18th International Toki Conference (ITC18)

Development of Physics and Technology of Stellarators/Heliotrons

"en route to DEMO"

Proceedings

Ceratopia Toki, Gifu, Japan, December 9 – 12, 2008

Organized by National Institute for Fusion Science

International Organizing Committee

O. Motojima(Japan, Chair), M. Abdou(USA), B. Blackwell(Australia),
D. Campbell(EU), J. Jacquinot(France), P. Kaw(India), T. Klinger(Germany),
G.S. Lee(Korea), J. Li(China), J. Sanchez(Spain), M. Tendler(Sweden),
M. Thumm(Germany), M. Zarnstorff(USA), T. Hino(Japan), S.Imagawa(Japan),
O. Kaneko(Japan), K. Kawahata(Japan), A. Komori(Japan), S. Matsuda(Japan),
K. Mima(Japan), O. Mitarai(Japan), T. Mutoh(Japan), N. Nakajima(Japan),
Y. Ogawa(Japan), K. Ohsawa(Japan), N. Ohyabu(Japan), A. Sagara(Japan),
F. Sano(Japan), M. Sasao(Japan), M. Sato(Japan), S. Sudo(Japan), H. Yamada(Japan),
N. Yoshida(Japan)

International Program Committee

Y. Ogawa(Japan, Chair), S. Kubo(Japan, Secretary), S. Bosch(Germany),
L. Kovrizhniykh(Russia), M. Kwon(Korea), F. Najmabadi(USA), M. Shats(Australia),
Dai-Kai Sze(USA), R. Wolf(Germany), B.N. Wan(China), A. Ando(Japan),
S. Imagawa(Japan), T. Imai(Japan), K. Kawahata(Japan), M. Kondo(Japan),
R. Kumazawa(Japan), O. Mitarai(Japan), T. Mizuuchi(Japan), S. Murakami(Japan),
T. Mutoh(Japan), N. Nakajima(Japan), N. Ohno(Japan), S. Okamura(Japan),
A. Sagara(Japan), H. Sakagami(Japan), T. Seki(Japan), T. Shimozuma(Japan),
M. Tanaka(Japan), K. Tobita(Japan), H. Yamada(Japan), H. Zushi(Japan)

Local Organizing Committee

T. Mutoh(Chair), T. Shimozuma(Scientific Secretary), S. Oi(Secretary), M. Emoto,
S. Hamaguchi, H. Igami, M. Ito, H. Kasahara, N. Kasuya, M. Kondo, S. Kubo,
R. Kumazawa, J. Miyazawa, Y. Nakamura, H. Nakane, M. Nishiura, K. Saito,
H. Sakagami, T. Seki, M. Skoric, T. Sugiyama, H. Takahashi, H. Tamura, M. Tanaka,
S. Toda, M. Tokitani, T. Tsuji, F. Tsutsumi, T. Uda, Y. Yoshimura, M. Yoshinuma

Preface

18th International Toki Conference (ITC18) was held in Toki (Japan) December 9-12 2008 organized by the National Institute for Fusion Science (NIFS). More than 150 experts in fusion research, especially in stellarator/heliotron research from Australia, Belgium, China, France, Germany, Hungary, India, Iran, Italy, Japan, Korea, Serbia, Spain, Sweden, Switzerland, and the United States of America gathered at the conference. The International Organizing Committee (IOC) chaired by O. Motojima, the International Program Committee (IPC) chaired by Y. Ogawa and the Local Organizing Committee (LOC) chaired by T. Mutoh have played the leading role in the elaboration of the scientific program of the conference. NIFS has organized the ITC as an annual meeting for fusion related sciences since its establishment in 1989. The IPC arranged 2 plenary talks, 1 review talk, 34 invited talks in addition to 109 contributed presentations including 6 oral talks.

Recent developments in the experimental, theoretical and technical research show the clear route to the realization of a stellarator/heliotron type demo fusion reactor. ITC18 was devoted to review the recent developments and to discuss the next steps forward to the demo reactor realization of stellarator/heliotron type. In the conference, recent experimental results from both tokamak and stellarator/heliotron devices are reviewed and the experimental and theoretical physics of plasma confinement in toroidal devices are also discussed and confirmed that the physical base of the fusion reactor is well developed. The development of steady state operation, heating, fueling, diverters, plasma wall interaction and wall materials, advanced diagnostics for reactor relevant plasma, blanket materials as well as super conducting magnets are discussed as inevitable key physics and technologies for the DEMO reactor.

Slides of all oral presentations as well as the proceedings are available at http://itc.nifs.ac.jp/. Extended papers of major contributions will be published in the special issue of Plasma and Fusion Research (http://www.jspf.or.jp/PFR/).

Chair of ITC-18 Local Organizing Committee

Takashi MUTOH

Contents

Invited Talks

Oral Talks

Poster Presentations 1

Poster Presentations 2

Invited Talk

I-01 - I-34

Proceedings of ITC18,2008

Wendelstein 7-X – a technology step towards Demo

Hans-Stephan Bosch and the Wendelstein 7-X Team
Max-Planck-Institut für Plasmaphysik, IPP-EURATOM Association,
D-17491 Greifswald, Germany

The Wendelstein 7-X stellarator, presently under construction in Greifswald, will be the first "fully-optimized" stellarator device which combines a quasi-symmetric magnetic field configuration with superconducting coils, a steady state exhaust concept, steady state heating at high power and a size sufficient to reach high nTτ-values. W7-X has been optimized numerically by J. Nührenberg et al., based on the concept of quasi-isodynamicity. Its key element is an optimized magnetic field configuration, generated by 50 non-planar superconducting coils. It is the mission of this project to demonstrate the reactor potential of the optimized stellarator line.

Most of the components have been fabricated already and four out of ten half-modules of the magnet system have been assembled already. This paper presents an overview of the status of construction and a summary of the future developments.

Keywords: Wendelstein 7-X, optimized stellarator, construction, assembly

1. Introduction

Wendelstein 7-X (W7-X), presently under construction in the IPP branch-institute in Greifswald, is a fully optimized stellarator. Its optimisation is based on the concept of quasi-isodynamicity [1].

The W7-X configuration has a five-fold symmetry and is described by a rotational transform $\iota/2\pi$ of about 1 ($0.72 < \iota/2\pi < 1.25$) with low shear (i.e. a small variation of $\iota/2\pi$ across the magnetic surfaces). The major radius of the plasma is 5.5 m, the effective (i.e. averaged) minor radius is 0.55 m, and the magnetic axis is helical.

W7-X will have to prove the properties predicted by the numerical optimization, i.e. confinement in the range of that observed in tokamaks of comparable size. Apart from this proof of the concept of numerically optimizing the stellarator magnetic configuration, a main goal of W7-X will be to demonstrate the suitability of optimized stellarators as a fusion power plant and to bring forward the technology towards "Demo". One key element that is still to be developed for a future fusion power plant, is steady state operation under reactor-relevant conditions, i.e. at high density and high power with suitable power and particle exhaust. To allow for steady-state operation (i.e. pulse lengths of 30 minutes- limited by the water cooling system), W7-X will apply a superconducting magnet system composed of 50 non-planar coils and 20 planar coils, an ECRH-system capable of delivering 10 MW for 30 minutes [2] and will also develop further the island divertor [3] and will address the plasma-wall interaction in long plasma pulses.

This paper will give an overview on the main components of W7-X and describe the status of device assembly.

author's e-mail: bosch@ipp.mpg.de

2. Main components of Wendelstein 7-X

Figure 1 shows a schematic overview of the basic device. It is clearly visible, that the plasma has a pentagon-shape. The device is therefore set-up from five identical modules. Each of those, however, is made out of two flip-symmetric half-modules, so that in fact the device is composed of 10 identical half-modules.

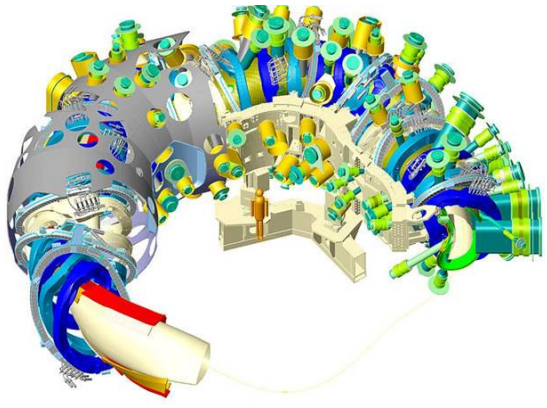

Fig.1 *Cutaway of a CAD drawing of W7-X showing the plasma and the divertor plates (lower left), the magnetic coils around the plasma vessel with inner support structure (upper right) and the Outer Vessel (upper left).*

2.1 Magnet system

The magnet system is made from 50 modular (non-planar) coils and 20 planar coils to allow for a

variation of the magnetic field configuration, a bus-bar system to connect these coils electrically with each other and with the power supplies (not visible in Fig. 1), a central support structure and a set of support elements fixing the coils to the central ring and supporting them against each other. The total cold mass of this magnet system will be 432 tons. According to the symmetry described before, each half-module is equipped with 5 non-planar coils of a different type and two planar coils (again different types).

The 50 non-planar coils that comprise the centerpiece of the magnet system have been manufactured by a German-Italian consortium of BNG and ASG [4]. For each coil 6 lengths of superconductor are wound as a double-layer with 18 turns each, i.e. 108 windings per coil. Very stringent tolerances on the

Fig.2 *Non-planar coil AAB54 (type 4) on a transport frame. Clearly visible are the Copper stripes on the coil casing and the cooling tubes. In the lower right part of the picture, the header area with the five interlayer joints and the two superconductor tail ends can be seen.*

geometric dimensions of the winding packages of less than 3 mm had to be kept. This leaves a margin for assembly tolerances of about the same order, i.e. 2 mm.

The six superconductor lengths in one coil are connected in series through low resistance joints which are also used to introduce the liquid He for the cooling of the superconductor. Figure 2 shows the non-planar coil AAB54. The insulation in the header region, i.e. at the exit of the layers from the winding pack and around the interlayer joints has proven to be an especially difficult area requiring extensive rework. Paschen tests, i.e. HV tests at different pressure levels, have proven to be a very effective tool for testing the quality of this insulation [5] and for unveiling problematic areas like small voids, areas of pure, unfilled resin or insufficient insulation of quench detection wires.

As of now, all 50 coils have been delivered. Thirtyeight of these coils have been tested individually at cryogenic temperatures in full-current operation and have proven the expected properties [6]. These cryogenic tests are being performed for all non-planar and planar coils at CEA in Saclay/France as part of the final acceptance test.

The 20 planar coils, supplied by Tesla in the UK, have casings that are made from two vertical rings and top and bottom plates bolted to them [7]. As of today, all coils have been delivered and nineteen of them have already successfully completed the cryogenic tests in Saclay.

To connect the coils with each other (seven groups of 10 identical coils in series) and with the current leads (which lead to the power supplies at ambient temperature), a superconducting bus-bar system is required which is being designed and manufactured by the research centre Jülich (FZJ, Germany) [8]. The same conductor is used as for the coils and the routing is done in a bifilar way to reduce error fields from the bus-bar. The design of the bus-bar system has been finished and manufacturing has started. The first 48 conductors (i.e. conductors for two modules) have been delivered, together with the corresponding supports (holders and clamps).

The connection between the power supply lines outside the cryostat (i.e. at ambient temperature and pressure) and the bus-bar system inside the cryostat (i.e. at about 4 K during operation and under vacuum) requires fourteen current leads that bridge the temperature and pressure transition. As the power supplies are located below the W7-X, these current leads are mounted in the bottom of the device and have the cold end at top, the warm end at the bottom and therefore require a special design. A design for such current leads, able to carry 20 kA each and using high temperature superconductor inserts, has been developed in collaboration with the research centre Karlsruhe, Germany (FZK). Development and manufacturing of these current leads is now under way at FZK.

The seven groups of superconducting coils are powered by seven power supplies manufactured by the Swiss company ABB. Each power supply delivers a direct current of up to 20 kA at a voltage of up to 30 V. This system has undergone the final acceptance tests and

has proven that the output currents can be stabilized to the required accuracy of 2×10^{-3}[9]. The quench detection system, developed in co-operation with FZK, will consist of almost 400 quench detection units that check permanently the differential voltages between double-layers of all coils and between all sectors within the bus-bar system [10]. The prototype units have been tested successfully and series production will start soon.

2.2 Magnet Support System

The 50 non-planar and the 20 planar coils will all be fixed to a central support ring, which is manufactured by ENSA in Spain. This structure is composed of 10 identical, welded segments which are bolted together to form a pentagon-shaped ring of 5 modules. Cast extensions for holding the coils are welded to this ring [11]. As the coils have to be kept in their precise position, also during cool down and operation, the half-modules of this central ring have to be machined to a high accuracy of a few tenth of a millimeter. The continuous refinement of structural calculations resulted in different modifications to the detailed design of the structure, thereby delaying the manufacturing. The first six segments of the support ring (see Fig. 3) have been delivered up to the end of 2008.

Fig.3 *Final work on the first segment of the central support ring (1/10 of the full ring). The picture shows also the cast extensions and the contact surfaces for fixing the coils.*

Ten cryo-supports will carry the support structure and provide a thermal barrier between the cold magnet system and the machine base. Fabrication of these cryo-supports is under way, their delivery is expected early in 2009.

Each coil is fixed radially to the ring in two points, where the magnetic forces (up to 4 MN) and bending moments (up to 350 MNmm) have to be taken up. A bolted solution using long and slender Inconel bolts (which better absorb deformations) and sleeves to limit the loss of pre-load during cooling down to 4K has been developed to keep the coils firmly in place [12].

Also in toroidal direction, the non-planar coils have to be supported against each other with a system that can take up the forces and moments and keep the positions of the coils to a high accuracy. Therefore, on the inner side of the coil ring, where the coils are very close to each other, so-called Narrow Support Elements (NSE, see [13]) and on the outboard side the so-called Lateral Support Elements (LSE) are foreseen. These LSE will be a rigid connection made of half-boxes which are welded between the neighboring coils. The crucial issue with this design is the proper control of welding shrinkage and distortion which is essential to comply with the magnet system assembly tolerances. An extensive test program has been carried out to optimize the layout and welding procedures for these elements.

The situation is different for the NSE because on the inboard side of the coils accessibility restrictions do not allow any welded or bolted solution. Based on refined FEM calculations which revealed that contact forces up to 1.5 MN and sliding distances of up to 5 mm with a tilting up to 1 degree have to be expected during magnet energization, a sliding pad solution has been selected. After an extensive test program, Al-bronze with a MoS_2 coating has been selected as the material for thick, low friction pads which are fixed in a pad holder to one coil, sliding on the support block of the other coil. To validate the basic design and to identify the best pad coating, a wide test program has been undertaken, including full scale friction tests at room temperature and cryo-vacuum tests at 77 K to test the full scale mock-ups in a more representative environment. A design similar to the one for the NSE is used for the so-called Planar Supports which support the planar coils against the non-planar coils.

2.3 Cryostat

The cryostat, providing the thermal insulation of the cold magnet system described before, consists of the plasma vessel, the outer vessel, the ports [14] and the thermal insulation of these components towards the cold mass.

The vacuum vessel of W7-X has been manufactured by the German company Deggendorfer Werft und Eisenbau (MAN DWE). A major issue in the design of this vacuum vessel was the optimization of its shape to allow for maximum space for the plasma and to simultaneously keep sufficient clearance to the coils. These requirements resulted in a tolerance of only $\pm$ 3 mm for the shape of the plasma vessel. The full plasma vessel is made up from 200 rings that are connected by welding. Each ring is made of four segments that are

exactly bent to the exact shape and 20 rings form one half-module. Water pipes on the outer side of this vessel allow a bake-out at 150^0 C and temperature control during plasma operation. All ten sectors of the plasma vessel have been delivered before the end of 2005.

The outer vessel, also manufactured by MAN DWE, is produced in 5 modules; each of them is divided in two (upper and lower) half-shells to allow assembly of the magnet module (plasma vessel module with 14 coils, support structure and the corresponding bus-bars) inside the outer vessel module. The outer vessel will have about 524 openings for ports, supply lines, manholes and diagnostic feedthroughs. The first four modules have been finished (see Fig. 4), the last one will be finished in spring of 2009.

Fig.4 *First module of the outer vessel during fabrication at Deggendorf.*

W7-X will be equipped with 254 ports of different shape and dimensions (up to 40 x 100 cm^2 rectangular ports) to allow access from the outside to the plasma vessel. 112 of these ports will be used for plasma diagnostics, 17 for heating systems, 25 for gas inlet and for pumping the vacuum vessel and 100 for supply of in-vessel components. All ports have been received from the Swiss company Romabau Gerinox.

Efficient operation of the superconducting coils requires very effective reduction of heat conduction as well as shielding of radiation from the room temperature components of the cryostat. The thermal insulation of W7-X (also manufactured and assembled by MAN DWE) is composed of two components, a multi-layer insulation of aluminized Kapton-foils (20 layers) and a rigid thermal shield. As the space limitations for this insulation between the vacuum vessel and the non-planar coils require again a tolerance of ± 2 mm, a novel technique has been developed. The thermal shield is now fabricated from glass-fiber panels with embedded Cu-meshes to improve heat transport within the panel. Cooling pipes on the outboard side of the panels are connected to the Cu meshes through Cu-braids. For each half-module of the vacuum vessel, eight panels of the shield with attached multi-layer insulation are fabricated. They are assembled on the plasma vessel in parallel with the threading of the coils. Recently, assembly of the thermal insulation in the outer vessel of the first module has started. For the outer vessel and the ports the shields are made from copper and brass.

2.4 In-vessel components

At the plasma edge, i.e. outside the closed flux surfaces, the magnetic configuration of W7-X forms a m=5 island structure to be used as an island divertor to control the power and particle exhaust from W7-X [14]. According to the field structure described above, also the divertor will have a five-fold symmetry, i.e. it will be composed of 10 units, five on top and five on the bottom. The full system of the in-vessel components includes several plasma-facing elements as well as cryo pumps and correction coils to modify the extent and location of the islands on the target plates. This system has been designed for steady-state operation at the full ECRH-heating power of 10 MW and for 10 s pulses of 15 MW NBI heating power [3].

For the plasma-facing components three different areas have to be distinguished which require different technical solutions respectively. The divertor target (with a horizontal and a smaller vertical target plate) will experience high power fluxes of up to 10 MW/m^2. The baffle shielding the neutrals in the target chamber versus the main plasma chamber, experiences lower stationary power fluxes of only up to 0.5 MW/m^2. The wall protection, covering the rest of the plasma vessel surface, is subjected to neutral particles and plasma radiation and is designed for power fluxes of 0.2 MW/m^2.

3. Assembly of Wendelstein 7-X

3.1 assembly sequence

Assembly of the stellarator comprises two major stages, i.e. pre-assembly of the five magnet modules and assembly of the torus. A detailed description of this sequence can be found in Ref. [16].

In the first step of the pre-assembly, which is performed roughly in parallel on two assembly rigs (Ia and Ib) for two half-modules, the seven coils are strung over the vacuum vessel which is covered with the thermal insulation. Then all coils are fixed to one segment of the central support ring and the inter-coil support elements are mounted (see Fig. 5). In the next step, on assembly rig II, the two corresponding half-modules are joined, i.e. the support ring segments are bolted and the plasma vessel half-modules are welded. Then the bus-bar holders are mounted and the conductors are fitted and cut to length.

On assembly rig III, the first part of the cryo-pipes (for helium cooling of the coils and the support structure) is assembled, then the bus-bar system, including the bus-bar joints, and the second part of the cryo-pipes, thereby completing a magnet module.

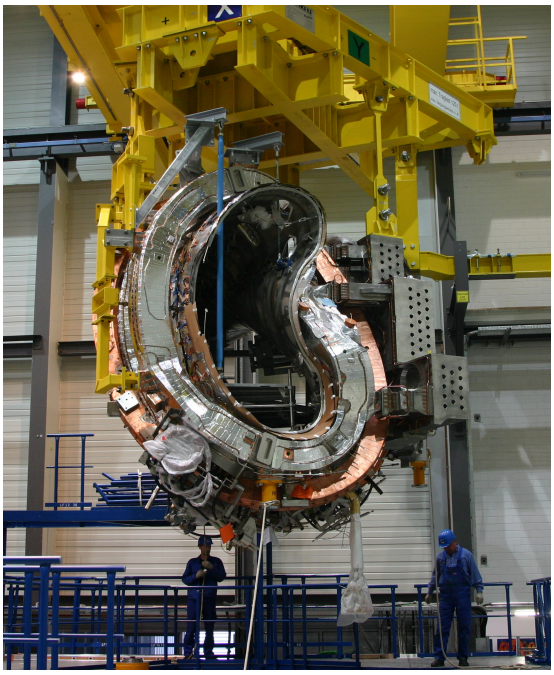

Fig.5 *First magnet half-module being transported to assembly rig II (February 2008). The central support ring with its step flange for connection of the two half-modules is visible on the right as well as the extensions for coil fixation.*

Final assembly starts with the insertion of the magnet module into a lower shell module of the outer vessel (first equipped with the thermal insulation and with three plasma vessel supports per module) which is then closed with the upper shell. At this stage, the module is located at its final place on the machine base. Then the installation of the ports can start. After a final measurement of the magnet modules geometry and after final adjustment of their position, the modules are welded to finally form a torus. As soon as two adjacent modules are connected, the last ports, i.e. those at the module separation plane, are inserted and then the current leads and the in-vessel components can be assembled.

After the completion of the torus, the peripheral components (heating structures, ex-vessel diagnostics, water-cooling and other media supplies) can be installed.

3.2 general assembly works

In parallel to these main steps of the device assembly, a large effort is required for the preparation of the components delivered from industry, mainly with regards to cleaning, instrumentation, and measuring and final rework of the outer geometry.

For all the assembly steps described before, the assembly technology had to be developed, including special tooling for the handling of the coils, for handling and stiffening of the outer vessel shells and for the assembly of ports and of in-vessel components. A very special task was the development of welding procedures because for welding of the Lateral Support Elements or for the connection of vessel modules, large weld seams (up to 25 mm thick) have to be performed while weld seam shrinking has to be kept to a minimum due to the very strict tolerances (in the order of a few mm) of the stellarator.

The small tolerances required for the geometry, especially of the magnet system, also requires an extensive measuring program, involving 3D measurement techniques like laser trackers, photogrammetry and laser scanning [17]. Geometry control is an essential task in this project, as Wendelstein 7-X is a very complex but also compact device with very narrow installation space for all its components. Clearance of all these components during cooling down and especially under magnetic loads has to be assured, but is difficult to reach as the device is very compact and the distances in many cases are not far beyond the tolerances. Therefore an extensive effort has been put into measuring the as-built geometry of the major components and into the collision control of these components under the different load conditions. This process already enters into the design of components like the cryo-piping or the thermal insulation of outer vessel and ports, often requiring several iterations or – as mentioned above – the rework on components ready for assembly, like for coil casings or ports [18].

3.2 status of assembly

At present, three out of the five modules are in the assembly process. On the first of these modules, which is presently on assembly rig III, the first lots of the cryo-pipes are being mounted. Due to the narrow installation space, mentioned above, design of these pipes requires several iteration cycles of design and collision control, making this process even more time-consuming than expected. Figure 6 illustrates the narrow assembly space with a CAD-model of the cebtral support ring with the bus-bars and the cryo-pipes. The second module on assembly rig II and the third one (still in two half-modules on rigs Ia and Ib) are assembled on a routine basis.

In late spring of 2009 the first module will be put into the lower shell of the outer vessel and in fall of 2009, assembly of the first ports is scheduled to start.

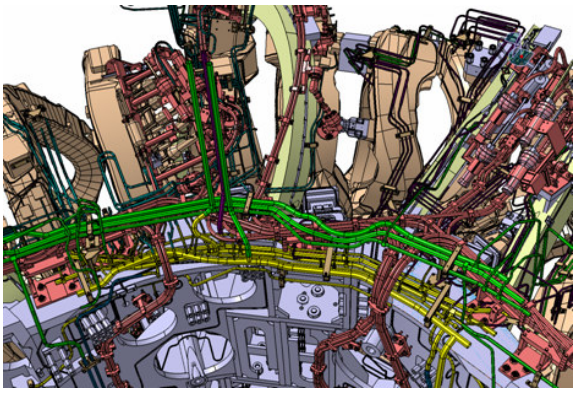

Fig.6 CAD-view of the central support ring with some coils and bus-bars (brown) and cryo-pipes (yellow, green and black), illustrating the very tight assembly space inside the cryostat.

There are still many assembly steps ahead, which have been developed, but have not yet been performed. Therefore the schedule bears still some uncertainty for the technical risks, especially in these new processes. With these considerations in mind, a full review of the assembly process has been performed in 2007 which resulted in an integrated assembly schedule incorporating several measures to minimize technical and schedule risks, e.g. only 245 out of the 299 ports foreseen initially, will be installed, additional assembly equipment will be used to enhance the parallelization of assembly work and many assembly steps will be brought forward into the component preparation.

Another important decision was that, for the first operation phase, the steady state divertor described above will not yet be installed. Instead, a Test Divertor Unit (TDU) with inertially cooled target plates will be installed [3]. All other in-vessel components described above, will be installed from the beginning, but in the first operation phase will not be water-cooled.

Based on a risk assessment of all assembly steps, time buffers for the technical risk were included in the schedule, summing up to more than a year on the critical path. Also the funding required for these times was included in the projects planning.

4. Summary

While the timely delivery of the super-conducting coils for W7-X is no longer critical, other components like the cryo-piping, parts of the bus-bar system, thermal insulation of outer vessel and ports, parts of the in-vessel components and the current leads (feedthroughs) still require stringent attention as their delivery might become time-critical. The project has implemented counter measures to decrease the schedule risks.

Assembly at present runs according to the schedule planned in 2007 and the first milestones have been kept. The current delays in design, fabrication and assembly of the cryo-pipes can be countered by some reorganization of other assembly steps, but the assembly schedule requires strict attention and continuous consideration.

As there are still some assembly processes to be developed in further detail (assembly of some special ports and of some in-vessel components), it has to be considered that at least some of the time buffers mentioned above, will have to be used. But still the project schedule foresees the start of commissioning of Wendelstein 7-X in May 2014.

References

[1] J. Nührenberg, *et al.*, Trans. Fusion Techn. **27**, 71 (1995).
[2] V. Erckmann *et al.*, *Radio Frequency Power in Plasmas*, (AIP, Melville, NY, 2005) p. 246.
[3] R. Stadler *et al.*, this conference.
[4] C. Sborchia *et al.*, IEEE Trans. Appl. Superconductivity **16**, 848 (2006).
[5] H. Scheller ***et al.***, IEEE Trans. Appl. Superconductivity **16**, 759 (2006).
[6] J. Baldzuhn, IEEE Trans. Appl. Superconductivity **18**, 509 (2008).
[7] H. Viebke *et al.*, Fusion Eng. Design **75-79**, 201 (2005).
[8] M. Sauer *et al.*, Fusion Eng. Design **82**, 1460 (2007).
[9] F. Füllenbach *et al.,* Fusion Eng. Design **82**, 1391 (2007).
[10] D. Birush *et al.,* Fusion Eng. Design **82**, 1400 (2007).
[11] A. Benito *et al.*, Fusion Eng. Design **82**, 1579 (2007).
[12] A. Dudek *et al.*, Fusion Eng. Design **82**, 1500 (2007).
[13] J. Reich *et al.*, 26th IEEE Symposium on Fusion Eng., Albuquerque, 2007
[14] A. Cardella *et al.*, Fusion Eng. Design **82**, 1911 (2007).
[15] H. Renner *et al.*, Fusion Science Techn. **46**, 318 (2004).
[16] L. Wegener *et al.*, 25th Symp. Fusion Techn., Rostock 2008, to be published
[17] T. Bräuer *et al.*, 25th Symp. Fusion Techn., Rostock, 2008, to be published.
[18] C. Baylard *et al.*, 25th Symp. Fusion Techn., Rostock, 2008, to be published.

Proceedings of ITC18, 2008

Configuration Control Experiment in Heliotron J

H. Okada, S. Kobayashi, K. Nagasaki, T. Mizuuchi, S. Yamamoto, G. Motojima[a], S. Watanabe[b], K. Mukai[b], S. Mihara[b], Y. Kowada[b], K. Hosaka[b], A. Matsuyama[b], Y. Nakamura[b], K. Hanatani, N. Nishino[c], Y. Nakashima[d], K. Nagaoka[a], T. Mutoh[a], Y. Suzuki[a], M. Yokoyama[a], A.C. Fernández[e], Á,A, Cappa[e], S. Konoshima, K. Kondo[b] and F. Sano.

Institute of Advanced Energy of Kyoto University, Uji 611-0011, Japan

[a] National Institute for Fusion Science,, Toki 509-5292, Japan

[b] Graduate School of Energy Science, Kyoto University, Uji 611-0011, Japan

[c] Graduate School of Engineering, Hiroshima University, Higashi-Hiroshima 739-8527, Japan

[d] Plasma Research Center. University of Tsukuba, Tsukuba 305-8577, Japan

[e]Laboratorio Nacional de Fusión, EURATOM-CIEMAT, Madrid 28040, Spain

Heliotron J is a flexible configuration device to explore a new concept optimization for the helical-axis heliotron configuration. The field ripple along the toroidal direction, which is called 'bumpiness' is a key component for the improvement of the particle confinement. From the fast ions generated by the ICRF minority heating, the high bumpy configuration is most favorable and the fast ions of about 30 keV are observed. The toroidal current control is also important for the Heliotron J field configuration. Using the combination of the change of the bumpiness and the deposition position, the toroidal current can be controlled by about 7 kA. The bumpy field dependence on the global confinement is investigated for ECH and NBI plasmas. The confinement in the high and medium bumpy configurations is better than that in the low bumpy configuration. The difference of the bumpy dependence for the ECH and NBI plasmas is possibly caused by the improved fast-ion confinement for the NBI plasmas in the high bumpy configuration.

Keywords: helical-axis heliotron, bumpiness control, fast ion confinement, non-inductive current, improved confinement

1. Inroduction

The optimization of the field configuration is very important for helical systems since there is large ripple loss in the collisionless regime for simple stellarator/heliotron. There are various advanced concepts proposed for this purpose, for example, quasi-omnigeneity [1], quasi-helical symmetry [2], quasi-axisymmetry [3] and so on. Heliotron J belongs to a quasi-omnigeneous concept among them, and is a low-shear helical-axis heliotron (major radius of the torus R_0 = 1.2 m, minor radius of the plasma a = 0.1-0.2 m, magnetic field on the axis $B_0 \leq$ 1.5 T, helical-coil pole number L = 1, pitch number M = 4) [4, 5, 6]. Using controllable five sets of coil systems, Helitoron J realizes a wide range of configurations by changing the coil-current ratios.

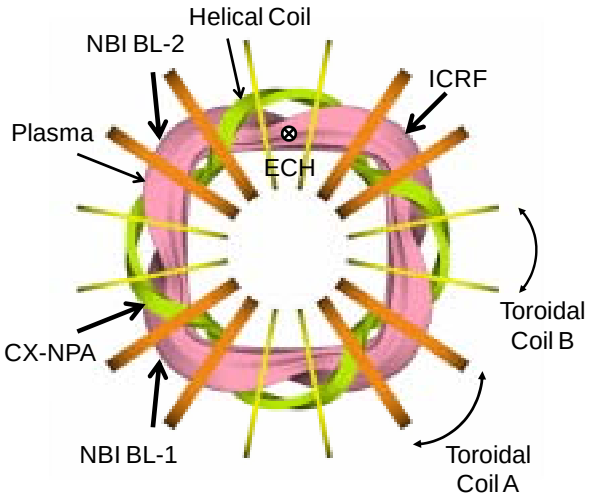

Fig. 1 Top view of Helitoron J. The helical coil and the two types of toroidal coils are illustrated. The positions of the three heating systems (ECH, NBI and ICRF) are also indicated.

The top view of the helical coil and the plasma is shown in Fig. 1. Three heating systems, which are the neutral beam injection (NBI), the ion cyclotron range of frequency (ICRF) and the electron cyclotron (EC) heating devices are installed in Heliotron J. A plasma is generated by using vertically-injected ECH, which is the second harmonic (70 GHz) X-mode and has power of 450 kW. The direction of the toroidal field is clockwise in Fig.1 for the normal operation. The two tangential-injection NB devices are installed; whose injection power and

author's e-mail: okada@iae.kyoto-u.ac.jp

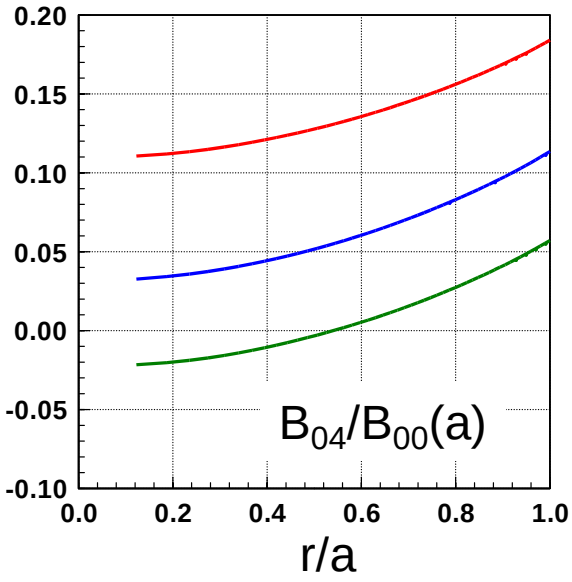

Fig. 2 The profiles of the bumpy ripples for the three bumpy configurations.

acceleration voltage are 700 kW and 30 kV for each unit. Two loop antennas for the ICRF heating are installed on the low field side of the corner section (upper-right corner in Fig. 1). The frequency of the ICRF is 19 - 23.2 MHz and the injection power is 400 kW for each antenna.

In this paper, the results of the control experiments by changing the bumpiness in the field configuration, which is one of the Fourier components in the Boozer coordinates, are described. The bumpy field component is a field ripple along the toroidal direction. This component is generated by the two sets of toroidal coils and the helical coil. If the current ratio of the toroidal coil A to the toroidal coil B (See Fig. 1) is unity, the sign of the bumpy component is equal to that of the helical ripple. Both the value of the bumpiness and the radial profile is effective for the improvement of the particle confinement in this magnetic configuration. The effectiveness of the bumpy component is investigated for (i) high energy ion confinement using ICRF minority heating, (ii) a non-inductive current in ECH plasmas and (iii) energy confinement for ECH or NBI plasmas. The configurations used in this study are as follows; the bumpiness (B_{04}/B_{00}, where B_{04} is the bumpy component and B_{00} is the averaged magnetic field strength) are 0.15 (high), 0.06 (medium) and 0.01 (low) at the normalized radius of 0.67, respectively. The profiles of the bumpy components are shown in Fig. 2. The other field components such as the iota, the toroidicity and the helicity are kept constant among the three cases. The plasma volume, the major radius and the minor radius are also constant.

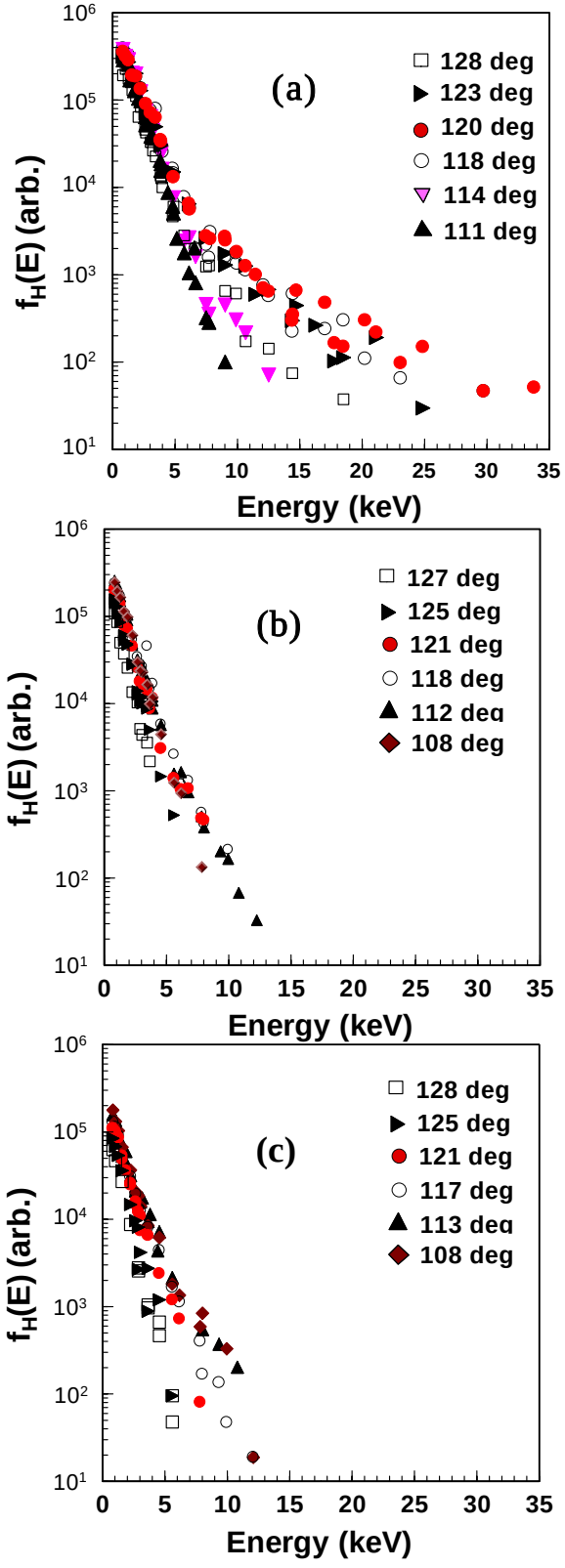

Fig. 3 Minority hydrogen spectra for various pitch angles in the high bumpy (a), the medium bumpy (b) and the low bumpy (c) configurations. By changing the toroidal and poloidal angles of the CX-NPA, the energy spectra are measured. The line of sight of the CX-NPA crosses the magnetic axis for all cases.

2. Fast Ion Confinement

High energy ions up to 30 keV were investigated by charge-exchange neutral particle analyzer (CX-NPA) for both NBI ions [7] and accelerated ions by ICRF. The former mainly includes passing particles and the latter, trapped particles. Here, the accelerated ions by ICRF are discussed. For keeping the ECH resonance position constant, the magnetic field strength is adjusted to be constant at the ECH injection position. Therefore, the magnetic field strength in the corner section where the ICRF antenna is installed is changed for each bumpy configuration, slightly. The frequency of the injected ICRF wave is adjusted so that the resonance layer is positioned near the magnetic axis: 23.2 MHz for the high bumpiness and 19 MHz for the medium and low bumpy cases. An ICRF pulse of 23.2 MHz or 19 MHz is injected into an ECH target plasma where $T_i(0)$ = 0.2 keV, $T_e(0)$ = 0.8 keV and $\overline{n}_e$ = 0.4 x 10^{19} m^{-3}. The ICRF injection power is in the range from 250 kW to 300 kW and The ECH power is about 300 kW. The minority heating mode is selected to generate fast ions with deuterium as the majority species and hydrogen as the minority species.

A CX-NPA is equipped to analyze the energetic ions, which has the ability of scanning in the toroidal and poloidal directions in order to research ions in the wide area of velocity space. It can be scanned in the toroidal direction from -10 to +18 deg and in the poloidal direction from -3 to 10 deg in order to observe charge-exchange neutrals in various pitch angles. The origin is the normal direction to the torus for the toroidal angle and the horizontal direction for the poloidal angle. The poloidal direction of the CX-NPA for measurement of each pitch angle or the field configuration is determined so that the line of sight of the CX-NPA crosses the magnetic axis.

Figure 3 shows measured minority hydrogen energy spectra for various pitch angles by changing the toroidal angle of the CX-NPA for the three bumpy cases mentioned in Section 1. In the high bumpy case (a), the ion flux is observed up to 34 keV at the pitch angle of 120 deg. Such high energy particles cannot be observed in the medium and low bumpy configurations. The highest tail is observed at about 30 deg from the perpendicular direction to the magnetic field. Toward 90 deg, the tail component decreases as shown in Fig. 3(a). The tail decreases from the angle of 120 deg as the pitch angle increases, since there is no acceleration mechanism in the parallel direction.

The high energy ion confinement is improved by increasing bumpiness. However, the measurable real space and velocity space is limited for the CX-NPA. The results of the analysis using Monte Carlo method roughly agree with the experimental results including pitch angle distribution of fast ions. The energy spectrum in the high bumpiness shows the largest high energy tail as a whole in the calculation results. The bumpiness can control the loss cone structure in this range of experiment [9].

3. Non-inductive Current

A non-inductive toroidal current plays an important role for Heliotron J since it could affect the transport through the field structure change whereas no current is required to form the confinement field. From this point of view, a non-inductive current is investigated in Heliotron J plasmas [10]. The electron cyclotron (EC) wave is injected vertically from the top port. However, the magnetic axis is not horizontal in the injection point of the EC wave. Therefore, the refractive index in the parallel direction, $n_{//}$ becomes finite. In this experiment, $n_{//}$ is 0.44. In Heliotron J plasmas, a bootstrap current, an EC driven current and a beam driven current by NBI heating are considered as the non-inductive toroidal current. Here, the BS current and the EC driven current are discussed for ECH plasmas. The BS current and the EC driven current are separated by the procedure that the EC driven current is estimated from the addition of the measured currents in the normal magnetic field and the reversed magnetic field and the BS current is from the subtraction since only the BS current changes its direction by field reversal. The BS current flows according to the field geometry and plasma parameters. The bootstrap current ($\leq$ 2 kA) flows in the co-direction in most cases as shown in Fig. 4. Here, the magnetic field strength at the axis is determined so that ω_0/ω is 0.5, where ω_0 is the cyclotron frequency at the axis and ω is the injected EC wave frequency. The current is largest in

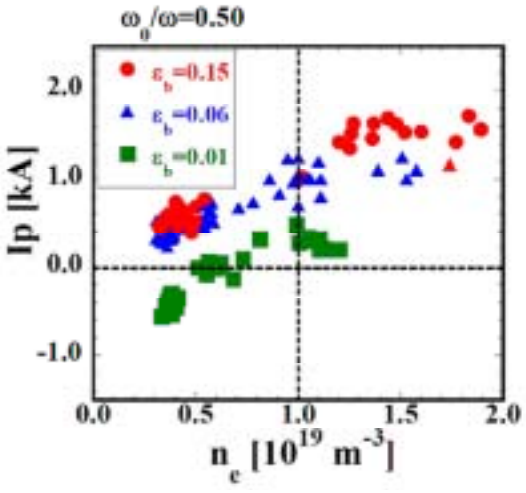

Fig. 4 Density dependence of the measured toroidal current in the three bumpy cases (in Ref. [10]). The injection condition of ω_0/ω is 0.5.

the high bumpiness and lowest in the low bumpiness. However, in the low density region for the low bumpiness,

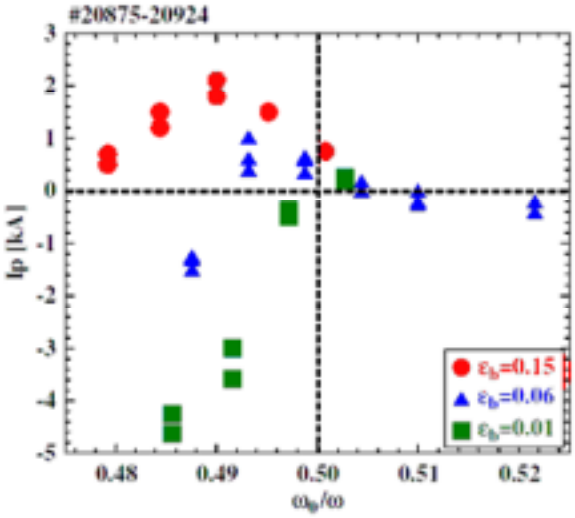

Fig. 5 The dependence of the toroidal current on the deposition position for the three bumpy cases (in Ref. [10]). The line-averaged electron density is 0.5 $\times 10^{19}$ m^{-3}.

the flow direction is reversed. The EC driven current in this condition (ω_0/ω = 0.5) is very small, then, the toroidal current is mostly a BS current in Fig. 4. The negative BS current in the low bumpy case can be explained by the neo-classical theory taking account of the possible radial electric field.

The magnitude of the EC driven current depends on the position of the EC power deposition since the effectiveness depends on the accelerated electron trajectory and its confinement. When the deposition is changed, the orbit of the energetic electron accelerated by

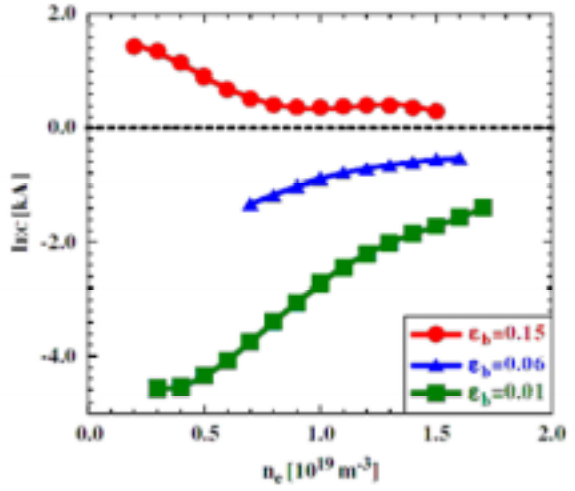

Fig. 6 Density dependence of the EC driven current at ω_0/ω = 0.49 for the three bumpy cases (in Ref. [10]).

the EC wave is considered to be changed. For example, the energetic electron in the transit orbit moves to the trapped orbit by changing acceleration position. At that time, the toroidal current component generated via Fisch-Boozer effect [11] will be changed to the opposite component generated via Ohkawa effect [12]. By changing the field strength, the toroidal current dependence on the deposition position is measured for the three bumpy cases. Near ω_0/ω = 0.49, a large toroidal current is observed for all cases as shown in Fig. 5. It is noted that the current direction can be altered by changing the bumpiness.

The EC driven current at ω_0/ω = 0.49 is estimated separately as shown in Fig. 6. A positive EC driven current is generated in the high bumpiness, while a negative EC driven current is generated in the medium and the low bumpiness. The maximum EC driven current of -4.6 kA has been observed for the low bumpy configuration. The maximum current drive figure of merit is $n_e R I_p / P_{EC}$ = 8.4 × 10^{16} AW^{-1} m^{-2} (I_p = 3.2 kA, n_e = 0.7 × 10^{19} $m^{-3}$and P_{EC} = 320 kW) [10]. Here we take the injected ECH power as P_{EC}. This current drive efficiency is lower than that predicted by the linear theory. The driving mechanism for the both directions in EC current drive, which is the Fisch-Boozer effect and the Ohkawa effect, must be considered.

4. Energy Confinement

The energy confinement for ECH or NBI plasma is also studied for the three bumpy configurations. Figure 7

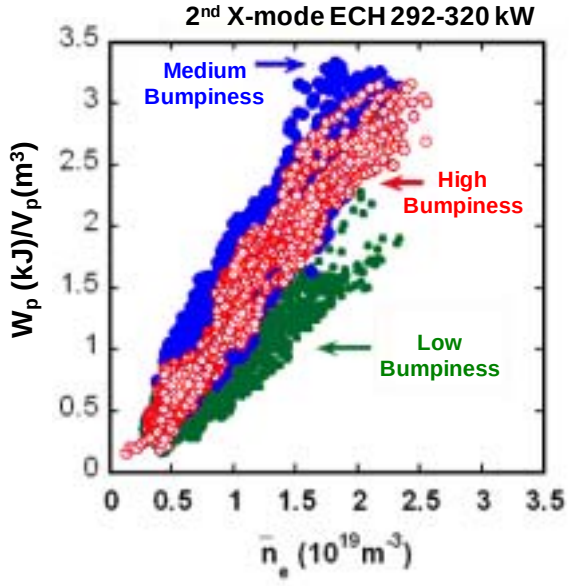

Fig. 7 Volume normalized plasma stored energy as a function of density in the three bumpy cases for ECH plasmas under the almost constant ECH power.

shows the volume normalized plasma stored energy attained as a function of density. The energy confinement is good for the medium and the high bumpy cases. The medium case is slightly better than the high bumpy case [13, 14].

For the study of NBI plasmas, one counter-injected NB unit is used since no transition phenomena to H-mode have been observed in counter injection, then the study is focused on the L-mode plasma [15, 16]. Figure 8 shows the plasma stored energy as a function of the absorbed NBI power in the three bumpy configurations for the constant density condition of 2×10^{19} m^{-3} [17]. The absorption power is estimated by using a birth-point calculation code (HFREYA), an orbit tracing code (MCNBI) and a Fokker-Planck code (FIT) [18]. The difference of the beam absorption ratio among the three

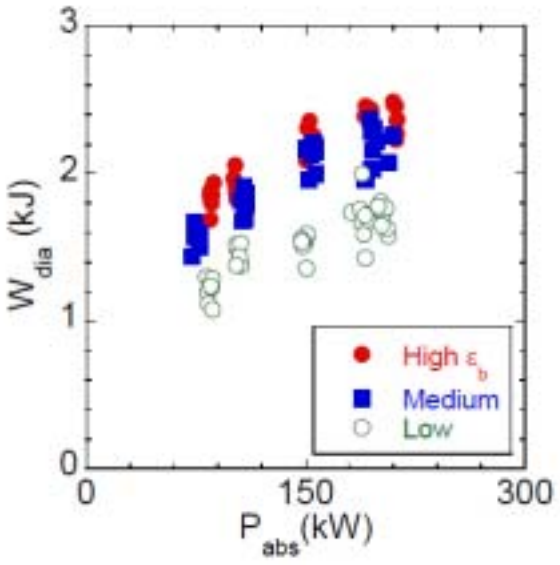

Fig. 8 Plasma stored energy as a function of absorbed NBI power for three bumpy cases. The neutral beam is injected in the counter direction under the line-averaged electron density of 2×10^{19} m^{-3}.

bumpy configurations is several percent for the density range from 1×10^{19} m^{-3} to 3×10^{19} m^{-3}. The plasma stored energy in the high and the medium bumpy cases is larger than that in the low bumpy case. The high bumpy case is best for the attained stored energy although the difference of the stored energy between the high and medium bumpy cases is not so large.

In Fig. 9, the relation between the experimental energy confinement time and the international stellarator scaling law (ISS95) is shown [17]. The beam component in the stored energy estimated from the Fokker-Planck analysis, which is less than 7%, is subtracted from the obtained stored energy. The enhancement factor of energy confinement time for the ISS95 is about 1.8, 1.7 and 1.4 in the high, the medium and the low bumpy

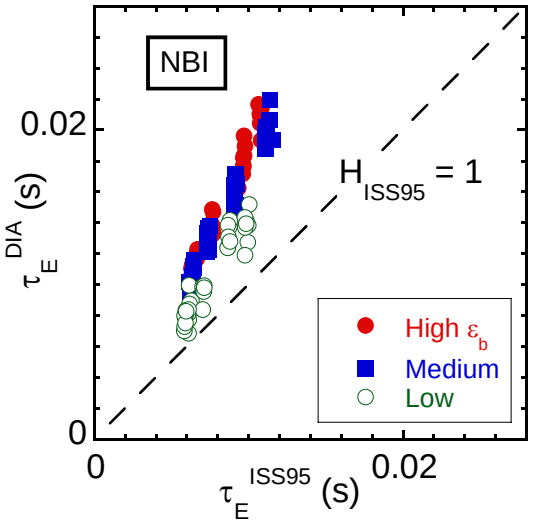

Fig. 9 The relation between the experimental energy confinement time and the international stellarator scaling law (ISS95) for the NBI plasma in the three bumpy configurations.

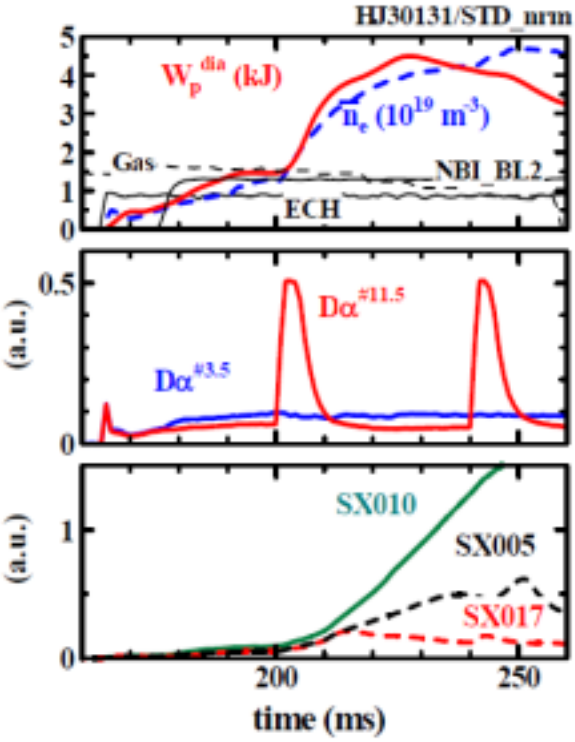

Fig. 10 The time traces of plasma parameters due to the SMBI fueling during the NBI and EC heating.

configurations, respectively. These results indicate the better confinement of the high and medium bumpy configurations. However, the medium bumpiness was most favorable for ECH plasmas in the experiment of the same density range. This difference is under investigation.

For the extension of the plasma operation region and the improvement of the confinement, the supersonic molecular beam injection (SMBI) system has been

installed [19]. This technique has been developed by L. Yao et al. [20, 21, and 22]. The SMBI fueling is performed for the plasma heated by NBI (0.6 MW) and EC wave (0.35 MW). The time traces of the line-averaged electron density ($\overline{n}_e$), the plasma stored energy (W_p), H_α, the signals of the three channels of an SX-array are shown with two pulses of SMBI in Fig. 10. After the first SMBI, the density and the stored energy are increased. The increment of the stored energy by the first pulse is large and it reaches 4.5 kJ. This value is about 50% higher than the maximum value attained by the normal gas-puff fueling for the same heating condition in Heliotron J. The plasma stored energy attained by using SMBI is extended from those by the gas-puff, which is limited at about 3 kJ for the similar EC and NBI heated plasmas. The SMBI fueling is considered to be a useful method for the optimization of the fueling for the Heliotron J plasmas.

5. Summary

The bumpy field control experiment aiming the improvement of the plasma confinement in Heliotron J has been performed.

The fast ion confinement is expected to be deeply connected to the bumpy control in Heliotron J magnetic configuration. By using ICRF minority heating, the fast ion formation and confinement is investigated in the low density condition of 0.4×10^{19} m^{-3}. The fast ion flux measured by the CX-NPA is largest in the high bumpy configuration. The flux near 30 keV is observed only in the high bumpy configuration. The high bumpy configuration is favorable for the fast-ion formation and confinement.

The non-inductive current is generated as a BS current and an EC driven current by the obliquely injected EC wave. Both the BS current and the EC driven current depend on the field configuration and plasma parameters. By changing the bumpy component, the non-inductive current at $\omega_0/\omega = 0.50$, which is mainly a BS current is changed by about 1 kA. Using the combination of the change of the bumpiness and the deposition position, the toroidal current can be controlled by about 7 kA.

For the global energy confinement, the bumpy dependence is also observed. In ECH plasmas, the medium and high bumpy configurations are better than the low bumpy configuration and the medium bumpy case is slightly better than the medium bumpy case. However, the dependence in the NBI plasmas is different from the ECH case. The high bumpy case is most favorable for the energy confinement although the difference between the high and medium cases is small. In addition to the improvement of the bulk electron confinement due to the bumpy control, it is possible that the better fast ion confinement in the high bumpy configuration improves the heating efficiency during slowing-down process of fast ions. The SMBI fueling has been performed and the stored energy of 4.5 kJ is attained. The optimization of the fueling is in progress.

Acknowledgements

This work is performed with the support and under the auspices of the Collaboration Program of the Laboratory for Complex Energy Processes, Institute of Advanced Energy, Kyoto University and the National Institute for Fusion Science (NIFS) Collaborative Research Program of NIFS04KUHL005, NIFS04KUHL002, NIFS04KUHL003, NIFS04KUHL006, NIFS06KUHL007, NIFS06KUHL009, NIFS06KUHL010, NIFS07KUHL011, NIFS07KUHL014, NIFS07KUHL015, NIFS07KUHL016, NIFS08KUHL020 and NIFS08KUHL022, the Formation of International Network for Scientific Collaborations as well as the Grant-in-Aid for Sci. Research.

References

[1] S. Gori *et al*., in Theory of Fusion Plasmas (Proc. Joint Varenna-Lausanne Int. Workshop, Varenna, 1996), Editrice Compositori, Bologna, 335 (1997).
[2] J. Nührenberg and R. Zille, Phys. Lett. A **129**, 113 (1988).
[3] J. Nührenberg *et al*., in Theory of Fusion Plasmas (Proc. Joint Varenna-Lausanne Int. Workshop, Varenna, 1994), Editrice Compositori, Bologna, 3 (1994).
[4] F. Sano *et al*., J. Plasma and Fusion Res. Series **3**, 26 (2000).
[5] M. Wakatani *et al*., Nucl. Fusion **40**, 569 (2000).
[6] T. Obiki *et al*., Nucl. Fusion **41**, 833 (2001).
[7] S. Kobayashi *et al*., IAEA-CN-116/EX/P4-41 (2004)
[8] H. Okada *et al*., Fusion Sci. Technol. **50**, 287 (2006).
[9] H. Okada *et al*., Nucl. Fusion **47**, 1346 (2007).
[10] G. Motojima *et al*., Nucl. Fusion **47**, 1045 (2007).
[11] N.J. Fisch and A.H. Boozer, Phys. Rev. Lett. **45**, 720 (1980).
[12] T. Ohkawa, General Atomics Report GA-A13837 (1976).
[13] T. Mizuuchi *et al*., Fusion Sci. Tech. **50**, 352 (2006).
[14] F. Sano *et al*., IAEA-CN-149/EX/5-5Ra (2006).
[15] S. Kobayashi *et al*., in 11th IAEA TM on H-mode Phys. Trans. Barriers (Tsukuba, 2007).
[16] T. Mizuuchi *et al*., Joint Conf. "17th Int. Toki Conf. on Phys. Flows & Turbulence in Plasmas" and "16th Int. Stellarator/Heliotron Workshop" (Toki, 2007) O-02.
[17] S. Kobayashi *et al*., in this conference.
[18] S. Murakami *et al*., Trans. Fusion Tech. **27**, 259 (1995).
[19] T. Mizuuchi *et al.,* in this conference.
[20] L. Yao, in "New Developments in Nuclear Fusion Research" (Nova Sci. Pub., 2006) pp.61-87.
[21] L. Yao *et al.*, Proc. 20th EPS Conf. on Controlled Fusion and Plasma Phys. (Lisbon, 1993) vol. **17C(I)**, p303.
[22] L. Yao *et al*., Nucl. Fusion **47**, 1399 (2007).

Proceedings of ITC18,2008

Recent study of the high performance confinement and the high beta plasmas on the Large Helical Devices

K.Y. Watanabe, A. Komori, H. Yamada, K. Kawahata, T. Mutoh, N. Ohyabu, O. Kaneko, S. Imagawa, Y. Nagayama, T. Shimozuma, K. Ida, T. Mito, K. Nagaoka, R. Sakamoto, S. Ohdachi, R. Kumazawa, H. Funaba, Y. Narushima, S. Sakakibara, Y. Suzuki, T. Morisaki, S. Sudo, O. Motojima and LHD experimental Group

Author affiliations should be centered 10-point italic type National Institute for Fusion Science,322-6 Oroshi-cho, Toki 509-5292, Japan

Some topics of the recent LHD (Large Helical Device) experimental results related with the extension of the operational regime to the fusion reactor are reviewed. LHD experiments can demonstrate the high ion temperature discharge with confinement improvement similar to the internal transport barrier. Super high density and high pressure plasmas with IDB (internal diffusion barriers) are obtained. The central electron density exceeds $1.1x10^{21}m^{-3}$ and IDB discharges enable good confinement regime to be extended to the high density operation regime. 5.1% volume averaged beta plasma is transiently produced by pellet fuelling and 5% plasma is maintained in quasi-steady state by gas-puff fuelling. By using an IDB, high central beta plasma comparable with standard high beta operation has been achieved. On the steady state operation, the pulse time with high input power operation is extended by the replacement of the divertor plate with good heat conductivity. The future subjects on LHD experiments to reactor are also discussed.

Keywords: Large Helical Device, recent progress, high ion temperature, internal transport barrier, super high density, internal diffusion barrier, high beta, resistive interchange, steady state, high heat load

1. Introduction

The LHD (large helical device) is the largest super-conducting helical machine in the world [1]. The experiment started at the end of the March 1998. Up to Dec. 5th 2008, 90426 discharges were done. As the typical plasma parameters, the plasma major radius is around 3.7m, the plasma volume is around $30m^3$. The maximum operational magnetic field strength is 3T. The central rotational transform is less than 0.4 and the edge rotational transform is more than 1.5. At the core, the magnetic shear is week and at the edge, it is strong.

In this paper, we will show some topics of the recent LHD experimental results related with the extension of the operational regime to the fusion reactor. In the table 1, the recent achievement in LHD experiments and the designed targets are shown. On the central temperature, 5.2 keV at n_e~$1.6x10^{19}m^{-3}$ for ion and 10keV for electron are achieved. On the beta value, which is a key parameter to construct the economical fusion reactor, the volume averaged beta reaches 5.1% transiently. Steady state discharges with the 490kW input power for over 54minutes, 1.1MW for 800s are maintained. The maximum operational density exceeds $10^{21}m^{-3}$ in the center. The available heating power is increasing. Now more than 25MW heating power is available by NBI, ECH and ICH. As the heating power increases, the plasma stored energy also increases. Now it exceeds 1.6GJ, which is comparable to the big tokamaks. These extension of the operational plasma parameters enable the systematic study near the fusion reactor plasmas.

This paper is organized as follows. At first, the characteristics of the high ion temperature discharges with

	Achieved	Designed Target
Central Ion Temperature	5.2keV ($1.6x10^{19}m^{-3}$)	10keV ($2x10^{19}m^{-3}$)
Central Electron Temperature	10keV ($0.5x10^{19}m^{-3}$)	10keV ($2x10^{19}m^{-3}$)
Central Density	$1.1x10^{21}m^{-3}$ (0.3keV) $1x10^{20}m^{-3}$ (1.5keV)	$1x10^{20}m^{-3}$ (1keV)
Volume averaged β	5.1% (0.425T)	> 5% (1-2T)
Long pulse operation with high heating power	54m28s (490kW) 800s (1100kW)	1hour (3,000kW)
Fusion Triple product	$5x10^{19}kemV^{-3}s$ $[n_{e0}\tau_E T_{e0}]$	$5x10^{19}kemV^{-3}s$ $[<n_e>\tau_E<T_e>]$

Table.1 Achieved plasma parameters (up to Dec. 2008) and the designed target.

author's e-mail:jkiyowata@LHD.nifs.ac.jp

confinement improvement like ITB (Internal transport barrier) are shown. Next the high density operation with IDB (internal diffusion barrier) is mentioned. And the high beta plasma and its characteristics are shown. The steady state operation with high input power and high heat load is also mentioned. Finally we summarize the recent LHD experimental results and discuss the future subjects on LHD experiments to reactor.

2. Recent experimental results

2.1 High ion temperature discharges

In the high ion temperature (high-T_i) operation, a key issue is the updated NBI heating systems. At present, LHD has 4 beam lines of NBI system, which consists of 3 tangential beam lines and 1 perpendicular beam lines. Tangential beams are characterized high energy with negative-ion sources. Then, electrons are mainly heated. Perpendicular beam lines are updated recently [2]. It is characterized as low energy ion sources, and it is effective to heat ions. Moreover it works as a diagnostic beam for CXRS.

The productions of high-T_i plasmas with low Z_{eff} have been performed by high power NB heating in LHD with the inwardly-shifted configurations with 3.575m < R_{ax} < 3.7m [3]. The inward shifted configuration has a good particle confinement. A typical wave form of high-T_i discharge is shown in Fig. 1. The time evolution of the core ion and electron temperature (T_i and T_e), the heating power and the line averaged electron density are shown in Fig.1(a) and(b). At the beginning of the discharge, the target plasma was started by ECH and sequentially connected to the low power NB heating phase with P-NBI (positive NBI) alone. After superposition of N-NBIs (negative-NBIs), the central T_i and T_e significantly increases. Finally, T_i exceeds T_e (high-T_i phase). The typical density at high- T_i phase is 1~2x$10^{19}$$m^{-3}$. High-$T_i$

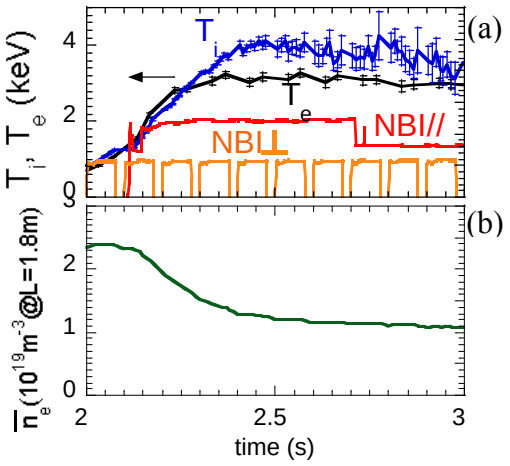

Fig.1 The time evolution of the core ion and electron temperature, the heating power and the line averaged electron density are shown in the high-T_i discharge.

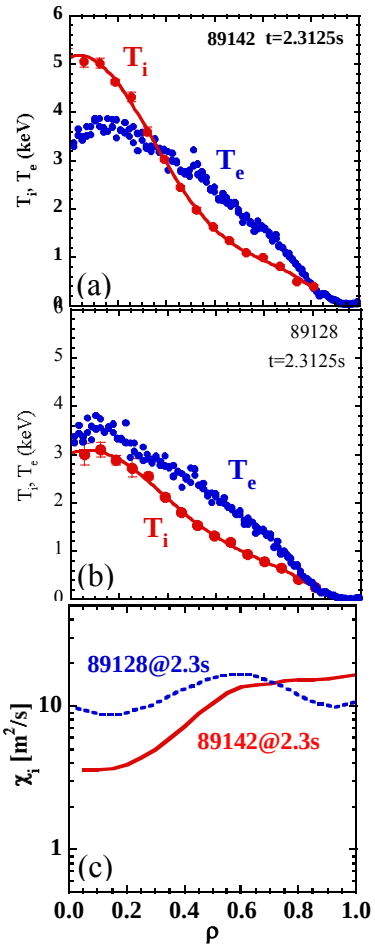

Fig.2 The typical radial profile of the T_i and T_e at the high-T_i phase (a) and the normal discharges, L-mode, (b). (c) The radial profile of the ion thermal conductivities for L-mode and high-T_i phase.

phase is maintained for 200 ms, which is almost several times longer than the energy confinement time.

Figure 2(a) shows the typical radial profile of the T_i and T_e at the high-T_i phase, where n_e ~ 1.6x$10^{19}$$m^{-3}$. The temperature profile at the high-T_i phase is characterized as the higher T_i comparison with T_e at the center and the much steeper T_i gradient than T_e at the core, which suggests the achievement of the improved confinement with ITB formation. On the contrary, the radial temperature profile in the normal discharges (L-mode) is shown in Fig.2(b). It should be noted that ITB formation is typically observed for the larger ion heating power per the ion density comparing with the normal discharges. Figure 2(c) shows the radial profile of the ion thermal conductivities for L-mode and high-T_i phase. In the core region, the thermal transport is improved in the high-T_i phase. It should be noted that the radial electric field is negative in the ITB region according to the preliminary measurement of the electric potential by the heavy ion beam probe, which is consistent with the theoretical prediction based on the neoclassical ambipolar particle flux condition. The reduction of the anomalous part of the ion thermal

conductivity is considered more dominant on the ITB formation comparing with that of neoclassical one. The mechanism of ITB structure formation has not been understood well yet. The understanding is one of our future subjects.

2.2. High density operation

In LHD, super high density and high pressure plasmas are obtained with IDB, which is the distinguished feature because this kind of feature has not been observed in tokamaks [4,5]. Super high density is obtained just after the multi-pellet injection And the high central pressure is obtained during the density decay phase. Maximum central density exceeds 10^{21}m^{-3}, and the maximum central pressure reaches 150kPa.

In the IDB region, the temperature profile is relatively flat and the IDB plasma is not accompanied by an improvement in thermal transport, while the temperature gradient is established in the small density region outside of IDB. The IDB plasmas is characterized as the large Sharanov shift, and the large stochastic region is predicted in the large electron temperature gradient region as shown in Fig.3 according to HINT [6] calculation. However, the large degradation of the thermal transport is not observed in the predicted stochastic region.

As an advantage of the IDB discharges, it enable the plasmas to extend the good confinement to the higher density operation regime. Figure 4 shows the dependence of the stored energy on the line averaged density for the almost same heating power. In Fig.4, the open squares, the blue circles and the red circles correspond to the discharges fuelled by the gas-puff, the pellets without IDB formation and the pellets with IDB formation. In the gas-puff operations, the confinement performance degrades as the density increases. On the contrary, in the pellet operations, the good confinement performance region extends to the higher density region comparing with the gas-puff

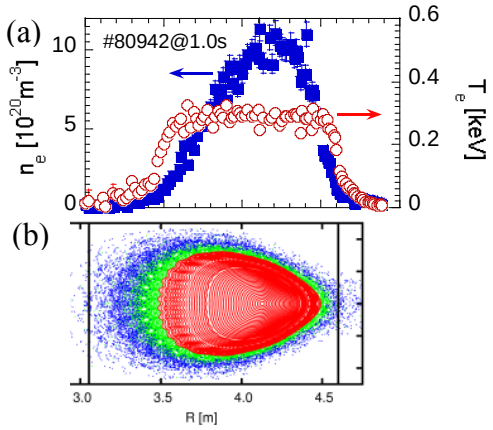

Fig.3 (a) Density and electron temperature profile of the IDB plasma with the highest central density. (b) The predicted magnetic surface structure for IDB plasma by HINT code.

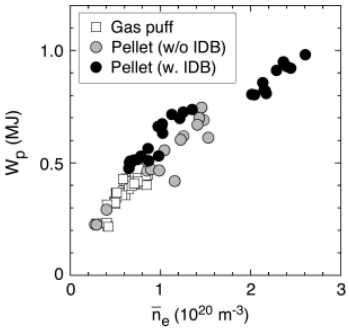

Fig.4 The plasma stored energy as the function of density for the discharges with various density profiles and by various fueling methods.

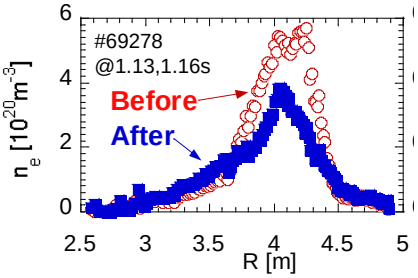

Fig.5 The density profiles just before and after a CDC event.

operations.

Next we will discuss the operational limit of the IDB plasmas. In IDB plasmas with high central pressure, the core density collapse (CDC) events are often observed [7]. Figure 5 shows the density profiles just before and after a CDC event. At the CDC event, core density is abruptly expelled. The electron temperature profiles little changes before and after a CDC event. The typical time of the collapse is ~100μs, It is much shorter than that of the collapse due to the MHD instabilities in LHD, which is more than 5 ms [8, 9]. And in the collapse due to the MHD instabilities, the changes of the electron temperature profile is significant. Here it should be noted that the temperature gradient is much larger than the density gradient in the core at the conventional MHD driven collapse. Sometimes MHD events are observed around CDC events. However, the driving mechanism is not clear yet. And another limitation of IDB formation is by lack of central heating power. High density plasma inhibit NB penetration to the core. Then the density rise by pellet is limited.

2.3. High beta discharges

The high beta regime has been extended to the volume averaged diamagnetic beta <β> of 5% mainly by optimizing the magnetic configuration and the increase in the NBI heating power [9]. Figure 7 shows the waveform of the <β> ~ 5% plasma, which corresponds to the maximum beta value. In Fig.7(a), the averaged beta value and the NBI heating power are shown and the magnetic fluctuations resonated with the edge region in Fig.7(b)-(d). Operational magnetic field strength is 0.425T. The plasma

is produced and maintained by mainly tangential NBI. Density is controlled by gas-puffing. High beta plasma near the 5% is maintained without disruption. In this discharge, the duration time near the 5% is limited for 40 times energy confinement time due to the termination of a NBI unit. If we can keep the power, the 5% beta plasma would be maintained in steady state. On the properties of the low mode number MHD activities in high beta region, only resonating mode width peripheral surfaces appear, and the core resonant MHD mode is not observed. Figure 8 shows the beta profile at <β> = 5%. Though some fine structures like a flattening and asymmetry in the profile appear, the effects on a global confinement look small. According to theoretical analysis for low mode number ideal and/or resistive MHD instability, only the instabilities with narrow radial mode width are predicted.

Next we discuss the effect of MHD instabilities on the confinement [10]. Figure 8(a) shows the characteristics of the local confinement properties at the edge normalized gyro-Bohm anomalous transport model. It should noticed that ISS95 empirical confinement scaling has the similar dependence of Gyro-Bohm anomalous transport model.

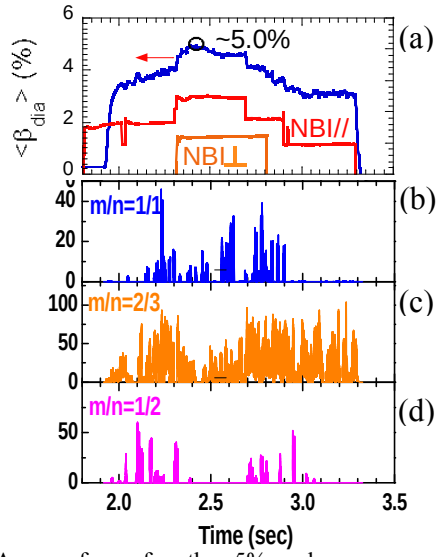

Fig.6 A waveform for the 5% volume averaged beta discharges. (a) beta value and the heating power by NBI. (b), (c) and (d) are the magnetic fluctuation with m/n=1/1, 2/3 and 1/2 mode numbers, respectively. Here m and n are the poloidal and toroidal mode numbers.

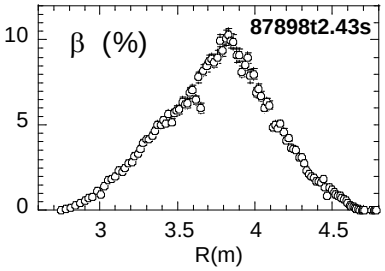

Fig.7 The beta profile evaluated by the electron density and the electron temperature, where Z_{eff}=1 and T_i=T_e are assumed.

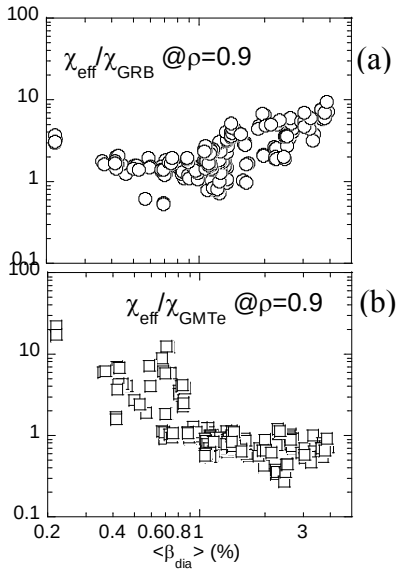

Fig.8 The normalized peripheral thermal transport coefficients as the function of the beta value (a) by the gyro-Bohm anomalous model and (b) the resistive interchange mode driven turbulence.

The local confinement performance at the edge gradually degrade as beta increases. Figure 8(b) shows the peripheral transport properties normalized by a resistive interchange mode driven turbulence proposed by Dr. Carreras et al [11]. In high beta region, the beta dependence of experiment data is well reproduced by that, which suggests the resistive interchange mode make a important roll on the local transport properties in edge region. In the resistive MHD instability, the magnetic Reynolds number, S is a key parameter and the anomalous transport driven by it would decrease as S increases. The S is proportional to the cubic of the magnetic field strength under a scaling. If we can obtain 4% beta discharges in 1T, the S is expected 10 times larger than the present 5% beta plasmas. To confirm the influence of the resistive interchange mode turbulence driven transport by the extension of the magnetic field, we need to extend the high beta regime to the operations with the higher magnetic field.

Recently another high beta plasma production is established by using an IDB scenario with the multiple pellet injections [7]. As the magnetic field strength decreases, CDC effect in IDB discharges on confinement

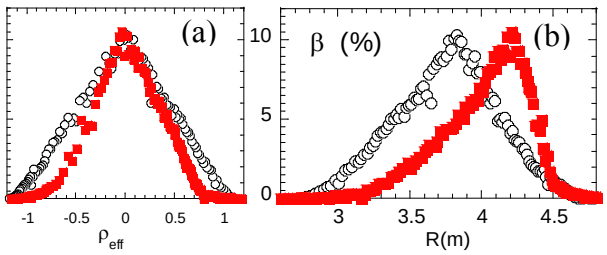

Fig.9 The beta profile as the function of the normalized minor radius (a) and the major radius (b) for the IDB discharge (close squares) and the standard high beta discharge (open circles).

becomes small. Then in low field operation with IDB plasmas, high central beta plasma comparable with standard high beta operation has been achieved. The beta profiles are shown as a function of the normalized minor radius in Fig.9(a) and of the major radius in Fig.9(b). In Fig.9, the closed circles denotes the beta profiles produced by IDB scenario and the open circles by the standard high beta scenario, which is exactly same with Fig.7. $\beta_0 \sim 10\%$ is transiently achieved under $<\beta> \sim 3\%$, which is comparable to that of the standard high beta operation with $<\beta> \sim 5\%$. The beta profiles by the IDB scenario is characterized as the steeper gradient of beta in the core comparison with that in the edge and the larger Shafranov shift. The production of the peaked pressure profile has the advantage for the MHD stability because of the large Shafranov shift and the steep pressure gradient and for the high fusion power output because it is proportional to the square of beta value not to the beta value itself.

2.4. Steady state operation

In LHD long pulse discharges, the extension of the duration time of discharges with the high heating power after the achievement of the world record of the largest heating energy (integrating heating power). The long pulse discharges with the high heating power is considered useful for a progress of the investigation on the impurity transport, the plasma-wall interaction and so on, characteristic time scales of which are long, because the discharges with the higher heating power have closer performance to the reactor. Recently the pulse time with high input power operation is extended by the replacement of the divertor plate and a model of the upper limit of the duration time of the long pulse discharges against the heating power based on the accumulated experimental data [12].

The duration times of the discharges, τ_{pl} are shown as a function of the heating power, P_H in Fig.10. The open circles corresponds to the experimental data before the replacement of the improved divertor plates with good heat conductivity, and the closed squares to ones after the replacement. The duration time data of the discharges before the replacement of the divertor plates were obtained for the wide range of heating power, which suggests the existence of a limitation of τ_{pl}. The envelope of the maximum of τ_{pl} is approximately expressed by the solid curve shown in Fig.10 and by the following equation:

$$\tau_{pl} \propto \log\left(P_H/\left(P_H - P_c\right)\right), \qquad (1)$$

which corresponds to empirical scaling low of the τ_{pl} against the heating power. In eq.(1), P_c is a constant. In Fig.10, the dashed line corresponds to the contour of the integrated heating power. From the solid line and the

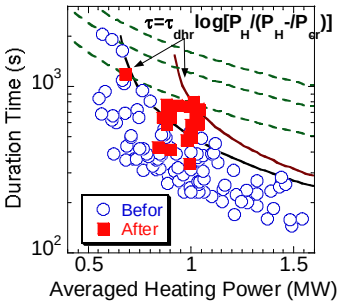

Fig.10 The duration times of the discharges, τ_{pl} as a function of the heating power, P_H. The open circles corresponds to the data before the replacement of the improved divertor plates, and the closed squares to ones after the replacement.

dashed lines, the larger integrated heating power discharges are easily obtained in the lower input power discharges for LHD. The empirical scaling low of the τ_{pl} is consistent with the following model. The upper limit of the temperature of the divertor plate, $T_{div\text{-}cr}$ is assumed to keep the discharges stationary for long time. And the temperature of the divertor plate is determined by its time constant of the heat removal, τ_{dhr}, where the saturated temperature is assumed proportional to heating power, P_H and the τ_{dhr}. The strong correlation between the temperature of the divertor plate and the penetration of the high Z impurity to the balk plasma from the divertor plate is observed in the LHD long pulse discharges up to date [12]. Under the above assumption, the predicted duration times of the discharges is expressed as

$$\tau_{pl-pre} = \tau_{dhr} \log\left(P_H/\left(P_H - P_{cr}\right)\right). \qquad (2)$$

Here $P_{cr} = T_{div-cr}/C\tau_{dhr}$ and C is a constant depending on the magnetic configurations, the plasma parameters and the heating methods. Eq.(2) coincides the empirical scaling based on the LHD experiments and it suggested the improvement of the heat conductivity of the divertor plate is the most important critical issue to extend the duration time of the discharges with the high heating power. As shown by the black squares in Fig.12, the duration time of the discharges with high heating power is extended after the replacement of the improved divertor plates with good heat conductivity: from 400s to 800s for the discharges with 1MW heating power, where the high central electron temperature with 1.5keV at n_e = $0.6\text{x}10^{19}\text{m}^{-3}$ is maintained. From Fig.10 and Eq.(2), it is speculated that the replacement of the divertor plate improve the capability of the heat removal by ~1.4 times as the time constant of the heat removal.

3. Summary and discussion

In this paper, the recent progress of the LHD experimental results related with the extension of the operational regime to the fusion reactor is reviewed.

LHD experiments can demonstrate the high ion

temperature discharge with confinement improvement similar to Internal Transport Barrier (ITB), which is characterized as the higher T_i comparison with T_e at the center and the much steeper T_i gradient than T_e at the core. In the LHD, super high density and high pressure plasmas with internal diffusion barriers are obtained, which is the distinguished feature because this kind of feature has not been observed in tokamaks. The central electron density exceeds $1.1x10^{21}m^{-3}$ and IDB discharges enable good confinement regime to be extended to the high density operation regime more than several $10^{20}m^{-3}$. 5.1% volume averaged beta plasma is transiently produced by pellet fuelling and 5% plasma is maintained in quasi-steady state by gas-puff fuelling. Up to 5% beta, disruptive phenomena is not observed. However, the gradual degradation of the energy confinement is observed with beta value, which would result in the enhancement of the resistive interchange mode turbulence due to the small magnetic Reynolds discharges. By using an IDB, high central beta plasma comparable with standard high beta operation has been achieved. On the steady state operation, the pulse time with high input power operation is extended by the replacement of the divertor plate with good heat conductivity: from 400s to 800s for the discharges with 1.1MW heating power. A model of the upper limit of the duration time of the long pulse discharges against the heating power based on the accumulated experimental data is established. According to the model, the heating energy would extend to 2000s when the heating power is 0.9MW.

Finally we discuss the subjects on LHD experiments to the reactor. At present, for LHD type reactor, 2 operation scenarios are considered; high temperature scenario and high density scenario. High temperature scenario is a conventional scenario. In principle, LHD target parameters as shown in table I were designed based on the high temperature scenario. As the subjects to high temperature scenario, the following items are picked up. (1) reduction of neoclassical transport in low collisional regime. In order to demonstrate it, the achievement of the positive electric field in the low collisional regime, the so-called "electron root in the n-regime" and the improvement of the ion thermal transport are necessary. Moreover, the high performance confinement comparing with the ISS95 scaling in low collisionality and high beta regime under low beam pressure should be demonstrated because the present high beta discharges are obtained only in the relatively high collisionality regime and under the non-negligible beam pressure, and their confinement properties are poorer with the higher collisionality, which is equivalent to the higher magnetic Reynolds number. In high beta regime around 5%, the beam ratio to diamagnetic energy is estimated ~30%. LHD high beta discharges are operated at the relatively low density and low magnetic field, and the tangential high energy particles have good confinement properties even in low magnetic field. That is the why the beam contribution is fairly large in LHD high beta discharges. The effect on MHD instabilities and equilibrium should be investigated. After discovery of the super high density operation with IDB plasmas, the high density scenario is proposed and its capabilities have been investigated [4]. As the subjects to high density scenario, the following items are picked up; (1) development of particle fueling method in the core with high density and relatively high temperature repeatedly. (2) understandings of CDC mechanism to avoid it. (3) study of transport property in stochastic regime. As the subjects related with steady state operation, the following items are picked up; (1) study of impurity transport. (2) development of suppression method of heat load to divertor. These subjects are common for the above 2 scenario.

References

[1] A. Iiyoshi *et al*., Nucl. Fusion **39**, 1245 (1999).
[2] Y. Takeiri *et al*., Plasma Fusion Res. **3**, S1001 (2008).
[3] K. Nagaoka *et al*., 22nd IAEA Conf. on Fusion Energy (Geneva, 2008) EX/8-2Ra.
[4] N. Ohyabu *et al*., 21st IAEA Conf. on Fusion Energy (Chengdu, 2006) EX/8-1.
[5] R. Sakamoto *et al*., 22nd IAEA Conf. on Fusion Energy (Geneva, 2008) EX/8-1Ra.
[6] K. Harafuji, T. Hayashi and T. Sato, J. Comput. Phys. 81, 169 (1989)
[7] S. Ohdachi *et al*., 22nd IAEA Conf. on Fusion Energy (Geneva, 2008) EX/8-1Rb.
[8] S. Ohdachi *et al*., 21st IAEA Conf. on Fusion Energy (Chengdu, 2006) EX/P8-15.
[9] S. Sakakibara *et al*., 21st IAEA Conf. on Fusion Energy (Chengdu, 2006) EX/7-5.
[10] H. Funaba *et al*., Plasma Fusion Res. **3**, 022 (2008).
[11] B.A. Carreras and P.H. Diamond, Phys. Fluids B 1, 1011 (1989).
[12] R. Kumazawa *et al*., 22nd IAEA Conf. on Fusion Energy (Geneva, 2008) EX/P6-29.
[13] O. Mitarai *et al*., 22nd IAEA Conf. on Fusion Energy (Geneva, 2008) FT/P3-19.

Proceedings of ITC18, 2008

Recent experiments towards to the steady-state operation in the EAST and HT-7 superconducting tokamaks

Baonian Wan for the EAST and HT-7 teams and collaborators
Institute of Plasma Physics, Chinese Academy of Sciences, Hefei, China

Abstact

The first plasma has been successfully obtained just after EAST engineering construction and followed by achievement of diverted plasma configuration in the second campaign under the full metal wall condition. To support the long pulse diverted plasma discharges, new capabilities including the fully actively water cooled in-vessel components, current drive and heating powers, diagnostics, real-time plasma control algorithm were developed. These developments were primarily validated in recent experimental campaign, such as realization of RTEFIT/ISOFLUX control algorithm, LHCD long pulse discharges over 20 seconds, etc. Recent experiments in HT-7 focused on long pulse discharges under different scenarios. The long pulse discharges up to 400s renews the records in HT-7 after a series of system modification.

Key words: superconducting tokamak, long pulse discharge, lower hybrid current drive

1. Introduction

EAST (Experimental Advanced Superconducting Tokamak) was completed its engineering construction and achieved the first plasma in 2006[1,2]. First divertor plasma in EAST was obtained in the second campaign in 2007. As first full superconducting tomakak with highly shaped plasma configuration, EAST is aimed to the high performance plasma and relevant technologies under steady state condition. To meet these requirements, EAST has the actively cooled plasma facing components (PFCs) and is equipped with lower hybrid current drive (LHCD) and ion cyclotron resonant heating (ICRH) systems. It could address a number of issues regarding the technology of steady-state divertor control and physics of long pulse operation with non-inductive current drive.

In last few years, HT-7 experiments were strongly oriented to support the EAST project both physically and technically[3], such as long pulse discharges, high performance plasma investigation, etc. Experience and experiments from the HT-7 become one important part of the EAST basis and certainly speeds up the EAST procedure. This paper will report the main progress of machine modification and operation on EAST and long pulse experiments on HT-7.

2. System Development

The long pulse high performance operation of a tokamak requires specific in-vessel structures and PFCs, which should be capable to handle the particle and heat fluxes in a variety of operation scenarios under steady-state condition. The in-vessel structure on EAST is a complicated integration of multi-systems as shown in Fig.1. They are composed of the fully actively water cooled PFCs and supporting structures, a full set of magnetic inductive sensors for machine operation and plasma control, the divertor cryopump, the actively water cooled internal coils for vertical

author's e-mail: bnwan@ipp.ac.cn

stabilization control, divertor probe arrays, baking system and thermal coupler etc. The system of the actively cooled PFC is a key element in construction of the new in-vessel structure. Fig.2 shows the EAST in-vessel structure together with ICRF antenna and LHCD launcher after full construction. The in-vessel geometry is designed as top–bottom symmetry to accommodate both double null or single null divertor configuration.

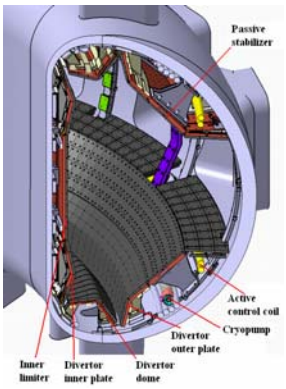

Fig.1 Elevation view of EAST in-vessel structure

Fig.2 Picture of in-vessel together with the ICRF antenna and LHCD launcher

Present PFCs structure can handle a peak heat flux up to 3.6MW/m^2 on the divertor plates and 0.5MW/m^2 on other plates. Bolted tiles affixed to an actively cooled heat sink are employed in the initial PFCs engineering. All plasma facing surface are made by one kind of multi-element doped graphite materials[**4**]. Such a structure with 2 t/h water mass flow rate for inner target, outer target and dome can maintain plasma facing surface temperature around 800℃ under peak heat load up to 3.6MW/m^2 according to the thermo-hydraulic analysis. Each of the upper and lower divertor structures consist of three high heat flux targets: inner, outer and private baffle (dome) plates. The vertical targets and dome form a “V” shape. Two gaps between inner, outer target and dome were provided with total 180m^3/s gas conductance for particle and impurity exhaust by cryopump, which was installed behind first wall and diverter plates. All PFCs were divided into 16 modules in toroidal direction for easy maintenance and modification. Two movable molybdenum limiters have been installed, which allow radial movement from 2.26m to 2.42m. In-vessel coils close to plasma with fast power supplies are utilized for vertical stabilization, which are also shown in Fig.1. The coils have been actively water cooled and can be operated at a current up to 20kA/turn under steady-state condition.

EAST vacuum chamber has double layer structure and can be baked up to 250℃ by high pressure hot nitrogen gas. The PFCs can be baked up to 350℃ also by hot nitrogen gas flowing in the cooling lines of the heat sinks. Other components including the 4 DC glow discharge anodes and 2 RF conditioning antenna were installed for wall conditioning. The RF conditioning is used normally for boronization and wall cleaning. The thermal couplers are attached on the chamber and port

extension walls and embed in the graphite titles of the liner, limiter and divertor for wall conditioning and also plasma discharges.

All magnetic sensors are newly manufactured and installed in vacuum chamber as a part of the integration of whole in-vessel components. They provide sufficient information for machine operation, plasma control and physics analysis. Two Langmuir probe and mach probe arrays were integrated on the specific divertor and dome modules. They were made by graphite rode and cooled through thermal conducting to the heat sink of the module, which is actively water-cooled. The probes were installed both in top and bottom diverter plates and dome respectively. The individual probe tips can be easily configured as triplet probe array along the divertor plates with a poloidal resolution of 2cm. The mach probe has 4 tips, which are oriented for toroidal and poloidal velocity measurements.

An advanced x-ray imaging crystal spectrometer (XCS) in collaboration with PPPL and NFRI has been installed at the end of the main pumping duct for ion and electron temperatures measurements[5]. There is a single channel laser interferometer with the vertical sight line at R = 1.9 m, which provide a line integrated density for density feedback control. Two visible CCD camera look at plasma in tangential sight line to monitor plasma discharges. Additional 20 diagnostics installed presently can provide measurements of electron temperatures, surface temperature of the liner or divertor plates, radiation power, and information of soft-X ray, visible to near UV radiation of impurities, H_α radiation etc. Hard-X ray and neutron flux measurements are also available for LHCD experiments and monitoring the runaway electrons.

The RF systems at ICRF with 1.5MW, 30~110MHZ and at LHF with 2MW, 2.45GHz are available for heating and current drive experiments as well as wall conditioning and discharge pre-ionization.

3. The experiments with new PFCs

EAST as a full superconducting tokamak has new features compared to conventional tokamak and also those tokamaks only with the toroidal superconducting coils. The key issue is to reduce the PF current variation rate by optimizing plasma operation scenarios, particularly, during plasma current buildup phase, which is important for stability and safety of the superconducting magnets with fixed cooling capability under steady-state condition. To achieve reliable break down and plasma current ramping up, the RF cleaning and boronization were used as routine wall conditioning on EAST. The working gas was hydrogen in 2007 and switched to deuterium for recently campaign in 2008.

The experiments have firstly performed using pre-programming shape control and feedback control for plasma position and current with the internal control coils (ICs) for vertical stabilization. To verify the shaping capabilities of the poloidal field system and vertical stabilization of ICs, highly shaped plasma at various configurations has been stably produced. The following configurations have been stably produced: double null configuration

with kappa=1.9 and delta=0.50; top or bottom single null configurations with kappa=1.7 and delta=0.64 with a plasma current up to 0.6MA. Above results almost cover all designed configuration in EAST and confirm the capabilities of the poloidal field systems including ICs and their power supplies for the present operation regime. Such experiments provide the important basis for algorithm development and optimization of real time plasma shape control.

The full reconstruction of the equilibrium has be performed by using EFIT[6] code routinely between shots. This kind of reconstruction was made to be real-time (RTEFIT) and sufficiently fast for the real-time shape control in DIII-D by using a fast loop and a slow loop calculations on separate CPUs. While RTEFIT has been done at a control cycle, the control reference points were determined at first. The flux difference between measured and pre-defined at the reference points were controlled to be zero based on the called RTEFIT/ISOFLUX algorithm, This control algorithm was primarily realized on EAST in 2008 campaign, which provides good basis for RF coupling.

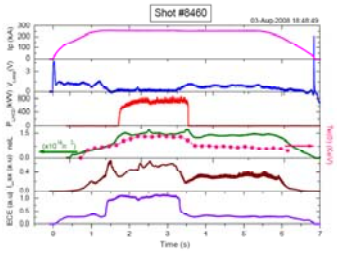

Fig.3 delivered 800kW LHCD power for nearly full non-inductive current drive

The LHW was used for current drive both in sustaining plasma discharges and assisting the plasma start-up. The plasma shape and position were optimized to maximize the wave coupling into the plasma. Nearly 0.8MW LHW at a fixed $N_{||}^{peak}$=2.3 has been successfully delivered, from what about 0.65MW power has been coupled into the plasma shown in Fig.3. This power can nearly sustain a fully non-inductive plasma discharge at Ip=250kA and line averaged density of ~ $1.5*10^{19}m^{-3}$. The current driving efficiency under this condition is about $0.8*10^{19}$ $Am^{-2}W^{-1}$ shown. Significant electron heating by LHW has been observed, while ion heating is very weak. The plasma discharges can be sustained over 20 seconds in such operation scenarios (Fig.4) under present condition. The LHCD experiments were also performed at different plasma current. At present conditions, LHCD can sustain plasma discharges of 400kA and line averaged density of ~ $1.5*10^{19}m^{-3}$ for a duration longer than 10s. Maxima current drive efficiency up to $1.0*10^{19}$ $Am^{-2}W^{-1}$ has been achieved. It means the possibility to sustain fully non-inductive plasma discharges at 500kA and line averaged density of ~ $2.0*10^{19}m^{-3}$ with presently available LHW power of 2MW, which will be a next goal.

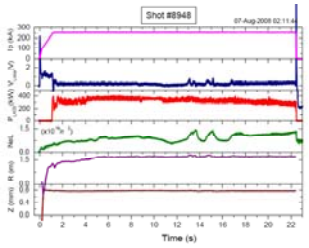

Fig.4 Long pulse discharge sustained by LHCD for 22s

Plasma initiation, ramp up and control are very important issues for a full superconducting machine. Full use of the PF capability can create a loop voltage of ~6.5V with a reasonable null field configuration, which will produce vessel currents up to 150 kA [2] at

breakdown and lead to a loss of poloidal magnetic flux of about 0.3 V*s. Low loop voltage startup has beneficial not only for safety of the machine operation, but also for reduce loss of poloidal magnetic flux due to vessel current. Break down at a toroidal electric field of 0.3V/m has been achieved by optimizing the null field configuration, gas pressure and assistance of the LHW of 100kW and well conditioned wall, which increases the safety margin of PF coils significantly due to reduced the PF current ramping rate. At the same time, the loss of poloidal magnetic flux due to vessel current (<100kA) is only 0.1V*S. Very low plasma ramp rate of 0.12MA/s during plasma current ramping up phase have been obtained with assistance of LHCD, which can significantly reduce the current ramping rate in PF coils or voltage applied at PF coils for the same plasma current ramping rate. This operation mode, on one hand, minimized the heat deposition on the PF coils caused by AC losses, and hence, increases safety of machine operation. On another hand, it allows better plasma control, particularly, during shaping phase due to the larger voltage regulation margin of PF power supply.

4. Experiments in HT-7

In last few years, experiments in the HT-7 tokamak focused on long pulse discharges under different scenarios to support EAST experiments both physically and technically. To meet the long pulse operation requirements, several systems around HT-7 were modified. The plasma control algorithm was implemented based on real time magnetic equilibrium reconstruction with the improved magnetic diagnostics. The iron core is simplified by using the "spool" model [7] and gaps of the last closed flux surface from the PFCs is adopted for the plasma control. New heat sink technology and material were utilized to replace the belt limiter at high field side for validation and supporting construction of the EAST in-vessel components.

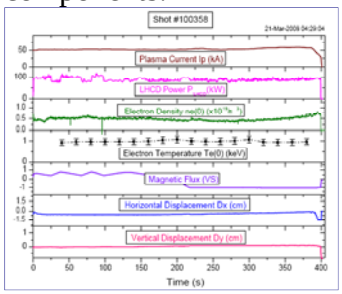

Fig.5 A long pulse discharge for 400s

The long pulse experiment was performed by driving the plasma current fully non-inductively through the use of LHCD, which was realized in two different scenarios. The first one is via feedback control of the magnetic swing flux of the transformer at a constant. The second way is so-called transformer-less discharges, which was realized by over current drive up to reversed saturation of the transformer and then switch off the current in the central solenoid. Experimental observation by hard X-ray pulse height analysis indicates that the cut-off energy of supra thermal electrons are smaller in the transformer-less discharges than in the first scenarios. These techniques has been used successfully to sustain the plasma discharges for 400s at Ip~50 kA shown in Fig 5, which is the new record in HT-7. The magnetic flux of the transformer was controlled at a constant during first 150s in these three shots and then over current drive led to switching off the central solenoid at about 200s, 210s, and 270s respectively. There was no observable hot spot during transformer-less discharges, which

might be correlated with vanish of further acceleration of fast electrons driven by LHCD. In such an operation mode, the surface temperature of the belt limiter could be well controlled below a certain value for whole plasma discharge duration as shown in Fig.20. These long pulse experiments indicate success of the new built belt limiter, and more important is to validate the same heat sink material and structure applied for the EAST PFCs. The well controlled surface temperature also suggests important role of supra thermal electrons on the heat load at the limiter. The limitation for even longer pulse is due to uncontrollable density rise caused by out-gassing mainly from the first wall, which was heated by plasma radiation and not actively cooled.

5. Summary and near future plan

Significant progress in construction of the fully actively water-cooled in-vessel components and plasma control in obtaining highly shaped plasma has been made on EAST. The primary achievements, particularly, the experiences from last two years provide us confidence that the highly shaped plasma with relevant performance could be sustained by RF powers for long duration, although some improvements are needed for reliable machine operation and effective experiments.

Totally 8MW RF systems will be available in 2009 and additional heating and current drive power of 8MW is expected before end of 2010. The flexibilities of heating scenarios and current drive in controlling power deposition and current density profile provide the possibilities to operate EAST in high performance regime with edge and/or internal transport barrier, which allow investigation focused on advanced scenarios for long pulse. In the next two years, diagnostics on EAST will provide measurements of all key profiles, which should be sufficient to describe the basic plasma performance and for integrated modeling and data analysis.

Acknowledgements

This work was supported by the National Natural Science Foundation of China under Grant No. 10725523 and No. 10721505 and partially by the Core-University Program of Japanese Society of Promote Sciences.

Reference

[1] Yuanxi Wan, et al., “Overview progress and future plan of EAST Project” Fusion energy 2006, Proc. of 21th Int. Conf. (Chengdu, China 2006) (Vienna: IAEA) CD-ROM file OV/1-1 and http://www-naweb.iaea.org/napc/physics/fec/fec2006/datasets/index.html

[2] Baonian Wan, et al., “First plasma in EAST” Fusion energy 2006, Proc. of 21th Int. Conf. (Chengdu, China 2006) (Vienna: IAEA) CD-ROM file PD/P6-5 and http://www-naweb.iaea.org/napc/physics/fec/fec2006/datasets/index.html

[3] Baonian Wan, et al., *Nucl. Fusion* **45**, S132 (2005).

[4] Baonian Wan, et al., *Journal of Nuclear Materials* **Vol. 313–316** 127–134 (2003)

[5] M. Bitter, et al., Rev. Sci. Instrum. **70**, 292 (1999)

[6] Lao, L.L., et al., *Nucl. Fusion* **25** 1611(1985)

[7] E. R. Solano et al, Nucl. Fusion, **30**, 1107 (1990)

Proceedings of ITC18,2008

KSTAR Construction and Commissioning

H. L. Yang, J. S. Bak, Y. S. Kim, Y. K. Oh, I. S. Whang, Y. S. Bae, Y. M. Park, K. W. Cho, Y. J. Kim, K. R. Park, W. C. Kim, M. K. Park, T. H. Ha and the KSTAR Team

National Fusion Research Institute

Gwahangno 113, Yuseong-Gu, Daejeon, 305-333, Korea

KSTAR's twelve years project has been officially completed by declaring the first plasma achievement on July 15th, 2008. KSTAR, the first Nb_3Sn-based fully superconducting tokamak device, has come a long path, overcoming many difficult situations. The detailed engineering design and infrastructure setup for R&D have been completed in 2001. In March 2008, after the construction period of seven years, the KSTAR assembly has been completed, by connecting the cryogenic transfer lines between the tokamak and the cryogenic distribution system within six months in the condition of preliminary study. The commissioning on KSTAR has been progressed from April to July, through the following four steps: vacuum, cryogenic cool down, superconducting magnet test, and plasma start-up. KSTAR has successfully passed the vacuum and cool down commissioning at the first trial. As scheduled, the basic environment with the vacuum at 3×10^{-8} mbar and the temperature below 4.5K has maintained without any cold helium leak. Next, all of the superconducting magnets have been conducted using the integrated plasma control system (PCS) for fast current and position control. The first plasma discharge has been initiated under time synchronized operation of the power supplies, the ECH pre-ionization system, the gas-puffing system, and the initial set of diagnostics systems. After about 400 successive test plasma discharges, during which plasma was successfully controlled with a flat-top current of 120 KA, duration of up to 800 ms has been obtained at KSTAR.

All of the commissioning contents, such as objectives, must-check items, target parameters, and commissioning results, will be presented in this paper. Specifically, various histories, such as vacuum, temperature, stress, plasma shot, and machine failure, will be reported.

Keywords: KSTAR, Vacuum Vessel, Nb_3Sn SC Coil, CS Pre-loading, KSTAR Assembly, KSTAR Commissioning, KSTAR First Plasma, ECH pre-ionization, Cool-down, SC transition

1. Introduction

Since the KSTAR (Korea Superconducting Tokamak Advanced Research) project started from the end of 1995 for the development of an advanced superconducting(SC) tokamak to establish a scientific and technological basis for an attractive fusion reactor [1], all related systems have been rigorously developed through early R&D and design phase which was actually terminated in middle of 2002. The R&D and design period provided key technologies and a crucial basis for the actual construction of the machine, which started in early 2002 [2]. The machine construction phase proceeded from 2002 and was finished by August of 2007. During the construction period, various kinds of important construction activity were simultaneously implemented. Among these various areas, the main tokamak system such as i) a vacuum vessel (VV) and cryostat, ii) thermal shields, iii) SC coils and structure, iv) SC interface system including current feeder system, v) machine assembly and system integration was a crucial engineering area of which the quality and schedule could decisively affect the success of the KSTAR construction efforts. All activities related to the systems mentioned above have been successfully carried out by August 2007. As a result, the KSTAR team finally declared the machine construction in September 2007. The integrated commissioning started from March 2008 after 6 months-preparation of final helium distribution box (HDS #2). The integrated commissioning has been successfully progressed without any serious problem and completed in first trial attempt. At last, the KSTAR has been officially completed by declaring the first plasma achievement on July 15th 2008. All commissioning results were verified by a special committee, whose members were nominated by the Minister of Education, Science, and Technology.

Warm-up of the machine started on July 20th was completed by end of August. Warm-up process was

author's e-mail: hlyang@nfri.re.kr

performed with two steps: forced helium circulation and natural warm-up. Now the machine is in the stage of preventive maintenance and system upgrade for next campaign.

2. History of the Construction

2.1 Vacuum Vessel (VV) and Cryostat

The VV of the KSTAR is one of the most important structures as it provides ultra-high vacuum conditions for the generation and confinement of the tokamak plasma. Therefore, all structures and fabrication techniques for the VV should meet the general requirements as described in detail in the literature [3]. The VV was designed by the end of 2001 to meet the requirements by both the KSTAR staff and by Hyundai Heavy Industries (HHI). The major parameters of the KSTAR VV are illustrated in Table 1.

Table 1. Major parameters of the VV

Parameters	Values
Inner radius of the torus	1.1 m
Outer radius of the torus	2.99 m
Height/width	3.387 m/ 1.880 m
Rib thickness	20 (40) mm
Double wall thickness	50-190 mm
Total weight	72 ton (with support)
Surface area (inner shell)	100 m2 (without port)
Relative permeability	<1.10 (after welding)
Shell thickness	12 mm
Resistance	> 40 μΩ

The cryostat is a single-walled vacuum vessel that provides a vacuum environment for the entire space in which all of the SC magnets and sub-systems are contained. This cryostat structure is mainly composed of large three parts: the base, the cylinder, and the lid. It achieves a target vacuum pressure ($< 1\times10^{-2}$ Pa) to allow the cool-down start of the cold mass. The total weight and height of the cryostat are 180 tons and 8.56 m, respectively. The fabrication of the cryostat started in middle of 2002 by HHI. As the diameter of the cryostat is 8.8 m, as mentioned above, it was impossible for the entire cryostat structure to be transported from the factory to the site. This technical problem was solved through the breakdown of the fabrication of the cryostat system into several sub-units in the factory. These sub-units were finally welded together at the site. Two halves of the cryostat base were completed in the fabrication process at the factory by the end of 2003 and were welded to each other at the site to form the entire base structure by February of 2004. The cryostat cylinder was divided into four quadrants, and the cryostat lid was divided into three pieces of a knuckle and a crown with ports. Both the cylinder and the lid were delivered to the site and were completed through site welding in June of 2004.

2.2 SC Magnet System

As detailed description is explained in the literature [4], the SC magnet system consists of 16 toroidal field coils and 14 PF coils. Both the TF and PF coil systems use internally cooled superconductors. The TF coil system provides a magnetic field of 3.5 T at the plasma center, with a peak flux density at the TF coil of 7.2 T. The nominal current of the TF coil is 35.2 kA. The PF coil system, which consists of 8 coils in central solenoid (CS) coil system (PF1-4) and 6 outer PF coils (PF5-7), provides 17 Vs and sustains the plasma current of 2 MA for 20 s, inductively. PF1-5 coils use Nb_3Sn CICC in the Incoloy908 conduit and PF6-7 coils use NbTi CICC in a modified stainless steel 316LN conduit. The fabrication procedure of the TF coils is (i)delivery of the CICC in spool, (ii)coil winding using three dimensional continuous scheme, (iii)attachment of joints and helium stubs, (iv)heat treatment in a vacuum furnace, (v) insulation taping on CICC and ground wrap, (vi)impregnation(VPI), and (vii)acceptance test. The joint of TF coil is strand-to-strand joint with solder between Nb_3Sn cable of TF coil and NbTi cable of busline. The last TF coil was finished in the fabrication by January 2006. The PF6 and PF7 coils, which are made of NbTi conductor, have been fabricated at the KSTAR building due to the difficulties in transportation. Fabrication of the 30 superconducting coils was completed by January 2006 with fabrication finish of the PF5U coil.

The KSTAR magnet structure consists of 16 TF structures, one CS structure, and 80 PF structures. Most of structures are made of stainless steel 316LN. The major fabrication procedure of the TF structures are; (i) fabrication of C-shaped coil case welded with inter-coil structure, (ii) fabrication of flat cover plate welded with inter-coil structure, (iii) coil encasing, (iv) final enclosure welding, (v) second vacuum pressure impregnation, (vi) final machining and delivery, and (vii) toroidal insulation attachment. Figure 8 shows the final machining process and assembly. The 16 TF structures have been finished in fabrication by January 2006. Current feeder system consists of SC buslines with joints, current leads with current lead boxes, and helium lines with electrical isolators. The superconductor of the buslines are made of NbTi strands in circular CICC. The current leads are vapor-cooled type leads, which are made of brass to minimize the helium consumption during zero current. The current lead boxes has been fabricated and installed

at the basement pit of the KSTAR tokamak.

2.3 SC Coil Test

A large SC coil test facility has been constructed and the performance test of the full size TF prototype coil, TF00 coil, and a pair of CS model coil were carried out in the test facility [5]. The major objective of the test is to confirm the validity of the design and the fabrication process. The results of the cool-down and current excitation test of the TF00 coil over than 30 kA showed that the TF coil design and fabrication procedure were acceptable. The CS model coil test has been implemented similar procedure of cool-down and current excitation as those of TF00 coil. The peak field measured at coil inner surface was about 8.6 T when charged up to 20 kA.

2.4 Thermal Shields

There are three types of KSTAR thermal shield: a vacuum vessel thermal shield (VVTS), a cryostat thermal shield (CTS), and a port thermal shield (PTS). The main shield panel is fabricated from a 316L plate 3 mm in thickness and a stainless steel pipe with a 7 mm ID. A wall with a thickness of 1.5 mm is welded on the panel. The shield panel has roughly two types of support made of epoxy glass to minimize heat transfer by conduction. As the VVTS is placed in the narrow gap between the TF superconducting magnet and the vacuum vessel, the VVTS panel is coated with silver at a thickness of 10 ㎛ in place of the use of multi-layer insulation (MLI) [6]. The VVTS has a double-pipeline configuration for redundancy. The CTS consists of three parts: the lid TS, the body TS, and the base TS in the cryostat. Each part is toroidally divided into 16 sectors like the VVTS. Its space is such that 30 layers of MLI are used to mitigate the effects of thermal radiation from the cryostat surface to the superconducting coils. There are 72 penetration ports classified into seven types to connect the vacuum vessel body and the cryostat. PTS coated with silver covers these ports. The VVTS fabrication started from the early 2004 and completed by the end of 2004.

2.5 KSTAR Assembly

The KSTAR assembly of which details are described in the lieterature [7] was divided into four stages. The first stage started at the beginning of 2004 and lasted until June of 2004. The first stage assembly included assembly of the cryostat base, gravity support for SC magnets, and main assembly jigs. The second stage started in July 2004 after completion of the main assembly jigs. The second stage included assemblies of major structures such as the VV, VVTS, TF magnets, and VV supports. In March of 2005, the main jig system was partly removed and the VV and VVTS were installed on the tokamak pit. The TF magnets were assembled from April of 2005 to May of 2006. The last sectors of the VVTS and VV, as well as that of the VV supports, were assembled in turn by June of 2006 as the final assembly step of the second stage. The third stage assembly mainly included assembly of all PF and CS coils. After the PF6L, PF7L, PF7U, PF6U coils were installed onto the TF structure in turn, the PF5L coil and the PF5U coil were assembled by October 2006. The CS coils were sub-assembled in the main experimental hall during the assembly period of the PF coils. The CS coil system after the sub-assembly process was finally assembled on the TF magnet system by October of 2006 as shown in Fig. 1. The third stage also covered final installation and system tests for all in-cryostat components of the SC bus line, SC joints, helium piping system, and all of the cryogenic and strain sensors. After most of the in-cryostat components were installed in the third stage, the cryostat cylinder was assembled in early January of 2007, as shown in Fig. 2.

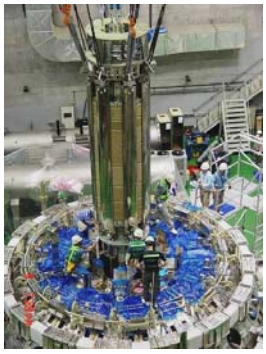

Fig.1 Assembly of the CS

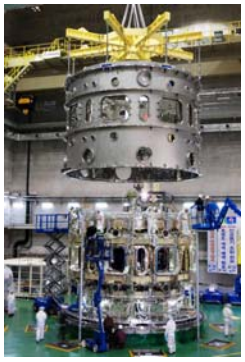

Fig.2 Assembly of the cryostat cylinder

Assembly of the cryostat cylinder provided a condition for the final welding of the VV ports. Subsequent procedures were the assembly of the cryostat lid and the assembly of the vertical ports. Two pumping duct systems for the VV and cryostat were simultaneously assembled during the assembly of the vertical port. As a final step for the assembly, all of the VV ports were blanked for vacuum sealing by the end of April of 2007.

3. Ancillary Systems

In addition to the construction of the main tokamak system, every ancillary system was simultaneously developed and installed to meet the target date of KSTAR

first plasma. The 9 kW Helium Refrigeration System (HRS) was finished in system commissioning and final acceptance test by March 2008.

The magnetic diagnostics for the first plasma have been also installed and completed the system test. Other crucial diagnostics such as ECE, single-channel interferometer, visible TV system, H_α monitoring system, and filter-scope were finally ready for first plasma. The ECH system (84 GHz, 500 kW, 2 sec) was also rigorously tested for ECH-assisted pre-ionization using 2nd harmonic [8]. The ICRH system (30~60 MHz, 2 MW, 300 sec) were fully tested with dummy load. However, the ICRH system was utilized ICRH discharge cleaning under TF field within 30 kW owing to the absence of cooling system for the ICRH antenna. The Magnet Power Supply (MPS) was successfully tested with dummy coil at room temperature [9]. As a result, all the system for start of integrated commissioning and first plasma were completed in system installation and self-commissioning before start of integrated commissioning. Figure 12 shows the KSTAR device and all of the ancillary system in the main experimental hall.

4. Vacuum Commissioning

KSTAR has two separate vacuum regions: one is the vacuum vessel for plasma discharge and the other is the cryostat for thermal insulation of superconducting magnets. The main task of the vacuum commissioning is to check the base pressure and leak rate of whole system to guarantee long-term operation. The commissioning was performed with two steps. The first step was taken after the assembly finish in June 2007. In the first trial, the cryostat vacuum was not achieved due to very tiny leak from a bellows in the cooling pipe of the cryostat thermal shields. After repairing the leaked bellows, there were no detectable He leaks on the all of the in-cryostat components. The second step commissioning began in March 2008. Figure 3 shows the vacuum history during the entire commissioning period. As shown in Fig. 3 (a), the primary vacuum reached below 5.0×10^{-5} Pa within 12 hours from evacuation, and the pressure was maintained in the range of 2.5×10^{-6} Pa before baking. While the vacuum vessel is baked up to 100 degree Celsius, the pressure continuously increased to 10^{-5} Pa range. After the baking process, the RF-assisted glow discharge cleaning (GDC) was implemented using hydrogen and helium gas. As shown in Fig. 3 (b), the vacuum pressure of the cryostat also reached 2.5×10^{-4} Pa within one day. In the final leak test in which all the SC magnets and the thermal shield were pressurized to 20 bars, there was no symptom of the helium leak. As the machine was cooled down toward 4.5 K, the secondary vacuum gradually decreased to 2.5×10^{-6} Pa. Especially, the cryostat vacuum drastically decreased at around 40 K. The entire pumping system, including control and interlock unit, were very stably operated through the entire commissioning period.

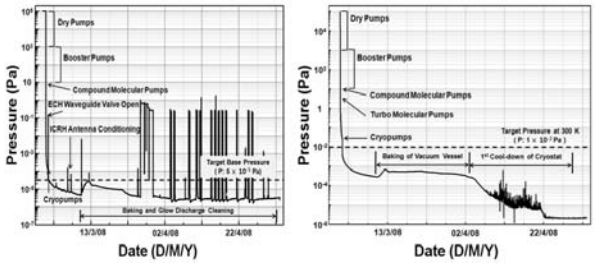

(a) (b)

Fig. 3 Vacuum history (a) VV, (b) cryostat

5. Cool-down Commissioning

The main tasks in this commissioning step were to check helium cold leak, mechanical stress of cold components, superconducting transition of coils, joint resistances, and operating characteristics of all cryogenic loops. All cold systems were cooled down to their operating temperature within 23 days, without serious trouble disturbing the cool-down process.

5.1 Temperature Control and Helium Cold Leak

The cool-down was carried out by manually controlling the inlet temperature from room temperature to 4.5 K. Figure 4 shows the temperature history of the first cool-down. Temperature was controlled with two limitations not to have excess contraction stress: one was to keep within temperature gradient of 50 K across the coils and structures, and was to restrict temperature difference of 25 K between inlets and outlets. The cryostat pressure decreases smoothly from 2.5×10^{-4} Pa to 2.5×10^{-6} Pa. The helium partial pressure kept around 4.0×10^{-7} Pa until warm-up. To identify whether it had a cold leak, the helium leak rate was measured by changing the pressure of helium gas up to 20 bars. The change of leak rate was not found. This proved that the cryostat did not have a helium cold leak. In any events, the total leak rate was less than 8.9×10^{-9} Pa m^3/s, which was much less than acceptable value of 1.0×10^{-5} Pa m^3/s.

5.2 Mechanical Stress Change

To monitor the structural stress behavior during cool-down, 239 strain gauges were instrumented on the various cold components. They were measured in the range of 15 MPa ~ 93 MPa, which is just within 13 % of

the maximum allowable stress. A maximum hoop stress of 93 MPa was observed at the lower outboard leg because there were more constraint structures on the lower part. On the other hand, tensile and compressive stresses were observed in the PF6 and PF7 structures, which were resulted from the relative difference of the thermal contraction between the TF structure and PF coils. Radial displacements of the 4 segmented toroidal ring at 10 K were in the range of 7.66 mm ~ 7.93 mm. Another important issue was to check the preload change of the central solenoid structure. The central solenoid (CS) was mechanically preloaded with 747 tons at room temperature [10]. As shown in Fig. 5, the preload value of CS structure was reduced to 600 tons at 5 K and then back to almost same value after warm-up.

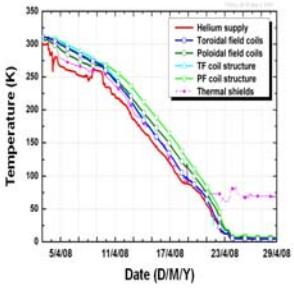

Fig.4 Cool-down history

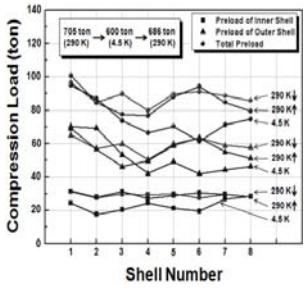

Fig.5 Pre-load change of CS

5.3 SC Transition and Joint Resistance

As the coil temperature went down to 20 K, the transition into superconducting state of the Nb_3Sn coils; 16 TF, and PF1-PF5 coils, was observed by directly measuring the coil voltage drop at a current of 100 A. Subsequently, the superconducting transition of NbTi coils; PF6, 7 coils, was observed as shown in Fig. 6. The transition temperatures of Nb_3Sn and NbTi coils were around 18 K and 9 K, respectively. After the bus-lines were fully cooled, voltage drops were measured at bus-line interval which had 5 or 6 lap joints. The joint resistances were evaluated by linear fitting of the measured I-V curves. Most of the joints have resistances of less than 2 nΩ, which are below the design allowance of 5 nΩ. From this result, it is verified that KSTAR silver-coated lap joints have reliable and uniform performance [5].

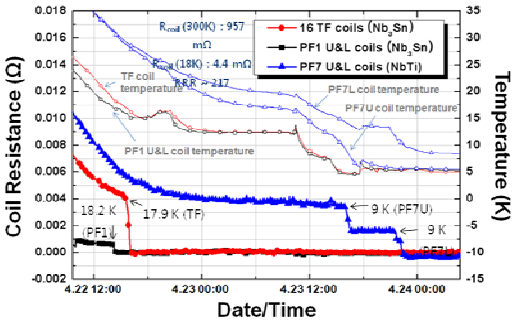

Fig. 6 SC transition of the KSTAR magnets

5.4. Magnet Commissioning

The TF system was tested by increasing the current level in steps. Figure 7 shows operating characteristics of TF magnet. The toroidal magnet was excited to 15 kA corresponding to 1.5 T at R=1.8 m, and has been operated stably with temperature rise less than 0.1 K in current change interval. To investigate the magnetic effect of Incoloy 908, intensive field measurements were also performed [11]. The vertical remnant field measured about 10 Gauss in zero TF current, reduced to 2 Gauss at TF current of 15 kA. The maximum mechanical stress of the TF structure at 15 kA was measured to be about 41 MPa. The quench detection system also operated reliably without any false activation. The maximum detected voltages were less than 25 mV at the instant of current charge started. During the entire commissioning period, no quench was found

Prior to real PF coil test, each power supply was tested with copper dummy coils. The current was controlled by the PCS system which was developed under KSTR-DIII-D cooperation. Control of reference current waveform, fast current change using the blip resistor and mutual inductance effects between adjacent coils were tested with each 7 PF power supply. After the successful performance tests with dummy coils, major tests with the superconducting coils were carried out. After the every single coil test, integrated tests with 7 PF coils were carried out. Seven PF power supplies were operated in a uni-polar condition because there was not a protection circuit. The typical PF current waveform had a 3s ramp-up and a 4s flat-top time before the blip of 100 ms duration. As shown in Fig. 8, blip tests were performed up to changing rate of 17.1kA/s for PF6 and up to 98.9 kA/s for PF3, respectively.

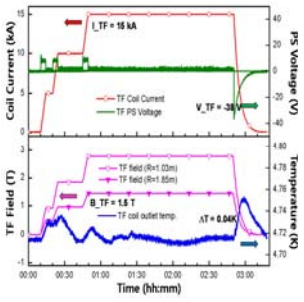

Fig. 7 Operating features of TF magnet

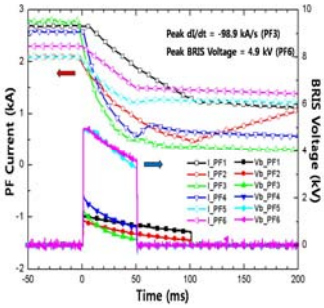

Fig. 8 Blip test results of PF magnets

6. First Plasma Experiments

6.1 Key Features in Start-up

Experiments on the initial field null configurations were performed with two different types of IM scenarios. Usual "conventional mode" scenario to have maximum field null size to get stable initial breakdown was tried. Flux contributions of this mode come mainly from the central solenoids PF1~4 and weakly from PF6~7. The expected loop voltage was ~4.5 V without plasma with flux of 0.89 Wb. The "dipole mode" scenario was developed to get higher loop voltage and poloidal magnetic flux for higher plasma performance. This was achieved by charging-up of the PF6 and PF7, and it increased the available magnetic flux significantly. The loop voltage was 5.1 V with flux of 0.95 Wb. To compensate for the low loop voltage, an 84 GHz ECH system with 500 kW power was utilized as the second harmonic ECH assisted pre-ionization. Pre-ionization by the ECH system was highly reliable. With ECH heating during the current ramp-up, the discharges were less sensitive to wall conditioning. To control the wall reflux during the plasma shots, ICRH-assisted discharge cleaning was implemented during shot-to-shot interval under the TF field.

6.2 Experimental Results

After several tens of breakdown shots, the first plasma was achieved on June 13th (shot 794). Figure 9 shows a plasma image of the shot 794. In this experiment, ECH was very critical system in initiating the discharge. Without the ECH power, plasma could not be discharged. With TF current of 15kA, ECH resonance layer was formed at R=1.8 m [12]. Under the IM conditions of the conventional scenario, the blip resistors were inserted for 100ms. The ECH power was on 30 ms before the applying toroidal loop voltage and lasted for 200 ms with 350 kW power. For this, the force balance with the current ramping was adjusted in feed forward manner. With the dipole mode IM scenario, more initial magnetization and higher plasma current could be obtained. In this mode, plasma current and position could be controlled to get longer plasma durations. As a result, we could achieve maximum plasma current was 133 kA and longest plasma length was 862 ms [13].

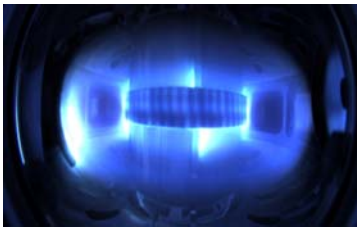

Fig.9 Image of ohmic discharge plasma

7. Conclusion

After about 400 successive test plasma discharges, successfully controlled plasma with flat-top current of 100 kA, duration up to 862ms was achieved at KSTAR. It was verified that the construction and the test results of the past twelve years were very successful through this commissioning. Looking at all of the commissioning results, it is certain that the success and lessons of KSTAR will greatly help with the upcoming construction of the superconducting tokamak. Especially, the engineering and commissioning progress of KSTAR will certainly benefit and contribute considerably to the construction of ITER. The KSTAR now plans to upgrade its power supply, plasma facing components, and heating devices as quickly and feasibly as possible, so that the overall performance of the machine can be greatly improved. The full performance experiments for advanced tokamak physics with a 300 sec long pulse will be exploited within 2012.

Acknowledgment

This work is supported by the Ministry of Education, Science, and Technology. The author would like to thank all the KSTAR participants from Korea domestic and international collaboration partners who gave efforts to make successful construction and commissioning.

References

[1] G.S. Lee, *et al.*, Nuclear Fusion 41 (2001) 1515-1523.
[2] J.S. Bak, *et al.*, IEEE trans. Plasma Science, vol. 32, p757 (2004).
[3] B.C. Kim, *et al.*, Fusion Engineering and Design, vol. 83, 573-579 (2008)
[4] K. Kim, *et al.*, Nuclear Fusion vol. 45 p783 (2005).
[5] Y.K. Oh, *et al.*, Advances in Cryogenic Engineering Materials, vol. 49, p241 (2004).
[6] W.C. Kim and J. S. Bak, Journal of the Korean Physical Society 49 (2006) 282-286.
[7] H.L. Yang, *et al.*, Nuclear Engineering and Technology, vol. 40, 439-450 (2008)
[8] Y.S. Bae, et al., Nucl. Fusion **49** (2009) to be published.
[9] J.H. Choi, H.L. Yang, *et al.*, Nuclear Engineering and Technology, vol. 40, 459-466 (2008)
[10] H.L. Yang, *et al.*, "KSTAR Assembly", in 2006 Proc. of 21st IAEA Fusion Energy Conference, China, FT2-2 (2006)
[11] Y.K. Oh, *et al.*, "Commissioning and Initial Operation of KSTAR Superconducting Tokamak", in 25th SOFT, Rock, Germany, S8.3 (2008).
[12] J.S. Bak, *et al.*, "Overview of Recent Commissioning Result of KSTAR", in 2008 Proc. of 22nd IAEA FEC, Geneva, Switzerland, FT/1-1 (2008)

Proceedings of ITC18, 2008

Advanced Tokamak Research in JT-60U and JT-60SA

Akihiko ISAYAMA for the JT-60 team

Japan Atomic Energy Agency, Naka, Ibaraki 311-0193, Japan

Results of experiment in JT-60U and design study in JT-60SA (Super Advanced) are described focusing on the development of advanced tokamak. In JT-60U, a high-integrated performance plasma with the normalized beta β_N=2.6, confinement enhancement factor $H_{H98(y,2)}$=1.0–1.1 and bootstrap current fraction f_{BS}=0.4 has been sustained for 25 s (14 times current diffusion time (τ_R)). Neoclassical tearing mode (NTM) with the poloidal mode number m = 2 and the toroidal mode number n = 1 has been stabilized with modulated electron cyclotron current drive (ECCD) in synchronization with the mode frequency (~5 kHz). A high-beta plasma exceeding the ideal MHD limit without conducting wall has been sustained for 5 s (~$3\tau_R$) by suppressing resistive wall mode (RWM). In addition, two new instabilities in the high-beta regime, *Energetic particle driven Wall Mode* (EWM) and *RWM precursor*, have been observed. In JT-60SA, exploration of full non-inductive steady-state operation with current drive by neutral beams and electron cyclotron waves is planned. In addition, NTM control with ECCD and RWM suppression with external coils are planned.

Keywords: advanced tokamak, ITER, Hybrid Scenario, NTM, RWM, JT-60U, JT-60SA

1 Introduction

Steady-state sustainment of high integrated performance is essential for a fusion reactor, where simultaneous achievement of high values of the normalized beta (β_N), confinement enhancement factor ($H_{H98(y,2)}$), non-inductive current drive fraction (f_{NI}) and so on is required. For example, in one of the advanced scenarios in ITER, so called the Hybrid Scenario, β_N=2–2.5, $H_{H98(y,2)}$=1–1.2 and f_{NI}=0.5 are assumed to obtain the fusion gain Q~5 with the discharge duration of longer than 1000 s [1]

To develop the scenario of the advanced tokamak operation and clarify physics issues and their solution, advanced tokamak research has been extensively performed in JT-60U by fully utilizing its capability. In JT-60U, two major scenarios have been developed for the advanced tokamak research [2]: high-β_p H-mode scenario and reversed shear scenario. Sustainment of high-performance plasmas for longer than current diffusion time have been achieved in both scenarios. This paper focuses only on the advanced tokamak research with high-β_p H-mode.

In obtaining a stationary high-beta plasma, one of the magnetohydrodynamic (MHD) instabilities to be suppressed or controlled is a neoclassical tearing mode (NTM). The NTM is destabilized by bootstrap current in a plasma with positive magnetic shear and degrades the plasma performance. Among possible mode numbers, NTMs with m/n=3/2 and 2/1 should be controlled since confinement degradation by them is large. Here, m and n are the poloidal and toroidal mode numbers, respectively.

In JT-60U, two scenarios for NTM suppression have been developed. One is avoidance of NTM onset through the optimization of pressure and current profiles. To be more specifically, the location of steep pressure gradient, which is typically located at 0.3–0.7 in the averaged minor radius, is adjusted so that it is far from the mode rational surfaces. This scenario is advantageous in that NTMs can be suppressed without additional heating/current drive systems other than those for the high-performance plasma. In JT-60U, systems for plasma control, heating/current drive and diagnostics were upgraded to obtain a long-duration plasma with auxiliary heating using neutral beams (NBs) and electron cyclotron (EC) waves up to 30 s in 2003 [3,4]. After the installation of ferritic steel tiles in 2005, a higher-confinement plasma was obtained through the reduction of fast ions [5, 6]. In 2007, pulse width of 3 units of the perpendicular NBs was extended to 30 s, which enabled central plasma heating for longer time.

The other scenario for NTM suppression is active stabilization using electron cyclotron current drive (ECCD). In JT-60U, NTM stabilization has been performed since the installation of the first 110 GHz gyrotron in 1999 [7], and stabilization by real-time mirror steering [8], preemptive stabilization [9] and simulation with the TOPICS code [10–12] have been performed.

In a higher beta regime above the ideal beta limit without conducting wall ('no-wall limit'), a resistive wall mode (RWM) appears and terminates the discharge. RWM had been observed in reversed shear discharges before the installation of the ferritic steel tiles [13]. After the installation of the ferritic steel tiles, RWM study in a positive-shear plasma, which requires higher NB power to reach the no-wall limit, became possible. Detailed scan of toroidal velocity utilizing the capability of various NB injection pattern in JT-60U, the minimum required toroidal rotation velocity was found to be 0.3% of the Alfvén velocity [14].

The operation of JT-60U was concluded with great success in August 2008. A superconducting tokamak, JT-60SA (Super Advanced), is being constructed to take

author's e-mail: isayama.akihiko@jaea.go.jp

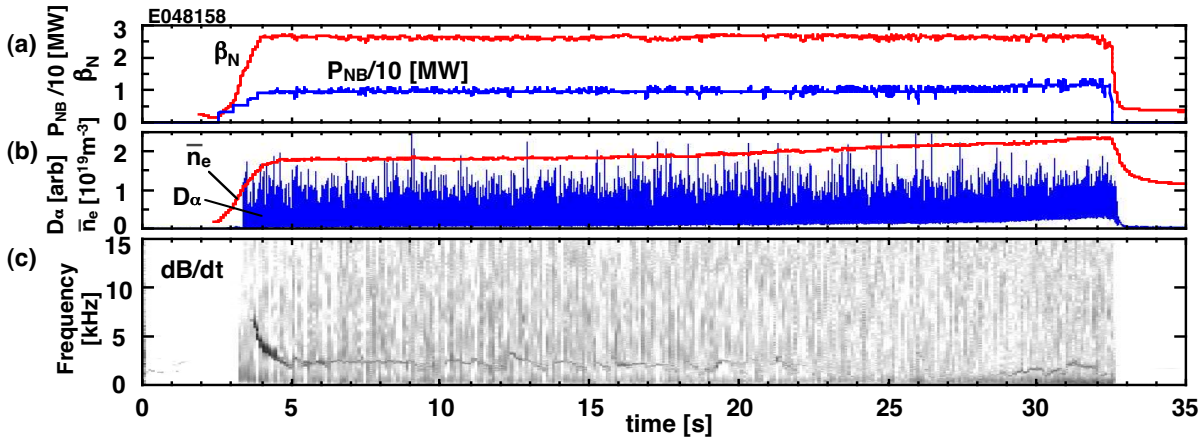

Fig. 1 Typical discharge of a long-pulse high-beta plasma. (a) Normalized beta and NB injection power, (b) line-averaged electron density and D_α intensity, (c) frequency spectrum of magnetic perturbations.

over and drive forward the advanced tokamak research as a combined program of the ITER Satellite Tokamak Program of Japan and EU and the Japanese National Program.

This paper describes results from JT-60U experiments and JT-60SA design study with emphasis on advanced tokamak research. After this introduction, long-duration sustainment of a high-beta plasma through NTM avoidance is described in Sec. 2. Active stabilization of an m/n=2/1 NTM with modulated ECCD is described in Sec. 3. Suppression of RWM by rotation control and newly observed instabilities are described in Sec. 3. Design and physics assessment in JT-60SA is described in Sec. 4. Finally, summary is described in Sec. 5.

2 Long-duration sustainment of high integrated performance plasma [15]

In JT-60U, the maximum pulse duration of 3 units of NBs was extended to 30 s in 2007, which enabled central heating for longer time. Typical discharge of a long-duration high-beta discharge is shown in Fig. 1. Plasma parameters in this discharge are as follows: the plasma current I_p=0.9 MA, the toroidal field B_t=1.54 T, the major radius R=3.36 m, the minor radius a=0.88 m, the plasma volume V_p=67 m^3, safety factor at 95% flux surface q_{95}=3.2. From t=2.5 s neutral beam was injected stepwise to avoid onset of NTMs. The central value of safety factor q was nearly unity, but large sawtooth oscillation was not observed. The value of the normalized beta, $\beta_N \equiv \beta_t/(I_p/aB_t)$, reached 2.6 by about 10 MW NB injection, and was sustained by feedback control. It can be seen that the injection power is almost the same, and H-mode with edge localized mode (ELM) is sustained stationarily. From t~20 s, D_α intensity and electron density gradually increased, and NB injection power slightly increased, showing confinement degradation. Frequency spectrum of magnetic perturbations (Fig. 1(c)) shows that no large instability such as NTMs is observed throughout the discharge. Although infrequent sawtooth oscillations are observed at ~2 kHz, confinement degradation is not visible. Profiles of ion and electron temperatures and safety factor at t =27 s are shown in Fig. 2. While the the temperature gradually decreased as the electron density increased, peaked profiles were maintained until the end of the high-beta phase. In addition, internal and edge transport barriers were also maintained. It can be seen that the q=1.5 and 2 surfaces are located at the peripheral region with small temperature gradient, which is effective in avoiding NTM onset.

The value of confinement enhancement factor against the H-mode scaling, $H_{H98(y,2)}$, is 1.0–1.1, and the fraction of bootstrap current to the total plasma current, f_{BS}, is 0.43–0.46 from ACCOME code calculation. These parameters satisfy the requirement for the ITER Hybrid Scenario [1]. Current diffusion time, τ_R, is 1.8 s. Here, $\tau_R \equiv \mu_0 \langle\sigma\rangle a^2/12$, μ_0 is permeability and $\langle\sigma\rangle$ is volume-averaged neoclassical conductivity [16]. Thus, the sustained period in Fig. 1 corresponds to about $14\tau_R$. Actually, safety factor profile measured with motional Stark effect diagnostic is fully relaxed and flat q-profile with $q(0)$~1 is sustained stationarily.

Progress in long-duration sustainment of high-beta plasma is shown in Fig. 3. Before 2003, confinement was not high ($H_{H98(y,2)}$~0.8–0.9) although pulse duration was significantly increased from 10 to 30 s, and β_N=2.3 was sustained for 22.3 s [3, 4]. Insertion of ferritic steel tiles contributed to extending the pulse duration as well as enhancing the confinement by reducing loss power and thus increasing available power in the later phase of discharges. Extension of the pulse width of the 3 perpendicular NBs in 2007 made it possible to further extend the duration of high-beta plasma, and as shown in Fig. 3, β_N=2.6 was sustained for 25 s, and β_N=2.3 was sustained for 28.6 s. Since the maximum pulse duration in the present JT-60U system is 30 s, the sustained period is nearly equal to the maximum pulse width of the NBs.

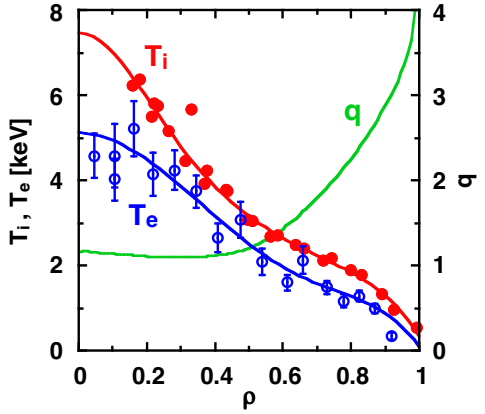

Fig. 2 Profiles of ion and electron temperatures and safety factor at t=27 s.

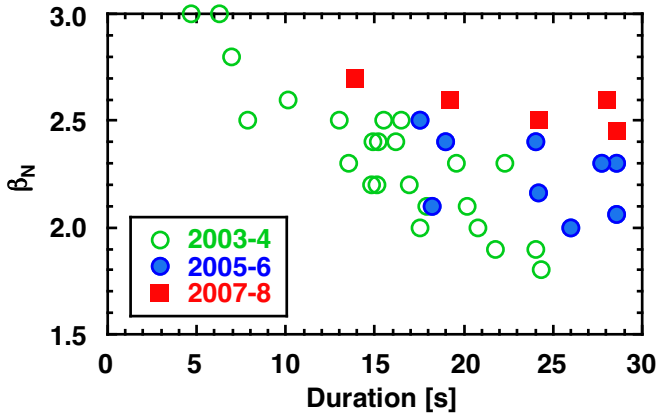

Fig. 3 Progress in the duration of a high beta plasma. Open circles, closed circles and closed squares correspond to the result in 2003–4, 2005–6 and 2007–8, respectively.

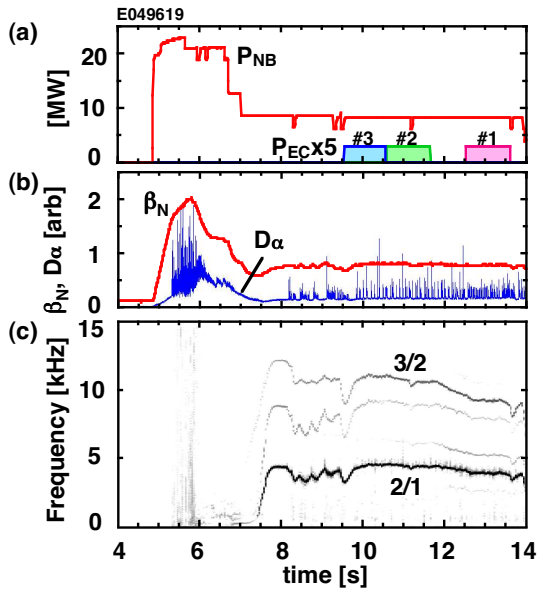

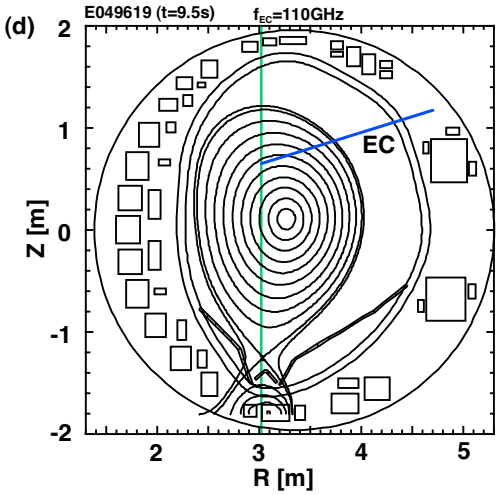

Fig. 4 Typical discharge of stabilization of an m/n=2/1 NTM with ECCD. (a) Injection power of NB and EC wave, (b) the normalized beta an D_α intensity, (c) frequency spectrum of magnetic perturbations, (d) plasma cross section. In Fig. 4(d), contour is drawn every 0.1 in the volume-averaged normalized minor radius.

3 Active stabilization of neoclassical tearing mode by localized electron cyclotron current drive [17]

In JT-60U, modulation frequency of gyrotrons has been increased year by year through continuous modification and conditioning. In 2008, modulation at about 7 kHz was successfully achieved [18, 19]. For NTM stabilization with modulated ECCD, EC wave is needed to be synchronized with the rotation of the NTM. In JT-60U, magnetic probe was used to generate a trigger signal for the modulation of gyrotron power. In addition, control system for the gyrotrons has been upgraded so that modulation frequency can be changed automatically by monitoring the magnetic probe signal in real time [19]. By using this system, phase difference between the magnetic perturbations and the modulated EC wave power can be fixed even if the NTM frequency changes in time during a discharge [19]. In 2008, stabilization of an m/n=2/1 NTM with modulated ECCD was performed.

Typical discharge waveform and plasma cross section in an NTM stabilization experiment are shown in Fig. 4, where typical plasma parameters are as follows: I_p=1.5 MA, B_t=3.7 T, R=3.18 m, a=0.80 m, q_{95}=4.1. In this series of discharges, NBs of about 25 MW was injected to destabilize a 2/1 NTM, and β_N increased to about 2. An m/n=2/1 NTM appeared at t~5.7 s, and the value of β_N decreased to about 1.2. At t=6.7–7 s, NB power was decreased and the direction of the tangential NBs was changed from balanced injection to counter injection to raise the mode frequency. The 2/1 NTM started to rotate

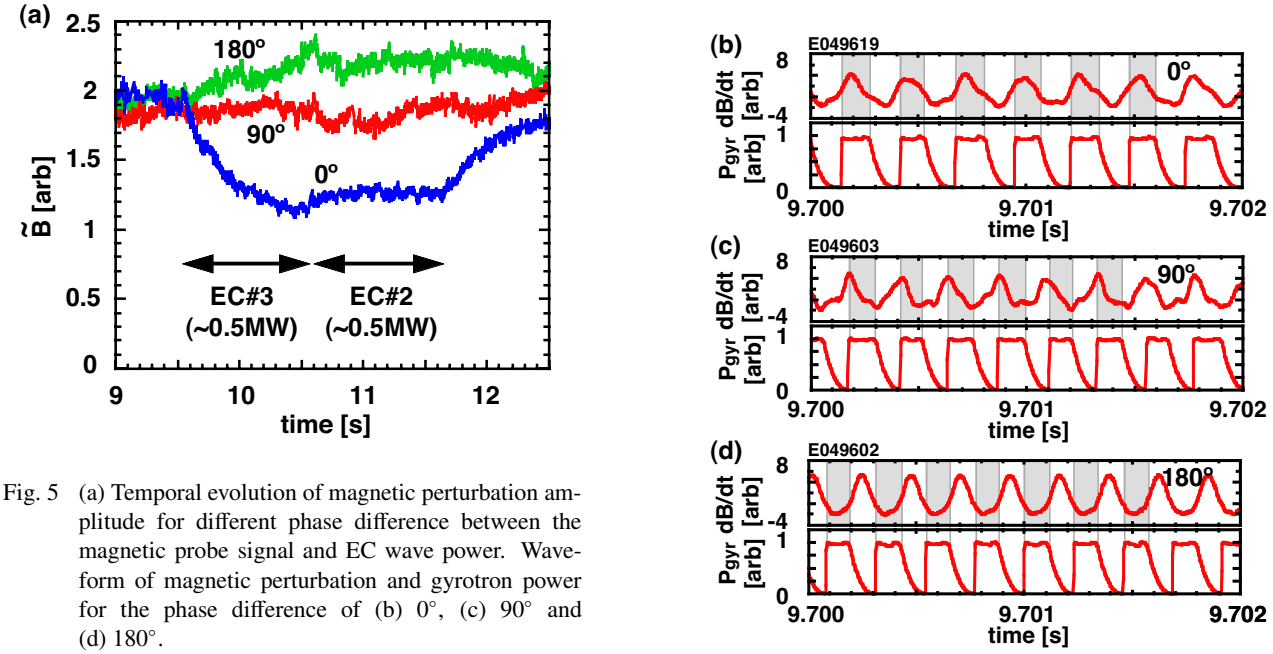

Fig. 5 (a) Temporal evolution of magnetic perturbation amplitude for different phase difference between the magnetic probe signal and EC wave power. Waveform of magnetic perturbation and gyrotron power for the phase difference of (b) 0°, (c) 90° and (d) 180°.

in the counter direction at t=7.5 s, and the mode frequency reached about 4–5 kHz as shown in Fig. 4(c). Electron cyclotron wave with the frequency of 110 GHz was injected at t=9.5 s from the low-field side as shown in Fig. 4(d). The 2/1 mode is located at ρ~0.6, where ρ is volume averaged normalized minor radius. According to calculation with ACCOME and EC-Hamamatsu codes, the total EC-driven current is 3 kA, and the peak EC-driven current density corresponds to ~20% of bootstrap current density at the q=2 surface.

Temporal evolution of magnetic perturbation amplitude is shown in Fig. 5(a), where phase difference between magnetic probe signal and gyrotron power $P_{\rm gyr}$ is 0°, 90° and 180°. For the 0° case, the mode amplitude decreases during the ECCD. For the 90° case, no clear effect of ECCD is seen, and for the 180° case, increase of mode amplitude, that is, NTM destabilization is observed. Detailed scan of the phase difference shows that O-point ECCD corresponds to the case when the phase difference is about −10°. Thus, the 0° case and the 180° nearly correspond to O-point ECCD and X-point ECCD, respectively. From this figure, it can be seen that phase difference should be properly controlled to stabilize an NTM efficiently. Expanded figure of magnetic probe signal and gyrotron power for each case is shown in Figs. 5(b)–(d). As shown in these figures, the phase difference is successfully scanned by using the newly developed system. It was also found that the stabilization effect defined by the initial decay time of the magnetic perturbation amplitude increases with deviating from the optimum phase difference: the decay time is doubled when the deviation becomes ±50°.

It is considered that modulated ECCD is more effective in stabilizing an NTM than unmodulated ECCD. However, experimental verification for an m/n=2/1 NTM has not been done yet. In JT-60U, it was found that the initial decay time for modulated ECCD is less than half of that for unmodulated ECCD with almost the same (peak) EC wave power. This shows that required EC wave power can be reduced significantly by modulating the EC wave.

4 Long duration sustainment of high-beta plasmas above no-wall limit through resistive wall mode suppression [20]

In the 2008 campaign, experiments on high-beta plasmas above the no-wall limit are focused on the extension of the duration. Typical discharge of a high-beta discharge is shown in Fig. 6, where plasma parameters are as follows: $I_{\rm p}$=0.9 MA, $B_{\rm t}$=1.44 T, R=3.43 m, a=0.91 m, q_{95}=3.2. As shown in Fig. 6(a), the plasma volume is relatively large to enhance the wall stabilization effect, but not so large as to increase metal impurity from the wall. In this discharge, beta value was first increased by positive-ion-based NBs alone, and then some of the perpendicular NBs were turned off to replace with negative-ion-based NBs. The change of the injection pattern is effective in avoiding the instabilities which trigger RWMs (described later) by increasing in the plasma rotation velocity and at the same time reducing trapped particle component of fast ions. The value of the normalized beta was kept at ~3.0 by feedback control on NBs. The no-wall beta limit, $\beta_{\rm N}^{\rm no\text{-}wall}$, calculated by an ideal MHD stability code MARG2D [21] is ~2.6, which corresponds to $3.0\ell_{\rm i}$. Here, $\ell_{\rm i}$ is the internal inductance. The beta limit with an ideal wall, $\beta_{\rm N}^{\rm ideal\text{-}wall}$, is calculated to be ~3.2 corresponding to $3.8\ell_{\rm i}$. The value of

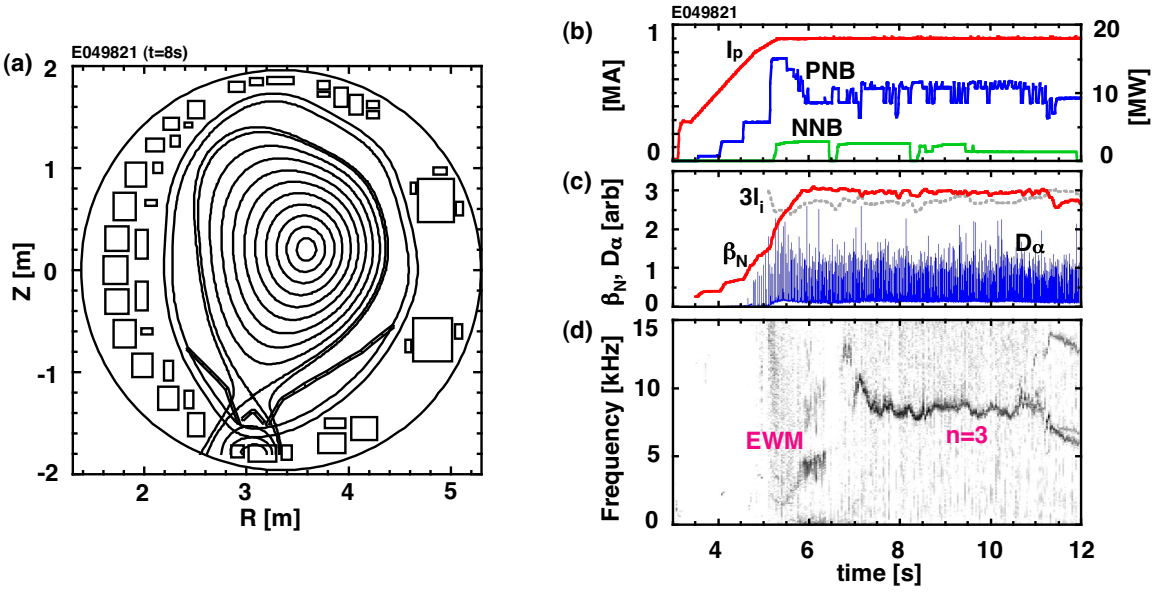

Fig. 6 Typical discharge of sustainment of a high-beta plasma above the no-wall limit. (a) Plasma cross section, (b) plasma current and injection power of NB, (c) normalized beta and D_α intensity, (d) frequency spectrum of magnetic perturbations, .

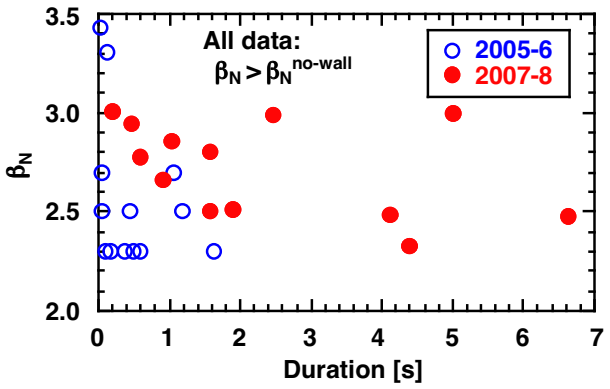

Fig. 7 Sustained value of the normalized beta versus duration. All data reach a beta value above the no-wall limit. Open circles and closed circles correspond to the data in 2005–6 and 2007–8, respectively.

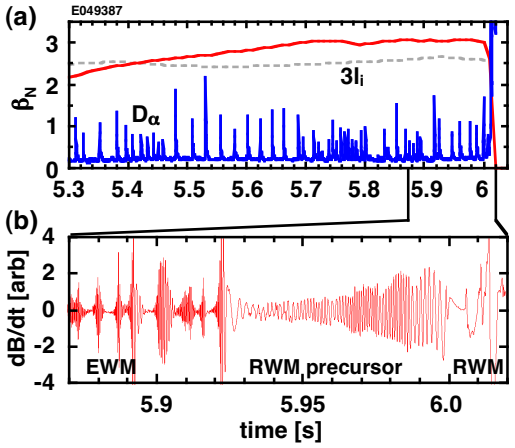

Fig. 8 Example of EWM and RWM precursor. (a) β_N and D_α intensity and (b) expanded figure of magnetic perturbations.

$C_\beta \equiv (\beta_N - \beta_N^{\text{no-wall}})/(\beta_N^{\text{ideal-wall}} - \beta_N^{\text{no-wall}})$, which indicates how close to the ideal wall limit the beta value is, reaches about 0.3. In this discharge, the no-wall beta limit gradually increases in time due to current penetration and β_N becomes smaller than $3\ell_i$ at t=11.2 s. The duration of high beta above the no-wall limit is about 5 s, which corresponds to 3 times the current diffusion time. Progress in sustained duration of high-beta plasmas above the no-wall limit is shown in Fig. 7. Note that all of the data points are the ones with $\beta_N > \beta_N^{\text{no-wall}}$. Although the duration was limited to less than 1.6 s in 2005–6, it has been significantly extended in 2007–8.

In this series of discharges, two kinds of instabilities appeared and limited the discharge duration through the onset of RWM: one is a fishbone-like instability termed *Energetic particle driven Wall Mode* (EWM), and the other is a slowly glowing mode termed *RWM precursor*. Both instabilities are observed only at $\beta_N > \beta_N^{\text{no-wall}}$, and one of them or both of them appeared in many of the high-beta discharges. Figure 8 shows an example where both EWM and RWM precursor are observed before an RWM. It is found that the EWM is triggered by an ELM or an EWM and has the following characteristics: (a) the growth and decay time are a few milliseconds, which is comparable to the resistive wall time τ_w, (b) n=1 and m=3–4, (c) no phase inversion in electron temperature measured with electron cyclotron emission diagnostics, that is, no island structure, (d) much larger amplitude at the low-field side than at the high-field side, (e) frequency chirping, (f) mode amplitude correlating with the power of perpendicular NBs. The EWM is different from the so-called fishbone instability in that the EWM is observed even when the central safety factor is above unity. The RWM precursor has the following

characteristics: (a) the growth time is 10–50 ms ($\gg\tau_w$), (b) n=1 and m=2–3, (c) no island structure, (d) a kink-ballooning-like mode structure, (e) it decreases V_t and/or dV_t/dr. In this series of experiments, it was found that the EWM appears and triggers RWM even when rotation velocity and its shear are enough high for RWM stability. In addition, the RWM precursor decreases the rotation velocity and its shear and triggers RWM. Thus, control of energetic particles and rotation velocity/shear was found to be important for RWM stability.

5 Physics assessment for JT-60SA

The JT-60SA device, equipped with toroidal and poloidal coils with superconducting magnets, will be installed in the present JT-60 torus hall [22, 23]. A birds-eye view of JT-60SA is shown in Fig. 9. The mission of JT-60SA is early realization of fusion energy by supporting exploitation of ITER and performing research toward DEMO. The maximum plasma current is 5.5 MA with a low aspect ratio (~2.5) plasma, and ~3 MA for an ITER-shaped plasma. Inductive operation with a flat top duration up to 100 s will be possible within the total available flux swing. As in the JT-60U experiments, control of NTM and RWM is an important issue in JT-60SA. For RWM control, in-vessel coils are to be installed in addition to passive conducting wall. For NTM control, the 110 GHz EC wave system will be reused with improvements in the pulse width and power. Other components for the JT-60U facility, such as NB and diagnostic system, will be reused. Since the heating/current drive system is needed to be upgraded for the JT-60SA operation, R&D activities are being done in parallel with the construction.

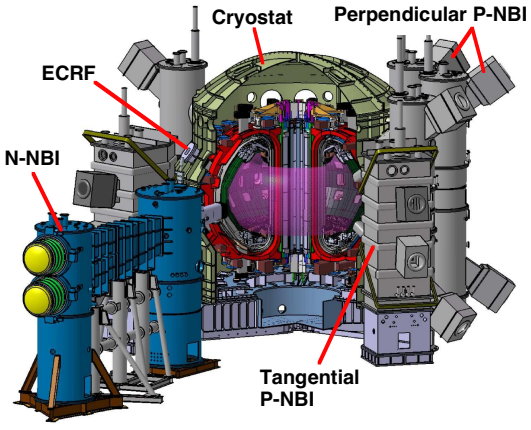

Fig. 9 Birds-eye view of JT-60SA.

6 Summary

Significant progress has been made in JT-60U advanced tokamak research until the very end of its experimental campaign in August 2008. A high-integrated performance plasma with β_N~2.6, $H_{H98(y,2)}$=1.0–1.1, f_{BS}~0.4, which satisfies the requirement of the ITER Hybrid Scenario, has been stationary sustained for 25 s ($14\tau_R$). Stabilization of an m/n=2/1 NTM with modulated ECCD has been successfully performed by modulating EC wave at ~5 kHz in synchronization with mode frequency. The superiority of modulated ECCD to unmodulated ECCD by a factor more than 2 has been shown experimentally. A high-beta plasma above the no-wall limit has been sustained for ~5 s (~$3\tau_R$). Two new instabilities which appear only at $\beta_N > \beta_N^{\text{no-wall}}$, energetic particle driven wall mode (EWM) and RWM precursor, have been observed. Design activity for JT-60SA is undergoing. Physics assessment is also being done for advanced tokamak research.

[1] M. Shimada, D.J. Campbell, V. Mukhovatov *et al.*, Nucl. Fusion **47**, S1 (2007).
[2] Y. Kamada, T. Fujita, S. Ishida *et al.*, Fusion Sci. Tech. **42**, 185 (2002).
[3] S. Ide, the JT-60 team, Nucl. Fusion **45**, S48 (2005).
[4] A. Isayama, the JT-60 Team, Phys. Plasmas **12**, 056117 (2005).
[5] H. Takenaga, the JT-60 team, Nucl. Fusion **47**, S563 (2007).
[6] N. Oyama, A. Isayama, T. Suzuki *et al.*, Nucl. Fusion **47**, 689 (2007).
[7] Y. Ikeda, A. Kasugai, S. Moriyama *et al.*, Fusion Sci. Technol. **42**, 435 (2002).
[8] A. Isayama, Y. Kamada, N. Hayashi *et al.*, Nucl. Fusion **43**, 1272 (2003).
[9] K. Nagasaki, A. Isayama, S. Ide *et al.*, Nucl. Fusion **43**, L7 (2003).
[10] N. Hayashi, A. Isayama, K. Nagasaki *et al.*, J. Plasma Fusion Res. **80**, 605 (2004).
[11] K. Nagasaki, A. Isayama, N. Hayashi *et al.*, Nucl. Fusion **45**, 1608 (2005).
[12] A. Isayama, N. Oyama, H. Urano *et al.*, Nucl. Fusion **47**, 773 (2007).
[13] S. Takeji, S. Tokuda, T. Fujita *et al.*, Nucl. Fusion **42**, 5 (2002).
[14] M. Takechi, G. Matsunaga, N. Aiba *et al.*, Phys. Rev. Lett. **98**, 055002 (2007).
[15] N. Oyama, the JT-60 Team, *Fusion Energy 2008* (Proc. 22nd IAEA Fusion Energy Conf., Geneva (IAEA, Vienna)) IAEA-CN-165/OV/1-3 (2008).
[16] D.R. Mikkelsen, Phys. Fluids B **1**, 333 (1989).
[17] A. Isayama, G. Matsunaga, T. Kobayashi *et al.*, *Fusion Energy 2008* (Proc. 22nd IAEA Fusion Energy Conf., Geneva (IAEA, Vienna)) IAEA-CN-165/EX/5-4 (2008).
[18] S. Moriyama, T. Kobayashi, A. Isayama *et al.*, *Fusion Energy 2008* (Proc. 22nd IAEA Fusion Energy Conf., Geneva (IAEA, Vienna)) IAEA-CN-165/FT/P2-26 (2008).
[19] T. Kobayashi, M. Terakado, F. Sato *et al.*, submitted to Plasma Fusion Res. (2008).
[20] G. Matsunaga, Y. Sakamoto, N. Aiba *et al.*, *Fusion Energy 2008* (Proc. 22nd IAEA Fusion Energy Conf., Geneva (IAEA, Vienna)) IAEA-CN-165/EX/5-2 (2008).
[21] S. Tokuda, T. Watanabe, Nucl. Fusion **6**, 3012 (1999).
[22] M. Kikuchi, *Fusion Energy 2006* (Proc. 21st IAEA Fusion Energy Conf., Chengdu (IAEA, Vienna)) IAEA-CN-149/FT/2-5 (2006).
[23] M. Matsukawa, M. Kikuchi, T. Fujii *et al.*, Fusion Eng. Design **83**, 795 (2008).

Proceedings of ITC18, 2008

Issues of Perpendicular Conductivity and Electric Fields in Fusion Devices

Michael TENDLER[1)]

[1)]*Alfvén Laboratory, KTH, Stockholm, Sweden*

At present it is well understood that the key element in the transition physics is the origin of the strong radial electric field and suppression of the turbulence fluctuation level by a strong poloidal rotation in the $\boldsymbol{E} \times \boldsymbol{B}$ fields. As a result, the transport coefficients are strongly reduced at fixed places and transport barriers with steep density and temperature gradients are formed near the separatrix or the last closed flux surface (ETB) or in the core region (ITB). The key element in the transition physics is the origin of the strong radial electric field. The issue depends crucially on the perpendicular conductivity. The impact of the momentum transport is brought to light.

Keywords: LH transitions, ExB shear suppression, Anomalous Momentum Transport

1 Introduction

Turbulence can be regarded as randomly fluctuating rapid motion of the fluid. It is an ubiquitous phenomenon in nature and is an effective way of transporting energy quickly as opposed to neoclassical collisional diffusion which is a very slow process in comparison. In fusion plasma parameter gradients determine turbulence and various transport modes which is the process through which particles, and energy in the centre of the plasma are lost to surrounding walls.

We need to gain insights into the control of plasma turbulence which is the most important factor working against the efforts towards fusion. There is accumulating evidence from fusion experiments that regimes with improved confinement can achieve higher values of confinement, beta and bootstrap current than had been thought plausible until recently. In spite of the extra free energy available from increased gradients in the improved confinement state, the $\boldsymbol{E} \times \boldsymbol{B}$ velocity shear allows the plasma to organize itself into a state of lower turbulence and transport.

This new way to improve confinement is bound to have a major impact on fusion as an energy source for the future. Transport barrier dynamics is the key scientific concern at present. The interest is enhanced by the fact that a continuously operated fusion reactor will not be operated at a steady-state, since for control purposes, it will necessarily require barriers to be created or lowered from time to time in different portions of a plasma to facilitate a reactor operation. Transport barriers will have to be controlled for operation purposes.

Recently, strong arguments addressing the validity and the experimental evidence in favour of the crucial role played by the profile of the electric field during LH transitions has been brought to light. Indeed, it was shown that the radial electric field is negative in the core region and positive in the SOL provided no momentum injection is employed to accelerate plasma in the toroidal direction [1,2]. Radial electric field inside the separatrix is close to the neoclassical electric field profile for a wide set of plasma profiles provided no external momentum injection by unbalanced neutral beam is employed [3]. In contrast, toroidal rotation is governed by the anomalous viscosity, shear Reynolds stress and zonal flows [4, 5].

In hindsight, the bifurcation models aimed at explaining the LH transitions and invoking current caused by the ion orbit loss [6, 7] were not confirmed experimentally. There, the current caused by the ion orbit loss is balanced by the current driven by non-linear neoclassical parallel viscosity yielding the bifurcation of the poloidal rotation. Yet, it was demonstrated experimentally [2] that the LH transition can be obtained also at a high collisionality regime where the ion orbit loss impact is negligible. Moreover, the poloidal rotation, which should be of the order of the poloidal sound speed also contradicts the experiment, where the radial electric field is determined by the density and temperature gradients. Furthermore, from the theoretical viewpoint the anomalous (specifically momentum) transport has been neglected. In addition, the ultimate necessity to reconcile their model put forward to explain transitions into regimes with improved confinement with first principles should not be overlooked [8]. To this end, it has been emphasized that models based only on ion–orbit loss mechanism do not satisfy this fundamental constraint due to the inherent inconsistency with the neoclassical theory. The error emerges because the $\boldsymbol{j} \times \boldsymbol{B}$ force (caused either due to ion orbit losses or any other reason) has obviously no parallel component whereas the parallel neoclassical viscosity cancels exactly in the toroidal direction according to the neoclassical theory.

Along alternative school of thought, the turbulence has been put forward as a major player behind the transition into regimes with improved confinement. The spin-up of the poloidal rotation has resulted from the poloidal asymmetry of anomalous transport or the shear Reynolds

author's e-mail: mtendler@kth.se

stress [9, 10]. However, the impact of the toroidicity has been either totally or partially neglected and the neoclassical flows and currents were overlooked. Here, it is iterated that many experimentally observed features may be assessed employing the synergy of the neoclassical theory for the electric field profiles with an anomalous momentum transport mechanism emerging due to zonal flows. The radial electric field profile is determined by the momentum balance equations including both neoclassical effects and zonal flows [11]. They have demonstrated that the radial electric field is close to the neoclassical value for not too steep density and temperature profiles. However in contrast to standard neoclassical theory, the toroidal rotation velocity is mainly determined by anomalous transport of the parallel and toroidal momentum via effective anomalous viscosity. Furthermore, the radial electric field shows no bifurcation and the origin of the strong electric field shear is governed by the self-consistent evolution of plasma profiles and electric fields. The bottom line is the sensitivity of the solution of transport equations with diffusivities governed by the shear of the electric field to subtle details of equilibrium density and temperature profiles. Indeed, they are dependent on both gradients and curvatures of evolving profiles. Boundary conditions imposed on the interface of plasmas with discontinuous values of the electric field play also a crucial role yielding unconventional solutions. Hence, it is important to bear in mind that transport is not determined by local densities or temperatures, but globally by subtle details of their profiles thereby making diffusive time scales in principle irrelevant. Indeed, the high sensitivity of a diffusivity (this may be particle, momentum, energy etc.) to subtle details of equilibrium profiles arising due to the dependence of fluxes on the first and second derivatives of equilibrium profiles has been put to light within the framework of the $\boldsymbol{E} \times \boldsymbol{B}$ shear suppression paradigm [12].To this end, the notion of subthreshold transitions (lacking a bifurcation and below the power limit) has been brought about. Scenarios describing this kind of transitions occur primarily due to mentioned above peculiarities of anomalous diffusivities. They have been coined "Tunneling Transitions" in analogy with Quantum Mechanics.

Finally, an insight is offered addressing both Internal and Edge Transport Barriers (ITB and ETB) from the same angle. These might have their common origin caused by the interface of plasmas with different configurations of confinement thereby providing a large shear of the electric field. The eloquent example of this idea takes place at the separatrix where the electric field within the SOL is governed by a contact with plates. This has to match the self-generated electric field on closed field lines governed by plasma flows and magnetic field geometry. Another example is confronted within the bulk plasma when chains of islands located in the vicinity of rational surfaces interface with the main plasma body yielding the amplification of the shear of the electric field. Within the SOL plasma the impact of the shear of the electric field maybe also important for the dynamics of blobs. Within the framework of neoclassical theory, the focus is on a confined region and this matching procedure may be provided by the impact of boundary conditions.

2 The Impact of the $\boldsymbol{E} \times \boldsymbol{B}$ Shear on Turbulence

The bottom line of the $\boldsymbol{E} \times \boldsymbol{B}$ shear concept consists of two issues: the impact of the $\boldsymbol{E} \times \boldsymbol{B}$ drifts on a residual turbulence and a more difficult question about a plausible origin of significant temporal and spatial variations of the electric field within the plasma volume [13].

Turbulence almost always coexists with large mean flows. In plasmas flows are self-generated either due to toroidicity (neoclassical) or due to turbulence (zonal) or externally imposed due to any form of physical or virtual biasing. Turbulence is fed into plasmas via energy cascades due to local or global instabilities. In the L mode turbulent 3D flows prevail characterized by strong turbulent fluctuations causing small mean shear flows. If this is the case particle trajectories are chaotic and turbulent transport is very large. In contrast, in the H mode turbulent fluctuations are strongly reduced. Strong mean shear flows emerge and more regular trajectories lead to the reduced transport of moments.

Energy cascades to larger scales in magnetized plasmas is a well-known phenomenon describing a mean flow at low k numbers due to the spectral condensation. It is the finite-system-size phenomenon requiring low dissipation in a bounded system. Mean flow generation provides the evidence for suppression of turbulence by a mean shear of the flow. Shearing acts more efficiently on large scales. Assuming an appearance of the mean flow due to the drift in the electric field, theory predicts complete stabilisation of various modes with the increment $\gamma_{\max}$ by the $\boldsymbol{E} \times \boldsymbol{B}$ rotational shear rate γ_{E} provided

$$\gamma_{\mathrm{E}} > \gamma_{\max} \tag{1}$$

$$\gamma_{\mathrm{E}} = \frac{RB_\theta}{B} \frac{\partial (E_r / RB_\theta)}{\partial r}, \gamma_{\max} - \text{linear growth rate}$$

Therefore, the complete stabilisation is the mode specific feature providing for the ample suppression of a dominant turbulence channel (i.e . Ion Temperature Gradient mode driven turbulence in discharges with the ITB's). The main physical effect relies upon an amplified damping due to an interaction between an unstable mode with a nearby, stable mode and the resulting from it the increase of the Landau damping of an unstable mode.

However, a bulk of other modes usually unstable and detrimental to confinement under conventional tokamak operation mode such as Trapped Electron and/or Electron Temperature Gradient modes remain the cause of enhanced losses.

In general, the turbulence consists of short-lived eddies, rather than coherent vortices. Therefore, the break-up of coherent vortices described above has never been observed experimentally.

In reality, the shear leads to the reduction in the eddy lifetimes according to the following formula. Shearing rate can be calculated as the function of the poloidal velocity profile as

$$\gamma_{\rm E} = L \times \left[\frac{{\rm d}\Omega}{{\rm d}r} = \frac{1}{r}\frac{{\rm d}V_\theta}{{\rm d}r} - \frac{V_\theta}{r^2} \right]$$

where L is the scale of a plasma slab.

Indeed, the effective growth rate $\gamma_{\rm c}$ can be shown to decrease dramatically according to

$$\gamma_{\rm c} = (\Delta\omega_{\rm D}\gamma_{\rm E}^2)^{1/3} \tag{2}$$

where $\Delta\omega_{\rm D}$ is the nonlinear decorrelation rate in absence of the $\boldsymbol{E} \times \boldsymbol{B}$ shear.

Hence, the imposed rotation by the $\boldsymbol{E} \times \boldsymbol{B}$ flow leads to turbulence reduction. In more detail, mean flows enforce vortices into the relative motion to the magnetic field thereby reducing energy input into the turbulence drive. The mechanism has a potential to benefit confinement provided an option to affect the electric field profile may be found.

3 The Origin and Features of the Electric Field

The difficult issue is how plasma can generate an electric field profile in order to fulfill stringent requirements for turbulence suppression imposed on the shear of the electric field profile. To elucidate the origin of the electric field in plasma and possible causes for the omnipresence the following equation stringently derived from the neoclassical theory provides the first insight

$$E_{\rm r} = \frac{1}{Z_{\rm i} e n_{\rm i}}\frac{\partial p_{\rm i}}{\partial r} - B_\phi v_\theta + B_\theta v_\phi \tag{3}$$

Here, the beneficial impact of the electric field seems to be assured if an electric field $E_{\rm r}$ and contributing to it poloidal and toroidal rotation velocities provide for the stringent requirement imposed on the shear. Therefore, there are basically three "knobs" (diamagnetic drift, poloidal and toroidal rotations) affecting the radial electric field. In real conditions, all of them evolve simultaneously both in space ant in time thereby contributing to the complexity of the issue.

According to standard neoclassical theory (i.e. ignoring regions with steep gradients of plasma parameters) this is found in toroidal geometry to yield

$$E_{\rm r}^{(NEO)} = \frac{T_{\rm i}}{e}\left[\frac{{\rm d}\ln n}{{\rm d}r} + (1-k)\frac{{\rm d}\ln T_{\rm i}}{{\rm d}r} \right] + B_\theta v_\phi \tag{4}$$

where k is the constant dependent on collisionality.

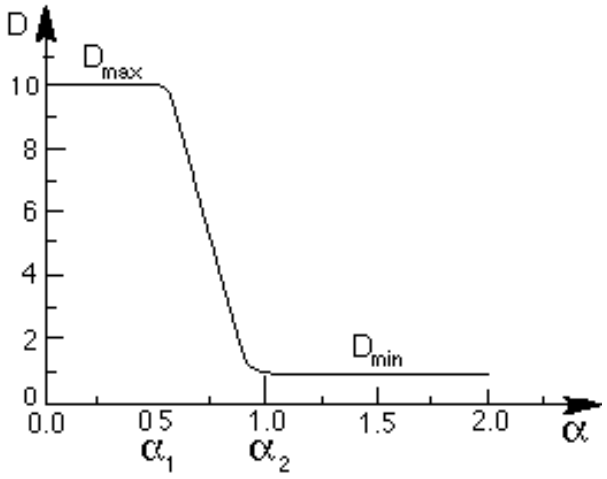

Fig. 1 Tentative dependence of a diffusivity on the shear of the electric field.

Although Eq.(4) is the subject to stringent constraints (the absence of unbalanced neutral beam injection and the lack of regions with steep gradients of the order of the poloidal gyroradius) it provides many useful insights, in particular during an initial stage of the transition. Indeed, employing Eq.(4) the shear of the electric field results to depend on both gradients and curvatures of density and temperature profiles.

4 Main Features of the Model

The transport barrier is modeled by diffusion equations with arbitrary diffusivities taken as functions of the shear of the electric field ${\rm d}E/{\rm d}r \sim \alpha$ Hence, the system of governing equations reads

$$\frac{\partial n}{\partial t} - \frac{\partial}{\partial r}\left[D(\alpha)\frac{\partial n}{\partial r} - V(\alpha)n \right] = S. \tag{5}$$

This model equation is assumed to describe any kind of transport such as the particle and heat transport, the toroidal and poloidal momentum transport and the turbulence transport. The parameter α is proportional to the shear of the radial electric field. Tentative plot of diffusivities $D(\alpha)$ as the function of shear α is shown on Fig.1.

At first, in order to gain insights into the physics governing transport under these assumptions few comments following from simple analytical considerations are offered. To this end, we wish to make an important point commenting on the crucial importance of the dependence of transport on the first order versus the second order derivatives of plasma profiles. In more detail, the flux either emerges to be a function of only gradients and/or curvature of density and temperature profiles. If the former situation is the case then the plot of the flux $\Gamma = -D{\rm d}n/{\rm d}r$ versus the gradient takes the useful form yielding the effect of the flux bifurcation usually invoked in order to explain the LH transition (the S - curve).

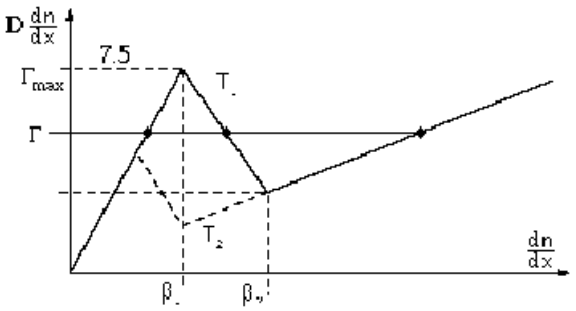

Fig. 2 Simplified picture of transitions ignoring second derivatives of plasma profiles.

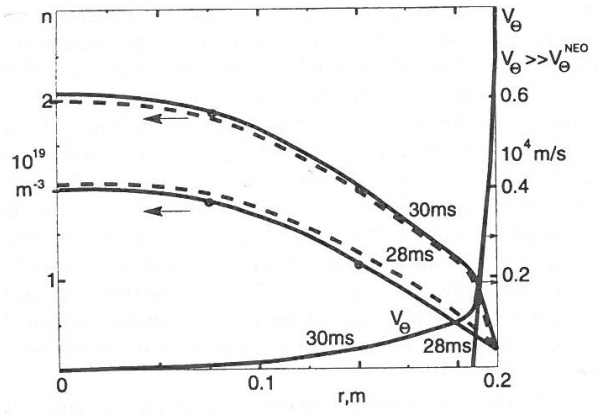

Fig. 3 Scenarios of two LH transitions. Full curves are transitions triggered by poloidal rotations, broken curves are transitions triggered by density depletions with poloidal rotation imposed to zero.

Therefore, ignoring the dependence of the shear of the electric field on the second derivative of a profile the scenario of the transition is significantly simplified and emerges either as dwelling on the left or the right branches of this curve. The straightforward and fast transition occurs then $\Gamma > \Gamma_{max}$. The case of $\Gamma = \Gamma_{max}$ describes the situation when prelude profiles prior to the transition represent an equilibrium unstable to an arbitrary perturbation. Therefore, an option of the transition caused entirely due to the diamagnetic drift (without employing a change in plasma rotation see Eq.(3)) emerges. In reality, the flux is a function of both gradients and/or curvatures of density and temperature profiles. Employing the first term in square parenthesis for the self-consistent electric field as yielded by the neoclassical theory one obtains an important estimate for the shear of the electric field

$$\alpha \sim \left| \mathrm{d}E_r/\mathrm{d}r \right| \sim \mathrm{d}^2 \ln n/\mathrm{d}r^2 \sim \left[(n'/n)^2 + n''/n \right] \quad (6)$$

Focussing on the first term the beneficial effect for a transition of an amplification of the density gradient without changing the local density at the same time is clearly seen from Eq.(6) because it provides more shear of the electric field for given values of other parameters. This may be brought about at the plasma edge by injecting small pellets tangentially as shown also in recent experiments addressing H-mode and Internal Transport Barriers carried out on the DIII-D tokamak and the LHD stellarator, where H and ITB plasmas have been directly produced by injecting frozen deuterium pellets into the L-mode plasma. The pellet triggers the transition at lowered edge temperatures indicating that a critical plasma temperature is not required for the transport barrier. The pellets are also able to lower the threshold power required to produce the H-mode transition indicating an agreement with predictions of the model.

On the other hand, it is obvious that for a given gradient of a density profile, it is easier to trigger a transition scenario at locations with a lower density i.e. at the edge of a confined region born out during the LH transition. Hence, it becomes obvious why LH transitions with the pedestal located at the edge were the first to be found among plentiful other regimes with improved confinement.

Notwithstanding transparency and clarity of arguments based upon Eqs. (5 and 6), it is important to bear in mind that within a spatial range of a plasma body characterised by steep gradients (i.e. plasma parameters within the transport barrier) the neoclassical expression Eq.(4) cannot be adopted everywhere because assumptions employed in deriving them are not justified uniformly. Therefore, the electric field has been found self-consistently from the poloidal balance coupled with the concurrent evolution of plasma profiles [3]. Note, it can be shown that Eqs.(5 and 6) unfold when neoclassical terms dominate. In other words, the neoclassical parallel viscosity is the governing factor providing for the ambipolarity.

At this point, the issue of causality for transitions into regimes with improved confinement such as the LH transition comes to mind. Indeed, the problem is whether the trigger is due to a change in the rotational $\boldsymbol{V} \times \boldsymbol{B}$ term or the pressure gradient term of main ions. Here, it is important to keep in mind that a steep pressure gradient has a potential to provide for large local values of the electric field by its own virtue according to Eq.(3). However, this effect can be either counteracted or reinforced depending on a quantitative impact rendered by both poloidal and toroidal rotations.

To this end, it has to be kept in mind that due to technical difficulties, it is almost impossible to answer questions related to causality experimentally because the resolution of the majority of diagnostics adopted on many devices is too slow to address the causal dependence in depth. Furthermore, data reported from JET on the magnitude and sign of the poloidal rotation contradicts the same data obtained by the DIII-D team. Yet, a scenario of the transition triggered entirely by the diamagnetic term emerges spontaneously provided the given form of prelude profiles is assumed. Importantly, the explicit dependence of the shear on the curvature merits a special emphasis because this enables a transition below the threshold $\Gamma < \Gamma_{max}$. This result

is supported both by analytical and numerical calculations. In more detail, the scenario of the transition resulting from solutions of the model Eq.(7) yields a very fast propagation of the front of improved confinement (see Fig.3) in comparison with the random walk estimate (straight line in Fig.3) based upon the conventional diffusive model. The main reason for this is the decorrelation of fluctuations carried up and down between the moving front of improved confinement and a separatrix. Therefore, the solution of the model Eq.(5) obtains convective features significantly reducing the effective time scale required by the transition. Hence, experimental studies showing the quench of turbulence on a very rapid time scale of the about 0.1 ms during the transition find its theoretical explanation.

In general, the transport is scale-free and any effective time scale does not exist at all under these circumstances because of the peculiarity of this kind of diffusivity. Hence, the important signature of self-organised systems relying upon intermittence and yielding avalanches is recovered. Two different scenarios along these lines were

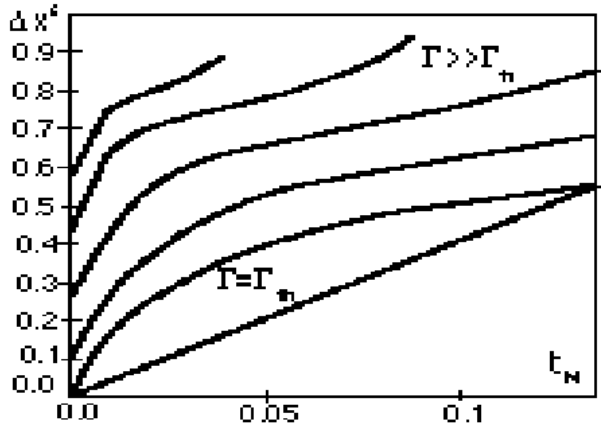

Fig. 4 Propagation of the front of Improved Confinement. Random walk width normalized to the width of the Barrier versus time in ms.

demonstrated before. It has been shown that the direct LH transition emerges provided the particle influx at the interface between the core and the thermal barrier was kept constant during the transition above the threshold value. In contrast when a possibility of the feedback has been taken into account the second (time dependent nonlinear regime) arises due to an interaction between inlet and outlet boundary conditions resulting from the feedback of the flux in the core on the flux into the SOL. The second constraint required obtaining a monotonic and time dependent solution is due to the dependence of the core flux on the varying density at the interface.

In the first scenario, the steepening of the density evolves gradually from the separatrix up the interface due to the reduced diffusion, thereby bringing about the bifurcation evolving into the thermal barrier. In the second scenario, the outflow at the separatrix ($\sim D_\alpha$ signal) dithers, being linked to the flux at the interface whereas absolute values of density vary insignificantly. In general, if the dependence on the second derivative is taken into account the picture of the transition gets dramatically modified. Thence, there is a more global relation strongly dependent on the distribution of sources of moments within the plasma. Furthermore, even for a given distribution of sources, the relation between fluxes and gradients is not unique anymore. Hence, additional boundary conditions are required because the governing system of transport equations obtains the form of the higher order. Therefore, the peripheral plasma plays the crucial role in controlling the global confinement and affecting plasma profiles and local transport diffusivities. Moreover, properties of the plasma within the SOL must be within the restricted range if a stationary solution of transport equations is to be found at all.

Indeed, it has been shown before that a steady state solution does not emerge outside the narrow range of boundary conditions imposed on the density gradient at the separatrix. The only solution found for mixed Dirichlet boundary conditions describes autonomous oscillations implying dithering between the Low and the High Confinement. This regime has been also demonstrated on many devices. Time dependent solutions appear to be a subtle phenomenon arising due to peculiar features of the model equation and the choice of boundary conditions. Another important application along these lines arises considering the interface of chain of islands located at rational q surfaces with the rest of the plasma core. Therefore, the ITB may stem from the necessity to force a uniform electric field generated within a chain of magnetic islands (dwelling on rational q – surfaces) to match the neoclassical electric field primarily governed by temperature and density profiles. The electric field within the chain of magnetic islands is a constant due to fast mixing, while the neoclassical values are employed within the main plasma body. Therefore, steep gradients of the electric fields result from the matching because of the helical structure of neighboring magnetic surfaces. Indeed, the close proximity occurs at the location of O points poloidally whereas the maximum is at X points. Thus, the shear of the electric field is significantly amplified locally thereby triggering the front of the improved confinement to propagate inwards. Thus, the shear of the electric field emerges at these locations naturally and self-consistently. This conclusion appears to be generally valid and is not pertinent to any specific magnetic configuration.

5 The Link between the MHD activity and the Improved Confinement

It is specially interesting to apply this idea at the edge of the plasma, where rational surfaces are crowded and occasionally overlapping due to the MHD activity. In-

deed, during rise of the MHD activity the change of the edge radial electric field from negative (directed inward) to positive (directed outward) values has been observed in the Ohmic discharges on TUMAN-3M tokamak [14].Measurements were performed by means of Doppler reflectometry method and by using probe technique. According to the heavy ion beam probe (HIBP) diagnostics the potential in the central region of TUMAN-3M also changed sign and became positive during MHD events while normally it is negative. There are experimental evidences that MHD activity is associated with the rise of magnetic island at q =3 flux surface in the core few centimeters inside from the last close flux surface (LCFS). Also the rise of smaller islands at q=4 and q =2 surfaces is reported. Indeed, the overlapping of neighboring magnetic surfaces results in formation of a stochastic layer in the LCFS vicinity provided the width of the island is of the same order as the minimum distance between rational q-surfaces.

Along these lines, the model for the origin of the positive radial electric field during the rise of the MHD activity has been developed [15]. It is based on the emergence of a strong electron radial flux resulting from the formation of an ergodic layer. The radial electron flux requires the same radial flux of ions to provide quasineutrality. Hence, the emerging positive radial ion current provides the torque in the toroidal direction forcing the radial electric field to become more positive (see Eq.3). This situation is similar to the biasing experiments and corresponding theory has been already developed [11]. In the extreme case, when the electron conductivity associated with the stochastic layer dominates over the neoclassical ion cross-field conductivity, the radial electric field becomes positive inside the stochastic layer. In more detail, the radial ion current generates toroidal rotation in the co-current direction by the toroidal $\boldsymbol{j} \times \boldsymbol{B}$ torque, so the ergodic layer becomes the source of the toroidal momentum of the same kind as the NBI injection. The co-current toroidal rotation has to be transported outside the ergodic layer to the core by the anomalous cross-field viscosity thus creating the co-current toroidal rotation in the center of a tokamak even without external sources of momentum injection. The co-current toroidal rotation makes the radial electric field more positive also outside the ergodic layer and for sufficiently fast toroidal rotation the radial electric field becomes positive also in the central regions in accordance with the neoclassical theory.

In the tokamak physics there are several other areas, where the return ion current and associated plasma toroidal acceleration plays a crucial role. The external current of fast ions generated during NBI should be compensated by return radial current of the main ions. The external ion current can be also associated with the ICRH heating causing the loss of fast ions. Externally imposed toroidal magnetic field ripples or islands used for the divertor operation may be the source of the externally generated radial currents. Resonant Magnetic Perturbations normally not resulting in the stochastization of the magnetic field and corresponding loss of electrons can be successfully used for the mitigation of ELM's crucial for the ITER performance [16].

6 Transport within the Scrape-Off Layer

Recently, transport of edge plasmas in magnetic confinement fusion devices has been recognized to be mostly convective and intermittent. There is an ample experimental evidence of large amplitude turbulence interacting with polarization drifts. Highly inhomogeneous filaments easily penetrating across magnetic fields were coined "blobs". As a theoretical explanation, blobs which are long-living coherent structures have been invoked. Blobs are a transversal phenomena appearing in different toroidal magnetic devices, both tokamaks and stellarators. This phenomenon is strongly adverse to the divertor operation of fusion devices. It demonstrates the ubiquitous nature of transport phenomena at the periphery. A blob has the potential of significantly redistributing heat loads on the surrounding structures of a fusion reactor. It might also intervene with the divertor performance thereby affecting the ignition scenario on ITER. The role blobs play in the global edge plasma transport was highlighted by the experimental data from Alcator C-Mod showing that a large fraction of the plasma particle flux coming from the core into the SOL was indeed transported radially by blobs to the chamber walls and not toroidally to the divertor, as generally expected. The properties of turbulence-induced structures, namely radial velocities and radial scale lengths of blobs, together with the statistics of fluctuations of the plasma density and the particle radial drift flux were studied in the peripheral region of the High Field Side of the FT-2 tokamak. Also, the edge plasma poloidal velocity is measured through cross-correlation of floating potential signals. The experimental results were compared with existing theoretical models and other reported results [17]. A first model for individual blob dynamics considers isolated blobs to be the fundamental entity for convective transport in the SOL. It is assumed that due to an unknown non-linear processes, a filament with large plasma density is peeled off the bulk plasma, in some region close to the last closed flux surface (LCFS) and on the Low Field Side of a fusion device. Effective gravity drifts on this side of the torus (due to a curvature and a gradient of magnetic fields) caused by an $\boldsymbol{F} \times \boldsymbol{B}$ particle drift, will then result in a vertical charge polarization. The associated electric field generated will in turn gives rise to a radial $\boldsymbol{E} \times \boldsymbol{B}$ convection of the blob against the chamber wall. The resulting convection speed will depend on the magnitude of the electric field which in turn will be determined from the balance of perpendicular and parallel currents inside these structures. An equivalent circuit and possible current pathways elucidating the physical picture can be invoked and alternative closures for such

circuit can be envisaged, ranging from the current flowing through the electrode sheath on the divertor plates limited by the saturation to the cross-field ion polarization currents flowing through ambient SOL plasmas. Theoretical scalings of an isolated blob treated as a 2D structure, in order to compare blob properties and dynamics were compared with results obtained experimentally.

When the blob is assumed to be in the far SOL and parallel current is small and governed by the sheath "resistivity", we have a sheath-connected blob and arrive to a solution with the form of an isolated blob of plasma density traveling in radial direction with an estimated speed V_b given by:

$$V_\mathrm{b} = 2c_\mathrm{s}\left(\frac{\rho_\mathrm{s}}{\delta_\mathrm{b}}\right)^2 \frac{L_\parallel}{R} \tag{7}$$

Where c_s is the sound speed, ρ_s is the ion gyro-radius, δ_b is the poloidal scale length of the blob, $L_\parallel$ is the blob parallel length, and R the major radius. Alternative current closures besides the one already mentioned for the so-called sheath-connected (C) regime, are related to linear edge instabilities being the resistive ballooning (RB) or the ideal strong ballooning (IB) dependent on specific experimental conditions. In RB mode the current loops close locally in the mid-plane region of a fusion device. The scaling for the radial blob velocity in both RB and IB modes is given by the same analytical expression on Eq.(8).

$$V_\mathrm{b} = c_\mathrm{s}\sqrt{\delta_\mathrm{b}}/\sqrt{R} \tag{8}$$

Note that Eq.(7) stands for the C model and that both scalings are for isolated blobs propagating on vacuum, i.e. the influence of the background plasma is not taken into account. The effect of the background plasma can be seen on the decrease of the order of magnitude of the predicted acceleration of the filaments by a factor of 2-3. An expression to estimate the blob drift velocity similar to the one presented before for the C model:

$$V_\mathrm{b} = \frac{T_\mathrm{e}^\mathrm{plasma}}{eB\delta_\mathrm{b}} \tag{9}$$

This estimate employs the condition that the short-circuited parallel current density and the ion saturation current passing through the sheath are of the same order. It is assumed that in the H- mode regime with ELM's this condition might be satisfied. The comparison with experimental results is presented in [17]. The experimental data available for both HFS and LFS in tokamaks and stellarators concerning the blob characterization has also been reviewed, and the lack of a reasonable amount of results for the HFS has been emphasized.

Blob velocities and sizes were obtained by analysis of the time-resolved signals of radial flux and density. It was observed a predominant direction on the movement of the blobs towards the wall, especially in periods of time of the discharge prior to the LH transition. The order of magnitude of the experimental values for sizes and velocities of blobs was found comparable with the theoretical estimates. However, the experimental dependence between these two parameters, size and velocity, was only and roughly in agreement with one theoretical prediction, given for the so-called Ballooning modes given by Eq.(8). One should bear in mind though that the models invoked are for the LFS. Nevertheless, according to simple reasoning the potential should be constant along magnetic field lines and hence HFS blobs should also move outwards as predicted by the LFS models. We see both inwards and outwards directions of blob movements, which is a question left for theoretical understanding. It is important to emphasize that blobs moving inwards may provide an important source of fuelling the core in the super dense mode discovered recently on LHD. We have also suggested the introduction of an additional coefficient to better fit the experimental values with the equation deduced for the ballooning modes.

The characterization of blobs is a task not yet complete. 3 Dimensional models based on PIC simulations may provide important information on the self-consistent evolution of ion density and electric field profiles. There is a need to improve the world's database on these structures in order to better understand this phenomena and the convective radial transport caused by turbulence in synergy with the convection.

7 Conclusions

The model invoking the paradigm of shear suppression addresses many effects observed experimentally. Indeed, it yields novel insights and conclusions consistent with measurements. For example, it points us toward the insight that both zonal and neoclassical flows are crucial for improvements in confinement. In general, it has to be kept in mind that the phenomena of transport barriers are very robust and sensitive only to prelude profiles. The most important practical conclusion from ideas and insights offered above that issues of perpendicular conductivity and electric fields are crucial for progress of the fusion research.

Acknowledgements

The work was supported by the Royal Swedish Academy of Engineering Sciences. Numerous discussions with Drs. O. Motojima, V.Rozhansky and G.VanOost are gratefully acknowledged.

[1] M. Tendler, Plasma Phys. and Controlled Fusion **13**, 191 (1990).
[2] K Ida *et al.*, Phys.Rev. Lett. **86**, 5297 (2001).
[3] V.Rozhansky and M. Tendler, *"Reviews of Plasma Physics"* vol.**19**, ed. B.B.Kadomtsev (New York and London, Consultants Bureau) (1996).
[4] A.Fujisawa *et al.*, **82**, 2669 (1999).

[5] K. Itoh *et al.*, Phys. Plasmas **12**, 072512 (2005).
[6] S.-I.Itoh and K.Itoh, Phys.Rev.Lett. **60**, 2276 (1988).
[7] K.C.Shaing and E.C.Crume, Phys.Rev.Lett **63**, 2365 (1989).
[8] Y.B. Kim and F. Hinton, Phys. Fluids **B4**, 278 (1992).
[9] A.Hassam *et al.*, Phys.Rev.Lett **66**, 309 (1991).
[10] B.A.Carreras *et al.*, Phys. Fluids **B3**, 696 (1991).
[11] V. Rozhansky and M.Tendler, Phys. Fluids **B4**, 1877 (1992).
[12] M.Tendler, Plasma Phys. and Controlled Fusion **B39**, 371 (1997).
[13] H. Biglari, P.Diamond and P.W.Terry, Phys. Fluids **B2**, 1 (1990).
[14] L. Askinazi *et al.*, Plasma Phys. and Controlled Fusion **48**, A85 (2006).
[15] E. Kaveeva, V. Rozhansky and M. Tendler, Nucl. Fusion **48**, 075003 (2008).
[16] T.Evans, *et al.*, Nucl. Fusion **48**, 024002 (2008).
[17] J.Vicente, S.I Lashkul, E. Vekshina and M.Tendler, Plasma Phys. and Controlled Fusion *in press* (2009).

Proceedings of ITC18, 2008

Experimental Confinement Studies Beyond ITER

Akihide FUJISAWA

National Institute for Fusion Science, Oroshi-cho, Toki 509-5292, Japan

The advantages of stellarators are discussed with a strong emphasis on the high density limit more than 10 times higher than that of tokamaks with the equivalent magnetic field strength. The comparison between stellerators and tokamaks in the light of the new paradigm of plasma turbulence and zonal flows is presented to propose a new optimization principle of magnetic field configuration. The roles of low-temperature devices should be recognized for further understanding of the plasma confinement even in the era of burning state plasmas

Keywords: tokamaks, stellerators, density limit, zonal flows, flow damping, principle of configuration optimization, low temperature devices

1 Introduction

The research aiming at realizing a sun on the earth has been carried out for more than fifty years. The efforts have advanced the physics of magnetically confinement along with the development of fusion technologies. A wide variety of the toroidal magnetic field confinement have been tested, such as tokamaks, spherical tokamaks, stellarators including many kinds of configurations (*e.g.,* heliotron, heliac, and helias), reversed field pinches, bumpy tories, magnetic mirrors, and so on.

At present a device, ITER, is being constructed to realize a tokamak plasma in burning state. This is because the tokamak is the leading concept of the magnetically confinement fusion, where a number of records, in fact, have been made. The followings have been achieved for instance; the ion temperature of 40 keV and the fusion product of 1.5×10^{20} m$^{-3} \cdot$ s $\cdot$ kev in JT-60U, the electron temperature of 20 keV in ADEX-U, the confinement time of 1.2 s and the stored energy of 17 MJ in JET. The spherical tokamak, with an extremely low aspect ratio of less than 2, has achieved the highest β of ~40%, together with high plasma confinement due to the large capacity of plasma current [1].

The studies of other magnetic configurations, however, should still continue to be carried out to demonstrate their own advantages or individualities that can supplement the absent characteristics of standard tokamaks. For example, the nominal currentless characteristic of stellarators makes the steady state operation of the discharges much easier. The comparative studies of various concepts should be necessary to optimize magnetic field configuration in terms of confinement, energetic particle behaviour etc., and to realize an advantageous device adopting the merits of different concepts in terms of the economic and steady state operation. This paper will discuss several physical and experimental topics for obtaining a better solution of a magnetically confined fusion device in future.

author's e-mail: fujisawa@nifs.ac.jp

2 Advantages of Stellarators

2.1 High Density Operation of Stellarators

The simple coil geometry of tokamak requires the internal plasma current to produce rotational transform for the plasma confinement. The resultant confinement field has an axisymmetric nature to serve the good confinement property, however, the external current drive is mandatory for steady state operation. Moreover, the toroidal current is the cause to determine the density limit of the modern tokamak operation before the Murakami limit is met where the radiation should be balanced to the input heating power [2]. The empirical formula to describe the density limit of the modern tokamaks is known as the Hugil-Greenwald limit [3], which is expressed as

$$\bar{n}_{limit} \propto \frac{I_p}{\pi a^2}$$

where I_p represents the plasma current. It has been experimentally supported that the density limit in the tokamak plasma should be bounded by the violent deterioration of the confinement [4].

On the other hand, the density limit of stellarators is known to be described by an empirical law, termed Sudo scaling [5, 6] which is approximately written as

$$\bar{n}_{limit} \propto \sqrt{P_{\rm abs} B}$$

where $P_{\rm abs}$ and B represent the absorbed power and confinement magnetic field, respectively. This expression suggests that the stellarator density limit should be deeply associated with the condition of radiation balance with the absorbed heating power, since the radiation should be proportional to the square of density, *i.e.,* $P_{\rm abs} \propto n_e^2$.

It has been also well known that the density limit of stellarators is well above the Greenwald limit. Figure 1 shows an example of the high density limit of the LHD heliotron, compared to the Greenwald limit of tokamaks. Moreover, the stellarators do not show any violent plasma

behavior around the density limit, while the tokamak operation near the density limit leads the plasma to disruptions.

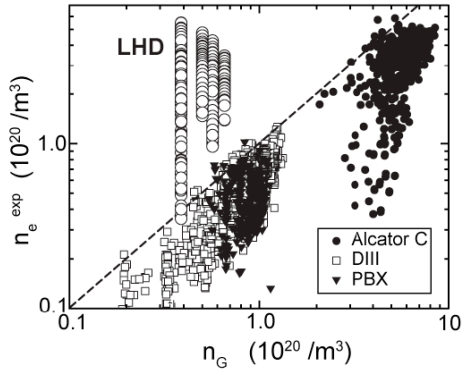

Fig. 1 Comparison between operational density in LHD and several tokamaks. The obtained density is plotted as the function of the corresponding Greenwald density. The achieved density in LHD is obviously ten times or much more higher than the Greenwald density (Courtesy of Prof. H. Yamada).

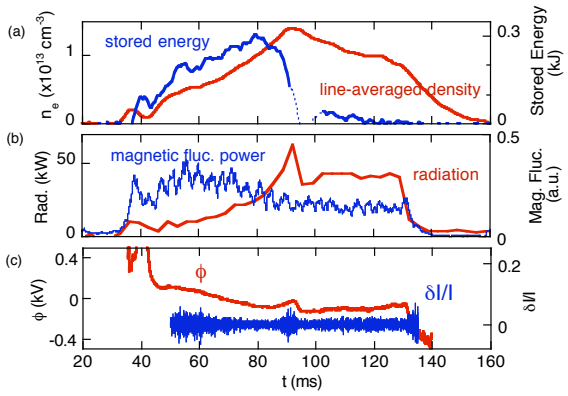

Fig. 2 Behavior of the ECR-heated CHS plasma at ∼ 100 kW. Time evolutions of (a) line-averaged density, stored energy, (b) radiation, magnetic field fluctuation power less than 50 kHz, (c) potential, and density fluctuations measured with HIBPs. The density limit is achieved or a transition happens at $t \simeq 90$ ms.

2.2 Behavior near Density Limit in Stellarators

A number of scenarios have been reported for stellarator plasmas around the density limit. In addition to the behavior like apparent radiation collapses, the rapid decrease in the stored energy and the following recovery, called *breathing*, is found around the density limit of the NBI plasmas in LHD [7] and W7-AS [8], when the magnetic field strength is properly selected at a fixed heating power.

In CHS an interesting behavior suggesting a transition is observed at the density limit. Figure 2 shows the temporal evolutions of line-averaged density, radial power, stored energy, and so on. The plasma is sustained with electron cyclotron resonance (ECR) heating with rather low power of ∼ 100 kW. In this case the line-averaged density increases gradually to reach a density limit. At the beginning of the exponential growth of radiation, a concomitant decrease with the stored energy is observed without any significant increase in MHD activities in a Mirnov coil signal. Just after the radiation reaches its maximum, the rapid decrease of radiation occurs and the radiation relaxes into a constant value. The potential signal observed with an HIBP also shows a rapid decrease in potential simultaneously with the radiation.

According to the observation, the plasma behavior before and after the density limit (or maixmum) point can be regarded as a transition from a state with high stored energy (or temperature) to the other one with extremely low stored energy (or temperature). On the other hand, the density fluctuations observed with an HIBP, or intermittent activity of density, show a rise and fall to increase during this transition. This observation suggests that turbulent transport could play an important role in the plasma behavior around the density limit, which should relate the inclusion of magnetic field dependence in the Sudo scaling to the turbulent transport, *i.e.*, $n_{\rm limit} \propto \sqrt{B}$.

2.3 Attractive Confinement Regimes in Stellrators

Recent studies in stellarators have found many interesting operational regimes, such as super dense core (SDC) in LHD [9, 10]. In the SDC discharge, the achieved density is 4.5×10^{20}m^{-3} with electron temperature of 0.85 keV. This is attained with a series of pellet injections. Besides, the high density H (HDH) mode was found in W7-AS [11, 12, 13] where the density up to 4×10^{20}m^{-3} is sustained in a rather stationary manner.

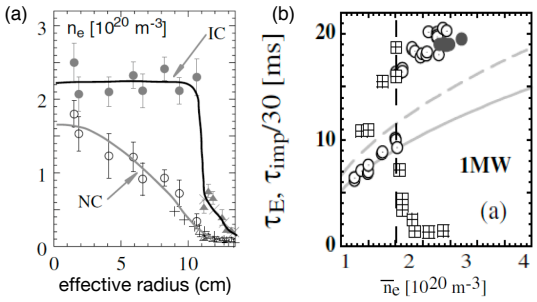

Fig. 3 HDH mode discovered in W7-AS. (a) The comparison between density and temperature profiles in normal confinement (NC) and improved confinement (HDH) mode. (b) The difference between confinement times of NC and HDH mode. The squares indicate the impurity confinement time.

As is shown in Fig. 3(a), the extremely sharp gradient is created in the density profile at the plasma edge. In contrast to usual H-mode in tokamaks, the HDH-mode is

that the transition happens above a critical density. Another special feature with the HDH-mode is the favorable reduction of impurity confinement. As is shown in Fig. 3(b), the impurity confinement time is sharply deteriorated the above the critical density, while the bulk particle confinement is clearly enhanced. Similar behavior of carbon impurity is found in LHD, or the outward movement of carbon is observed when high toroidal rotation of plasma is induced by higher power of neutral beam injection (NBI). This feature is an advantage because spontaneous ash-removal can be expected if this phenomenon is valid for helium ions.

3 Transport and New Paradigm

3.1 Collisional Transport and Symmetry

The transport in magnetically confinement plasma is described as the total of collisional and turbulent transport. The diffusive coefficient of collisional process is generally expressed as $D \propto \Delta^2 \nu_{\rm ei}$, where Δ and ν_{ei} are the effective step width and collision frequency, respectively. The effective step width is related with the deviation of a particle orbit from the magnetic field flux surface, and can be large if the collisionality is sufficiently low to allow the particles to be trapped in the magnetic field mirror associated with the inhomogeneity of the confinement magnetic field. Therefore, the effective step width is a function of collisionality and geometrical property of confinement field.

In tokamaks, the poloidal inhomogeneity of the magnetic configuration gives birth to the particles trapped in poloidal mirror field, termed banana particles. The existence of banana particles enhances the collisional transport. On the other hand, non-axisymmetric (or three dimensional) stellarator configurations produce the other kind of trapped particles, so-called helically trapped particles. These particles give the bipolar diffusion nature to the cross-field transports of ion and electron in addition to enhancing the collisional transport. It is known that the bipolar diffusion nature should be the dominant process to form the radial electric field in stellarators. In a steady state the radial electric field should be determined by the balance between collisional ion and electron fluxes denoted $\Gamma_{\rm ion}(E_r)$ and $\Gamma_{\rm electron}(E_r)$, respectively, *i.e.,* $\Gamma_{\rm ion}(E_r) - \Gamma_{\rm electron}(E_r) = 0$ in stellarators, while the generation mechanism of radial electric field is still an open question in tokamaks. Moreover, the nonlinear dependence of collisional fluxes on radial electric field causes the bifurcation nature of radial electric field in stellarators [14, 15].

3.2 Bipolar Difffusion and Barrier Formation

The bifurcation nature of radial electric field with stellarators has been found to be the cause of internal transport barrier commonly observed in stellarators [16, 17, 18, 19]. The formation scenario is identical with the model proposed for the explanation of H-mode initially [20, 21]. In a stellarator plasma core where temperature is above a critical value, the radial electric field makes a transition into a strongly positive branch (or electron root) with the radial electric field outside still remaining in a weakly positive branch (or ion root). As is shown in Fig. 4(a), the transition creates the transient layer between the two branches. The rather large electric field shear is produced in the layer to reduce the turbulence and form the transport barrier according to the $E \times B$-shearing of turbulence [22, 23, 24, 25, 26].

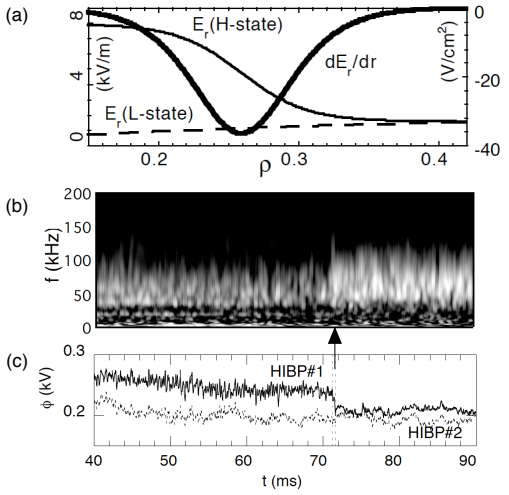

Fig. 4 The property of transport barrier in stellarator. (a) The profiles of radial electric field and its shear around the internal transport barrier in CHS. (b) Electric field fluctuations at the barrier before and after the collapse of the barrier, and (c) potential drop inside the barrier indicating the collapse of the barrier, together with the potential outside.

On the other hand, as is shown ins Fig. 4(b), the sudden increase in fluctuation is observed in the connection layer or the position of the ITB after the back-transition indicated by the sudden drop of potential (Fig. 4(c)). The observed transition time scale of radial electric field is in the range of a few dozen microseconds, being consistent with that prediction of the neoclassical theory [27], The time scale is much faster than the confinement time scale, therefore, this means that the existence of multi-steady states of electric field.

Accordingly, the ITB in stellarators is an exceptionally clear example to demonstrate that the electric field bifurcation can be the cause for the barrier formation. In contrast the formation of the H-mode or edge transport barriers both in tokamaks and stellarators still allows of many candidate mechanisms; some experimental results suggest the balance between fast ion loss and parallel viscosity, while some others suggest the turbulent Reynolds stress should play an important role. The non-axisymmetric fea-

ture, instead of the anxiety of collisional transport, could give stellarators an advantage in the transport barrier formation, of which cause is clearly identified thus theoretically predictable rather easily.

3.3 Zonal Flows and New Paradigm

The magnetic well and shear have been known to be the concepts to measure the magnetic configuration property to stabilize the linear MHD and drift wave instabilities. Therefore, these concepts have been used as the major factors to optimize the magnetic field configuration. The recent development of theories and plasma diagnostics also has shown a new paradigm [28, 29], which could be common for magnetically confined plasmas, to understand the saturation mechanisms of the plasma turbulence and the resultant transport. In other words, the new paradigm can be a new factor to evaluate the property of the magnetic field configuration in terms of turbulent saturation mechanism, while the magnetic shear and well serves as the factors to assess the linear growth of the instabilities [30, 31].

In the new paradigm, the turbulence should be recognized as a system of zonal flows and drift waves. Inhomogeneity of plasma (*i.e.,* temperature and density gradients) causes drift wave turbulence to result in the enhancement of plasma transport. Then the drift waves generate and transfer the energy to zonal flows through the $v\nabla v$-nonlinearity. Moreover, the zonal flows give back-reactions on the drift waves, such as $E \times B$-shearing, wave trappings, and so on, to work as further reduction of drift-waves. The symmetric nature of zonal flows causes no radial or cross-field transport. Therefore, the increase in the zonal flow fraction in the turbulence contributes to lessen the anomalous transport. The fraction of zonal flows in the power spectrum of electric field fluctuations, therefore, is a key to determine the turbulent transport level.

The direct measurements of electric field fluctuations in CHS have proven the existence of zonal flows experimentally, together with the couplings between zonal flows and the background turbulence [32, 33, 34]. A number of experimental reports have been accumulated to show the existence of Geodesic Acoustic Modes (GAMs), an oscillatory branch of zonal flows [29], and their couplings with the background turbulence [35] using direct and indirect measurements of flow or electric field. Therefore, the new paradigm of plasma turbulence and transport is widely prevailed nowadays. Figure 5 shows the radial correlation function between the electric field fluctuations corresponding to the stationary zonal flows, visualizing the radial pattern of zonal flows.

3.4 Confinement and Flow Damping Rate

The essential requirement for detecting the zonal flows is to measure the fluctuations of plasma flows or electric field directly. This imposes a quite difficult constraint on the present plasma diagnostics, therefore, limited data have been available. However, the comparison between fluctuation spectra of flow (or electric field) in tokamak and stellarator is possible. Figure 6 shows the electric field spectra directly measured with HIBPs in the core of CHS stellarator, and the flow fluctuation spectra indirectly measured with BES in the edge region of DIII-D tokamak [36].

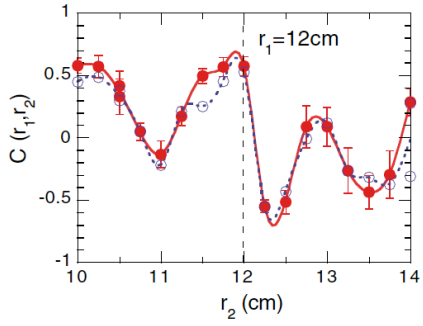

Fig. 5 The identified radial pattern of zonal flows in CHS. The radial structure of zonal flows is represented in the radial correlation function.

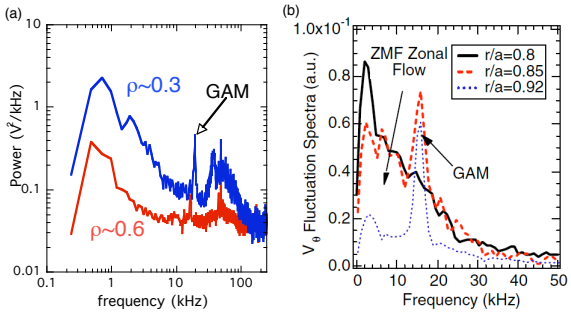

Fig. 6 The comparison between spectra of (a) electric field fluctuations measured with HIBP (CHS), and (b) poloidal flow fluctuations measured with BES (DIII-D).

In spite of the difference of magnetic field configuration and the observed locations, the comparison shows the common features, i) a region corresponding to stationary zonal flows exists, ii) the oscillatory branches, GAMs, are observed as sharp peaks, and iii) regions with broad band fluctuations corresponding to drift waves with a higher frequency from a few dozen kHz to a hundred kHz are present. In the case of CHS stellarator, the fraction of turbulent power increases being accompanied with the increase of zonal flow fraction to that of the drift waves around $\sim$ 50 kHz, probably due to the enhancement of temperature gradient in the plasma core region. In the case of DIII-D tokamak, the GAM fraction decreases with an increase in zonal flow amplitude as the observation point goes inward.

It has been found that the absolute value of GAM amplitude should be much larger in tokamak that in stellarator. The HIBP observations in JIPPT-IIU [37] showed that the GAM potential amplitude can exceed $\sim$ 100 V, while

that in CHS stellarator should be in the range of a few volts. This may be ascribed to the larger parallel viscosity of stellarators. Figure 7 shows the comparison between toroidal flows driven by NBI in stellarator (CHS) and tokamak (JFT-2M). Obviously, the resultant toroidal rotation velocity in tokamak is much faster than that in stellarator, although the input NBI power is in the same range in both experiments of CHS [38] and JFT-2M [39]. Thus, the inhomogeneity should give a large damping effect on plasma flows.

As for the internal transport barrier in stellarator, the transport inside the barrier is also found to be improved without any significant electric field shear. Recently, it has been confirmed in CHS that this improvement is caused by the enhancement of zonal flow fraction, as is shown in Fig. 8, due to the reduction of flow damping rate [40, 41]. The zonal flows (or zonal radial electric field) are driven by turbulence, therefore, the turbulent radial current to drive the zonal flows, $\delta j_{\rm turb}$, should be balanced with the neoclassical radial current (or total radial flux of ions and electrons) in stellarators, this condition is expressed as $\delta j_{\rm turb} + (\partial j_{\rm neo}/\partial E_r)\delta E_r = 0$, where $(\partial j_{\rm neo}/\partial E_r)$ could be called the effective neoclassical viscosity. The low effective viscosity in electron root is experimentally confirmed, as is shown in the inset of Fig. 8, in addition to the prediction by neoclassical collisional transport theories.

These facts suggest that the zonal flow fraction should be large as the flow-damping rate is low. Hence, the magnetic field configuration with lower parallel viscosity or magnetic inhomogeneity should give a better confinement owing to the possible enhancement of zonal flow fraction. The new paradigm could provide an optimization principle for the magnetic field configuration in the light of turbulence transport by its saturation mechanism.

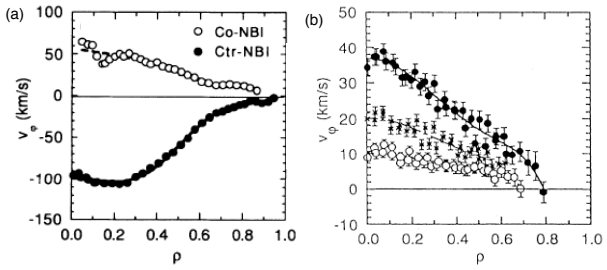

Fig. 7 The comparison between induced toroidal flows in tokamak (JFT-2M) and stellarator (CHS). (a) The profile of toroidal flow velocity in JFT-2M and (b) that in CHS. The toroidal flows are measured with charge exchange recombination spectroscopy.

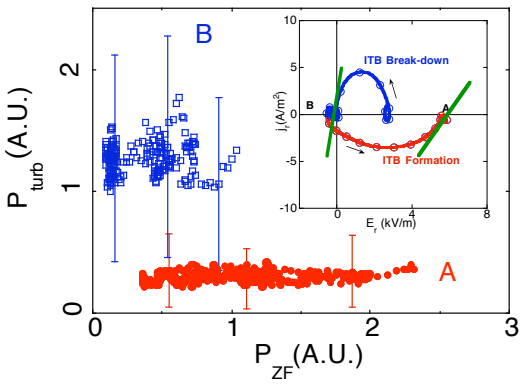

Fig. 8 The fractions of zonal flows and drift waves in the state with and without confinement improvement in CHS. The measurement was carried out at a point inside the position of internal transport barrier. The increase in zonal flow fraction should be ascribed to the decrease in effective viscosity accompanied with the transition from ion (point B) into electron root (point A). The effective viscosity corresponds to the slope of the tangential lines at the stable points of radial electric field in the inset. It is clear that the slope of ion root is steeper than that of electron root solution.

4 Beyond Simple Comparison

4.1 Roles of Low Temperature Devices

High accessibility and flexibility must be of essential need for the experiments aiming at finding the physical laws underlying the structural formation of plasmas. The role of low temperature devices should be emphasized in addition to exploring new possible diagnostics for high temperature plasmas. Low temperature devices, even a linear cylindrical device, provide good environments to study the fundamental processes of plasma turbulence and transport.

For instance, in low temperature toroidal device, H1-heliac, the fundamental processes of plasma turbulence has been extensively studied [42, 43]. In TJ-K the dependence of turbulence characteristics on dimensionless parameters, such as normalized Lamor radius, ρ^*, collisionlity ν^*, and so on, has been pursued for the first principle understanding of the dimensionless scaling law of plasma confinement [44]. The simultaneous measurements of both radial and poloidal wavenumbers using 2-dimensional probes in TJ-K succeeded in clarifying the fundamental process of magnetized plasma turbulence, *i.e.,* the nature of dual cascade in a two dimensional flow system [45].

Besides, a number of excellent experimental results have been reported from cylindrical linear devices in university laboratories. In CSDX, a cylindrical laboratory plasma, the momentum balance between the turbulent Reynolds stress drive and viscous damping was investigated and successfully demonstrated that the turbulent Reynolds stress should be the cause of the zonal flow generation [46]. In a cylindrical machine, LMD-U, the streamer formation has been identified with an efficient use of the combination of 64 channel azimuthal probe array and 2 dimensionally movable probes [47].

Recently, In a laboratory cylindrical plasma of Kyushu university, the detailed processes of sheared flow

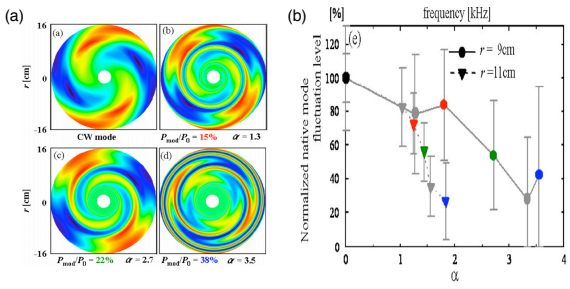

Fig. 9 Observation to demonstrate the interplay between the sheared flows and a pressure driven mode in a linear cylindrical plasma. The sheared flow strength is controlled by the degree of the modulation of ECR-heating. (a) The reconstructed images of the interplay between sheared flows and the mode. (b) The suppression degree as a function of a parameter to indicate the shear flow strength, α.

effect were observed in externally induced sheared flow using the modulation of the plasma heating power [48]. In the device, a pressure-driven instability is observed in electron cyclotron heated plasma as a sharp peak without any modulation of ECR-heating. By applying the ECR-heating modulation, the sheared flows are induced to interact with and suppress the native mode. Figure 9 shows the images of the change of the reconstructed potential fluctuation patterns according to the modulation intensity of heating power, and the suppression ratio of the native mode as a function of the strength of the induced sheared flow. The results clearly demonstrate how the native mode is altered as the shear flow becomes stronger, suggesting that the process of three wave coupling should play a role in the suppression.

4.2 Concluding Remarks

Tokamak is the leading concept for fusion reactor, however, it is necessary to overcome a number of issues for realizing an economically compatible reactor. The advantageous properties of the other toroidal devices, therefore, should be incorporated into a Demo and following reactors; for instance, the advantage with stellarators, the high density operation exceeding the Greenwald limit without any disruptive activities, would be desired to be adopted to the tokamak concept even though the axisymmetric nature giving a good plasma confinement may be partially destroyed. In order to realize a device with a combined concept or an optimizing configuration, it is absolutely essential to understand the plasma behavior to determine the operational boundaries and the plasma confinement from the first principle, which should result in the precise and accurate prediction of magnetically confined plasma performance to any given configurations. Therefore, the important roles of medium and small sized devices oriented for physical understanding of toroidal plasmas are strengthen even in the era of burning plamsas.

[1] M. Gryaznevich et al., Phys. Rev. Lett. **80** 3972 (1998).
[2] M. Murakami et al., Nucl. Fusion **16** 347 (1976).
[3] M. Greenwald et al., Nucl. Fusion **28** 2199 (1988).
[4] D. L. Brower et al., Phys. Rev. Lett. **67** 200 (1991).
[5] S. Sudo et al., Nucl. Fusion **30** 11 (1990).
[6] J. Miyazawa et al., Nucl. Fusion **48** 015003 (2008).
[7] B. J. Peterson et al., Nucl. Fusion **41** 519 (2001).
[8] L. Giannone et al., Plasma Phys. Control. Fusion **42** 603 (2000).
[9] N. Ohyabu et al., Phys. Rev. Lett. **97** 055002 (2006).
[10] R. Sakamoto et al., Nucl. Fusion **46** 884 (2006).
[11] K. McCormick et al., Phys. Rev. Lett. **89** 015001 (2002).
[12] F. Wagner et al., Plasma Phys. Control. Fusion **48** A217 (2006).
[13] M. Hirsch et al., Plasma Phys. Control. Fusion **50** 053001 (2008).
[14] L. M. Kovrizhnykh, Nucl. Fusion **24**,435 (1984).
[15] D. E. Hastings, Phys. Fluids **27** 935 (1984).
[16] A. Fujisawa *et al*., Phys. Rev. Lett. **82** 2669 (1999).
[17] U. Stroth et al., Phys. Rev. Lett. **86** 5910 (2001).
[18] A. Fujisawa, Plasma Phys. Control. Fusion **45** R1 (2003).
[19] M. Yokoyama et al., Nucl. Fusion **47** 1213 (2007).
[20] S. -I. Itoh, K. Itoh, Phys. Rev. Lett. **60** 2276 (1988).
[21] K. C. Shaing, E. C. Crume Jr., Phys. Rev. Lett. **63** 2369 (1989).
[22] K. C. Shaing et al., *Proceedings of 12th International Conference on Plasma Physics and Controlled Nuclear Fusion Research*, Nice, 1988, (International Atomic Energy Agency, Vienna, 1989), Vol. 2, p. 13
[23] H. Biglari, P. H. Diamond, P. W. Terry, Phys. Fluids B **2** 1 (1990).
[24] K. Itoh et al., Plasm Phys. Control. Fusion **36** 123 (1994).
[25] T. S. Hahm, K. H. Burrel, Phys. Plasmas **2** 1648 (1995).
[26] Z. Lin et al., Science **281** 1835 (1998).
[27] A. Fujisawa et al., Phys. Rev. Lett. **79** 1054 (1997).
[28] P. H. Diamond et al., Plasma Phys. Control. Fusion **47** R35 (2005).
[29] A. Fujisawa et al., Nucl. Fusion **47** S718 (2007).
[30] J. Nührenberg, R. Zille, 1986 Phys. Lett. **114A** 129.
[31] J. Nührenberg, R. Zille, 1988 Phys. Lett. **129** 113.
[32] A. Fujisawa et al., Phys. Rev. Lett. **93** 165002 (2004).
[33] A. Fujisawa et al., Plasma Phys. Control. Fusion **49** 211 (2007).
[34] A. Fujisawa et al., J. Phys. Soc. Jpn. **76** 033501 (2007).
[35] Y. Nagashima et al., Phys. Rev. Lett. **95** 095002 (2005).
[36] D. K. Gupta et al., Phys. Rev. Lett. **97** 125002 (2006).
[37] Y. Hamada et al , Nucl. Fusion **45** 81 (2005).
[38] K. Ida et al., Phys. Rev. Lett. **67** 58 (1991).
[39] K. Ida et al., Phys. Rev. Lett. **68** 182 (1992).
[40] K. Itoh et al., Phys. Plasmas **14** 020702 (2007).
[41] A. Fujisawa et al., Phys. Plasmas **15** 055906 (2008).
[42] M. G. Shats, H. Xia, H. Punzmann, Phys. Rev. E **71** 046409 (2005).
[43] H. Xia, M. G. Shats, H. Punzman, Phys. Rev. Lett. **97** 255003 (2006).
[44] U. Stroth et al., Phys. Plasma **11** 2558 (2004).
[45] P Manz et al., Plasma Phys. Control. Fusion **50** 035008 (2008).
[46] G. R. Tynan et al., Plasma Phys. Control. Fusion **48** S51 (2006).
[47] T. Yamada et al., Nature Phys. **4** 721 (01 Sep. 2008).
[48] H. Tsuchiya et al., Plasma Phys. Control. Fusion **50** 055005 (2008).

Proceedings of ITC18,2008

On the physics of shear flows in 3D geometry

C. Hidalgo and M.A. Pedrosa

Laboratorio Nacional de Fusión, EURATOM-CIEMAT, Madrid, Spain

Recent experiments have shown the importance of multi-scale (long-range) mechanisms in the transition to improved confinement regimes and the key role of electric fields to amplify them. Flows driven by turbulence might explain such experimental observation, which would imply to consider the importance of 3-D effects on the energy transfer between flows and turbulence. Comparative studies in different magnetic configurations (tokamaks vs stellarators), diagnostic development and large-scale simulation are needed to assess the importance of multi-scale physics in the development of sheared flows.

Keywords: Transport, Flows, Turbulence, Transport Barriers.

.

1. Introduction

The discovery of the transition to edge improved confinement regimes at the beginning of the 1980's brought on a new era in magnetic confinement fusion. After more than 25 years of active research, most experimental evidences support the paradigm of sheared electric field suppression of turbulence to explain transport barrier physics, although the underlying mechanisms that generate the electric fields still remain as the fundamental open issue confronting the fusion community.

As pedestal plasma parameters have a strong impact on global confinement, prediction of the ITER pedestal parameters and the H-mode transport barrier width remain a key and fully open research area. Indeed, large uncertainties are still present in the empirical description of the L-H transition power threshold, with significant implications for the overall structure of the ITER research plan.

Critical tests of models for transport barriers based on second order (turbulent driven flow) and first order (pressure gradient driven flows) phase transition as well as role of equilibrium flows and edge localized neutral particle sources are needed for the development of a comprehensive theory of the L-H transition and transport barriers. In the case of edge transport barriers, the influence of plasma boundary conditions on empirical power threshold should be also addressed. Due to the times/spatial scales involved this research area is a real challenge for both theorists and experimentalists.

Recent experiments have shown the importance of multi-scale (long-range) mechanisms in the transition to improved confinement regimes and the key role of electric fields to amplify them [1]. The detection of lon-range correlations in stellarators [2, 1] and tokamaks [3] is consistent with the theoretically predicted (low frequency) zonal flows.

The possible interplay between turbulent and neoclassical transport mechanisms has been recently reported; Ion temperature gradient driven turbulent simulations have shown an enhancement of zonal flows in stellarator configurations optimized for reducing neoclassical transport [4].

2. Long-range correlations and transition to improved confinement regimes

In the TJ-II stellarator sheared flows can be easily driven and damped at the plasma edge by changing the plasma density or during biasing experiments [5 , 6]. The experimental results on the emergence of the shear flow layer in TJ-II have some of the characteristics of a transition and are consistent with the expectations of second-order transition models of turbulence driven sheared flows [7].

In addition, the TJ-II is equipped with a unique system for multi-scale physics studies: two Langmuir probe arrays (measuring ion saturation current, floating potential and poloidal electric fields) located in two different toroidal positions installed on fast reciprocating drives. One of the probes (P 1) is located in a top port entering vertically through one of the "corners" of its beam-shaped plasma and at $\phi \approx 35^{o}$ (where ϕ is the toroidal angle in the TJ-II reference system). The other probe (P

author's e-mail: carlos.hidalgo@ciemat.es

2) is installed in a bottom port at ϕ ≈195º and enters into the plasma through a region with a higher density of flux surfaces (i.e. lower flux expansion) than P 1 (Fig. 1).

This unique experimental set-up (with probe toroidally separated in the order of 5 m) allows the simultaneous investigation of short (in the range of few millimeters) and long-range (in the order of ten meters) fluctuation scales in the plasma edge .

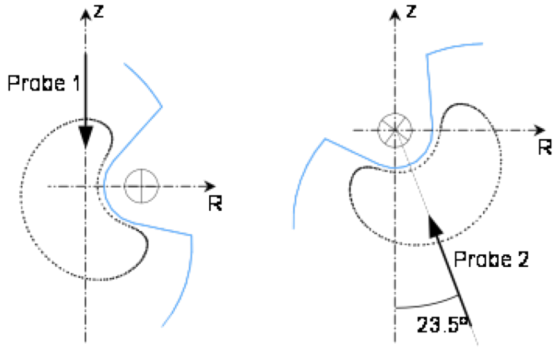

Fig.1 Schematic view of the location of the two probes (thick line arrows) and their positions relative to the TJ-II plasma.

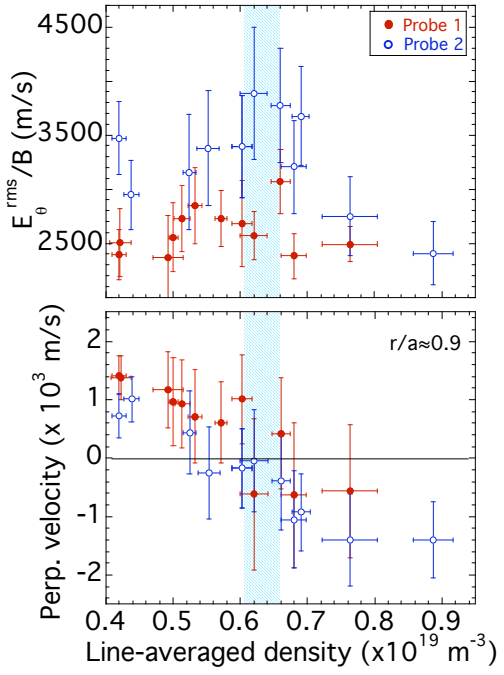

Fig.2 Averaged electric field fluctuations and perpendicular velocity measured at two toroidal locations and at approximately the same radial position (r/a≈0.9) as a function of plasma density.

It has been previously shown that the development of sheared flows at the plasma edge of the TJ-II requires a critical value of plasma density or density gradient that depends on global plasma parameters [5, 6]. For densities above the threshold, and once sheared flows are fully developed, fluctuations level and the turbulent transport slightly decreases and the edge gradients become steeper. Edge sheared flows are developed at the same threshold density in the two toroidal positions (probes P1 and P2) (Fig. 2). Floating potential signals measured at both toroidal locations show a striking similarity mainly for low frequency components, contrary to that observed in the ion saturation current signals. This similarity is observed at different time scales but it is more clear during fluctuation events with time scales in the range of (0.1 – 1) ms related to the shear flow development. To quantify the similarity between probe signals the toroidal cross-correlation defined as

$$\gamma_{xy}(\tau) = \frac{E\left\{\left[x(t+\tau)-\bar{x}\right]\left[y(t)-\bar{y}\right]\right\}}{\sqrt{E\left\{\left[x(t)-\bar{x}\right]^2\right\}.E\left\{\left[y(t)-\bar{y}\right]^2\right\}}}$$

has been computed for a wide range of TJ-II plasma conditions, including a line-averaged density scan as well as with and without electrode bias in plasmas without MHD activity as showed the pick-up coils installed in TJ-II.

Figure 3 illustrates the dependence of the toroidal floating potential correlation on the line-averaged density (for the same shots presented in figure 2). It is observed that the cross-correlation depends on the density, being larger as density increases up to n ≈ 0.6 x 10^{19} m^{-3}, which corresponds to the threshold density for shear flow development

Figure 4 shows the time evolution of plasma density and the cross-correlation between floating potential and ion saturation signals during biasing induced improved transitions (for probes 1 and 2). It shows clearly in the increase in the cross-correlation during the biasing phase. Once the biasing is turned off, the density decreases in the time scale of the particle confinement time (in the range of 10 ms) whereas both the electric field and the degree of long range correlation decreases in a much faster time scale. These results shows that the high degree of long-range correlation observed in floating potential signals in coupled to the value of radial electric fields and

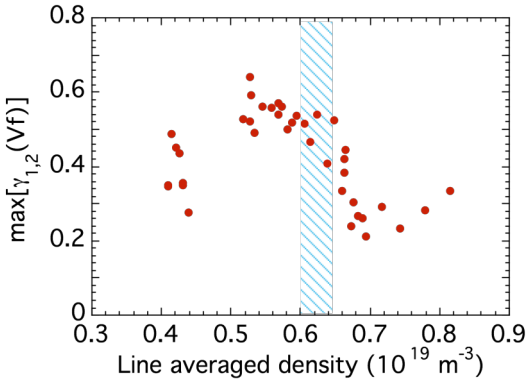

Fig.3 Maximum value of the cross-correlation between floating potential signals measured at r/a = 0.9 as a function of the plasma density. The shadow area indicates the threshold density for the development of edge sheared flows.

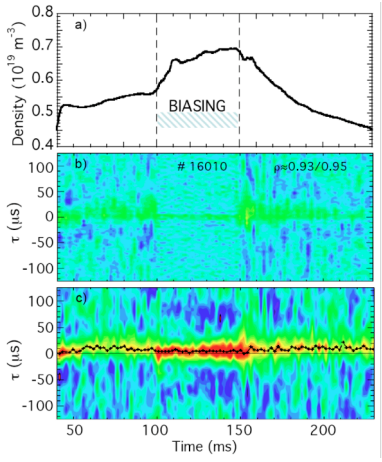

Fig.4 Time evolution of plasma density during biasing induced improve confinement regimes in TJ-II and cross-correlation function between b) ion saturation current and c) floating potential signals measured toroidally apart and at the plasma edge as a function of time for one shot during biasing experiments.

not to the plasma density.

Recent experiments with Li-coating and NBI heating have shown evidence of spontaneous bifurcations characterized by the increase of plasma density and stored energy with a concomitant reduction in the H_a emission (showing a decrease of the outward particle flux) together with the reduction of the level of broadband fluctuations and a steeper density gradients. All these phenomena are characteristic of plasma bifurcations to improved confinement regimes (H-mode) [8 9]. Experimental evidence of long (spatial) range correlations has been recently observed during the L-H transition in the TJ-II stellarator.

3. Driving and damping mechanisms of multi scale mechanisms

TJ-II results, showing the amplification of multi-scale physics features during spontaneous transport bifurcations and more recently during the development of spontaneous L-H transition, can help to provide a critical test for L-H transition models.

The resistance of fluids to shearing motion is a well known observation. The tendency of sheared motion to be reduced with the passage of time, if no other forces are at work to maintain it, leads to the concept of (positive) coefficient of viscosity, the constant of proportionality relating the stress to the shear. In a turbulent flow, when the momentum flux perpendicular to the mean flow direction is directed from regions of larger values toward regions of smaller values of mean flow, it is said that a turbulent (eddy) viscosity is present.

The concept of a reverse effect (e.g. negative viscosity) is something which appears to be again common sense [10]. However, for certain kind of flows (e.g. planet´s atmosphere and plasmas [11]) evidence of negative viscosity effects have been reported. In this case the mean flow can gain kinetic energy from the turbulence with direct impact in the development of sheared flows. Some conditions must be fulfilled in the system to show negative viscosity behaviour in steady state plasmas (Fig. 5). First eddies which transport the momentum contrary to the gradient of mean flow must have a supply of turbulent kinetic energy (otherwise they will die out). Second, the mean flow should experience some form of braking (i.e. positive viscosity) so that its value does not increase without limit. However, this braking should be low enough to allow the generation of differential rotation. Third, some kind of turbulent irregularity must be present. In steady state the turbulent drive is equal to the damping, i.e. for the poloidal dynamics

$$d\langle \tilde{v}_r \tilde{v}_\theta \rangle / dr = \mu V_\theta$$

In the framework of bifurcation transition models based on second order phase transitions triggered by zonal flows (i.e. via negative viscosity mechanisms), fluctuations are expected to show long range correlations in the order parameter related with the electric fields. Then, TJ-II findings reported in section 2 are consistent

with this theoretical framework.

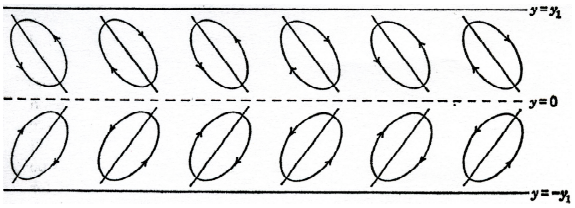

Fig.5 Some kind of turbulent irregularity must be present to get flow driven by instabilities in plamas. This ingredient is illustrated in the figure, showing a flow with some hypothetical pattern producing a convergence of momentum into the mid-channel [10].

The poloidal rotation is damped by the magnetic pumping (i.e. the plasma rotation in the presence of inhomogeneous magnetic field heats up the plasma and leads to an irreversible transformation of the kinetic energy of rotation into thermal energy which damps the rotation) [12]. Also, a neoclassical theory of plasma rotation is available and the main result is that the poloidal rotation is proportional to the gradient of the ion temperature [13]. It should be noted that multi-scale physics might be also expected in the framework of other L-H transition models like those based on particle orbit losses or Stringer spin-up [14]. However because radial electric fields are expected to reduce both edge particle losses and the degree of poloidal asymmetries during transition to improved confinement regimes [15], it remains to be clarified why multi-scale physics mechanisms should be amplified at the H mode regime if those mechanisms are playing a leading role during the development of transport bifurcations.

3. The 3-D energy transfer between edge flows and turbulence

Experiments in tokamaks and stellarators have shown that the edge velocity shear layer appears to organize itself to reach a condition in which the radial gradient in the poloidal phase velocity of fluctuations is comparable to the inverse of the correlation time of fluctuations (1/t). This result suggests that ExB sheared flows organized themselves to be close to marginal stability (i.e. $\omega_{ExB} \approx 1/\tau$). Considering that this property has been observed in different devices with tremendous differences in the magnetic topology (e.g JET tokamak and the TJ-II stellarator), we conclude that this result should be considered as a fundamental property of spontaneous edge shear flow in fusion devices (and so an important ingredient in the modelling of the L-H transition).

From this perspective, an important question is to identify which mechanism allows fluctuations and sheared flows to organize themselves to be close to marginal stability. It is easy to understand why turbulent driven flows (e.g. via Reynolds stress) allow sheared flows and fluctuations to reach marginal stability condition $\omega_{ExB} \approx 1/\tau$. The Reynolds stress tensor (whose components can be quantified as the quadratic cross-correlation of fluctuating velocity components) allows the interchange of energy (and momentum) between mean flows and fluctuations. Once the Reynolds stress driven sheared flows reach the critical value to modify fluctuations a negative feedback mechanism will be established which will keep the plasma near the condition ω_{ExB} critical.

Experiments in the TJ-II stellarator [16] have investigated the evolution of turbulence during edge shear development by quantifying the quadratic term of fluctuating radial and parallel velocities. Radial variations in the radial-parallel Reynolds stress components are developed in the proximity of the threshold density to trigger the development of edge sheared flows. In addition, experiments using fast cameras and probes suggest that also the quadratic term (radial-perpendicular Reynolds stress component) is modified during edge shear flow development in the TJ-II stellarator [17] and the JET tokamak [18]. The fact that different quadratic terms in fluctuating velocities (radial-parallel and radial-perpendicular) changes during edge sheared flow development has an important consequence: shear flow physics involves 3-D physics phenomena in which both perpendicular and parallel dynamics are involved.

3. Conclusions

Recent experiments have shown the importance of multi-scale (long-range) mechanisms in the transition to improved confinement regimes and the key role of electric fields to amplify them. Flows driven by turbulence might explain such experimental observation, which would imply to consider the importance of 3-D effects on the energy transfer between flows and turbulence. Comparative studies in different magnetic configurations (e.g. tokamak, stellarators and RFPs), diagnostic development and large-scale simulation are needed to assess the importance of multi-scale physics in the development of sheared flows.

References

[1] M. A. Pedrosa et al., Phys Rev. Lett. **100**, 215003 (2008)

[2] A. Fujisawa et al., Phys. Rev. Lett. **93**, 165002 (2004)

[3] D. K. Gupta et al., Phys. Rev. Lett. **97** 125002 (2006).

[4] T. Watanabe et al., LHD reference Phys Rev. Lett. **100**, 195002 (2008).

[5] C. Hidalgo et al., Phys. Rev. E **70**, 067402 (2004).

[6] M.A. Pedrosa et al., Plasma Phys. Control. Fusion **47**, 777 (2005).

[7] B. A. Carreras et al., Phys. Plasmas **13**, 122509 (2006).

[8] F. L. tabarés et al., Plasma Phys Control Fusion (2008).

[9] J. Sánchez et al., Nuclear Fusion (2008).

[10] V. P. Starr, "Physics of Negative Viscosity Phenomena" (1968) McGraw-Hill.

[11] P. Diamond et al., Plasma Physics and Controlled Fusion **47**, R35 (2005).

[12] A. B. Hassam and R. Kulsrud Phys. Fluids **21**, 2271 (1978).

[13 J. H. F. Severo et al., Nuclear Fusion **43**, 1047 (2003).

[14] J W Connor and H R Wilson Plasma Phys Control Fusion **42**, R1 (2000).

[15] G. Tynan et al., Phys. Rev. Lett. **68**, 3032 (1992).

[16] B. Gonçalves et al., **96**, 145001 (2006).

[17] J. A. Alonso et al., Plasma Phys. Control. Fusion **48**, B465 (2006).

[18] E. Sánchez et al., J. of Nuclear Materials **337**, 296 (2005).

Proceedings of ITC18,2008

Status and High Power Performance of the 10-MW 140-GHz ECH System for the Stellarator W7-X

M. Thumm[1,2], P. Brand[4], H. Braune[3], V. Erckmann[3], G. Gantenbein[1], S. Illy[1], W. Kasparek[4], S. Kern[1], H. P. Laqua[3], C. Lechte[4], N.B. Marushchenko[3], G. Michel[3], B. Piosczyk[1], M. Schmid[1], Y. Turkin[3], M. Weissgerber[3] and the W7-X ECH-Teams at FZK Karlsruhe[1], IPP Greifswald[3] and IPF Stuttgart[4]

[1]*Forschungszentrum Karlsruhe, Association EURATOM-FZK,Institut für Hochleistungsimpuls- und Mikrowellentechnik, D-76021 Karlsruhe, Germany*

[2]*Universität Karlsruhe, Institut für Höchstfrequenztechnik und Elektronik, D-76131 Karlsruhe, Germany*

[3]*Max-Planck-Institut für Plasmaphysik, EURATOM Association, Teilinstitut Greifswald, D-17491 Greifswald, Germany*

[4]*Universität Stuttgart, Institut für Plasmaforschung, D-70569 Stuttgart, Germany*

During the last years, electron cyclotron heating (ECH) was proven to be one of the most attractive heating schemes for stellarators because it provides net-current-free plasma startup and heating. Both the stellarator Wendelstein 7-X (W7-X) and the ITER tokamak will be equipped with a strong ECH and current-drive system. Both ECH&CD systems are comparable in frequency and have continuous-wave (CW) capability (140 GHz, 10 MW for W7-X and 170 GHz, 27 MW for ITER). The heating- and current drive scenarios, which support W7-X operation at various magnetic fields and in different density regimes are reviewed. The ECH plant consists of ten RF-modules with 1 MW power each. The commissioning of the entire ECH installation is in an advanced state. All supporting systems like the superconducting magnets, the water cooling plant, the cryogenic plant, the main power supply and all high-voltage modulators are completed and operating. The ten gyrotrons at W7-X will be arranged in two 5 MW subgroups symmetrically to a central beam duct in the ECH hall. The mm-wave beams of each subgroup will be combined and transmitted by a purely optical multibeam-waveguide transmission line from the gyrotrons to the torus. The mm-wave power will be launched to the plasma through ten synthetic diamond barrier windows and in-vessel quasi-optical plug-in launchers, allowing each 1-MW mm-wave beam to be steered independently. The polarization, as well as the poloidal and toroidal launch angles, will be adjusted individually to provide optimum conditions for different heating and current-drive scenarios. Integrated high power CW tests of the full transmission system (except the in vessel components) were performed recently and are in excellent agreement with theory and low power measurements. The work presently concentrates on the acceptance tests of the gyrotrons, on the front end of the transmission system near the W7-X torus and on the in-vessel components.

Keywords: Nuclear Fusion, Stellarator, Steady State Operation, Electron Cyclotron Heating, Gyrotron, Quasi-Optical Transmission

1. Inroduction

Wendelstein 7-X (W7-X) is the next step in the stellarator line towards thermonuclear magnetic fusion power plants. Stellarators have inherent steady state operation capability, because the confining magnetic field is totally generated by external coils. W7-X will be equipped with a superconducting coil system and a continuously operating (CW) 140 GHz Electron Cyclotron Heating and Current Drive (ECH&CD) system with 10 MW gyrotron power. An actively pumped divertor with 10 MW heat removal capability for stationary energy and particle control will be installed after an initial testing phase using an inertially cooled divertor in pulsed operation. An ECH power of 10 MW is required to achieve reactor relevant plasma parameters [1] at the nominal magnetic field of 2.5 T. The ECH&CD operation scenarios and the status of the in-vessel components are reported in Sec. 2. Tests experiments on

author's e-mail:manfred.thumm@ihm.fzk.de, *This paper was carried out within the framework of EFDA.*

gyrotrons are summarized in Sec. 3. The ECH plant is in a well-advanced state, integrated high power tests of the transmission line are reported in Sec. 4.

2. Operation scenarios and in-vessel components

The ECH&CD system at W7-X has to fulfill many different functions. It has to provide plasma start-up, heating and current control routinely at the different resonant confining magnetic fields. It is the only heating system, which will be fully available for long-pulse operation from beginning of the experiment. For plasma start-up and "low" plasma density ($<1.2\cdot10^{20}$ m^{-3}) operation heating with the second harmonic X-mode (X2) at 140 GHz is foreseen. Its single-pass absorption is sufficiently high that nearly total absorption is guaranteed up to the cut-off density ($<1.2\cdot10^{20}$ m^{-3}). At low density plasma temperatures of above 10 keV are expected. The heating power of 10 MW should be sufficient to sustain a plasma at $1.0\cdot10^{20}$ m^{-3} with a temperature of 4 keV. X2 operation at 103.8 GHz is also envisaged (see next chapter). In addition start-up at the third harmonic (X3) will be explored. Although in stellarators neither a permanent ECCD for the plasma confinement nor any NTM- stabilization is needed, the control of the divertor strike point position requires a permanent control of the edge rotational transform iota. In addition it should be avoided that the iota profile does approach any main rational resonance. Therefore ECCD will be used for residual bootstrap current [2] compensation and iota control on a fast time scale. For long time scales (<100s) iota will be controlled by the currents in the coil system. With the installed ECH power of 10 MW up to 300 kA current can be driven at $1.0\cdot10^{19}$ m^{-3} by ECCD. Even at $1.0\cdot10^{20}$ m^{-3} an ECCD current of up to 30 kA is expected, which will be sufficient to compensate the estimated bootstrap current of about 20 kA.

The main challenge of the first experimental campaign will be to develop an operation scenario, where the slowly growing bootstrap current is continuously compensated by a well matched central and off-axis ECCD. Efficient divertor operation probably may require a plasma density well above the X2-cutoff density. Here second harmonic O-mode heating (O2) with a plasma density of up to $2.4\cdot10^{20}$ m^{-3} is foreseen [3,4]. In contrast to X2 heating O2 single-pass absorption is well below 100%. Depending on plasma density and central plasma temperature a single-pass absorption of 50-90% is expected. The similar situation is found for X3-heating (B_{res}= 1.66 T, $n_e < 1.6\cdot10^{20}$ m^{-3}), which is a promising scenario for operation at reduced confining magnetic field. An example for X3 single-pass absorption calculations with 10 MW input power is shown in Fig. 1 (top). The related electron and ion temperatures resulting from a transport code [5] are also shown.

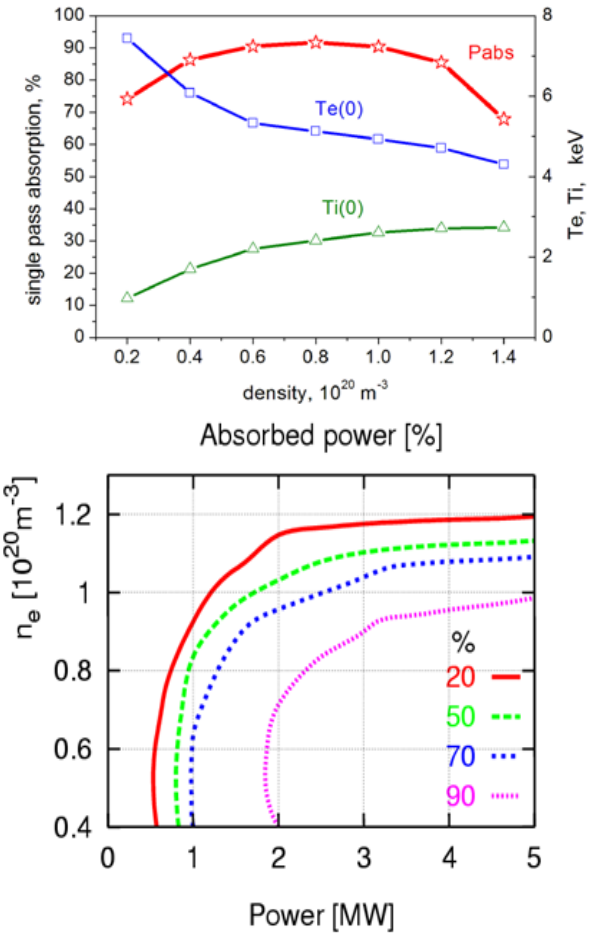

Fig. 1 Top: X3 single-pass absorption P_{abs} at 140 GHz from ray-tracing calculations as a function of the plasma density. The central electron and ion temperatures $T_e(0)$, $T_i(0)$ are also shown. Bottom: O2 triple-pass absorption at 104 GHz. Contours of constant absorbed power (in %) as a function of plasma density n_e and ECH power.

The non-absorbed part of the mm-wave beams would thermally overload the graphite tiles at the heat shield, which is opposite to the ECH antennas. Therefore several selected tiles will be replaced by specially shaped tiles made of TZM, which is a molybdenum alloy with small amounts of titanium and zirconium. These tiles reflect the mm-wave beams into a second pass through the plasma center onto a water-cooled stainless-steel reflector panel in between the ECH ports. This reflector will provide a third pass through the plasma as shown in Fig 1. (bottom)

and in Fig 2. Thus the total absorption will be significantly increased. The same reflector system can be used for the X3-heating scenario, where also an incomplete single-pass absorption is expected. The launching angle for both heating scenarios is about 12° at the position of the most elongated plasma cross-section. Therefore the beam deflection by plasma refraction is below 3 cm at the tiles, which can be easily compensated by the movable antennas. The ECCD capability at O2 will not be sufficient to compensate the bootstrap current for all magnetic configurations, but stellarator operation with a finite bootstrap current is also feasible.

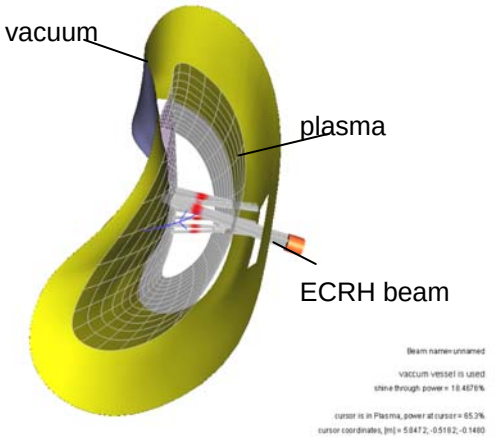

Fig. 2 Three-pass ray-tracing calculations for one selected mm-wave beam with O2-mode polarization.

For operation at ultra high plasma densities above the O-cutoff density Bernstein wave heating employing the OXB-mode conversion scenario is envisaged [6]. The transmission line and the in-vessel antennas are well designed to provide the required optimal launching angle of 55° in respect to the magnetic field direction and the nearly circular polarization. Two additional ports (N-type) are foreseen at W7-X for special ECH physics experiments with two mm-wave beams (2 MW). Here the beams will propagate along the B=const surfaces in order to localize the interaction in the phase space. Therefore advanced ECCD scenarios with supra-thermal electrons can be investigated. In addition, the N-port is also foreseen as the mm-wave injection port for the Collective Thomson Scattering diagnostics (CTS).

The in-vessel components will enable the above mentioned operational scenarios. The design of the front steering ECH antennas is compatible with full power CW requirements. Four antenna plugs are under construction, each block can handle three mm-wave beams (incl. two spare beam lines for a possible later upgrade) as shown in Fig. 3. The movable mirrors allow a poloidal steering range of ±25° and a toroidal steering range between ±15° and ∓35°, which complies with all operation scenarios.

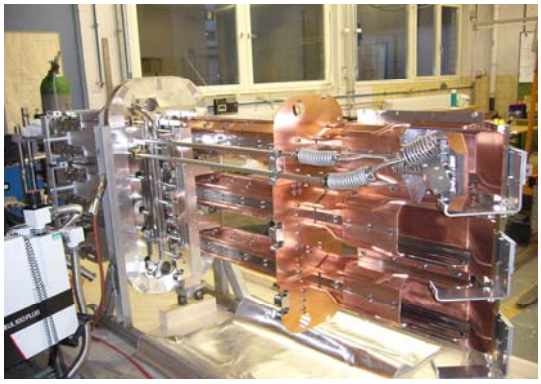

Fig. 3 Photo of the assembly of one of the four ECH antenna plugs.

The critical antenna components like the ceramic bearings and the flexible tube spirals for the cooling water supply had been already successfully tested in a mechanical mock-up under vacuum conditions and in ECH stray radiation environment. The mirror design is identical with the well proven transmission-line type. Most of the antenna components are already manufactured and the assembly has started (see Fig. 3).

The N-ports are very narrow and a remote steering scheme [7] will therefore be employed which is based on the imaging properties of a square corrugated waveguide. A solution with a bent waveguide was chosen. This makes the integration of the waveguides easier and provides a lower antenna beam divergence due to an increased waveguide cross-section. However, thorough optimization of the position of the miter bend and the vacuum valve in the waveguide are required.

The TZM reflectors for O2 and X3 heating scenarios have to sustain a mm-wave power of 0.5 MW on a surface of 120 cm^2 each. High power test (0.5 MW) of a prototype tile mounted on the original W7-X cooling plate showed an absorption of 0.3% which is in agreement with the theoretical value calculated from the material properties. With the resulting thermal load of 1.5 kW the tile reached after 200 s a steady state temperature of 470 °C at the surface and 390 °C at the cooling plate, which is acceptable for W7-X operation.

Reliable ECH operation requires special ECH-related diagnostics. The beam direction, its polarization and the absorbed power should be known with a high precision. In particular the latter is one of the most important plasma parameters, since the energy confinement time is the ratio of plasma energy and absorbed heating power.

120 pick-up antennas (open circular waveguides), which are incorporated in the heat shield tiles, will serve as diagnostics. These mono-mode waveguide tubes are combined into four bundles, which run along the vacuum vessel wall towards four B-type ports, where the signal is transmitted through the vacuum-air interface. Any contribution to the original polarization due to multiple waveguide bending will be compensated by appropriate phase shifters before the signal is detected by mm-wave diodes. A prototype of a waveguide bundle was already manufactured and is ready for a test assembly inside the W7-X vacuum vessel (see Fig. 4). The total absorbed power will be measured by at least five sniffer probes located in each of the five stellarator modules. These detectors measure the none-absorbed ECH stray radiation, which is distributed inside the vacuum vessel. Its signal will be used to detect any unintended reduction of ECH absorption in order to avoid severe machine damage of inappropriately armored in-vessel components by direct beam irradiation or mm-wave stray radiations. In addition it is planned to monitor the heat shield, which is opposite to the ECH antennas, by infrared cameras.

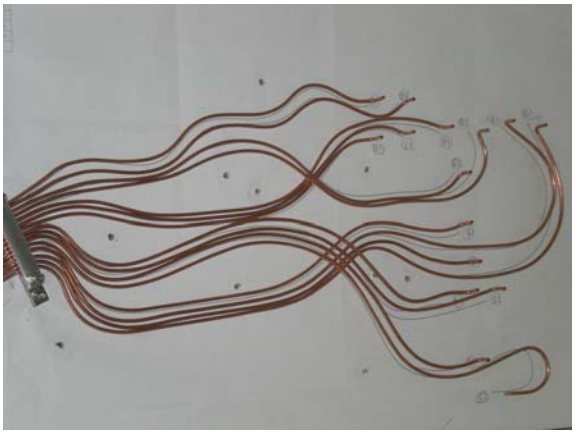

Fig. 4 Pre-shaped waveguide bundle prototype for assembly and routing tests inside the W7-X vacuum vessel.

3. Gyrotron testing and two-frequency operation

The first series gyrotron SN1 manufactured by Thales Electron Devices (TED) has been tested successfully at FZK and IPP in 2005. It has fulfilled all the specifications (0.91 MW in fundamental Gaussian mode, 30 min. pulse duration, 45% efficiency). During the acceptance test no specific limitations were observed. In order to keep the warranty this gyrotron has been sealed, the two equally performing prototype gyrotrons are routinely used for test experiments on advanced ECH components.

The next series gyrotrons showed a more or less different behavior with respect to parasitic oscillations excited in the beam tunnel region. These oscillations result in an excessive heating of the absorbing ceramic rings. The gyrotrons, re-opened after operation, showed significant damages due to overheating at the ceramic rings and the brazing of the rings. This limited in general the pulse length in full power operation to a few ms or the power in long-pulse operation to 0.6–0.7 MW.

In a first attempt to improve the situation, the manufacturer opened the series gyrotrons SN2 and SN3 and installed ceramic rings with a better brazing (SN2a, SN3a) and changed the sequence of the ceramic rings with different inner diameter (SN5). But both measures did not improve the situation significantly.

Therefore, FZK started in 2008 first designs to overcome this issue and to come to a more robust beam tunnel which suppresses the excitation of parasitic oscillations more efficiently. In order to validate a new beam tunnel as much as possible, it is planned to perform tests with a 170 GHz coaxial cavity gyrotron and a frequency step tunable 140 GHz gyrotron with a structurally modified beam tunnel which represents only a small change in the existing design.

In the following we will report on the experimental results obtained with the series gyrotrons SN2a, SN3a and SN5, all equipped with the original beam tunnel.

In 2008 acceptance tests have been continued with the repaired serial gyrotron SN2a at IPP Greifswald. The tube achieved 0.83 MW at 3 min and 0.71 MW at 25 min. pulse length. However, during conditioning of the tube the pressure level increased and complicated further progress. The control of the vacuum system of the gyrotron did not show a leakage. The acceptance tests of the tube were stopped by a crack of the output window which occured during operation without any alarm message from the interlock system. The gyrotron was sent back to the manufacturer for opening and detailed failure analysis.

The serial gyrotron SN3a has been tested at FZK in short pulse (~ ms) and long pulse (up to 30 min) operation with power levels of up to 0.8 MW and 0.5 MW, respectively. The output beam pattern has been measured and analyzed. The beam parameters are very close to those obtained in the first version of the gyrotron which shows a stable and reliable quasi-optical output system (see Table 1). Parasitic oscillations at a lower frequency (120 – 130 GHz) were observed which are supposed to be excited in the beam tunnel region and limit the performance of the gyrotron. After conditioning of the gyrotron, it was possible to operate the tube with a maximum power of about 0.72 MW for 3 min and

Table 1: Gaussian output beam parameters of the TED 140 GHz gyrotrons calculated from measured patterns.

Gyrotron	w_{0x}; w_{0y} beam waist	z_{0x}; z_{0y} location of beam waist	TEM_{00} [%]
Maquette	19.3; 17.4	-82.8; 61.2	95
Prototype	18.6; 21.3	202; 71	97
TED SN1	17.7; 21.6	126.9; 126.0	97.5
TED SN2	20.2; 22.5	103.5; 39.8	97
TED SN 2a	18.7; 22.2	127.0; 30.0	95
TED SN3	17.5; 20.6	130; 90	97
TED SN3a	17.6; 20.5	24; 77	96
TED SN 4	18.1; 18.5	105; 51	97

0.5 MW for 30 min, the specified 0.9 MW output power could not be achieved.

Acceptance tests of the serial gyrotron SN5 have been started at FZK. This tube has been equipped with a beam tunnel with a small modification of the inner contour which should suppress the excitation of parasitic oscillations. In short pulse operation the gyrotron delivered up to 0.95 MW. However, parasitic oscillations (120-130 GHz) were still limiting the performance of the tube. Furthermore and independent from the beam tunnel issue, the parameter optimization of this gyrotron had to be stopped as a shift of the mm-wave output beam at the window caused frequent arcing, raising the risk of a failure of the diamond disk.

The W7-X gyrotrons are optimized for single-frequency operation at 140 GHz, for details see ref. [8]. Their synthetic diamond windows have a resonant thickness of $4\lambda/2$ (1.8 mm) at 140 GHz and are also transparent at 105 GHz corresponding to $3\lambda/2$. Two modes, the $TE_{21,6}$ (103.8 GHz) and the $TE_{22,6}$ (106.3 GHz) exist in the vicinity of the desired frequency. Both modes could be exited by tuning the gyrotron magnetic field and adjusting the operation parameters (I_{beam} = 40 A and U_{acc} = 62 kV). We have focused on the $TE_{21,6}$ mode operation, because the output beam was almost perfectly centered at the output window, whereas the beam from the $TE_{22,6}$ mode was located somewhat off center. Using the TED prototype gyrotron a maximum output power of about 0.52 MW was achieved without collector voltage depression corresponding to an efficiency η = 21 %, which is compatible with theoretical predictions. The output power drops with increasing depression voltage while the efficiency increases from 21 % to 27 %. The corresponding collector loading at 0 and 8 kV depression voltage is 1.9 and 1.7 MW, respectively, which is incompatible with the collector-loading limit of 1.3 MW. Thus only operation at 0.4 MW with reduced beam current around 34 A can be handled safely. The mm-wave beam was transmitted through 7 mirrors of the quasi-optical transmission line into a calorimetric CW-load. Transmission losses of about 20 kW were measured, which compares well with the transmission loss fraction at 0.9 MW, 140 GHz operation. It is worth noting, that both the beam matching mirrors as well as the set of polarizers can be used without modification. Assuming, that all series gyrotrons behave similar to the prototype, the ECH&CD system of W7-X will be operated as a two-frequency system with a total power of 4 MW at the lower frequency. The operation range of experiments can then be extended towards different resonant magnetic fields of 1.86 T (X2 and O2 mode) and 1.25 T (X3 mode). An example for the O2-mode absorption at 103.8 GHz after 3 transits through the plasma is shown in Fig. 1 (bottom) as a function of plasma density and ECH power. The same transport code as for Fig. 1 (top) was used. An interesting parameter regime (absorption > 90 %) is accessible with moderate power at the reduced magnetic field. The calculated electron temperatures range from 3.5 to 5 keV, depending on plasma density and ECH power. Once plasma start-up could be achieved with the X3-mode, which is not clear yet, operation at 1.25 T is of particular interest, because ECH then could provide a target plasma for neutral beam injection heating for high-ß physics studies, which is most promising at low confining magnetic field.

4. High power tests of transmission system

The transmission system consists of single-beam waveguide (SBWG) and multi-beam waveguide (MBWG) components. For each gyrotron, a beam conditioning optics of five single-beam mirrors is used. Two of these mirrors match the gyrotron output to a Gaussian beam with the correct beam parameters. Two corrugated mirrors are used to set the appropriate polarization for optimum absorption of the radiation in the plasma. A fifth reflector directs the beam to a plane mirror array, the beam combining optics, which is situated at the input plane of a multi-beam waveguide (MBWG) [1]. The MBWG is designed to transmit up to seven beams from the gyrotron hall (entrance plane) to the stellarator hall (output plane). A mirror array separates the beams again at the output plane and distributes them via CVD-diamond vacuum barrier windows to the individually movable launchers in the W7-X torus. Two symmetrically arranged MBWGs are used to transmit the power of all gyrotrons. A major work package was the design completion and manufacturing of the transmission system near the torus. This comprises the reflectors type M13 and M14, which will be installed

in two "towers" in front of the W7-X ports as sketched in Fig. 5 (left). Both towers are completed, and the installation of control systems for reflectors and launchers, support structures, and granite absorbing plates has started, see Fig.5 (right).

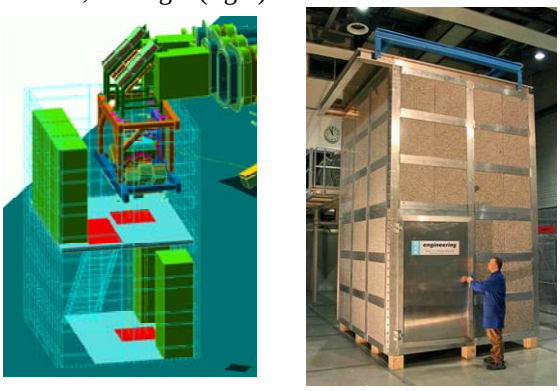

Fig. 5 Left: CAD sketch of the beam-distribution optics and control racks inside the two-storey tower. Right: ECH tower with mm-wave absorbing granite-wall structure.

Tests of the entire transmission line can only be performed, once the W7-X construction is completed and access to the main torus hall is provided. Therefore, we had installed retro-reflectors in the underground beam-duct in the image plane at half distance of the MBWG transmission line. Long-distance transmission can be simulated and tested by transmitting the high power mm-wave beams half way in forward direction and then back via the reflectors into the dummy load. First calorimetric high-power measurements are shown in Fig. 6, where the calorimetrically measured transmitted power is plotted versus the incident power. As a guide for the eye, the 'no-loss' line is also plotted. Total losses of 2.6±0.4% were measured for 10 reflections on the 2 x 3 MBWG mirrors and the 4 additional guiding mirrors over a total length of about 40 m.

The measured total losses are compared to the calculated losses for the individual components in Table 2. Good agreement is found with calculations and previous low power measurements. This result confirms the high quality of the quasi-optical concept for high power, long-distance transmission.

5. Summary

The ECH&CD system for W7-X is the most ambitious and largest CW plant presently under construction. It is designed to satisfy the physics demands for stationary heating and current drive at 2nd harmonic with X- and O-mode, 3rd harmonic with X-mode, as well as mode conversion heating in the high density regime with Bernstein modes. The 10 MW, CW mm-wave power from 10 gyrotrons is transmitted via an optical multi-beam waveguide system operating at atmospheric pressure, which is a unique feature of this system. The optical transmission offers favorable characteristics such as broadband transmission and a large margin for power handling. This allows operation of the system at two frequencies and with the option of a later power upgrade without modification of the transmission line.

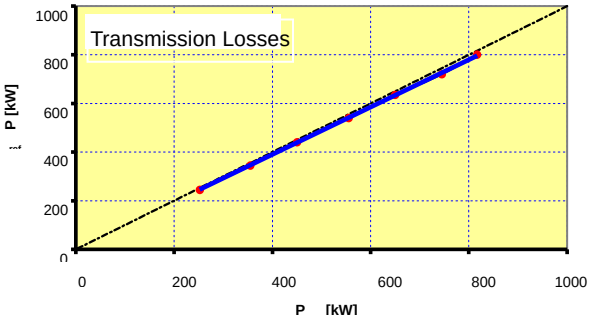

Fig. 6 Calorimetric measurement of the mm-wave power P_{refl} (after transmission through 10 mirrors) as a function of the incident power P_{inc}. The dashed-dotted line indicates no-loss transmission.

Tab. 2 Calculated transmission losses for different optical transmission components under normal atmospheric pressure (140 GHz). The sum of the different contributions is compared to the measured losses.

ITEM	OHMIC (%)	DIFFRACTION (%)	TOTAL (%)
M5, M6, M7	0.39	0.2	0.59
2 SR	0.26	0.1	0.36
M5, M6, M7	0.39	0.2	0.59
M4	0.13	0.1	0.23
SD	0.13	0.1	0.23
Atmospheric	0.68		0.68
SUM			**2.68**
MEASURED			**2.6 ± 0.4**

References

[1] V. Erckmann, *et al.*, Fus. Sci. and Techn., **52**, 291 (2007)

[2] N.B. Marushchenko, *et al.*, to be published in *Proc EPS 2007, Warsaw, Poland*

[3] M. Rome,*et al.*, Plas. Phys. Contr. Fus. **40,** 511 (1998)

[4] Yu. Turkin, *et al.*, to be published in *Proc EPS 2007, Warsaw, Poland*

[5] Yu. Turkin, *et al.*, Transport Simulations for W7-X. 33rd EPS Conference on Plasma Phys. Rome, 19 - 23 June 2006 ECA Vol.30I, P-2.113 (2006)

[6] H. P. Laqua, *et al.*, Phys. Rev. Lett. ***78***, 3467 (1997)

[7] B. Plaum, *et al.*, Fus. Sci. and Techn., ***50***, 1 *(2006)*

[8] M. Thumm *et al.*, IEEE Trans. Plas. Sci., **35**, 143 (2007)

Proceedings of ITC18,2008

A High-Power Gyrotron and high-power mm wave technology for Fusion Reactor

Keishi Sakamoto, Ken Kajiwara, Atsushi Kasugai, Yasuhisa Oda, Koji Takahashi, Noriyuki Kobayashi, Takayuki Kobayashi, Akihiko Isayama, Shinichi Moriyama

Japan Atomic Energy Agency, 801-1, Mukoyama, Naka, Ibaraki, Japan 311-0193

Recent activities on the developments of high power gyrotrons and high power millimeter wave technologies in JAEA are presented. A basic criterion of ITER gyrotron was satisfied using a JAEA $TE_{31,8}$ mode gyrotron. The output power from the gyrotron is used for developments of transmission line components and ITER launcher. The gyrotron is being operated for 3 years, and demonstrated operational reliability. As a next step, a new gyrotron was designed and fabricated, which operates at higher order resonator mode to enable the operation at greater than 1 MW. In parallel, feasibility studies of power modulation and dual frequency gyrotron were carried out. On 110GHz gyrotron system of JT-60U, 2.9MW power injection into the plasma was demonstrated for 5 sec pulse duration. The EC technologies under development for ITER and JT-60SA are applicable also for future fusion reactors such as DEMO.

Keywords: Gyrotron, mm-wave technology, $TE_{31,8}$ mode, ITER, DEMO

1. Introduction

On ITER (International Thermonuclear Experimental Reactor), a 20 MW electron cyclotron heating and current drive (EC H&CD) system is being planned for a plasma initiation, heating, current drive and MHD instability control [1,2]. As a power source, 1MW 170GHz long pulse gyrotron is required. A development of the 170 GHz gyrotron has been carried out from EDA phase (Engineering Design Activities) in Russia, Europe and Japan [3,4]. In 1990's, important breakthrough technologies for high power long pulse gyrotrons, such as a high efficiency mode converter [5], depressed collector [6], diamond window [7-9], were developed, which gave a route to the realization of 170 GHz 1MW CW gyrotron. In 2000's, quasi-CW operations were demonstrated by some gyrotrons. On 140 GHz gyrotron developed for Wenderstein 7X, by using an advanced built-in mode converter, 30 min operations were demonstrated by EU and US in 2003-2005 [10,11]. In 2006, a stable 1MW 170 GHz oscillation was demonstrated at CW-relevant pulse duration. Here, the efficiency was 55 % with a depressed collector at the optimum oscillation parameters in the so-called hard excitation region [12]. The achieved parameters satisfy a basic criterion required for the ITER gyrotron. Using this gyrotron as a power source, R&D of a transmission line and a launcher for ITER procurement is underway in addition to the reliability test of the gyrotron. As a next activity, the gyrotron development of higher power generation using a higher resonator mode has started. A resonator diameter is raised by increase the mode number in the resonator, which reduces a heat load density on the resonator wall. And, feasibilities of a power modulation for application to the Neo-classical Tearing Mode (NTM) suppression of ITER plasma and frequency tunability are studied for advanced operation. In parallel, the EC H&CD technologies developed for ITER have been applied for 110 GHz system on JT-60U.

In this paper, recent activities and next plan for EC H&CD technologies at JAEA are described. In section 2, present deign of ITER EC H&CD system is introduced. In section 3, experimental results of 170 GHz gyrotron are described, and tests of transmission line and launcher are described in section 4. R&D for an advanced gyrotron is discussed in section 5. In section 6, results of 110 GHz EC H&CD system on J-60U are summarized. A conclusion is given in section 7.

2. EC H&CD system of ITER

For the 20 MW EC H&CD system of ITER, 24 tubes of 1 MW-170 GHz gyrotron will be adopted assuming a transmission efficiency of 83 %. In the transmission line, various components such as a matching optics unit (MOU) that interfaces the gyrotron output power with the waveguide, 8~9 miter bends, 1~2 isolation valves, a torus window for tritium shielding, and a launcher, are included. The development of the launcher and demonstration of high efficiency high power transmission are important R&D issues for ITER EC H&CD system (section 4). The 24 gyrotrons are placed in the third floor of the RF building to be built adjacent to

author's e-mail: sakamoto.keishi@jaea.go.jp

the assembly hall of ITER as shown in Fig.1 [13]. Main power supplies are placed in the first floor, and beam acceleration power supplies [14] are placed in the second

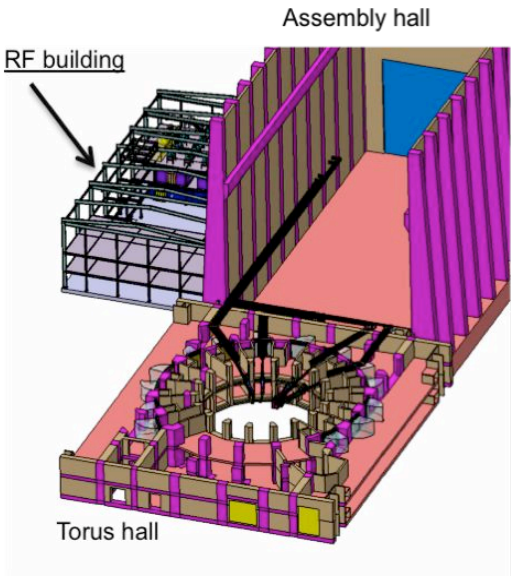

Fig.1 Layout of RF heating system and torus hall of ITER. (Courtesy of M.Henderson of ITER/IO)

floor of the RF building. The length of the transmission line will be ~150 m. Two types of the launcher are installed. One is the launcher installed in an equatorial port to perform the heating and current drive. Other is four launchers in upper ports, which have the control function of MHD instability [2].

3. 170GHz 1MW Gyrotron for ITER

The JAEA gyrotron has following feature [15]. An electron gun is a triode-type magnetron injection gun (MIG). In the beam tunnel, which indicates a section between the MIG and a resonator, conical silicon carbides are installed to suppress a parasitic oscillation. The resonator is a cylindrical cavity, whose Q-factor is 1530 at 170 GHz-$TE_{31,8}$ mode. A built-in mode converter placed at the downstream of the resonator is designed to generate a Gaussian beam using CCR-LOT and Surf3D codes [16]. The RF beam radiated from the converter is transformed with 4 mirrors and is outputted through the diamond window of 1.853 mm in thickness. The disk edge is coated by Copper to protect the bonding material between the cuffs and the diamond from the corrosion. In the operation, a pitch factor of the electron beam can be controlled by the changing the anode voltage V_{ak}. With a combination of resonator field B_c (magnetic field at the resonator), electron parameters (cyclotron frequency and pitch factor) can be optimized actively during the oscillation.

In Fig.2, a history of the gyrotron operation is shown. Operation begun at March 2006, and some important results, such as 1 hour oscillation, 1 MW/800 s/55 %, 0.8

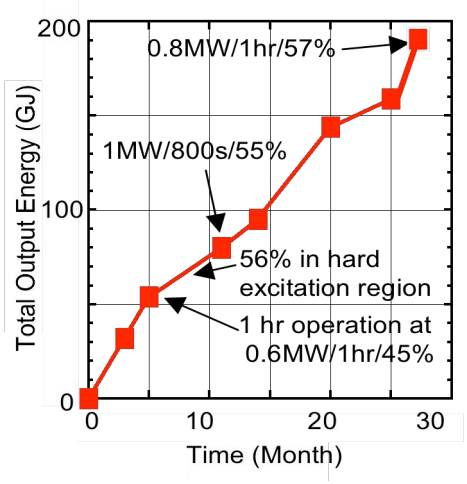

Fig.2: History of integrated RF energy outputted from the JAEA170 GHz gyrotron. Start was March of 2006.

MW/1 hour/57 %, have been demonstrated as indicated in the figure. The total output energy is ~200 GJ. The output power and deposition power in the tube was measured calorimetrically [17]. Sum of measured powers, i.e., output power from the window (1020 kW), collector deposition (742 kW), a stray radiation (24kW) and ohmic loss (63 kW), agrees well with the DC input power. In Fig.3, the beam current dependence of the output power and the efficiency with and without the depressed collector are shown. Pulse durations for all data are greater than 5 min. By the active control of V_{ak} and B_c, the operation parameters (electron cyclotron frequency and its pitch factor in the resonator) are optimized for each data in the hard excitation region. The maximum efficiency was ~60 % at 0.6 MW output. Fig.4 shows a time evolution of one-hour operation for the applied voltages, beam current (~30A), magnetic field at the resonator, light signal observed in the tube, RF signal at the directional coupler, vacuum in the tube at the output power of 0.8 MW. The efficiency was 57%. The oscillation was very stable during the shot. The pressure increased for 40 min, however, that kept a constant value after 40min. This pressure stabilization can be explained as follows. During the operation, the electron beam ionizes neutral particles in the tube. These positive ions are accelerated by the strong electric field applied for the depressed collector and those are absorbed by the collector wall. In other words, the depressed collector gyrotron acts as an ion pump inherently. When the

operation ended, such pumping effect disappears. Consequently, increase in the pressure occurs because the ions are released from the collector wall and no additional pumping effect.

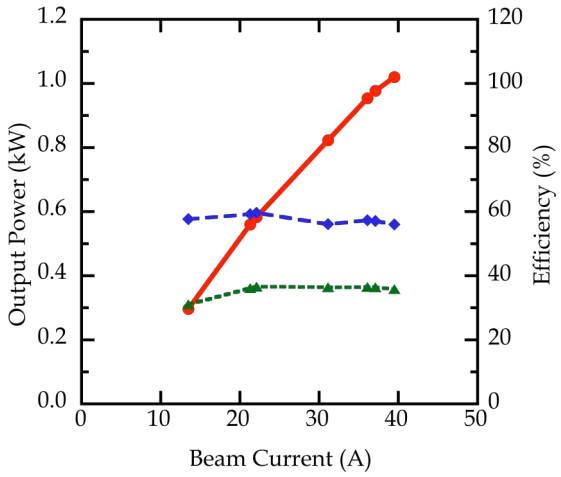

Fig.3: Experimental result of beam current dependence of output power at 170 GHz (red), oscillation efficiency (green) and overall efficiency with depressed collector (blue). Beam voltage is ~72 kV, anode voltage, depressed collector voltage, B_c are optimized for each data points. Pulse durations are greater than 5min.

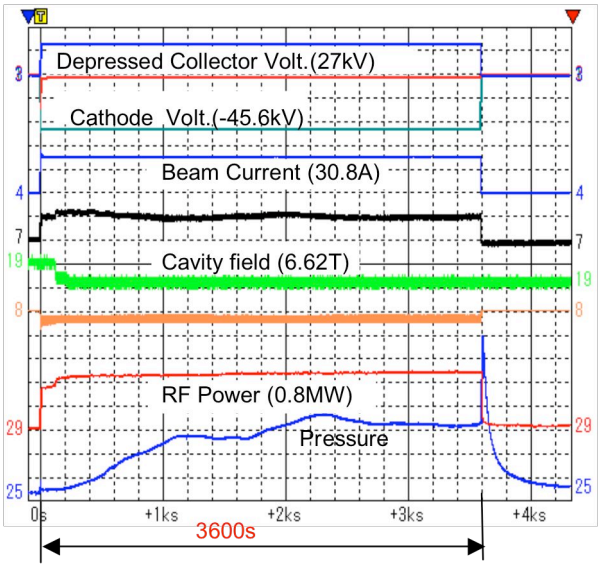

Fig.4: Time evolution of 1-hour operation of 170 GHz gyrotron at 0.8 MW. The efficiency is 57 % with the depressed collector.

As a simulation of gyrotron operation on ITER, a high repetitive RF generation was demonstrated at 0.8 MW. Ten shots were repeated for every 30 min with the pulse duration of 400sec. The efficiency with the depressed collector was ~56%. No major trouble was observed, which gives a prospect of stable operation in ITER experiment [18].

4. RF power transmission and launcher for ITER

The output power of the gyrotron is used for developments of transmission line and launcher components [19]. In Fig.5, picture of the test transmission line in JAEA is shown. The output power couples with the waveguide of 63.5mm in diameter via two-phase correlation mirrors in a matching optics unit (MOU), and 92 % of the output power was transmitted to the dummy load via 40 m evacuated transmission line including 7 miter bends. Here a power loss in the MOU is ~4.5 %. At the end of the transmission line, components, such as a torus window for ITER, arc detector, low loss miter bend, polarizer, are connected for high power and long pulse tests. Furthermore, as with the practical system, a test launcher is connected after the transmission line.

For this purpose, a preliminary launcher mock-up was manufactured as shown in Fig.6. Fig.6(a) shows one of three quasi-optical RF beam lines of the equatorial launcher [20]. Fig.6 (b) is a picture of the launcher mock-up fabricated based on the updated design of the equatorial launcher. High power mm wave is outputted from one waveguide, and radiated from the movable mirror. The radiated power is reflected by two mirrors and outputted from the launcher as a bundle of the beams. The surfaces of two mirrors are optimized to minimize the heat load on the mirrors [21]. The angle of the final

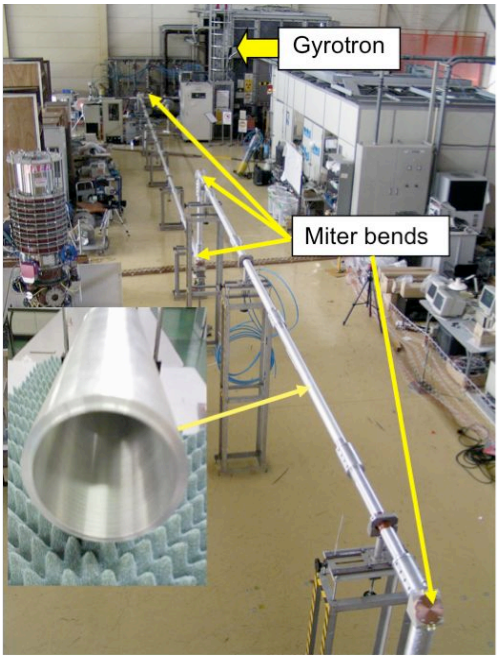

Fig.5: Picture of transmission line of JAEA test stand.

mirror can be controlled using an ultra-sonic motor. The power is received by a metal dummy load.

The test system includes most of the essential parts of ITER EC H&CD system. The test on this system will provide useful database for the detailed design of the system.

5. Advanced Gyrotron

5.1 Higher mode oscillation of 170 GHz gyrotron

The R&D of a high power gyrotron using a higher mode oscillation has started. The oscillation mode is $TE_{31,12}$ cylindrical resonator. By increasing the oscillation mode, the resonator diameter increases from 17.9 mm to 21.84 mm, and the heat load on the resonator wall significantly decreases. This will contribute to the higher power generation and relax a thermal stress on the resonator. On the other hand, careful setup and operation will be required to establish the stable and high efficiency oscillation. The MIG is the same configuration with the $TE_{31,8}$ gyrotron. As a first step, a short pulse gyrotron was fabricated and tested. The output power of ~1.57 MW was obtained at 170 GHz. Based on the result, a long pulse $TE_{31,12}$ mode gyrotron was fabricated as shown in Fig.7. The experiment will be done soon.

5.2 Power modulation

In ITER, high frequency power modulation up to 5 kHz will be required for suppression of NTM instability. For this purpose, a test of high power modulation of JAEA gyrotron is planned using a voltage modulation of a body power supply [14]. Generally, when the power modulation is applied, the collector heat load increases since the non-workout electron beams impact the collector. In case of the JAEA gyrotron, however, the modulated voltage of the body V_m appears as a decrease in the anode-cathode voltage V_{ak} of the triode MIG since the anode-body voltage is kept constant. Since a beam current decreases as the V_{ak} does, the current drop by the voltage modulation must be much larger than the diode type MIG. Furthermore, if the anode modulation is added on, V_{ak} will decrease to 0V. Consequently, the beam current could be reduced to small level. Then, the averaged collector heat load can be suppressed significantly, which will permit the operation at larger beam current to increase the oscillation power on the identical gyrotron.

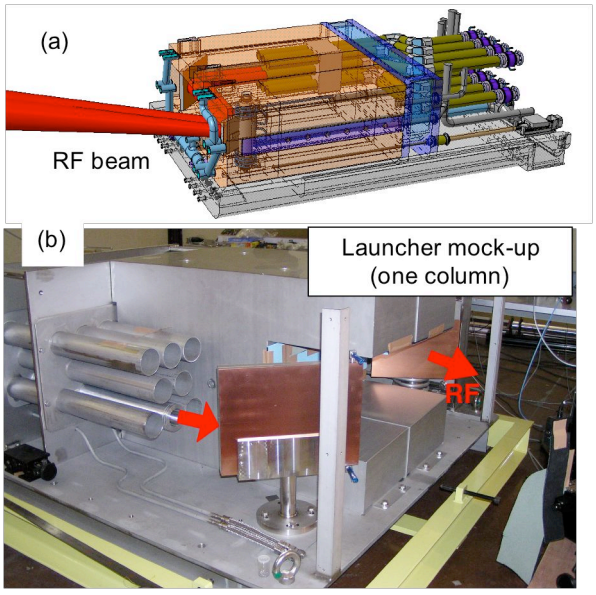

Fig.6: Mockup of equatorial launcher. (one of three beam lines).

Fig.7: Picture of 170 GHz gyrotron. Oscillation mode is $TE_{31,12}$, and Gaussian beam output.

5.3 Dual Frequency gyrotron

High power multi-frequency gyrotrons have been studied by many institutes [22-24]. These gyrotrons have a diode MIG. Generally, the triode has a larger flexibility than the diode for determination of electron beam parameters such as beam radius, pitch factor at fixed beam voltage. Therefore, the triode type MIG is much suitable for the multi-frequency gyrotron. Here, a set of $TE_{31,11}$ and $TE_{25,9}$ modes for 170 GHz and ~137 GHz, respectively, are proposed. The mode corresponds to the transparent frequency of the diamond window of 1.853 mm in thickness. By adjusting the anode voltage the mirror ratio between the resonator and MIG fields,

optimized pitch factor can be selected at any beam voltage. Consequently, 1 MW high efficiency oscillation will be available at both modes. The high efficiency mode conversion is also available from the oscillation mode to the Gaussian beam for both modes.

5.4 Fast field control super conducting magnet

For a step tunable frequency control at reasonable beam parameters, a magnetic field control should be accompanied. For a fast control of B_c, He-free super conducting magnet with an additional sweeping coil was developed [25]. A diameter of a room temperature bore is 240 mm, and the 7 T at the center. Using commercially available DC power supplies, the magnetic field sweeping was demonstrated with a speed of 0.4 T/10 sec at 7T.

6. 110 GHz gyrotron for JT-60U and JT-60SA

The 110 GHz gyrotron has been designed firstly in 1998 taking into account the results of 170 GHz gyrotron in ITER. The basic configuration is the same with the 170 GHz gyrotron. The oscillation mode is $TE_{22,6}$ at 110 GHz. The MIG is the triode gun, and the depressed collector is adopted. The thickness of the diamond window is 1.715mm. The EC H&CD system was firstly applied on JT-60U in 1999, and upgraded to 4-gyrotron system in 2001. Liquid He free magnets have been used for all gyrotrons, and no major trouble had occurred. The EC H&CD was used on JT-60U, and many important results were demonstrated on the large sized plasma, such as electron heating to 26 keV [26], plasma initiation by second harmonic ECR [27] and NTM suppression [28]. In 2008, the total injection power of 2.9 MW for 5 sec was demonstrated [29] and its operation has ended on JT-60U. In the last experiment campaign, modulated ECCD at 5-7 kHz synchronized to NTM was achieved by real time control of anode voltage [30] and stronger stabilization effect was obtained than un-modulated ECCD by a factor of more than 2 [31]. The improvement of EC H&CD system has started aiming 100sec operation on the future JT-60SA. In parallel, the effort for improvement of 110 GHz gyrotron performance is continued after the JT-60U shutdown. Up to now, the demonstration of 1.5 MW/1 sec has succeeded [32]. Here, the beam voltage and the beam current are 86 kV, 62.8 A with the depressed collector voltage of ~26 kV. In the near future, the experiment will be continued using the gyrotron where the improved mode converter is installed.

7. Conclusion

A basic requirement of the ITER gyrotron performance was demonstrated with the JAEA 170 GHz gyrotron. As the next activity, higher order mode gyrotron is under development for a higher power generation. In parallel, the demonstration of the power modulation is planned for ITER application. And, a design of a dual frequency gyrotron was proposed. The high power gyrotron is used as a power source for the developments of transmission line and ITER launcher. The full performance of EC H&CD system was demonstrated on JT-60U with 110 GHz gyrotrons, where 2.9 MW/5 sec injection was attained. These activities give a prospect for the procurement for ITER and JT-60SA. As the EC technologies have a generality, R&D carried out for ITER and JT-60SA are also applicable for all kind of magnetic fusion devices and future reactor DEMO since the present design of the magnetic filed strength is similar level [33].

Acknowledgments

Authors would thank to the encouragement of Drs.M.Akiba, R.Yoshino, H.Takatsu and T.Tsunematsu.

References

1. How J. (ed) 2007 Project Integration Document PID ITER_D_2234RH Ver3.0 and https://user.iter.org/?uid=2234RH&version=v3.0.
2. M.Henderson, G.Saibene, Nuclear Fusion, **48**(5) 054017 (2008).
3. M.Thumm, Int.J.Infrared and mm waves, **26**, 4, 483 (2005).
4. K.Sakamoto, Fusion Sci. &Tech., **52**, 145 (2007).
5. G.G.Denisov, et al., Int.J.Electronics, 72, 1079 (1992).
6. K.Sakamoto, et.al., Phys.Rev.Lett., 73, 3532 (1994).
7. O.Braz, et al., Inj.J.Infrared and mm waves, **18**, 1945 (1997).
8. A. Kasugai, et al., Rev.Sci.Instrm., **69**, 2160 (1998).
9. K.Sakamoto, et.al., Rev.Sci.Instrm., **70**, 208 (1999).
10. K.Felch, et al., J.Phys.Conf.Ser., **25**, 13 (2005).
11. G.Dammertz, et al., IEEE Trans. Plasma Sci., 34, 173 (2006).
12. K.Sakamoto, et al., Nat.Phys., vol.3, p.411 (2007).
13. C.Darbos, et al., in Proc. of 25th Symp. on Fusion Technology, Rostock, Germany, P3.11 (2008).
14. T.Bonicelli, et al., Proc.22nd Symp. Fusion Technology (SOFT02), Helsinki, Finland, September 2002, p.543 (2002).
15. K.Sakamoto, et.al., Nucl.Fusion, **43** 729(2003).
16. J.Neilson, IEEE Trans.Plasma Science, **34**, 635 (2006).
17. A.Kasugai, et.al., Nucl.Fusion, **48**, 5, 054009 (2008).
18. K.Kajiwara, et al., to be published in J.Plasma and Fusion Res. (2009).
19. K.Takahashi, et al., to be submitted.
20. K.Takahashi, et al., Nucl.Fusion, **48**, 5, 054014 (2008).

21. K.Kajiwara, Fusion Eng. Design, **84**, 1, 72 (2009).
22. M.Thumm, et al., Fus.Eng.Des., **53**, 407 (2001).
23. D.Wagner, et al., Nucl.Fusion, **48**, 05406(2008).
24. G.G.Denisov, Nucl.Fusion, **48**, 05407(2008).
25. K.Sakamoto, et al., J.Phys. Conf.Ser., **25**, 8 (2005).
26. T.Suzuki, et al., Nucl.Fusion **44** 7, 699 (2004).
27. K.Kajiwara, et al., Nucl.Fusuin, **45** 7, 694 (2005).
28. A.Isayama, et al., Nucl.Fusuin, **43,** 10, 1272 (2003).
29. 27. S.Moriyama, et al., in Fusion Energy Conf. FT/P2-26 (2008).
30. T.Kobayashi, et al., submitted to J.Plasma and Fusion Res. (2009).
31. A.Isayama, et al., in Fusion Energy Conf. EX/5-4 (2008).
32. T.Kobayashi, et al., J. Plasma and Fusion Res. **3**, 014 (2009).
33. K.Tobita, et al., Fusion Eng.Des., **81** 1151 (2006).

Proceedings of ITC18, 2008

Ion cyclotron frequency range (ICRF) power on the way to DEMO

J.-M. Noterdaeme

Max Planck Institute for Plasmaphysics, EURATOM Association, D-85748 Garching, Germany
University Gent, EESA Department, B-9000 Gent, Belgium

The use made of "auxiliary" systems, such as the ICRF power system, the environment in which those systems will operate and the requirement they must fulfill, will change drastically between present systems, systems for ITER and those for DEMO. Some characteristics, now presently barely relevant, will become increasingly important. The paper draws attention to the changes, gives an overview of the ICRF system for ITER and highlights where extrapolations with respect to present systems are required. It moves on to DEMO and shows where the strength of ICRF is and proposes an approach to mitigate its weak points.

Keywords: ICRF, ITER, DEMO, heating, control, T breeding, maintenance, availability, economics

1. Introduction

Since in DEMO type machines only a limited number of plasma heating and control systems will be acceptable, the selection of the systems to be installed will be severe. The selection criteria, guided by characteristics relevant for DEMO, will be quite different from the present ones.

Some characteristics of the heating and control systems, of no considerable importance in present machines, will become increasingly significant as machines move from present experiments to DEMO type machines. This is due to the major changes that will occur in 1. the use that will be made of the systems 2. the environment in which the systems will operate and 3. the requirements they must fulfill.

An ICRF system scores well on the relevant characteristics and is therefore a strong candidate as one of the heating and control systems in DEMO type machines. There are however areas that need to be addressed in present and future machines.

The paper gives an overview of the ICRF system for ITER and highlights where extrapolations with respect to present systems are required. These need to be taken up with high priority in existing machines and on test stands. Critical aspects are the voltage standoff in the antenna and absolutely reliable arc detection methods. Impurity production in a high-Z metallic wall environment may become an issue in a later stage of ITER, but proposals for mitigation can and should be investigated in ASDEX Upgrade and Alcator C-mod.

The paper proceeds to elucidate the role of ICRF on DEMO. Experiments on present-day machines and on ITER could strengthen the case for ICRF on DEMO.

author's e-mail: noterdaeme@ipp.mpg.de

It is fit to highlight, at a Toki conference, the interesting synergy between ICRF and steady state helical concepts. The steady aspects of the helical concept has allowed ICRF in LHD to demonstrate the long pulse capability of ICRF systems and thus to reinforce suitability of ICRF for the long pulse/steady state machines of the DEMO type. In the other direction, ICRF systems can contribute significantly to qualify the helical concept for ITER/DEMO type machines: experiments on fast ions confinement with ICRF in present helical machines have shown that the helical concepts can confine energetic particles [1].

2. Use made of the system

Present "auxiliary systems" are mainly used for heating, whereas other functions such as control of the current profile, density profile or rotation only come into play to increase the experimental flexibility or for demonstration purposes.

For ITER, heating to ignition will be an important function, but only for a fraction of the time. The remaining time, the heating system will be either idle or, if possible, used for burn, current and density profile control. An important application could be wall conditioning.

For DEMO, the use of the system for heating to ignition will and should be a negligible fraction of the time. If the confinement concept chosen for DEMO requires a plasma current, then driving current and/or controlling the current profile will likely be the dominant use of a least one auxiliary system. Other applications will include burn and density profile control.

The need to limit the number of "auxiliary" systems on DEMO, will favor systems that can perform more than

one function. ICRF systems have been used for heating, both electrons [2] and ions [3]. Its use for burn control was investigated on JET with positive results [4]. Control of sawtooth, using current profile modification has been extensively demonstrated [5][6][7]. Central current drive was shown in D-III-D [8], while ICRF power can also be used for wall conditioning [9], even in conditions where glow discharge cleaning is no longer possible due to the presence of a permanent magnetic field. In general it was shown that ICRF could be utilized for many other purposes than heating alone [10].

On this basis, ICRF is clearly a good candidate for a machine where the number of "auxiliary" systems is limited and therefore systems are favored that can perform more than one function.

2. Environment in which the system needs to operate

Most of the present experiments operate with short pulses. In current experiments also, the presence of neutrons does not have an major influence neither on the design of the components near the plasma, nor must the shielding/ neutron streaming effect due those components on the regions further removed from the machine be considered. Remote maintenance is sometimes needed, such as in JET, but is mostly the exception.

In ITER, even when operated in pulsed mode, the timescales for the auxiliary systems will be such that they need to be designed for steady state. The presence of neutrons influences the choice of materials and the location of certain components, but it is mainly the biological aspects of the radiation that dictate the use of remote maintenance. Shielding or neutron streaming due to the presence or absence of certain components in the ports is an important design parameter. When neutron streaming cannot be avoided (such as in the case of NBI), measures have to be taken to shield the neutrons at a more remote location. Overall dimensions are larger, leading also to larger plasma-antenna distances, a negative aspect if wave-coupling structures are used.

In DEMO, the presence of neutrons will dominate the choice of materials as neutron damage will influence how often components need to be replaced, and how much waste is produced. Neutron streaming through large opening in the blanket will be difficult to accept. The systems exposed to large neutron fluxes must be simple and sturdy, and should not impose constraints on the materials used. Remote maintenance will be essential, but should be limited for the auxiliary systems to times when other major components (such as blankets) need to be replaced. In addition, in a pure fusion DEMO, tritium breeding will be indispensable, favoring systems with small openings in blanket and shields.

It is conceivable that, because of the importance of T breeding, the number of ports will be severely restricted in machines of the DEMO type. Whereas in ITER the ICRF antenna is part of a port plug, it would be preferable for ICRF antennas in DEMO to be integrated in the blanket and the opening through the blanket limited to the transmission line only. The resulting impact on T breeding is then minor. Neutron streaming, already small along those small penetrations, can be further reduced by proper measures. The power density calculated based on the area of the transmission line is high, while the power density at the surface of the antenna can be low. Insulators, required in the vacuum feedthrough of the line, can put in an area of sufficient low neutron flux, and, as already foreseen in ITER the system should be designed such that they can be replaced separately. The replacement of components exposed to neutrons near the machine should be compatible with scheduled remote maintenance and not require more frequent intervention than needed for the blanket components.

3. Requirements

In present experiments, the choice and number of systems is determined more by the desired experimental flexibility and by what each of the systems can do best, more than by capital cost considerations. The cost of operation is a non-issue. The availability of the system is important but non-essential, and none of the systems operate all the time at their maximum power. Reliability is desired, but, if need be, a shot can usually be repeated.

For ITER, the capital cost of the "auxiliary system" becomes an important issue, with 10% of the total cost devoted to the "auxiliary" systems. Operating cost, in terms of cost of electricity to provide the power during the pulse is not a significant matter. As such, the plug to power efficiency of the auxiliary system does not play a major role in its selection. The system should not prevent ITER to operate, or lead to long down time, therefore a high availability is valuable. As each discharge will count, reliability will be paramount.

For DEMO, meant in part to provide the basis for the demonstration of the economic viability of a fusion power plant, the capital cost of a system may be a key criterion for its inclusion or rejection. Here the cost per MW plays a role as well as the amount of power that needs to be installed. The power that needs to be installed depends on how efficiently the system acts on the plasma. For example, if current drive is needed, the current drive efficiency will play a defining role in the power to be

installed, and thus in the capital cost of the auxiliary system.

Since DEMO should be running a substantial fraction of the time, cost linked directly with the operation of the auxiliary systems will play a crucial role. Small recirculating power will be essential, emphasizing the need for systems with high plug-to-power efficiency, as well as a high efficiency in its action on the plasma.

Availability is, together with the capital cost, a term in the cost of electricity, and therefore of paramount importance for the economic viability of fusion. It means that the systems must have a large mean time between failure (MTBF), and a low mean time to repair (MTTR). These requirements lead to a preference for systems where components that need maintenance and or replacement are easily accessible (far from the machine), and sufficiently low cost that some redundancy can be provided. Modern nuclear power plants achieve a ratio of supplied TW_e h during one year to the product of *installed* power times number of hours in one year, of more than 0.9, which is equivalent to saying that, except for one month per year, the plant operates continuously at *full* power. This is a benchmark that fusion will certainly not achieve in DEMO, nor in the first fusion power plants. Those values were also not achieved from the early days of nuclear fission, nor are they reached by all nuclear power plant, but it gives an indication of the goal.

Since losing a system during operation may lead to disastrous consequence (if burn control fails, an emergency turn-off of the reactor may be needed), a very high reliability will be required. Sturdy systems, with no moving parts, operating well away from limits, will therefore be favored.

ICRF has among the auxiliary systems, the lowest cost in terms of cost/installed power and the largest plug to power efficiency (power supply, transmission, generator, coupling: typically 0.5). Thus, except if ICRF were to be used for current drive, both the capital and operating cost of an ICRF system would be one of the lowest among the existing auxiliary systems. The efficiency of driven current/installed power is for ICRF presently low, so that either ICRF should better not be used for this, or substantial progress in this area is necessary. Most of the ICRF components, except for the antennas, are located far from the machine. The unit size and cost of the RF generators are such that some redundancy can be provided. If a unit breaks down the redundant units can be used, while the remote location of the generators allows the repair of the broken one, during continued operation of the others. The ILA JET antenna and the ITER antenna operate at high power density close to operating limits, making it a critical component of the ICRF system. For DEMO, making the antennas part of the blanket could mitigate this. With antennas located in such a way the power density could be low, and those components would be operating much further from existing limits.

4. Extrapolations needed for ITER

The ICRF system for ITER [11] foresees to deliver 20 MW through one or two antennas with a size of approximately 1.75m (toroidal) x 2.2m (poloidal), designed for operation between 40 and 55 MHz. The design and manufacturing of the antenna [12] are the responsibility of the European partner. The present design, developed by the CYCLE consortium (Cyclotron Cluster for Europe – a consortium of the associations: UKAEA, CEA, ERM-KMS, IPP and Politechnico de Torino) has 8 triplets of straps arranged in an array of 4 in the toroidal direction and 2 in the poloidal direction (see Fig. 1). The matching systems and coaxial transmission lines are the responsibility of the US partner. Standard type short-circuited stubs, line stretchers and capacitors will do the matching of the impedance of the antenna to the impedance required by the generators. The generators will be shielded from fast transients by 3 dB couplers [13]. A generator power of 20 MW (eight generators rated a 2.5 MW for VSWR=2) will be installed. The generators are the responsibility of the Indian ITER partner.

The ILA antenna on JET [14] incorporates many of the features that will be present in the ITER antenna: the close array of short strap, with non-negligible cross coupling and resulting challenging matching procedure, the high power density and high voltages. On ILA, voltages of 45 kV have been achieved, higher than the 40 kV design voltage on ITER. Even in this tightly coupled array, automatic matching has been achieved. Though the design values of the coupled power (8 MW/m^2 for 7.2 MW coupled) have not yet been achieved, there is confidence that the experience gathered on the ILA will allow to qualify the new tools (TOPICA) to calculate the expected coupling of the ITER antenna. Those tools did not yet exist when the ILA was designed.

The transmission line system does not present a substantial extension of the state of the art. Challenging will be to find the right balance between cost and operating limits for steady state operation at high power. Which part of and how to cool actively the transmission lines and matching components will be choices that need to be carefully made. LHD has developed liquid stub tuners that are basically suited for steady state, but have not yet achieved the needed values of voltage strength.

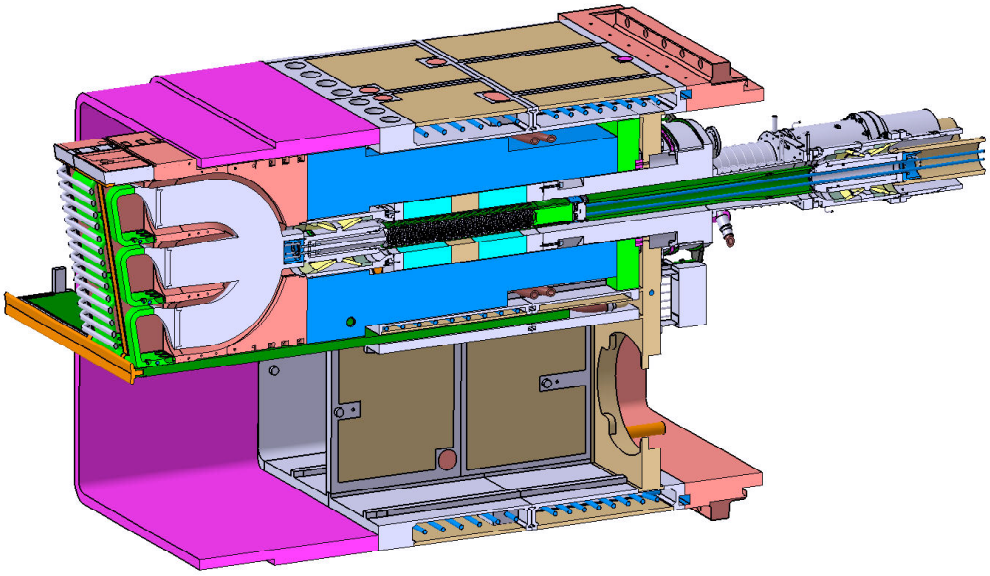

Fig.1 Present design of the ITER antenna. Eight triplets of straps (one triplet shown) are arranged in an array of 4 in the toroidal and two in the poloidal direction. Each of the triplets is fed by a transmission line that incorporates two double conical feedthroughs. They are replaceable without having to remove the whole antenna [14].

No RF generator exists yet that has achieved the required values. Closest is the Korean development with 1.9 MW for 300s achieved at a single frequency, and for a specific load [15]. It is as yet not clear whether the required parameters can be achieved with existing tetrodes or whether new types of tubes will need to be developed.

From this brief overview, we can conclude that the extrapolations in the technical area needed for ICRF on ITER will be moderate and that we are already well on our way to achieve the required design parameters.

One area where substantial work is required is the question of impurity production with ICRF when high Z metallic walls are used in the immediate neighborhood of the antenna.

In ASDEX Upgrade where such conditions are present, the use of ICRF is possible but presently restricted to operation at large plasma-wall distances and with additional gas puffing [16]. The impurity production is understood to be the result of acceleration of ions (mostly impurity ions) in the rectified sheath near the wall. The sheaths themselves are due to rectification of parallel electric fields induced along field lines, mostly by currents induced at the boundaries of antenna structures. Results from newly developed electromagnetic codes, supported by experiments, indicate that it is possible to reduce those RF electric fields [17][18], and thus of the impurity production. Experiments on ASDEX Upgrade and Alcator C-mod [19], in particular with new, optimized antennas should be able to clarify the compatibility of ICRF and high-Z metallic walls.

A second area where progress is needed is the arc detection systems. In most present machines arcing in antennas sets the operational limits. The voltage limits achieved vary between 30 kV and 45 kV (in the ILA antenna), and are still not completely understood. Several types of arcs can occur [20], and several methods will need to be developed to detect them with required reliability. Whereas most present system can cope with limited failures of the arc detection systems, the steady state cooling needs of the components in systems like Tore Supra and JET, and in all future machines, leads to catastrophic consequences (water leaks and sometimes major flooding) if an arc is not detected in time.

Except for those two areas (impurity production and arc detection) the extrapolation from present system to ITER is of a quantitative nature, and most of the parameters such as unit power, pulse length, voltages, power densities have already been achieved or are well on their way of being achieved.

5. Extrapolations needed for DEMO

The changes for the auxiliary systems in their use, the environment in which they operate and the requirements placed upon them will be substantial compared to the present systems and to ITER and qualitative aspects will play a major role.

Those changes were indicated in the corresponding sections, and it was shown there that ICRF is well positioned to be one of the auxiliary systems for DEMO.

A number of areas, where ICRF needs further progress are addressed here briefly and a proposal is made which could contribute simultaneously to progress in those areas. These areas are the impurity production, the voltage limits and the small current drive efficiency.

The parallel electric fields, induced on field lines in front of the antenna which lead to rectified sheath, and thus to impurity production, are themselves dominated by the currents at the antenna boundaries. Antennas where the toroidal variation of the current is smoother as in [21], lead to less induced currents at the boundaries, less induced parallel electric fields and thus less impurities.

The high voltage in the antennas and related danger for arc and damage of antenna structures is directly related to the high power density. Antennas with lower power densities would lead to lower voltages and reduce the likelihood of arcs.

On the basis of simple arguments, it can be shown that current drive efficiency increases with the velocity squared of the electrons the wave couples to, if the wave accelerates electrons with high parallel velocity (this is the region of the lower hybrid wave) and with one over the velocity of the electrons, if low parallel velocity electrons are accelerated – assuming trapped particles effects do not reduce this efficiency (this is the region of ohmic current drive). ICRF couples to the electrons whose parallel velocity is close to the phase velocity of the wave and near the minimum of both branches.

One could consider in DEMO the use of a continuous array of low power density antennas, distributed over the whole outer circumference of the machine. The antennas would be an integral part of the blanket. The only penetrations though the outer chamber walls and blanket would be the transmission lines. By proper phasing between the antennas of the continuous array a well-defined toroidal wave number, with a well defined toroidal standing wave pattern would be generated. The resulting low $k_{//}$ would increase the coupling, while the smooth toroidal variation of the current would avoid induced currents at discontinuities and therefore large $E_{//}$ fields. By an appropriate slow phasing variation, a slow rotation of this wave pattern can be achieved. Since the rotation of this standing pattern can be arbitrarily slow, and if electrons can be accelerated using this slow rotation, one could possibly be on the branch of the current drive efficiency curve where the efficiency increases with 1/velocity. This is reminiscent of the rotamak type current drive [22].

Should this concept work, 3 critical areas of the use of ICRF would be, if not solved, at least substantially improved (impurity production, high voltage, low current drive efficiency) improving the prospect of ICRF for DEMO and machines beyond it.

References

[1] Mutoh T., *Steady-state operation ans high energy particle production of MeV energy in the Large Helical Device*, Nucl. Fusion 47 (2007) 1250-1257.

[2] Mantsinen M.J., *Localized bulk electron heating with ICRF mode conversion in the JET tokamak*, Nuclear Fusion 44 (2004) 33-46.

[3] Mantsinen M.J., *Fast ion distributions driven by polychromatic ICRF waves on JET*, Plasma Physics and Controlled Fusion 47 (2005) 1439-1457.

[4] Jones T.T.C., *Simulation of Alphy Particle Plasma Self-Heating Using ICRH under Real-Time Control*, in Controlled Fusion and Plasma Physics, (Funchal (Madeira), Portugal, 2001), Vol. ECA 25A, EPS (2001) 1197-1200.

[5] Mantsinen M.J., *Analysis of ion cyclotron heating and current drive at omega approximate to 2 omega(cH) for sawtooth control in JET plasmas*, Plasma Physics and Controlled Fusion 44 (2002) 1521-1542.

[6] Eriksson L.-G., *Destabilisation of fast ion induced long sawteeth by localised current drive in the JET tokamak*, Phys.Rev.Lett. 92 (2004) 235004.

[7] Parisot A., *Sawtooth period changes with mode conversion current drive on Alcator C-Mod*, Plasma Physics and Controlled Fusion 49 (2007) 219-235.

[8] Petty C.C., *Fast wave current drive at high ion cyclotron harmonics on DIII-D*, Plasma Phys. and Contr. Fusion 43 (2001) 1747.

[9] Lyssolvan A., *New scenarios of ICRF wall conditioning in TEXTOR and ASDEX upgrade*, Journal of Nuclear Materials 363 (2007) 1358-1363.

[10] Mantsinen M., *Application of ICRF waves in tokamaks beyond heating*, in Plasma Physics and Controlled Fusion 45 (2003) A445-A456

[11] Sakamoto K., *Progress in ITER Heating and Current drive system*, in IAEA Fusion Energy, (Geneva, 2008), IAEA to

be published.

[12] Nightingale M., *RF and mechanical design of the ITER ICRF antenna*, in IAEA Fusion Energy, (Geneva, 2008), to be published.

[13] Noterdaeme J.M., *Matching to ELMy plasmas in the ICRF domain*, Fusion Engineering and Design 74 (2005) 191-198.

[14] Nightingale M., *Development of the JET ion cyclotron resonance frequency heating system in support of ITER*, in IAEA Fusion Energy, (Geneva, 2008), to be published.

[15] Kwak J.G., *Acievement of 1.9 MW for 300s during commissioning of the KSTAR ICRF transmitter*, in SOFT, (Rostock, 2008), to be published

[16] Bobkov V.V., *Compatibility of ICRF antennas with W-coated limiters for different plasma geometries in ASDEX Upgrade*, Journal of Nuclear Materials 363 (2007) 122-126.

[17] Bobkov V., *Assessment of compatibility of ICRF antenna operation with full-W in ASDEX Upgrade*, in IAEA Fusion Energy, (Geneva, 2008), to be published.

[18] Zammuto I., *ICRF Antennas optimized for operation with a high-Z metallic wall in ASDEX Upgrade*, in SOFT, (Rostock, 2008), to be published.

[19] Wukitch S., *Ion Cyclotron Antenna Impurity Production and Real Time Matching in Alcator C-Mod*, in IAEA Fusion Energy, (Geneva, 2008), to be published

[20] D'Inca R., *Characterization of arcs in ICRF transmission lines*, in SOFT, (Rostock, 2008), to be published

[21] Cattanei G., *A Toroidally Broad Antenna for Ion Cycloctron Resonance Heating of Large Tokamaks*, Nucl. Fusion 29 (1989) 15-26.

[22] Majeski R., *Studies of rotamak current drive in DDX-U*, in APS Meeting of the Plasma Physics Division, (Seattle, 1999), APS

Proceedings of ITC18,2008

Configuration effect on energetic particle and thermal energy confinement in NBI plasmas of Heliotron J

S. Kobayashi[1)], T. Mizuuchi[1)], K. Nagasaki[1)], H. Okada[1)], K. Kondo[2)], S. Yamamoto[1)], S. Murakami[3)], D. Katayama[2)], Y. Suzuki[4)], T. Minami[4)], K. Nagaoka[4)], Y. Takeiri[4)], K. Murai[2)], Y. Nakamura[2)], M. Yokoyama[4)], S. Konoshima[1)], K. Hanatani[1)], G. Motojima[4)], K. Hosaka[2)], K. Toushi[1)], F. Sano[1)]

1) Institute of Advanced Energy, Kyoto University, Gokasho, Uji 611-0011, Japan

2) Graduate School of Energy Science, Kyoto University, Gokasho, Uji 611-0011, Japan

3) Graduate School of Engineering, Kyoto University, Kyoto 606-8501, Japan

4) National Institute for Fusion Science, Toki, Gifu, 509-5292, Japan

The configuration effect on the energetic ion and the global energy confinement has been investigated in the NBI plasmas of Heliotron J with regard to the effect of the bumpy magnetic field (bumpiness) being the key factor of the drift optimization in the helical-axis heliotron configuration. The configuration scan experiments have been carried out by changing the bumpy magnetic field (ε_b) with keeping plasma volume, plasma axis position and edge rotational transform almost constant. It has been found that the 1/e decay time of high energy CX flux after the NB turned-off has increased with bumpiness. The co-going ion flux of fast ions induced by energetic-ion-driven MHD modes has been observed by installing the hybrid directional Langmuir probe system. The preferable energy confinement time to the international stellarator scaling law ISS95 has been obtained in the high and medium-ε_b configurations. The improvement in the electron temperature mainly contributes to the enhancement of the plasma performance in the high- and medium-ε_b configurations The control of bumpiness is effective not only in the energetic particle transport but also in the global energy confinement in NBI plasmas of Heliotron J.

Keywords: Helical-axis heliotron configuration, Heliotron J device, neutral beam heating, drift optimization, bumpiness magnetic field component, energetic particle confinement and energy confinement.

1. Introduction

For the optimization of helical/stellarator magnetic configurations toward the fusion reactor, it is important subject to reduce the ripple loss of helically trapped particle and to control the neoclassical transport since the magnetic field has the three-dimensional structure. The configuration optimization in terms of “drift optimization” has been achieved by aligning the drift orbit surface to the magnetic flux one. In the planner axis heliotron configurations such as LHD, Heliotron E and CHS [1-3], the drift orbit surface has been optimized when the magnetic axis was shifted inwardly and the reduction in neoclassical transport coefficient in the $1/\nu$ regime has been found [4]. From the viewpoint of the Boozer coordinate system, the side-band of the helical magnetic field is adjusted in the inwardly-shifted configuration, which plays a key role to reduce the loss of trapped particles. An improvement in the energetic particle confinement has been obtained experimentally in the inward-shifted configuration. In such a case, the enhancement factor of the experimental energy confinement time to the international stellarator scaling (ISS) law has also become better than that of the outward-shifted configurations [5,6]. This suggests that the drift optimization is a candidate to mitigate the anomalous transport.

A helical-axis heliotron device Heliotron J [7,8] is designed based on the omnigeneous optimization scenario [9,10]. In the helical-axis heliotron configuration, the theoretical analysis has predicted that the control of the toroidal mirror ratio, bumpiness, in the Boozer coordinate system has been important for the drift optimization. The neoclassical diffusion coefficient and the loss rate of the energetic particles have had a dependence on bumpiness. Therefore it is important to investigate experimentally the bumpiness effect both on the energetic particle transport and bulk plasma confinement.

In this paper, we describe the configuration effect on the energetic and energy confinement in the NBI plasmas of Heliotron J, focusing on the effects of the bumpy magnetic field. The experimental setup and the characteristics of the configurations used in the bumpiness scan experiments are explained in section 2. The energetic particle transport in the NBI plasmas is shown in section 3. The dependence of the energetic ion transport on bumpiness magnetic field is investigated

author's e-mail:kobayashi@iae.kyoto-u.ac.jp

experimentally with charge exchange neutral particle analyzer (CX-NPA). The experimental result of the energetic-ion-driven MHD activities is shown by installation of the hybrid directional Langmuir probe system. The bumpiness effect on the global energy confinement is described in section 4. Summary is given in section 5.

2. Experimental Setup

2.1. Heliotron J Device

Heliotron J is the medium sized (R_0/a_p = 1.2m/0.17m) helical-axis heliotron device with an L/M = 1/4 helical winding coil, where L and M are the pole number of the helical coil and helical pitch, respectively. Figure 1 shows the bird's-eye view of Heliotron J including the coils and the heating systems. To achieve a flexible configuration control in Heliotron J, five sets of coils are installed, i.e. helical and main vertical (H+V), toroidal A and B (TA and TB) and inner and auxiliary vertical (IV and AV) coils. The TA coils are located at so-called "corner" section where tokamak like magnetic field is formed. On the contrary, the magnetic field in the "straight" section in which the TB coils are set has a local quasi-omnigeneous magnetic field. As shown in Fig. 1, two tangential beamlines of the hydrogen neutral beam injection (NBI) system have been installed in Heliotron J (BL1 and BL2). Each beamline has two bucket-type ion sources and the maximum beam power and acceleration voltage of 0.7 MW and 30 keV, respectively. The mean pitch angle of the beam ions is about 155 (25) degree in the co- (counter-) injection case of the standard configuration of Heliotron J. The numerical analysis of the NBI absorption power is described in section 4. An E//B type CX-NPA system can measure the hydrogen and deuterium charge-exchange neutral fluxes separately. This system also has a capability to scan both poloidal (θ_{NPA}) and toroidal (ϕ_{NPA}) angles with the ranges of $-3^o < \theta_{NPA} < +10^o$ and $-10^o < \phi_{NPA} < +18^o$. The initial

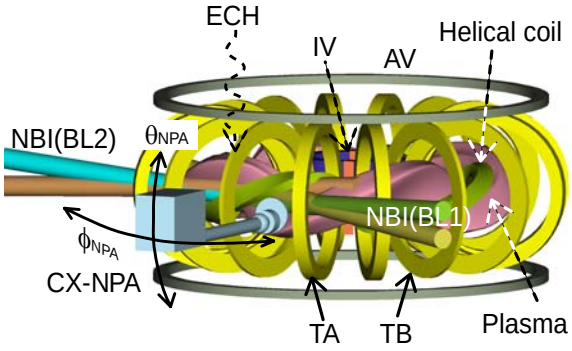

Fig. 1 Schematic view of Heliotron J including coil, heating and diagnostic systems.

plasma is produced by 2nd harmonic 70 GHz ECH with a maximum injection power of 0.4 MW. The deuterium gas was used for working gas to obtain the energy spectra for bulk (D^+) and beam (H^+) ions separately.

2.2. Configuration Characteristics in Bumpiness Scan Experiment

In this study, we selected three bumpiness ε_b (= B_{04}/B_{00}) configurations of high (ε_b = 0.15), medium (0.06) and low (0.02) at r/a = 2/3 by changing the current ratio of TA and TB coils with keeping the edge rotational transform ($\iota(a)/2\pi$ = 0.56), plasma volume (V_p = 0.7 m^3), and magnetic axis position (R_{ax} = 1.2 m) almost constant. Figures 2(a)-(c) show the radial profiles of the magnetic well, bumpiness, helicity ε_t (= B_{14}/B_{00}) and toroidicity ε_t (= B_{10}/B_{00}), where B_{mn} is the Fourier component of the field strength with m/n mode numbers in the Boozer coordinate system. The standard configuration of Heliotron J corresponds to medium-ε_b configuration. In the low-ε_b configuration the bumpiness can change its sign in the core region. As shown in Figs. 2(a)-(c), other main Fourier

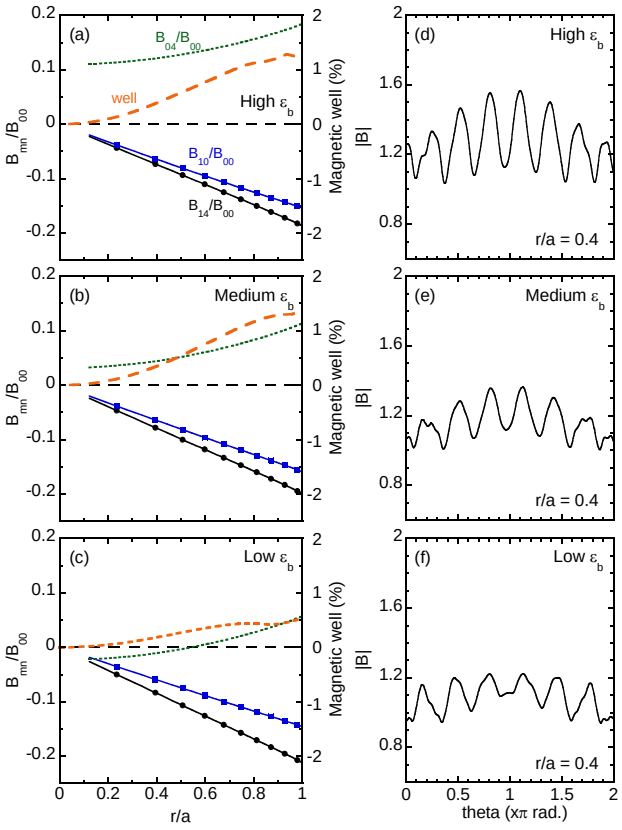

Fig. 2. (a)-(c) Radial profile of magnetic well, helicity, toroidicity and bumpiness in Boozer coordinate systems and (d)-(f) field strength along the field line in the high-, medium and low-ε_b configurations.

components, i.e. helicity and toroidicity, are almost unchanged to clarify the bumpiness effect on the energy confinement. The magnetic well in the entire plasma region is formed in the three ε_b configurations. Figures 2(d)-(f) illustrate the magnetic field strength at r/a = 0.4 along a field line in the Boozer coordinate system. In the case of high-ε_b, the ripple amplitude is higher than the others and the minimum values of field strength at the bottoms of the ripple are relatively flat. In contrast, in the configuration with low-ε_b, the strength of the ripple bottoms varies along the field line. From the viewpoint of the Boozer coordinate system, it has been found that the difference between $\boldsymbol{B}$ and $\nabla\boldsymbol{B}$ becomes small as increasing bumpiness [11], which expects the reduction in the gap between drift and flux surfaces in the high-ε_b configuration.

3. Energetic Ion Transport

3. 1. Dependence on Bumpiness

The decay of the CX flux just after NB turned-off investigated because this provides information regarding the slowing down and the confinement time of the beam ions [11]. Figure 3(a) shows the time evolution of the CX flux (E = 18 keV) after the NB turned-off for high, medium and low ε_b cases. The base plasma was sustained by 70 GHz ECH at the line-averaged electron density ($\bar{n}_e$) of 0.8×10^{19} m^{-3}. The NPA toroidal angle was set to be ϕ_{NPA} = +12 ^{o} to measure the CX flux having more similar pitch angle to the tangentially injected beam ions. The gap between the pitch angle of beam ion and observation one is around 25 degree, since the pitch angle of the detected particle at the plasma axis is about 130 degree in the medium ε_b configuration. In that case, the numerical calculation shows that CX-NPA observes passing particles. A clear dependence of the decay of the CX flux on bumpiness is found, i.e. the observed 1/e decay time of the CX flux after the NB turned-off, which is much smaller than the classical beam energy slowing down time as described below, increases with bumpiness.

From an aspect of the classical collision processes, the loss term of fast ion is mainly classified into orbit loss, pitch angle scattering, slowing-down, and charge exchange. The orbit calculation predicts that loss time of the ions where CX-NPA observes at ϕ_{NPA} = +12 ^{o} is longer than 5 ms and there is no difference on the bumpiness configuration, since these particles correspond passing particles. Figure 4 shows the time evolution of the loss rate of the energetic ions deduced by the orbit following calculation with the initial energy of 18 keV for the three bumpiness ε_b cases [11]. The bumpiness dependence on the loss rate appears in the trapped particles, that is, growth of the loss rate becomes slower with bumpiness. This is consistent with the slow grad-$\boldsymbol{B}$ drift due to the control of bumpiness as expected. At the quasi-steady-state condition after t = 0.1 ms, the difference in the loss rate is 29 % and 25 % for the high- and low-ε_b cases, respectively, which corresponds to the loss cone angle. The slowing-down time was estimated to be around 60 ms and its difference among

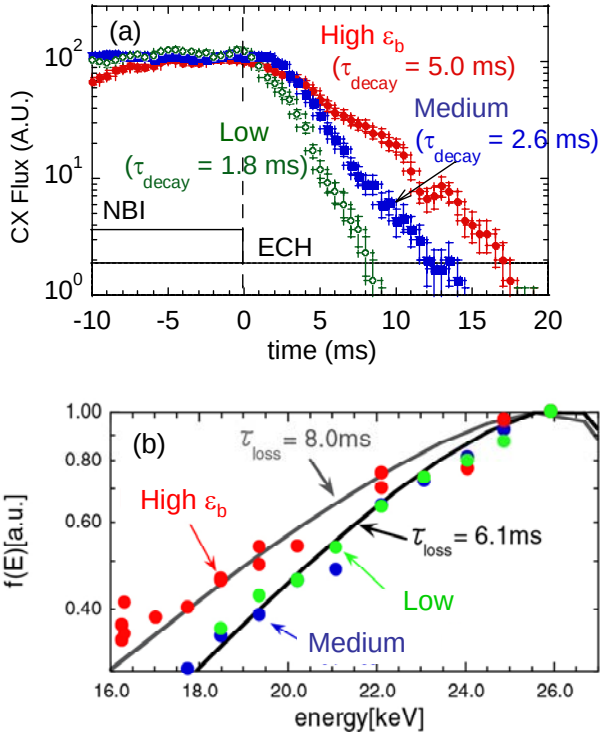

Fig. 3 (a) time evolution of the CX flux (E = 18 keV) just after the NB turned-off for high-, medium- and low-eb configurations, respectively, [11] and (b) energy spectrum obtained in the CX-NPA measurement and Fokker-Planck calculation. [12]

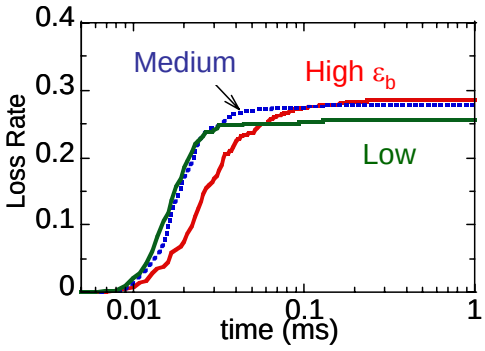

Fig. 4 Time evolution of the loss rate of fast ion (E = 18 keV) deduced by the ion orbit following calculation for ion guiding center. The orbit calculation was done until the test particles from the initial position at ρ = 0.25 strike the wall. [11]

the three configurations was negligibly small under the experimental condition. The CX loss time is considered to be unchanged in the experiments, since the H_α/D_α intensity normalized by $\bar{n}_e$ did not change. In order to interpret the measurement result with CX-NPA, the Fokker-Planck analysis for the fast ion distribution is carried out using a zero-dimensional Fokker-Planck equation taking the effective loss time into account [12]. Figure 3(b) shows the measured and calculated CX energy spectra in the energy range from half- to full-energy of beam ion in the three bumpiness configurations. The effective loss time in the high-ε_b configuration is longer than that for the medium and low-ε_b cases. These results indicate that the effective confinement of the energetic ions improves as bumpiness increases.

3. 2. Energetic-ion-driven MHD activities

Interaction of fast ions with MHD activities is one of the most important issues in burning plasma physics, because it may decreases α-particle heating efficiency. In low-magnetic-shear helical devices, global Alfvén eighenmode (GAE) is a candidate of most unstable modes when fast ion pressure becomes fairly high. GAEs have been observed at several magnetic configurations in NBI plasmas of Heliotron J, however, strong bursting GAE has not been observed in low ε_b configuration [13]. In order to investigate the ion transport in detail, we installed Hybrid Directional Langmuir probe (HDLP) system into Heliotron J [14]. HDLP can measure the co-directed and counter directed ion fluxes separately using some pairs of probe tip. This system can control the radial, poloidal and rotation angles simultaneously to detect the spatial distribution of fast ions and to align the pair of the probe tip with the magnetic field line.

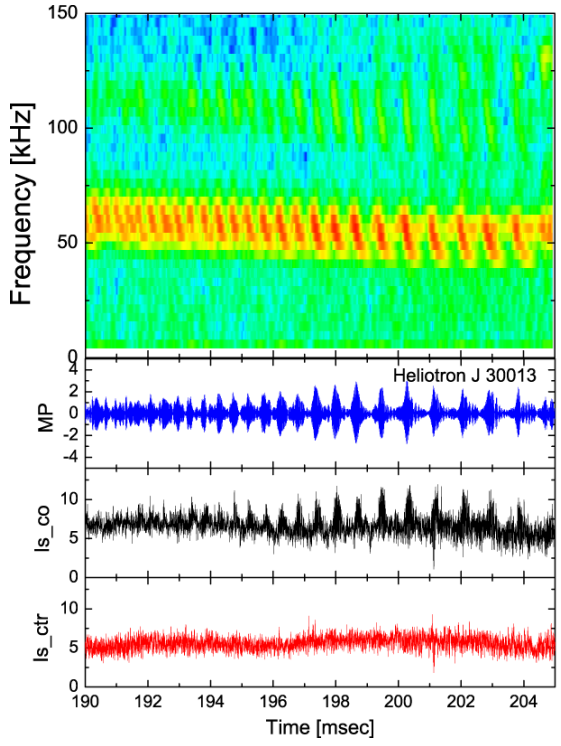

Fig. 5 The contour map of the power spectrum by magnetic fluctuation and its wave forms located on the chamber wall, co- and counter-directed (Is_co and Is_ctr) ion currents measured by HDLP at r/a= 0.9 [14].

Figure 5 shows the time evolution of the bursting GAE occurred in NBI and ECH plasmas [14]. The frequency of GAE chirped down quickly from 70 kHz to 40 kHz. The co-directed ion flux synchronized with GAE burst was observed and it was sensitive to the burst interval and amplitude. On the contrary, the response of the counter-going ion flux to GAE burst was weak. Then the co-going ion flux of fast ions is considered as a resonant convective oscillation [14]. These results indicate that the influence of GAE on the energetic ion confinement should be taken into account for further optimization of the helical-axis heliotron configuration toward fusion reactor.

4. Global Energy Confinement

In order to investigate the bumpiness effect on the energy confinement in NBI plasmas, we carried out bumpiness scan experiment in the NBI sustained plasmas. To clarify the absorbed power dependence, the power scan experiments are performed with keeping the line-averaged electron density almost constant. Figure 6 shows the plasma stored energy as a function of the absorbed NBI power (P_{abs}) in the three bumpiness configurations [15]. These data were obtained at the averaged electron density of 2×10^{19} m^{-3}. The counter-direction neutral beam is injected to cancel out

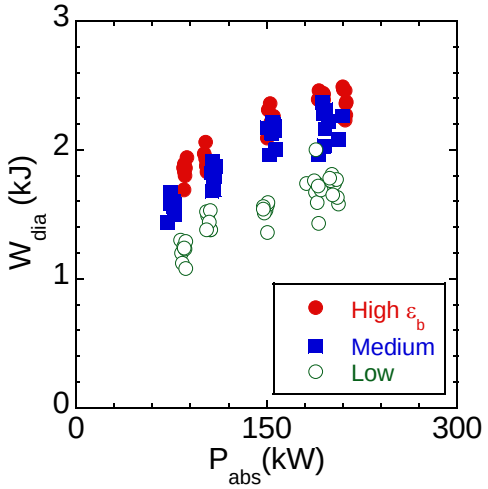

Fig. 6 Stored energy as a function of absorbed NBI power P_{abs} obtained in high-, medium- and low-ε_b configurations [15].

the change in the rotational transform by beta effects. The stored energy is evaluated by the diamagnetic loop data. The stored energy in the high- and medium-ε_b configurations is clearly higher than that in the low ε_b case. The difference of W_{dia} between the high- and medium-ε_b configurations is small, but the W_{dia} in high-ε_b case is more than 5% higher than that of the medium-ε_b configuration.

The beam absorption profile and the total absorption rate are estimated by the following steps [16]; (1) calculation of birthpoints of the beam ions using Monte-Carlo method (HFREYA), (2) estimation of orbit loss and the redistribution of the beam ions by orbit calculation for ion guiding center (MCNBI) and (3) analysis of heating profile using Fokker-Planck equation (FIT) [17]. The Monte-Carlo code HFREYA is modified to apply the three-dimensional shape of the plasma and the inner vacuum vessel of Heliotron J. The ion orbit is calculated only at the initial energy of beam ions without slowing down process. The slowing down process of fast ions and the energy transfer to both the bulk electrons and ions are calculated by the Fokker-Planck analysis including the CX loss of fast ions. The density profiles are assumed to be parabolic. The shape of the radial profile of the electron (ion) temperature is also parabolic with the core temperature of 400 eV (300 eV). The edge neutral density is assumed to be 2×10^{16} m^{-3}. In case of $\bar{n}_e$ = 2×10^{19} m^{-3}, the absorption fractions is about 35 % for the three bumpiness configurations. The detailed evaluation of the orbit loss of fast ions including the slowing down process remains as a future work.

Figure 7(a) shows the bulk (deuterium) ion temperature deduced by CX-NPA as a function of the NBI absorption power P_{abs} obtained in the three ε_b configurations. A slightly increase in the ion temperature as increasing ε_b is observed, that is, the ion temperature in the high, medium- and low-ε_b configurations are 0.23, 0.20 and 0.18 keV at P_{abs} of 200 kW, respectively. The ion temperature dependence on the NBI power is weak. As shown in Fig. 7(b), the electron cyclotron emission intensity (I_{ECE}) at the core region increased with P_{abs} in high- and medium-ε_b cases, while a relatively weaker dependence of the ECE intensity on P_{abs} is obtained in the low-ε_b configuration. The ECE measurement indicates an increase in the electron temperature both in high- and medium-ε_b configurations. Although the calibrated ECE measurement is not available at present, the configuration dependence of the stored energy plotted in Fig. 6 can be explained qualitatively in terms of the difference in the electron temperature. The improvement in the electron temperature mainly contributes to the enhancement of the plasma performance in the two ε_b configurations.

Figure 8 shows the comparison of the energy confinement time between experimentally obtained τ_E^{DIA} and International Stellarator Scaling law ISS95 τ_E^{ISS95} [18]. The energy confinement time is deduced by $\tau_E^{DIA} = (W_{dia} - W_{beam})/P_{abs}$, where W_{beam} is the beam component of the stored energy deduced from the Fokker-Planck analysis, which is less than 7 % under these conditions. In the present experimental conditions, the electron

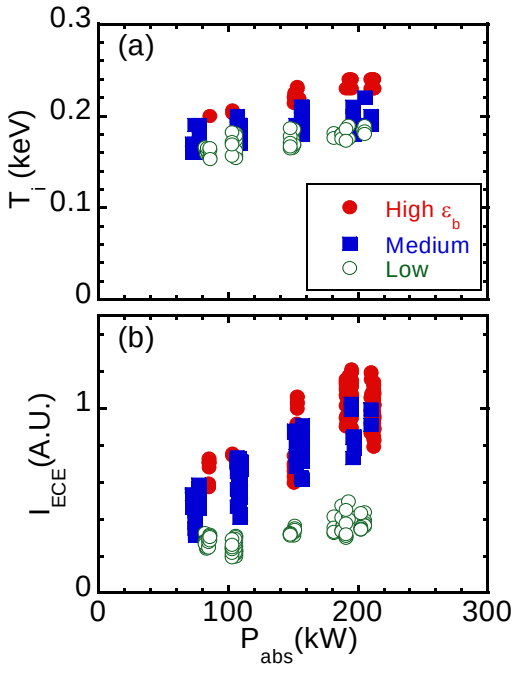

Fig. 7 (a) Bulk (deuterium) ion temperature and (b) ECE intensity as a function of P_{abs} in high-, medium- and low-ε_b configurations [15].

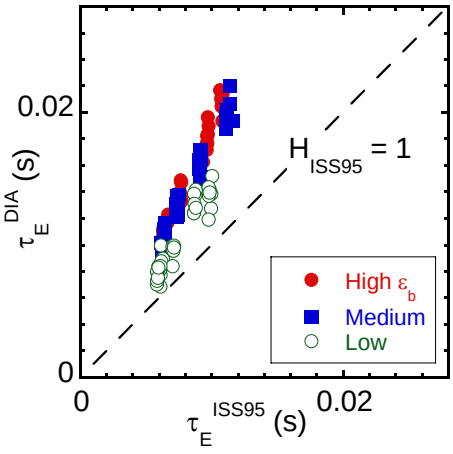

Fig. 8 Relationship between experimental energy confinement time and international empirical scaling law, ISS95, obtained in the NBI plasmas at the three bumpiness configurations [15].

collisionality is in the plateau regime. The enhancement factor of the energy confinement to the scaling ($H_{ISS95} = \tau_E^{DIA}/\tau_E^{ISS95}$) is about 1.8, 1.7 in the high and medium ε_b configurations, respectively, which is higher than the low-ε_b case of 1.4. These results suggest that the high and medium-ε_b configurations have better confinement characteristics for bulk plasma than that for the low-ε_b configuration in these experimental conditions.

Since the data shown in Fig. 8 were obtained at the constant density condition, the dependence of the energy confinement time on the heating power is investigated. Figure 9 shows the experimental energy confinement time as a function of NB absorption power. τ_E^{DIA} is proportional to $P_{abs}^{-0.72}$, $P_{abs}^{-0.66}$ and $P_{abs}^{-0.68}$ for the high-, medium- and low-ε_b cases, respectively. The power dependence is almost similar to the ISS95 scaling ($\tau_E^{ISS95} \propto P^{-0.59}$), although the beam absorption was calculated under the assumed density and temperature profiles.

5. Summary

The energetic particle and global energy confinement in the NBI plasmas of Heliotron J has been investigated. The bumpiness control experiments have revealed the effectiveness of the control of bumpiness on the confinement both for the energetic particle and the bulk plasma. Under the present experimental conditions, the temperature dependence on bumpiness suggests that the electron energy transport mainly dominates the global energy confinement. Further experiments and analyses are needed to clarify the physical mechanism of the bumpiness effect on the anomalous electron transport.

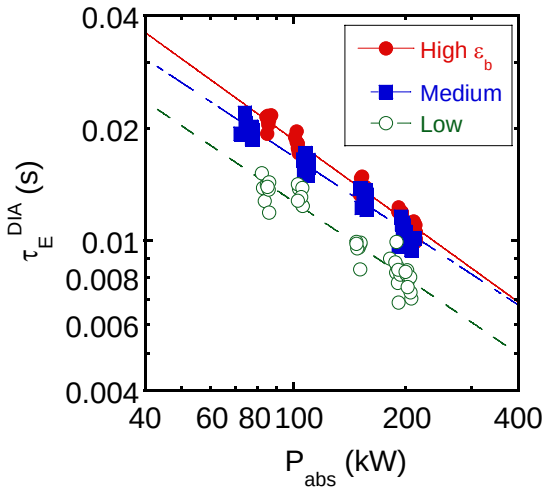

Fig. 9 Experimentally obtained energy confinement time as a function of NB absorption power.

Acknowledgements

The authors thank the Heliotron J staff for conducting the experiments and discussions. This work was supported by NIFS/NINS under the NIFS Collaborative Research Program (NIFS04KUHL005, NIFS04KUHL003, NIFS04KUHL006, NIFS05KUHL007, NIFS06KUHL007, NIFS06KUHL010, NIFS07KUHL011, NIFS07KUHL015 and NIFS08KUHL020) and under a project sponsored by the Formation of International Network for Scientific Collaborations. This work was partly supported by a Grant-in-Aid for Scientific Research from the Japan Society for the Promotion of Science No. 20686061.

References

[1] O. Motojima, et al., Nucl. Fusion **47** (2007) S668-S676.
[2] T. Obiki, et al., IAEA-CN-56/C-1-2 (1996).
[3] S. Okamura, et al., Nucl. Fusion **45** (2005) 863–870.
[4] S. Murakami, et al., Nucl. Fusion **42** (2002) L19–L22.
[5] H. Yamada, et al., Plasma Phys. Control. Fusion **43** (2001) A55–A71.
[6] S. Okamura, et Al 1999 Nucl. Fusion **39** (1999) 1337.
[7] F. Sano, et al., J. Plasma Fusion Res. SERIES **3** (2000) 26.
[8] T. Obiki, et al., Nucl. Fusion **41** (2001) 833.
[9] M. Wakatani, et al., Nucl. Fusion **40** (2000) 569.
[10] M. Yokoyama, et al., Nucl. Fusion **40** (2000) 261.
[11] S. Kobayashi, et al., IAEA-CN-116/EX/P4-41 (2004).
[12] M. Kaneko, et al., Fusion Sci. Tech. **50** (2006) 428.
[13] S. Yamamoto, et al., Fusion Sci. Tech. **51** (2007) 93.
[14] K. Nagaoka, et al., Proc. ICPP2008, P2-156 (2008).
[15] S. Kobayashi, et al., IAEA-CN-165/EX/P5-13 (2008).
[16] S. Murakami, et al., Trans. Fusion Tech. **27** (1995) 259.
[17] M. G. Mccoy, et al., Compt. Phys. Commu. **24** (1981) 37.
[18] U. Stroth, et al., Nuclear Fusion **36** (1995) 1063.

Proceedings of ITC18,2008

Steady-state operation scenario and the first experimental result on QUEST

K.Hanada[1)], K.N.Sato[1)], H.Zushi[1)], K.Nakamura[1)], M.Sakamoto[1)], H.Idei[1)], M.Hasegawa[1)], Y.Takase[2)], O.Mitarai[3)], T.Maekawa[4)], Y.Kishimoto[4)], M.Ishiguro[5)], T.Yoshinaga[6)], H.Igami[6)], N.Nishino[7)], H.Honma[5)], S.Kawasaki[1)], H.Nakashima[1)], A.Higashijima[1)], Y.Higashizono[1)], A.Ando[8)], N.Asakura[9)], A.Ejiri[2)], Y.Hirooka[6)], A.Ishida[10)], A.Komori[6)], M.Matsukawa[9)], O.Motojima[6)], Y.Ogawa[2)], N.Ohno[11)], Y.Ono[2)], M.Peng[12)], S.Sudo[6)], H.Yamada[6)], N.Yoshida[1)], Z.Yoshida[2)].

[1)] Research Institute for Applied Mechanics, Kyushu University,

[2)] University of Tokyo

[3)] Tokai University,

[4)] Kyoto University,

[5)] IGSES, Kyushu University,

[6)] National Institute for Fusion Science,

[7)] Hiroshima University

[8)] Tohoku University,

[9)] Japan Atomic Energy Agency,

[10)] Niigata University,

[11)] Nagoya University,

[12)] Fusion Energy Division, ORNL

QUEST focuses on the steady state operation of the spherical tokamak by controlled PWI and electron Bernstain wave current drive. One of the main purposes of QUEST is an achievement of long duration discharge with MW-class injected power. As the result, QUEST should be operated in the challenging region on heat and particle handling. To do the particle handling, high temperature all metal wall up to 600K and closed divertors are planned, which is to realize the steady-state operation under recycling ratio, R=1. This is a dispensable check to DEMO, because wall pumping should be avoided as possible in the view of tritium retention. The program to execute QUEST experiments will be developed in increment step such as, I. low β steady state operation in limiter configuration, II. low β steady state operation in divertor configuration, III relatively high β steady state operation in closed divertor configuration. Phase I in the project corresponds to these two years, and final goal of phase I is to make full current drive plasma up to 20kA. Closed divertor will be designed and tested in the Phase II. QUEST is running from Oct., 2008 and the first results is introduced.

Keywords: steady state operation, spherical tokamak, electron Bernstain wave, plasma wall interaction

1. Inroduction

It is important to obtain the academic basics to support high beta and steady state operation approaches. The QUEST (Q-shu University Experiment with Steady State Sperical Tokamak) project focuses on the steady state operation of the spherical tokamak (ST) which has the capability to attain high β rather than conventional tokamaks. A final target of the project is the steady state operation of ST with relatively high β (10%) under controlled plasma wall interaction (PWI).

The main difference between a pulsed operation and a steady one is the difficulties of handling of the heat and the particles loads. Although the transient huge heat load comes from plasma in the pulsed operation, the condition of the plasma facing components (PFCs) does not affect the performance of the plasma so much. While in the steady state operation, the erosion and the supptering of the material make serious effect in the maintenance of the high performance plasmas [1,2]. The continuous heat load makes large damages to the material of PFCs. The particle handling is more complicate in steady state operation. Because the wall pumping works well even on the divertor configuration, therefore the temperature and the number of absorbed particles of the PFCs should be controlled during discharges. Long duration discharges were sometimes terminated by the

author's e-mail: hanada@triam.kyushu-u.ac.jp

wall saturation phenomenon that the particles stored in the wall come back to the plasma abruptly. When the wall saturation phenomenon takes place, the in-flux of the particles increases and the particle handling could not work well and as the result the plasmas were terminated [3]. To avoid the appearance of the wall saturation phenomenon, the control of the wall temperature and the number of the absorbed particles to the wall should be done [4].

The QUEST program will be developed in increment step such as, I. low β steady state operation in limiter configuration, II. low β steady state operation in divertor configuration, III relatively high β steady state operation in closed divertor configuration. The specific purpose in phase I is:

(1) To examine the steady state current drive and the generation of closed flux configuration by electron Bernstain wave (EBW) current drive (CD).

The purposes in Phase II are:

(1) To comprehensively establish recycling control based on wall temperature control, advanced wall control under high plasma performance.

(2) To improve diverter concepts and to establish the way of controlling particles and heat loads during long duration operation.

(3) To obtain relatively high β (10%) under high elongated plasma shape and additional heating power in short pulse discharge down to 1 s.

In this paper, the physical design and the specification of QUEST are described in Section 2, and the first experimental results are shown in Section 3 and the summary is described in Section 4.

2. Physical design and specification of QUEST

2.1 Machine size decision

Machine size is the most important parameter of the project, because the appropriate size should be naturally derived from the mission of the project. The final goal of the project mission is to provide an academic basis for steady state high β operation at low aspect ratio as contributed to ST-based CTF, which is an important step to develop a fusion power plant. We should select the machine size to attain the final goal of the mission in the view of scientific consideration.

Before the investigation for the machine size, the limitation associated with the machine site should be shown. The commercial power source at the site is limited up to 7MVA and a MG of 125 MJ (effective power is 60 MJ within 1 sec) is available in the shout pulse operations. When toroidal magnetic field of 0.25 T at 0.64 m would be applied to the machine, the electric power source of 4MVA is required continuously and it will be supplied from commercial power source. Avaiable heating power of 3-5MW will be restricted by the capability of MG up to 1sec. In particular, the maximum plasma current have the strong relation to the machine size and the capability of available power source and is compelled to be restricted up to 0.3 MA in the case of major radius of 0.64 m. When the larger machine size is selected, the maximum plasma current will be reduced to the lower level because of the increment of the electric power source required to operate poloidal field (PF) coils. When we would like to sustain the plasma in steady state, all of electric power should be supplied from commercial power source. Therefore the maximum plasma current is limited to 100kA under the heating power is less than 1 MW. RF heating power of 8.2GHz up to 400kW, 170GHz up to 200kW and 2.45 GHz up to 50kW was prepared for plasma heating. The maximum power of 170GHz RF source is due to the output power of the gyrotron, the power supply can be applied to 500kW heating source. The power supply for a gyrotron of 170 GHz will be converted to different RF heating system, because the gyrotron frequency is not suitable for plasma heating at the low toroidal magnetic field such as QUEST. After the conversion, we can operate 1MW power source for plasma heating in Phase II.

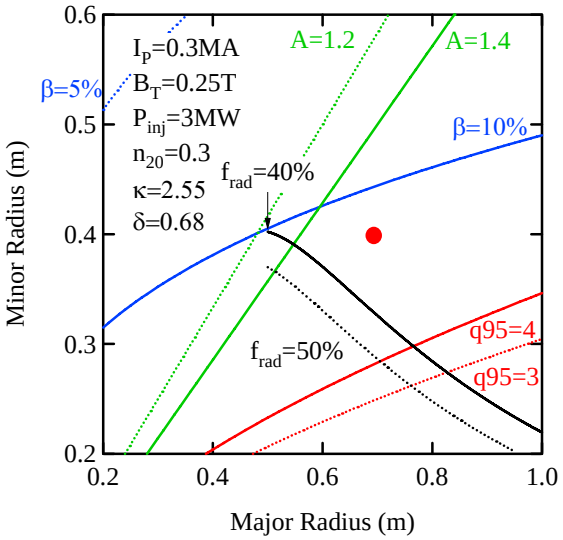

Fig. 1 Operation window in the case of L-mode confinement scaling [5] provide from the data base for conventional tokamaks under the condition of I_P=300kA, B_T=0.25T, P_{inj}=3MW, κ=2.55, δ=0.68, n_{20}=0.3. The heat load is estimated from the width of heat flux on the midplane in low field side [6] and it is not considered about the expansion of magnetic flux surface on the divertor plate. A dot shows the selected parameter. f_{rad} shows the fraction of radiation loss to the input power.

Figure 1 shows an operation window on minor and major radii considering under the above-described site limitation for heating power, plasma current and toroidal magnetic field. The solid and dotted red lines show the line for q_{95}=4 and 3, respectively. Generally speaking, it is difficult to operate on q95<3 in tokamaks and the solid red line provide a low q limit. The solid black line shows the heat load limitation to a divertor plate under the condition of the fraction of radiation, P_{rad}=40% in double null configuration. In steady state, the heat load to PFCs should be kept down on less than 10MW/m^2. This is also the requirement for ITER [5]. When the major radius is less than the black line, the heat load to divertor plate goes beyond the boundary of the ITER requirement. The solid and dotted green lines show the aspect ratio, A=1.4 and 1.3, respectively. The reduction of aspect ratio leads to the difficulty of the construction of the machine because of the technical limit to construct the machine. The solid and dotted blue lines show the constant β of 10% and 5% based on the ITER 89P L-mode scaling under the condition of I_P=300kA, B_T=0.25T, P_{inj}=3MW, κ=2.55, δ=0.68, n_{20}=0.3 respectively. This indicates the possibility to complete the mission of the project. The machine size window to attain β=10% is not so large and the selected machine size (red point on the figure) has the candidate to attain the mission. The vacuum vessel and TF, PF coils of QUEST are shown in Fig. 2 and the selected parameters are listed in Table 1.

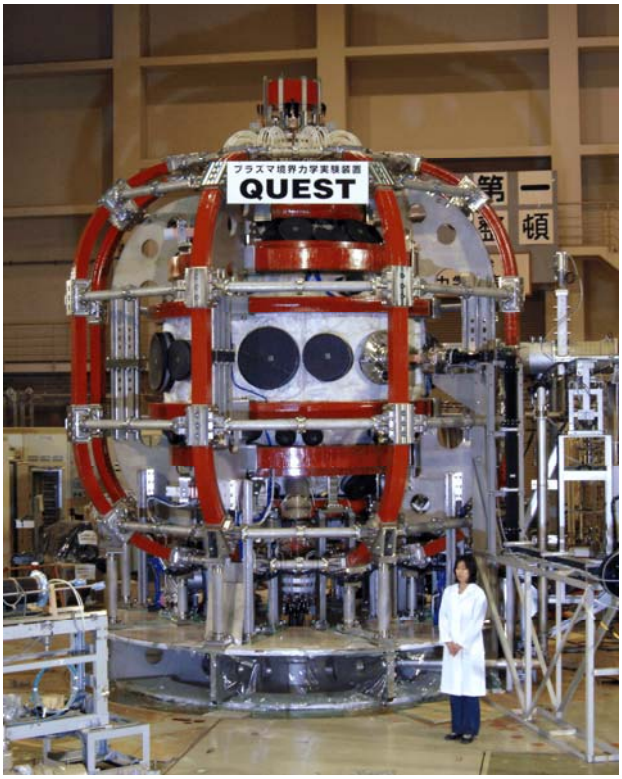

Fig. 2 The vacuum vessel and TF, PF coils of QUEST

	Phase I	Phase II		Phase III
	Steady	Pulse	Steady	Steady
R(m)	0.68			
a(m)	0.4			
B_T (T)	0.25	0.5	0.25	0.25
I_P (kA)	20	300	100	300
P_H(MW)	0.45	3	1	5

Table 1: Specifications and major parameters of QUEST

2.2 Non-inductive Current Drive in Phase I and II

In Phase I, the most important issue of the QUEST project is to achieve steady state operation. Non-inductive current drive is indispensable for steady state operation. As discussed in section 4.1, the different way to drive the plasma current from that in conventional tokamaks should be developed. Lower hybrid wave (LHW) is one of the promising methods to make current and the long duration discharge more than 5h was achieved on TRIAM-1M [7,8]. However LHW cannot penetrate to the center part of the high density plasmas under the low magnetic field condition because of accessibility of the wave. As for electron cyclotron current drive (ECCD), it is difficult to avoid the cut-off of electron cyclotron wave (ECW) under the low field condition. Instead of LHW current drive (LHCD), electron Bernstein wave current drive (EBWCD) and higher harmonics fast wave current drive (HHFWCD) are candidates to establish the maintenance of plasma current in steady state on STs. As we do not have any heating source for HHFWCD in the view of frequency at present, EBWCD is suitable way to apply to QUEST in Phase I.

In Phase II, upgraded heating source (NBI) up to 2MW will be prepared. At that time, NBCD and bootstrap current are additional candidates to provide sufficient plasma current. The current drive efficiency of NBCD is mainly decided by the fast ion thermal process that is classical slowing down process. In ST, the confinement of fast ion is crucial issue for NBCD because of low toroidal magnetic field. A present fast ion orbit calculation predicted better fast ion confinement than conventional tokamaks. In this section, it is difficult to discuss about the current drive efficiency including fast ion confinement. We assume that the fast ion confinement in ST is the similar to the conventional tokamaks. Before discuss about the current drive efficiency of NBCD, the beam energy to inject plasma should be decided, because large amount of through power is dangerous as well as inefficient. The absorption of the beam is decided by the cross-section for the processes, which are charge exchange, ionization by ion, and ionization by electron.

In QUEST, the machine size is not so large and plasma density is in medium range. Therefore the suitable beam energy may be around 20-30keV, where the charge exchange process will be dominant. When electron density is 5 x 10^{19} m^{-3}, $n\sigma_{cx}$=5 [m^{-1}] at 10keV of hydrogen beam, $n\sigma_{cx}$=3 [m^{-1}] at 20keV and $n\sigma_{cx}$=2 [m^{-1}] at 30keV. As tangent length of QUEST is 1.7m, 96% absorption can be expected at 30keV beam. We assume that 30keV hydrogen beam will be injected to tangential direction for the estimation of efficiency of NBCD. In this case, several 100kA can be expected.

Investigation of estimation of current drive efficiency of EBWCD is done under the given machine size and heating source in Phase I and II. At first, two excitation scenario of EBW (O-X-B and X-B) should be discussed, because injection way of RF depends on the scenario of wave excitation. The O-X-B scenario is utilized a mode conversion from O-mode to X-mode at the cut-off region for O–mode. The conversion rate from O-mode to X-mode is well-understood and depends on the injection angle to the cut-off layer. When we are willing to adopt this scenario, the adjustment of the injection angle is crucial. The converted X-mode will transfer to the upper hybrid resonance (UHR) from high field side and it will convert to EBW. EBW propagates inwards again and is absorbed bulk electrons effectively. By the effect of the magnetic shear, EBW has the single directed momentum in specified situation and it delivered to plasma. Accordingly plasma is provided single directed momentum from EBW and plasma current can be driven. The X-B scenario is the same in delivery and receipt of the momentum, however the mode conversion process is different. The RF will injected perpendicular to the magnetic field and 3 wave coupling play an essential role in mode conversion process and the mode conversion efficiency significantly depends on the scale length of electron density at UHR. To convert to EBW, we should control the density gradient at UHR.

Experimental observations of EBWCD are obtained in various devices. Driven current of 100 kA at 60GHz 600kW was achieved in COMPASS-D on the O-X-B scenario [9]. Full non-inductive plasma current up to 20 kA in a sequence of plasma start-up on CS-less configuration was achieved for 5 sec on LATE [10]. The X-B scenario was executed on TST-2 by appropriating RF power source of 8.2 GHz, 200kW. Plasma heating could be observed in the case of application to ohmic heated plasma. Full non-inductive plasma current of 4kA for 0.3 sec could be sustained by only-RF on TST-2 [11].

In order to study the wave propagation and absorption of EBW, the wave trajectory has been calculated with some ray tracing codes [12]. The wave trajectory of the incident wave was calculated using the TASK/WR ray-tracing code [13]. The local wave electric fields were evaluated in the ray trace calculation, and used for the Fokker-Planck (TASK/FP) [13] analysis. The driven-current profile was estimated in the FP analysis. The geometrical coordinates were taken as a simple tokamak configuration with circular poloidal cross-sections. The major and minor radii were R_0=0.64m and a=0.36m in this study. The profiles of electron density and temperature, and plasma current were assumed to be parabolic. The central electron density and temperature were n_{e0} = $0.2\times10^{19}$$m^{-3}$ and T_{e0} = 100eV, respectively. The total plasmacurrent was 20kA. The *O*-cutoff was at the plasma radius r=0.2. The local wave electric fields were calculated in the ray trace calculation, and used for the Fokker-Planck (TASK/FP) analysis. In the TASK/FP code, a quasi-linear RF operator in the velocity space was evaluated from the wave field , and the bounce averaged velocity distribution function was calculated to evaluate the plasma current driven by the EBWH/CD. The nonlinear collision operator was used with the trapped electron effect. As the results I_p/P_H=0.11 [A/W] can be obtained [14].

Bootstrap current will play a significant role in driving non-inductive current at low collisional region. We try to calculate the bootstrap current at some given plasma parameters. Expression provided by S.P. Hirshman [15] is utilized in the calculation. Total value of bootstrap current is 36kA even in high β (~ 20 %) plasma. To confirm the result, modification of density and temperature profile were executed, however total bootstrap current did not change so much. This indicates that the bootstrap current may not play an essential role in non-inductive current drive in QUEST.

2.3 Control of Plasma Wall Interaction

Control of plasma wall interaction (PWI) is the key issue to maintain plasmas in steady state. In TRIAM-1M, strong wall pumping played an essential role in the particle balance in ultra long duration discharge [16]. The estimated value of wall pumping rate depended on plasma parameters such as density, therefore it was difficult to control wall pumping rate during plasma discharge [16]. Moreover the property of the wall pumping was alternatively turned on and off [16] and the wall sometimes modified to source of particles. When the wall works as particle source, the control of plasma density becomes to be difficult and finally plasma termination may take place. To avoid this difficulty of particle handling in long duration discharge, high temperature wall (HTW) is quite effective, because HTW can hold recycling rate of particles to unity. This property of the wall made sure in laboratory experiments [17]. We

would like to install HTW in the vacuum vessel on QUEST as shown in Fig. 3. The temperature of HTW will be decided by the desorption property of Hydrogen from the wall. At the first year in Phase II, HTW will be installed on the vacuum vessel.

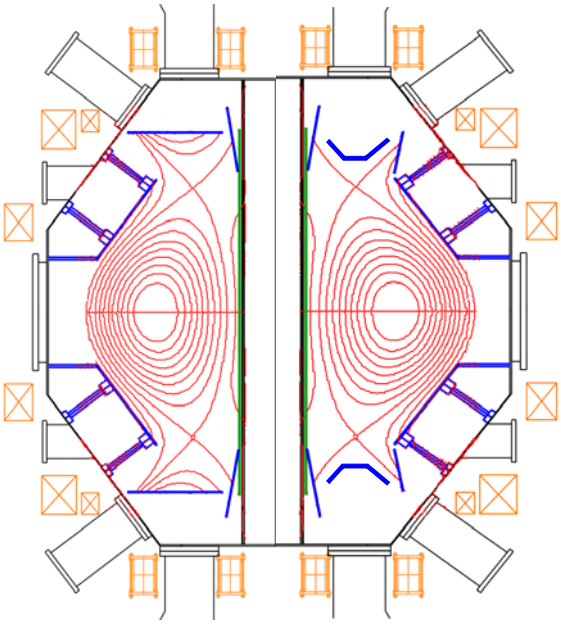

Fig. 3 Schematic view of the plan of the installation of the first wall on QUEST is shown. Left half of the figure illustrates the situation of the first step (the flat divertor plates and HTW). Right half shows the second step (the closed divertor and HTW).

To handle heat and particle load, the divertor is a key component. The plan of the construction of divertor structure is also shown in Fig. 3. In Phase I, limiter configuration is mainly used. The center stack is surrounded by limiters made of SUS306 coated by Tungsten. The flat divertor plates are installed on the top and bottom side of the vacuum vessel as shown in left half of Fig. 3 and its surface will be also coated by Tungsten. In the first step, diagnostics to monitor heat and particle flux during discharges will be installed and the estimated heat and particle flux will be used for the design of closed divertor structure.

3. Results of the first experiments

The first experiments on QUEST started on Oct., 2008. The purpose of this experimental campaign is to make sure the soundness of the machine and to obtain tokamak plasma. In this experimental campaign, it is impossible to operate the machine in steady state and the pulse duration is limited up to a few seconds because of the limitation of power supply for TF coil. The power supply will be improved in next year and steady state operation will be done.

Figure 4 shows the time trace of 2D image of Hα in first formation of tokamak configuration. The center solenoid with the cancel coil and a pair of PF coil were used to achieve this discharge. Peak of plasma current is about 10kA and plasma shifts outwards at 0.50595s because of poor equilibrium due to weak vertical field. At first plasma was produced by power of RF and a cylindrical plasma around electron cyclotron resonance (ECR) layer can be observed at 0.4545 s. And then the current of center solenoid increases gradually and plasma deformation appears due to the upwelling of return magnetic field from the seam of coils of the center solenoid, which is composed of three independent coils. At 0.486675 s, the plasma was divided into three parts. The center part of plasma forms tokamak configuration afterwards. At 0.4923 s, a bright point appears on the surface of inner limiter and this bright point expanded as shown the picture at 0.49365 s. Just before the appearance of the bright point, a glimmers at the top side of limiter can be observed. At 0.49875s, tokamak configuration was formed tentatively and the plasma shifts outwards because of weak vertical field. These pictures will be useful to understand the formation of closed flux surface.

After this experiment, we try to obtain the formation of closed flux surface without the assistance of magnetic flux from the center solenoid. This is the crucial point to achieve the steady state operation of ST.

4. Summary

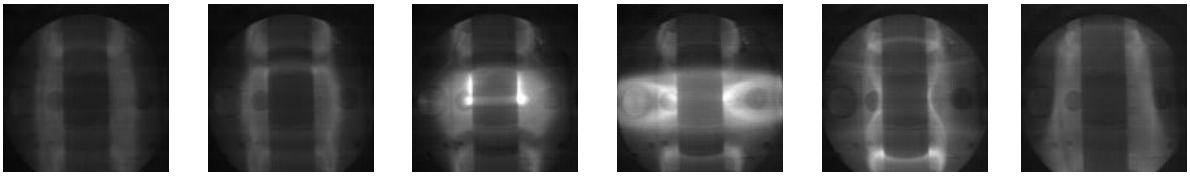

Fig. 4 Time traces of 2D image of Ha on the first formation of tokamak plasma measured with high speed camera. The center stack can be seen at the center part of each picture.

Physical design of the machine size of QUEST is shown. Conventional tokamak scaling indicated the expected plasma parameters, and ray trace and Fokker-Plank calculation for EBWCD were executed. As the result, the specification of QUEST is consistent with the mission. Heat and particle handing is the crucial issue to obtain steady state operation, and it is shown that the combination of closed divertor and high temperature wall is a candidate to resolve the difficulty. In QUEST the concept will be adopted and the preparation will proceed.

Acknowledgements

This work is performed with the support and under the auspices of the NIFS Collaboration Research Program (NIFS05KUTR014, NIFS08KUTR022). This work is partially supported by a Grant-in-aid for Scientific Research from Ministry of Education, Science and Culture of Japan.

References

[1] M.Chatelier *et al.*, Nuclear Fusion **47**, S579-589 (2007)
[2] R.Bhattacharyay *et al.*, J.Nuclear Material **363-365**, 938-943 (2007).
[3] K.Hanada Nucl. Fusion **41**, 1539-1542 (2001).
[4] R.Bhattacharyay *et al.*, Nucl. Fusion **47** 864-874 (2007).
[5] ITER Physics Basis, Nucl.. Fusion, **39**, No12 (1999).
[6] A.Loarte *et al.*, J. Nuclear Material **266-269**, 587-592 (1999)
[7] H.Zushi, *et al.*, Nucl. Fusion **45** S142-S156 (2005).
[8] K.Hanada *et al.*, Fusion Engineering and Design, **81** 2257-2265 (2006).
[9] V.Shevchenko *et al.*, PRL, **89** 265005 (2002).
[10] T.Yoshinaga *et al.* PRL **96**, 125005 (2006).
[11] A.Ejiri *et al.*, Nucl. Fusion, **46** 709-713 (2006).
[12] T. Maekawa *et al.*, J. of the Phy. Soc. of Japan, **48** 247 (1980).
[13] A. Fukuyama, Fusion Eng. and Design, **53**, 71 (2001).
[14] H.Idei *et al.* H. Idei *et al.* Proc. 32nd International Conf. on Infrared and Millimetre Waves, 2007.
[15] S.P. Hirshman, Phys. Pluids 31, pp3150 (1988).
[16] M.Sakamoto *et al.*, Nucl. Fusion, **42** 165-168 (2002).
[17] M.Miyamoto *et al.*, J. Nuclear Material **337-339**, 436-440 (2005)

Proceedings of ITC18,2008

Integrated Performance and Critical Issues Towards Steady-State Operation in JT-60U

YOSHITERU SAKAMOTO and the JT-60 team

Japan Atomic Energy Agency, 801-1, Mukouyama, Naka, Ibaraki-ken, 311-0193, Japan

This paper reports the integrated performance, achieved in JT-60U, towards the steady-state operation foreseen in ITER and DEMO reactor. Advanced tokamak plasmas with weak shear or reversed shear have been optimized to confront the critical issues such as the high-beta operation with high confinement, the compatibility of high-density operation with high confinement, and long sustainment with high non-inductive current drive. As a result, high-integrated performances were achieved in both plasma regimes. For example, high confinement reversed shear plasmas with high bootstrap current fraction exceeding no-wall beta limit are obtained in reactor relevant regime, where $\beta_N \sim 2.7$, $\beta_p \sim 2.3$ is achieved with reversed q profile with $q_{min} \sim 2.3$, and then $HH_{98y2} \sim 1.7$, $n_e/n_{GW} \sim 0.87$ and $f_{BS} \sim 0.9$ are also obtained at $q_{95} \sim 5.3$.

Keywords: advanced tokamak, integrated performance, DEMO reactor, high beta, high density, high confinement, long sustainment

1. Introduction

High fusion performances were achieved so far in JT-60U, which is one of the largest tokamak in the world. For example, the record values of fusion triple product $n\tau T = 1.53 \times 10^{21}$ m^{-3}skeV [1] and the DT equivalent fusion gain $Q_{DT}^{eq} = 1.25$ [2]. Towards steady-state operation of tokamak, however, high-integrated performance is required, where high values of confinement enhancement factor over ELMy H-mode scaling (HH_{98y2}), normalized beta (β_N), bootstrap current fraction of plasma current (f_{BS}), non-inductive driven current fraction of plasma current (f_{CD}), fuel purity, the ratio of radiation loss power to absorbed heating power (f_{rad}) and normalized electron density by Greenwald density limit (n_e/n_{GW}) should be sustained long time [3]. For example, ITER steady-state operation scenario foresees $HH_{98y2} = 1.61$, $\beta_N = 2.93$, $f_{BS} = 0.46$, $f_{CD} = 1.0$, fuel purity of 0.82, $f_{rad} = 0.53$ and $n_e/n_{GW} = 0.78$ [4]. Furthermore, other reactor relevant conditions are also important in which the operation region of $q_{95} \sim 5$, electron temperature nearly equal to ion temperature and low momentum input due to alpha heating.

In JT-60U, two types of advanced tokamak plasmas with an internal transport barrier (ITB) and an edge transport barrier (ETB) have been optimized towards high-integrated performance [5]. One is a high β_p H-mode plasma, the so-called a weak shear plasma, which is characterized by safety factor (q) profile with weak positive magnetic shear in the core region, the parabolic-type weak ITB and a higher beta limit compared with that of reversed shear plasmas. The other is a reversed shear H-mode plasma, which is characterized by q profile with negative magnetic shear in the core region, the box-type strong ITB and larger bootstrap current and higher confinement compared with those of weak shear plasmas.

Critical issues towards the high-integrated performance focused in this paper are as follows. First issue is simultaneous achievement of high beta and high confinement, because these performances directly enhance the fusion performance. Second issue is the compatibility of high density with high confinement. Since the large amount of particle fueling by gas puff degrades temperature in the core region, we should develop the high-density operation with keeping the high confinement. Third issue is long sustainment, where demonstration of steady-state plasma with high non-inductive current drive fraction over the characteristic timescales, for example energy confinement time (τ_E), current diffusion time (τ_R) and wall saturation time (τ_W) and so on, is required.

Progress of integrated performances achieved in weak shear and reversed shear plasmas on JT-60U is described in this paper and which is organized as follows. High-beta operation above no wall beta limit is described in section 2. High-density operation with high confinement is described in section 3. Long sustainment with high non-inductive current drive fraction is described in section 4. A summary is presented in section 5.

author's e-mail: sakamoto.yoshiteru@jaea.go.jp

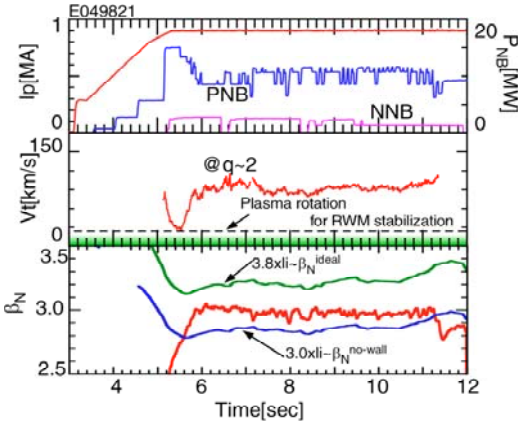

Fig.1 Waveforms of the stationary sustained weak shear plasma with wall stabilization.

2. High beta operation above no wall beta limit

The stability limit of ideal low n kink modes is significantly improved when a plasma is close to a perfectly conducting wall. However resistive wall modes (RWMs), which are a branch of ideal low n kink modes, are destabilized due to the finite resistivity of the conducting wall when the plasmas exceed no-wall beta limit due to the ideal low n kink modes. The RWM can be stabilized by using externally applied nonaxisymmetric magnetic field with coils [6] and/or by sufficient plasma rotation [7]. Recent experiments in JT-60U and DIII-D identified that a low toroidal rotation threshold for stabilizing RWM, where the toroidal rotation velocity at the low order rational surface plays important role [8, 9]. High beta experiments above no-wall beta limit were performed in weak shear and reversed shear plasma in JT-60U.

In weak shear plasma regime, high $\beta_N \sim 4$ was transiently achieved by wall stabilization [10]. Recently, quasi-steady state weak shear plasma with wall stabilization was obtained by utilizing the control of toroidal rotation velocity to keep above critical velocity [11]. Figure 1 shows the waveform of the stationary sustained weak shear plasma above no-wall beta limit, where $\beta_N \sim 3$ sustained for ~ 5s. In the discharge, low power of neutral beam (NB) heating was applied during Ip ramp-up phase to produce the weak positive shear configuration, and high power NB heating with negative ion-based neutral beam (N-NB) was injected to produce ITB. The β_N was sustained by using feedback control of stored energy via perpendicular NBs. The toroidal rotation velocity at q ~ 2 surface is much faster than the critical velocity ~ 20 km/s as shown in the figure. The no-wall beta limit is roughly indicated as 3.0 times the internal inductance, while the ideal wall beta limit as 3.8 times the internal inductance, which is confirmed by MARG2D code [12]. According to ACCOME code [13], which solves the inductive and non-inductive current density profiles that are consistent with plasma equilibrium, $f_{CD} > 0.8$ and $f_{BS} \sim 0.5$ were achieved. Since the large volume configuration was utilized for wall stabilization, lower confinement ($HH_{98y2} \sim 0.8$) is attributed to the lack of strong central heating. The duration is determined by the increase of no-wall beta limit due to gradual penetration of inductive field. Furthermore, some MHD instabilities cause the disruption in the high beta weak shear plasmas above no-wall beta limit. In particular, n = 1 bursting mode and slowly growing mode as a RWM precursor have been observed [11]. The bursting mode, so-called energetic particle driven wall mode (EWM) [*], is the energetic particle branch as the results of the interaction between the energetic particle and a marginally stable RWM, and then directly triggers RWM despite of enough toroidal rotation velocity for RWM stabilization. The slowly growing mode, which has longer growth time than the resistive wall time, makes toroidal rotation velocity and its shear at the rational surface reduce, and then the RWM is destabilized.

In reversed shear plasma regime, typical waveforms of the discharge with above no-wall beta limit are shown in Fig. 2, where the plasma parameters are as follows: plasma current $I_p = 0.8$MA, toroidal magnetic field $B_T = 2.0$T, $q_{95} \sim 5.3$ and the ratio of the wall radius to the plasma minor radius d/a ~ 1.3 [15]. The value of q_{95} is actually close to the design parameter of DEMO reactors. The discharge was established under the low momentum input condition expected in DEMO reactors, where tangential neutral beams (NBs) were injected by balanced

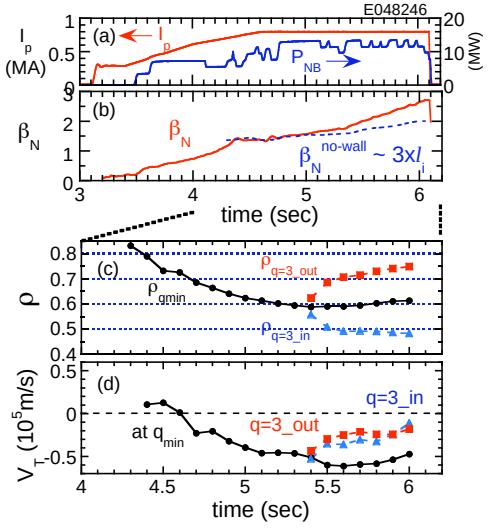

Fig.2 Waveforms of the wall-stabilized reversed shear discharge.

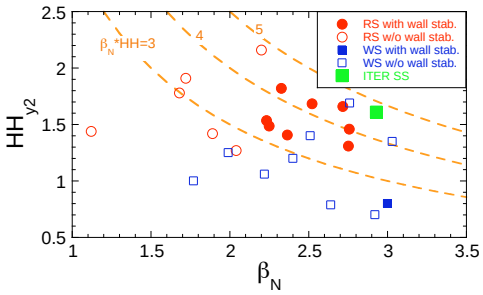

Fig.3 Simultaneous achievement of high normalized beta and high confinement.

way in which the injected power of co-tangential NBs is similar to that of ctr-tangential NBs. The normalized beta increased continuously by following the stored energy feedback control. However, the discharge was terminated by disruption at t ~ 6.1s. The MHD instability (n = 1) was observed just before the disruption, of which growth time is the order of the resistive wall time (τ_W ~ 10ms), suggesting RWM. In this discharge, β_N ~ 2.7 was achieved just before disruption, and the achieved high β_p ~ 2.3 leads to high f_{BS}. The achieved value of β_N is much higher than reversed shear plasmas with β_N ~ 1.7 - 2.2 at d/a ~ 1.5. The no-wall beta limit is estimated at about three times the internal inductance as shown in the figure. Actually, the detail analysis of MHD stability using the MARG2D code indicates that the ideal wall beta limit is β_N ~ 2.9 and the no-wall beta limit is ~1.9, resulting C_β ~ 0.8, where $C_\beta = (\beta_N - \beta_N^{\text{no-wall}}) / (\beta_N^{\text{ideal-wall}} - \beta_N^{\text{no-wall}})$. It should be noted that values of q such as q_{95} and q_{min} is very similar to those of ITER steady-state scenario (VI) for strong negative shear in which q_{95} ~ 5.4, q_{min} ~ 2.3 and q(0) ~ 5.9 are expected [4]. Thanks to ITBs, high confinement enhancement factor HH_{98y2} ~ 1.7 was obtained at high normalized density (n_e/n_{GW} ~ 0.87), and the ratio of electron and ion temperatures was T_e/T_i ~ 0.9 at the center. Furthermore, extremely high bootstrap current fraction of ~ 92% is obtained in the plasma, which is evaluated from ACCOME code. The RWM became unstable when toroidal rotation velocities at q = 3 surface decreased to the critical toroidal rotation velocity as shown in Fig. 2(d). By comparison of balanced- and co-injected discharges, the toroidal rotation velocity at outer q = 3 surface might play the important role for RWM stabilization.

Figure 3 shows simultaneous achievement of high beta and high confinement in both weak shear and reversed shear plasmas with/without wall stabilization. Beta limit was improved by RWM stabilization, especially in reversed shear plasmas with keeping high confinement. The high value of β_N ~ 3 was achieved with high HH_{98y2} ~1.5 in both plasma regimes, which is expected in ITER steady-state operation scenario. In weak shear plasmas, high β_N and high confinement was obtained even without wall stabilization as shown in the figure. Since the large volume configuration was utilized for wall stabilization discharges, lower confinement in the weak shear plasma with wall stabilization is attributed to the lack of strong central heating.

3. High-density operation with high confinement

Although the high-density operation above Greenwald density is preferable in DEMO reactors, confinement degradation was observed in the ELMy H-mode plasmas without ITBs [16]. In the plasmas with ITB, strong central heating is required for sustaining high confinement especially in weak shear plasmas. However it is difficult to keep a centrally peaked heating profile at high density due to the attenuation of neutral beam for heating.

Figure 4 shows the comparison of high-density operation in weak shear plasma discharge with pellet injection and with gas fueling [17], where the electron density was enhanced up to n_e/n_{GW} ~ 0.7 under the conditions of B_T = 3.6 T, I_p = 1.0 MA, q_{95} ~ 6.5, δ ~ 0.45 and q_{95} ~ 6.5. The pellets were injected from high field side. In addition, negative-ion based neutral beam (N-NB), which have high beam energy (~360 keV), was injected at high-density phase in order to keep a centrally peaked heating profile. In the pellet-injected discharge, the confinement enhancement factor over the L-mode scaling (H_{89PL}) stays almost constant even with increasing electron density, as shown in Fig. 4**(a)**, where HH_{98y2}

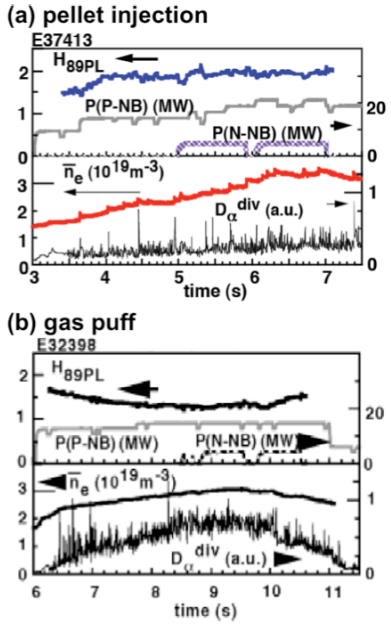

Fig.4 Waveforms of high-density operation by utilizing (a) pellet injection and (b) gas puff.

=1.05, β_N =2.2 and f_{BS} ~ 60% was simultaneously achieved at n_e/n_{GW} ~0.7. On the other hand, H_{89PL} decreases with increasing electron density in the gas fueled discharge as shown in Fig. 4(b). The ITBs in temperature profile were sustained and the density profile was peaked in the pellet-injected discharge, while the ITBs produced in the early phase disappeared in the gas-fueled discharge. One of the differences is seen in the pedestal parameter. The electron density at the pedestal is almost similar in both discharges, while the temperatures at the pedestal in the pellet-injected discharge are higher than that in the gas-fueled discharge. The pedestal temperature and density increases gradually in time in the pellet-injected discharge, where the core-edge parameter linkage plays an important role [17]. On the other hand, the temperature decreases with increasing density, which leads to decrease in the core temperatures and the energy confinement.

In reversed shear plasma regime, on the other hand, stronger ITBs are produced including electron density profile. The wide ITB radius can contribute the high-density operation with keeping high confinement characteristics. Figure 5 shows the electron density profile normalized to the Greenwald density in the high-density reversed shear plasma at before ITB formation and at fully developed ITB phase [18]. Here, B_T = 2.5T, I_p ~ 1.0MA, q_{95} ~ 6.1, and NB and LHRF heating were utilized. It should be noted that the density increases with NB fueling only. The density profile changes from relatively flat to a broad central peaked profile, where the density inside ITB increases, while the edge density remains almost constant. Although the edge electron density is smaller than $0.4n_{GW}$, the central electron density largely exceeds n_{GW} due to the wide radius of ITB. Therefore the high n_e/n_{GW} is obtained due to the peaked density profile inside the wide ITB. Thanks to ITBs, HH_{98y2} =1.3, β_N ~ 2 and f_{BS} ~ 70% were simultaneously achieved at n_e/n_{GW} = 1.1. It should be

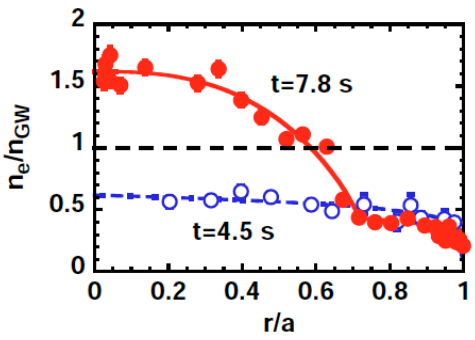

Fig.5 Profiles of electron density normalized by Greenwald density obtained in high-density reversed shear plasma.

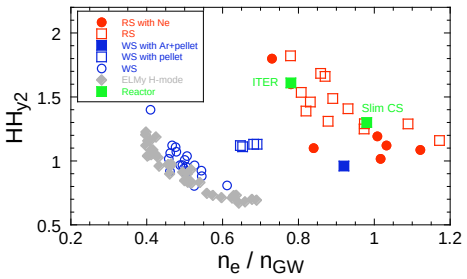

Fig.6 Compatibility of high density and high confinement in weak shear and reversed shear plasmas together with ELMy H-mode.

mentioned that the pedestal pressure is lower than that in the ELMy H-mode plasmas, and the core-edge parameter linkage is weak compared to weak shear plasmas.

Figure 6 shows the compatibility of high density and high confinement in both weak shear and reversed shear plasmas, where standard ELMy H-mode and impurity seeded plasmas [18] are also shown. Basically confinement performance is degraded with increasing n_e/n_{GW} in ELMy H-mode, weak shear and reversed shear plasmas. High-density operation region is expanded in weak shear plasmas with small degradation of confinement property by utilizing capability of density profile control such as pellet injection as described above, and impurity seeding with Argon, and then the high confinement region of HH_{98y2} > ~ 1 was achieved up to n_e/n_{GW} ~ 0.9. Furthermore, high-density operation region at n_e/n_{GW} ~ 1, foreseen in ITER steady-state operation scenario and DEMO reactor such as Slim CS, was obtained in reversed shear plasmas with very high confinement property (HH_{98y2} = 1.3 -1.7). In addition to high-density operation, high radiation loss fraction (f_{rad} > 0.9) was also obtained in the cases of impurity-seeded discharge. It is noted that HH_{98y2} ~ 0.95 at n_e/n_{GW} ~ 0.7 was obtained so far under the wall saturated condition, which is expected in steady-state plasmas [19].

4. Long sustainment with high non-inductive current drive fraction

Towards steady state operation of tokamak, the long sustainment of plasmas with full non-inductive current drive condition should be demonstrated. Critical issues for long sustainment are avoidance of neoclassical tearing modes in weak shear plasmas and the disruption in reversed shear plasmas.

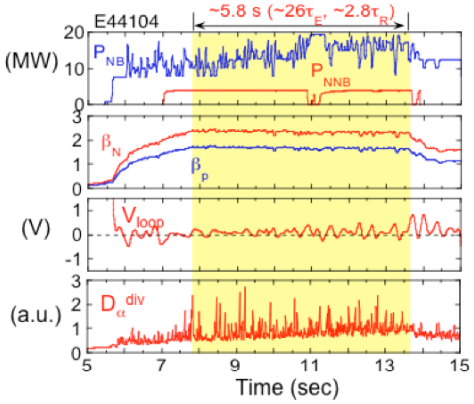

Fig.7 Waveforms of long sustained weak shear plasma with nearly full CD.

In the weak shear plasma regime, suppression of NTMs was demonstrated by electron cyclotron current drive [20]. However it is required for the complete avoidance of the NTM with m/n = 3/2 that the value of q in the whole plasma region is beyond 1.5. Typical waveform of such a scenario is shown in Fig. 7 [21], where I_p = 1 MA, B_T = 2.4 T, κ = 1.44, δ = 0.5 and q_{95} ~ 4.5. The plasma with β_N ~ 2.4 (β_p ~ 1.7) has been sustained for 5.8 s. This duration corresponds to ~ 26 τ_E and ~2.8 τ_R. Loop voltage was reduced near zero, which indicates the nearly full non-inductive current drive condition. The analysis of non-inductive current drive indicates that f_{BS} ~ 50-43% and f_{BD} ~ 52-47% were obtained. The sustained duration was determined by the pulse length of N-NB (~ 4 MW, ~ 6.5 s). In this discharge, HH_{98y2} ~1.0 was obtained at n_e/n_{GW} ~ 0.54. It should be emphasized that no NTM was observed in this discharge by the optimization of q profile.

In reversed shear plasma regime, one of the difficulties to obtain a long sustainment is avoidance of disruption due to the lower beta limit without wall stabilization. The reversed shear q profile gradually changes towards the stationary condition, where the value of q in core plasma region, including q_{min} and its location, decreases continuously due to the penetration of inductive current. Therefore the value of q_{min} passes through integer values until reaching stationary condition. Then the discharges frequently terminate by disruption when q_{min} goes across the integer values. In order to avoid disruptions, the pressure gradient at the ITB should be decreased when the plasma becomes unstable. The technique of the control of the ITB strength had been developed in JT-60U reversed shear discharges by the control of toroidal rotation, where local reduction of E_r shear affects the whole ITB layer [22]. For the long sustainment of the reversed shear plasmas with large f_{BS} under nearly full non-inductive current drive condition, we attempted the toroidal rotation control to avoid a

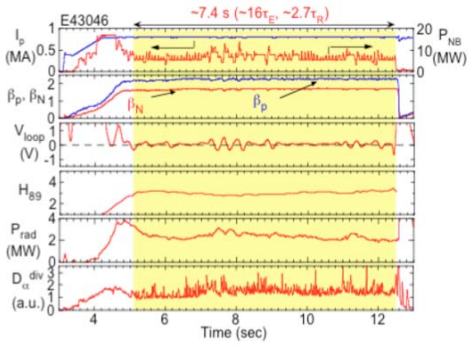

Fig.8 Waveforms of long sustained reversed shear plasma with nearly full CD.

disruption. Typical waveform of the long sustained reversed shear discharge are shown in Fig. 8, where I_p = 0.8 MA, B_T = 3.4 T, q_{95} ~ 8.3, κ_x = 1.6, δ_x = 0.42 [21]. Utilizing the feedback control of the stored energy by the perpendicular NBs, β_N ~ 1.7 (β_p ~ 2.4) was maintained from t ~ 5.1 s until the end of the NB heating (t = 12.5 s). Loop voltage decreased to nearly zero and was kept nearly constant, which indicates the nearly full non-inductive current drive condition. The high HH_{98y2} of ~1.9 was also maintained thanks to ITBs at n_e/n_{GW} ~ 0.6. According to ACCOME code, f_{CD} > 0.9 and f_{BS} ~ 0.75 were achieved. In this discharge, toroidal rotation control for pressure gradient control was applied during t = 7 – 8s at q_{min} being 4, where ctr-NB was switched off, and then the disruption was successfully avoided. The sustained duration of f_{BS} ~ 0.75 is ~ 7.4 s, which corresponds to ~ 16 τ_E and ~ 2.7 τ_R. At the stationary phase, the profile of measured total current density agrees closely with that of non-inductive current density, which implies the plasma approached the stationary condition.

Figure 9 shows progress of long sustainment of weak shear and reversed shear plasmas with high f_{BS}. By optimizing profiles of current and pressure, the sustained duration of both plasma regimes is extended under the nearly full non-inductive current drive condition. The plasmas with high f_{BS} expected in ITER steady state scenario and DEMO reactor is sustained for longer than current diffusion time scale, which is typically ~ 2 s in JT-60U. Durations are limited by pulse length of NB or N-NB.

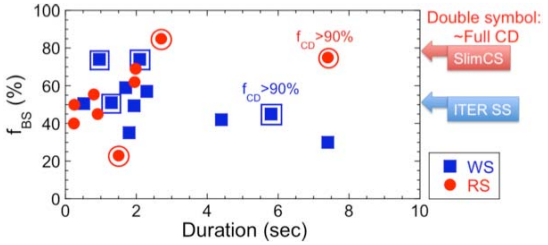

Fig.9 Progress of long sustainment of high bootstrap current fraction plasmas.

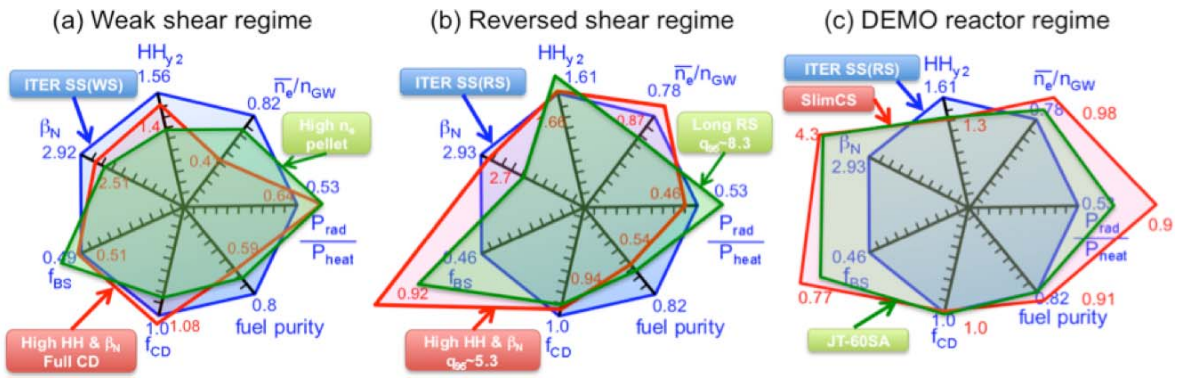

Fig. 10 Integrated performance achieved in (a) weak shear plasmas and (b) reversed shear plasmas. (c) Comparison of integrated performance among ITER, Slim CS and JT-60SA.

5. Summary

JT-60U tokamak optimized weak shear and reversed shear plasmas towards steady-state operation of tokamak and demonstrated (1) high beta and high confinement simultaneously, (2) compatibility of high density with high confinement, and (3) long sustainment under the nearly full non-inductive current drive condition. As the results, high-integrated performances were achieved in both plasma regimes. Achieved integrated performance in weak shear and reversed shear plasmas is shown in Fig. 10(a) and 10(b) together with the design parameter of the ITER steady-state scenarios [4]. In weak shear plasma regime, the discharge with high confinement and high beta plasma under the full non-inductive current drive condition [3] and the discharge with high density produced by pellet injection are shown in the figure. In reversed shear plasma regime, the discharge with high confinement and high beta plasma at reactor relevant q_{95} ~ 5.3 and the long pulse discharge at high q_{95} ~ 8.3 are shown in the figure. In both plasma regimes, high-integrated performance compared to ITER steady-state scenario was achieved. However some parameters are not satisfied simultaneously. And also long sustainment is still one of the remaining issues.

Concerning DEMO reactor, Slim CS [23] is one of the examples of economical and compact DEMO reactor with high β_N ~ 4.3 and high f_{BS} ~ 0.77. Figure 10(c) shows comparison of integrated performance among ITER steady state scenario, Slim CS and JT-60SA [24]. There are large gaps in design parameter between Slim CS and ITER, especially in β_N, f_{BS} and f_{rad}. JT-60SA will address the key issues for DEMO, as satellite tokamak of ITER, where demonstration of high beta operation by RWM control coils, and heat and particle control with divertor pumping capability. Then we hope ITER scenario can be improved by results of JT-60SA.

Acknowledgments

The authors would like to acknowledge the members of the Japan Atomic Energy Agency who have contributed to the JT-60U projects.

References

[1] S. Ishida et al., Proc. 16th Int. Conf. Plasma Physics and Controlled Nuclear Fusion Research, Montreal, Canada, October 7-11, 1996, Vol. 1, p. 315, International Atomic Energy Agency (1997).
[2] T. Fujita et al., Nucl. Fusion **39**, 1627 (1999).
[3] Y. Kamada and the JT-60 team, Nucl. Fusion **41**, 1311 (2001).
[4] Plasma Performance Assessment 2004 section 3.4, ITER Technical Basis ITER EDA Documentation Series.
[5] Y. Kamada et al., Fusion Science and Technology **42**, 185 (2002).
[6] C. M. Bishop, Plasma Phys. Control. Fusion **31,** 1179 (1989).
[7] A. Bondeson and Ward, D.J. Phys. Rev. Lett. **72**, 2709 (1994).
[8] M. Takechi et al., Phys. Rev. Lett. **98**, 055002 (2007).
[9] H. Reimerdes et al., Phys. Rev. Lett. **98**, 055001 (2007).
[10] M. Takechi et al., Proc. 21st Int. Conf. on Fusion Energy (Chengdu, 2006) (Vienna: IAEA) EX/7-1Rb.
[11] G. Matsunaga et al., Proc. 22nd Int. Conf. on Fusion Energy (Geneva, 2008) (Vienna: IAEA) EX/5-2.
[12] Tokuda, S. and Watanabe, T., Phys. Plasmas **6**, 3012 (1999).
[13] Tani, K., et al., J. Comput. Phys. **98**, 332 (1992).
[14] G. Matsunaga et al., submitted to Phys. Rev. Lett.
[15] Y. Sakamoto et al., Proc. 22nd Int. Conf. on Fusion Energy (Geneva, 2008) (Vienna: IAEA) EX/1-1.
[16] H. Urano et al., Plasma Phys. Control. Fusion **44**, 11 (2002).
[17] Y. Kamada et al., Plasma Phys. Control. Fusion **44**, A279 (2002).
[18] H. Takenaga et al., Nucl. Fusion **45**, 1618 (2005).
[19] N. Asakura et al., Proc. 22nd Int. Conf. on Fusion Energy (Geneva, 2008) (Vienna: IAEA) EX/4-4Ra.
[20] A. Isayama et al., Nucl. Fusion **43** 1272 (2003).
[21] Y. Sakamoto et al., Nucl. Fusion **45**, 574 (2005).
[22] Y. Sakamoto et al., Nucl. Fusion **41** 865 (2001).
[23] K. Tobita et al., Nucl. Fusion **47**, 892 (2007).
[24] T. Fujita et al., Nucl. Fusion **47**, 1512 (2007).

Proceedings of ITC18,2008

Status of plasma facing material studies and issues toward DEMO

Yoshio Ueda

Graduate School of Engineering, Osaka University, 2-1 Yamadaoka, Suita, Osaka 565-0871, Japan

This review paper presents status of research activity of plasma facing materials, mostly tungsten and critical issues towards DEMO reactors. A helium effect on tungsten surface morphology and its impact on fusion reactors and a pulsed heat effect to tungsten are briefly summarized. For DEMO, effects of steady-state operation and heavy neutron irradiation are important subjects to investigate. Present understandings on these are briefly summarized. Finally, issues of helical system towards DEMO will be discussed.

Keywords: plasma facing materials, graphite, tungsten, helium effects, neutron effects, deposition control, surface protective coating

1. Introduction

Plasma facing materials in divertors in fusion reactors are subject to high heat load up to ~10 MW/m^2. To withstand this heat flux, only materials with high thermal conductivity and high melting (sublimation) points can be used. Tungsten and CFC (Carbon Fiber Composite) graphite are the sole candidates. Both materials, however, have concerns: for CFC enhanced erosion of graphite by chemical sputtering, for tungsten cooling of fusion plasma by core accumulation in the burning plasma.

In ITER, serious discussion on the choice of plasma facing materials for divertor is going on. The safety issues are the most critical such as keeping in-vessel tritium retention below the administrative limit (presently set at 700 g [1]) and also amount of dusts (especially dusts on hot surfaces) should be below the limit[1]. In ITER, coolant of water will be used with its inlet temperature of about 100 °C, leading to relatively low wall surface temperature (200~300 °C) except for high heat flux region. Under this temperature condition, any material will potentially contain non-negligible amount of tritium even for metallic materials. It is believed that the use of tungsten is the best choice with regard to these viewpoints, since carbon materials will keep significant amount of tritium in codeposition layers with high T/C ratio (up to 0.4 for plasma facing side).

For DEMO, several operation conditions are essentially different from those of ITER such as steady-state operation (up to several years), high temperature walls (more than 500 °C), and high fluence neutron dose (more than 10 dpa). Under these conditions, tritium retention problem will be probably eased, while neutron effects at elevated temperature will become critical. Tritium permeation from the plasma facing surface to the coolant will need to be properly evaluated.

author's e-mail:yueda@eei.eng.osaka-u.ac.jp

In this paper, material issues of tungsten and CFC graphite for ITER and DEMO will be reviewed and critical issues for DEMO reactors will be presented.

2. Basic properties of graphite and tungsten

Graphite has been widely used for many magnetic confinement devices, and gives excellent plasma performance and new confinement regime because of less impact on plasma confinement than metallic materials. CFC graphite has also an excellent feature as a divertor material such as non-melting feature and high thermal shock resistance. However, erosion by plasma ion bombardment is quite large due to chemical sputtering. In addition, redeposition layers contain tritium, which would be dominated for in-vessel T retention. Therefore, CFC can probably be used only in the first phase of ITER. Although wall temperature could be high enough to neglect T retention in graphite in DEMO, hydrocarbon transport to remote area, leading to thick deposition with T retention, is serious concerns. In addition, heat shock resistance of CFC materials (NB31) may not be very high under repetitive heat pulse irradiation[2]. For NB31, pitch fibers are arranged perpendicular to a plasma facing surface. The fibers were broken at 10~100 μm from the top, which will be eventually released as dust particles and lead to enhanced erosion.

Tungsten has also good performance under high heat flux plasma exposure because of a high melting point and low sputtering by fuel ions. However, there is quite a concern because of a melting feature and brittleness such as low temperature brittleness, recrystallization brittleness, and neutron irradiation brittleness. Once tungsten melts, material strength is greatly reduced. After solidification, yield stress is greatly reduced and internal stresses is generated during a solidification process. These changes will cause cracking and destruction of high heat flux components in the worst case. Helium effects are very

important and critical to use tungsten as plasma facing materials. Details will be shown in Sec. 3. The neutron effect will not be a big concern for ITER since neutron fluence to wall materials is not high (up to about 1 dpa for tungsten). But for a steady-state rectors such as DEMO, it would be the most critical issue for tungsten divertor. Details will be shown in Sec. 5-2.

3. Helium effects

Recently, helium effects on tungsten have attracted increasing attention in terms of material degradation[3], leading to exfoliation and grain ejection (dust formation). Helium atoms have high trapping energy with point defects (4.0 eV – 4.4 eV) in tungsten, while hydrogen atoms have much lower binding energy with point defects (~1.4 eV for a single vacancy, ~2.1 eV for a void). Therefore, He atoms are hardly detrapped from these defects even at elevated temperatures. In addition, when tungsten temperature exceeds recrystallization temperature (1300 °C), helium and defect complexes becomes mobile and tend to agglomerate to form, so-called, helium bubbles. Below this temperature range (more than about 800 °C), nanoscopic structure is formed [4,5]. The typical nanostructure is shown in Fig. 1[5]. The

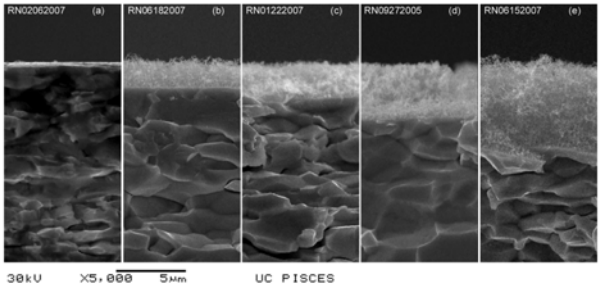

Fig. 1 He plasma induced nanostructure on tungsten [4]

thickness of nanostructure increases with square root of time, indicating diffusion-like behavior.

There are several disadvantages for He bubble- or nano-structure on tungsten. At first, it can be pointed out that the bubble structure in the subsurface region significantly reduce thermal diffusivity, leading to melting and evaporation of surface layer by transient heat loads. Secondly, dust formation associated with enhanced erosion would take place by the He effects. At elevated temperature, He bubbles diffuse into the bulk of tungsten and tend to be trapped at grain boundaries. He bubbles along the grain boundaries reduce adhesion between the grains, which are easily ejected by the effects of thermal stress or internal stress caused by hydrogen isotopes and/or helium containment. Figure 2 shows the ejected grain particles on the tungsten sample surface. This tungsten sample was exposed to He plasma at 1,600 K to the fluence of 9 x 10^{25} m^{-2} at first, followed by deuterium

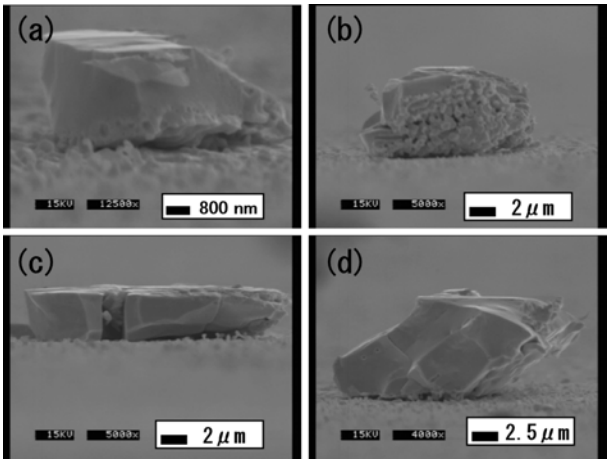

Fig. 2 Grain ejection of tungsten surface after deuterium plasma exposure at 550 K subsequent to He plasma pre-exposure at 1,600 K. (D. Nishijima et al.[5]).

plasma exposure at 550 K to the fluence of 2.5x 10^{25} m^{-2}. It was recrystallized during He plasma exposure and He bubbles with the diameters less than 1 μm were densely formed along grain boundaries. Therefore, the grain ejection in this case took place probably due to reduced adhesion between grains by He bubble accumulation.

Therefore, it is important to study formation conditions, effects to core plasma, and suppression technique (if necessary) for He bubbles and nanostructure in fusion reactor environments.

Recent studies have shown that He bubble layers act as a hydrogen isotope diffusion barrier. By this effect, reduction of deuterium retention and suppression of blistering take place[6], see Fig. 3. In ITER, since wall

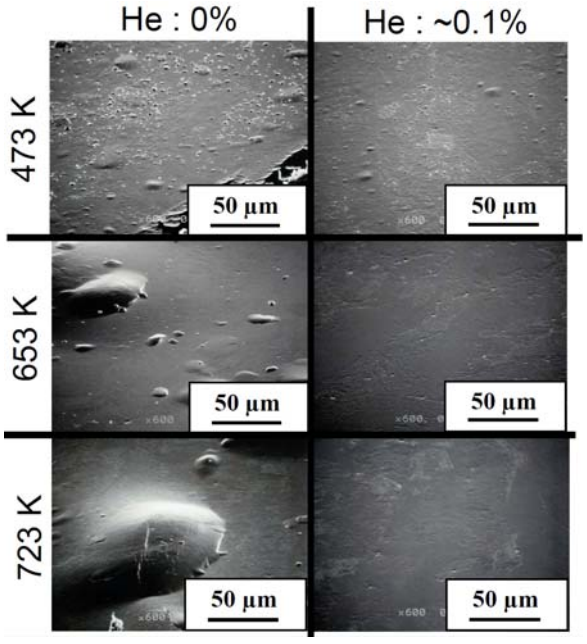

Fig. 3 Temperature dependence of surface morphology of ion irradiated W by 1 keV H, C, and He mixed ion tungsten [6] .

temperature except for near strike points is low (200~300 °C), this effect greatly affects T retention in a tungsten wall material. For DEMO, T retention in wall materials will not be a issue but T permeation to coolant tubes is a matter of concern. The barrier effect of He bubbles could greatly reduce T permeation. According to the reference[6], this effect is effective at least up to the temperature of 450°C (723 K). Over this temperature, more studies are needed to understand T behavior in first walls of DEMO.

4. Pulsed heat load effects

For more than 20 years, many good confinement modes of core plasmas have been found in tokamak devices and are the keys to achieve economical fusion reactors. One of them is H-mode, which has transport barriers near the edge plasma (so called pedestal). This mode, however, is known to be accompanied by repeated energy and particle ejection, so-called ELM (Edge Localized Mode). For ITER, a pulse length and a heat load of Type I ELMs were predicted to be ~0.2 ms and 0.5–1.2 MJ/cm^2, respectively[7,8]. This Type I ELM pulse can raise the surface temperature of tungsten above the melting point of tungsten (3422˚C). Once tungsten melts, grain growth and significant reduction of yield strength will occur, leading to crack formation and dust generation. Therefore, it is believed that the mitigation of the ELM pulse energy is of great importance for fusion reactors.

Recently it has been pointed out that even under non-melting conditions the repetitive ELM pulse effects could be serious[9]. Repetitive heat pulse cause surface expansion and contraction alternately, which would cause metal fatigue and cracking. Particle induced processes, mainly due to helium ions, could enhance this effects. More studies will be needed to comprehensively understand this effect and to avoid serious effect in fusion reactors for tungsten walls.

So far, no similar repetitive heat pulse to wall materials like ELM's in tokamak has not been found in the helical system. But it is noted than ELM is associated with pedestals near the separatrix, which appears as a result of improved plasma confinement, known as H-mode. So in the future, there still remain some possibility to obtain good confinement regimes with ELM-like edge plasma behavior in helical system. In this case, repetitive heat pulse must be reduced or suppressed to an acceptable level.

5. Issues for reactor environment

5-1. Steady-state operation

Plasma duration in present magnetic confinement devices are limited to a few hours. Especially for high performance plasmas with the fusion energy gain factor around 1, the duration is limited to an order of seconds. On the other hand, the discharge duration of DEMO reactors will be an order of several months. There still remains a significant gap between the present and next step device, even ITER, and DEMO.

There are several time constants in terms of plasma wall interaction. Wall saturation for fuel atoms (hydrogen isotopes) is one of the important time constant. If wall saturation do not take place, walls always suck tritium, eventually the tritium wall retention exceeds accepted level (~700 g for ITER). In addition, wall pumping of tritium reduces usable tritium produced in blankets, leading that requirements of TBR (Tritium Breeding Ratio) should be raised in blankets. According to present reactor design study[12], TBR is very marginal compared with the required value (~1.1). Therefore, wall pumping should be terminated in an acceptable short operation duration.

In JT-60U, plasma performance under these wall-saturated conditions have been investigated[10]. The wall saturation time in this case is an order of minutes. This is acceptable because it is much shorter than expected operation time of DEMO. In Tore Supra, however, wall saturation has not been observed for 2 min discharge and wall pumping continued at least up to the cumulative discharge time of 5 hours[11]. In these devices, wall materials were graphite and the relatively low first wall temperature (less than 300 ˚C).

In DEMO, in the case of metallic wall materials (tungsten as a leading candidate), implanted tritium will diffuse into the bulk to be trapped at intrinsic or neutron induced trapping sites or permeate to the rear surface or interface with structural materials (low activation materials such as RAF, vanadium alloys, SiC as present candidates). For metallic structural materials, tritium will permeate through to reach coolants. On the other hand, for ceramic materials such as SiC, since this is a strong diffusion barrier of tritium, tritium will not permeate to the coolants. If the wall temperature is high enough, tritium will not accumulate in metallic armor materials and permeate to the coolants, which are the most desirable situation in terms of tritium retention. But if the coolant temperature is not very high (ex. 300 °C of water), tritium could accumulate around coolant tubes. This will not only increase tritium retention but also will affect deterioration of material properties. In addition, as was mentioned in the section 3, helium bubble layers tend to work as tritium diffusion barrier. If there are two diffusion barriers both on the plasma facing side (ex. He bubble layer) and on the rear side (ex. SiC/SiC composite), tritium tends to be confined in wall materials between these diffusion barriers, which increase tritium retention and

probably deteriorate the wall materials. Therefore, in DEMO reactors, issues of tritium implanted from the plasma facing side are closely related to the design of divertor and blankets. This issue, however, have not been studied so far, and will be one of the most important R&D subjects for blanket development.

As was described, tritium retention in codeposited layers is a matter of concern for ITER. Even in DEMO, since erosion of wall materials does not have a clear limit, formation of codeposition layers would continue during plasma operation. It is known that hydrocarbon molecular radicals have low sticking coefficients on high temperature walls. These molecules are transported far from plasma facing walls through exhaust ducts. Even if the surface temperature of in-vessel components are high enough for these radicals not to stick, there are low temperature surface somewhere in remote area (vacuum pumps etc.). Hydrocarbon radicals will deposit on these surface and produce T retained deposition layers. This is also a concern related to the use of carbon contained walls for steady-state reactors. To solve this issue, complete understandings of transport of hydrocarbon radicals and effective removal methods of T retained deposit must be needed.

Degradation of wall materials under steady-state conditions also needs to be investigated. There have been quite a few studies for the effects of plasma exposure to wall materials. Ion fluence of these studies, however, are limited up to 10^{28} m^{-2}, while ion fluence to divertor plates in fusion reactors will reach 10^{31} m^{-2} in a year. At present, no plasma device can simulate wall materials under this fluence condition, and there are even no plans for it. We need to make a strategy for the development of reliable wall materials under very high fluence conditions.

5-2. Heavy neutron irradiation

As was pointed out, one of the most significant differences between ITER and DEMO is neutron fluence. In fact, ITER will provide a test bed of 14 MeV neutron irradiation for materials and components. Its fluence, however, is much lower than that in DEMO due to low duty plasma operation. ITER will be able to provide the average neutron fluence of about 0.3 MWm^{-2} year. On the other hand, neutron fluence to wall materials of fusion reactors would reach about 10 MWm^{-2} year[12].

Fusion neutrons (14 MeV) will have several effects on wall materials. Radiation damages produced by elastic collision with lattice atoms. These damages will result in hardening, swelling and some other material degradation. In addition, transmutation of materials needs to be taken care of due to very high fluence in DEMO. For example, some of tungsten isotopes are transmuted to Re, then Os[13]. Thermal conductivity of tungsten contained with Re was studied by Fujitsuka et al.[14]. Their study showed that thermal conductivity of tungsten decreases with Re concentration. Tungsten with 10at% Re has lower thermal conductivity than pure tungsten by about 30% at 1000 K. Under fusion neutron irradiation, this composition would be reached in about 2 years of operation. The other heavy-atom transmutation effects have not been known well.

In addition, (n, α) reaction will produce He atoms which appears with the neutron energy more than 10 MeV (tungsten). This means fission neutron (less than a few MeV) cannot cause this reaction. As already mentioned, helium could cause deteriorating effects on metals due to the formation of He bubbles. Therefore, definitely we need some facilities other than fission reactors or dedicated experiments to examine transmuted He effects on tungsten bulk material property.

New tungsten material with the resistance to neutron irradiation is being developed by Kurishita et al.[15]. This new material, UFG-W(Ultra Fine Grained W) with TiC dispersoids, has much smaller grain sizes (less than sub-micrometer) which greatly improve embrittlement of ordinary tungsten. This material has also desirable feature under high flux plasma exposure environment. For ordinary tungsten, high flux plasma exposure produces blisters[16], but UFG-W did not show blisters up to the fluence of about 10^{26} m^{-2}[17]. In addition, D retention is not higher than that in ordinary tungsten (stress relieved tungsten with the grain size of a few micrometer). Although it is necessary to examine at higher fluence conditions, UFG-W clearly has some advantages over ordinary tungsten as plasma facing materials for ITER and DEMO.

For CFC graphite, neutron effects would be very serious. Most important effects are reduction of thermal conductivity and dimensional change[18]. Reduction of thermal conductivity changes appear even in ~0.01 dpa. The reduction is larger at lower temperatures. Over about 1000 °C, reduction is small because of the annealing of radiation damage. On the other hand, dimensional change takes place during annealing process of damage, which makes new graphitic plane and expand graphite crystal along c-axis[19]. For carbon fibers, neutron irradiation leads to shrinkage in the direction parallel to the fibers and to swelling in the perpendicular direction. Since this process increases with the increase in temperature, the most serious effects of dimensional change would appear in CFC graphite tiles at strike points of divertor. Although we do not have database under reactor relevant high fluence conditions, this effect could be inevitable and the most serious problem for the use of CFC in DEMO.

5-3 Strategy needs for DEMO

Design of tokamak based DEMO device has been carried out by several research groups[20,21]. Handling of divertor heat load is always an issue. The heat load of 10 MW/m^2 to the divertor is a typical standard of a design parameter. In terms of high heat flux technology, development of high heat flux components for DEMO has more limitation than ITER. Coolant tubes for ITER can be made of copper alloys (ex. CuCrZr alloy for ITER) due to high thermal conductivity. But this alloy is subject to hardening under heavy neutron irradiation. Therefore, under DEMO environment, the other materials need to be examined. One of the candidate materials in the JAEA design is RAF[22]. Design of water cooled tungsten monoblock divertor with the RAF coolant tube can handle the maximum heat flux of 13 MW/m^2, while 25 MW/m^2 can be handled by the module with the Cu coolant tube. Heat removal capability for the plasma facing components in DEMO and the commercial reactors must have some tolerance for safety operation and material degradation during long term operation. Therefore, heat removal capability of the divertor with the abovementioned RAF cooling tube would not be enough for the 10 MW/m^2 heat flux. The heat flux to the divertor plates in DEMO should be substantially reduced in comparison with ITER as long as solid materials would be used.

In the roadmap shown in ITER home page[23], the DEMO reactor construction will start just before the second DT operation phase in ITER and the operation phase 1 in DEMO will start before the end of the ITER operation. IFMIF will be employed simultaneously with the ITER operation, which provide the opportunity to select and optimize blanket structural materials. For plasma facing components, however, there is no plan to make a selection and qualification test of the components for the steady-state operations of DEMO.

The test conditions of divertor components are very complicated. They should include high heat flux irradiation up to 10-20 MW/m^2, high fluence irradiation of 14 MeV neutron up to about $10MW{\cdot}year/m^2$, and high fluence D/T and He (5~10%) plasma irradiation up to the fluence of about 10^{31} m^{-2}. Combination of these mixed irradiation is extremely important. For example, thermal stress caused by temperature gradient would be closely related to neutron irradiation creep. Neutron damage and helium bubbles would strongly affect hydrogen isotope and helium behavior, and its effect on material degradation in tungsten.

This combination test should be done before the installation of divertor modules in steady-state operation of DEMO. The relevant facilities (ideas) are CTF (Component Test Facility, steady-state magnetic confinement plasma for a volume neutron source), IFMIF with a high density plasma device, and the use of the operation phase 1 of DEMO. In any case, we need to seriously consider the strategy for R&D and a qualification test of divertor modules for DEMO.

7. Towards helical reactors

Helical reactors also have similar requirements as tokamak reactors in terms of plasma wall interaction. The important issues are avoidance of impurity accumulation in the core plasmas, and power and particle (He) control to the divertor. LHD type helical reactors already have several advantages over tokamak devices such as no major disruption associated with current quenching and natural divertor configuration with edge ergodic layers[24]. Since the connection length between divertor plates and X points is shorter in helical devices than tokamak devices, the role of the ergodic layers is very important to control impurity influx to the core plasma. Kobayashi et al. showed that the edge surface layer plays an important role in impurity retention, where the friction force significantly dominates over the thermal force in LHD[25]. In a short pulse discharge (an order of seconds), experimental data proved that this layer effectively blocked wall impurities from penetrating into the core plasma. In the future, investigation on impurity behavior in this ergodic layer for much longer time scale is needed.

Power and particle control (He ash exhaust) is another important issue in helical system towards DEMO. As was mentioned before, it is better to reduce divertor heat load to much less than 10 MW/m^2 for realistic solution for solid divertor system. According to the reactor design FFHR[24], divertor heat flux of 1.6 to 2.3 MW/m^2 was a design parameter. This number is very attractive in terms of heat removal. In general, as particle flux to the divertor plate is low, neutral pressure near evacuation slot is also low, leading to reduction of He exhaust efficiency. The important issue is to achieve compatibility of low heat flux to the divertor plate and high He exhaust efficiency. Appropriate divertor design would be a key to find optimization of these.

8. Conclusion

Although there still remain several important issues on plasma facing components for ITER, there will be more challenging issues towards DEMO because of steady-state operation and high neutron dose. Feasibility study and development of relevant tungsten materials under steady-state fusion reactor environments must be pursued. For these purposes, we need clear strategy for the development of plasma facing components.

Acknowledgements

The author greatly thanks Dr. Masuzaki, Dr. Morisaki, and Dr. Yoshimura in NIFS for providing useful

information and fruitful discussion.

References

[1] J. Roth, E. Tsitrone, T. Loarer, V. Philipps, S. Brezinsek, A. Loarte, G. Counsell, R. Doerner, K. Schmid, O. Ogorodnikova and R. Causey, Plasma Phys. Control. Fusion, 50 103001 (20pp)

[2] J. Linke et al, presented at ICFRM13 (Nice, 2007)

[3] N. Yoshida H. Iwakiri, K. Tokunaga, T. Baba, J. Nucl. Mater. 337–339 (2005) 946.

[4] S. TAKAMURA, N. OHNO, D. NISHIJIMA and S. KAJITA, *Plasma and Fusion Res.,* 1, (2006) 051.

[5] M.J. Baldwin and R.P. Doerner, Nucl. Fusion 48 (2008) 035001.

[6] D. Nishijima, K. Amano, N. Ohno, N. Yoshida and S. Takamura, J. Plasma Fusion Res., 81, (2005) 703.

[7] A. Raffray, D. Haynes and F. Najmabadi, J. Nucl. Mater., 313-316 (2003) 23.

[8] G Federici, J.N Brooks, D.P Coster, G Janeschitz, A Kukuskhin, A Loarte, H.D Pacher, J Stober, C.H Wu, J. Nucl. Mater., 290-293, (2001) 260.

[9] Y. Ueda, M. Fukumoto, J. Yoshida, Y. Ohtsuka, R. Akiyoshi, H. Iwakiri, N. Yoshida, J. Nucl. Mater. in press (2009)

[10] H. Takenaga, T. Nakano, N. Asakura, H. Kubo, S. Konoshima, K. Shimizu, K. Tsuzuki, K. Masaki, T. Tanabe, S. Ide and T. Fujita, Nucl. Fusion 46 (2006) S39.

[11] J. Bucalossi, C. Brosset, B. Pégourié, E. Tsitrone, E. Dufour, A. Eckedahl, A. Geraud, M. Goniche, J. Gunn, T. Loarer, P. Monier-Garbet, J.C. Vallet and S. Vartanian, J. of Nucl. Mater., 363-365 (2007) 759.

[12] Y. Ueda, K. Tobita, Y. Katoh, J. Nucl. Mater. 313–316 (2003) 32.

[13] T. Noda , M. Fujita, M. Okada, J. Nucl. Mater. 258-263 (1998) 934.

[14] M. Fujitsuka, B. Tsuchiya, I. Mutoh, T. Tanabe, T. Shikama, J. Nucl. Mater. 283-287 (2000) 1148.

[15] H. Kurishita, S. Matsuso, H. Arakawa, T. Hirai, J. Linke, M. Kawai, N. Yoshida, Advanced Mater. Res. 59 (2009) 18.

[16] W.M.Shu, Appl. Phys. Lett., 92, (2008) 211904.

[17] M. Miyamoto et al., to be submitted.

[18] V. Barabash, G. Federici, M. Rodig, L.L. Snead, C.H. Wu, J. .Nucl. Mater. 283-287 (2000) 138.

[19] T. Munsat, Fusion Eng. Des. 54 (2001) 249.

[20] A.R. Raffray, L. El-Guebaly, S. Malang, I. Sviatoslavsky, M.S. Tillack, X. Wang and The ARIES Team, Fusion Eng. .Des. 82 (2007) 217.

[21] K. Tobita, S. Nishio, M. Enoeda, M. Sato, T. Isono, S. Sakurai, H. Nakamura, S. Sato, S. Suzuki, M. Ando, K. Ezato, T. Hayashi, T. Hayashi, T. Hirose, T. Inoue, Y. Kawamura, N. Koizumi, Y. Kudo, R. Kurihara, T. Kuroda, M. Matsukawa, K. Mouri, Y. Nakamura, M. Nishi, Y. Nomoto, J. Ohmori, N. Oyama, K. Sakamoto, T. Suzuki, M. Takechi, H. Tanigawa, K. Tsuchiya and D. Tsuru, Fusion Eng. Des. 81 (2006) 1151.

[22] K. Ezato, S. Suzuki, M. Dairaku and M. Akiba, Fusion Eng. Des. 75-79 (2005) 313.

[23] ITER home page, http://www.iter.org/a/index_nav_1.htm

[24] A. Sagara, O. Mitarai, S. Imagawa, T. Morisaki, T. Tanaka, N. Mizuguchi, T. Dolan, J. Miyazawa, K. Takahata, H. Chikaraishi, S. Yamada, K. Seo, R. Sakamoto, S. Masuzaki, T. Muroga, H. Yamada, S. Fukada, H. Hashizume, K. Yamazaki, T. Mito, O. Kaneko, T. Mutoh, N. Ohyabu, N. Noda, A. Komori, S. Sudo, O. Motojima, Fusion Eng. Des. 81 (2006) 2703.

[25] M. KOBAYASHI, Y. FENG, S. MORITA, K. SATO, M. B. CHOWDHURI, S. MASUZAKI, M. SHOJI, Y. NAKAMURA, M. TOKITANI, N. OHYABU, M. GOTO, T. MORISAKI, I. YAMADA, K. NARIHARA, N. ASHIKAWA, H. YAMADA, A. KOMORI, O. MOTOJIMA, Plasma and Fusion Res. 3, (2008) S1005.

Proceedings of ITC18,2008

Steady-State In Vessel Components for the WENDELSTEIN 7-X Stellarator

R. Stadler(1), A. Vorköper(2), J. Boscary(1), A. Cardella(1),
F. Hurd(1), Ch. Li(1), B. Mendelevitch(1), A. Peacock(1), H. Pirsch(1)
(1) Max-Planck-Institut für Plasmaphysik, EURATOM Association, 85748 Garching, Germany
(2) Max-Planck-Institut für Plasmaphysik, EURATOM Association, 17491 Greifswald, Germany

The WENDELSTEIN 7-X (W7-X) stellarator, presently under construction in Greifswald, Germany, will be a "fully-optimized" stellarator device with the aim to demonstrate the reactor potential of the HELIAS line at steady operation close to fusion relevant parameters.
The in-vessel components of W7-X are designed for steady state operation with high heat flux divertor target plates designed to withstand 10 MW/m^2 power loading. The plasma vessel and the ports are further protected by a series of water cooled graphite tiles clamped on CuCrZr cooling structure and of stainless steel panels. Behind the divertor components are the cryo vacuum pumps and the sweep/control coils.
For the first operation phase in 2014, an inertial cooled divertor of the same geometry as the high heat flux divertor will be installed as well as all in-vessel components except cryo vacuum pumps. Mostly, the components will be operated without water-cooling since during this phase the power will be restricted to 8 MW for 10s and 1 MW for 50s.
This paper describes the selected technical solutions and the present status of the various in-vessel components of W7-X with a focus on the high heat flux divertor.

Keywords: WENDELSTEIN 7-X, stellarator, in-vessel components, divertor, wall protection.

1. Introduction

The experiment WENDELSTEIN 7-X (W7-X), at present under construction at the Greifswald branch of the Max-Planck-Institut für Plasmaphysik (IPP), with a superconducting magnet system and actively cooled in-vessel components (IVC), is the largest stellarator project to date [1]. The design of W7-X will allow steady state operation, with a 140 GHz ECRH cw input power of 10 MW over a pulse length of up to 30 min. Additional heating sources, ICRH and NBI, will provide additional power for flexible experimentation [2]. The IVC, shown in Fig. 1, consist of the divertor and the wall protection of the plasma vessel. Behind the divertor components are the cryo vacuum pumps (CVP) and the sweep/control coils (CC).

For the first operation phase in 2014 [3] an inertial cooled divertor (TDU) will be installed, this will be replaced later for steady-state operation by the high heat flux (HHF) divertor. The TDU has the same geometry as the HHF divertor. This phase aims at determining the correct positioning of the target plates. This approach will minimize the necessary commissioning of the HHF divertor in steady-state operation.

The other IVC except CVP will be installed at the beginning but mostly operated without active water cooling. This is possible as the input power will be restricted to 8 MW for 10s and 1 MW for 50s. This paper presents the selected technical solutions and the present status of the IVC.

The complete IVC have a weight of 33.8 tons, covering a total surface of 265 m^2. The intrinsic challenge of this project is the 3D-geometry of the machine and the limited available space within the vacuum vessel. IVC

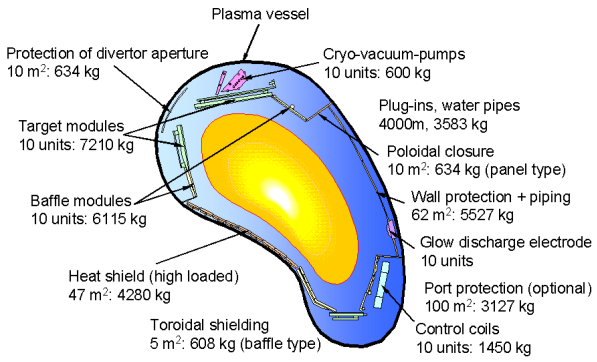

Fig.1 Location of IVC in the W7-X plasma vessel at the "bean-shape" cross-section.

author's e-mail: Reinhold.Stadler@ipp.mpg.de

have been designed to maximize the plasma volume and require a high level of accuracy.

2. IVC Project

The development and construction of the IVC is managed in IPP Garching, in close cooperation with the team at IPP Greifswald.

A large part of the IVC is manufactured and tested in the IPP Garching workshop. The manufacturing contract for target elements (TE) of the HHF divertor has been awarded to PLANSEE SE, Austria. The sweep/control coils have been manufactured by BNG, and the wall panels (WP) are being delivered by MAN-DWE, both companies are located in Germany.

3. Divertor Components

The divertor consists of ten similar discrete units, arranged above and below in each of the five modules. The plasma facing components are the target modules (TM) and the baffle modules (BM). Behind them are the CVP and CC. The highest thermally loaded parts are the target plates with a surface area of ~25m² to allow a wide range of plasma configuration and magnetic parameters.

3.1 High Heat Flux Divertor

The ten similar units of the HHF divertor are divided into nine horizontal and three vertical TM, with an intermediate pumping gap between horizontal and vertical TM. The horizontal part consists of four HHF-TM, two clamped low heat flux modules (LHF) and three additional HHF-TM in a row along the toroidal circumference.

Each HHF TM consists of eight to twelve actively cooled TE (Fig. 2). The HHF divertor requires the production of about 900 TE of 13 different types. These

Fig.2 Two full scale prototype HHF target modules with dummy target elements, already mounted on adjustable frame.

Fig.3 GLADIS HHF-test facility, with new designed vacuum lock

elements are each designed to remove a maximum power of 100 kW and to withstand a steady-state heat load of 10 MW/m².

The design comprises flat carbon fiber composite (CFC) tiles bonded to actively water-cooled CuCrZr heat sinks. For the TE production, the initial approach was to use as much as possible well-known technologies. A large experience in the manufacturing in large quantities of HHF elements designed for similar loading conditions was gained during the fabrication of about 600 finger elements for the toroidal pump limiter of Tore Supra [4]. The contract was awarded to the same company that successfully produced these finger elements, in order to avoid significant R&D activities. The strategy consisted of a preliminary phase of pre-series activities to qualify the manufacturing process to be adapted to the different geometry of target elements (longer, wider, trapezoidal), followed by the launching of the serial fabrication of the required 900 elements.

In addition, Sepcarb® NB31 CFC material was selected instead of N11 for Tore Supra produced by the same company, namely Snecma Propulsion Solide, France. This grade offers higher mechanical properties to cope with the loading occurring during the fabrication and operation at the critical interface between the CFC and Cu. Many unexpected difficulties occurred during this fabrication and significant differences in the obtained mechanical properties between delivered batches were observed. This required substantial additional qualification activities, and approximately 900 kg CFC was finally successfully delivered to IPP.

The heat sink is manufactured by joining by electron beam welding two plates of CuCrZr into which have been machined semi-circular channels. Swirl tapes are inserted and the plates are welded together. This design can suffer from leakage between adjacent channels with a

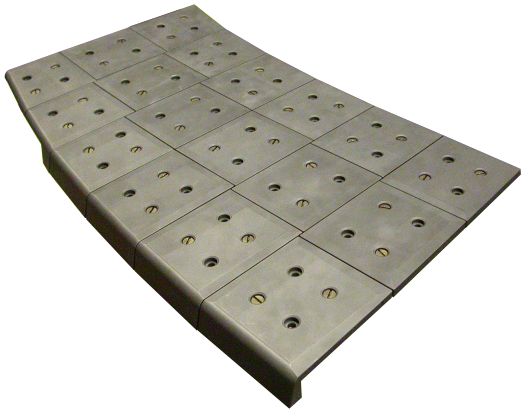

Fig.4 Baffle Module with graphite tiles temporarily clamped during acceptance tests.

significant reduction of the thermal performance which affects the critical interface with CFC tiles. Additional efforts have been dedicated to the improvement of this weld design.

The bonding technology between CFC tiles and heat sink underwent also significant improvement. The initial Active Metal Casting (AMC) technology will be improved by a bi-layer technology: a copper layer is active metal cast to CFC tiles, and then an OF-copper layer is added by hot isostatic pressing. The tiles are finally bonded by electron beam welding onto the cooling structure, with the same process used by Tore Supra. This solution, as shown in samples, is expected to improve the reliability and the robustness of the bond for all types of TE under thermal cycling, and to avoid or reduce crack propagation at the interface. However, adaptation of the Tore Supra solution to the new geometry showed that several problems have to be overcome resulting in a significant pre-series effort.

About sixty prototype TE have been evaluated during pre-series activities. All elements were tested in the HHF ion beam facility GLADIS (Fig. 3) of IPP Garching in fatigue tests of 100 cycles @ 10 MW/m² for 10 seconds.

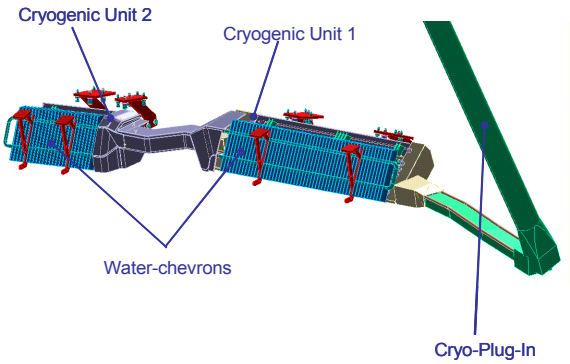

Fig.5 CAD model of Cryo Vacuum Pump

The last delivered elements showed no visible defects at the end of the test campaign. In addition, one element survived 10.000 cycles without visible damage. Tests with increased power were also performed. A critical heat flux of 31 MW/m² was achieved on an element without tiles, compared to the 25 MW/m² specified. A screening test with heat fluxes up to 24 MW/m² was also achieved. With these promising results a sufficient margin for experimental steady-state operation can be expected and shall be verified by an additional development program.

The LHF-units are designed for 1 MW/m² steady-state and use the same technology as the BM. The divertor pumped volume is closed by toroidal and poloidal closure plates. For the toroidal part a water cooled structure similar to the BM is used and for the poloidal closure stainless steel panels are used.

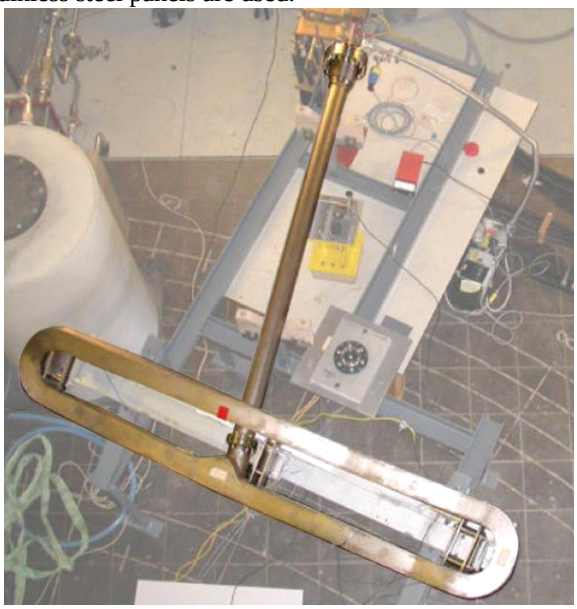

Fig.6 Control coil in IPP test facility.

3.2 Baffle Modules

The 170 BM are designed for a maximum steady-state heat load of 500 kW/m². The BM consists of CuCrZr plates vacuum brazed to stainless steel tubes that form the cooling circuit. Graphite tiles are clamped to the structure using TZM screws (Fig. 4). A compliant layer of soft carbon is used to provide the thermal contact.

3.4 Cryo-Vacuum Pump

The CVP are located behind the horizontal TM in the divertor volume. Each CVP is built up of two units, which are shielded by water cooled chevrons against radiation loads (Fig. 5). The CVP are designed for an optimum pumping speed of 75 m³/s in front of the chevrons.

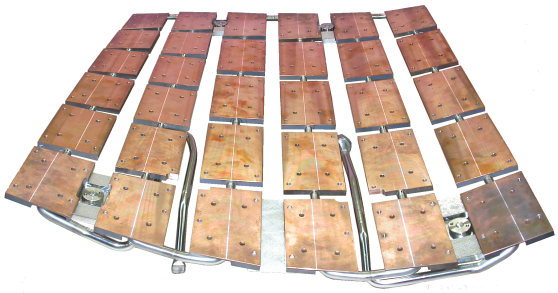

Fig.7 Heat shield, shown without clamped graphite tiles.

3.5 Control Coils

The ten CC (Fig. 6) are located behind the BM. The CC allow to compensate for symmetry breaking error fields and to sweep the strike point and spread the power deposition along the target surface in order to increase steady-state reliability of the TE.

4. Wall Protection

The plasma vessel wall and the ports are protected by actively cooled components. On the inboard side, close to the plasma surface, graphite protected heat shields (HS) are installed. The outboard side is covered by stainless steel wall panels (WP).

4.1 Heat Shields

The HS (Fig. 7) use similar technology to the BM, but are designed for a maximum heat load of 300 kW/m^2. Some of the 162 HS include beam dump elements for the neutral beam injection (NBI), the ECRH heating and the diagnostic-injector, as well as special solutions for integrated diagnostics systems.

Fig.8 Wall panel, rear view.

4.2 Wall Panels

The outboard region of the plasma vessel and the pumping gap area will be covered by 320 steel WP (Fig. 8). They are designed for a heat load of up to 200 kW/m^2.

For the layout of the WP, the plasma vessel geometry was divided into facets with small cylindrical shaped segments. This reduced significantly manufacturing effort by allowing 1D-bending on the individual WP.

Each WP is made from two stainless steel sheets that are welded together and quilted by overpressure to form a meander of cooling channels. Along the circumference a vacuum tight weld seals the WP.

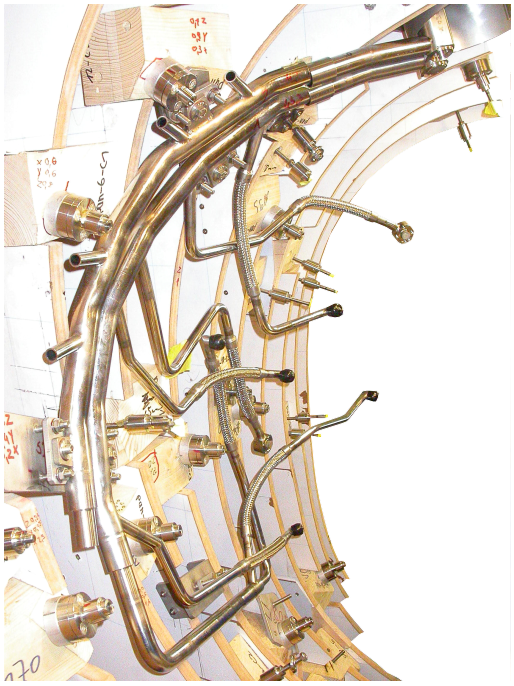

Fig.9 Prototype cooling circuit during installation in the wooden mock-up.

4.4 Port Liner

Some ports, that require internal protection during HHF operation, are equipped with WP-type port liners. The NBI ports – due to the higher thermal loads - will be equipped with graphite and CFC tile protection similar to the BM.

5. Internal Cooling Supply

All 1500 plasma facing components are actively cooled during steady state operation. 4.5 km of pipe work is installed as 150 individual cooling loops. The cooling circuits are the first to be installed. Design and manufacturing technology were verified with a prototype, installed and hydraulically tested in a wooden mock-up of a plasma-vessel segment (Fig. 9).

7. Test Facilities used for the IVC-activities

Several test facilities are used regularly to perform acceptance tests of all IVC.

A vacuum chamber, with 3 m length and 1.2 m diameter, is used for leak and out-gassing tests (Fig. 10), hot leak tests for the plasma facing components at (160°C) and cold tests at LN2 temperature for the CVP.

Hydraulic tests and temperature distribution analysis to identify hot spots on the WP with an infrared camera are also used.

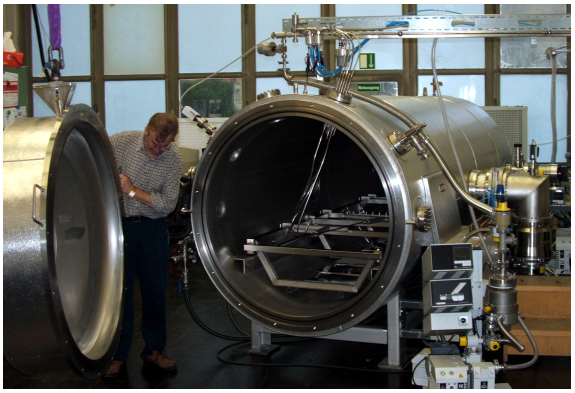

Fig.10 Vacuum chamber for testing of IVC-components.

8. Conclusions

The IVC for W7-X are designed for steady-state operation at 10 MW and the components are actively cooled.

Prototype HHF testing has shown encouraging results for the development of the technology for the standard TE. A significant development program is still required before all 13 types of TE for W7-X are fully qualified. Manufacturing of the HS, WP and BM is well progressed. Procurement of graphite tiles is on-going. Serial production of the cooling loops was initiated, all CC are delivered. First delivery of the components to IPP Greifswald has started.

The present time schedule, based on the experience gained throughout the project, shows that all components, including the TDU, will be available for installation to allow machine commissioning in 2014.

References

[1] B. Streibl et.al, Manufacturing of the WENDELSTEIN 7-X divertor and wall protection, Fusion Engineering and Design 75-79, (2005) 463-468

[2] J. Feist, Systemspezifikation WENDELSTEIN 7-X – Zentrale Maschine, IPP (1999)

[3] A. Peacock et.al., Design and Development of the Test Divertor (TDU) of the Experiment W7-X, IPP, 25th. SOFT (2008), submitted for publication in Fus. Eng. Des.

[4] J.J. Cordier, Preliminary results and lessons learned from upgrading the Tore Supra actively cooled plasma facing components (CIEL project), Fus. Eng. Des. 66-68 (2003) 59-67.

[5] J. Boscary et.al., Results of the Examinations of the W7-X preseries target elements, Fusion Engineering and Design 82, (2007) 1634-1638

[6] J. Boscary et.al., Fabrication and Testing Route for the serial Fabrication of W7-X Target Elements, IPP, 25th SOFT (2008), submitted for publication in Fus. Eng. Des.

[7] H. Greuner et.al., High Heat Flux Facility GLADIS: Operational Characteristics and Results of W7-X Pre-Series target Tests, Journal of Nuclear Materials 367-377, (2007) 1444-1448

[8] H. Greuner et.al., High Heat Flux Tests of the WENDELSTEIN 7-X Pre-Series target Elements; Experimental Evaluation of the thermo-mechanical behaviour, Fusion Engineering and Design 82, (2007) 1713-1719

[9] H. Greuner. et.al., Review of the High Heat Flux Testing as an integrated Part of W7-X Divertor Development, IPP, 25th SOFT (2008), submitted for publication in Fus. Eng. Des.

[10] R. Stadler et.al, The In-Vessel Components of the Experiment WENDELSTEIN 7-X, IPP, 25th SOFT (2008), submitted for publication in Fus. Eng. Des.

Proceedings of ITC18, 2008

Spatial heterodyne spectro-polarimetry systems for imaging key plasma parameters in fusion devices

John HOWARD[1)], Ahmed DIALLO[1)], Roger JASPERS[2)] and Jinil CHUNG[3)]

[1)]*Plasma Research Laboratory, Australian National University. Canberra ACT 0200, Australia*
[2)]*FOM institute for Plasmaphysics Rijnhuizen, 3430 BE Nieuwegein, The Netherlands*
[3)]*National Fusion Research Institute, Gwahangno 113, Yusung-Gu, Daejeon, 305-333, Korea*

(Received January 2008 / Accepted)

Imaging diagnostics systems are very important to aid the understanding of core and edge confinement in 3D helical magnetic devices. In this paper we consider recent developments in optical "coherence imaging" interferometric systems that open new diagnostic capabilities for next generation devices, with particular focus on Motional Stark Effect (MSE) imaging. We present preliminary results obtained using a hybrid spatio-temporal heterodyne snapshot imaging polarimeter-interferometer for motional Stark effect imaging of the q-profile in the TEXTOR tokamak.

Keywords: Polarimetry, spectroscopy, Motional Stark Effect, coherence, interferometry

DOI: 10.1585/pfr.1.001

1 Introduction

Motional Stark Effect spectro-polarimetry has become a routine diagnostic for high power fusion devices that employ diagnostic or heating neutral beams. In tokamaks, measurement of the polarization state of the Stark split multiplet is used to infer the internal toroidal current density profile [1, 2], while for stellarators MSE can be used to help determine the plasma equilibrium. Until now, because of various technical limitations, especially in low field compact systems where the Stark multiplet is difficult to resolve or is contaminated by other spectral features, MSE systems have been limited to 10 or 20 discrete channels viewing positions across the injected beam.

The MSE technique relies on the splitting of the Doppler-shifted neutral beam Balmer α light into orthogonally polarized σ and π components as a result of the motion-induced strong electric field $\boldsymbol{E} = \boldsymbol{v}\times\boldsymbol{B}$ experienced in the rest frame of the neutral atoms. The Doppler shift, which arises due to observation at an angle to the energetic beam, conveniently shifts the multiplet away from the background H_α radiation. When viewed in a direction perpendicular to $\boldsymbol{E}$ the Stark split σ and π components are polarized respectively perpendicular and parallel to the direction of $\boldsymbol{E}$. When viewed along $\boldsymbol{E}$ the σ components are unpolarized and the π components have no brightness. The Stark separation of adjacent Balmer alpha spectral components varies as $\Delta\lambda_S = 2.7574 \times 10^{-8} E$ nm where $E = |\boldsymbol{v}\times\boldsymbol{B}|$ is the induced electric field [3]. Integrated over wavelength, the Stark multiplet is nett unpolarized and no orientational information can be obtained.

The magnetic field pitch angle is usually estimated by isolating and measuring the polarization direction of the central cluster of σ lines. This requires a tunable narrowband filter to spectrally resolve the multiplet in order to obtain a nett polarization that is analysed by a modulated polarimeter. Every spatial channel thus requires a dedicated filter whose passband must be optimized by tilt or thermal tuning. Recently we have proposed a variety of optical systems that can capture the full polarimetric information about the entire Stark multiplet in a single snapshot [4]. This is achieved by using interfero-polarimetric methods to produce orthogonal spatial carrier fringes which encode the optical coherence (spectrum) and polarimetric information.

In the slightly simpler scheme described here, a spatial heterodyne polarization interferometer is used to provide spectral discrimination and to imprint interference fringes on an image of the neutral beam. The contrast and phase of the fringes depend on the spectral separation of the Stark components and their mean wavelength. A front end polarimeter which employs a switching liquid crystal waveplate modulates the fringe phase in proportion to the local polarization orientation of the entire Stark multiplet. Successive independent images can then be phase demodulated to recover an image of the local magnetic field pitch angle. Because of the spatial encoding and the ability to accept a relatively wide spectral window, it becomes feasible to undertake two-dimensional magnetic field imaging. Moreover, the resulting extracted image of the Stark multiplet polarization orientation is insensitive to arbitrary unpolarized spectral contamination such as the wing of the H_α emission, or leakage from adjacent beam energy components. Under certain conditions, it is also insensitive to background radiation that has become polarized due to reflections from various surfaces.

This paper is organized as follows. Section 2 gives a brief description of the optical system, its operating principle and its implementation on TEXTOR for observations

author's e-mail: john.howard@anu.edu.au

of the H_α multiplet. First observations are presented in Sec. 3. The experimental images when compared with modeling results, suggest that line-of-sight integration effects may be important for the interpretation of the pitch angle images. The results also suggest a number of tests and crosschecks which will be undertaken during a dedicated day of operations in March 2009. These issues are considered in Sec. 4.

2 MSE imaging spectro-polarimeter

2.1 Measurement principle

Figure 1(a) shows the optical arrangement for a simple polarization interferometer comprising a polarizer, birefringent delay plate (of phase delay ϕ) with fast axis at 45° to the polarizer axis, and final analyzer parallel to the first polarizer. Within a factor, the interferometric signal is given by

$$S = I_0(1 + \zeta \cos\phi) \tag{1}$$

where I_0 is the brightness, ζ is the fringe visibility at optical delay $\phi = 2\pi LB/\lambda_0$, L is the birefringent plate thickness, B is the birefringence and λ_0 is the wavelength.

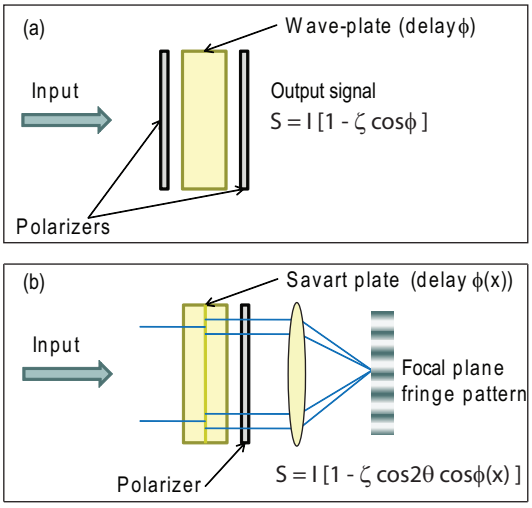

Fig. 1 (a) A simple polarization interferometer. The fringe visibility ζ depends on the optical coherence at phase delay ϕ. (b) When the input light is already polarized, the first polarizer can be omitted. The fringe contrast then also depends on the input polarization orientation with respect to the final analyzer. A shearing Savart wave-plate produced a sinusoidal fringe pattern in the lens focal plane.

If the light source is already polarized, the first polarizer can be removed and the signal becomes

$$S = I_0(1 + \zeta \cos 2\theta \cos\phi) \tag{2}$$

where θ is the polarization angle with respect to the final analyzer axis. If the wave-plate is replaced with a Savart shearing plate [5], the phase delay becomes a function of position and an interference fringe pattern is formed in the focal plane of a final imaging lens. The fringes carry the polarization orientation through the amplitude term $\zeta \cos 2\theta$.

If a quarter wave plate with fast axis parallel to the analyzer is installed as the first element in the optical chain, the polarization orientation is shifted to the phase domain and the detected image is

$$S = I_0\left[1 + \zeta \cos(\phi - 2\theta)\right]. \tag{3}$$

Because the phase delay $\phi(x)$ is generally not known absolutely, it is necessary to introduce a modulating element in order to extract the polarization orientation. In our case, we insert a ferroelectric liquid crystal (FLC) half wave-plate between the first quarter wave plate and the following optical delay plate (see Fig. 2). Nominally the FLC fast axis is aligned parallel to the delay plate and ϕ becomes $\phi + \pi$. By reversing the polarity of a low voltage bias of order 5V across the FLC cell, the birefringent axes rotate through 45° so that the fast axis is now crossed with the axes of the quarter wave-plate, reversing the sense of the quarter-wave delay and changing the sign of the term 2θ in Eq. (3). The images in the two FLC states are respectively

$$S_1 = I_0\left[1 - \zeta \cos(\phi - 2\theta)\right] \tag{4}$$

$$S_2 = I_0\left[1 + \zeta \cos(\phi + 2\theta)\right] \tag{5}$$

and it is clear that a suitable demodulation procedure applied to successive images will produce an image of 4θ.

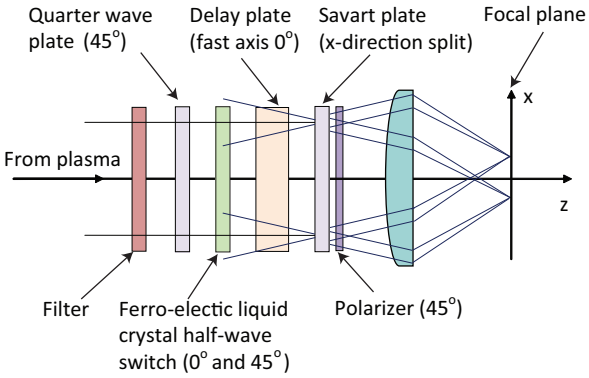

Fig. 2 Layout of the hybrid spectro-polarimeter. The quarter-wave plate and FLC switch constitute the polarimeter. The primary delay plate and polarizer provide spectral discrimination. The Savart plate imprints a sinusoidal spatial carrier wave in the x-direction.

Because the MSE multiplet is nett unpolarized the signs of the π and σ contributions to the image of the complete multiplet are opposite and, in the absence of spectral discrimination, the fringe pattern vanishes. However, by appropriately choosing the optical delay offset ϕ it is possible to maximize the difference between ζ_π and ζ_σ to ensure

good fringe visibility, even when the ratio of the separation to width of the multiplet components is small [4].

2.2 The TEXTOR optical system

The TEXTOR neutral beam and viewing geometry is depicted in Fig. 3. A custom turning prism mounted in vacuum is used to direct light from the beam through a fused-silica window into the spectro-polarimeter. The instrument is constructed from the various optical birefringent components of diameter 25mm housed in a 40 mm diameter turret that screws into the filter thread of a 17 mm focal length wide-angle C-mount imaging lens (see Fig. 6). The lens (focused at infinity) forms an image of the plasma onto an 8 mm × 6 mm imaging fibre bundle array which transports the image to a Cooke sensicam CCD camera. The turret, lens and fibre cable are inserted into a re-entrant port and positioned adjacent to the fused-silica vacuum window.

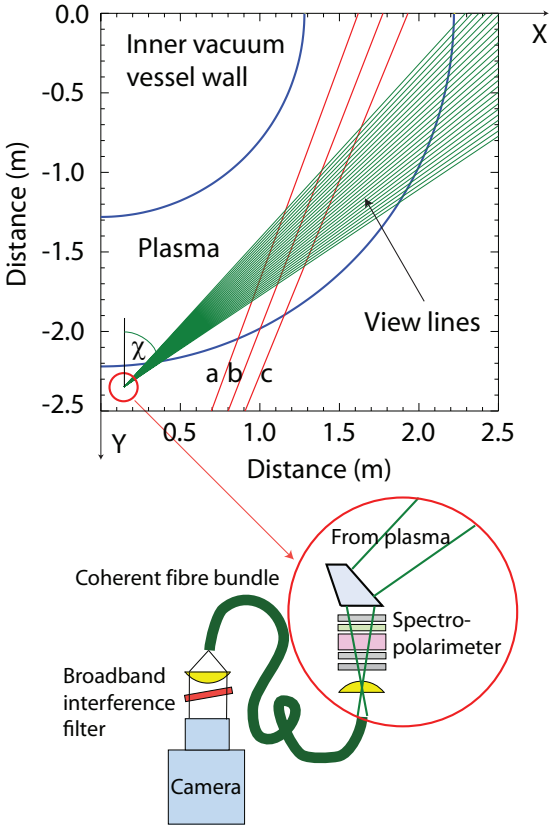

Fig. 3 The TEXTOR system geometry. The neutral beam spans the region designated by the lines labeled 'a', 'b' and 'c'. A coherent fibre bundle transports the image to a broadband interference filter and CCD camera synchronized to the FLC switch.

At the fiber cable exit a 55 mm focal length F-mount lens collimates the light through tiltable 2nm pass-band interference filter centered on 662.5nm. The filter is adjusted so that the centre wavelength approximately tracks the variation in Doppler shift of the multiplet across the beam image. A final 50 mm focal length F-mount lens forms the final image.

We have constructed a numerical model of the TEXTOR system to calculate the expected spectrum and associated nett fringe contrast versus optical delay as a function of viewing angle to the beam [4]. The results shown in Fig. 4 indicate that an optical delay of approximately 1000 waves at 663 nm should give excellent nett fringe contrast across the viewing region. The delay is obtained using a field-widened lithium niobate delay plate of total thickness 6 mm and effective diameter 30 mm. A conventional calcite Savart shearing plate of thickness 1 mm is used to generate the spatial heterodyne fringe pattern in the focal plane of the focusing lens.

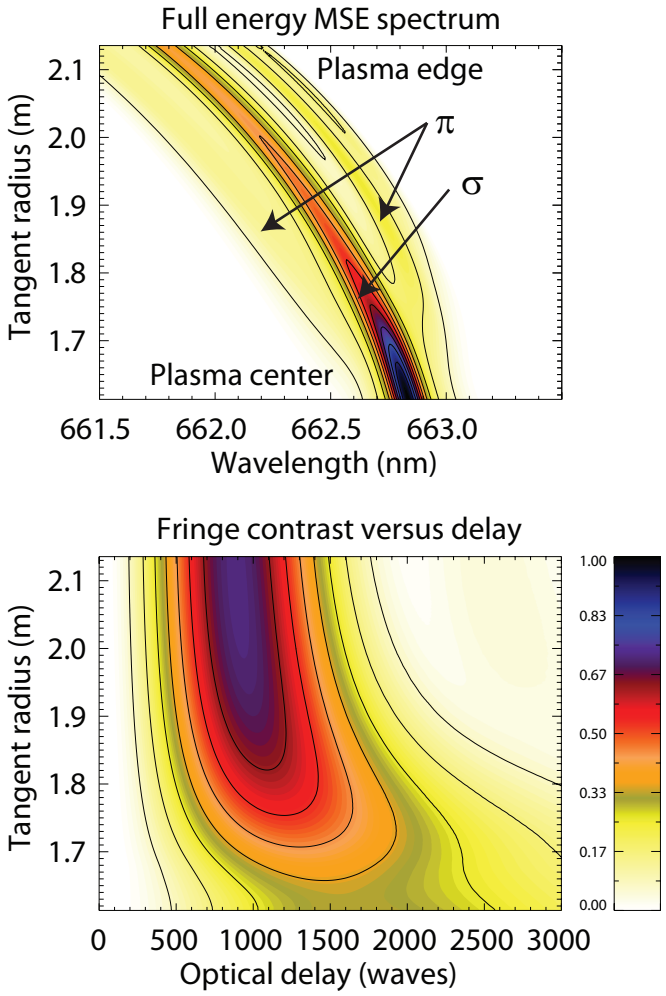

Fig. 4 Top: The model MSE spectrum for the imaging arrangement on TEXTOR and Bottom: the corresponding fringe contrast versus optical delay. The fringe contrast is poorer near plasma center where the separation between Stark components is small.

Figure 5(a) shows the interior of the TEXTOR vacuum vessel as viewed by the spectro-polarimeter. Various image features such as port openings and flanges are used to calibrate the observed field of view. The 2×2 binned images (688×520 pixels) have been cropped to show only regions accepted by the spectro-polarimeter optical system.

Figures 5(b) and (c) show images of plasma light in the 660 nm filter pass-band without and in the presence of the neutral heating beam respectively. The color scales are in units of photo-electrons and the image exposure time was 4 ms. Note that the plasma light image shows no evidence of interference fringes, indicating the absence of polarized features of spectral width comparable to the MSE multiplet components. As evident in Fig 5(c), the spatial fringes have been oriented parallel to the horizontal midplane in order to maximize the radial spatial resolution. The resulting radial resolution ~ 3mm is set by fibre cable resolution and image binning, while the vertical resoution of ~ 15 – 20 mm is set by fringe period. While the observed fringe curvature can be eliminated by field-widening the Savart plate [5], it is of no consequence in the present optical configuration where the fringe phase can be recovered by demodulating the images column-by-column.

2.3 Optical system calibration

The system polarimetric response is calibrated by filling the field-of-view using Balmer-alpha light from a hydrogen lamp and replacing the 663 nm filter with a filter at 656 nm. A rotatable polarizer is used to vary the incident polarization and image sequences are acquired and processed for a range of polarizer angles spanning 90°. A typical calibration arrangement is shown in Fig. 6. Central horizontal slices for a sequence of calibration phase images for polarizer angles between 0° and 90° in increments of 10° ± 1° are shown in Fig. 7. We have implemented both wavelet and Hilbert transform demodulation algorithms. The latter method, which is based on fast Fourier transforms and is therefore quite fast, generally suffices when the signal to noise ratio is good (as is the case for data presented in this paper). Image lines show typical root mean square phase noise of ~ 0.5°. Small systematic departures from uniformity may be due to component alignment inaccuracies which will be addressed in the next version of the instrument. These distortions, which are nevertheless quite small, have not been compensated in the results presented in this article.

3 Results

To illustrate performance the system performance we consider an image sequence for discharge #108250 during which the toroidal magnetic field was 2.25T on axis and the toroidal current was ~ 350 kA. For this discharge, the camera exposure time was 2 ms, the frame period was ~50 ms and the image size was 344 × 260 pixels. The time history of the interferogram brightness averaged over a central cell of dimensions 10 × 10 pixels is shown in Fig. 8. Note the strong modulation in the beam brightness and accompanying phase modulation of amplitude ~ 0.2 radians corresponding to a periodic modulation in the beam energy of

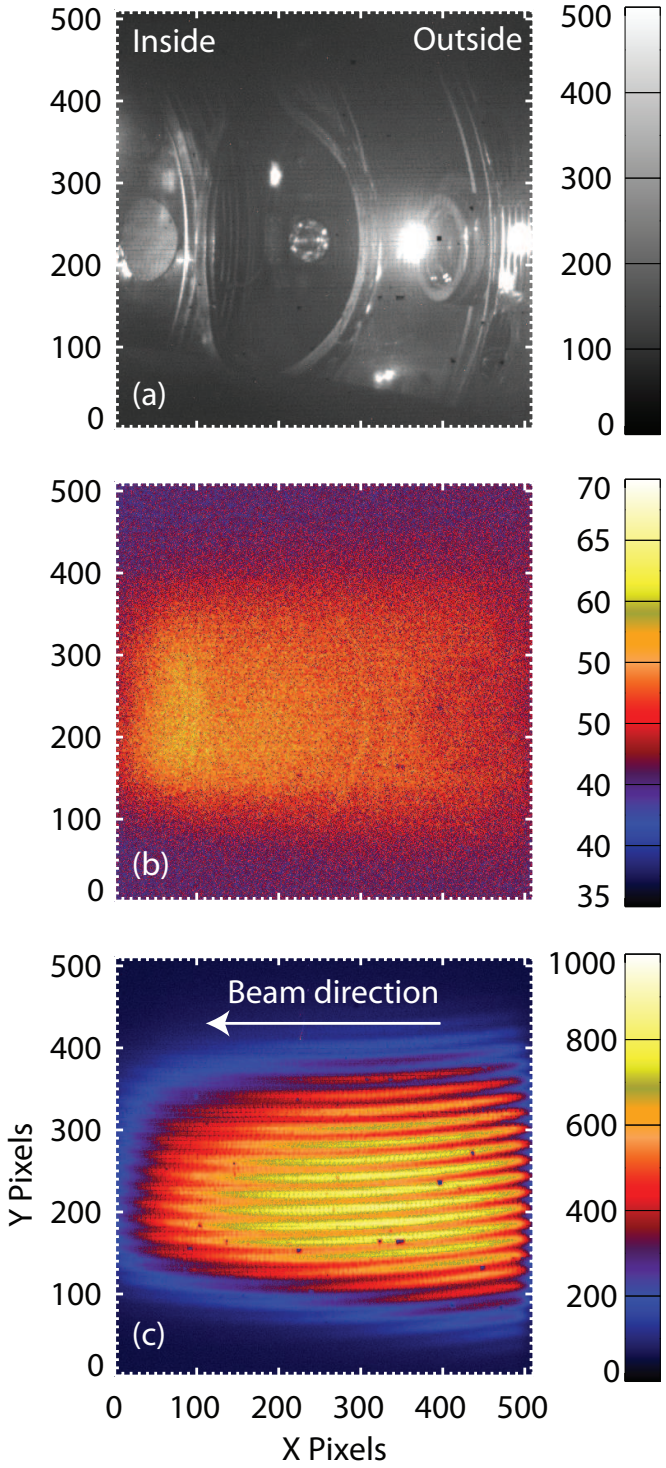

Fig. 5 (a) Image of interior of TEXTOR vacuum vessel as recorded by the spectro-polarimeter. (b) Plasma emission within the 660nm filter pass-band (no neutral beam emission) for discharge #108248. Notice the absence of interference fringes. (c) Image of the neutral beam. Visible interference fringes indicate that the light is polarized. Successive images can be demodulated for the polarization orientation.

amplitude ~ 0.4 keV - consistent with independent beam energy measurements. It is important that the image ex-

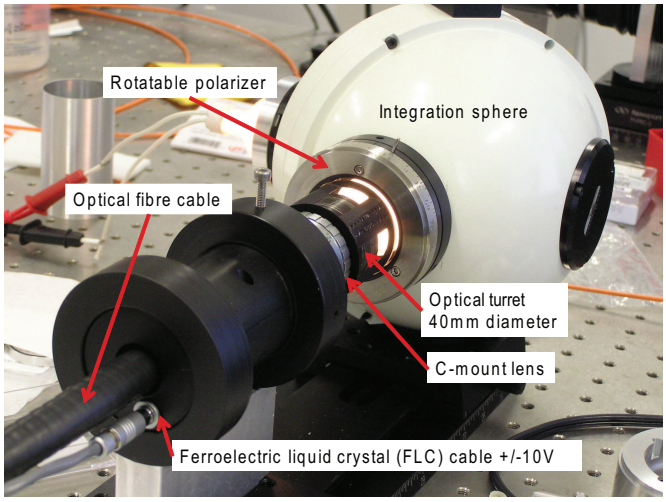

Fig. 6 A photograph of the optical head during calibration procedure. The optical head is inserted into a re-entrant port that views the plasma and neutral beam through a turning prism and fused silica window

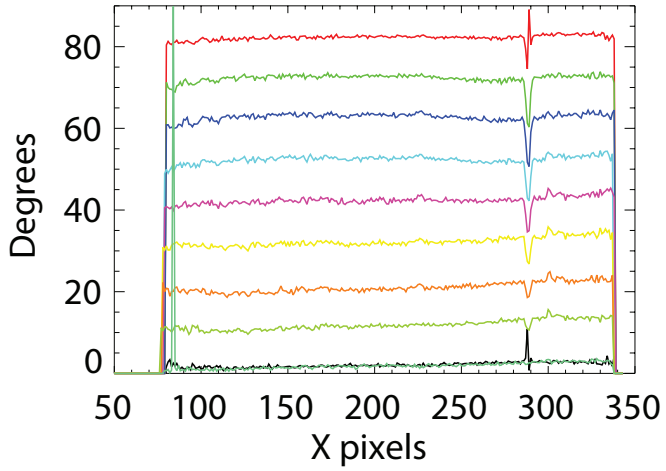

Fig. 7 Central horizontal slices for a sequence of calibration phase images for polarizer angles between 0° and 90° in increments of 10° ± 1°. The image discontinuities are due to a faulty optical cable pixel.

posure time be less than the modulation period in order to maintain good fringe visibility.

The interferograms have been demodulated using a wavelet-based algorithm and images of the fringe visibility and inferred polarization orientation θ versus image coordinate angles (χ, ψ) where χ is the angle between the line of sight and tokamak Y-axis as shown in Fig. 3 and ψ is the vertical angle above the horizontal midplane. Representative images taken at time 1.8 s in the discharge are shown in Fig. 9. As expected, the fringe contrast deteriorates towards the center of the plasma where the multiplet splitting decreases (compare with Fig. 4). We have not corrected for weak instrumental fringe contrast variations.

To interpret the experimental polarization tilt angle image, we have developed a numerical model to calcu-

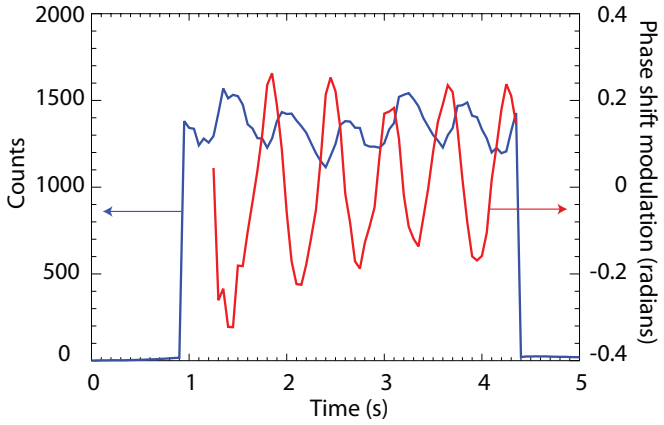

Fig. 8 Temporal behaviour of central image brightness and carrier phase. A strong modulation in the beam parameters is evident. See text for discussion.

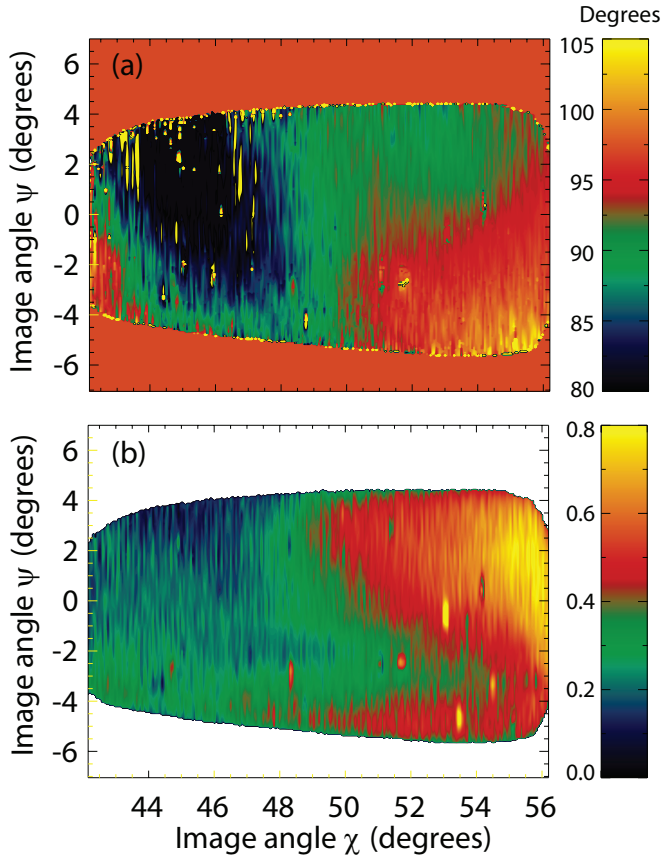

Fig. 9 (a) Demodulated polarization tilt angle image at 1.8 s and (b) corresponding fringe visibility image. See text for discussion.

late the expected inclination distribution for the TEXTOR viewing geometry. We assume a toroidal current distribution of the form $j(r) = j_0(1-r^2/a^2)^\gamma$ and in the simulations reported here, have taken the value $\gamma = 2$ for the exponent and the plasma minor radius is $a = 0.47$m. To calculate the polarization orientation, for each point in the field of view, we project the local $\boldsymbol{E} = \boldsymbol{v} \times \boldsymbol{B}$ onto a measurement Cartesian coordinate system having z axis connecting the mea-

surement pixel and the field point and x-axis in the tokamak horizontal plane. Because the beam is extended both vertically and toroidally, the measured polarization angle at a given image point can be derived from the summation of the Stokes vectors describing the polarization state for all points on the z-axis that intersect the beam.

While the brightness weighting along the view line is unknown, it is nevertheless instructive to calculate the electric field orientation on vertical planes intersecting the beam on axis (label 'b' in Fig. 3) and on planes labeled 'a' and 'c' in Fig. 3 that are 1° displaced either side of the axis with respect to the model beam origin. These planes are at angles within the estimated divergence of the 50 keV hydrogen heating neutral beam. The calculated polarization angle distributions are shown in Fig. 10. As or Fig. 9(a), the color contours span the range $[80°, 105°]$ while the vertical angular extent for each of the images is set by the beam model and geometric perspective effects. We observe a strong dependence on beam inclination that suggests that path integration effects may be important in the TEXTOR case. Moreover, we note that the three computed images taken together tend to capture many of the features observed in the experimental image and match satisfactorily the observed range of inclination angles. Additional experiments and crosschecks are required to confirm these results.

4 Discussion and future work

Polarization interferometers have a number of advantages for spectro-polarimetric imaging, including high throughput, simple and compact optics with easy alignment and 2-d imaging capability. By obviating the need for narrowband filters, the spectro-polarimeter described here allows MSE imaging for the first time. Importantly, the technique is insensitive to unpolarized or wideband polarized background contamination. There would also seem to be some sensitivity advantage in that the instrument is sensitive to 4 times the polarization inclination.

The preliminary results reported here suggest a number of cross-checks and validation experiments, including beam into gas calibration, reversal of field direction etc. which will be undertaken during dedicated experiments in 2009. Clearly it will be necessary to attempt to quantify and possibly unfold line-of-sight integration effects. In addition, a custom compound optical system to undertake double-spatial-heterodyne snapshot imaging will be implemented. Ultimately, a snapshot imaging system will be deployed for high speed imaging using a CMOS camera for studies of MHD relaxation and other transient phenomena.

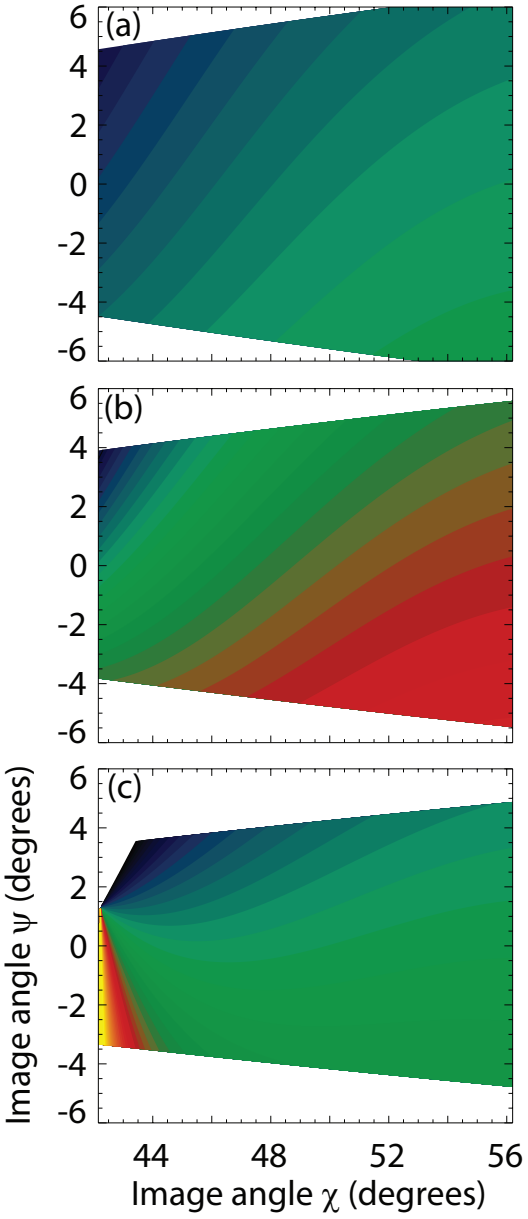

Fig. 10 (a)-(c): Calculated pitch angle distributions in vertical planes along lines a-c respectively as shown in Fig. 3.

Acknowledgements

This work is supported by International Science Linkages established under the Australian Government's innovation statement, "Backing Australia's Ability". We also wish to thank Dr R. König for providing the imaging fibre array for these experiments.

Bibliography

[1] F. M. Levinton *et al.*, Phys. Rev. Lett. **63**, 2060 (1989).
[2] D. Wroblewski *et al.*, Rev. Sci. Instrum. **61**, 3552 (1990).
[3] B. W. Rice, Fusion Eng. Design **34-35**, 135 (1999).
[4] J. Howard, Plasma Physics and Controlled Fusion **50**, 125003 (18pp) (2008).
[5] M. Francon and S. Mallick, *Polarization Interferometers* (Wiley-Interscience, London, 1971).

Proceedings of ITC18,2008

From Wendelstein 7-X to a Stellarator Reactor

R.C. Wolf, C. Beidler, H. Maaßberg, R. Burhenn, J. Geiger, M. Hirsch, J. Kisslinger, A. Weller, A. Werner and the Wendelstein 7-X Team

Max-Planck-Institut für Plasmaphysik, IPP-EURATOM Association, D-17491 Greifswald, Germany

Wendelstein 7-X is a drift optimized stellarator with improved thermal and fast ion confinement. Additional optimization criteria are a stiff equilibrium configuration and MHD stability up to a volume averaged β of 5%. The main objectives are to demonstrate reactor relevant plasma performance under steady state conditions including power and particle exhaust with an island divertor. To that effect Wendelstein 7-X has superconducting coils with a maximum average magnetic field of 3 T and will be equipped with actively cooled plasma facing components for heat fluxes of up to 10 MW/m^2. Besides fulfilling this research mission, the extrapolation from Wendelstein 7-X to a stellarator reactor will depend on the comparison with the results from other stellarators, the ITER results and here in particular the experience gained with α-particle heating and operating a nuclear device, and the possibility to extrapolate these results by first principle theory.

Keywords: Wendelstein 7-X, stellarator optimization, Helically Advanced Stellarator

1. Introduction

Wendelstein 7-X (W7-X) is a drift optimized low magnetic shear stellarator to demonstrate basic reactor capability of the stellarator concept [1]. With a major radius, R, of 5.5 m and an average minor radius, <a>, of 0.5 m the resulting plasma volume of 30 m^3 lies between those of ASDEX Upgrade and JET. The maximum magnetic field is 3 T, corresponding to 600 MJ of magnetic field energy. The rotational transform, ι, ranges from 5/6 to 5/4 and, in contrast to the partially optimized predecessor of W7-X, Wendelstein 7-AS (W7-AS) [2], is practically independent of the plasma β.

The design of W7-X is based on an elaborate optimization procedure to overcome the essential deficiencies of the stellarator concept: (1) The introduction of quasi-symmetry – in case of W7-X a quasi-isodynamic configuration has been chosen – yields reduced neoclassical transport and, in particular, good fast ion confinement which is a prerequisite for any type of fusion reactor. Since in a stellarator the neoclassical diffusion scales like $\varepsilon_h T^{7/2}$, the helical ripple, ε_h, has to be kept as small as possible. (2) By minimizing the Pfirsch-Schlüter and bootstrap currents the Shafranov shift is minimized and thus a high equilibrium limit is achieved. (3) Finally, the magnetic field configuration provides sufficiently large magnetic well to avoid pressure drive instabilities such as interchange modes, aiming at an volume averaged $<\beta>$ of 5%.

High power steady state operation of W7-X will be approached in two steps: (1) An inertially cooled test divertor will allow pulses from 10 to 50 s, corresponding to heating power levels from 8 to 1 MW. During this initial phase three heating systems will be available: Neutral beam injection (NBI), ion cyclotron resonance heating (ICRH) or electron cyclotron resonance heating (ECRH). Depending on the combination of the heating methods, the available heating power will vary between 8 and 11 MW. (2) After the installation of the actively cooled divertor and the completion of the water cooling of all plasma facing components, 30 minutes plasmas with 10 MW ECRH [3] are foreseen. Later upgrades will include increases of the neutral beam heating power from 10 to 20 MW and of the ion cyclotron heating power from 2 to 10 MW.

Various studies of a HElical Advanced Stellarator (HELIAS) reactor have been conducted already (see e.g. [4,5]). The HELIAS reactor is basically an extrapolation from the W7-X design, which in itself is based on results from the W7-AS stellarator, the first advanced stellarator experiment. Essentially, three requirements form the basis of the HELIAS reactor concept: (1) Sufficiently good confinement has to be guaranteed to reach ignition. Probably owing to the different weighting of neoclassical and anomalous transport in the different stellarator devices, a unified scaling law does not exist. Recent studies have shown that the cross-device scaling improves with the introduction of a configuration factor, which appears to correlate with the degree of neoclassical optimization [6]. Therefore, conservatively an confinement improvement, such as observed in the H-mode, has not been assumed. (2) To provide a super-conductor with sufficient ductility for the fabrication of the non-planar modular coils, NbTi has been chosen. At the temperature of super-fluid helium of 1.8 K maximum magnetic fields of 10 T are possible, corresponding to 5 T on axis. (3) For the blanket a space

author's e-mail: robert.wolf@ipp.mpg.de

with 1.3 m thickness has been reserved between plasma and coils. Although no detailed design for the blanket has been made up to now, this is thought to be sufficient. With $<\beta> = 4 – 5\%$, the resulting HELIAS reactor concepts have 3 GW of fusion power. Three types with different aspect ratios, but similar plasma volumes, have been investigated [7]: The HR22/5 with a five-fold symmetry, a major radius of R = 22 m, an aspect ratio of A = 12 and 50 modular coils, the HR18/4 with R = 18 m, A = 9 and 40 modular coils, and the HR3/15 with R = 15 m, A = 6 and 30 modular coils. Less coils for a given plasma volume means lower cost. However, the limit for reducing the aspect ratio is given by the α-particle losses, which for the HR3/15 already become critically high. Therefore, the HR18/4 is regarded as the best compromise between a reasonably small number of coils and sufficient α-confinement. Because of the low volume to surface ratio, the advantage of a large aspect ratio is a low neutron flux to the wall which for the HR4/18 is calculated to be on average 1 MW/m^2 reaching peak values of 1.6 MW/m^2.

Recently the European fusion facilities have undergone an extensive review to assess their relevance for the future fusion programme. Seven R&D missions have been defined which provide an efficient and focused implementation of the fusion programme [8]. Their titles are burning plasma, reliable operation, operation compatible with first wall, technology and physics for steady state operation, predicting fusion performance, operation in nuclear environment and DEMO integrated design. The following discussion of the W7-X programme will be made with respect to these R&D missions. The last two missions, however, do not apply, as W7-X is neither a nuclear device (no deuterium-tritium operation) nor will DEMO components such as a breeder blanket be tested in W7-X.

2. Burning Plasma

The confinement of the fast helium ions or α-particles from the D-T fusion reactor is a prerequisite for a future fusion reactors. While in tokamaks it has been demonstrated that at least for low fast ion pressure α-particles are confined [9] and heat the plasma [10], in stellarators this is not so easily achieved. Without optimization of the stellarator magnetic field configuration, in the long mean-free path regime fast ions tend to drift radially and thus leave the confinement region. The quasi-isodynamic symmetry of W7-X solves this problem by increasing the magnetic field in transition areas between the five field periods, basically establishing a system of linked mirrors [11]. The trapped particles oscillate between these regions of high magnetic field, making a net poloidal rotation but no radial movement as they are kept away from zones of high field inhomogeneity. Fig. 1 shows the orbits of 50 keV protons calculated for W7-AS and W7-X. It can be seen that for the partially drift-optimized W7-AS the fast ions are not confined for all pitch angles.

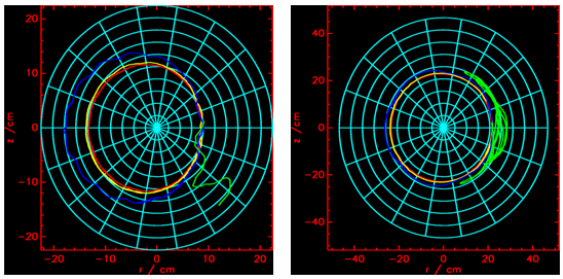

Fig. 1 Orbits of 50 keV protons in the poloidal projection for W7-AS (left) and W7-X (right). The colors denote the pitch angle: 0°, 50°, 70°, 80°

A particular characteristic of the W7-X configuration is that the collisionless fast particle confinement requires a finite β of about 2–3% [12]. As a consequence, full demonstration of fast ion confinement will be possible only during the 2nd phase of operation, as power and pulse duration are limited during the 1st phase. To reach a fully equilibrated magnetic field configuration the pulse duration has to be of the order of $\tau = L/R \approx 20$ s.

Extrapolated to the HELIAS reactor (HR4/18) a α-loss fraction of 2.5% is predicted. With respect to the power balance this is in any case not critical, but in a fusion reactor the α-losses have to be kept this low, as undue localized fast ion fluxes leaving the plasma damage first wall components.

3. Reliable Operation

To achieve a high fusion power density, a fusion reactor requires high β and high plasma density. This, however means, that reliable operation near operational boundaries will be needed. Here, stellarators have a clear advantage as, without current driven instabilities and disruptions, the plasma behaviour at the β-limit is fairly benign. In addition, much higher densities can be achieved in stellarators as the Greenwald limit, known from tokamaks, has not been observed [2].

While W7-AS still showed pressure driven modes, the W7-X design should include sufficient magnetic well to provide stability up to $<\beta> = 5\%$, at least for the standard and high mirror configurations. However, also in W7-AS examples exist where the increase of $<\beta>$ eventually led to a stabilization of these modes. This is explained by the formation of a magnetic well as the configuration changes with rising $<\beta>$. Owing to a small Shafranov shift also to equilibrium limit of W7-X should not curtail the value of $<\beta> = 5\%$.

Already during the 1st operational phase high density

will be addressed. To this effect W7-X is equipped with an ECRH system prepared for 2nd harmonic O-mode which works above electron densities of $n_e = 1\times10^{20}$ m^{-3}. Based on neoclassical transport in the plasma core (and an anomalous edge) at a density of 1.8×10^{20}m^{-3} and 10 MW of ECRH, electron and ion temperatures of $T_e = 6.2$ keV and $T_i = 4.2$ keV, corresponding to $\langle\beta\rangle = 4.1\%$, are predicted. Depending on the actual confinement, high β might be possible only at lower magnetic field (meaning below 2.5 T, which is the nominal field for 140 GHz ECRH). During the 2nd phase of operation β- and equilibrium limit studies will become possible at power levels of 20 MW and above.

With $\langle\beta\rangle = 4$–5% and $n_e = 2$-3×10^{20} m^{-3} the HELIAS does not exceed the values envisaged for W7-X. Confinement time (1.6 – 2.3 s) and ion temperature ($T_i = 11 - 15$ keV) are of course higher.

4. Operation Compatible with First Wall

On the one hand, an undue contamination of plasma with impurities from the first wall has to be avoided and, on the other hand, wall erosion and tritium retention have to be limited. Therefore, carbon is ruled out as a first wall material and tungsten is considered as a candidate material for a fusion reactor [13].

Nevertheless, W7-X will start operation with carbon covering the high heat flux target elements (≥ 1 MW/m^2). For stellarators in particular, because of effectively missing temperature screening effect, impurity accumulation is a critical issue. For the power and particle exhaust W7-X is equipped with an island divertor which utilizes the large magnetic islands forming at the plasma boundary at $\iota = 1$. This concept was for the first time successfully tested in W7-AS. In W7-AS the introduction of the island divertor also led to the discovery of the high density H-mode (HDH-mode), which not only showed improved energy confinement, but at the same time much reduced impurity confinement [14]. This very favourable behaviour is illustrated in Fig. 2. The explanation for the low impurity confinement are strong density gradients at the plasma edge, which hinders the penetration of impurities, and an additional outward impurity transport. The latter, however, is not understood. Because of these properties the HDH-mode is the candidate scenario for high density steady state plasma operation in W7-X. However it is unclear how the HDH scales to W7-X.

During the 1st phase of W7-X operation first the divertor topology will have to be investigated. Here, the inertially cooled test divertor has the advantage that, because of its intrinsically robust design, overheating or damaging the cooling structure does not have to be considered. Subsequently, first attempts to re-establish the HDH-mode will be made. The 2nd phase of operation will then address full steady state power and particle exhaust. Eventually also high-Z wall materials, such as tungsten, will have to be considered. Here, a gradual increase of the wall coverage as successfully demonstrated in ASDEX Upgrade [15] could be a feasible approach.

5. Technology and Physics for Steady State

W7-X is the first optimized stellarator with an integrated design for steady state operation. This includes super-conducting coils made of NbTi for a magnet field of up to 3 T on axis, an actively cooled first wall for heat fluxes of up to 10 MW/m^2 [16], and device control, data acquisition, diagnostics and an ECRH system [3] developed for continuous plasma operation. Many aspects of these technologies are similar to the ITER requirements.

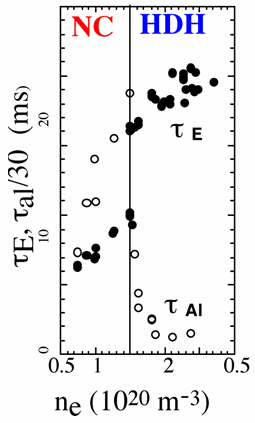

Fig. 2 Energy and impurity confinement time as a function of plasma density. The transition from normal confinement, NC, to the HDH-mode becomes evident in a rise of τ_E and a simultaneous drop of τ_{al} (which is the measured decay time of aluminum injected by laser blow-off).

During the 1st operational phase of W7-X stationary plasma operation is only possible at very low power levels of the order of 100 kW to test basic system properties. Going to 1 MW, 50 s pulse will already give some insight into plasma behaviour for times longer than the *L/R* time. In addition to what is described in the previous chapters, short pulses (8 MW for ~10 s) will be used to verify the improved neoclassical transport. In the 2nd phase the objective is to develop a fully steady state high power plasma scenario demonstrating the reactor capability of the stellarator.

The plasma control requirements of W7-X are generally very low. This also applies to the necessity to control the magnetic field. One of the optimization criteria of the W7-X design is the minimization of the bootstrap current. While the smallest bootstrap current is expected in the high mirror configuration, calculations show that depending on confinement and density bootstrap currents

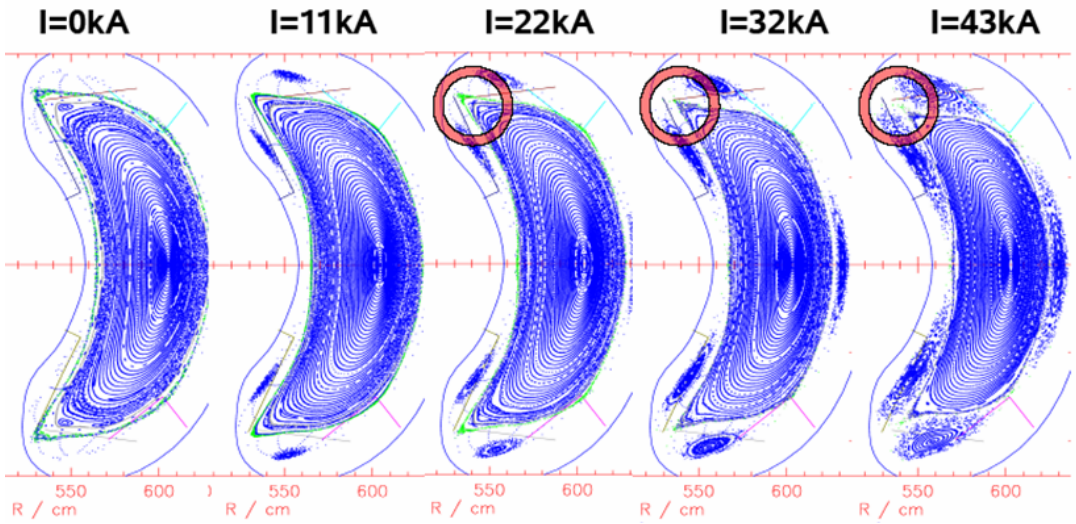

Fig. 3 Sequence of W7-X equilibria with different amounts of plasma currents simulating the current diffusion while a bootstrap current of 43 kA is building up. The red circles show the critical regions near the edges of the divertor tiles.

of up to 50 kA might develop at 5 MW heating power. This level is thought to be adequate to go from 2nd harmonic X-mode to 2nd harmonic O-mode, as in O-mode the microwave absorption strongly increases with electron temperature and a thermal collapse has to be avoided [17]. As a consequence of the bootstrap current the plasma equilibrium will show an initial temporal evolution. To illustrate this effect, a sequence of equilibria with different amounts of toroidal currents have been calculated using the VMEC code and a field extender for the magnetic island regions outside the last closed flux surface (Fig. 3). The current diffusion is simulated by assuming that the bootstrap current, I_{BS}, is initially balanced by an ohmic current, $\int \sigma E \, dA$ (E: toroidal electric field, $\int dA$: integral over poloidal cross-section), where the electrical conductivity, σ, is essentially given by the temperature distribution. The ohmic current is then successively reduced, until finally the total current, $I = I_{BS} + \int \sigma E \, dA$ matches the bootstrap current. Fig. 3 shows an example where the final equilibrium with the fully developed plasma current is consistent with the island divertor operation. However, on the way to this configuration, the edges of the divertor tiles and the pumping gap will be loaded with plasma. To avoid high thermal loads at these regions, either current drive has to be applied simultaneous with ECRH or the rotational transform has to be adjusted. In W7-X the latter should be in principle possible by using the planar coils, but is technically limited due to a limited number of allowed load cycles of the magnets. An additional option is the introduction of protection limiters.

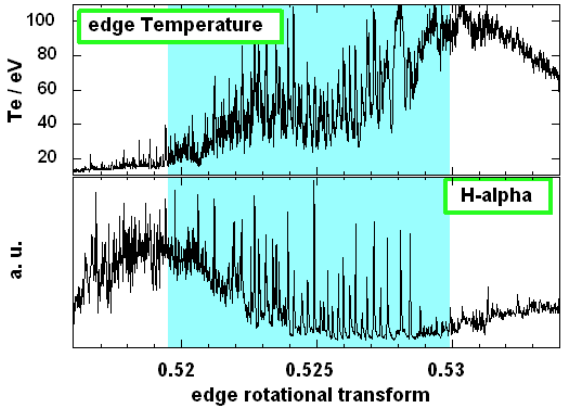

Fig. 4 Variation of the edge electron temperature and the ELM characteristic (from Hα signal) with edge rotational transform in W7-AS [2].

6. Predicting fusion performance

The prime objective of W7-X is to demonstrate the basics reactor capability of the stellarator. W7-X will have to verify the theory based optimization criteria and thereby also improve the theoretical understanding of stellarator physics. In a more general context, there are however also a range of physics issues related to 3D effects concerning both stellarators and tokamaks. E.g., in stellarators the generation of ambipolar electric are caused by the open magnet field lines in the plasma boundary. Recently, the effect of such electric fields on momentum transport has been observed in tokamaks with an ergodic divertor [18]. The control of edge localized modes (ELMs) using dedicated perturbation coils to ergodize the plasma edge is now one of the methods to mitigate ELMs in ITER. In this context W7-X could provide information on ELM control without strong

plasma currents and, thus, without the contribution of current driven instabilities. As an example Fig. 4 shows the effect of the change of the rotational transform on the ELM signature in W7-AS [2].

The size of the step from W7-X to a larger stellarator device towards a stellarator reactor will depend on the ability to extrapolate the results. This includes the transferability of the ITER results to stellarators, and here in particular the α-particle heating, and will strongly depend on the progress made with first principle theories and their applicability to 3D magnetic field configurations. In this context Wendelstein 7-X fits well into the ITER schedule and the development plan for high performance computing.

7. Summary and Conclusions

Wendelstein 7-X is an optimized stellarator designed for steady state operation. Its main objective is the demonstration of the basic reactor capability of the stellarator.

W7-X addresses the main physics issues for the development of a stellarator reactor: (1) Fast particle confinement and fast particle driven instabilities in a 3D configuration. Owing to the high plasma densities a reduced drive is expected for the latter. (2) Neoclassical versus turbulent transport. Latest calculations suggest also for the turbulent transport a dependence on the degree of neoclassical optimization [19]. (3) Impurity confinement. Plasma scenarios, such as the HDH-mode have to be further developed to avoid impurity accumulation. Also here the possible role of a turbulent drive has to be investigated. (4) 3D divertor configuration. W7-X will utilize the natural magnetic islands at the plasma boundary and combine them with actively cooled divertor targets.

Correspondingly specific stellarator technology issues are: (1) Coil configuration, coil support structure and the choice of superconductor. In a stellarator with modular non-planar coils the forces on the support structure need particular attention. (2) Divertor. In a 3D magnetic field configuration a divertor is also technically more complicated, requiring very accurate alignment to avoid unbalanced heat load distributions. (3) Depending on the aspect ratio, the possibility to provide enough space can be very limited in stellarators. (4) In addition, both accessibility and maintainability need to be thoroughly investigated in future stellarator reactor studies.

The further optimization of stellarators has to include also simplified engineering solutions. To that effect a first-of-a-kind device such as W7-X is not optimized. Future stellarator reactor studies will have to combine in a more rigorous way physics and engineering optimization.

[1] G. Grieger et al., Phys. Fluids B4 (1992) 2081
[2] M. Hirsch et al., Plasma Phys. Control. Fusion 50 (2008) 053001
[3] M. Thumm et al., this conference
[4] H. Wobig, Plasma Phys. Control. Fusion **41** (1999) A159
[5] C. D. Beidler et al., Nucl. Fusion 41 (2001) 1759
[6] A. Dinklage et al., Fusion Sci. Techn. 51 (2007) 1
[7] Yu. Igitkhanov et al., Fusion Engineering and Design 81 (2006) 2695
[8] J. Pamela, private communication
[9] M. J. Mantsinen et al., Phys. Rev. Lett. 88 (2002) 105002
[10] Thomas et al., Phys. Rev. Lett. 80 (1998) 5548
[11] E. Strumberger, Nucl. Fusion 40 (2000) 1697
[12] W. Lotz et al., Plasma Phys. Control Fusion 34 (1992) 1037
[13] M. Kaufmann and R. Neu, Fusion Engineering and Design 82 (2007) 521
[14] K. McCormick et al., Phys. Rev. Lett. 89 (2002) 015001
[15] R. Neu, J. of Nucl. Materials 363–365 (2007) 52
[16] R. Stadler et al., this conference
[17] Yu. Turkin et al., 34th EPS Conference on Plasma Phys. Warsaw (2-6 July 2007) ECA Vol.31F, P-1.148
[18] K.-H. Finken et al., Phys. Rev. Lett. 94 (2005) 015003
[19] F. Jenko et al., this conference

Proceedings of ITC18, 2008

High-density, low temperature ignited operations in FFHR

O. Mitarai, A. Sagara[(a)], R.Sakamoto[(a)], N. Ohyabu[(a)], A. Komori[(a)], and O. Motojima[(a)]
Liberal Arts Education Center, Kumamoto Campus, Tokai University, 9-1-1 Toroku, Kumamoto 862-8652, Japan
(a) National Institute for Fusion Science, 322-6 Oroshi-cho, Toki, 509-5292, Japan
Keyword: helical reactor, thermally unstable, high density, low temperature, ignition

Abstract New control method of the unstable operating point in the helical reactor FFHR makes the ignition study on the high density and low temperature operation possible. Proportional-integral-derivative (PID) control of the fueling with the error of the fusion power of $e(P_f)= -(P_{fo}-P_f)$ can stabilize the unstable operating point. Here $P_{fo}(t)$ is the fusion power set value and $P_f(t)$ is the measured fusion power. Although the large parameter variation would lose its control due to the inherently unstable nature, it is possible to control the ignited operation by pellet injection with the pellet size between 12 mm and 16 mm. Unstable ignited operation is robust against disturbances such as impurity increments by fueling feedback alone. However, if the heating power feedback control is added, robustness to the disturbances is improved, and an operational regime with respect to the integration time and derivative time is expanded.

1. Introduction

Achievement of the superdense-core (SDC) plasmas in LHD experiments [1][2] stimulates the study on the stabilization method of the thermal instability in a fusion reactor. Recently, new, simple and comprehensive control method of the unstable operating point is proposed for the high-density and low temperature ignited operation for the FFHR helical reactor [3,4]. PID feedback control of the fueling based on the error of the fusion power with an opposite sign of $e'_{DT}(P_f)= -(P_{fo}-P_f)$ can stabilize the unstable operating point and the desired fusion power is obtained at the same time. Here P_f is the measured fusion power and P_{fo} is its set value. Using this control algorithm, the operating point with the box type density profile can reach the high-density and low temperature steady state condition ($n(0)\sim 1\times10^{21}$ m^{-3}, $T(0)\sim 6.4$ keV, and $\langle\beta\rangle\sim 2.5$ %) from the initial very low temperature and density regime [5]. Although this control was demonstrated using the zero-dimensional analysis, it can be also applied to one-dimensional simulation code and implemented in a reactor because linearization is not necessary in equations different from previous studies [6-11].

Although the high-density and low temperature ignited operation is inherently unstable, it is demonstrated that the steady state can be maintained even when plasma parameters are disturbed by pellet injections [5]. So far feedback control was used for fueling, and not for the external heating power [4,5]. Although preprogramming of the heating power is enough for ignited operation in FFHR in many cases, it may expand the operational capability if it can be developed.

author's e-mail: omitarai@ktmail.tokai-u.jp

In this study we demonstrate that feedback control of the external heating power is possible and expands the operational regime for ignited operation. Especially, it improves control robustness to disturbances such as the change in the impurity fraction than that without the feedback control of the heating power.

2. Zero-dimensional equations and density profiles of SDC plasma

In this analysis, the global power balance equation is used,

$$\frac{dW}{dt} = P_{EXT} - \left(P_L + P_B + P_S - P_\alpha\right) \qquad (1)$$

where P_{EXT} is the external heating power, P_L is the total plasma conduction loss, P_B is the total bremsstrahlung loss, P_S is the total synchrotron radiation loss, which is negligible in the low temperature operation, and P_α is the total alpha heating power. The ISS95 confinement scaling is used for the plasma conduction loss where γ_{ISS} represent the confinement enhancement factors over the ISS95 scaling. POPCON is the contour map of the heating power of $P_{HT} = \left(P_L + P_B + P_S - P_\alpha\right)$ plotted on the n-T plane. Sudo density limit scaling on the line density of the core plasma with the density limit factor of $\gamma_{SUDO}=5.5$ is used as a measure of density. In the power balance equation the equal ion and electron temperature was assumed due to very high density [3-5].

The combined particle balance equation using the charge neutrality condition is

$$\frac{dn_e(0)}{dt} = \frac{1}{1-8f_O}\left[(1+\alpha_n)S_{DT}(t) - \left\{\frac{f_D+f_T}{\tau_p^*} + \frac{2f_\alpha}{\tau_\alpha^*}\right\}n_e(0)\right] \quad (2)$$

where f_o is the impurity fraction, α_n is the density profile factor, S_{DT} is the D-T fueling rate, f_D is the deuterium fraction, f_T is the tritium fraction, f_α is the helium ash fraction, τ_p^* is the D-T fuel particle confinement time, and τ_α^* is the helium ash confinement time. The helium ash confinement time ratio of τ_α^*/τ_E=3, and the fuel particle confinement time ratio of τ_p^*/τ_E=3 have been used in the helium ash particle balance equation unless otherwise noted. We assumed the box type density profile n(x) for SDC plasma using hyperbolic tangent, and used the broad temperature profile T(x) with α_T=0.25 [5] as shown in Fig. 1.

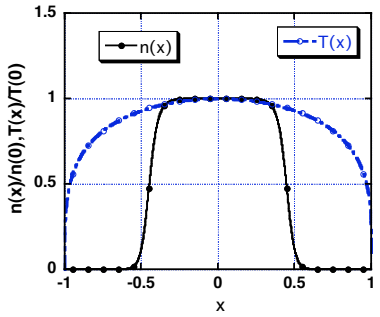

Fig. 1. Assume box type SDC density and temperature profiles.

3.Unstable ignition control algorithm

3.1. Feedback control of fueling

Stable ignition in FFHR reactor is controlled by the continuous D-T fueling rate:

$$S_{DT}(t) = S_{DT0}G_{fo}(t)\left\{e_{DT}(P_f) + \frac{1}{T_{int}}\int_0^t e_{DT}(P_f)dt + T_d\frac{de_{DT}(P_f)}{dt}\right\} \quad (3)$$

where the PID control is used based on the fusion power error of $e_{DT}(P_f) = +(1-P_f(t)/P_{fo}(t))$, where $P_{fo}(t)$ is the fusion power set value and $P_f(t)$ is the measured fusion power [13]. However, the opposite sign of $e_{DT}(P_f)= -(1-P_f(t)/P_{fo}(t))$ can stabilize the thermal instability [3-5].

This behavior is understood as shown in POPCON in Fig. 2 for the continuous fueling. When P_f is larger than P_{fo}, the operating point (A) moves toward the higher density and lower temperature side. This operating point slightly shifts to the higher temperature side due to ignition nature between (A) and (B). When it enters in the sub-ignition regime (B), it goes to the lower temperature side due to sub-ignition nature and crosses the constant P_{fo} line (C). The fueling is now decreased and the operating point proceeds to the lower density and higher temperature side, and goes into the ignition regime (D), and crosses the constant P_{fo} line. Thus, oscillations take place and are damped away.

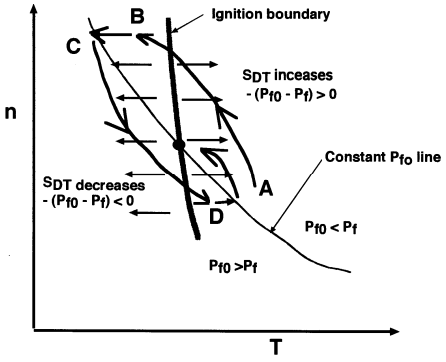

FIG. 2. Schematic movement of the operating point around the unstable ignition point on POPCON for continuous fueling[3-5].

On the other hand, fueling is digitized for pellet injection. The PID signal Error(P_f), based on the fusion power error of $e_{DT}(P_f) = -(1-P_f/P_{fo})$,

$$Error(P_f) = \left\{e_{DT}(P_f) + \frac{1}{T_{int}}\int_0^t e_{DT}(P_f)dt + T_d\frac{de_{DT}(P_f)}{dt}\right\} \quad (4)$$

determines the timing when the pellet is injected or not. Injected fueling quantity is discriminated by

$$\begin{cases} S_{DT}(t) = S_{DTpellet} & for\ Error(P_f) > 0 \\ S_{DT}(t) = 0 & for\ Error(P_f) \le 0 \end{cases} \quad (5)$$

where $S_{DTpellet}$ is the fueling particle number per the plasma volume by one pellet as given below. In this case the operation path moves straightly, and crosses the unstable ignition boundary along the constant beta line.

3.2. Pellet size:

As the D-T solid molar volume is 19.88 mm^3/mol [12], D-T ice density is given by $\{6.02\times10^{23}\times2\}/19.88[mm^3/mol]=6.05\times10^{28}\ m^{-3}$. For

the pellet size of L_p=14 mm diameter and L_p=14 mm length, the total D-T particle number is $N_{pell}=\pi(L_p/2)^2L_p x 6.05x10^{28}=130x10^{21}$. Therefore, fueling particle number per plasma volume of V_o=827 m^3 is S_{DTpell}= $1.57x10^{20}$ m^{-3}/(1 pellet pulse) , which corresponds to fueling rate in the continuous fueling operation (see Fig 3-(d)). As three consecutive pellets are injected and no injection in the successive duration, the minimum repetition time of pellet injection is 0.12 s. Here, the calculation time step is Δt=0.02 s. Detailed pellet injection algorithm was described in the reference [13].

3.3. Feedback control of the heating power

In the stable ignition the external heating power is feedback controlled using the density limit scaling [14]. However, as it is difficult to use the density limit scaling in the unstable operation, the different control algorithm must be developed. In this study we used the fusion power error as used in the ITER ignition study [15]. When the fusion power is smaller than the set value, the heating power is applied by the following algorithm.

$$P_{EXT}(P_f)=P_{EXTO}\left\{e_{EXT}(P_f)+\frac{1}{T_{P\,\mathrm{int}}}\int_0^t e_{EXT}(P_f)dt\right\} \qquad (6)$$

where P_{EXT0}=500 MW, $e_{EXT}(P_f)=(1-P_f/P_{fimp})$, and P_{fimp} is the set value given by $P_{fimp}(t)=P_{fo}(t)(1.8/1.9)$. In the steady state P_{fimp}=1.8 GW is lower than 1.9 GW in order to prevent the heating power application during the fusion power oscillation. Here, PI feedback control has been used with T_{Pint}=15 s.

4. Ignition access to the unstable operating point

Figure 3 shows the temporal evolution of plasma parameters for the pellet size of L_p=14 mm in FFHR2m with R=14 m, $\overline{a}$ =1.73 m, B_o=6 T, P_f=1.9 GW and γ_{ISS}=1.6. For the fusion power rise-up time of $\Delta\tau_{rise}$=20 s and the maximum external heating power of P_{EXT}=90 MW, the time averaged density is initially built up to ~$0.6x10^{21}$ m^{-3} by the density feedback (NGW trace) until 12.8 s and then raised up to n(0)~$1x10^{21}$ m^{-3} and decreased to $8.9x10^{20}$ m^{-3} by the fusion power control switched on at 12.8 s. The external heating power is preprogrammed to decrease it to 0 at 24 s. We see that even by fueling at the discrete time the ignition access is possible. When the density is increased by three consecutive pellets, the temperature is dropped. Their variations are out of phase due to adiabatic process by the power balance equilibrium in a short time. We found that the density variation of Δn~ $5x10^{19}$ m^{-3} is allowed for ignited operation.

Especially for τ_α^*/τ_E=5, the time averaged peak temperature at the steady state is $T_i(0)$~7.14 keV, the volume averaged beta value is $<\beta>$~ 2.55 %, the helium ash fraction is 8.9 %, the effective charge is Z_{eff}~1.60, and the average neutron wall loading is Γ_n~1.5 MW/m^2. As the confinement time is increased to 4.1 s due to high-density operation, the plasma conduction loss P_L is decreased, reducing the divertor heat load to Γ_{div}~6.3 MW/m^2 for the 10cm width of the divertor plate at the right angle to the magnetic field line.

The ratio of the bremsstrahlung loss power P_B to the alpha heating power P_α is as large as P_B/P_α ~ 70 %. The variation of the diverter heat flux is $\Delta\Gamma_{div}/\Gamma_{div}$~0.5/6.3=8 %, and variation of the first wall heat flux is $\Delta P_{HF}/P_{HF}$~0.018/0.23=8 %.

In Fig. 4 is shown the operation path to the unstable ignition point on POPCON corresponding to Fig. 3-(a). The operation is stabilized by cooling with fueling and by heating with the fueling reduction, which is controlled by the error of the fusion power $e_{DT}(P_f)$ = -(1- P_f/P_{fo}). We see that the operating point never go beyond 7.2 keV, which may avoid the neo-classical transport.

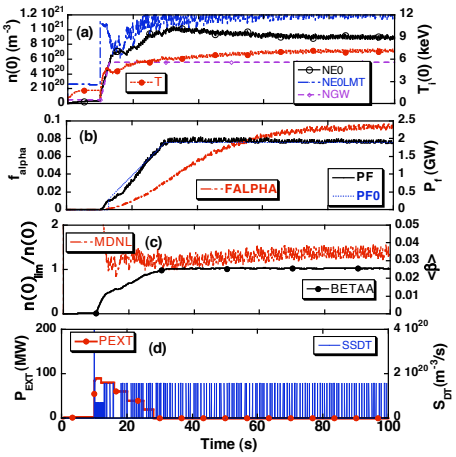

Fig.3. Temporal evolution of the plasma parameters for τ_α^*/τ_E=5 and *the pellet size of 14 mm. (a) Peak temperature, peak density, density limit, (b) alpha ash fraction, fusion power and its set value, (c) density limit margin, beta value, and (d) D-T pellet fueling rate, and the heating power. (T_{int}=8 s and T_d=0.26 s). The density variation is Δn~$5x10^{19}m^{-3}$.*

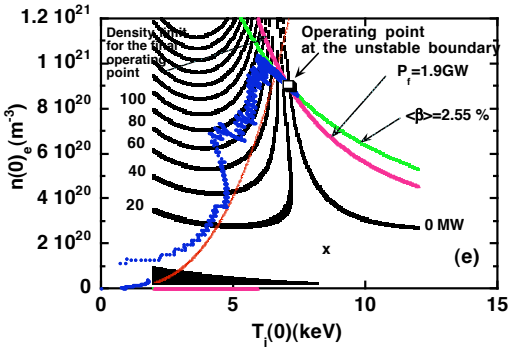

Fig. 4. The operation path to the unstable ignition point on POPCON corresponding to Fig.3-(a).

For the larger pellet size of 16 mm, ignition can be accessed although the density variation becomes as large as $\Delta n \sim 8 \times 10^{19}$ m^{-3}. For the larger pellet size of 17 mm, ignition is terminated at t=50 s due to large density variation. At the termination phase, the density and the temperature are both decreased at the same time, and their variations are in phase.

5. Operation parameters with pellet injection

So far, the integration time of T_{int}=8 s and the derivative time of T_d=0.26 s have been used for fueling control. By adjusting these time constants, the fusion power waveform can be optimized.

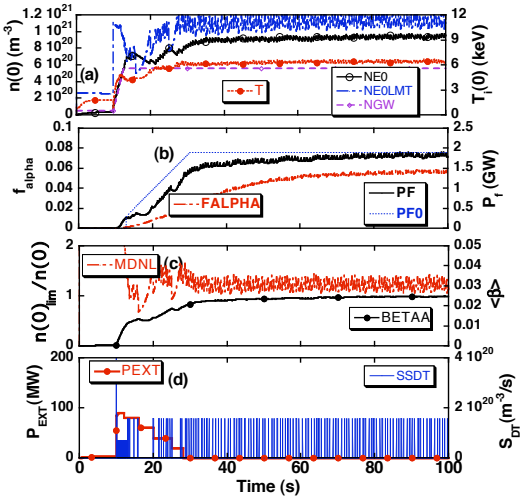

Fig. 5. Temporal evolution of the plasma parameters for T_{int}=45 s and T_d=0.39 s. The fusion power delays with respect to the set value for τ_α^*/τ_E=3.

For example, in the case of T_{int}=45 s and T_d=0.39 s as shown in Fig. 5, the fusion power rise-up is delayed due to decrease in the temperature by frequent pellet injection just after 12.8 s which is caused by the large derivative term. Advancing the phase by the large derivative time rather delays the fusion power rise-up. This time delay can be improved by the feedback control of the heating power. However, as 100 MW heating power should be applied for a long time, it is not efficient at all.

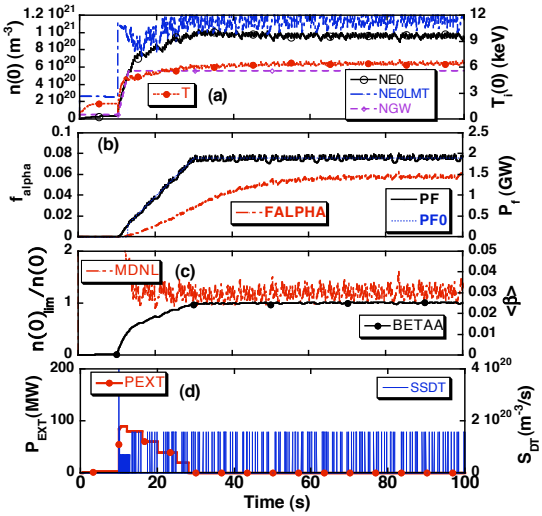

Fig. 6. Temporal evolution of the plasma parameters for T_{int}=45 s and T_d=0.001 s with the pellet size of 14 mm. The fusion power is not delayed with respect to the set value.

On the other hand, the fusion power rise-up is not delayed by the smaller derivative time of T_d=0.001 s as shown in Fig. 6. As the calculation time step is Δt=0.02s, corresponding to $T_d \sim 0$, the derivative term does not play any role. Therefore, just after 12.8 s, pellets are not injected due to negligible derivative term. Thus, the temperature does not decrease and the fusion power rises up linearly. Although the heating power helps the operation, fueling should be optimized at first by these control parameters.

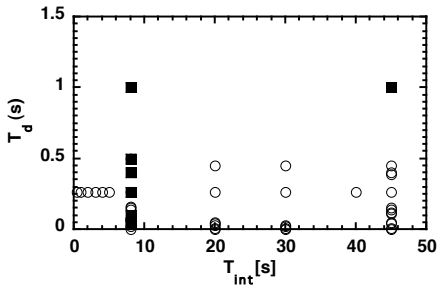

Fig. 7. Operation regime for the integration and derivative times for 14 mm pellet. Open circle shows without the heating power feedback and solid square with the heating power feedback.

The ignited operational regime with respect to the integration time T_{int} and derivative time T_d is shown in Fig. 7. In this study T_{int}=8 s and T_d=0.26 s are used unless otherwise noted. It s seen that the operation regime is expanded by the feedback control of the heating power.

6. Control robustness to the disturbances with/without heating power feedback control

Without heating power feedback control, ignition can be maintained by the feedback control of the pellet fueling alone when the impurity fraction is increased from f_o=0.0075 to 0.013 as shown in Fig. 8. When impurity fraction is larger than 0.013, ignition is terminated.

However, when the heating power feedback control is switched on at 15 s, the heating power is automatically applied and reduced to zero after some oscillation as shown in Fig. 9. When the impurity fraction is increased up to f_o=0.021 after 40 s, the heating power is automatically applied to prevent the fusion power drop during impurity increment as shown in Fig. 9, and then ignition is recovered. Thus, feedback application of the heating power is found to be effective to keep ignition when disturbances exist.

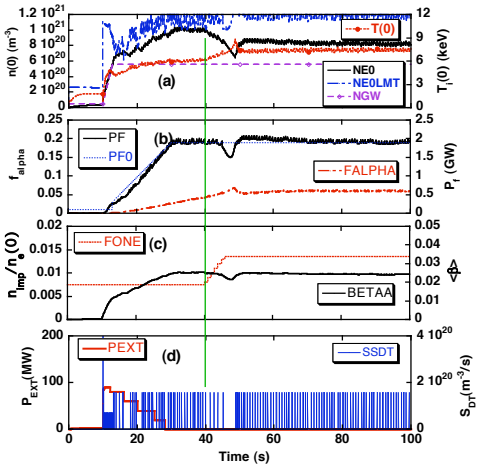

Fig. 8. Temporal evolution of the plasma parameters after impurity increment from f_o=0.0075 to 0.013.

7. Shutdown in the unstable operation

The fusion power shutdown is also important for ending discharge and machine operation. It was studied whether shutdown can be done without problems with the feedback control of pellet injection

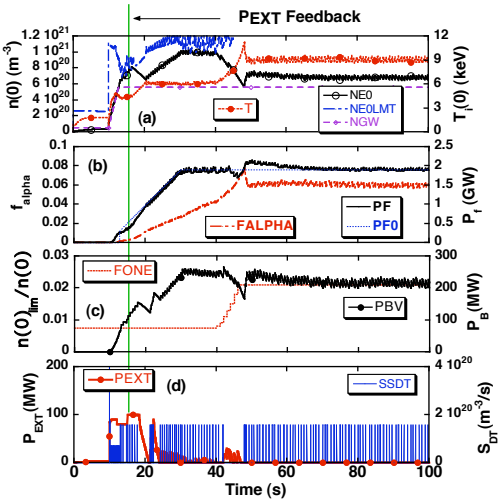

Fig. 9. Temporal evolution of the plasma parameters after impurity increment from f_o=0.0075 to 0.021. Ignition is maintained by fueling and heating power feedback control.

alone. In Fig. 10 is shown the shutdown phase using the preprogram of the heating power. In the late shutdown phase after 70 s, the external heating power of 20 MW is applied for smoother shutdown. The divertor heat load does not increase at all during the shutdown phase. For smooth fusion power shutdown the heating power should be applied because the operating point should pass the contour map of the heating power on POPCON to come back to the initial low temperature and density regime. Therefore, when the heating power is not applied during the fusion power shutdown phase, the fusion power abruptly decreases.

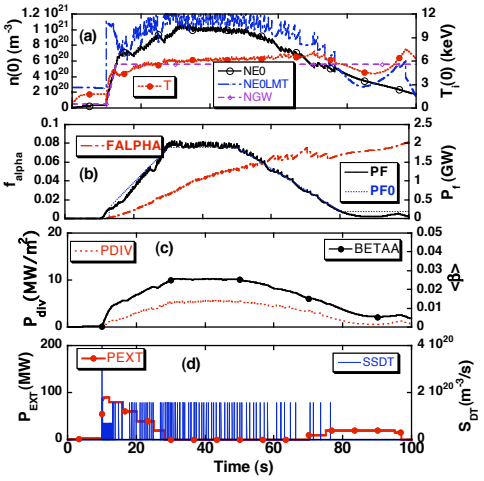

Fig. 10. Temporal evolution of the plasma parameters during the shutdown phase without the heating power feedback control.

When the fueling is stopped at 65 s during the shutdown phase, the operation loses its control, and the fusion power is excessive and the divertor heat load would increase to 39 MW/m^2 for the 10 cm divertor plate with the right angle to the magnetic field line as shown in Fig. 11. Therefore in the shutdown phase, fueling should not be stopped when operated in the unstable ignition regime. A large quantity of fueling provides rather safer operation in the whole discharge.

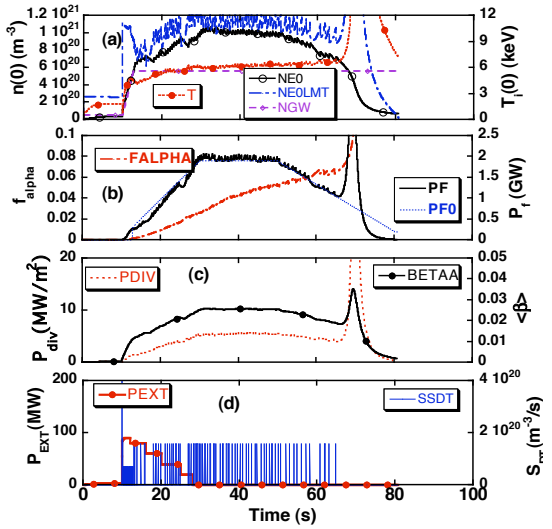

Fig. 11. Temporal evolution of the plasma parameters during the shutdown phase without the heating power feedback control. At 65 s fueling is stopped externally.

When feedback control of the external heating power is applied at 15 s during the fusion power rise up phase, the heating power is automatically switched off and then automatically applied during the shutdown phase. But as calculation was terminated before 80 s, after 75 s in the late shutdown phase the heating power of 20 MW was applied for smoother shutdown.

8. Discussion and summary

In this study we have used a larger confinement factor of 1.6, and the helium ash confinement time ratio of 3 and 4. Detailed studies were conducted for other parameters [5]. To lower the operating temperature for good pellet penetration, the helium ash confinement time ratio should be as small as possible.

In this study we demonstrated that thermally unstable ignited operation is stabilized when the pellets are injected repetitively. The operational regime is expanded when the feedback control of the heating power based on the fusion power is applied as well as fueling.

Unstable ignition control used in this study is robust to disturbances such impurity injection during the discharge with the feedback control of the heating power. However, as we studied the transient response to the set value and disturbances only in an ignited operation, further studies are required for the unified control algorithm applicable to ignition and sub-ignition.

This work is performed with the support and under the auspices of the NIFS Collaborative Research Program NIFS04KFDF001, NIFS05ULAA116 and NIFS07KFDH002.

References

[1] N. Ohyabu, T. Morisaki, S. Masuzaki, et al., Phy. Rev. Lett., **97**, (2006) 055002-1.
[2] R. Sakamoto et al., in 21th IAEA conference (Geneva, Switzerland, Oct 13, 2008) EX/8-1Ra.
[3] O. Mitarai, A. Sagara, N. Ohyabu, R. Sakamoto, A. Komori and O. Motojima, Plasma and Fusion Research, Rapid Communication, Vol.2 (2007) 021-1-3
[4] O. Mitarai, A. Sagara, N. Ohyabu, R. Sakamoto, A. Komori and O. Motojima, submitted in 2008
[5] O. Mitarai, A. Sagara, N. Ashikawa, R. Sakamoto, M. Yoshinuma, M. Goto, T. Morisaki, et al., in 21th IAEA conference (Geneva, Switzerland, Oct 13, 2008) FT/P3-19
[6] K. Maki, Fusion Technology, **10**, (1986) 70.
[7] J. Mandrekas and W. M. Stacy Jr., Fusion Technology, **19**, (1991) 57.
[8] E. Bebhan and U. Vieth, Nucl. Fusion, **37,** (1996) 251.
[9] W. Hui et al., Fusion Technology, **25**, (1994) 318.
[10] E. Schuster et al., Fusion Science and Technology, **43**, (2003) 18.
[11] J. E. Vitela and J. J. Martinell, Plasma Physics & Controlled Fusion, **40**, (1998) 295.
[12] P.C.Souers, "Hydrogen Properties for Fusion Energy", University of California Press (1986) p80.
[13] O. Mitarai, et al., Fusion Engineering and Design, **70**, (2004) 247.
[14] O. Mitarai, A. Sagara, et al., Nucl. Fusion, **47**, (2007) 1411.
[15] O. Mitarai and K. Muraoka, Nucl. Fusion, **39**, (1999) 725

Proceedings of ITC18,2008

The Design Windows and Economical Potential of Heliotron Reactors

Yasuji Kozaki, Shinsaku Imagawa and Akio Sagara

National Institute for Fusion Science

Abstract. The design windows analysis and economical evaluation on Heliotron reactors have been carried out based on the recent experiment results of LHD and the technology-cost basis of magnets developed for LHD and ITER. We found that the Heliotron reactors have the technically and economically attractive design windows, where the major radius is increased as large as for the sufficient blanket space, but the magnetic stored energy is decreased to reasonable level because of lower magnetic field with the physics basis of H factor near 1.1 to the ISS04 scaling and beta value of 5%.

Keywords: reactor design, heliotron, design windows, cost analysis, superconducting magnet

1. Inroduction

The Heliotron reactors are characterized by a pair of helical coils with large major radius but moderate aspect ratio, which give us different approaches for power plants from tokamak reactors.

For design studies on magnetic fusion reactors many integrating system design codes had been developed and guided design studies, such as Generomak (J. Shefield, 1986) and system design codes in ARIES design studies. Most of the previous studies showed the importance of the mass power density, and suggested the much higher beta value and the smaller reactor size is necessary to achieve economical fusion reactors. But as far as magnetic confinement fusion the direction for the compact reactor has become suffer from severe neutron wall loads, diverter heat loads, and tritium beading ratios. For practical fusion power plants, we should consider adequate size and mass power density.

To remove those misunderstandings on the necessity of compactness, we must investigate design windows with estimating the detail mass-cost relationships, especially on magnets and blankets. We have much experience on costs of fusion device through preparing ITER construction. Now we can discuss the costs of magnet and major facility with some reality with the ITER database.

2. The HeliCos code for system design

2.1 Major design parameters and relationships

The major relationships between plasma parameters and reactor parameters in the HeliCos code are identified as follows.

author's e-mail: kozaki.yasuji@nifs.ac.jp

1) Basic geometry of plasma and helical coils

The geometry of plasma and helical coils are similar to LHD, i.e. polarity l=2, field periods m=10, coil pitch parameter $\gamma=(m/l)/(R_c/a_c)=1.15\sim1.25$. We consider a_p, a_c (minor radius of plasma and coil) and a_{pin} (inner minimum plasma radius) are also similar to LHD inward shift plasma case. The plasma radius a_p is given by the LCFS (Last closed flux surface) of the LHD magnetic field calculations depending on γ. The larger plasma volume and the better plasma confinement conditions are discussed in the LHD inward shift cases. We should consider making the largest plasma volume given by optimizing the LCFS conditions, also with making the ergodic layer thin as possible.

We can describe the relationships between a_p and a_c, or R_p, as an equation of a linear regression and also an index regression only depending on γ, in the $\gamma=1.15\sim1.25$, based on LHD experiment.

$$a_p=a_c(-1.3577+1.603\times\gamma)$$

$$a_p=0.2904\times\gamma^{3.495}\ a_c=0.06292\times\gamma^{4.495}\ R_p$$

The plasma volume V_p is expressed by the R_p and γ.

$$V_p=2\pi^2a_p^2R_p=0.0841\times R_p^3\ \gamma^{8.87}$$

2) The space for blanket: Δd

The Δd is described with the configuration of plasma and helical coils as follows (Fig. 1),

$$\Delta d=a_c-(R_c-R_p)-a_{pin}-H/2-\Delta t \quad \text{----------(1)}$$

$$a_{pin}=(-1.2479+1.2524\ \gamma)\times(R_c/3.9)$$

$$H=(I_{HC}/(j\times W/H))^{0.5}$$

$$I_{HC}=R_P\ B_0/(2m)\times10$$

I_{HC}, j: helical coil current and current density,

H, W: height and width of helical coils,

Δt: thermal insulation space.

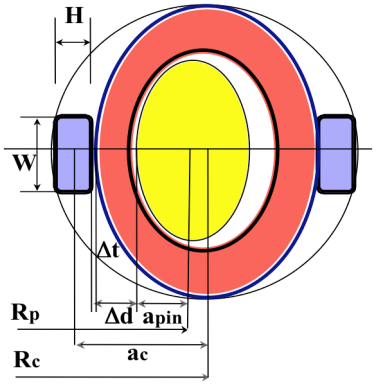

Fig.1 The profile of plasma, helical coil and blanket. The required blanket space constraints the minimum R_p.

The current density j depends on the B_{max}, which is given by the ratio of B_{max}/B_0,

B_{max}/B_0
$=(0.4819+0.41847(a_c/H)+0.0066851(a_c/H)^2) \times(R_p/R_c)$

The minimum blanket space Δd depends not only on the blanket-shield design but also the ergodic layer depth, of which optimization is one of the most important issues.

3) Fusion power given with B_0, β, and V_P

The fusion power is calculated by the volume integration of fusion power density p_f using the following reaction rate $\langle\sigma v\rangle_{DT}$ and the plasma profile assumptions in the HeliCos code.

$p_f = n_T n_D \langle\sigma v\rangle_{DT} V_p \times 17.58(MeV) \times 1.6021\times10^{-19}$ (J/eV) $\times10^{-3}$ [GW]

$\langle\sigma v\rangle_{DT}=0.97397\times10^{-22}\times\exp\{0.038245(\ln(Ti))^3$
$- 1.0074(\ln(Ti))^2 + 6.3997\ln(Ti) -9.75\}(m^3/s)$

We might use a simple parabolic profile, index a_n for plasma density, and a_T for temperature to consider peaking factors. As we can calculate P_f easily by a good approximation, $\langle\sigma v\rangle_{DT} \propto T_i^2$ for T_i~10keV to be well known, we use a following equation for sensitivity studies.

$P_f=0.06272/(1+2a_n+2a_T)\times n_e(0)^2T_i(0)^2V_p\times10^{-6} \propto \beta^2 B_0^4 V_P$
[GW], n_e:$10^{19}/m^3$, T_i : keV (2)

4) Power balance with the confinement scaling ISS04

The power balance is described using the required energy confinement time τ_{Er},

$P_\alpha f_\alpha - R_{loss}=W_p / \tau_{Er}$
($P_\alpha=0.2P_f$, f_α : α heating efficiency, R_{loss}:Radiation loss
W_p : plasma stored energy, $W_p \propto n_e(0)T_i(0)V_p$)

We use the energy confinement scaling ISS04, which can be expressed only with the R_p and γ as geometrical parameters [1].

τ_E(ISS04)
$=0.134 (f_\alpha P_\alpha - R_{loss})^{-0.61} n_{el}^{0.54} B_0^{0.84} R_P^{0.64} a_p^{2.28} \iota_{2/3}^{0.41}$
$=6.23\times10^{-5} R_p^{1.09} \gamma^{2.98} (p_f(1- r_{loss}))^{-0.61} B_0^{0.84} n_{el}^{0.54}$
[ms]
($p_f = P_f / V_p$, $r_{loss} = R_{loss} /(0.2 f_\alpha p_f V_P)$,
r_{loss}: radiation loss rate)

The H factors are calculated using the density limit and density profile conditions as follows.

H_f (ISS04)= $\tau_{Er} / \tau_{E(ISS04)}$
$H_f =76.4\times f_{np}\times R_p^{-1.09} \gamma^{-2.98} p_f^{-0.16} (1-r_{loss})^{-0.66} B_0^{-1.11}$ (3)
f_{np} : density profile effect coefficient
(f_{np}=1.0 in the $n_{el}=1.2n_c$ and a_n=0.5 case)
$n_c=149.0\times p_f^{1/2} B_0^{1/2}$ [$10^{19}/m^3$], n_c : Sudo density limit

2.2 Major equations and calculation flow

We can calculate the major design parameters, B_0, R_p , γ, P_f , based on the three equations (1),(2),(3). Therefore the design points of the LHD-similar heliotron reactor are given with the cross points of the following three equations on the B_0-R_p plane.

1) The Δd-equation : $\mathbf{B_0(R_p, \gamma, \Delta d, j)}$ from eq.(1)
$B_0=(16j/R_p)((0.2633- 0.1312\ \gamma)\ R_p - 20.41(\Delta d +0.1))^2$
[T] (4)
2) The P_f equation : $\mathbf{B_0(R_p, \gamma, \beta, P_f)}$ from eq. (2)
$B_0=92.64\ P_f^{1/4} \beta^{-1/2} \gamma^{-2.22} R_p^{-3/4}$ [T] (5)
3) The H_f -equation : $\mathbf{B_0(R_p, \gamma, H_f, P_f)}$ from eq. (3)

The relationships between major equations, calculation flows and the issues to be considered are shown in Fig. 2.

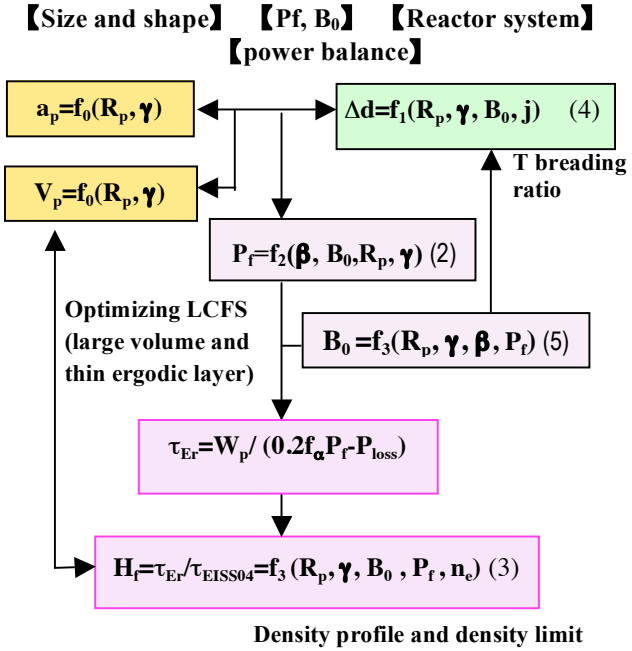

Fig.2 The major design parameters and calculation flows.

3 The design windows of Heliotron reactors

3.1 The constraints of design windows

In general the design spaces of magnetic fusion reactors are limited with following three constraints,

1) the Δd blanket space conditions necessary for tritium breading,
2) the B_0 and V_P conditions satisfying power balance with H factor limitation,
3) the upper magnetic stored energy (W) constraints for avoiding the difficulty of manufacturing.

Then the design space on the R_P-B_0 (or W) plane has the minimum R_P boundary given by the Δd constraints, the lower boundary of B_0 from H factor conditions, and the upper boundary of B_0 from the W constraints. With increasing γ the design points of helical reactors move to the larger R_P according to increasing plasma radius and much severe Δd constraints. For each γ Bo decreases with increasing Δ d, although W increases.

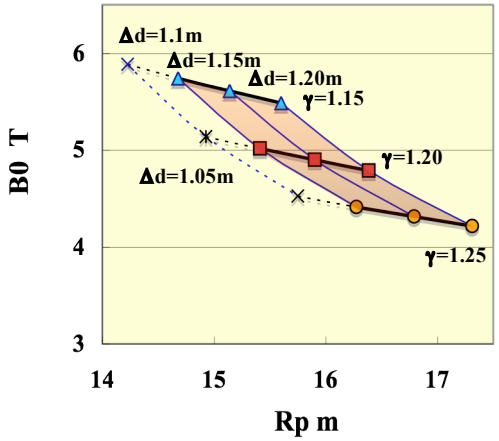

Fig. 3(a) Design windows on the R_p-B_0 plane.

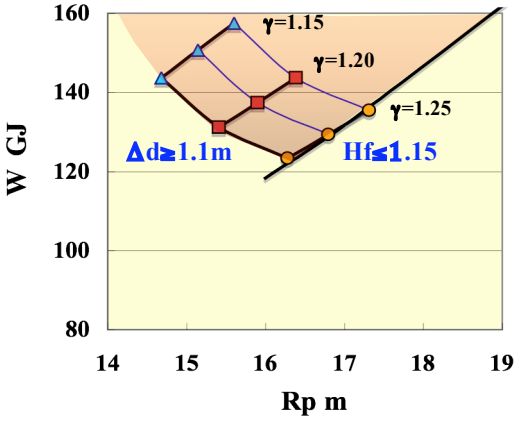

Fig. 3(b) Design windows on the R_p-W_0 plane.

Fig. 3(a), (b) Design windows are limited with the constraints of Δd≥1.1m, Hf≤1.15 and W<160G, depending on γ (β 5%, Pf 4GW case).

Though the minimum R_P increases with increasing γ, the B_0 decreases so much that the W also decreases with increasing the minimum R_P .

3.2 The design windows depending on γ and β

Searching for attractive fusion power plants a wide range of design options was investigated, β values from 3% to 5%, and fusion power P_f from 2GW to 4GW as shown in figure 4(1)~(3).

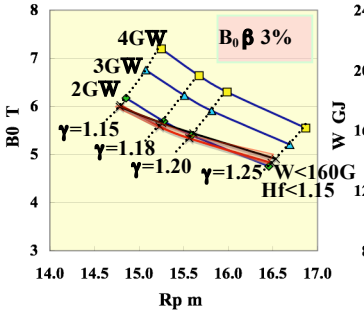

Fig. 4(1)(a) B_0 in β 3%

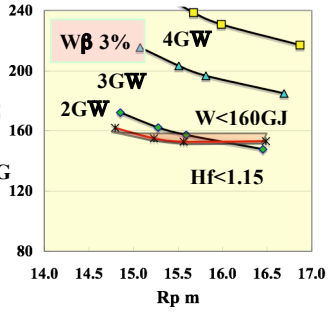

Fig. 4(1)(b) W in β 3%

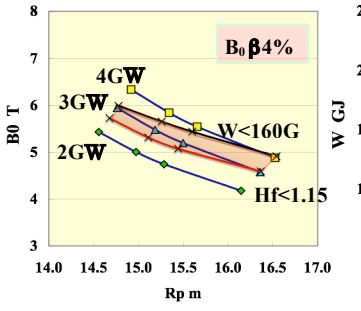

Fig. 4(2)(a) B_0 in β 4%

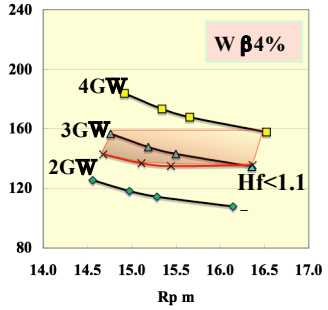

Fig. 4(2)(b) W in β 4%

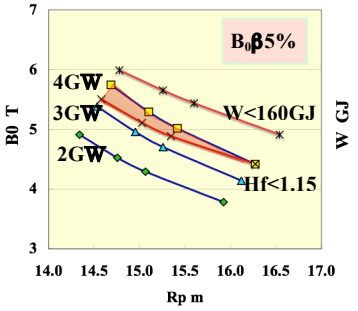

Fig. 4(3)(a) B_0 in β 5%

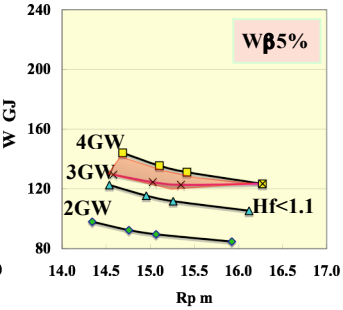

Fig. 4(3)(b) W in β 5%

Fig. 4(1)~(3) The design windows of Heliotron reactor strongly depend on γ and β, limited with the constraints of Δd=1.1m, H_f≤1.15, W<160GJ. The γ dependence are shown with the four points, γ=1.15, 1.18, 1.20, 1.25 on each line[4].

In the β 3% cases, even though in the smaller P_f plants, magnetic stored energy W is near upper boundary. In the β 4% cases, we can consider wide design space with B_0=5~6T, Pf=3~4GW, although W is rather large, ~150GJ.

In the β 5% cases, we can consider the optimum

design windows of P_f=3.3~4GW plants with R_P=14.6~16.3m, B_0=4.4~5.5T, and W=125~140GJ

We should notice that the H factor conditions in β 5% are severe in the smaller P_f case and the larger γ case. Therefore in the H_f=1.10 case we must consider the minimum P_f is 3.8GW for γ=1.15, and P_f is 4.5GW for γ=1.25. We should also notice that the design windows must shift the larger R_p and the larger W in the large Δd case, as shown in figure 3.

4. Cost model

4. 1 Cost estimating methods

The COE (Cost of Electricity) is calculated with the general cost estimating method and the unit cost data and scaling lows for BOP (balance of plant) [5,6]. The cost of magnets and blanket -shield are estimated based on mass cost analysis. The capital costs are calculated using rather low FCR (~0.0578:Fixed charge rate) used in the recent report of Japanese AEC for estimating nuclear power plants (40 years life time and 3% discount rate).

The operation cost of magnet should be taken special care for the inherent characteristics of long lifetime and easy maintenance. In regard to blanket the periodic replacement is necessary, and the availability factors are estimated in changing with neutron wall loads.

4. 2 Magnet cost estimation

We estimated the unit cost of magnets to be related to weights and magnetic stored energy, thorough analyzing the cost factors of magnet systems based on the LHD construction, ITER construction and the FFHR-2m1 design studies [2]. In the FFHR2m1 design we considered a CIC conductor for helical coils based on the engineering base for ITER and the winding technology of LHD helical coils.

The cost factors are estimated in breakdown components such as super conducting strands, conduits, support structures, and winding process in each coil systems. The costs of the conductors and the winding occupy about 70% of the total magnet costs (Fig. 5).

The total weight 16,000 ton and the total cost 210 BYen are estimated for the total magnet systems of the 3GW Heliotron power plant, in which the magnetic stored energy is 133GJ [3].

Comparing the helical reactor magnets to ITER magnets, the magnetic stored energy is about three times, the weight is 1.6 times and the cost is about 2 times of ITER (ITER 2002 report, and FDR1999 report).

For the superconducting magnets having similar configuration we could consider the costs are

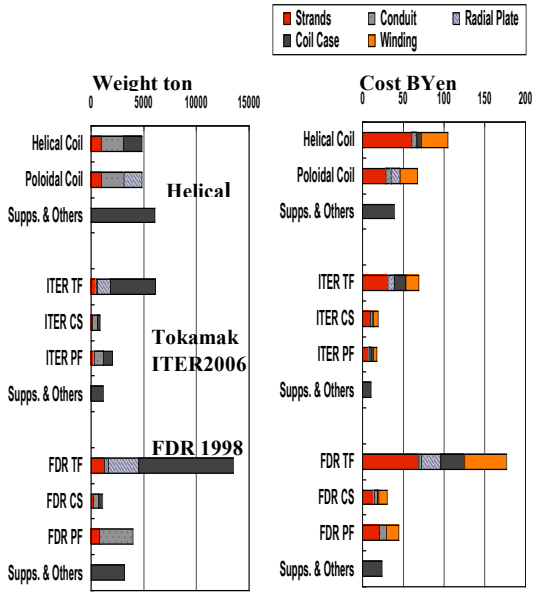

Fig. 5 The weight and cost of the magnets of the helical reactor (FFHR-2m1) and the tokamak reactor(ITER).

proportional to weights, which are approximately proportional to the stored energy. In HeliCos code we can use the above unit cost per ton that means the total unit cost is 1.59 BYen/GJ (14.4 M$/GJ).

5. Standard Heliotron power plants and economic analysis

5.1 Heliotron reactors of 3~ 4 GW fusion power

Table 1 shows the major design parameters and costs of typical Heliotron reactors. For 4GW fusion power plants β=5% is expected, but for 3GW plants the smaller β (~4.4%) is yet manageable. With selecting adequate γ we can consider the wide range of design parameters, R_p=14.6~16.3 m, B_0=4.2~5.7 T, and W=122~144 GJ.

We could understand the reason why the difference of design parameters for different γ is so large, by comparing plasma volume, i.e., 920 m^3 in γ=1.15 versus 2600 m^3 in γ=1.25. The sensitivity of increasing V_P versus decreasing B_0 is very interesting. The optimization of the LCFS (V_p) might be one of the most important issues.

The major parameters in Table 1 are dominated with the simple relationships shown in 2.2. But there are remaining many uncertainties regarding power flows and mass flows, especially in the local heat load to the diverter. Those problems on optimizing LCFS, controlling ergodic layer and diverter plasma must be critical issues to be considered in the next design studies.

Table1. The major design parameters and mass-cost estimation of standard Heliotron reactors

Design Parameters	Symbol (unit)	4GW standard plants			3GW
		β=5%, Hf=1.06-1.15			Hf=1.15
Coil pitch parameter	γ	1.15	**1.20**	1.25	1.20
Coil major Radius	R_c (m)	15.91	**16.70**	17.63	16.69
Coil minor radius	a_c (m)	3.66	**4.01**	4.41	4.00
Plasma major radius	R_p (m)	14.69	**15.42**	16.27	15.40
Plasma radius	a_p (m)	1.78	**2.27**	2.85	2.27
Inner plasma radius	a_{pin} (m)	0.78	**1.09**	1.44	1.09
Plasma volume	V_p (m^3)	916	**1565**	2604	1561
Magnetic field	B_0 (T)	5.74	**5.02**	4.42	5.00
Average beta	β	5.0	**5.0**	5.0	4.37
Fusion power	Pf (GW)	4.00	**4.00**	4.00	3.00
Energy confinement time (ISS95)	$\tau_{E(ISS95)}$ (msec)	0.84	**1.04**	1.25	1.14
Energy confinement time ISS04	$\tau_{E(ISS04)}$ (msec)	1.43	**1.78**	2.14	1.95
Required energy confinement time	τ_{Er} (msec)*	1.53	**1.95**	2.47	2.24
H factor to ISS04	Hf	1.064	**1.094**	1.151	1.150
Radiation loss **	Rloss (GW)	0.13	**0.12**	0.11	0.09
Electron density	$n_e(0)$ ($10^{19}/m^3$)	36.06	**25.77**	18.75	22.31
Line average density	n_{el} ($10^{19}/m^3$)	28.32	**20.24**	14.73	17.52
Density limit	n_c ($10^{19}/m^3$)	23.6	**16.87**	12.27	14.61
Ion Temperature	Ti(0)	14.68	**15.67**	16.69	15.69
Iota 2/3	ι(2/3)	0.904	**0.775**	0.641	0.775
Maximum field on coils	Bmax (T)	12.16	**11.91**	11.78	11.88
Coil current	I_{HC} (MA)	42.18	**38.67**	35.93	38.50
Coil current density	j (A/mm^2)	26.0	**26.0**	26.0	26.0
Helical Coil height	H (m)	0.90	**0.86**	0.83	0.86
Blanket space	Δd (m)	1.10	**1.10**	1.10	1.10
Neutron wall loads	f_n (MW/m^2)	2.9	**2.2**	1.7	1.7
Weight of Blanket and shield	Mbs (ton)	8580	**11360**	14920	11340
Magnetic stored energy	W (GJ)	144	**131**	123	130
Weight of magnets	Mmag (ton)	18000	**16400**	15400	16200
*Magnet cost (%)****	*Cmag*	*2079(34.6)*	***1893(31.0)***	*1780(28.0)*	*1875(33.7)*
*Blanket and shield cost (%)****	*Cbs (M$)*	*889(14.8)*	***1177(19.3)***	*1546(24.3)*	*1175(21.1)*
Total construction cost	*C (total)*	*7270*	***7393***	*7705*	*6735*
Net electric power	Pn (GW)	1604	**1601**	1598	1194
Total auxiliary power	Pa (GW)	109	**112**	115	91
Plant availability factor	f_A	0.680	**0.706**	0.726	0.727
Capital cost	*mill/kWh*	*44.0*	***43.2***	*43.8*	*51.2*
Operation cost	*mill/kWh*	*26.8*	***27.1***	*28.2*	*31.4*
Replacement cost	*mill/kWh*	*8.18*	***8.19***	*8.21*	*8.24*
Fuel cost	*mill/kWh*	*0.023*	***0.022***	*0.021*	*0.021*
COE(Cost of electricity)	*mill/kWh*	*79.0*	***78.5***	*80.3*	*90.9*

*Effective ion charge Zeff=1.32,

**Alpha heating efficiency 0.9, and profile index a_n=0.5,a_T=1.0.

*** The magnet costs, blanket and shield costs include the engineering indirect cost.

5. 2 Economic potentials of Heliotron reactors

We could consider the magnet cost and the blanket-shield cost are dominant cost factors in the magnetic confinement fusion reactor, as far as the normal steady operations are achieved with the reasonable recirculating power, and the sufficient plant availability factors without suffering from too high heat load or neutron load.

Using the magnetic stored energy and the unit cost mentioned in figure 5, we estimated the magnet costs shown in Ttable 1, which are 1800 M$ (γ=1.25, 15400 ton) to 2080 M$ (γ=1.15, 18000ton). Those magnet cost ratio to total plant cost are about 30%, which can make the Heliotron power plants of fusion power 3~4GW economically attractive.

In the LHD-similar-shape Heliotron reactors, when the major radius R_p and γ (i.e., a_p) increases, the magnetic field B_0 decreases much in the same β-P_f and Δd conditions as shown in figure 6(a). That is why the magnetic stored energy W decreases even if in the larger coil size. These characteristics between plasma volume (given with R_p, γ) and B_0, and magnet cost are shown in

figure 6(a). The costs of blanket and shield (Cbs) are estimated basing on FFHR-2m1 blanket design studies [2] and are increased in proportion with $R_p a_p$. The sensitivity analysis regarding current density, plasma profile and density limit are carried out.

When the R_p and γ increase, the magnet cost decreases but the blanket-shield cost increases. Therefore the COEs of Heliotron reactors, depending on R_p, γ, show the bottom as the result of the trade-off between the magnet cost and the blanket-shield cost, i.e., B_0 versus plasma volume

The COEs of Heliotron reactors shown in figure 6(b) suggest us that the technically and economically attractive design windows exist in the rather wide area of the large R_p (15~16m), medium γ (~1.20) and β values (~5%), and the reasonable magnetic stored energy (~130 GJ).

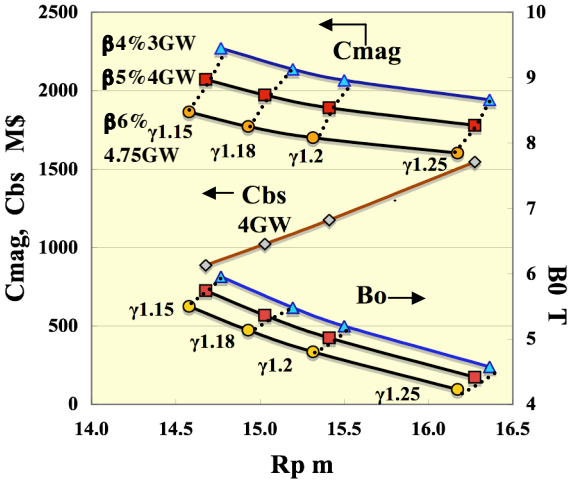

Fig. 6(a) The B_0, magnet cost (Cmag), and blanket Cost (Cbs) depend on R_p, γ and β. When R_p and γ increase, Cmag decreases but Cbs increases. Those plots on R_p (γ) are given with Δd=1.1m.

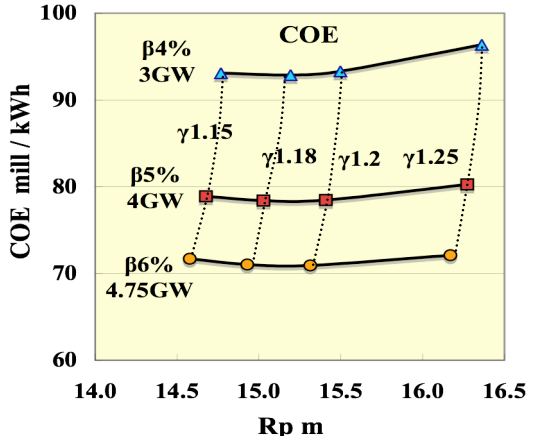

Fig. 6(b) The COEs of Heliotron reactors, which depend on plasma major radius R_p, coil pitch parameter γ and β, show the bottom near R_p=15~15.5m with blanket space condition Δd=1.1m.

6. Conclusions

We can summarize the results of analysis as follows,

1) LHD-type helical reactors have the attractive design windows in rather large plasma major radius of 15~16m, with the sufficient blanket space and the reasonable magnetic stored energy of 120~140 GJ based on the physics basis of H factor near 1.1 and β of 5%.
2) The β dependence is very important for selecting the optimum fusion power with reasonable magnetic energy, so that the confirming good confinement in the near β~5% plasma is the first priority of critical issues.
3) The γ dependence is essential in Heliotron reactors that is critically sensitive not only for optimizing LCFS (plasma volume) but for selecting the optimum blanket design.
4) There are many remaining subject to be studied, in especially, the problem of the particle and heat loads on the diverter are a critical issue to be considered in the next analysis.

References

[1] H. Yamada *et al.*, Nuclear Fusion 45, 1684 (2005).
[2] A. Sagara *et al.*, Nuclear Fusion 45, 258 (2005).
[3] S. Imagawa and A. Sagara, Plasma Science & Technology 7, 2626 (2005).
[4] Y. Kozaki *et al.*, 22nd IAEA Fusion Energy conf., FT/P3-18 (2008).
[5] Y. Kozaki *et al.*, Proc. Seventh Int. Conf. on Emerging Nuclear Energy Systems, 76 (1993)
[6] Y. Kozaki *et al.*, 19th IAEA-CN-94/FTP1/25 (2002)

Proceedings of ITC18,2008

Design Integration of the LHD-type Energy Reactor FFHR2 towards Demo

A. Sagara[1], S. Imagawa[1], Y. Kozaki[1], O. Mitarai[2], T. Tanaka[1], T. Watanabe[1], N. Yanagi[1], T. Goto[1], H. Tamura[1], K. Takahata[1], S. Masuzaki[1], M. Shoji[1], M. Kobayashi[1], K. Nishimura[1], H.Igami[1], T. Muroga[1], T. Nagasaka[1], M. Kondo[1], A. Nishimura[1], H. Chikaraishi[1], S. Yamada[1], T. Mito[1], N. Nakajima[1], S. Fukada[3], H. Hashizume[4], Y. Wu[5], Y. Igitkhanov[6], O. Motojima[1] and FFHR design group

[1]*National Institute for Fusion Science, Toki, Gifu 509-5292, Japan*

[2]*Tokai University, 9-1-1 Toroku, Kumamoto 862-8652, Japan*

[3]*Kyushu University, 6-10-1 Hakozaki, Fukuoka, Fukuoka 812-8581, Japan*

[4]*Tohoku University, Sendai 980-8579, Japana*

[5]*Institute of Plasma Physics, Chinese Academy of Sciences, Hefei, China.*

[6]*Max-Planck-Institut für Plasmaphysik, IPP-EURATOM Ass., Greifswald, Germany*

Three candidates to secure the blanket space are proposed in the direction of reactor size optimization without deteriorating a-heating efficiency and with taking cost analyses into account. For this direction the key engineering aspects are investigated; on 3D blanket designs, it is shown that the peaking factor of neutron wall loading is 1.2 to 1.3 and the blanket cover rate over 90% is possible by proposing Discrete Pumping with Semi-closed Shield (DPSS) concept. On large superconducting magnet system under the maximum nuclear heating of 200W/m^3, CICC and alternative conductor designs are proposed with a robust design of cryogenic support posts. On access to ignited plasmas, new methods are proposed, in which a long rise-up time over 300 s reduces the heating power to 30 MW and a new proportional-integration-derivative (PID) control of the fueling can handle the thermally unstable plasma at high density operations.

Keywords: helical reactor, blanket, COE, nuclear heating, superconducting magnet, ignition

1. Introduction

On the basis of physics and engineering results established in the LHD project, conceptual designs of the LHD-type helical reactor FFHR have made continuous progress from 1991 [1, 2]. Those design activities have led many R&D works with international collaborations in broad research areas [3, 4].

Due to inherent current-less plasma and intrinsic diverter configuration, helical reactors have attractive advantages, such as steady operation and no dangerous current disruption. In particular, in the LHD-type reactor design, the coil pitch parameter g of continuous helical winding can be adjusted beneficially to reduce the magnetic hoop force (Force Free Helical Reactor: FFHR) while expanding the blanket space, where $\gamma=(ma_c)/(lR_c)$ with a coil major radius R_c, a coil minor radius a_c, a pole number l, and a pitch number m.

2. Candidates to secure the blanket space

The design parameters of FFHR2 are listed in Table 1, which newly includes the recent results of cost evaluation based on the ITER (2003) design. In this base design, one of the main issues is the structural compatibility between blanket and divertor configurations. In particular, the blanket space at the inboard side is still insufficient due to the interference between the first walls and the ergodic layers surrounding the last closed flux surface.

From the point of view of a-heating efficiency over 0.95, the importance of the ergodic layers has been found by collision-less orbits simulation of 3.52MeV alpha

author's e-mail: sagara.akio@LHD.nifs.ac.jp

Table 1. Design parameters of helical reactor

Design parameters			LHD	FFHR2	FFHR2m1	FFHR2m2	SDC
Polarity	l		2	2	2	2	
Field periods	m		10	10	10	10	
Coil pitch parameter	¬		1.25	1.15	1.15	1.20	
Coil major Radius	R_c	m	3.9	10	14.0	17.3	
Coil minor radius	a_c	m	0.98	2.3	3.22	4.16	
Plasma major radius	R_p	m	3.75	10	14.0	16.0	
Plasma radius	$<a_p>$	m	0.61	1.24	1.73	2.35	
Plasma volume	Vp	m^3	30	303	827	1744	
Blanket space	¬	m	0.12	0.7	1.1	1.05	
Magnetic field	B_0	T	4	10	6.18	4.84	
Max. field on coils	B_{max}	T	9.2	14.8	13.3	11.9	
Coil current density	j	MA/m^2	53	25	26.6	26	
Magnetic energy		GJ	1.64	147	133		
Fusion power	P_F	GW		1	1.9	3	
Neutron wall load	$¬_n$	MW/m^2		1.5	1.5	1.5	
External heating pow	P_{ext}	MW		70	80	43	100
¬ heating efficiency	$¬_¬$			0.7	0.9	0.9	0.9
Density lim.improvement				1	1.5	1.5	7.5
H factor of ISS95				2.40	1.92	1.92	1.60
Effective ion charge	Z_{eff}			1.40	1.34	1.48	1.55
Electron density	$n_e(0)$	10^{19} m^{-3}		27.4	26.7	17.9	83.0
Temperature	$T_i(0)$	keV		21	15.8	18	6.33
Plasma beta	¬⊂ℜ	%		1.6	3.0	4.40	3.35
Plasma conduction lo	P_L	MW			290	453	115
Diverter heat load	$¬_{div}$	MW/m^2			1.6	2.3	0.6
Total capital cost	G$(2003)			4.6	5.6	7.0	
COE	mill/kWh			155	106	93	

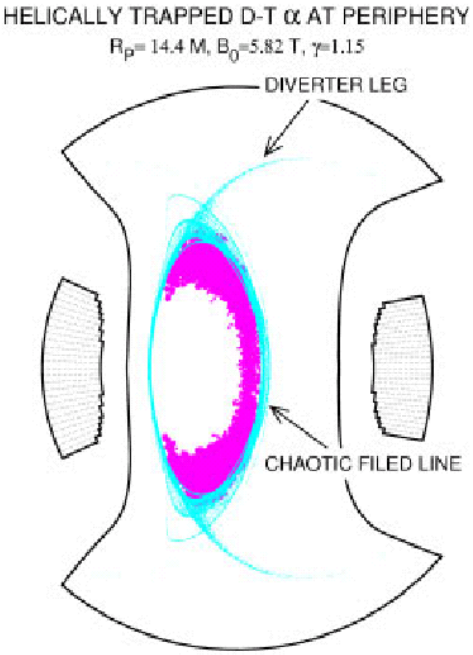

Fig.1 Poincare plot of helically trapped a particles (magenta dots) and the chaotic field lines (sky blue dots).

particles as shown in Fig.1. Therefore, the reactor size is increased. In this case, as shown in Fig.2, it is expected that there is an optimum size around R_c of 15m by taking into account the cost of electricity (COE), the total capital cost, and engineering feasibility on large scaled magnets.

3. Progress and issues on 3D blanket designs

In the direction of optimizing neutronics performances, the 3D distribution of neutron wall loading is basically important. Under the averaged neutron wall loading of 1.5 MW/m^2, the maximum loading for the uniform and helical source are 2 MW/m^2 and 1.8 MW/m^2, respectively, at the first wall of blankets on the helical coils. Therefore the peaking factor is estimated to be 1.2 to 1.3.

The FFHR blanket designs have been improved to obtain the total TBR over 1.05 for the standard design of Flibe+Be/JLF-1 and long-life design of Spectral-shifter and Tritium Breeding (STB) blanket [2, 3] by enhancement of the blanket cover rate to 80%. More increase of the cover rate over 90% is effectively possible by a new proposal of Discrete Pumping with Semi-closed Shield (DPSS) concept as shown in Fig.3, where the helical divertor duct is almost closed with partly opened at only the discrete pumping ports. This DPSS is very important not only to increase the total TBR over 1.2 but also to reduce the radiation effects on magnets. In fact, as shown in Fig.4, the first neutron fluxes at the poloidal coils just out side the divertor duct and at the side of the helical coils are successfully reduced to the acceptable

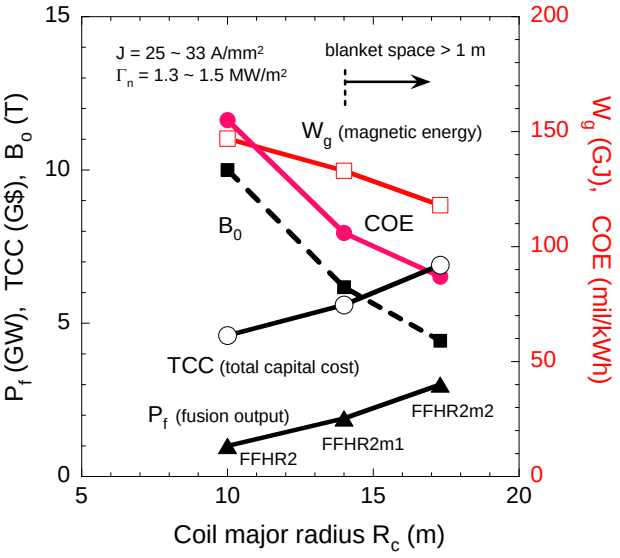

Fig. 2 R_c dependences of the fusion output P_f, the total capital cost (TCC), magnetic field B_0 at the plasma center, cost of electricity (COE) and magnetic energy W_g under almost same conditions on neutron wall loading Γ and current density J on helical coils.

level lower than $1x10^{22}$ n/m^2 in 40 years. The total nuclear heating is also reduced from 250kW to 40kW, which means the cryogenics power to be about 12MW and acceptable level below 1% of the fusion output.

4. Base design of large superconducting magnet system

The base design for the FFHR2m1 superconducting magnet system has been preliminary proposed on the engineering base of ITER-TF coils as a conventional option, where the magnet-motive force of helical coils is about 50 MA and the cable-in conduit conductors (CICC) of current 90 kA with Nb3Al strands are wound in the grooves of the internal plates. In this concept, react and wind method is preferred to use conventional insulator and to prevent huge thermal stress. The maximum length of a cooling path is about 500 m that is determined by the pressure drop for the required mass flow against the nuclear heat of 1000 W/m^3. This value has a 5 times margin of the maximum nuclear heating calculated on the FFHR helical coils, in which the gamma-ray heating is dominant and the maximum is about 200 W/m^3.

The total weight of the coils and the supporting structure exceeds 16,000 tons. As shown in Fig.5, this weight is supported by cryogenic support posts by adopting the same type of the LHD support post, which is a folded multi plates consisted of Carbon Fiber Reinforcement Plastic (CFRP) and stainless steel plates. Gravity per support is 16,000 ton / 30 legs ~ 530 ton, thermal contraction < max. 55 mm, and the total heat load to 4K is about 0.34 kW which is 1/20 of the case of stainless steel post.

The modal and dynamic response analysis using typical earthquake vibrations are the next issue for design optimization.

5. New proposals on access to ignited plasmas

Minimization of the external heating power to access self-ignition is advantageous to increase the reactor design flexibility and to reduce the capital and operating

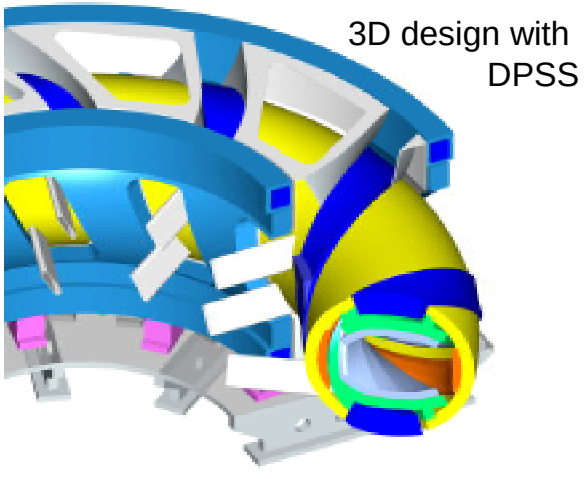

Fig.3 Discrete Pumping with Semi-closed Shield (DPSS) concept, where the helical divertor duct is almost closed with partly opened at only the

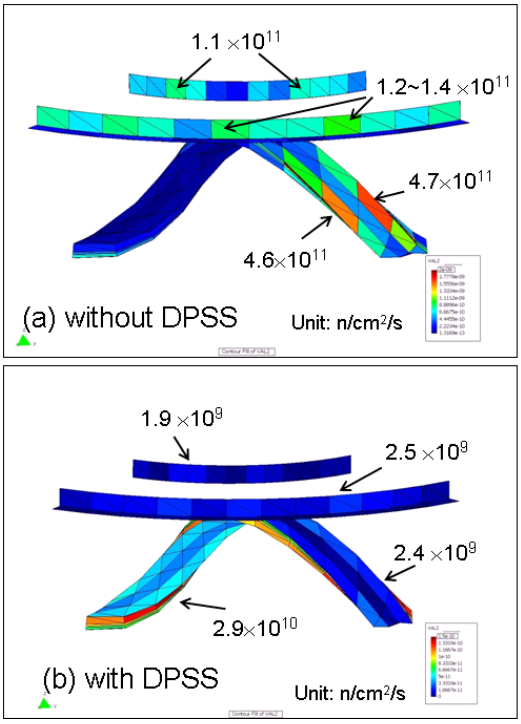

Fig.4 The first neutron fluxes at the poloidal and helical coils (a) without and (b) with the DPSS, where the flux at the rear side of helical coils is high in (a) and one order reduced in (b).

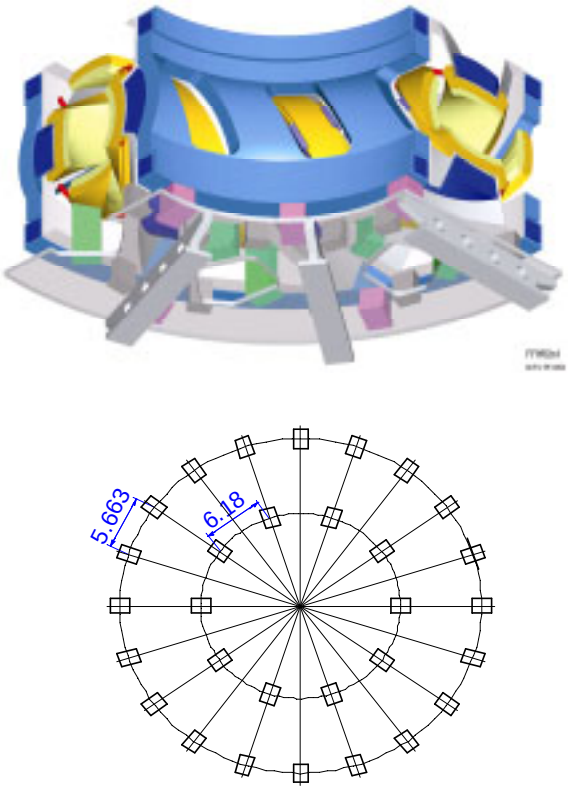

Fig.5 The cryogenic support posts of FFHR2m1.

costs of the plasma heating device in a helical reactor. While the fusion power rise-up time in a tokamak depends on the OH transformer flux or the current drive capability, any fusion power rise-up time can be employed in a helical reactor, because the confinement field is generated by the external helical coils. It has been recently found that a lower density limit margin reduces the external heating power, and over 300 s of the fusion power rise-up time can reduce the heating power from such as 100 MW to minimized 30 MW in FFHR2m1 [5].

A new and simple control method of the unstable operating point in FFHR2m1 is proposed for the ignited operation with high-density plasma [6], as demonstrated in Fig.6, where a new proportional-integration-derivative (PID) control of the fueling has been used to obtain the desired fusion power.

6. Summary

Recent activities on optimizing the base design of LHD-type helical reactor FFHR2m1 is presented. Three candidates to secure the blanket space are proposed in the direction of reactor size optimization without deteriorating a-heating efficiency and with taking cost analyses into account.

On 3D blanket designs, it is shown that the peaking factor of neutron wall loading is 1.2 to 1.3 and the blanket cover rate over 90% is possible by proposing Discrete Pumping with Semi-closed Shield (DPSS) concept. Helical blanket shaping along divertor field lines is a next big issue.

On large superconducting magnet system under the maximum nuclear heating of 200W/m^3, CICC designs of 500 m cooling path and 90 kA with Nb3Al strands and alternative Indirect cooling Nb3Sn conductor designs are proposed with the LHD-type robust design of cryogenic support posts.

On access to ignited plasmas, using the advantage of current-less plasma, new methods are proposed, which are a long rise-up time over 300 s to reduce the heating power to 30 MW and a new proportional-integration-derivative (PID) control of the fueling to handle the thermally unstable plasma at high density operations.

References

[1] A. Sagara, O. Motojima, K.Watanabe et al., Blanket and Divertor Design for Force Free Helical Reactor (FFHR), Fusion Eng. and Design, 29 (1995) pp.51-56.

[2] A. Sagara, S. Imagawa, O. Mitarai et al., Improved structure and long-life blanket concepts for heliotron reactors, Nuclear Fusion, 45 (2005) pp.258-263.

[3] A. Sagara, O. Mitarai, S. Imagawa et al., Conceptual design activities and key issues on LHD-type reactor FFHR, Fusion Eng. and Design, 81 (2006) pp.2703-2721.

[4] A. Sagara, T. Tanaka, T. Muroga et al., Innovative Liquid Breeder Blanket Design Activities in Japan, Fusion Sci. and Tech., 47 (2005) pp.524-529.

[5] O. Mitarai, A.Sagara, H.Chikaraishi et al., Minimization of the External Heating Power by Long Fusion Power Rise-up Time for Self-ignition Access in the Helical Reactor FFHR2m, presented at 21st IAEA Fusion Energy Conf., 2006, Chengdu, China.

[6] O. Mitarai, A. Sagara, N. Ohyabu, et al., New Control Method of the Unstable Operating Point in the FFHR Helical Reactor, Plasma and Fusion Research, Rapid Communications, 2, 021 (2007) .

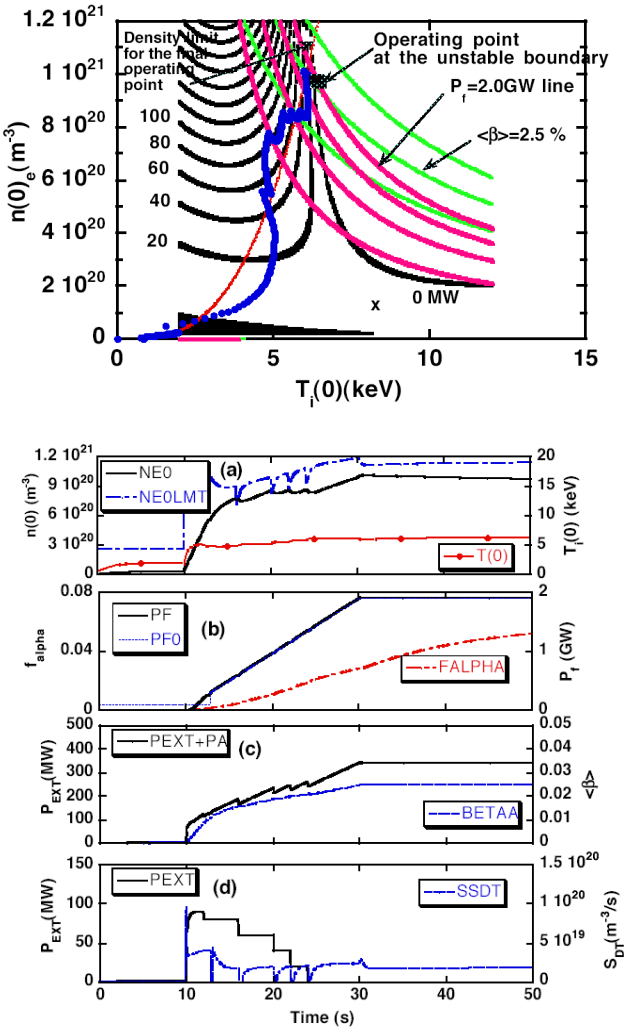

Fig.6 Temporal evolution of plasma parameters in FFHR2m1 at the thermally unstable boundary of high density operations, and the POPCON diagram.

Proceedings of ITC18, 2008

Fusion Education in the European Union

GuidoVan Oost[1)]

[1)]*Department of Applied Physics, Ghent University, B-9000 Ghent, Belgium*

Recent educational initiatives are outlined aiming to maintain the expertise that has placed the EU Fusion Programme at the forefront of international fusion research and engineering, and to ensure the availability of competent staff to construct and operate ITER and DEMO.

Keywords: education, EU fusion programme, Erasmus Mundus European Master, Fusion Education Network, human resource management, ITER, DEMO

1 Introduction

Fusion research is entering a new phase. The construction of ITER, the Broader Approach activities, and the preparation for DEMO require an expansion of the fusion programme and a shift of the emphasis from plasma physics to engineering and nuclear materials. There is also a growing need for competences on nuclear project related issues such as project management, nuclear licensing, quality assurance, risk assessment, and management of procurement processes, as well as a need for stronger collaboration with industry. Even within the fundamental plasma physics research there are important shifts of emphasis.

In Europe, research in the field of nuclear fusion by magnetic confinement is strongly integrated by EURATOM. There are no national research programmes in the strict sense. The EU programme is executed by more than 20 institutes associated with EURATOM (called Associations for Fusion). The large majority of EU countries plus Switzerland have signed Association contracts. A more specific working framework EFDA (European Fusion Development Agreement; www.efda.org) has been established for the exploitation of the largest fusion experiment in the world JET (Joint European Torus) and for technological developments necessary for future fusion installations. The EU fusion programme, a prototype of integrated European research, has maintained a complementarity of programmes and installations. This strongly integrated organization is at the origin of the dominating position of Europe in magnetic confinement fusion (MCF) research and of the decision to build the next step large international installation ITER in Cadarache.

In order to maintain the expertise that has placed the EU fusion programme at the forefront of international fusion research and engineering, and to ensure the availability of competent staff to construct and operate ITER and DEMO, a long-term Human Resource Management plan for the European Fusion Programme is needed, which should reflect the increase of the volume of the programme, the shifts in required competences, and the natural aging of the present population of professionals in the fusion community. It is estimated that at least 40 new researchers should come into the system each year.

A key element of this human resource strategy is a well-planned programme for education in fusion science and engineering, to make sure that a match between the required competences and the available professionals is realised, and that a sufficient number of new people enter the fusion system. In the framework of the Bologna declaration there is furthermore the need to harmonize advanced fusion education, training and professional qualification, and to strengthen interaction and exchange of academic resources in the European Research Area.

Fusion education is a field that lends itself by excellence for European collaboration, as it can build on the very well developed collaboration between the EURATOM Associations through the EFDA agreement. Coordinating fusion education across Europe allows the joint development of common educational goals and standards, high quality educational materials, and easy access to hands-on experiments and experimental facilities throughout Europe. A special role is played by the Joint European Torus JET, exploited jointly by the European researchers under the EFDA coordination, which as a joint European facility is a particularly inspirational environment for education and training.

Presently, the following activities exist in the field of fusion training and education in the EU:

- Mobility Scheme (starting usually from Post-Doc level)
- National schemes and fellowships by the associated laboratories
- European PhD in Fusion Science and Engineering
- European Training Scheme for ITER: selected laboratories offer posts on key topics for ITER R&D
- Erasmus Mundus Master in Nuclear Fusion Science & Engineering Physics
- EU CSA (Coordinated Support Action) << Fusion Education Network >>- FUSENET

The last two initiatives will be outlined below.

author's e-mail: guido.vanoost@ugent.be

2 Erasmus Mundus " European Master in Nuclear Fusion Science & Engineering Physics " (FUSION-EP)

The European Master in Nuclear Fusion Science and Engineering Physics (**FUSION-EP**) is offered by the following partners:

- Universiteit Gent, Belgium (coordinator)
- Université Henri Poincaré, Nancy, France
- Kungliga Tekniska Högskola (KTH) Stockholm, Sweden
- Universität Stuttgart, Germany
- Universidad Complutense de Madrid, Spain
- Universidad Carlos III de Madrid, Spain
- Universidad Polytécnica de Madrid, Spain

The ITER host country France is also member of the present Erasmus Mundus consortium. All the partners have a long relationship in the framework of the coordinated EURATOM research programme on nuclear fusion, guaranteeing a strong synergy and visibility. The aim of the Masters programme (**http://www.em-master-fusion.org**) is to provide a high-level multinational research-oriented education in fusion-related engineering physics, in close relation to the research activities of the partners, and with a well-integrated language and cultural experience. The combined and harmonized teaching &research of the 7 universities offers a far greater variety of competences in the field of fusion science and engineering physics than could be provided by each of the single universities, and therefore guarantees a significant added value for the students in terms of specialisation opportunities. The Joint European Master Programme offers a genuine European opportunity for Master level studies in a field which is of crucial importance to contribute to the solution of the ever more urgent and vital problem of world energy supply. A large number of scientists and engineers will be required in two main categories: " Fusion technology and engineering physics " and " Plasma physics " and their formation takes typically 10 years, requiring a structured European Master level education. Furthermore, fusion research shows an increasing and very important spin-off in many fields of science and engineering, such as new materials, nanotechnologies, superconducting coils, robotics, electronic components, high power RF sources, space propulsion. The EU framework described in offers many possibilities for summer schools and doctoral studies.

The studies in engineering physics are devoted to the technical applications of physics and strongly supported by the research activities in the different laboratories within the Consortium. By combining in a balanced way the basic concepts of a degree in engineering with the essentials of an education as a engineering physicist, these studies seek to train engineers capable of performing or leading technical and scientific research in universities, research establishments or industry.

The engineering component of the studies makes the physics engineer familiar with the analysis, design and optimization of new and existing systems, products, machines, materials, etc., in which simplification to manageable system descriptions (from rules of thumb to expert systems) is essential. In the physics component the reductionist approach holds centre stage; here experiments and mathematical modelling seek to reduce physical phenomena to their very essence and to discover the physical laws applicable. Even though the approach has a more philosophical slant, the rigorous attitude is essential and a physical theory should stand a validation by experiment.

Physics engineers are trained, first and foremost, for R&D purposes. Their wide-ranging education makes them fit for all companies and research establishments where interdisciplinary R&D requires in-depth knowledge of physics. They will constitute a substantial percentage of the large number of additional researchers required for the establishment of the EU as the best centre of excellence in the world. Both components of the studies especially qualify the physics engineer to fill executive jobs at a later stage.

In view of the expertise of the partners, the programme offers three programme tracks to the student: (i) Plasma physics (fusion-oriented); (ii) Computational methods in physics; and (iii) Instrumentation and Radiation. The programme structure is combined with a mandatory stay of the student at three universities in three countries: semesters1&2 at University A; semester 3 at B and semester 4 (Master thesis) in C. Semesters 3&4 are in a particular track. After semester 2 a summer event is organized in which the tracks and Master thesis topics are proposed. Student mobility is an inherent part of the programme structure and philosophy.

The admission criteria are: a bachelor degree in engineering physics, applied physics, physics or equivalent degrees. Sufficient bachelor level knowledge in classical and modern physics is mandatory together with the necessary mathematical and computer programming skills. No difference is made between third-country students, EU students, grantees and non-grantees. Applicants (students and scholars) from third countries (applying for a grant or not) will be subject to a well defined selection procedure aiming at high quality.

3 Erasmus Mundus International Network for Nuclear Fusion Education

For collaborations outside Europe, EURATOM establishes bilateral agreements, which are privileged channels for the Associations and institutes outside Europe. Global collaborations have been established in the framework of IAEA (International Atomic Energy Agency) and IAE (International Energy Agency). Collaborations are formalized in

the form of IAEA CRP 's (Coordinated Research Projects) and IAE Implementing Agreements. IAEA has provided the legal framework for the development of ITER since 1988. All the partners are involved in CRP 's and Implementing Agreements, and thus have privileged links with non-EU universities and research institutes. Furthermore, several FUSION-EP partners have close collaborations with NIS (New Independent States) institutes and universities in the framework of INTAS.

The European thinking about fusion R&D emphasizes an integrated and strongly coordinated approach which has resulted in the leading position of the EU in magnetic confinement fusion (MCF). The European Master in Nuclear Fusion Science and Engineering Physics - Erasmus Mundus programme (FUSION-EP) offers the opportunity to study this European vision on MCF R&D in Europe and to experience the diversity in its approaches and applications. Therefore, in addition to the FUSION-EP teaching and exchange programme, a new partnership has been established between the FUSION-EP Consortium and a number of high level key Third Country -institutions specialised in fusion research and education. The general objective of this network is to build and strengthen a worldwide network of EU and non-EU based centres of excellence in fusion R&D studies. The FUSION-EP Consortium - itself a partnership of renowned European institutes of research and training in fusion - aims at brokering an improved connection and coordination between different key non-EU institutions within its network range, in view of collaboration between EU and non-EU scientists and engineers in the international research project ITER.

Key Third Country-institutes have been selected on the basis of their competence, (inter)national network density, and longstanding links with the FUSION-EP Consortium partners. They are among the world 's most renowned and active institutes in the field of MCF studies.

- UCLA (USA)
- University of Wisconsin-Madison (USA)
- St. Petersburg State Polytechnic University (Russia)
- Moscow Engineering Physics Institute (Russia)
- University of Science and Technology of China (Hefei)
- Tsinghua University Beijing (China)
- Southwestern Institute of Physics, Chengdu (China)

The main political-economic spheres in fusion R&D (Europe, North-America, and Asia) are represented by two or three leading institutes as main network nodes. However, every institute has its own network partners downstream and thus plays a broker 's role in its own turn. It is this spirit of brokerage between different network nodes (' tertius iungens ' principle) that promises to allow for a dynamic learning network. This network brokerage between FUSION-EP and its non-EU partners can be visually imagined as a hub-and-spokes-model, with the FUSION-EP Consortium in the middle connecting different previously disconnected networks. Futhermore, all the countries involved are members of the large scale international research project ITER, and within these countries the partner institutions are main players.

The specific objective of this new partnership is to intensify the exposure and interaction of FUSION-EP institutes with non-EU fusion R&D approaches and education in the rest of the world. The interaction in this new partnership modality is being realized through outgoing mobility of EU students and scholars on the one hand and joint reflection and analysis seminars on the other hand. This interaction is deemed crucial to better adapt the FUSION-EP curriculum to non-EU students. Exposure of EU students and scholars to institutes in Third Countries is critical for a better understanding of the teaching needs of non-EU students with reference to the European model of fusion R&D. It also enhances the understanding of fusion R&D problems and solutions in Third Countries and thus allows for the integration of interesting approaches and practices from other regions in the teaching activities of the FUSION-EP.

The interaction will also increase the specialized knowledge on specific characteristics of fusion R&D in the hosting countries and thus contribute to more targeted future research and teaching collaboration. This new partnership will also allow the assessment of teaching plans/methods in the partner institutes with the aim to develop mutual standards and facilitate the future exchange between education institutes (e.g. by better preparation of Bachelor students wanting to follow the FUSION-EP). Through the exchange of students and in particular scholars we also want to strengthen the general interaction among EU and non-EU countries with respect to research, exchange of practices and policies of fusion R&D.

Finally, through this cooperation an increased outreach of FUSION-EP is envisaged. Firstly, by establishing reference institutes for future non-EU FUSION-EP students in different parts of the world. Partner institutes can not only distribute information on the FUSION-EP in their country or region, but also serve as information centres for students of that part of the world searching for more detailed information about the study programme of the FUSION-EP, the specific required skills (by e.g. the organisation of short preparatory courses in the partner institutes, $\cdots$). Partner institutes become in that way information and pre- selection antennas for the FUSION-EP. All this must help to increase the quality of the FUSION-EP programme. Secondly, offering the possibility to complete short training periods in non-EU institutes will also increase the appeal of the FUSION-EP programme to EU students. This Erasmus Mundus programme enforces the intercultural exchange among EU and non-EU students, sparks the interest to know the other countries better, and enhances mutual understanding and cooperation.

4 FUSENET

The European Fusion Education Network (FUSENET) for education in fusion science and technology started in October 2009, as part of a comprehensive package of coordination actions, in order to increase, enhance, and broaden fusion training and education activities in Europe. FUSENETconsists of eleven focussed work packages, with a total budget of 2.0 M€. The project brings together a broad representation of the European fusion community with 35 participants from 18 countries, of which 22 Universities and 13 EURATOM Associations. The FUSENET project will cover all education levels, from secondary school through Bachelor and Master level, to PhD.

The specific objectives of the FUSENET project are:

1. The sustainable establishment of the FUSENET Association, which provides a permanent platform for the coordination of existing actions, the initiation, development and execution of new EU-wide actions, and for the exchange and dissemination of information.
2. A coherent programme of EU-wide learning opportunities in the fusion programme and related industry, with jointly developed educational goals for different target groups, which is easily accessible and transparent through the central FUSENET website.
3. High quality teaching materials and hands-on experiments, which are used throughout Europe to create highly attractive and effective learning opportunities, and which lead to more coherence in the level and scope of knowledge of students.
4. A mobility system in which the best learning opportunities are available to students throughout Europe, and which leads to the forming of many interpersonal links among people in the fusion system.

The actions of FUSENET build upon the already strongly integrated European Fusion Research programme, coordinated under EFDA. The experimental facilities and research groups in this programme will play a major role in the educational programme, and optimizing the accessibility of those facilities for students is an important goal of FUSENET. A special role is played by the Joint European Torus JET, exploited jointly by the European researchers under the EFDA coordination, which as a joint European facility is particularly inspirational as a place for education and training.

The network will be given a permanent identity by the establishment of the FUSENET Association, which will provide a platform for the coordination of existing actions, the initiation, development and implementation of new EU-wide actions, and for the exchange and dissemination of fusion education information.

The envisaged concrete end result of the FUSENET project is an integrated fusion education system in Europe, with strong links between fusion institutes and higher education institutes. Through a central website, the programme will offer a transparent structure of coherent educational actions, accessible and inviting, in which students and teachers can easily find their way to a variety of attractive ways to participate in the fusion research programme.

The strategy of the work plan is directly connected to the goal of a broad base of knowledge transfer to secondary school and bachelor/master/technical students, and a high peak of PhD students. This leads to actions aimed at all levels of fusion education. There are three main elements to the strategy:

1. **Critical mass.** As the number of students in fusion subjects in most countries is not large enough to support specialised Master or PhD degrees, actions need to be coordinated and initiated on a European scale, in order to reach sufficient critical mass.
2. **Coherence.** To optimise the flow of students through the system, better links are needed between the different education layers. This means both a focus on secondary school teachers and good connections between higher education institutes and fusion institutes.
3. **Transparency.** Learning opportunities need to be more accessible to students across Europe, through dissemination of information, and improvement of mobility. The educational goals of bachelor/master and doctoral level courses need to be more aligned, to make it easier for students to navigate the fusion system.

The European Fusion Education programme should be considered as the natural counterpart of the European Fusion Research programme, coordinated under the EFDA agreement. The two will work in close harmony and the synergy will be obvious. The ultimate aims of the educational programme are the support of the fusion programme, either directly by training high level researchers, or indirectly by improving the rooting in society. More directly, FUSENET will contribute significantly to the coordination of high-quality research, because it

- enhances the participation and exchange of students and their teachers in the fusion programme,
- stimulates the creation of attractive student training opportunities,
- further strengthens the ties between research groups

To make the network sustainable, an association (the FUSENET Association) will be set up with the task to manage and further develop the network formed under the CSA. The organization of the network and its embedding in an Association is similar to that of the European Nuclear Energy Network (ENEN).

Acknowledgement

The author gratefully acknowledges the very valuable input of Prof. Niek Lopes Cardozo and Dr. Mark T. Westra from FOM (The Netherlands) who are responsible for the overall coordination of FUSENET.

Oral Talks

O-01 - O-07

Proceedings of ITC18, 2008

The Lithium Wall Stellarator Experiment in TJ-II

F.L. Tabarés[1], D. Tafalla, J.A. Ferreira, M.A Ochando, F. Medina, E. Ascasibar, T. Estrada, C. Fuentes, I. García-Cortés, J. Guasp, M. Liniers. I. Pastor, M.A. Pedrosa and the TJ-II Team*.

Laboratorio Nacional de Fusión. CIEMAT. Avenida Complutense 22, 28040 Madrid, Spain

** See author list in ref. 8*

In the last years, lithium wall conditioning has been carried out in several fusion devices by different techniques, providing in many instances record values of plasma parameters and enhanced plasma reproducibility and opening the possibility of developing high radiative, low recycling liquid divertor concepts of high potential for future reactors. This concept has been termed the Li Tokamak Reactor. Compared to tokamaks, stellarator plasmas show distinct features in their interaction with the surrounding materials. The lack of disruptions and type I ELMs make them more reliable for reactor operation. So it is the lack of MHD-driven density limit. On the other side, the intrinsic radiative character of the density limit of stellarators and the tendency to central impurity accumulation makes wall-material selection paramount. In the present work, the plasma performance of the TJ-II Heliac under Li-coated wall conditions is described. Compared to previous coatings, lithium has produced the best plasma performance to date, leading to the achievement of record values in plasma density and energy confinement. Plasma profiles free from impurity accumulation have been obtained under specific fuelling schemes. The development of L-H transitions has been characterized in terms of steep gradients in edge parameters and broadband fluctuation suppression.

Keywords: lithium, stellarator, fusion reactor, first wall materials, recycling, impurity accumulation, TJ-II, H-mode

1.Introduction

Plasma wall interaction issues are paramount in achieving fusion plasmas with high purity, controlled density and high confinement. Compared to tokamaks, stellarator plasmas show distinct features in their interaction with the surrounding materials. On the good side, the lack of disruptions and type I ELMs make the choice of plasma facing components less demanding. In addition, the lack of MHD-driven density limit [1] has allowed their operation at densities well above the corresponding Greenwald limit for tokamaks [2]. Since plasma collapse in stellarators seems to be mainly governed by local power balance considerations [3], changes in wall materials are ideally suited for the validation of the running models for the density limit in these devices. As a potential drawback, neoclassical transport characteristics of the core plasma in stellarators make them prone to impurity accumulation [4], thus stressing the use of low Z elements as PFC. A closed coupling between the divertor efficiency and the recycling characteristics of the wall has been recently evidenced in LHD, as shown by the achievement of the IDB-SDC mode in the absence of the LID operation, only under low recycling wall conditions [5]. Therefore, low Z, low recycling first wall scenarios look highly promising if a stellarator reactor concept is to be developed. Among the available low Z coating options (Be, C and B) lithium is a very attractive element due to its very low radiation power, strong H retention and strong O getter activity and excellent results have been achieved recently in tokamaks [6]. Also, and in direct connection to the lower recycling scenario leading to decreased CX losses and higher temperatures, important changes in energy confinement have been predicted and observed [7]. In the present work, the operation of a stellarator, the TJ-II Heliac [8], with lithium-coated walls is described. The most relevant changes on the plasma performance and confinement characteristics associated to the new wall scenario are described and analysed in terms of enhanced impurity and particle control.

2. Coating technique

The TJ-II stellarator has been operated under different first wall conditions since its beginning and details about the applied techniques and resulting plasma performance can be found in [9]. Basically, under ECR plasma generation and heating, the density control is hampered by the combination of low cut-off density (ne (0) <1.7 .10^{19} m^{-3}) and the fast saturation of the small (~0.5 m^2 vs. ~40 m^2) plasma-interacting

author's e-mail: tabares@ciemat.es

surface located at the grooved wall area which surrounds the two characteristic central coils.

For the results here reported (2007-08 campaign), a low recycling, low Z wall has been produced by *in situ* lithium coating. It is generated by evaporation under vacuum from four ovens, symmetrically spaced and oriented tangentially to the vacuum vessel in the equatorial plane of the machine. A total of 4g of metallic Li are evaporated during each conditioning cycle, at temperatures of 500-600 ºC over the chamber (at room temperature). Effusion from the ovens creates an atomic beam aiming at the remote region opposed to the corresponding flange. Under HV operation, the mean free path of the Li atoms is long enough to produce a thin layer at the vessel walls located midway between adjacent ovens. The initial deposition pattern, directly visible in the groove protecting the central coils, matches the line of sight flight of the Li atoms. However, plasma operation was found to redistribute the initial coating very efficiently and the beneficial effect of the coating extended far beyond that expected from the localized deposition. Nevertheless, in order to extend the lifetime of the Li coating, and due to the very high reactivity of this species with background gases (water, O_2, N_2, CO…) a ~50 nm boron layer was deposited by glow discharge in a He/o- carborane mixture prior to the evaporation (see [9] for more details). A He GD depleted the H from the B coating after its deposition. Also, He GD was applied every day on the Li layer in order to remove hydrogen from the areas not fully covered by the coating. A total of 12 g of Li were evaporated for the ~1000 discharges performed in a four month period.

3. Density control

The most remarkable change upon lithiation of TJ-II was a conspicuous improvement of particle control by external puffing compared to the former, B-coated scenario. Not only the required puffing levels were significantly higher, by a factor of 2-3, to obtain the same density (feed-forward operation mode), but also no sign of wall saturation was observed after a full day of ECRH operation. Particle balance measurements under the Li coated walls yields a total retention ~4.10^{21} H/m^2 after one day of operation (~45, 200 ms discharges), a factor 5 higher than the B wall saturation limit at room temperature, which takes place at total retained inventory of ~ 8.10^{20} H/m^2 (RT values). Of particular relevance on machine performance is the recovery of pumping walls characteristics after shots with densities above cut-off. Typically, one or two purges (dry discharges) were required in B scenarios. However, no such a need was found upon lithiation, the wall memory effect being basically washed out. All these observations concerning wall inventory under Li walls point to strong diffusion of the implanted H into the wall coating, which may be different from the initially deposited one after plasma operation.

The dynamic behaviour of plasma particles for H and He plasmas was investigated by perturbative experiments. A value of the effective confinement time, $t_p/(1-R)$, of ~8 ms were deduced for H plasmas in freshly deposited Li. Assuming no major changes in particle confinement respect to the boron and metal cases [10], a value of R<0.20 is obtained. This value was slowly evolving after some hundreds of shots up to values of R~0.5. Perturbative experiments in He fuelled discharges yields an R value of ~0.93. This, less than one, recycling coefficient value is in line with previous observations of He pumping in low temperature Li walls [6] and opens the possibility to selective removal of reactor fuel particles and resulting ashes. Of special challenge in TJ-II, density control in NBI plasmas was dramatically improved by the lithium coating. Both, plasma reproducibility and density control were significantly better than in previous campaigns [10]. As an example of density control in NBI heated plasmas, a high challenging issue under previous wall conditions, figure 1 shows the plasma density and fuelling waveform of three consecutive discharges. As seen, an almost flat density plateau is achieved by external puffing control. It is also worth noting that particle fluxes to the wall during the NBI phase, as monitored by the different Ha monitors located all over the machine, remain basically at the ECRH plasma level thus indicating a strong enhancement (up to a factor of 4) of global particle confinement. For high particle confinement and NBI pulse length of ~100 ms, the density rise should be ultimately limited by the beam fuelling rate which, for a 31keV, 0.5 MW power can be evaluated in ~10^{20} e$^-$/s.

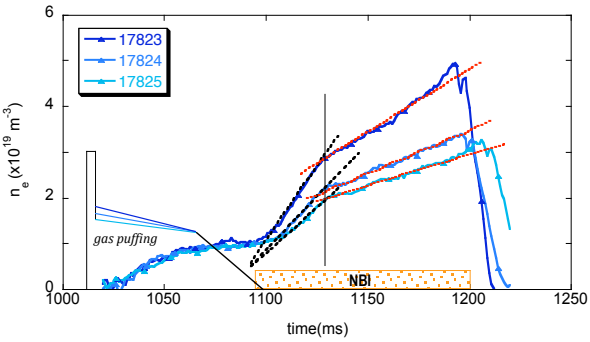

Fig.1. Density evolution for three consecutive NBI discharges under different fuelling waveforms.

This value was indeed experimentally observed. Furthermore, no sign of collapse was seen up to central density values of 8.10^{19} m^{-3}, depending on the shape of the resulting plasma profile (see below).

4. Impurity behaviour and plasma profiles

Significant effects concerning impurity concentration have been observed upon Li wall conditioning: the electron density-normalized signals from carbon emission, radiated power, neutral lithium and other impurity-related signals were seen to systematically decrease during the operation. A concomitant evolution of particle recycling towards lower levels was eventually observed. A spectroscopic estimate of the erosion yield of Li by the plasma was made from the calibrated intensities of the Ha and LiI (671 nm) lines. A yield of (0.5-1). 10^{-3} Li/H was deduced at several locations of the vessel. These figure is at least a factor 30 lower than expected from TRIM code [11] for the calculation of the corresponding sputtering yield at the measured edge temperature of 50-60 eV and the reason of this mismatch is still under investigation. Plasma spectroscopy and soft X ray measurements, together with the IONEQ impurity transport code [12] indicate that carbon still represents the main contaminant in Li-wall scenarios. Radial profiles of radiation losses were determined from absolutely calibrated bolometer arrays located at several toroidal and poloidal locations. Two different profiles developed depending on fuelling strategy and local plasma parameters. Examples of these profiles are shown in figure 2. For the broad, dome-type profile (on the left), central radiation levels are almost half than those observed in the peaked, bell-type counterpart (on the right). From the analysis of SXR emission profile, it is concluded that central values of Zeff differ, indicating an impurity accumulation in the bell-type scenario with central Zeff values up to 2.8. The radial shapes of plasma emissivity of figure 5 are mirrored by the Thomson Scattering data of plasma density, with central values up to 8.10^{19} m^{-3} in the bell-type profile and almost constant electron temperatures of 200-300 eV across the plasma minor radius.

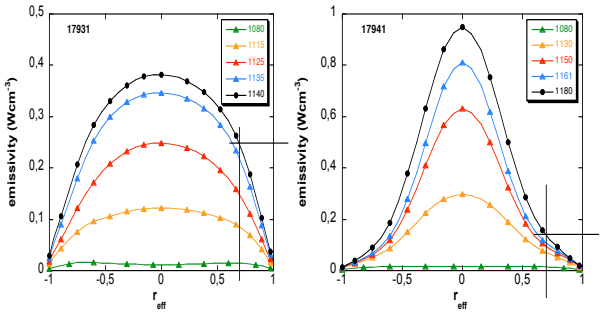

Fig.2. Radial profiles of plasma emissivity (bolometer) for two different type of profiles obtained under Li-wall operation: left: dome type, right: bell type. Note the different central and peripheral radiation levels.

In spite of their lower, total radiated power, development of the dome-type profile was systematically associated to a prompt plasma collapse. One of the possible causes of this fact can be found in the local power balance established at the plasma edge under central heating conditions. Indeed, the data shown in fig.3 indicate a significantly lower radiated power at the edge for the peaked, non-collapsing profiles. This balance has been called into play in defining the density limit in stellarators through the so-called *"low-radiative collapse"*[4]. Interestingly, transition from the bell to the dome type profile can be readily achieved by gas puffing during the NBI phase of the discharge.

5. Energy Confinement and L- H mode transition

Figure 3 shows the evolution of plasma energy content as a function of the average electron density for B and Li wall scenarios. The energy content is

evaluated by integration of the plasma Te, Ti and ne profiles.

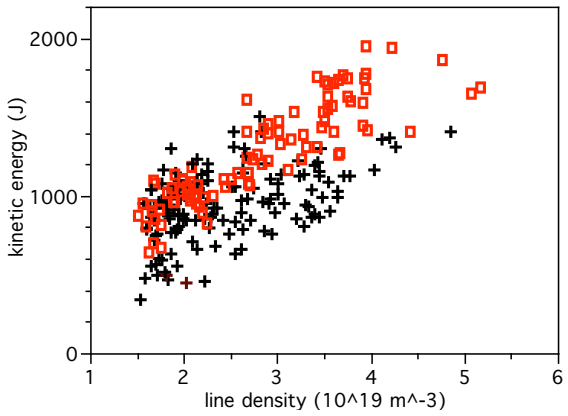

Fig.3. Plasma energy content versus line density for B (black pluses) and Li (red squares) coated-wall discharges in plasmas heated with only one NBI.

For the density span shown in the figure, a clear improvement of energy confinement from the B to the Li wall scenario takes place. Confinement times were evaluated at the maximum of diamagnetic energy content, Total injected power by the NBI system was measured by calorimetry and corrected by shine-through an ion losses effects. Total radiation was also taken into account for the available power coupled to the plasma. A strong dependence of t_E with <ne> was deduced at least from the Li-wall scenarios, with t_E up to 20 ms [13]. This enhancement of energy confinement with density is beyond that expected from usual scaling laws for stellarators [14]. Some evidence on the presence of transport bifurcations leading to enhanced confinement modes was provided through the conspicuous ELMy behaviour in the Hα signals observed under NBI operation. A periodic oscillation in the edge parameters, with sharp bursts of less than 300μs duration and a repetition rate of a few kHz, between two defined levels takes place at given line average density values and magnetic configuration. This plasma edge activity is correlated with important changes in the broadband density and electrostatic fluctuation levels at the edge, as detected by the reflectometer (in the density gradient region) and Langmuir probes (region around the LCFS), and it shows the characteristics of the L-H transition reported elsewhere [8,15]

6.Conclusions

In the last year, the TJ-II has been operated under lithium-coated wall conditions, the first time that this technique has ever been applied to a stellarator. Very encouraging results in terms of density control, plasma reproducibility and confinement characteristics have been obtained, dramatically enlarging the operational window of the machine even when only partial wall coverage with Li was achieved. NBI heated plasmas under stationary conditions have been produced up to record central densities of 8.10^{19} m^{-3}, with no sign of local thermal collapse under the limited NBI power available during the campaign. Two different types of plasma profiles were recorded, with different behaviour respect to impurity accumulation. Strong ELM-type activity has been detected, in close correlation to fluctuation suppression at the edge and enhanced confinement.

References

[1] H. Wobig. Plasma Phys. Control. Fusion **42** (2000) 931.

[2] O. Motojima et al. Phys Rev Lett. **97**(2006) 055002

[3] M.A. Ochando et al. Nucl. Fusion **37** (1997) 2

[4] Y. Takeiri et al. Plasma Phys. Control Fusion **42** (2000) 147

[5] A. Komori et al. 18th PSI Conference Toledo, Spain. 2008. To appear in JNM

[6] S.V. Mirnov et al Plasma Phys. Control. Fusion **48**(2006) 821 and refs. therein

[7] R. Majeski et al. Phys Rev Lett. **97** (2006) 075002

[8] J. Sánchez et al. Proc 2008 IAEA Conference. To appear in Nucl. Fusion

[9] F.L. Tabarés et al. J.Nucl. Mater **266-269** (1999) 1273. Also, D. Tafalla et al, ibid. **290-293** (2001) 1195

[10] F. L. Tabarés et al. Proc. 16th Intl. Stell. / Heliotron Workshop 2007. Toki, Gifu, Japan.

[11] J. László and W. Eckstein J. Nucl. Mater. **184** (1991) 22

[12] A. Weller et al., Report JET-IR- (87) 10 (1997)

[13] F.L. Tabarés et al. Plasma Phys. Control. Fusion **50** (2008) 124051

[14] H. Yamada et al. Nucl. Fusion **45** (2005) 1684

[15] P. W. Terry, Rev. Mod. Phys. **72** (2000) 109

Proceedings of ITC18, 2008

Present Progress of Plasma Transport Study on HL-2A

X.T.Ding[1)], W.W.Xiao[1)], X.L.Zou[2)], H.J.Sun[1)], Yi Liu[1)], L.H. Yao[1)], J. Rao[1)], B.B. Feng[1)], Z.T. Liu[1)], Y. Zhou[1)], Q.W. Yang[1)] , L.W. Yan[1)] , J.Q. Dong[1)] , X.R. Duan[1)] and HL-2A team

[1)]*Southwestern Institute of Physics, P.O. Box 432, Chengdu, China*

[2)]*Association Euratom-CEA, CEA/DSM/IRFM,CEA/Cadarache,13018 St Paul-lez-Durance, France*

The recent experiments of HL-2A tokamak have been focused on studying the physics of turbulence and transport. A spontaneous particle transport barrier has been observed in Ohmic discharges without any external momentum input. The barrier was evidenced by density perturbation study using modulated supersonic molecular beam injection (SMBI) and microwave reflectometry. The new features of the non-local transport effect induced with SMBI have been analyzed. The suppression of m/n = 2/1 tearing modes may be sustained by ECRH modulation at a frequency about 10 Hz. Continuous confinement improvement was observed after the mode suppression.

Keywords: Transport, Transient, Perturbation, Turbulence, ECRH, Modulation

1 Introduction

The understanding of transport physics and plasma confinement is an important subject for the design of future fusion reactors, especially the physics for particle transport [1–4], electron heat transport [5–8] and the internal transport barrier formation [9–11]. The recent experiments of HL-2A tokamak (R=1.65 m, a=0.4 m) have been focused on studying the physics of turbulence, transport, MHD instabilities and energetic electron dynamics. This paper presents some new experimental results for transport on HL-2A, including the spontaneous particle transport barrier, the non-local phenomena triggered by SMBI and the confinement features during modulated ECRH.

2 Present Status of the HL-2A Tokamak

The main operation parameters of the device are as follows: the toroidal magnetic field is 1.2-2.7 T, the plasma current is 150-450 kA and the plasma density is (1 - 6) $\times$ 10^{19} m^{-3}. ECRH system with four 68 GHz / 500 kW / 1 s gyrotrons has been built up in HL-2A. The ECRH power with both fundamental O-mode and second harmonic X-mode up to 2 MW is injected from the low field side of the device. The deposit position of ECRH is determined by the toroidal magnetic field. When toroidal magnetic field varies from 2.43T to 2.2T for O-mode, the resonance point can be replaced from the plasma core to the point at r=16 cm. The wave energy deposits in a range of 3cm. The efficiency of the transmission system is more than 80 %, so at least 1.6 MW power can be injected into plasmas. The electron and ion temperatures are 5 keV and 1.5 keV during 2MW ECRH respectively.

The supersonic molecular beam injection (SMBI) system has been improved with the modulation frequency reaching 50 Hz. Particles of the gas are accelerated by imposed pressure through the nozzle to get into the vacuum chamber of the tokamak. It is an attempt to enhance the penetration depth and fuelling effect. The penetration depth is very important to trigger the non-local transport phenomena. H_α intensity profile measured by H_α detector array and the density profiles measured by microwave reflectometry indicate that the penetration depth of the SMBI is more than ρ= 0.7. The SMBI injection has deeper penetration and better locality than conventional gas puffingthe system is not only an advanced technology for fuelling, but also a powerful tool (combined with microwave reflectometer or ECE) for particle as well as electron thermal transport studies.

The device is equipped with extensive and advanced diagnostics for transport study, including ECE and microwave reflectometry with high spatial and temporal resolution. There are also the Thomson scattering for electron temperature measurement, the 8 channel HCN laser interferometer for density profile, the five soft x-ray arrays for MHD study and the Doppler reflectometry for plasma rotation and core turbulence measurements.

3 Experimental results

3.1 Spontaneous internal particle transport barrier

On HL-2A tokamak, spontaneous particle transport barriers were observed in purely Ohmic heating plasmas without any external momentum input. The internal particle transport barriers (pITBs) were found to be formed when the line averaged electron density increases to a critical value in HL-2A experiments. Figure 1 shows the temporal evolution of the density profile measured by a broadband O-mode reflectometer for a representative discharge with

author's e-mail: dingxt@swip.ac.cn

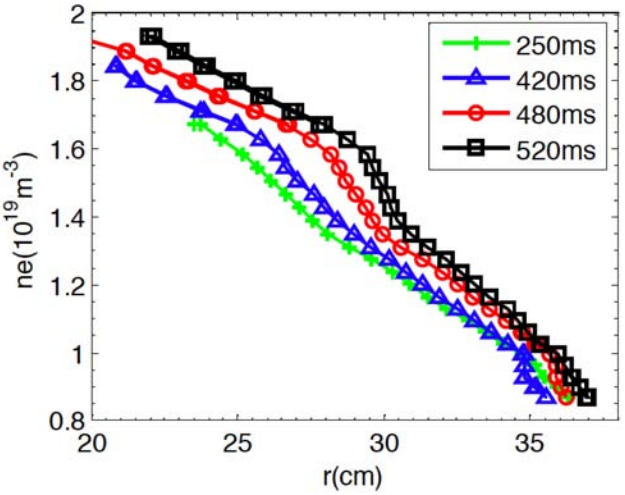

Fig. 1 Temporal evolution of the densityprofile at selected moments: before theappearance of the barrier (250 ms); at thebeginning of the appearance of the barrier(420 ms); strong barrier (480 ms); just after a particle pulse injection by SMBI(520 ms).

a transition to pITB formation. The pITB developed gradually around r = 29 cm. The critical line-averaged electron density corresponding to this transition is n_c = 2.2 × 10^{19}m^{-3}. The width of the barrier is 1-2 cm. There is a drastic change in the density gradient through the barrier: L_n ~10cm at the barrier, L_n ~ 50cm for r=20-28 cm and L_n ~25cm for r=30-36 cm.

To study the transport features of the pITB, the density modulation generated by SMBI has been employed. The modulation frequency and the pulse duration of the SMBI are 9.6 Hz and about 6 ms, respectively, while the gas pressure is 1.3 MPa in the experiments. The simulation with an analytical model for particle transport was carried out to characterize this barrier quantitatively. The phase and the amplitude of the 1st harmonic of the modulated density are displayed in Figs. 2 (a) and (b), where the solid lines and closed circles are the simulation and experimental results, respectively. The model diffusivity D and convective velocity V employed in the simulation are presented in Fig. 2(c): D_1 = 0.1 m^2/s, V_1 = 1.0 m/s in the domain I ($r < x_1$); D_2 = 0.045 m^2/s, V_2 = -2.7 m/s in the domain II ($x_1 < r < x_2$), and D_3 = 0.5 m^2/s, V_3 = 6.0 m/s in the domain III ($r > x_2$). The model apparently represents the experiment quite well. In comparison, a SMBI modulation experiment has also been performed for a discharge with a density (n_e = 1.9 × 10^{19} m^{-3}) lower than the critical density n_c. In this case, no barriers have been observed and the diffusivity obtained with the same method is D = 0.25 m^2/s for r = (28 - 31) cm. In addition, a negative convective velocity has been found as V = -2.2 m/s for r = (28 - 31) cm and V = -4.2 m/s for r = (31 - 33) cm. From the density modulation experiments, it may be concluded

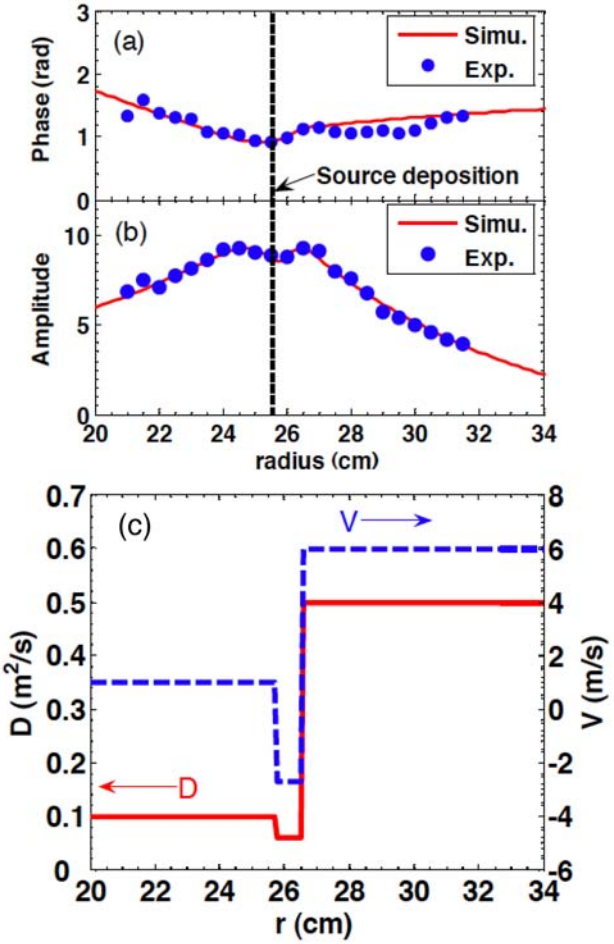

Fig. 2 Profiles of the phase (a) and amplitude (b) of the 1st Fourier harmonic of the modulated density.(c) Profiles of the diffusivity D and convective velocity V for the simulation.

that the convective velocity is negative when the density is lower than the threshold and positive when the density exceeds the threshold, except inside the barrier where the particle convective velocity remains negative. The diffusivity D is rather well-like instead of step-like.

The sign change of the convective velocity can be explained with the TEM/ITG turbulence regimes [10, 11]. The density threshold may correlate with the TEM/ITG transition via the collisionality. However, the mechanism leading to the pITB formation remains unclear at present. On the other hand, the formation of the barrier may coincide with the TEM/ITG transition. Thus, it is not excluded that the transport barrier is created initially by the discontinuity or jump in the convective velocity during the TEM/ITG transition, or more precisely, by two convective velocities in opposite direction (inward/outward) at the barrier. This speculation needs, of course, further experiments to be confirmed.

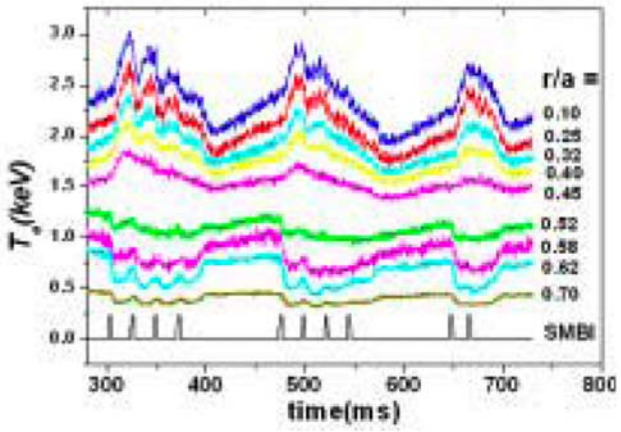

Fig. 3 Temporal evolution of T_e measured bythe ECE at different radii.

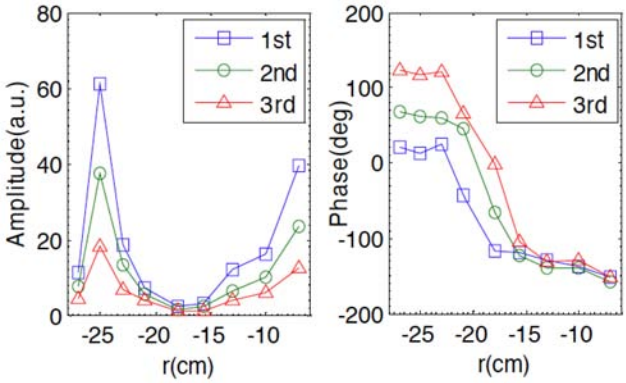

Fig. 4 Amplitudes and phases of the first three harmonics after FFT of the T_e measured by ECE(shot 8337, B_t = 1.4 T, n_e = 0.7 - 1.0 $\times 10^{19}$ m^{-3}, I_p= 180kA).

3.2 Non-local transport with SMBI

Since the first observation of the non-local electron thermal transport on TEXT-U in 1995 [12], a variety of edge cooling techniques [13–15] have been widely used in studying the effect, including impurity injection by laser ablation, ice pellet injection, carbon-based molecule injection, etc. The effect has been observed after supersonic molecular beam being injected the HL-2A tokamak. Shown in Fig.3 is the time evolution of electron temperature T_e, measured with ECE at different radii during modulated SMBI of 4 ms duration. The electron temperature sharp dropping in the edge and fast rising in the core after each SMB pulse are clearly shown. In addition, the duration of the core electron temperature rise may be prolonged by adjusting the time separation between two successive SMB pulses, which are 20 ms, 20 ms and 15 ms, respectively, for the three successive series here. Besides, both the thermal radiation and the H_α emission decrease when the non-local effect appears.

The transport properties of the non-local phenomena were analyzed with Fourier transformation of the modulated T_e measured with ECE. The results for the modulation of SMBI at f = 10 Hz are given in Fig. 4. A strong decrease in amplitude and a clear phase jump for all harmonics occur at $r \sim$ -18 cm, where the reverse of the electron temperature change takes place. The two peaks in each amplitude profile and the two corresponding troughs in each phase profile are apparent for all harmonics. These may indicate that two perturbation sources exist in the regions outside and inside the inversion radius, respectively. The position of the outer initial heat pulse was found to be at r = - 25 cm, depending on the deposition location of SMBI. The behaviour of the perturbation shows usual propagation features of SMBI cold pulse in this region. The value of $\chi_{e,HP}$ deduced from the Fourier analysis, showing agreement with the result from sawtooth pulse propagation, is in the range of (2 - 3) m^2/s. In the inner region, the initial perturbation was found to be in the core. The profiles of the amplitude and the phase of the first three harmonics are independent of the SMBI modulation frequency. The steeper profiles around the interface mean a reduction of heat transport and indicate formation of an internal transport barrier in this region. With the good flexibility and easy controllability of the SMBI parameters (gas pressure, modulation frequency, duty cycle, etc.), modulated SMBI has been proven to be an effective tool for studies of the non-local effect. Further investigation on the mechanism of the effect is undertaken on HL-2A.

3.3 Improved Confinement during Off- Axis ECRH

The investigation on the suppression of m = 2/ n = 1 tearing mode by off-axis ECRH has been performed. With the instability suppression, obvious increase of the plasma density and stored energy has been observed. A transient improved confinement was obtained after ECRH switch-off in the experiments with the ECRH power in the range of 0.6 < P_{ECRH}/P_{ohm} < 1. The interesting feature of the confinement after ECRH switch-off motivated us to apply successive ECRH pulses for sustaining MHD-free phase and obtaining a continuous confinement improvement.

The ECRH power must be deposited just around the flux surface where the m/n =2/1 magnetic islands were located in order to achieve perfect mode stabilization. The frequency and depth of the modulation were about 10 Hz and 100%, respectively, with a duty cycle of 50%. In this operation mode the maximum power that the gyrotron could deliver was limited to 250 kW. The results from two identical discharges with the ECRH power deposited at (#8207) and 3 cm inside (#8236) the q = 2 surface, respectively, are shown and compared in Figure 5. The behaviors of the line averaged density, the central electron temperature (soft x-ray), and the stored energy are the same in the two shots. The amplitude of the m/n=2/1 magnetic

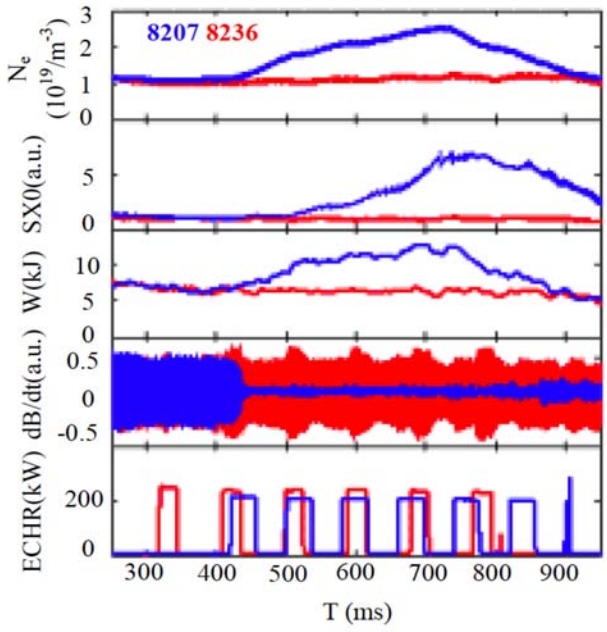

Fig. 5 Time traces of the density, the SXR intensity,the stored energy, the time derivative of thepoloidal magnetic field and the power of ECRH deposited at (the blue traces) and inside (the red traces) the q=2 surface.

fluctuations begins to decrease after the injection of modulated ECRH at 425ms in discharge #8207. Concurrently with the suppression of the tearing mode the plasma density, the stored energy, and the energy confinement time increase 80%, 50%, and 40%, respectively, indicating a significant confinement improvement. Thus, the experimental results clearly show that indeed a better suppression may be achieved with such a lower frequency modulated ECRH in the vicinity of the q = 2 surface. The suppression event is characterized by a feature of the continuous improvement of confinement, i.e. the steady increases of the plasma density, temperature, stored energy and energy confinement time throughout the modulated ECRH period.

4 Conclusions

A natural particle transport barrier has been evidenced firstly in the ohmic plasmas in HL-2A without any auxiliary heating and external momentum input. The barrier is located around r/a =0.6-0.7 with a width of 1-2 cm. A threshold in central line averaged density has been found for the observation of the particle transport barrier with n_c=2.2 $\times$ 10^{19} m^{-3}. By analysing the propagation of a particle wave, it is found that the diffusivity D is rather well-like than step-like with important reduction inside the barrier. The convection is found to be inward outside of the barrier, and outward inside the barrier.

The non-local phenomena triggered by SMBI have been observed on HL-2A firstly. The core electron temperature T_e rise increases from 18% to more than 40% and the duration of the T_e rise could be prolonged by changing the conditions of SMBs injection. Repetitive non-local effect induced by modulated SMBs allows Fourier transformation of the temperature perturbation, yielding detailed investigation of the pulse propagation. The suppression of m=2/n=1 tearing mode has been realized with heating located around q=2 surface. The continuous improvement of confinement increase steadily throughout the modulated off-axis ECRH.

Acknowledgement

This work was supported by the National Natural Science Foundation of China (Grant No.10335060) and supported partially by the JSPS-CAS Core University Program in the field of 'Plasma and Nuclear Fusion'.

[1] F. Wagner, G. Faussmann, D. Grave *et al.*, Phys. Rev. Lett. **53**, 1453 (1984).
[2] M.J. Greenwald, D.A. Gwinn, S. Milora *et al.*, Phys. Rev.Lett. **53**, 352 (1984).
[3] C.L. Fiore, J.E. Rice, P.T. Bonoli *et al.*, Phys. Plasmas **8**, 2023 (2001).
[4] E.J. Doyle, G.M. Staebler, L. Zeng *et al.*, Plasma Phys. Controlled Fusion **42**, A237 (2000).
[5] Ryter F, Leuterer F, Pereverzev G, Fahrbach H U, Stober J, Suttrop W and ASDEX Upgrade Team, Phys.Rev.Let. **86**, 2325 (2001).
[6] Ryter F. *et al.*, Plasma Phys.Contr.Fus. **48** ,B453 (2006).
[7] Garbet B. *et al.*, Plasma Phys.Contr.Fus. **46**, B557 (2004).
[8] Jacchia A, De Luca F, Cirant S, Sozzi C, Bracco G, Bruschi A, Buratti P, Podda S, Tudisco O, Nucl. Fusion **42** 1116 (2002).
[9] "Electron heated ITB in JET " G.M.D.Hogowij, *et.al.*, Plasma Physics & Control. Fusion **44**, 1155 (2002).
[10] Garbet X. Garzoti L. Mantica P. *et al.*, ., Phys. Rev. Lett. **91**, 035001 (2003).
[11] Bourdelle C. Garbet X. Imbaux F. *et al.*, ., Phys. Plasmas **14**, 112501 (2007).
[12] Callen J. D., Phys. Fluids **B4**, 2142 (1992).
[13] Gentle K. W. *et al.*, Phys. Rev. Lett. **74**, 3620 (1995).
[14] Hogeweij G. M. D. *et al.*, Plasma Phys .Contr. Fusion **42**, 1137 (2000).
[15] Zou X.L. *et al.*, ., Plasma Phys. Control. Fusion **42**, 1067 (2000).

Proceedings of ITC18, 2008

Recent results of ECRH/ECCD experiments on TCV

F. Felici, E. Asp[1)], S. Cirant[2)] S. Coda, E. Fable, T. Goodman, J. Graves, M. Henderson[3)], J. Paley, F. Piras, O. Sauter, G. Turri, V. Udintsev, C. Zucca and the TCV team

Centre de Recherches en Physique des Plasmas, Association EURATOM-Suisse, École Polytechnique Fédérale de Lausanne, EPFL, 1015 Lausanne, Switzerland
[1)]*EFDA-JET CSU, Culham, United Kingdom*
[2)]*Istituto di Fisica del Plasma, EURATOM-ENEA-CNR Association, Milano, Italy*
[3)]*ITER Organization, Cadarache, F-13108, St Paul-lez-Durance, France*

December 11, 2008

Keywords: ECRH, ECCD, MHD, plasma control, steady-state scenarios, transport barriers

1. Introduction

The Tokamak à configuration variable (TCV) [1] ($B_T <$ 1.5T, R/a = 0.88m/0.25m, $I_p \leq$ 1MA) is located at the Swiss Federal Institute of Technology (EPFL) in Lausanne. It has been conceived primarily as a platform for investigating the effects of different plasma shapes, which can be obtained thanks to a set of 16 independently powered poloidal field coils and an elongated vacuum vessel. This has allowed the study of greatly varying elongation $0.9 < \kappa < 2.8$ and triangularity $-0.6 < \delta < 0.9$.

The auxiliary heating system of TCV is comprised of a 4.5MW EC system [2]. TCV is equipped with 6 gyrotrons providing low-field side launched second harmonic X mode (X2) each 500kW, 82.6GHz and another 3 gyrotrons (500kW, 118GHz each) for top-launched third harmonic X mode heating (X3). The power from each of the X2 gyrotrons is transmitted through windowless transmission lines to a set of six independently steerable launchers. Each launcher has a series of focusing mirrors, of which the final one can move in real-time, adjusting the deposition location in the plasma during a shot. Additionally, the entire launcher assembly can be rotated around the longitudinal axis between shots to change the toroidal injection angle and allow a combination of ECH and co/counter-ECCD to be simultaneously injected in the plasma, both on- and off-axis. By injecting co-ECCD, the plasma current can be sustained non-inductively, using the ohmic transformer only for breakdown and plasma current ramp-up.

The flexibility provided by the X2 EC system is exploited in experiments on subjects such as transport barrier formation [3], [4], [5], current density profile modulation [6], fast electron physics [7], electron transport studies[8], and fully non-inductive, steady-state scenario development [9], [10], [11]. These experiments have contributed to progress in the understanding of physics aspects of EC heated plasmas. A recent, ongoing development is the integration of the ECRH/ECCD system into a digital real-time control system for TCV [12]. This has opened up the possibility for advanced real-time feedback control experiments and will offer increasing opportunities in the future. As ITER will rely on steerable EC launchers for suppression of MHD activity, this is an important line of research.

This paper will focus on several recent results of ECRH/ECCD experiments on TCV. A more complete overview of recent TCV results not specifically related to ECRH/ECCD is provided in [13]. In Section 2, results from real-time control experiments are presented which demonstrate feedback control of the sawtooth period and of the x-ray emission profile peak. Then, an overview is given of results from TCV plasmas featuring electron Internal Transport Barriers (eITBs) (Section 3). Particular attention will be devoted to plasmas with global oscillations. Finally, Section 4 will discuss how tearing modes have been created during off-axis current density profile modulation experiments, suggesting that TCV provides opportunity for studies of classical tearing mode stability and current density profile control .

2. Real-time plasma control using ECRH/ECCD

As mentioned, the angle of the final mirrors of the X2 launchers can be either driven by a feedforward reference or controlled in real-time feedback by the control system. Also the gyrotron power can be controlled in real-time. Previously, the gyrotron power has been controlled in experiments demonstrating the feedback control of ECCD current and global plasma elongation [14]. Recently, an upgraded system has been installed which allows fast ($\sim$ 10kHz) real-time analysis of diagnostic signals and subsequent control actions on local parameters such as magnetic shear[12]. The system is based on dTacq acquisition cards sharing a PCI bus with an embedded computer. Algorithms are designed and tested in

author's e-mail: federico.felici@epfl.ch

Simulink® from which C code is automatically generated and compiled on the target computer. This computer executes analysis/control algorithms and sends command signals to the DACs which control the EC system. The first applications, using the system to control the launcher injection angles, are discussed below.

2.1 Feedback control of the sawtooth period

The sawtooth instability manifests itself in Tokamaks as a periodic sudden decrease in the plasma pressure and temperature inside the $q=1$ surface. It is clearly visible in time traces of central soft X-ray chords and ECE channels as a sawtooth shaped trace. Besides causing a loss of confinement, sawteeth are also known to be possible triggers for Neoclassical Tearing Modes (NTMs) [4] and other MHD activity which may cause disruptions. On the other hand, it is likely that sawteeth will be required in burning plasmas as a mechanism for removing helium from the core [15]. For this reason, it is useful to be able to tailor the sawtooth period, either to stabilize the sawtooth – perhaps to such an extent that the sawtooth period becomes longer than the plasma lifetime– or to destabilize sawteeth, creating more frequent but less perturbing crashes.

It is well known [16] that one of the conditions for the occurence of a sawtooth crash is that the magnetic shear at the $q=1$ surface exceeds a critical limit $s_1 > s_{crit}$. As the core temperature builds up, the current carried in the core increases until the shear exceeds this limit, and the crash is triggered. The shear at the $q=1$ surface can be influenced by localized current injection, either directly by EC current drive or indirectly by local resistivity reduction using EC heating. In past TCV experiments, sweeps of the EC beams across the $q=1$ surface were used to investigate the variation of the sawtooth period, demonstrating that a maximum of the period is found as the beam is close to the $q=1$ rational surface [17]. It should be noted that another important factor determining the sawtooth period is the presence of fast particles, particularly in ICRH heated or burning plasmas [18] but also in NBI heated discharges [19]. However, since TCV does not have a neutral beam injector nor a dedicated ion heating system, fast particles play no role in TCV sawtooth stabilization

In a recent set of experiments, [20] this fact was exploited to control the sawtooth period in feedback. The sawtooth period is determined by analyzing a set of central soft x-ray channels. The period is compared to a requested reference period to generate an error signal which is fed to a controller. This controller moves the mirror of one launcher, which injects 500kW of EC power into the plasma with a combined heating and co-current drive effect. From feedforward sweeps of the mirror position, the response of the sawtooth period to the mirror angle was determined. This dependence, shown in Figure 1, is nonlinear with a clear peak as the deposition location moves from outside to inside the $q=1$ surface. Also, an hysteresis effect can be observed due to the global current density and q-profile modifications as the EC absorption location moves radially. Attention is focused on controlling the sawtooth period while moving the deposition location on the outside of the $q=1$ surface, thus staying on one side of the peak. However, in this region the response is the most nonlinear as can be observed from the increasing slope of the response. This results in an increased gain of the system to be controlled. As is well known from linear control theory [21], using a simple linear controller such as a PID controller may lead to instability if the system gain increases. Reducing the controller gain will however lead to a slow response of the closed-loop system.

In order to be able to obtain different sawtooth periods with the same controller, a nonlinear gain-scheduling controller was designed which moves the mirror at two different speeds depending on the requested sawtooth period. Figure 2 shows the performance and effectiveness of this controller. In the initial phase of the discharge, ECH is turned on with the controller off. The heating location was chosen such that the sawtooth period would increase and exceed the requested period. Then, the controller is switched on and moves the mirror away from the $q=1$ surface to obtain a smaller sawtooth period as requested. After some time, the target period is increased. The mirror then rapidly moves closer to the $q=1$ surface to increase the period. Initially, no change in period is observed due to the mentioned hysteresis effect, however after a while the requested period is obtained and maintained. This provides a demonstration of the possibility to control the sawtooth period in real-time feedback using EC deposition.

2.2 Feedback control of emission profiles

Another application of the real-time feedback of the EC injection angle is the control of profiles in TCV. As the deposition can be steered on- and off-axis simply by pointing the mirror angle towards or away from the plasma center, broader or more peaked profiles can be realised. As TCV lacks a real-time current density profile measurement and the ECE profile is not always straightforward to interpret due to insufficient optical thickness of the plasma, the most readily available diagnostic is the DMPX soft X-ray diagnostic situated at the bottom of the vacuum chamber. It provides good spatial and temporal resolution with 64 lines-of-sight at $<$ 200kHz [22]. All the DMPX channels are read by the real-time algorithm which filters the signals and performs a spline fit to obtain a profile. From the result of the spline fitting, one can derive other quantities – such as the total emission, the peak emission or the relative profile width – any of which can be chosen as control variables.

In a first experiment, the value of the peak emission (defined as the maximum value of the spline fitted profile) was controlled using a single gyrotron and launcher, set to 0° toroidal angle so providing mainly heating. The de-

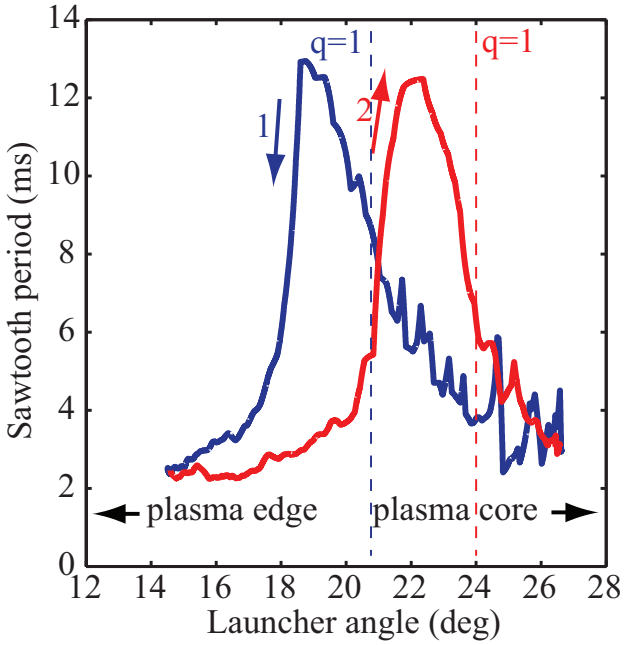

Fig. 1 TCV pulse #35807, Response of the sawtooth period to mirror angle sweep. As the mirror moves across the $q=1$ surface the period peaks and then decays again. The gradient of the curve varies greatly as one approaches the peak. Note that the $q=1$ surface moves during the sweep due to global changes to the current density profile, causing a hysteresis effect.

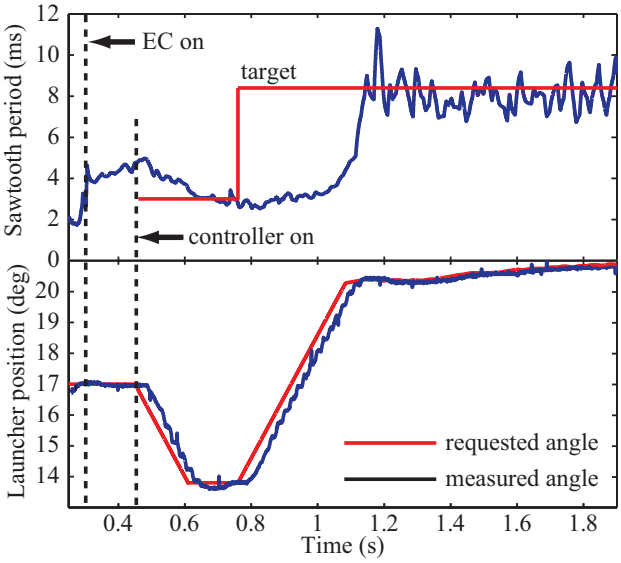

Fig. 2 TCV pulse #35833, demonstrating control of the sawtooth period using a nonlinear, gain-scheduling controller. As soon as the controller switches on the mirror moves to decrease the sawtooth period as is requested. A short time later, the requested period is changed to a higher value. The mirror moves as to move the deposition towards the plasma core in order to increase the sawtooth period. Initially, the period does not change due to the hysteresis effect illustrated in Figure 1.

tected profile peak is subtracted from a reference value and the result is fed into a PI controller. The controller then steers the launcher mirror such that the deposition is closer to the center (to increase the emission peak), or moved off-axis (to decrease it). The controller gains were chosen based on a rough model estimated from a previous pulse where a scan of the mirror angle was done using feed-forward control of the mirror position and were tuned only slightly between experiments. Unlike early tokamak experiments in which the EC *power* was controlled to change the central temperature, the controller here steers the injection angle to achieve the same objective.

Figure 3 demonstrates that the controller successfully obtains two different reference values during the shot. At 0.25s, the gyrotron is switched on while the launcher angle is set at a fixed angle. At 0.4s, the feedback controller is activated and attempts to reduce the peak by moving the deposition location more off-axis. When the reference value is reached, the movement stops. The reference is then increased and the controller responds by moving the launcher back, to provide more central heating. After the control is switched off the peak does not change much since the angle coincidentally stays at a preprogrammed position not far from where it ended up during the feedback control phase.

With these results as a starting point, this methodology will be extended in the next TCV campaign to allow control of several parameters of the emission profiles by varying in real-time the deposition location and power of several gyrotrons.

3. Scenarios with eITBs

Internal electron transport barriers (eITBs) manifest themselves as a marked increase of the core electron temperature and density, resulting in confinement properties superior to L or H modes. Confinement enhancements of 3-6 above the standard L-mode confinement scaling of TCV have been obtained. eITBs are routinely created in TCV discharges in a variety of conditions, including a) fully non-inductive scenarios and b) stationary discharges with a large EC current drive and bootstrap current component, combined with ohmic current [23] [3] [11] [4]. Typically, these plasmas have low density ($\sim 10^{19}\mathrm{m}^{-3}$) and current ($\sim$ 100kA). In previous TCV campaigns, it was demonstrated for the first time unambiguously that the essential requirement for obtaining eITBs is the presence of a negative shear region in the plasma center, and that increasingly negative shear leads to increasing core electron confinement [24]. This was demonstrated by inducing current density profile perturbations with neglibible input power using the ohmic transformer during fully non-inductive scenarios featuring eITBs and it has been confirmed by detailed modeling in [25]. Additionally, precise tailoring of the current and pressure profiles has allowed plasmas to be sustained having 100% bootstrap current in steady

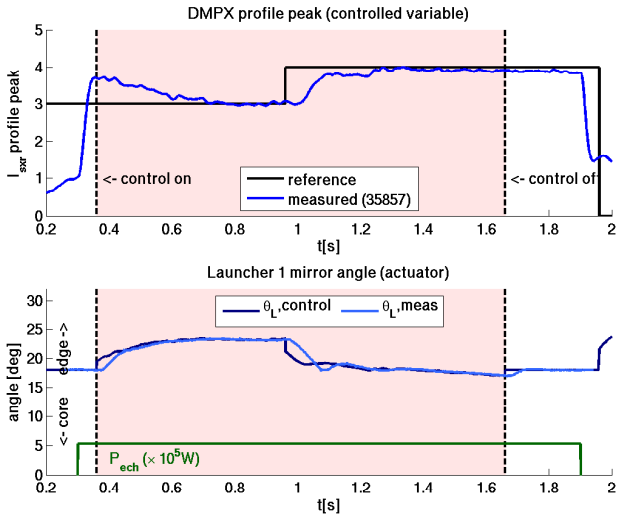

Fig. 3 Control of X-ray emission profile peak. A step reference is given to the controller, which adjusts the mirror angle to obtain more on- or off-axis deposition. The measured mirror angle lags slightly behind the controller reference due to the launcher mechanics and protection filters. The peak traces shown are the result of low-pass filtering and spline fitting of several DMPX channels.

state, lasting over several current redistribution times [26]. Plasmas featuring ITBs are promising candidates for long-pulse steady-state operation in advanced tokamak scenarios as they have a high bootstrap current fraction and good confinement properties. However, these scenarios are often affected by MHD activity, due to the proximity to the infernal stability limit. The interplay between this MHD activity and the eITB can lead to global oscillations of several plasma quantities [5], [27]. In order for ITB scenarios to be applicable to reactor-grade plasmas, such oscillations need to be investigated and methods for their suppression need to be assessed. TCV experiments have focused on these modes and have demonstrated how they can can be suppressed by perturbations of the current density profile.

3.1 Global plasma oscillations

Global oscillations are present in TCV discharges featuring eITBs with strong ECRH/ECCD [5], [27]. These oscillations are caused primarily by the presence of a strong pressure gradient in a region of low magnetic shear. In this case, it can be shown that the eITB plasmas are close to the ideal MHD limit, and so-called *infernal* modes [28] can be triggered. These modes then lead to a confinement degradation and a weakening of the transport barrier. The subsequent reduction of the bootstrap current – which forms a significant part of the total current fraction – leads to a global modification of the current density profile such that the MHD modes are suppressed, the reverse shear region is recovered and the transport barrier is formed again [5]. This cyclic behaviour manifests itself as an oscillation of plasma current, temperature, density and/or radial position, with a frequency of the order of $\sim$10Hz. Depending on the closeness to the ideal limit, the MHD modes may be of resistive (tearing) nature or ideal (crash-like) nature. Similar instabilities have been observed in other Tokamak experiments, notably Tore-Supra, [29] and TRIAM-1M [30]. Recent TCV experiments demonstrated how these oscillations can be suppressed or triggered by modifications of the current density profile.

3.2 Suppression of oscillations using current perturbations

In the experiments described below, eITBs were obtained by strong (typically 1.5MW) off-axis co-ECCD This creates the hollow current density profile required for the formation of the barrier. On-axis heating is also applied to increase the core temperature. Often this central heating is combined with a small counter-current drive component in order to make the current density profile more hollow and the transition more pronounced. Based on this scenario, several methods were tested to perturb the current density profile [27] [5]. The most straightforward perturbation method is the addition of more co-ECCD in the core. In one particular experiment 0.25MW of on-axis co-ECCD was added, effectively making the current density profile less hollow and resulting in a reduction of the barrier and the suppression of the oscillatory regime.

In a second experiment, illustrated in Figure 4, the oscillatory regime was again triggered in a fully non-inductive discharge with 1.5MW of ECCD off-axis and one centrally heating gyrotron with a counter-current drive compoment. This time, however, the co-ECCD power is gradually reduced from 1.5MW to 0.6MW between 1.5s and 2s. In this case, the oscillatory regime is suppressed, but this time it does not lead to a loss of the barrier. The reason for the suppression of the global oscillations has been found by studying the change in q profile due to the change of driven off-axis current. Since TCV does not have a direct measurement of the current density profile, the profiles were modelled by ASTRA [31] transport simulations combined with the CQL3D code [32] to calculate the ECCD current density profile. The result of these simulations is that the q profile minimum is close to 3 (within simulation error bars) in the initial oscillatory phase, but tends to increase as the off-axis ECCD decreases. The main resistive MHD mode (identified as $m/n = 3/1$) is therefore suppressed and the plasma oscillations disappear [27].

The change in ECCD power which causes the suppression of the oscillatory regime not only affects the current density profile, but inevitably also changes the total power deposition. For this reason, a different set of TCV discharges were performed using the ohmic transformer to induce co- or counter current in the plasma. As the plasma conductivity is highest in the center, this perturbation is peaked on axis and significantly affects the reverse shear

responsible for the barrier. It is important to note that ohmic current drive is an order of magnitude more efficient than ECCD, therefore the additional ohmic power is negligible. This experimental method, previously used to prove the link between transport barriers and hollow current density profiles, has also been applied to experiments for suppression of the oscillatory regime [5]. Depending on the sign of the ohmic current perturbation, the plasma can evolve in two different ways. In the case where counter current drive is induced, (making the current density profile more hollow) the barrier strength is increased and the plasma further approaches the ideal MHD limit. In this case, a minor disruption often follows, degrading or destroying the barrier and reducing the confinement. The eITB then recovers with a different q profile which can be oscillation-free. In the opposite case, where co-current drive is induced (making the current profile less hollow) the barrier strength is reduced. This reduces the β_N and the proximity to the MHD limit. The MHD mode is seen to disappear and the plasma maintains good confinement, albeit with a weaker transport barrier. In Figure 5, an example of the latter case is shown. Towards the end of this fully non-inductive discharge, a positive current perturbation (~ 60mV) is added. The low frequency MHD mode, which was initially responsible for the oscillatory plasma behaviour disappears. The central SXR trace shows that the oscillations stop while the barrier is maintained. This is confirmed by comparing Thomson profile measurements before and after the ITB phase [5]. Comparing the case with ECCD (Fig. 4) and ohmic current (Fig. 5) perturbations show that it is indeed the modification of the current density profile which is the key and not the actuators used.

These experiments provide insight into the dynamics of the global plasma oscallations in high-performance eITB scenarios and how they can be avoided. The results suggest that careful tailoring of the current density profile will be necessary in advanced tokamak scenarios in order to maintain a steady-state barrier.

4. Tearing mode triggering by current density profile tailoring

As a final example of the application of ECCD for current density profile modifications in TCV, we illustrate a series of experiments devoted to the modulation of the current density profile. In these so-called Swing-ECCD experiments, two groups of up to three gyrotrons each are set up such as to drive either co- or counter current at the same radial location in the plasma. The power of these two groups is then modulated, one group being on while the other is off. By taking care to carefully align the deposition locations from the different gyrotrons, it was possible to perform experiments modulating the current density profile only, keeping the total injected power constant. The objective of these experiments was to demonstrate the effect of the shear profile on elecron transport. The results of

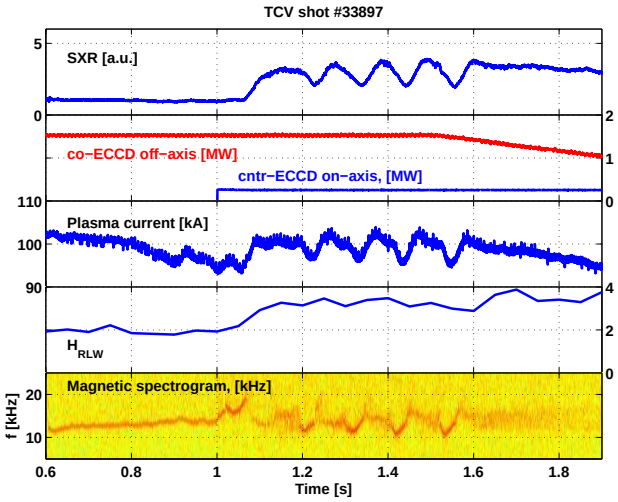

Fig. 4 Perturbation of the current density profile during an eITB discharge by ramp-down of the co-ECCD power combined with counter-ECCD on-axis. The disappearance of the MHD mode is attributed to the dissappearane of the $q = 3$ resonant surface. As can be seen from the SXR measurements, a weaker, oscillation-free barrier remains during the rampdown.

these experiments are detailed in [6] and will not be treated here. During these experiments, however, MHD modes were occasionally visible. These modes are identified as magnetic islands from soft x-ray channel signatures. It is well known that tearing modes can be destabilized classically when Δ' becomes positive [33]. The Δ' parameter depends on the local q profile and its derivatives, which is why local current density perturbations affects the classical tearing stability [34],[35]. Cylindrical tearing stability simulations of the TCV experiments have confirmed that this stabilization or destabilization effect can be achieved with the ECCD injected and it depends on both the direction of the induced current and the location of the current deposition with respect to the rational q surface. It is interesting to perform systematic experiments and comparison with theoretical predictions on the stabilization/ destabilization of tearing modes via localized current drive, not necessarily inside the island as is usually done for tearing mode stabilization and as is forseen in ITER. This should shed further light on the triggering mechanisms determining the onset of tearing modes and methods to prevent and/ or suppress them. These issues will be a focus in coming TCV experiments.

5. Summary and conclusions

This paper has provided an overview of recent experimental results in TCV plamas featuring ECRH/ECCD. Thanks to the localized deposition provided by ECRH or ECCD, many different effects arising from current density and temperature profiles modifications have been studied. Notably, the recent upgrades to the TCV control system have

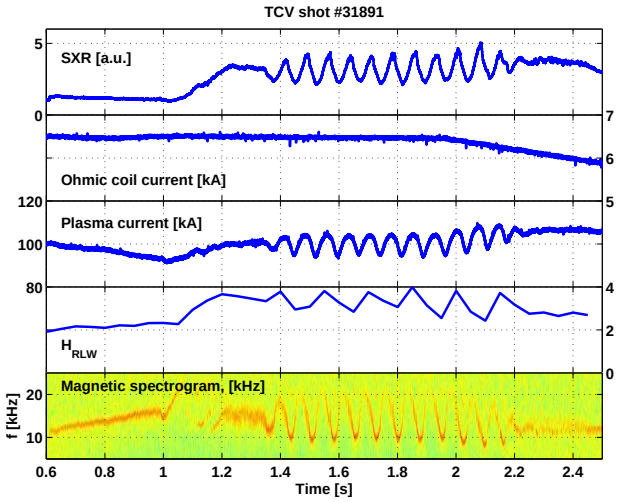

Fig. 5 Perturbation of the current density profile during an eITB discharge by co current induced by the ohmic transformer. The current density profile becomes less hollow, leading to a reduced barrier strength, reduced proximity to the MHD limit and disappearance of the MHD mode responsible for the global plasma oscillations. The gyrotron power does not change throughout the shot.

opened the way to advanced real-time feedback control experiments, demonstrating feedback control of the sawtooth period using a nonlinear controller and preparing the way for further feedback control of both current density and pressure profiles. Much attention has been devoted to scenarios featuring internal electron transport barriers. The fundamental role played by hollow current density profiles in the sustainment of transport barriers has been demonstrated. Furthermore, 100% bootstrap fractions have been achieved in which the bootstrap current profile and the high pressure gradient region are spontaneously well-aligned. In addition, global plasma oscillations often present in high-confinement discharges with eITBs have been studied, revealing that they are intrinsically linked to the appearance of modes due to the proximity to the ideal MHD limit. It has been shown that these modes can be suppressed in a variety of ways by changing the current density profile without necessarily losing the barrier itself. Finally, tearing modes appearing during shear modulation experments indicate that TCV can be a valuable tool for detailed studies of current drive effects on tearing mode stability.

Acknowledgements

This work was supported in part by the Swiss National Science Foundation.

[1] F. Hofmann et al., Plasma Physics and Controlled Fusion **36**, B277 (1994).
[2] T. Goodman and the TCV team, Nuclear Fusion **48**, 054011 (2008).
[3] M. A. Henderson et al., Physical Review Letters **93**, 215001 (2004).
[4] O. Sauter et al., Plasma Physics and Controlled Fusion **44**, 1999 (2002).
[5] G. Turri, V. S. Udintsev, O. Sauter, T. P. Goodman, and E. Fable, Plasma Physics and Controlled Fusion **50**, 065010 (2008).
[6] S. Cirant et al., Modulated ECCD experiments on TCV, in *21th IAEA Fusion Energy Conference*, 2006, Paper EX/P3-3.
[7] S. Coda et al., Nuclear Fusion **43**, 1361 (2003).
[8] Y. Camenen et al., Nuclear Fusion **47**, 510 (2007).
[9] O. Sauter et al., Phys. Rev. Lett. **84**, 3322 (2000).
[10] S. Coda et al., Plasma Physics and Controlled Fusion **42**, B311 (2000).
[11] T. P. Goodman et al., Plasma Physics and Controlled Fusion **47**, B107 (2005).
[12] J. Paley et al., Real time control of plasmas and ECRH systems on TCV, in *IAEA Conference 2008*, 2008.
[13] A. Fasoli, Overview of physics research on the TCV tokamak, in *IAEA Conference 2008*, 2008.
[14] J. I. Paley, S. Coda, and the TCV Team, Plasma Physics and Controlled Fusion **49**, 1735 (2007).
[15] T. Hender et al., Nuclear Fusion **47**, S128 (2007).
[16] O. Sauter et al., Phys. Rev. Lett. **88**, 105001 (2002).
[17] C. Angioni, T. Goodman, M. Henderson, and O. Sauter, Nuclear Fusion **43**, 455 (2003).
[18] J. P. Graves et al., Plasma Physics and Controlled Fusion **47**, B121 (2005).
[19] C. Angioni et al., Plasma Physics and Controlled Fusion **44**, 205 (2002).
[20] J. I. Paley, F. Felici, S. Coda, T. P. Goodman, and F. Piras, Submitted to Plasma Physics and Controlled Fusion (2008).
[21] K. Ogata, *Modern Control Systems*, Prentice Hall, 4th edition, 2002.
[22] A. Sushkov et al., Review of Scientific Instruments **79**, 023506 (2008).
[23] Z. A. Pietrzyk et al., Phys. Rev. Lett. **86**, 1530 (2001).
[24] O. Sauter et al., Physical Review Letters **94**, 105002 (2005).
[25] C. Zucca et al., Plasma Physics and Controlled Fusion **51**, 015002 (2009).
[26] S. Coda, O. Sauter, M. Henderson, and T. Goodman, Fully bootstrap discharge sustainment in steady state in the TCV tokamak, in *IAEA Conference 2008*, 2008.
[27] V. S. Udintsev et al., Plasma Physics and Controlled Fusion **50**, 124052 (2008).
[28] T. Ozeki, M. Azumi, S. Tokuda, and S. Ishida, Nuclear Fusion **33**, 1025 (1993).
[29] G. Giruzzi et al., Phys. Rev. Lett. **91**, 135001 (2003).
[30] K. Hanada et al., (2004).
[31] G. V. Pereverzev, IPP Report 5/42, Max Planck - IPP, 1991.
[32] R. W. Harvey and M. G. McCoy, in *Proc. IAEA TCM/Advances in Simulation and Modeling in Thermonuclear Plasmas*, Montreal, 1992.
[33] H. Furth, P. Rutherford, and H. Selberg, The Physics of Fluids **16**, 1054 (1973).
[34] E. Westerhof, Nuclear Fusion **27**, 1929 (1987).
[35] O. Sauter et al., in *Theory of Fusion Plasmas (Varenna 1998), ISPP-18*, page 403, Bologna, Italy, 1999, Editrice Compositori.

Proceedings of ITC18, 2008

Optimization of the accelerators for the ITER Neutral Beam Injector project

V. Antoni, P. Agostinetti, M. Cavenago[a], H.P.L. de Esch[b], G. Fubiani[c], N. Pilan, G. Serianni, P. Veltri and the NBI RFX Team

Consorzio RFX Euratom-ENEA Association, Padova, Italy

[a]INFN-LNL, Legnaro, Italy

[b]Association EURATOM-CEA Cadarache, IRFM/SCCP, France

[c]CNRS, LAPLACE, F-31062 Toulouse, France

M. Kashiwagi, M. Taniguchi, N. Umeda, T. Inoue

Japan Atomic Energy Agency, Japan

A joint Japan-EU R&D activity is in progress to optimize the accelerator for the ITER NBI. The accelerator baseline design is based on a five grids system which can be adapted to operate with three grids for initial operations at low voltage (500 kV). Moreover, in order to speed up the test of the NBI system at the Test Facility, a negative ion source with extraction voltage up to 100kV will be operated in parallel to the full injector. In this contribution the three accelerators mentioned above are presented discussing the procedure to optimize the grid geometry in order to assure optimum optics during operation when the grids undergo deformations and thermal stresses due to the particles that hit their surface

Keywords: ITER, heating and current drive, negative ion acceleration

1. Introduction

Two Neutral Beam Injectors (NBI) are foreseen in ITER in order to deliver a total of 33 MW of heating power. Each NBI is designed to operate at 1 MV and 40 A current in Deuterium and at 870 kV and 46 A in Hydrogen [1,2]. In recent years a joint revision of the NBI design for ITER performed by the Japan and EU Domestic Agencies in close contact with ITER has led to important changes which have improved the availability and reliability of the NBI system [3]. The insertion of an absolute gate valve between the NBI and the duct and the modification of the Beam Line Vessel with possibility of vertical access, have improved the availability of the system while shortening the time required for maintenance and repair in case of fault. The adoption of the air insulated High Voltage deck and the choice of the RF Ion Source have led to less demanding maintenance in particular for the source which does not require replacements of the filaments as it was for the arc driven source. Passive and active protection systems for the accelerator grids and power supplies are now implemented in the project therefore improving the reliability of the system. Finally the design of the Test Facility to be built in Padova and aimed to test and optimize the NBI and to assist the operations in ITER has been almost completed [4]. A robust R&D program is in progress at the 1 MV test facilities in Naka (JAEA) and Cadarache (CEA) to tackle and solve the remaining issues related to High Voltage holding and particle acceleration in the 1 MV range [5,6,7]. To assess a multi-aperture multi-grid (MAMuG) and a single-aperture single-gap (SINGAP) accelerator [8] concepts at the same test facility with the same diagnostics, a collaborative R&D was performed between JAEA and CEA Cadarache under an ITER task agreement. As a result of better voltage holding and less electron acceleration, the MAMuG was confirmed as the baseline design for ITER [5,7]. All these activities have led to a better understanding of the physics of the 1 MV accelerator and of the negative ion extraction which have allowed the accelerator design to be further advanced as discussed in the following.

2. The accelerator design

In the ITER NBI baseline design the accelerator is a MAMuG system based on five grids [9]. In order to provide auxiliary heating to the initial operation of ITER in Hydrogen at relatively low current, it has been proposed to operate one of the NBI as a three grid system at a reduced voltage of 500 kV. It has been verified that

author's e-mail: vanni.antoni@igi.cnr.it

the present grid support structure and power supply layout can easily be adapted to a three grids system. In this contribution three accelerators of interest for ITER, namely the five-grids 1 MV accelerator in the reference design, the three-grids 500 kV accelerator foreseen for initial operations and the single grid 100 kV accelerator to optimize the extraction in the Ion Source are presented. The criteria and the method applied to optimize the accelerator design are described. In particular the design of the accelerator grids has to provide optimum perveance, compatible with the finite size of the grids due to the cooling channels and the insertion of permanent magnets required to deflect the unwanted electrons co-extracted from the source or generated by stripping losses. The thermo-mechanical analysis of the grids has been performed by taking into account the power load due to co-extracted and secondary electrons. In order to minimize the grid bending and the thermal stresses the grids are actively cooled and the cooling channels have been carefully designed in order to be accommodated in a relatively narrow space.

The optimization process is therefore based on a sequence of the following steps which are reiterated up to final convergence:

a) The initial electric field distribution is computed.
b) The magnetic field distribution as obtained from the combination of magnetic filter and permanent magnets inserted in the grids is added
c) The particle trajectory is computed.
d) The interaction with the background gas is simulated by evaluating the stripping losses and the generation of secondary particles due to interaction of primary particles with material surfaces.
e) The new electric field distribution due to the charge distribution and the related trajectories are calculated up to convergence.
f) The thermal load due to ions and electrons intercepting the grids is evaluated and the deformation, when the cooling is applied, evaluated. The design of the grids (cooling channels size and layout and position of permanent magnets) is modified in order to minimize the deformation.
g) Steps from a) to f) are repeated until an optimum configuration is obtained for a single or a couple of beamlets.
h) Interaction among beamlets is evaluated to compensate for the divergence of the beamlets by a suitable mechanical displacement of the apertures

These steps are accomplished using different codes. The electric field and the initial trajectories are computed by using the code SLACCAD [10,11] and then by adding the magnetic field distribution. Recently a new code BYPO [12], which solves in a self-consistent way the trajectories with an initial distribution of magnetic and electric field, has been developed and the results applied to benchmark the results of SLACCAD. The interaction of the particles with background gas and material surfaces are described by the Monte Carlo Code EAMCC [13]. The thermal analyses are performed by using ANSYS. Finally the beamlet-beamlet interaction is studied by using the code OPERA [14]. This procedure has been applied to the optimization of the highest priority accelerator, namely the 100kV one, as in the present planning it is expected to enter into operation in three years from approval. This accelerator shares several characteristics with the accelerator required by the diagnostic neutral beam (DNB) [9] for operation in Hydrogen, so that the initial development of the accelerator has been performed in parallel with that of the DNB. The main requirements of this accelerator are a current of 60 A H^- (and later 40 A D^-) and an energy of 100 keV. In Fig. 1 a comparison of the beam profile for the three accelerators is shown.

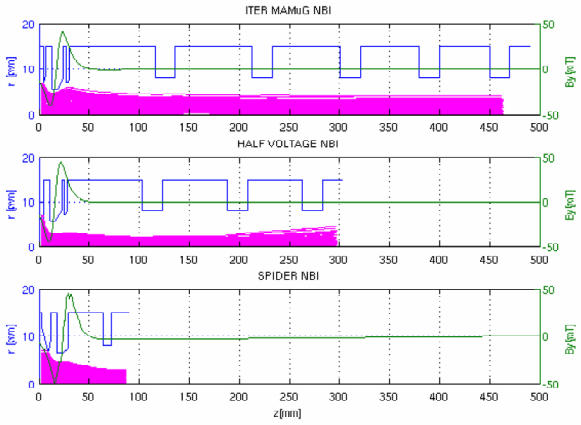

Fig. 1 - Ion beam trajectories simulated with SLACCAD. The aperture profiles and the magnetic field due to suppression magnets are also sketched.

3. Study of the beam optics

All three accelerators operate with multi-aperture grids biased at different potentials. Each grid features 1280 apertures. All systems have a Plasma Grid (PG) and an Extraction Grid (EG) at approximately 10 kV. The accelerations steps are respectively:

- 5 acceleration grids for ITER MAMuG (5 acceleration steps of 200 kV each)

- 3 acceleration grids for ITER Half-Voltage (3 acceleration steps of about 160 kV)
- 1 acceleration grid for SPIDER (a single acceleration step of 90 kV)

The interactions among particles inside the accelerator, like secondary particle production processes, are studied by the code EAMCC [13]. This is a 3-dimensional (3D) relativistic particle tracking code which allow macroparticle trajectories, in prescribed electrostatic and magnetostatic fields, to be calculated inside the accelerator. In the code, each macroparticle represents an ensemble of rays. This code needs as inputs the electric and magnetic fields inside the accelerator. The former was calculated with SLACCAD, as explained above. The latter was calculated by summing the field given by the SmCo permanent magnets and the field from the plasma grid filter current (calculated by assuming an infinitely thin electron sheath). Collisions are described using a Monte-Carlo method. Several types of collisions are considered in the code: (i) electron and heavy ion/neutral collisions with grids, (ii) negative ion single and double stripping reactions and (iii) ionization of background gas.
In Fig. 2 the trajectories of negative ions and stripping loss electrons for a single beamlet are shown. The corresponding thermal load is also shown [15].

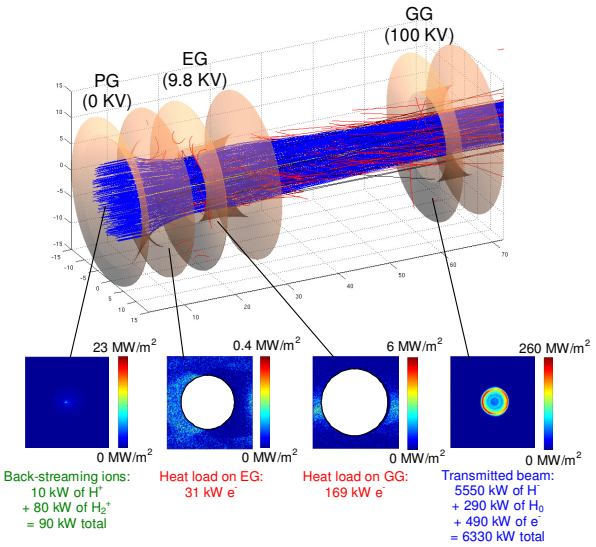

Fig. 2 - EAMCC simulation of negative ion beamlet in the 100 kV accelerator: the particle trajectories and stripping reaction are simulated with a Monte Carlo approach in a domain with electrical and magnetic fields. The power corresponding to the whole accelerator (1280 beamlets) is reported.

The transmitted beamlet power distribution features a ring that is hotter than the central part. These could be due to the chamfered shape of the PG apertures. In fact, this effect is reversed in case of a flat PG surface [15].
The backstreaming positive ions are concentrated in the center of the aperture area. The consequent heat power density is quite high, as it covers only an area of some tens of square millimeters. These ions could give rise to sputtering phenomena on the plasma source back plate and on the driver Faraday shields, with a consequent decay of the plasma purity and problems of surface integrity. The sputtering yield due to the backstreaming deuterium ions is generally reduced by a factor of about 5 if the copper surface is coated with Molybdenum. Hence, in order to minimize the detrimental effects consequent to sputtering, a layer of Molybdenum of some microns is foreseen to be applied on the plasma source back plate.

4. Thermo-mechanical optimization

The accelerator grids must be designed in such a way that the corresponding apertures stay well aligned during all the operating scenarios, in order to maintain good beam optics. For this reason and for manufacturing requirements the grids are vertically split in four segments, independently supported with a fixed pin at the left side and with a sliding pin at the right side [16]. For optical reasons, the maximum allowable misalignment between the corresponding apertures of the three grids is fixed to 0.4 mm, whose 0.2 mm due to thermal expansion.
The grids have also to withstand two categories of stresses: a) Cyclic thermal stress due to the temperature gradients between hotter and colder zones. These stresses must be maintained low in order to satisfy the requirement on fatigue life. b)Static stress due to the water pressure. The local values of equivalent stress must be lower than the allowable values for electrodeposited copper (fixed at 100 MPa). The position and dimensions of the cooling channels, as well as the water flow, must be optimized in order to satisfy all the requirements on alignment and stresses according to the ITER criteria [17] and in all foreseeable scenarios (conditioning, partial power, full power etc.).
Several analyses have been performed to estimate the temperatures and stresses along the grids [18]. It was found that the thermal stresses are causing also an out-of-plane deformation of the grids. The analyses have shown that these deformations can be minimized in order to keep within tolerable values the increase in the beam divergence.

5. Compensation of Beamlet repulsion

As one of the techniques applied to compensate beamlet deflection due to the beamlet-beamlet interaction, aperture offset was examined numerically in a three grid accelerator at 500 kV in JT60U [19]. The trajectories of fifty beamlets from 10 x 5 apertures were traced utilizing the three dimensional beam analysis code, OPERA-3d. Fig. 3 shows the calculated beam footprints at 3.5 m downstream from the grounded grid. In Fig. 3a, the centers of all calculated beamlets are represented by points. They moved outward from the aperture positions due to the beamlet-beamlet interaction. The maximum deflection angle was 6 mrad in beamlet coming from peripheral apertures. The proper aperture offset to compensate 6 mrad of beamlet deflection was evaluated to be 0.7 mm according to thin lens theory. Fig. 3b shows that all beamlets stay in the positions extrapolated from the apertures by proper aperture offset at the bottom of extractor. The results have shown that a proper aperture offset within 1 mm is enough to correct the beamlet deflection by the beamlet-beamlet interaction. This compensation technique is to be applied to design 100 kV, 500 kV and 1 MeV accelerators.

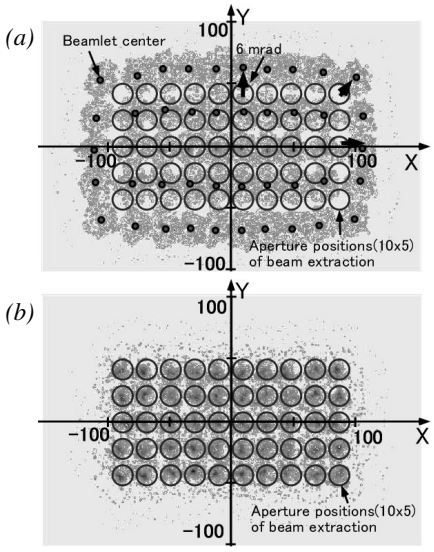

Fig. 3 - Calculated beam footprints at 3.5 m downstream from the grounded grid (a) before and (b) after proper aperture offset in the extractor. The beam parameter is 110 A /m^2 of D$^-$ ion beam current density and 340 keV at beam energy. Opened circles represent the original aperture positions.

6. Conclusions

The better understanding of the physics and the numerical tools available allow the optimisation of the accelerators for ITER to be carried out.

The procedure to optimize the 100 kV accelerator for ITER has been described with the present design of the accelerator. Using this procedure, the design of the extraction and acceleration system for the ITER NBI and related experiments can been accomplished by taking into account at the same time physics and engineering requirements.

References

[1] R. S. Hemsworth *et al*. Neutral beams for ITER. Rev. Sci. Instrum. 67, Issue 3, 1120 (1996).
[2] T. Inoue *et al*. Design of neutral beam system for ITER-FEAT, Fus. Eng. and Design 56-57 (2001) 517-521
[3] R.S. Hemsworth *et al*. Rev. Sci. Instrum. 79, 02C109 (2008).
[4] P. Sonato *et al*. The ITER full size plasma source device design. 25th Symposium on Fusion Technology,15-19 September 2008, Rostock, Germany.
[5] M. Taniguchi *et al*. Development of 1 MeV H- accelerator at JAEA for ITER NB, to be published in Conf. Proc. of American Inst. Phys. 2008.
[6] H.P.L De Esch *et al*. Results of the SINGAP neutral beam accelerator experiment at JAEA, to be published to Fusion Eng. Design.
[7] M. Kashiwagi *et al*. R&D progress of high power negative ion accelerator for ITER NB system at JAEA, to be published to Nuclear Fusion.
[8] H.P.L. de Esch, R.S. Hemsworth and P. Massmann. Updated physics design ITER-SINGAP accelerator. Fusion Eng. Des. 73 (2005) 329.
[9] ITER Technical Basis 2002, Neutral beam heating & current drive (NB H&CD) system, Detailed Design Document (section 5.3 DDD5.3) (Vienna: IAEA)
[10] J. Pamela. A model for negative ion extraction and comparison of negative ion optics calculations to experimental results. Rev. Sci. Inst. 62 (1991) 1163.
[11] W.B. Hermannsfeld. Electron Trajectory Program, SLAC report, Stanford Linear Accelerator Center, SLAC-226 (1979)
[12] M. Cavenago *et al*. IEEE Trans. Plasma Sci. 36, 1581 (2008)
[13] G. Fubiani *et al*. Modeling of secondary emission processes in the negative ion based electrostatic accelerator of the International Thermonuclear Experimental Reactor. Phys. Rev. Special Topics Accelerators and Beams 11, 014202 (2008)
[14] "OPERA-3d", Vector Fields Co.Ltd.
[15] P. Agostinetti *et al*. Design of a low voltage, high current extraction system for the ITER Ion Source. AIP Proceedings of the 1st International Conference on Negative Ions, Beams and Sources, 2008, Aix en Provence, France.
[16] D. Marcuzzi *et al*. Detail design of the RF Source for the 1 MV Neutral Beam Test Facility. 25th Symposium on Fusion Technology,15-19 September 2008, Rostock, Germany.
[17] Various Authors. ITER MPH. Material Properties Handbook. ITER Document No. G 74 MA 16.
[18] P. Agostinetti, S. Dal Bello, M. Dalla Palma and P. Zaccaria. Thermomechanical design of the SINGAP accelerator grids for ITER NB Injectors. Fusion Eng. Des. 82 (2007) 860-866.
[19] M. Kashiwagi *et al*. Compensation of beamlet repulsion in a large negative ion source with a multi aperture accelerator. AIP Proceedings of the 1st International Conference on Negative Ions, Beams and Sources, 2008, Aix en Provence, France.

Proceedings of ITC18,2008

The development of 6 MeV Heavy Ion Beam Probe system in LHD

A. Shimizu, T. Ido, M. Nishiura, S. Nakamura, H. Nakano, S. Ohshima[1)], A. Nishizawa, M. Yokoyama, Y. Yoshimura, S. Kubo, T. Shimozuma, H. Igami, H. Takahashi, N. Tamura, I. Yamada, T. Minami, K. Narihara, T. Akiyama, T. Tokuzawa, K. Tanaka, K. Kawahata, K. Toi, M. Isobe, F. Watanabe, K. Ogawa, K. Nagaoka, K. Ikeda, M. Osakabe, K. Tsumori, Y. Takeiri, O. Kaneko, S. Kato, M. Yokota, Y. Hamada, LHD Group

National Institute for Fusion Science, 322-6 Oroshi-cho, Toki, Gifu 509-5292, Japan

[1)]Osaka University, 2-6 Yamadaoka, Suita, Osaka 565-0871, Japan

The 6 MeV Heavy Ion Beam Probe (HIBP) was installed to Large Helical Device (LHD) and it has been developed. The radial profile of potential in the region where normalized minor radius, ρ, is less than 0.5 was measured, and the electric field obtained from the fitting function of experimental data was compared with the neoclassical theory. The experimental results fairly coincided with the theory. The negative pulses were observed in potential signal in the case of the inward shifted magnetic configuration. The time constants of these pulses were less than the energy confinement time. Potential fluctuations of coherent modes were also observed, and one of their frequencies coincided with the geodesic acoustic mode (GAM). In this report, the present status of potential measurements with HIBP system in LHD is described.

Keywords: Large Helical Device, heavy ion beam probe, potential, tandem accelerator, tandem analyzer

1. Introduction

In the toroidal magnetized plasmas, radial electric field is a very important parameter. In transition phenomena, such as H-mode transition, the change of radial electric field structure was observed in tokamak [1-3]. In helical devices, the bifurcation phenomenon is predicted from the neoclassical theory, and the confinement property is improved by the produced radial electric field. In the experiment of helical device, this type of phenomenon was observed and an internal transport barrier (ITB) was created [4-6]. It is considered that the poloidal shear flow plays a very important role in the production of ITB because the shear flow can reduce the anomalous transport by suppressing the turbulence in plasma [7]. In the torus plasma, the radial electric field is related to the poloidal flow, therefore, the shear of electric field is also important. Thus, measurements of radial electric field are very essential to study these attractive physics in toroidal plasmas.

Heavy Ion Beam Probe (HIBP) [8] is a very useful tool to study these attractive physics, because it can directly measure plasma potential in the inside of high temperature toroidal plasma. Moreover, this tool can measure it with good spatial/temporal resolution, without disturbing plasma. In order to measure the radial structure of potential and its fluctuation in Large Helical Device (LHD), the 6 MeV Heavy Ion Beam Probe was installed and has been developed [9,10]. In this report, the present status of HIBP in LHD is described and the recent results obtained from our system are shown. Up to now, the operation of this system at the acceleration energy of 6 MeV was done, however the resolution of potential measurement was not good because the acceleration voltage was not stable above ~ 1.3 MV (Acceleration energy in this case corresponds to 2.6 MeV). Therefore, most data shown here were obtained on the condition of the acceleration voltage being less than 1.3 MV.

author's e-mail: akihiro@nifs.ac.jp

2. HIBP system in LHD

In Fig.1, the schematic view of HIBP system in LHD is shown. The toroidal magnetic field strength of LHD is 3 T, and the typical major/minor radius is 3.6 m / 0.6 m. In order to inject the Au^+ probing beam to the center of plasma, the acceleration energy of 6 MeV is required. To reduce the required voltage to be half, the tandem accelerator is used in our system. The negative ion, Au^-, is produced in the target sputter ion source [11]. The Au^- is extracted and pre-accelerated up to 50 keV. After that, this beam is injected to the tandem accelerator and accelerated to 3 MeV. In the gas cell located in the center of the tandem accelerator, Au^- ions are stripped two electrons and changed to positive ions, Au^+. These ions are re-accelerated to 6 MeV. This beam is guided to plasma through several components: the charge separator, the 4.8 m cylindrical deflector, the 7.8 degree deflector, and so on. The orbit of probing beam has three

dimensional structure in the plasma. The injection angle and the ejection angle of probing beam are controlled by two 8-pole electric deflectors (sweeper) at the injection and ejection ports. By controlling these angles, the observation point is changed. The injected Au^{+} is stripped an electron by the collision with plasma, and at this time it obtains the potential energy at this ionized point. Here, we call the Au^{+} beam as the primary beam, and the produced Au^{2+} beam as the secondary beam. By measuring the difference of energy between the primary and the secondary beam, the plasma potential at the ionized point can be measured. The ionized point is called as a sample volume. The sample volume positions are arranged three dimensionally in plasma, because that the beam orbit has three dimensional geometry. The projection of sample volume positions on the vertically elongated cross section are shown in Fig.2, on the condition that the toroidal magnetic field strength is 1.5 T, the major radius of magnetic axis is 3.75 m, the acceleration energy is 1.376 MeV. The potential in the domain of the normalized minor radius from 0 to 0.5 can be measured with our HIBP system.

For the energy analyzer, if the traditional Proca-Green type of energy analyzer [12] is used, the required voltage reaches to 500 kV - 1 MV for the beam energy of 6 MeV. The electric power supply for this voltage costs much and is not realistic. Therefore the tandem type of energy analyzer is applied [13] in our system. With this analyzer, the required voltage is reduced to 120 kV with keeping the second order focusing property of the beam injection angle. There are three slit holes at the entrance of this analyzer, so

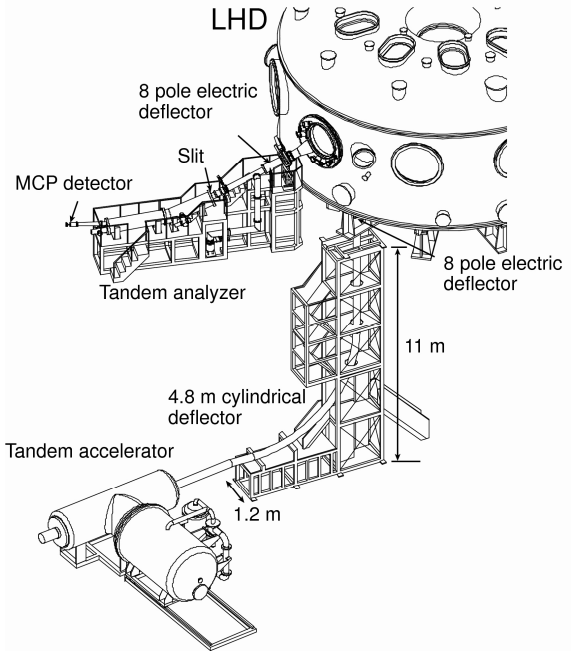

Fig.1 Schematic view of HIBP system in LHD is shown. The negative ion source is omitted in this figure.

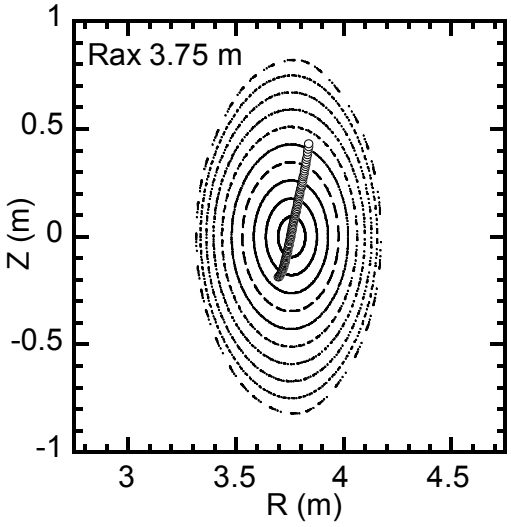

Fig.2 The projection of sample volume positions on the vertically elongated cross section and magnetic surfaces for the configuration of R_{ax} 3.75 m are shown.

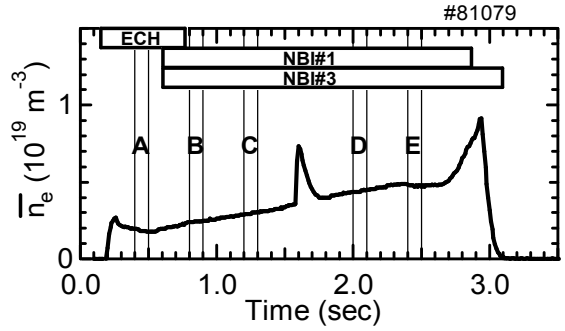

Fig.3 The temporal evolution of line averaged electron density and heating methods are shown. The potential was measured in the duration from A to E.

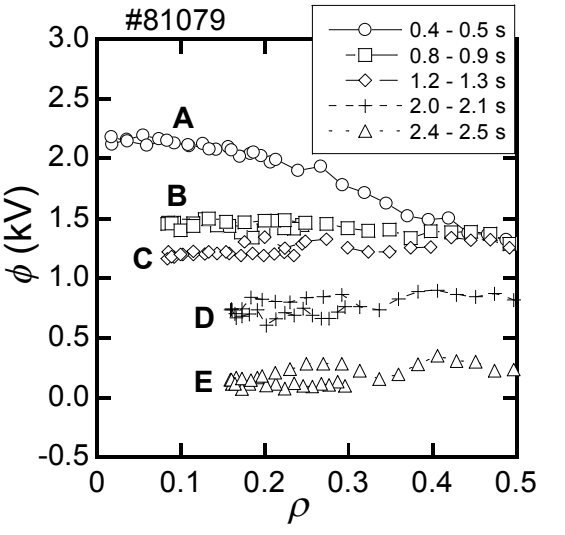

Fig.4 The radial profiles of potential measured with HIBP are shown. The characters from A to E correspond to the durations in Fig.3.

the potential of neighboring 3 sample volumes can be measured. For detecting secondary beam current, high gain detector, micro channel plates (MCPs) are used, by which a very small amount of secondary beam current can be detected. In LHD, the order of detected current is about a few tens pA - nA. The ratio of detected secondary beam current to injected primary beam current is 10^{-5} - 10^{-4} in the density range of 0.5 - 1.0 × 10^{19} m^{-3}.

3. The radial profile of potential

With our HIBP system, the radial profile of potential was measured. The magnetic configuration of LHD can be characterized by the major radius of the axis, R_{ax}, the toroidal magnetic field strength, B_t, the pitch parameter, γ, and the quadrupole component of magnetic field, B_q. The radial potential profile was measured in the magnetic field configuration of a standard one, R_{ax} = 3.75 m, B_t = 1.5 T, γ = 1.254, B_q = 100 %. The energy of probing beam was 1.376 MeV. The plasma was produced by ECH and sustained by NBI heating. The line averaged density was about 0.2 × 10^{19} m^{-3} at ECH phase, and it gradually increased. Fig.3 shows the temporal evolution of line averaged density and the heating methods. Central temperature was about 2.5 keV in ECH phase and 1.0 keV in NBI phase. The position of sample volume was changed by changing the injection angle of probing beam at 10 Hz. The radial profiles of potential obtained from HIBP in the duration from A to E are shown in Fig.4. In ECH phase, the potential was positive at the center, and it gradually decreased as the density increased. In the NBI phase, the potential at the central region was positive however the electric field was almost zero or a little negative.

By fitting these experimental data with polynomial functions and differentiating them, the profiles of electric field were obtained and compared with the neoclassical theory as shown in Fig.5. Fig.5 (a) shows the radial profile of electric field obtained from the fitting function of experimental results and Fig.5 (b) shows the calculation results estimated from the neoclassical theory. In Fig.5 (b), in the region where ρ > 0.25, the multiple roots exist. In this region, the largest positive one corresponds to the electron root, and the smallest negative one or almost zero corresponds to the ion root. The one between these roots is the unstable root. The theoretical calculations are

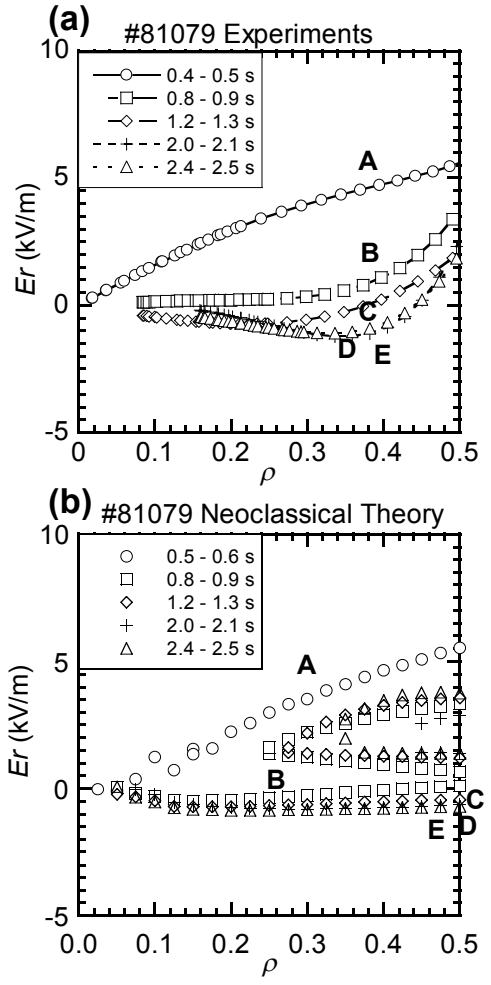

Fig.5 (a) Radial profiles of radial electric field obtained from the derivatives of the fitting functions of experimental data are shown. (b) Radial profiles of radial electric field calculated from the neoclassical theory are shown.

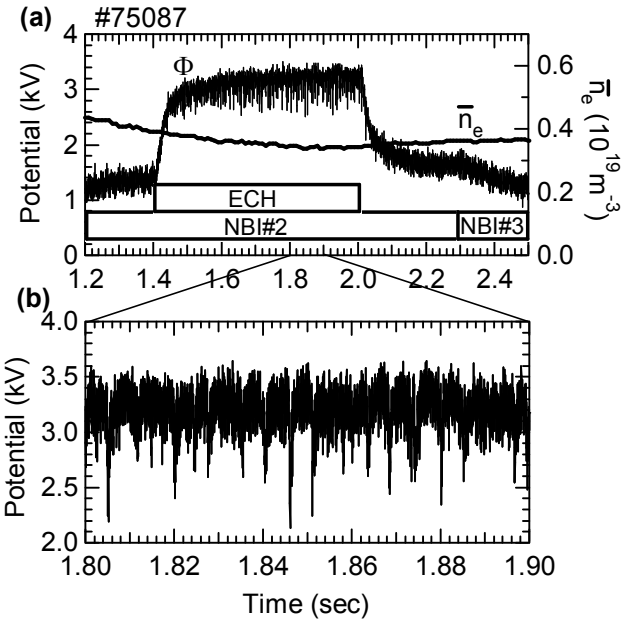

Fig.6 (a) Temporal evolutions of potential, line averaged density, heating methods are shown. (b) The magnification of potential signal from 1.8 to 1.9 sec is shown.

almost consistent with experimental results, so we can conclude that the electric field in the core region of this experiment is almost determined by the neoclassical theory.

3. Negative pulses observed in potential signal

In the case of the inward shifted configuration, the negative pulses were observed in the potential signal. The parameters for this magnetic configuration were as follows: R_{ax} = 3.6 m, B_t = 1.5 T, γ = 1.254, B_q = 100 %. In this case, the probing beam energy of HIBP was 1.562 MeV. Plasma was produced by co-injection NB heating and sustained by it. Temporal evolutions of heating methods, line averaged density, and potential are shown in Fig.6 (a). The line averaged density is about 0.4×10^{19} m^{-3}. At the 1.4 sec, the ECH was additionally applied. In the ECH phase, negative pulses were observed as shown in Fig.6 (b). The normalized minor radius of the sample volume position was fixed at ~ 0.3. Negative pulses can be seen in the temporal evolution of potential signal. The typical time constants are 90 μs in the drop phase and 500 μs in the recovering phase as shown in Fig.7. The energy confinement time is ~ 100 ms in LHD. The time constant of negative pulses were much faster than the energy confinement time, so these phenomena are considered to be the bifurcation of the electric field.

In CHS, such bifurcation phenomena were observed [14,15], which is called as "pulsation". In CHS, various types of pulsation were observed. In the case of low density, the drop of potential was very large. The potential at the center in the additional ECH phase was ~ 1 keV in the electron root, and it dropped to a few hundreds eV in the ion root. The change of potential was ~ 1 keV. However, in the high density case in CHS, the drop of potential was small: the change of potential was about 100 ~ 200 eV. The result of LHD is very similar to the high density case of CHS. These negative pulses were observed only the inward shift case, R_{ax} = 3.6 m, and were not observed in the other configuration at present. The reason for it may be the difference of configuration property in the context of neoclassical theory.

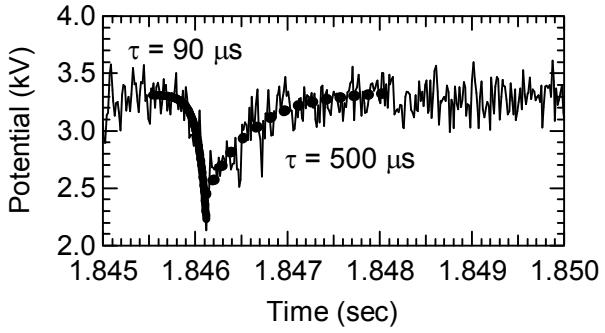

Fig.7 The time constants of negative pulse are shown. These were faster than the energy confinement time.

4. Observation of coherent modes

The signal to noise ratio of our system was improved, so coherent modes were observed in LHD. An example of it is shown in Fig.8. As shown in Fig.8 (a), the plasma was produced and sustained by NB heating. The line averaged density was about 0.1×10^{19} m^{-3}, relatively low. The ECH was applied from 1.0 to 1.6 sec, which was injected for co-directed current drive. In Fig.8 (b), the spectrogram of potential signal are shown. The position of sample volume was $\rho \sim 0$. These signals had the coherence with signals of magnetic probes, therefore these are considered to be the coherent modes caused by MHD instabilities. In this case, the rotational transform at the central region was increased by ECH current drive, and the shear in the rotational transform profile in the central regime becomes small. Then, it is considered that a sort of Alfven Eigen modes were excited. Around the frequency of 20 kHz from 1.68 to 1.76 sec, the fluctuation having constant frequency was seen, which coincided with the geodesic acoustic mode (GAM) [16,17]. This mode

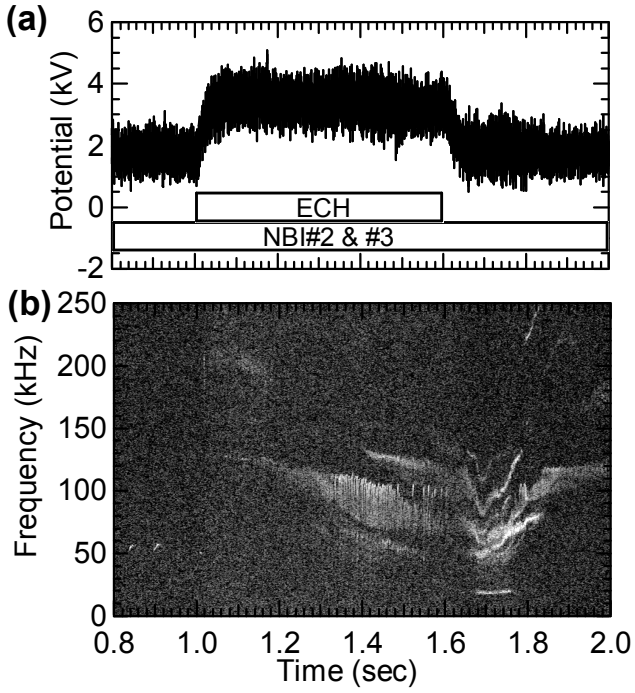

Fig.8 (a) The temporal evolution of potential and heating methods are shown. (b) The spectrogram of potential fluctuation is shown.

was localized to the central region of plasma [18]. The fluctuation amplitude was several hundreds volts.

Up to now, the fluctuation caused by turbulence was not measured clearly in the potential signal, because the signal to noise ratio of our system was not sufficient. The more improvement of S/N ratio is needed in the future.

5. Summary

In LHD, 6 MeV Heavy Ion Beam Probe has been developed. On the condition of the acceleration energy begin below 2.6 MeV, the acceleration energy was stable, so the potential in plasma could be measured with a good signal to noise ratio. The radial potential profile was measured in the magnetic field configuration R_{ax} = 3.75 of LHD. Results were compared with the neoclassical theory. The radial profile of electric field obtained from the experiment fairly coincides with the theoretical calculation. In the inward shifted configuration (R_{ax} = 3.6), the negative pulses were observed in potential signal. The fluctuations of coherent modes were measured with HIBP. The frequency of one of them coincided with the GAM. The fluctuation amplitudes were about several hundreds volts.

Acknowledgments

This work was supported by the NIFS budget under contract No. ULBB 505, 514, 515, and was partly supported by MEXT Japan under Grant-in-Aid for Young Scientists (Nos. 16760674, 18760640), and NIFS/NINS under the project of Formation of International Network for Scientific Collaborations. The authors wish to thank for continuous support of scientific and technical staff in LHD.

References

[1] K. Ida, S. Hidekuma, Y. Miura, T. Fujita, M. Mori, K. Hoshino, N. Suzuki, T. Yamauchi *et al*., Phys. Rev. Lett. **65**, 1364 (1990).

[2] R. J. Groebner, K. H. Burrell, R. P. Seraydarian *et al*., Phys. Rev. Lett. **64**, 3015 (1990).

[3] T. Ido, K. Kamiya, Y. Miura, Y. Hamada, A. Nishizawa, Y. Kawasumi, Phys. Rev. Lett. **88**, 055006 (2002).

[4] A. Fujisawa, H. Iguchi, T. Minami, Y. Yoshimura, H. Sanuki, K. Itoh, S. Lee, K. Tanaka *et al*., Phys. Rev. Lett. **82**, 2669 (1999).

[5] A. Fujisawa, H. Iguchi, T. Minami, Y. Yoshimura, K. tanaka, K. Itoh, H. Sanuki, S. Lee, M. Kojima, S. -I. Itoh, M. Yokoyama, S. Kado, S. Okamura, R. Akiyama, K. Ida *et al*., Phys. Plasmas **7**, 4152 (2000).

[6] T. Estrada, A. Alonso, A. A. Chmyga, N. Dreval, L. Eliseev, C. Hidalgo, A. D. Komarov, A. S. Kozachok *et al*., Plasma Phys. Control. Fusion **47**, L57 (2005).

[7] K. H. Burrell, Phys. Plasmas **4**, 1499 (1997).

[8] T. P. Crowley *et al*., IEEE Trans. on Plasma Sci. **22**, 291 (1994).

[9] T. Ido, A. Shimizu, M. Nishiura, A. Nishizawa, S. Katoh, K. Tsukada, M. Yokota, H. Ogawa, T. Inoue, Y. Hamada *et al*., Rev. Sci. Instrum. **77**, 10F523 (2006).

[10] A. Shimizu, T. Ido, M. Nishiura, H. Nakano, I. Yamada, K. Narihara, T, Akiyama, T. Tokuzawa, K. Tanaka *et al*., J. Plasma Fusion Res. **2**, S1098 (2007).

[11] M. Nishiura, T. Ido, A. Shimizu, S. Kato, K. Tsukada, A. Nishizawa, Y. Hamada, Y. Matsumoto *et al*., Rev. Sci. Instrum. **77**, 03A537 (2006).

[12] G. A. Proca and T. S. Green, Rev. Sci. Instrum. **41**, 1778 (1970).

[13] Y. Hamada, A. Fujisawa, H. Iguchi, A. Nishizawa, Y. Kawasumi, Rev. Sci. Instrum. **68**, 2020 (1997).

[14] A. Fujisawa, H. Iguchi, H. Idei, S. Kubo, K. Matsuoka, S. Okamura, K. Tanaka, T. Minami, S. Ohdachi, S. Morita, H. Zushi *et al*., Phys. Rev. Lett. **81**, 2256 (1998).

[15] A. Fujisawa, H. Iguchi, T. Minami, Y. Yoshimura, K. Tanaka, K. Itoh, H. Sanuki, S. Lee, M. Kojima, S. -I. Itoh *et al*., Phys. Plasmas **7**, 4152 (2000).

[16] N. Winsor, J. L. Johnson, J. M. Dowson, Phys. Fluids **11**, 2448 (1968).

[17] P. H. Diamond, S. -I. Itoh, K. Itoh, T. S. Hahm, Plasma Phys. Control. Fusion **47**, R35 (2005).

[18] T. Ido, A. Shimizu, M. Nishiura, H. Nakano, S. Ohshima, S. Kato, Y. Hamada, Y. Yoshimura, S. Kubo, T. Shimozuma, H. Igami, H. Takahashi, K. Toi *et al*., Rev. Sci. Instrum. **79**, 10F318 (2008).

Poster Presentations 1

P1-02 - P1-44

Proceedings of ITC18, 2008

Modeling of Collisional Transport in Ergodic Region

Ryutaro KANNO[1,2)], Masanori NUNAMI[3)], Shinsuke SATAKE[1)], Hisanori TAKAMARU[4)], Masao OKAMOTO[4)] and Nobuyoshi OHYABU[1,2)]

[1)]*National Institute for Fusion Science, Toki 509-5292, Japan*
[2)]*Department of Fusion Science, Graduate University for Advanced Studies, Toki 509-5292, Japan*
[3)]*Research Institute for Sustainable Humanosphere, Kyoto University, Japan Science and Technology Agency, CREST, Uji 611-0011, Japan*
[4)]*Department of Computer Science, Chubu University, Kasugai 487-8501, Japan*

In recent tokamak experiments it is found that so-called stochastic diffusion theory based on the "field line diffusion" overestimates the radial energy transport in collisionless edge plasma affected by resonant magnetic perturbations, though the perturbations induce chaotic behavior of the field lines. These results imply that the conventional modeling of the edge transport should be reconsidered for covering the range from lower to higher collisionalities. It is required to construct the modeling extracting information contributing to the transport in macro-scale from kinetic motions in micro-scale. A simulation study of collisional transport in the ergodic region is attempted for estimating the transport coefficients according to the modeling. By using a drift kinetic equation solver without the assumption of nested flux surfaces (the KEATS code), it is possible to execute the estimation. In this paper, we report the modeling constructed from the viewpoint of stochastic approach and the simulation study of the ion transport in the ergodic region under the assumption of neglecting effects of an electric field and neutrals.

Keywords: collisional transport, ergodic region, chaotic field line, stochastic analysis, diffusion process, δf simulation

1 Introduction

In recent tokamak experiments it is found that so-called stochastic diffusion theory based on the "field line diffusion" [1] overestimates the radial energy transport in the edge added resonant magnetic perturbations (RMPs) [2, 3]. This fact is discovered in the experiments of edge localized modes (ELMs) suppression by adding RMPs to the edge plasma. (The idea of suppressing the ELMs by using RMPs has been proposed in Ref. [4].) When the RMPs induce a chaotic behavior in the field lines, the theory predicts that a thermal diffusivity is given by "diffusion of the field lines." In collisionless edge ergodized plasma, the experimental thermal-diffusivity $\chi^{\rm exp} = -q_{\rm r}/(n\nabla T)$ is inconsistent with the prediction of the stochastic diffusion theory $\chi^{\rm ql}$; i.e. $\chi_{\rm e}^{\rm exp}/\chi_{\rm e}^{\rm ql} \ll 1/10$ for the electron thermal diffusivity [3], where $q_{\rm r}$ is the radial energy flux, n the density, and T the temperature measured in the experiments. The above experimental results imply that the conventional modeling of transport in the ergodic region should be reconsidered in torus plasmas, and kinetic modeling is required for understanding stochastic transport in the ergodic region [5].

For construction of kinetic modeling, statistical properties of the guiding center orbits in the ergodic region are previously studied in the monoenergetic test-particle simulations in detail [6]. The doubt on the validity of the stochastic diffusion theory for the collisionless limit has been reported; i.e. guiding center orbits in the ergodic region are not Brownian for lower-collisionality. On the other hand, for the collisional limit, the radial behavior of the guiding center orbits is numerically observed to be a standard diffusion process. These results mean that it is not a trivial problem whether the transport coefficients in the ergodic region can be always estimated by tracing monoenergetic test-particle orbits. We should note that the statistical properties of the neoclassical radial diffusion for the range from lower to higher collisionalities in a magnetic configuration having nested flux surfaces are confirmed through direct comparison with a Brownian process in configuration space given by tracing monoenergetic test-particle orbits [7]. It is important to construct the modeling extracting information contributing to the collisional transport in macro-scale from the kinetic motions in micro-scale, even if the guiding center orbits themselves are non-Brownian. The modeling of the transport should be reconsidered from the viewpoint of stochastic approaching the statistics of kinetic motions exposed to noise caused by the RMPs.

In order to estimate transport coefficients in the ergodic region, we develop a new transport simulation code without the assumption of nested flux surfaces; the code is named "KEATS" [8, 9, 10]. The code is programmed by expanding the well-known Monte-Carlo particle simulation scheme based on the δf method [11, 12, 13]. By

author's e-mail: kanno@nifs.ac.jp

using the KEATS code, it is possible to execute the estimation.

In this paper, we discuss the modeling of the transport exposed to noise caused by chaotic behavior of field lines, and apply the KEATS code to a torus plasma having the ergodic region for estimating the transport coefficients (in particular, thermal diffusivity). Here, because of a limited computational-time we treat ions (protons) in higher-collisionality for our numerical study of the transport in the ergodic region. The modeling and simulations are useful for understanding transport properties in the ergodic region generated in the edge of a helical plasma. The details of the modeling are discussed in Sec. 2. In Sec. 3, the simulation results are shown. Finally, summary is given in Sec. 4.

2 Modeling of Collisional Transport

First, we consider the collisional transport in macro-scale under the assumption of neglecting effects of chaotic field lines, an electric field, and neutrals. For a fluid quantity $u(t, \boldsymbol{x})$, i.e. the density $u = n(t, \boldsymbol{x})$ or energy $u = (3/2)nT$, the fluid equation is given as [14, 15]

$$\frac{\partial u(t,\boldsymbol{x})}{\partial t} + \nabla\cdot(\boldsymbol{V}u) - \frac{1}{2}\nabla\cdot(\mathsf{D}\cdot\nabla u) + \nu u = h(t,\boldsymbol{x}), \quad (1)$$

where $\nabla = \partial/\partial\boldsymbol{x}$, a position in Euclidean space $\boldsymbol{x} \in \mathbf{R}^3$, time $t \in [0, t_1)$, the initial condition $u(0, \boldsymbol{x}) = \phi(\boldsymbol{x})$ at $t = 0$, and the boundary condition $u(t, \boldsymbol{x}) = g(t, \boldsymbol{x})$ at the boundary. Here, the mean velocity $\boldsymbol{V}$ and the diffusion coefficient $\mathsf{D} = (D^{ij})$ are assumed to be given functions of t and $\boldsymbol{x}$.

The above fluid equation is the initial-boundary value problem (written for t replaced by $t_1 - t$):

$$(L + \nu_*)u + \frac{\partial u}{\partial t} = h_*(t,\boldsymbol{x}) \quad \text{in } Q = \mathcal{M}\times[0,t_1), \quad (2)$$

$$u(t_1,\boldsymbol{x}) = \phi(\boldsymbol{x}) \quad \text{on } \mathcal{M}, \quad (3)$$

$$u(t,\boldsymbol{x}) = g(t,\boldsymbol{x}) \quad \text{on } \mathcal{S}, \quad (4)$$

where $\mathcal{M}$ is a bounded domain with the boundary $\partial\mathcal{M}$, $\mathcal{S} = \partial\mathcal{M}\times[0, t_1)$, and

$$Lu := \left\{\frac{1}{2}D^{ij}\frac{\partial^2}{\partial x^i\partial x^j} + V_*^i\frac{\partial}{\partial x^i}\right\}u, \quad (5)$$

$$V_*^i = -V^i + \frac{1}{2}\frac{\partial D^{ij}}{\partial x^j}, \quad (6)$$

$$\nu_* = -\nu - \frac{\partial V_i}{\partial x^i}, \quad (7)$$

$$h_* = -h. \quad (8)$$

The solution of Eqs. (2)-(4) is given as [16]

$$\begin{aligned} u(t,\boldsymbol{x}) = {} & E_{t,\boldsymbol{x}}g(\tau,\boldsymbol{\xi}(\tau))\exp\left[\int_t^\tau \nu_*(s,\boldsymbol{\xi}(s))\mathrm{d}s\right]\chi_{\tau<t_1} \\ & + E_{t,\boldsymbol{x}}\phi(\boldsymbol{\xi}(T))\exp\left[\int_t^\tau \nu_*(s,\boldsymbol{\xi}(s))\mathrm{d}s\right]\chi_{\tau=t_1} \\ & - E_{t,\boldsymbol{x}}\int_t^\tau h_*(s,\boldsymbol{\xi}(s))\exp\left[\int_t^s \nu_*(\lambda,\boldsymbol{\xi}(\lambda))\mathrm{d}\lambda\right]\mathrm{d}s, \end{aligned} \quad (9)$$

where $E_{t,\boldsymbol{x}}$ is the expectation operator given by the diffusion process:

$$\mathrm{d}\xi^i(t) = \sigma_j^i(t,\boldsymbol{\xi}(t))\mathrm{d}w^j(t) + V_*^i(t,\boldsymbol{\xi}(t))\mathrm{d}t \quad (10)$$

having $D^{ij} = \sigma_k^i \mathrm{g}^{k\ell}\sigma_\ell^j$, $\mathrm{g}^{k\ell}$ is the metric, $\boldsymbol{w}(t)$ is a Brownian motion, χ_A is the indicator function of a set A, τ is the first time $\lambda \in [t, t_1)$ that $\boldsymbol{\xi}(\lambda)$ leaves $\mathcal{M}$ if such a time exists and $\tau = t_1$ otherwise. Therefore, the transport in macro-scale is expressed by using the diffusion process given as Eq. (10).

The diffusion process given as Eq. (10) is originally caused from the collision operator. Let us take the following collision operator $C(f)$:

$$C(f) = \nu_{\mathrm{col}}\frac{\partial}{\partial\boldsymbol{v}}\cdot\left\{\boldsymbol{v}f + v_{\mathrm{th}}^2\frac{\partial f}{\partial\boldsymbol{v}}\right\}, \quad (11)$$

where $f = f(t,\boldsymbol{x},\boldsymbol{v}) = f_{\mathrm{M}}(t,\boldsymbol{x},\boldsymbol{v};\boldsymbol{V}(t,\boldsymbol{x})) + \delta f(t,\boldsymbol{x},\boldsymbol{v})$ is a distribution function expressing statistics of kinetic motions in micro-scale, f_{M} is a shifted Maxwellian background, $\nu_{\mathrm{col}} = \nu_{\mathrm{col}}(\boldsymbol{x})$ is the collision frequency, v_{th} the thermal velocity, $(\boldsymbol{V} + \boldsymbol{v})$ the velocity of a guiding center, and $\boldsymbol{V} = \boldsymbol{V}(t,\boldsymbol{x})$ the mean velocity [17]. The operator (11) is simpler, but is used only to get a rough idea of collisional effects [18].

We consider the motion of a guiding center along a field line for estimation of radially spreading the guiding centers in a perturbed field. The guiding center motion exposed to the collisions (11) is given as an Ornstein-Uhlenbeck process:

$$\mathrm{d}\boldsymbol{x}(t) = (\boldsymbol{V} + \boldsymbol{v})\mathrm{d}t, \quad (12)$$

$$\mathrm{d}\boldsymbol{v}(t) = \sigma\mathrm{d}\boldsymbol{w}(t) - \nu_{\mathrm{col}}\boldsymbol{v}\mathrm{d}t, \quad (13)$$

where a perturbation field is neglected in the above equations, $\boldsymbol{V} = V_\parallel\boldsymbol{b}$, $\boldsymbol{b} = \boldsymbol{B}/B$ the unit vector along a field line, $\sigma = v_{\mathrm{th}}\sqrt{\nu_{\mathrm{col}}}$, and $\boldsymbol{B}$ the unperturbed magnetic field. Here, the effects of toroidal and helical ripples are neglected for simplicity. Here, v_{th} and ν_{col} are assumed to be constant.

One may consider that effect of a perturbation field on the guiding center motion is interpreted as noise on the motion. If the effect is expressed as a linear operator $\tilde{\mathcal{N}}(\boldsymbol{V}+\boldsymbol{v})$, then instead of Eq. (12) the motion of a guiding center is described as

$$\mathrm{d}\boldsymbol{\zeta} = \left\{(\boldsymbol{V} + \boldsymbol{v}) + \tilde{\mathcal{N}}(\boldsymbol{V} + \boldsymbol{v})\right\}\mathrm{d}t. \quad (14)$$

After sufficient exposure to the collisions $t \gg 1/\nu_{\mathrm{col}}$ ($\nu_{\mathrm{col}} \to \infty$ and $v_{\mathrm{th}}/\sqrt{\nu_{\mathrm{col}}} = \text{const.}$), the stochastic process $\boldsymbol{\zeta}(t)$ (written for t replaced by $t_1 - t$) becomes

$$\mathrm{d}\boldsymbol{\zeta}(t) \approx \frac{v_{\mathrm{th}}}{\sqrt{\nu_{\mathrm{col}}}}(1 + \tilde{\mathsf{N}})\cdot\mathrm{d}\boldsymbol{w}(t) - (\boldsymbol{V} + \tilde{\boldsymbol{V}})\mathrm{d}t, \quad (15)$$

where $\tilde{\boldsymbol{V}} = \tilde{\mathcal{N}}\boldsymbol{V}$, and $\tilde{\mathsf{N}} = (N_j^i)$ is assumed to be a continuous function in t, together with its first t-derivative. Here, the noise expressed as $\tilde{\boldsymbol{V}}$ and $\tilde{\mathsf{N}}$ is bounded, i.e. there exist V_0 and N_0 satisfying $|\tilde{\boldsymbol{V}}| \le V_0$ and $|N_j^i| \le N_0$.

From Eqs. (9) and (10), the collisional transport in macro-scale is described as diffusion phenomenon, thus the process $\boldsymbol{\zeta}(t)$ is projected onto a diffusion process:

$$\lim_{\epsilon\to 0+}\frac{1}{\epsilon}E\left[\zeta^i_{t-\epsilon,\boldsymbol{x}}(t)-x^i\middle|\mathcal{P}_t^{t-\epsilon}\right]=U^i_*(t,\boldsymbol{x}), \tag{16}$$

$$\lim_{\epsilon\to 0+}\frac{1}{\epsilon}E\left[\left\{\zeta^i_{t-\epsilon,\boldsymbol{x}}(t)-x^i\right\}\times\left\{\zeta^j_{t-\epsilon,\boldsymbol{x}}(t)-x^j\right\}\middle|\mathcal{P}_t^{t-\epsilon}\right]=\tilde{D}^{ij}(t,\boldsymbol{x}), \tag{17}$$

where $\boldsymbol{\zeta}_{t-\epsilon,\boldsymbol{x}}(t)$ is a path $\boldsymbol{\zeta}(t)$ satisfying $\boldsymbol{\zeta}(t-\epsilon)=\boldsymbol{x}$, and $\boldsymbol{U}_*$ is the mean velocity affected by the noise: $\boldsymbol{U}_*=-\{\boldsymbol{V}+E[\tilde{\boldsymbol{V}}|\mathcal{P}_t^{\zeta}]\}$. Here, $E[\,\cdot\,|\mathcal{P}_t^{t-\epsilon}]$ denotes the conditional expectation with respect to $\mathcal{P}_t^{t-\epsilon}$, and the σ-algebra $\mathcal{P}_t^{t-\epsilon}$ is generated by the set of sample paths $\{\boldsymbol{\zeta}_{t-\epsilon,\boldsymbol{x}}(s); t-\epsilon\le s\le t\}$ [19]. Note that $E[\,\cdot\,|\mathcal{P}_t^{t-\epsilon}]$ is $\mathcal{P}_t^{t-\epsilon}$ measurable, i.e. $\lim_{\epsilon\to 0+}E[\,\cdot\,|\mathcal{P}_t^{t-\epsilon}]$ is a function of t and $\boldsymbol{x}$. The diffusion process extracted from the process $\boldsymbol{\zeta}(t)$ is given as

$$\mathrm{d}\xi^i(t)=\tilde{\sigma}^i_j(t,\boldsymbol{\xi}(t))\mathrm{d}w^j(t)+U^i_*(t,\boldsymbol{\xi}(t))\mathrm{d}t, \tag{18}$$

i.e., the diffusion in velocity space for micro-scale becomes the diffusion in configuration space for macro-scale, see the first term in the right hand side of Eq. (18), where $\tilde{D}^{ij}=\tilde{\sigma}^i_k g^{k\ell}\tilde{\sigma}^j_\ell$. In this case, the partial differential operator L given by the diffusion process $\boldsymbol{\xi}(t)$ is derived as

$$\begin{aligned}-\frac{\partial u(t,\boldsymbol{x})}{\partial t}&=\lim_{\epsilon\to 0+}\frac{u(t-\epsilon,\boldsymbol{x})-u(t,\boldsymbol{x})}{\epsilon}\\&=\lim_{\epsilon\to 0+}\frac{1}{\epsilon}E\left[u(t,\boldsymbol{\xi}_{t-\epsilon,\boldsymbol{x}}(t))-u(t,\boldsymbol{x})\right]\\&=\frac{1}{2}\tilde{D}^{ij}(t,\boldsymbol{x})\frac{\partial^2 u(t,\boldsymbol{x})}{\partial x^i\partial x^j}+U^i_*(t,\boldsymbol{x})\frac{\partial u(t,\boldsymbol{x})}{\partial x^i},\end{aligned} \tag{19}$$

where $u(t-\epsilon,\boldsymbol{x})=E[u(t,\boldsymbol{\xi}_{t-\epsilon,\boldsymbol{x}}(t))]$ and $E[u(t,\boldsymbol{x})]=u(t,\boldsymbol{x})$.

3 Results of KEATS Code

For estimation of the radial fluxes in the ergodic region, we use a magnetic configuration which is formed by adding RMPs into a simple tokamak field having concentric circular flux surfaces, where the major radius of the magnetic axis $R_{\rm ax}=3.6$ m, the minor radius of the plasma $a=1$ m, and the magnetic field strength on the axis $B_{\rm ax}=4$ T. The unperturbed magnetic field is approximately given as $B_R=-(B_{\rm ax}R_{\rm ax}/q)Z/R^2$, $B_\varphi=-B_{\rm ax}R_{\rm ax}/R$, and $B_Z=(B_{\rm ax}R_{\rm ax}/q)(R-R_{\rm ax})/R^2$ [20], where q is the safety factor and $q^{-1}=0.9-0.5875(r/a)^2$, and $r=\sqrt{(R-R_{\rm ax})^2+Z^2}$. The RMPs causing resonance with, for example, the rational surfaces of $q=m/n=3/2, 10/7, 11/7$ are numerically given by using the perturbation field $\delta\boldsymbol{B}=\nabla\times(\alpha\boldsymbol{B})$ [6], and order of the strength is $O(|\delta B_{\rm r}/B_{\rm t}|)\sim 10^{-1}$. Here, the function α, which has unit of length, is used to represent the structure of perturbed magnetic field; $\alpha(R,\varphi,Z)=\sum_{m,n}\alpha_{mn}(\psi(R,Z))\cos\{m\theta(R,Z)-n\varphi+\varphi_{mn}\}$, where ψ is a label of magnetic flux surfaces and φ_{mn} is the phase. The

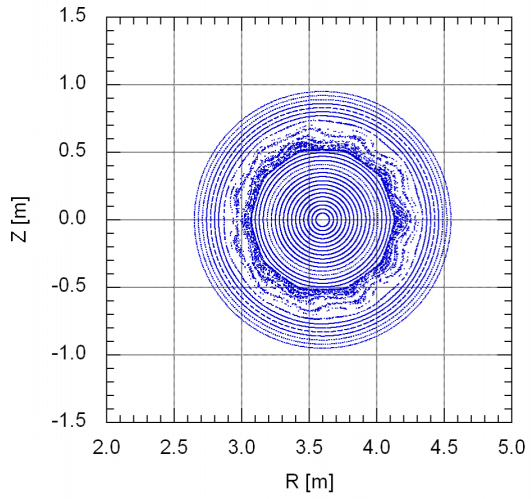

Fig. 1 Poincaré plots of the magnetic field lines on a poloidal cross section for case of $\Delta_{\delta B}=\delta B/\delta B^{(0)}=1$, where $\delta B=|\delta\boldsymbol{B}|$ is the strength of RMPs and $\delta B^{(0)}$ is the strength of the RMPs in the case b) of Fig. 2. The ergodic region is placed between $r/a=0.5$ and 0.7, where $r=\sqrt{(R-R_{\rm ax})^2+Z^2}$ and $R_{\rm ax}=3.6$ m.

Poincaré plots of the magnetic field lines on a poloidal cross section are shown in Fig. 1. The ergodic region appears in $r/a\approx 0.7\sim 1$. In the KEATS code, the number of marker particles is $N_{\rm MP}=16,000,000$.

To investigate effect of the existence of the ergodic region on the transport phenomena, we evaluate the energy flux of ions (protons) $\boldsymbol{q}_{\rm i}$, because the evaluation of electron energy flux is highly time-consuming. The calculation time for ions is about 40 hours in real time to get the result with sufficient numerical-accuracy by using the vector-parallel supercomputer SX-7, and the calculation time for electrons is estimated to be about 40 ($\approx\sqrt{m_{\rm i}/m_{\rm e}}$) times longer than the one for ions if the number of PEs (processing elements) is fixed, where 64 PEs are used in this paper.

The evaluation of the ion energy flux is carried out in the configuration having lower temperature $T_{\rm edge}\sim 100$ eV at a center of the ergodic region. The temperature profile is given as $T_{\rm i}=T_{\rm ax}\{0.02+0.98\exp[-4(r/a)^{2.5}]\}$ with $T_{\rm ax}=250$ eV, which neglects the existence of the ergodic region. The density profile is set homogeneous, $n_{\rm i}=\text{const.}=1\times 10^{19}$ m^{-3}. The radial profiles of thermal diffusivities estimated from the KEATS computations are shown in Fig. 2, where from the modeling of the transport given in the previous section the thermal diffusivity can be estimated as $\chi^{\rm i}_{\rm eff}=q_{\rm r}/(n_{\rm i}|\partial T_{\rm i}/\partial r|)$, and $q_{\rm r}$ the radial energy flux evaluated by the KEATS code. Here, the radial mean velocity $V_{\rm r}$ is neglected because of $|V_{\rm r}/v_{\rm th}|\ll 1$. For simplicity, the radial energy fluxes are given by neglecting the existence of the ergodic region, because we have no magnetic coordinate system including several magnetic field structures as the core and ergodic regions. The energy flux $\boldsymbol{q}_{\rm i}$ is averaged over concentric circular shell region in the whole toroidal angles as if there were nested flux surfaces.

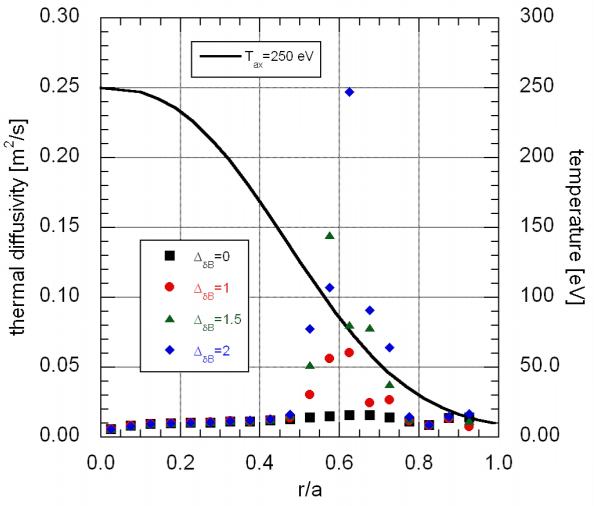

Fig. 2 Radial profile of the ion thermal diffusivity χ_r for a) no RMP (black squares), b) $\Delta_{\delta B} = \delta B/\delta B^{(0)} = 1$ (red circles), c) $\Delta_{\delta B} = 1.5$ (green triangles), and d) $\Delta_{\delta B} = 2$ (blue lozenges), where $\delta B = |\delta \boldsymbol{B}|$ is the strength of RMPs and $\delta B^{(0)}$ is the strength of the RMPs for the case b). Radial profile of temperature is fixed as $T_i = T_{ax}\{0.02 + 0.98\exp[-4(r/a)^{2.5}]\}$ with $T_{ax} = 250$ eV (black solid line), where $r = \sqrt{(R - R_{ax})^2 + Z^2}$ and $R_{ax} = 3.6$ m. The center of the ergodic region is located at $r/a \approx 0.6$.

Here, in the KEATS computations the energy flux is given as [9, 10]

$$\boldsymbol{q}_i(\boldsymbol{x}) = \overline{\int \mathrm{d}^3 v \, \frac{m_i v^2}{2}(\boldsymbol{v}_\parallel + \boldsymbol{v}_d)\delta f}, \qquad (20)$$

where $\overline{\cdots}$ means the time-average, and the averaging time is longer than the typical time-scale of δf (both the orbit and collision times). It is confirmed that the energy flux evaluated by the KEATS code becomes quasi-steady after a sufficient time. The radial profiles of the thermal diffusivities χ_r in Fig. 2 show that the diffusivity in the ergodic region is proportional to the square of the strength of RMPs.

4 Summary

We have been developing the modeling of collisional transport to study the transport phenomena in the ergodic region. For estimation of transport coefficients, we apply the KEATS code to ions in the ergodic region disturbed by resonant magnetic perturbations under the assumption of neglecting effects of an electric field and neutrals, and find that the coefficients are proportional to the square of the strength of RMPs.

For a lower-collisionality case, the transport is strongly affected by the existence of the ergodic region. The strong particle and energy fluxes cause the time-evolution of the background described by the fluid equations. Further simulation study of the transport by solving simultaneously both the kinetic and fluid equations is needed for understanding of the collisionless edge ergodized plasma; the interim report of developing the KEATS code is written in Ref. [9].

Acknowledgements

This work was performed with the support and under the auspices of the NIFS Collaborative Research Program NIFS08KLDD016 and NIFS08KTAD004.

[1] A.B. Rechester and M.N. Rosenbluth, Phys. Rev. Lett. **40**, 38 (1978).
[2] K.H. Burrell *et al.*, Plasma Phys. Control. Fusion **47**, B37 (2005).
[3] T.E. Evans *et al.*, Nature Phys. **2**, 419 (2006).
[4] N. Ohyabu *et al.*, Nucl. Fusion **27**, 2171 (1987).
[5] I. Joseph *et al.*, J. Nucl. Mater. **363-365**, 591 (2007).
[6] A. Maluckov *et al.*, Physica A **322**, 13 (2003).
[7] A. Maluckov *et al.*, Plasma Phys. Control. Fusion **43**, 1211 (2001).
[8] M. Nunami *et al.*, Research Report NIFS Series No. NIFS-871 (2007).
[9] R. Kanno *et al.*, Contrib. Plasma Phys. **48**, 106 (2008).
[10] R. Kanno *et al.*, Plasma Fusion Res. **3**, S1060 (2008).
[11] W.X. Wang *et al.*, Plasma Phys. Control. Fusion **41**, 1091 (1999).
[12] S. Satake *et al.*, Plasma Fusion Res. **1**, 002 (2006).
[13] S. Satake *et al.*, Plasma Fusion Res. **3**, S1062 (2008).
[14] Y. Feng *et al.*, J. Nucl. Mater. **266-269**, 812 (1999).
[15] A. Runov *et al.*, Nucl. Fusion **44**, S74 (2004).
[16] B. Øksendal, *Stochastic Differential Equations* (Springer-Verlag, Berlin Heidelberg, 2003).
[17] P.C. Clemmow and J.P. Dougherty, *Electrodynamics of Particles and Plasmas* (Addison-Wesley, Reading, Mass., 1969).
[18] D.R. Nicholson, *Introduction to Plasma Theory* (John Wiley & Sons, New York, 1983).
[19] A. D. Wentzell, *A Course in the Theory of Stochastic Processes* (McGraw-Hill, New York, 1981).
[20] J. Wesson, *Tokamaks* 3rd ed. (Oxford Univ. Pr., New York, 2004).

Proceedings of ITC18, 2008

Implementation of NBI heating module FIT3D to hierarchy-integrated simulation code TASK3D

Masahiko SATO, Sadayoshi MURAKAMI[1)], Atsushi FUKUYAMA[1)], Yuji NAKAMURA[2)], Kiyomasa WATANABE, Shinichiro TODA,Masayuki YOKOYAMA, Hisamichi FUNABA, Hiroshi YAMADA and Noriyoshi NAKAJIMA

National Institute for Fusion Science, Toki 509-5292, Japan
[1)]*Graduate School of Engineering, Kyoto University, Kyoto 606-8501, Japan*
[2)]*Graduate School of Energy Science, Kyoto University, Kyoto 611-0011, Japan*

TASK3D is an hierarchy-integrated simulation code for toroidal helical plasmas. For the further development of the TASK3D, new module for neutral beam injection (NBI) heating, FIT3D, has been implemented to the TASK3D. In order to check the applicability of the FIT3D module, test simulation for the FIT3D module has been performed together with MHD equilibrium VMEC module, one-dimensional diffusive transport TR module, radial electric field ER module and neoclassical transport database DCOM/NNW module.

Keywords: integrated simulation, helical plasma, NBI heating

1 Introduction

In order to systematically clarify confinement physics in toroidal magnetic confinement systems, a hierarchy-renormalized simulation concept is being developed under domestic and international collaborations with universities and institutes [1]. The hierarchy-renormalized simulation model in toroidal magnetic confinement systems consists of a hierarchy-integrated simulation approach and a hierarchy-extended simulation approach. The hierarchy-integrated approach is mainly based on a transport simulation combining various simplified models describing physical processes in different hierarchies. This approach is suitable for investigating whole temporal behavior of experimentally observed macroscopic physics quantities. For the hierarchy-integrated simulation approach, the integrated modeling code for three dimensional configurations (TASK3D) is being developed on the basis of an integrated modeling code for tokamak plasmas, TASK (Transport Analyzing System for tokamaK) [1], which was developed in Kyoto University. In order to extend the TASK code to be applicable to three dimensional configurations, the transport equations for the rotational transform and the radial electric field have been reformulated by taking the three-dimensional nature of configurations into account. With this new formulation, new modules for the rotational transform (EI module)[2-4] and radial electric field (ER module) [5] have been developed and implemented. The TASK3D has also been extended to read LHD experimental data in Ufile format[5].

The TASK3D has a modular structure as shown in Fig.1. The modular structure of the TASK3D allows us to conduct simulations using an individual module or combination of some modules according to the user's objective. For example, in ref[2-4], calculations on the temporal evolution of the rotational transform and non-inductive current for an LHD experiment have been performed by using the combination of VMEC module for MHD equilibrium, EI module for rotational transform and BSC/FIT module for bootstrap current and Ohkawa current. In ref[6], the MHD stability beta limit in LHD has been analyzed by using VMEC module for MHD equilibrium and TR module for diffusive transport. In this analysis, a linear stability module was used together with these modules to include the effect of MHD instabilities. From the analysis, it is found that the volume average beta value is expected to be beyond 6% in LHD.

In this paper, the further development of the TASK3D, implementation of the NBI (Neutral beam injection) heating module (FIT3D module), is reported. In order to check the applicability of the FIT3D module, test simulations have been performed by using the combination of VMEC module, TR module, ER module, DCOM/NNW module and FIT3D module.

This paper is organized as follows. In Section 2, the numerical scheme of the test simulation for the application of the FIT3D module and the modules used here are explained. In Section 3, we show the numerical result of the test simulation for an NBI heating plasma in LHD. Finally, Section 4 is devoted to brief summary.

2 Numerical scheme of test simulation on application of FIT3D module

The FIT3D is an neutral beam injection (NBI) heating module. The FIT3D has been developed based on three simulation codes[7]: HFREAYA, MCNBI and FIT, where HFREYA evaluates beam ion birth points using Monte-Carlo method and MCNBI calculates radial redistribution

author's e-mail: masahiko@nifs.ac.jp

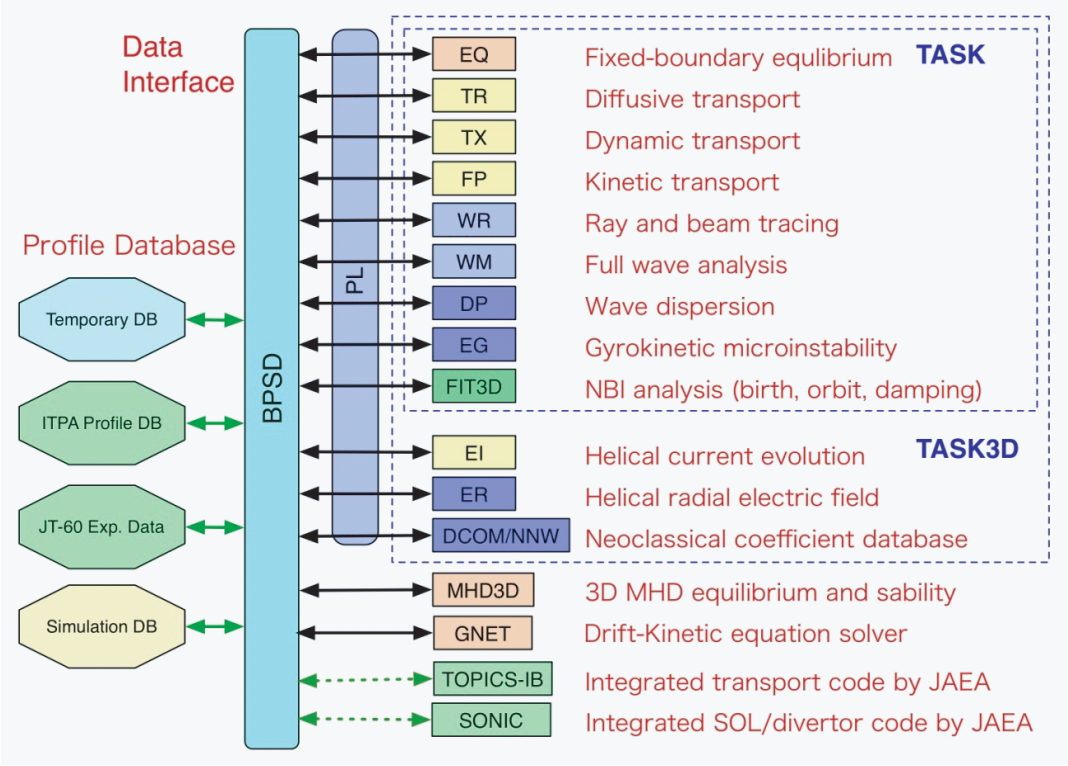

Fig. 1 Module structure of TASK3D.

of beam ions due to prompt orbit effects. Then, heating profiles are obtained by FIT code solving the Fokker-Planck equation. In order to check the applicability of the FIT3D module, test simulation has been performed by using the combination of VMEC module, TR module, ER module, DCOM/NNW module and FIT3D module. The numerical scheme of the test simulation on application of the FIT3D module is shown in Fig.2. The TR module is a one-dimensional diffusive transport module for solving particle transport and heat transport equations. In this test simulation, the density profile is fixed. Hence, the following heat transport equation is solved;

$$\frac{1}{V'^{5/3}}\frac{\partial}{\partial t}\left(\frac{3}{2}n_s T_s V'^{5/3}\right) = -\frac{1}{V'}\frac{\partial}{\partial \rho}\left(V'\langle|\nabla\rho|\rangle\frac{3}{2}n_s T_s V_{Es} - V'\langle|\nabla\rho|^2\rangle n_s \chi_s \frac{\partial T_s}{\partial \rho}\right) + P_s, \quad (1)$$

where n_s is density, T_s is temperature and s expresses species of particles. $V_{Es} = V_{Ks} + \frac{3}{2}V_s$, where V_{Ks} is a heat pinch velocity and χ_s, V_s are a thermal diffusion coefficient, and a particle pinch velocity which consist of neoclassical part and anomalous part. t, ρ, V are time, minor radius variable of magnetic surface and volume enclosed by the magnetic surface, respectively. The prime denotes the derivative with respect to ρ, and $\langle\rangle$ represents the magnetic surface average. P_s is the energy source (or sink). The NBI heating power is included in the energy source

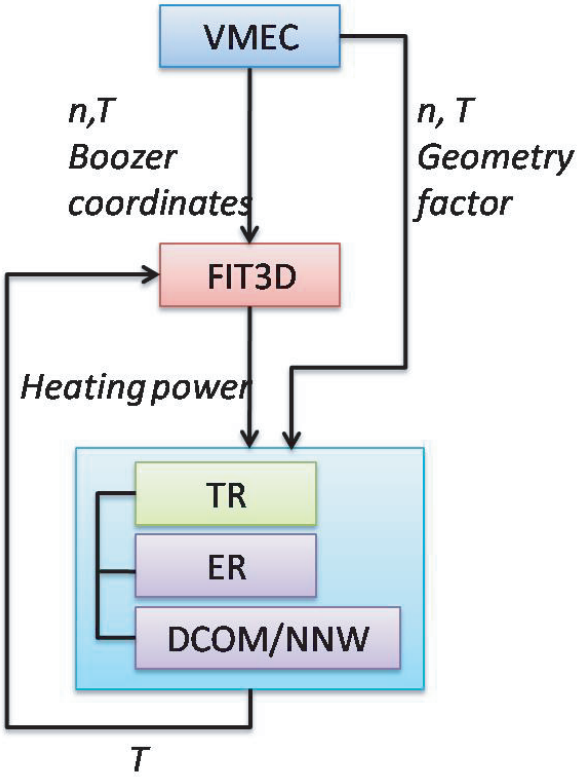

Fig. 2 Numerical scheme of test simulation on application of the FIT3D module, where n is density and T is temperature.

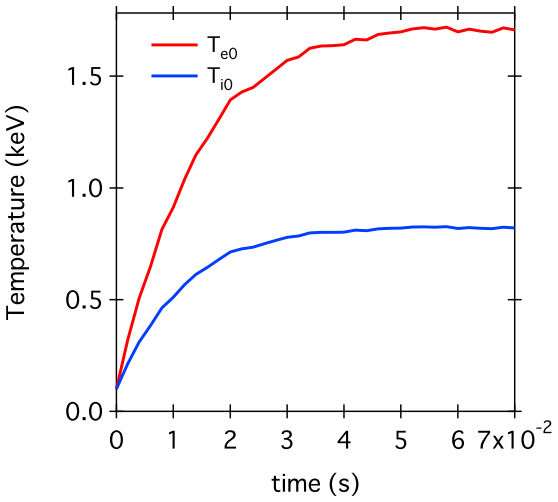

Fig. 3 Time evolution of electron (T_{e0})and ion (T_{i0}) temperature at the plasma center.

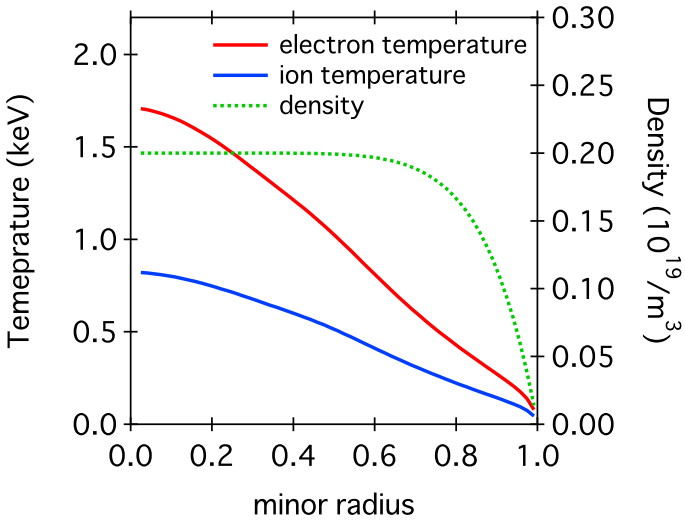

Fig. 4 Radial profiles of electron and ion at t=0.07[s]. The density profile (green line) is fixed.)

term P_s, which is calculated by the FIT3D module. The geometry factors V', $\langle|\nabla\rho|\rangle$, $\langle|\nabla\rho|^2\rangle$ in eq.(1) are calculated by the VMEC module. In the test simulation, the profiles of the geometry factors are fixed after the MHD equilibrium is calculated for the initial state by the VMEC module.

Since the ambiplolar condition is not satisfied intrinsincally due to the non-axisymmetry of helical plasmas and the radial electric field E_r is determined by neoclassical transport. For this purpose, ER module is calculated the radial electric field from the ambipolar condition $\Gamma_e = \Gamma_i$, where Γ_e and Γ_i are electron and ion neoclassical particle flux, respectively. For the evaluation of the neoclassical transport flux, DCOM/NNW module is used. The DCOM/NNW is the database of the neoclassical diffusion coefficients being constructed by the DCOM/NNW (Diffusion Coefficient Calculator by Monte Carlo Method / Neural NetWork) [8], based on the Monte-Carlo code, DCOM.

By the TR module, the profiles of the temperature of the electron and ion are updated and then the updated profiles are used for input parameters of the FIT3D module. Then, the heating power is recalculated for new temperature profiles.

3 Numerical result of test simulation on application of the FIT3D module

In order to check the applicability of the FIT3D module, test simulation has been performed for an LHD plasma according to the numerical scheme shown in Fig.2. In this section, numerical result of the test simulation is shown. In the test simulation, the initial temperature profiles of electron and ion are chosen as $T_s = (T_{s,0} - T_{a,s})(1-\rho^2) + T_{a,s}$, where $T_{s,0} = 0.1$[keV] and $T_{a,s} = 0.01$[keV]. We set the density profile as $n = (n_0 - n_a)(1-\rho^8) + n_a$, where $n_0 =$

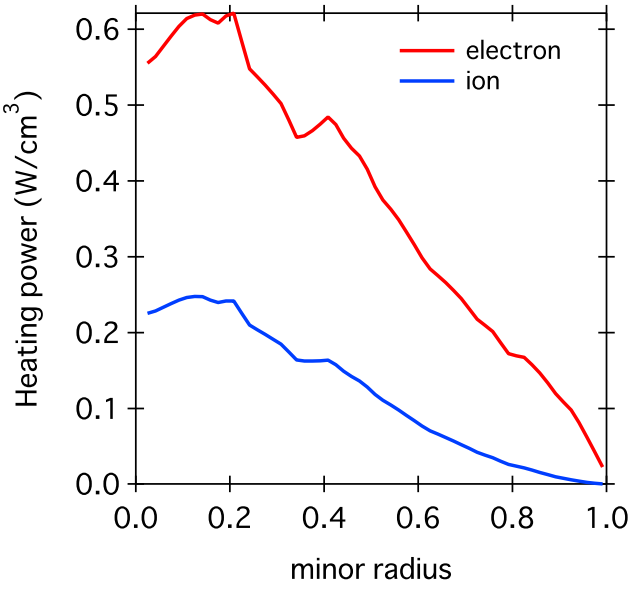

Fig. 5 Radial profiles of electron and ion heating power at t=0.07[s].

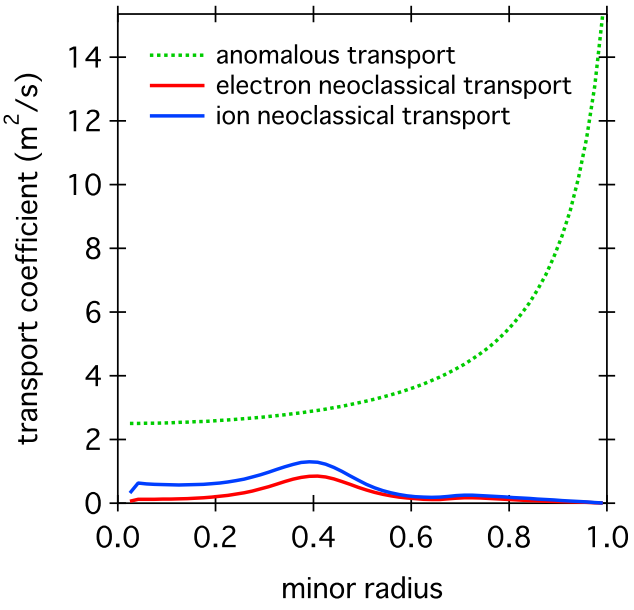

Fig. 6 Radial profiles of electron and ion neoclassical transport coefficient and anomalous transport coefficient at t=0.07[s].

$2[10^{19}/\mathrm{m}^3]$ and $n_a = 0.01[10^{19}/\mathrm{m}^3]$. Anomalous transport coefficient is assumed to be $\chi^{an} = 2/(1 - 0.85\rho^2)$ [m^2/s]. The profiles of the density and the anomalous transport coefficient are fixed. The magnetic field strength is set to be B=2.5[T]. For the NBI heating, three tangential NBI in LHD are considered. Their injection beam ion energy E_b and beam power P_b are set to be (E_b, P_b) = (170 [keV],3.45 [MW]), (150 [keV],2.75 [MW]),(148 [keV], 2.75 [MW]), respectively. Figure 3 shows time evolution of the temperatures of the electron (T_{e0}) and the ion (T_{i0}) at the plasma center. The temperatures T_{e0} and T_{i0} are saturated at about t=0.05[s]. The profiles of the temperature, heating power and transport coefficient at t=0.07[s] are shown in Figs.4, 5 and 6, respectively. The heating power for the electron is about three times that of the ion as shown in Fig.5. On the other hand, the temperature of the electron is about twice that of the ion as shown in Fig.4.

4 Summary

The NBI heating module, FIT3D, has been implemented to TASK3D. In order to check the applicability of the FIT3D module, test simulation of a NBI heating plasma for LHD has been performed by the combination of VMEC, FIT3D, TR, ER and DCOM/NNW modules. From the test simulation, the applicability of the FIT3D module and the linkage of essential modules for analysis of the transport phenomena in LHD have been confirmed. In this paper, the anomalous transport coefficient is fixed for simplicity. The evaluation of the energy confinement time for various anomalous transport model is a future work.

[1] A.Fukuyama *et al.*, Proc. of 20th IAEA Fusion Energy Conf. (Villamoura, Portugal, 2004) IAEA-CSP-25/CD/TH/P2-3.
[2] Y. Nakamura *et al.*, Fusion Sci. and Tech. 50 (2006) pp.457-463.
[3] Y. Nakamura *et al.*, Proc. of 21st IAEA Fusion Energy Conf. (Chengdu, China, 2006) IAEA-CN-149/TH/P7-1.
[4] Y. Nakamura *et al.*, Plasma Fusion Res. 3 (2008) S1058.
[5] M. Sato *et al.*, Plasma Fusion Res. 3 (2008) S1063.
[6] M. Sato *et al.*, Proc. of 22nd IAEA Fusion Energy Conf. (Geneva, Switzerland, 2008) TH/P9-18.
[7] S. Murakami *et al.*, Trans. Fusion Technol. 27 (1995) 259.
[8] A. Wakasa *et al.*, Jpn. J. Appl. Phys. 46 (2007) 1157.

Proceedings of ITC18, 2008

High-wavenumber ballooning-like modes with a finite parallel flow in LHD

Hideaki MIURA[1,2] and Noriyoshi NAKAJIMA[1,2]

[1)]*National Institute for Fusion Science, Gifu 509-5292, Japan*

[2)]*The Graduate University for Advanced Studies (SOKENDAI), Gifu 509-5292, Japan*

Fully three-dimensional, compressible and nonlinear MHD simulations are carried out to study nonlinear evolution of ballooning-like modes in LHD. A near-ideal dynamical evolution shows that growths of ballooning modes in brings about drastic deformations of the pressure. Another simulation which starts under a finite-amplitude flow parallel to the magnetic field lines suggests that the ballooning modes, which are obtained by the near-ideal simulation, are not sensitive to the parallel perturbation. In the nonlinear stage, only the parallel component of the velocity with $n = 1$ wavenumber survives the nonlinear saturation and the perpendicular velocity components become less energetic. Consequently, the saturated profile of the simulation with flow becomes more organized than that in the simulation without flow.

Keywords: MHD simulation, stability, parallel flow

1 Introduction

Study of magnetohydrodynamic (MHD) instability is one of the most basic and important subjects in the magnetic confinement research. In the Large Helical Device[1], pressure-driven instabilities are expected especially for the position of vacuum magnetic axis position $R_{ax} < 3.75m$ (*inward-shifted* magnetic axis position). Although some MHD signals are observed under an inward-shifted magnetic configuration (typically $R_{ax} = 3.6m$), the MHD activities do not bring about critical deterioration of the plasma profile and a high β-value of $\langle\beta\rangle \simeq 5\%$ has been been achieved.[2, 3, 4]

In order to clarify the mechanisms of a hot plasma to overcome the instabilities in LHD, we have been carrying out the fully three-dimensional, compressible and nonlinear MHD simulations by the use of the MHD In the Non-Orthogonal System (MINOS) code.[5, 6, 7, 8] The series of the MINOS simulations have revealed that there are some mechanisms which can reduce the impact of the instability, such as the profile modification (local fattenings) of the pressure, the release of the free-energy as the parallel kinetic energy, and the linear compressibility effect to reduce the growth rates of the unstable modes. However, we have also found that these mechanisms are not necessarily sufficient to suppress the high-wavenumber ballooning modes when the growths of them are near ideal.[8] Because of the overlapping of linear eigen-functions of the high-wavenumber ballooning modes, a local flattening of the pressure at one rational surface cannot stop growths of the multiple ballooning modes. In the simulations the considerable part of the free energy to drive the instability is released in the direction parallel to the magnetic field lines and the compressibility reduce the growth rates. However, these two mechanisms are not sufficient when the initial equilibrium is strongly unstable.

These results in conjunction with some simulations with the parallel heat conductivity suggest that the mild saturations in the LHD might be achieved through dissipative processes (including some sorts of turbulent viscosities caused by turbulence, which are out of scope of the single-fluid MHD), not through the processes in the frameworks of ideal MHD dynamics. Here we have to note that the suggestions or speculations are based on the simulations starting from an unstable equilibrium with very small random perturbations. While starting simulations from the equilibrium with small perturbations is basic and essential in the framework of the linear stability theory, it also makes senses to consider the plasma dynamics with finite-amplitude perturbations, or finite flows. In fact, the toroidal velocity in LHD experiments reaches to about 40~50 km/s[9], which is not negligible in comparison with the Alfvén velocity, though it is also pointed out in the reference that the flow velocity is not sufficient to stabilize the MHD modes.

Since the computations of the equilibrium with finite flows for fully three-dimensional configurations are not prepared sufficiently yet, it is still difficult to discuss the evolutions of unstable linear eigen-modes in the LHD now. Nevertheless, it may be worth carrying out MINOS simulations starting from the equilibrium with finite-amplitude perturbations, since such a computation can serve as a sort of numerical experiment to examine sensitivity of the linear eigen-modes without the flow to the strong perturbations. Here we concentrate on an initial flow in the direction parallel to the magnetic field lines, since the parallel flow is not directly related with the linear stability theory of the static equilibrium and thus we may be able to understand the time evolutions in the frame work of the stability theory of the static equilibrium. In the next section, we study numerical results of simulations with flows. The

author's e-mail: miura.hideaki@nifs.ac.jp

concluding remarks will be in §.3.

2 Nonlinear Simulation

A MINOS simulation with an initial finite-amplitude parallel flow is provided as follows. We make use of the numerical results of the near-ideal simulation in Ref.[8] as reference data. The number of grid points is $193 \times 193 \times 640$. Dissipative coefficients are set as the resistivity $\eta = 1 \times 10^{-6}$, the shear viscosity $\mu = 1 \times 10^{-6}$, the isotropic part of the heat conductivity $\kappa = 1 \times 10^{-6}$. We make use of a snap shot of the time evolution at $t = 64$ in the reference data as a part of the initial condition because the linear eigen-functions of the ballooning modes are formed at this time.[8] We perturb this initial data by adding a flow parallel to the magnetic field lines. The parallel flow is provided so that the velocity profile in the minor radial direction has the same profile as the pressure, for simplicity. It means $\mathbf{B} \cdot \nabla v_{//} = 0$ initially where $v_{//}$ is the parallel velocity. Then the most unsteady effect is expected in the centrifugal force. Here we set the maximum parallel velocity as the $\rho_0 v_{//}^2 / p = 1/1000$ at the position of the magnetic axis, where v_A is the Alfvén velocity and ρ is the mass density. Note that we have provided the initial equilibrium in the reference data with the peaked beta value $\beta_0 = 3.7\%$. A simple ordering of the right-hand-side terms of the momentum equation suggests that the centrifugal force of the parallel flow is quite smaller than the pressure gradient an the Lorentz force so that the parallel flow can be considered as a sort of the (finite-amplitude) perturbation to the equilibrium without flow.

In Fig.1, time evolutions of the (a)parallel and (b)sum of the normal and binormal components of the velocity with some specific poloidal (m) and toroidal (n) wavenumbers are shown. The wavenumbers are chosen so that the Fourier coefficients are the representatives of the linear eigen-functions. In Fig.1(a), many of the Fourier coefficients grow rapidly, while the $m/n = 0/0$ coefficients of the parallel component of the velocity has extremely large amplitude and stay almost constant. The $m/n = 2/1$ coefficient is perturbed initially due to numerical noise in the preparation of the perturbation. The perpendicular counter part of the $0/0$ coefficient in Fig.1(b) is only $1/10000$ of the parallel one, although it is also sufficiently large compared to the amplitudes of the other ($n \geq 1$) coefficients. A quick comparison of Fig.1 to Figs.2(b) and (c) in Ref.[8] reveals that the growth of the Fourier coefficients in Fig.1 are more rapid than those in Figs.2(b) and (c). Furthermore, the growths of the Fourier amplitudes in Fig.1 are slightly curved, suggesting the contributions of the nonlinear couplings through the dynamical evolutions.

In Fig.2, we see the radial profiles of the $n = 1$ pressure Fourier coefficients in the reference data and the perturbed simulation. It has been verified that the Fourier coefficients compose the linear eigen-function of the ballooning mode in Ref.[8]. We find that the Fourier coefficients in the perturbed simulation are very similar to that in the reference data.

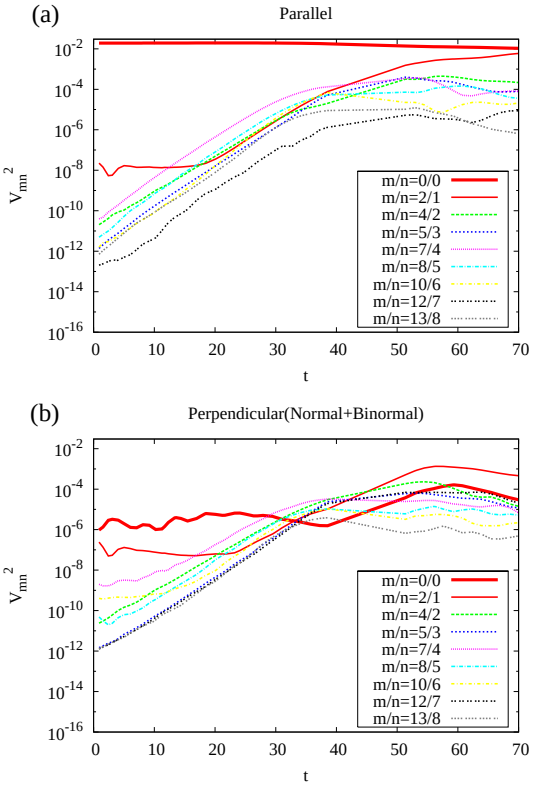

Fig. 1 Time evolutions of the Fourier amplitudes of (a)the parallel and (b)the perpendicular components of the velocity. The wavenumbers are selected as representatives of the linear eigen-modes of in the reference simulation.

In Figs.3 and Figs.4, we see the radial pressure profiles of the $n = 9$ and 15 modes respectively in the reference data and the perturbed simulation. The coefficients in Figs.3(c), (d) and Figs.4(c), (d) are the linear eigen-functions of the ballooning modes obtained in the reference data. Again we find that the Fourier coefficients in Figs.3(a), (b) and Figs.4(a), (b) are very similar to the linear eigen-functions. These observations suggest that the linear eigen-functions are not sensitive to the finite parallel perturbations and they might be good references to study the dynamical evolutions with the flow before the study of the stability theory for the equilibrium with flows are progressed.

In Fig.5(a), the three-dimensional view of the saturated state are shown. The isosurface and contours on a poloidal cross-section (left-hand-side to the paper) of the pressure are shown. The contours on a cross-section in the right-hand-side to the paper are for the pressure fluctuations. It is clear in the contour plots of the pressure fluctuations that the positive fluctuations are localized in the inner-side of the torus while the negative fluctuations are in the outer-side of the torus. The localization is mostly contributed by the $m/n = 2/1$ structure of the parallel ve-

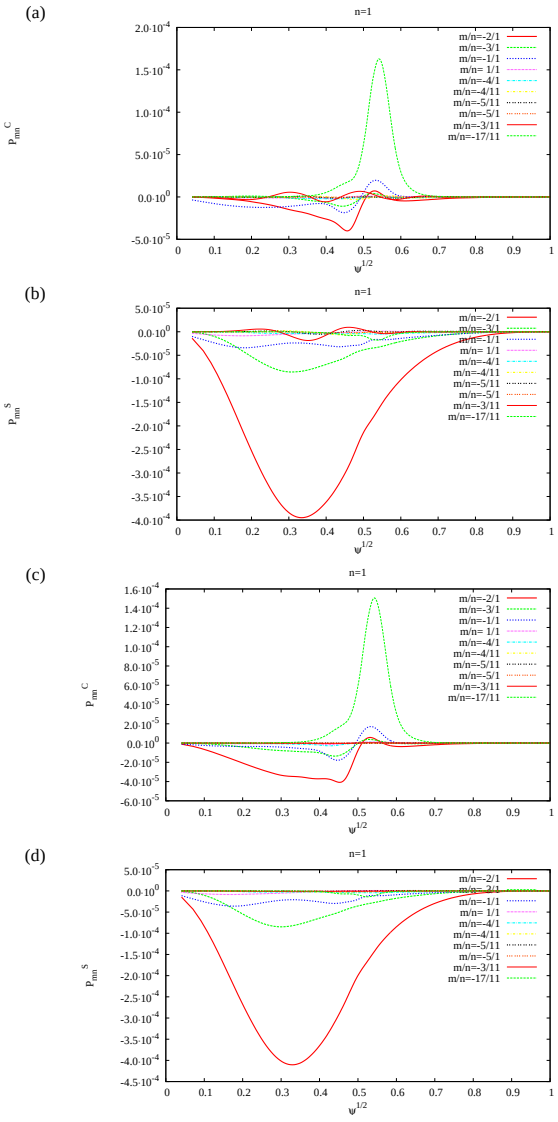

Fig. 2 Comparisons of the radial profiles of $n = 1$ Fourier coefficients. The (a)cosine and (b)sine parts of the Fourier coefficients in the perturbed simulations are compared to those in the reference simulation data (c) and (d), respectively.

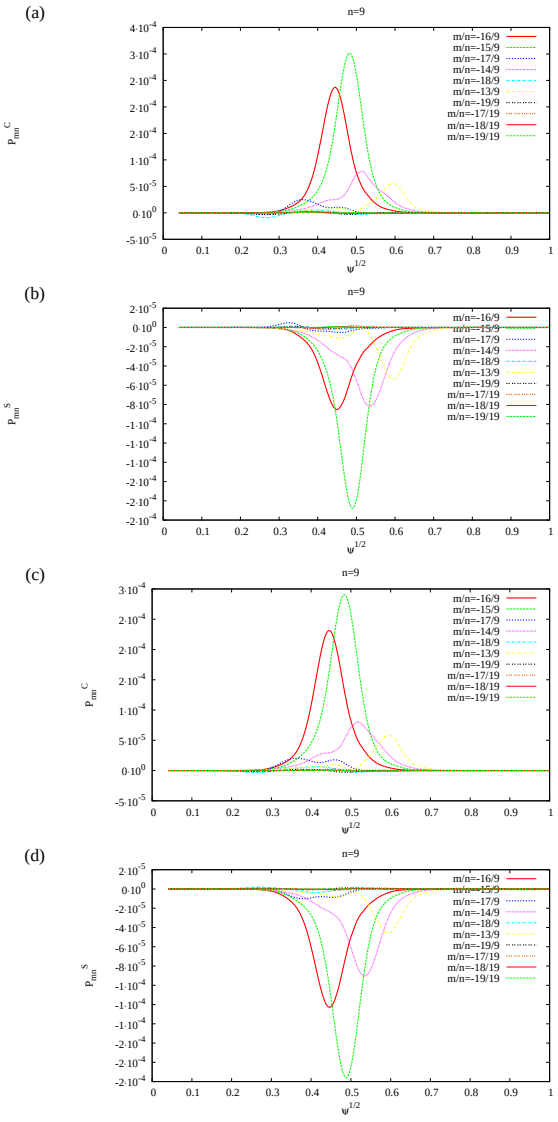

Fig. 3 The radial profiles of the pressure Fourier coefficients with $n = 9$ wavenumber. The(a)cosine and (b)sine parts of the Fourier coefficients in the perturbed simulations are compared to those in the reference simulation data (c) and (d), respectively.

locity as is seen in Fig.1(a) and the centrifugal force of the parallel motions appear being less important. In Fig.5(b), the $m/n = 0/0$ pressure profile of the perturbed simulation at the saturated time is compared to that in the reference data. Note that we have already seen in Ref.[8] that the local fattenings of the pressure can not stabilize the growths of high-wavenumber, near-ideal ballooning modes sufficiently and the $0/0$ profile of the pressure is drastically modified. However, it is easily found that the radial profile in the perturbed simulation is improved to that in the reference data.

3 Concluding Remarks

In this article, we have seen a very primitive view of an influence of the finite perturbations to the linearly-unstable MHD system. It appears that the linear stability theory of an equilibrium without flow can be a starting point to study the dynamical evolution with the parallel flow when neither an equilibrium with flow nor the stability analysis around the equilibrium for the three-dimensional helical configuration are prepared. Although the introduction of the initial parallel flow does not stabilize the instability sufficiently, the mean pressure profile appears better-organized than that in the near-ideal simulation without the parallel flow.

The numerical simulations in this articles have been

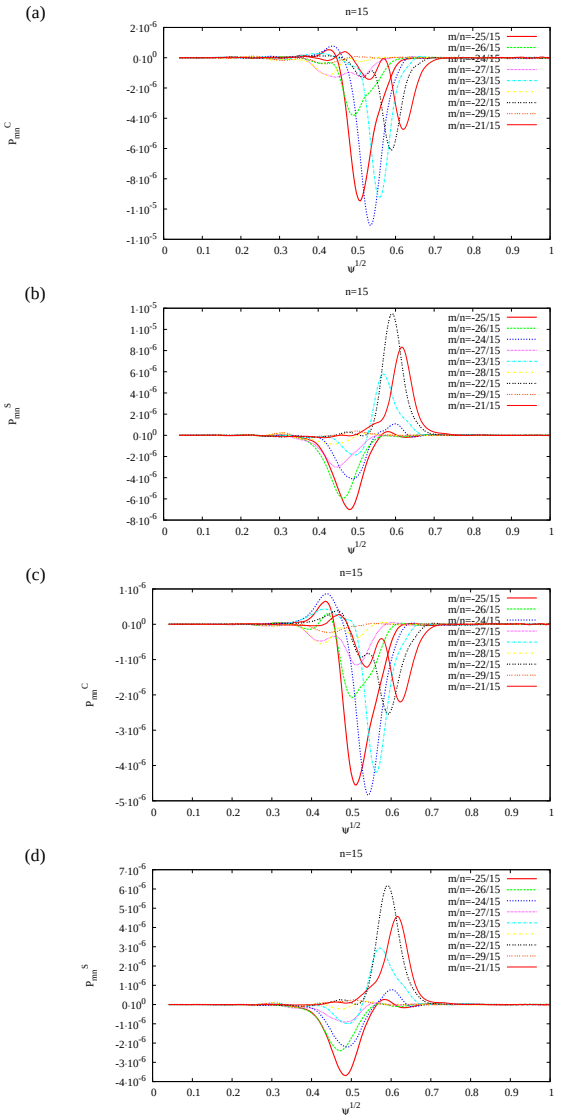

Fig. 4 The radial profiles of the pressure Fourier coefficients with $n = 15$ wavenumber. The(a)cosine and (b)sine parts of the Fourier coefficients in the perturbed simulations are compared to those in the reference simulation data (c) and (d), respectively.

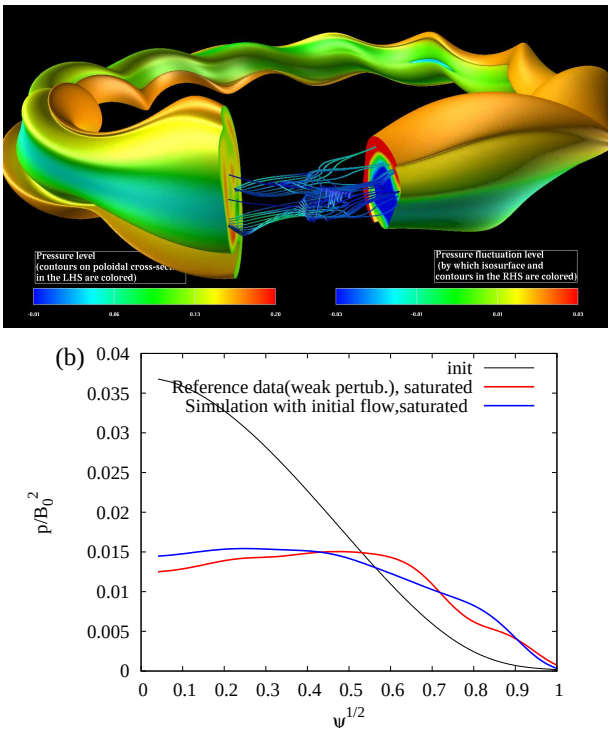

Fig. 5 (a)The three-dimensional view of the saturated state. The isosurface and contours on a poloidal cross-section of the pressure are shown. The contours on a cross-section in the right-hand-side to the paper are for the pressure fluctuations. (b) A comparison of $m/n = 0/0$ pressure profile between the reference data and the perturbed simulation.

carried out by the use of NEC SX-7 “Plasma Simulator” and SX-8 “LHD Numerical Analysis System” of National Institute for Fusion Science, Japan. This research was partially supported by Japan-China Core University Program.

[1] MOTOJIMA, O., et al., “Initial physics achievements of large helical device experiments”, Phys. Plasmas **6** (1999) 1843-1850.
[2] SAKAKIBARA, S., et al., “MHD characteristics in the high beta regime of the Large Helical Device”, Nuclear Fusion **41** (2001) 1177-1183.
[3] MOTOJIMA, O., et al., “Overview of confinement and MHD stability in the Large Helical Device”, Nuclear Fusion **45** (2005) S255-S265.
[4] KOMORI, A., et al., “Development of Net-Current Free Heliotron Plasmas in the Large Helical Device”, 22th IAEA Fusion Energy Conference (2008) OV/2-4.
[5] H. Miura, T. Hayashi and T. Sato, Phys. Plasmas **8** (2001) p. 4870.
[6] H. Miura et al., IAEA-CSP-25/CD/TH2/3, Proc. 20th IAEA Fusion Energy Conference (1-6 Nov. 2004, Villamoura, Portugal)
[7] H. Miura et al.,x TH/P9-18, 22th IAEA Fusion Energy Conference (12-18 October 2008, Geneva, Switzland)
[8] H. Miura and N. Nakajima, TH/P9-18, 22th IAEA Fusion Energy Conference (12-18 October 2008, Geneva, Switzland)
[9] M. Yoshinuma et al, EX/P5-1, 22th IAEA Fusion Energy Conference (12-18 October 2008, Geneva, Switzland)

Proceedings of ITC18, 2008

Numerical Study of Non-Resonant Pressure Driven Mode in Heliotron Plasma

Katsuji ICHIGUCHI[1)] and Benjamin A. CARRERAS[2)]

[1)]*National Institute for Fusion Science, Oroshi-cho 322-6, Toki 509-5292, Japan*
[2)]*BACV Solutions Inc., 110 Mohawk, Oak Ridge, Tennessee 37831, USA*

Linear and nonlinear properties of a non-resonant pressure driven mode localized around the magnetic axis in a heliotron plasma are studied numerically. The non-resonant mode is destabilized when there exist fairly large region around the magnetic axis with steep pressure gradient, rotational transform is close to the mode rational number and the magnetic shear is weak. The nonlinear analysis indicates that the mode can induce sawtooth-like oscillations.

Keywords: Heliotron, MHD, non-linear simulation, non-resonant mode

1. Introduction

In the Large Helical Device (LHD) configuration with the vacuum magnetic axis located at 3.6m (R_{ax}=3.6m), sawtooth-like oscillations were observed with the soft X-ray camera system in fairly high density plasmas produced by pellet injection, although the effect of the MHD activity on the global confinement was small[1]. The instability is localized around the magnetic axis and has an m = 3 mode structure. For this magnetic configuration and as shown in Fig.1, there is no magnetic surface with ι = 1/3. Therefore, there is a possibility that the mode observed experimentally is a non-resonant mode.

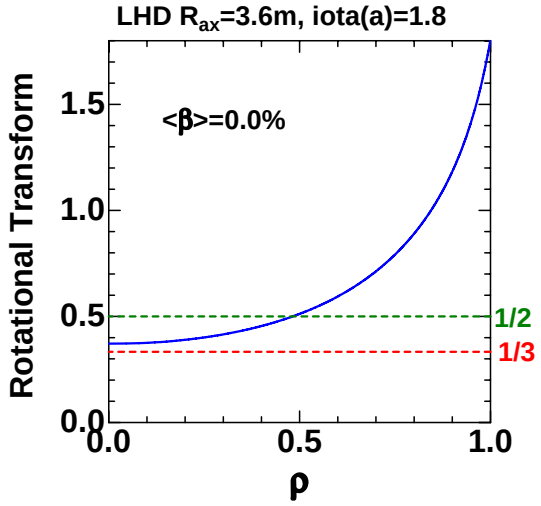

Fig. 1 Rotational transform in vacuum LHD configuration with R_{ax}=3.6m.

Here, we numerically study the properties of such a non-resonant mode. In this study, we analyze its linear ideal stability properties and its nonlinear dynamics in the beta increasing phase. We utilize the VMEC code[2] to calculate the three-dimensional equilibrium under the constraints of the free boundary and the no net-current. We utilize the NORM code[3, 4] for the linear stability and nonlinear dynamics of the mode. This code is based on the reduced MHD equations.

author's e-mail: ichiguch@nifs.ac.jp

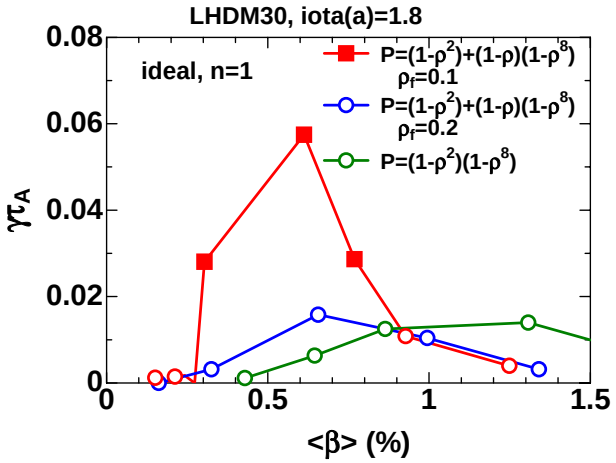

Fig. 2 Growth rates of n = 1 ideal modes.

2. Linear Stability Analysis

The unstable ideal non-resonant mode is obtained only for a steep pressure profile. Figure 2 shows the growth rate of the n = 1 ideal modes for the pressure profile given by

$$P(\rho) = P_0 \begin{cases} (1-a\rho^2) & for \quad 0 \le \rho \le \rho_f \\ b(1-\rho)(1-\rho^8) & for \quad \rho_f \le \rho \le 1 \end{cases} \quad (1)$$

with ρ_f = 0.1. Here, ρ denotes a square-root of the normalized toroidal flux. The factors of a and b are determined so that the value and the first derivative of P are continuous at $\rho = \rho_f$. The growth rate for the profiles of eq.(1) with ρ_f = 0.2 and $P = P_0(1-\rho)(1-\rho^8)$ is also plotted as reference. A non-resonant (m,n) = (3, 1) mode is unstable only in the range of $0.3\% \lesssim \langle\beta\rangle \lesssim 0.8\%$ for the pressure profile of eq.(1) with ρ_f = 0.1. In other cases, the (m,n) = (2, 1) mode can be unstable. The non-resonant mode is also stable for the $P = P_0(1-\rho^2)^2$ and $P = P_0(1-\rho^2)^3$ profiles.

The comparison of these pressure profile shown in Fig.3 indicates that a large pressure gradient around the magnetic axis is necessary for the destabilization of the mode. Hereafter, we focus on the pressure profile of eq.(1) with $\rho_f = 0.1$.

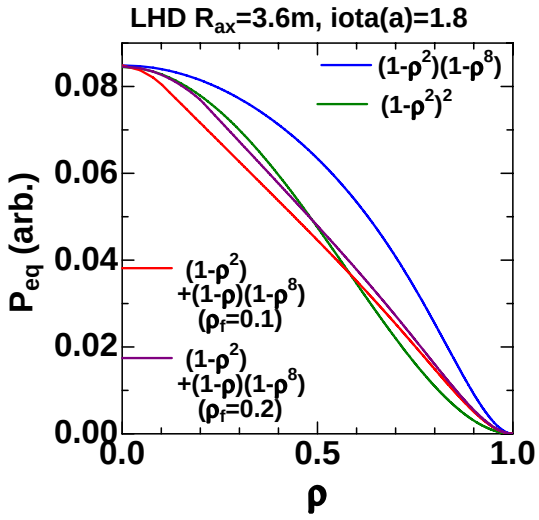

Fig. 3 Pressure profiles examined in linear stability analysis.

In order to investigate the equilibrium properties when the non-resonant mode is destabilized, we examine the beta dependence of the rotational transform. As shown in Fig.4, the rotational transform at the axis decreases and approaches to 1/3 for $\langle\beta\rangle \leq 0.6\%$, and then increases as the beta value increases. Simultaneously, the magnetic shear is reduced in the region of $\rho \lesssim 0.2$ for $0.3\% \lesssim \langle\beta\rangle \lesssim 0.6\%$. Consequently, the non-resonant mode can be destabilized when the pressure profile is steep, the rotational transform is close to the rational number of the mode and the magnetic shear is weak around the axis. These features are similar to those of the infernal mode[5].

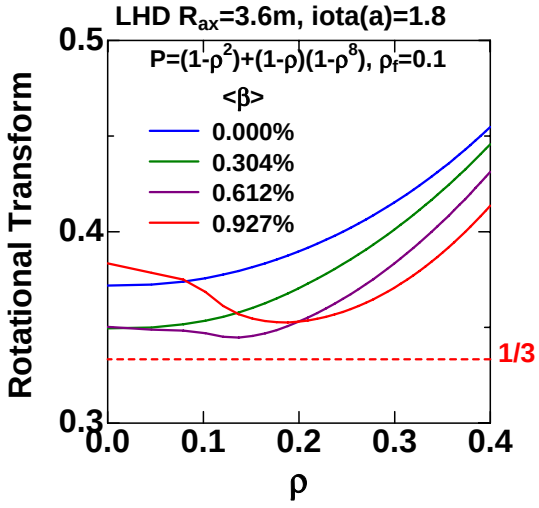

Fig. 4 Beta dependence of rotational transform around the axis.

The non-resonant mode structure is quite different from that of the interchange mode. Figure 5 shows the profile of the stream function of the $n = 1$ mode for $\langle\beta\rangle = 0.612\%$. All components are localized around the magnetic axis. The sidebands of the mode are fairly large and the mode structure is similar to that of the ballooning mode. However, the contour of the perturbed pressure shows a clear $m = 3$ structure, as shown in Fig.6. This structure is consistent with the soft X-ray image shown in Ref.[1].

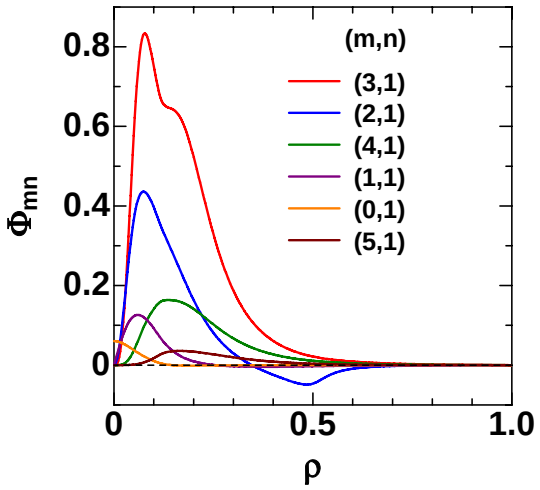

Fig. 5 Stream function of $n = 1$ ideal mode at $\langle\beta\rangle = 0.612\%$.

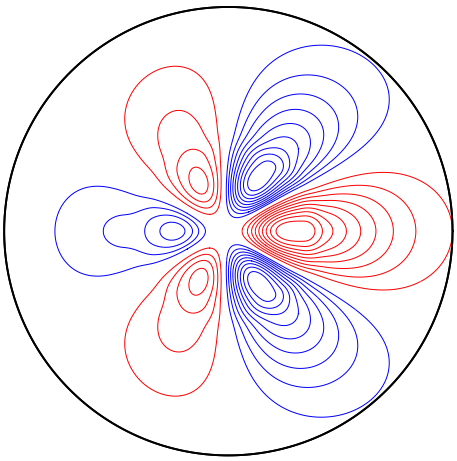

Fig. 6 Contour of perturbed pressure at $\langle\beta\rangle = 0.612\%$ plotted in the region of $\rho \leq 0.3$.

3. Analysis of Non-Linear Dynamics with Multi-Scale Approach

In order to investigate whether the $(m, n) = (3, 1)$ non-resonant mode is actually destabilized as a dominant mode, we examine the nonlinear behavior as beta increases. For this purpose, we utilize the multi-scale numerical scheme[6, 7]. In this scheme, both the effects of the nonlinear dynamics of the perturbation and the pressure increase due to an external source are incorporated in the time evolution of the pressure. In the present analysis,

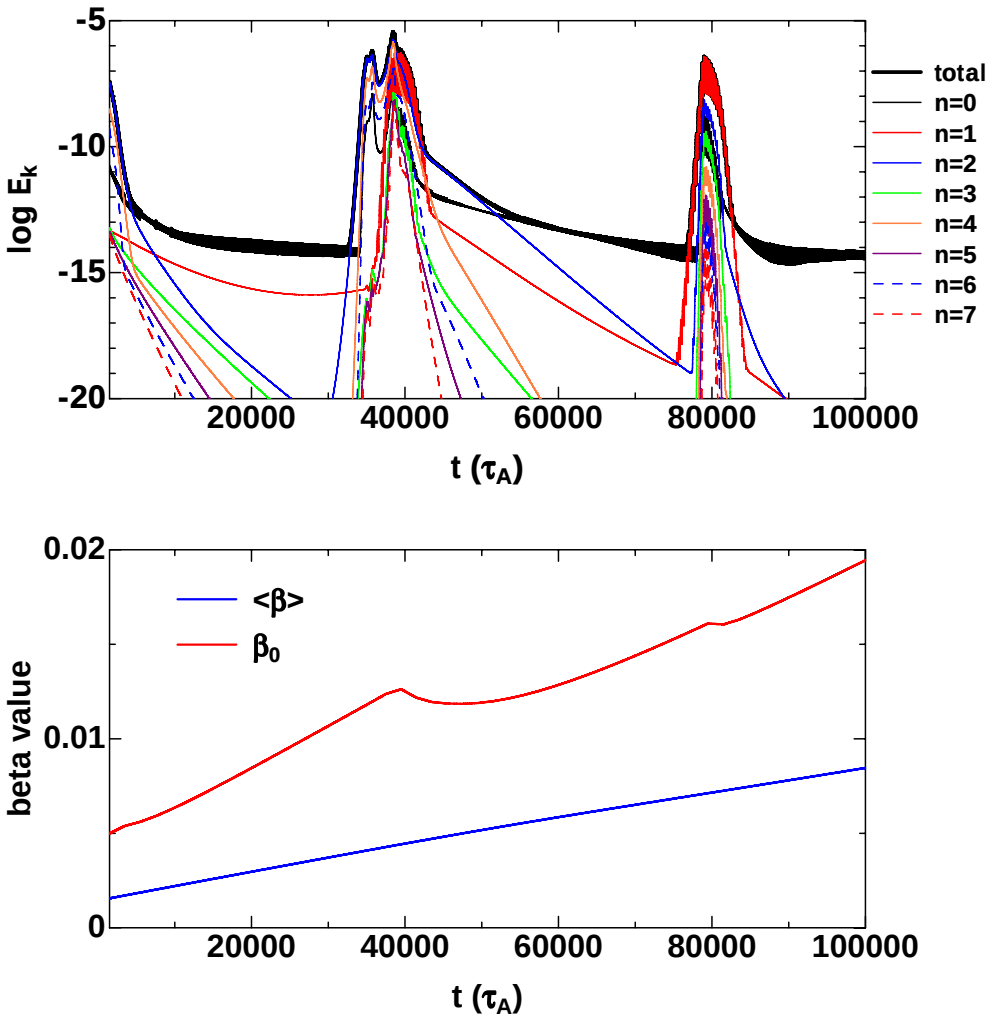

Fig. 7 Time evolution of kinetic energy (top) and beta values (bottom).

we assume the profile given by eq.(1) for the external pressure increment. We also assume the resistivity is such that $S = 10^6$.

Figure 7 shows the time evolution of the kinetic energy of the perturbation and the beta values for the LHD plasma with R_{ax}=3.6m. Two peaks appear during the time evolution of the kinetic energy at $t \sim 39000\tau_A$ and $t \sim 79000\tau_A$. The axis beta degrades after the kinetic energy peaks, while the average beta increases monotonously. The feature of the axis beta seems to be consistent with the experimental results[1] because the axis beta shows a sawtooth-like behavior.

The dominant mode is an $(m, n) = (3, 1)$ mode at both peaks. Figure 8 shows the profiles of the total average pressure and the rotational transform at the peaks. The minimal value of the rotational transform is $\iota = 0.34613$ at $\rho = 0.03125$ for $t = 39950\tau_A$ ($\langle\beta\rangle = 0.442\%$) and $\iota = 0.34865$ at $\rho = 0.13020$ for $t = 79950\tau_A$ ($\langle\beta\rangle = 0.712\%$). In both cases, the magnetic shear is very weak and the pressure gradient is quite steep in the region of $\rho \lesssim 0.2$. Hence, it is the $(m, n) = (3, 1)$ non-resonant mode excited around the axis that causes the reduction of the axis beta. The total pressure profile around the axis is deformed into triangular shape, as shown in Fig.9.

4. Conclusions

The linear stability of the ideal non-resonant mode with $(m, n) = (3, 1)$ is analyzed for the LHD configurations with R_{ax}=3.6m by using the NORM code. The mode becomes unstable only when the pressure profile is steep at a weak shear region with the rotational transform close to the rational value of the mode. This feature is similar to the infernal mode. The nonlinear dynamics of the non-resonant mode is also analyzed by applying the multi-scale approach. A degradation of confinement due to the mode is obtained. The time evolution of the beta value indicates a sawtooth-like activity, which seems to be consistent with the LHD experimental results.

Acknowledgments

This work is supported by NIFS cooperation programs NIFS07KLDD012 and by the Grant-in-Aid for Scientific Research (C) 17560736 of the Japan Society for the Pro-

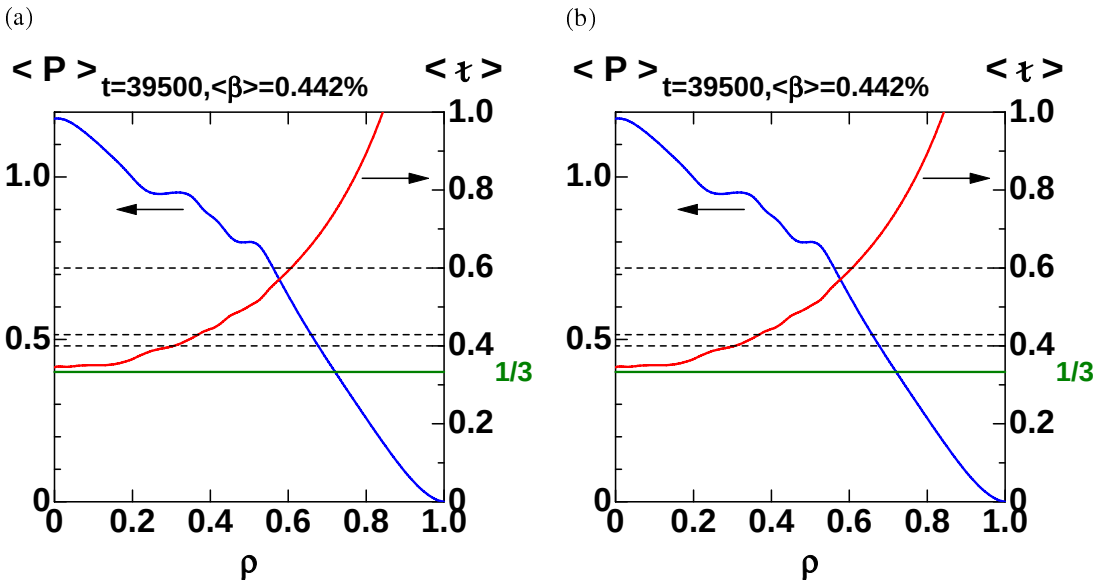

Fig. 8 Profiles of total average pressure and rotational transform at (a) $t = 39950\tau_A$ and (b) $t = 79950\tau_A$.

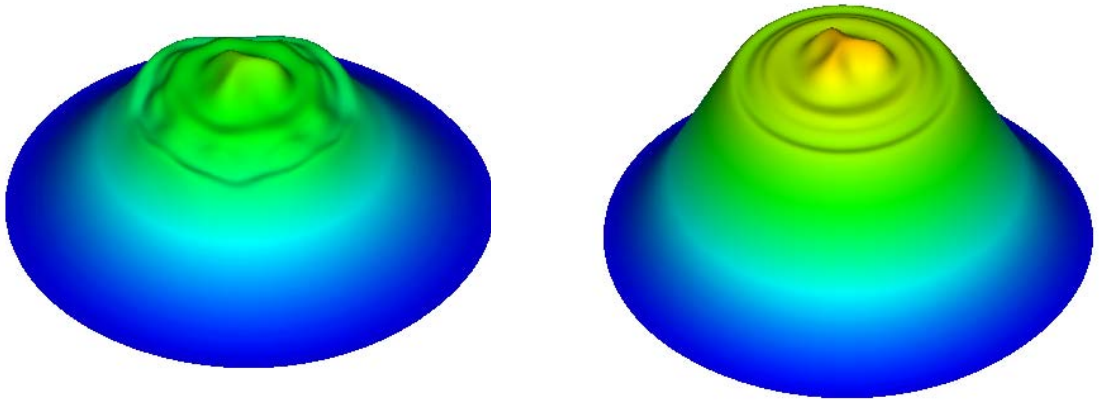

Fig. 9 Bird's eye view of the pressure at $t = 39500\tau_A$ and $\langle\beta\rangle = 0.442\%$ (left) and $t = 79500\tau_A$ and $\langle\beta\rangle = 0.712\%$ (right).

motion of Science.

[1] S. Ohdachi et al., Proc. Fusion Energy Conf. 2006, EX/P8-15.
[2] S.P. Hirshman, et al., Comput. Phys. Commun. **43**, 143-155 (1986).
[3] K. Ichiguchi, et al., Nucl. Fusion **43**, 1101-1109 (2003).
[4] K. Ichiguchi, et al., Fusion Science and Technology **46**, 34-43 (2004).
[5] *for example,* J. Manickam, et al., Nucl. Fusion **27**, 1461-1472 (1987).
[6] K. Ichiguchi, B. A. Carreras, J. Plasma Phys. **72** (2006) 1117-1121.
[7] K. Ichiguchi, B. A. Carreras, Plasma and Fusion Research **3** (2008) S1033.

Proceedings of ITC18, 2008

Effects of Static Magnetic Islands on Interchange mode in Straight Heliotron Configuration

Kinya SAITO[1)], Katsuji ICHIGUCHI[1,2)] and Nobuyoshi OHYABU[1,2)]

[1)]*The Graduate University for Advanced Studies, Toki 509-5292, Japan*
[2)]*National Institute for Fusion Science, Toki 509-5292, Japan*

The interaction between resistive interchange mode with single helicity and static islands due to an external perturbed field is numerically studied in a straight heliotron configuration based on the reduced MHD equations. Especially, the dependence of the island width in the saturation state of the interchange mode on the static island width or the external field magnitude is focused. The dependence is different between the large and small static island cases. In the large static island case. the saturated island width increases as the static island width. In this case, the interchange mode reduces the island width. On the other hand, in the small static island case, the saturated width has an oscillatory tendency with respect to the static island width.

Keywords: magnetic island, resistive interchange mode

1. Introduction

In the magnetic confinement of the fusion plasma, a configuration with nested surfaces is the most favorable. However, error magnetic field originated from such as misalignment of the field coils and the terrestrial magnetism induces static magnetic islands. The static islands have a possibility to degrade the plasma confinement substantially. Particularly, the heliotron configuration is easily affected by the static islands because all of the confinement magnetic field is generated by the outer coils. In the Large Helical Device (LHD), which is a typical heliotron device, the Local Island Divertor coils are installed in the system to control the static islands with $(m, n) = (1, 1)$ actively and investigate the effects on the global confinement[1], where m and n are the poloidal and toroidal mode numbers, respectively.

On the other hand, the interchange mode is a crucial MHD mode in the heliotron configurations. A lot of theoretical analyses have been done for the behavior in the nested surface configurations. However, only a few works treated the behavior of the interchange mode in the existence of the static islands. Therefore, comprehensive study about the direct interaction between the interchange mode and the static islands has not been carried out. Thus, the interaction between the static magnetic island and the dynamics of the interchange mode is numerically analyzed in the present work. Particularly, the island width in the saturation state of the interchange mode is focused. To investigate the basic mechanism, we employ a straight heliotron configuration corresponding to the LHD.

2. Basic Equations and Incorporation of Static Magnetic islands

Since the nonlinear treatment is inevitable for the study of the magnetic islands, we utilize the NORM code[2]. This code solves the nonlinear reduced MHD equations for the poloidal magnetic flux Ψ, the stream function Φ and the plasma pressure P. In the straight heliotron configurations, the equations in the cylindrical coordinates (r,θ,z) are given by

$$\frac{\partial}{\partial t}\left(\frac{\tilde{\Psi}}{R_0}\right) = -\frac{1}{\mu_0}\mathbf{B}\cdot\nabla\tilde{\Phi} + \eta\tilde{J}_z \tag{1}$$

$$\rho\frac{d}{dt}\tilde{U} = -(\mathbf{B}\cdot\nabla\tilde{J}_z + \tilde{\mathbf{B}}\cdot\nabla J_{z\ eq}) + \nabla\Omega_{eq}\times\nabla\tilde{P}\cdot\hat{z} + \nu\nabla_\perp^2\tilde{U} \tag{2}$$

and

$$\frac{dP}{dt} = \kappa_\perp\nabla\cdot\nabla_\perp\tilde{P} + \kappa_\parallel\frac{\mathbf{B}}{B_0}\cdot\nabla(\frac{\mathbf{B}}{B_0}\cdot\nabla\tilde{P}), \tag{3}$$

where the subscript 'eq' refers to the equilibrium quantity and the tilde denotes the perturbed quantity. The factors of ρ and μ_0 are the mass density and the vacuum permeability, respectively. The magnetic differential operator and the convective time derivative are given by

$$\mathbf{B}\cdot\nabla = B_0\frac{\partial}{\partial z} + \hat{z}\times\nabla\Big\{\frac{1}{R_0}(\Psi_{eq} + \tilde{\Psi})\Big\}\cdot\nabla \tag{4}$$

and

$$\frac{d}{dt} = \frac{\partial}{\partial t} + \tilde{\mathbf{v}}_\perp\cdot\nabla, \tag{5}$$

respectively, where $\tilde{\mathbf{v}}_\perp = \nabla\tilde{\Phi}\times\hat{z}$. The operator $\nabla_\perp$ is defined as $\nabla_\perp = \nabla - \hat{z}(\partial/\partial z)$ and $\hat{z}$ is the unit vector in the z direction. The vorticity $\tilde{U}$ and the current density $\tilde{J}_z$ are expressed by $\tilde{U} = \nabla_\perp^2\tilde{\Phi}$, $\tilde{J}_z = \nabla_\perp^2(\tilde{\Psi}/R_0)$, respectively. The average field line curvature Ω_{eq} is given by

$$\Omega_{eq} = \frac{1}{4\pi^2}\int_0^{2\pi}\int_0^{2\pi} d\theta d\zeta\left(\frac{R}{R_0}\right)^2\left(1 + \frac{|\mathbf{B}_{eq} - \overline{\mathbf{B}_{eq}}|^2}{B_0^2}\right). \tag{6}$$

The viscosity and the perpendicular and parallel heat conductivity are introduced with the coefficients of ν, $\kappa_\perp$ and

author's e-mail: saito.kinya@nifs.ac.jp

$\kappa_{//}$, respectively. The resistivity η is also introduced, which is measured by the magnetic Reynolds number S hereafter.

The effects of the static island are incorporated by assuming the existence of an external poloidal magnetic flux perturbation at the plasma boundary[3]. The poloidal flux corresponding to the (m, n) magnetic islands in vacuum configuration is given by the solution of the current-free equation,

$$\nabla_{\perp}^2 \tilde{\Psi} = 0 \tag{7}$$

with the boundary condition,

$$\tilde{\Psi}_{(r=1)} = \Psi_b \cos(m\theta - n\frac{z}{R_0}). \tag{8}$$

The size of the static magnetic islands is controlled by changing the value of Ψ_b. Here, Ψ_b corresponds to the magnitude of the external perturbed magnetic field. We use the solution of Eq.(7) as the initial condition of $\tilde{\Psi}$ for the nonlinear calculation. By following the time evolution of the interchange mode under the boundary condition (8), we can investigate the effects of the static island on the dynamics of the mode. In the present work, the magnetic island $(m, n) = (1, 1)$ is examined.

We study the interaction between the static islands and the interchange mode with $(m, n) = (1, 1)$. For this purpose, we assume that the perturbations have a single helicity of $n/m = 1$ as follows:

$$\tilde{\Psi}(r, \theta, z) = \sum_{n=0, m=n}^{N} \Psi_{m,n}(r) \cos(m\theta - n\frac{z}{R_0}) \tag{9}$$

$$\tilde{\Phi}(r, \theta, z) = \sum_{n=0, m=n}^{N} \Phi_{m,n}(r) \sin(m\theta - n\frac{z}{R_0}) \tag{10}$$

$$\tilde{P}(r, \theta, z) = \sum_{n=0, m=n}^{N} P_{m,n}(r) \cos(m\theta - n\frac{z}{R_0}), \tag{11}$$

where $N = 30$ is employed in the present calculation. The magnetic energy of the perturbation is defined as $E_M = \Sigma_n E_M^n$ and $E_M^n = \frac{1}{2}\int |\nabla_{\perp}\Psi_{nn} \cos(n\theta - n\frac{z}{R_0})|^2 dV$.

3. Equilibrium and Linear Stability

We examine a straight heliotron equilibrium corresponding to the LHD configuration with the vacuum magnetic axis located at 3.6m. The equilibrium is obtained by utilizing the cylindrical part of a three-dimensional equilibrium, which is calculated with the VMEC code[4] under the no net current and the free boundary conditions. We assume the pressure profile of the $P = P_0(1 - r^4)^2$ with the beta value at the axis of $\beta_0 = 4\%$. Figure 1 shows the profiles of the pressure and rotational transform ι. The rational surface of $\iota = 1$ is located at $r = 0.85$ with substantial pressure gradient.

In order to enhance the effect of the interchange mode, we use a large resistivity of $S = 10^4$. We also choose the dissipation parameters of ν, $\kappa_{\perp}$ and $\kappa_{//}$ so that

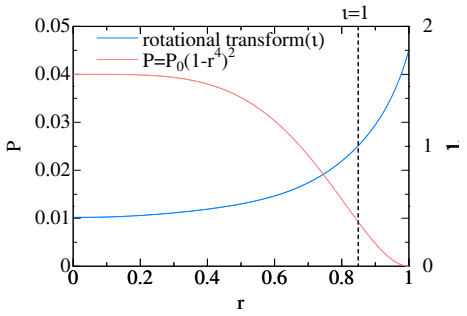

Fig. 1 Profiles of pressure and rotational transform.

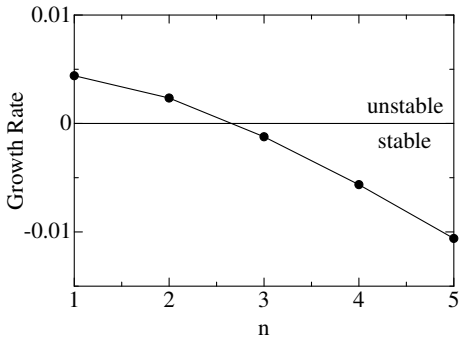

Fig. 2 Linear growth rates of the interchange mode with $\Psi_b = 0$ versus toroidal mode number n.

the $n = 1$ mode should be dominant. Figure 2 shows the linear growth rares for these parameters. The growth rate decreases as the toroidal mode number n. Only the $n = 1$ and $n = 2$ modes are linearly unstable. The growth rate of the $n = 1$ mode is almost twice of that of the $n = 2$ mode.

4. Development of Magnetic Islands due to Nonlinear Dynamics of Resistive Interchange Mode

We examine the development of the magnetic islands in the nonlinear evolution of the resistive interchange mode discussed in Sec.3. Figure 3 shows the dependence of both widths of the initial static islands at $t = 0\tau_A(w_i)$ and the islands in the saturation state at $t = 14,000\tau_A(w_s)$ on the external poloidal flux Ψ_b. Positive and negative values correspond to the magnetic islands with the X-points located at $\theta = 0$ and $\theta = \pi$ in the $z = 0$ poloidal cross section, respectively. The width of initial island w_i is a monotonous function of Ψ_b. However, the tendency of the island width in the saturation state w_s varies depending on Ψ_b.

At first, we look at the case of $w_i = 0$ ($\Psi_b = 0$) as the reference of the case without the static islands. In this case, a typical evolution of the resistive interchange mode is obtained. Figure 4 shows the time evolution of the magnetic energy. There exists a stationary saturation region after the linear growth of the mode. The $(m, n) = (1, 1)$ mode is dominant in the whole region as expected in Sec.3. Figure 5 shows the contour of the helical magnetic flux in the

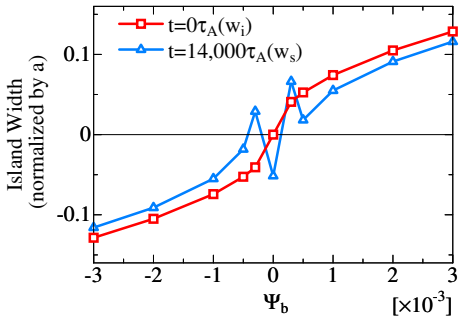

Fig. 3 Dependence of island width in the initial state(w_i) and the saturation state(w_s) on Ψ_b. The width is normalized by the minor radius.

saturation state at $t = 14,000\tau_A$, which is defined as

$$\Psi_h(r,\theta,z) = \Psi_{eq}(r) + \tilde{\Psi}(r,\theta,z) - \frac{r^2}{2}\frac{n}{m}\frac{B_0}{R_0}. \qquad (12)$$

The $(m,n) = (1,1)$ island is generated by the resistive interchange mode even $\Psi_b = 0$. This is due to the assumption of the large resistivity of $S = 10^4$ and the cylindrical geometry. The X-point is generated at $\theta = \pi$ in $z = 0$ poloidal cross section in this case. Dashed line shows the position of the rational surface with $\iota = 1$. The vortex flow occurs so that the plasma inside $\iota = 1$ surface moves toward the X-point.

Next, we consider the cases of the finite initial static islands. The dependence of w_s on w_i or Ψ_b is different between large and small cases of $|w_i|$.

In the large $|w_i|$ case of $|w_i| \geq 5.3 \times 10^{-2}$ ($|\Psi_b| \geq 5.0 \times 10^{-4}$), there exists a tendency that $|w_s|$ increases as $|w_i|$ as shown in Fig.3.

Figure 6 shows the time evolution of the magnetic energy for $w_i = 0.10$ ($\Psi_b = 2.0 \times 10^{-3}$). As in the case of $w_i = 0$, there exits a stationary saturation state, however, the behavior of the mode in the linear region is different. Since $\Psi_{1,1}$ has a large and constant amplitude due to static magnetic islands, the growth rate of $\Psi_{1,1}$ is almost zero. The growth rates of other modes are determined by the convolution with $\Psi_{1,1}$, therefore, each mode has almost the same growth rate. This property of the linear growth rate is common for all finite w_i, but quite different from that in the case of $w_i = 0$ shown in Fig.4.

In the initial state for $w_i = 0.10$ ($\Psi_b = 2.0 \times 10^{-3}$), the X-point is located at $\theta = 0$ as shown in Fig.7(a). This point remains at the same position in the saturation state as shown in Fig.7(b). That is, the phase of the island in the saturation state is determined by that in the initial state, which is independent of the island phase of $w_i = 0$. In this case, $|w_s|$ is smaller than $|w_i|$ and the vortices are generated so that the plasma inside of the $\iota = 1$ surface moves from the X-point to the O-point as shown in Fig.7. This result indicates that the interchange mode reduces the island width in the nonlinear evolution. This property is common for large initial island cases of $|w_i| \geq 5.3 \times 10^{-2}$ ($|\Psi_b| \geq 5.0 \times 10^{-4}$).

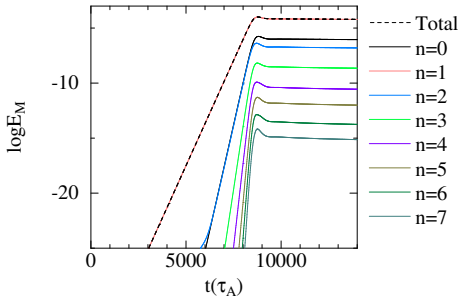

Fig. 4 Time evolution of the magnetic energy for $w_i = 0$.

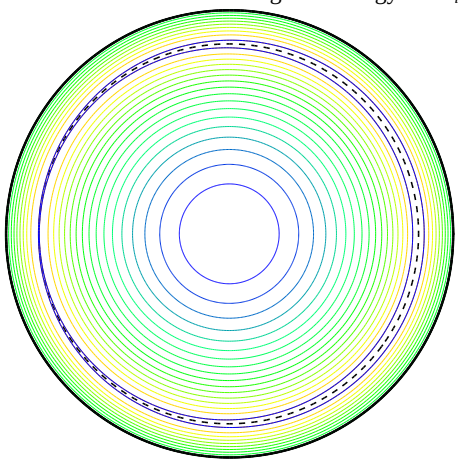

Fig. 5 Contour of helical magnetic flux in $z = 0$ poloidal cross section at $t = 14,000\tau_A$.

On the other hand, in the small initial static island case of $|w_i| < 5.3 \times 10^{-2}$ ($|\Psi_b| > 5.0 \times 10^{-4}$), the dependence of w_s on w_i or Ψ_b is not monotonous, rather oscillatory, as shown in Fig.3. The property of the island development is different from that in the large initial island case.

Figure 8 shows the change of the magnetic islands for $w_i = 4.1 \times 10^{-2}$ ($\Psi_b = 3.0 \times 10^{-4}$). In this case, the phase of the islands are the same as that for $|w_i| = 5.3 \times 10^{-2}$, however, w_s is larger than w_i as shown in Fig,8(a) and (b). Figure 8(c) shows that the vortices are generated so that the plasma inside of the $\iota = 1$ surface moves from the O-point to the X-point. This flow is considered to enhance the reconnection at the X-point. Therefore, the interchange

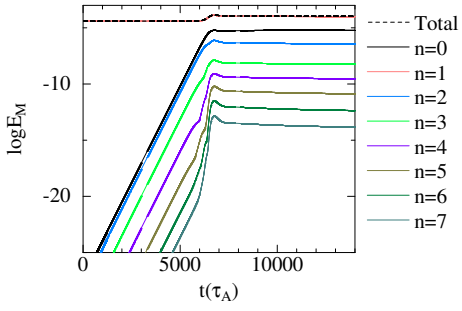

Fig. 6 Time evolution of magnetic energy .

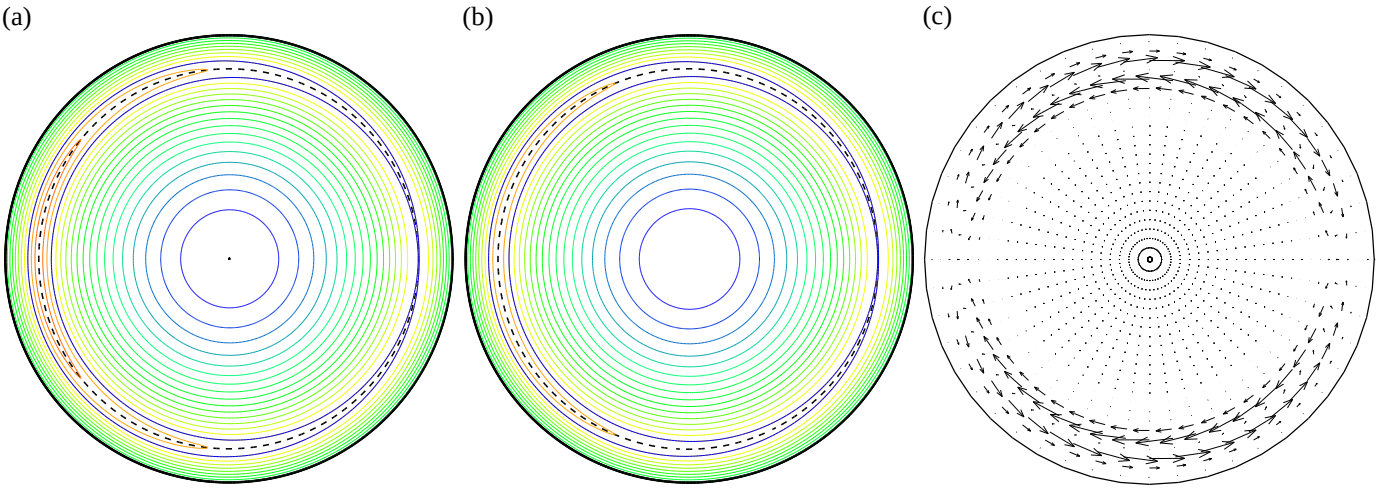

Fig.7 Contour of helical magnetic flux for $w_i = 0.10$ at (a) t=0τ_A and (b) $t = 14,000\tau_A$, and (c) flow pattern at $t = 14,000\tau_A$ for the same w_i.

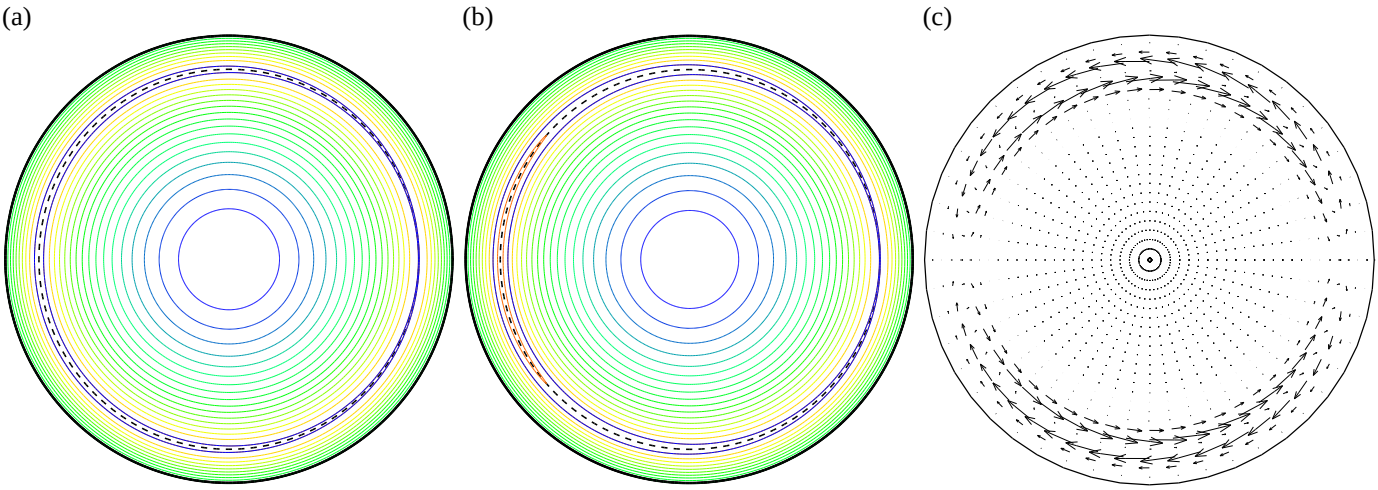

Fig.8 Contour of helical magnetic flux for $w_i = 4.1 \times 10^{-2}$ at (a) t=0τ_A and (b) $t = 14,000\tau_A$, and (c) flow pattern at $t = 14,000\tau_A$ for the same w_i.

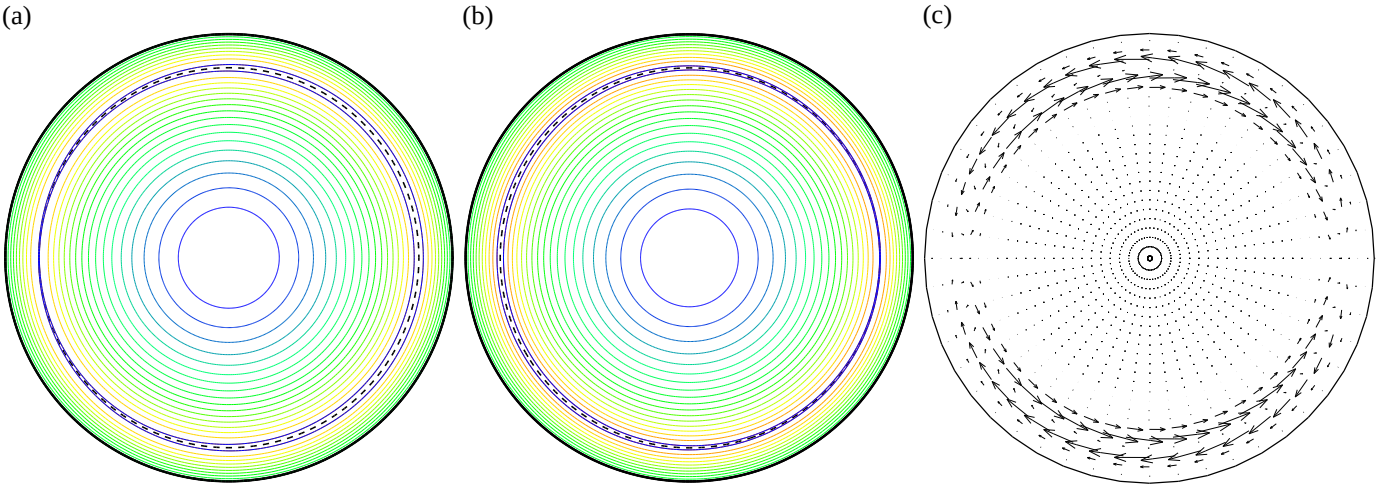

Fig.9 Contour of helical magnetic flux for $w_i = -4.1 \times 10^{-2}$ at (a) t=0τ_A and (b) $t = 14,000\tau_A$, and (c) flow pattern at $t = 14,000\tau_A$ for the same w_i.

mode enhances the island width in the case.

In the case of $w_i = -4.1 \times 10^{-2}$ ($\Psi_b = -3.0 \times 10^{-4}$), we obtain another behavior of the island. In this case, the phase of the island changes in the nonlinear evolution of the interchange mode. The X-point is located at $\theta = \pi$ at $t = 0$, while the point is located at $\theta = 0$ at $t = 14,000\tau_A$ as shown Fig. 9(a) and (b). The vortices are generated so that the plasma inside the $\iota = 1$ surface moves from X-point to O-point in the initial island as shown in Fig. 9(c). The direction of the flow is the same as in the large initial island case, however, it may be strong enough to change the island phase.

5. Conclusions

We study the interaction between the $(m, n) = (1, 1)$ static magnetic islands and the nonlinear dynamics of the resistive interchange mode with the single helicity of $n/m = 1$ by following the time evolution of the mode. Particularly, the dependence of the island development on the width of the initial static island w_i is focused.

At first, we obtain a common feature in the linear state of the time evolution of the interchange mode for all finite w_i. The $(m, n) = (1, 1)$ component of the magnetic energy is dominant and almost constant due to the existence of the initial state islands in the present analysis. Therefore, other components have almost the same growth rate because these components are mainly generated by the convolution with the dominant mode.

As the interchange mode evolves nonlinearly, the width and the phase of the magnetic islands can change. Such change are considered to be attributed to the vortex flow generated by the interchange mode. A common tendency between the flow and the change of the islands is also found for all finite w_i. When the flow is generated so that the plasma moves toward the initial O-point, the island width is reduced or the phase of the island is changed. On the other hand, the flow is generated so that the plasma moves toward the initial X-point, the island width is enhanced.

The dependence of the island width in the saturation state on w_i is different between the cases of the large and small $|w_i|$. In the large initial island case for $|w_i| \geq 5.3 \times 10^{-2}$, the island width in the saturation state increases monotonously as $|w_i|$. The location of the O-points and the X-points is determined by the positions in the initial islands and independent of the island phase for $w_i = 0$. In this case, the interchange mode has a contribution to reduce the island width for each w_i.

On the other hand, in the small island case for $|w_i| < 5.3 \times 10^{-2}$, the island development does not have such a definite tendency as in the large island case. The dependence of the island width in the saturation on w_i is not monotonous. In one case, the width is enhanced by the interchange mode evolution with the phase fixed. In other case, the island phase changes so that the positions of the X-point and the O-point are replaced in the saturation state. Such behavior in the small island cases may be due to the existence of a large island for $w_i = 0$, which results from the choice of the large resistivity of $S = 10^4$ in this analysis.

Acknowledgments

This work is supported by NIFS cooperation programs NIFS08KLDD015 and NIFS08KNXN129 and by the Grant-in-Aid for Scientific Research (C) 17560736 of the Japan Society for the Promotion of Science.

References

[1]N. Ohyabu et al., J. Nucl. Mater. **266-269** 302 (1999).
[2]K. Ichiguchi et al., Nucl. Fusion **43**, 1101-1109 (2003).
[3]T. Unemura et al., Phys. Plasmas **11** 1545 (2004).
[4]S. P. Hirshman et al., Comput. Phy. Commun. **43** 143 (1986).

Proceedings of ITC18, 2008

Identification of magnetic islands in Heliotron J experiments

Yasuhiro SUZUKI[1,2], Satoshi YAMAMOTO[3], Satoru SAKAKIBARA[1,2], Hiroyuki OKADA[3], Kazunobu NAGASAKI[3], Shinji KOBAYASHI[3], Kiyofumi MUKAI[3], Shinya WATANABE[3], Tohru Mizuuchi[3], Yoshiro NARUSHIMA[1,2], Yuji NAKAMURA[4], Kiyomasa WATANABE[1,2] and Fumimichi SANO[3]

[1]*National Institute for Fusion Science, Toki 509-5292, Japan*
[2]*Graduate University for Advanced Studies, SOKENDAI, Toki 509-5292, Japan*
[3]*Institute of Advanced Energy, Kyoto University, Uji 611-0011, Japan*
[4]*Graduate School of Energy Science, Kyoto University, Uji 611-0011, Japan*

The equilibrium response on the magnetic island produced by external perturbed coils is studied in a Heliotron J plasma. In order to identify the equilibrium response, the magnetic diagnostic system is developped. This system consists of two parts. One is the diagnostic system based on the toroidal array of the magnetic probe. Another is a numerical code based on the 3D MHD equilibrium calculation code. Using the diagnostic system, the perturbation field friven by the equilibrium response is identified.

Keywords: magnetic island, equilibrium response, magnetic diagnostics, HINT2

1 Introduction

Generating and keeping clear flux surfaces are an aim of magnetic confinement researches, because magnetic islands and stochasticity of magnetic field leads the degradation of the confinement connecting and overlapping filed lines. In tokamaks, the degradation of the confinement due to generating islands like the locked mode and neoclassical tearing mode (NTM) were observed and studied [1, 2]. The same degradations is also observed in helical system [3]. Thus, understanding and controlling of island dynamics are urgent and critical issues to aim the fusion reactor.

A method to identify magnetic islands is measuring electron temperature and density. However, if islands are rotating or healing, the profile measurement cannot identify island structure. Another method is the magnetic diagnostics. Since the magnetic diagnostics detects the change of magnetic flux directly, above problems are resolved but the diagnostics must be installed appropriately to detect perturbed field of islands.

In this study, we study island dynamics using the magnetic diagnostics in Heliotron J plasmas. Heliotron J is an $L = 1/M = 4$ helical axis heliotron configuration. A characteristic is the rotational transform profile with low magnetic shear ($\iota \sim 0.5$) to improve the particle confinement. This means there is a possibility of generating of large magnetic islands with coupling the perturbation. If low-n resonances are superposed, low-n/m islands appear. This is an advantage to study the equilibrium response on those islands. Thus, in order to generate low order magnetic islands and study the impact of the equilibrium response, external perturbation coils are designed and installed in Heliotron J device. In next section, the external coil to produce low-n perturbation field and magnetic diagnostic system are explained. Then, first result of the island experiment is shown. Lastly, we summarize this study and show the outlook.

author's e-mail: ysuzuki@LHD.nifs.ac.jp

2 Experimental setup

2.1 Heliotron J device

The Heliotron J device is a medium sized helical-axis heliotron device ($R_0 = 1.2$[m], $a_p = 0.17$ [m], $B_0 \leq 1.5$ [T]) with an $L = 1/M$=4 helical coil. Figure 1 shows a schematic view of the experimental system. In this experiment, the initial plasma is produced by using the second harmonic X-mode ECH (70 GHz, < 0.45 MW, non-focusing Gaussian beam) launched from a top port. To measure the perturbed field, four magnetic probes (MP01~04) are installed along the toroidal direction. These probes detect the perturbation along the toroidal direction.

2.2 Installation of external perturbation coils

The magnetic island is produced by the perturbed field from the 'MHD instability' and 'MHD equilibrium response' (equilibrium response). The identification of the perturbation on the MHD instability is easy because only detection of the perturbation from the equilibrium field is done. However, the identification of the perturbation on the equilibrium response is difficult because the equilibrium response driven by the equilibrium current (the Pfirsh-Schlüter (P-S) current, inductive and non-inductive net toridal currents) along rippled field lines is very small. To detect the perturbation and identify the mode, the improvement of the magnetic diagnostic is necessary. As a

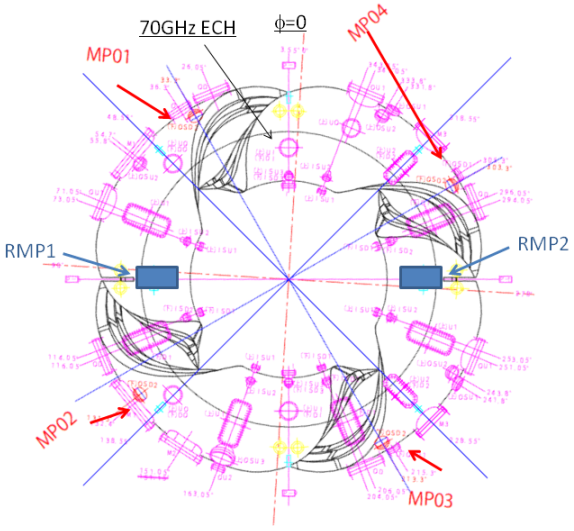

Fig. 1 Experimental setup

first step, we measure the distortion of the P-S current flow on a low-n (n=1) magnetic island. In theoretical analyses, spontaneous generation of the magnetic island by the equilibrium response is only for $n \geq 4$ because of M=4. In order to appear the distortion of the P-S current on the low-n island, the external perturbation with n=1 is necessary. Thus, we designed and installed two pair of resonant magnetic perturbation (RMP) coils in Heliotron J device. RMP coils to generate n=1 perturbation were installed at hatched positions in fig. 1. Poincaré maps of magnetic field lines are plotted at ϕ=0. Bold lines in the figures indicate the wall of the vacuum vessel. In Fig. 1(a), an island chain by n/m=4/8 natural resonance appears. On the other hand, in figs.1(b) and (c), large magnetic islands with n/m=1/2 appear by the external perturbed field and the phase of islands is different in both cases. The external perturbed field is the quadrupole field and it is generated by two pairs of trim coils. The phase of islands can be changed by controling the current of the trim coil. Figure 2 shows radial profiles of the rotational transform as a function of the major radius R at ϕ=0. Although the external perturbed field is superimposed, profiles and positions of the magnetic axis are hardly changed.

3 Equilibrium response on low-n islands

Since the profile of the plasma pressure becomes flat on the island, the P-S current changes with flattering pressure profile. The distortion of the P-S current leads the equilibrium response. The magnetic diagnostic identifies the response localized along the toroidal direction.

To study the equilibrium response due to the finite β

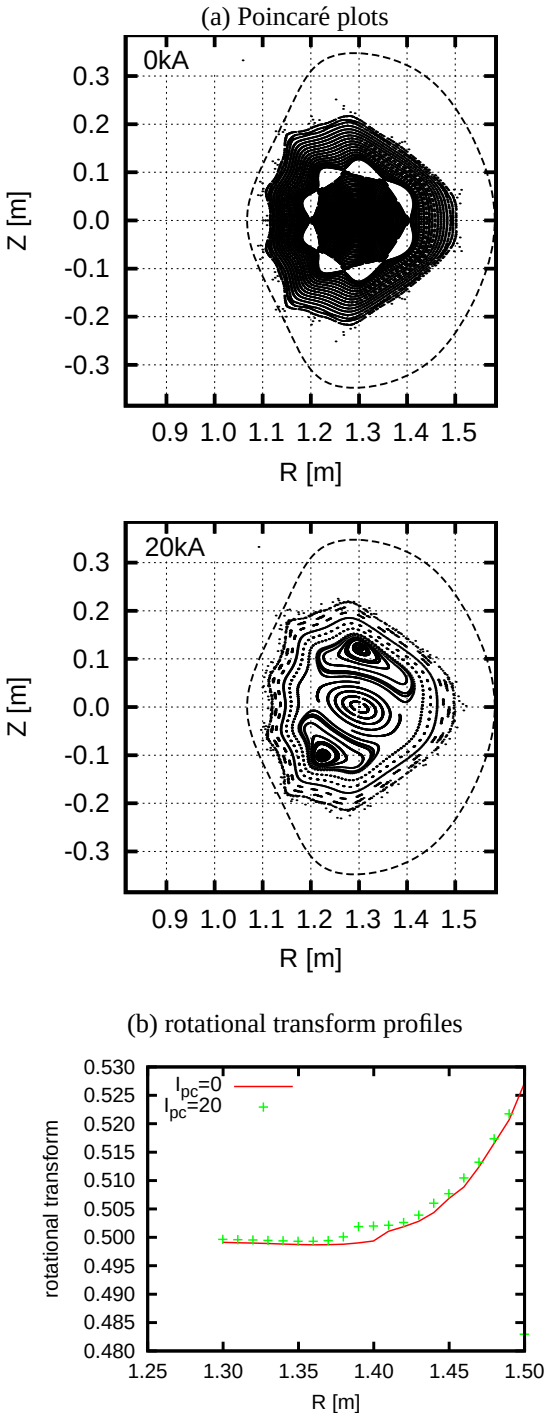

Fig. 2 Poincaré plots of magnetic field lines with and without the RMP and profiles of the rotational transform as the function of R are plotted at $\phi=\pi 4$. Wth the RMP, I_{RMP} is 20kA.

effect, the MHD equilibrium is caluclated by the HINT2 code [4], which is a 3D MHD equilibrium solver without an assumption of nested flux surfaces *a priori*. In fig. 3, Poincaré plot of magnetic field lines and the rotational transform are shown for $<\beta>\sim 0.2\%$ corresponding to fig. 2. For the comparison, the rotational transform for the vacuum is also shown in fig.3(b). Increased β, the ratational transform on the axis increases and the resonant surface with n/m=1/2 disappears. Thus, islands with n/m=1/2 also disappear. However, flux surfaces sitll distort due to external RMP field.

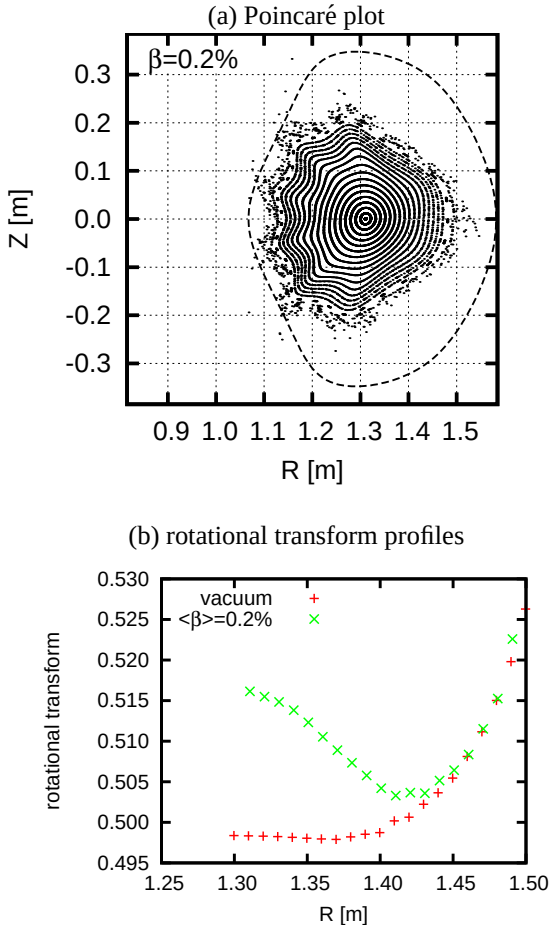

Fig. 3 Poincaré plots of magnetic field lines with and without the RMP and profiles of the rotational transform as the function of R are plotted at $\phi=\pi 4$. Wth the RMP, I_{RMP} is 20kA.

To identify the equilibrium response due to the finite-β effect, the pressure-induced driven by the plasma is calculated. In fig. 4, the normal component of pressure-induced field, B_n, is shown. Poloidal and toroidal angle are normalized by 2π and θ=0 is the ourtermost position on Z=0 plane. The marginal difference appears along ϕ=0.9 line. On the other hand, the poloidal component of pressure-induced field, B_θ, is plotted along the position of magnetic probes in fig. 5. the poloidal field changes along the toroidal angle ϕ. However, the change along ϕ is very small because of $\delta B_\theta < 1[G]$. Since the difference is very small,

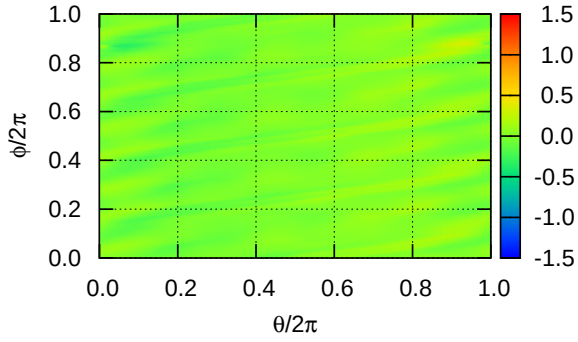

Fig. 4 The normal field component on the vacuum vessel

the observation by the magnetic probe is difficult. In order to observe significantly, the improvement of S/N ratio by the flux loop is necessary. This result will be the basis to design the flux loop in Heliotron J device.

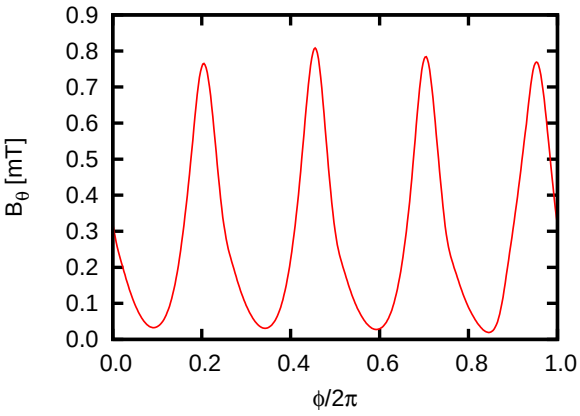

Fig. 5 The poloidal field at magnetic probes

Finally, we show the first result of the experimants with the RMP. For a typical shot (#32741) in this experiments, the density was kept $\sim 10^{19}$ and small net-toroidal current (< 1kA) flowed in the plasma. Unfortunately, in this experiment, the profiles of electron temperature and densitycould not be observed. In fig. 6, signals of magnetic probes with (#32741) or without (#32745) the RMP, respectively. Comparing fig. 6 (a) and (b), differences appeared in both cases. With the RMP, there are no signals of MP02~04. This suggests a possibility that the P-S current flow was distorted by the magnetic island and the external field driven by the P-S current was changed. However, this is still a speculaion. The identification of the equilibrium response is a future subject. The signal observed by the magnetic probe was very small. Since the equilibrum response is guessed ver small, the flux loop is efficient to observe small perturbation field. The design of flux loop to Heliotron J device is another future subject.

(a) I_{pc}=0kA

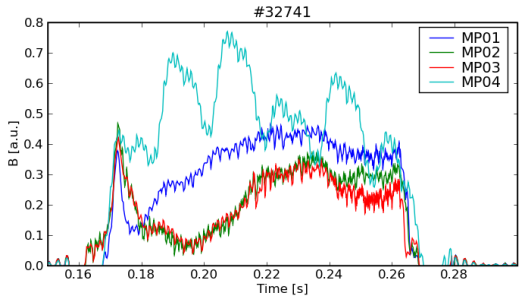

(b) I_{pc}=20kA

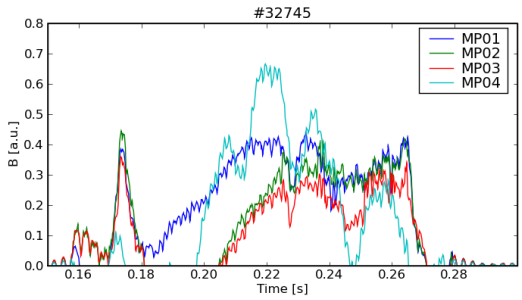

Fig. 6 Signals of magnetic probes in two shot (no RMP and RMP). With the RMP, I_{RMP} is 20kA.

4 Summary

we designed and installed external RMP coils to Heliotron J device. These coils can produce low-*n* magnetic island in the plasma. To detect the distortion of the equilibrium current flow by large magnetic islands, we can study the effect of the equilibrium response on the spontaneous changing magnetic islands. We also show the fisrt result of the configuration with the RMP field. The difference on signals of magnetic probes appeared by superposing the RMP field.

Acknowledgements

The authors thank the Heliotron J staff for conducting the experiments and discussions. This work was supported by NIFS/NINS under the NIFS Collaborative Research Program (NIFS07KOAP018, NIFS07KUHL011, NIFS07KUHL016, NIFS06KTAT023, NIFS07KNXN104) This work was partly supported by Grant-in-Aid for Scientific Research from the Japan Society for the Promotion of Science No. 17206094, 19360419 and 20760585.

[1] J. A. Snipes, D. J. Campbell, P. S. Haynes et al., Nucl. Fusion **28**, 1085 (1988)
[2] R. Carrera, R. D. Hazeltine, and M. Kostchenreuther, Phys. Fluids **29**, 899 (1986)
[3] N. Ohyabu et al., Phys. Rev. Lett. **97**, 055002 (2006)
[4] Y. Suzuki et al., Nucl. Fusion. **46**, L19 (2006)

Proceedings of ITC18, 2008

High-beta toroidal equilibria with flow in reduced fluid models

Atsushi ITO and Noriyoshi NAKAJIMA

National Institute for Fusion Science,322-6 Oroshi-cho, Toki 509-5292, Japan

A reduced set of equations for high-beta tokamak equilibria with flow comparable to the poloidal sound velocity are solved analytically for the single-fluid MHD case and numerically for the case of two-fluid model with ion Finite Larmor radius (FLR). The analytical solution for single-fluid MHD equilibria shows that the shift of the magnetic axis from the geometric axis is enhanced by a slightly super-poloidal-sonic flow and it produces a forbidden region of equilibrium by the poloidal-sonic flow. Numerical analysis shows that there are regular solutions for the two-fluid model with FLR that are singular for the single-fluid and Hall MHD models, and that the solutions depend on the sign of the $E \times B$ flow compared to that of the ion diamagnetic flow.

Keywords: two-fluid model, finite Larmor radius, equilibria with flow, magnetohydrodynamics

1 Introduction

In magnetically confined plasmas, equilibrium flows may suppress instability and turbulent transport to give rise to improved confinement modes where high-β is achieved. In such equilibria, the scale lengths characteristic of microscopic effects not included in single-fluid magnetohydrodynamics (MHD) cannot be neglected. Small scale effects on flowing equilibria due to the Hall current have been studied with two-fluid or Hall MHD models [1]. However, these models are consistent with kinetic theory only for cold ions. A consistent treatment of hot ions in a two-fluid framework must include the ion gyroviscosity and other finite Larmor radius (FLR) effects. In the fluid formalism of collisionless magnetized plasmas, these effects are incorporated by means of asymptotic expansions in terms of the small parameter $\delta \sim \rho_i/a$, where ρ_i is the ion Larmor radius and a is the macroscopic scale length. With a slow dynamics ordering, $v \sim \delta v_{th}$ where v and v_{th} are the flow and thermal velocities respectively, the ion FLR terms [2] are much simplified in the reduced models for large-aspect-ratio, high-β tokamaks [3] after relating δ to the inverse aspect ratio expansion parameter $\varepsilon \equiv a/R_0 \ll 1$, where R_0 is the characteristic scale length of the major radius.

We have derived reduced sets of two-fluid equations for axisymmetric equilibria with flow in the orders of the poloidal sound velocities [4]. The poloidal-sonic flow can be described by the reduced model with the relation $\delta \sim \epsilon$. This reduced set can describe the three models: single-fluid (ideal) MHD, Hall MHD, two-fluid model with ion FLR. For the single fluid case, we can find analytical solutions and study the effects of poloidal-sonic flow on the equilibrium profiles (Sec. 3). For the case of two-fluid model with ion FLR, we have found numerically regular solutions that depend on the sign of the $E \times B$ flow compared to that of the ion diamagnetic flow (Sec. 4).

author's e-mail: ito.atsushi2@nifs.ac.jp

2 Basic equations

The equations for two-fluid equilibria with hot ions are

$$\nabla \cdot (n\mathbf{v}) = 0, \tag{1}$$

$$\nabla \times \mathbf{E} = 0, \tag{2}$$

$$m_i n \mathbf{v} \cdot \nabla \mathbf{v} = \mathbf{j} \times \mathbf{B} - \nabla (p_i + p_e) - \lambda_i \nabla \cdot \Pi_i^{gv}, \tag{3}$$

$$\mathbf{E} + \mathbf{v} \times \mathbf{B} = \frac{\lambda_H}{ne} (\mathbf{j} \times \mathbf{B} - \nabla p_e), \tag{4}$$

$$\mu_0 \mathbf{j} = \nabla \times \mathbf{B} \tag{5}$$

$$\mathbf{v} \cdot \nabla p_i + \gamma p_i \nabla \cdot \mathbf{v} + \lambda_i \left(\frac{2}{5} \gamma \nabla \cdot \mathbf{q}_i \right) = 0, \tag{6}$$

$$(\mathbf{v} - \lambda_H \mathbf{j}/ne) \cdot \nabla p_e + \gamma p_e \nabla \cdot (\mathbf{v} - \lambda_H \mathbf{j}/ne) + \lambda_e \left(\frac{2}{5} \gamma \nabla \cdot \mathbf{q}_e \right) = 0, \tag{7}$$

where m_i is the ion mass, n is the density, $\mathbf{v}$ is the ion flow velocity, $\mathbf{E}$ and $\mathbf{B}$ are the electric and magnetic fields, $\mathbf{j}$ is the current density, p_i and p_e are the ion and electron pressures, Π_i^{gv} is the ion gyroviscous tensor, $\mathbf{q}_i$ and $\mathbf{q}_e$ are the ion and electron heat fluxes respectively, and $\gamma = 5/3$. The diagonal components of the pressure tensors are assumed to be isotropic. The electron mass m_e is neglected because $m_e \ll m_i$. The electron gyroviscosity is also neglected since $\rho_e \ll \rho_i$. We have introduced the artificial indices λ_i, λ_e and λ_H that label the two-fluid, non-ideal terms: $(\lambda_i, \lambda_e, \lambda_H) = (0, 0, 0)$ for single-fluid (ideal) MHD, $(0, 0, 1)$ for two-fluid MHD with adiabatic electron pressure but zero ion Larmor radius (Hall MHD) and $(1, 1, 1)$ for two-fluids with finite ion Larmor radius. Here we shall consider the corresponding toroidal axisymmetric equilibria, where, in cylindrical coordinates (R, φ, Z), the magnetic field $\mathbf{B}$ can be written as

$$\mathbf{B} = \nabla \psi(R, Z) \times \nabla \varphi + I(R, Z) \nabla \varphi \tag{8}$$

The asymptotic expansion is defined in terms of the inverse aspect ratio $\varepsilon \equiv a/R_0 \ll 1$ where a and R_0 are

the characteristic scale length of the minor and major radii respectively. The following high-β tokamak orderings for compressible reduced MHD are applied,

$$B_p \sim \varepsilon B_0, \quad p_i \sim p_e \sim \varepsilon\left(B_0^2/\mu_0\right), \quad |\nabla| \sim 1/a.$$

The variables are expanded as $f = f_1 + f_2 + f_3 + \ldots$ We assume slow dynamics ordering,

$$v \sim \delta v_{thi}, \quad m_i n v^2 \sim \|\Pi_i^{gv}\| \sim \delta^2 p_{i,e},$$

$$q_i \sim v p_{i,e} \sim \delta v_{thi} p_{i,e}.$$

The energy of flows in the order of the poloidal sound speed $v \sim C_{sp} \equiv (B_p/B_0)(\gamma p/n m_i)^{1/2}$ is the third order of the magnetic energy,

$$m_i n v^2 \sim \varepsilon^2 p \sim \varepsilon^3\left(B_0^2/\mu_0\right).$$

The equation for ψ_1 is identical to the reduced GS equation for single-fluid, static equilibria,

$$\Delta_2 \psi_1 = -\mu_0 R_0^2 \left[\left(\frac{2x}{R_0}\right) p_1' + g_*'\right] - \left(\frac{I_1^2}{2}\right)', \tag{9}$$

where $\Delta_2 \equiv (\partial^2/\partial R^2 + \partial^2/\partial Z^2)$, $p_1 \equiv p_{i1} + p_{e1}$ and

$$p_{i2} + p_{e2} + \frac{B_0}{\mu_0 R_0} I_2 \equiv g_*(\psi_1). \tag{10}$$

The following quantities are shown to be arbitrary functions of ψ_1,

$$n_0 = n_0(\psi_1), \quad p_{i1} = p_{i1}(\psi_1),$$
$$p_{e1} = p_{e1}(\psi_1), \quad I_1 = I_1(\psi_1). \tag{11}$$

The effects of flow, two-fluid and ion FLR appears in the equation for ψ_2 [5, 4].

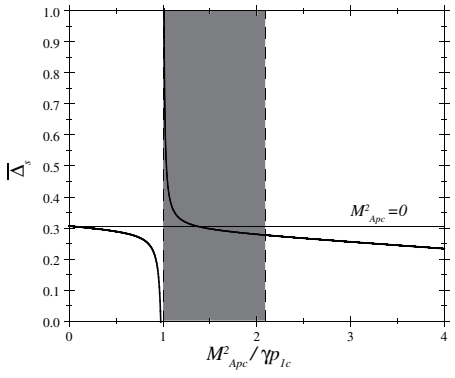

Fig. 1 The Shafranov shift as a function of poloidal Mach number. The shaded region is beyond the equilibrium beta limit.

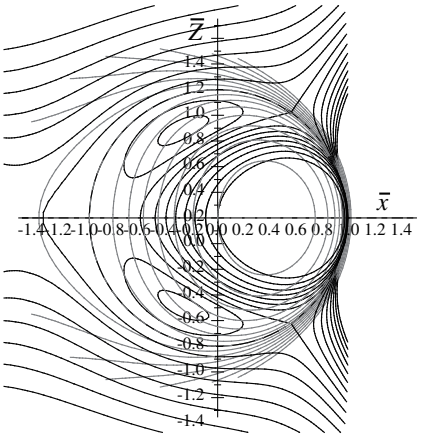

Fig. 2 The magnetic surfaces for $M^2_{Apc} = 0$ (gray) and for $M^2_{Apc} = 1.05\gamma p_{1c}$ (black).

3 Single-fluid equilibria

Single-fluid MHD equilibria are given by setting $(\lambda_i, \lambda_e, \lambda_H) = (0, 0, 0)$. For linear profiles of the lowest-order quantities, we have derived analytical equilibria of high-beta tokamaks with poloidal-sonic flow and the expressions for the shift of the magnetic axis, the shift of the pressure maximum and the equilibrium beta limit [6]. We assume linear profiles for the following free functions,

$$p_1 = \varepsilon\left(B_0^2/\mu_0\right) p_{1c}(\psi_1/\psi_c), \tag{12}$$

$$g_* + \frac{I_1^2}{2\mu_0 R_0^2} = \varepsilon^2\left(B_0^2/\mu_0\right) g_c\left(\frac{\psi_1}{\psi_c}\right), \tag{13}$$

$$M_{Ap}^2 = \varepsilon M_{Apc}^2(\psi_1/\psi_c), \tag{14}$$

$$M_{Ap}(\psi_1) \equiv -\left[\mu_0 m_i n_0(\psi_1)\right]^{1/2} R_0 \Phi_1'(\psi_1)/B_0 \tag{15}$$

is the leading order of the poloidal Alfvén Mach number, $\beta_1 \equiv \gamma p_1/(B_0^2/\mu_0)$. The fixed boundary conditions for ψ_1 and ψ_2 are given by assuming circular cross section as

$$\psi_1(a,\theta) = \psi_2(a,\theta) = 0. \tag{16}$$

We have also solved for the vacuum region $1 \le r$ assuming that ψ_1 and ψ_2 are smoothly connected at the plasma-vacuum boundary $r = a$. We then apply the following normalization

$$r/a \equiv \bar{r}, \qquad \psi_1/\psi_c \equiv \bar{\psi}_1, \qquad \psi_2/\psi_c \equiv \varepsilon\bar{\psi}_2,$$

$$a/R_0 \equiv \varepsilon, \quad \psi_c/B_0 R_0 a \equiv \varepsilon B_p.$$

(For figures 1 - 8, $\varepsilon = 0.1$, $g_c = 4$, $p_{1c} = 3.2$ and $B_p = 1$.) The solution indicates the modification of the magnetic structure and the departure of the pressure surfaces from the magnetic surfaces by sub- or super-poloidal-sonic flows. We have shown that the shift of the magnetic axis

from the geometric axis is enhanced by a slightly super-poloidal-sonic flow and it produces a forbidden region of equilibrium by the poloidal-sonic flow (Fig. 1). Figure 2 shows the magnetic structure for $M^2_{Apc}/\gamma p_{1c} = 1.05$, where the equilibrium beta limit is violated since the separatrix appears in the plasma region. The physical mechanism of the shift of the pressure maximum from the magnetic axis due to the poloidal-sonic flow can be explained in analogy to those of the geodesic acoustic mode and the slow magnetosonic wave.

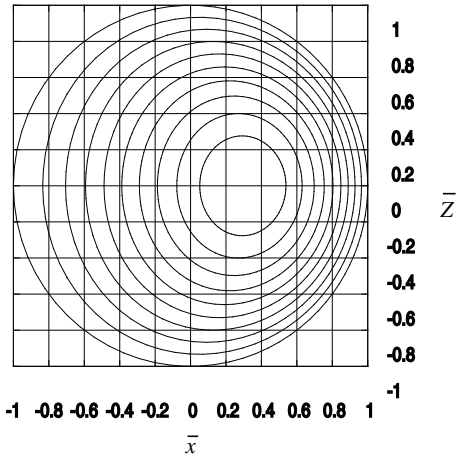

Fig. 3 Isosurfaces of ψ for $V_{Ec} = -\sqrt{\gamma p_{1c}}$ and $V_{dc} = -1$.

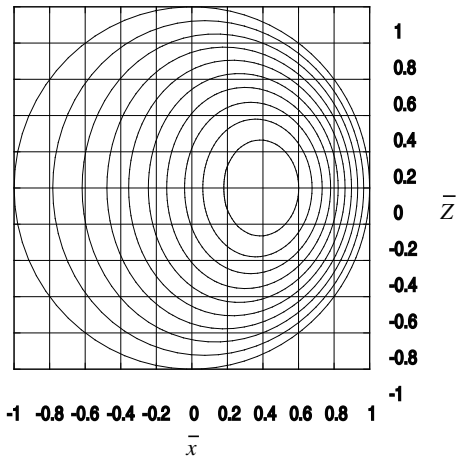

Fig. 4 Isosurfaces of p for $V_{Ec} = -\sqrt{\gamma p_{1c}}$ and $V_{dc} = -1$.

4 Two-fluid equilibria with FLR

Two-fluid equilibria with FLR are obtained by setting $(\lambda_i, \lambda_e, \lambda_H) = (1, 1, 1)$. From Faraday's law (2), we obtain $\mathbf{E} \equiv -\nabla\Phi$. The generalized Ohm's law (4) is rewritten as

$$\mathbf{E} + \mathbf{v}\times\mathbf{B} = \frac{\lambda_H}{ne}\left(\nabla p_i + m_i n\mathbf{v}\cdot\nabla\mathbf{v} + \lambda_i\nabla\cdot\Pi_i^{gv}\right). \quad (17)$$

The ion flow velocity $\mathbf{v}$ is defined from Eq. (17) up to the second order as

$$\mathbf{v} \equiv \mathbf{v_E} + \lambda_H\mathbf{v}_{di} + v_\parallel(\mathbf{B}/B), \quad (18)$$

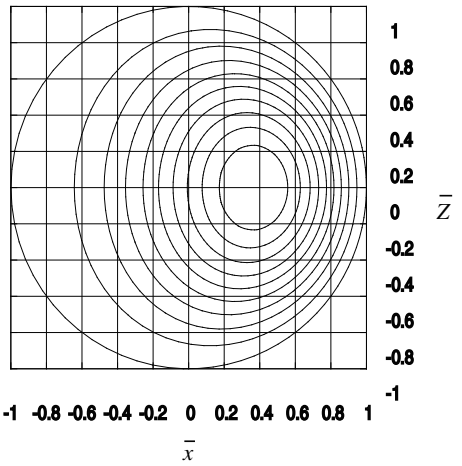

Fig. 5 Isosurfaces of Ψ for $V_{Ec} = -\sqrt{\gamma p_{1c}}$ and $V_{dc} = -1$.

$$\mathbf{v}_E \equiv -\frac{\nabla\Phi\times\mathbf{B}}{B^2}, \quad \mathbf{v}_{di} \equiv -\frac{\nabla p_i\times\mathbf{B}}{enB^2}. \quad (19)$$

The ion gyroviscous force is needed only in their leading orders [5],

$$\nabla\cdot\Pi_i^{gv} \simeq -\frac{m_i}{eB_0}(R_0\nabla\varphi\times\nabla p_{i1})\cdot\nabla\mathbf{v} - \nabla\left(\chi_v + \chi_q\right), \quad (20)$$

Unlike for single-fluid equilibria, the profile of n_0 must be specified in order to give the profiles of $E\times B$ and diamagnetic flows for two-fluid equilibria. We assume the linear profile of n_0,

$$n_0 = n_c\overline{\psi}_1. \quad (21)$$

Then the $E\times B$ and the diamagnetic flows are given by

$$V_E/V_{Ap} = \sqrt{\varepsilon}V_{Ec}\overline{\psi}_1^{1/2}, \quad (22)$$

$$V_{di}/V_{Ap} = \sqrt{\varepsilon}V_{dc}p_{i1c}\overline{\psi}_1^{-1/2}, \quad (23)$$

$$V_{de}/V_{Ap} = -\sqrt{\varepsilon}V_{dc}p_{e1c}\overline{\psi}_1^{-1/2}, \quad (24)$$

where

$$V_{dc} \equiv -\sqrt{\varepsilon\mu_0 m_i n_{0c}}\frac{R_0\left(B_0^2/\mu_0\right)}{en_{0c}B_0\psi_c}. \quad (25)$$

We solve the GS equation for ψ_2 by using the finite element method with 40×40 grid points. Figures 3 - 5 show the isosurfaces of ψ, p and the ion stream function Ψ respectively for $V_{Ec} = -1$ and $V_{dc} = -1$. The single-fluid equilibria with $V_{Ec}^2 = \gamma p_{1c}$ is singular because of the poloidal-sonic singularity. The Hall-MHD equilibria also have singularity at $\bar{r} = 1$ because the convective term in the equation for ψ_2,

$$M_{Ap}\left(M_{Ap} - \lambda_i\frac{V_{di}}{V_{Ap}}\right)$$

goes to infinity for the given profiles. Thus, this solution is regular in the presence of both two-fluid and FLR effects. Figures 3 - 5 also show that the isosurfaces of ψ, p and Ψ do not coincide with each other due to the two-fluid effect.

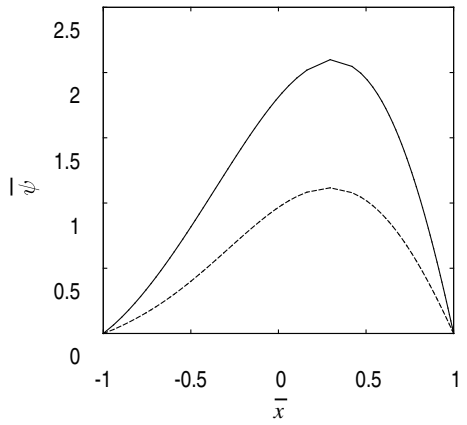

Fig. 6 The profiles of ψ in the mid plane.

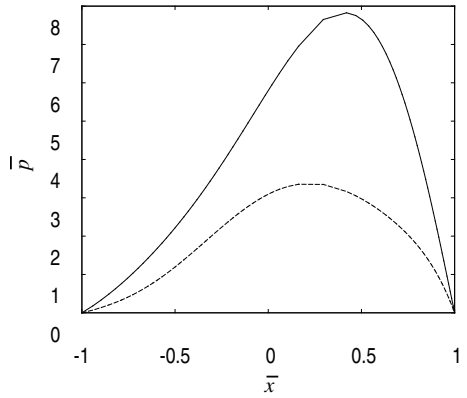

Fig. 7 The profiles of p in the midplane.

Figures 6 - 8 show the profiles of ψ, p and the ion stream function Ψ respectively in the midplane for $V_{Ec} = \pm 1$ and $V_{dc} = -1$. The solid lines are for $V_{Ec} = V_{dc}$ and the dashed line are for $V_{Ec} = -V_{dc}$. These results show that the equilibrium solutions for two fluid equilibria with FLR depend on the sign of the $E \times B$ flow.

5 Summary

We have solved a reduced set of equations for high-beta tokamak equilibria with flow comparable to the poloidal sound velocity analytically for the single-fluid MHD case and numerically for the case of two-fluid model with ion Finite Larmor radius (FLR). The analytical solution for single-fluid MHD equilibria shows that the shift of the magnetic axis from the geometric axis is enhanced by a slightly super-poloidal-sonic flow and it produces a forbidden region of equilibrium by the poloidal-sonic flow. Numerical analysis shows that there are regular solutions for the two-fluid model with FLR that are singular for the single-fluid and Hall MHD models, and that the solutions depend on the sign of the $E \times B$ flow compared to that of the ion diamagnetic flow.

[1] A. Ito, J. J. Ramos, and N. Nakajima, Phys. Plasmas **14**, 062501 (2007).

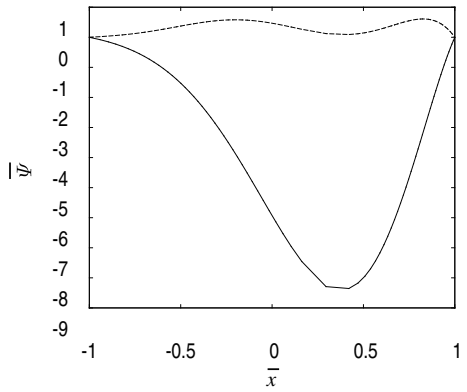

Fig. 8 The profiles of Ψ in the midplane.

[2] J. J. Ramos, Phys. Plasmas **12**, 052102 (2005).
[3] H. R. Strauss, Phys. Fluids **20**, 1354 (1977).
[4] A. Ito and N. Nakajima, *Theory of Fusion Plasmas*, AIP Conference Proceedings **1069**, 121 (2008).
[5] A. Ito, J. J. Ramos, and N. Nakajima,Plasma Fusion Res. **3**, 034 (2008).
[6] A. Ito and N. Nakajima, Plasma Phys. Contr. Fusion, in press.

Proceedings of ITC18, 2008

Intrinsic rotation of magnetic island with finite width

Ken UZAWA, Akihiro ISHIZAWA and Noriyoshi NAKAJIMA

National Institute for Fusion Science, 322-6 Oroshi-cho Toki-city, GIFU 509-5292, Japan

The direction of island rotation is investigated by using a two fluid equations, which includes effects of poloidal beta and also diamagnetic drifts of both ion and electron. It is found that the island rotates toward the electron diamagnetic drift in all cases in the linear regime. The parameter beta plays an important role in determining the direction of the island rotation in the nonlinear regime. It is also found that when the island width is small comparable to the ion Larmor radius, the real frequency strongly is affected to rotate toward the ion diamagnetic direction.

Keywords: island rotation, neoclassical tearing mode, two fluid model

1 Introduction

Tearing modes are resistive Magnetohydrodynamic (MHD) instabilities which break topology of ideal magnetic field and lead to the formation of helically perturbed structures called magnetic islands by tearing or reconnecting magnetic field line around the resonant surfaces in magnetic confinement devices such as LHD. The linear theory shows that the classical tearing mode is stable when the stability parameter

$$\Delta' = \frac{1}{\tilde{\psi}} \left[\left. \frac{d\tilde{\psi}}{dx} \right|_{x=+0} - \left. \frac{d\tilde{\psi}}{dx} \right|_{x=-0} \right]$$

is negative, which is given by the logarithmic jump of the perturbed magnetic flux around the rational surface[1]. However, the new type of tearing modes which can occur even when classically stable (the stability parameter is negative) due to helically perturbed bootstrap current in recent low collisional plasmas. The metastable (linearly stable but nonlinearly unstable) tearing modes are called neoclassical tearing modes (NTMs). The NTMs are found to limit the achievable beta in high performance discharges and deteriorate plasma confinement leading to plasma disruption. Therefore, much attention has been focused on NTMs both theoretically and experimentally[2, 3, 4].

To understand NTM dynamics theoretically, the modified Rutherford equation is often used as the model equation describing temporal evolution of magnetic island width,

$$\frac{\tau_s}{r_s}\frac{dw}{dt} = r_s\Delta' + \beta_p \left(\frac{\Delta_b w}{w^2 + w_0^2} - \frac{\Delta_p}{w^3} \right), \qquad (1)$$

where $\tau_s = \mu_0 r_s^2 / 1.22\eta$ is the resistive diffusion time at the magnetic surface of radius r_s, η is the neocalssical resistivity, Δ' is the classical tearing stability parameter which is discussed above, β_p is the poloidal beta at r_s, w_0 is the characteristic island width. The coefficients Δ_b and Δ_p represent destabilizing bootstrap current effect and polarization current effect, respectively. Typical representation of Δ_p is

$$\Delta_p = \frac{L_s^2}{k v_A^2}\omega(\omega - \omega_{*i}),$$

where ω is island rotation frequency, ω_{*i} is ion diamagnetic drift frequency, L_s is the magnetic shear length, k is the wave number of the mode, and $v_A = \sqrt{B_0^2/4\pi n m_i}$ is the Alfven velocity[5]. It clearly shows that when $\Delta_p < 0$ the polarization term plays a stabilizing role on NTM growth. And note that the island growth depends on rotation of island direction. It is of much importance to determine the direction of the island so much works have been investigated by using several models[5, 7, 8, 9]. However, effects of finite beta and also ion and electron diamagnetic drifts are not fully investigated. In this work, we investigated numerically the rotation of magnetic island for various island width including both effects.

2 Model Equations

Since there is no degree of freedom determining the island rotation in conventional MHD models, we have investigated the rotation of the island based on a reduced two fluid model which includes both effects of ion and electron diamagnetic drifts. The model equations used here is a two dimensional slab version of the four-field model[6], which consists a set of four equations that describes temporal evolutions of the magnetic flux ψ, the electrostatic potential ϕ, the perturbed electron pressure p, and the parallel ion velocity $v_\parallel$, i.e.,

$$\frac{\partial U}{\partial t} = -[\varphi,\ U] - \nabla_\parallel J + \nu\nabla_\perp^2 U - \frac{\delta\tau}{2}\left([p,\ U] + [\varphi,\ \nabla_\perp^2 p] + \nabla_\perp^2 [p,\ \varphi] \right),$$

author's e-mail: uzawa.ken@nifs.ac.jp

$$\frac{\partial \psi}{\partial t} = -\nabla_\parallel \varphi + \eta J + \delta \nabla_\parallel p,$$

$$\frac{\partial p}{\partial t} = -[\varphi,\ p] - 2\beta\delta \nabla_\parallel J - \beta \nabla_\parallel v + \frac{1}{2}\beta\eta(1+\tau)\nabla_\perp^2 p,$$

$$\frac{\partial v}{\partial t} = -[\varphi,\ v] - \frac{1}{2}(1+\tau)\nabla_\parallel p + D_v \nabla_\perp^2 v,$$

with vorticity $U = \nabla_\perp^2 \phi$, and z-directed current density $J = \nabla_\perp^2 \psi$. Usual Cartesian coordinate (x, y, z) is adopted. The validity of two dimensional calculation is justified in low beta plasmas, where the magnetic field is represented by $\boldsymbol{B} = B_0 \hat{\boldsymbol{z}} + \nabla\psi \times \hat{\boldsymbol{z}}$, where B_0 is the ambient magnetic field along the z-axis. The normalization used here is $(x,\ y,\ t,\ \psi,\ \phi,\ n,\ v_{\parallel i}) = (x/a,\ y/a,\ v_A t/a,\ \psi/\varepsilon B_0 a,\ c\phi/v_A B_0 a,\ n/n_0,\ \delta v_{\parallel i}/v_A)$. Here, a is the minor radius, c is the light speed, ε is the inverse aspect ratio, ν is the viscosity, η is the resistivity, and both equilibrium ion and electron density n_0 are constant due to charge neutrality. We suppose that ion and electron temperatures are constant by incroducing the ratio of them $\tau = T_i/T_e$. And two parameters are introduced as two fluid parameters $\delta = (2\omega_{ci}\tau_A)^{-1}$, which is related to the ion skin depth, and $\beta = [1 + (1+\tau\beta_e)/2\beta_e]^{-1}$, where $\omega_{ci} = \sqrt{4\pi n_0 e^2/m_i}$ is the ion plasma frequency and $\beta_e = 8\pi n_0 T_e/B_0^2$ is the electron beta value, and T_e is the constant electron temperature. We note that the parameters are related to the ion Larmor radius, i.e., $(\rho_i/a)^2 = 2\tau\beta\delta^2$. The operator $[,\ ]$ denotes the Poisson bracket, $[A,\ B] = \nabla_\perp A \times \nabla_\perp B \cdot \hat{\boldsymbol{z}}$, and total derivative $d/dt = \partial/\partial t + [\varphi,\ ]$ includes only $E \times B$ drift velocity.

3 Numerical Results

3.1 Numerical Settings

The model equations are solved numerically by using pseudo spectral code in two dimensional slab geometry. We impose the zero boundary condition for radial direction x, so all components are automatically set to zero at the radial boundary. A finite-differential method is applied to the direction and the periodic boundary condition is imposed for the poloidal direction y. The domain of numerical simulation is $x = [0, 1]$ and $y = [0, 1]$. The number of grids in a simulation box is chosen to 400×20. Temporal evolution is calculated by using a predictor-corrector method with time step $\Delta t = 10^{-3}$. The pressure and magnetic flux equilibrium profiles are $p_{eq}(x) = 0.25\,(1 - \tanh(x - 0.5))\,/L_p$, and $\psi_{eq}(x) = L_s \ln[\cosh(x - 0.5)/L_s]$. And no equilibrium parts are considered for electrostatic potential ϕ and ion parallel velocity v, i.e., $\phi = \tilde{\phi},\ v = \tilde{v}$. In all simulations, we have $\nu = 10^{-4}$, $\eta = 10^{-4}$, and $D_v = 10^{-4}$.

3.2 Linear Resluts

At first, we examine the island rotation by performing linear calculation. A perturbed quantity $A(x, y, t)$ in the slab coordinates is assumed to varies as

$$\tilde{A}(x, y, t) = \sum_m A_m(x) \exp \mathrm{i}(my - \omega t) + c.c.,$$

where m is the poloidal wave number. Then model equations are reduced to

$$\frac{\partial \tilde{U}}{\partial t} = \frac{\partial \psi_{eq}}{\partial x}\frac{\partial \tilde{J}}{\partial y} - \frac{\partial \tilde{\psi}}{\partial y}\frac{\partial J_{eq}}{\partial x} + \nu\nabla_\perp^2 \tilde{U} + \delta\tau\left(-\frac{\partial p_{eq}}{\partial x}\frac{\partial \tilde{U}}{\partial y} - \frac{\partial^2 p_{eq}}{\partial x^2}\frac{\partial^2 \tilde{\varphi}}{\partial x \partial y}\right),$$

$$\frac{\partial \tilde{\psi}}{\partial t} = \frac{\partial \psi_{eq}}{\partial x}\frac{\partial \tilde{\varphi}}{\partial y} + \eta\nabla_\perp^2 \psi + \delta\left(-\frac{\partial \psi_{eq}}{\partial x}\frac{\partial \tilde{p}}{\partial y} + \frac{\partial p_{eq}}{\partial x}\frac{\partial \tilde{\psi}}{\partial y}\right),$$

$$\frac{\partial \tilde{p}}{\partial t} = \frac{\partial p_{eq}}{\partial x}\frac{\partial \tilde{\varphi}}{\partial y} + 2\beta\delta\left(\frac{\partial \psi_{eq}}{\partial x}\frac{\partial \tilde{J}}{\partial y} - \frac{\partial J_{eq}}{\partial x}\frac{\partial \tilde{\psi}}{\partial y}\right) + \beta\frac{\partial \psi_{eq}}{\partial x}\frac{\partial \tilde{v}}{\partial y} + \frac{\beta\eta}{2}(1+\tau)\nabla_\perp^2(p_{eq} + \tilde{p}),$$

$$\frac{\partial \tilde{v}}{\partial t} = \frac{1+\tau}{2}\left(\frac{\partial \psi_{eq}}{\partial x}\frac{\partial \tilde{p}}{\partial y} - \frac{\partial p_{eq}}{\partial x}\frac{\partial \tilde{\psi}}{\partial y}\right) + D_v\nabla_\perp^2 \tilde{v}.$$

In Fig.1, the dependence of real frequency of $m = 1$ island is illustrated as a function of τ for various δ. Here, β value is chosen to 0.01, and the ratio of the shear scale length L_s to the density scale length is chosen to 2/3. The real frequency is normalized by the electron diamagnetic drift velocity, $\omega_{\star(e)} = \delta m p_0'$. Note that the island is rotating with pure electron diamagnetic drift velocity when normalized Ω is unity. It is found that the real frequency reduces with respect to τ in small δ case, but in large δ case the dependence is less effective and the island is almost rotating in the direction of electron diamagnetic drift.

Figure 2 shows the dependence of real frequency with respect to δ for various β. Here, $\tau = 1$ and $L_s/L_p = 2/3$ is chosen. It is found that the real frequency increases with respect to δ, indicating that effects of finite Larmor radius weaken island rotate in the direction of the ion diamagnetic drift. The dependence is same as beta increases. Totally the direction of island rotation points the electron diamagnetic drift.

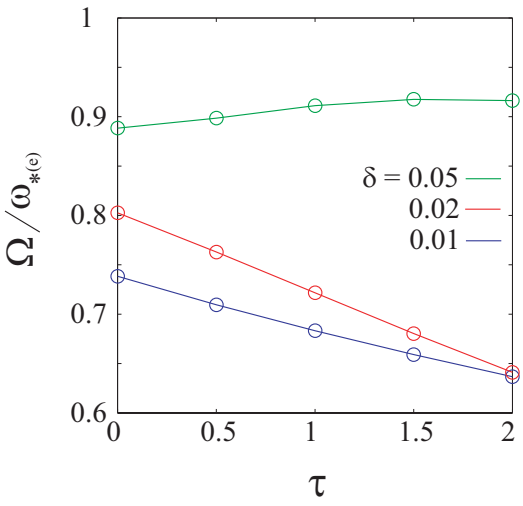

Fig. 1 The dependence of real frequency as a function of τ for various δ. Other parameters are $\beta = 0.01$ and $L_s/L_p = 2/3$.

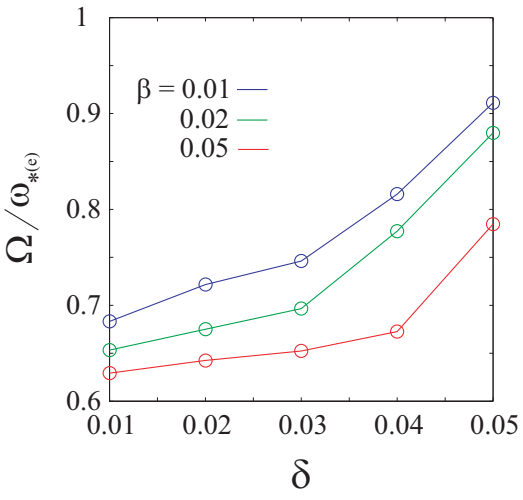

Fig. 2 The dependence of real frequency as a function of δ for various β. Other parameters are $\tau = 1$ and $L_s/L_p = 2/3$.

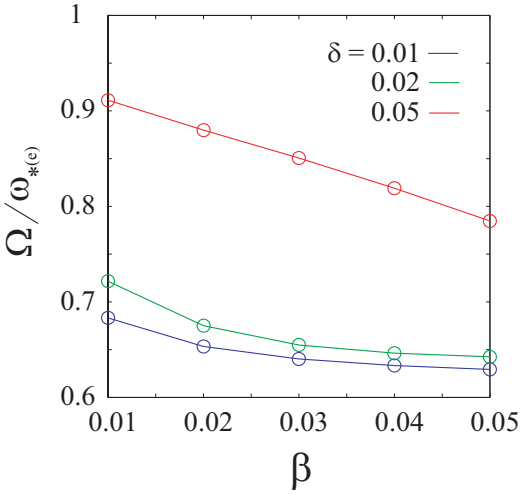

Fig. 3 The dependence of real frequency as a function of β for various δ. $\tau = 1$ and $L_s/L_p = 2/3$.

Figure 3 illustates the dependence of real frequency with respect to β for various δ. Parameters for τ and L_s/L_p are same as used in Fig.2. It is found that the real frequency monotonically decreases with respect to β. The tendency is same for different δ value. As shown in these resuls, the island rotates toward electron diamagnetic drift in the linear regime.

3.3 Nonlinear Results

Next, we examine the island rotation in the nonlinear regime. Here, δ and L_s/L_p is chosen to $\delta = 0.01$, $L_s/L_p = 2/3$. Only $m = 1$ mode grows up and saturate with finite island width because of positive Δ' in this parameter. In Figure 4 the real frequency is illustrated as a function of the island width in the case of $\beta = 0.01$. The island width w is defined as the distance between the separatrix at magnetic neutral surface which is approximately given by $w \simeq 4\sqrt{\tilde{\psi}/\psi_{eq}''}$. The ion Larmor radius is estimated as $\rho_i \simeq 0.001$ in this case. The dotted lines indicate the real frequencies calculated from linear theory. It is found that when the island width is small comparable to the ion Larmor radius, the real frequency drastically decreases to that estimated by the linear calculation. Through the transient phase from $w \simeq 0.04$ to 0.12, the real frequency varies across the line $\Omega = 0$ when it saturates. Therefore, the island finally rotates in the direction of ion diamagnetic drift whereas it is rotating toward electron diamagnetic drift in the linear regime.

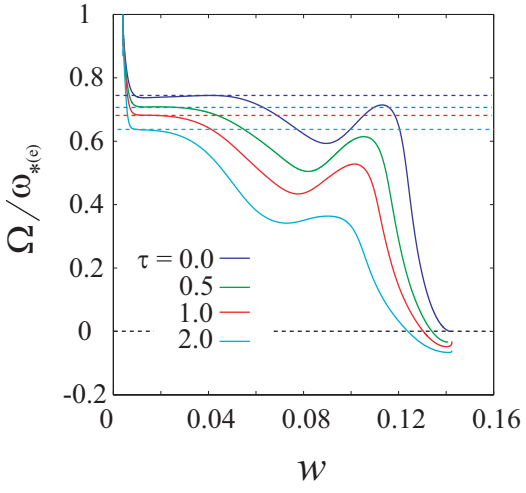

Fig. 4 The dependence of real frequency as a function of the island width for various τ. Other parameters are chosen to $\beta = 0.01$, $\delta = 0.01$, and $L_s/L_p = 2/3$.

Figure 5 shows the real frequency with respect to the island width in the case of $\beta = 0.02$, with $\rho_i \simeq 0.002$. We can also see the reduction of real frequency when the width is around the ion Larmor

radius. And it has wide plateau region where linear analysis is enough valid with respect to the width, and finally becomes approximately zero and the island has locked.

Figure 6 illustrates the real frequency as a function of the island width in the case of $\beta = 0.05$. The ion Larmor radius is estimated as $\rho_i \simeq 0.01$. The real frequency has a finite positive value when the island saturates. The island is still rotating in the direction of electron diamagnetic drift. The parameter beta plays an important role in determining the direction of the island.

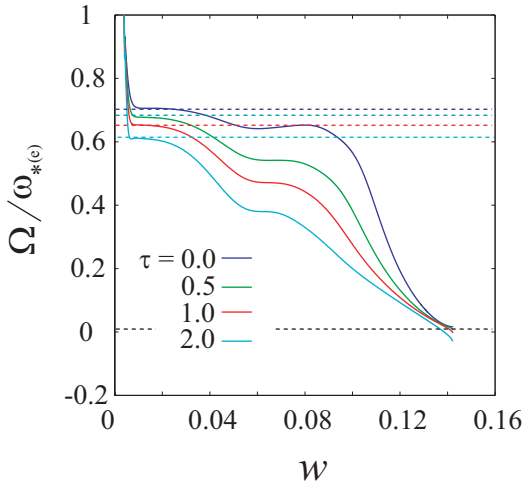

Fig. 5 The dependence of real frequency as a function of the island width for various τ in the case of $\beta = 0.02$. Other parameters are same as used in Fig.4.

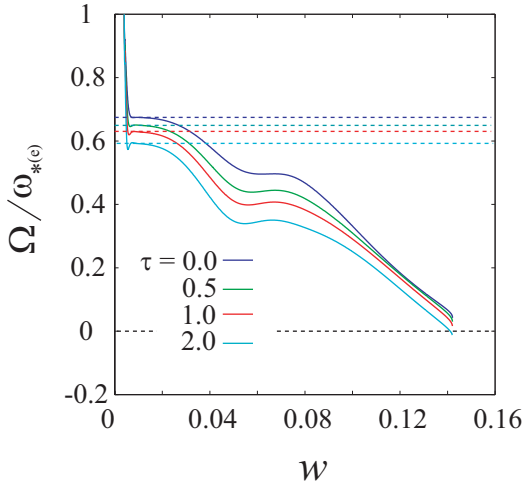

Fig. 6 The dependence of real frequency as a function of the island width for various τ in the case of $\beta = 0.05$. Other parameters are same as used in Fig.4.

We have also investigated dependence of δ on the island rotation. It is found that the growth rate of the island susceptibly depends on δ. In linearly stable region where island remains small comparable to initial noise, island rotates toward the electron diamagnetic drift.

4 Conclusion

We have investigated the intrinsic rotation of magnetic island based on a reduced two-fluid model which includes both effects of ion and electron diamagnetic drifts as well as the ion parallel motion. In nonlinear regime, the direction of island rotation strongly depends on β, whereas it rotates toward the electron diamagnetic drift in the linear regime. It is also found that when the island width is small comparable to the ion Larmor radius, the real frequency is affected to rotate toward the ion diamagnetic direction.

[1] H. P. Furth, J. Killeen, and M. N. Rosenbluth, Phys. Fluids **6**, 459 (1963).
[2] R. J. La Haye, Phys. Plasmas **13**, 055501 (2006).
[3] A. Isayama, Y. Kamada, T. Ozeki, and N. Isei, Plasma. Phys. Control. Fusion, **41**, 35 (1999).
[4] R. Fitzpatrick, Phys. Plasmas **2**, 825 (1995).
[5] J. W. Connor, F. L. Waelbroeck, and H. R. Wilson, Phys. Plasmas **8**, 2835 (2001).
[6] R. D. Hazeltine, M. Kotschenreuther, and P. J. Morrison, Phys. Fluids **28**, 2466 (1985).
[7] F. L. Waelbroeck, Phys. Rev. Lett. **95**, 035002 (2005).
[8] R. Fitzpatrick and F. L. Waelbroeck, Phys. Plasmas **12**, 022307 (2005).
[9] R. Fitzpatrick, F. L. Waelbroeck, and F. Militello, Phys. Plasmas **13**, 122507 (2006).

Proceedings of ITC18, 2008

3D MHD equilibrium calculations for Tokamaks with resonant magnetic perturbations: TEXTOR as an example

Christopher WIEGMANN[1)], Yasuhiro SUZUKI[2)], Joachim GEIGER[3)], Yunfeng LIANG[1)], Detlev REITER[1)], Robert C. WOLF[3)]

[1)]*Institut für Energieforschung - Plasmaphysik, Forschungszentrum Jülich GmbH, Assoziation EURATOM-FZJ, Trilateral Euregio Cluster, 52425 Jülich, Germany*

[2)]*National Institute for Fusion Science, 322-6 Oroshi-cho, Toki 509-5292, Japan*

[3)]*Max-Planck-Institut für Plasmaphysik, Assoziation EURATOM-IPP, 17491 Greifswald, Germany*

For the first time three dimensional equilibrium calculations for the tokamak TEXTOR with dynamic ergodic divertor are presented. These calculations were performed with the HINT2 code which was applied for the first time to tokamaks with high net toroidal current and island structures. The results are compared with the often used vacuum superposition approach. In case of the DED in 6/2 mode the differences are found to be minor. In case of the DED in 3/1 mode, a large appearing 1/1 island in the core plasma shows that a further understanding of the treatment of the net toroidal current density has to be achieved.

Keywords: MHD equilibrium, TEXTOR, DED, HINT2

1 Introduction

The application of **R**esonant **M**agnetic **P**erturbations (RMP) to tokamaks recently gained a lot of attention due to the possibility of ELM suppression or mitigation [1, 2]. The iron core tokamak TEXTOR with circular plasma cross-section is specially suited to study the 3D effects of RMPs due to its **D**ynamic **E**rgodic **D**ivertor (DED) [3]. The DED consists of 16 helically aligned perturbation coils installed in-vessel at the high-field side and can be operated in several base modes (m/n = 12/4, 6/2 and 3/1) with either DC or AC current supply. The penetration depth of the RMPs depends on the choosen poloidal mode number m.
Knowledge of the magnetic field topology is a necessary prerequisite for further studies concerning e.g. the transport charateristics. Earlier work on error field penetration has shown strong indications that screening and amplification of RMPs play an important role in determining the magnetic field topology (see e.g. [4, 5]). Nevertheless, in this study a full penetration of the RMPs is assumed. The focus lies on the effect of the RMPs on the plasma equilibrium itself as the equilibrium force balance is distorted. The converged 3D equilibria will be compared with the simple vacuum assumption.

2 HINT2 code

To investigate the resulting 3D equilibrium the HINT2 code [6, 7] is applied. This code is an Eulerian initial value solver which relaxes the given initial magnetic field configuration into an equilibrium by solving resistive MHD equations. Screening of the RMPs due to plasma rotation is not taken into account.
HINT2 uses a quasi-eulerian helically rotating grid (u^1, u^2, u^3) which in case of tokamak calculations reduces to a cylindrical like coordinate system whose relation to normal cylindrical coordinates is given by

$$r = R_0 + u^1 \tag{1}$$

$$z = u^2 \tag{2}$$

$$\phi = -u^3 \,. \tag{3}$$

The relaxation process is carried out in two steps. Instead of solving the evolution equation for the pressure, the pressure distribution is relaxated in step A with fixed magnetic field by a field line tracing method. The pressure is adjusted to satisfy a vanishing pressure gradient along the field lines ($\mathbf{B}\cdot\nabla p = 0$) by evaluating the line integral along a field line

$$p^{i+1} = \bar{p} = \frac{\int_{-L_{in}}^{L_{in}} F p^i \frac{dl}{B}}{\int_{-L_{in}}^{L_{in}} \frac{dl}{B}}, \quad F = \begin{cases} 1 & : \text{ if } L_C \geq L_{in} \\ 0 & : \text{ if } L_C < L_{in} \,. \end{cases} \tag{4}$$

On field lines which leave the computational region or intersect with a limiting contour the pressure is set to zero. Depending on the value of L_{in} a finite pressure in the stochastic edge region can be sustained. Hence, L_{in} plays a crucial role in describing the vacuum-plasma transistion.
In step B, a set of resistive MHD equations with fixed pres-

author's e-mail: c.wiegmann@fz-juelich.de

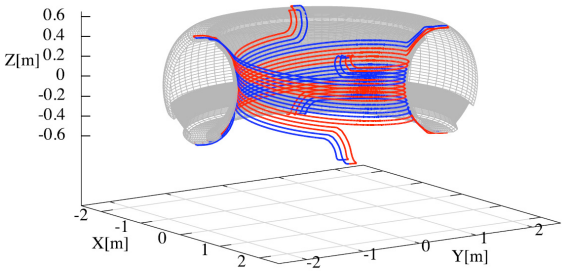

Fig. 1 DED in 6/2 configuration with the limiting contour used in HINT2 calculation.

sure distribution is solved

$$\frac{\partial \mathbf{v}}{\partial t} = -f_{CFL}\left(\nabla p + (\mathbf{J} - \mathbf{J_0}) \times \mathbf{B}\right) \quad (5)$$

$$\frac{\partial \mathbf{B}}{\partial t} = \nabla \times \left\{ \mathbf{v} \times \mathbf{B} - \eta \left(\mathbf{J} - \mathbf{J_0} - \mathbf{B} \frac{\langle \mathbf{J} \cdot \mathbf{B} \rangle_{net}}{\langle B^2 \rangle} \right) \right\} \quad (6)$$

$$\mathbf{J} = \nabla \times \mathbf{B}, \quad \mathbf{J_0} = \nabla \times \mathbf{B_{vac}}. \quad (7)$$

The factor f_{CFL} is necessary to ensure that the Courant-Friedrich-Levy condition is satiesfied in case that field coils are located inside the computational domain. $\mathbf{J_0}$ denotes the vacuum current density due to the poloidal and toroidal coils within the computational domain. The net toroidal current density $\mathbf{B}\frac{\langle \mathbf{J}\cdot\mathbf{B}\rangle_{net}}{\langle B^2\rangle}$ is made up by the ohmic current, the bootsstrap current, currents due to heating and current drive schemes. A functional dependence on the normalized toroidal flux is assumed.

3 Calculation results

The input data for the HINT2 calculation were prepared as follows. Usually, a 3D free boundary equilibrium calculation assuming nested flux surfaces, typically done with the VMEC code [8,9], is used to initialize the HINT2 calculations. In case of TEXTOR, this procedure is not applicable due to the existing iron core and a missing 3D model taking the iron core effects into account. Instead, a version of the 2D equilibrium code DIVA, specially adapted for TEXTOR and the iron core, is used to provide an axisymmetric 2D equilibrium. The perturbation field of the DED is calculated via Biot-Savart from the given polygon description which also includes the current feeds (see Fig.1). The initial total magnetic field for HINT2 is than a superposition of the 2D equilibrium, an $1/R$ toroidal field corrected for the diamagnetic behaviour of the plasma and the vacuum perturbation field. To obtain an initial 3D pressure distribution, the calculated 2D pressure of DIVA is mapped toroidally. The net toroidal current density profile is obtained by surface averaging the toroidal current density profile of DIVA and mapping this with the help of the safety factor profile onto the normalized toroidal flux.
As the DED coils are located very close to the plasma itself, the usage of a limiting contour in the calculation is in-

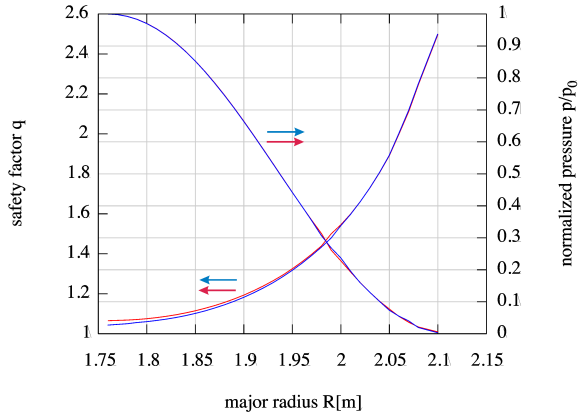

Fig. 2 Pressure and safety factor profiles of vacuum superposition (red) and 3D equilibrium (blue) of DED in 6/2 configuration, both at the toroidal angle $\phi = 0$.

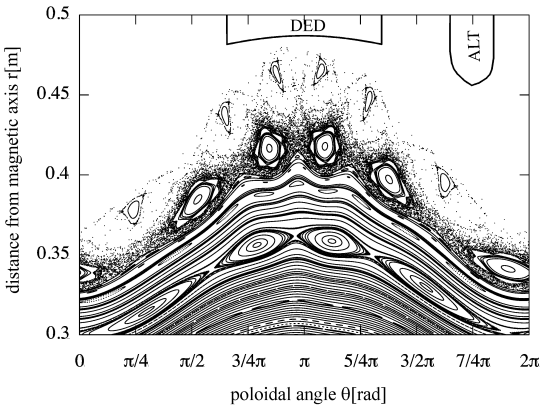

Fig. 3 Edge region of the 3D converged equilibrium for the DED 6/2 case at $\phi = 0$. At the top, the limiting structures of the DED (middle) and of the ALT-limiter (upper right) can be seen. The 4/2 island chain inside the core plasma and the remanent 5/2 and 6/2 island chains are clearly visible.

evitable. Otherwise, stochastic field lines extending from the plasma into the coil region could be captured there and could lead to an additional build up of a finite pressure in the plasma edge region as their connection length exceed L_{in}.

3.1 TEXTOR with DED 6/2

Here, a 3D equilibrium for TEXTOR with a DED 6/2 perturbation field was calculated. Due to the perturbation field symmetry only a half torus calculation was necessary. The resolution was chosen to be $129 \times 129 \times 184$ grid points (u^1, u^2, u^3) corresponding to a spacial resolution of $1.02cm$ in a poloidal plane and about $1°$ in toroidal direction. The underlying 2D equilibrium had the following parameters: $I_p = 245kA$, $B_{tor}(@1.75) = 1.3T$ and a central axis pressure of $p_{axis} = 16kPa$.
In step A, $L_{in} = 200m$ was used for the pressure relax-

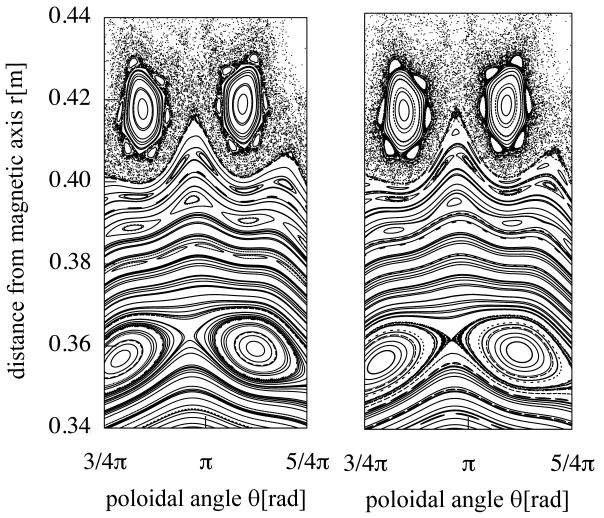

Fig. 4 Enlarged area of vacuum superposition (left) and converged 3D equilibrium (right) for the DED 6/2 case.

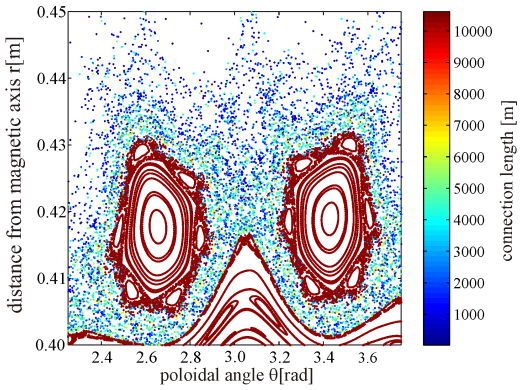

Fig. 5 Connection length plot of enlarged area of vacuum superposition of DED in 6/2 configuration at $\phi = 0$.

ation to ensure that the inner islands are traced out completely and the pressure profile is flattened there accordingly. In Fig.2 the profiles for the safety factor q and the pressure p as functions of the major radius are shown for the vacuum superposition and the converged 3D equilibrium. Both profiles do not differ very much from each other. Deviations in the pressure profiles can especially be seen in the plasma edge and can be assigned to the location of the islands and stochastic region. The q-profiles agree well in the edge region but the 3D equilibrium one has a slightly lower value in the core region. This is caused by the changed net toroidal current distribution. Furthermore, the q-profiles can only be computed up to a major radius of $2.1m$ as it is not possible to compute a q-value further out due to the ergodicity of the edge region. The Differences around $r_{minor} = 1.98 - 2.0m$ are due to the $3/2$ island chain.

The magnetic field structure of the converged equilibrium is shown in Fig.3 for the edge region. The gross structures agree very well between the vacuum superposition and the 3D equilibrium. This can be attributed to the

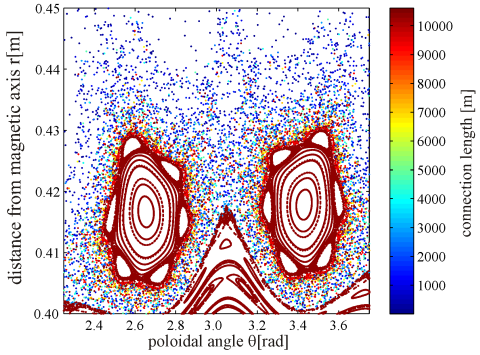

Fig. 6 Connection length plot of enlarged area of converged 3D equilibrium of DED in 6/2 configuration at $\phi = 0$.

low plasma pressure and current in the edge region resulting in a very small modification of the magnetic topology due to the equilibrium response. Having a closer look, a starting ergodisation of the X-point of the $4/2$ island chain at $r \approx 0.36m$ can be observed in the converged equilibrium case (see Fig.4). Furthermore, the island width of the high m island chain at $r \approx 0.39m$ has decreased. Connection length plots for both cases are shown for an enlarged area in Fig.5 and Fig.6, respectively. In both cases a sharp separation between the stochastic region and the remanent $5/2$ islands as well as the core area can clearly be seen. But in case of the converged 3D equilibrium the separation between the remanent $5/2$ islands and the surrounding stochastic region is no longer that pronounced as it is in the vacuum superposition case.

3.2 TEXTOR with DED 3/1

As the perturbation field of the DED 3/1 configuration offers no symmetry, a full torus calculation is necessary. The resolution was chosen to be $121 \times 121 \times 184$ resulting in a spacial resolution of exactly $1.0cm$ in a poloidal plane. The toroidal resolution had to be decreased to 2° due to computational costs, especially memory needs. As underlying 2D equilibrium the following parameters were choosen: $I_p = 300kA$, $B_{tor}(@1.75m) = 2.25T$ and an axis pressure of $p_{axis} = 8.6kPa$. As TEXTOR discharges tend to be sawtooth unstable in this scenario, an axis value of the safety factor below one was chosen for the underlying DIVA equilibrium. Consequently, by adding the DED field a large $1/1$ island appears. The vacuum superposition and the converged equilibrium solution are shown in Fig.7 and Fig.8, respectively. The $1/1$, $2/1$, $3/1$ and $4/1$ islands are clearly visible. Major changes in the magnetic field topology can be observed around the magnetic axis and the $1/1$ island in the converged equilibrium case. A closer analysis shows then that these changes are not caused alone by physics but that the pressure profile is not flattened accordingly within the $1/1$ island evenso the value of L_{in} was choosen sufficiently high. An accurate

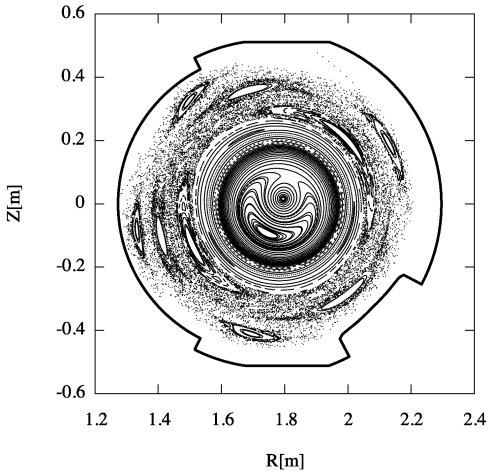

Fig. 7 Vacuum superposition of the DED in 3/1 configuration and 2D equilibrium at $\phi = 0$.

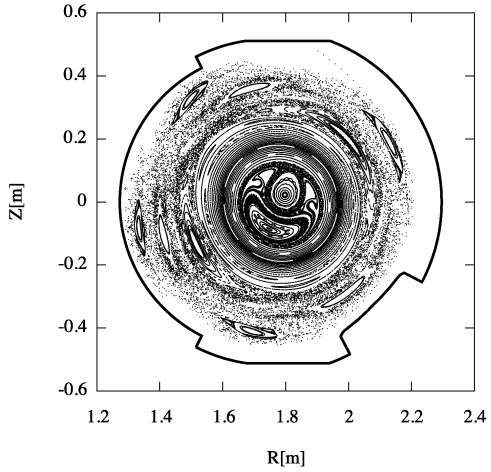

Fig. 8 Converged 3D equilibrium of the DED in 3/1 configuration at $\phi = 0$.

flattening is a necessity in case of tokamak calculations with the HINT2 code as the toroidal flux distribution is calculated from the relaxated pressure distribution and than used for distributing the net toroidal current density. Here, a small deepening of the pressure profile within the 1/1 island leads to a deepening of the calculated toroidal flux distribution and then to a wrong scaling of the net toroidal current. This causes a net toroidal current distribution, which compromises island confinement, as shown in Fig.9, and drives then via Eq.(6) the modification of the magnetic field topology, which in this case is partly caused by numerics.

4 Conclusions

The presented DED 6/2 case shows only very minor changes in the converged equilibrium solution so that the vacuum superposition appears to be a resonable approximation for the considered case. The low equilibrium response can be attributed to the low pressure gradient and current density in the edge. Furthermore, the chosen parameter $L_{in} = 200m$ leads to a smoothed pressure distribution in the ergodic edge region. Lower values of L_{in} could give a better resemblance of the local pressure distribution and could lead to a higher pressure in the edge region but will cause an insufficient profile flattening of the core islands. The effect of different values for L_{in} will be studied in the future.

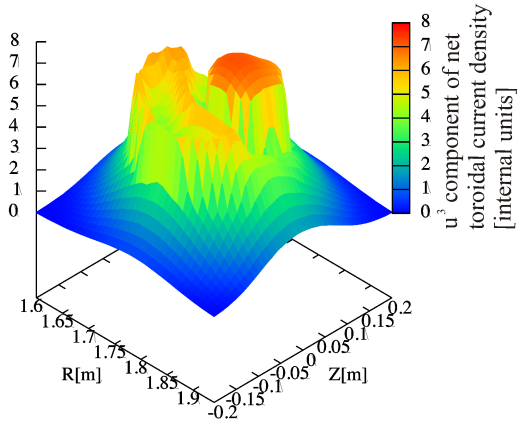

Fig. 9 Surface plot of the net toroidal current density [internal units] in the plasma core region of the converged 3D equilibrium of the DED in 3/1 configuration at $\phi = 0$.

For the 3/1 configuration, the picture is different. Here, a large 1/1 island in the core plasma causes numerical problems in the distribution of the net toroidal current density due to an inaccurate normalized toroidal flux distribution. For studying the 3/1 configuration with safety factor profiles, whose value is below one at the axis, or tokamak equilibria with large internal islands an improvement of the pressure flattening algorithm or of the calculation of the flux distribution will be necessary. Furthermore, the grid dependence of these effect has to be studied.

Acknowledgements One of the authors (C.W.) gratefully acknowledges support by a "Pre/Postdoctoral Scholarship for North-American and European Researchers (Short Term)" of the Japan Society for the Promotion of Science (JSPS).

[1] Y.Liang et al., Phys. Rev. Lett. **98**,265004 (2007).
[2] T.E. Evans et al., Nature Phys. **2**, 419 (2006)
[3] K.H. Finken et al., *The structure of magnetic field in the TEXTOR-DED*, Schriften des Forschungszentrum Jülich, Energy Technology **45**, ISSN 1433-5522 (2005)
[4] Q. Yu et al., Nucl. Fusion **48**, 024007 (2008)
[5] Y. Kikuchi et al., Plasma Phys. Control. Fusion **48**, 169-183 (2006)
[6] Y. Suzuki et al., Nucl. Fusion **46**, L19-L24 (2006)
[7] K. Harafuji et al., J. Comp. Phys. **81**, 169-192 (1989)
[8] S.P. Hirshman and D.K. Lee, Comput. Phys. Commun. **43**, 143 (1986)
[9] S.P. Hirshman et al., Comput. Phys. Commun. **43** (1986)

Proceedings of ITC18, 2008

Electron parallel heat transport in the scrape-off layer using a particle-in-cell code

Aaron FROESE[1)], Tomonori TAKIZUKA[2)] and Masatoshi YAGI[3)]

[1)]*IGSES, Kyushu University, Kasuga 816-8580, Japan*
[2)]*Japan Atomic Energy Agency, Naka 311-0193, Japan*
[3)]*RIAM, Kyushu University, Kasuga 816-8580, Japan*

Electron heat transport parallel to the magnetic field in the scrape-off layer plasma is investigated with the use of a particle-in-cell code PARASOL. Coulomb collisions are simulated correctly by a binary collision model. The heat flux is lost by radiation cooling, in addition to the convection/conduction to the divertor plates. It is confirmed for the collisional case that the conductive heat flux is given by the Spitzer-Härm expression. For the long mean free path case, the conductive heat flux is limited to a factor α_e of the free streaming value. It is found that α_e is small (~ 0.1 of the sheath-limited value) for the low radiation condition, but becomes large (~ 1.0) for the high radiation condition.

Keywords: tokamak scrape-off layer, conductive heat flux, PIC simulation, PARASOL, collisionless flux limit

1 Introduction

The divertor design in a tokamak reactor produces a separatrix system with closed magnetic field lines surrounded by open field lines terminating at the divertor plates. The burning core plasma lies inside the separatrix and exhibits good containment, though a large amount of heat is lost by anomalous transport and ELMs across the separatrix to the scrape-off layer (SOL). The heat in the SOL is carried mainly by the parallel transport along the open magnetic field lines to the divertor plates. Therefore, the SOL acts as a mediator between the hot core and the solid divertor plates.

Many features must be addressed in the SOL that are absent in the core; the plasma can no longer be assumed to be collisionless and strong parallel gradients develop that negatively affect the containment. In order to reduce the huge heat load on the plates, divertor simulation studies using fluid modelling are devoted to optimizing the divertor configuration and operation scenario. However, assumptions regarding kinetic effects, such as boundary conditions at the wall, heat conductivity, and plasma viscosity, are significant liabilities for the fluid model and are typically addressed by introducing primitive approximations [1, 2], which must be validated separately by full kinetic modelling. This can be accomplished by particle methods that suffer from large statistical errors or finite-difference methods that suffer from inefficient phase-space coverage. In this paper, electron heat transport parallel to the magnetic field in the SOL plasma is investigated with the use of a particle-in-cell code PARASOL in which Coulomb collisions are simulated correctly by a binary collision model.

author's e-mail: aaron@riam.kyushu-u.ac.jp

2 Parallel heat conduction

Parallel heat conduction by electrons is given by

$$q_e = \frac{m_e}{2} \int d\mathbf{v} \cdot V^2 V_{\parallel} f_e(\mathbf{x}, \mathbf{v}),$$

where m_e is the electron mass, $\mathbf{v}$ is the velocity, $\mathbf{V} = \mathbf{v} - \mathbf{u}$ is the velocity relative to the fluid velocity $\mathbf{u}$, and $f_e(\mathbf{x}, \mathbf{v})$ is the phase-space distribution function. In a collisional plasma, this evaluates to the Spitzer-Härm expression [3].

$$q_{SH} = -n_e \chi_e^{SH} \nabla_{\parallel} T_e \qquad \chi_e^{SH} = 3.2 v_{te} \lambda_{ee} \tag{1}$$

where n_e is the electron density, $v_{te} = (T_e/m_e)^{1/2}$ is the thermal speed, $\lambda_{ee} = v_{te}\tau_{ee}$ is the thermal mean free path, and $\tau_{ee} \propto v_{te}^3$ is the electron-electron collision time. Since χ has a strong dependence on thermal speed, which in turn depends on particle mass, so the ion conduction is negligible. However, this expression is not general due to the proportional relationship with the mean free path. The maximum heat flux in a collisionless plasma is the order of the free-streaming flux

$$q_{FS} = n_e T_e \left(T_{e\parallel}/m_e\right)^{1/2}. \tag{2}$$

We wish to determine the collision-dependent behavior of the heat flux, so as to replace it with a simpler expression that retains resonable accuracy. The preferred method is using the harmonic average form [1],

$$q_{eff} = \left(\frac{1}{q_{SH}} + \frac{1}{\alpha_e q_{FS}} \right)^{-1}, \quad \alpha_e = \lim_{\lambda_{ee} \to \infty} \frac{q}{q_{FS}}, \tag{3}$$

where α_e is the flux-limiting coefficient, *i.e.* the ratio between free-streaming and actual heat fluxes in the collisionless limit. Since the Spitzer-Härm heat flux is proportional to the mean free path, when the collisionality is high, $q_{SH} \ll \alpha_e q_{FS}$ becomes small and $q_e \simeq q_{SH}$, but when

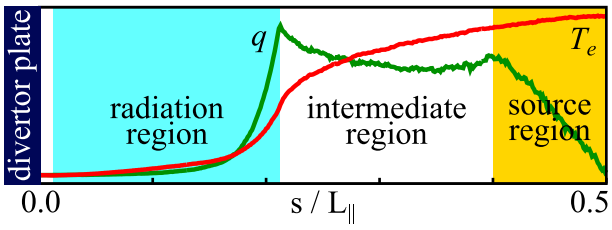

Fig. 1 Diagram of PARASOL half-system showing the temperature and heat flux profiles in the system with $f_{rad} = 0.5$ and $\lambda_{mfp}/L = 0.1$. The divertor plate (navy) and radiation (blue), intermediate (white), and source (yellow) regions are marked.

the collisionality is low, $q_{SH} \gg \alpha_e q_{FS}$ becomes large and $q_e \simeq \alpha_e q_{FS}$. A number of studies using kinetic simulations have produced widely disparate values for α_e, ranging from 0.03 to 3 [2]. However, there has been little inquiry into the cause of this range of results, with the exception of an investigation of the effect of collisionality using BIT1 [4]. In this study, we look at both collisionality as well as temperature gradient by adjusting the particle mean free path length and radiation loss from the SOL, respectively.

3 Simulation model

PARASOL is a 1d2v electrostatic particle-in-cell model on a closed domain with energy sources and sinks mirrored across the midpoint. The plasma is free to move in the spatial dimension s parallel to the separatrix magnetic field (Fig. 1a), but approximated as homogenous in the perpendicular directions. A hot ambipolar plasma source is in the domain center $s/L_{\|} = [0.4, 0.5]$ to mimic diffusion from the plasma core. Particles generated at the source are given a thermal velocity distribution consistent with the temperature of the particles already occupying the hot source region, essentially causing the core and SOL to equilibrate. Ions that strike the divertor plate are reintroduced as a hot ion-electron pair, maintaining a constant ion number in the simulation. Due to the fact that electrons escape sooner than ions, this leads to a slightly positive charge in the plasma.

Energy loss occurs via a radiative loss region and flow to the divertor plates. For this study, recycling at the divertor has been deactivated and neutrals are ignored. The divertor plate is set at an angle $\theta = 20°$ to the magnetic field, such that the connection length is related to the system length by $L = \theta L_{\|}$. The radiative energy sink lies beside the divertor $s/L_{\|} = [0.01, 0.21]$ to simulate radiation into the private plasma. During each time step, all electrons occupying the radiation region lose a small fraction of their kinetic energy with no change in direction. The input parameter $f_{rad} = Q_{rad}/Q_{tot}$ specifies the ratio of the radiative energy-loss flux to the total energy flux.

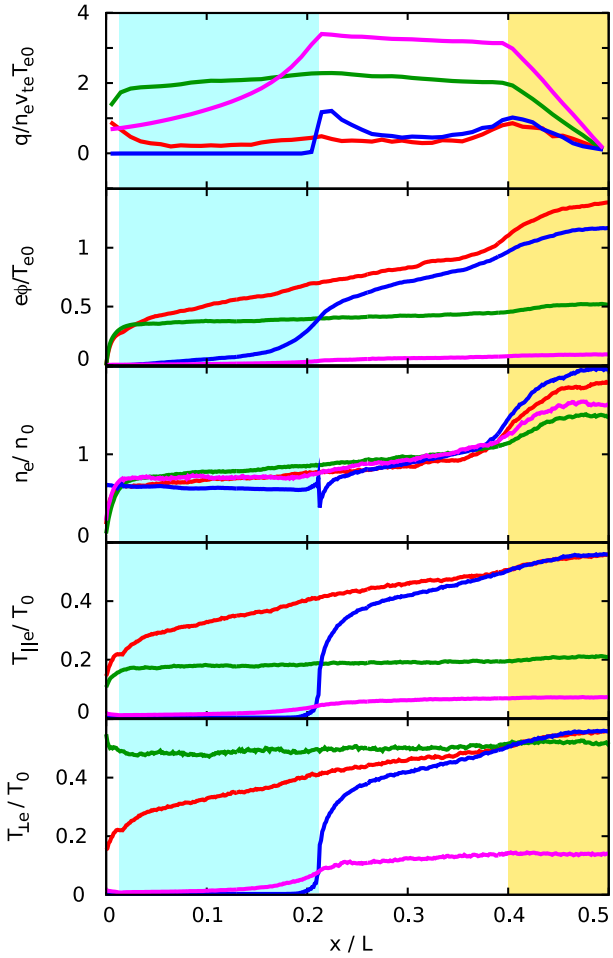

Fig. 2 Spatial variation profiles of conductive heat flux, potential, and electron density and temperature for plasma with the following properties:
(red) low rad. $f_{rad} = 0.1$, collisional $\lambda_{mfp}/L = 10^{-2}$
(green) low rad. $f_{rad} = 0.1$, collisionless $\lambda_{mfp}/L = 10^{2}$
(blue) high rad. $f_{rad} = 0.5$, collisional $\lambda_{mfp}/L = 10^{-1}$
(purple) high rad. $f_{rad} = 0.5$, collisionless $\lambda_{mfp}/L = 10^{3}$

Coulomb collisions are treated using a binary collision model, where in each time step each particle is paired with both an ion and another electron in the same cell, and given a collision angle proportional to the length of the time step. While the initial mean free path is specified as the input parameter $\lambda_{mfp0} \equiv 3^{3/2}\lambda_{ee}$, it evolves with the local plasma density and temperature such that $\lambda_{mfp}/\lambda_{mfp0} = (T_{e\|}/m_e)^{1/2}(3T_e/T_{e0})^{3/2}$. Ions progress in time via a kinetic equation and electrons by a drift kinetic equation. The ion gyro-radius is set to $\rho_i/L = 5\times10^{-3}$, the number of spatial cells to 800, and the number of particles per cell to greater than 100. Except where specified, the ion-electron mass ratio is always $m_i/m_e = 1800$.

4 Results

A cursory glance at the plasma profiles of high versus low collisionality and high versus low radiation rates shows

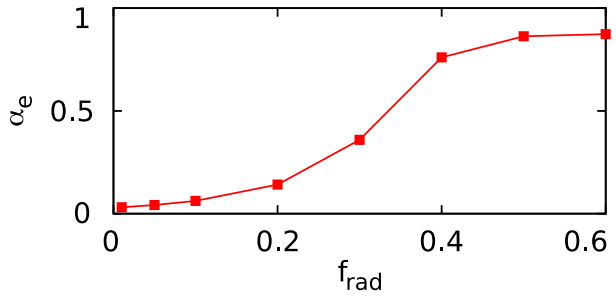

Fig. 3 Dependence of α_e in collisionless limit on radiation f_{rad}.

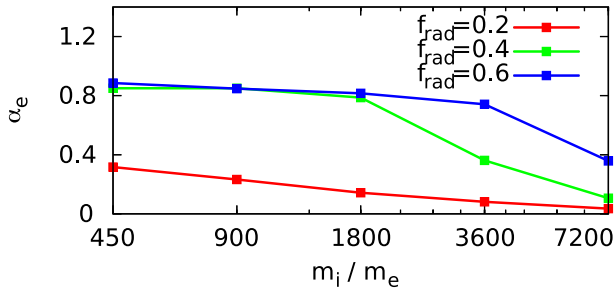

Fig. 4 Dependence of α_e in collisionless limit on ion-electron mass ratio m_i/m_e. Mass ratio 3600 corresponds to a deuterium plasma.

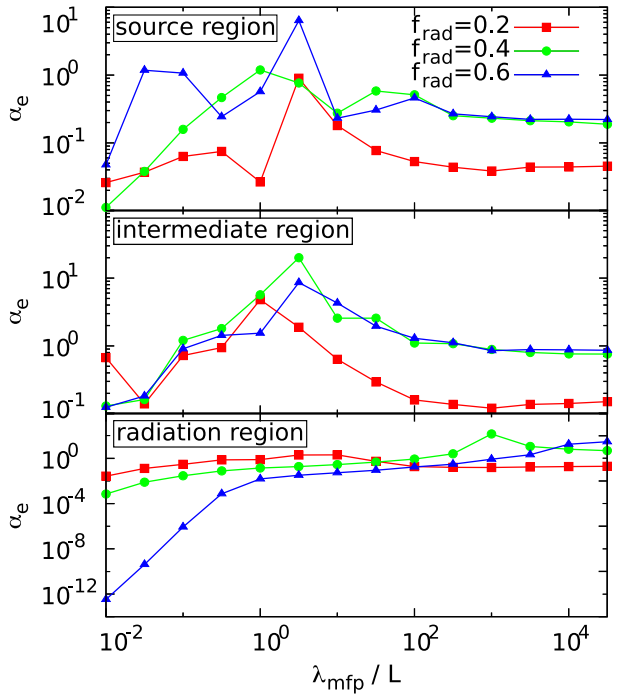

Fig. 5 Dependence of α_e on mean free path by region. Each point represents a poloidally-average over the indicated region with error bars omitted for clarity.

that the heat flux changes drastically in the four cases (Fig. 2). The collisional cases (red and blue) exhibit large gradients in potential, density and temperature compared to the collisionless cases (green and purple). They consequently have much smaller heat fluxes. As is expected, increasing the radiation causes the temperature and heat flux to drop precipitously before the divertor plate, but actually increases the rate of energy loss from the core plasma. In the collisional plasmas, the thermal energy is equally partitioned between all three dimensions, such that $T_\parallel = T_\perp$, whereas in the collisionless plasmas, the thermal energy is equally partitioned parallel and perpendicular to the magnetic field, such that $T_\parallel = T_\perp/2$.

The PARASOL code has previously been used to determine α_e to be a relatively high value of 0.75 for an ion electron mass ratio of $m_i/m_e = 400$ [5]. Our results show that this falls within the range of possible values seen in Fig. 4. The collisionless limit α_e has a simple harmonic form relationship with the radiation loss, growing from near zero when there is no radiation to nearly one when the energy reaching the divertor is negligible Fig. 3. The point of transition shifts to higher radiation as the mass ratio is increased, as Fig. 4 of ion-electron mass ratio dependence m_i/m_e shows. This shift occurs because high mass ions are less prone to collisional effects, spend less time in the radiation region, and therefore, the radiation becomes effectively less.

While α_e is defined as a collisionless limit without local energy sources or sinks, we wish to check if Eq. 3 can be used in the general case, as it often is. Therefore, the dependence of α_e on position and collisionality is of interest, with the results presented in Fig. 5. As expected, α_e always asymptotes to a constant value in the collisionless limit. This limit does not appear to depend on position (and hence energy balance) much, in keeping with the expectation that a sheath-limited plasma is almost uniform. The collisional limit, on the other hand, strongly changes with the local energy balance. In the source region, $q \simeq q_{SH}$, which results in large errors in the calculated value of α_e. The intermediate region shows a radiation-independent nearly linear growth with $\alpha_e \propto \lambda_{mfp}$ that results in a peak when the mean free path is on the order of the connection length. The radiation region exhibits similar linear growth, except that high radiation produces a much more rapid increase in α_e than low radiation.

We wish to examine the validity of using q_{eff} in Eq. 3 as a general substitute for the heat flux as calculated by a fully kinetic simulation. Figure 6 shows the relationship q/q_{eff} over a range of collisionalities and radiation rates. Of course, the function converges to unity at the collisionless limit because of the previous fitting to the free parameter α_e. However, without any fitting, the collisional limit also correctly shows that the heat flux approaches the Spitzer-Härm limit $q \to q_{SH}$. Unfortunately, as the function transitions from the Spitzer-Härm limit to the free-streaming limit, the simple model deviates from the actual heat flux. When the radiation rate is high, the match between q_{eff} and q is acceptably within error. However, as the radiation is reduced, such that particles become more likely to pass from the radiation region back into the inter-

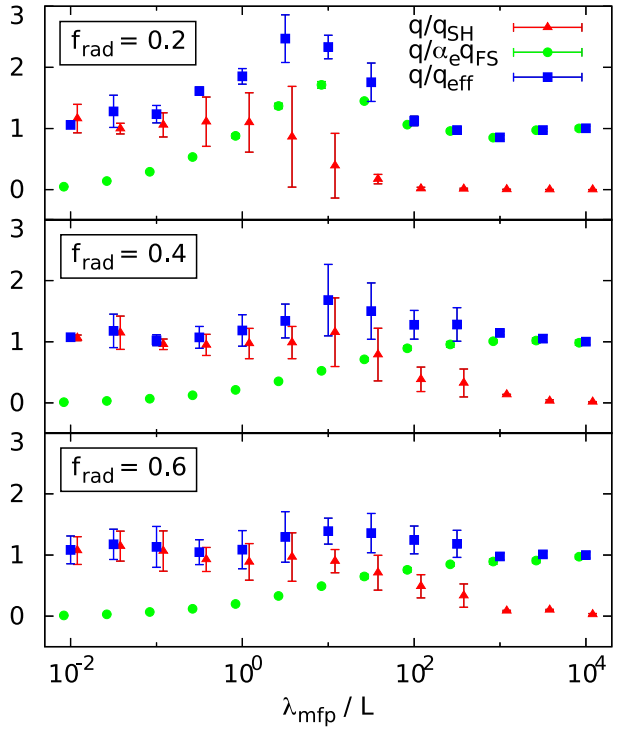

Fig. 6 Ratios of measured heat flux to Spitzer-Härm limit, α_e-adjusted free-streaming limit, and effective heat flux (Eq. 3) for different radiation rates and measured in the intermediate region. The values of α_e for each case are taken from the results in Fig. 6.

mediate region, the ratio $q/\alpha_e q_{FS}$ alone rises above unity for a moderate mean free path length. This result is due to both a rise in the heat flux, as well as a reduction in the free-streaming heat flux. This may be attributable to the fact that the temperature gradient falls drastically with collisionality in the high radiation case, but almost not at all in the low radiation case.

5 Summary

Electron heat transport parallel to the magnetic field in the SOL plasma is investigated with the PARASOL simulation. It is confirmed that in the collisional case the conductive heat flux is given by the Spitzer-Härm expression. In the collisionless case, conductive heat flux is limited to a factor α_e of the free-streaming value, with α_e small (~ 0.1 of the sheath-limited value) when little energy is lost to radiation, but becomes large (~ 1.0) when the radiation is high. Outside these limits, the currently used model of the conductive heat flux is an insufficient approximation for q_e. The model deviates strongly from the calculated results for a moderately collisional plasma with low radiation. Behavior in regions with energy sources or sinks also requires a multiply-defined α_e. Constraining usage of the model to regimes that behave correctly is not practical, and therefore, a more robust model is required. Due to the relative economy of system memory, a database lookup for q_e as a function of electron density and temperature may be the most tenable solution.

[1] P. C. Stangeby, *The Plasma Boundary of Magnetic Fusion Devices* (Taylor & Francis, New York, 2000) p. 660.
[2] W. Fundamenski, Plasma Phys. Control. Fusion **47**, R163 (2005).
[3] S. I. Braginskii, *Review of Plasma Physics Vol. 1, edited by M. A. Leontovich* (Consultants Bureau, New York, 1966) p. 205.
[4] D. Tskhakaya *et al.*, Contrib. Plasma Phys. **48**, 89 (2008).
[5] T. Takizuka *et al.*, Trans. of Fusion Technol. **39**, 111 (2001).

Proceedings of ITC18, 2008

Numerical simulation on the flute instabilities in the GAMMA10 magnetic field

Isao KATANUMA[1)], Katsuya YASHIRO[1)], Tsuyoshi IMAI[1)] and Vladimir P. PASTUKHOV[2)]

[1)] *Plasma Research Center, University of Tsukuba, Tsukuba 305-8577, Japan*

[2)] *RRC "Kurchatov Institute", Kurchatov Square, 1, 123182 Moscow, Russia*

We apply the computer simulation code, which was developed to study the flute modes fluctuation in the divertor, to the GAMMA10 tandem mirror.

Keywords: divertor, flute, interchange, simulation, mirror

1. Introduction

Flute modes are the most dangerous instabilities for open magnetic systems such as GAMMA10 tandem mirror. So that the GAMMA10 contains the non-axisymmetric minimum-B mirror regions for the suppression of the flute instabilities. The non-axisymmetric magnetic field, however, causes the neoclassical radial transport of ions in the central cell, so that the fully axisymmetric tandem mirror is desirable. A divertor magnetic mirror is a candidate for the axisymmetric tandem mirror stable to the flute modes as a future device [1]. There is a plan to replace one of anchor cell in GAMMA10 with an axisymmetric divertor mirror cell [2].

We have derived a set of the basic equations to analyze the flute mode fluctuations in the axisymmetric magnetic divertor and have developed a computer simulation code [3, 4]. In the present paper, we will apply the computer code to the GAMMA10 magnetic field and will perform the computer simulation on the flute mode fluctuations and the associated plasma radial transport.

In order to apply the computer code, where the basic equations used in the code were derived in the axisymmetric systems, to the GAMMA10 with the non-axisymmetric mirror regions, we make the following assumption. The stability criterion of the flute modes is given as [5, 6]

$$\int_{-L}^{L} \frac{(\tilde{p}_\perp + \tilde{p}_\parallel)}{B} \kappa_\psi \mathrm{d}\zeta \geq 0 \qquad (1)$$

Here the anisotropic pressures are written by the separation of variables as $p_\perp(\psi, \zeta) = \tilde{p}_\perp(\zeta)\nu(\psi)$, $p_\parallel(\psi, \zeta) = \tilde{p}_\parallel(\zeta)\nu(\psi)$ and κ_ψ is the normal curvature described in the flux coordinates (ψ, φ, ζ) with $\boldsymbol{B} = \nabla\psi \times \nabla\varphi$,

$$\hat{e}_\parallel \cdot \nabla \hat{e}_\parallel \equiv \boldsymbol{\kappa} = \kappa_\psi \nabla\psi + \kappa_\varphi \nabla\varphi \qquad (2)$$

The familiar stability criterion of the flute modes with isotropic plasma pressure is [7]

$$\delta \int_{-L}^{L} \frac{\mathrm{d}\zeta}{B} < 0 \quad \Rightarrow \quad \frac{\partial U}{\partial \psi} < 0\,, \quad U \equiv \int_{-L}^{L} \frac{\mathrm{d}\zeta}{B} \qquad (3)$$

author's e-mail: katanuma@prc.tsukuba.ac.jp

Noticing that $\partial U/\partial\psi = -2\int \kappa_\psi \mathrm{d}\zeta/B$ in the vacuum magnetic field, where $\nabla_\perp B = B\boldsymbol{\kappa}$, we redefine the specific volume of a magnetic field line U as

$$U = \int_{-L}^{L} \frac{(\tilde{p}_\perp + \tilde{p}_\parallel)}{B} \mathrm{d}\zeta \qquad (4)$$

This definition of specific volume U in eq.(4) satisfies the stability criterion eq.(1) with the axial pressure profile such as in Fig.1. So the simulation code can be applied to the non-axisymmetric magnetic field with anisotropic plasma pressure if the specific volume U defined in eq.(4) is axisymmetric.

2. Application to the GAMMA10 tandem mirror

GAMMA10 is an effectively axisymmetrized tandem mirror, which is designed to satisfy that the integral $\int \kappa_\psi \mathrm{d}\zeta/B$ does not depend on the azimuthal coordinate φ. The definition of U in eq.(4) retains the axisymmetric character of U, and the computer code [3, 4] can be used to calculate the flute mode fluctuations in GAMMA10. The axial plasma pressure profile adopted here is shown in Fig.1.

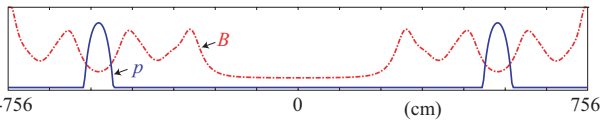

Fig. 1 GAMMA10 axial pressure model. Here $p = \tilde{p}_\perp + \tilde{p}_\parallel$.

Figure 2 plots the radial profiles of the specific volume U for the various ratio $pc \equiv (\tilde{p}_\perp + \tilde{p}_\parallel)_{Anchor}/(\tilde{p}_\perp + \tilde{p}_\parallel)_{central}$. In light of stability criterion eq.(1) or eq.(3), the cases of Figs.2(b) and 2(c) are stable to the flute modes near axis.

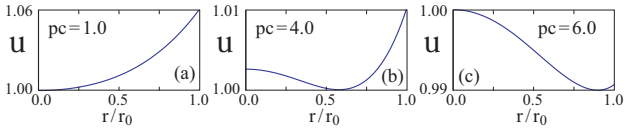

Fig. 2 Radial profiles of $u \equiv U(r)/U(0)$ of GAMMA10.

The basic equations adopted in the code are that the equation of motion of vorticity $\hat{w}$,

$$\partial_t|_\psi \hat{w} + [\![\Phi,\, \hat{w}]\!] - [\![\hat{\rho},\, \langle \frac{v_\alpha^2}{2} \rangle]\!] + \frac{1}{U^\gamma}\frac{\partial U}{\partial \psi}\frac{\partial(\hat{\rho}_0\tilde{T} + \hat{T}_0\tilde{\rho})}{\partial \varphi} = \{DT\}_w \qquad (5)$$

where $\hat{w}$ is related to the specific volume integrated vorticity $\nabla \times (\hat{\rho}\boldsymbol{B} \times \nabla\Phi/B^2)$ due to plasma $\boldsymbol{E} \times \boldsymbol{B}$ drift flux, i.e.

$\hat{w} = wU$. The transport equation of density $\hat{\rho}$ integrated along a magnetic field line, i.e. $\hat{\rho} = \rho U$, is

$$\partial_t|_\psi \hat{\rho} + [\![\Phi, \hat{\rho}]\!] = \{DT\}_\rho \tag{6}$$

And the transport equation of heat $\hat{T}$ integrated along a magnetic field line, i.e. $\hat{T} = TU^{\gamma-1}$, is

$$\partial_t|_\psi \hat{T} + [\![\Phi, \hat{T}]\!] = \{DT\}_T \tag{7}$$

Here the terms $\{DT\}_{w,\rho,T}$ are the classical dissipative terms [3, 4, 8], and $[\![\Phi, \hat{w}]\!] \equiv (\partial\Phi/\partial\psi)\partial\hat{w}/\partial\varphi - (\partial\Phi/\partial\varphi)\partial\hat{w}/\partial\psi$ is known as the Poisson bracket. The quantities with subscript 0 means the equilibrium ones and γ is the adiabatic index $\gamma = 5/3$. The symbol $\langle v_\alpha^2 \rangle$ is the square of plasma flow velocity, and the vorticity $\hat{w}$ can be represented by the scalar potential Φ as

$$\hat{w} = \partial_\psi(\hat{\rho}\langle r^2\rangle\partial_\psi\Phi) + \partial_\varphi\left(\hat{\rho}\langle 1/r^2B^2 + \lambda^2B^2\rangle\partial_\varphi\Phi\right) \tag{8}$$

where $\langle A \rangle$ means the average of A along a magnetic field line.

The linear dispersion relation obtained from eqs.(5)-(8) is

$$\begin{aligned}&(\omega - m\partial_\psi\Phi_0)^2 m^2\hat{\rho}_0\langle 1/r^2B^2 + \lambda^2B^2\rangle \\ &+ (\omega - m\partial_\psi\Phi_0)\left(m(\partial_\psi\hat{\rho}_0)\partial_\psi(\langle r^2\rangle\partial_\psi\Phi_0) - m\partial_\psi\hat{w}_0\right) \\ &- \left((m^2/2)(\partial_\psi\overline{\langle v_\alpha^2\rangle})\partial_\psi\hat{\rho}_0 + (m^2/U^\gamma)(\partial_\psi U)\partial_\psi(\hat{\rho}_0\hat{T}_0)\right) = 0\end{aligned} \tag{9}$$

Here m is the azimuthal mode number and ω is the frequency of the mode. In the case of $\partial_\psi\hat{w}_0 = 0$ and $\partial_\psi\hat{\rho}_0 = 0$, eq.(9) gives the simple dispersion relation of

$$\omega = m\partial_\psi\Phi_0 + \left((1/U^\gamma)(\partial_\psi U)(\partial_\psi\hat{T}_0)/\langle 1/r^2B^2 + \lambda^2B^2\rangle\right)^{1/2} \tag{10}$$

Equation (10) indicates that the mode drifts azimuthally with the $\boldsymbol{E}\times\boldsymbol{B}$ drift velocity, and is unstable if $(\partial_\psi U)\partial_\psi\hat{T}_0 < 0$ which is just the same as the stability condition of flute modes of eqs.(1) or (3).

3. Motivation of the simulation and flute instability

The GAMMA10 tandem mirror improves the axial ion confinement with the help of plug potential formation in the end-mirror cells. Figure 3 is a copy of Fig.6 in [9] as it was. The authors discussed the effects of Neutral beam injection (NBI) on the line densities measured in GAMMA10 in their article [9]. But we are interested in the behavior of the diamagnetism ($\mathsf{DM_{cc}}$) in Fig.3(c) around Time $\simeq$ 130ms. The figure indicates that the diamagnetism dropped suddenly just when the plug ECRH was turned on. We suppose the mechanism of the sudden drop of $\mathsf{DM_{cc}}$ to be the flute mode fluctuations, and carry out the numerical simulation on the flute mode fluctuations.

What kind of effects does the plug-ECRH bring into the GAMMA10 confinement region? It is reasonable to understand that the plug ECRH brings the charge density perturbation into the system, because the plug-ECRH is expected to create the plug potential. The potential, however, is created by the vortex within the framework of MHD as

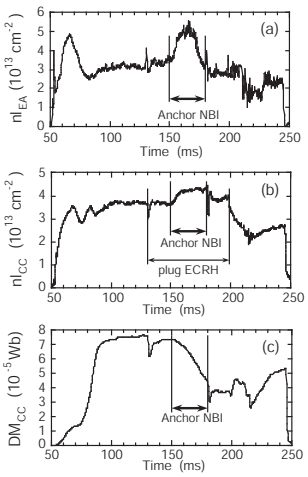

Fig. 3 Time evolution of (a) east anchor line density, (b) central cell line density, and (c) central cell diamagnetism. This figure and the caption are a copy of Fig.6 in [9].

shown in eq.(8), so that the plug ECRH is assumed to bring the vortex into the system.

At first we carry out the simulation in the case of $pc = 1.0$, where the axial pressure is constant and so the specific volume U is Fig.2(a). The flute modes are unstable because of $\partial U/\partial\psi > 0$. The initial condition is that $\hat{w}(x,\varphi) = +1$, $\hat{\rho}(x,\varphi) = 1$, $\hat{T}(x,\varphi) = \exp\{-2x^2\}u^{2/3}$, where all quantities are normalized, and the radial profile of temperature is $T(x,\varphi) = \hat{T}(x,\varphi)/u^{2/3}$. Here $x \equiv r/r_0$, where $r_0 = 18$cm is chosen as the radial position of a limiter. The constant $\hat{w}$ gives the rigid azimuthal rotation of plasma by $\boldsymbol{E}\times\boldsymbol{B}$.

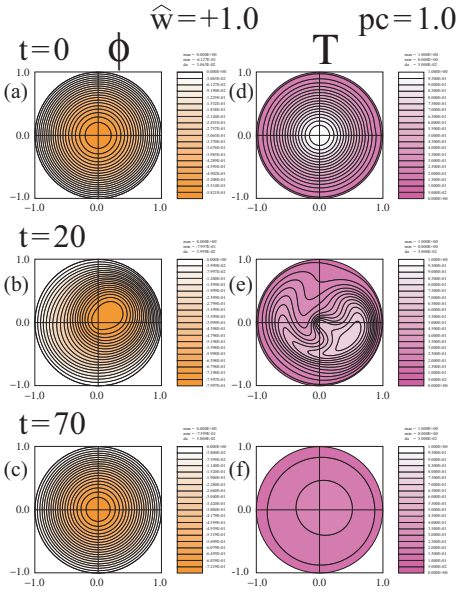

Fig. 4 Contour plots of potential Φ and temperature T at $t = 0$ in (a), (d), at $t = 20$ in (b), (e) and at $t = 70$ in (c), (f). Here each $\Phi(x,\varphi)$ is normalized by its maximum value at each time, while each $T(x,\varphi)$ is normalized by its maximum value at $t = 0$.

Figures 4(a) and 4(d) plot the contour surfaces of the initial potential Φ and initial temperature T profiles, where a small initial perturbation is added to $T(x)$ which is too small to be seen in Fig.4(d). It can be seen that the flute

instability makes the temperature profile flat at $t = 70$.

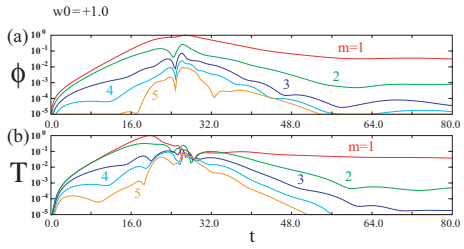

Fig. 5 Time evolution of Fourier components of Φ and T for various azimuthal mode numbers m at $x = 1/2$.

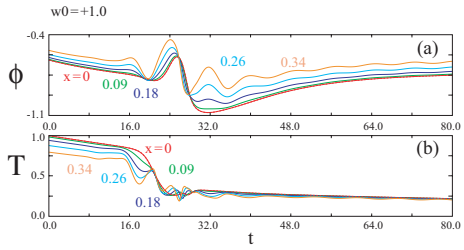

Fig. 6 The time variation of magnitudes of $T(x, \varphi)$ and $\Phi(x, \varphi)$ is plotted as a function of t at $x = 0,\ 0.09,\ 0.18,\ 0.26,\ 0.34$. All data points are at $\varphi = 0$.

Figures 5 shows the time evolution of Fourier components of Φ and T at $x = 1/2$ and Fig.6 plots the time evolution of Φ and T at various x and $\varphi = 0$. Before the flute instability saturates, a large transport of T occurs in Fig.6(b), when the potential profile deviates from the axisymmetry in Fig.4(b). The flute instability saturates when the temperature profile becomes flat radially like Fig.4(f).

4. Effects of the anisotropic potential

The flute instability causes a large energy transport due to the anisotropic potential profile generated by the instability shown in Fig.4(b). If the external μ-wave for plug potential formation (ECRH) brings the perturbed vorticity in the system, the resultant anisotropic potential can cause a large transport just like the flute instability. To investigate this mechanism of transport we carry out the numerical simulation with initial conditions of non-uniform vorticity $\hat{w}$ in Fig.7.

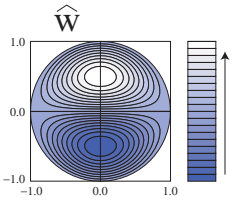

Fig. 7 Initial condition of $\hat{w}(x, \varphi)$.

The initial condition of $\hat{w}$ in Fig.7 is given by

$$\hat{w}(x, \varphi) = w_0 + w_f \sin\{\pi x\} \sin\varphi \qquad (11)$$

Here w_0 and w_f are constants which give the initial potential $\Phi(x, \varphi)$ as shown in Fig.8. The following simulation adopts $pc = 4.0$, that is the radial profile of U is given by Fig.2(b). By changing the coefficients w_0 and w_f, various anisotropic initial potential profile is realized in Fig.8.

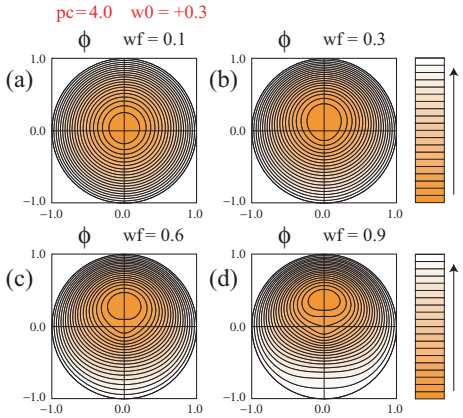

Fig. 8 Initial condition of potential, which is obtained by eqs.(8) and (11) for various w_f. Here the case $w_0 = +0.3$ is plotted.

We show the simulation results of $w_f = 0.1,\ 0.3,\ 0.6,\ 0.9$ with $w_0 = +0.3$. Figures 9–12 plot the time variation of potential $\Phi(x, \varphi = 0)$ and temperature $T(x, \varphi = 0)$ at $x = 0,\ 0.09,\ 0.18,\ 0.26,\ 0.34$, respectively. The temperature T at each local spatial point decreases slowly in time in Figs.9 and 10.

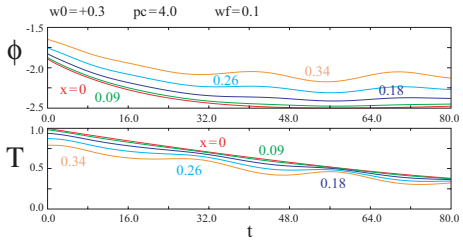

Fig. 9 The time evolution of the potential Φ and T measured at the same positions as Fig.6 for the case of $w_f = 0.1$.

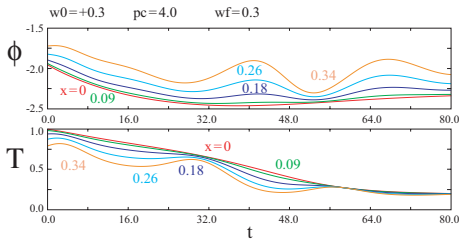

Fig. 10 The time evolution of the potential Φ and T measured at the same positions as Fig.6 for the case of $w_f = 0.3$.

However, a large transport results from the initial anisotropic potential in Figs.11 and 12. After $t = 40$ in Fig.11 and after $t = 30$ in Fig.12 the temperature radial profiles becomes almost flat. So the initial anisotropy of potential has the strong influence on the transport. The oscillations of potential observed in Figs.9–12 comes from the anisotropy of the potential, which means that the initial anisotropy of potential survives for a long time. This can be seen clearly in Fig.13.

Figure 13 plots the time evolution of Fourier amplitudes of potential. The dominant mode is $m = 1$, amplitude of which is order of magnitude larger than other modes $m \neq 1$. The system is not unstable to the flute modes, be-

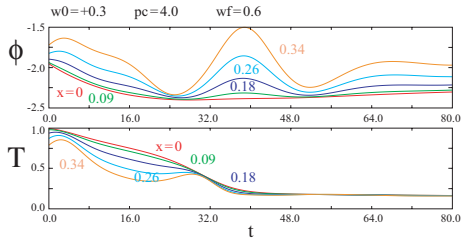

Fig. 11 The time evolution of the potential Φ and T measured at the same positions as Fig.6 for the case of $w_f = 0.6$.

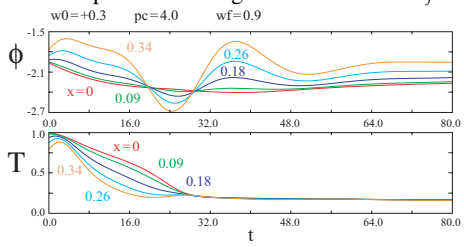

Fig. 12 The time evolution of the potential Φ and T measured at the same positions as Fig.6 for the case of $w_f = 0.9$.

cause the $m = 1$ initial perturbation of Φ does not grows in time, but the system is in the marginally stable state.

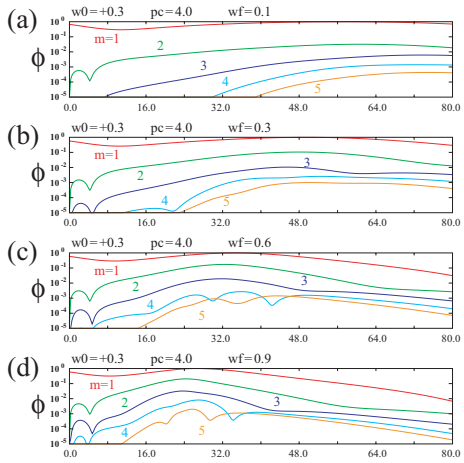

Fig. 13 The time evolution of Fourier amplitudes $m = 1 \sim 5$ for $w_0 = 0.3$.

The cases of high potential of $w_0 = +3.0$ are plotted in Figs.14, 15. The anisotropy of initial potential is given by the ratio w_f/w_0 only. The comparison of two cases $w_0 = +0.3$ and $w_0 = +3.0$ indicates that a larger magnitude of potential cause larger transport as long as the ratio w_f/w_0 is the same. This results is supported by the consideration that the transport results from the $\boldsymbol{E} \times \boldsymbol{B}$-drifts, that is the larger magnitude $\boldsymbol{E}$ cause the larger magnitude of drifts.

The time evolution of Fourier amplitude of potential Φ in the case $w_0 = +3.0$ is plotted in Fig.16. The $m = 1$ initial perturbation of Φ is the dominant mode in this case, and which decreases in time so that the system is stable.

5. Summary

We applied the simulation code, which developed for the axisymmetric system, to the non-axisymmetric tandem mirror, taking into account the effect of axial pressure profile to the magnetic specific volume U. In the case of the

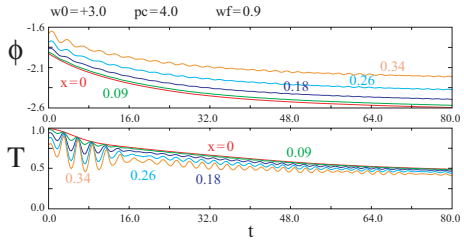

Fig. 14 The time evolution of the potential Φ and T measured at the same positions as Fig.6 for the case of $w_0 = 3.0$ and $w_f = 0.9$.

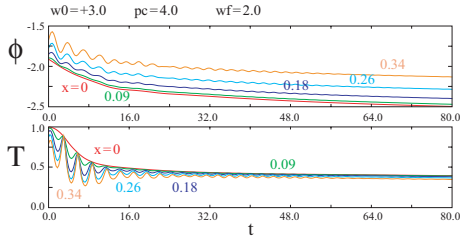

Fig. 15 The time evolution of the potential Φ and T measured at the same positions as Fig.6 for the case of $w_0 = 3.0$ and $w_f = 2.0$.

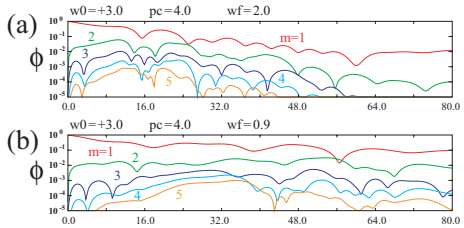

Fig. 16 The time evolution of Fourier amplitudes $m = 1 \sim 5$ for $w_0 = 3.0$.

uniform axial pressure profile, the system was unstable to the flute modes which caused a large energy transport.

The initial anisotropy of potential, which is realized by the initial anisotropic vorticity $\hat{w}$, causes a large energy transport even in the system stable to the flute modes. The mechanism of transport comes from the $\boldsymbol{E} \times \boldsymbol{B}$-drift in the radial direction due to the flute-like fluctuations having a long life time. The life time of this flute-like fluctuations becomes shorter in a very stable state to the flute modes in Fig.2(c) than that in Fig.2(b)

[1] I.Katanuma, Y.Sasagawa, Y.Tatematsu, Y.Nakashima, T.Cho, V.P.Pastukhov; Nucl. Fusion, **46**, 608(2006).
[2] I.Katanuma, H.Saimaru, Y.Mizoguchi, K.Yashiro, T.Cho, V.P.Pastuhkov; Trans. Fus. Sci. Tech. **51**, 122(2007).
[3] I.Katanuma, V.P.Pastukhov, T.Imai, M.Ichimura, T.Kariya et al.; J. Plas. Fus. Res. **84**, 279(2008).
[4] I.Katanuma, et al.; J. Plas. Fus. Res. **84**, 279(2008).
[5] *Physics Basis for MFTF-B, ed. D.E.Boldwin, B.G.Logan, T.C.Simonen; UCID-18496-Part 2 (1980).*
[6] I.Katanuma, T.Tatematsu, K.Ishii, T.Saito and K.Yatsu; J. Phys. Soc.Jpn. **69**, 3244(2000).
[7] M.N.Rosenbluth and C.L.Longmire, Ann. Phys. **1**, 120(1957).
[8] S.I.Braginskiin *Reviews of Plasma Physics*, ed. A.M.A.Leontovich (Consultants Bureau, New York, 1965) Vol. 1.
[9] K.Yatsu, et.al.; Nucl. Fusion, **41**, 613(2001).

Proceedings of ITC18,2008

Effects of MHD-activity-induced low-*n* error magnetic fields on the neoclassical viscosities in helical plasmas

Shin Nishimura

National Institute for Fusion Science, Oroshi-cho 322-6, Toki, 509-5292, Japan

Effects of the perturbed magnetic field with low toroidal mode numbers (n) are considered. One cause of this type of perturbation, which has recently been studied in tokamaks, is MHD-activities. In helical/stellarator, this low-n perturbation is sometimes artificially added for island diverters. In viewpoint of the neoclassical viscosities, these perturbed magnetic fields affect on both of bounce center drifts of toroidally trapped and ripple-trapped particles. However, in usual neoclassical analyses in helical/stellarator devices assuming periodic magnetic field strength, these effects had not been studied. For future studies in helical/stellarator devices, a method to use bounce-averaged drift kinetic equation for the toroidally trapped particles is proposed.

Keywords: neoclassical transport, neoclassical viscosity, drift kinetic equation, rotational stabilization of RWM, island diverter

1. Inroduction

Neoclassical analyses in helical plasmas often assume the toroidally periodic magnetic field strength of $B=\Sigma B_{mn}\cos(m\theta-nN\zeta)$ [θ, ζ : poloidal and toroidal angles, N: the toroidal period number] and thus effects of the low-n ($n<N$) error magnetic fields in a more general expression $B=\Sigma B_{mn}\cos(m\theta-n\zeta)$ had not been investigated. However, in recent tokamak studies [1-3], this kind of low-n error magnetic field component induced by MHD-activities is considered to be important since it causes various additional neoclassical effects relating to the rotational stabilization of the resistive wall mode and island physics. The toroidal viscosity caused by additional bounce-averaged bounce center motions has been mainly investigated in these studies in tokamaks. When the low-n modes exist in helical and stellarator configurations, it affects not only on the toroidally trapped (berely trapped) particles but also on the ripple-trapped (deeply trapped) ones. It also should be noted that this type of low-n error fields is sometimes added artificially for island diverters. Although these effects for the viscosity are already covered by a recently proposed basic framework for the neoclassical transport in general non-symmetric toroidal plasmas [4], the "full torus" calculation including the low-n modes will be huge if we adopt the numerical procedures (such as variational methods and Monte Carlo methods) described in Ref.[4]. Practically usable methods to obtain the viscosity coefficients have still remained as future theme. Even in our previous study deriving and testing various analytically approximated formulas [5], the bounce-averaged effects due to the low-n modes are not included. Therefore we recently started to study an extension of the analytical approximation methods for the drift kinetic equation in helical and stellarator configurations to include these additional drift effects [6]. This understanding for the trapped particles' dynamics will be useful not only for studies of mean flows [1-3] but also for studies investigating a relation of the neoclassical transport with the zonal flow [7-8].

As an important implicit basis of the neoclassical transport analysis, we assume here existences of nested closed magnetic flux surfaces [4]. This assumption means that only resonant modes of $m-n\psi'/\chi'=0$ in the Fourier expansions of $1/B^2$ in the Boozer coordinates and of B^2 in the Hamada coordinates are forbidden. Here, χ' and ψ' are radial derivatives ('=d/ds with the arbitrary label of flux surfaces s) of the poloidal and toroidal magnetic fluxes, respectively, and (m,n) are the poloidal and toroidal Fourier modes in the expansions. We shall define the flux coordinates (s,θ,ζ) there to make the safety factor to be positive $q\equiv\psi'/\chi'>0$. Non-resonant low-n modes of $|m-nq|\approx 1$, and nearly resonant modes $m-nq\approx 0$ in other functions still can exist without breaking the flux surfaces. For the non-bounce-averaged guiding center drift effects such as the parallel viscosity force determining the parallel plasma flows, we already derived analytical formulas which is applicable to arbitrary Fourier spectra of the magnetic field including this type of low-n error fields. Therefore we shall focus on the bounce-averaged bounce-center drifts of the toroidally trapped and ripple-trapped particles in so-called $1/\nu$ collisionality regime. In contrast to the non-averaged effects, in which all of Fourier coefficients B_{mn} are

author's e-mail: nishimura.shin@lhd.nifs.ac.jp

required, the effective range of (m,n) is limited in calculation of the bounce-averaged effects. For e.g., contributions of extremely high frequency modulation along the **B**-field line with $|m-nq| \gg |Nq-L|$ vanish in the bounce averaging and are not important for both of the ripple-trapped and toroidally trapped particles. Here (L.N) are the basic poloidal and toroidal modes of the helical modulation, which is used in a "conventional" model expression with the assumption of the toroidal periodicity [5,7,9,10,11,12]

$$B/B_{00} = 1 + \varepsilon_{\mathrm{T}}(\theta) + \varepsilon_{\mathrm{H}}(\theta)\cos\{L\theta - N\zeta + \gamma(\theta)\} \quad (1)$$

for the ripple-trapping effects. It should be noted here that the analytical bounce-averaging for the ripple-trapped particles [11,12] assumes that the phase term $\gamma(\theta)$ is a slowly varying small function. Furthermore, in the analytical bounce-averaging for the toroidally trapped particles, we shall treat this high frequency modulation (helical and bumpy ripples) $\varepsilon_{\mathrm{H}}(\theta)\cos\{L\theta - N\zeta + \gamma(\theta)\}$ by a ripple-averaging. Also in this "ripple-averaging" of the toroidally trapped particles' motion, this characteristic of $\gamma(\theta)$ is favorable. In existing helical/stellarator devices, this characteristic is not attained in the Hamada coordinates (s, θ_{H}, ζ_{H}), which are used in some theories for tokamaks [3,4]. The Boozer coordinates (s, θ_{B}, ζ_{B}) are better for analyses of helical/stellarator devices and thus we assume the use of the Boozer coordinates though we omit the subscript "B" indicating "Boozer". Methods to include the low-n perturbed fields and to truncate nonessential B-field spectra in the bounce-averaged kinetic equation depend on the trapped orbit topologies and thus we consider them separately in the next section. It also is assumed in these discussions that $Nq-L$ is positive and $Nq-L \gg 1$, which is satisfied in general helical/stellarator configurations.

2. Expressions of the Magnetic Field Strength for the Bounce-averaged Motions

For a simplicity, we assume the stellarator symmetry of the B-field strength $B(-\theta,-\zeta)=B(\theta,\zeta)$. In the bounce-averaged drift kinetic equations [3,11,12], parallel drift term [4] $V_{\|}f_{a1} \equiv v_{\|}\mathbf{b}\cdot\nabla_{(\mu=\mathrm{const})}f_{a1}$ vanishes as a result of the averaging $\oint \mathrm{d}l/v_{\|}$, and the substantially remaining guiding center drift is that due to $\nabla s \times \mathbf{B}\cdot\nabla v_{\|}$ in the radial drift term [4]

$$\sigma_1^{+} \equiv \mathbf{v}_{\mathrm{d}a}\cdot\nabla s = -\frac{m_a c}{e_a}\frac{4\pi^2}{V'}\frac{v_{\|}B}{\langle B^2\rangle}\times \left(B_\zeta^{(\mathrm{Boozer})}\frac{\partial}{\partial\theta_{\mathrm{B}}} - B_\theta^{(\mathrm{Boozer})}\frac{\partial}{\partial\zeta_{\mathrm{B}}}\right)_{(\mu=\mathrm{const})}\left(\frac{v_{\|}}{B}\right) \quad (2)$$

and/or

$$\sigma_{Xa} \equiv -\sigma_1^{+} - \frac{m_a c}{e_a}V_{\|}\left(v_{\|}\widetilde{U}\right) = \frac{m_a c}{e_a}\frac{4\pi^2}{V'}\frac{v_{\|}}{\langle B^2\rangle B}\times \left(B_\zeta^{(\mathrm{Boozer})}\frac{\partial}{\partial\theta_{\mathrm{H}}} - B_\theta^{(\mathrm{Boozer})}\frac{\partial}{\partial\zeta_{\mathrm{H}}}\right)_{(\mu=\mathrm{const})}\left(v_{\|}B\right) \quad (3)$$

However, B-field strength modulation along the field line $\mathbf{B}\cdot\nabla B$ also is still implicitly included as the $v_{\|}$ modulation and as a factor determining the positions of trapped particles' reflection points. Procedures carrying out this averaging analytically depend on the trapped orbit topologies; the toroidally trapped orbits in the barely trapped pitch-angle range where $v_{\|} \simeq \mathrm{const}$ along the **B**-field line in a ripple period, and the ripple-trapped orbits in the deeply trapped range where $v_{\|} \neq \mathrm{const}$ in the period. This difference in a characteristic of the parallel drift velocity $v_{\|}$ results in different treatments of B_{mn} components around $m\sim L$, $n\sim N$. For the toroidally trapped particles with the long bounce period over larger poloidal angle ranges, the reflection points are almost determined only by the envelop function $1+\varepsilon_{\mathrm{T}}(\theta)+\varepsilon_{\mathrm{H}}(\theta)$ in Eq.(1) and the bounce-averaging of $\nabla s \times \mathbf{B}\cdot\nabla v_{\|}$ can be carried out with an approximation of $v_{\|} \simeq \mathrm{const}$ in the ripple period. In this case, the parallel modulation $\mathbf{B}\cdot\nabla B$ in $\nabla v_{\|}$ due to non-axisymmetric ($n\neq 0$) B_{mn} modes is not essentially important, and the B_{mn} are separated into only two types; axisymmetric modes $n=0$ causing the trapping, and the non-axisymmetric modes as a cause of the bounce-averaged radial drifts. In the tokamak theory assuming $\varepsilon_{\mathrm{H}}(\theta) \approx 0$ [2,3], a following expression of B is used to calculate effects of $m\sim nq$ non-axisymmetric modes on the toroidally trapped particles' parallel velocity $v_{\|}$.

$$B = \sum_m B_{m0}\cos(m\theta) + \sum_{n\neq 0}\left[\cos(n\zeta_0)\sum_m B_{mn}\cos\{(m-nq)\theta\} - \sin(n\zeta_0)\sum_m B_{mn}\sin\{(m-nq)\theta\}\right] \quad (4)$$

Here, $\zeta_0 \equiv q\theta - \zeta$ is a label of the magnetic field lines. We shall use this method also for toroidally trapped particles in helical/stellarator devices. It should be noted that only non-axisymmetric modes of $|m-nq| < Nq-L$ effectively remain in the field-line integral per the ripple-period in the case of $v_{\|} \simeq \mathrm{const}$, and this remaining poloidal mode (m) range becomes narrower in the integral for longer bounce periods.

On the other hand, we should take into account both of $\nabla s \times \mathbf{B}\cdot\nabla B$ and $\mathbf{B}\cdot\nabla B$ in $\nabla v_{\|}$ for the ripple-trapped

particles with $v_{\|} \neq \text{const}$ in the ripple-period. For this calculation, we consider a use of differential $\nabla s \times \mathbf{B} \bullet \nabla J_{\mathrm{r}}$ of the adiabatic invariant J_{r} [11,12], for which an analytically approximated expression for the model field in Eq.(1) is given by

$$J_{\mathrm{r}} \equiv \oint v_{\|} \mathrm{d}l = \frac{16 B_{\zeta}/B_{00}}{N - L/q} \frac{\pi - 2\sin^{-1}\alpha^{*}}{\pi} \left(\frac{\mu B_{00} \delta_{\mathrm{eff}}}{m_a} \right)^{1/2} \times \left\{ E(\kappa) - (1-\kappa^2) K(\kappa) \right\} \quad (\text{for } \kappa^2 < 1) \quad . \quad (5)$$

Here, $K(\kappa)$ and $E(\kappa)$ are the complete elliptic integrals of the first and second kind, respectively, and the pitch-angle parameter κ^2 in them is defined by $\kappa^2 \equiv \{w - \mu B_{00}(1+\varepsilon_{\mathrm{T}} - \delta_{\mathrm{eff}})\}/(2\mu B_{00}\delta_{\mathrm{eff}})$. Although detailed definitions of the effective ripple-well depth δ_{eff} and the length correction α^* are shown in Ref.[9], approximations of $\delta_{\mathrm{eff}} \cong \varepsilon_{\mathrm{H}}$ and $\alpha^* \cong 0$ can be used in many helical/stellarator devices as stated in Ref.[5]. In contrast to the toroidally trapped cases, the axisymmetric B-field modulation n=0 scarcely has the trapping effects ($\mathbf{B} \bullet \nabla B$) and substantially has only radial drift effects ($\nabla s \times \mathbf{B} \bullet \nabla B$) for the ripple-trapped particles. Although the non-axisymmetric modulations $n \neq 0$ cause both of them, there are two types of the $n \neq 0$ modes; high frequency modulation along the field line $\varepsilon_{\mathrm{H}}(\theta) \cos\{L\theta - N\zeta + \gamma(\theta)\}$, and the low frequency ones $\mathbf{B} \bullet \nabla \cos(m\theta - n\zeta) \approx 0$. If the non-axisymmetric mode satisfies $\nabla s \times \mathbf{B} \bullet \nabla \cos(m\theta - n\zeta) \simeq \text{const}$ in a ripple period, it is appropriate to include it into $\varepsilon_{\mathrm{T}}(\theta)$, but this treatment neglects the $v_{\|}$ modulation due to this mode. In case of the ripple-trapping, we should avoid this neglect as long as contributions of the $n \neq 0$ modes keeps an important characteristic of $\varepsilon_{\mathrm{H}}(\theta)$ as a slowly varying function along the **B**-field line. For this calculation, we shall consider an expression of B

$$\begin{aligned} B = & \sum_m B_{m0} \cos(m\theta) \\ & + \sum_{l=1}^{\infty} \left[\cos\{l(L\theta - N\zeta)\} \sum_m B_{m,\, lN} \cos\{(m - lL)\theta\} \right. \\ & \left. \quad - \sin\{l(L\theta - N\zeta)\} \sum_m B_{m,\, lN} \sin\{(m - lL)\theta\} \right] \\ & + \sum_m \left[\cos(m\theta_0) \sum_{n \neq 0,\, lN} B_{mn} \cos\{(m/q - n)\zeta\} \right. \\ & \left. \quad - \sin(m\theta_0) \sum_{n \neq 0,\, lN} B_{mn} \sin\{(m/q - n)\zeta\} \right] \end{aligned} \quad . \quad (6)$$

Here, $\theta_0 \equiv \theta - \zeta/q$ in the third term is another label of the magnetic field lines. In previous stellarator theories [5,7,9-12], the first and second terms are used as $1 + \varepsilon_{\mathrm{T}}(\theta)$ and $\varepsilon_{\mathrm{H}}(\theta) \cos\{L\theta - N\zeta + \gamma(\theta)\}$ in Eq.(1), respectively, and the third term is neglected there. Even though it is well-known that $l \geq 2$ in the second term is truncated in Ref.[11], these higher harmonics can be included in the analytically approximated calculation of J_{r} and $\nabla s \times \mathbf{B} \bullet \nabla J_{\mathrm{r}}$ by some methods such as that in Ref.[12], and thus we retain here the $l \geq 2$ terms. Also in this Eq.(6), effective poloidal mode (m) range, which remains in the integral along the field line per ripple-period is limited. Similarly to Eq.(4), only a range of $|m/q - n| < N - L/q$ is important in the first and third terms, and the third term with this truncation has a role as the low frequency modulation along the field line analogous to $1 + \varepsilon_{\mathrm{T}}(\theta)$ in Eqs.(1),(5). In the second term, as discussed in Ref.[9], only a range of $|m - lL| < Nq - L$ should be included to keep $\varepsilon_{\mathrm{H}}(\theta)$ as a slowly varying function compared with $\cos\{L\theta - N\zeta + \gamma(\theta)\}$. Therefore, only for this limited (m,n) region, we can include both of $\mathbf{B} \bullet \nabla \cos(m\theta - n\zeta)$ and $\nabla s \times \mathbf{B} \bullet \nabla \cos(m\theta - n\zeta)$ in $\nabla s \times \mathbf{B} \bullet \nabla J_{\mathrm{r}}$. The trapping effects due to $\mathbf{B} \bullet \nabla \cos(m\theta - n\zeta)$ vanish on the line of $m \cong nq$ in the (m,n) space, and it is appropriate to be included in $\varepsilon_{\mathrm{H}}(\theta) \cos\{L\theta - N\zeta + \gamma(\theta)\}$ for the modes in $m < Nq + (l-1)L$ which do not include this line. The modes in $m > Nq$ being high frequency contributions in $\varepsilon_{\mathrm{H}}(\theta)$ must be separated from this term and be treated in the third term in Eq.(6) to include only $\nabla s \times \mathbf{B} \bullet \nabla \cos(m\theta - n\zeta)$ since $\mathbf{B} \bullet \nabla \cos(m\theta - n\zeta) \approx 0$ near this line $m \cong nq$. Although contributions of $m \sim L \ll nq$ with $n \neq 0$, lN in the third term do not automatically vanish only by the bounce-averaging for the ripple-trapped orbits with $v_{\|} \neq \text{const}$, they are substantially slight toroidal modulations of $\varepsilon_{\mathrm{H}}(\theta)$ and $\gamma(\theta)$, and are not important in the final flux-surface-averaged results. Therefore only $\nabla s \times \mathbf{B} \bullet \nabla \cos(m\theta - n\zeta)$ in the range of $|m - nq| < Nq - L$ is retained in the third term.

The low frequency B-field strength modulation along the field line $\varepsilon_{\mathrm{T}}(\theta)$ in Eq.(1) is now extended to include non-axisymmetric component $\varepsilon_{\mathrm{T}}^{(\mathrm{na})}(\theta,\zeta)$ by

$$\begin{aligned} B/B_{00} \cong & 1 + \varepsilon_{\mathrm{T}}^{(\mathrm{as})}(\theta) + \varepsilon_{\mathrm{T}}^{(\mathrm{na})}(\theta,\zeta) \\ & + \varepsilon_{\mathrm{H}}(\theta) \cos\{L\theta - N\zeta + \gamma(\theta)\} \end{aligned} \quad , \quad (7)$$

where the non-axisymmetric component is defined by

$$\begin{aligned} & \varepsilon_{\mathrm{T}}^{(\mathrm{na})}(\theta,\zeta) \\ & \equiv \frac{1}{B_{00}} \sum_{|m - nq| < Nq - L} \left[\cos(m\theta_0) \sum_{n \neq 0, lN} B_{mn} \cos\{(m/q - n)\zeta\} \right. \\ & \qquad \left. - \sin(m\theta_0) \sum_{n \neq 0, lN} B_{mn} \sin\{(m/q - n)\zeta\} \right] \\ & + \frac{1}{B_{00}} \sum_{\substack{|m - nq| < Nq - L \\ m > Nq + (l-1)L}} \left[\cos(m\theta_0) \sum_{n = lN} B_{mn} \cos\{(m/q - n)\zeta\} \right. \\ & \qquad \left. - \sin(m\theta_0) \sum_{n = lN} B_{mn} \sin\{(m/q - n)\zeta\} \right] \end{aligned} \quad ,$$

and the axisymmetric component $\varepsilon_{\mathrm{T}}^{(\mathrm{as})}(\theta)$ is defined by

$$\varepsilon_{\mathrm{T}}^{(\mathrm{as})}(\theta) \equiv \frac{1}{B_{00}} \sum_{|m-nq|<Nq-L} B_{m0}\cos(m\theta) \quad .$$

As mentioned in the introduction, practically interesting B-field perturbations are low-frequency modulation $|m-nq| \le 1$ with low toroidal modes of $n \ll N$ in both of the MHD-activity induced and artificially added perturbations, and thus $n \ge N$ in $\varepsilon_{\mathrm{T}}^{(\mathrm{na})}(\theta,\zeta)$ is not actually important. By these considerations, however, we find that the definition of the "low frequency modulation along the **B**-field lines" differs depending on the pitch-angle (κ^2) range. The treatment of $(n-N)q + L < m < Nq + (l-1)L$ at $n=lN$ differs in two ranges discontinuously; toroidally trapped particles in $\kappa^2>1$, and ripple-trapped particles in $\kappa^2<1$. This difference corresponds to that of bounce- (or ripple-) averaged $\nabla v_{\|}$ effects in two pitch-angle ranges $\kappa^2>1$ and $\kappa^2<1$. In contrast to Eq.(5) for $\kappa^2<1$, the ripple-averaged parallel velocity for $\kappa^2>1$ is given by [12],

$$J_{\mathrm{t}} \equiv \oint_{\substack{\mathrm{ripple}\\ \mathrm{period}}} v_{\|}\mathrm{d}l = \frac{16 B_{\zeta}/B_{00}}{N - L/q}\left(\frac{\mu B_{00}\delta_{\mathrm{eff}}}{m_a}\right)^{1/2} \kappa E(1/\kappa) . \quad (8)$$

Although J in Eqs.(5),(8) and σ_1^+, σ_{Xa} in Eqs.(2),(3) are continuous at $\kappa^2=1$, ∇J and the bounce average of σ_1^+, σ_{Xa} are discontinuously change at $\kappa^2=1$. An aforementioned approximation $v_{\|} \simeq \mathrm{const}$ in a ripple period at $\kappa^2>1$, in spite of a fact that $v_{\|} \neq \mathrm{const}$ at $\kappa^2<1$, is motivated by this discontinuous change. It may be thought that one problem in this definition of "low frequency" in the ripple-trapped pitch-angle range $\kappa^2<1$ is a discontinuous change of our treatment at a boundary regime in the (m,n) space $m \cong Nq+(l-1)L$. In the Fourier expansion of B on the magnetic flux surface coordinates (Boozer coordinates in many practical cases) making the phase function $\gamma(\theta)$ to be a slowly varying small function, however, B_{mn} in this region are small, and thus the discontinuous change is not a serious problem. In addition to it, since the poloidal mode (m) limiters of $|nq-m| < Nq-L$, $|m-lL| < Nq-L$, and so on in Eqs.(4),(7) are actually implemented by low-pass filters in $\partial/\partial\theta$ operation [9], the contributions of the modes do not change discontinuously.

A method to obtain approximated values of $\varepsilon_{\mathrm{H}}(\theta)$ for an approximation of

$$\frac{1}{B_{00}}\sum_{l=1}^{\infty}\left[\begin{array}{l}\cos\{l(L\theta - N\zeta)\}\sum\limits_{|m-lL|<Nq-L} B_{m,\,lN}\cos\{(m-lL)\theta\} \\ -\sin\{l(L\theta - N\zeta)\}\sum\limits_{|m-lL|<Nq-L} B_{m,\,lN}\sin\{(m-lL)\theta\}\end{array}\right]$$
$$\cong \varepsilon_{\mathrm{H}}(\theta)\cos\{L\theta - N\zeta + \gamma(\theta)\} \quad , \quad (9)$$

which corresponds to retaining only first lowest mode term in the Todoroki's "phase" Fourier series [12], is already described in Ref.[9] and will not be shown here. It only should be emphasized here on this high frequency modulation term $\varepsilon_{\mathrm{H}}(\theta)\cos\{L\theta - N\zeta + \gamma(\theta)\}$ that its amplitude $\varepsilon_{\mathrm{H}}(\theta)$ is more essential rather than the form of the modulation $\cos\{L\theta - N\zeta + \gamma(\theta)\}$ in calculating the bounce-averaged radial drifts. The higher harmonics of $n=N$ with $l=2,3,4,\ldots$ can contribute to this amplitude $\varepsilon_{\mathrm{H}}(\theta)$ and are sometimes non-negligible [9]. The $1/\nu$ component of the ripple-trapped particle distribution function can be obtained only by replacing $\partial\varepsilon_{\mathrm{T}}/\partial\theta$ by $\partial\left\{\varepsilon_{\mathrm{T}}^{(\mathrm{as})}(\theta) + \varepsilon_{\mathrm{T}}^{(\mathrm{na})}(\theta)\right\}/\partial\theta$ in the previous ripple diffusion theories [11,12] and their applications [5,7,9,10]. In the next section, we describe only a method to obtain the $1/\nu$ component in the toroidally trapped particle distribution.

3. Bounce-averaged Solution for the Toroidally Trapped Particles

Another reason for aforementioned choice of the Boozer coordinates is a fact that we cannot fully include all of $\nabla s \times \mathbf{B}\cdot\nabla B$, $\mathbf{B}\cdot\nabla B$ in $\nabla v_{\|}$ and neglect some parts of $\mathbf{B}\cdot\nabla B$ in the bounce-averaging as discussed in the previous section. Although the radial drift term σ_1^+ given in the Boozer coordinates in a form of $\nabla s \times \mathbf{B}\cdot\nabla(v_{\|}/B)$ as shown in Eq.(2) is suitable this analytical approximation, use of σ_{Xa} in Eq.(3) requires more exact calculation of $\mathbf{B}\cdot\nabla v_{\|}$ even in the bounce averaged equation. One more reason is that contributions of the boundary regime in the (m,n) space $|m-lL| \simeq Nq-L$ should be small in determining the envelop function $\varepsilon_{\mathrm{H}}(\theta)$ in Eq.(9). Therefore, to derive the $1/\nu$ diffusion coefficient, we execute a procedure in Ref.[3] in the Boozer coordinates, in which the Jacobian is given by $\sqrt{g_{\mathrm{B}}} = (V'/4\pi^2)\langle B^2\rangle/B^2$ [4], although this previous theory is originally written using the Hamada coordinates ($\sqrt{g_{\mathrm{H}}} = V'/4\pi^2$). In this derivation, we allow also existence of helical and bumpy ripple $\varepsilon_{\mathrm{H}}(\theta)\cos\{L\theta - N\zeta + \gamma(\theta)\}$ and therefore the ripple-averaged parallel velocity is given by Eq.(8), while the velocity in the axisymmetric limit is used in Ref.[3]. By rewriting Eq.(6) as

$$B/B_{00} = 1 + \varepsilon_{\mathrm{T}}^{(\mathrm{as})}(\theta) + \sum_{n=1}^{\infty}\left\{A_n(\theta)\cos(n\zeta_0) + B_n(\theta)\sin(n\zeta_0)\right\} \quad , \quad (10)$$

and with a boundary condition at $v_{\|}=0$ making $\partial G_{Xa}/\partial\mu$ to be finite,

$$\frac{\partial G_{Xa}}{\partial \mu} = -\frac{c}{e_a \chi' \nu_{\mathrm{D}}^a} \frac{\oint \frac{|v_{//0}|}{\left(B_{\mathrm{axisymmetric}}\right)^2} \frac{\partial B}{\partial \zeta_0} \mathrm{d}\theta}{\oint \frac{|v_{//0}|}{\left(B_{\mathrm{axisymmetric}}\right)^2} \mathrm{d}\theta} \qquad (11)$$

is obtained. The integral period length for $\oint \mathrm{d}\theta$ is determined by the envelope function $1+\varepsilon_{\mathrm{T}}^{(\mathrm{as})}(\theta)+\varepsilon_{\mathrm{H}}(\theta)$, and $|v_{//0}|$, $B_{\mathrm{axsymmetric}}$ in this integral are defined by

$$|v_{//0}| \equiv \frac{4/\pi}{N - L/q}\left(\frac{\mu B_{00}\delta_{\mathrm{eff}}}{m_a}\right)^{1/2} \kappa E(1/\kappa). \qquad (12)$$

$$B_{\mathrm{axisymmetric}} \equiv B_0\left\{1+\varepsilon_{\mathrm{T}}^{(\mathrm{as})}(\theta)\right\}$$

Note that $E(\kappa)$ in $0\le\kappa\le1$ is a monotonically decreasing function in a range of $1\le E(\kappa)\le\pi/2$, and thus the ripple-averaged parallel velocity coincides with the axisymmetric value $|v_{//0}| = v(1-\mu B_{\mathrm{axisymmetric}}/v)^{1/2}$ in the small ripple limit of $\delta_{\mathrm{eff}}\to0$. Results shown in Refs.[2-3] are those for this $\delta_{\mathrm{eff}}\to0$ limit with only one axisymmetric B-field modulation B_{10} (B_{m0}=0 for $m\ge2$). As a result of $v_{\|} \simeq \mathrm{const}$ in a ripple period and resulting

$$\oint_{\substack{\mathrm{ripple}\\ \mathrm{period}}} v_{\|}(\partial B/\partial\zeta_0)\mathrm{d}l \cong \frac{N-L/q}{2\pi B_\zeta/B_{00}}\left\{\oint_{\substack{\mathrm{ripple}\\ \mathrm{period}}} (\partial B/\partial\zeta_0)\mathrm{d}l\right\}\left\{\oint_{\substack{\mathrm{ripple}\\ \mathrm{period}}} v_{\|}\mathrm{d}l\right\},$$

Eq.(11) has a identical form to the $\partial\varepsilon_{\mathrm{T}}/\partial\theta$ term in the stellarator ripple diffusion theories [11-12]. If at least one of $v_{\|}$ and $\partial B/\partial\zeta_0$ is almost constant in the period, this result is obtained. This approximation cannot be used for the ripple-trapped particles, and therefore $\partial J_{\mathrm{r}}/\partial\theta$ including $\partial\varepsilon_{\mathrm{H}}/\partial\theta$ is calculated by using Eq.(5) for the deeply trapped pitch-angle range of $\kappa^2<1$ [11-12]. The approximation of $v_{\|} \simeq \mathrm{const}$ for the barely trapped pitch-angle range $\mu\sim v/B_{\mathrm{M}}$ [B_{M}: maximum value of B in the flux surface] is justified by a fact that the $1/\nu$ diffusions without the low-n and nearly resonant B-field modes of $n<N$ and $|m-nq|\le1$ are almost determined only by those of ripple-trapped particles in various helical/stellarator configurations [4,5,9,10]. This fact means that the toroidally trapped particles do not have effective bounce-averaged radial drift in spite of the break of the axisymmetry due to the ripples, and only $\partial B/\partial\zeta_0$ due to additional perturbation fields with $|m-nq|\le1$ can cause their bounce-averaged drift. In cases with the stellarator symmetry $B(-\theta,-\zeta)=B(\theta,\zeta)$, the contribution of $B_n(\theta)$, which is an odd function of θ, vanish in Eq.(11), and thus $\partial B/\partial\zeta_0$ is given there by $(1/B_{00})\partial B/\partial\zeta_0 = -\sum nA_n(\theta)\sin(n\zeta_0)$. By further pitch-angle integral with the boundary condition G_{Xa}=0 at the circulating/trapped boundary $\mu=v/B_{\mathrm{M}}$, the $1/\nu$ diffusion coefficients (the diagonal mono-energetic viscosity coefficient L^* defined in Ref.[4]) can be obtained in a form of

$$L^*_{(\mathrm{MHD})} \propto \frac{1}{\nu_{\mathrm{D}}^a}\int_{\mathrm{trapped}} \mathrm{d}\mu \frac{\sum_{n=1}^{\infty} n^2\left\{\oint \frac{|v_{//0}|}{\left(B_{\mathrm{axisymmetric}}\right)^2} A_n(\theta)\,\mathrm{d}\theta\right\}^2}{\oint \frac{|v_{//0}|}{\left(B_{\mathrm{axisymmetric}}\right)^2}\mathrm{d}\theta}.$$

Though this integral can only be obtained numerically, this estimation is still easier than applications of existing numerical methods for helical/stellarator devices [4].

4. Conclusion

In this paper, we investigated effects of the nearly resonant magnetic field spectra on two types of trapped particles' drifts (toroidally trapped and ripple trapped) by extending and combining the analytical methods for tokamak neoclassical viscosity [2-3] and the ripple diffusions in helical/stellarator devices [5-12]. The analytical bounce-averaging methods for these particles' bounce-center drifts in the $1/\nu$ collisionality regime are proposed.

Acknowledgement

This work is supported by a coordinated research program of the National Institute for Fusion Science NIFS07KNXN103.

[1] E.Lazzaro, R.J.Buttery, et al., Phys.Plasmas **9**, 3906 (2002)
[2] W.Zhu, et al., Phys.Rev.Lett. **96**, 225002 (2006)
[3] K.C.Shaing, Phys.Plasmas **10**, 1443 (2003); ibid. **14**, 049903 (2007)
[4] H.Sugama and S.Nishimura, Phys.Plasmas **9**, 4637 (2002); ibid. **15**,042502(2008)
[5] S.Nishimura, H.Sugama, and Y.Nakamura, Fusion Sci.Technol. **51**,61 (2007)
[6] S.Nishimura, D.R.Mikkelsen, et al., in 21st US TTF WS (Boulder, Colorado, USA, March 25-28, 2008) P51
[7] H.Sugama and T.-H.Watanabe, Phys.Rev.Lett.**94**,115001 (2005)
[8] H.E.Mynick and A.H.Boozer, Phys.Plasmas **14**, 072507(2007)
[9] S.Nishimura, D.R.Mikkelsen, D.A.Spong, et al., Plasma Fusion Res. **3**, S1059 (2008)
[10] S.Nishimura and Heliotron-J group, to be published in JPFR SERIES
[11] K.C.Shaing and S.A.Hokin, Phys.Fluids **26**, 2136 (1983)
[12] J.Todoroki, J.Phys.Soc.Jpn **8**, 2758 (1990)

Proceedings of ITC18, 2008

Development of neoclassical transport database for LHD: DGN/LHD

A. Wakasa, S. Murakami [a)], C.D. Beidler[b)], H. Maassberg [b)], M. Yokoyama[c)], and S. Oikawa

Graduate School of Engineering, Hokkaido University, Sapporo 060-8628, Japan
[a)] *Department of Nuclear Engineering, Kyoto University, Kyoto 606-8501, Japan*
[b)] *Max-Planck-Institute für Plasmaphysik, EURATOM Ass., Greifswald, Germany*
[c)] *National Institute for Fusion Science,322-6 Oroshi-cho, Toki 509-5292, Japan*

Abstract

In helical systems, the neoclassical transport is one of the important issues in addition to the anomalous transport, because of a strong temperature dependency of heat conductivity and an important role in the radial electric field determination. Thus the development of a reliable tool for the neoclassical transport analysis is necessary for the transport analysis in LHD. We have developed a neoclassical transport database for LHD plasmas, DCOM/NNW. The mono-energetic diffusion coefficients are evaluated based on the Monte Carlo method by DCOM code and the mono-energetic diffusion coefficient database is constructed using a neural network technique. The input parameters for the database are the collision frequency, the radial electric field, the minor radius and the configuration parameters (R_{axis}, beta, etc). Recent increment of heating power raises the plasma temperature in LHD. Because the collision frequency decreases in proportion to $T^{3/2}$, we have to estimate the diffusion coefficient in the more collisionless regime. However, DCOM code requires huge calculation time to obtain the diffusion coefficient in such collisionless regime.

In this paper, we improve the DCOM code to reduce the computation time in order to obtain the mono-energetic diffusion coefficients in the more collisionless regime. As a result the DCOM calculation becomes about 6 times faster than previous version. Also we apply GSRAKE code which solves the ripple-averaged drift kinetic equation to obtain further collisionless regime. Finally we construct a neoclassical transport database DCOM-GSRAKE/NNW for LHD (DGN/LHD). The neoclassical transport analyses of high temperature LHD plasma are done using DGN/LHD.

Keywords: LHD, neoclassical transport, neural network, Monte Carlo method

1. Introduction

In helical systems, neoclassical transport is one of the important issues for sustaining high-temperature plasma. In particular, in the long-mean-free-path (LMFP) regime, the neoclassical transport coefficient increases as collision frequency decreases ($1/\nu$ regime), and neoclassical transport plays an important role as well as anomalous transport by plasma turbulence. Moreover, the neoclassical transport plays an important role in the radial electric field determination in helical systems.

The neoclassical transport coefficient has been evaluated using the Monte Carlo method directly following particle orbits, where the mono-energetic diffusion coefficients are estimated by the radial diffusion of test particles [1-3]. This method has a good property in the LMFP regime except for its long calculation time. Thus, we have developed a Monte Carlo simulation code, the Diffusion Coefficient Calculator by Monte Carlo Method (DCOM) code [4], which is optimized in performance in the vector computer. The DCOM code can calculate the mono-energetic diffusion coefficient without convergence problem even if in LMFP regime, especially with finite beta, a large number of Fourier modes of the magnetic field in the Boozer coordinates must be used.

To evaluate the neoclassical diffusion coefficient of thermal plasma, we must take energy convolution into account. Therefore, it is necessary to interpolate discrete data by the DCOM. In a non-axisymmetric system, the diffusion coefficient shows complex behavior and strongly depends on collision frequency and radial electric field (e.g., $1/\nu$, $\sqrt{\nu}$ and ν regimes). The interpolation based on a traditional analytical theory has a problem with connected regions between two regimes.

We apply the neural network (NNW) [5] method to the fitting of the diffusion coefficient of LHD, which shows a complex behavior in several collisional regimes, i.e., ν, $\sqrt{\nu}$, $1/\nu$, plateau and

author's e-mail: wakasa@fusion.qe.eng.hokudai.ac.jp

P-S regimes. We used a multilayer perceptron NNW with only one hidden layer, generally known as MLP1. The neoclassical transport database, DCOM/NNW [6], has been constructed with input parameters r/a, ν^* and G, and D^* can be obtained as an output of the NNW, where ν^* is the normalized collision frequency, G is the normalized radial electric field and D^* is the normalized diffusion coefficient respectively.

However, as shown in the above-mentioned, the DCOM code has a problem of the computing time. When we calculate the diffusion coefficient of the finite beta plasma which has a complex magnetic field, because we have to consider a large number of Fourier modes of the magnetic field, the computational cost of the calculating the sum of all Fourier modes of the magnetic field become expensive. And when we calculate the diffusion coefficient in the extremely low collision frequency regime, because we have to trace the particle long time, the DCOM code requires a large computing time. In these cause, DCOM/NNW does not have sufficient data in the finite beta plasma or in the extremely low collision frequency regime.

For overcoming these problems, first, we have improved the DCOM code to reduce the CPU time. We also apply the results of the GSRAKE [7] code to the neoclassical transport database using NNW in the extremely low collision regime. Thus, we reconstruct a new neoclassical transport database, DCOM+GSRAKE/NNW for LHD, DGN/LHD.

2. Reconstruction of the neoclassical transport database for LHD

2.1 Improvement of DCOM code

DCOM code evaluates a monoenergetic local diffusion coefficient, D, using the Monte Carlo method. In the simulation, monoenergetic N particles are released from initial minor radius position r_0, where the particle randomly distribution in the poloidal and toroidal coordinates, and in the pitch angle space. The test particle orbits are monitored by solving the equations of motion in Boozer coordinates. The DCOM code has to calculate the summation of all Fourier modes of the magnetic field in the Boozer coordinate described as, $B=\sum_{m,n} B_{m,n}(\psi)\cos(m\theta-n\zeta)$, whenever time step advances. When we evaluate the diffusion coefficient in the finite beta plasma which has a complicated magnetic configuration, we have to consider a large number of Fourier modes of the magnetic field and a large CPU time is required.

Therefore, we assume that the particles are subjected to forces from the magnetic field at initial position instead of from the magnetic field at the position where the particles moved. This enables us to use 2D-spline interpolation for expression of the magnetic field. By using 2D-spline table of only one magnetic surface for calculating the magnetic field, we can calculate the magnetic field quickly without calculating the summation of Fourier modes as before. Here, we call the DCOM(F) which calculates the magnetic field by adding up the Fourier modes and the DCOM(S) which calculates the magnetic field using 2D-spline table.

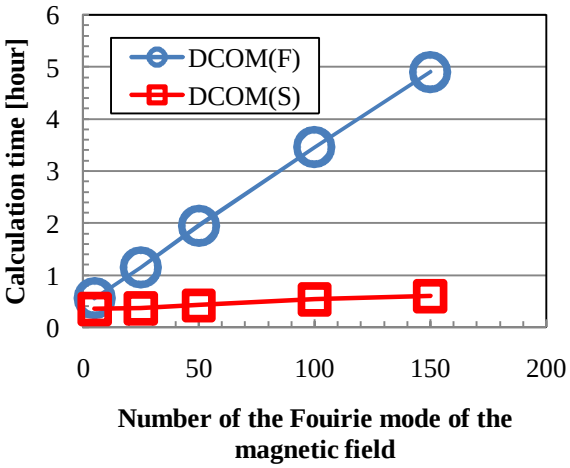

Fig. 1 Calculation time as a function of the number of the Fourier mode of magnetic filed.

In Fig. 1, the calculation time as a function of the number of the Fourier mode of magnetic field are shown. When calculating the diffusion coefficients by the DCOM(F), the necessary CPU time increases as the number of the Fourier mode of the magnetic field increases. In contrast, when calculating by DCOM(S), the CPU time is almost constant even if the magnetic field is complicated. Figure 1 shows that the CPU time reduces to about 1/6 when the number of Fourier mode is 50 and to about 1/10 when the number of Fourier mode is 150. Even when calculating the diffusion coefficient in the finite plasma needing a large number of the Fourier modes, the DCOM(S) can expeditiously calculate.

2.2. Combine the results of the DCOM code with the results of GSRAKE code

In the LMFP regime, a necessary computing time of the DCOM code increases in inverse proportion to the collision frequency. Especially, in extremely low collision regime, the CPU time of over 500 hours is required for calculating the diffusion coefficient on the super computer, the SX-8. Consequently, the data concerning in the extremely low collision frequency regime are insufficient in the DCOM/NNW.

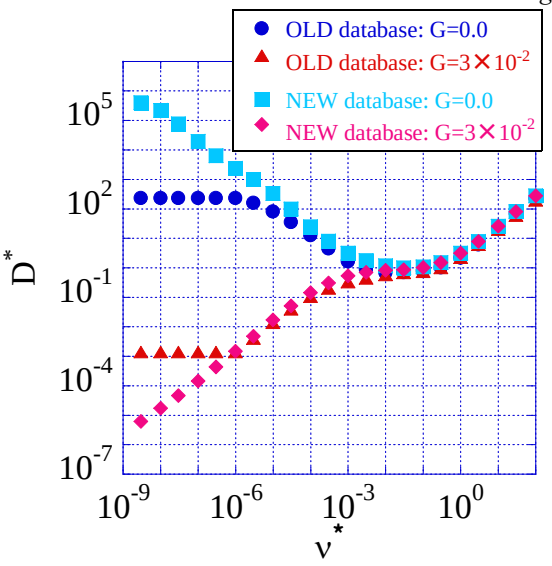

Fig. 2 The normalized diffusion coefficient, D^* as a function of the normalized collision frequency, ν^*, which are outputs of old database, DCOM/NNW and the outputs of new database, DGN/LHD.

Therefore, in extremely low collision frequency regime, we combine the results of the GSRAKE code with the results of the DCOM to construct the neoclassical transport database. GSRAKE is a code which solves general solution of the ripple-averaged kinetic equation. Though GSRAKE can treat few Fourier modes of the magnetic field, a necessary CPU time is small even for calculation in which collision frequency is very small. We supplemented the neoclassical transport database with the GSRAKE results for extremely low collision regime and have improved the neoclassical transport data base.

Because the DCOM and GSRAKE results are discrete monoenergetic diffusion coefficients, it is necessary to interpolate them. We apply the NNW method to the fitting of the diffusion coefficient of LHD. We consider a multilayer perceptron (MLP) NNW model which is the most widely used. We use the MLP1 model which has only one hidden layer. The accuracy of the NNW depends on the number of hidden units. We have to appropriately select the number of hidden units so that the NNW has a good generalization performance. In this research, we evaluate the generalization performance by using information criterion, the Minimum Description Length criterion (MDL criterion) [8] and we assume the number of hidden unit is set to 12.

Figure 2 shows the outputs of the old database, DCOM/NNW, and the outputs of the new database, DCOM+GSRAKE/NNW for LHD (DGN/LHD). At the plasma which has a standard profile of temperature and of density, whose collision frequency, ν^*, are over 10^{-6} in the energy integral, the outputs of old database, DCOM/NNW, are accurate enough. However, in extremely low collision frequency regime, because the computational results of the DCOM don't exist, the outputs of the old database, DCOM/NNW are inaccurate. Because the newly neoclassical transport database, the DGN/LHD, contains the result of the GSRAKE, the outputs of the DGN/LHD are appropriate even in the extremely low collision frequency regime. By using the new neoclassical transport database, DGN/LHD, accurate evaluations of the neoclassical transport in high-temperature plasma and finite beta plasma become possible.

3. Neoclassical transport analysis using the DGN/LHD

We compare the neoclassical transport analysis by the DGN/LHD and by the DCOM/NNW. In this analysis, we consider the hydrogen plasma and R_{axis} = 3.6 m configuration in LHD and β_0=0%. We assume the low-collisional plasma which temperature and density profiles of electron and ion are,

$$T_e = T_i = 4\times(1-(r/a)^2)+1 \text{ [keV]},$$

$$n_e = n_i = 3.5\times(1-(r/a)^2)+1.5[10^{18}/m^3].$$

In these profiles, the energy integral up to $\nu^*=1\times 10^{-7}$ is necessary.

In Fig. 3(a) and 3(b), the electron and ion particle fluxes, Γ_e and Γ_i, at r/a=0.5 are shown as function of radial electric field, E_r. When E_r is from about -20kV/m to 15kV/m, Γ_e calculated using DGN/LHD increases more than using DCOM/NNW and when E_r is from about -3kV/m to 3kV/m, Γ_i using DGN/LHD increases more than using DCOM/NNW. The reason of increases by using DGN/LHD is that DGN/LHD is considering the diffusion coefficient in extremely low collision regime.

Figure 4 shows the ambipolar radial electric field as a function of r/a. There are electron and ion root both using DGN/LHD and using DCOM/NNW. E_r don't make much difference whether by DGN/LHD or by DCOM/NNW. However, as shown in Fig. 5, the thermal conductivities of electron, χ_e, by DGN/LHD and by DCOM/NNW are different. In electron root, χ_e, by DGN/LHD increases to about 1.5 times that of by DCOM/NNW and in ion root, χ_e, by DGN/LHD increases to about 2 times that of by DCOM/NNW.

4. Summary

We have improved the DCOM code to reduce the CPU time. Even in the case with a large number of Fourier modes of the magnetic field, DCOM(S) can calculate the diffusion coefficient at high speed. The GSRAKE results in the extremely low collision regime have been included in the neural network database. The outputs of the new neoclassical transport database, DGN/LHD, which

contains the GSRAKE results, are appropriate even in the extremely low collision frequency regime. By using the new neoclassical transport database, DGN/LHD, accurate evaluations of the neoclassical transport in high-temperature plasma and finite beta plasma become possible.

References

[1] A. H. Boozer and G. Kuo-Petravic: Phys. Fluids **24** (1981) 851.
[2] W. Lotz and J. Nu¨hrenberg: Phys. Fluids **31** (1988) 2984.
[3] C. D. Beidler and W. N. G. Hitchon: Plasma Phys. Control. Fusion **36** (1994) 317.
[4] A. Wakasa, S. Murakami et al.: J. Plasma Fusion Res. SERIES 4 (2001) 408
[5] C. M. Bishop: Rev. Sci. Instrum. **65** (1994) 1803.
[6] A. Wakasa, S. Murakami *et al.*: Jpn. J. Appl. Phys. **46** (2007) 1157.
[7] C. D. Beidler and W. D. D'haeseleer, Plasma Phys. Control. Fisoin **37** (1995) 463
[8] J. Rissanen, Stochastic Complexity in Statistical Inquiry, World Scientific, 1989.

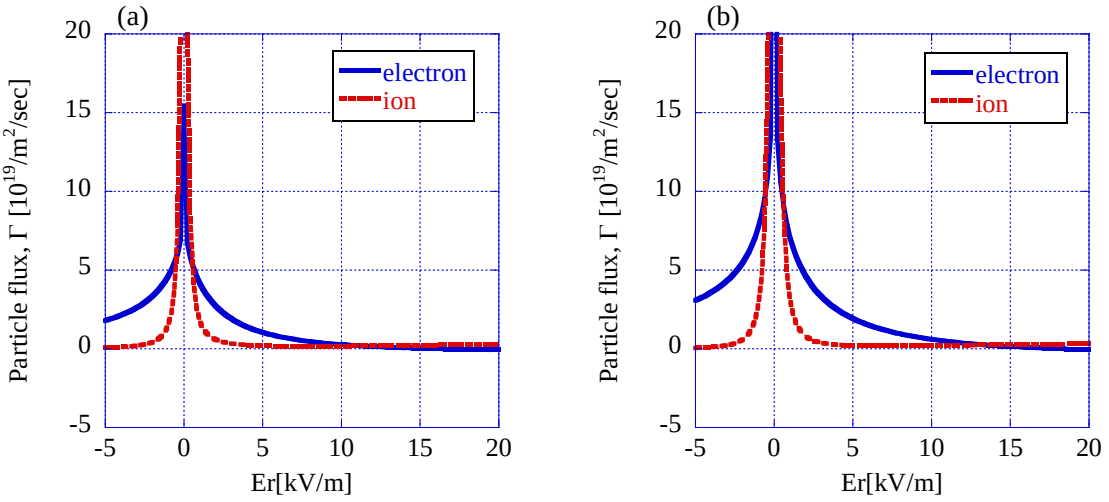

Fig. 3. Particle fluxes, Γ, as a function of radial electric field, E_r at r/a = 0.5 by (a) DCOM/NNW and (b) DGN/LHD.

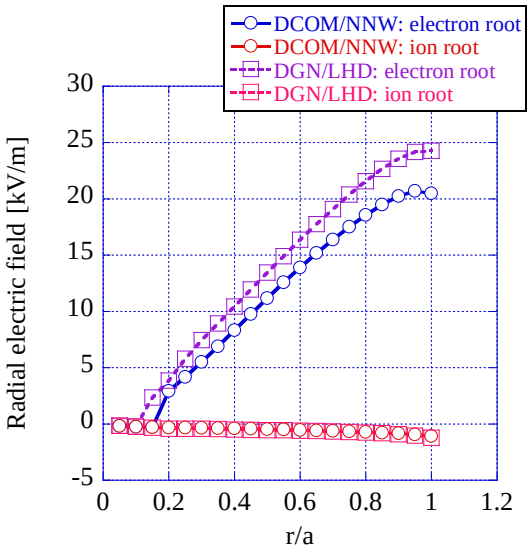

Fig. 4. Radial electric field, E_r, as a function of r/a by DCOM/NNW and by DGN/LHD.

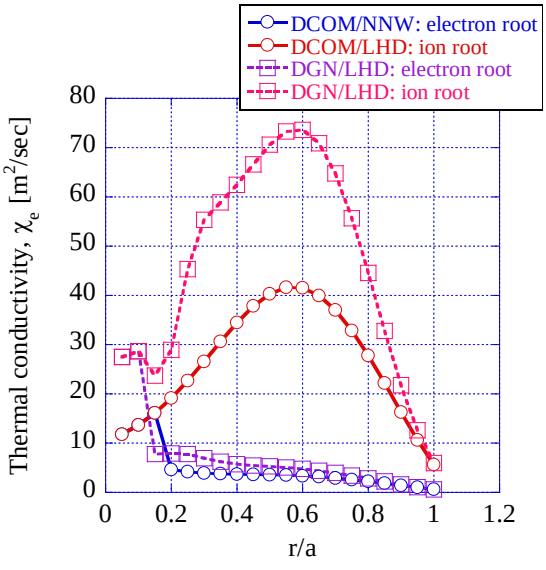

Fig. 5. Thermal conductivity of electron, χ_e, as a function of r/a by DCOM/NNW and by DGN/LHD.

Proceedings of ITC18, 2008

Peripheral Plasma Turbulence Measurement of Heliotron J plasmas

N. Nishino, T. Mizuuchi[1)], S. Kobayashi[1)], K. Nagasaki[1)], H. Okada[1)], F. Sano[1)], S. Yamamoto[1)], and K. Kondo[2)]

Graduate School of Engineering, Hiroshima University

1) Institute of Advanced Energy, Kyoto University

2) Graduate School of Energy Science, Kyoto University

Using a fast camera with tangential view motion of the filamentary structures in peripheral regions was observed. It was already confirmed that motion of this turbulence was dithering during "Phase I" in former SMBI (supersonic molecular beam injection) experiment. During "Phase I" Heliotron J plasma did not always reach the H-mode nor radiation collapse even though the electron density was larger than the threshold. Moreover, the electron density may be controllable in "Phase I" plasma. It was favorable for fusion reactor plasma. This time SMBI experiment with careful adjustment of gas puff quantity was demonstrated for realizing "Phase I" and it was successful to obtain higher confinement energy shot. In this paper the fast camera measurement of this experiment is described.

Keywords: turbulence, peripheral plasma, L-H transition, H-mode, Heliotron J, fast camera

1. Introduction

Fast cameras have been installed in Heliotron J [1,2] since several years [3-5]. Recent progress of fast cameras enables us to get information on the peripheral plasma turbulence. In particular, using a conventional gas puff, supersonic molecular beam injection (SMBI) [5], and solid target such as limiter [3] are very useful to visualize complex peripheral plasma behavior. Also, a combination of conventional peripheral plasma measurement (Langmuir probe, magnetic probe, etc) and fast cameras gives us the powerful method to study plasma turbulence [4].

In the first SMBI experiment of this year it was found that after SMBI a kind of improved confinement mode "Phase I" [6-8] appeared instead of the H-mode. Camera images show filamentary structure of peripheral plasma rotated with L-mode direction (if this was ErxB drift, Er is positive.), and sometimes the rotation changed to the H-mode direction (if this was ErxB drift, Er is negative). That was called "dithering", and this was one of the feature of "Phase I" in Heliotron J. In this experiment, low frequency MHD activity occurred after SMBI with large gas quantity (too high pressure), and the energy confinement degraded.

author's e-mail: nishino@hiroshima-u.ac.jp

However, some shots maintained, "Phase I" and they did not reach H-mode. The latter case the electron density rose more than the transition threshold.

In Heliotron devices the rise of the electron density after H-mode is uncontrollable, and usually plasma reach radiation collapse with short time after the transition.

This phase I sometimes did not reach H-mode, therefore the energy confinement is not better than H-mode. However, it did not reach radiation collapse and it is prominent improved mode to be able to control the density.

In this experiment the gas quantity of SMBI was adjusted carefully and higher confinement energy shot was realized after SMBI. In this paper the fast camera measurement of this SMBI shot was reported.

2. Experimental Setup

Heliotron J device is a medium sized helical-axis heliotron device (averaged R/a=1.2m/0.17m, B=1.5T) with l=1, m=4 helical coil configuration. Figure 1 shows top view of Heliotron J and main diagnostics used in this paper and the camera location.

In general the initial plasma is produced by ECH (70GHz, 0.45MW, non-focusing Gaussian beam)

launched from a top port. Two NB system (BL-1,2; 30keV, 0.7WM) are installed with tangential port, and they faced each other. Selecting one of the two beam-lines or changing the direction of the confinement field, Co- or CTR-injection can be performed.

One SMBI and four conventional gas puff systems with piezoelectric valves are installed at the outer side and inner side ports, respectively.

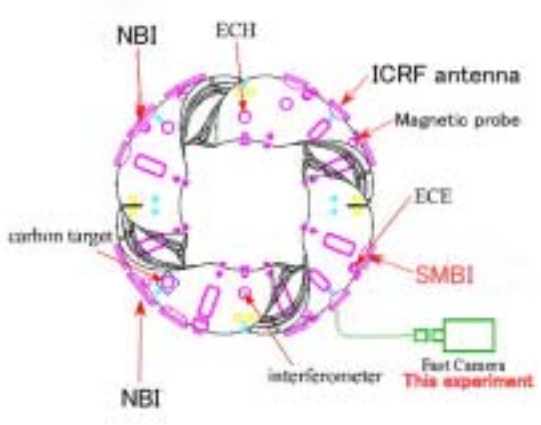

Fig.1 Top view of Heliotron J
The fast camera can view the ICRF antenna and SMBI.

3. Results and discussion

The waveforms with or without SMBI are shown in Fig.2 and 3, respectively. After SMBI the diamagnetic signal rose gradually, and ~13 ms later the diamagnetic signal began to decrease.

From ECE and AXUV signals (not shown in the figure) it was inferred that the electron temperature decreased due to SMBI [9,10] and the electron density increased. It seemed that these effects cancelled out each other, and the diamagnetic signal did not increased just after SMBI. Afterwards the diamagnetic signal increased gradually due to NBI. However, more precise profile information is needed to conclude this scenario.

The important thing is that after SMBI the electron density became larger than the threshold of the L-H transition, however, plasma did not reach H-mode. Therefore, plasma terminated without the radiation collapse. This feature is called 'Phase I' in Ref [5].

The fast camera images with 40000 FPS show that filamentary structure was seen near the ICRF antenna, and it was brighter when filament hit the antenna. Fig.4 shows the fast camera image during SMBI. Near ICRF antenna the motion of filamentary structure rotate with unti-clockwise firstly. However, after ~190ms sometimes rotation direction changed to clockwise. Therefore, it was recognized that plasma was 'dithering phase' after ~190ms. To visualize this motion clearly two-dimensional phase images of 8.75kHz frequency component were shown in Fig. 5.

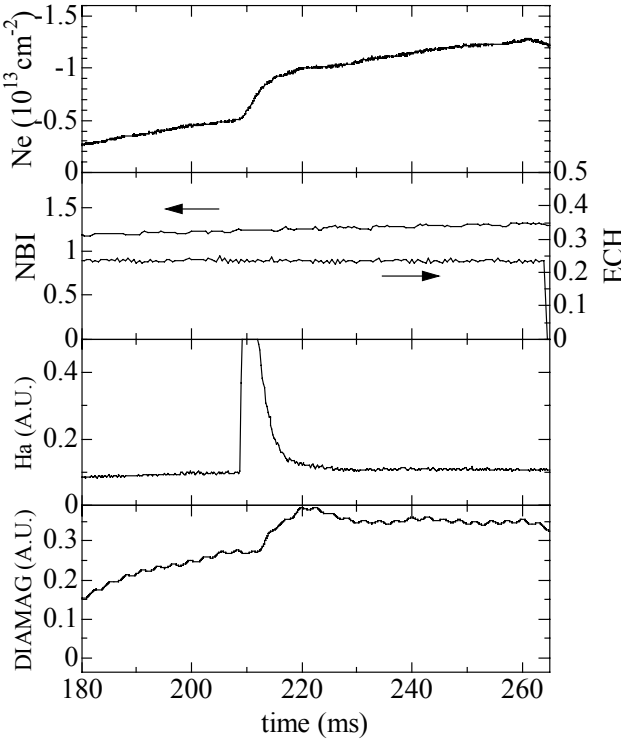

Fig.2 Typical waveform of Heliotron J plasma with SMBI (#32816)

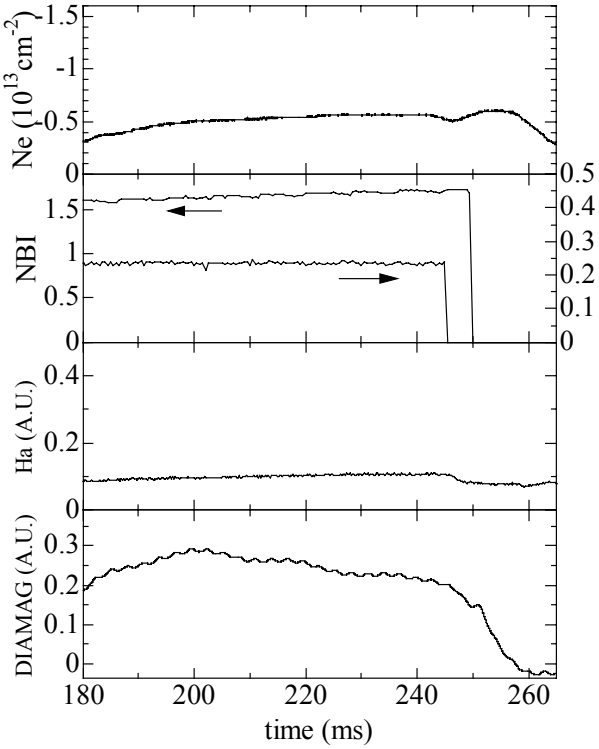

Fig.3 Typical waveform of Heliotron J plasma without SMBI (#32783)

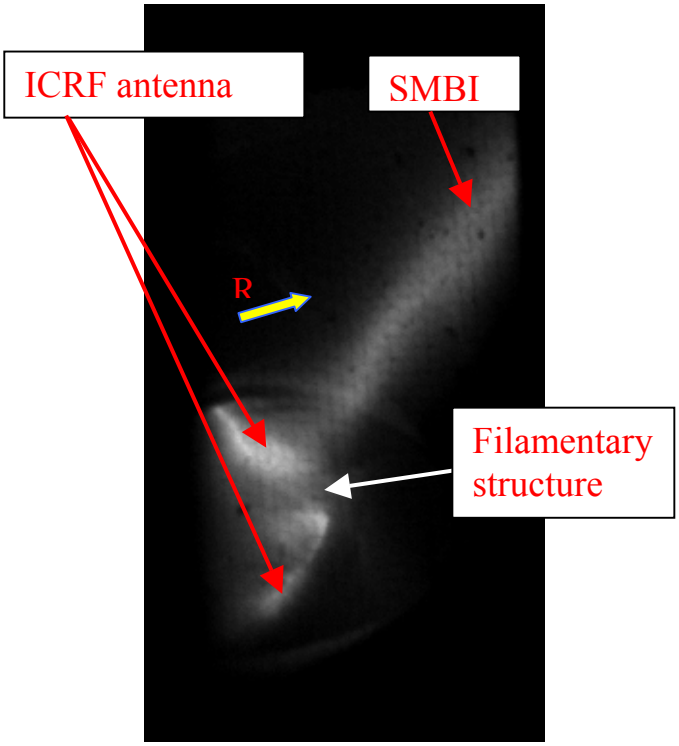

Fig.4 Fast camera image during SMBI

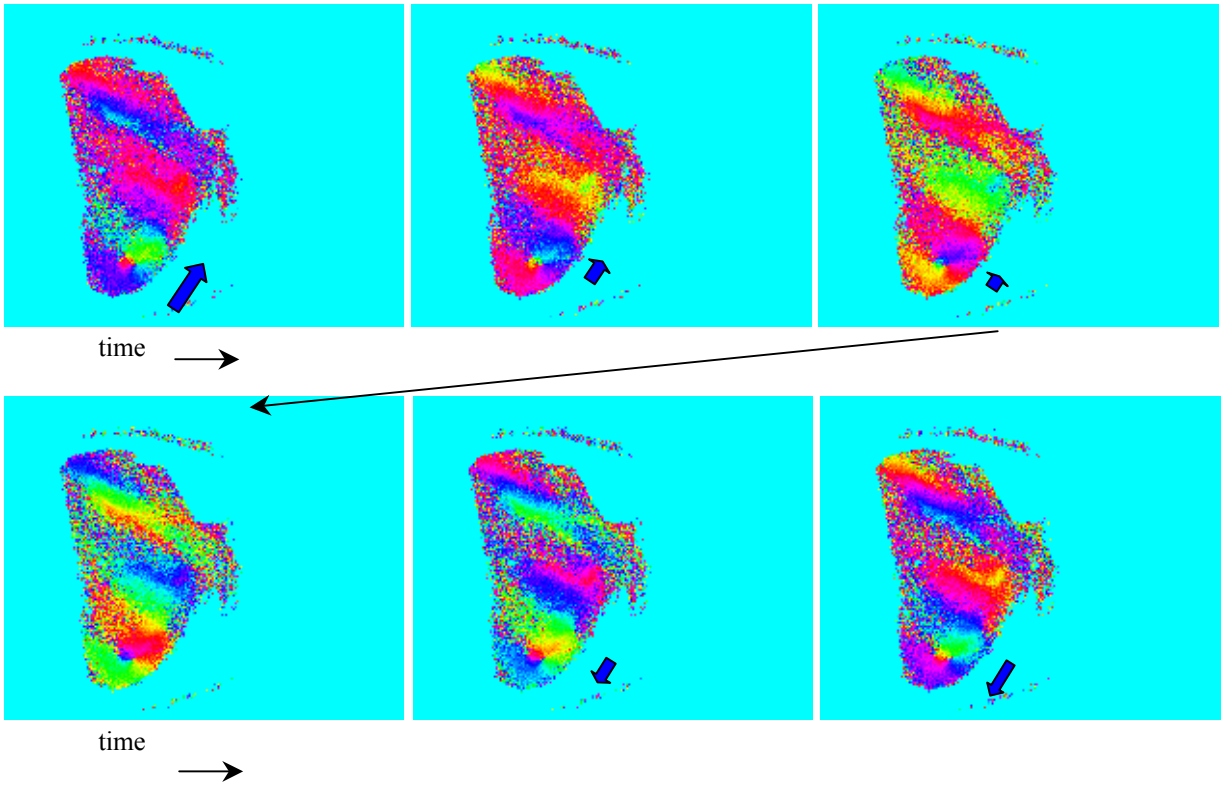

Fig.5 Two-dimensional phase images during “dithering phase”
A part of images near the ICRF antenna are shown.

The way to create these images is that first the frequency peak in the power spectra from FFT during suitable period for one pixel data in ROI (region of interest) is selected, and second the phases of the same frequency for all pixels are colored by color chart. Therefore, this phase images show the wavelength of the turbulence at the selected frequency and its motion. If there was no frequency peak in the spectra obtained by pixel data in ROI, typical frequency of the turbulence in Heliotron J plasma could be selected.

This time typical frequency of 8.75kHz in the frequency range of the peripheral turbulence (5-10kHz) in Heliotron J plasma was selected.

Just after SMBI the whole plasma began brighter and the whole picture was the same color in two-dimensional phase image, but afterwards the turbulent motion was recognized. The apparent filamentary structure motion was recognized “dithering phase”, and that meant plasma was “Phase I”.

Without SMBI shot the “dithering phase” was confirmed after ~190ms, and it was believed that plasma was “Phase I”

This SMBI experiment reproduced the former SMBI experiment very well, and it was not found the difference of the filamentary structure motion between the camera images before and after SMBI.

Figure 6 shows the magnetic probe signal for MHD activity. The time slices of the spectrum of this signal are shown in Fig. 7.

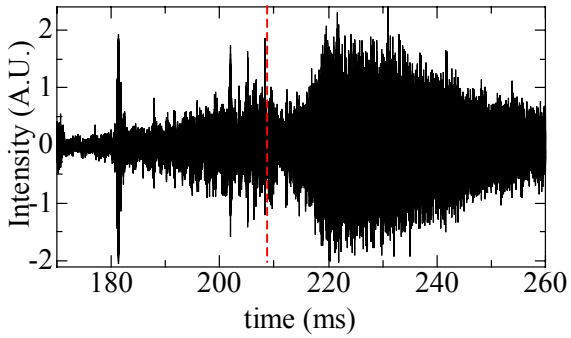

Fig.6 Magnetic probe signal (raw data)
Red line shows SMBI time. MHD activity was decreased due to SMBI.

The MHD activity in low frequency range of 10-20kHz grew from ~190ms and after 210ms (time of SMBI) this activity was decreased temporary. Afterwards (~220ms) this activity was growing again. It seemed that the effect of SMBI reduced this activity. There were another frequency peaks in high frequency range and those were thought as GAE mode (global Alfven eigen-mode). However, those GAE mode existed with no relation to SMBI, therefore GAE mode in this experiment did not affect the characteristics of the energy confinement.

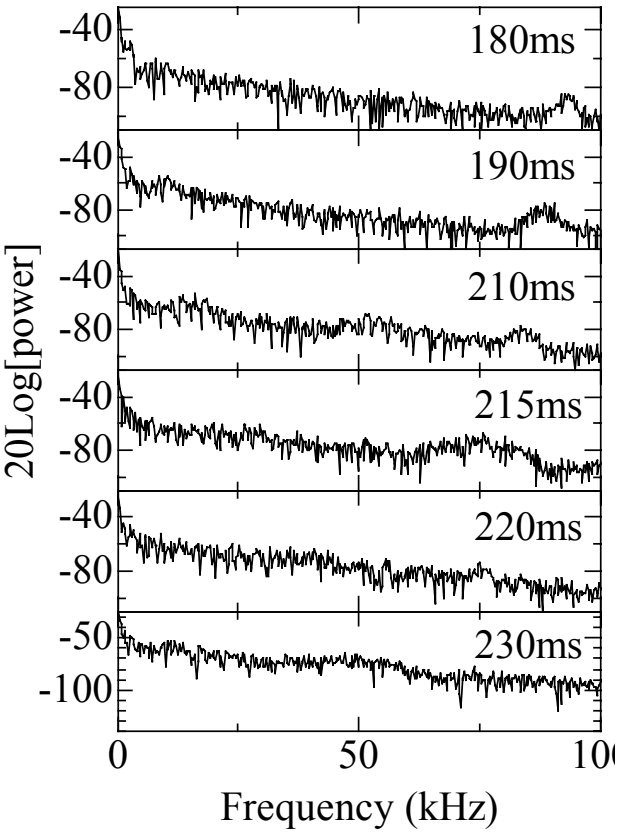

Fig.7 Spectra of magnetic probe signal
SMBI starts at 209ms and reduction of low frequency activity at 215ms was recognized.

Only difference between with or without SMBI was the former low frequency MHD activity. Thus, it possibly relate to the energy confinement of Heliotron J plasmas.

Unfortunately in this experiment plasma was not so bright before and after SMBI, and the camera images could be taken up to 40000 FPS. Therefore, the turbulence of these frequency ranges could not be obtained. Plasma is very bright during SMBI using the view port of this experiment, thus the view port at other toroidal section is needed for turbulence measurement included in SMBI period. Because Hα signals strongly depend on the toroidal section during SMBI.

This is the experimental problem to be solved.

4. Conclusion

Using SMBI high confinement energy shots, which could not be reached by conventional gas puff, were obtained. Also it was confirmed that these shots were a kind of improved mode “Phase I” by the fast camera images.

Further investigation is necessary to understand the

physical mechanism why “Phase I” plasma did not reach H-mode even though the electron density is over the threshold of the L-H transition. For this purpose the experiments are in progress in Heliotron J.

Acknowledgements

This work is performed with the support and under the auspices of the Bi-directional Collaborative Research Program (NIFS04KUHL006)

References

[1] F. Sano, et al., J. Plasma Fusion Res. SERIES 3, 26 (2000).
[2] T. Obiki, T. Mizuuchi, K. Nagasaki, et al., Nucl. Fusion **41** 883 (2001).
[3] N. Nishino, K. Takahashi, H. Kawazome, et al., J. Nucl. Mater. **337** 1073 (2005).
[4] N. Nishino, T. Mizuuchi, K.Kondo, et al., J. Nucl. Matter. **363-365** 628 (2007)
[5] N. Nishino, T. Mizuuchi, et al., to be published in JFPR.
[6] T. Mizuuchi, W. L. Ang, Y. Nishioka, et al., J. Nucl.
[7] T. Mizuuchi, et al., J. Nucl. Matter. **337-339** 332 (2005)
[8] F. Sano, T. Mizuuchi, K.Kondo, et al., Nucl. Fusion **45** 1557 (2005).
[9] T.Mizuuchi, et al., this conference
[10] S.Watanabe, et al., this conference

Proceedings of ITC18, 2008

Langevin Equation for Guiding Center Motion and its Application to Neoclassical Transport Theory

Akinobu MATSUYAMA[1)] and Kiyoshi HANATANI[2)]

[1)]*Graduate School of Energy Science, Kyoto University, Uji 611-0011, Japan*
[2)]*Institute of Advanced Energy, Kyoto University, Uji 611-0011, Japan*

Neoclassical transport in toroidal plasmas is addressed by the Langevin equation. To ensure the diffusive nature of a stochastic process, the dynamics of test particles is expressed in terms of the Langevin equation with the assumption of sufficiently small radial orbit width. The transport coefficients are evaluated by the time integration of auto- and cross-correlation functions for each pair of time-reversal expressions of microscopic fluxes. As a test of this method, the neoclassical viscosity coefficients are calculated numerically and are shown to agree with analytical formulas.

Keywords: Neoclassical Transport, Langevin Equation, Linear Response Theory

1 Introduction

The Langevin equation[1] is used to describe the transport processes in a system close to thermal equilibrium. An advantage of the Langevin-type description is that it can be easily simulated using a quasi-random number generator. The Monte Carlo methods have been extensively used in the stellarator/heliotron research, in particular, to estimate the $1/\nu$ radial diffusion[2], which gives the irreducible minimum of the transport level in a toroidal configuration. The calculation of parallel transport such as bootstrap currents is also important for predicting the non-inductive currents which are observed in experiments.

Mathematically, the Langevin equation is an example of stochastic differential equations(SDEs)[3]. When we consider a stochastic variable $X(t)$ in a Gaussian random process with t, a time variable, the evolution of $X(t)$ can be written in terms of SDEs by

$$dX(t) = a(X;t)\,dt + b(X;t)\,dW(t), \tag{1}$$

where $a(X;t)$ is the deterministic part of test particle motion, while $b(X;t)$ denotes the random acceleration with the standard Wiener process $W(t)$. In most cases, we need not solve exact trajectories of test particles. Instead, the Wiener increments $dW(t)$ are approximated by relatively simple random variables, such as the two-point or uniform ones. The Monte Carlo collision operator introduced by Boozer and Kuo-Petravic[2] is an example of using the two-point random variables as an approximation of the Wiener increments.

On the other hand, the transport theory in such a stochastic system can be treated quantitatively by the correlation-function method[4]. The transport coefficients are then calculated from the time-integration of correlation function between microscopic fluxes carried by each particle. This method is also known as the Green-Kubo formula[5, 6]. In the linear response theory of stochastic process[7], this approach is valid in a variety of transport phenomena, provided that the evolution of a system is dominated by Gaussian probability distributions.

In the present paper, we propose a method for computing neoclassical transport matrix using the Langevin equation and correlation function. Although it is not easy to calculate the correlation function in general, the neoclassical ordering[8] enables us to evaluate it as a function of magnetic surface label. In Sec. 2, we derive the Langevin equation for guiding center motion. Section 3 describes the correlation-function method for neoclassical transport theory, in which we calculate the neoclassical viscosity coefficients[9] as a numerical test. In Sec.4, we summarize the main finding of this work and comment on future studies.

2 Langevin Equation

We now wish to derive the Langevin equation for describing the neoclassical transport in toroidal plasmas. Here, we note that the phase-space coordinates of guiding center are regarded as stochastic variables. The test particle experiences the deterministic friction and random acceleration together with the complex Hamiltonian motion, which is formulated by the drift Hamiltonian theory[10]. If we denote the guiding center coordinate by $z_i\,(i = 1,\ldots,5)$, its Hamiltonian motion is expressed by the Pois-

author's e-mail: matuyama@center.iae.kyoto-u.ac.jp

son bracket $\{\bullet, \bullet\}$ or Poisson tensor $\omega_{ij} \equiv \{ z_i, z_j \}$ as

$$z_i = \{ z_i, H \} = \omega_{ij} \frac{\partial H}{\partial z_j}, \tag{2}$$

where H is the drift Hamiltonian[10]. If we take into account the Coulomb collisions, equations of motion must be written in terms of SDEs like Eq.(1). Therefore,

$$dz_i(t) = \left[a_i^{(H)}(t, \mathbf{z}) + a_i^{(F)}(t, \mathbf{z}) \right] dt + b_{ij}(t, \mathbf{z})\, dW_j(t), \tag{3}$$

where we divided the deterministic part a_i into the Hamiltonian $a_i^{(H)} = \omega_{ij}\, \partial H / \partial z_j$ and the friction part $a_i^{(F)}$. We note that Eq.(3) becomes non-Hamiltonian and stochastic because of the friction force and random scattering.

In the present work, we retain only the pitch angle scattering in the collision operator. We used the coordinate system $(s, \theta, \zeta, v, \xi)$, where s is the surface label, θ and ζ are the poloidal and toroidal angles, respectively, v is particle velocity, and ξ is the pitch variables. This choice is convenient because, in our case, the particle energy becomes manifestly a constant of motion, and the non-Hamiltonian terms are included only in ξ. We also note that the Boozer coordinates[11] were used to describe the guiding center position. From Eq.(3), we can write the stochastic motion of guiding center by

$$\begin{aligned} ds &= \{ s, H \}\, dt, \\ d\theta &= \{ \theta, H \}\, dt, \\ d\zeta &= \{ \zeta, H \}\, dt, \\ dv &= 0, \\ d\xi &= \{ \xi, H \}\, dt - \nu_D \xi\, dt + \sqrt{(1-\xi^2)\nu_d}\, dW_t, \end{aligned} \tag{4}$$

where ν_D is the deflection frequency. The Poisson brackets appeared in Eqs.(4) represent the guiding center equations used in the orbit calculation. Equations (4) contain the guiding center drifts up to the first order of dimensionless parameter $\epsilon \equiv \rho_L / L$, where ρ_L is the Larmor radius and L_c is the characteristic scale length in the radial direction. In the local and diffusive picture of neoclassical transport[8], however, the effect of finite radial orbit width is neglected so that the particle dynamics relevant to the transport can be expressed only by the terms up to zeroth order. Therefore, we approximate the Poisson brackets up to the lowest order:

$$\begin{aligned} ds &= 0, \\ d\theta &= \frac{v\xi}{B} \frac{\chi'}{\sqrt{g_B}}\, dt, \\ d\zeta &= \frac{v\xi}{B} \frac{\psi'}{\sqrt{g_B}}\, dt, \\ d\xi &= -\frac{v(1-\xi^2)}{2B} \left[\frac{\chi'}{\sqrt{g_B}} \frac{\partial \ln B}{\partial \theta} + \frac{\psi'}{\sqrt{g_B}} \frac{\partial \ln B}{\partial \zeta} \right] dt, \\ &\quad -\nu_D \xi\, dt + \sqrt{(1-\xi^2)\nu_D}\, dW_t, \end{aligned} \tag{5}$$

where χ and ψ are the poloidal and toroidal flux function, respectively, the prime denotes the derivative with respect to the surface label s, and the Jacobian $\sqrt{g_B}$ is of Boozer coordinates. For simplicity, we did not consider the poloidal and toroidal drifts induced by the radial electric field in Eqs.(5). As discussed in the next section, the radial drift term $\{s, H\}$ affects the transport only through the linear response to the radial thermodynamic force. Accordingly, the dynamics of test particles involves only the motion along magnetic field lines. In this approximation, the treatment using the Poisson bracket guarantees conservation of energy.

The numerical solution of Eqs.(5) gives the stochastic motion of test particles. Those ensemble relax to the stationary probability distribution, P_0, within the statistical error due to the finite number of test particles. We use P_0 as the initial condition of test particle distribution when we calculate the correlation function.

3 Correlation Function Method

In this section, we discuss the correlation-function method for calculating the neoclassical transport matrix. The transport matrix determines the phenomenological relation between the macroscopic fluxes and thermodynamic forces[12], and it can be evaluated through the auto- and cross-correlations of the microscopic fluxes.

The correlation function of microscopic fluxes, $\sigma_i(\mathbf{z})$ and $\sigma_j(\mathbf{z})$, is given by

$$R_{ij}(t) = \int d\mathbf{z}\, P_0(\mathbf{z})\, \sigma_i(\mathbf{z}(0))\, \sigma_j(\mathbf{z}(t)), \tag{6}$$

where we assumed that $\sigma_i(\mathbf{z})$ and $\sigma_j(\mathbf{z})$ have the time-reversal symmetry (an even function of pitch variable) and the test particles are distributed with P_0 at $t = 0$. If the thermodynamic force is switched on at $t = 0$, the first-order flux such as radial drifts will be driven as a linear response. The time-dependent transport coefficient, which is called as the running transport coefficient[13], is evaluated by

$$D_{ij}(t) = \int_0^t d\tau\, R_{ij}(\tau). \tag{7}$$

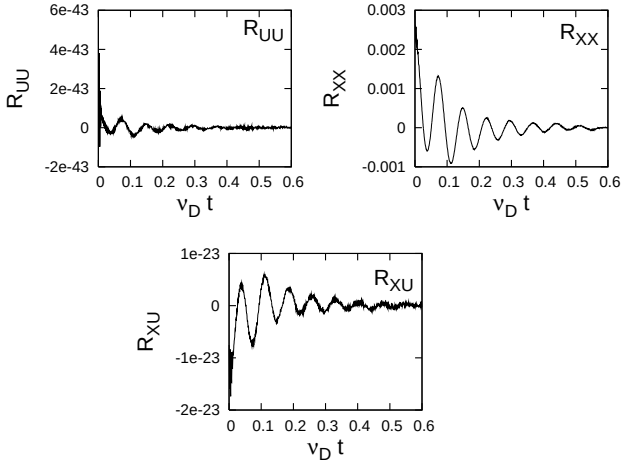

Fig. 1 The correlation functions R_{UU}, R_{XX} and R_{XU} numerically calculated by Eq.(6). The collisionality is $\nu_D/v = 1 \times 10^{-3}$, the banana regime. The horizontal axis denotes the time normalized by ν_D.

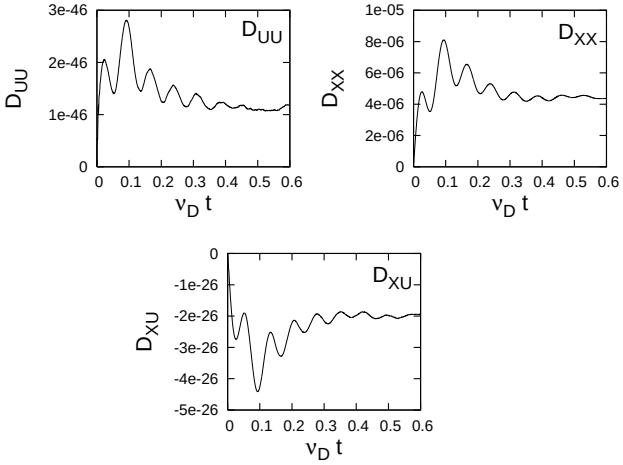

Fig. 2 The running transport coefficients D_{UU}, D_{XX}, and D_{XU} calculated by the time integration in Eq.(7) for the correlation functions in Fig.(1). The horizontal axis denotes the time normalized by ν_D.

This quantity will converge to a finite value if the transport process is characterized by diffusive nature[13].

In Eq.(6), we choose $\sigma_i(\mathbf{z})$ and $\sigma_j(\mathbf{z})$ by[9]

$$\sigma_U \equiv -mv^2 P_2(\xi)\,\mathbf{B}\cdot\nabla \ln B, \quad (8)$$

$$\sigma_X \equiv -v^2 P_2(\xi)\,\frac{B}{\Omega}\left(\tilde{U}\mathbf{b} + \frac{\nabla s\times\mathbf{b}}{B}\right)\cdot\nabla \ln B, \quad (9)$$

where m is the particle mass, $P_2(\xi)$ is the second order Legendre polynomial and $\mathbf{B}$ is the magnetic field, $B = |\mathbf{B}|$, $\mathbf{b} = \mathbf{B}/B$, and Ω is the Larmor frequency. The quantity $\tilde{U}$ is defined by the solution of

$$\mathbf{B}\cdot\nabla(\tilde{U}/B) = \mathbf{B}\times\nabla s\cdot\nabla(1/B^2), \quad \langle B\tilde{U}\rangle = 0. \quad (10)$$

The bracket denotes the surface averaging operation. We calculate the auto- and cross-correlation functions of σ_U and σ_X as

$$\begin{aligned} R_{UU}(t) &= \int d\theta d\zeta d\xi\, P_0\,\sigma_U(t=0)\,\sigma_U(t), \\ R_{XU}(t) &= \int d\theta d\zeta d\xi\, P_0\,\sigma_X(t=0)\,\sigma_U(t), \\ R_{XX}(t) &= \int d\theta d\zeta d\xi\, P_0\,\sigma_X(t=0)\,\sigma_X(t), \end{aligned} \quad (11)$$

where the integrals are evaluated by the Monte Carlo methods. We note that the correlation functions parametrically depend on the initial surface label and particle velocity because $ds = 0$ and $dv = 0$ in Eqs.(5).

The evolution of correlation functions for each pair of fluxes are given in Figs. (1). The magnetic field model used here is the same with that in Ref.[9]. For this case, magnetic field strength is given by $B = B_0[1 - \epsilon_t\cos\theta - \epsilon_h\cos(l\theta - m\zeta)]$ with $\epsilon_t = 0.1$ and $\epsilon_h = 0.01$, where l and m are the poloidal and toroidal field periods, respectively. The collisionality is set as $\nu_D/v = 1\times10^{-3}$ (Banana regime). We observed that the correlation functions decayed within the relaxation time. Figure (2) shows the running transport coefficients, which are denoted by D_{UU}, D_{XU}, and D_{XX}, respectively, were converged to the finite values, asymptotically.

The choice of microscopic fluxes given in Eqs.(8) and (9) is useful because the neoclassical viscosity coefficients[9] can be evaluated by D_{UU}, D_{XU}, and D_{XX}. We calculate the neoclassical viscosity coefficients, L, M, and N by

$$M = \frac{1}{T}D_{UU}\left[1 - \frac{3D_{UU}}{2mT\nu_D K\langle B^2\rangle}\right], \quad (12)$$

$$N = \frac{1}{T}D_{XU}\left[1 - \frac{3D_{UU}}{2mT\nu_D K\langle B^2\rangle}\right], \quad (13)$$

$$L = \frac{1}{T}D_{XX} + \frac{3D_{XU}^2}{2mT^2\nu_D K\langle B^2\rangle} \times\left[1 - \frac{3D_{UU}}{2mT\nu_D K\langle B^2\rangle}\right], \quad (14)$$

where T is the temperature in energy units and $K \equiv mv^2/2T$. Once we obtain the collisionality dependence of L, M, and N (or the geometric factor instead of N, defined by $G_{\rm BS} = -e\langle B^2\rangle N/M$), we can calculate the Onsager-symmetric viscosity matrix using the energy integral[9].

Figures (3), (4) and (5) show the collisionality dependence of normalized viscosity coefficients L^*, M^*, and $G_{\rm BS}$ for the same magnetic field strength with that used in Fig.(1) and (2). The solid lines represent the analytical

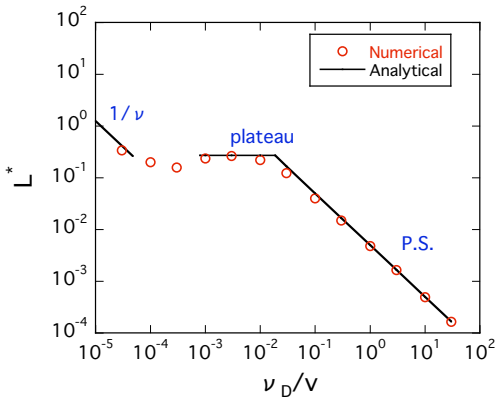

Fig. 3 The collisionality dependence of radial diffusion coefficients $L^* \equiv L/[\frac{1}{2}(v_T/T)(Bv_T/\Omega)^2K^{3/2}]$, where $v_T = \sqrt{2T/m}$ is the thermal velocity.

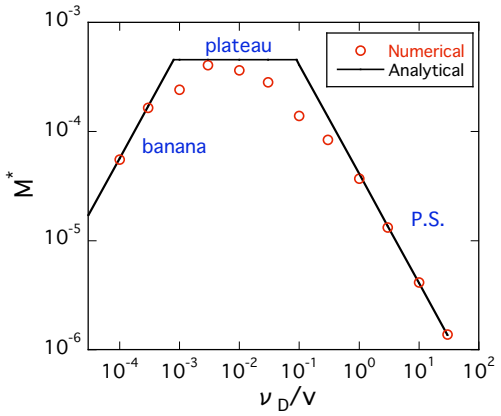

Fig. 4 The collisionality dependence of Parallel viscosity coefficients, $M^* \equiv M/(mv_TK^{3/2})$, against parallel flows.

asymptotic expressions given in Ref.[9]. In these figures, the numerical results obtained by the correlation-function method show reasonable agreements with the analytical values. Therefore, we have concluded that the correlation-function method in Eq.(11) has been successfully verified through the calculation of neoclassical viscosity coefficients.

4 Conclusions

In the present work, we derived the Langevin equation of guiding center motion and developed the method for computing neoclassical transport using the correlation-function method. As noted in Sec.2 and 3, the neoclassical ordering for the Langevin equation is important to ensure the local and diffusive nature of neoclassical transport. We should also mention that, owing to this assumption, the explicit calculation of correlation functions becomes possible.

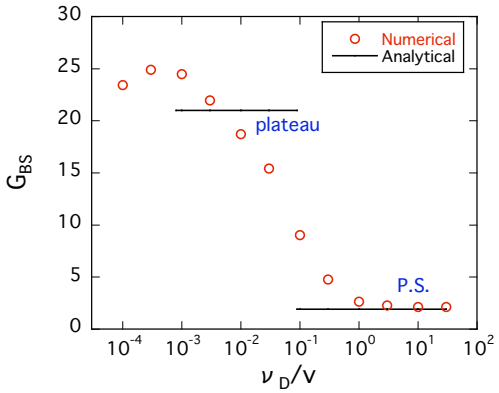

Fig. 5 The collisionality dependence of geometric factor $G_{\rm BS}$.

As a specific example, we evaluated the neoclassical viscosity coefficients, L^*, M^* and $G_{\rm BS}$, which are used in the moment-equation method[9] for obtaining the viscosity-flow relation. We showed that the viscosity coefficients can also be calculated by the correlation-function method, which is based not on the kinetic but on the stochastic approach using the Langevin equation.

In future work, the effect of radial electric field should be taken into account in Eqs.(5) and we will test the method for realistic toroidal MHD equilibria.

Acknowledgement

This work is supported in part by the Global COE Program in Graduate School of Energy Science, Kyoto University, Japan.

[1] F.Schwabl, *Statistical Mechanics* (Springer, Berlin, 2000)
[2] A.H.Boozer and G.Kuo-Petravic, Phys. Fluids **24**, 1999 (1981)
[3] P.E.Kloeden and E.Platen, *Numerical Solution of Stochastic Differential Equations* (Springer-Verlag, Berlin, 1992)
[4] H.Mori, Phys. Rev. **112**, 1829 (1958)
[5] M.Green, J.Chem. Phys. **20**, 1281 (1952)
[6] R.Kubo, J. Phys. Soc. Jpn. **12**, 570 (1957)
[7] P.Hänggi and H.Thomas, Phys. Rep. **4**, 207 (1982)
[8] F.L.Hinton and R.D.Hazeltine, Rev. Mod. Phys. **42**, 239 (1976)
[9] H.Sugama and S.Nishimura, Phys. Plasmas **9**, 4637 (2002)
[10] R.G.Littlejohn, Phys. Fluids **24**, 1730 (1981)
[11] A.H.Boozer, Phys. Fluids **26**, 1288 (1983)
[12] S.R.de Groot and P.Mazur, *Nonequilibrium Thermodynamics* (North-Holland, Amsterdam, 1962)
[13] R.Balescu, *Statistical Dynamics: Matter out of Equilibrium* (Imperial College Press, London, 1997)

Proceedings of ITC18, 2008

2D density turbulence measured by MIR in TPE-RX

Z B Shi[1)], Y Nagayama[2)], S Yamaguchi[3)], D Kuwahara[4)], T Yoshinaga[2)], M Sugito[2)], Y Hirano[5)], H Koguchi[5)], S Kiyama[5)], H Sakakita[5)], K Yambe[5)],C Michael[6)]

[1)] *The Graduate University for Advanced Studies, Toki 509-5292, Japan*
[2)] *National Institute for Fusion Science, Toki 509-5292, Japan*
[3)] *Kansai University, Suita 564-8680, Japan*
[4)] *Department of Energy Science, Tokyo Institute of Technology, Tokyo 152-8550, Japan*
[5)] *Advanced Industrial Science and Technology, Tsukuba 305-8568, Japan*
[6)] *UKAEA, Abingdon, Oxfordshire OX14 3DB, United Kingdom*

September 15, 2008

Two-dimensional (2D) turbulence measurement by using microwave imaging reflectometry (MIR) has been performed in the reversed field pinch (RFP) plasma in TPE-RX. In this work, the maximum entropy method (MEM) is used to estimate the 2D k-spectrum. The turbulences between the pulsed poloidal current drive (PPCD) and the high Θ plasmas are studied. The m=1 modes are dominant in PPCD plasma, while in high Θ plasma the k spectrum expands to the high k range and the turbulence propagates in the electron drift direction. The preliminary result shows that PPCD plasma switches off the turbulence, and the high Θ plasma has strong turbulence.

Keywords: MIR, MEM, density fluctuation

1. Introduction

Microwave reflectometry, based on the radar technique, is a powerful tool to measure the plasma density profile and density fluctuation [1, 2]. In a reflectometry system, the launching wave is reflected by the cutoff layer in the plasma. The phase difference between the launching wave and the reflection wave can be detected, and the phase fluctuation is mainly modified by the density fluctuations near the cutoff region in 1D geometric approximation [1].

However, 2D configuration of the fluctuation may cause a complicated interference pattern on the detection plane due to the diffraction effects [1–4]. Microwave imaging reflectometry (MIR) uses large aperture optical technique to correct the disturbed wave front. The image of the cutoff surface is made by the wide aperture lens onto the 2D detector array located at the detector plane. The feasibilities of MIR for 2D turbulence measurement have been investigated in theories and experiments intensively [1–7].

To obtain the fine structures of the fluctuations, a big detector array is required. However, the detector size is often smaller than the correlation length of the fluctuation. The measurement area in plasma is limited by the small window. On the other hand, the turbulent signals are often mixed with long distance correlation and short distance correlation modes, leading to the complicated 2D cross-correlation function. The traditional two-point cross-correlation can't distinguish the multiple modes. To obtain the useful information from the limited experimental data, it is necessary to develop a new numerical method to estimate the turbulence structure from the signals obtained by a few detectors.

In this paper, we have developed a MIR system to investigate the 2D turbulence in the reversed field pinch (RFP) [8] plasma in TPE-RX. The maximum entropy method (MEM) [9, 10] is used to improve the spectral resolution. The turbulences between the pulsed poloidal current drive (PPCD) and the high Θ plasmas are studied. The preliminary result shows that the PPCD plasma switches off the turbulence which agrees with the nonlinear MHD dynamo model [8]. The paper is organized as follows: Section 2 presents the MIR system in TPE-RX. The analysis methods are described in section 3. The turbulences between PPCD and the high Θ plasmas are discussed in section 4. The summary is given in section 5.

2. MIR system in TPE-RX

TPE-RX is a large RFP device with major radius R =1.72 m and minor radius a =0.45 m [11, 12]. The experiments with MIR have been performed with the plasma current of 200-300 kA and electron density of $(0.5-1)\times10^{19}$ cm^{-3}. In the TPE-RX plasma, the cutoff radius of 20 GHz mainly located at the region of r_{cut}/a=0.6-0.9 because the density profile usually becomes flat or hollow in the case of PPCD and gas-puffing operations. This region is near the reversed field surface. It is useful for the calibration of the optical aberration of MIR optical system.

Figure 1 shows the schematic diagram of the MIR system in TPE-RX [13]. It consists of a optical system and a 2D receiver system. The quartz window of the TPE-RX viewing port is located at r = 67 cm. The RF wave illuminating from the horn antenna is

author's e-mail: shi.zhongbing@nifs.ac.jp

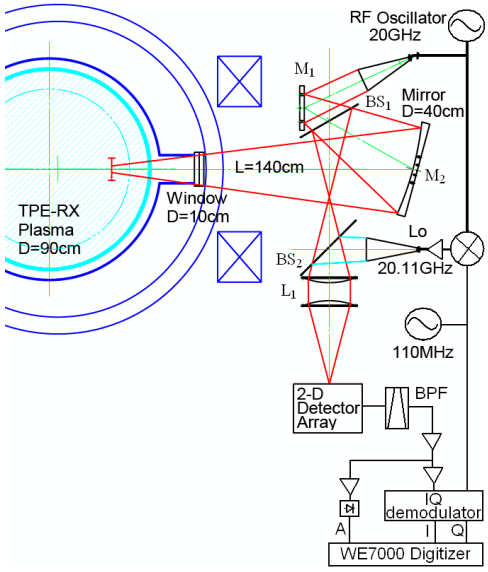

Fig. 1 Schematic diagram of the MIR system on TPE-RX

reflected by the first plain mirror (M_1). The RF wave passes through the first beam splitter (BS_1) to the main mirror (M_2). The main mirror, which is an elliptic concave mirror with the size of 40 cm in diameter at $r = 140$ cm, makes a parallel illumination beam in the plasma. The reflected wave is collected by the main mirror and is separated from the illumination beam by the first beam splitter (BS_1). The local oscillation (LO) wave and the reflected wave are mixed at the second beam splitter (BS_2). The image of the plasma fluctuation is made on the detector surface by the Teflon lens (L_1). The optical system has been designed and tested carefully, and good agreement between the measured beam profiles and those obtained by a ray tracing simulation was confirmed.

The receiver system consists of a planer Yagi-Uda antenna, a Schottky barrier diode, low pass filter, intermediate frequency (IF) amplifier and phase-detector. The Yagi-Uda antenna array is made on the Teflon printed circuit board (PCB). On the design of antenna system, a computer code for electro-magnetic field is employed. The 4 by 4 2D antenna and detector circuits are made by the micro strip line technology, which enables high sensitivity measurement. 4 elements are set on a PCB with a distance of 12 mm, and 4 PCBs are stacked with a distance of 15 mm. The spacial resolution of the detector array in the plasma is about 3.7cm.

A Gunn oscillator generating the microwave with frequency of 20 GHz is used. The RF wave illuminates in the O-mode, so the cutoff density is $n_{ecut} = 0.5 \times 10^{19}$ m^{-3}. The LO wave with the frequency of 20.11 GHz is made by mixing the RF wave (20 GHz) and the low frequency wave (110 MHz) at an up-converter. By mixing the reflected wave and the LO wave, the 2D mixer array makes intermediate frequency (IF) signal of 110MHz. This IF signal contains the amplitude A and the phase ϕ of the density fluctuation in plasma. The amplitude is obtained by rectifying the IF signal with a diode detector. The phase is obtained by comparing the IF frequency and the mixed signal by the phase demodulator.

3. Analysis technique

3.1 2D cross-correlation

The two-point cross-correlation [14] is a traditional analysis method to study the correlation between two fluctuations, given as

$$\Gamma_{ij} =< n_i n_j >= \int_{\Delta t}\int_{\Delta\omega} n_i(\omega,t) n_j^*(\omega,t)\, d\omega dt \quad (1)$$

where the asterisk $*$ denotes complex conjugation, $n(\omega,t)$ is the Fourier transform of the time series, i and j represent different channels. The cross-correlation spectrum array can be obtained by doing the cross-correlation between the reference channel and every channel in the detecting region. The cross-correlation spectrum is the inverse Fourier transforms of the power spectrum. According to the Wiener–Khinchin theorem, the power spectrum is the Fourier transform of the autocorrelation function, defined as

$$S(k_x,k_y) = \int\int \Gamma(x,y) e^{-i(k_x x + k_y y)}\, dxdy \quad (2)$$

where, k_x and k_y are the toroidal and the poloidal wavenumbers, respectively. $\Gamma(x,y)$ is the average autocorrelation array which is averaged over different reference channels.

Figure 2 shows the power spectrum estimated by equation 2. The spectrum shows a dominant broad peak with distinct sidelobes caused by too small detector size. The broad spectrum with the dominant energy might conceal the other modes with small power density. It shows pool spectral resolution. Therefore, the traditional Fourier transform fails to resolve the spectral peaks.

3.2 MEM

The power spectrum estimated by Fourier transform is similar as using a bandpass filter in the unknown autocorrelation function we want to solve. If one can extend the correlation measurements outside the measured region, the power spectrum with high resolution can be restored. One possible way is trying to find the filter coefficients by autoregressive method. However, the result is sensitive to the noise and is not very reliable sometimes. It may cause spurious peaks if we fail to set the convergence condition and fail to select the optimized order of the autoregressive

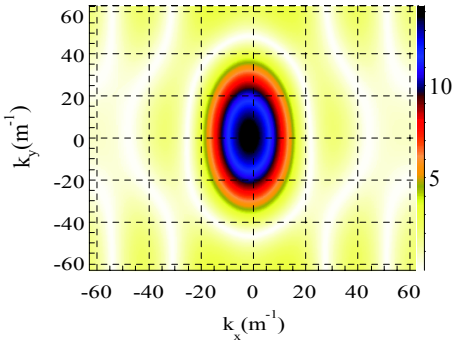

Fig. 2 The power spectrum $S(k_x, k_y)$ obtained by Fourier transform

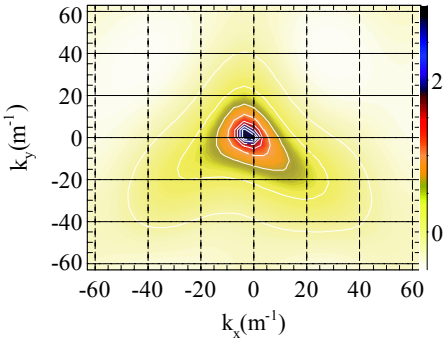

Fig. 3 The power spectrum $\log(S(k_x, k_y))$ of PPCD plasma (r_c=0.85) obtained by MEM

filter. So far, many numerical methods such as autoregressive, maximum likelihood method and Pisarenko methods have been used to the power spectral estimation. Among them, 2D MEM is the most powerful and effective method because of better spectral resolution [9, 10]. In this study, the Skilling MEM will be used, because it is a model-free method which can give more reliable result than the other MEM algorithms, for example the method based on the autoregressive model. The entropy is defined as

$$H(S) = \int\int \log(S(k_x, k_y))\, dk_x dk_y \tag{3}$$

Define the constraint statistic, chi-squared, to estimate the misfit between the experimental value and expectation value.

$$\begin{aligned} C(S) &= \chi^2(S) - \chi^2_{tar.} \\ &= \sum_{i=1}^{N_{ch}} (\Gamma_{meas.} - \Gamma_{aim})^2/\sigma^2 - \chi^2_{tar.} \end{aligned} \tag{4}$$

The entropy is changed as solve the following equation in maximum.

$$P(S) = H(S) - \lambda C(S) \tag{5}$$

under the constrain of $C \to 0$. Here λ is the Lagrange multiplier. $\Gamma_{meas.}$ is the 2D autocorrelation function given by equation 1. Γ_{aim} is the autocorrelation function estimated by MEM. σ is the standard error of $\Gamma_{meas.}$. $\chi_{tar.}$ is the target to converge maximum of equation 5 within reasonable calculation time. The maximum condition is satisfied when $\Gamma_{meas.} = \Gamma_{aim}$ and it is possible for the 1D MEM. However, the maximization process of equation 5 in 2D array requires non-linear optimization. $\chi_{tar.}$ should be equal to channel number but it is determined empirically for good convergence. This problem is solved iteratively by searching for maximum entropy over three well chosen search directions [10, 15].

Figure 3 shows the power spectrum $\log S(k_x, k_y)$ estimated by MEM in PPCD plasma. Note that the logarithm axis is used. The peak in the power spectrum is much higher than the background fluctuations. Therefore, the k-spectrum estimated by MEM shows high 2D spectral resolution.

4. Turbulence of PPCD and high Θ plasmas

The RFP configuration is generated by the relaxation process and sustained by the dynamo effect, which is caused by the turbulences and instabilities. The nonlinear MHD dynamo model is used to explain the dynamo mechanism [16]. This model assumes that the fluctuation-induced electromotive electric field sustains the field aligned current against resistive decay. The plasma current is given as

$$\eta j_{//} = E_{//} + < \tilde{v} \times \tilde{B} >_{//} \tag{6}$$

where, η is the electric resistivity. $j_{//}$ is the parallel equilibrium current, $\tilde{v}$, $\tilde{B}$ are the fluctuating fluid velocity and magnetic field, respectively. <> denotes the average over an equilibrium flux surface. $E_{//}$ is the external electric field parallel to the magnetic field. $< \tilde{v} \times \tilde{B} >_{//}$ represents the dynamo term.

In the high Θ plasma the dynamo is dominant. The pinch parameter Θ is defined as the ratio of the poloidal magnetic field at the edge to the volume averaged toroidal magnetic field, $\Theta = B_p(a)/ < B_t >$. The high Θ is defined as Θ>1.6. The fluctuation becomes more coherent and the fluctuation amplitude of the magnetic probe increases as the Θ increases. The sawtooth crashes are often observed during high Θ operation [11, 12]. In PPCD operation, an external pulsed poloidal field drives the poloidal current, so that the Taylor state is sustained without the help of the dynamo effect. As a result, the dynamo-related fluctuations can be suppressed.

The turbulences of PPCD and high Θ plasmas are compared between the 2D k spectra estimated by MEM. As shown in figure 3, the peaked power is observed at k_x=-3±3 m^{-1} and k_y=3±3 m^{-1} in PPCD

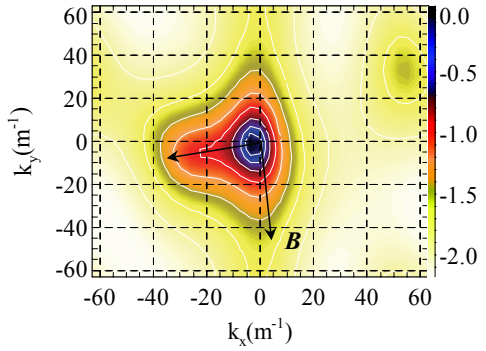

Fig. 4 The power spectrum $\log(S(k_x, k_y))$ of high Θ plasma (r_c=0.7) estimated by MEM

plasma. The mode energy is limited at the low k range which means low turbulence in PPCD plasma. The dominant mode is m=-1/n=7 with the error of Δm=1/Δn=7. This is the single helicity mode which is dominant in many case of TPE-RX PPCD plasma. Figure 4 shows the power spectrum $\log(S(k_x, k_y))$ in the case of high Θ plasma. The cutoff radius is about r/a= 0.7. The peaked power is observed at k_x=-3±5 m^{-1} and k_y=-3±6 m^{-1}. The dominant modes are m=-1±2/n=-7±14. It is wider than that of PPCD plasma. Therefore, the spectrum of high Θ plasma expands to the high k range.

The revered surface can be obtained by the modified Bessel function model [8]. Generally, the reversed surface is at about r/a=0.9 in the high Θ plasma, while it is at about r/a=0.8 in the typical PPCD plasma due to the driving of the external field. In PPCD plasma, the cutoff surface of MIR is at about r/a=0.85 because the electron density profile is rather high. MIR detects the density fluctuation outside of the reversed field surface. In the high Θ plasma, the cutoff surface of MIR is at about r/a=0.7 due to the low density. MIR detects the density fluctuation inside of the reversed field surface.

The evolutions of the tearing modes during a dynamo event have been discussed by using magnetic probe [11, 12]. Those observations show that the multi-modes will be excited during the dynamo event in the high Θ plasma. At the low k region it shows a flat peak which agrees with the multi-modes in the high Θ plasma.

The expansion direction in k spectrum of the high Θ plasma is mainly in toroidal direction which indicates by an arrow shown in figure 5. The magnetic field is mainly poloidal near the reversed field surface. The expansion direction is perpendicular to the magnetic field line. It is in the electron drift direction. Therefore, the turbulence in the high Θ plasma propagates in the electron drift direction. The expansion in high k range means the strong turbulence in the high Θ plasma. This result agrees with the nonlinear MHD dynamo model.

5. Summary

In summary, 2D turbulence measurement by using MIR has been done in the RFP plasma in TPE-RX. A large aperture optical system is used to make an image of the cutoff surface onto the 4 by 4 detectors array located at the imaging plane. The 2D k spectrum obtained by the traditional Fourier method shows poor spectral resolution due to the small detector array whose size is smaller than the cross-correlation length of the fluctuation. The MEM is used to estimate the k spectrum, and the spectrum shows high spectral resolution.

The turbulences between the PPCD and the high Θ plasmas are studied. The low k mode is dominant in PPCD plasma, while in high Θ plasma it shows multi-modes in the low k region. The k spectrum of the high Θ plasma expands to the high k range and the turbulence propagates in the electron drift direction. The preliminary result shows that PPCD plasma switches off the turbulence, and the high Θ plasma has strong turbulence, which agrees with the nonlinear MHD dynamo model.

This work is carried out as one of the NINS Imaging Science Project (Grant No. NIFS08KEIN0021). This work is also supported by NIFS (Grant No. NIFS08ULPP525), and SOKENDAI (Grant No. NIFS08GLPP003). A part of this study was financially supported by the Budget for Nuclear Research of the Ministry of Education, Culture, Sports, Science and Technology of Japan, based on the screening and counseling of the Atomic Energy Commission.

[1] E. Mazzucato Rev. Sci. Instrum. **69**, 2201 (1998).
[2] H. Park et al., Rev. Sci. Instrum. **74**, 4239 (2003).
[3] E. Mazzucato et al., Phys. Plasmas **9**, 1955 (2002).
[4] Y. Lin et al., Plasma Phys. Control. Fusion **43**, L1 (2001)
[5] M. Ignatenko et al., Nucl. Fusion **46**, S760 (2006)
[6] T. Estrada et al., Phys. Plasmas **8**, 2657 (2001).
[7] S. Yamaguchi et al., Rev. Sci. Instrum. **77**, 10E930 (2006).
[8] H.A.B. Bodin Nuclear Fusion **30**, 1717 (1990)
[9] Jae S. Lim et al., IEEE trans. on acoustics, speech, and signal proc. **Assp-29**, 401 (1981)
[10] J. Skilling et al., Mon. Not. R. astr. Soc. **211**, 111, (1984)
[11] Y. Hirano et al., Nuclear Fusion **36**, 721 (1996)
[12] P.R. Brunsell et al., Phys. Fluids B **5**, 885 (1993)
[13] Y. Nagayama et al., Plasma and Fusion Research **3**, 053 (2008)
[14] Ch.P. Ritz et al., Rev. Sci. Instrum. **59**, 2201 (1988).
[15] C.A. Michael et al., Plasma and Fusion Research **2**, S1034 (2007)
[16] H. Ji et al., Physical review letters **73**, 668 (1994)

Proceedings of ITC18,2008

Quasi-Coherent Modes in the High Density H-mode Regime of W7-AS

E. Belonohy[1], M. Hirsch[2], K. McCormick[3], G. Papp[4], G. Pokol[4], H. Thomsen[2], A. Werner[2], S. Zoletnik[1] and the W7-AS Team

[1]*MTA KFKI RMKI, EURATOM Association, Budapest, Hungary*

[2]*MPI für Plasmaphysik, EURATOM Association, Greifswald, Germany*

[3]*MPI für Plasmaphysik, EURATOM Association, Garching, Germany*

[4]*Dept. of Nuclear Techniques, Budapest Univ. of Technology and Economics, EURATOM Association, Budapest, Hungary*

The high density H-mode (HDH) is an ELM-free H-mode regime at the Wendelstein 7-AS (W7-AS) stellarator exhibiting no impurity accumulation. Quasi-Coherent (QC) modes found recently on Mirnov coil signals are thought to be prime candidates responsible for the low impurity concentration in this regime based on their strong correlation to impurity radiation. These modes are high frequency (50-150 kHz), high poloidal mode number (m~40), possibly pressure-driven oscillations, showing strong amplitude modulation. QC modes are occasionally accompanied by low frequency oscillations (principle frequencies <50 kHz plus higher harmonics) not unique for the HDH regimes detected by both the Mirnov coils and Langmuir probes, as well as high frequency oscillations (250-350 kHz) that - when present - decrease the QC amplitude. QC modes on W7-AS show similarities to quasi-coherent modes found on the Alcator C-Mod tokamak, responsible for the low impurity concentration in the similar ELM-free, high density H-mode called Enhanced D-alpha mode, prompting a careful comparison between the two modes.

Keywords: ELM-free H-mode, high density H-mode, quasi-coherent modes, impurity transport, W7-AS

1. Introduction

The High Density H-mode (HDH) [**1**] is a stationary ELM-free improved H-mode regime at the Wendelstein 7-AS (W7-AS: major radius R = 2 m, minor radius $a_{eff} \leq$ 0.16m, toroidal magnetic field $B_t \leq 2.5$T) [**2**] stellarator not subject to impurity accumulation even at high line averaged electron densities up to $4 \cdot 10^{20}$ m^{-3}. It has been obtained above a threshold density after the realization of the island divertor concept on W7-AS. It is characterized by flat density profiles, edge-localized radiation and energy confinement times about $2 \cdot \tau_e^{ISS95}$ beside significantly low impurity retention times. This is of particular interest as future fusion-oriented devices are mainly preferred to be run at high densities, a regime often susceptible to impurity accumulation and ensuing radiation collapse as it is the case for the standard ELM-free H-mode regime of W7-AS called the Quiescent H-mode (H*). The mechanism responsible for this low impurity concentration of the HDH regime has not yet been identified.

Recent investigations of Mirnov coil data found an MHD mode appearing in the HDH phase showing remarkable correlation with the impurity radiation making it a promising candidate for the impurity flushing mechanism.. The mode was named quasi-coherent (QC) mode due to its similarity to the QC modes [**3**] found in the Enhanced D-alpha (EDA) regime [**4**] of the Alcator C-Mod tokamak, responsible for the low impurity concentration in that high density ELM-free regime. Characteristics of these modes and their relation to the impurity transport are reported here. Other MHD modes accompanying the QC modes are investigated here as well. A careful comparison of the QC modes to other similar MHD modes present in stable ELM-free regimes of other devices is attempted as well, in order to gain better insight into the nature of these modes.

author's e-mail: belonohy@rmki.kfki.hu

2. Quasi-Coherent Modes in Wendelstein 7-AS

Quasi-coherent modes are bursty, narrow band (~10-15 kHz) oscillations in the 50-150 kHz frequency range detected in the poloidal magnetic field fluctuations showing good correlation with the impurity radiation. Fig. 1. shows a spectrogram of a Mirnov coil signal and the corresponding impurity radiation from bolometry for two ELM-free H-mode time windows, namely the quiescent H* and the HDH mode. In H* the impurity radiation increases due to impurity accumulation in the core and broadband fluctuations can be observed that appear to be the reminiscent of small ELMs. In the HDH phase a QC

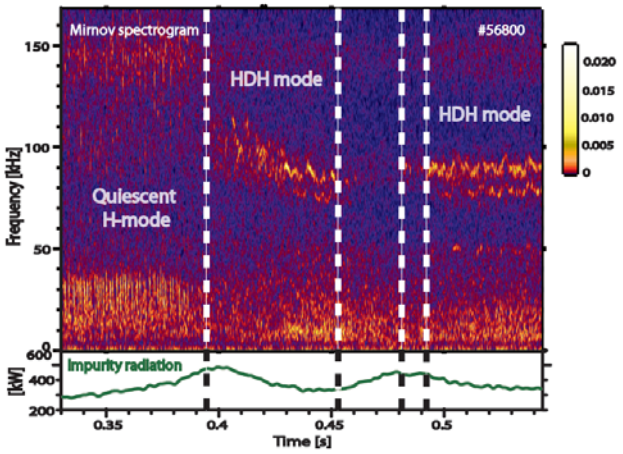

Fig. 1. Spectrogram of the magnetic fluctuations measured by a Mirnov coil for the Quiescent H-mode and HDH phase showing the presence of a quasi-coherent mode. The corresponding impurity radiation is indicated as well.

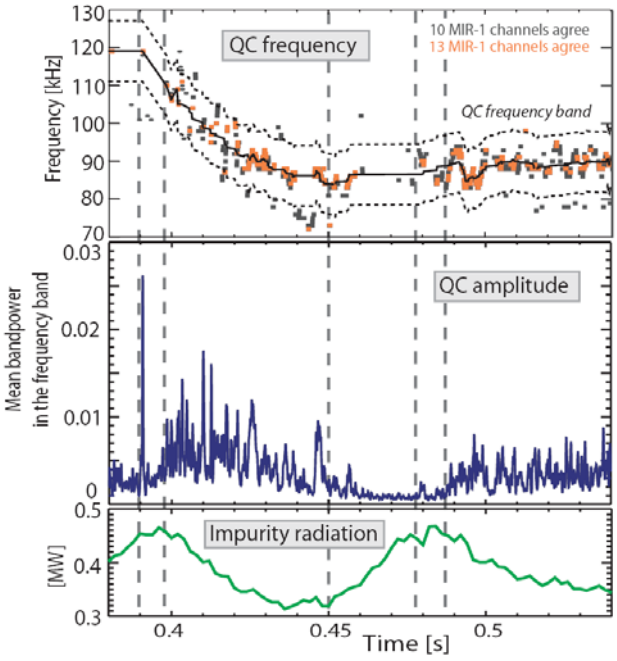

Fig. 2. Frequency band (dotted lines) and QC amplitude (defined as the mean normalized bandpower for the given frequency band for the 16 poloidal Mirnov coil array. The corresponding impurity radiation is indicated as well.

mode appears with its frequency sweeped down from about 120 kHz to 90 kHz, and the impurity radiation decreases corresponding to an outward flux of impurities. Bolometer tomography confirms that the radiation profile becomes strongly localized to the edge in the HDH phase [2]. At around 0.455-0.48 s the mode's amplitude drops an order of magnitude whereas the impurities start to accumulate anew and the radiation increases. This phase is then followed by a stable HDH phase with the QC mode reappearing at 90 kHz. A subsequent accompanying oscillation is present as well around 78 kHz, its presence is however not correlated with the impurity behaviour. For a quantitative comparison between radiation and the QC mode amplitude first, the frequency of the QC mode is obtained from a 16 channel poloidal Mirnov array by determining the frequencies present in at least a preset (10 and 13) number of Mirnov coil signals. The QC amplitude is then defined as the mean of 16 normalized bandpower signals [**5**] in the narrow frequency band containing the QC frequency obtained from the 16 Mirnov coil signals. The frequency band, QC amplitude and impurity radiation is shown in Fig. 2. The clear correlation between the QC mode amplitude and the radiation is obvious. The strong amplitude modulation of the QC mode can also be seen.

Determination of the mode number has been attempted from three poloidal Mirnov coil arrays (16, 8 and 8 channels respectively) by time-windowed Fourier decomposition of the signals and analysing the relative phase shift of the fluctuations. No poloidal mode number (m<6) could be obtained, indicating a higher value than what the limited number of Mirnov channels could resolve. A reciprocating probe housing two poloidal field pick-up coils (MRCP), based on the concept of Snipes et al [**6**], has been inserted into the plasma measuring the radial decay of the magnetic field perturbations along the distance to the separatrix. As shown in Fig. 3., the amplitude of the mode falls off rapidly, in about 2 cm-s, with the distance from the separatrix with an exponential decay length of k_r~2.82 (±0.78) cm^{-1} and k_r~ 3.18 (±0.79) cm^{-1} respectively for the 90 kHz and 110 kHz QC modes. By assuming a field aligned perturbation and using the Laplace equation outside the fluctuating current layer (method described in [**6**]) $k_r \approx k_{pol}$ (as $k_{tor} \sim k_{pol} \cdot 0.037$ can be neglected). Thus using this rapid radial decay of the amplitude a rough estimate of the poloidal mode number of m ~ 40 is obtained. This corresponds to roughly n~20.

In order to get information on the driving force of the QC modes, the end phase of the discharge is studied in detail. Fig. 4 shows main plasma parameters at and after the shut down of the NBI heating (at 0.9s). Spectrogram of the Mirnov coil signal is shown as well, including the corresponding amplitudes for the QC mode at 90 kHz and the second MHD mode at 78 kHz. Two back-transitions can be observed, first after about 5 ms the impurities start to accumulate indicated by the increase of the radiation power as the plasma transitions back from HDH to H-mode. At about 10 ms the plasma goes through a second transition, i.e. an H-L back-transition indicated by

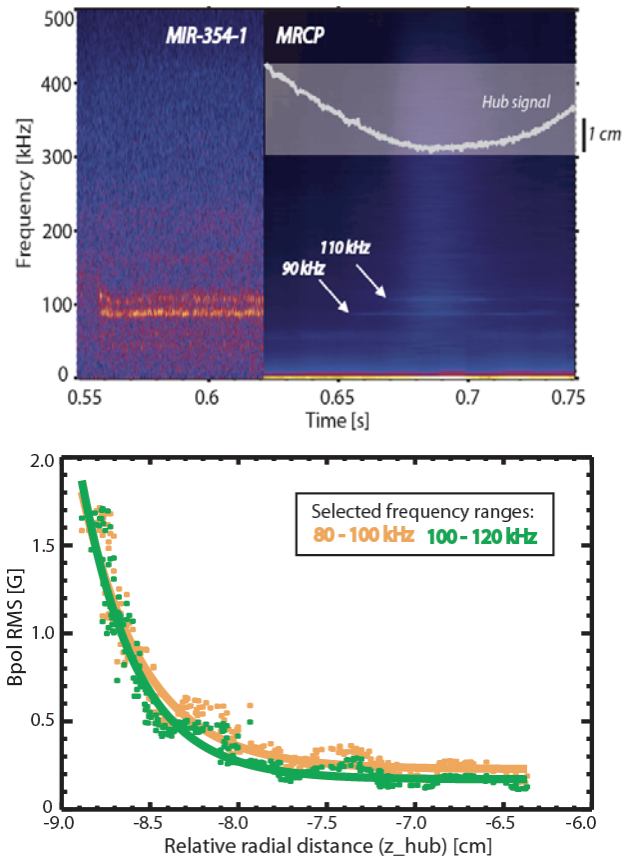

Fig. 3. (a) Spectrogram of the magnetic fluctuation measured by the high resolution Mirnov coil array and the MRCP coil including the Hub signal showing the relative distance of the MRCP coil to the separatrix (#56172). (b) Radial decay of the magnetic fluctuations measured by the MRCP probe in the frequency range of the QC modes respectively.

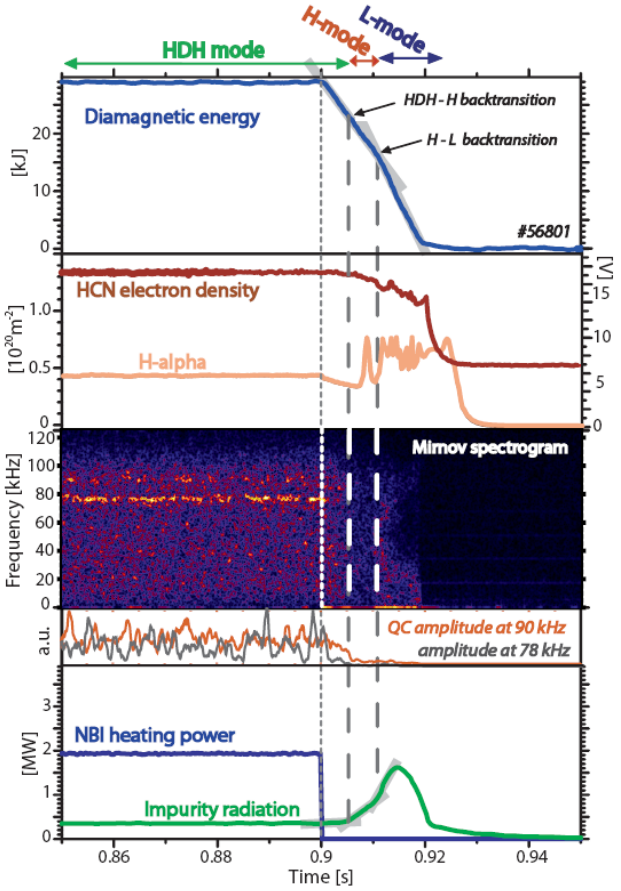

Fig. 4. Overview of the global parameters and Mirnov coil spectrogram including the amplitudes of the two MHD modes present in the discharge (#56801).

the change in the diamagnetic energy, H-alpha signal and the impurity radiation (a single ELM can be seen in the H-alpha signal before). By studying the disappearance of the MHD modes, an indication at their driving forces can be obtained. The QC mode at 90 kHz disappears about 5 ms after the shut down of the NBI in correlation with the HDH-H mode back-transition, indicating that it could be a pressure-gradient driven mode, whereas the second MHD mode at 78 kHz disappears rapidly, in only about 1-2 ms, indicating that it could have a different drive.

QC modes are not the only MHD oscillations present in the HDH regime. They are occasionally accompanied by low (LFO) and high (HFO) frequency oscillations. LFOs are oscillations with principle frequencies below 50 kHz often with higher harmonics detected by Mirnov coils, H-alpha diagnostic and Langmuir probes. These modes are not unique for the HDH phase, are often present in Quiescent H-mode as well, and do not correlate well with the impurity accumulation. HFOs are, on the other hand, observed in HDH regimes with frequencies of 250-350 kHz. They are detected by high resolution 1 MHz) Mirnov coil signals operated only in a relatively short time window, thus its relation to the impurity transport or more information on these modes could not be obtained. Preliminary analysis shows that both these low and high frequency oscillations are accompanied by quasi-coherent modes, whereas the amplitude of the QC modes seem to decrease in the presence of HFOs.

The detection and localisation of the QC modes remains an open question. It is still unresolved whether these modes are present in all HDH phases. The investigations are based on three poloidal arrays of Mirnov coils (16 channels sampled at 350 kHz, two 8 channel arrays at 1 MHz for limited time intervals) for given time interval and a single Mirnov channel at 250 kHz available throughout the discharge. Fig. 5. shows the setup of the MIR-1 16 channel poloidal Mirnov array and the magnetic reconstruction of the discharge series shown in Fig. 1,2 and 4.

At present, the modes are only detected in the magnetic fluctuations measured by Mirnov coils, as other diagnostics fail to measure the needed frequency regime and location due to the very high densities. The Lithium Beam Emission Spectroscopy did not detect these modes in the SOL, thus the location of these modes is thought to be inside the separatrix, presumably in the pedestal area. This is also supported by the fact that the QC mode frequency appears to be extremely sensitive to small changes in the rotational transform, therefore it is probably localized to a narrow radial region in the pedestal.

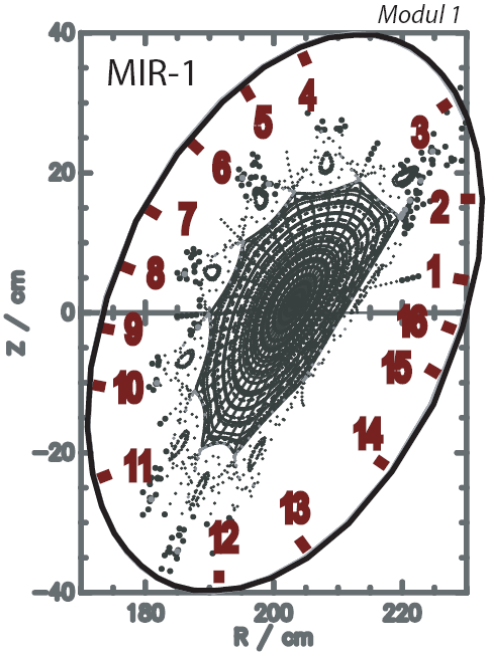

Fig. 5. Setup of the 16 poloidal Mirnov coil array and magnetic reconstruction of flux surfaces (#56801).

The universality of the QC mode is tested by analysing specific parameter scan, such as density scans for given heating powers (1, 2 MW NBI), magnetic configurations (different divertor configurations and iota values) and isotope plasmas (Hydrogen or Deuterium). An example is shown in Fig. 6. for 2 MW NBI, Deuterium plasma discharges at an iota value of 0.55. The mean coherence between Mirnov coil signal pairs is plotted for a normal confinement phase (n_e= $2.25 \cdot 10^{20}$ m^{-3}) and an HDH phase (n_e= $2.38 \cdot 10^{20}$ m^{-3}), just before and just after the density threshold of the 2 MW NBI HDH regime. At the HDH phase, modes are present appearing to be QC modes. The universality of the QC modes is, however, still unresolved. It should be noted that detection can be clearly hampered by the high mode numbers and small plasma sizes. In large plasmas (increase of 2cm in the plasma minor radius compared to standard configurations, shown in Fig. 1,2,4) a clear behaviour of QC modes is observed. They are present in and through all HDH phases showing remarkable correlation to the impurity radiation.

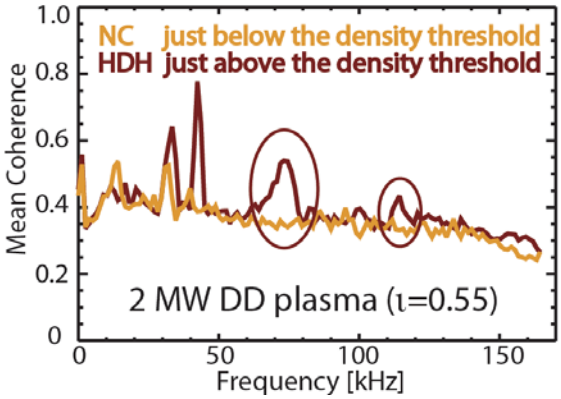

Fig. 6. Mean coherence between pairs of mirnov coil signals of two discharges in normal confinement and the HDH phase, just below and above the density threshold for the HDH regime respectively. The QC mode peaks are circled.

3. Conclusion

Quasi-coherent modes found in the HDH regime are high mode number (m~40), high frequency (f~50-150 kHz), and possibly pressure-driven oscillations that show strong amplitude modulation and correlation to the impurity radiation. At this time, no definite answer can yet be given, whether the QC mode is the mechanism responsible for the enhanced impurity transport in the HDH regime or it is a by-product of the real mechanism. The strong correlation, however, makes it a promising candidate. Further work is under way to deepen the physical understanding of this mode. At the Alcator C-Mod tokamak, similar QC modes are known to be responsible for the impurity transport in the ELM-free, stable, high density H-mode regime, the Enhanced D-alpha (EDA) H-mode. This prompts a careful comparison of the QC modes in the two regimes to gain more insight into the nature of these modes.

References

[1] K. McCormick *et al*., Phys. Rev. Lett. **89**, 015001 (2002).
[2] M. Hirsch *et al*., Plasma Phys. Control. Fusion **50** (5), 1-2004 (2008)
[3] A. Mazurenko *et al*., Phys. Rev. Lett. **89**, 225004 (2002).
[4] M. Greenwald *et al*., Phys. Plasmas **6**, 1943 (1999).
[5] G. Pokol, *et al*., Plasma Phys. Control. Fusion **49,** 1392 (2007)
[6] Snipes *et al*., Plasma Phys. Control. Fusion **43**, L23-L30 (2001)

Proceedings of ITC18, 2008

A closed divertor configuration for reduction of the heat load and efficient particle control for helical fusion reactors

Mamoru Shoji, Masahiro Kobayashi, Suguru Masuzaki, Akio Sagara, Hiroshi Yamada, Akio Komori and LHD Experimental Groups

National Institute for Fusion Science, 322-6 Oroshi-cho, Toki 509-5292, Japan

An innovative closed helical divertor concept is proposed for reduction of a heat load on the divertor plates and efficient particle control/pumping. The closed divertor configuration is investigated by a neutral particle transport simulation code coupled with a one-dimensional plasma fluid analysis on the divertor legs for a helical fusion reactor in which the geometry of the plasma and the magnetic field line configuration is same as that in the large helical device (LHD). The closed divertor configuration practically utilizes intrinsic three-dimensional magnetic field line configurations in the plasma periphery (an ergodic layer and divertor legs). The divertor configuration is optimized to an inward shift magnetic configuration in which the best energy confinement time has been achieved, a highly ergodized magnetic field line structure is formed in the inboard side of the torus, and the neutral density there is higher than that in the other region in the LHD vacuum vessel. It means that the divertor configuration is compatible with good main plasma confinement, effective divertor heat load reduction and efficient particle control/pumping from the inboard side. The analysis in this closed helical divertor configuration shows many advantageous over that in the other divertor concepts.

Keywords: neutral particle transport simulation, closed divertor, helical fusion reactor, plasma fluid analysis, ergodic layer, particle control, plasma periphery, LHD.

1. Introduction

The most critical issue for realizing fusion reactors is reduction of a heat load on the divertor plates with efficient particle control in the plasma periphery. For solving this issue, closed divertor configurations are designed and investigated in many plasma confinement devices. A new innovative closed helical divertor configuration which practically utilizes intrinsic magnetic field line structures in the plasma periphery (ergodic layer and divertor legs) in helical systems can solve the above critical issues.

Recent plasma experiments in the Large Helical Device (LHD) demonstrate that control of the peripheral plasma density is an important factor for achieving super dense core (SDC) plasmas [1]. The closed helical divertor configuration can contribute to sustaining the SDC plasmas by active pumping of neutral particles in the plasma periphery. An operational regime for sustaining the SDC plasma can propose a more attractive operational scenario in a helical fusion reactor with significant reduction of a heat load on the divertor plates.

In this paper, the neutral particle density profile and a heat load on the divertor plates in the optimized closed helical divertor configuration for a helical fusion reactor is investigated by a three-dimensional neutral particle transport simulation code coupled with a one-dimensional plasma fluid analysis on the divertor legs. Many advantages of the closed helical divertor configuration over the other divertor concepts are also mentioned.

2. Magnetic field line structures in the LHD plasma periphery

The LHD is the largest super-conducting helical device [2]. The magnetic configuration for plasma confinement is produced by external two twisted helical coils and three pairs of circular poloidal coils, forming helically twisted plasma ($\bullet/m$=2/10, where $\bullet$ and m are the polarity and the toroidal field period). Non-axsymmetric magnetic components by the helical coils produce three-dimensionally complicated magnetic field line

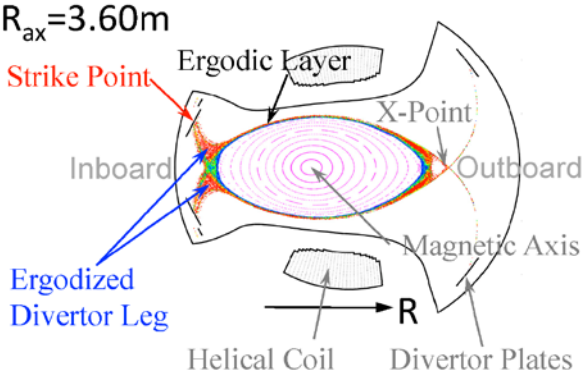

Fig.1 Poincare plots of magnetic field lines in the present open divertor case.

author's e-mail: shoji@LHD.nifs.ac.jp

structures (ergodic layer) in the plasma periphery in which the connection length of the magnetic field lines reaches to several km. These magnetic field lines are bundled and directly connected to the divertor plates at strike points along divertor legs on which the connection length is only a few meter. The radial position of the magnetic axis is flexibly controlled by changing the coil current in the poloidal coils.

Figure 1 shows the Poincare plots of magnetic field lines in the present open divertor case in an inward shift magnetic configuration (R_{ax}=3.60m) on a poloidal cross section where the plasma is horizontally elongated. The Poincare plots indicate that most of the magnetic field lines in the ergodic layer are bundled into the divertor legs in the inboard side of the torus with highly ergodized magnetic field line structure, indicating that most of the strike points (neutral gas source) locate in the inboard side in this magnetic configuration.

3. Design of an optimized closed helical divertor configuration

An optimized closed helical divertor configuration has been designed by using a fully three-dimensional neutral particle transport simulation code (EIRENE) coupled with a one-dimensional plasma fluid analysis on the divertor legs [3]. A plan of the three-dimensional geometry of the closed divertor components viewed from an outboard side of the torus is illustrated in Figure 2. The closed divertor consists of the following four main components: a V-shaped dome, slanted divertor plates, back plates and target plates. These four components contribute to concentration of the position of the strike points in the inboard side and enhancement of the neutral particle density there. Pumping ducts are placed behind the dome for particle pumping form the inboard side. An analysis by the neutral particle transport simulation predicts that enhancement of the neutral pressure by more than one order of magnitude compared to that in the present open divertor configuration [4].

Figure 3 is the Poincare plots of the magnetic field lines in the plasma periphery including a particle diffusion effect for the inward shift magnetic configuration. The particle diffusion effect (D~0.1m^2/s) is necessary for explaining the experimental results of the toroidal/poloidal distribution of the heat load on divertor plates measured with thermo-couples embedded in the divertor plates [5]. The poloidal cross section of the closed divertor components is also illustrated in this figure. The plasma wetted area on the divertor plates is enlarged in this closed divertor configuration due to the highly ergodized divertor legs in the inboard side of the torus, which contributes to

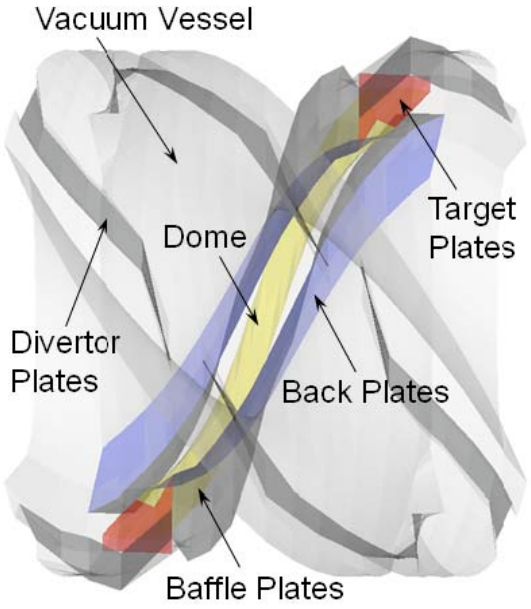

Fig.2 Three-dimensional geometry of the closed divertor configuration planned in LHD.

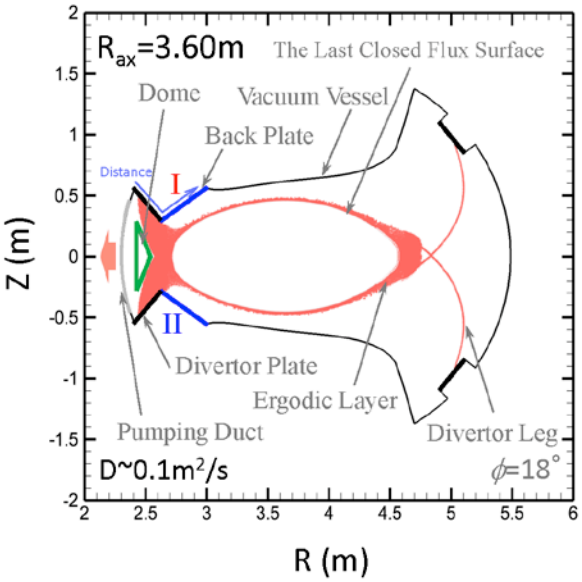

Fig.3 Poincare plots of the magnetic field lines including a particle diffusion effect in the closed divertor case.

strong reduction of the heat load on the divertor plates. This divertor configuration has the following four advantages over other closed divertor concepts [6]:

1. The highly ergodized magnetic field line structure on inner divertor legs extends the plasma wetted area on the divertor plates, which can be effective for mitigation of the heat load on the divertor components. The plasma on the divertor legs effectively prevents the outflow of the neutral particles from the divertor region to the main plasma due to ionization of neutral particles on the ergodized divertor legs.
2. The curved divertor legs toward the inboard side of the torus are also favorable for efficient particle

control/pumping from the inboard side. This is because most of neutral particles and impurities released from the slanted divertor plates directly reach to the pumping ducts through the space between the V-shaped dome and the inner vacuum vessel.

3. The ergodic layer functions as a shield against impurity penetration, which has been experimentally confirmed by comparing the measurements of carbon emission and the calculations by a three-dimensional plasma fluid code (EMC3-EIRENE) [7, 8]. The long connection length of the magnetic field lines in the ergodic layer contributes to cooling down the plasma temperature in the periphery.
4. Most of the strike points (about 80%) are directly connected to the divertor and the target plates in the inboard side for the inward shift magnetic configuration, which is favorable for efficient neutral particle control. This is because neutral particles are pumped out from the inboard side with no interference with plasma heating and diagnostic systems which have to be installed in outboard side of the torus.

4. Neutral particle transport analysis in the closed divertor configuration

The neutral particle transport simulation code has been applied to calculate the neutral density profile in the closed divertor region. In this simulation, trajectories of many test particles (representative of neutral particles) are traced in a three-dimensional grid model. We constructed a model for simulating a helical fusion reactor in which the shape of the plasma/vacuum vessel and the closed divertor components is identical to that planed in LHD. The size of the geometry is linearly extended to a Force Free Helical Reactor (FFHR) size (R_0=14.0m) from the LHD size (R_0=3.9m), where R_0 means the major radius of the device center [9]. Some closed divertor components (the V-shaped dome and the target plates) are approximated as assemblies of triangular plates in this model. Because of the arbitrary shape of the two components which crosses over toroidal sections, these components are included in the model by using a function 'additional surface' implemented in the code. The entrance of the pumping duct is set on the vacuum wall in the inboard side of the torus (behind the V-shaped dome). A special surface is introduced for simulating the entrance of the duct which absorbs test particles with a probability satisfying a predefined pumping speed there. Two surfaces at the both toroidal ends of the model are treated as a periodic one on which the position of an injected test particle are moved to another surface, and the direction of the particle is rotated at the one-toroidal pitch angle (36°) on the machine axis.

The trajectories of the test particles are determined by a Monte-Carlo method including various atomic/molecular processes in pasmas. Some parameters of neutral particles released from divertor plates are determined by using a database on plasma-wall interactions calculated by the TRIM code. We regard the surface of all vacuum components in the model as carbon. The particle reflection coefficient of the vacuum components is set to be 1.0 (no particle absorption) for modeling a steady state plasma discharge operation. The absorption probability of the special surfaces at the entrance of the duct is set to be 0.01 which provides a reasonable pumping rate (~72 m^3/s) for the helical fusion reactor.

The particle source profile on the divertor/target plates is obtained from the calculations of plasma parameters on the divertor legs. The parameter profiles are calculated by solving one-dimensional plasma fluid equations of three invariances (plasma density, momentum and energy) along the magnetic field lines on the divertor legs. The equations are solved under the boundary condition between the outer edge of the ergodic layer and the upstream of the divertor legs for satisfying the Bohm criterion on the divertor plates [10]. The parameter profiles are determined by an iteration process with the calculation of neutral particles by the neutral transport simulation.

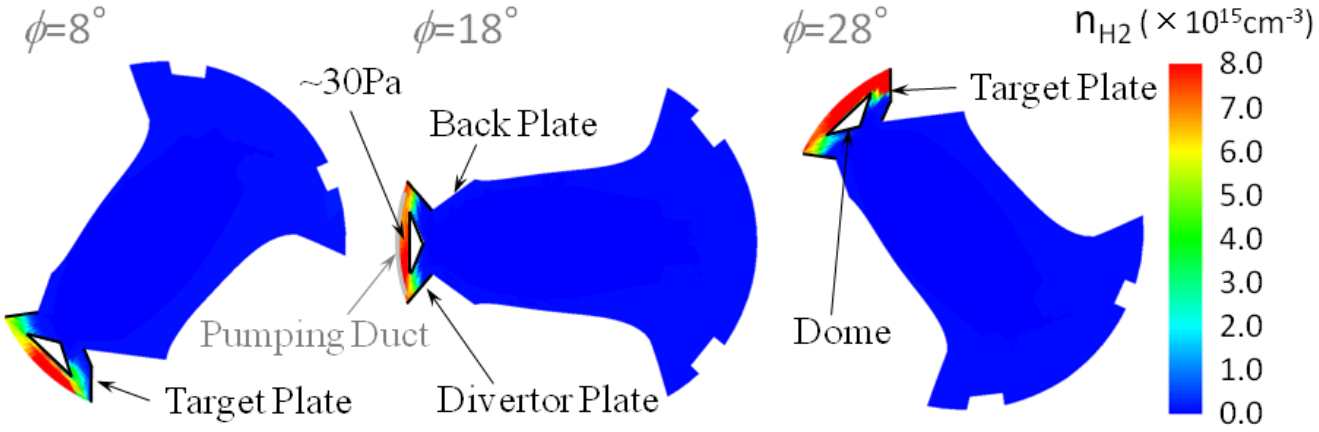

Fig.4 Calculations of the three poloidal cross sections of the density profile of neutral hydrogen molecules for the closed divertor configuration in a helical fusion reactor case.

The plasma parameter profiles inside of the ergodic layer are calculated by the EMC3-EIRENE code for the FFHR (no divertor leg version, P_{output}=284MW, T_e^{LCFS}~400eV, n_e^{LCFS}~1×10^{20}m^{-3}, Γ_{output}=1.6×10^{6}A), where P_{output} is the total output power from the ergodic layer, T_e^{LCFS}, n_e^{LCFS} are the electron temperature and the plasma density at the last closed flux surface, respectively, and Γ_{output} means the total current of the plasma flow at the upstream of the divertor legs [11].

When the plasma temperature at a position on magnetic field lines in the divertor legs equals to nearly zero for solving the three differential equations, we regarded that the plasma is fully dissipated and recombined by the background neutral particles at the position. It is assumed that a volume source which equals to that of the dissipated plasma is formed there. The heat load onto the divertor plates is calculated by plasma parameters at the front of the plates including the effect of the plasma sheath. Conversion of the calculations of the plasma parameter profiles along the divertor legs to the volume averaged values in the three-dimensional grid model is based on a procedure adopted in a track length estimator.

5. Calculation of the neutral density profile and a heat load distribution on the divertor plates

Figure 4 gives the calculation of the three poloidal cross sections of the density profile of neutral hydrogen molecules in the closed divertor configuration. The density of hydrogen molecules at the front of the pumping duct is about 7×10^{15}cm^{-3} (~30Pa). Local formation of the high neutral pressure there contributes to mitigation of requirements for the vacuum pumping system in the helical fusion reactor. The calculation shows that most of neutral particles are ionized in the divertor legs. Ionization in the ergodic layer near the X-points is very low (about 2% of the neutral particles released from the divertor plates). It indicates that plasmas produced by the ionization of neutral particles released from the divertor plates are almost recycled in the inner divertor region. The highly ergodized divertor legs in the inboard side contribute to effective ionization of the neutral particles in this region.

Figure 5 indicates the calculated profile of the plasma density on a poloidal cross-section where the plasma is horizontally elongated. The plasma density at the front of the divertor plates in the inboard side is significantly low. A high density and low electron temperature plasma (n_e>8×10^{13}cm^{-3}, T_e<0.1eV) is formed at the upstream on the inner divertor legs by strong interactions between the plasma and neutral particles released from the divertor plates. This low electron temperature is effective for enhancing plasma recombination processes on the divertor legs, which leads to strong reduction of head load on the divertor plates. The heat load on the divertor components is

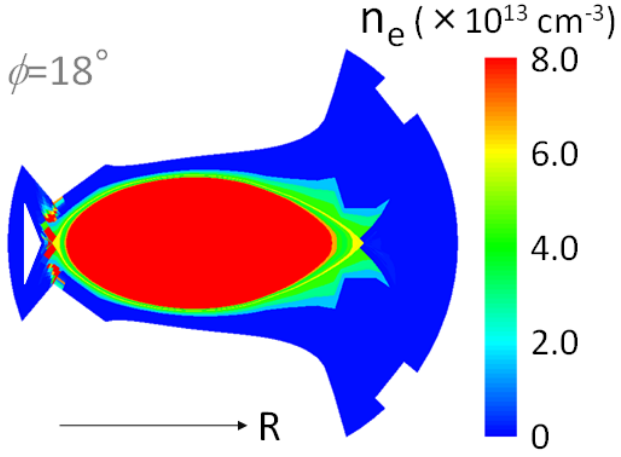

Fig.5 Poloidal cross-section of the calculated plasma density in the closed divertor case.

estimated to be less than a few MW, which is due to a combined effect of the large plasma wetted area (~600m^2), ion energy loss by ionization of high neutral particle density in the inboard side, plasma recombination process on the divertor legs, and formation of the low plasma temperature in the ergodic layer.

6. Summary

An innovative closed helical divertor concept for a helical fusion reactor is proposed for an effective particle control/pumping with reduction of the head load on the divertor plates with keeping good main plasma energy confinement in the inward shift magnetic configuration. The neutral particle transport simulation with a plasma fluid analysis of the divertor legs predicts high neutral density at the entrance of the pumping duct (behind the dome), which is enough for efficient particle pumping from the inboard side of the torus. The simulation also shows reduction of the heat load on the closed divertor components by combined effect of ion energy loss by ionization and recombination, large plasma wetted area, and low plasma temperature in the ergodic layer.

References

[1] N. Ohyabu *et al.*, Phys. Rev. Lett. **97**, 05502 (2006).
[2] O. Motojima *et al.*, Nucl. Fusion **40**, 559 (2000).
[3] D. Reiter *et al.*, Fusion Sci. Technol., **47**, 172 (2005).
[4] M. Shoji *et al.*, Plasma Fusion Res. **3**, S1038 (2008).
[5] S. Masuzaki *et al.*, Nucl. Fusion **42**, 750 (2002).
[6] R König *et al.*, Plasma Phys. Control. Fusion **44**, 2365 (2002).
[7] Y. Feng *et al.*, Plasma Phys. Control. Fusion **44**, 611 (2002).
[8] M. Kobayashi *et al.*, Plasma Fusion Res. **3**, S1005 (2008).
[9] A. Sagara *et al.*, Nucl. Fusion **45**, 258 (2005).
[10] P. C. Stangeby, *The plasma boundary of magnetic fusion devices* (Institute of Physics Publishing, Bristol and Philadelphia, 2000) p.423.
[11] M. Kobayashi *et al.*, Fusion Sci. Technol., **52**, 566 (2007).

Proceedings of ITC18, 2008

1D fluid model of LHD divertor plasma and hydrogen recycling

Gakushi KAWAMURA[1)], Yukihiro TOMITA[1)], Masahiro KOBAYASHI[1)],and David TSKHAKAYA[2,3)]

[1)]*National Institute for Fusion Science, Gifu 509-5292, Japan*

[2)]*Association Euratom-ÖAW, Institute of Theoretical Physics, University of Innsbruck, Technikerstrasse 25/II, Innsbruck A-6020, Austria*

[3)]*Permanent address: Institute of Physics, Georgian Academy of Sciences, 380077 Tbilisi, Georgia*

One dimensional plasma and neutral models of the divertor plasma in Large Helical Device is presented. The plasma is described by stationary fluid equations for electron and ion. The atomic processes such as dissociation of hydrogen molecules released from the divertor plate, ionization of hydrogen atoms, charge exchange and recombination are included in equations of neutrals. This model is intended to be employed in an integrated simulation where an equilibrium of the upstream plasma and plasma-surface interactions at the divertor plate are solved in different numerical codes separately. From the computational point of view, the numerical code for the divertor plasma is developed for 1D flux tube where the boundary conditions of both ends are specified. The calculation time is less than one second and reasonably short to use in future integrated simulations. In the results, interactions between plasma and neutrals and dependence of the energy loss on the plasma density are studied. In low density case, the energy is lost through ionization and charge exchange but the total amount of the loss is small and the impurity loss is negligibly small. In high density, or high recycling case, the ionization loss and impurity cooling increases much larger than the charge exchange loss and causes the drop of the heat flux at the divertor plate.

Keywords: LHD, divertor, fluid, neutral, recycling

1 Introduction

The Large Helical Device (LHD) [1] is a heliotron / tersatron type device with helical divertors. The LHD plasma has an ergodic layer [2] outside the core plasma. The divertor plasma is connected to the ergodic layer and parallel flow along the magnetic field is dominant there. The plasma profiles such as density and temperature determine the motion and the charge state of impurities. Therefore, physical understandings of the divertor plasma and its modeling are important issues in the LHD boundary plasmas.

In this paper, we present plasma and neutral models in the divertor plasma to determine the plasma profiles from input parameters such as heat flux coming from the ergodic layer and the plasma density at the upstream boundary. The model presented here is intended to be employed in our future studies as a divertor leg model to connect the following two simulation codes; EMC3 code [2] for the ergodic layer and ERO code [3] for the plasma-surface interactions at the divertor. The former code solves fluid equations to obtain equilibrium plasma profiles in the stochastic magnetic field and the latter solves the equations of motion for impurity particles to obtain the sputtering yield, time evolution of surface conditions and impurity transport near a target plate. In order to avoid a numerical difficulty arising from the strong magnetic shear in the LHD boundary plasma and to keep the amount of the computational resources in reasonable level, we developed 1D model along the magnetic field line, i.e. a flux tube model.

The plasma fluid equations are described in Sec. 2.1. They include interaction with neutrals and impurity cooling [4–7]. The differences of our model from these models are the neutral equations discussed in Sec. 2.2, which includes atomic processes such as dissociation and ionization of hydrogen molecules and atoms. In Sec. 3, comparisons with our previous model [8] and discussion of heat flux and energy loss are given. Finally in Sec. 4, conclusions are presented.

2 Divertor plasma and neutral models

2.1 Fluid equations of plasma

We use Braginskii-type two fluid equations [9] to describe the divertor plasma. Since 1D fluid equations along the magnetic field and the method of numerical solution was reported in the previous work [8], we summarize them briefly here. We denote the plasma density, velocity, electron and ion temperatures and electrostatic potential by $n(s)$, $v(s)$, $T_e(s)$, $T_i(s)$ and $\phi(s)$, respectively. The position along the magnetic field is described by s and has zero value, $s = 0$, at the upstream boundary and the connection length, $s = l_c$, at the entrance of the magnetic presheath [10]. The four conservation equations of density, momentum and temperatures and Ohm's law, or electron momentum conservation, are given by

$$\frac{dnv}{ds} = S_n, \qquad (1)$$

author's e-mail: kawamura.gakushi@nifs.ac.jp

$$\frac{d}{ds}\left[m_{\rm i}nv^2 + n\left(T_{\rm e}+T_{\rm i}\right)\right] = S_{\rm p}, \quad (2)$$

$$\frac{d}{ds}\left[\frac{5}{2}nvT_{\rm e} - \kappa_{\rm e0}T_{\rm e}^{5/2}\frac{dT_{\rm e}}{ds}\right] = env\frac{d\phi}{ds} - \frac{3m_{\rm e}n}{m_{\rm i}}\nu_{\rm eq}(T_{\rm e}-T_{\rm i}) - Lr_{\rm imp}n^2 + S_{\rm Ee}, \quad (3)$$

$$\frac{d}{ds}\left[\frac{m_{\rm i}nv^3}{2} + \frac{5nvT_{\rm i}}{2} - \kappa_{\rm i0}T_{\rm i}^{5/2}\frac{dT_{\rm i}}{ds}\right] = -env\frac{d\phi}{ds} + \frac{3m_{\rm e}n}{m_{\rm i}}\nu_{\rm eq}(T_{\rm e}-T_{\rm i}) + S_{\rm Ei}, \quad (4)$$

$$\frac{1}{n}\frac{dnT_{\rm e}}{ds} + 0.71\frac{dT_{\rm e}}{ds} - e\frac{d\phi}{ds} = 0 \quad (5)$$

where the electron and ion mass, carbon impurity ratio, the heat conduction coefficients and temperature equilibration coefficient were denoted by $m_{\rm e}$, $m_{\rm i}$, $r_{\rm imp}$, $\kappa_{\rm i0} = 1.2\times10^{69}$ [W/mJ$^{7/2}$], $\kappa_{\rm e0} = 5.0\times10^{67}$ [W/mJ$^{7/2}$] and $\nu_{\rm eq} = 6.9\times10^{17}nT_{\rm e}^{3/2}$ [11]. The source terms associated with neutrals in the right-hand side, i.e. $S_{\rm n}$, $S_{\rm p}$, $S_{\rm Ee}$ and $S_{\rm Ei}$, are discussed later in Sec. 2.2. The following conditions and relations are assumed in these equations; i) the temperature anisotropy time is negligibly short compared with the particle dwell time, i.e. $T_\perp = T_\parallel = T$, ii) ambipoler flow, i.e. $v_{\rm e} = v_{\rm i} = v$, iii) quasineutral condition, i.e. $n_{\rm e} = n_{\rm i} = n$.

In this paper, we use variables with subscripts '0' and '1' to indicate boundary values at $s = 0$ and $l_{\rm c}$, respectively. The plasma equations, Eqs. (1) – (5), are integrated numerically from the wall to the upstream boundary. Since our model is intended to be employed to connect different simulation codes at $s = 0$ and $l_{\rm c}$, the plasma density and heat flux at the upstream boundary are implemented as free parameters. The integral of the plasma equations, however, requires boundary values at $s = l_{\rm c}$ as initial values. Therefore we utilize the Newton's method to determine the initial values satisfying the density and heat flux at $s = 0$ and the following four conditions; i) equality of the Bohm criterion at $s = l_{\rm c}$, i.e. $v_1 = c_{\rm s} \equiv \sqrt{(T_{\rm e1}+T_{\rm i1})/m_{\rm i}}$, ii) potential $\phi_1 = 0$, iii) and iv) electron and ion heat fluxes at $s = l_{\rm c}$ determined by the sheath theory [8, 11].

2.2 Modeling of neutral particle

In order to describe interactions of plasma, hydrogen molecules and atoms, we choose five dominant reactions in the divertor plasma.

(d1) $\mathrm{H_2 + e^- \rightarrow 2H + e^-}$,
(d2) $\mathrm{H_2 + e^- \rightarrow H^+ + H + 2e^-}$,
(cx) $\mathrm{H + H^+ \rightarrow H^+ + H}$,
(iz) $\mathrm{H + e^- \rightarrow H^+ + 2e^-}$,
(rc) $\mathrm{H^+ + 2e^- \rightarrow H + e^-}$.

The fist and second reactions represent the dissociation of hydrogen molecule to atoms. The reaction (d2) consists of two reaction, $\mathrm{H_2 + e^- \rightarrow H_2^+ + 2e^-}$ and $\mathrm{H_2^+ + e^- \rightarrow H^+ + H + e^-}$, but the dissociation rate of $\mathrm{H_2^+}$ is relatively high and the particle speed of $\mathrm{H_2}$ is slow. Thus these two reactions are regarded as one reaction in this work. The last three reactions, (cx), (iz) and (rc), represent charge exchange, ionization and recombination, respectively. The rate coefficient of these reactions [12, 13] are denoted by $\langle\sigma_{\rm d1}v\rangle$, $\langle\sigma_{\rm d2}v\rangle$, $\langle\sigma_{\rm cx}v\rangle$, $\langle\sigma_{\rm iz}v\rangle$ and $\langle\sigma_{\rm rc}v\rangle$, respectively.

There are several types of expressions to obtain the neutral profiles; Monte Carlo simulation, kinetic equation, fluid equation and diffusion equation. Since the mean-free-path (MFP) of hydrogen atom, e.g. approximately 2 [m] for a typical neutral density 10^{19} [m^{-3}], is comparable to the plasma size and much longer than the neutral decay length [8]. Therefore the diffusion process is negligible in the divertor plasma and also the fluid equation of the neutral gas does not correctly describe the characteristics of the wide range of particle energy such as few eV of dissociation atoms and tens eV of charge exchange atoms. Therefore in this paper, we use simplified kinetic-type equations.

We classify the neutrals into four components; molecules released from the divertor plate, dissociated atoms from the molecules, charge exchange atoms and recombination atoms. The particle speed of each component is treated as a constant; $v_{\rm m}$, $v_{\rm d}$, $v_{\rm cx}$ and $v_{\rm rc}$, respectively. The density of each component is denoted by $n_{\rm m}$, $n_{\rm d}^{\pm}$, $n_{\rm cx}^{\pm}$ and $n_{\rm rc}^{\pm}$, respectively. The superscript '±' corresponds to two components with opposite direction, i.e. positive and negative velocity on s-coordinate. They have each characteristic temperature, or energy, determined from their sources. The molecule temperature $T_{\rm m}$ is same as that of the divertor plate. The temperature of dissociation atoms is determined from the Frank-Condon dissociation energy, i.e. $T_{\rm d} \sim 2.5[eV]$. The temperatures of charge exchange and recombination atoms, $T_{\rm cx}$ and $T_{\rm rc}$, are determined from the averages energy of the generated atoms by each processes over $s = 0$ to $l_{\rm c}$. The velocity of each component are calculated from corresponding temperature; $v_{\rm m} = \sqrt{T_{\rm m}/\pi m_{\rm i}}/\cos\varphi$, $v_{\rm d} = \sqrt{2T_{\rm d}/\pi m_{\rm i}}$, $v_{\rm cx} = \sqrt{2T_{\rm rc}/\pi m_{\rm i}}$ and $v_{\rm rc} = \sqrt{2T_{\rm cx}/\pi m_{\rm i}}$. The angle of the magnetic field measured from the surface normal on the divertor plate was denoted by φ and used to obtain the equivalent velocity of molecules. This conversion is due to the existence of the difference between the directions of plasma and neutral flows.

The particle conservation equations of neutrals are given by

$$-v_m\frac{dn_{\rm m}}{ds} = \left(\langle\sigma_{\rm d1}v\rangle + \langle\sigma_{\rm d2}v\rangle\right)n_{\rm m}n, \quad (6)$$

$$\pm v_{\rm d}\frac{dn_{\rm d}^{\pm}}{ds} = \left(2\langle\sigma_{\rm d1}v\rangle + \langle\sigma_{\rm d2}v\rangle\right)n_{\rm m}n - \left(\langle\sigma_{\rm iz}v\rangle + \langle\sigma_{\rm cx}v\rangle\right)n_{\rm d}^{\pm}n, \quad (7)$$

$$\pm v_{\rm H_{cx}}\frac{dn_{\rm cx}^{\pm}}{ds} = (1-r_{\rm pl})\frac{v_{\rm cx}\pm v}{2v_{\rm cx}}\langle\sigma_{\rm cx}v\rangle n_{\rm a}n - \left(\langle\sigma_{\rm iz}v\rangle + \langle\sigma_{\rm cx}v\rangle\right)n_{\rm cx}^{\pm}n, \quad (8)$$

$$\pm v_{\rm rc}\frac{dn_{\rm rc}^{\pm}}{ds} = (1-r_{\rm pl})\frac{v_{\rm rc}\pm v}{2v_{\rm rc}}\langle\sigma_{\rm rc}v\rangle n^2 - (\langle\sigma_{\rm iz}v\rangle + \langle\sigma_{\rm cx}v\rangle)\, n_{\rm rc}^{\pm} n, \quad (9)$$

where the total density of hydrogen atoms were denoted by $n_{\rm a} \equiv n_{\rm d}^{+} + n_{\rm d}^{-} + n_{\rm cx}^{+} + n_{\rm cx}^{-} + n_{\rm rc}^{+} + n_{\rm rc}^{-}$. Since the source of the hydrogen is the molecules released from the divertor plate, we use the boundary condition, $n_{\rm m1}v_{\rm m} = n_1 v_1/2$. The particle loss of generated hydrogen atoms was introduced as a constant ratio $r_{\rm pl}$ in Eqs. (8) and (9). We note that each equations, (7) – (9), consists of two equations for positive and negative velocities. The coefficients of the first terms in the right-hand side of Eqs. (8) and (9), $(v_{\rm cx} \pm v)/2v_{\rm cx}$ and $(v_{\rm rc} \pm v)/2v_{\rm rc}$, represent the momentum conservation in the charge exchange hydrogen atoms and ions. In order to conserve the total energy when $r_{\rm pl} = 0$, the temperature $T_{\rm cx}$ and $T_{\rm rc}$ are calculated as

$$T_{\rm cx} = \frac{\int_0^{l_{\rm c}} \left(T_{\rm i} + m_{\rm i}v^2/3\right)\langle\sigma_{\rm cx}v\rangle n_{\rm a} n\, ds}{\int_0^{l_{\rm c}}\langle\sigma_{\rm cx}v\rangle n_{\rm a} n\, ds}, \quad (10)$$

$$T_{\rm rc} = \frac{\int_0^{l_{\rm c}} \left(T_{\rm i} + m_{\rm i}v^2/3\right)\langle\sigma_{\rm rc}v\rangle n^2\, ds}{\int_0^{l_{\rm c}}\langle\sigma_{\rm rc}v\rangle n^2\, ds}. \quad (11)$$

The source terms in Eqs. (1) – (4) are given by

$$S_{\rm n} = \langle\sigma_{\rm d2}v\rangle n_{\rm m} n_{\rm e} + \langle\sigma_{\rm iz}v\rangle n_{\rm a} n_{\rm e} - \langle\sigma_{\rm rc}v\rangle n_{\rm i} n_{\rm e}, \quad (12)$$

$$S_{\rm p} = m_{\rm i}\langle\sigma_{\rm cx}v\rangle n_{\rm i}\left[\left(n_{\rm d}^{+} - n_{\rm d}^{-}\right)v_{\rm d} + \left(n_{\rm cx}^{+} - n_{\rm cx}^{-}\right)v_{\rm cx} + \left(n_{\rm rc}^{+} - n_{\rm rc}^{-}\right)v_{\rm rc} - n_{\rm a}v\right], \quad (13)$$

$$S_{\rm Ee} = -25e\langle\sigma_{\rm iz}v\rangle n_{\rm a} n, \quad (14)$$

$$S_{\rm Ei} = \frac{3}{2}\left(\langle\sigma_{\rm iz}v\rangle n_{\rm e} + \langle\sigma_{\rm cx}v\rangle n_{\rm i}\right)\left[\left(n_{\rm d}^{+} + n_{\rm d}^{-}\right)T_{\rm d} + \left(n_{\rm cx}^{+} + n_{\rm cx}^{-}\right)T_{\rm cx} + \left(n_{\rm rc}^{+} + n_{\rm rc}^{-}\right)T_{\rm rc}\right] + 4.3e\langle\sigma_{\rm d2}v\rangle n_{\rm e} n_{\rm m} - \langle\sigma_{\rm cx}v\rangle n_{\rm s} n_{\rm i}\left(\frac{3}{2}T_{\rm i} + \frac{1}{2}m_{\rm i}v^2\right). \quad (15)$$

3 Results and discussions

We modified the numerical code in Ref. [8] to solve the plasma equations (1) – (5) and the neutral equations (6) – (9) self-consistently. The plasma equations and neutral equations with negative velocity are integrated from the wall boundary, $s = l_{\rm c}$, and the neutral equations with positive velocity are integrated from the upstream boundary, $s = 0$. The integrals are carried out numerically by the fourth order Runge-Kutta method and the step width is changed adoptively. Since the plasma profiles and neutral profiles depend on each other, we obtain solutions by solving plasma and neutral equations iteratively. The total calculation time including the iterations is less than one second on an ordinary PC. Although the time is longer than that of the previous code [8], it is still reasonable for the integrated simulation in the future plan.

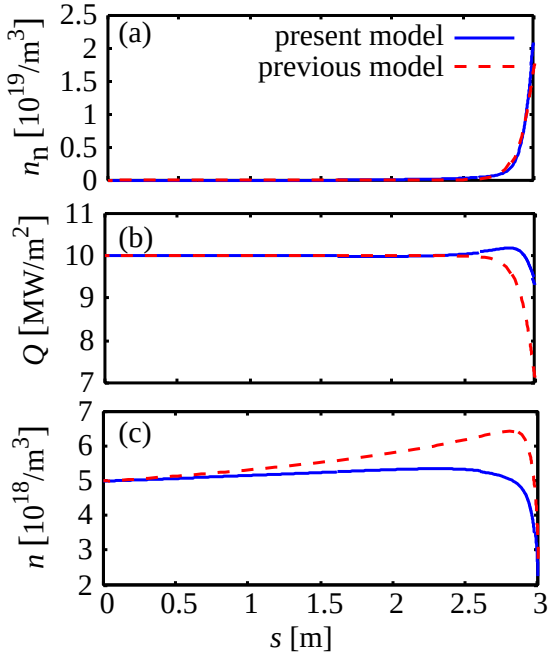

Fig. 1 (a) neutral density, (b) heat flux and (c) plasma density profiles obtained from the previous and present models.

Comparisons of the solutions between present and previous models are shown in Fig. 1. The plasma density and electron and ion heat fluxes at $s = 0$ were chosen as $n_0 = 5 \times 10^{18}$ [m^{-3}], $Q_{\rm e} = Q_{\rm i} = 5$ [MW/m^2]. Temperature of the hydrogen molecules, angle of the magnetic field, particle loss ratio and impurity ratio were $T_{\rm m} = 600$ [K], $\varphi = 80°$, $r_{\rm pl} = 0.2$ and $r_{\rm imp} = 3\%$, respectively. The global recycling coefficient was calculated as 84% from the particle fluxes at $s = 0$ and $l_{\rm c}$. The density profiles of neutrals, $n_{\rm n} = n_{\rm a} + n_{\rm m}$, in Fig. 1(a) were similar each other in this case. The heat flux Q of the previous model in Fig. 1(b), however, had lower value than that of the present one near the divertor plate. The reason of the difference is due to the overestimate of the energy loss by charge exchange in the previous one. A small peak in front of the wall was observed in the Q profile of the present model. It is caused by the interaction of the ion and neutral energy. High speed neutrals are generated through the charge exchange processes and their energy are transported by the neutral flow. The neutrals remaining in the plasma region are ionized and their energy returns to the plasma. Therefore the small peak represents energy transport by neutrals from the vicinity of the wall to $s \sim 2.7$ [m]. The overestimate of the plasma density in Fig. 1(c) is also caused by the overestimate of the energy loss, or underestimate of the ion temperature.

The heat fluxes at the divertor plate, $s = l_{\rm c}$, are shown as functions of the plasma density at $s = 0$ in Fig. 2(a). The electron, ion and total heat fluxes were denoted by $Q_{\rm e1}$, $Q_{\rm i1}$ and Q_1, respectively. The input heat flux is fixed to $Q_{\rm e0} = Q_{\rm i0} = 5$ [MW/m^2]. When the density is rela-

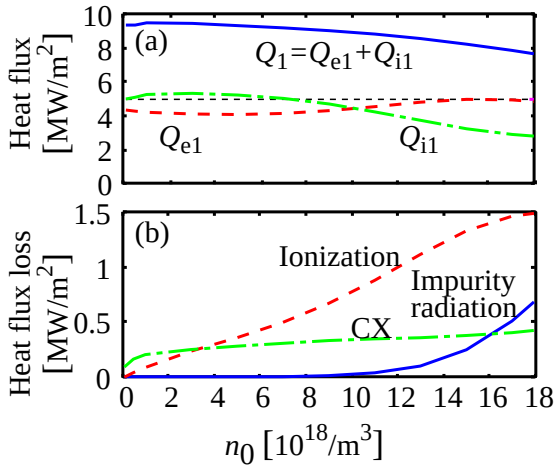

Fig. 2 (a) heat flux at the divertor plate and (b) heat flux loss as functions of plasma density at upstream boundary n_0. Electron, ion and total heat fluxes were denoted by Q, Q_e and Q_i.

tively low, e.g. $n_0 < 10^{19}$ [m^{-3}], almost all heat flux coming from the upstream boundary deposits on the divertor plate, while in the high recycling regime the heat flux decreases and especially the ion heat flux becomes half. The contributions of three main energy sinks to the heat flux are compared in Fig. 2(b). The largest energy loss is caused by radiation due to the electron impact ionization. The loss caused by ionization and impurity radiation increases in high recycling regime because the electron temperature decrease to about 10 [eV], while the charge exchange loss does not change. From above discussions we can identify the energy transfer channels. In the low recycling regime, $n_0 \sim 5 \times 10^{18}$ [m^{-3}], electron and ion energies are lost by ionization loss and charge exchange loss, respectively. The each amount of the loss is comparable and much smaller than the total heat flux coming from the upstream plasma. In the high recycling regime, $n_0 > 1 \times 10^{19}$ [m^{-3}], ionization and impurity losses increases and the plasma energy is lost through the electon channel mainly. The impurity cooling increases more rapidly than ionization for $n_0 > 1.5 \times 10^{19}$ [m^{-3}].

4 Conclusions

A fluid model of LHD divertor plasma and a neutral model were presented. The atomic processes such as dissociation and ionization of hydrogen molecules and atoms were included. We developed a numerical code which has boundary conditions relevant to code connections at the both end of the calculation region, i.e. $s = 0$ and l_c. The self-consistent solutions were obtained by iterative calculations of the plasma and neutral equations. The calculation time is less than one second and it is reasonably short for integrated simulation of future studies.

Comparisons of heat flux, neutral and plasma density profiles between the previous [8] and present models were carried out. Although the deviation of the neutral density was negligibly small, the heat flux and plasma density profiles changed significantly. By treating the interaction of energy between plasma and neutrals directly, the amount of energy loss due to the energetic neutral atoms are included correctly in the model, and thus the overestimate of the energy loss is improved.

The dependence of the heat flux on the plasma density were studied by using the code. In the low density case, the plasma loses its energy by ionization and charge exchange, but effect of the loss on the heat flux decrease is small. On the other hand in the high density, or high recycling case, the ionization loss and impurity cooling becomes large and the heat flux decreases by 20% when the plasma density at the upstream boundary is 1.8×10^{19} [m^{-3}]. We confirmed that the ion energy is transfered to electron and it is lost by ionization and impurity radiation.

In the paper, we employed constant impurity ratio. The dynamics of impurities is important to obtain the impurity profiles and to elucidate the role of the divertor plasma on the core plasma. Implementation of a fluid impurity model and the application of the model to the integrated simulation will be future issues.

Acknowledgments

The contribution of the last author was carried out under the European Fusion Development agreement, supported by the European Communities. The views and opinions expressed herein do not necessarily reflect those of the European Commission.

[1] N. Oyabu *et al.*, Nucl. Fusion, **34**, 387 (1994)
[2] M. Kobayashi *et al.*, J. Nucl. Mater., **363–365**, 294 (2007)
[3] A. Kirschner *et al.*, Nuclear Fusion, **40**, 989 (2000)
[4] P. C. Stangeby and J. D. Elder, J. Nucl. Mater., **196-198**, 258 (1992)
[5] K. Shimizu *et al.*, J. Nucl. Mater., **196-198** 476 (1992)
[6] Rajiv Goswami *et al.*, Phys. Plasmas, **8**, 857 (2001)
[7] Deok-Kyu Kim and Sanh Hee Hong, Phys. Plasmas, **12**, 062504 (2005)
[8] G. Kawamura, Y. Tomita, M. Kobayashi and D. Tskhakaya, *"1D fluid model of plasma profiles in the LHD divertor leg"*, to be published in J. Plasma Fusion Res. Ser.
[9] S. I. Braginskii, Rev. Plasma Phys., **1**, 205 (1965)
[10] D. Tskhakaya and S. Kuhn, Plasma Phys. Control. Fusion, **47**, A327 (2005)
[11] Peter C. Stangeby, *The Plasma Boundary of Magnetic Fusion Devices*, Institute of Physics Publishing (Bristol and Philadelphia 1999).
[12] R. L. Freeman and E. M. Jones, *Atomic Collision Processes in Plasma Physics Experiments*, Culham Laboratory, Abingdon, England, Report CLM-R 137 (1974).
[13] E. M. Jones, *Atomic Collision Processes in Plasma Physics Experiments*, Culham Laboratory, Abingdon, England, Report CLM-R 175 (1977).

Proceedings of ITC18,2008

First result on Z_{eff} Profile Analysis from Visible Bremsstrahlung Measurement for Different Density Profiles in LHD

Hangyu Zhou[1], Shigeru Morita[2], Motoshi Goto[2]

[1]*Department of Fusion Science, Graduate University for Advanced Studies, Toki 509-5292, Gifu, Japan*

[2]*National Institute for Fusion Science, Toki 509-5292, Gifu, Japan*

Visible bremsstrahlung emission has been measured using a optimized Czerny-Turner spectrometer newly installed on LHD. The bremsstrahlung emission profile has been successfully observed in some limited discharge conditions having no asymmetric strong edge bremsstrahlung emissions which are originated in the ergodic layer. Z_{eff} profiles are analyzed for peaked, flat and hollow density profiles as the first trial of the analysis. As a result, a flat Z_{eff} profile is obtained for all different density profiles. It indicates that the partial impurity pressure is basically constant against the plasma radius.

Keywords: Z_{eff} profile, visible bremsstrahlung, density profile

1. Introduction

Fuel dilution and enhanced radiation loss caused by impurity buildup are still one of serious problems in magnetic confinement fusion research. Impurity transport study becomes therefore important for understanding the impurity behavior and for improving plasma performance [1,2]. In Large Helical Device (LHD), a variety of electron density profiles such as peaked, flat and hollow profiles have been observed in different experimental conditions, which are quite different from the density profile usually seen in tokamaks, i.e., peaked profile. It is very interesting to study the impurity transport in such different density profiles. For the purpose full-vertical Z_{eff} profiles have been measured in LHD to obtain important information necessary for the impurity transport study, especially in plasma core region.

Visible bremsstrahlung emission has been measured with an optimized Czerny-Turner visible spectrometer [3] newly installed on LHD The instrument can entirely eliminate line emissions from the bremsstrahlung signal, which was one of serious problems in old bremsstrahlung measurement system with interference filter [4]. The new visible spectrometer system consists of 44 fiber array, an astigmatism-corrected Czerny-Turner visible spectrometer and a charge-coupled device (CCD) with vertical spatial resolution of 2.6cm and time resolution of 100ms. However, an asymmetric bremsstrahlung profile has been still observed after changing the diagnostic system. As a result of detailed data analysis, it was found that the asymmetric part of the signal originates in edge bremsstrahlung emission from thick ergodic layer. Fortunately, we could confirm that the lower half of the vertical bremsstrahlung profile had no influence from the edge emission in inwardly shifted magnetic configurations ($R_{ax} \leq 3.6$m) where the ergodic layer thickness is relatively thin. The local bremsstrahlung emission is calculated from chord-integrated signals after Abel inversion using elliptical magnetic surface with finite-β effect. The Z_{eff} profile is finally obtained with considering electron density and temperature profiles measured by Thomson scattering diagnostic [5]. In this paper the Z_{eff} profiles from LHD are presented in different density profile cases.

2. Experimental setup

The Czerny-turner visible spectrometer consists of a toroidal mirror, a flat mirror, two spherical mirrors and three gratings. A short focal length of 300mm is adopted to achieve a highly bright system. The three gratings of 120 (blaze: 330nm), 300 (500nm) and 1200 (200nm) grooves/mm are set in the turret. In the usual LHD experiments, the 300 grooves/mm grating is mainly used to observe wider wavelength range of 500nm to 600nm with relatively higher spectral resolution. The brightness of the 300 grooves/mm was very similar to the 120 grooves/mm. Vertical fiber array ($-0.6\text{m} \leq z \leq 0.6\text{m}$) is installed with parallel view chords at horizontally

author's e-mail: zhou.hangyu@nifs.ac.jp

elongated plasma cross-section of LHD. The fiber array consists of 44 quartz optical fibers with core diameter of 100μm and clad diameter of 125μm. The spatial resolution, e.g., 30mm at the plasma center, is defined by optical lens with focal length of 30mm, which is coupled with each optical fiber. The output spectra are detected by CCD. The CCD has detection area of 13.3 × 13.3 mm^2 (1024 × 1024 channels, 13 μm × 13 μm/pixel). It is generally operated at -20°C to reduce the thermal noise. Exposure time of 31ms and temporal resolution of 100ms are selected in the present study with readout speed of 11 μs/line and 0.4 μs/pixel.

3. Analysis of radial Z_{eff} profile

Density profiles in LHD basically changes according to heating power, magnetic field strength, magnetic axis position and fuel method.

The peaked density profile is easily produced by hydrogen multi-pellets injection. The Z_{eff} profile is analyzed for the peak density profile formed in high-density range with the pellet injection. A typical waveform of such a discharge is traced in Fig.1. Ten H_2 pellets are repetitively injected in magnetic axis of 3.85m during 1.70-2.02s. Plasma energy quickly increases during pellet injection and reaches 0.9MJ. Line-averaged electron density evaluated from density profile measured with Thomson scattering continuously increases and reaches $3.5\times10^{14}cm^{-3}$, whereas electron temperature in the plasma center dramatically decreases down to 0.3keV. Chord-integrated bremsstrahlung emission also increases in the same way as density behavior and reaches a quite large value of $490\mu Wcm^{-2}nm^{-1}$. The β value is largely increased and becomes 1.13%. At 1.822s after the third pellet injection, the radial Z_{eff} profile is analyzed with electron density and temperature profiles in addition to local bremsstrahlung emissivity after Abel inversion. It is shown in Fig.2. The temperature profile is entirely flat at ρ<0.8 and quickly decreases at ρ>0.8. The outside boundary of the edge temperature expands to ρ=1.2 in the ergodic layer. The bremsstrahlung emissivity profile is also peaked as density profile. The Z_{eff} profile analyzed from the peaked density profile is fairly flat at the core plasma region inside ρ =1.0. The values of Z_{eff} distribute around 1.13. In the ergodic layer, which is denoted with yellow square hatch in Fig.2, it is difficult to analyze the Z_{eff} because of large uncertainties in density and temperature profiles of Thomson scattering. Error bars of the Z_{eff} profile basically originated in the density and temperature profiles are considerably inside ρ= 0.7. However, it gradually increases at edge plasmas, e.g., 23% at ρ=1.0. The fitting curves for electron density and temperature profiles used in the present analysis are also indicated in Fig.2 (a) and (b). Another important point on uncertainty of the Z_{eff} profile is in the selection of magnetic surface deformed by plasma pressure. The magnetic surface is of course necessary for Abel inversion of the line-integrated bremsstrahlung signal.

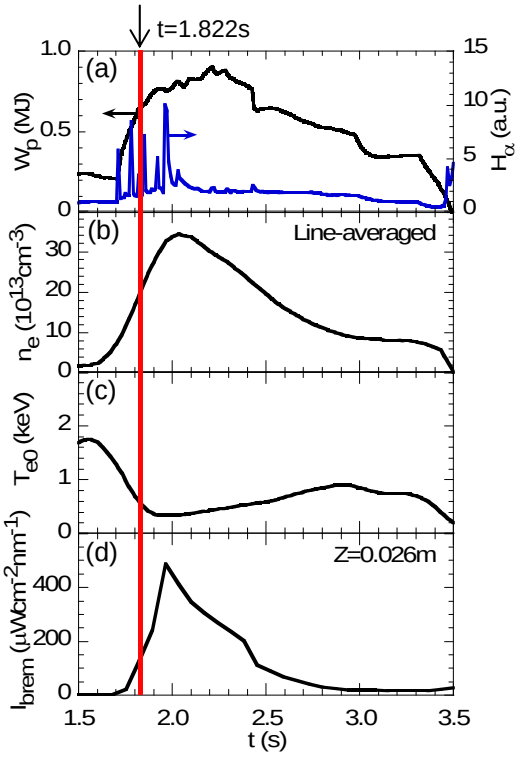

FIG.1 Waveform of high-density discharge with multi-pellets injection for peak density profile.

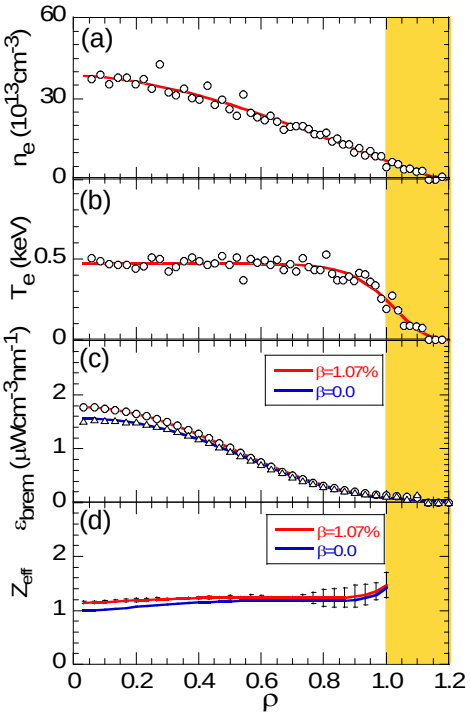

FIG.2 Profiles as a function of normalized radius at t=1.822s for multi-pellets injection discharge.

The uncertainty of the Z_{eff} profile due to magnetic surface deformation is checked using different two magnetic surfaces with β=0 and 1.07. Two bremsstrahlung emissivity profiles are obtained from the two magnetic surfaces, as shown in Fig.2 (c). The two bremsstrahlung emissivity profiles are quite similar, whereas a small difference is appeared in the plasma core. Since the visible bremsstrahlung is horizontally observed from outboard side of the torus, the effect on the magnetic surface distortion becomes much less compared to vertical measurement. Especially, the difference in the Z_{eff} value can be neglected at the outer plasma region, because the magnetic surface distortion is mainly occured in the plasma core. It is then strongly suggested that the uncertainty in the Z_{eff} profile on the assumed magnetic surface is quite small compared to that on the density and temperature profiles in the present diagnostic system.

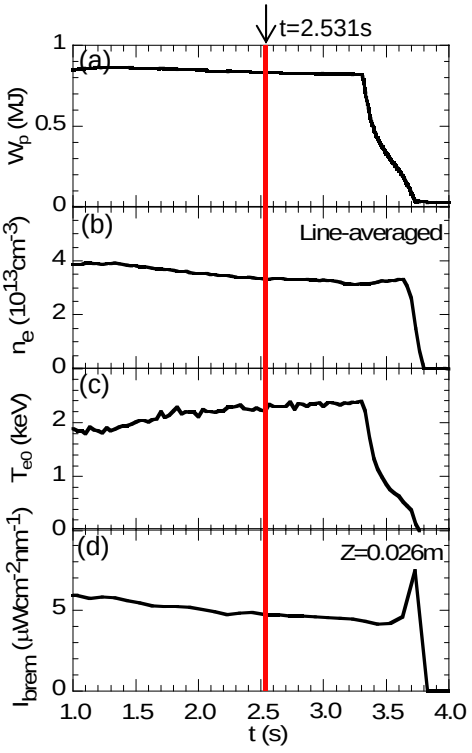

FIG.3 Time evolvement of stable discharge for flat density profile.

Next, the Z_{eff} profile is analyzed for flat density profile. The data are taken from stable plasma discharge in R_{ax}=3.6m. The discharge waveform is traced in Fig.3. The plasma energy is constantly sustained from 0.8s to 3.3s. The line-averaged electron density is roughly kept at 3.5x10^{13}cm^{-3} and the central electron temperature slightly increases from 2.0keV to 2.2keV during the steady phase accroding to the gradual decrease in the density. The chord-integrated bremsstrahlung behaves similar to the desnity. The β value is 0.88% at the steady phase. The Zeff profile is calculated at 2.531s with electron density and temperature profiles as shown in Fig.2 (b). The density profile is entirely flat at ρ < 0.9, whereas the temperature profile is peaked. The bremsstrahlung emissivity profile after Abel inversion becomes a little hollow. This indicates small temperature dependence in the visible bremsstrahlung emission. The Z_{eff} profile is flat with values near 2.05. The analysis in the ergodic layer is still difficult. Error bars of the Z_{eff} profile gradually increase toward plasma core and the maximum error bar is appeared as 12% at the plasma center. It is clear that the error bars increased at the plasma core is originated in the local emissivity calculation of the bremsstrahlung based on Abel inversion method.

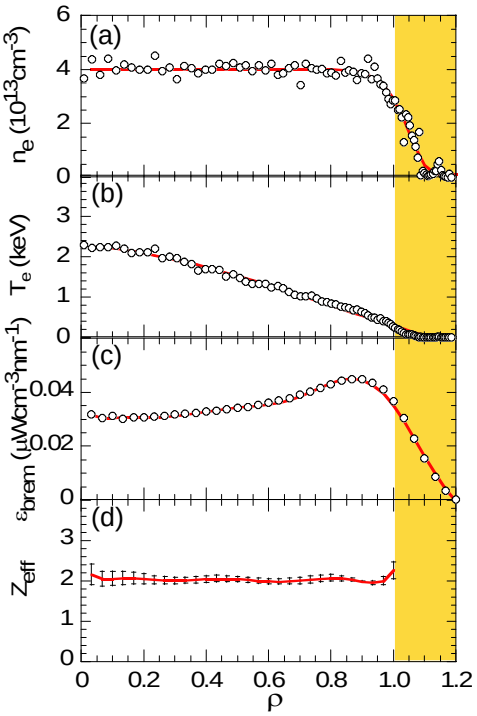

FIG.4 Radial profiles at t=2.531s produced by stable discharge.

Finally, the Z_{eff} profile is analyzed for hollow density profile. The hollow density profile is observed at density rise phase in R_{ax}=3.60m. The discharge waveform used in the analysis is shown in Fig.3 (a). The line-averaged electron density gradually increases during 0.5-1.5s and finally reaches 6x10^{-13}cm^{-3}, although the plasma energy is kept constant. The central plasma temperature then decreases from 1.8 to 1.2keV. The chord-integrated bremsstrahlung also increases according to the density rise. The β value is 0.88% in the discharge. At 2.531s, The Z_{eff} profile is analyzed at 2.531s. The electron density and temperature profiles are shown in Fig.3 (b) with local bremsstrahlung emissivity profile. The hollow density profile is formed having its peak value at ρ=0.9. On the contrary the

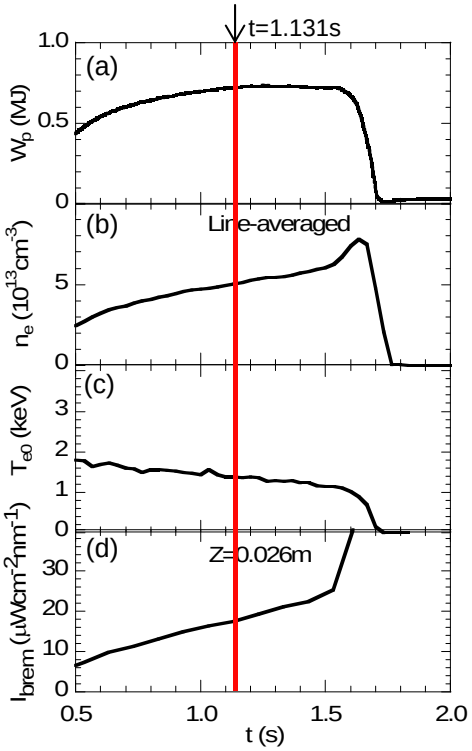

FIG.5 Trace of stable discharge for hollow density profile.

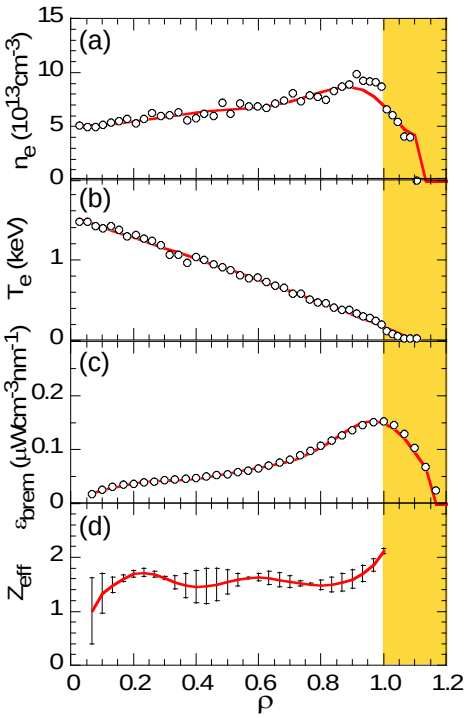

FIG.6 Profiles as a function of normalized radius at 1.131s during stable discharge.

temperature profile is peaked and forms a triangle shape.The bremsstrahlung emissivity largely decreases at the plasma core and the profile becomes much hollower than the density profile. The Z_{eff} profile is also flat with values around 1.58. In case of the hollow density profile, the analysis is generally difficult because of relatively large error bars in the density profile and difficulty in the Abel inversion calculation. The error bars in the Z_{eff} profile become also large in this case, i.e., ~20% at ρ = 0.4 and ~30% at plasma core. At present, any discussions can not be therefore done on the detailed structure in the Z_{eff} profile.

4. Summary and Discussion

Z_{eff} profile from visible bremsstrahlung measurement is analyzed for peaked, flat and hollow density profiles in LHD plasmas. The flat Z_{eff} profile is basically obtained for all different density profiles. It indicates that the impurity partial pressure is constant in general discharges of LHD. The error bars seen in the Z_{eff} profiles are mainly originated in fitting curves to express the electron temperature and density profiles and in process in the Abel inversion calculation. The uncertainty on magnetic surface distortion is relatively small. More precise Z_{eff} profile analysis will be done after optimizing the magnetic surface used in the calculation and modifying the method on Abel inversion calculation.

[1] D. P. Schissel et al., Phys. Fluids **31**, 3738 (1988).
[2] S. Morita, M.Goto et al., Physica Scripta T91, 48 (2001).
[3] H. Y. Zhou, S. Morita, M.Goto, M. B. Chowdhuri, Rev. Sci. Instrum. 79, 10F536 (2008)
[4] H. Nozato, S. Morita, M. Goto, J. Plasma Fusion Res. 5, 442 (2002)
[5] K.Nrihara et al., Rev. Sci. Instrum. 72, 1122 (2001)

Proceedings of ITC18,2008

Transport analysis of high-Z impurity with MHD effects in tokamak system

Ikuhiro YAMADA, Kozo YAMAZAKI, Tetsutarou OISHI, Hideki ARIMOTO and Tatsuo SHOJI

Department of Energy Engineering and Science ,Nagoya University,
Furo-cho, Chikusa-ku, Nagoya 464-8603 Japan

In fusion reactors, extremely high heat load on divertor plates is one of the serious problems, and the use of high-Z material is planned in terms of consistency between “ignited fusion burning” and “plasma facing component (PFC) materials”. However, high-Z impurity from these PFC causes large radiation loss even if its content is quite little amount. High-Z impurity transport analysis with MHD effects is carried out using TOTAL code. The critical level of impurity concentration in ITER is found 4.0% for carbon, 0.1% for iron, and 0.008% for tungsten with respect to electron density. The ITB formation for electron density can prevent high-Z impurity accumulation. It is also shown that sawtooth oscillation is beneficial for the reduction of radiation loss from plasma core (~20%), although it might leads to unfavorable fusion power fluctuation of 10%.

Keywords: impurity transport, sawtooth oscillation, internal transport barrier, Tokamak,

1. Introduction

In fusion reactors, the divertor plate and other PFC material get some interactions with hot plasma, by ion backscattering, chemical and physical sputtering processes, and then yield impurities into plasma. Especially heat loads on divertor plates are predicted to be very large, and high-Z materials such as tungsten will be used in such parts due to its high heat conductivity and low erosion rate. However, resulting high-Z impurity tends to accumulate in plasma core due to strong inwardly directed drift velocities caused by neo-classical convection and cause large radiation loss. Besides they displace reacting ions by large number of electrons released by them and cause fuel dilution.

The radial distribution of impurity in tokamak and helical system is calculated by using a 1.5D transport code TOTAL (toroidal transport analysis linkage) [1]. In Section 2, a simulation code used in this paper is described. In Section 3, typical machine parameters and plasma parameters are described. In Section 4, simulation results are presented. First, we clarify the permissible impurity level for ITER plasma. Secondly we make a study of impurity behavior in plasmas with internal transport barrier (ITB). Thirdly, effects of sawtooth oscillation on impurity are investigated. In Section 5, summary and conclusion are presented.

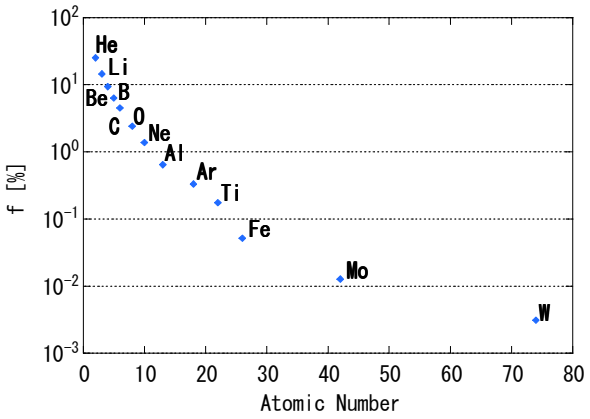

Fig.1 Fractional impurity level which produces radiation power equal to 10% of the total fusion power.

2. Numerical Model

2-1. Transport Model

To investigate transport of fuel and impurity ions in tokamak and helical system, we used 1.5-D (1-D transport / 2-D equilibrium for tokamak), or 2.0-D (1-D transport / 3-D equilibrium for helical) time-dependent simulation model with low-Z gas and high-Z metal impurity dynamics. The plasma density n_e, n_i and temperature T_e, T_i are described by

$$\frac{\partial n_e}{\partial t}+\frac{1}{V'}\frac{\partial}{\partial \rho}V'\Gamma_e = S_P \quad (1)$$

$$\sum_i z_i n_i \approx n_e \quad (2)$$

$$\frac{3}{2}\frac{\partial n_e T_e}{\partial t}+\frac{1}{V'}\frac{\partial}{\partial \rho}\left\{V'\left(q_e+\frac{5}{2}\Gamma_e T_e\right)\right\} = P_{He}-P_{ei}-P_{rad}-\Gamma_e E_r \quad (3)$$

$$\frac{3}{2}\frac{\partial n_i T_i}{\partial t}+\frac{1}{V'}\frac{\partial}{\partial \rho}\left\{V'\left(q_i+\frac{5}{2}\Gamma_i T_i\right)\right\} = P_{Hi}-P_{ei}-P_{cx}-z_i\Gamma_i E_r \quad (4)$$

author’s e-mail: i-yamada@ees.nagoya-u.ac.jp

Using the normalized radius ρ and the volume V defines by the equilibrium magnetic surface. The radiation loss P_{rad} is the summation of bremsstrahlung radiation, impurity line radiation and synchrotron radiation powers.

For the anomalous part of the transport coefficients, a Bohm-type model is used in this paper;

$$\chi_e = \chi_i = \alpha_B \frac{T_e}{B_T} q_\Psi^2 / L_{Pe} \quad , \tag{5}$$

where, T_e, B_t and q_Ψ are the electron temperature, toroidal magnetic field and MHD safety factor, respectively. L_{Pe} is the scale length of the pressure gradient normalized by the minor radius.

We examined high-Z impurities with a model for impurities in TOTAL: the multi-species dynamic impurity code IMPDYN was used to model the ionization states and the NCLASS code was used for the full neoclassical transport of each charge state considering arbitrary aspect ratio and collisionality.

2-2. Impurity Model

For the impurity dynamics [2,3], the rate equation and the diffusion equation are solved using IMPDYN code coupled with ADPAK atomic physics package which can calculate cooling rate:

$$\frac{\partial n_k}{\partial t} = -\frac{1}{V'}\frac{\partial}{\partial \rho}(V'\Gamma_k) + [\gamma_{k-1} n_{k-1} + \alpha_{k+1} n_{k+1} - (\gamma_k + \alpha_k) n_k] n_e + S \, . \tag{6}$$

$$\Gamma_k = \Gamma_k^{NCs} + \Gamma_k^{NCa} - D_k(\rho)\frac{\partial n_k}{\partial \rho} + V_k(\rho) n_k \tag{7}$$

with ionization rate γ_k , recombination rate α_k and particle source term S_k. Here, diffusion constant D_k and simply modeled velocity V_k=V(a)・(r/a) are used for anomalous transport (V_k>0 corresponds to outward velocity). The main fuel neutrals are calculated by the AURORA Monte Carlo code.

The neoclassical impurity flux in tokamak is expressed by

$$\Gamma_k^{NCs} = -D_k^{NC}\nabla n_k + D_k^{NC} n_k \left[\sum_{l \neq k} (g_{nl \to k} \nabla n_l / n_l) + g_{Ti} \nabla T_i / T_i + g_{Te} \nabla T_e / T_e \, . \right] \tag{8}$$

The neoclassical ripple transport coefficient in helical system is given by the density gradient, temperature gradient and the radial electric field

$$\Gamma_k^{NCa} \propto D_{rip\nabla n} \nabla n / n + D_{rip\nabla T} \nabla T / T - Z E_r / T \tag{9}$$

Here, we adopted the neoclassical expression of fuel ions to include the impurity ions in addition to the tokamak-like axi-symmetric neoclassical flux.

The radial electric field in the helical system is determined by the neoclassical transport flux including impurity ions as follows,

$$\left(\sum_k z_k \Gamma_k^{NCa}(E_r) - \Gamma_e^{NCa}(E_r)\right) = 0 \tag{10}$$

Here, the subscript k denotes fuel ions (D & T), helium and impurity ions. The neutral impurity density is given by

$$\nu_0 \frac{\partial n_k}{\partial \rho} = S_0 n_e n_0 \tag{11}$$

Here, v_0 is neutral impurity velocity, and S_0 and n_e is ionization coefficient and electron density at plasma boundary.

In the simulation, the impurity source was defined as the impurity neutral flux on the plasma boundary. When steady state conditions have been established, continuous neutral impurity influx was introduced, and after a transient phase the system settles into a new radiation-enhanced steady state.

3. Model of Tokamak and Helical Plasmas

We considered three reacting or burning plasmas; JET, ITER and helical reactor HR-1.

Table.1 Typical machine and plasma parameters.

	ITER	JET	HR-1
R [m]	6.2	2.9	13
a [m]	2	0.95	2.54
κ	1.7	1.6	-
δ	0.3	0.2	-
B [T]	5.35	3.45	4.6
IP [MA]	9.5	4	-

4. Simulation Results

4-1. Permissible Impurity Level

We clarify the critical impurity content for tokamak plasma. As a result, in ITER, critical concentrations of impurity is 4.0% for carbon, 0.1% for iron, and 0.008% for tungsten impurity with respect to electron density to maintain Q>10.

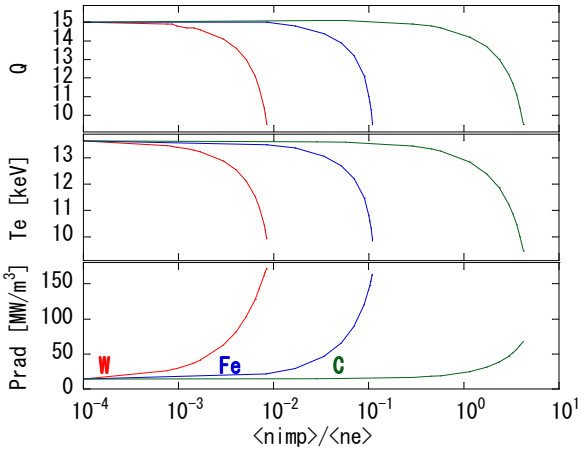

Fig.2 Change of plasma parameters versus impurities concentration.

Regardless of same decrease of Q value for each impurity, they have different radiation power individually. In the case of High-Z impurity (W), the main effect is large radiation loss. On the other hand, it is considered that Low-Z impurity (C) dominates other influence on plasma, such as fuel dilution, rather than radiation itself.

4-2. Effects of Internal Transport Barrier

To control impurity influx, the modification of edge plasma density profile might be beneficial. According to the neoclassical theory, a finite gradient of temperature (i.e. negative $\nabla T/T$) might contribute to the impurity shielding effect. But finite density gradient leads to impurity pinching effect. Figure 3 shows the effects of edge electron density profile in the case of ITB foot-point at ρ=0.8. When the edge density profile becomes rather flat due to strong gradient at temperature ITB, the impurity line radiation can be reduced as shown in the figure.

This result indicates that ITB formation, such as by pellet injection, can prevent high-Z impurities from accumulating inside the ITB.

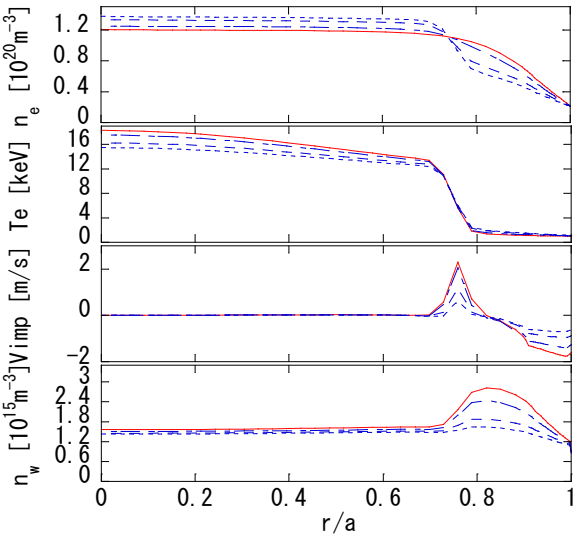

Fig.3 Effect of edge density profile on impurity transport in ITER ITB plasma.

4-3. Effects of Sawtooth Oscillation

Sawtooth oscillations are periodic and MHD-initiated mixing events that occur in a tokamak plasma in the near axis region where the safety factor q is less than or equal to unity. It is known to affect the transport of main plasma and impurity by flattening radial profile of densities and temperatures periodically in the core plasma. Thus, if inward anomalous convection is present, small sawtooth may be considered as beneficial in preventing the accumulation of impurities in the core region. In this paper, we simulate the argon seeding experiments in JET[4,5] and

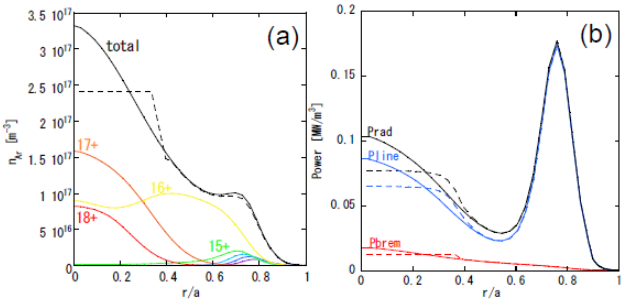

Fig.4 Results of sawtooth oscillation effect on impurity in JET plasma. Figure (a) and (b) shows total impurity density profile, and total radiation profile in the case of argon respectively before (solid line) and after (dashed line) sawtooth crash.

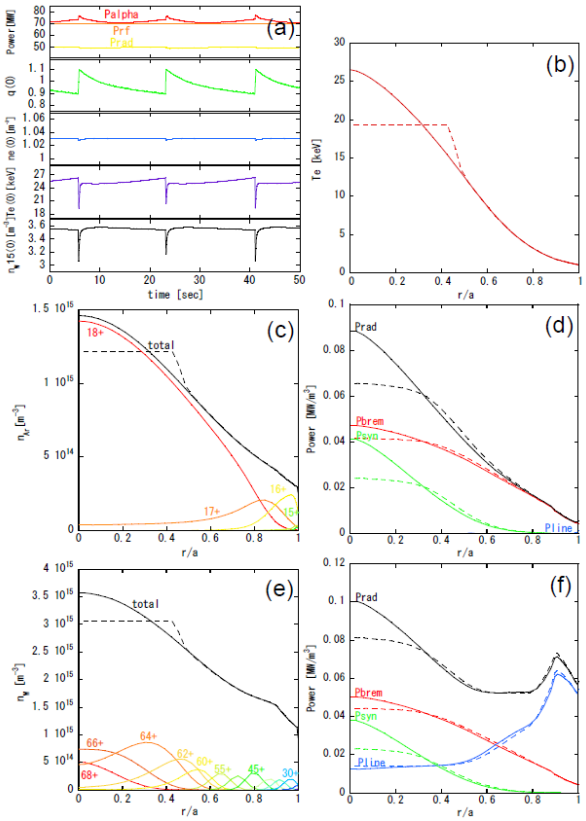

Fig.5 Results of sawtooth oscillation effect on impurity in ITER plasma. Figure (a) and (b) shows time evolution of main plasma parameters and electron temperature, respectively. Figure (c) and (d) shows total impurity density profile and total radiation profile in the case of argon, respectively, before (solid line) and after (dashed line) sawtooth crash. Figure (e) and (f) are the same for tungsten.

also predict the impurity (Ar/W) behavior in ITER discharge with sawtooth in the case of existing relatively large inward drift velocity for impurity.

Simplified sawtooth model is included in the TOTAL code which evolves the plasma profiles between crashes. In the model, the profile is made to be flat inside the inversion radius at the crash, based on the Kadomtsev's full magnetic reconnection model.

As a result, in JET experiments, sawtooth oscillation is found to be effective for controlling impurity [4,5]. Figure 4 shows that sawtooth oscillation in JET can prevent impurity from accumulating into plasma core and can reduce corresponding impurity line radiation about 25% and total radiation loss about 26% from plasma core. The results roughly agree with experimental data.

On the other hand, in ITER, as shown in Fig.5, since argon impurity is almost fully ionized, corresponding line radiation is nearly zero along whole radius except plasma boundary. Similarly, the case of tungsten impurity, existence of highly charged ion in core region makes profile of line radiation hollow. In both cases, sawtooth oscillations reduce bremsstrahlung radiation and synchrotron radiation from plasma core, and about 20% reduction in radiation loss is realized, although it is not affect line radiation profile. It is shown that sawtooth activities can effectively reduce radiation loss from plasma core, which is caused by the temperate and density drop due to internal disruption and might fluctuate about 10% of fusion power. Moreover, the sawtooth event might initiate a seed island for neoclassical tearing mode (NTM). Therefore, the sawtooth avoidance is important for ITER operations.

5. Summary and Conclusion

We investigated transport of high-Z impurity with MHD effects and show the following results:

(1) In ITER, the critical level of impurity concentration is, 4.0% for carbon, 0.1% for iron, and 0.008% for tungsten with respect to electron density.

(2) ITB formation for electron density, such as pellet injection, can prevent high-Z impurity from accumulating inside the ITB region.

(3) Sawtooth oscillation is beneficial for reduction of radiation loss from plasma core (~20%), although it leads to unfavorable fusion power fluctuation of 10%. Moreover, to avoid its harmful effects on NTM excitation and so on, the control of sawtooth oscillation is necessary in spite of impurity exhaust.

References

[1] K. Yamazaki, T. Amano, Nucl. Fusion **32**, 633 (1992).

[2] Y. Murakami, T. Amano *et al*., J. Nucl. Material **313-316**, 1161 (2003)

[3] K. Yamazaki *et al.*, J. Plasma Fusion Res. SERIES, **7**, 102 (2006)

[4] M.E. Puiatti *et al*., Plasma Phys. Control. Fusion **44** (2002) 1863.

[5] M.E. Puiatti *et al*., Plasma Phys. Control. Fusion **45** (2003) 2011.

Proceedings of ITC18,2008

Formation condition of fiberform nanostructured tungsten by helium plasma exposure

W. Sakaguchi, S. Kajita[a], N. Ohno, M. Takagi, H. Kurishita[b],

Department of Energy Eng. and Sci., Graduate School of Eng., Nagoya University, Nagoya 464-8608, Japan

[a]EcoTopia Science Institute, Nagoya University, Nagoya 464-8608, Japan

[b] International Research Center for Nuclear Materials Science, Institute for Materials Research (IMR), Tohoku University, Oarai, Ibaraki 311-1313, Japan

Tungsten samples were irradiated by high density helium plasma in the divertor plasma simulator NAGDIS-II to investigate the formation condition of the fiberform nanostructured tungsten. Experimental result indicates that the surface temperature threshold exists around 1000 K. When the surface temperature is above 1130 K, when the incident ion energy is 50 eV, the fiberform nanostructure thickens with the increase of the sample temperature. Three samples manufactured by different procedure (ultra fine grained tungsten, ITER-reference tungsten grade and powder metallurgy tungsten) were exposed to helium plasma, and the nanostructure was formed in all the samples.

Keywords: Helium plasma, Tungsten, Optical reflectivity, Nanostructure, NAGDIS-II

1. Introduction

Recently, it has been found that the fiberform nanostructured tungsten is formed on tungsten surface by irradiating helium plasma [1]. Tungsten is a candidate material for divertor armor in ITER [2] because of its good thermophysical properties, high melting point, low sputtering yield and a low tritium inventory. Additionally, tungsten is also a candidate material for in-vessel mirror material in fusion devices [3]. When it is used as a material of these positions, the nanostructure may cause serious problems because it could lead to the decrease of the optical reflectivity [4] and the thermal conductivity [5]. Therefore, it is necessary to investigate the formation condition and the formation mechanism of the fiberform nanostructure.

Until now, it has been revealed that the high helium ion fluence ($>10^{25}$ m^{-2}) is necessary to cover the surface with the fiberform nanostructured tungsten [1,4,6]. Moreover, it has been found that the incident ion energy is an important parameter to form the nanostructured tungsten. When the incident helium ion energy was above 30 eV, the fiberform nanostructure was formed at the surface temperature of 1800 K, although only the helium bubbles and holes were formed when the incident ion energy was 15 eV [4]. Additionally, it is reported that a nanostructured layer thickness of 5μm is observed by irradiating helium plasma at the fluence of 1.1×10^{27} m^{-2} [6].

In this paper, to investigate the formation condition in detail, helium plasma irradiations are performed at different surface temperatures with fixed incident ion energy. In addition, experiments are performed by using the tungsten samples manufactured by different procedure. The fluence of the helium ion to form the nanostructure is evaluated by the measurement of the optical reflectivity because the optical reflectivity decreases to ~ 0 % due to its complicated structure when the surface is covered with the nanostructure. The surface is analyzed by scanning electron microscope (SEM) after the helium plasma exposure.

2. Experimental setup

Experiments were performed in the divertor plasma simulator NAGDIS-II (NAGoya university DIvertor Simulator-II). Figure 1 shows a schematic view of the experimental setup. High density helium plasma, which is produced by dc arc discharge, was irradiated to tungsten samples situated in parallel to the magnetic field line. The sample, which is powder metallurgy tungsten provided by Nilaco Co. with 99.95 % purity, was polished by sandpapers and alumina suspension. In order to control the incident ion energy to the samples, the samples were electrically biased in the helium plasma. The optical reflectivity of the sample was measured by using a He-Ne laser, of which wavelength is 632.8 nm, and a photodiode with a band-pass optical filter to exclude the emission of plasma. The surface temperature of the samples was measured by a pyrometer and the incident ion flux was derived by the ion current. After the helium plasma irradiation, the samples were analyzed by a SEM and were

author's e-mail: w-sakaguchi@ees.nagoya-u.ac.jp

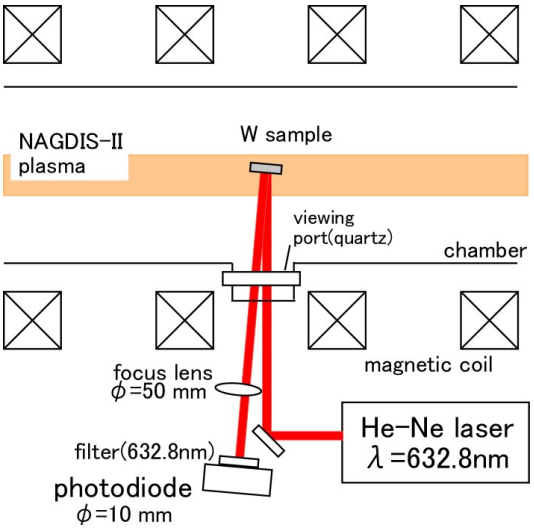

Fig. 1 Schematic illustration of the experimental setup in the divertor simulator NAGDIS-II.

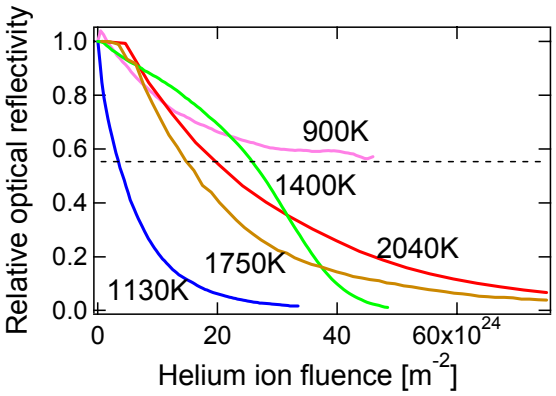

Fig. 2 Measured reflectivity of tungsten under helium plasma exposure at different sample temperatures from 900 K to 2040 K

measured with a spectrophotometer (Nihon Bunkosya: ARV-47S) for the wavelength between 200 and 900 nm.

3. Results

3. 1. Surface temperature dependence

Figure 2 shows the relative optical reflectivity as a function of helium ion fluence while helium plasma was irradiated. Five samples were irradiated to the helium plasma at different surface temperatures from 900 K to 2040 K. The incident helium ion energy was fixed to 50 eV. When the sample temperature was 900K, the relative optical reflectivity decreased to 0.55 at the fluence of 4.5 x 10^{25} m^{-2} and the surface had a metallic luster even after the helium irradiation. On the other hand, when the sample temperature was 1130 K, the relative optical reflectivity decreased to ~ 0 at the fluence of 3.0 x 10^{25} m^{-2} and the surface color changed to black. Figure 3 shows the SEM micrographs of samples after the helium plasma exposure. The surface irradiated at 900 K was modified to the wavy structure (Fig. 3, (a)). However, the surface irradiated at the temperature from 1130 K to 2040 K was covered with the fiberform nanostructure (Fig. 3, (b)~(e)). It is indicated that the sample temperature should be greater than ~ 1000 K to form the nanostructure.

The size of the fiberform nanostructured tungsten is different by the temperature of the samples. The size of the structure are, typically, < 40 nm at 1130 K (Fig. 3 (b)), < 200 nm at 1750 K (Fig. 3 (c)), and < 1 μm at 2040 K (Fig. 3 (e)). The structure irradiated at 1750 K is complicated, but the average size is < 1 μm (Fig. 3 (d)). It is indicated that the size of nanostructure thickened with the increase of the sample temperature. Besides, more helium fluence was required to decrease the relative optical reflectivity to ~ 0 with the increase of the sample temperature from Fig. 2.

Figure 4 shows the wavelength dependence of reflectivity of polished sample, and samples after the helium plasma exposure. The optical reflectivity at the wavelength of 632.8 nm corresponds to the one that was measured by the photodiode. For the wavelength λ = 900 nm, the reflectivity decreases by ~ 20 %; on the other hand, it decreases by ~ 70 % for λ = 200 nm. The degree of reflectivity reduction increases as the decrease of the wavelength. From Fig. 3 (a), the size of the surface roughness is approximately several tens nm. Thus, it is suspected that the roughness does not nave significant influence on the optical reflectivity if the wavelength is ten times greater than the structure. When the irradiation temperature was higher and the surface is covered by the fine structure, the optical reflectivity becomes 0 in the range of 200 < λ < 900 nm.

It has been reported that helium ions produce bubbles and holes on the surface at the incident ion energy below the threshold value of physical sputtering [7-9]. When the surface temperature is higher than ~ 1600 K and the incident ion energy exceeds ~ 5 eV, the micrometer-sized bubbles and holes are formed [9]. This paper shows that the necessary minimum sample temperature to form the fiberform nanostructure is approximately 1000 K when the incident ion energy is 50 eV. This temperature is lower than the threshold of the micrometer-sized bubble and hole formation. Meanwhile, the nanometer-sized bubbles formation is reported at the temperature of 700 K [10]. Since the bubble size increases due to the high sample temperature, the nanostructure thickens with the increase of the sample temperature. We believe that the nanometer-sized bubbles formation and their coalescence

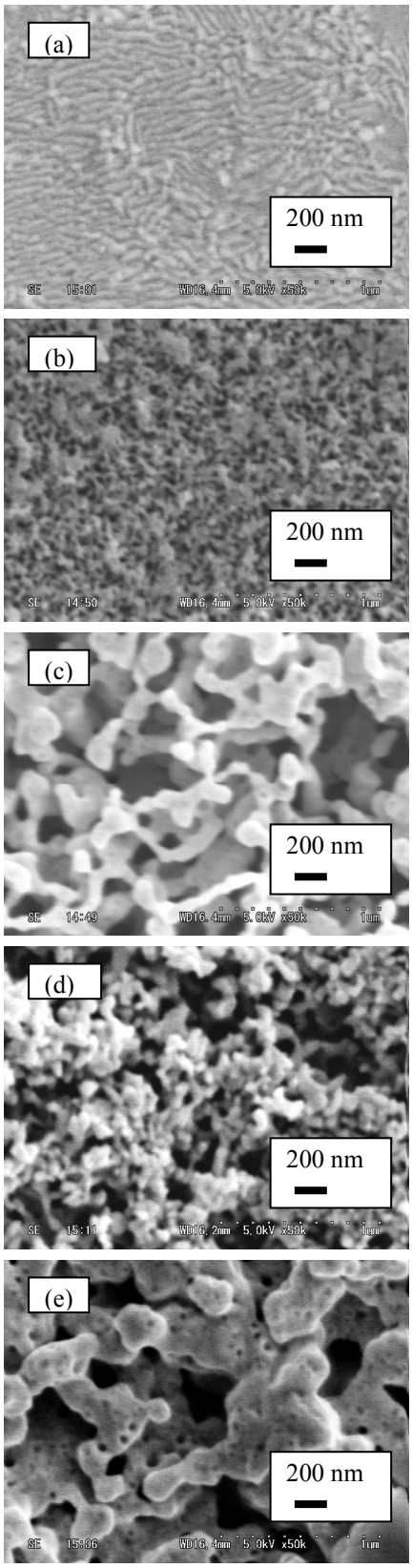

Fig. 3 SEM micrographs of the tungsten surface after the helium plasma exposure. The sample temperatures are (a) 900 K, (b) 1130 K, (c) 1400 K, (d) 1750 K and (e) 2040 K, respectively.

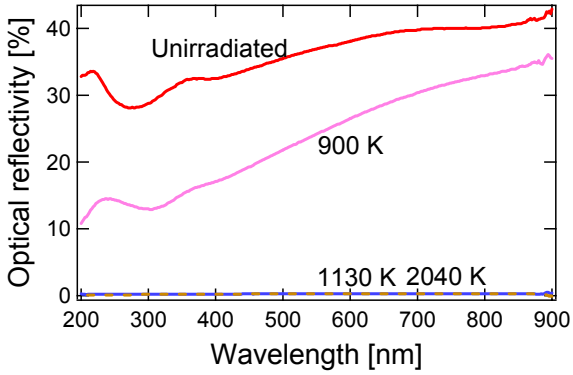

Fig. 4 Reflectivity of polished samples and samples irradiated at 900 K, 1130 K, 2040 K.

play a role to form the fiberform nanostructured tungsten. The incident helium ion energy threshold of the nanostructure formation is ~ 30 eV which is higher than that of the bubble formation at the surface temperature of ~ 1800 K. The formation mechanism of the nanostructure is not understood well yet.

3. 2. Different manufacturing procedure

Figure 5 shows the optical reflectivity as a function of helium ion fluence. Three samples, which were manufactured by different procedure, were irradiated to the helium plasma. First one is the ultra fine grained (UFG) W-0.5 wt. % TiC consolidate which is fabricated utilizing mechanical alloying in purified Ar and hot isostatic pressing [11]. The grain size is approximately 70 nm. Second one is the ITER-reference tungsten grade (ITER). The grain size is approximately 20 μm. Third one is the powder metallurgy tungsten. The incident ion energies were 50 eV and the surface temperatures were 1700 K, 1880 K and 1750 K, respectively. The fiberform nanostructured tungsten was formed on all the samples. Figure 6 shows the SEM micrographs of UFG and ITER after the helium plasma exposure. The size of the nanostructure is almost same. The fluence to form the nanostructure was almost same at ~ 10^{26} m^{-2} from Fig. 5. Clear differences on the formation of the nanostructure were not observed even when the manufacturing procedure and grain size are different. It is noted that the surface temperature was higher than the recrystallization temperature. Thus, the recrystallization process may modify the originality of each sample. For further work, it is expected that the irradiation at lower temperature make it clear the difference between them.

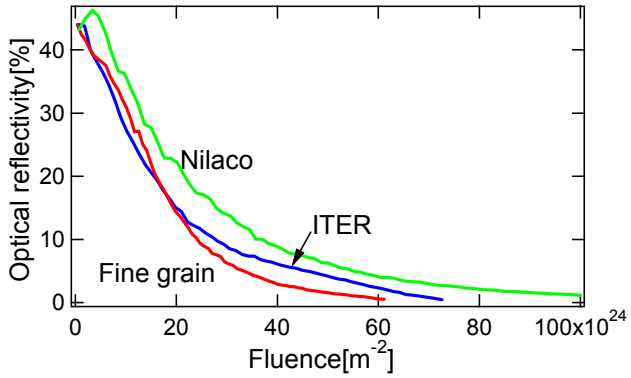

Fig. 5 Measured reflectivity of three samples which were manufactured by different procedure

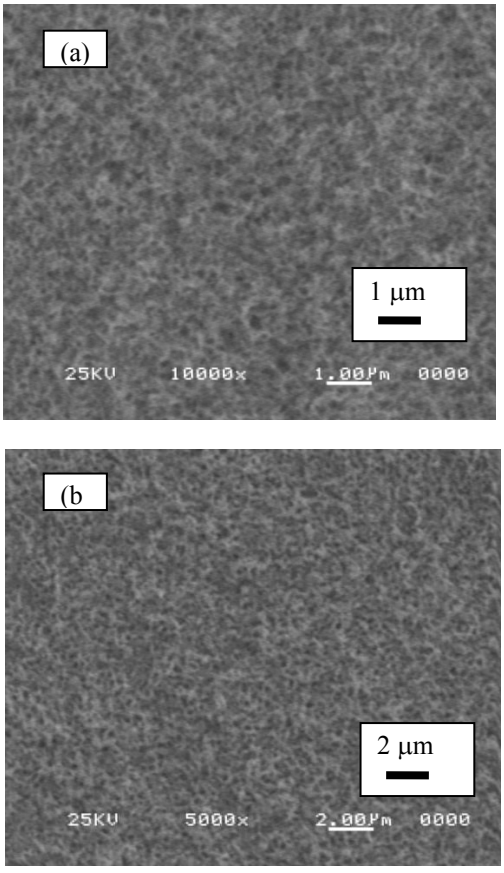

Fig. 6 SEM micrographs of tungsten surface (a) UFG and (b) ITER after helium plasma exposure.

4. Conclusion

Helium plasma irradiation experiments have been performed to investigate the necessary conditions for the formation of the fiberform nanostructure. This paper reveals that the necessary minimum sample temperature to form the nanostructure is approximately 1000 K when the incident ion energy is 50 eV. Moreover, it has been reported that the incident ion energy threshold of the nanostructure formation is ~ 30 eV. Considering the use of tungsten as divertor and mirror materials, the formation of the fiberform nanostructured tungsten has to be prevented. Thus, it is necessary for the fusion device materials to keep a material temperature under ~ 1000 K or to keep the incident helium ion energy under ~30 eV.

The nanostructure thickens with the increase of the sample temperature. We consider that the size of helium bubbles influence the size of the nanostructure. No clear differences on the formation of the nanostructure were observed at the temperature of ~ 1800 K even when the manufacturing procedure and the grain size are different.

References

[1] S. Takamura, N. Ohno, D. Nishijima, S. Kajita, Plasma Fusion Res. **1** 051 (2006).
[2] ITER Physics Basis, Nucl. Fusion **39** 2137 (1999).
[3] A. Litnovsky, V.S. Voitsenya, A. Costley, A.J.H. Donne, Nucl. Fusion **47** 833 (2007).
[4] W. Sakaguchi, S. Kajita, N. Ohno and M. Takagi, to be published in Journal of Nuclear Materials.
[5] S. Kajita, S. Takamura, N. Ohno, D. Nishijima, H. Iwakiri and N. Yoshida, Nucl. Fusion **47**, 1358 (2007).
[6] M.J. Baldwin, R.P. Doerner, Nucl. Fusion **48** 035001 (2008).
[7] M. Y. Ye, N. Ohno, S. Takamura, J. Plasma Fusion Res. **3** 265 (2000).
[8] D. Nishijima, M.Y. Ye, N. Ohno, S. Takamura, J. Nucl. Mater. **313-316** 99 (2003).
[9] D. Nishijima, M.Y. Ye, N. Ohno, S. Takamura, J. Nucl. Mater. **329-333** 1029 (2004).
[10] D. Nishijima, H. Iwakiri, K. Amano, M. Y. Ye, N. Ohno, K. Tokunaga, N. Yoshida, S. Takamura, Nucl. Fusion **45** 669-674 (2005)
[11] H. Kurishita, S. Matsuo, H. Arakawa, et al., Mater. Sci. Eng. A **477** 162-167 (2008).

Proceedings of ITC18, 2008

Hydrogen Concentration and Crystal Structure of Carbon Film Produced at the Duct of Local Island Divertor in Large Helical Device

Tomoya Hirata[1)], Yuji Nobuta[1)], Tomoaki Hino[1)], Suguru Masuzaki[2)], Naoko Ashikawa[2)], Yuji Yamauchi[1)], , Yuko Hirohata[1)], Akio Sagara[2)], Kiyohiko Nishimura[2)], Nobuyoshi Ohyabu[2)], Nobuaki Noda[2)], Akio Komori[2)], Osamu Motojima[2),] LHD Experimental Group[2)]

1) Laboratory of Plasma Physics and Engineering, Hokkaido University, Sapporo, 060-8628, Japan

2) National Institute of Fusion Science, Toki-shi, Gifu-ken, 509-5292, Japan

Two sets of material probes were installed at the pumping duct of the Local Island Divertor (LID) in the Large Helical Device (LHD) during 9th (2005) and 10th (2006) experimental campaign. One set of the material probes were faced to the LID head which consists of carbon fiber composite (CFC) tiles, and the other set were far from the head. After the campaigns, the material probes were extracted, and their surface morphology, the depth profile of atomic composition, thickness of the deposition layer on them, the amount of retained hydrogen in the layer and crystal structure of the layer were investigated. The value of hydrogen concentration in the carbon layers on the probes faced to the LID head was H/C = 0.55 in the atomic ratio. On the other hand, the value on the probes far from the head was significantly large, H/C = 1.25 in the atomic ratio. The microstructure analysis of the carbon deposition layers using Raman spectroscopy indicates that the layers were polymer like amorphous hydrogenated carbons, which was possibly resulted from the large deposition of chemically sputtered hydrocarbon on the probes. As the result, the co-deposited layers with a large amount of hydrogen were formed.

Keywords: Carbon deposition layer, Co-deposition, Hydrogen retention, Local Island Divertor, Large Helical Device,

1. Introduction

One of the important issues for ITER is to evaluate in-vessel tritium inventory because the retained amount of tritium in ITER is limited below 350 g. Carbon fiber composite (CFC) will be used for a divertor plate material of ITER. Carbon materials are easily eroded by incident hydrogen isotopes ions for physical and chemical sputtering, and carbon co-deposits with plenty of hydrogen isotopes in the vicinity of the divertor. When tritium is employed for fuel gas in ITER, large amount of tritium will be retained in the deposited carbon layer. So the characterizations of the carbon co-deposition layer and its hydrogen isotope retention are important concerns associated with the reactor safety [1].

In tokamak devices, hydrogen retention behaviors in carbon components, such as divertor tiles, have been investigated so far [2-4]. It was found that the tritium retention in the shadow area could be significantly large. The CFC was also employed for divertor material of the local island divertor (LID) in the Large Helical Device (LHD).

The CFC tiles were eroded by hydrogen ion bombardment and carbon co-deposits with hydrogen in the pumping duct of LID, which is shadowed from the plasma.

In this paper, we focused on the co-deposited carbon layer produced in the pumping duct of LID in 9th (2005) and 10th (2006) experimental campaign. The relationship between the structure of carbon layer, wall temperature and hydrogen concentration was investigated.

2. Experimental

In LHD, the LID experiments have been conducted since 2003, in addition to intrinsic helical divertor experiments [5]. Figure 1 shows a schematic view of the LID configuration. A divertor head that is covered by the neutralizer plates made of CFC is inserted into the m/n=1/1 magnetic island in the horizontally elongated cross-section where the width of the island is maximum (about 20 cm). The pumping duct surrounds the divertor head, and it works as a baffle. Outer separatrix of the island connects the divertor head as the divertor legs, and the last closed flux surface is determined by the inner separatrix of the island. Plasma-surface interaction occurs only at the divertor head ideally, and thus the wet area (< 0.1 m^2) is less than one tenth of that of helical divertor. Therefore, the divertor head receives much higher heat and particle fluxes than those to the helical divertor plates, and a considerable amount of carbon was eroded and co-deposited with hydrogen during the experiments [6]. The crystal structure and the hydrogen retention properties of the co-deposited carbon layers in the vicinity of LID head were investigated with a technique of material probe [7]. During each 9th (2005) and 10th (2006) experimental campaign, silicon and stainless steel (SUS316L) probes were installed at four

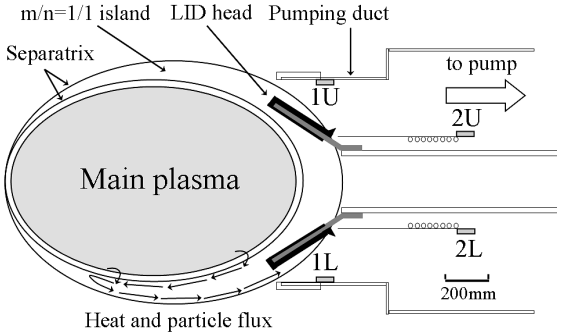

Fig.1 Schematic view of the LID configuration. The LID head is inserted into the m/n=1/1 magnetic island. The black parts on the LID head are made of carbon (graphite or CFC), and the gray parts are the base structure of the head that is made of SUS316. Material probes (1U, 1L, 2U, 2L) were installed inside the pumping duct. The neutral gas pressure in the pumping duct close to the LID head was considered to be ~1 Pa.

author's e-mail: y-nobuta@eng.hokudai.ac.jp

positions in the pumping duct as shown in Fig.1. Two probe sets (1U, 1L) were placed inside the pumping duct, which was faced to the LID head and have 200 mm distance from the tip of the pumping duct. The other sets of probes (2U, 2L) were 870 mm far from the tip of the pumping duct and had shallow line of sight to the head. In these experimental campaigns, hydrogen gas was employed for the LID discharges. The numbers of the discharge with the LID configuration were 707 (9th) and 313 (10th).

The stainless steel probes were used for analysis of surface morphology and gas retention, and silicon probes were used to investigate depth profile of atomic composition, the thickness and the crystal structure of the deposited carbon layers, respectively. The size of each probe is 10 mm × 20 mm × 1 mm. Typical surface temperatures of the head near the strike point and the pumping duct near the LID head estimated from thermocouple measurements were approximately 1000 K and 600 K, respectively. At the probe position close to the head (1U, 1L), the maximum wall temperature during the discharge was ~570 K. In the case of the other probe position far from the head (2U, 2L), the wall temperature during discharge was in the range from RT to 323 K.

After each experimental campaign, the probes were extracted and analyzed using scanning electron microscope (SEM), Auger electron spectroscopy (AES), surface roughness meter, thermal desorption spectroscopy (TDS), X-ray deflection, and Raman spectroscopy.

3. Results and discussion

3.1 Surface morphology

Figures 2 (a) and (b) show the SEM photographs of the 1U and 2U surfaces after the 9th experimental campaign. On the surface of 1U, sub-micron size protuberant structures were observed. On the other hand, the surface of 2U was smooth compared to 1U. The surfaces conditions of 1L and 2L were similar to those of 1U and 2U, respectively. This difference of surface morphologies between 1U and 2U might be caused by the deposition process of sputtered carbon atoms. The neutral gas pressure in the pumping duct close to the LID head reached up to ~1 Pa. Therefore, sputtered carbon particles were scattered before they redeposit on the probes. And then, they incident to the surface of the probe close to the head from random angle and deposit selectively on the protuberant structure. This is one of the possible explanation for the formation of protuberant structure. On the other hand, the smooth surface might result from the direct deposition of chemically sputtered hydrocarbon.

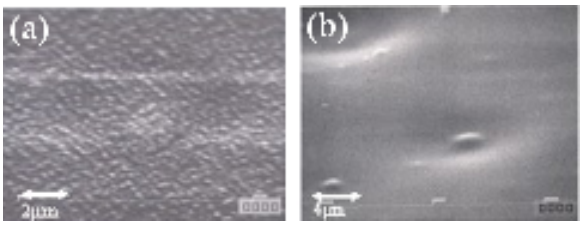

Fig.2 SEM images of the surface morphologies of the stainless steel probes, (a) 1U and (b) 2U after 9th experimental campaign.

3.2 Atomic composition and film thickness of deposited layer

In AES analysis, Ar ion with an energy of 3keV was used for sputtering. The depth of the crater formed by the Ar ions bombardment was measured by a surface roughness meter, and then the depth was estimated from the sputter-etching time. The concentration of oxygen was below 1 at.%, which were similar to those of other probes. Figure 3 shows the thickness of the deposition layer measured by using the surface roughness meter. The thickness of the layers on 1L and 1U after 9th experimental campaign was in the range from 500 to 700 nm. On the other hand, the thickness on 2L and 2U was in the range from 160 to 200 nm. In 10th experimental campaign, the thickness was approximately a half of that in 9th experimental campaign. This is owing to the reduced number of hydrogen discharge in 10th experimental campaign. Assuming the typical duration time in a LID discharge to be 2 s, the deposition rates of the carbon on 1U and 2U are estimated to be 0.64 nm/s and 0.14 nm/s, respectively

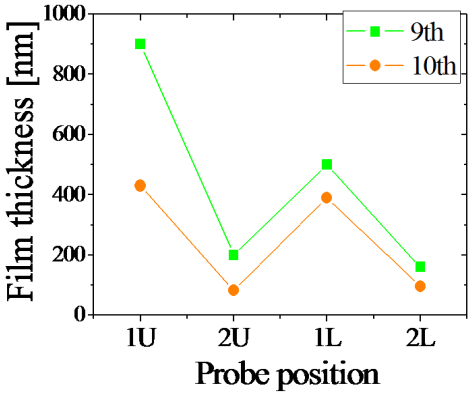

Fig.3 The thickness of the deposition layer on the probes.

3.3 Hydrogen retention

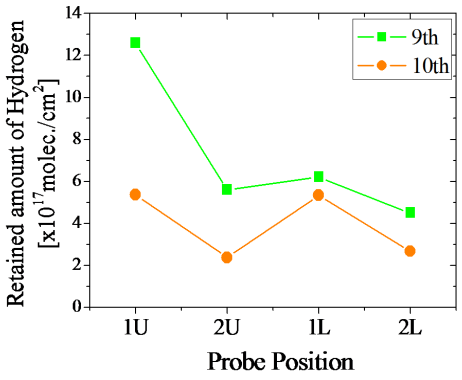

Fig.4 Retained amounts of hydrogen of the deposited carbon films on the probes.

Figure 4 shows the retained amounts of hydrogen in the probes. Most of retained hydrogen desorbed in form of hydrogen molecular during the TDS measurements. In the case of 10th experimental campaign, the retained amount of hydrogen was approximately a half of that in 9th experimental campaign. These results indicate that the retained amount of hydrogen of each position was roughly proportional to the deposited carbon film thickness.

3.4 Crystal Structure of Carbon Films

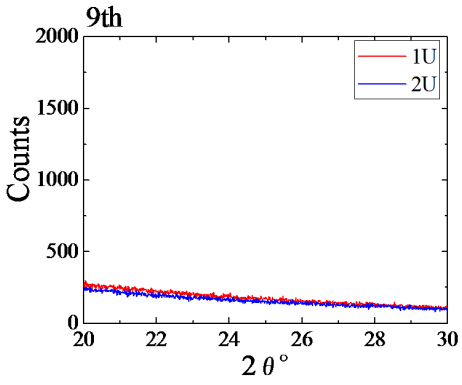

Fig.5 X-ray diffraction patterns of the deposited carbon films after 9th experimental campaign.

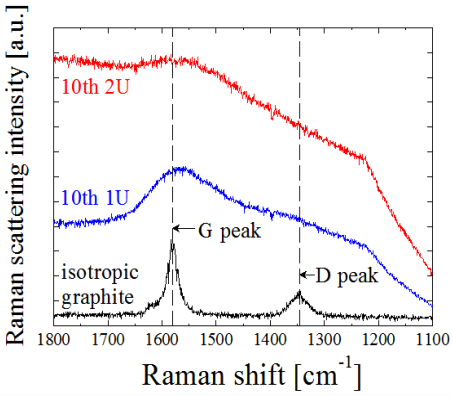

Fig.6 Raman spectra of the surface of the carbon film on the probes after 10th experimental campaign.

Figure 5 shows X-ray diffraction patterns of the carbon deposition layers after 9th experimental campaign. In the case of graphite, (002) X-ray deflection peak appears around 2θ =26 degree. In the case of the probes, however, no peak was observed. This result indicates that the structures of the carbon layers on 1U and 2U probes were amorphous. Figure 6 shows Raman spectra of the carbon layers on the probes in 10th experimental campaign. Raman spectrum of isotropic graphite has two peaks as shown in the figure with the black line. The peak at 1580 cm^{-1} is called "G" peak which originates from graphite structure. The other peak at 1355 cm^{-1} is called "D" peak which originates from defects [16]. The spectra of the carbon films on the probes were not similar to that of isotropic graphite but were similar to that of polymer-like amorphous hydrogenated carbon film [16]. The spectra of 1U have a broad peak around 1580 cm^{-1}, indicating that this layer contained carbon hexagonal structure like graphite. On the other hand, the "G" peak was not clear in the spectra of 2U. The carbon layer of 2U is considered to be more polymerized than 1U, which might have been caused by deposition of chemically sputtered hydrocarbon at low temperature.

3.5 Hydrogen concentration

In the present study, the mass densities of the carbon layers on the probes were not measured directly. For the estimation of hydrogen concentration, it is necessary to evaluate the density of carbon layers produced in the LID experiments. For this purpose, we prepared amorphous hydrogenated carbon film (a-C:H film) by using a magnetron sputtering device. The discharge gases in this device were argon and hydrogen gas with the mixture ratio of 1/20 in H_2/Ar. Input power was 1 kW. The distance between substrate and graphite target was 3.5 cm. The discharge pressure was kept at 1.5 Pa. The discharge time was 2 hours. The film thickness of the produced a-C:H film was estimated to be 160 nm by using the surface roughness meter. The mass density of the a-C:H film was estimated to be 0.98 g/cm^3 by a weight gain measurement. Next, we measured the etching rate of the a-C:H film by Ar ion etching in the AES apparatus to compare the rate to that of the LID samples. For the etching rate is proportional to the mass density, we can estimate the mass densities of the LID samples. The density of carbon film on the probes close the LID head (1U, 1L) was estimated to be 0.93 g/cm^3 and that of the probes far from the head (2U, 2L) was estimated to be 0.90 g/cm^3. These values were lower than that of isotropic graphite (1.8 g/cm^3), and thus, they are so called "soft" deposition layer. Using the volume of the deposition layer, which was calculated using the surface area and the thickness of the layer, and the estimated mass density, a number of carbon atoms in the carbon layer was obtained. Using the number and the measured amount of the retained hydrogen with the TDS measurement, the hydrogen concentration (H/C) was obtained for each sample. The atomic ratios of H/C for 1U, 1L, 2U and 2L were estimated to be 0.53, 0.55, 1.26 and 1.24 after 9th experimental campaign, and H/C = 0.52, 0.58, 1.25 and 1.27 after 10th experimental campaign. Fig.7 shows the relationship between the atomic ratio of H/C for the probes and the maximum temperature of the probes during the LID discharge. The deuterium concentrations in graphite after the irradiation of deuterium ion beam with the energy of 1.0 keV at different graphite temperature [11,13] are also plotted in Fig.7. In the laboratory experiment, the deuterium concentration in graphite, D/C, after deuterium ion irradiation at the temperature from room temperature

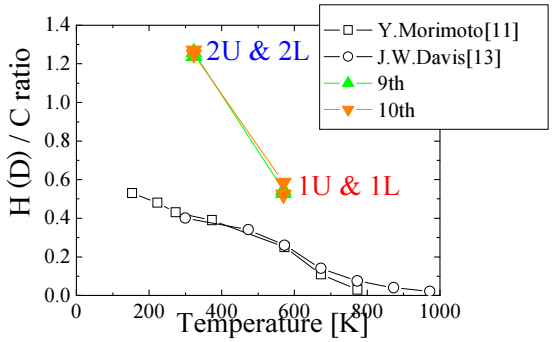

Fig.7 The relationship between the hydrogen concentrations of carbon films produced in the location of probes and the temperature on the surface of probes. In addition, the data of the deuterium concentration in graphite after deuterium ion irradiation with the energy of 1.0 keV at temperature from 153 K to 773 K is also shown. [11, 13]

to 570 K is approximately D/C=0.3 [11, 12, 13]. The H/C ratios on 1U and 1L probes were double of this value. For the carbon layer on 2U and 2L probes, the hydrogen concentrations were approximately triple of the graphite case. The large hydrogen concentration in 2U and 2L probes was associated with for polymerized amorphous structure in the carbon layers deposited on 2U & 2L probes. This result suggests that the characteristics of the carbon layers produced in the pumping duct of the LID were dominated by the deposition of hydrocarbon. In JT-60U, the atomic ratio of D/C for a carbon film deposited on the divertor tile was < 0.04 with the divertor temperature above 600 K [14]. Compared with this value, the atomic ratio of H/C in the carbon film produced in the vicinity of LID head was much higher. On the other hand, the D/C ratio for the carbon film deposited on the divertor tiles in JET MK-IIA divertor with the temperature below 500 K [14] was 0.1~0.4, and the D/C ratio in the re-deposited layers on the louvers, which was shadowed from the plasma and was kept at low temperature, was 0.8 [2,15]. This value was close to that of the co-deposited carbon film produced in the vicinity of LID obtained in the present study. The present results indicates that the hydrogen concentration of co-deposited layer could be large compared to that at the plasma-wetted region.

4. Conclusion

The relationship between the structure of carbon layer and hydrogen concentration in the layer on material probes in the vicinity of LID in LHD was investigated. The hydrogen concentration in the carbon films (H/C) on the probes close to the LID head (1U and 1L) where wall temperature was 570 K was around 0.55. On the othedddr hand, H/C in the carbon films on the probes far from the head (2U and 2L) where wall temperature 327 K was significantly large, 1.25. These values were several times larger than those in graphite after deuterium ion beam irradiation. The structures of these carbon films were polymer like amorphous hydrogenated carbon. This suggests that the hydrogen concentration in co-deposited carbon layer formed could be large due to deposition of hydrocarbon.

Acknowledgements

This work was supported by the Collaboration Research Program for Large Helical Device (NIFS04KOBS005, KLPP301) in National Institute for Fusion Science, and partly supported by the JSPS-CAS Core University Program in the field of Plasma and Nuclear Fusion.

Reference

[1] G. Federici et al, Nucl. Fusion **41**, 1967 (2001).
[2] J. P. Coad et al, J. Nucl. Mater. **290-293**, 224 (2001).
[3] M. Mayer et al, J. Nucl. Mater. **290-293**, 381 (2001).
[4] K. Masaki et al, J. Nucl. Mater. **337-339**, 553 (2005).
[5] T. Morisaki et al, J. Nucl. Mater. **337-339**, 154 (2005).
[6] S. Masuzaki et al, J. Nucl. Mater **363-365**, 314 (2007)
[7] T. Hino et al, Nucl. Fusion **44**, 496 (2004).
[8] Y. Yamaichi et al, Vacuum. **47**, 6-8, 973 (1996)
[9] J. Winter et al, Nucl. Instr. And Meth. In Phys. Res. **B23**, 538(1987).
[10] Y. Ishimoto et al, J. Nucl. Mater. **350**, 301 (2006)
[11] Y. Morimoto et al, J. Nucl. Mater. **313-316**, 595 (2003).
[12] J. Roth et al, J. Nucl. Mater. **93-94**, 601 (1980).
[13] J. W. Davis et al, J. Nucl. Mater. **217**, 206 (1994).
[14] T. Tanabe, Fusion Eng. Des. **81**, 139 (2006)
[15] Y. Hirohata et al, J. Nucl. Mater. **363-365**, 854 (2007)
[16] Paul K. Chu et al, Mater Chem and Phys. 96 (2006) 253-277

Proceedings of ITC18, 2008

Study of α particle Confinemet in the LHD Type Reactor

Y. MASAOKA[1)], S. MURAKAMI[1)]

[1)]*Department of Nuclear Enginieering, Kyoto University, Kyoto 606-8501, Japan*

The α-particle confinement of the heliotron type reactor is investigated based on three typical LHD configurations with different magnetic axis positions in the major radius. The GNET code is applied, in which the drift kinetic equation for the α-particle is sloved including the particle collisions with background plasma, is applied to evaluate the velocity space distributions, the radial profiles and energy loss rates.

It is found that the inward shift of magnetic axis improves the alpha-particle confinement strongly and a sufficient confinement of alpha-particle for fusion reactor is obtained in the strongly inward shifted configuration.

Keywords: LHD, α-particle, confinement, finite-β, GNET

1 Introduction

D-T fusion reaction produces a high energy α-particle which has the energy of 3.5MeV and the plasma heating by the energetic α-particle is necessary to sustain a high ion temperature plasma in the fusion reactor. Therefore, it is important to confine the energetic α-particles until the energy slow-down to the thermal energy. Also, the lost of the high energy α-particles may cause the damage of the first wall of the reactor. Therefore, a sufficient confinement of the high energy α-partiles is required. In helical systems, the magnetic configuration is mainly genereated by the coil currents so that we can obtain steady state plasma without an additional plasma current drive system. However, the behaviores of trapped energetic particles are complicated due to the three-dimensional (3D) magnetic configuration compared with that in the tokamak configuration. Thus, the detail analysis of the α-particle confinement is necessary for the reactor desing assuming helical configurations.

In this paper we study the α-particle confinement in the LHD type heliotron reactor extending the LHD configuration. The LHD can be flexible about the configuration and we can move the plasma horizontally to shift the magnetic axis position inward or outward relative to the center of helical coils by controlling the axisymmetric poloidal fields. The shift of the magnetic axis position alters characteristics of the ripple-induced transport and, especially, a strong inward shift reduces the ripple-induced transport to the comparable level of "advanced stellarators"[1] The trapped particle orbits are also improved as the magnetic axis shifts to the inward (Fig.1), from $R_{ax} = 3.75$ to $R_{ax} = 3.53$.

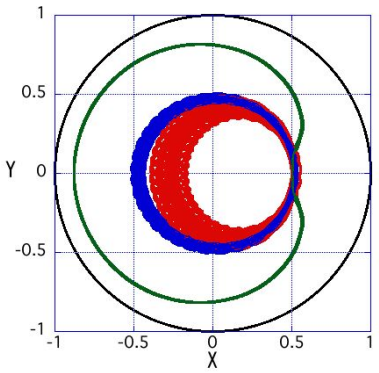

Fig. 1 Trapped particle orbits in the typical magnetic configuration of LHD.

2 Simulation Model

The α-particle confinements are investigated assuming reactor sized devices base on three typical configuration of LHD with different magnetic axis position in the major radius. The first one is the "OS" configuration based on the Rax=3.75m (standard heliotron configuration) of the LHD. The secound is the "IS" configuration based on the Rax=3.6m (σ -optimized configuration) and the last one is the "NO" configuration based on the Rax=3.50m (near the neoclassical-tarnsport-optimized configuration). The optimum axis position for the ripple-induced transport is 3.53m and a good confinement of energetic particle is expected in the NO configuration. The assumed parameters for extending to the heliotron reactors are the plasma volume : 1000m^3 and the magnetic field strength : 5T.

The GNET code [2] is applied to study the α-particle confinement. The drift kinetic equation in the

author's e-mail: masaoka@p-grp.nucleng.kyoto-u.ac.jp

5D phase-space

$$\frac{\partial f}{\partial t} + (\boldsymbol{v}_{\parallel} + \boldsymbol{v}_D) \cdot \nabla f + \dot{\boldsymbol{v}} \cdot \nabla_V f = C^{coll}(f) + L^{particle}(f) + S_\alpha, \quad (1)$$

is solved with the pitch angle and the energy scattering, where f is the particle flux and C^{coll} is the collision operator term. $L^{particle}$ and S_α are the loss and the source terms of the α- particle, respectively.

The source term, $S_\alpha$is evaluated assuming the temperature profiles and thefollowing density .

$$T_e(r) = 9.5 \times 10^3 \left[1 - \left(\frac{r}{a}\right)^2\right] + 5.0 \times 10^2 \quad [\mathrm{eV}], \quad (2)$$

$$n_e(r) = 1.90 \times 10^{20} \left[1 - \left(\frac{r}{a}\right)^8\right] + 1.00 \times 10^{19} \quad [\mathrm{m}^{-3}]. \quad (3)$$

Fig. 2 shows the radial profile of the source term of the α- particle.

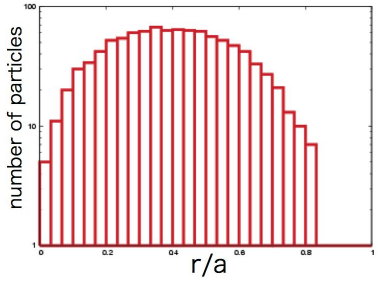

Fig. 2 Plot of the source term of the α-partile.

3 Simulation Results

We steady α-particle confinement in the heliotron reactor extending the typical three configurations of LHD; OS, IS, and NO. As a first step we study the configurations in a low beta limit to show a flexibility of LHD magnetic configuration. We run the GNET code until the steady state of the α-partile is obatined. The typical time to obtain the steady state is t = 0.2s.

Fig. 3 shows the velocity space distribution of the α-particle in the NO and OS configurations. We can see the slowing-down distribution of the α-particle from the energy of 3.5MeV. It is also found that the distribution near $V_{\parallel} = 0$ rigion (trapped particle region) is decreased compared with other regions due to the radial diffusion and the orbit loss of trapped particles. Also the less decrement is found in the NO configuration than that in the OS configuratin.

Fig. 4 shows the radial profile of the α-particle after the slowing-down to the thermal particle; t = 0.2s. We can see the radial broadening of the α-particle from the initial profile in both cases and the larger change in the radial profile is found in the OS configuration than that in the NO configuration.

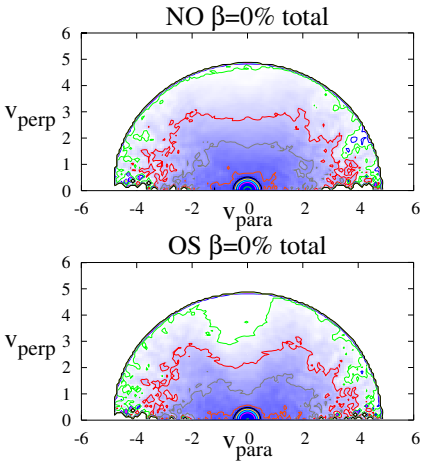

Fig. 3 The velocity space distributions of the α-particle; in the NO (top) and OS (bottom) configurations.

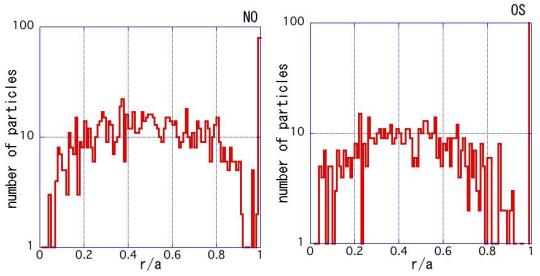

Fig. 4 The radial profiles of the α-particle after slowing-down in the NO (top) and OS (bottom) configurations.

Next we study the distribution of the lost α-particle in the energy and velocity space. The energy spectrum of the lost α-particle in the OS configuration is shown in Fig. 5. The large loss near the initial energy 3.5MeV can be seen in the OS configuration and this indicates the large prompt orbit loss of particle. This loss is strongly reduced in the NO configuration where the trapped particle orbit is improved largely.

Fig. 6 shows the velocity distribution of the lost α-particle in the OS configuraton. It is found that the lost α-particle has the similar pitch angle close to the trapped and passing particle boundary in the velocity space. This shows that the radial diffusion of the transition particle between the trapped and passing motions is large.

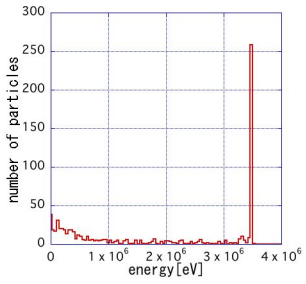

Fig. 5 Energy spectrum of lost α-particles in the OS configuration.

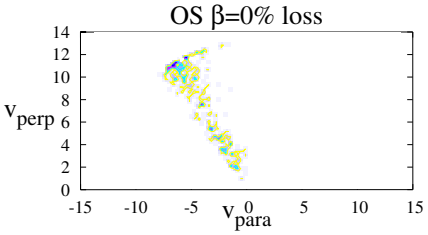

Fig. 6 Velocity space distribution of lost α-particles in the OS configuration.

We, next, show the time development of the energy loss rate of α-particle in Fig.7. We can see large energy loss after very short time ($t < 10^{-3}$s) in the OS configuration due to the prompt orbit loss and the initial loss is very small in the IS and NO configurations. The loss rate increased to about 5% in the NO configuration.

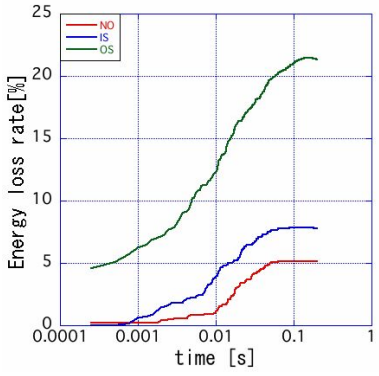

Fig. 7 Energy loss rate

4 Conclusion

We have studied the α-particle confinement of the heliotron type reactor assuming reactor sized LHD based on three typical configurations with different magnetic axis positions in the major radius. The GNET code has been applied, in which the drift kinetic equation for the α-particle is sloved including the particle collisions with background plasma. The velocity space distributions, the radial profiles and energy loss rates have been evaluated chainging the magnetic configurations. It is found that the inward shift of magnetic axis improves the alpha-particle confinement strongly and a sufficient confinement of alpha-particle for fusion reactor is obtained in the strongly inward shifted configuration.

[1] S. Murakami, et al., Nucl. Fusion, 42 (2002). L19
[2] S. Murakami, et at., Fusion Sci. Technol. 46 (2004) 241.

Proceedings of ITC18,2008

Influence of Neutral Beam Injection Direction on Fast Ion Distribution Function in Large Helical Device (LHD)

Evgeny Alexandrovitch VESHCHEV[1], Tetsuo OZAKI[1], Tsuguhiro WATANABE[1], Shigeru SUDO[1] and LHD Experimental Group[1]

1) National Institute for Fusion Science, Toki, Gifu 509-5292, Japan

Effective ion heating and good fast ion confinement are essential for ignition. Therefore the influence of various types of plasma heating on fast ion distribution function in various configurations of magnetic field should be studied. To study distribution of fast ions in LHD plasma a new Angular Resolved Multi-Sightline Neutral Particle Analyzer (ARMS-NPA) has been developed [1-3]. It scans plasma by 20 sightlines and can provide detailed information about angular and radial distribution of fast particles. In this paper the influence of co- and counter-Neutral Beam Injection (NBI) on angular distribution of suprathermal particle tail is shown (Fig.1). Measurements were made for different directions of magnetic field in inward- (R=3.6m) and outward-shifted (R=3.9m) magnetic axis position. Dependence of width of suprathermal ion tail angular distribution during co- or counter- NBI was measured for different magnetic field strength and demonstrated in current work. The simulation results of fast particle orbits are shown as well in order to explain the experimental results.

Keywords: fast ion heating, neutral particles, angle resolved measurements, fast particle flux simulation, diagnostic, fast particle orbits, energy resolved measurements, angular distribution function, ion distribution.

1. Inroduction

Fast ion distribution plasma may suffer significant changes under various plasma heating mechanisms in different magnetic field configurations and plasma parameters. Therefore, as effective ion heating and good fast ion confinement are essential for ignition, fast ion distribution function should be studied properly. For this purpose numerous diagnostic tools have been developed on modern fusion devices and on LHD in particular. LHD plasma has a very complex 3D shape that complicates diagnostics and investigations of fast particle distribution function.

One of recently developed is Angular Resolved Multi-Sightline Neutral Particle Analyzer (ARMS-NPA) scanning plasma by 20 sightlines and being upgraded currently up to 40 sightlines. Among previously used NPAs on LHD for angular resolved measurements of fast particles there was only one “multi-sightline” Silicon Detector based NPA (SD-NPA) with 6 scanning chords [4]. However, the angular resolution of SD-NPA was not enough for profound investigations of fast particle angular distribution in a single plasma discharge and for studying of such an effect as predicted by theory existence of fast particles loss-cone regions in helical plasma.

The key feature and unique advantage of ARMS-NPA is the possibility to make detailed time-, angular- and energy-resolved measurements of fast particle distribution in plasma in a single plasma discharge.

First experimental results demonstrated the possibility of loss-cone existence in LHD plasma [3,5]. Same time, as comparisons of fast particle population in plasmas shifted in and out in major radius are important in the suprathurmal ion confinement studies, investigations of fast particle angular distribution has been started in inward-shifted (Rax=3.6m) and outward-shifted (Rax=3.9m) magnetic axis position configurations in [3]. As Neutral Beam Injection is widely used for fast particle heating and considered to be one of the heating mechanisms in future fusion devices as well, it is important to study how does direction of neutral beam particles influence on fast ion distribution in different plasma conditions and different magnetic axis positions.

In this paper experimental results of fast particle angular distribution obtained by ARMS-NPA are shown for inward-shifted (Rax=3.6m) and outward-shifted (Rax=3.9m) magnetic axis positions for co- and counter-injected NB for every case of magnetic axis position. Experimental results are compared with theoretical predictions based on fast ion orbit calculations.

2. Experimental Setup

The position of ARMS-NPA on LHD versus NB injectors and ICRF antennas is shown on Fig.1. For investigation of influence of NBI direction on angular

author’s e-mail: veshchev.evgeny@lhd.nifs.ac.jp

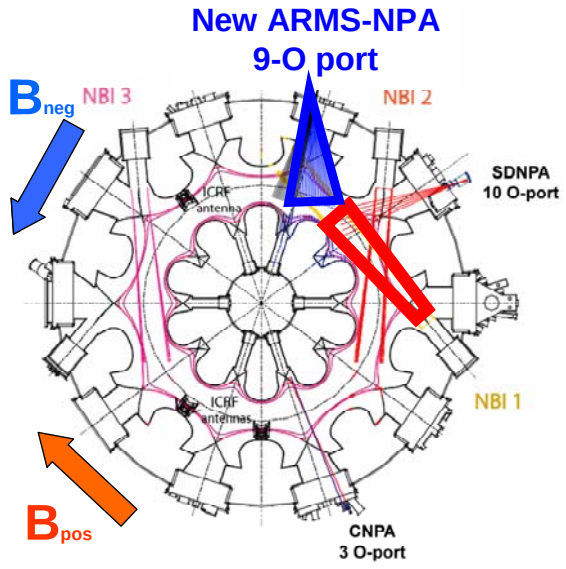

Fig.1 ARMS-NPA location on LHD (blue) versus NBI#1 (red).

distribution of fast particles NBI#1 was used with the energy of injected particles equal to 180keV. In the case with positive magnetic field (marked by orange on Fig.1) NBI#1 serves as counter-injector and in the case with negative magnetic field (marked by blue on Fig.1) as co-injector.

3. Experimental Results

Experimental angular-resolved fast particle spectra are shown on Fig.2. Spectra on Fig.2a) and 2b) correspond to co- and counter-injected NBI#1 regimes correspondingly with inward-shifted (Rax=3.6m) magnetic axis position. Spectra on Fig.2c) and 2d) correspond to co- and counter-injected NBI#1 regimes correspondingly with outward-shifted (Rax=3.9m) magnetic axis position. The colored scale units of every picture correspond to the ln(Γ(E)), where Γ(E) [counts] is the flux of fast particles detected by diagnostic.

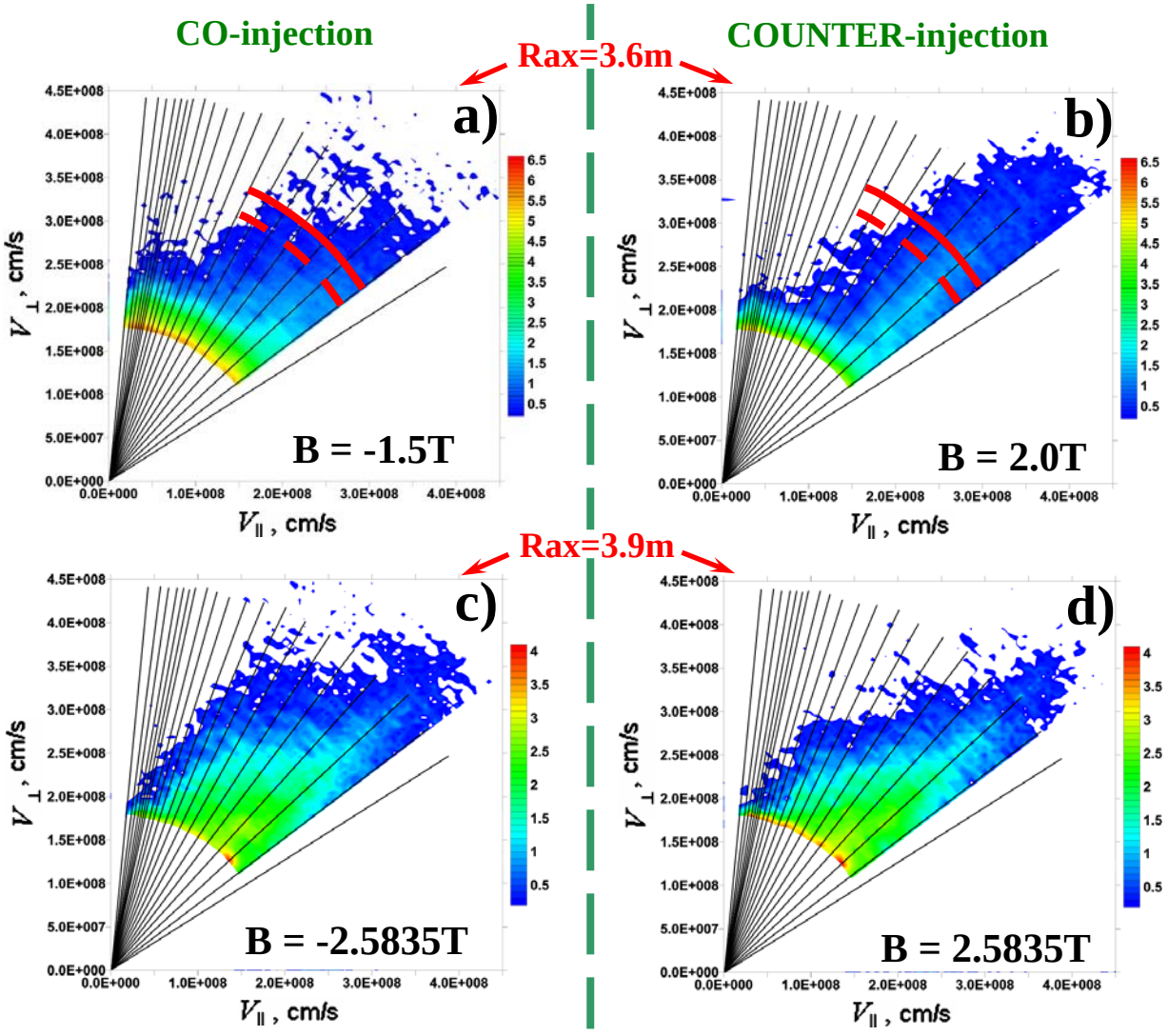

Fig.2 Comparison of experimental fast particle angular distribution in co- and counter-injected NBI#1 regimes for Rax=3.6m and R=3.9m magnetic axis positions

Let's compare spectra obtained in co- and counter-regimes, *i.e.* compare Fig.2a) with Fig.2b) and compare Fig.2c) with Fig.2d). From these comparisons one can notice that angular distribution of high-energy tail from NBI#1 is wider during co-injection for both outward- and inward magnetic axis positions.

Let's compare spectra obtained in co-injected regimes with inward (Rax=3.6m) and outward (Rax=3.9m) magnetic axis positions and spectra obtained in counter-injected ones, *i.e.* compare Fig.2a) with Fig.2c) and compare Fig.2b) with Fig.2d). From these comparisons one can notice that although total flux has been reduced in regimes with outward-shifted magnetic axis (colored scale limit is equal to 4 for Rax=3.9m against scale limit equal to 6.5 for Rax=3.6m), the high high-energy tails from NBI#1 in outward-shifted magnetic axis configuration are wider than those ones in inward-shifted magnetic axis configuration.

In order to confirm if such a difference has appeared due to increased magnetic field strength (B=2T for Rax=3.6m case against B= 2.6T for Rax=3.9m) or due to magnetic axis shift effect, dependence of fast ion angular distribution on magnetic field strength has been measured for the case of Rax=3.6m. The magnetic field strength was varied from -0.75T to -2.811T. Results of such measurements are shown on Fig.3. It shows angular distribution of fast particles with the energies of 65÷70keV as it is marked, for example, on Fig.2a) and Fig.2b) by red colored arcs. Black circles of Fig.3 correspond to the positive magnetic field direction and counter-injecting NBI#1 correspondingly. All other colored dots correspond to the negative magnetic field direction and co-injecting NBI#1. Black circles and colored dots except blue dots correspond to magnetic axis position at Rax=3.6m, blue dots correspond to slightly shifted out magnetic axis position at Rax=3.65m.

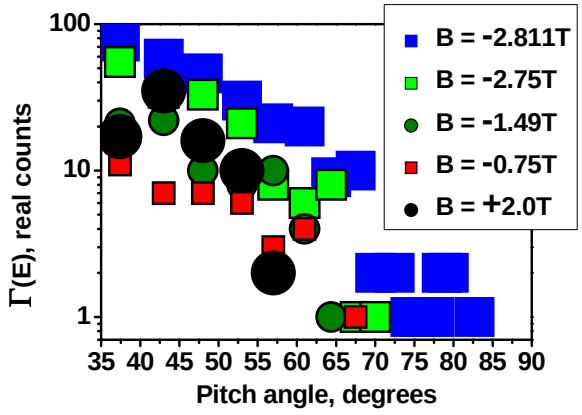

Fig.3 Angular distribution of high energy tail particles from NBI#1 (particles energies are in the range of 65÷70keV). Blue squares correspond to Rax=3.65m magnetic axis position. All other dots correspond to Rax=3.6m. Black dots correspond to positive direction of magnetic field and , accordingly, to counter-injecting NBI#1, all other dots correspond to negative magnetic field and , accordingly, to co-injecting NBI#1.

It can be noticed on the Fig.3 that although the flux of fast particles is increasing with increasing of magnetic field strength (for the case of negative magnetic field), the angular range of suprathermal ion tail remains the same (35°÷67°) degrees for the case of negative magnetic field and magnetic axis position at Rax=3.6m. However, the slight shift of magnetic axis to the outward direction (Rax=3.65m) together with increasing of magnetic field strength (B=-2.811T) leads to the broadening of angular distribution (35°÷80°) together with increasing of fast particles population.

Same time from Fig.3 it can be clearly seen that fast particles angular distribution for the case of B=2T is narrower than those ones for the case of negative magnetic field and, accordingly, co-injected NBI#1 in the whole range of scanned magnetic field strength from -0.75T to -2.811T.

Therefore, from experimental results it may be concluded that co-injecting NB is more effective than counter-injecting NB for fast ion heating on LHD.

In addition to that, outward shift of magnetic axis is more favorable than inward shift of magnetic axis for fast ion heating from the point of view of creating a broader angular distributed high energy tail from NB.

Accordingly, outward shifted magnetic axis configuration with co-injecting NBI (in our case it is Rax=3.9m, B=-2.5835T and operating NBI#1) is the most appropriate for broad heating of fast ions by tangential NBI in LHD plasma.

4. Simulation Results

Obtained experimental results can be explained by fast particle orbit simulation results, which predicted that co-injection is more favorable for fast ion heating than counter-injection on LHD [5]. These simulation results from manuscript [5] can be seen on Fig.4, which shows the most outermost drift surfaces of co-injected (by red color) and counter-injected (by green color) NB particles with E=180keV. Magnetic axis radius is Rax=3.6m for both cases and magnetic field strength at the axes is B=0.5T for Fig.4a) and B=2.75T for Fig.4b).

From the Fig.4b) it can be seen that in usual LHD operating range (Bax=2.75T E=180keV) the confinement region of the counter-injected NB particles is slightly smaller than the Last Closed Flux Surface (LCFS) and the confinement region of co-injected NB particles reaches

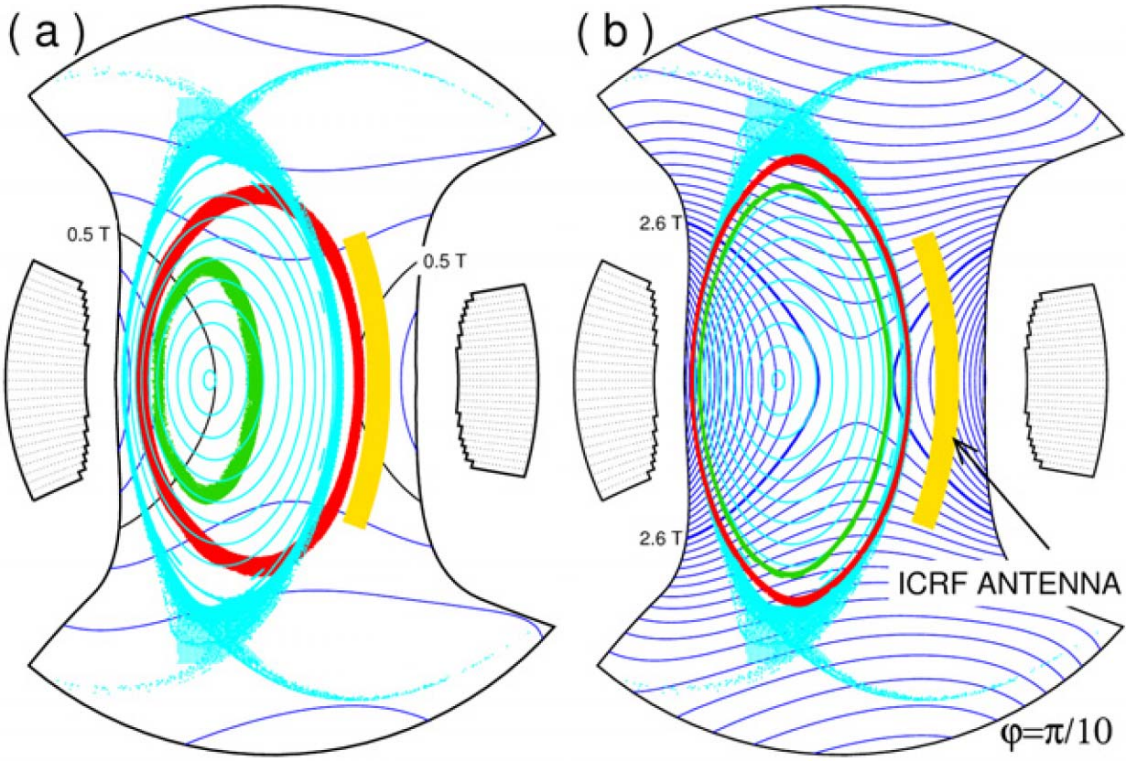

Fig.4 Relations between the magnetic surface, the outermost drift surfaces and magnetic field intensity are shown by the Poincar´e plots at the poloidal cross section of $\varphi = \pi/10$. Red (green) color dots show the almost outermost drift surface of co-NBI (counter-NBI) particle with E = 180 keV. Cyan color dots show the structure of lines of force. Position of magnetic axis is 'inward shifted' one (Rax = 3.6 m). (*a*) Low magnetic field case (Bax = 0.5 T). (*b*) Standard magnetic field case (Bax = 2.75 T).

even the boundary of the chaotic field line layer exceeding the LCFS. However, in the low magnetic field operation case, the effect of the $B \times \nabla B$ drift motion increases. The drift surface of the co-NBI can extend fairly outside the LCFS and the drift surface of counter-NBI is reduced fairly compared with the LCFS as it is shown on figure Fig.4a).

References

[1] E. A. Veshchev *et.al.*, Rev. Sci. Instrum., **77**, 10F129 (2006).
[2] E. A. Veshchev *et.al.*, Plasma and Fusion Research, **2**, S1073 (2007).
[3] E. A. Veshchev *et.al.*, Plasma and Fusion Research, **3**, S1035 (2008).
[4] J.F. Lyon *et al.*, Rev. Sci. Instrum., **74**, 1873 (2003).
[5] T.Watanabe *et.al.,* Nucl. Fusion, **46**, 291-305 (2006).

Proceedings of ITC18, 2008

A Theoretical Model of Ripple Resonance Diffusion of Alpha Particles in Tokamaks

Hideyuki MIMATA[1)], Hiroaki TSUTSUI[1)], Shunji TSUJI-IIO[1)], Ryuichi SHIMADA[1)] and Keiji TANI[2)]

[1)]*Tokyo Institute of Technology, 2-12-1-N1-11 Ookayama, Meguro-ku, Tokyo 152-8550, Japan*
[2)]*Nippon Advanced Technology Co., Ltd. Naka Office, 801-1 Mukoyama, Naka 311-0193, Japan*

A theoretical model of ripple resonance diffusion of fusion-produced α particles in tokamaks is presented. An M-shaped energy dependence of diffusion coefficients around ripple resonance conditions, in which the toroidal precession motion of banana particles resonates to the field strength with ripples, was numerically obtained. The M-shaped dependence comes from both island structure and initial distribution of α particles in a $(N\phi, \psi)$ phase space, where N is the number of toroidal field coils, and $(N\phi, \psi)$ is the coordinate of the reflection point of a banana particle in the toroidal angle and the poloidal flux space. Although the particles have periodic motions and a normalized hamiltonian $C(N\phi, \psi)$ is conserved without collisions, pitch angle scattering by collisions changes constant parameters in C and causes the diffusion whose characteristic step size and time are the island size and a variance time to the separatrix respectively, while the characteristic time just outside of the separatrix is determined by a collisionless process.

Keywords: α particle, tokamak, diffusion, ripple resonance

1 Introduction

The confinement of fusion produced α particles is important to maintain burning plasmas in tokamaks. Although α particles are well confined in axisymmetric fields, it has been shown that the loss of α particles due to magnetic field ripple is dominant in the diffusion process in actual tokamaks [1, 2]. However the understanding of the loss processes in detail is not sufficient.

The pitch-angle scattering of fusion-produced α particles in one bounce motion is small enough to maintain banana orbits. Then collisonless orbits are important for the diffusion process. Since the radial displacement of a banana orbit by ripples depends on the toroidal phase at the banana tip [3], the cumulated radial displacement becomes resonantly large when the difference in the toroidal angles of successive banana tips is a multiple of the toroidal angle of adjacent TF coils (the ripple resonance). This toroidal distance of successive banana tips is determined by a toroidal precession ϕ_p. Yushmanov theoretically analyzed this ripple resonance diffusion by means of the banana-drift kinetic equation without the radial change of the toroidal precession $\partial\phi_\mathrm{p}/\partial r$ [4]. Since the toroidal precession, however, strongly depends on the radial position in an actual tokamak, we investigated the ripple resonance diffusion in a realistic system with the radial change of the toroidal precession by numerical calculations. Then the diffusion coefficients with an M-shaped energy dependence around the ripple resonance energy was represented [8]. In this paper, we analyze the physical phenomena of the ripple resonance diffusion using a theoretical representation of collisionless orbits.

Section 2 shows the numerical calculation of the ripple resonance diffusion. Then the importance of the collisionless orbit is explained. In Sec. 3, we analyze the physical phenomena of the ripple resonance diffusion using the theoretical representation of collisionless orbits. The conclusions are given in Sec. 4.

author's e-mail: hmimata@nr.titech.ac.jp

2 Ripple Resonance Diffusion

In axisymmetric field, the toroidal canonical momentum,

$$P_\phi = mv_\parallel I/B + e\psi = e\psi_\mathrm{b}, \tag{1}$$

where $v_\parallel$ is the velocity parallel to the magnetic field and $I = RB_\phi$, is conserved and corresponds to the poloidal magnetic flux at a banana tip, ψ_b. However it is not conserved in rippled fields and has displacements depneding on the toroidal angle of the banana tip [3, 5, 6, 7],

$$\Delta\psi = \Delta_\mathrm{b} \sin(N\phi \mp \pi/4), \tag{2}$$

$$\Delta_\mathrm{b} = I\gamma\rho_\mathrm{L}\sqrt{\pi Nq/(\varepsilon|\sin\theta_\mathrm{b}|)}, \tag{3}$$

where γ is the ripple strength, ρ_L is the Larmor radius, θ_b is the poloidal angle of the banana tip, $\mp$ corresponds to the upper and lower banana tip, $\varepsilon = r/R_0$, and each parameter is evaluated at the banana tip. Then the cumulated radial displacement becomes resonantly large when the difference in the toroidal angles of successive banana tips is a multiple of the toroidal angle of adjacent TF coils. This ripple resonance conditon is given by

$$2N\phi_\mathrm{p} = 2k\pi \ \ (k = 0, \pm1, 2, 3, \cdots), \tag{4}$$

where ϕ_p is the toroidal precession during half bounce [6]. Yushmanov theoretically analyzed this ripple resonance diffusion without the radial change of the toroidal precession and diffusion coefficients have peaks at resonance energies [4]. Since the toroidal precession, however, strongly depends on the radial position in an actual tokamak, we investigated the ripple resonance diffusion in a realistic system with the radial change of the toroidal precession and found that it has an M-shaped energy dependence around the resonance energies [8] (Fig. 1). The diffusion coefficient also changes with the ripple strength and the plasma density. The value of the coefficients is proportional to the ripple strength, while the energy range where diffusion is enhanced by the ripple becames wider with increasing ripple strength. Diffusion coefficients are roughly proportional to the collision frequency.

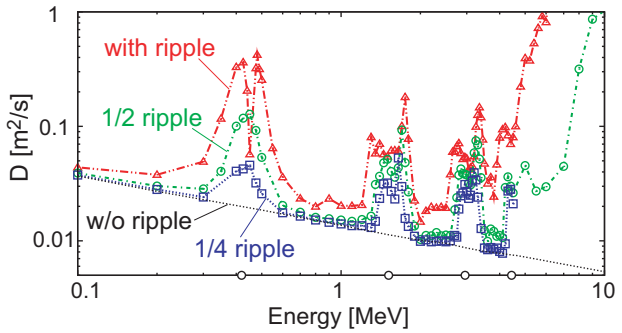

Fig. 1 Energy dependence of the diffusion coefficient changes with the ripple strength. In this configuration, 0.4, 1.5, and 2.9 MeV are the ripple resonance energies without ripples (open circles). Particles start from the same banana tip at any energies. Diffusion coefficients have an M-shaped dependence around each resonance energy. At energies over about 5 MeV, the diffusion coefficient increases with the energy, since this range is nealy stochastic [5].

Next, we investigated collsionless orbits in rippled fields using a mapping model to understand the M-shaped dependence of diffusion coefficients. Then,

$$\left((\psi-\psi_k)/\Delta_p\right)^2+\cos\left(N\phi+\Phi_k\right)=C\,, \tag{5}$$

$$\Delta_p=\sqrt{2\Delta_b\cos(\Phi_k-\pi/4)}/\left(N(\partial\phi_p/\partial\psi)|_{\psi_k}\right) \tag{6}$$

is obtained except for the singular point, $\cos(\Phi_k-\pi/4)=0$, where ψ_k is the resonance surface satisfying Eq.(4),

$$\Phi=N(\phi_b(\psi)+\phi_p(\psi))/2, \tag{7}$$

ϕ_b is the toroidal length of the banana orbit,

$$\phi_b=2q\theta_b, \tag{8}$$

and $\Phi_k=\Phi(\psi_k)$. Equation (5) determines the island width and location. Around the resonance surface $\psi=\psi_k$, an island structure is formed and the width of the island is determined by Δ_p. The integration constant C determines the collisionless orbit and C is conserved in collisionless cases, and $C=1$ and $-1<C<1$ correspond to the separatrix and an orbit inside the separatrix, respectively. The change in the island structure mainly depends on ψ_k, Φ_k and Δ_p. The position of the O-point and the width of the island are specified by (Φ_k,ψ_k) and Δ_p, respectively. When particles outside the separatrix enter inside the saparatrix by collisions, they can jump about the width of the island, leading to the enhancement in the diffusion. Therefore we numerically evaluated the diffusion coefficients starting from each collisionless orbit on the Poincaré map. The results are shown in Fig. 2. C obtained from the guiding center orbit computation is not constant. Then, we introduce a label of each trajectory, $\tilde{C}$, defined by

$$\tilde{C}=\left((\psi-\psi_k)/\tilde{\Delta}_p\right)^2-1, \tag{9}$$

where $2\sqrt{2}\tilde{\Delta}_p$ is the width of the island skimmed from the Poincaré map of the guiding center orbits. Just outside of the separatrix, the diffusion coefficient is large and it becomes small with the distance from the separatrix. On the other hand, inside the separatrix, diffusion coefficients are small. Since the collisionless orbit is important for the ripple resonance diffusion, we consider a theoretical model of the ripple resonance diffuion from the analytical representation of the collisionless orbit, Eq. (5).

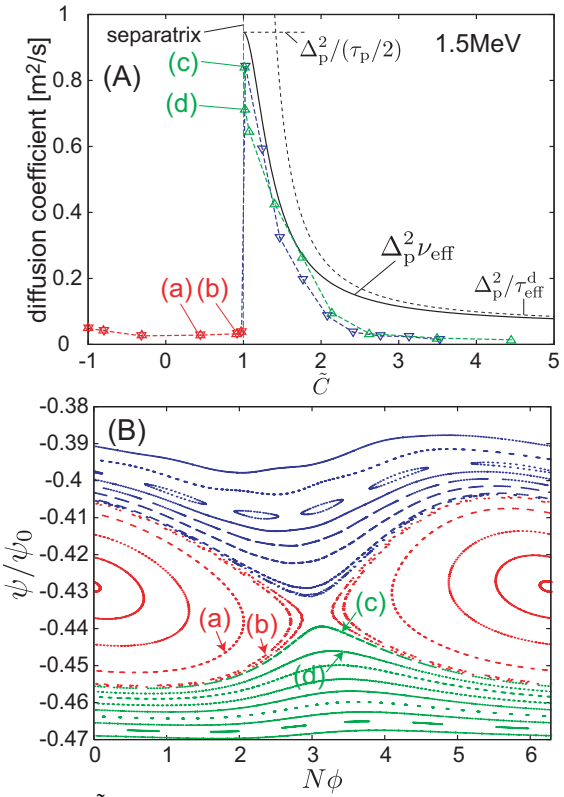

Fig. 2 (A) $\tilde{C}$-dependence of diffusion coefficients at 1.5 MeV from which the neoclassical diffusion is subtracted. $\tilde{C}>1$, two plots correspond to the trajectory upper and lower side of the island. (B) Initial trajectories of the calculation of each diffusion coefficient in (A). Initial positions are randomly given from a few hundred bounce motions on these collisionless trajectories.

3 Theoretical Model of the Ripple Resonance Diffusion

In this section, we analyze the ripple resonance diffusion by a model consistent with the results of the previous section: the step size of the diffusion is the width of the island, Δ_p, and the characteristic time of the diffusion is the time in which particles reach the separatrix by collision. Here we assume particles are uniformly distributed on a constant C orbit, and hence the characteristic time must be much greater than the bounce time. We evaluate this characteristic time below. As shown in the previous section, the island structure is determined by ψ_k and Φ_k. Since the separatrix is determined by $C = 1$, the characteristic time is the time in which C becomes 1 by collisions.

The energy, W, and the magnetic moment, μ_m, of the particle are conserved in collisionless cases and these are changed by Coulomb collisions. The time evolution of the average and variance of W and $\sin^2\zeta = (v_\perp/v)^2 = \mu_\mathrm{m}B/W$ (ζ is the pitch angle) by collisions is represented by the slowing-down time, τ_s, the deflection time, τ_d, and the energy-exchange time, τ_ε, by taking emsemble average. Parameters, ϕ, ψ, Φ_k and ψ_k, which determine the C value of the particle, is changed by the change in W and $\sin^2\zeta$, then a change in C is occured. A change in the position of the particle by collisions brings a change in C,

$$\Delta C_\phi = -\sin(N\phi + \Phi_k) N\Delta\phi, \tag{10}$$

$$\Delta C_\psi = \pm(2/\Delta_\mathrm{p})\sqrt{C - \cos(N\phi + \Phi_k)}\,\Delta\psi, \tag{11}$$

where $\pm$ is corresponds to each case, $\psi > \psi_k$ and $\psi < \psi_k$. When the toroidal angle of the banana tip varies, a phase difference to the map is occured and C is changed. While a change of the resonance surface, ψ_k, and the phase, Φ_k, of the island by collision bring a change in C,

$$\Delta C_{\Phi_k} = [(C - \cos(N\phi + \Phi_k))\tan(\Phi_k - \pi/4) - \sin(N\phi + \Phi_k)]\,\Delta\Phi_k, \tag{12}$$

$$\Delta C_{\psi_k} = \mp(2/\Delta_\mathrm{p})\sqrt{C - \cos(N\phi + \Phi_k)}\,\Delta\psi_k. \tag{13}$$

Since the contribution of the change in ψ and ψ_k to a change in C depends on the width of the island, the ripple strength γ and the spatial change in the toroidal precession, $\partial\phi_\mathrm{p}/\partial\psi$, are important. When ϕ_p is changed by collisions, resonance surface ψ_k moves to satisfy the resonance condition (4). Since a change in ψ_k becomes large with the decrease of $\partial\phi_\mathrm{p}/\partial\psi$, the contribute of ψ_k depends on $\partial\phi_\mathrm{p}/\partial\psi$ while the analysis by Yushmanov [4] is the case, $\partial\phi_\mathrm{p}/\partial\psi = 0$. In this paper, we consider the magnetic configulation with $\psi/\phi_\mathrm{p}(\partial\phi_\mathrm{p}/\partial\psi) \gg \varepsilon^2 S/Nq$, $\varepsilon^2\phi_\mathrm{p}/(Nq)^2 \ll N\Delta_\mathrm{p}(\partial\phi_\mathrm{p}/\partial\psi) < \pi/2\sqrt{2}$ and collision times with $\tau_\mathrm{d}/\tau_\mathrm{s} \ll (Nq/\varepsilon)^2\Delta_\mathrm{p}(\partial\phi_\mathrm{p}/\partial\psi)/\phi_\mathrm{p}$, $\tau_\mathrm{d}/\tau_\varepsilon \ll 1$.

As described above, a change in the orbit C by collisions is described by the a change in W and $\sin^2\zeta$ via a change in the parameters, ϕ, ψ, Φ_k, and ψ_k. Then the time evolution of the average and the variance of C is described by collision times by taking the emsemble average. First, we evaluate the time evolution of the average of C by collisions. The average of ΔC_ψ is zero because the change in back and forth banana motion calncels each other. Because we consider the particles outside the separatrix in this model, ΔC_ϕ and the second term of ΔC_{Φ_k} are vanished by taking average over ϕ. Then, the time evolution of average of C is given by

$$\frac{\mathrm{d}}{\mathrm{d}t}\left\langle\langle C\rangle_\phi\right\rangle = \left(\mp\frac{2\sqrt{C+1}}{\Delta_\mathrm{p}}E\left(\sqrt{\frac{2}{C+1}}\right) + C\tan(\Phi_k - \pi/4)N\theta_\mathrm{b}\frac{\partial q}{\partial\psi}\right)\frac{\phi_\mathrm{p}}{\partial\phi_\mathrm{p}/\partial\psi}\frac{1}{\tau_\mathrm{s}}, \tag{14}$$

where $\langle\rangle_\phi$ means average over ϕ, $E(k)$ is the complete elliptic integral of the first kind. bThe first term arises from the change in the resonance surface ψ_k and the second term arises from the change in the width of the island by the change in Φ_k. The characteristic time, in which C becomes unity is given by the inverse of Eq. (14),

$$\tau^\mathrm{s}_\mathrm{eff} = (1 - C)\mathrm{d}t\Big/\mathrm{d}\left\langle\langle C\rangle_\phi\right\rangle. \tag{15}$$

Next, we evaluate the time evolution of the variance of C. With the condition $\psi/\phi_\mathrm{p}(\partial\phi_\mathrm{p}/\partial\psi) \gg \varepsilon^2 S/Nq$ and $\varepsilon^2\phi_\mathrm{p}/(Nq)^2 \ll N\Delta_\mathrm{p}(\partial\phi_\mathrm{p}/\partial\psi)$, the contribution of the $\left\langle(\Delta C_\psi)^2\right\rangle$ and $\left\langle(\Delta C_{\psi_k})^2\right\rangle$ is much smaller than $\left\langle(\Delta C_{\Phi_k})^2\right\rangle$. Moreover, $\left\langle(\Delta C_\phi)^2\right\rangle / \left\langle(\Delta C_{\Phi_k})^2\right\rangle \sim (\phi_\mathrm{p}/q\varepsilon)^2$ is much less than unity. Ignoring τ_ε since $\tau_\mathrm{d} \ll \tau_\varepsilon$, the time evolution of the variance of C is given by

$$\frac{\mathrm{d}}{\mathrm{d}t}\left\langle\left\langle(C - \langle C\rangle)^2\right\rangle_\phi\right\rangle = \left[\left(C^2 + \frac{1}{2}\right)\tan^2(\Phi_k - \pi/4) + \frac{1}{2}\right] \times\left(\frac{NqR_0}{r\sin\theta_\mathrm{b}}\right)^2\frac{1}{2}\left\langle\sin^2 2\zeta\right\rangle_\mathrm{b}\frac{1}{\tau_\mathrm{d}}, \tag{16}$$

where $\langle\rangle_\mathrm{b}$ means the average over the bounce time. The main contributions are the changes in the width of the island and in the phase, and these are caused by the change in Φ_k. The particles on C spread to the separatrix, when the variance of C changes 0 to $(C-1)^2$. Because of $\psi/\phi_\mathrm{p}(\partial\phi_\mathrm{p}/\partial\psi) \gg \varepsilon^2 S/Nq$ and $\varepsilon^2\phi_\mathrm{p}/(Nq)^2 \ll N\Delta_\mathrm{p}(\partial\phi_\mathrm{p}/\partial\psi)$, the change in C comes from the change in ψ and ψ_k is much smaller than the width of the island, then the change in the averege of C is much less than the change in the variance of C. Therfore the change in the average of C can be ignored during C spreads. Then the characteristic time is given by $(C-1)^2$ over the rate of change at C, Eq. (16),

$$\tau^\mathrm{d}_\mathrm{eff} = (C-1)^2\,\mathrm{d}t\Big/\mathrm{d}\left\langle\left\langle(C - \langle C\rangle)^2\right\rangle_\phi\right\rangle. \tag{17}$$

The average of C changes proportionally to τ_s^{-1} and the variance of C changes proportionally to τ_d^{-1}. However, as mentioned above, the change in C by the change in the variance of C is dominant. Then the effective collision frequendy is $\nu_\mathrm{eff} = 1/\tau^\mathrm{d}_\mathrm{eff}$ and the diffusion coefficient is

evaluated by $D \sim \Delta_p^2 \nu_{\rm eff}$. In this diffusion model, diffusion coefficient becomes small with C which corresponds to the distance from the separatrix and the particles inside the separatrix ($-1 < C < 1$) do not contribute to the diffusion. Since, however, at the separatrix, the diffusion coefficient becomes infinity, other characteristic time determines the peak of the diffusion.

We considered when a particle reachs a separatrix, it can jump the width of an island so far. However, it takes half a time in which particle rounds the island on a collisionless orbit (τ_p) to jump the width of an island. Therefore we assume the effective collision frequency is

$$\nu_{\rm eff} = 1/(\tau_{\rm eff}^{\rm d} + \tau_p/2). \qquad (18)$$

Here τ_p is evaluated at $\psi - \psi_k = \Delta_p$ in the axisymmetric field,

$$\tau_p = 2\pi\tau_b \Big/ \left[N\Delta_p(\partial\phi_p/\partial\psi)|_{\psi_k}\right] \quad (C \le 1)\,, \qquad (19)$$

where τ_b is the bounce time. Then the diffusion coefficient at the separatrix is evaluated, $D \sim \Delta_p^2\nu_{\rm eff} = \Delta_p^2/(\tau_p/2)$. It has a dependence $D \propto W$ and $D \propto \gamma^{1/2}$ since $\Delta_p \propto W^0$, $\Delta_p \propto \gamma^{1/2}$ and $\tau_p \propto W^{-1}$, $\tau_p \propto \gamma^{-1}$. Meanwhile, the dependence of diffusion coefficients becomes $D \propto W^{-3/2}$ and $D \propto \gamma$ when particles are away from the separatrix because of the deflection time $\tau_d \propto W^{3/2}$.

Fig. 2 also shows the comparison between above theoretical model (solid line) and the numerical results. In this magnetic configulation, $\tau_p/2 \sim 9\tau_b$ and the peak of the diffusion coefficients at the separatrix is about $1.0\,{\rm m}^2/{\rm s}$. and the main contribution to the change of C is the change of the island width determined by Eq. (12). Thus particles of $C > 2(1/\cos\Phi_k)^2 - 1$ can not enter inside the separatrix since the island width is limited and cannot be extended to all region by collisions. However trajectories on large C can be changed to unity by the changes in the width of the island and the phase in the theoretical model. Then Eq. (17) has a finite value at $C = \infty$ and there is difference between the theoretical model and the numerical results at large C in Fig. 2.

If the diffusion coefficients at the separatrix is determined by τ_p, it does not depend on the collision frequency. Fig. 3 shows the dependence of the diffusion coefficients on the plasma densisy (collision frequency). Except for just outside the separatrix, diffusion coefficients are propotional to the plasma density. However the diffusion coefficients just outside the separatrix are independent of the plasma density. Therefore the peak of the diffusion coefficients at the separatrix is considered to be determined by a collisionless process, the physical mechanism for which is left for future work.

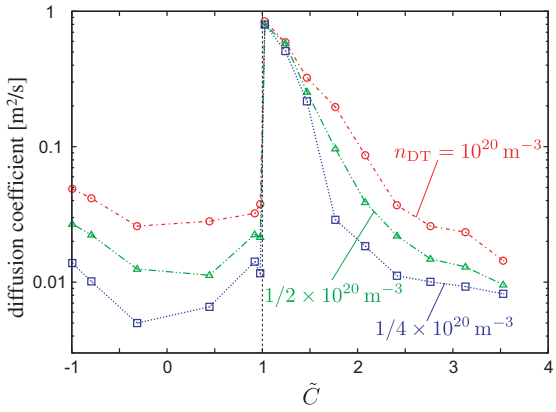

Fig. 3 The dependence of the diffusion coefficients (Fig. 2) on the plasma density. The peak of the diffusion coefficients at the separatrix do not depend on the plasma density.

4 Conclusions

The diffusion coefficients were found to have an M-shaped energy dependence around resonance energies by the numerical calculation and it was shown to be caused by the collisionless orbit in the phase space. The ripple resonance diffusion was analyezed by the theoretical model: step size of the diffusion is about the width of the island, Δ_p and characteristic time of the diffusion is the time in which particles reach the separatrix by collisions. Concluding remarks are made as follows,

1. In the magnetic configuration with $\psi/\phi_p(\partial\phi_p/\partial\psi) \gg \varepsilon^2 S/Nq$ and $\varepsilon^2\phi_p/(Nq)^2 \ll N\Delta_p(\partial\phi_p/\partial\psi) < \pi/2\sqrt{2}$, particles enter inside the separatrix, jump the island then cause the large diffusion by collisions via the change in the phase of the island, which has root in the chage in the poloidal angle of the banana tip.
2. The peak of the diffusion coefficient at the separatrix is determined by a collisionless process. Meanwhile, the dependence of diffusion coefficients becomes $D \propto W^{-3/2}$ and $D \propto \gamma$ when particles are away from the separatrix.

[1] K. Tani, T. Takizuka, M. Azumi, and H. Kishimoto, Nuclear Fusion **23**, 657 (1983)
[2] K. Tani, T. Takizuka and M. Azumi, Nuclear Fusion **33**, 903 (1993)
[3] R. J. Goldston and H. H. Towner, J. Plasma Physics, **26**, 283 (1981)
[4] P. N. Yushmanov, Nuclear Fusion **23**, 1599 (1983)
[5] R. J. Goldston, R. B. White and A. H. Boozer, Phys. Rev. Lett **47**, 647 (1981).
[6] P. N. Yushmanov, Rev.Plasma Phys., **16**, 117 (1990).
[7] R. B. White, R. J. Goldston, M. H. Redi, and R. V. Budny, Phys. Plasmas, **3**, 3034 (1996).
[8] H. Mimata, K. Tani, H. tsutsui, K. Tobita, S. Tsuji-Iio, and R. Shimada, submitted to Plasma and Fusion Res.

Proceedings of ITC18,2008

Comparison of neutral particle flux decay times on the NBI plasmas in Large Helical Device

Tetsuo Ozaki, Pavel R. Goncharov*, Evgeny A. Veshchev, Shigeru Sudo, Tsuguhiro Watanabe, High-Energy Particle Group and LHD Experimental Group

National Institute for Fusion Science, Toki, Gifu 509-5292, Japan

We compare the decay times of charge exchange neutral particle fluxes in various NBI plasmas after switching-off NBI by using the Compact Neutral Particle Analyzer in Large Helical Device. Here the decay times at co-, counter and perpendicular injections are observed at the magnetic axis of R_{ax}=3.65. The decay times are determined mainly by the electron drag in tangential NBI. The decay time decreases by the weak magnetic field same as the simulation. The decay time at the perpendicular beam NBI is several – ten ms, which is less than one tens of that at the tangential injections. The decay time determined by the ion-ion collision, which is the main process of the energy loss and the pitch angle scattering at the injection energy of 40 keV, is about 10-20 ms. The observed decay times are still several times smaller than those values. The results are compared with the results from Angular Resolved Multi-Sight line neutral particle.

Keywords: Loss cone, Chaotic region, Decay time, Compact Neutral Particle Analyzer, Angular Resolved Multi-Sight line neutral particle analyzer, LHD, NBI

1. Introduction

Helical Devices have plasma stabilities even if the plasma density is high, because the magnetic field to confine the plasma is created by the external coil current. Recently the high-density scenario [1] toward the achievement of Lawson criterion for the nuclear fusion has been proposed in Large Helical Device (LHD) [2]. In this scenario, the heat load at the first wall can be reduced because the plasma temperature can keep low although the plasma density is extremely high. However the loss particle in loss region, which reduces the plasma quality and damages the first wall, still remains in helical devices. In LHD, the loss cone is minimized by the magnetic configuration so as there is no loss cone within one third of the minor radius [3] at the high magnetic field and at the inner magnetic axis shift. In this design, all particles outer from the last magnetic surface are assumed to be lost. In real, some particles re-enter to the plasma although partially particles are lost by the enhanced charge exchange at the outer region of the plasma. There is also the chaotic region near the last magnetic surface, which consists of the un-closed magnetic field line [4]. The chaotic region actually can be relax the particle loss because the particle in this region can be alive with longer life-time than in the loss cone.

From previous experiments in LHD, the loss cone is not serious for the high-energy particle confinement at the strong magnetic field and at inner magnetic shift indirectly by observation and simulation. Actually the energetic particle over 1 MeV, can be observed on the ion cyclotron heating plasma. This fact means there is not a big loss cone in LHD. Perpendicular neutral beam heating (NBI) [5] is applied to the perpendicular direction against the magnetic axis, where is near the loss cone (of the traditional prediction). However the NBI heating is successfully performed if the base plasma exists.

The decay times of the neutral flux can provide to understand the loss mechanism indirectly. Here we discuss them at the switching-off the heating on different NBI directions. Each beam is individually used instead of the beam modulation overlapped base plasma [6] in order to obtain clear signals. The decay time consists of the classical atomic process and another loss mechanism. Therefore quick decay time may be due to additional loss mechanism. We also measure the loss cone directly by the Angular Resolved Multi-Sight line neutral particle analyzer (ARMS). The results are compared each other.

2. Experimental Apparatus

LHD has a toroidal mode number of m=10, and a helical mode number of l=2. The major and minor radius are 3.9 m, 0.6 m, respectively. The helical ripple is 0.25 and the magnetic field is a maximum of 3 T. Although the standard magnetic axis is 3.75 m, it can be changed from 3.4 m to 4.1 m by applying a vertical magnetic field. The maximum electron temperature of over 10 keV can be observed by using Thomson scattering and electron cyclotron emission. The electron density can be changed

*) *Current address; St. Petersburg Poly-technical University, Polytekhnicheskaya st., 29 St. Petersburg, 195251 Russia*

author's e-mail: ozaki@nifs.ac.jp

from 0.01 to 1x10^{21} m^{-3}. The density profile is measured with a multi-channel interferometer [7]. The stored energy is monitored by a magnetic probe.

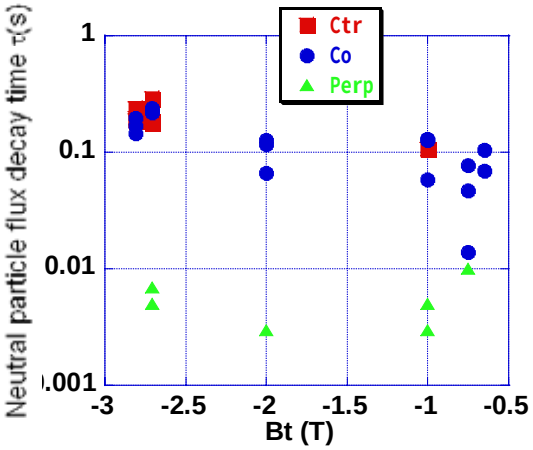

Fig. 1. The magnetic field dependence of the neutral flux decay time at R_{ax}=3.65 m. Ctr, Co and Perp mean the NBI injection direction against the magnetic field, counter, co and perpendicular, respectively.

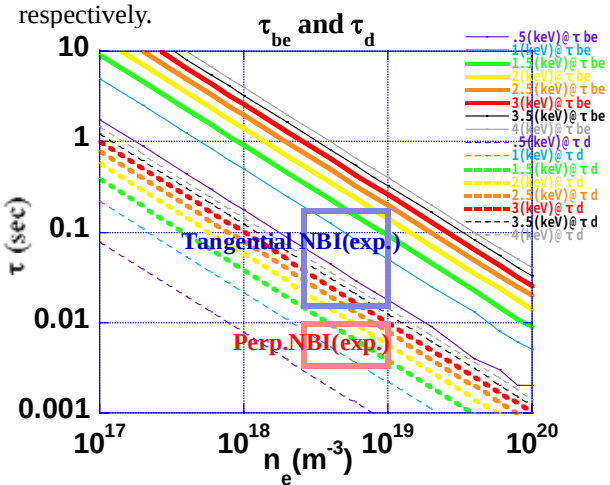

Fig. 2. Comparison between τ_{be}, τ_d and the experimental results. τ_{be} and τ_d can be obtained from eqs. (1)-(4).

Time and energy resolved charge exchange neutral particle is measured by the Compact Neutral Particle Analyzer (CNPA) [8], which is installed in the perpendicular direction against LHD plasma near the mid-plane. CNPA is a traditional E//B particle analyzer with a diamond-like carbon film as a stripping foil, a permanent magnet for the energy analysis of particles and condenser plates for particle mass separation. Mainly hydrogen ions with the energy range from 0.8 to 168 keV can be observed using 40 rectangular channeltrons.

It is determined that the spatial resolution is 5 cm using several apertures in the neutral particle flight. Time resolution is set to be 0.1 ms.

ARMS is the silicon detector with different sight lines of 20 channels. It has the energy range from 20 keV to 1000 keV with the energy resolution of few keV. The time resolution is 5 ms. A detail specification of ARMS is mentioned in the reference [9].

3. Experimental Results (CNPA)

In experiments, the NBI plasmas are created at the same magnetic axis and various magnetic fields. The neutral particle flux is observed by CNPA when the NBIs#1-4 are applied. NBI#1 and #3 have the same tangential direction. NBI#2 is also a tangential injection although it is different direction from NBI#1 and 3. NBI#4 is a perpendicular direction. Here we compare the neutral particle flux decay times when the co-, counter and perpendicular NBIs are applied at the magnetic axis of R_{ax}=3.65 m. In simulation, the chaotic region is minimized and the energetic particle is well confined at R_{ax} =3.65 m [4]. The decay time of the neutral particle flux with a certain energy, which is originated from NBI, is determined by the electron drag (at the high energy region), the charge exchange loss (at the middle and low energy regions), the pitch angle dispersion (which is occurred in low energy region), and the orbit loss in the loss cone or chaotic region. Former three effects may be independent on the injection direction of NBI. Therefore if there is large discrepancy of the decay times between the tangential and perpendicular injections, the orbit loss is the most probable candidate of the loss mechanism.

Figure 1 shows the decay times in different magnetic fields. The difference between the beam directions can be found clearly. The energy loss time due to the electron drag τ_{be} is given by [10]

$$\tau_{be} = \frac{3\pi\sqrt{2\pi}\varepsilon_0^2 m_b T_e^{3/2}}{n_e Z_b^2 e^4 \sqrt{m_e}\ln\Lambda}, \qquad (1)$$

where, ε_0, m_b, m_e, T_e, n_e, Z_b, e and lnΛ are the permittivity in vacuum, the beam ion mass, the electron mass, the electron temperature, the electron density, the beam charge state, the electron charge and the Coulomb logarithm, respectively. If the experimental parameters are chosen, the decay time is almost agreed with the energy loss time by the electron. This means the decay of the neutral particle is determined by the electron drag. When the magnetic field increases, the decay times in the tangential NBIs also increase. Two possibilities are proposed. One candidate is that the electron temperature is high because the good particle confinement can be achieved in the high magnetic field. Another possibility is that the chaotic region is narrow in the high magnetic field.

In the perpendicular NBI case, the decay time is from several ms to 10 ms. Here maximum injection energy is 40 keV. Therefore the ion-ion collision is essential for the

energy relaxation and the pitch angle scattering. The neutral particle from the tangential NBI has uniform angular distribution when the particle injects to the CNPA. However we must be aware of the escape from the sight line because the sight line of CNPA is also perpendicular. The energy loss time τ_{bi} by the ion-ion collision is given by [10]

$$\tau_{bi} = \frac{2\pi\varepsilon_0^2 A_b A_i m_p^2 V_b^3}{n_i Z_i^2 Z_b^2 e^4 \ln\Lambda}, \qquad (2)$$

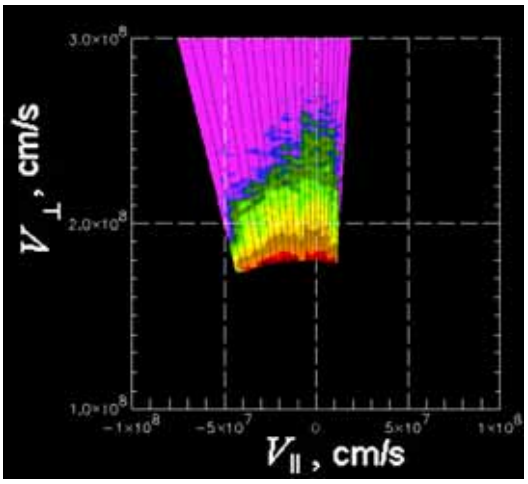

Fig. 3. The ARMS signal in NBI#4 plasma. The intensity of the flux is colored. The analyzer is covered from 70 to 100 degrees of the pitch angle.

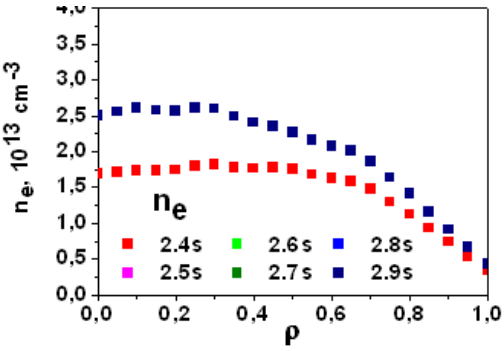

Fig. 4(a). Plasma density profiles at the tangential NBI experiments. The penetration depth of the background neutral depends on the plasma density.

where A_b, A_i, m_p, V_b, n_i and Z_i are the beam mass number, the plasma ion mass number, the proton mass, the beam velocity, the plasma ion density and the plasma ion charge state, respectively. For typical plasma parameters, the energy loss time by the plasma ion τ_{bi} is 100 ms. The value is too large than the experimental value. The ion-ion collision time τ_{ii} for occurring the pitch angle is given by [11]

$$\tau_{ii} = \frac{25.8\sqrt{\pi}\varepsilon_0^2\sqrt{m_i}T_i^{3/2}}{n_i Z_i^4 e^4 \ln\Lambda}, \qquad (3)$$

For typical plasma parameters, ion-ion collision time τ_{ii} is about 10 ms, which is smaller than τ_{bi}. This means the decay of the perpendicular NBI is determined mainly by the escaping from the sightline due to the ion-ion collision. Therefore the decay time τ_d is defined by the convolution of those times as,

$$\tau_d = \frac{1}{\tau_{bi}^{-1} + \tau_{ii}^{-1}}, \qquad (4)$$

The perpendicular injected particle is lost from the sight line with the ion-ion collision time, and decays with the beam-ion decay time. The observed decay time is still slightly small than the calculation value.

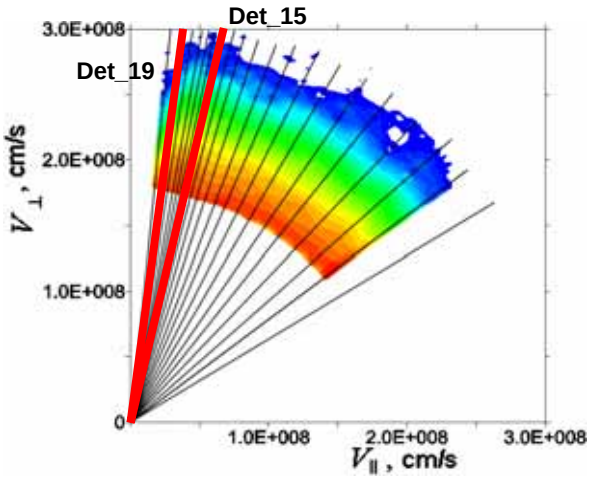

Fig. 4(b). The ARMS signal in tangential NBI plasma. To study the loss region, we compare two signals of the different chords, No. 15 (non-loss), No. 19 (loss).

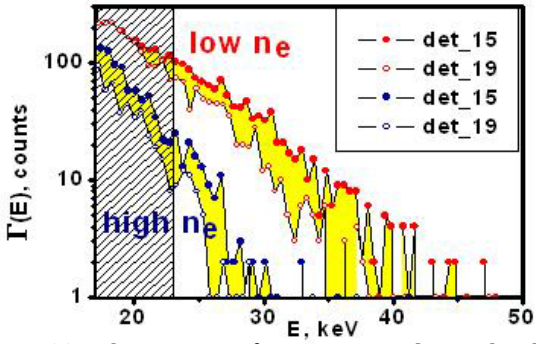

Fig. 4(c). The spectra of ARMS signals in chords, No.15 and No.19. The spectra of two different chords are compared at the high- and low-density case. At less than 30 keV, the particle loss is large in the high-density plasma.

Figure 2 shows the comparison between the calculation of τ_{be} (strait lines) and τ_d (broken lines) obtained from eqs. (1)-(4) and the experimental results. The experimental data areas are shown by the rectangular in Fig. 2. In τ_{be} and τ_d, the experimental decay times both

in the tangential and perpendicular NBIs are smaller than the calculated values. However it is not true that the most of particles are lost in the classical loss cone because the loss time should be several μs if there is a large loss cone. . The particle loss from the classical loss cone or chaotic region is not so large especially in the high magnetic field.

4. Experimental Results (ARMS)

Figure 3 shows the neutral particle angular distribution around the pitch angle of 90 degrees obtained by ARMS when the perpendicular NBI is applied. The horizontal and vertical velocities of the neutral particles are on the horizontal and vertical axes. Therefore the radial axis means the particle speed. The logarithmic flux of the particle is colored.

In Fig. 3, the flux near 90 degrees is observed slightly intensive but broad because the NBI is applied to the perpendicular direction. This means the trapped particle near 90 degrees is well confined. The particle, which is injected to the perpendicular, is decreasing its energy and pitch angle by the ion-ion collision. In decreasing of the total particle flux over 15 keV at the pitch angle of 85 degrees or less, the effect from the loss cone or loss from the chaotic region may be involved. The uniform angular distribution can be obtained from short ion-ion collision time of 10 ms.

Figure 4 shows the pitch angle distribution when the tangential NBI is applied. When the tangential NBI is applied, the beam energy decreases by the electron drag, it has the large pitch angle at the low energy by the beam ion collision. Therefore the angular distribution of the beam is uniform at the low energy. However we find that the beam with the pitch angle over the 85 degrees strongly decreases (dent) from the measurement by ARMS. This suggests there is the loss region around there.

It is very important to know where is the loss region and it is serious or not. For this purpose, we check the change of the dent near the pitch angle of 85 degrees by the plasma density. Figure 4(a) shows the density profiles of two different discharges with same NBI heating. Here we assume that the dent is due to the particle loss from the loss region. Usually the dent should change by the electric field in the plasma. The negative electric field enhances the loss, this means, makes deep dent. If the plasma density is high, the electric field becomes negative [12]. Therefore the dent should be deep. But the dependence between the density and electric field is not so strong at the density over 10^{-19} m^{-3}. Actually at Fig. 4(a), the electric fields may be almost the same. On the other hand, the flux will decrease because the background neutral, which is source of the charge exchange, cannot invade to the plasma at high-density case. The fluxes at the high and low-density plasmas come from the plasma outer and the whole region, respectively. Therefore by the comparison of the flux from between the high- and low-density plasma, we can estimate where the charge exchange occurs. Figure 4(b) shows the spectra of two different sight lines at the high and low-density plasmas. At one sight line (No.15), the energetic particle is well confined. Another sight line (No. 19) reflects the loss region. We compare the discrepancy between the No.15 and No.19 at the high- and low- density plasmas. The discrepancy at the high-density plasma is larger than that at the low-density plasma. This means that the loss region is localized at the outer plasma. According to Aurora code calculation [13], the penetration depth of the background neutral is changed at $\rho=1/3$. Therefore there may be the loss region out of $\rho=1/3$ same as the original design of LHD.

5. Summary

We compare the flux decay times from CNPA at the end of NBIs. In co- and counter- tangential NBIs, the decay times are determined by the electron drag. The decay time is smaller than the escaping time from the sight line, which is determined by the ion-ion collision. But it is long enough than the specific time by the loss cone. This means part of the particles are lost. For checking this, we observe the angular distribution of the neutral flux by using ARMS. The loss region can be seen near 85 degrees. To specify the position of the loss region, we compare the angular distributions at different density plasmas. The loss region may be localized near the plasma edge. This means the loss region is not serious especially at the high magnetic field.

Acknowledgements

This work was performed under NIFS-ULBB509, the grants aid of No. 17540475 and 18035013.

References

[1] R.Sakamoto, et al., IAEA EX8-1Ra (2008).
[2] O. Motojima, et al., Fusion Eng. Des., 20 (1993) 3-14.
[3] T. Kamimura, private communication.
[4] T. Watanabe et al., Nuclear Fusion, 46 (2006) 291-305.
[5] O. Kaneko, et al., Fusion Eng. Des., 26 (1995) 1-4,455.
[6] M.Osakabe, private communication.
[7] K. Kawahata, et al., Fusion Eng. Des., 26 (1997) 34-35,393.
[8] T. Ozaki, et al., Plasma 2005 (2006) 812, 399.
[9] E. Veshchev, et al.,Rev. Sci. Instrum., 77, (2006) 10F129-1.
[10] S. Takamura, “Basic Plasma Heating”, in Japanese, p.74.
[11] K. Miyamoto, “Plasma Physics for Fusion Researcher”, in Japanese, p.554.
[12] K. Ida, et al., Phys. Plasma 8,(2001)1-4.
[13] S. Murakami, private communication.

Proceedings of ITC18,2008

Analysis of particle orbits in spherical tokamak-stellarator hybrid system (TOKASTAR) and experiments in Compact-TOKASTAR device

Y. Taira, K. Yamazaki, H. Arimoto, T. Oishi, T. Shoji
Department of Energy Engineering and Science, Nagoya University, Furo-cho, Chikusa-ku, Nagoya, Japan

A compact spherical tokamak-stellarator hybrid system TOKASTAR was proposed, and particle orbit analysis in this configuration has been carried out. In the original configuration, the average rotational transform is rather small, and several improved configurations were evaluated. The confinement improvement of fast particles was clarified. For the experimental demonstration of this configuration concept, a Compact-TOKASTAR device (C-TOKASTAR) was constructed, and the existence of these magnetic surfaces was suggested using an electron-emission impedance method.

Keywords: TOKASTAR, tokamak, stellarator, hybrid system, magnetic surface, particle orbit

1. Introduction

A tokamak magnetic configuration system is widely accepted as a future attractive toroidal fusion reactor, because of axisymmetric simple coil configuration, and good plasma confinement properties. It has smaller and more compact coil system than the helical coil system. However, to operate in steady state, external power for plasma current drive is required and the risk of plasma current disruption should be considered. On the other hand, helical magnetic confinement systems are superior to tokamaks for steady-state operation and possible disruption-free operations, but non-axisymmetric configuration properties give rise to the loss of fast ions. Here, a compact spherical tokamak-stellarator hybrid system TOKASTAR was proposed[1,2], which has a compact and simple coil system and natural diverter[3].

In this paper, we evaluated characteristics of particle orbit confinement in a Compact-TOKASTAR device (C-TOKASTAR). Figure 1 shows the C-TOKASTAR concept with toroidal number N=2. Two helical coils are combined at center of the system and one pair of poloidal coils is installed outside of helical coils to cancel vertical magnetic field made by helical coils. Plasma can be confined in this system and a natural divertor surface exits outside the last closed magnetic surfaces [3].

2. Method of calculation

In the configuration analysis, magnetic field tracing code HSD (helical system design) is used to calculate vacuum magnetic surfaces. We define coil configuration and its electric coil current as input parameters, and

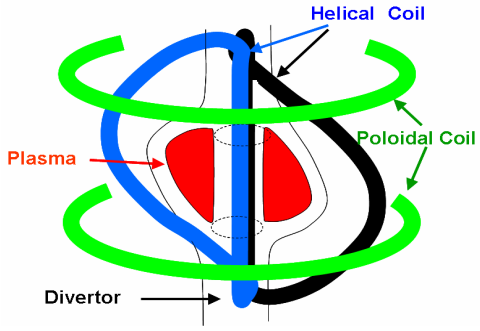

Fig.1 N=2 TOKASTAR Concept

calculate magnetic field lines by the Biot-savart's law in the HSD code. The guiding-center orbit theory is used to calculate the orbit trajectory of fast ions. The guiding-center equation which we used in this research is as follows;

$$\frac{dv_{//}}{dt} = -\frac{v_{\perp}^{2}}{2B}(\vec{b}\cdot\nabla)B \quad , \tag{1}$$

$$\frac{1}{v}\frac{d\vec{r}}{dt} = \frac{v_{//}}{v}\vec{b} + \rho\left(\frac{\beta^{2}}{2}\frac{B}{B_0} + \frac{v_{//}^{2}}{v^{2}}\right)\frac{B_0}{B}\left(\vec{b}\times\frac{\nabla B}{B}\right) \quad , \tag{2}$$

where

$$\rho = \frac{mv}{eB_0} \quad ,$$

$$\beta = \alpha\sqrt{\frac{B_0}{B_i}}$$ (B_0 is the toroidal magnetic field at magnetic axis, and the suffix i denotes values at starting point).

author's e-mail: y-taira@ees.nagoya-u.ac.jp

3. Analysis of magnetic surface and particle confinement in TOKASTAR system

Figure 2 shows a schematic drawing of the analysis layout in the case of circular magnetic surfaces. Here, θ is poloidal angle, r is minor radius of plasma, and R is major radius. In this figure we divided cross-sections into 3 sections, "1/3 magnetic surface", "2/3 magnetic surface" and "LCMFS (last closed magnetic field surface)" from magnetic axis in order.

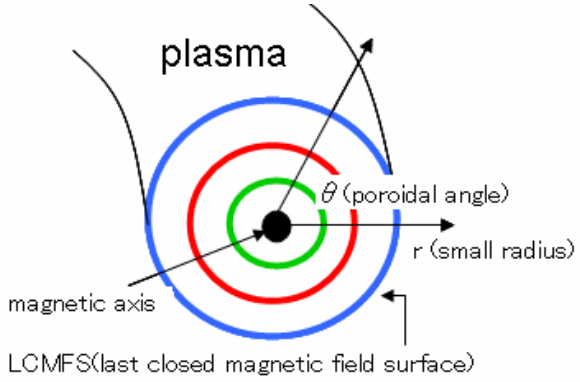

Fig.2 Layout of plasma analysis

The average and local vacuum rotational transforms are shown in Figs. 3(a) and (b), respectively. The average vacuum rotational transform decreases as a function of small radius. The vacuum rotation transform of the present

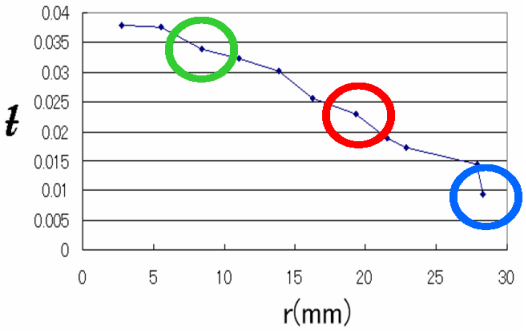

Fig.3(a) Average vacuum rotational transform in TOKASTAR. Colored circles corresponds to Fig.2

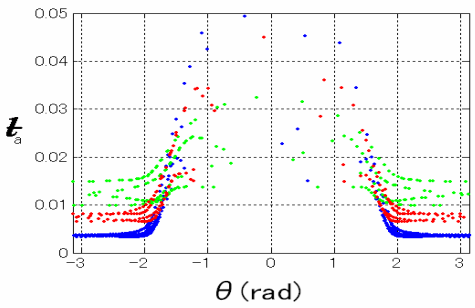

Fig.3(b) Local rotational transform as a function of poloidal angle θ in TOKASTAR

TOKASTAR system is smaller than 0.14 which might be a critical value of disruption-free operations. Moreover in Fig. 3(b), we can see the vacuum rotational transform is very small on the inner side of the system (θ < 2rad, θ > 2rad). The reason why the vacuum transform is small is TOKASTAR system does not have helical magnetic components inside this system.

Secondly, we studied confinement of fast ions in TOKATAR (Fig.4). The fast ions in LCMFS is confined (passing particles), and there are some ions which are localized in TOKASTAR system in pitch angle~90degrees domain. Moreover, in this research we show that there are many fast ions in random out of LCMFS which are passing or localized in TOKASTAR. The particle confinement comparisons with this N=2 TOKASTAR and the N=6 standard heliotron configuration has already been done in ref.[4].

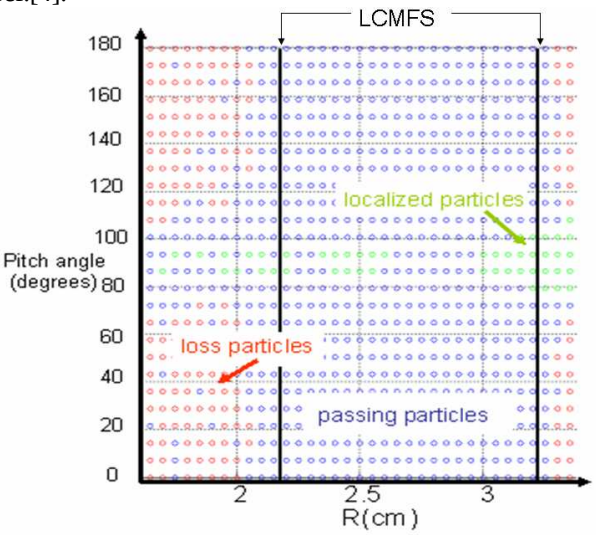

Fig.4 Fast ion confinement diagram of TOKASTAR

4. Proposal of improved TOKASTAR

We showed in Sec.3 that C-TOKASTAR has a low vacuum rotational transform. In order to raise rotational transform we propose improved TOKASTAR which has helical component in the inner side of this system as shown in Fig.5. In this figure, we define ha and hb as outer helical radius and inner helical radius, respectively.

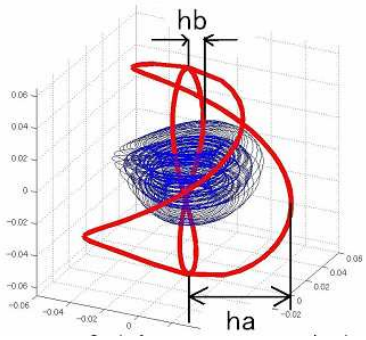

Fig.5 Improved TOKASTAR with inner helical coil

We clarify that with increase in the ratio hb/ha, the vacuum rotational transform improves (Fig.6). When hb/ha is 0.14, the rotational transform becomes ~0.1. But, with the increase in hb/ha, the plasma volume becomes smaller. When hb/ha is 0.14, the plasma small radius of improved TOKASTAR is 1/3 as large as that of TOKASTAR.

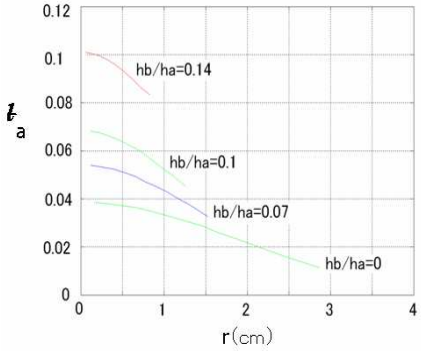

Fig. 6 Rotational transform in the improved TOKASTAR with central helical coil modification

Generally, when average vacuum rotational transform increases, the deviation Δ between fast ions orbit and magnetic surface will decrease and, fast ions confinement can be improved. We confirm its relationship between the rotational transform and the shift Δ (Fig.7). In Table 1, we show the effect of inner helical modifications on rotational transform increase and loss particle reduction in improved TOKASTAR systems. In Fig.7, as the vacuum rotational transform increase, 2 Δ /2a, ratio of the orbit shift Δ and the plasma small radius a, is decrease. When the vacuum rotational transform is 0.092, the shift Δ becomes nearly zero. As shown in Table 1, the increase in vacuum rotational transform leads to the improvement of fast ions confinement. When hb/ha is 0.14, a ratio of loss particles is about 8.3%.

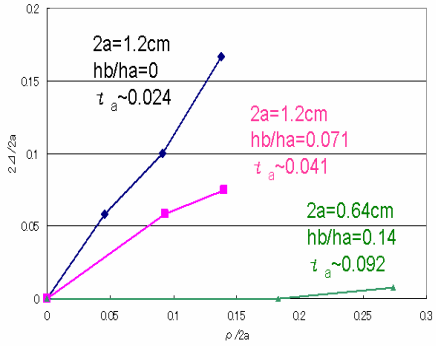

Fig.7 Average rotational transform as a function

Secondly, we proposed improved TOKASTAR(3) which reduces magnetic ripple on the outer side of TOKASTAR system. As shown in Fig.8, a large outer

Table 1 A ratio of loss particle in improved TOKASTAR

	hb/ha	vacuum rotational transform	ratio of loss particles
TOKASTAR	0	0.024	0.133
Improved TOKASTAR #1	0.071	0.041	0.127
Improved TOKASTAR #2	0.14	0.092	0.083

coil system is adopted for this analysis. We move helical component away from plasma, and magnetic ripple σ decreases on the outside of this system (left figure of Fig.8). The comparisons between improved #3 and original configurations are as follows;

σ =0.007/0.09=0.078 (improved TOKASTAR #3),
σ =0.76 (original TOKASTAR).

We expected that the outer helical ripple reduction causes improvement of fast ions confinement, but the ratio of loss particles increase (66.1%). It is because when we reduce helical ripple component, vacuum rotational transform decreases at the same time. So the present model #3 is not effective to improve fast particle confinement.

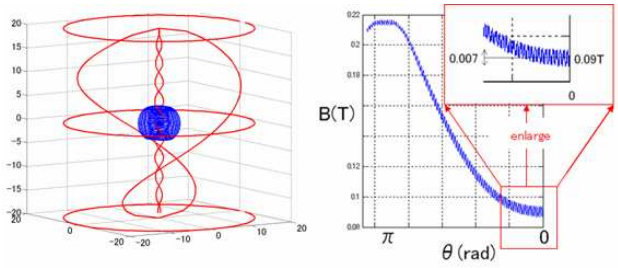

Fig.8 Improved model #3 (left), and its magnetic ripple as a function of θ (left).

Thirdly, we proposed improved TOKASTAR #4 which have 4 helical coils as shown in Fig.9. It has ultra low aspect ratio as

A~2 (improved TOKASTAR #4),
A~2.7 (original TOKASTAR).

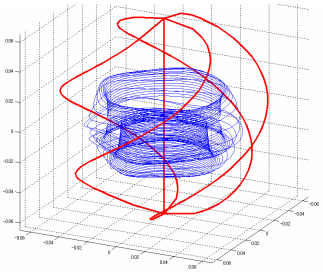

Fig.9 model #4 TOKASTAR with N=4 symmetry.

5. Impedance method in C-TOKASTAR experiments

In order to check the existence of magnetic surface in C-TOKASTAR device, an electron-emission impedance method is used. Table 2 shows parameters of C-TOKASTAR device with double 10-turn helical coils and a pair of 20-turn poloidal coils. As shown in Fig.10, we insert electron gun filament in C-TOKASTAR, and detect the electron current. When the magnetic surface is formed, the electrons go round magnetic surface and go out to the ground finally. So larger circuit impedance can be detected than that when magnetic surface does not exist.

Table 2 Parameters of C-TOKASTAR device

major plasma radius (typical)	35mm
radius of poloidal coil	140mm
radius of spherical helical coil	130mm

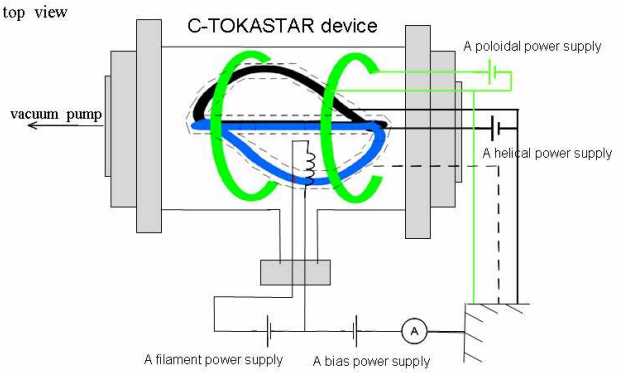

Fig.10 Experimental layout of electron-emission impedance method in C-TOKASTAR

In Fig. 11(a) and (b), we show result of impedance method. In Fig. 11(a), we light an electron gun filament for about 18min, and during that we change helical coil current (H(A/turn)) and poloidal coil current (P(A/turn)). In this experiment a bias power supply voltage is 9.4V. In this figure we also show magnetic surfaces analyzed by HSD. When H/P is 6~10, magnetic surfaces are formed. This result agrees with that analysis.

In Fig.11(b), we first energize helical and poloidal coils and then light an electron gun filament, which turn is reversed from Fig.12. The electrons are emitted for about 30second per shot, and 9 shot results are shown in Fig. 11(b). In this experiment with bias voltage of 19.2V, we confirm an influence of a magnetic field. When H/P is 10, the impedance becomes smallest. By this electron-emission impedance method, we can confirm influence of a magnetic field, and suggest the existence of magnetic surface.

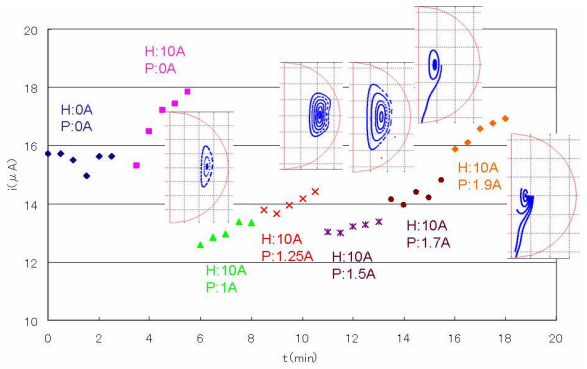

Fig.11(a) Impedance method with quasi-steady electron emission by changing magnetic configuration

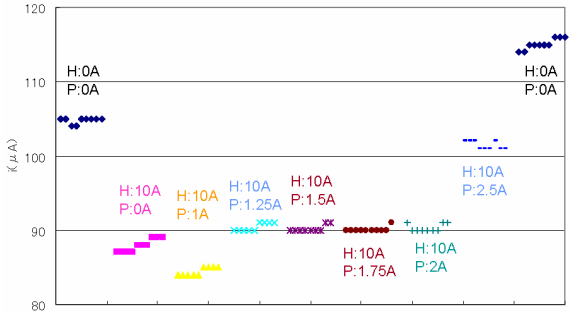

Fig.11(b) Impedance method with short electron emission in quasi-steady magnetic configuration

6. Conclusion

We analyzed fast particle orbit in a compact spherical tokamak-stellarator hybrid TOKASTAR. Several concepts with inner helical coils are proposed to improve particle confinement, and the particle loss reduction in is clarified. A miniature machine C-TOKASTAR was constructed and an electron-emission impedance method is applied for checking magnetic surfaces. We found by comparisons with HSD analysis that magnetic surfaces might be formed in this C-TOKASTAR device

References

[1] K. Yamazaki and Y. Kubota, Proceedings of Plasma Science Symposium 2005 and the 22nd Symposium 2005 and the 22nd Symposium on Plasma Processing (PSS2005/SPP-22) (2005) P3-094.

[2] K. Yamazaki and Y. Abe, Research Report of the Institute of Plasma Physics, Nagoya, Japan, IPPJ-718 (1985).

[3] T. Sawafuji, Analysis of magnetic surface in Spherical Tokamak-Stellarator (TOKASTAR), Department of Energy Engineering and Science, Nagoya University, a master thesis (in Japanese) (2008)

[4] K. Yamazaki, Y. Taira et al., 14th International Congress on Plasma Physics (ICPP2008) (September 8-12, 2008, Fukuoka)

Proceedings of ITC18,2008

Proposal of Split and Segmented-type Helical Coils for the Heliotron Fusion Energy Reactor

Nagato Yanagi[1], Kiyohiko Nishimura[1], Gourab Bansal[2], Akio Sagara[1] and Osamu Motojima[1]

1) National Institute for Fusion Science, 322-6 Oroshi-cho, Tok, Gifu 509-5292, Japan

2) Institute for Plasma Research, Bhat, Gandhinagar, Gujarat, 382-428 India

Configuration optimization is carried out for the heliotron-type fusion energy reactor FFHR. One of the important issues is to find sufficient clearances between the ergodic region outside the nested magnetic surfaces and blankets at the inboard side of the torus so that direct loss of alpha particles is minimized and the heat flux on the first walls is reduced. Though the primary option is to have a fairly large major radius R_c of the helical coils to be ~17 m in the present design, it has been found that equivalent clearances are obtained with R_c = 15 m by employing a lower helical pitch parameter and by splitting the helical coils in the poloidal cross-section at the outboard side of the torus. On the other hand, splitting the helical coils provides another modified configuration with R_c ~ 17 m that ensures magnetic well formation in the fairly large nested magnetic surfaces with outward shifted configurations. From the engineering viewpoint, we propose that such helical coils can be constructed by prefabricating half-pitch segments using high-temperature superconductors and the segments are to be assembled on site.

Keywords: heliotron, FFHR, configuration optimization, split-type helical coils, high-temperature superconductor, segmented-type helical coils

1. Introduction

Based on the successful progress of fusion relevant plasma experiments in the Large Helical Device (LHD) [1], the conceptual design studies on the heliotron-type fusion energy reactor FFHR are being conducted both on physics and engineering issues [2]. For FFHR, a magnetic configuration similar to that of LHD is employed so that the confined plasma is net current-free with steady-state operations. Though configuration optimization is still being pursued, the present choice gives the major radius of 14-18 m with the toroidal magnetic field of 6-4 T in order to generate ~3 GW of fusion power. The stored magnetic energy of the superconducting coil system should be in the range of 120-150 GJ.

In these studies, the helical pitch parameter γ defined by $(m/l)(a_c/R_c)$ for continuous helical coils (having the toroidal pitch number m, poloidal pole number l, average minor radius a_c and major radius R_c) has been chosen to be lower than 1.25 that was adopted for the present LHD. This choice is made for the purpose of ensuring a sufficient blanket space (thickness > 1 m) between the ergodic region of magnetic field lines (outside the nested magnetic surfaces) and the blankets [3]. At the same time, the lower γ reduces the electromagnetic hoop-forces on the helical coils. The configuration proposed in 2005, "FFHR-2m1", has m = 10, l = 2, R_c = 14 m and a_c = 3.22 m with γ = 1.15.

One of the difficult issues with this configuration is the still observed interferences between the ergodic region and blankets especially at the inboard side of the torus. In order to reduce the heat flux on the blankets, the "helical x-point diverter (HXD)" was proposed [4]. However, this choice gives an extremely high heat flux on the limiter-like structures. Moreover, the confinement of alpha particles is deteriorated by cutting the magnetic field lines in the ergodic region where alpha particles are still confined.

In this respect, two approaches are being considered to secure more sufficient clearances. One is to enlarge the major radius of the helical coils, and the latest design, "FFHR-2m2", gives R_c = 17.33 m and a_c = 4.02 m with γ = 1.20. The vacuum magnetic surfaces of this configuration are shown in Fig. 1, and the blanket space of 0.95 m is secured at the inboard side. As shown in Fig. 1, the magnetic axis is shifted inward (located at R_p = 16.0 m) in order to have good particle confinement.

The other approach is to find optimized magnetic configurations by modifying the winding laws of the helical coils. In this respect, we found that favorable configurations could be obtained by splitting the helical coils in the poloidal cross-section. The new configurations were named "FFHR-2S", and two options of FFHR-2S, namely, "Type-I" and "Type-II" are proposed in this paper.

From the engineering viewpoint, we also propose that such complicated helical coils with the continuous manner and huge size can be constructed by prefabricating half-pitch segments of the windings using high-temperature superconductors (HTS), and the segments are to be assembled on site.

author's e-mail: yanagi@LHD.nifs.ac.jp

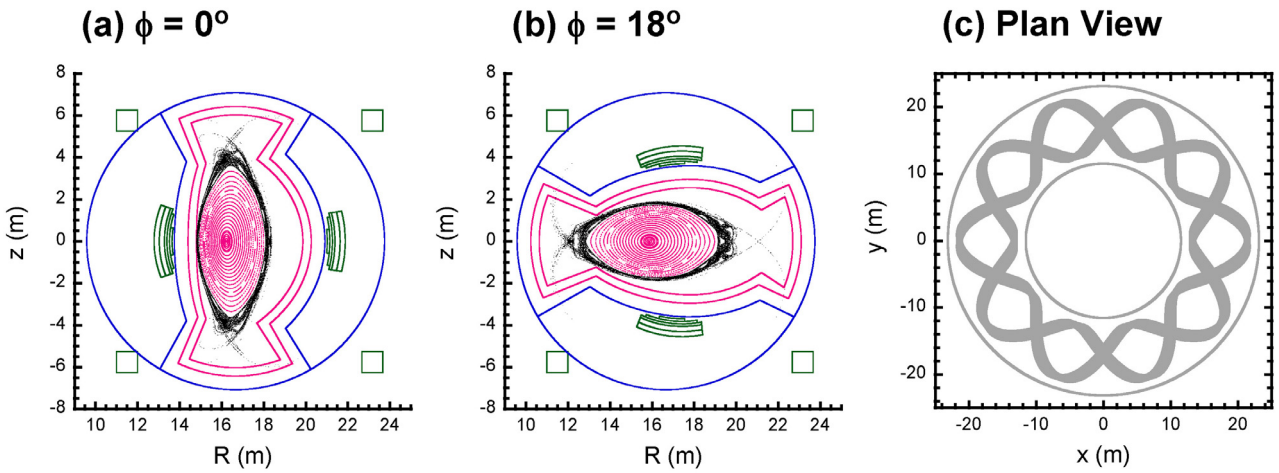

Fig. 1 Vacuum magnetic surfaces at (a) the toroidal angle ϕ = 0° and (b) ϕ = 18°of FFHR-2m2 (Type-A) with R_c = 17.33 m, a_c = 4.02 m and γ = 1.2. The magnetic axis is shifted inward at R_p = 16.0 m. (c) Plan view of the coils.

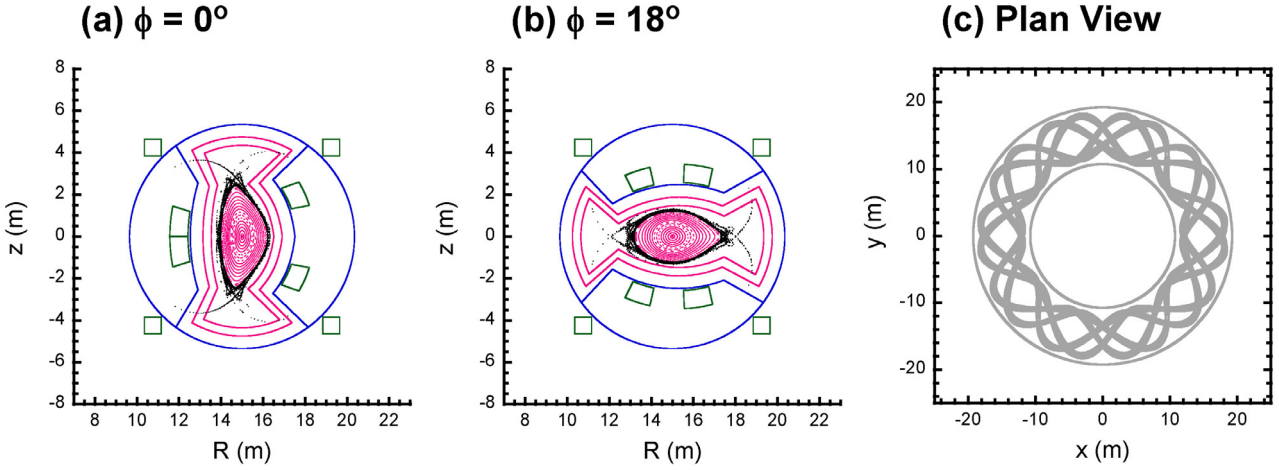

Fig. 2 Vacuum magnetic surfaces at (a) the toroidal angle ϕ = 0° and (b) ϕ = 18° of FFHR-2S Type-I with R_c = 15.0 m, a_c = 3.0 m and γ = 1.0. The magnetic axis is at the center of the helical coils (R_p = 15.0 m). (c) Plan view of the coils.

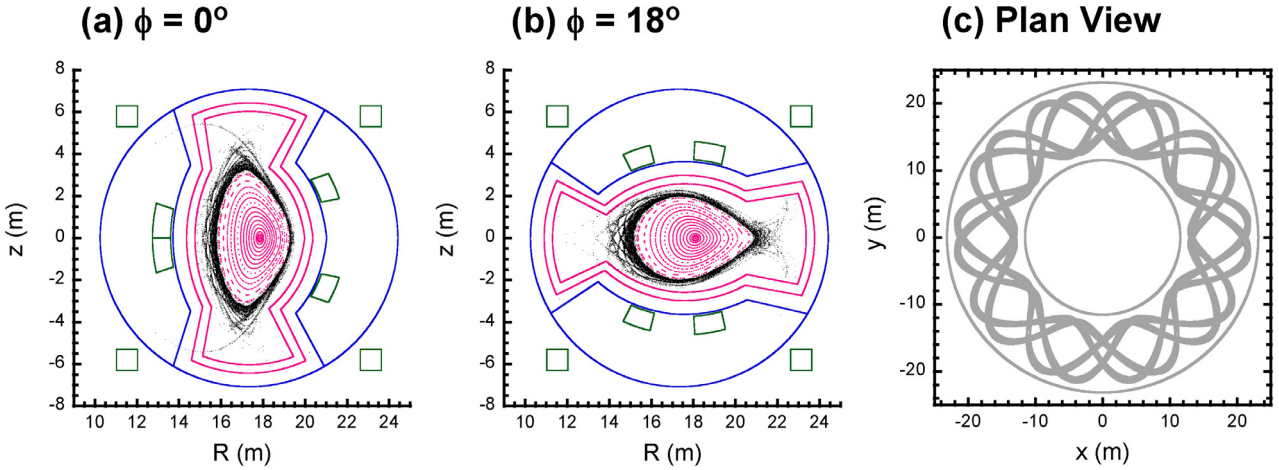

Fig. 3 Vacuum magnetic surfaces at (a) the toroidal angle ϕ = 0° and (b) ϕ = 18°of FFHR-2S Type II with R_c = 17.33 m, a_c = 4.02 m and γ = 1.2. The magnetic axis is shifted outward at R_p = 18.0 m. (c) Plan view of the coils.

2. Proposal of split-type helical coils

It was previously found that the symmetry of magnetic surfaces is significantly improved by increasing the current density of the helical coils at the inboard side of the torus while decreasing at the outboard side [5, 6]. This situation can be practically realized by splitting the helical coils in the poloidal cross-section at the outboard side. It should be reminded, on the other hand, that good symmetry of magnetic surfaces is usually obtained by shifting the magnetic axis inward with conventional heliotron magnetic configurations, like that of LHD.

Here, we newly found that drastically large nested magnetic surfaces (or the plasma volume) can be obtained by the symmetry improvement with split-type helical coils even if the original configuration (without splitting the helical coils) possesses a fairly large ergodic region outside the relatively small nested magnetic surfaces. In this respect, we first found that sufficient clearances are obtained even with a smaller major radius of R_c = 15.0 m (than that of the standard configuration of FFHR-2m2 with R_c = 17.33 m) by splitting the helical coils and at the same time by reducing the helical pitch parameter to be as low as γ = 1.0 [7]. The vacuum magnetic surfaces of this configuration are shown in Fig. 2. The magnetic axis is located at the center of the helical coils and the blanket space of ~1 m is secured at the inboard side. Here we should note that such a low helical pitch parameter has never been examined so far, as it is well known that one is almost in the so-called forbidden-zone for generating magnetic surfaces with a l = 2 heliotron configuration [8]. We understand that the low helical pitch parameter is effective for compacting the separatrix while the splitting of helical coils at the outboard side ensures larger nested magnetic surfaces by the symmetry improvement. This configuration is named "FFHR-2S Type-I". Owing to the smaller major radius, we design that the toroidal magnetic field is as high as 6 T, while it is 4.84 T for FFHR-2m2.

We then found that split-type helical coils could provide another configuration based on the same concept of symmetry improvement. The FFHR-2m2 has the inward shifted magnetic surfaces, which ensures good particle confinement properties. On the other hand, it has been recently found in the LHD plasma experiments that high electron density is achieved with the "superdense core (SDC)" at outward shifted configurations [9]. However, one of the problems with this configuration is that the nested magnetic surfaces become considerably smaller than those at inward shifted cases. Here, we propose that fairly large nested magnetic surfaces can be obtained even with outward shifted configurations as we split the helical coils. Figure 3 shows an example of the vacuum magnetic surfaces with this concept, which is named "FFHR-2S Type-II". The basic parameters of this configuration are the same as those for FFHR-2m2 except for the split-type helical coils, and the magnetic axis is located at R_p = 18.0 m where the toroidal magnetic field is 4.3 T. Though the original configuration gives ~35% reduction of the average minor radius at R_p = 18.0 m compared to that at R_p = 16.0 m, it is only ~7% with FFHR-2S Type-II. Here, it should be noted that a similar idea had been previously proposed in [6].

Figure 4 shows the radial profiles of rotational transform and magnetic well depth for three configurations: FFHR-2m2, FFHR-2S Type-I and FFHR-2S Type-II. As shown in Fig. 4, magnetic well is formed within the entire magnetic surfaces of FFHR-2S Type-II. On the other hand, the rotational transform as well as shear are lower with this case than those of other configurations. For all these configurations, the field properties including the plasma beta should be investigated in our future studies.

We here note that split-type helical coils are useful not only for configuration optimization but also for some other purposes, such as injecting pellets and/or RF waves from the high field side through the gaps of helical coils at the outboard side. It is proposed in [10] that ICRF heating has good accessibility in case of FFHR-2S configurations.

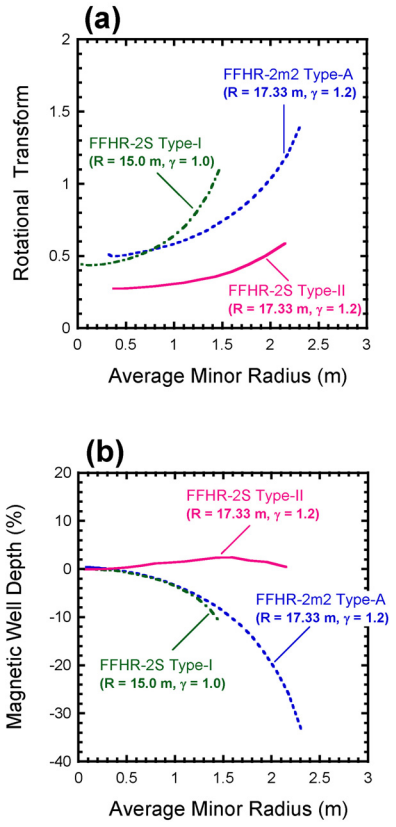

Fig. 4 Radial profiles of (a) rotational transform and (b) magnetic well depth for FFHR-2m2, FFHR-2S Type-I and FFHR-2S Type-II.

3. Proposal of segmented-type helical coils

From the engineering viewpoint for realizing the complicated winding of split-type helical coils with the huge size of FFHR, here we propose "segmented-type" fabrication [11], which could drastically ease the construction process. As shown in Fig. 4 (b), we employ a number of joints between the half-pitch segments which are prefabricated separately. Here we also propose that high-temperature superconductors (HTS) are adopted with indirect-cooling scheme and the surplus refrigeration power operated at 20-30 K is effectively used to remove the joule heating generated by the joints between segments [12]. Our proposal is to employ RE123-based coated-conductors, and Fig. 3(a) shows a conductor design. Here, the HTS tapes are packed without transposition, and the bending strain is limited to be 0.05%. Good mechanical properties are secured also by using a stainless-steel jacket. It should be noted that we have successfully carried out proof-of-principle experiments of HTS conductors with 10-15 kA critical current at 8 T and 20 K [12]. At the joint locations, the HTS conductors are cut in step-like structures, then overlapped and joined with superconducting sides facing each other [11].

Since the HTS conductor has a large temperature margin, the temperature rise at a joint may not be a big concern in terms of the cryogenic stability. For a temperature rise of 5 K, the power density of 990 W/m^3 can be allowed, which means that a joint resistance of 3 nΩ is acceptable [11]. On the other hand, according to the joint resistance measured with single tapes, it is expected that the overall joint resistance of a 100 kA conductor can be as low as 0.06 nΩ, which requires only 300 kW of additional refrigeration power for the entire system. Moreover, helical coils assembled in segments may have a further possibility that they can be demountable for maintenance as was originally proposed in [13] with NbTi superconductors and more recently in [14] with HTS conductors.

4. Summary

Configuration optimization is being carried out for the heliotron-type fusion energy reactor FFHR by splitting the helical coils in the poloidal cross-section at the outboard side of the torus, which is effective in having good symmetry of magnetic surfaces. Together by choosing a low helical pitch parameter of $\gamma = 1.0$, the FFHR-2S Type-I configuration provides a smaller major radius of $R_c = 15$ m to secure sufficient blanket space of ~1 m which is equivalent with that obtained for FFHR-2m2 with $R_c = 17.33$ m. On the other hand, by splitting the helical coils with the FFHR-2m2 design, the FFHR-2S Type-II configuration provides magnetic well formation in the entire region of the fairly large nested magnetic surfaces with outward shifted configurations. It is also proposed that continuous helical coils with such complicated structure can be assembled by prefabricating half-pitch segments using HTS conductors.

Acknowlegments

The authors are grateful to Drs. T. Watanabe, S. Imagawa, Y. Kozaki, T. Goto and other members in the FFHR design group for valuable discussion and support.

References

[1] O. Motojima *et al.*, Nuclear Fusion **47**, S668 (2007).
[2] A. Sagara *et al.*, Fusion Eng. Des. **81**, 2703 (2006).
[3] S. Imagawa *et al.*, J. Plasma Fusion Res. SERIES **5,** 537 (2002).
[4] T. Morisaki *et al.*, Fusion Eng. Des. **81,** 2749 (2006).
[5] K. Nishimura and M. Fujiwara, J. Phys. Soc. Japan **64**, 1164 (1995).
[6] H. Akao, T. Watanabe and K. Nishikawa, JSPS Report 63050027 (1988) 345 (*in Japanese*).
[7] N. Yanagi *et al.*, Proceedings of 17th International Toki Conference (2007).
[8] K. Uo, Nuclear Fusion **13**, 661 (1973).
[9] H. Yamada *et al.*, Plasma Phys. Control. Fusion **49**, B487 (2007).
[10] K. Saito *et al.*, *this conference*.
[11] G. Bansal *et al.*, Plasma and Fusion Research **3**, S1049 (2008).
[12] G. Bansal *et al.*, IEEE Trans. Appl. Supercond. **18**, 1151 (2008).
[13] K. Uo *et al.*, Proc. 14th Symp. Fusion Techonol. **2**, 1727 (1986).
[14] H. Hashizume *et al.*, Fusion Eng. Des. **63**, 449 (2002).

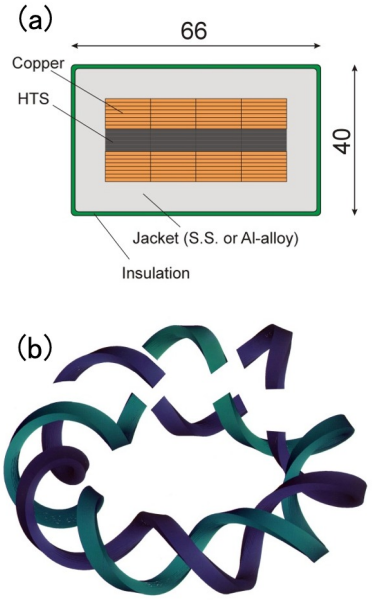

Fig. 5 (a) Conceptual design of an HTS superconductor with 100 kA current capacity and (b) illustrative image of segmented-type helical coils.

Proceedings of ITC18,2008

Environmental and economical assessment of various fusion reactors by the calculation of CO_2 emission amount

S. Uemura, K. Yamazaki, H. Arimoto, T. Oishi, T. Shoji

Department of Energy Engineering and Science, Nagoya University, Furo-cho, Chikusa-ku, Nagoya, 466-8603, Japan

We compared several fusion rectors from the view point of CO_2 emission amount. Magnetic confinement systems we evaluated are Tokamak Reactor (TR), Helical Reactor (HR) and Spherical Tokamak reactor (ST). These models are calculated by Physics Engineering Cost (PEC) code. Parameters of Inertial confinement fusion Reactor (IR) is simply calculated by given pellet gains. In addition, different blanket modules and fuels are considered in TR designs. To calculate CO_2 emission amount of fusion reactor defined by plasma parameters and radial build, we used basic unit for CO_2 weights (k-t-CO_2/t-material). Calculation results indicate that CO_2 is the most emitted from the construction stage of coil systems for magnetic confinement fusion reactors. For the IR design, the construction stage of driver system and pellet purification stages involve much CO_2 emission. By comparing fusion reactors with other power generation systems from the view point of CO_2 emission amount, we confirmed that fusion reactor emits less CO_2. Therefore, there is little influence on economics of fusion reactors by introducing carbon tax.

Keywords: Tokamak Reactor (TR), Helical Reactor (HR), Spherical Tokamak reactor (ST), Inertial confinement fusion Reactor (IR), blanket, CO_2 emission amount, Cost Of Electricity (COE)

1. Introduction

Fusion reactor is expected to be one of abundant energy resources in the future. However there are many technological problems to be solved. In addition it is essential to assess safety, economics and environmental burden of fusion reactor. In this paper we calculated the Cost Of Electricity (COE) and CO_2 emission amount for several types of fusion reactors. And to assess economics and environmental issues at once, we considered the case of introduction of carbon tax.

2. Assessment procedure

Confinement systems we evaluated here are three types of magnetic confinement fusion reactors (Tokamak Reactor (TR), Helical Reactor (HR) and Spherical Tokamak reactor (ST)) and Inertial confinement fusion Reactor (IR). Several blanket modules and fuel systems (D-T or D-^{3}He) are considered in TR. We used Physics Engineering Cost code (PEC code) [1, 2] to calculate COE of magnetic confinement fusion reactors. PEC code is a code which calculates plasma parameters and radial build of fusion reactor with input parameters such as net electric power output and ignition margin.

The calculation flow of IR parameter is shown in Fig.1. Driver systems quoted here are Kr-F laser of SIRIUS-P [3] (driver energy is 3.4 MJ with 7.5% efficiency) and heavy ion beam (HIB) [4] (driver energy is 7 MJ with 20.4% efficiency). Repetition rate is calculated by given driver energy and pellet gain. Chamber size is approximated by some other reactor designs [3, 4]. Cost of plant systems except for driver system and pellet production are calculated by the same scaling as PEC code. Driver system and pellet production cost are given by the scaling described in Ref. [4].

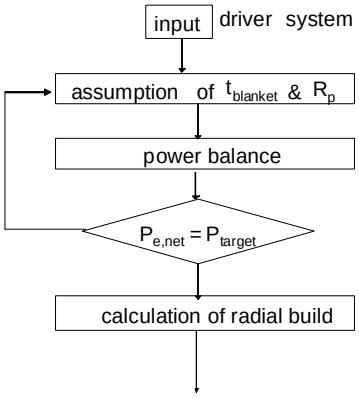

Fig.1 Calculation flow of IR.

To estimate CO_2 emission amounts, we used basic unit for CO_2 weight (k-t-CO_2/t-material) [2, 5, 6]. CO_2 emissions from mining, transport and fabrication are included in this factor.

3. Assessment models

Models of confinement systems and blanket models adopted here are explained below. To compare all of fusion

author's e-mail:s-uemura@ees.nagoya-u.ac.jp

Table1 Main parameters of several magnetic confinement fusion reactors calculated by PEC code

	TR		ST	HR
confinment scaling	ITER Elmy H mode			ISS mode
fuel	D-T	D-^{3}He	D-T	D-T
normalized β value β_N average β value <β> (%)*	β_N=4	β_N=6	β_N=6	<β>=4%
Aspect ratio <A>*	3.5	3.5	1.6	7.8
Average temperature <T> (keV)*	15	42.5	15	10
Plasma major radius R_p (m)	6.3	13.9	4.3	14.9
Toroidal field B_t (T)	6.2	8.4	2.5	4.7
Total fusion power P_{fus} (MW)	3478	4823	4188	2346
Average density <n> (10^{20}/m^3)	1.5	1.5	1.0	1.0

* input parameter

Table2 Main parameters of inertial confinement fusion reactors. Driver systems considered here are Kr-F laser system and Heavy Ion Beam (HIB).

laser system	Kr-F	HIB
Driver energy (MJ)*	3.4	7
Driver efficiency*	0.075	0.206
Pellet gain*	120	120
Repetition rate f_{rep}(Hz)	6.5	2.7
Chamber size R_{fw} (m)	4.4	5.8
Total fusion power P_{fus} (MW)	2644	2260

* input parameter

Table.3 Several blanket parameters in TR design

Blanket module	Li/V	Flibe/FS	LiPb/SiC	Li2O/SiC	F-F hybrid
Thermal efficiency*	0.46	0.4	0.5	0.49	0.4
FW/Blanket lifetime W_{life} (MWy/m^2)*	18	15	20	20	15
Toroidal field B_t (T)	6.1	6.2	6.1	5.9	4.7
Total fusion power P_{fus} (MW)	2909	3478	2618	2682	592
Thickness of FW/Blanket $t_{blanket}$ (m)	0.4	0.6	0.8	0.5	0.9
Thickness of shield t_{shield} (m)	0.8	0.7	0.4	0.8	0.6
Neutron wall load L_{wall} (MW/m^2)	3.0	3.3	2.8	2.7	0.9

* input parameters

reactors under the same conditions, 1000MWe net electric power output, 30 years operation period and 0.75 utilization factor are assumed.

In the reference case normalized beta value (average beta value for HR) is determined by the technical performance of reactor models which is considered now. When TR employs D-^{3}He fuel, high temperature and high maximum toroidal field is required to design sufficiency compact and economical reactor. So D-^{3}He fuel reactor is assumed to have high performances (high temperate, magnetic field and beta). Because of the low neutron generation rate of D-^{3}He fuel, we assumed that there is no blanket exchange during D-^{3}He fuel fusion reactors. Main parameters of magnetic confinement fusion reactors calculated by PEC code are listed in Table1.

Pellet gain of IR is given as an input in our calculation. And pellet gain is selected same value for Kr-F laser system reactor and HIB reactor. Li breeder liquid wall chamber is adapted to IR and we assumed that there is no blanket exchange during its operation period. The main

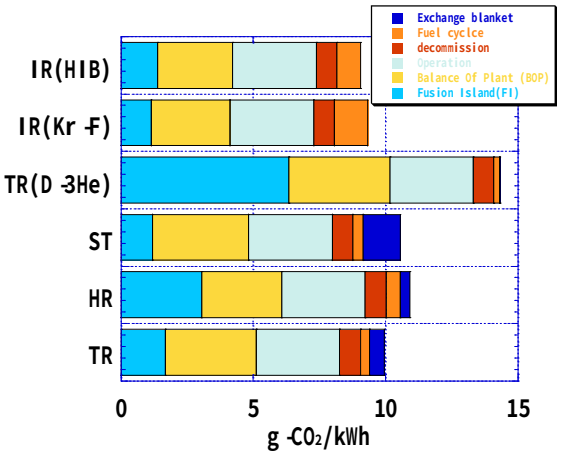

Fig.2 CO_2 emission amount of several fusion reactors.

parameter of the reference case of IR is listed in Table2.

Blanket modules we adapted to TR are Li breeder with V structural material blanket (Li/V), Flibe breeder with ferrite steel structural material blanket (Flibe/FS), LiPb breeder with SiC structural material blanket (LiPb/SiC), Li_2O breeder with SiC structural material blanket (Li_2O/SiC) and fission fusion hybrid (F-F hybrid) blanket [7]. There is UO_2 in F-F hybrid blanket model so its neutron energy multiplication rate is very high (We assumed 6.0). Each model has a difference in thermal efficiency and wall life time in PEC code [2]. Main parameter of the TR reactor which has different blanket is shown in Table3.

4. Results

The CO_2 calculation results of reference fusion reactors are shown in Fig.2. The coil construction phase is the most CO_2 emitting stage of magnetic confinement fusion reactors. CO_2 emission amounts from coil system construction account for 10%, 8% and 20% of lifetime CO_2 emission amount of TR, ST and HR, respectively. HR and D-^{3}He fuelled TR needs rather larger coil than D-T fuelled TR and ST, and more CO_2 are emitted at the Fusion Island (FI) construction stage. ST needs more re-circulating power including ohm loss at the normal conducting coil, and more CO_2 are emitted at the Balance Of Plant (BOP) construction stage. On the contrary, HR requires less re-circulating power, and less CO_2 is emitted at the BOP construction stage. Dependence of CO_2 emission amount and plasma major radius on beta value is shown in Fig.3. The achievement of higher beta value leads to more compact system and less CO_2 emission.

CO_2 emission amounts of tokamak reactors with different blanket module are shown in Fig.4. Thermal efficiency is an influential factor to design fusion reactor. A

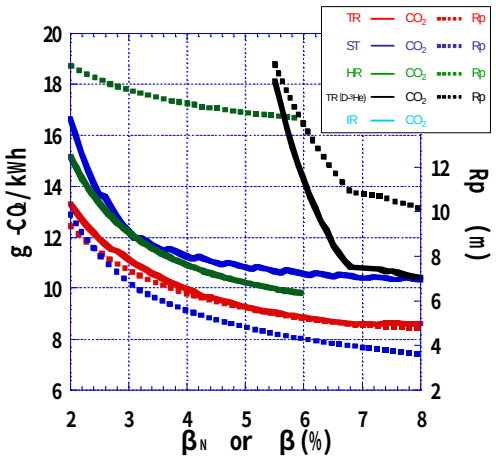

Fig.3 Dependence of CO_2 emission amount and plasma major radius on beta value.

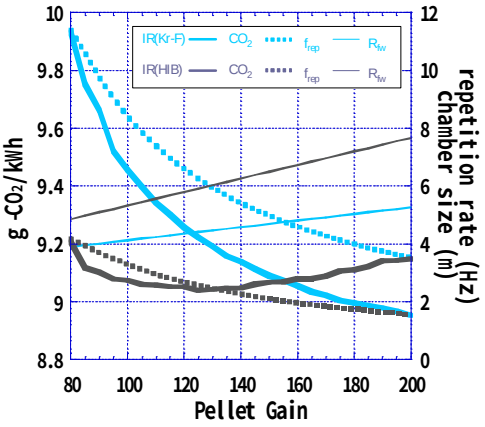

Fig.5 Dependence of CO_2 emission amount, laser repetition rate and chamber size on pellet gain.

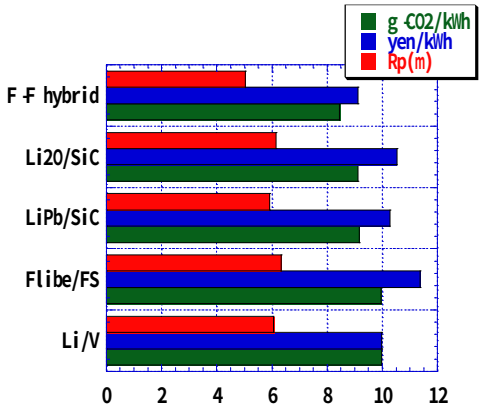

Fig.4 CO_2 emission amount, Cost Of Electricity (COE) and plasma major radius Rp of several TR designs with different blanket modules.

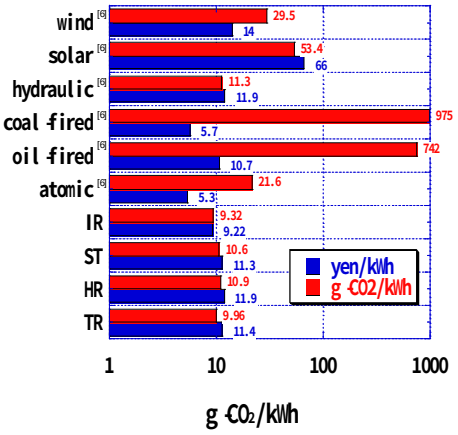

Fig.6 Comparison among fusion reactors and other conventional power plants from the aspect of COE and CO2 emission amount.

higher thermal efficiency model, such as LiPb/SiC or Li_2O/SiC model, can give rise to more compact system and less CO_2 emission than other blanket models. Vanadium needs much electric power to fabricate, so the CO_2 emission amount of Li/V blanket model is rather higher than others. F-F hybrid blanket model modify FI requirements because of its high neutron multiply factor. Therefore it is possible to construct with lower cost and less CO_2 emission amount. But there exists another problem; high level radioactive waste disposal.

Driver construction stage is the most CO_2 emitting stage of IR. Additionally IR emits more CO_2 than magnetic confinement fusion reactor at the fuel cycle stage. However, total CO_2 emission amount from IR is lower than that from magnetic confinement fusion reactors because of its compactness and the assumption that no blanket exchange is required during its operation period. Dependence of CO_2 emission amount, laser repetition rate and chamber size on pellet gain is shown in Fig.5. When pellet gain is low, high laser repetition rate is necessary to attain desired net electric power. High laser repetition rate requires many pellets, and CO_2 emission during fuel cycle is increased. Whereas, when high pellet gain is assumed, large chamber size is necessary to tolerate high fusion heat pulse.

Figure 6 shows the comparison of fusion power pants and other power generation systems from the view point of COE and CO_2 emission amount. Fusion reactors emit less CO_2 than other conventional power plants do [6]. When comparing fusion reactor with atomic power plant, atomic power plant emits more CO_2 in its fuel cycle. Atomic power plant needs uranium concentration, whereas fusion power plant needs tritium separation. In this paper, tritium separation of fusion reactor is optimistically evaluated, so it might be necessary to reconsider it well.

COE of fusion reactor and other power plants in the case of carbon tax introduction is shown in Fig.7. CO_2

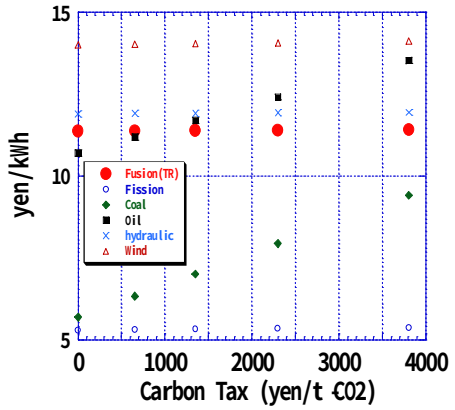

Fig.7 COE of fusion reactor and other power plants in case some carbon tax is introduced

emission amount from fusion reactor during its life time is far less than those from thermal power plants. Introduction of carbon tax has little impact on COE of fusion reactors alike conventional clean energy recourses like solar and wind power etc. Carbon taxes assumed here are 1350, 3808, 655 and 2300 yen/kWh (actual example of Norway, actual example of Sweden, a plan of Japanese environment ministry and recommendation of Central Research Institute of Electric Power Industry [8], respectively.)

5. Conclusion

We calculated CO_2 emission amount from various fusion reactors including inertial confinement fusion reactor. CO_2 is emitted mainly at the magnet system construction stage for magnetic confinement fusion reactors. So HR and D-^{3}He fuelled fusion reactors with bigger magnet system emits more CO_2 during its construction stage. FI of ST is so compact that CO_2 is less emitted during its construction, but BOP construction stage involves much CO_2 emission because of its large re-circulating power. For inertial confinement fusion reactors CO_2 is emitted mainly at the driver system construction stage. The chamber size and quantity of pellet decided by repetition rate are also strongly related to CO_2 emission amount. After comparing fusion reactors with other power generation systems from the view point of CO_2 emission amount, we conclude that fusion reactor emits less CO_2. There is little influence on economics of fusion reactors even by introducing carbon tax.

References

[1] K. Yamazaki and T. J. Dolan, Fusion Engineering and Design **81**, 1145 (2006).

[2] S. Uemura and K. Yamazaki *et al*., Transactions of the Atomic Energy Society of Japan. **8**, to be published (2009).

[3] M. A. Abdou *et al*., UWFDM-950 (1993).

[4] I. N. Sviatoslavsky *et al*., Fusion Engineering and Design **23**, 251 (1993).

[5] H. Hondo *et al*., Socio-economic Research Center, Reo. **Y95013** (1996).

[6] H. Hondo *et al*., Socio-economic Research Center, Reo. **Y99009** (2000).

[7] L. J. Qiu *et al*., Fusion Engineering and Design **25**, 169 (1994).

[8] T. Hattori *et al*., Socio-economic Research Center, Reo. **Y01007** (2001).

Proceedings of ITC18,2008

Development of System Design Code for Heliotron Reactor

Takuya Goto, Akio Sagara, Shinsaku Imagawa

National Institute for Fusion Science

Heliotron reactors inherently have suitable properties for a DEMO reactor; no need of current drive power, easiness in steady state operation. To clarify a possible path to the DEMO reactor with utilizing such properties of heliotron reactors, system design code for heliotron reactors is being developed. Assuming the use for sensitivity analysis over a wide design space, computational time needs to be reduced as much as possible. Whereas calculation of an equilibrium magnetic surface, which requires long computational time including numerical integral, is indispensable to obtain several key engineering and physics variables in a system design. Here magnetic field configuration of heliotron system is considered to be described by geometric configuration of helical coil only. Thus it is expected that magnetic field configuration can be estimated by some empirical scaling laws and approximation formulae. In this paper, current status and some technical issues of code development are reviewed.

Keywords: heliotoron reactor, system design code, simplified calculation method, scaling law

1. Introduction

The construction of international thermonuclear experimental reactor (ITER) has been started and the development of fusion energy source now enters into a quite important phase in which controlled and continuous fusion burn is demonstrated. Then the detailed design study of a DEMO reactor, which succeeds to ITER, should be started in the near future. Helical system, which confines plasma by the magnetic field generated by external conductors only, inherently has suitable properties for a DEMO reactor; no need of current drive power, easiness in a steady state operation. Thus it is quite meaningful to clarify a possible path to the DEMO reactor that fully utilizes such properties. The study of helical system parallel to tokamak is also important from the viewpoint of maintaining flexible developmental strategy of fusion energy.

Generally, sensitivity analysis over a wide design space is an effective way to clarify the design direction of a reactor system. Helical system, however, has high degree of freedom in its design and requires the consideration of complicated three-dimensional effects and fast calculation with simple formulae is difficult. Thus system design code for helical system has not yet been built except for the use in the optimization study within a limited design space. Whereas, heliotron system, which uses 2 continuous helical coils for the plasma confinement, has achieved excellent plasma properties through the experimental studies by Large Helical Device (LHD) [1], and the design of a DEMO reactor can be extrapolated from these achievements. Thus design study of a DEMO reactor with heliotron system is quite significant. We can reduce a degree of freedom in design by specializing for heliotron reactors. The probable design space has been also narrowed down through the past experimental studies. In such a restricted area, we can obtain a valid estimation of the reactor performance by using several empirical scaling laws or approximation formulae. Then it becomes possible to build a system design code for heliotron reactors. In this paper, current situation and several critical issues of code development are reviewed.

2. Application and Required Performance of System Code

As described in the previous section, we assume the use of a system design code for sensitivity analyses over a wide design space. Then system code needs to be able to calculate core plasma performance, engineering design criteria, and plant performance (i.e., electric power output, cost, the amount of radioactive waste, etc.) simultaneously and with a consistent manner. Whereas computational time is required to be reduced as much as possible. Since scanning of 6 patterns of each 6 parameters yield 46,656 design points and only 3 patterns of 10 parameters yield 59,049. Then the computational time per one parameter set point is limited to be <1 sec to carry out a parametric scan with sufficient design points (more than 100,000) within reasonable computational time (e.g., about a day). However, in heliotron system, the position, shape, and current of helical and poloidal coils are the critical factors that determine its design feasibility. For example, the information of magnetic surface structure including ergodic layer is indispensable for the blanket and shield design. The design of vacuum vessel also cannot be fixed without the information of divertor strike points. Magnetic surface structure can be changed by adjusting position and

author's e-mail:goto.takuya@LHD.nifs.ac.jp

current of poloidal coils. But its degree of freedom is also limited by stored magnetic energy of the coil system. Then we need to consider these effects even in preliminary phase of the parametric scan to find viable design points. Though it is not described in this paper, we also need to consider feasibility of the sufficient TBR (tritium breeding ratio) achievement, the effect of maintenance time and frequency on plant availability, and operation scenario including transient phase (e.g., plasma lump-up and shutdown).

3. Simplified Calculation Method

In the system design of heliotron system, magnetic field calculation is necessary to get several important parameters (e.g., maximum field on coil, minimum minor plasma radius, etc.). However, it requires significant computational time because it cannot be solved analytically and needs numerical integral. Here we only need a moderate accuracy of the calculation result for the application in a parametric scan. The vacuum magnetic field configuration is uniquely determined by the coil geometric configuration and simplified calculation (e.g., approximation formula and inter- or extrapolation of tabulated data) can yield the sufficient accuracy. In the following, a brief description of such simplified calculation methods is given.

3.1 Magnetic filed ratio scaling

The estimation of the maximum magnetic field on coil $B_{\max}$ and average toroidal field on magnetic axis $\langle B_0 \rangle$ with reasonable accuracy is indispensable in a system design. $\langle B_0 \rangle$ of tokamak system can be easily calculated from $B_{\max}$ and shape of toroidal field coil by using a simple $1/R$ scaling. Whereas $\langle B_0 \rangle$ of heliotron system can be obtained by Ampere's law as

$$\langle B_0 \rangle = \frac{\mu_0 m I_c}{2\pi R_c} \qquad (1)$$

where μ_0, m, I_c, R_c are vacuum magnetic permeability, toroidal pitch number, helical coil current, and helical coil major radius. But $B_{\max}$ of heliotron system cannot be calculated by an analytical way. Here the ratio of these 2 parameters $B_{\max}/\langle B_0 \rangle$ is a non-dimensional parameter and determined by coil geometric configuration only. Thus the magnetic field ratio can be described by a function of several non-dimensional parameters related to geometric factors. Such scaling law has already been proposed by Yamazaki in the design optimization of Large Heclical Device (LHD) [2] as:

$$\frac{B_{\max}}{B_0} = 2.1\left(\frac{j_c}{40}\frac{R_c}{B_0}\right)^{0.40}\left(\frac{10}{m}\right)^{-0.853}\left(\frac{\gamma_c}{1.2}\right)^{0.05}, \qquad (1)$$

where j_c is helical coil current density and γ_c is helical pitch parameter $\gamma_c = m a_c / (\ell R_c)$. This scaling well reproduces the magnetic field ratio of heliotron system that has similar coil shape to LHD. However, it cannot reproduce that of recent designed heliotron reactors; FFHR-2m1 and FFHR-2m2 [3]. This is because that the coil cross-sectional shape of FFHR series is different from that of LHD. Thus we tried to build a new magnetic ratio scaling law including this effect. If we assume 2 helical coils has the same rectangular cross-section, the geometrical configuration of helical coils is uniquely determined when the following parameters are given; R_c, m, coil minor radius a_c, pitch modulation parameter α, coil cross-sectional area S_c, and the ratio of coil width to height $x=W/H$. After some consideration, we selected 5 non-dimensional parameters: m, α, γ_c, the parameter defined as $\zeta \equiv \sqrt{S_c}/R_c$, and the parameter related to the maximum field on infinite-length linear conductor with rectangular cross-section;

$$\xi = \sqrt{x}\left\{\ln\left(1+\frac{4}{x^2}\right)+\frac{4}{x}\tan^{-1}\left(\frac{x^2}{2}\right)\right\}. \qquad (2)$$

Then we calculated magnetic field ratio of various heliotron system by using finite volume current element code developed based on Todoroki's theory [4] and carried out regression analysis of the result. Here we assumed that poloidal coils were located at each vertex of the rectangle that has the inscribed circle with the same radius as the outer edge of the helical coil; $a_c+H/2$.. According to the result of regression analysis, we proposed magnetic ratio scaling as following;

$$\frac{B_{\max}}{\langle B_0 \rangle} = 0.85(1+\alpha)^{-0.117} m^{-0.853} \gamma_c^{0.156} \xi^{0.796} \zeta^{-0.815}. \qquad (3)$$

As shown in Fig. 1, this scaling well reproduce the magnetic field ratio calculated by finite volume current element code within 2% error over wide range of design parameters: $4 \le R_c \le 20$, $m = (8,10,12)$, $1 \le \gamma_c \le 1.4$, $-0.2 \le \alpha \le 0.2$, $0.07 \le \zeta \le 1$, $1 \le \xi \le 2$.

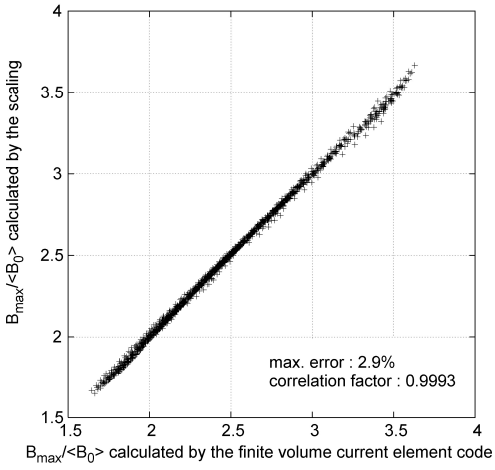

Fig.1 Comparison of magnetic field ratio estimated by the proposed scaling (eq. (3)) and the calculation result by finite volume current element code..

3.2 Calculation of Vacuum Magnetic Surface

To achieve fast calculation in evaluation of plasma performance, we consider the use of ISS (International Stellarator Scaling) [5,6]. ISS scaling law consists of average plasma minor radius $<a_p>$, major radius of last closed flux surface (LCFS) R_{geo}, average toroidal field strength B_t, rotational transform ι at normalized radius of ρ=2/3. To obtain these parameters, calculation of an equilibrium magnetic surface is indispensable. But calculation of a magnetic surface needs filed line tracing, which requires long computational time. Whereas magnetic field structures including ergodic layer generated by similar shape 2 coils are always similar to each other. Thus it is expected that parameters related to magnetic configuration can be obtained by inter- or extrapolation of database generated by the detailed calculation with several data points.

To calculate equilibrium magnetic field, the location and current of poloidal coils needs to be determined. Helical coil inevitably generate net vertical field in plasma confinement region. This vertical field is canceled out by poloidal coils symmetrically located against the equatorial plane. Generally two pairs of helical coils, one is located at inner side of torus and the other at outer side, are used to reduce leakage field. Then 6 parameters, radius, height and current of inner and outer poloidal coil, needs to be determined. For simplicity, here we assumed inner and outer poloidal coil has same height and located on the circle that shares its center with helical coil winding center. Then the location of poloidal coil is fixed by two parameters, the radius of circle R_{PC} and angle between outer poloidal coil and equatorial plane θ_{PC} (see Fig. 2). Once the locations of poloidal coils are given, there remains two degree of freedom; currents of inner and outer poloidal coil. There are two main parameters used to determine the current of poloidal coils: cancellation of dipole field generated by helical coil (BD), that of quadrapole field (BQ). BD value coincides to the shift of vacuum magnetic axis. Here we gave BD value and BQ was fixed to be 100%. And R_{PC} and θ_{PC} are selected to maximize the volume enclosed by the last closed flux surface.

Table I shows the comparison of the parameter set of LHD at several magnetic axis positions with the calculation result obtained by the interpolation of database. This database is generated by the detailed calculation with parameter set: γ_c=1.1, 1.2, 1.3 and ζ=0.07, 0.08, 0.09, 1.0. As shown in the table, the parameters of LHD with magnetic axis position R_{ax}=3.9m and 3.75m (coincides to the BD values of 96.01% and 101.84%) were reasonably reproduced. But the parameters of LHD with R_{ax}=3.6m deviate from the result of equilibrium magnetic surface calculation. One reason of this deviation is the difference in

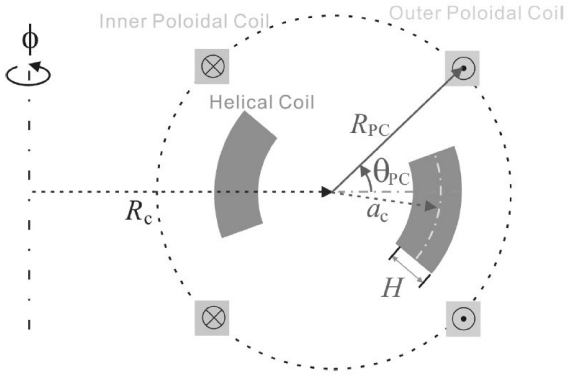

Fig.2 Schematic viewing of poloidal cross-section of heliotron system.

the position of poloidal coils. In the case of BD=107.91%, the difference in current and position of poloidal coils from those of LHD is larger than the other cases. The largest deviation of magnetic axis position also shows this difference. Another reason is that the position and current of poloidal coils have not been fully optimized. The magnetic field generated by helical coil is monotonous function of coil geometric parameters. However, magnetic field structure around LCFS strongly depends on the position and current of poloidal coils. Then the volume enclosed by LCFS varies non-monotonically with the coil geometrical configuration. Therefore, the design of poloidal coils need to be optimized to obtain a database that can serve consistent data at any design point by inter- or extrapolation.

Table I Comparison of parameters related to magnetic surface structure of LHD at several vacuum magnetic axis positions with the value obtained by interpolation of database. The values in left row are results of equilibrium magnetic surface calculation, those in right row are obtained by interpolation of database.

	LHD R_{ax}=3.9m		LHD 3.75m		LHD 3.6m	
BD	0.9601	←	1.0184	←	1.0791	←
$<a_p>$	0.535	0.552	0.589	0.593	0.636	0.584
ι_0	0.432	0.402	0.349	0.334	0.378	0.306
ι_a	0.964	1.049	1.214	1.257	1.571	1.229
R_{ax}	3.9	3.903	3.75	3.767	3.6	3.651
R_{geo}	3.816	3.811	3.740	3.738	3.672	3.694

4. Conclusion

System design code for heliotron reactors is being developed. To reduce computational time, we introduced several simplified calculation methods. For calculation of magnetic field ratio (the ratio of maximum field on coil B_{max} to average toroidal field on magnetic axis $<B_0>$), we proposed a new scaling described by exponential law of

non-dimensional parameter related to coil geometrical configuration. We also tried to establish tabulated database of parameters related to magnetic field and magnetic surface structure at several specific design point. We expected that we can obtain these parameters at any design point by inter- or extrapolation of the database. Magnetic field components generated by helical coils can be well reproduced. But magnetic surface structure strongly depends on current and position of poloidal coils and we have not yet established perfect database that can be installed in the system code. Though we need further optimization of them to establish a consistent database, we had a perspective to build system design code that satisfies the required performance.

To achieve high reliability of the system design code, we plan to refine ISS scaling law by considering the effect of vacuum magnetic axis position and density/temperature profile and build it into the system code. We also need to consider finite beta effect on the magnetic configuration. Simplified evaluation method of tritium breeding ratio (TBR), plant availability, and operation scenario is also required to find viable design window. It is also quite important to clarify the design space with high robustness to the model uncertainty for assured development to a DEMO and commercial reactor instead of local optimization. To install procedures that can achieve these analyses, we can find the design point of the heliotron reactor that has high reliability and feasibility.

Acknowledgement

The authors appreciate the all members of helical reactor design group in National Institute for Fusion Science for provide valuable advises.

References

[1] O. Motojima *et al*., Nucl. Fusion **40**, 599 (2000).
[2] K. Yamazaki *et al*., Fusion Technology **21**, 147 (1992).
[3] A. Sagara *et al*., Nucl. Fusion **45**, 258 (2005).
[4] J. Todoroki, Kakuyugo Kenkyu **57** (1987) 318 [*in Japanese*].
[5] U. Stroth *et al*., Nucl. Fusion **36**, 1063 (1996).
[6] H. Yamada *et al*., Nucl. Fusion **45**, 1684 (2005).

Proceedings of ITC18,2008

Water-Cooled Solid Breeding Blanket for DEMO

K. Tobita, S. Nishio, A. Saito, M. Enoeda, C. Liu, H. Tanigawa,
S. Sato, D. Tsuru, T. Hirose, Y. Seki and M. Yamada*

*Japan Atomic Energy Agency, *Computer Software Development Co. Ltd.*

For tokamak fusion DEMO, neutronics and thermal design was carried out to find a blanket concept with reality. For the continuity with the Japanese ITER-TBM options, this study considered water-cooled blanket with solid breeding materials of Li ceramics (Li_4SiO_4, Li_2TiO_3 and Li_2ZrO_3) and Be multipliers (Be and $Be_{12}Ti$). On the based on multilayered structure with Li_4SiO_4 pebbles, Be plate and mixture of Li_4SiO_4/$Be_{12}Ti$, the local TBR of 1.42 (corresponds to the net TBR of 1.05) was obtained. In addition, it was concluded that in-between conducting shell structure can be placed at r_w/a = 1.32-1.35 with satisfying fuel self-sufficiency.

Keywords: blanket, tritium breeding ratio, solid breeder, DEMO, fusion reactor

1. Introduction

Blanket of fusion reactor must meet three major requirements, 1) tritium self-sufficiency, 2) removal of nuclear heating, and 3) structural strength against electromagnetic forces acting on disruptions. The common maneuver in blanket design is to minimize the areas of coolant and structural materials so as to ensure fuel (tritium) self-sufficiency. Generally, it is difficult to ensure fuel self-sufficiency in itself. It is even more difficult to find a consistent solution satisfying all these requirements. Water-cooled solid breeding blanket treated in this paper, is regarded as a conservative and less challenging blanket concept. However, the fact is that the concept still has difficult problems to be resolved. In this paper, we report the blanket design study for a compact low aspect ratio DEMO "SlimCS" and clarify the critical design issues.

2. Basic concept of blanket

The DEMO reactor, SlimCS, has a major radius of 5.5 m, aspect ratio (A) of 2.6, maximum field of 16.4 T, normalized beta (β_N) of 4.3 and fusion output of 2.95 GW [1]. The average neutron wall load is 3 MW/m^2. The reactor is characterized by a reduced-size central solenoid (CS) whose main function is plasma shaping rather than plasma current ramp-up. The CS has an outer radius of 0.7 m, being capable of moderate plasma shaping (triangularity of ~0.35) and plasma current ramp of 3.8 MA. Although such a CS provides a constraint in tokamak operation, especially in the current ramp-up phase, it has advantages to allow us to introduce a thin toroidal coil system, decreasing the reactor weight and perhaps contributing a reduction of the construction cost. In addition, the reduced-size CS produces the possibility of low A, which leads to advantages in physics design such as high elongation of plasma, high plasma current, high Greenwald density limit and high beta limit.

author's e-mail: tobita.kenji30@jaea.go.jp

The DEMO blanket is required to consider continuity with the Japanese ITER-TBM program [2] in which water-cooled solid breeder blanket using lithium ceramics (breeder), Be or $Be_{12}Ti$ (neutron multiplier) and F82H [3] (structural material) will be developed. In addition, a conducting shell structure should be installed near the plasma (preferablly, r_w/a ~ 1.3) on the outboard side. For this purpose, the blanket consists of replaceable and permanent blanket, and the front and side plates of the permanent blanket are 0.07 m in thickness so that the plates have the function of the conducting shell (called "Kameari shell") [4] assembly, as indicated in Fig.1. Since the first wall area on the outboard side is wide in a low-A reactor like SlimCS (inboard 27%, outboard 73%), the demand for tritium breeding on the high field side is comparatively reduced. This leads to the breeding blanket concept consisting of small inboard blanket and large outboard blanket modules. For this reason, SlimCS is designed to have replaceable and permanent blankets on the outboard side while no permanent blanket is installed on the inboard side.

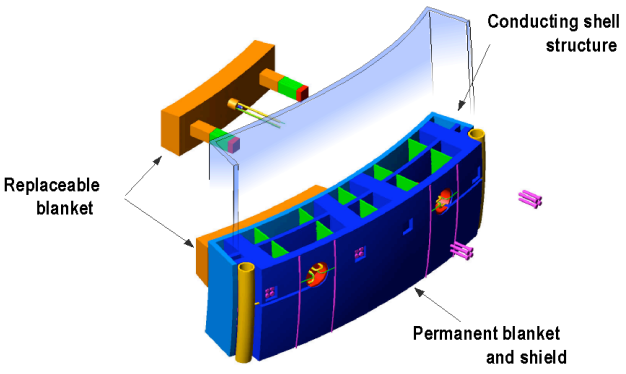

Fig.1 Replaceable and permanent blanket concept of SlimCS.

The temperature range and pressure of the coolant is one of the key design issues. The coolant temperature is required to be about 300ºC at least so as to avoid corrosion by radiation-produced hydrogen peroxides and radiation embrittlement like light water reactors. However, use in the PWR conditions (15 MPa, 285-325ºC) will be problematic in that the required large amount of coolant in the blanket can detract the self-sufficiency of tritium production. On the other hand, use of supercritical water (25 MPa, 280-510ºC), which can allow heat removal with a smaller amount of water because of wide operating temperature range, is expected to lead serious corrosion of F82H. Accordingly, we decided to use water in the subcritical water condition of ~23 MPa and 290-360ºC ($\Delta T = 70K$).

3. Blanket Structure

3.1. Blanket segmentation

A challenging issue in the blanket design is to assure robustness of the blanket casing and its support against disruptions. This requirement is a difficult issue especially for the replaceable blanket. Because it must not only withstand enormous electromagnetic (EM) forces acting on disruptions, but be easily de-installable and installable for periodic replacement. From the point of view of structural robustness, smaller blanket casing is desirable while such a casing seems to be problematic regarding tritium breeding. After all, the blanket casing should be large as long as it withstands disruptions.

In order to determine a reasonable blanket casing in terms of the EM forces, eddy current due to a disruption and the resulting EM force moments were estimated. On the basis of the analysis on various blanket casings for a disruption (plasma current quench time of 0.03 s, without suffering vertical displacement event), we come to a conclusion that toroidally-long blanket casing has advantage in the viewpoint of support against disruptions [5] when the blanket is fixed with supports in the toroidal direction (Fig.1).

3.2. Neutronics and thermal design of blanket

The purpose of this research is to find a promising candidate of blanket concept. In this early stage of research, the one-dimensional analysis with simplified models is efficient to flexibly deal with a try and error process in the design. The code used in this study is an ANIHEAT code that calculates the nuclear heating distribution and solves heat transfer in the blanket. Eventually, the code provides the temperature profile in the blanket and the local tritium breeding ratio (TBR). The required local TBR for SlimCS is estimated to be ≥ 1.38 to reach the net TBR of ≥ 1.05.

Based on the result of various model calculations, the blanket is designed to have multilayered structure as shown in Fig.2. This is because such structure installing breeder and multiplier zones alternately can provides the highest TBR. Compared with other lithium ceramics such as Li_2TiO_3 and Li_2ZrO_3, Li_4SiO_4 has high Li density per unit volume (Table 1) and Si has low cross section for inelastic collisions in MeV range (Fig.3). This suggests that Li_4SiO_4 is anticipated to have the highest TBR among them. Actually, the calculated TBR is as expected. A distinctive feature of the blanket interior is to use both Be plate and $Be_{12}Ti$ pebbles in accordance with the intension. From the point of view of chemical stability, $Be_{12}Ti$ is favorable as neutron multiplier. However, we determined not to use $Be_{12}Ti$ in the forward multiplier zones (in the first and second multiplier zones). This is to avoid neutron absorption in MeV range by Ti of $Be_{12}Ti$. Be intrinsically has excellent thermal conductivity (nominally, 200 W/mK). When it used as pebbles, however, the conductivity decreases to as low as 7 W/mK [6], which will make the thermal design of Be layers. For this reason, Be plates are allocated in the forward multiplier zones. Incidentally, Be plates are canned to avoid the reactive decomposition of Li_4SiO_4 by Be. In the backward multiplier zones of the blanket, neutron absorption by Ti of $Be_{12}Ti$ becomes less important because of reduced energy of neutrons. In fact, there is an affirmative reason for using $Be_{12}Ti$ in the backward. This is because $Be_{12}Ti$ is allowed to use in the mixture of Li_4SiO_4 without any partition due to its chemical stability, which contribute to increasing TBR.

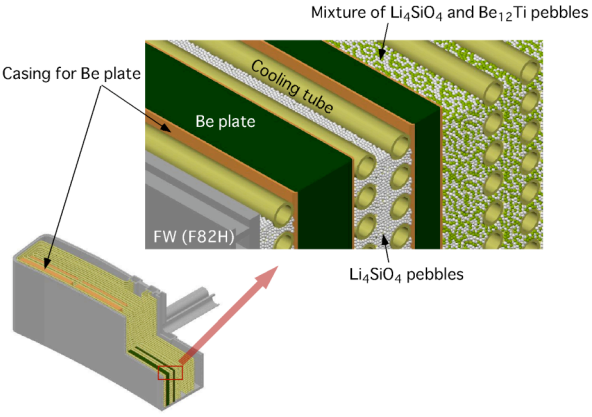

Fig.2 Interior of replaceable blanket

The blanket structure shown in Fig.2 is modeled one-dimensionally and the nuclear heating and the temperature in the steady state are calculated. Figure 4 is an optimized arrangement in which the thickness of each material is determined to satisfy the operating

temperature; ≤ 900ºC for Li_4SiO_4 and $Be_{12}Ti$, and 600ºC for Be. The coolant temperature is assumed to be same as the outlet temperature (360ºC) and the neutron wall load is 5 MW/m^2 which corresponds to the peak wall load in the reactor when the average neutron wall load is 3 MW/m^2. Notice that the nuclear heating of Li_4SiO_4 in the first and second breeder zones is as high as 100 W/cm^3. Since the heat thermal conductivity of Li_4SiO_4 pebbles is low (about 1 W/mK [7]), the zones must be as thin as 1 cm to meet the operating temperature.

Table 1 Comparison of lithium ceramics

	Li_4SiO_4	Li_2TiO_3	Li_2ZrO_3
Li density (g/cm^3)	0.51	0.43	0.38
Thermal conductivity (W/mK)	2.4	1.8	0.75
Swelling ΔV/V (%)	1.15	0.8	0.5
Reactivity with H_2O	small	none	none

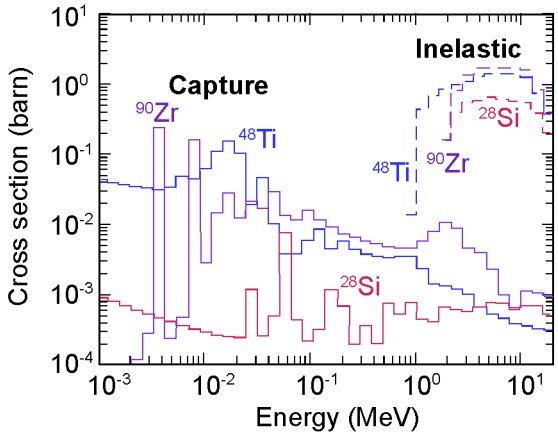

Fig.3 Cross section for neutron capture and inelastic collision for metals of Li ceramics.

The calculated local TBR is summarized in Table 2, indicating that the required local TBR (≥ 1.38) is satisfied for both cases with Li_4SiO_4 and Li_2TiO_3 pebbles. In addition, most of tritium is produced on the outboard side. The thickness of the replaceable and permanent is about 40 cm and 30 cm, respectively. Despite the thickness, the permanent blanket contributes little to the TBR. Figure 5 illustrates the distribution of the local TBR at each breeder stage (zone) for the Li_4SiO_4 case. The figure suggests that the importance of the design for the replaceable blanket, especially for the forward breeder stages of the blanket.

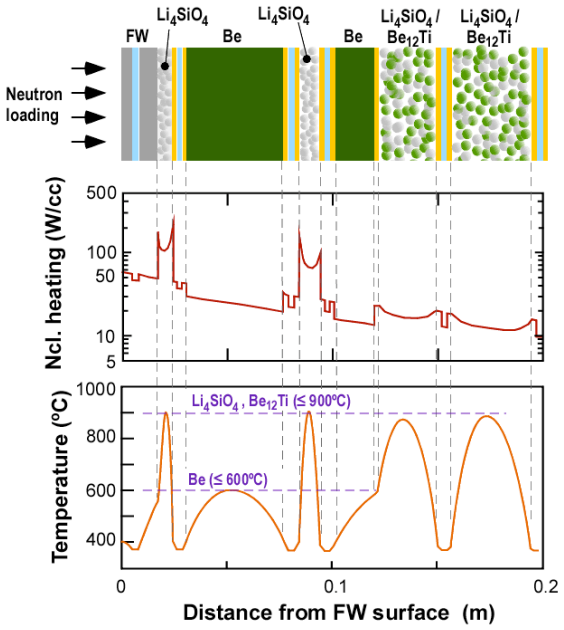

Fig.4 One-dimensional model of blanket and the calculated nuclear heating and temperature distribution.

Table 2 Local TBR for Li_4SiO_4 and Li_2TiO_3 pebbles

		Li_4SiO_4	Li_2TiO_3
Inboard	Replaceable blanket	0.31	0.30
Outboard	Replaceable blanket	1.07	1.04
	Permanent blanket	0.04	0.04
Total		1.42	1.38

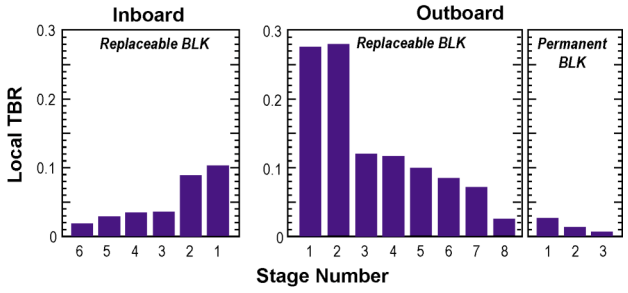

Fig.5 Local TBR produced in each breeder zone in the blanket using Li_4SiO_4 pebbles.

3.3. Conducting wall position and TBR

In SlimCS, the problem on the conducting wall position is equivalent to the problem on the segmentation of replaceable and permanent blankets. This is because the front plate of the permanent blanket plays a role of a conducting wall as shown in Fig.1. From the point of view of plasma design, the wall position should be close

to the plasma as possible for high β_N access and vertical stability of plasma. On the other hand, the conducting shell attenuates neutron flux, leading to a reduction in TBR. As the calculated TBR of the present blanket options is near the verge of fuel self-sufficiency, the relation between the conducting shell position and TBR becomes a critical issue regarding blanket design. Since fuel self-sufficiency is a necessary requirement of fusion reactor, one might have to accept a setback of wall position to ensure fuel self-sufficiency even if the design value of β_N decreases.

Figure 6 shows the summation of the local TBR between the inboard blanket and the n-th breeder stage (zone) of the replaceable blanket. When the conducting shell structure is located just behind the breeder stage (this means the replaceable blanket has n stages of breeder), the local TBR in the breeding zones behind the wall is expected to be as low as 0.05. Therefore, in order to meet fuel self-sufficiency, the summation of the local TBR must be 1.33 (= 1.38-0.05) or higher. The figure indicates that this condition is satisfied when the number of breeder stages is seven or more. This indicates a necessity to arrange the conducting shell at r_w/a = 1.32 – 1.35, which may impose compromise on the design value of β_N.

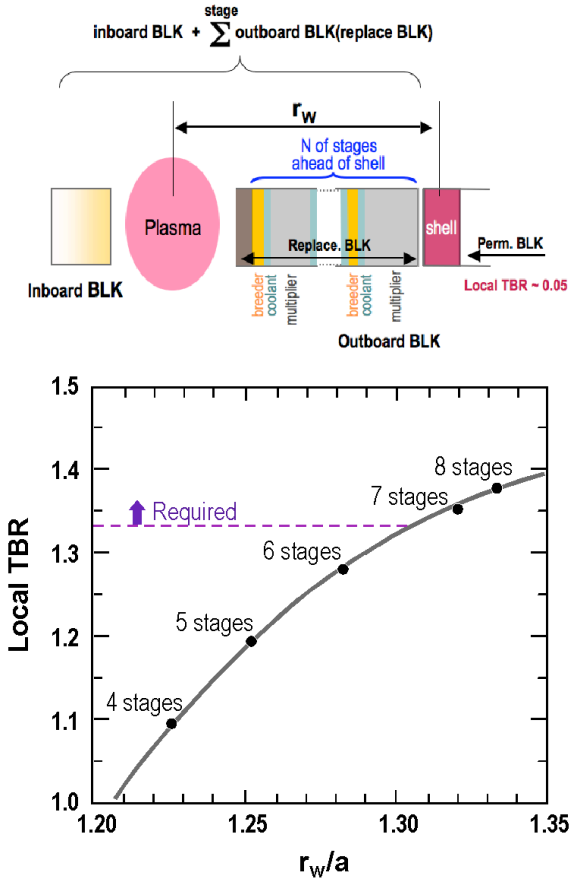

Fig.6 Relation between r_W/a and the number of breeder stages of the replaceable blanket on the outboard.

4. Summary

The present study focused on the neutronics and thermal design of water-cooled solid breeding blanket on SlimCS. Findings of this study are:

1) In the modeled calculation, a blanket concept satisfying fuel self-sufficiency can be envisaged using the presently available data.
2) In-between conducting shell structure can be placed at r_w/a = 1.32-1.35 with satisfying fuel self-sufficiency.

However, it must be noted that the present model calculation includes uncertainty in the treatment of contact heat resistance. This kind of heat transfer can be said to be an intrinsic difficulty in the design of solid breeding blanket. In order to pursuit reality of blanket design, it is necessary to find a concept that reduces uncertainty of contact heat resistance. For example, inserting a thin Be pebble layer between the Be plate and the casing improves the situation although it has a demerit in heat conductivity. In addition, more information on irradiation effect on heat conductivity of breeder and multiplier is required for reliable design.

References

[1] K. Tobita et al., Nucl. Fusion **47**, 892 (2007).
[2] M. Enoeda *et al.*, Fusion Eng. Design **81**, 415 (2006).
[3] S. Jitsukawa et al., J. Nucl. Mater. **307-311**, 179 (2002).
[4] S. Nishio et al., Fusion Eng. Design **81**, 1271 (2006).
[5] K. Tobita et al., Proc. in Fusion Energy Conference 2008, Geneva, FT/P3-9 (2008).
[6] M. Uchida et al., Fusion Eng. Design **69**, 499 (2003).
[7] G. Piazza, M. Enoeda A. Ying, Fusion Eng. Design **58-59**, 661 (2001).

Proceedings of ITC18, 2008

Practical Calculation of Nuclear Fusion Power for a Toroidal Plasma Device with Magnetic Confinement

P.R. Goncharov

St.Petersburg Polytechnical University, 195251, Russia

An algorithm has been developed and realized as a FORTRAN code to calculate the volume integral power of a magnetic confinement nuclear fusion reactor and the fusion rate function in a general case taking as input data the nuclei energy distributions, fusion cross-sections and the magnetic surface geometry. Two fast and simple analytic models of practical magnetic flux surface shapes have been introduced and the corresponding Jacobian determinants have been found. The developed method has been applied to obtain the radial profiles of the nuclear fusion reaction rate and the volume integral power for both Maxwellian and suprathermal D and T particle distributions. Gaussian kernel empirical probability density estimation has been proposed to reconstruct the ion energy probability density function from experimentally obtained random samples of escaping neutral atom energy. Neutral particle diagnostic database may serve as a basis for an experimentally confirmed calculation technique for reactor power and ignition criterion.

Keywords: fusion reactor power, nuclear fusion rate, ion distribution function, high energy particles, non-Maxwellian rate coefficients, plasma volume integration

1. Introduction

The power of a magnetic confinement fusion reactor P [W] and the fulfillment of the ignition criterion are quantitatively determined by the nuclear fusion reaction rate $\mathcal{R}_{\alpha\beta}$ [$m^{-3}s^{-1}$] integrated over the plasma volume using the known magnetic surface geometry:

$$P \propto \int \mathcal{R}_{\alpha\beta}(\mathbf{r}) d^3\mathbf{r} = \int \mathcal{R}_{\alpha\beta}(\rho,\vartheta,\varphi) R(\rho,\vartheta,\varphi) |J| \, d\rho d\vartheta d\varphi , \qquad (1)$$

where

$$J = \begin{vmatrix} \frac{\partial R}{\partial \rho} & \frac{\partial R}{\partial \vartheta} & 0 \\ \frac{\partial Z}{\partial \rho} & \frac{\partial Z}{\partial \vartheta} & 0 \\ 0 & 0 & 1 \end{vmatrix} \qquad (2)$$

is the Jacobian determinant for the transformation from cylindrical coordinates (R, Z, φ) to flux coordinates $(\rho, \vartheta, \varphi)$ with ρ, ϑ and φ designating the magnetic surface label, the poloidal angle and the toroidal angle respectively. Azimuthally symmetric magnetic surfaces are assumed in (2).

The rate of the nuclear fusion reaction between the species α and β,

$$\mathcal{R}_{\alpha\beta} = \frac{n_\alpha n_\beta}{1+\delta_{\alpha\beta}} \tilde{\mathcal{R}}_{\alpha\beta}, \qquad (3)$$

in turn, is proportional to the rate coefficient $\tilde{\mathcal{R}}_{\alpha\beta} = \langle \sigma(v) v \rangle$ averaged over the velocity distribution functions of the reacting species by integrating over the six-dimensional velocity space:

$$\tilde{\mathcal{R}}_{\alpha\beta} = \int \sigma(v) v f_\alpha(\mathbf{v}_\alpha) f_\beta(\mathbf{v}_\beta) d^3\mathbf{v}_\alpha d^3\mathbf{v}_\beta , \qquad (4)$$

where $v = |\mathbf{v}_\alpha - \mathbf{v}_\beta|$ is the relative velocity and $\delta_{\alpha\beta}$ is the Kronecker symbol reflecting the fact that when the reacting species are identical as in DD and TT reactions, and their density is n, the rate is proportional to $C_n^2 = \frac{1}{2} n(n-1) \approx \frac{n^2}{2}$.

The FORTRAN code for nuclear fusion rate and power calculation is based on (1) - (4) and nuclear cross-section approximations from [1-3]. Particle density profiles and the magnetic surface geometry are used as input data. Either analytic ion distribution functions based on theoretical models, or experimentally obtained ion distributions may be used for the calculations.

2. Analytic Models of Magnetic Surfaces

A rigorous treatment requires that Grad-Shafranov equation solutions are used. In order to increase the computation speed and simplify the code, two analytic models of magnetic surfaces have been used in the form of nested shifted D-shaped curves and nested shifted ellipses in the poloidal cross-section. The D-shaped last closed flux surface (LCFS) equation in cylindrical coordinates is

author's e-mail: goncharov@phtf.stu.neva.ru

$$Z^{\pm}_{LCFS}(R) = \pm\sqrt{(\kappa_1 + \kappa_2 R)} \times\sqrt{\sqrt{\kappa_3 R^2 + \kappa_4 R + \kappa_5} + \kappa_6 R + \kappa_7}\,, \qquad (5)$$

where $\kappa_1 = R_{out}/2\gamma$, $\kappa_2 = -1/2\gamma$, $\kappa_3 = 1-4\gamma$, $\kappa_4 = -2\left(\kappa_3 R_{out} + \delta(2\gamma-1)\right)$, $\kappa_5 = \kappa_3 R_{out}^2 + 2\delta \times(2\gamma-1)R_{out} + \delta^2$, $\kappa_6 = 1$ and $\kappa_7 = \delta - R_{out}$ are determined by three input parameters: outer plasma radius R_{out} [m], LCFS poloidal cross-section width δ [m] and dimensionless γ to control the LCFS poloidal cross-section width to height ratio. One more dimensional input parameter Δ [m] is to simulate the Shafranov shift. The magnetic axis position is then

$$R_0 = \frac{R_{in} + R_{out}}{2} + \Delta\,, \qquad (6)$$

where the inner plasma radius R_{in} [m] is calculated from the LCFS equation (5). The poloidal angle $\vartheta \in [0, 2\pi)$ is defined in the same way as the polar angle assuming $R = R_0$, $Z = 0$ to be the centre point and Z to be the polar axis.

As for the transformation between the cylindrical coordinates (R, Z, φ) and flux coordinates $(\rho, \vartheta, \varphi)$, the azimuthal (toroidal) angle $\varphi \in [0, 2\pi)$ preserves. For a given point (ρ, ϑ) in the poloidal plane the coordinate transformation to cylindrical (R, Z) is performed as follows. First,

$$\tilde{\vartheta} = \pi - (\pi - \vartheta)\, sign(\pi - \vartheta) \qquad (7)$$

is calculated, where $sign(y) = -1$ for $y < 0$ and $sign(y) = 1$ for $y \ge 0$. If $\tilde{\vartheta} = 0$, then $Z = 0$; $R = R_0 + \rho(R_{out} - R_0)$. If $\tilde{\vartheta} = \pi$, then $Z = 0$; $R = R_0 + \rho(R_{in} - R_0)$. If $\tilde{\vartheta} = \pi/2$, then $R = R_0$; $Z = \rho Z^{+}_{LCFS}(R_0)\, sign(\pi - \vartheta)$. Otherwise, the nonlinear equation

$$\frac{Z^{+}_{LCFS}(R_{LCFS})}{R_{LCFS} - R_0} - \tan\tilde{\vartheta} = 0 \qquad (8)$$

is resolved numerically with respect to R_{LCFS} sought within $[R_{in}, R_{out}]$. Then,

$$R = R_0 + \rho(R_{LCFS} - R_0)\,,$$
$$Z = \rho Z^{+}_{LCFS}(R_{LCFS})\, sign(\pi - \vartheta)\,. \qquad (9)$$

The ellipse-shaped LCFS equation in cylindrical coordinates is

$$Z^{\pm}_{LCFS}(R) = \pm\sqrt{\kappa_1 R^2 + \kappa_2 R + \kappa_3}\,, \qquad (10)$$

where $\kappa_1 = -b^2/a^2$, $\kappa_2 = 2b^2(R_{out} - a)/a^2$ and $\kappa_3 = b^2 - b^2(R_{out} - a)^2/a^2$ are determined by three

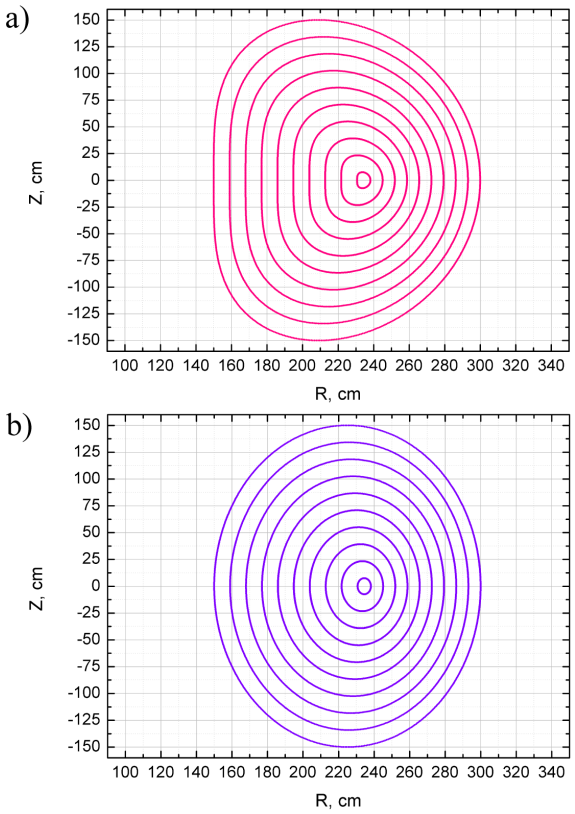

Fig. 1. a) D-shaped and b) ellipse-shaped isolines $\rho = const$ for R_{in} = 1.5 m, R_{out} = 3 m, Δ = 0.1 m.

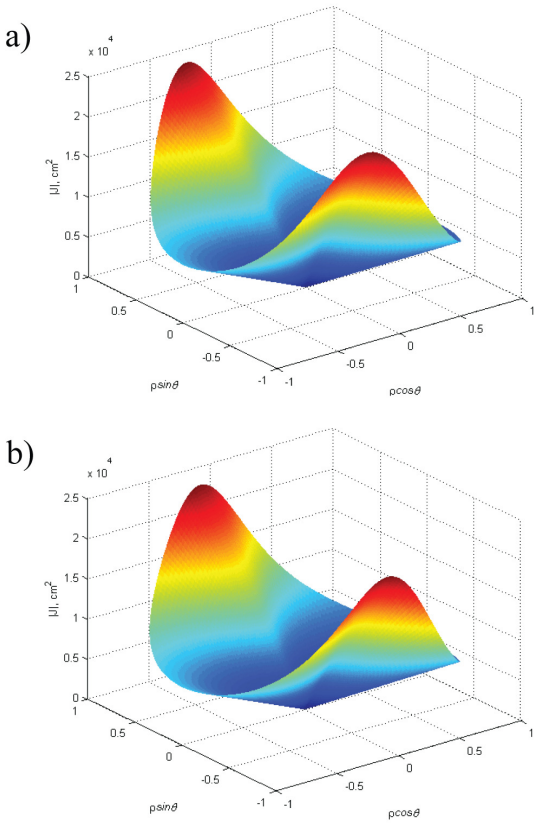

Fig. 2. Jacobian determinant for a) D-shaped and b) ellipse-shaped magnetic surface models.

dimensional input parameters: outer plasma radius R_{out} [m], major and minor ellipse semiaxes *a* [m] and *b* [m]. Again, one more dimensional input parameter Δ [m] is to simulate the Shafranov shift. The magnetic axis position is then

$$R_0 = R_{out} - a + \Delta . \qquad (11)$$

The coordinate transformation from (ρ, ϑ) to cylindrical (R, Z) is performed using formulas (8) and (9) analogously to the case of D-shaped curves substituting the proper function $Z^{+}_{LCFS}(R)$ given by (10) instead of (5).

Fig. 1 shows $\rho = const$ isolines obtained by using the coordinate transformation procedures for the two model magnetic surface shapes. The parameters are $\delta = 1.5$ m, $\gamma = 0.326426$ for Fig. 1 a); $a = 0.75$ m, $b = 1.5$ m for Fig. 1 b), $R_{in} = 1.5$ m, $R_{out} = 3$ m, $\Delta = 0.1$ m for both.

Since R and Z are implicit functions of ρ and ϑ, central difference derivative formulas are used to calculate the elements of the Jacobian determinant (2). Left and right difference derivatives are used at the range $\rho \in [0,1]$, $\vartheta \in [0, 2\pi)$ extremities. The resulting $|J|$ shown in Fig. 2 enables one to calculate the volume integral (1) for either of the two magnetic surface types.

These fast simple analytic models or their combination may be used as a satisfactory practical approximation of a tokamak magnetohydrodynamic equilibrium whenever chord or volume integration, or mapping of plasma parameters as functions of magnetic surfaces to real space coordinates is required in physical and engineering tasks. For stellarator configurations more complicated full 3D models are needed.

3. Nuclear Fusion Rate Coefficients

3.1. Monoenergetic beam and Maxwellian target

For the monoenergetic and monodirectional distribution of species α interacting with a Maxwellian target β,

$$f_\alpha(\mathbf{v}_\alpha) = \delta(\mathbf{v}_\alpha - \mathbf{V}), \quad f_\beta(\mathbf{v}_\beta) = \left(\frac{m_\beta}{2\pi T}\right)^{3/2} e^{-\frac{m_\beta v_\beta^2}{2T}}, \qquad (12)$$

the rate coefficient (4) is reduced to

$$\tilde{\mathcal{R}}^{(BM)}_{\alpha\beta}\left(V, m_\beta/T\right) = \frac{1}{V}\left(\frac{2m_\beta}{\pi T}\right)^{1/2} e^{-\frac{m_\beta V^2}{2T}} \times \int_0^{+\infty} v^2 \sigma(v) \sinh\left(\frac{m_\beta v V}{T}\right) e^{-\frac{m_\beta v^2}{2T}} dv . \qquad (13)$$

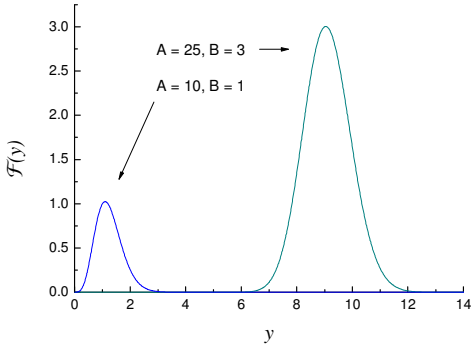

Fig. 3. Function $\mathcal{F}(y)$ in the integrand in (15).

Denoting the atomic velocity unit as $v_0 \approx 2.188 \times 10^8\ cm/s$ and introducing a dimensionless variable $y = v^2/v_0^2$ and dimensionless constants $A = \frac{m_\beta v_0^2}{2T}$ and $B = V/v_0$, consider a dimensionless function

$$\mathcal{F}(y) = \sqrt{y}\left(e^{2AB\sqrt{y} - Ay - AB^2} - e^{-2AB\sqrt{y} - Ay - AB^2}\right). \qquad (14)$$

Then,

$$\tilde{\mathcal{R}}^{(BM)}_{\alpha\beta}\left(V, m_\beta/T\right) = \frac{v_0}{2\sqrt{\pi}} \frac{\sqrt{A}}{B} \int_0^{+\infty} \sigma(y)\mathcal{F}(y) dy . \qquad (15)$$

To avoid arithmetic overflows, the constant e^{-AB^2} should not be taken outside the integral. $\mathcal{F}(y)$ is a nonnegative, slightly asymmetrically bell-shaped exponentially decaying function as shown in Fig. 3. The maximum position depends on the parameters. Qualitatively, function $\mathcal{F}(y)$ can very roughly be thought of as a Gaussian curve corresponding to the Maxwellian distribution of target particles, shifted along the abscissa axis by a value corresponding to the beam particle velocity. The exact maximum condition is expressed by a nonlinear equation

$$\tanh z = \frac{2AB^2 z}{z^2 - 2AB^2}, \qquad (16)$$

where $z = 2AB\sqrt{y}$. Equation (16) can be solved numerically, taking as an initial left-hand approximation to its root the positive root of the quadratic equation corresponding to the unit right hand side.

Assuming the cross-section $\sigma(y)$ to be a smoother function compared to $\mathcal{F}(y)$, the integral in

(15) can first be evaluated over a finite interval around the maximum of $\mathcal{F}(y)$. Then, at every subsequent step one should broaden the initially chosen arbitrary integration limits until the integral value becomes close enough to the one obtained at the previous step. Thus, the required relative precision may be achieved.

3.2. Isotropically distributed projectiles and Maxwellian target.

In the case when the velocity distribution of species α is expressed by an isotropic function $F(v_\alpha)$ and the distribution of species β is Maxwellian as in (12), the rate coefficient is calculated as

$$\tilde{\mathcal{R}}_{\alpha\beta}^{(FM)} = 4\pi \int_0^{+\infty} v_\alpha^2 F(v_\alpha) \tilde{\mathcal{R}}_{\alpha\beta}^{(BM)}\left(v_\alpha, m_\beta/T\right) dv_\alpha . \quad (17)$$

The technique to compute $\tilde{\mathcal{R}}_{\alpha\beta}^{(BM)}\left(v_\alpha, m_\beta/T\right)$ is described above. The practical realization of formula (17) depends on the specific function $F(v_\alpha)$. In particular, for suprathermal ion distributions occurring due to fast neutral beam injection heating the upper integration limit in practice appears to be finite. Another characteristic case of a bell-shaped exponentially decaying integrand implies that one should step-by-step broaden the integration range around the maximum position comparing the integral values until the required relative precision is achieved.

3.3. Isothermal Maxwellian case.

This is an important particular case of 3.2 above. For two Maxwellian species α and β at thermal equilibrium $T_\alpha = T_\beta = T$ the rate coefficient is

$$\tilde{\mathcal{R}}_{\alpha\beta}^{(MM)}\left(\mu_{\alpha\beta}/T\right) = \frac{2}{\sqrt{\pi}} v_0 \gamma^{3/2} \int_0^{+\infty} \sigma(y) f(y) dy , \quad (18)$$

where the dimensionless function $f(y) = ye^{-\gamma y}$, the dimensionless variable $y = v^2/v_0^2$ and the dimensionless constant $\gamma = \frac{\mu_{\alpha\beta} v_0^2}{2T}$. The value v_0, as above, denotes the atomic velocity unit and $\mu_{\alpha\beta} = m_\alpha m_\beta/(m_\alpha + m_\beta)$ is the reduced mass. The maximum of $f(y)$ is attained at $y = 1/\gamma$. Assuming the cross-section $\sigma(y)$ to be a smoother function compared to $f(y)$, the integral in (18) can first be evaluated over a finite interval around the maximum of $f(y)$. Then, at every subsequent step one should broaden the initially chosen arbitrary integration limits until the integral value becomes close enough to the one obtained at the previous step. Thus, the required relative precision may be achieved.

4. Fast Neutral Beam Injection-Induced Suprathermal Ion Distribution

In order to describe the neutral beam injection heating-induced fast ion distribution, one can use the classical nonstationary slowing down distribution function for a delta-like fast ion source

$$S\left(v_\alpha - v_{inj}\right) = \frac{S_0}{4\pi v_\alpha^2} \frac{e^{-\frac{\left(v_\alpha - v_{inj}\right)^2}{\epsilon^2}}}{\epsilon\sqrt{\pi}} \quad (19)$$

$$F\left(v_\alpha\right) = \frac{\mathrm{K}}{v_\alpha^3 + v_c^3}\left(erf\left(\frac{v^*\left(v_\alpha, t\right) - v_{inj}}{\epsilon}\right) - erf\left(\frac{v_\alpha - v_{inj}}{\epsilon}\right)\right), \quad (20)$$

where K is a normalization constant, the slowing down time

$$\tau_s = \frac{3 m_\alpha T_e^{3/2}}{4\sqrt{2\pi} n_e Z_\alpha^2 e^4 \Lambda m_e^{1/2}}, \quad (21)$$

cube of the critical velocity

$$v_c^3 = \frac{3\sqrt{2\pi} T_e^{3/2}}{2 m_\alpha m_e^{1/2}}, \quad (22)$$

Λ is the Coulomb logarithm, and, as shown in [4],

$$v^*\left(v_\alpha, t\right) = \left(\left(v_\alpha^3 + v_c^3\right) e^{3t/\tau_s} - v_c^3\right)^{1/3} . \quad (23)$$

The normalization constant K is determined by numerical integration. The ion velocity $v_\alpha = \sqrt{2E/m_\alpha}$, v_{inj} is the injection velocity corresponding to the injection energy E_{inj}, the values S_0 and ϵ in (19) determine the source rate and peak width, respectively, and t is the time since the commencement of the fast particle source action.

5. Experimentally Obtained Suprathermal Ion Distributions

Radial and angle dependence of the ion distribution function is studied experimentally by means of passive line-integral and also active localized charge exchange

neutral particle diagnostics [5, 6]. An extensive diagnostic database of this kind should enable one to predict the local ion distribution function evolution for a given plasma discharge regime in a certain device, for a specific heating method and time diagram.

Using the diagnostic data in the form of an array of energies (E_1, …, E_N) of escaped neutral particles measured along a certain observation direction, where N is the total number of particles collected during a certain time interval, one can construct an empirical probability density function

$$f^{(K)}(E) = \frac{1}{Nh}\sum_{j=1}^{N} K\left(\frac{E-E_j}{h}\right), \quad h>0 \qquad (24)$$

with Gaussian kernel function $K(z)=e^{-z^2/2}/\sqrt{2\pi}$. The optimal kernel bandwidth h selection algorithm and the ion distribution function reconstruction are discussed in [7].

Thus, a possibility exists to perform a correct experimentally confirmed calculation of the time evolution of the local fusion rate coefficient (4) and the fusion reactor power (1). Particular MHD equilibrium data can then be used rather than analytic approximations.

6. Calculation Examples

Assuming the radial density profiles to be

$$n_{e,D,T}(\rho)=\left(n_{e,D,T}(0)-n_{e,D,T}(1)\right)\left(1-\rho^a\right)^b+n_{e,D,T}(1) \qquad (25)$$

and radial temperature profiles

$$T_{e,D,T}(\rho)=\left(T_{e,D,T}(0)-T_{e,D,T}(1)\right)\left(1-\rho^q\right)^r+T_{e,D,T}(1), \qquad (26)$$

let us introduce an additive non-Maxwellian distortion of the form (20) to the deuterium distribution so that

$$f_D(\mathbf{v}_D)=A\left(\frac{m_D}{2\pi T}\right)^{3/2} e^{-\frac{m_D v_D^2}{2T}}+(1-A)F(v_D), \qquad (27)$$

where $A\le 1$. $A=1$ corresponds to the pure undistorted Maxwellian case. The rate coefficient for the interaction of deuterium particles distributed according to (27)

$$\tilde{\mathcal{R}}_{DD}=A^2\tilde{\mathcal{R}}_{DD}^{(MM)}\left(\mu_{DD}/T\right)+2A(1-A)\tilde{\mathcal{R}}_{DD}^{(FM)} +(1-A)^2\tilde{\mathcal{R}}_{DD}^{(FF)} \qquad (28)$$

is then calculated using (17) and (18). The last term in (28) accounts for the "tail-tail" particle interaction rate. It is considered negligible because the non-Maxwellian distortion is assumed to be small, *i.e.* $(1-A)^2 \ll 1$.

In the case when deuterium component distributed according to (27) interacts with Maxwellian tritons

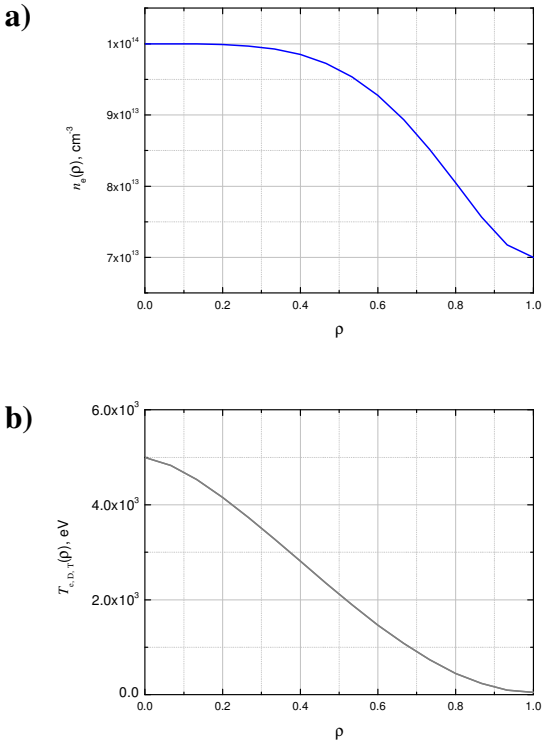

Fig. 4. a). Radial profile of deuterium and tritium density; b). Radial profile of deuterium and tritium temperature.

$$f_T(\mathbf{v}_T)=\left(\frac{m_T}{2\pi T}\right)^{3/2} e^{-\frac{m_T v_T^2}{2T}}, \qquad (29)$$

the rate coefficient is

$$\tilde{\mathcal{R}}_{DT}=A\tilde{\mathcal{R}}_{DT}^{(MM)}\left(\mu_{DT}/T\right)+(1-A)\tilde{\mathcal{R}}_{DT}^{(FM)}. \qquad (30)$$

The fusion rate radial profile and integral power calculation given below is for T(D,n)He^4 reaction. Fig. 4 a) shows the electron density profile with a = 4, b = 2, $n_e(0)=1.0\times10^{14}$ cm^{-3}, $n_e(1)=0.7\times10^{14}$ cm^{-3}. The nuclei densities are $n_D=n_T=n_e/2$. Fig. 4 b) shows the electron and ion temperature profile $T_e=T_D=T_T$ with q = 1.5, r = 2, $T_{e,D,T}(0)=5.0\times10^3$ eV, $T_{e,D,T}(1)=50$ eV.

Calculations have been performed for three variants of the deuteron velocity distribution function shown in Fig. 5, namely, for undistorted Maxwellian distribution and for the cases when there exists 2.5% or 5% population of suprathermal particles described by the classical slowing down model of beam particles with the injection energy E_{inj} = 150 keV. The non-locality, *i.e.*, the radial dependence

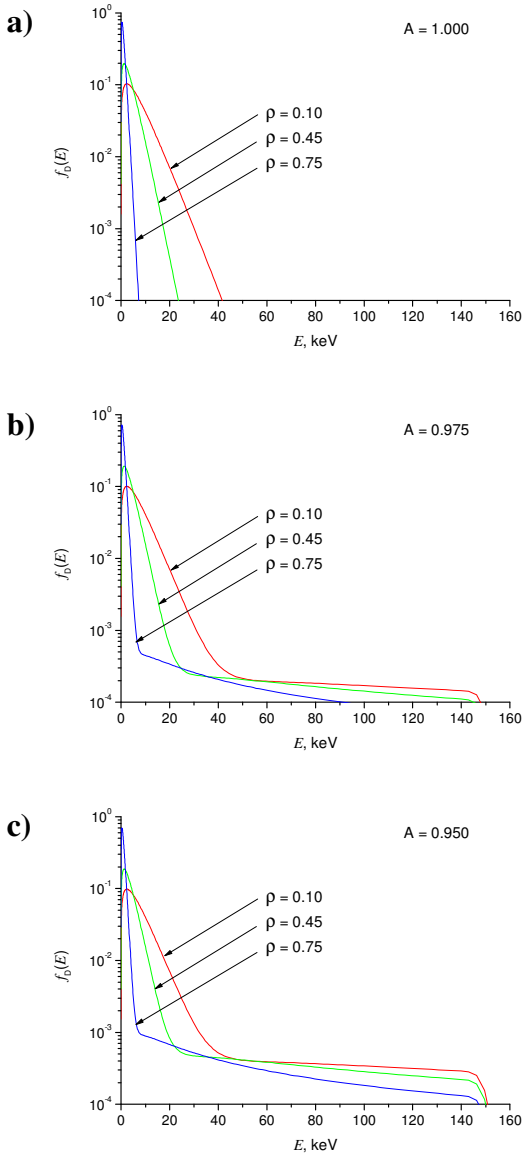

Fig. 5. Deuteron energy distribution function a) in the undistorted Maxwellian case for A = 1 and in the presence of suprathermal "tail" with b) A= 0.975 and c) A = 0.950.

of the ion distribution function in this model is due to the radial profiles of n_e and T_e, determining the slowing down time and the critical velocity values.

For each of the three variants of the distribution the radial profile of T(D,n)He^4 reaction rate has been calculated as well as the plasma volume integral power for two types of magnetic surfaces with D-shaped and elliptical poloidal cross-sections as shown in Fig. 1. Slight differences in the magnetic surface shape, as expected, have no significant direct "geometrical" influence on the power. Calculation results are shown in Fig. 6. In this example the presence of 5% suprathermal deuteron

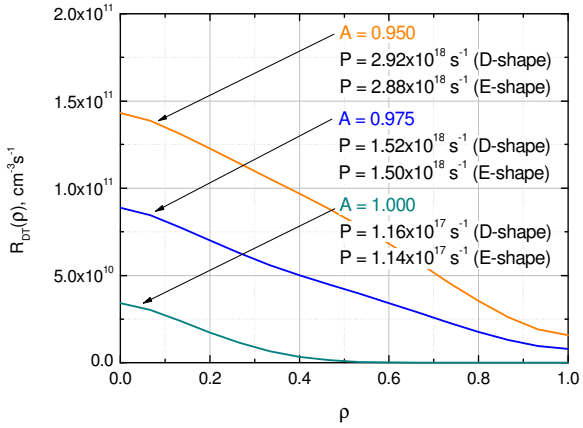

Fig. 6. Radial profiles of T(D,n)He^4 reaction rate for thermal tritons and three variants of deuteron energy distribution and the corresponding plasma volume integral power values for two types of magnetic surface geometry.

population leads to approximately 25 time increase in the fusion power compared to the pure Maxwellian case.

7. Summary

A general practical algorithm has been realized to calculate the nuclear fusion rate and power in a toroidal magnetic plasma confinement device. Volume integration is performed using analytical approximations of magnetic surfaces. A detailed description of velocity space integration technique for beam-Maxwellian, bi-Maxwellian and "isotropic function - Maxwellian" cases has been given. Fusion rate and power calculations can be done using either theoretical or experimentally obtained nuclei energy distribution functions.

A significant contribution to the nuclear fusion reaction rates comes from suprathermal ions from high-energy distribution tails. Therefore, the production and good confinement of fast ions play the essential role. Reliable experimental data and theoretical understanding of the formation of fast ion distribution tails are required.

The ion distribution function reflects the kinetic effects, the single particle confinement properties depending on the particular magnetic configuration, the finite β effects such as MHD induced fast ion losses, radial electric field effects, etc. As a method to investigate the ion component distribution function and its evolution due to the application of heating, measurements of kinetic energy distributions of neutral atoms escaping from the plasma may be used, which are often referred to as neutral particle analysis (NPA) diagnostics. Multidirectional passive measurements provide

information on the angular anisotropy, fast ion confinement, and distribution tail shapes. Line-integral energy-resolved neutral fluxes are obtained at different observation angles. Special mathematical techniques are required for the correct data analysis [5]. Another approach is to create a localized dense target for charge-exchange in the plasma. A diagnostic pellet ablation cloud can be used for this purpose (pellet charge exchange, or PCX method). Time-resolved measurements of the neutral flux from the cloud as it moves across the plasma column result in radially-resolved information on the fast particle energy distribution [6].

Smooth normalized probability density functions for the nuclei energies can then be calculated from NPA data using the method given in [7]. Thus, experimentally confirmed calculations of nuclear fusion rate and power are possible on the basis of diagnostic data.

References

[1] G.H. Miley, H. Towner, N. Ivich, Rept. COO-2218-17, University of Illinois (1974).

[2] B.H. Duane, Rept. BNWL-1685, Brookhaven National Laboratory (1972).

[3] H.-S. Bosch, G.M. Hale, Nucl. Fusion, **32**, 611 (1992).

[4] J.G. Cordey and M.J. Houghton, Nucl. Fusion, **13**, 215 (1973).

[5] P.R. Goncharov, T. Ozaki et al., Rev. Sci. Instrum., **79**, 10F311 (2008).

[6] P.R. Goncharov, T. Ozaki et al., Rev. Sci. Instrum., **79**, 10F312 (2008).

[7] P.R. Goncharov, T. Ozaki et al., Plasma and Fusion Research, **3**, S1083 (2008).

Poster Presentations 2

P2-01 - P2-65

Proceedings of ITC18, 2008

A Global Simulation Study of ICRF Heating by TASK/WM and GNET in Helical Plasmas

Tetsuya YAMAMOTO[1)], Sadayoshi MURAKAMI[1)] and Atsushi FUKUYAMA[1)]

[1)]*Department of Nuclear Engineering, Kyoto University, Kyoto 606-8501, Japan*

A global simulation code is developed to study the ICRF heating in helical plasmas combining two global simulation codes: a full wave field solver, TASK/WM, and a drift kinetic equation solver, GNET. The both codes can treat a 3-D magnetic configuration based on the MHD equilibrium by VMEC code. The developed code is applied to the ICRF minority heating in Large Helical Device (LHD). The ICRF wave propagation is solved by TASK/WM and the obtained RF electric field is used to solve the drift kinetic equation by GNET.

Keywords: ICRF heating, Simulation

1 Introduction

The ion cyclotron range of frequencies (ICRF) heating has long been considered a primary plasma heating method. The physics basis and the efficiency of ICRF heating have been confirmed by experimental, theoretical and simulation studies. However, there still remains several important issues in ICRF heating, e.g. finite orbit effect of energetic ions, current drive, toroidal flow generation, etc. In order to clarify these problems, a global simulation study which takes into account the wave-plasma interaction self-consistently is necessary.

In this paper, we study the ICRF heating in helical plasmas combining two global simulation codes: a full wave field solver TASK/WM [1] and a drift kinetic equation solver GNET [2], as a first step to develop a self-consistent simulation. The developed code is applied to the ICRF minority heating in the Large Helical Device (LHD). The realistic ICRF wave profile obtained by TASK/WM is used to solve a drift kinetic equation by GNET. The both codes can treat a 3-D magnetic configuration based on the MHD equilibrium by VMEC code.

In Sec. 2 the simulation models and codes are described and, then, simulation results are presented in Sec. 3. Finally, the obtained results are summarized in Sec. 4.

2 Simulation model

In this study we combine two simulation code to study the ICRF heating. The simulation model is illustrated in Fig. 1. First, Maxwell's equation for RF wave is solved by TASK/WM code, then the obtained RF wave electric field profile is used to solve a drift kinetic equation by GNET code. Finally, the steady state velocity distribution function of plasma is obtained.

TASK/WM code solves Maxwell's equation for RF wave electric field, $\boldsymbol{E}$, with complex frequency, ω,

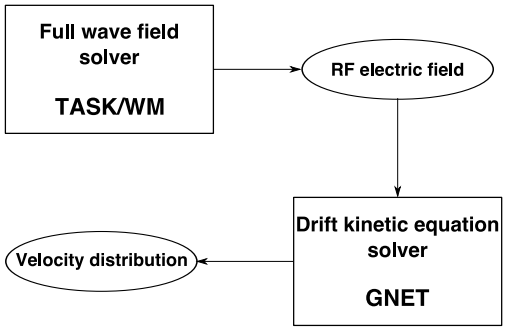

Fig. 1 The schematic diagram of simulation model

$$\nabla \times \nabla \times \boldsymbol{E} = \frac{\omega^2}{c^2} \overleftrightarrow{\epsilon} \cdot \boldsymbol{E} + i\omega\mu_0 \boldsymbol{j}_{\rm ext}, \tag{1}$$

where the external current density, $\boldsymbol{j}_{\rm ext}$ denotes the antenna current in ICRF heating, as a boundary value problem in the 3-D magnetic configuration. In the present analysis, a simple collisional cold plasma model is applied [3]. Maxwell's equation Eq. (1) is formulated by expansion to Fourier mode in poloidal and toroidal direction and finite different method in radial direction. Then the electric field is formulated as

$$\boldsymbol{E}(\psi_l, \theta, \varphi) = \sum_{mn} \boldsymbol{E}_{mn}(\psi_l) e^{i(m\theta + n\varphi)}, \tag{2}$$

where l, m, n are the radial grid number, poloidal and toroidal mode numbers, respectively.

GNET code solves a linearized drift kinetic equation for energetic ions including complicated behavior of trapped particles in 5-D phase space as

$$\frac{\partial f}{\partial t} + (\boldsymbol{v}_\parallel + \boldsymbol{v}_{\rm D}) \cdot \nabla f + \boldsymbol{a} \cdot \nabla_{\boldsymbol{v}} f - C(f) - Q_{\rm ICRF}(f) - L = S, \tag{3}$$

where $C(f)$ and $Q_{\rm ICRF}$ are the linear Coulomb collision operator and the ICRF heating term, respectively. S and L

author's e-mail: yamamoto@p-grp.nucleng.kyoto-u.ac.jp

are the particle source term by ionization of neutral particles and sink (loss) term including orbit loss and charge exchange, respectively.

In order to solve the linearized drift kinetic equation (3) by Monte Carlo method, the Green function, $\mathcal{G}$, is introduced as

$$\frac{\partial \mathcal{G}}{\partial t} + (\boldsymbol{v}_{\parallel} + \boldsymbol{v}_{\mathrm{D}}) \cdot \nabla \mathcal{G} + \boldsymbol{a} \cdot \nabla_{\boldsymbol{v}} \mathcal{G} - C(\mathcal{G}) - Q_{\mathrm{ICRF}}(\mathcal{G}) - L = 0 \tag{4}$$

with the initial condition $\mathcal{G}(\boldsymbol{x}, \boldsymbol{v}, t = 0 | \boldsymbol{x}', \boldsymbol{v}') = \delta(\boldsymbol{x} - \boldsymbol{x}')\delta(\boldsymbol{v} - \boldsymbol{v}')$. The $\mathcal{G}$ is evaluated by solving the equation of motion for guiding center of test particles expressed by the Hamiltonian of charged particle

$$H = \frac{1}{2} m v_{\parallel}^2 + \mu B(\psi, \theta, \varphi) + q\Phi(\psi) \tag{5}$$

in Boozer coordinate. In order to solve the equation of motion, 6th-order Runge-Kutta method is applied. The collisional effects are taken into account using the linear Monte Carlo collision operator [4].

The ICRF heating term is modelled by changing the perpendicular velocity of the test particle passing through the resonance layer, $\omega - k_{\parallel} v_{\parallel} = n\Omega$, by

$$\begin{aligned} \Delta v_{\perp} \approx & \left[\left(v_{\perp 0} + \frac{q}{2m} I |E_+| J_{n-1}(k_{\perp}\rho_{\mathrm{L}}) \cos\phi_{\mathrm{r}} \right)^2 \right. \\ & \left. + \frac{q^2}{4m^2} \{ I |E_+| J_{n-1}(k_{\perp}\rho_{\mathrm{L}}) \}^2 \sin^2\phi_{\mathrm{r}} \right]^{-\frac{1}{2}} - v_{\perp 0} \\ \approx & \frac{q}{2m} I |E_+| J_{n-1}(k_{\perp}\rho_{\mathrm{L}}) \cos\phi_{\mathrm{r}} \\ & + \frac{q^2}{8m^2 v_{\perp 0}} \{ I |E_+| J_{n-1}(k_{\perp}\rho_{\mathrm{L}}) \}^2 \sin^2\phi_{\mathrm{r}}, \end{aligned} \tag{6}$$

where E_+ and ϕ_{r} are the left-circularly polarized component of RF wave electric field and random phase, respectively. Also, q, m, ρ_{L}, J_n are the charge, mass, the Larmor radius of the particle and nth Bessel function, respectively. The time duration passing through the resonance layer, I, is given by the minimum value as, $I = \min(\sqrt{2\pi/n\dot{\Omega}}, 2\pi(n\ddot{\Omega})^{-1/3}\mathrm{Ai}(0))$, which corresponds to two cases; the simple passing of the resonance layer and the passing near the turning point of a trapped motion (banana tip).

In the simulation $|E_+|$ evaluated by TASK/WM is used in Eq. (6). We consider only fundamental ion cyclotron resonance. The finite larmor radius (FLR) effect, $J_{n-1}(k_{\perp}\rho_{\mathrm{L}})$ term in Eq. (6), is considered by evaluating the wave length, λ, from the electric field wave form directly as Fig. 2 and calculating the perpendicular wave vector, $k_{\perp} = 2\pi/\lambda_{\perp}$.

Assuming $B_{\varphi} \gg B_{\theta}$ for simplicity, $k_{\parallel}$ is evaluated as

$$k_{\parallel} \approx \frac{n}{R}, \tag{7}$$

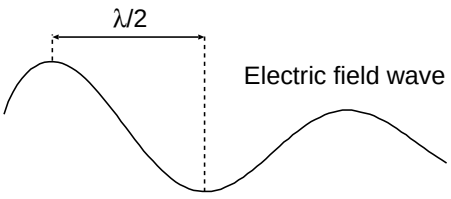

Fig. 2 Evaluation of wave length, λ, from electric field wave

where n is the toroidal mode number in Eq. (2) and R is the major radius.

Finally the velocity distribution function is calculated by integrating the particle in the phase space over initial position $(\boldsymbol{x}', \boldsymbol{v}')$ and initial time t' as

$$f(\boldsymbol{x}, \boldsymbol{v}, t) = \int_0^t dt' \int d\boldsymbol{x}' \int d\boldsymbol{v}' S\, \mathcal{G}(\boldsymbol{x}, \boldsymbol{v}, t - t' | \boldsymbol{x}', \boldsymbol{v}'). \tag{8}$$

3 Simulation results

We study the ICRF minority heating using the developed code in the helical plasma (LHD). The poloidal cross sections of the MHD equilibrium by VMEC code are shown in Fig. 3. The assumed plasma parameters are listed in Table 1. We assume deuterium (D) as a majority ion and hydrogen (H) as a minority ion.

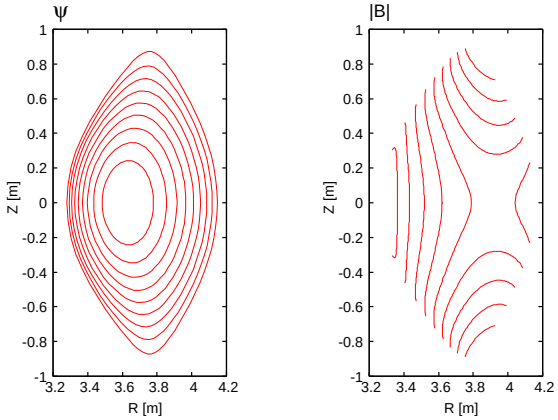

Fig. 3 Equilibrium data by VMEC and NEWBOZ, Contour plots of magnetic flux ψ (left) and absolute value of magnetic field (right) on a poloidal cross section

Table 1 Parameters of helical plasma (LHD)

Plasma major radius	R_0	3.6 m
Plasma minor radius	a	0.58 m
Magnetic field at magnetic axis	B_0	2.75 T
Temperature at magnetic axis	T_0	3.0 keV
Temperature on plasma boundary	T_s	0.3 keV
Density at magnetic axis	n_0	$0.7 \times 10^{20}/\mathrm{m}^3$
Density on plasma boundary	n_s	$0.07 \times 10^{20}/\mathrm{m}^3$
Antenna current density	j_{ext}	1.0 A/m
Wave frequency	f_{RF}	38.5, 40.0 MHz
Minority ion ratio	H/D+H	5 %
Collisionality	ν_s	0.003

We first analyze the ICRF wave propagation and absorption in the plasma by TASK/WM. Fig. 4 shows contour plots of the real part of left circularly polarized component of the RF electric field, Re E_+ (left) and the power absorption (right) on the poloidal cross section in the case of the ICRF wave frequency $f_{\mathrm{RF}} = 40.0$ MHz (on axis heating). Fig. 5 are the same manner in the case of $f_{\mathrm{RF}} = 38.5$ MHz (off axis heating). The ICRF waves are exited in the plasma from the antenna set on the outer side of the torus (right side). In the both cases, the Re E_+ component of the wave is absorbed by the plasma and the wave amplitude is damped near the minority ion cyclotron resonance layer (the minority ion cyclotron resonance layers are drawn as green lines in the left figure of Fig. 4 and 5). Then the amplitude is damped further near the two-ion-hybrid cutoff and resonance layers.

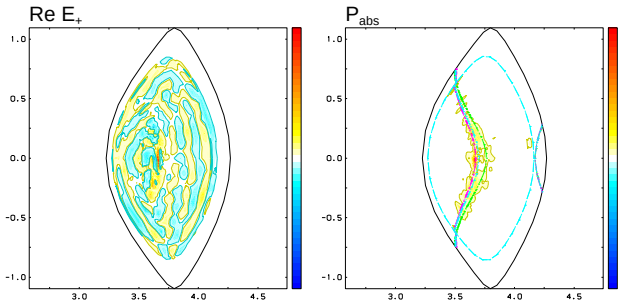

Fig. 4 Contour plots of Re E_+ (left) and P_{abs} (right) on the poloidal cross section in the case of $f_{\mathrm{RF}} = 40.0$ MHz.

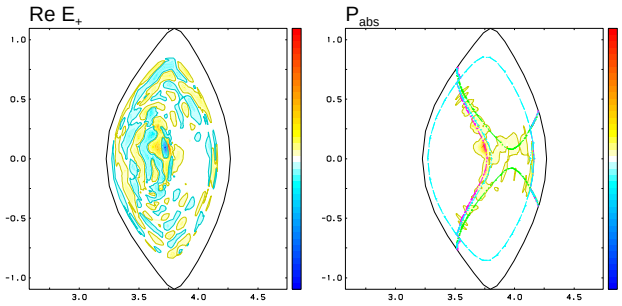

Fig. 5 Contour plots of Re E_+ (left) and P_{abs} (right) on the poloidal cross section in the case of $f_{\mathrm{RF}} = 38.5$ MHz

Next, we analyze the evolution of velocity distribution function of minority ions and the plasma heating efficiency by GNET. The RF electric field profile obtained by TASK/WM is used to accelerate the minority ions following Eq. (6). The $k_\perp$ is directly calculated from electric field waves by the method illustrated in Fig. 2. The $k_\perp$ and the $|E_+|$ are shown in Fig. 6. The same plasma parameters are

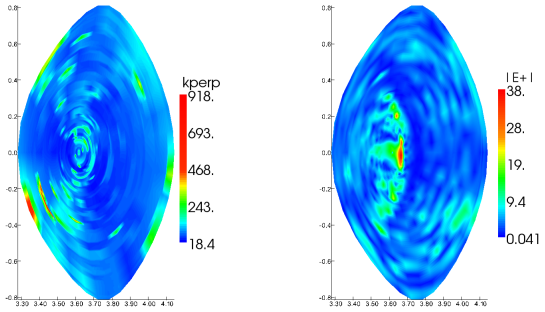

Fig. 6 $k_\perp$ (left) and $|E_+|$ (right) in the case of $f_{\mathrm{RF}} = 40.0$ MHz

assumed as in the TASK/WM calculation. The test particle orbits are followed for about 0.6 s to obtain the steady state of the distribution function.

The velocity distribution functions of minority ions are shown in Fig. 7 ($f_{\mathrm{RF}} = 40.0$ MHz) and 8 ($f_{\mathrm{RF}} = 38.5$ MHz). Fig. 7 are contour plots of the velocity distribution averaged on the flux surface between ρ ($= \sqrt{\psi/\psi_a}$) = 0.0 and 0.10 (left upper), $\rho = 0.31$ and 0.41 (right upper), and $\rho = 0.45$ and 0.55 (left lower), $\rho = 0.66$ and 0.76 (right lower) with $f_{\mathrm{RF}} = 40.0$ MHz. Fig. 8 shows in the same manner of Fig. 7 in the case of $f_{\mathrm{RF}} = 38.5$ MHz.

Figure 9 shows the radial profile of the ICRF wave

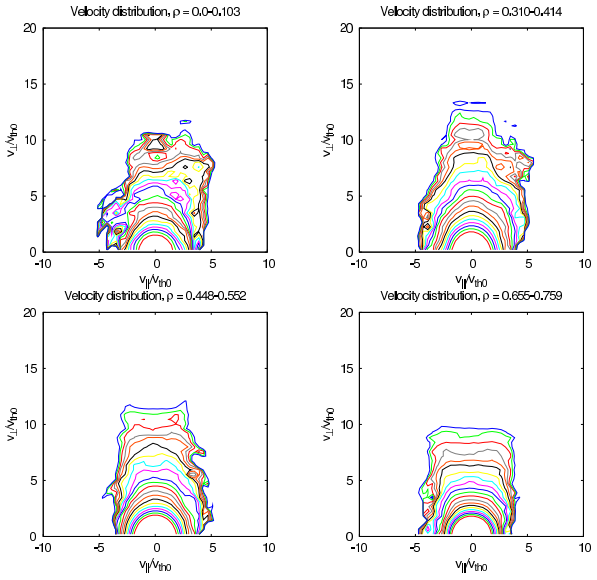

Fig. 7 Velocity distribution averaged in each radial ρ interval ($f_{\mathrm{RF}} = 40.0$ MHz)

power absorbed by minority ions in the case of $f_{\mathrm{RF}} = 40.0$ MHz (red line) and $f_{\mathrm{RF}} = 38.5$ MHz (green line). We can see that the radial profile of the absorbed ICRF

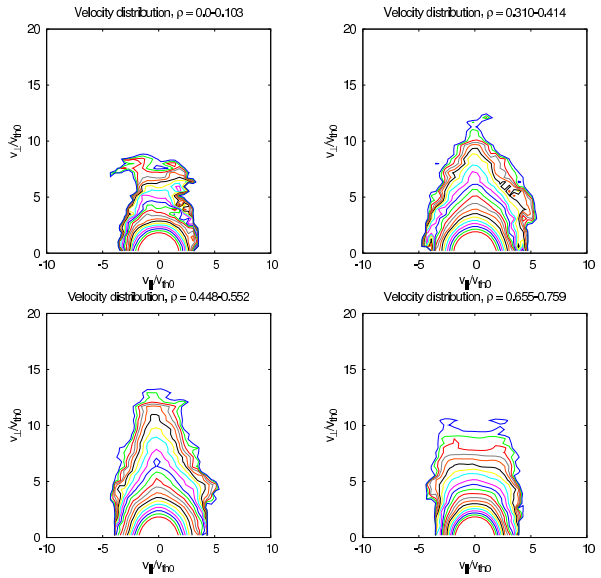

Fig. 8 Velocity distribution averaged in each radial ρ interval (f_{RF} = 38.5 MHz)

wave power depends on f_{RF} and peaks at a specific radial position. The ICRF wave power absorbed by minor-

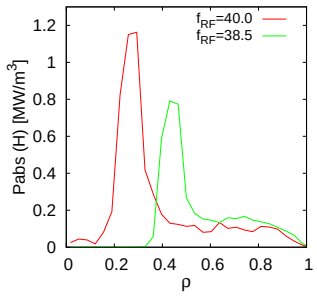

Fig. 9 Power profile absorbed by minority ions (H) in the case of f_{RF} = 40.0 MHz (red line) and f_{RF} = 38.5 MHz (green line)

ity ions is transferred to the background ions and electrons through particle collisions. The heating power profiles of background ions, P_{dep} (D), and electrons, P_{dep} (e), are shown in Fig. 10. Although the both P_{dep} (D) and P_{dep} (e) slightly peak at the same radial point, the profile of them are broader compared to that of P_{abs} (H). The heating efficiencies (Total heating power/Total power absorption) are 0.697 (f_{RF} = 40.0 MHz) and 0.396 (f_{RF} = 38.5 MHz), respectively.

4 Conclusion

We have carried out a global simulation of ICRF heating in the helical plasma (LHD) combining the full wave field solver (TASK/WM) and the drift kinetic equation solver (GNET). The realistic ICRF wave profile have been obtained by TASK/WM and been used to solve a drift kinetic

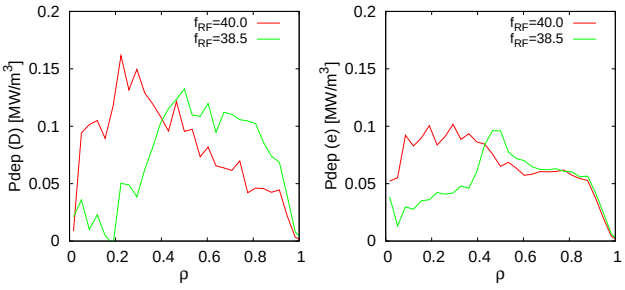

Fig. 10 Heating power profile of background ion (left) and electron (right) in the case of f_{RF} = 40.0 MHz (red line) and f_{RF} = 38.5 MHz (green line)

equation in the GNET. The wave number $k_{\perp}$ profile has been directly evaluated from the wave form.

The characteristics of the ICRF minority heating in the LHD have been shown.

[1] A. Fukuyama and T. Akutsu, *Proc. 19th Int. Conf. Fusion Energy 2002*, THP3-14.
[2] S. Murakami *et al.*, Nucl. Fusion **46** (2006) S425.
[3] T. Yamamoto, S. Murakami and A. Fukuyama, Plasma and Fusion Research **3** (2008) S1075.
[4] Boozer A.H. and Kuo-Petravic G., Phys. Fluids **24** (1981) 851.

Proceedings of ITC18, 2008

Analysis of Propagating Mode Contents in the Corrugated Waveguides of ECH System for Precise Alignment

Takashi SHIMOZUMA[1)], Hiroshi IDEI[2)], Michael A. SHAPIRO[3)], Richard J. TEMKIN[3)], Shin KUBO[1)], Hiroe IGAMI[1)], Yasuo YOSHIMURA[1)], Hiromi TAKAHASHI[1)], Satoshi ITO[1)], Sakuji KOBAYASHI[1)], Yoshinori MIZUNO[1)], Yasuyuki TAKITA[1)] and Takashi MUTOH[1)]

[1)] *National Institute for Fusion Science, 322-6 Oroshi-cho, Toki 509-5292, Japan*
[2)] *Research Institute for Applied Mechanics Kyushu University, Kasuga, Fukuoka 816-8580, Japan*
[3)] *Plasma Science and Fusion Center Massachusetts Institute of Technology, Cambridge, MA02139, USA*

A new method is proposed to analyze mode contents of high power electromagnetic waves that are propagating through corrugated waveguides in the electron cyclotron resonance heating (ECH) system for nuclear fusion devices. The method was applied to a 168GHz transmission line of the ECH system in Large Helical Device (LHD) to evaluate the waveguide alignment. Mode contents of the propagating wave could be well analyzed using this method. Furthermore, the wave field in the waveguide was reconstructed using the obtained information of the each mode content.

Keywords: ECH, gyrotron, corrugated waveguide, mode analysis, phase retrieval

1 Introduction

Electron Cyclotron resonance Heating (ECH) is one of the most powerful heating methods for plasma heating and current drive in fusion-oriented plasma devices. The high power millimeter-waves for ECH are usually transmitted by over-sized circular corrugated waveguides. The length of such transmission lines becomes longer and longer due to the huge size of plasma confinement devices. In the over-sized corrugated waveguides, tilt and offset of the waveguide axis easily cause conversion of the transmitted mode of HE_{11} to unwanted modes. Improvement of transmission efficiency is essential in view not only of increase of usable power but reduction of heat load to the millimeter-wave components by Ohmic loss. For example, to suppress a mode conversion loss $< 1\%$, tilt angle and offset of the beam center should be less than 0.1 deg. and 2.9mm, respectively, for the 168GHz transmission through the corrugated waveguide 88.9mm in diameter [1]. We already proposed an alignment method of transmission lines based on infrared (IR) images on a target irradiated by high power millimeter-waves [2].

As a next step, it is important to identify propagating mode contents in the corrugated waveguides for clarifying what kind of misalignment induces such mode conversion. One method of the mode-content analysis has been already proposed by using the irradiant waveguide modes [3]. We will report another method of mode-content analysis and reconstruction of the wave field in the corrugated waveguide. Figure 1 illustrates a flow chart of the mode-content analysis. At first, a target plate, which is set several tens centimeter away from the open edge of the corrugated waveguide, is irradiated by a high power millimeter-wave. The temperature rise of the target plate is measured by IR camera precisely for several target positions. Next, the phase information is retrieved by the phase retrieval method [4]. In parallel with this, the first and second moments of the radiation pattern are calculated to evaluate the position of the power center and the waist size of the beam. Once the information of the amplitude and phase at the exit of the waveguide is determined, mode contents can be analyzed by orthogonal-mode expansion in the corrugated waveguide. Finally, the electric field in the waveguide can be reconstructed up to its entrance using the obtained mode contents and the phase factor of each constituent mode.

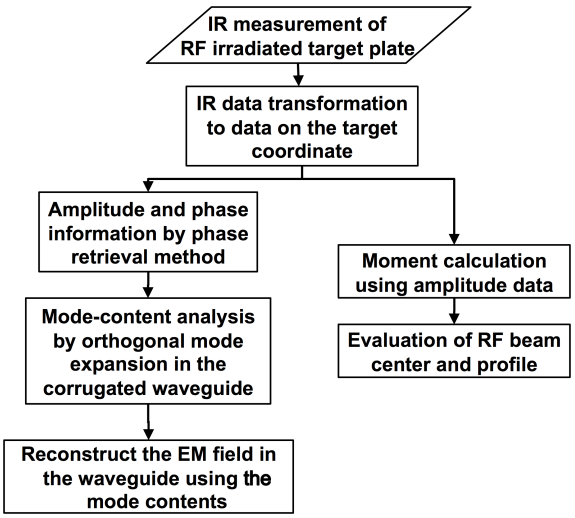

Fig. 1 A flow chart of the mode-content analysis and electric field reconstruction in the corrugated waveguide.

This paper is organized as follows. In Sec. 2, the

author's e-mail: shimozuma.takashi@LHD.nifs.ac.jp

method of mode-content analysis is described, and the results of its application to a 168GHz transmission line in LHD ECH system are given. In Sec. 3, a method and calculated results of the electric field reconstruction in the corrugated waveguide are described using the information of analyzed mode contents in Sec. 2, Finally, Section 4 will be devoted to a conclusion.

2 Method and Results of Mode-Content Analysis

In the process of designing phase correcting mirrors and performing waveguide alignment, the phase retrieval method was successfully used to reconstruct the phase information of the radiated waves using only measured intensity profiles at several positions [4]. By using the phase retrieval method, we can find the complex amplitude at radiating edge of the corrugated waveguide. It can be decomposed by the eigen modes in the corrugated waveguide. The expansion coefficients by the eigen modes give the mode contents of the corresponding eigen modes.

At the waveguide exit (z=0), the phase can be retrieved by the phase retrieval method. Such amplitude $A(x, y, 0)$ and phase $\varphi(x, y, 0)$ can be expanded by the orthogonal functions in the waveguide as,

$$A(x, y, 0)e^{j\varphi(x,y,0)} = \sum_{n=1}^{N} C_n e^{j\varphi_n} \phi_n(x, y) \tag{1}$$

, where C_n is the amplitude and φ_n is the phase of a mode n. On the contrary, the expansion coefficients are represented by

$$C_n e^{j\varphi_n} = \frac{\int_S A(x, y, 0)e^{j\varphi(x,y,0)} \cdot \phi_n^*(x, y)ds}{\int_S |\phi_n(x, y)|^2 ds}. \tag{2}$$

So, a fraction of the mode n, p_n, is calculated as,

$$p_n = \frac{|C_n|^2 \cdot \int_s |\phi_n|^2 ds}{\int_S |A|^2 ds} = \frac{|\int_S A(x, y, 0)e^{j\varphi(x,y,0)} \cdot \phi_n^* ds|^2}{\int_S |\phi_n|^2 ds \cdot \int_S |A|^2 ds}. \tag{3}$$

The eigen functions in an over-sized corrugated waveguide with the radius of a are approximately given by [5]

$$\phi_{n,m}^{even} = J_{n-1}(X_{n-1,m}\frac{r}{a}) \cdot \cos(n-1)\phi$$

$$\text{for } n, m = 1, 2, \cdots$$

$$\phi_{n,m}^{odd} = J_{n-1}(X_{n-1,m}\frac{r}{a}) \cdot \sin(n-1)\phi \tag{4}$$

$$\text{for } n = 2, 3, \cdots, m = 1, 2, \cdots$$

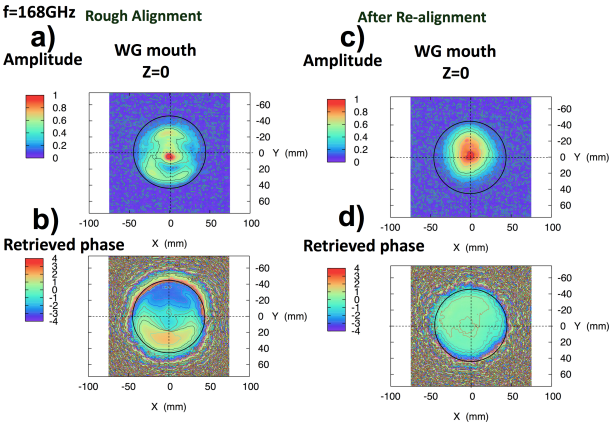

Fig. 2 Measured amplitude and retrieved phase at the radiating edge of the corrugated waveguide. The amplitude in a) and phase profile in b) for the rough alignment case. The amplitude in c) and phase profile in d) for the case after realignment.

Here, $X_{n-1,m}$ are m-th roots of Bessel function $J_{n-1}(X_{n-1,m}) = 0$ and $r = \sqrt{x^2 + y^2}, \phi = \tan^{-1}(y/x)$.

This method was applied to the 168GHz transmission line in the ECH system of LHD. Figure 2 shows measured amplitude and retrieved phase at the radiating edge of the circular corrugated waveguide. Figs. a) and b) correspond to the amplitude and phase profiles for the rough alignment case, respectively. Figs. c) and d) are the amplitude and phase profiles for the case after realignment of the waveguide. In the rough alignment case, the intensity pattern breaks into several peaks and the phase in the lower part is reverse to that in the upper part on the waveguide cross section. After realignment, the intensity profile was improved to be a Gaussian-like one and the phase distribution was almost constant.

These data were used for mode-content analyses. Figure 3 shows the analyzed mode contents of both cases in Fig. 2 for the orthogonal even- and odd-modes in the corrugated waveguide. In the rough alignment case, HE_{11} main propagating mode is only 13%. The major component is HE_{21} odd mode, which stems from the profile asymmetry with respect to x-axis as shown in Fig. 2 a) and b). HE_{12} mode of 18.5% is caused by a part of off-axis components in the amplitude profile. In the case after realignment, HE_{11} main propagating mode is recovered to dominate 89% and the other unwanted modes are HE_{21}/1.1%, HE_{12}/0.9% (even-mode) and HE_{21}/5.4% (odd-mode). The small fraction of HE_{21} odd mode attributes to the small offset of the intensity center from the waveguide axis in y-direction.

3 Field Reconstruction

On the contrary, the electromagnetic field at the arbitrary position, z, in the waveguide can be reconstructed by using the expansion coefficients of each eigen mode, $C_n e^{j\varphi_n}$, and

a) Rough Alignment Case

Mode	Even (%)	Odd (%)
HE11	**13.289**	**-**
HE12	**18.499**	-
HE13	0.337	-
HE14	0.584	-
HE15	0.173	-
HE21	0.440	**35.709**
HE22	0.213	**5.897**
HE23	0.020	0.451
HE24	0.064	0.986
HE25	0.022	0.218
HE31	**13.741**	0.723
HE41	0.465	**2.542**

b) After Re-alignment Case

Mode	Even (%)	Odd (%)
HE11	**88.841**	**-**
HE12	**0.910**	-
HE13	0158	-
HE14	0.118	-
HE15	0.161	-
HE21	**1.149**	**5.357**
HE22	0.140	**0.684**
HE23	0.079	0.131
HE24	0.012	0.086
HE25	0.036	0.177
HE31	**0.432**	0.048
HE41	0.147	0.021

Fig. 3 Results of mode-content analysis for even and odd modes in the corrugated waveguide.

propagation phase factor, $e^{(-j\beta_n z)}$, where β_n is a propagation constant of the mode n in the z-direction.

The amplitude and phase at the arbitrary z position in the corrugated waveguide are generally represented as follows,

$$A(x,y,z)e^{j\varphi(x,y,z)} = A_r(x,y,z) + jA_i(x,y,z) \quad (5)$$

$$= \sum_{n=1}^{N} C_n e^{j\varphi_n} \phi_n(x,y) \exp(-j\beta_n z) \quad (6)$$

, where

$$\beta_n = \sqrt{k^2 - \left(\frac{X_n}{a}\right)^2} \quad (7)$$

$$k = \frac{\omega}{c} = \frac{2\pi}{\lambda} \quad (8)$$

ω and λ are the angular frequency and wave length of a propagating wave, respectively. c is the speed of light. Finally the real and imaginary parts of the wave field, A_r and A_i, are expressed as follows,

$$A_r(x,y,z) = \sum_{n=1}^{N} \{C_n \cos\varphi_n \cos(\beta_n z) + C_n \sin\varphi_n \sin(\beta_n z)\}\phi_n(x,y) \quad (9)$$

$$A_i(x,y,z) = \sum_{n=1}^{N} \{-C_n \cos\varphi_n \sin(\beta_n z) + C_n \sin\varphi_n \cos(\beta_n z)\}\phi_n(x,y) \quad (10)$$

Figure 4 a) shows the intensity and phase profiles of the reconstructed field for the rough alignment case at several positions (z=0, -1.6m and -3.2m) as indicated in the illustration. The positions of z =-3.2m and z=0 correspond to the entrance and exit of a corrugated waveguide under test, respectively. In general, the n-th moment in the x-direction weighted by the intensity $A(x,y,z)^2$ can be defined as,

$$< x^n > (z) = \int x^n A^2(x,y,z)\mathrm{d}x\mathrm{d}y / \int A^2(x,y,z)\mathrm{d}x\mathrm{d}y \quad (11)$$

As a representative of the power density center, the first moment was calculated. The results are shown in Fig. 4 b). Since the beat wavelength between HE_{11} and HE_{21} (odd-mode), which is the most dominant mode among the unwanted modes, is about 9.8m, this results in a periodic change of the first moment $< y >$ of which period corresponds to about a beat wavelength. In x-direction, the non-axisymmetric unwanted even-mode of HE_{21} affects the value of $< x >$ and shows the same periodic change. Because HE_{12} is an axisymmetric mode, the first moment calculation is not affected by this mode.

Figure 5 a) shows the same intensity and phase profiles of the reconstructed field for the case after realignment. The peak position in the amplitude profile moves slightly in y-direction. This is due to the existence of the same dominant mode, HE_{21} (odd-mode). The phase pattern, however, keeps almost uniform along the waveguide axis. The first moment of the intensity profile are shown in Fig. 5 b). The changes of $< x >$ and $< y >$ show the same periodic change, and their periods correspond to the beat wave length between HE_{11} and HE_{21} (odd-mode). Although the center of intensity locates around the waveguide axis at the entrance, the calculated phase indicates an little inclined phase profile in the y-direction, which is about 0.3 degree. This caused a generation of the dominant unwanted mode of HE_{21} (odd-mode).

4 Conclusion

Mode contents of high power electromagnetic waves that are propagating through corrugated waveguide in ECH

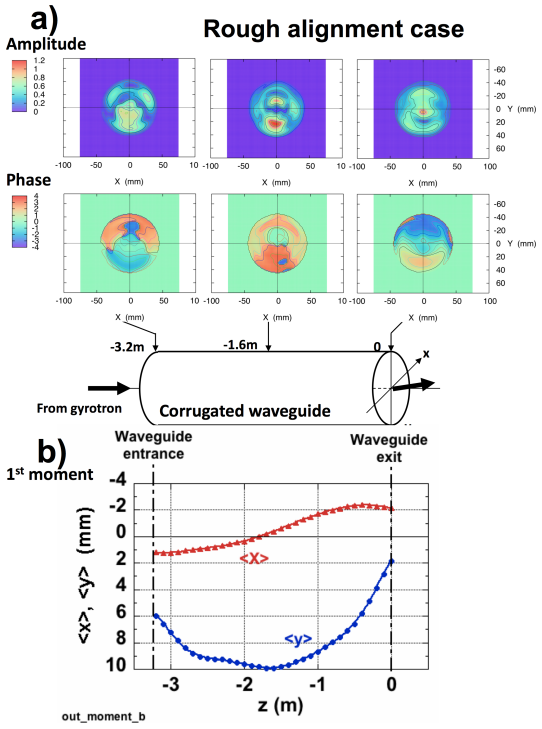

Fig. 4 For the rough alignment case, a) contour plot of amplitude and phase of reconstructed electric field at several positions (z=0, -1.6m and -3.2m) in the corrugated waveguide and b) the first moment calculation for x- and y- direction are given.

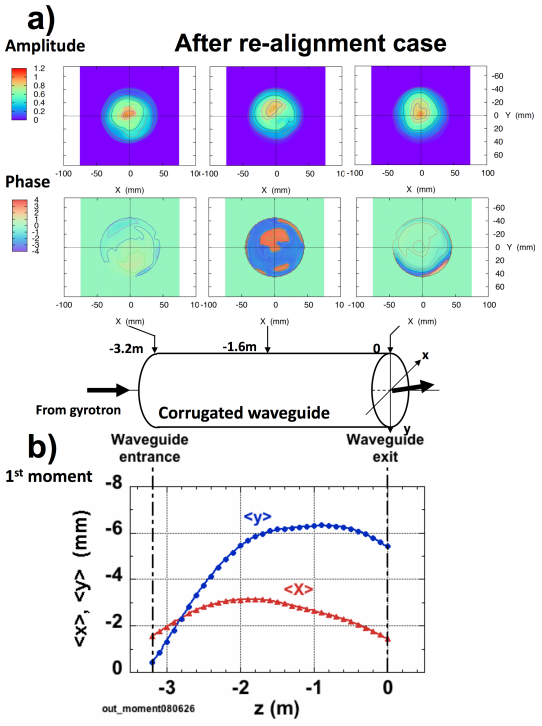

Fig. 5 For the case after re-alignment, a) contour plot of amplitude and phase of reconstructed electric field at several positions (z=0, -1.6m and -3.2m) in the corrugated waveguide and b) the first moment calculation for x- and y- direction are given.

system could be well analyzed using retrieved phase information, and the wave field in the waveguide was reconstructed on the basis of the complex amplitude of each eigen mode. The advantage of this method is that the used data are measured in the same configuration as the actual transmission system and as the same high power level. The obtained results can be useful to analyze the possible cause of degradation of transmission efficiency.

Two cases of the rough alignment and after realignment of the wave coupling were analyzed using this method as examples. The results of mode-content analysis clearly give the cause of misalignment between the incident beam axis and the waveguide axis. Subsequent field reconstruction in the waveguide gives the change of the field propagating through the waveguide and an unobservable phase information of the incident wave at the waveguide entrance. In special, the phase information at the waveguide entrance gives a good guidance for alignment. It was found that a burn-pattern measurement at two positions was insufficient for the beam alignment, because the center of measurable intensity distribution changes with a period of beat wavelength between the related modes. This suggest that burn-pattern measurement should be performed at several positions, quarter beat wave length between the main mode and unwanted modes, in special.

Acknowledgment

The authors gratefully acknowledge Professors A. Komori, S. Sudo and O. Motojima for their continuous guidance and encouragement. This work has been supported by NIFS under NIFS08ULRR501, 502, 503, and was partly performed under the collaboration organized by NIFS(NIFS08KCRR004). This work was also supported by Grant-in-Aid for Scientific Research from Ministry of Education, Science and Culture of Japan (19560051).

References

[1] K. Ohkubo, S. Kubo, H. Idei, M. Sato, T. Shimozuma and Y. Takita, Int. J. Infrared and Millim. Waves **18**, 23–41(1997).

[2] T. Shimozuma, H. Idei, M. A. Shapiro, R. J. Temkin et al., J. of Plasma and Fusion Research Vol.81, No.3, 2005, pp191-196.

[3] H.Idei, M. A. Shapiro, R. J. Temkin, T. Shimozuma and S. Kubo, Proc. of the 32nd Int. Conf, on Infrared and Millimeter waves, p67-68, MonA3-3 (2007).

[4] M. A. Shapiro, T. S. Chu, D. R. Denison et al., Fusion Eng. and Design, Vol. 53, 2001, pp537-544.

[5] N. L. Aleksandrov, A. V. Chirkov, G. G. Denisov and S. V. Kuzikov, Int. J. of Infrared and Millim. Waves, Vol. 18, No. 8, 1997, pp1505-1516.

Proceedings of ITC18,2008

Active steering system for the Neutral Beam Injector for ITER

Marco Cavenago[a], Gianluigi Serianni, Vanni Antoni, Nicola Pilan, Pierluigi Zaccaria

Consorzio RFX, EURATOM-ENEA Association, Corso Stati Uniti 4, I-35127 Padova, Italy

[a]*Laboratori Nazionali di Legnaro-Istituto Nazionale di Fisica Nucleare (LNL-INFN), Viale dell'Università 2, 35020 Legnaro (PD), Italy*

ITER requires an additional power injection of 33 MW from neutral beams, which can be provided by two injectors, delivering 16.5 MW each, having an ion current of 40 A and an accelerating voltage of 1 MV.

The requirement of on-axis and off-axis injection into ITER is presently accomplished by mechanical tilting of the injector source. To preserve the integrity of the beam line components, on the horizontal plane, very tight misalignment is tolerable (±3 mrad); such accuracy requires precise installation of the components. Breaking the vacuum and executing a long series of operations is required to provide proper beam alignment. It would be helpful if such alignments could be performed remotely.

A study has been conducted on the possibility of steering the negative ions by suitable magnetic fields, generated by dedicated coils located at the exit of the accelerator. It results that the magnetic system can meet the requirements in terms of beam alignment. The steering system will heavily affect the trajectory of the electrons extracted from the accelerator and can be used to deflect the electrons onto suitable dump plates.

The system can steer the ions and dump the electrons in a controlled way, even in case of modulation of the acceleration voltage; a flexible beam aiming system can be used to adapt the power deposition profile in ITER to the plasma characteristics; active steering can provide a suitable way to control the power deposition with respect to the possibility of exciting Alfvén eigenmodes, which can reduce the performances of ITER plasmas.

The present contribution reviews the preliminary design of the active steering system and provides an analysis of advantages and disadvantages.

Keywords: ITER, heating and current drive, plasma instabilities, beam steering, heat loads

1. Introduction

Depending on the operating scenario, ITER requires an additional power up to 33 MW from neutral beam injection; such power can be provided by two injectors, each one delivering 16.5 MW; the ion current should be 40 A and the accelerating voltage 1 MV [1]; this high particle energy implies the use of negative ions based on consideration of neutralisation efficiency [2].

It is required that the design allows both on-axis and off-axis injection into ITER; presently this is accomplished by mechanical tilting of the injector source. At the same time, on the horizontal plane, very tight misalignment is tolerable (±3 mrad), to preserve the integrity of the beam line components; such accuracy must be obtained by precise installation of the components.

Modifications of the alignment using these systems require breaking the vacuum and executing a long series of operations. Consequently it would be helpful if such alignments could be performed remotely.

Active aiming would allow to modify the power deposition profile in ITER according to the characteristics of the plasma; active steering can provide a suitable way to control the power deposition with respect to the possibility of exciting Alfvén eigenmodes, which can reduce the performances of ITER plasmas [3].

A study has been conducted on the possibility of steering the negative ions by magnetic fields, generated by suitable coils located at the exit of the accelerator.

As a by-product, the steering system would heavily affect the electron trajectories outside of the accelerator and deflect the electrons onto suitable dump plates.

Advantages of this system are the possibility of steering the ions and dumping the electrons in a controlled way, even in case of modulation of the acceleration voltage; aiming of the ions is provided without the need of moveable parts in vacuum and of flexible connections.

The present paper reviews the preliminary design of an active steering system for ITER and describes the numerical tools developed to give the main specifications; finally advantages and disadvantages are analysed.

2. Operating principle

The principle of operation of an active steerer is illustrated in Fig. 1: the negative ions emitted from the accelerator are deflected by the magnetic field produced by suitable coils. Two sets of coils are required to provide

author's e-mail: gianluigi.serianni@igi.cnr.it

vertical and horizontal steering. Since the effect of magnetic fields on electrons is larger than on ions, the system can be used to deflect the co-accelerated electrons and a suitable dump plate must be provided.

Two schemes are proposed for the system: a single steerer can be used to deflect the ions; the electrons leaving the accelerator are also deflected and are intercepted by the electron dump. The advantages of such a system are: little space required for magnetic field coils and simplicity of use; moreover, monopolar power supplies are required. The drawback is that the electron deflection is related to the deflection of negative ions; therefore the position of the panels intercepting the electrons requires a careful study, to comply with the requirements of beam steering in two directions. In this case the beam source is tilted and the steerer must recover the ion deflection at any time.

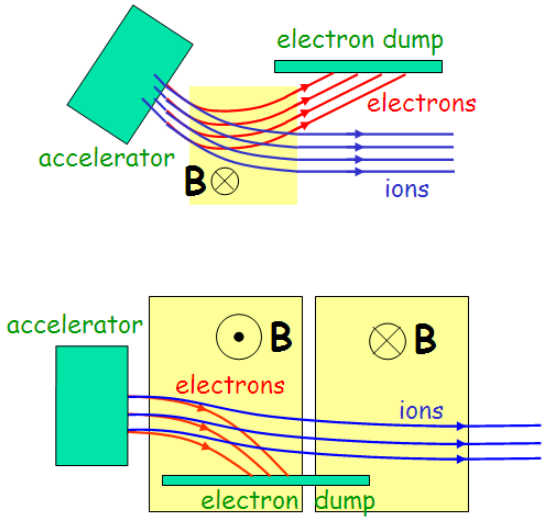

Fig.1 Operation of active steerers: in a single-stage steerer (top), electron and ion deflections are linked; ions are deflected separately from electrons in double-stage systems (bottom).

In the case of the double-stage steerer the magnetic field of the first stage filters the electrons, deflecting them towards the electron dump; the second stage compensates for the deflection undergone by the beam trajectory and gives the required deflection of negative ions. This solution allows to decouple electron dumping from beam steering, as the two sets of coils serve different purposes.

In both schemes an iron yoke is necessary, to prevent the steerer magnetic field from penetrating the acceleration region. It is worth noting that the iron yoke acts also as a protection for the cryopump panels, by intercepting the radiation emitted at the electron dump plates.

3. Numerical tools

Several numerical tools have been developed in the COMSOL Multiphysics environment [4] to investigate the performances of a steerer and to support its design.

To analyse the main features of the system, the paraxial approximation is adopted, according to which the sine of an angle can be approximated by the angle itself: $\sin\vartheta \approx \vartheta$.

So conservation of energy and Larmor radius for a particle of mass m_o and charge q_p in an accelareting voltage V read:

$$q_p V = m_o c^2(\gamma - 1) \qquad R_L = \frac{\gamma m_o v}{q_p B} \tag{1}$$

which give the particle deflection:

$$\Delta\vartheta = \frac{c\ q_p \int B_x \,\mathrm{d}z}{(q_o^2 V_p^2 + 2 m_o c^2 q_p V_p)^{1/2}} \tag{2}$$

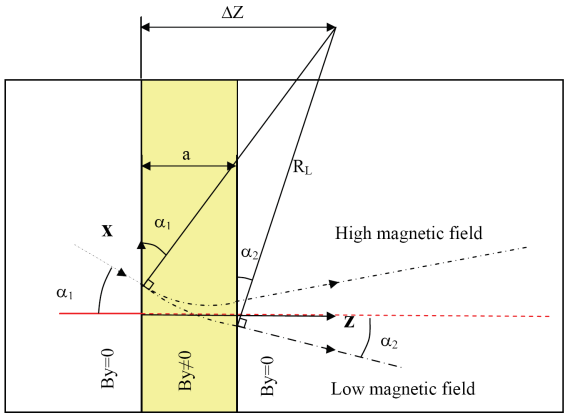

Fig.2 Ion trajectories for a single-stage steerer corresponding to minimum and maximum required deflections.

Eq. 2 shows that the deflection depends on the particle energy and on the integral of the magnetic field along the particle path. Hence uniformity of the deflection does not require uniformity of the magnetic field but uniformity of the integral of the magnetic field along the particle path: particles can have the same deflection after experiencing different magnetic fields along their paths.

The integral of the magnetic field along the particle path is intrinsically a two-dimensional quantity. This opens the possibility of increasing the spatial resolution of numerical estimates of the deflection, without resorting to huge numbers of degrees of freedom [5]. As a matter of fact the analysis of the magnetic configuration has been realised in COMSOL, using the *emqav* application module; likewise COMSOL has been used to compute the particle trajectories and to model the magnetic field coils [6].

A numerical method has been realised also to estimate the power deposited on material surfaces [6]. Specifically each beamlet is subdivided into several small areas and the corresponding contribution to the particle flux is computed. By following the particle motion, each of the beamlet subdivisions is mapped onto its final position and the

numerical estimation of the Jacobian of the transformation allows the computation of the initial-to-final ratio of the beamlet surface, giving a sort of intensifying factor for the heat flux. Since the energy of the beamlet is known, this procedure provides a local estimate of the heat flux.

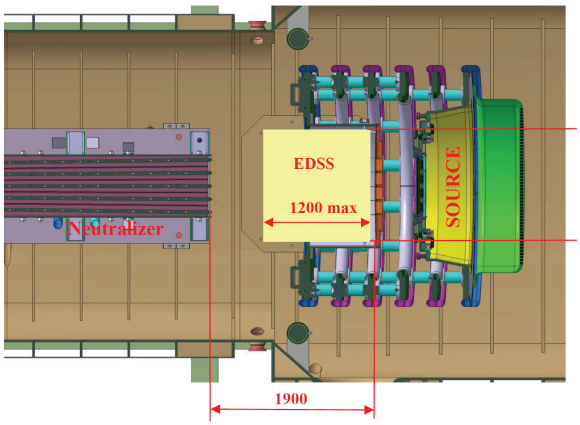

Fig.3 Proposed location of a steerer in ITER NBI.

4. Application to ITER

The feasibility of a steering system for ITER has been investigated [7]. The following requirements in terms of particle deflection have been assumed: ±3 mrad on the horizontal plane and ±14 mrad on the vertical plane.

The system has been located just downstream of the grounded grid (Fig. 3). In the vertical direction all the available space has been used; along the beam axis however, the necessity of pumping away the gas exiting the grounded grid limits the axial extension of the steerer. Due to the large difference between the vertical and the horizontal width of the beam at the exit of the accelerator, it seems better to install vertical electron dump plates. It is assumed that the plates extend 0.6 m in the axial direction.

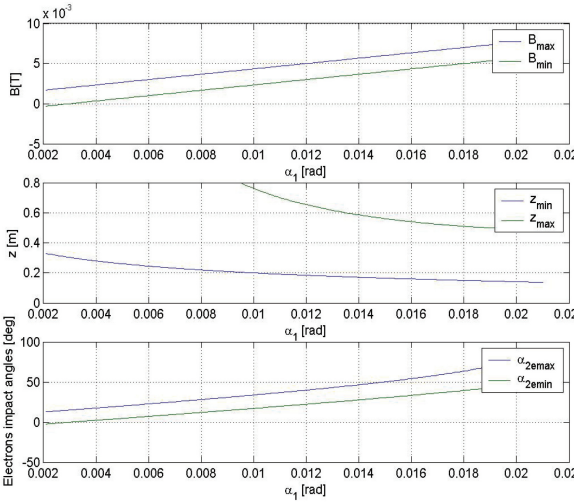

Fig.4 Single-stage steerer. Minimum and maximum magnetic fields corresponding to specified range of vertical deflection; corresponding minimum and maximum axial positions and incidence angles of impact of electrons on the electron dump.

As sketched in Fig. 2, the specified range of the ion deflection results in the specification of maximum and minimum values for the corresponding magnetic fields; in the case of a single-stage steerer, the results are shown in Fig. 4: as a function of the entrance angle of ions in the magnetic field, α_1, the required magnetic fields increase; the axial position where the electrons hit the dump plate decreases, their impact angle increases. These graphs can be used to define the minimum entrance angle of the particles, which results in the tilting angle of the beam source. A reduction of the plate length is desirable in terms of the reduction of the overall dimensions, but results in a larger impact angle and consequently in a large heat flux.

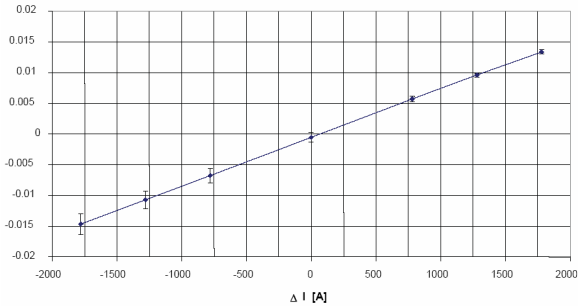

Fig.5 Negative ion deflection as a function of the current imbalance in the double-stage steerer.

In the case of the double-stage steerer, the first set of coils is dedicated to the horizontal deflection of electrons onto the dump plate; the second set of coils recovers the negative ion direction and provides the horizontal steering;

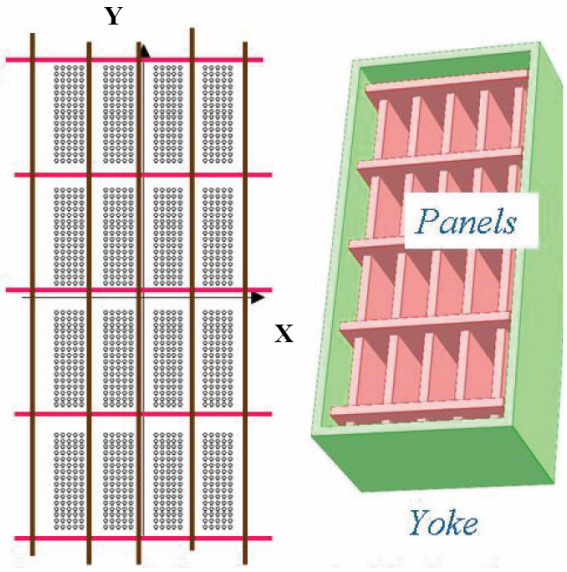

Fig.6 Conceptual design of a single-stage steerer. Electron dump plates, housing the coils, and magnetic yoke are shown.

another set of coils is interlaced to provide the vertical steering. Fig. 5 shows the ion deflection due to a current imbalance between the two sets of coils: it can be verified that the requirements are satisfied.

5. Conceptual design

A conceptual design has been developed for both steering systems; deflection of electrons is mainly performed on the horizontal plane.

Fig. 6 shows the case of the single-stage steerer. The magnetic coils are embedded in the electron dump plates. These plates are located between the beamlet groups, to shorten the distance between the plates and the apertures where electrons emerge. The magnetic yoke is also shown.

The double-stage steerer involves three sets of coils (see Fig. 7): the first stage forces the electrons onto the electron dump plates, which are vertical; a second set of coils compensates for the beam deflection induced by the previous set and provides the required horizontal steering of the beam; the last set of coils is interlaced with the second one and steers the beam in the vertical direction. The magnetic yoke surrounds the whole system.

5. Conclusions and future work

An active steerer can meet the requirements of ITER in terms of beam aiming, both horizontally and vertically. The system can be located in the space between the grounded grid and the neutraliser. The influence of the iron yoke on pumping efficiency is still to be assessed.

The advantages of active steering with respect to mechanical steering are: large flexibility, even at non-nominal acceleration voltages; control of power deposition profile and, consequently, of plasma instabilities; no need of mechanical tilting of the source; full control of beam aiming outside the vacuum vessel; controlled dumping of accelerated electrons; protection of cryopump panels from the radiation emitted at the electron dump plates.

Acknowledgments

This work was supported by the European Communities under the Contract of Association between EURATOM and ENEA. The views and opinions expressed herein do not necessarily reflect those of the European Commission.

[1] ITER Technical Basis 2002, “Neutral beam heating & current drive (NB H&CD) system”, Detailed Design Document (section 5.3 DDD5.3) (Vienna: IAEA)
[2] C. Gormezano *et al*., Nucl. Fusion **47**, S285 (2007)
[3] M. Ishikawa *et al*., Nucl. Fusion **47**, 849 (2007)
[4] Comsol Multiphysics 3.3, http://www.comsol.com
[5] M. Cavenago *et al*., COMSOL User Conf. 2007, Eds. Petit and O. Squali, Grenoble
[6] M. Cavenago *et al*., Annual Report 2006, INFN-LNL-217(2007), ISSN 1828-8545, 213
[7] N. Pilan *et al*., contract TW6-THHN-NBD1, report no. 3.4.3, part 3 (2008).

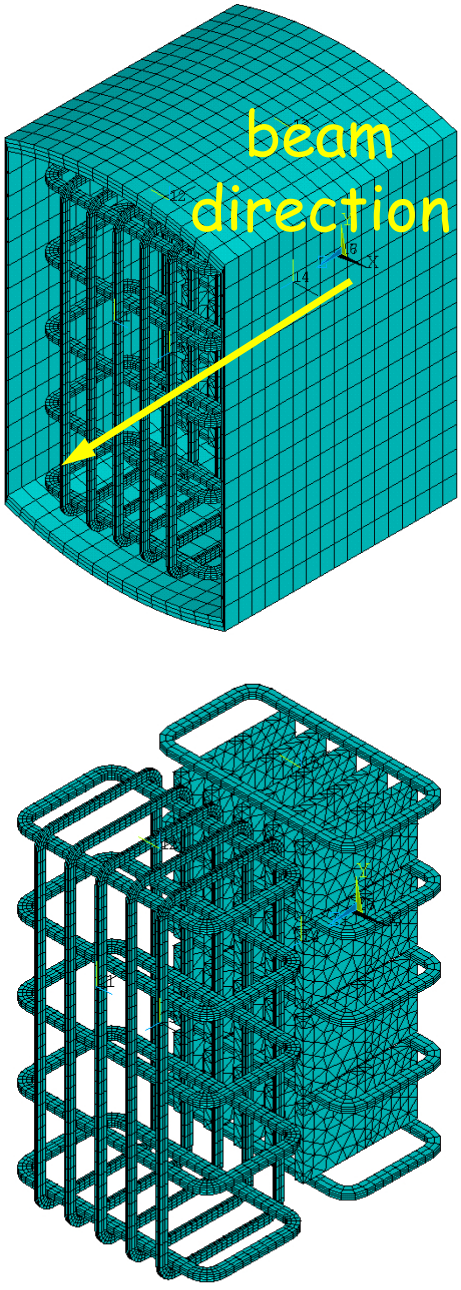

Fig.7 Conceptual design of a double-stage steerer. The three sets of coils are shown together with the electron dump plates and the magnetic yoke.

Proceedings of ITC18,2008

Photon Temperatures of Hard X-Ray Emission of LHCD Plasmas and Current Drive Efficiency in the HT–7 Tokamak

J. YOUNIS[1], B. N. WAN[1], S. Y. LIN[1], Z. Y. CHEN[2], Y. J. SHI[1], J. F. SHAN[1], F. K. LIU[1]

1. Institute of Plasma Physics, Chinese Academy of Sciences, Hefei 230031, P R China
2. Department of Physics, Yunnan Normal University, Kunming 650092, P R China

A comprehensive study of photon temperatures (Tph) of hard X-ray emission in the lower hybrid current drive (LHCD) plasmas and the current drive efficiency of lower hybrid waves in HT-7 tokomak is presented through a simple correlation. The photon temperature increases with increasing plasma current while it decreases with increasing plasma density. The current drive efficiency increases with the increase of the density in fully accessible condition of LHCD, with the decreased photon temperature T_{ph} and increased population density of the fast electrons at fixed plasma current. These experimental results reveal that photon temperature depends mainly on global effects of the fast electron population, synergy between the fast electron and the loop voltage and the coulomb slowing down.

Keywords: photon temperature, hard x-rays, current drive efficiency, HT-7 tokamak

1. Inroduction

Steady state operation of tokamak is the ultimate goal to realize a commercial fusion reactor. On the other hand, high performance, such as in advanced tokamak operation modes, is needed for the economic use of fusion reactors [1]. Lower hybrid (LH) waves are routinely used to drive currents in tokamak plasmas non-inductively, thus significantly extending the tokamak operation space to long-pulse, steady state discharges**.** In recent years lower hybrid (LH) waves have been successfully utilized for electron and ion plasma heating, to sustain and ramp-up toroidal plasma current, and to stabilize sawteeth in tokamak Investigations carried out in the HT-7 tokamak are contributing to these issues relevant to fusion reactors and the underlying physics. HT-7 is a medium sized tokamak with superconducting toroidal coils. Its main purpose is to explore high performance plasma operation under steady-state conditions. Since the very beginning of LHCD experiments in tokamaks, it has been recognized that hard X-ray emission from fast electrons provides considerable information on the LH wave power deposition profile and the fast electrons energy distribution. The measurement of the FEB emission in the hard X-ray energy range is the most efficient means for the investigation of LHCD experiments in plasma physics [2]. The photon temperature is just a parameter to characterize the level of anisotropy of the fast electron tail, which is determined by the exponential-like decrease of the FEB energy spectrum. The photon temperature is a commonly used parameter, to analyze qualitatively how the tail evolves with radio frequency wave parameters. The photon temperature indicates the "hardening" of the X-ray spectra, resulting from the interaction of fast electrons with residual loop voltage. It contains information of the energy distribution of fast electrons driven by the LH waves and residual electric field. For higher T_{ph}, the fraction of the energetic fast electrons population is larger, which means more plasma current carried by the fast electrons. The current drive efficiency is one of the most important parameter in non-inductive current drive for the evaluation of lower hybrid current drive experiments [3]. The experimental current drive efficiency is defined as $\eta = I_{rf} n_e R / P_{LH}$, where I_{rf} is the current driven by the lower hybrid waves, n_e is the central line average density, R is the major radius of the plasma and P_{LH} is the injected LH wave power absorbed by the plasma through landau damping. A fully non-inductive CD efficiency $\eta_o = I p n_e R / P_{LH0}$ is obtained when loop voltage approaches zero. P_{LH0} is the required LH power to attain zero loop voltage. The current related to RF power can be estimated by $I_{rf} = -(\Delta V / V_{OH}) I_p$, where $\Delta V = V_{LH} - V_{OH}$ is the loop voltage change between the LHCD phase and ohmic phase if total plasma current is unchanged. The purpose of this paper is to give a description of current drive efficiency in the LHCD plasma of HT-7 tokamak through such a simple way which is directly linked to the population and averaged velocity of fast electrons.

author's e-mail: jawad@ipp.ac.cn

.

2. Experimental Results and Discussion

HT-7 is a medium sized tokamak with superconducting toroidal coils and water-cooled graphite limiters in circular cross section [4]. It has a major radius of R_0 = 1.22 m, minor radius of a = 0.27 m, one toroidal water-cooling belt limiter at high field side and a new set of actively cooled toroidal graphite limiters at the bottom and top of the vacuum vessel. A LH power (P_{LH}) up to 1.2 MW at 2.45 GHz is available presently in the HT-7 machine. The power spectrum of the launched wave can be adjusted in the range $1.25 < n_{//} < 3.45$ by means of feedback control of the phase difference between adjacent wave guides of the couplers, where $n_{//}$ is the peak index of parallel refraction of the launched wave. The HT-7 tokamak is normally operated at I_p = 100–200 kA, B_t = 2 T, line-averaged density $n_e = (0.5 - 4) \times 10^{19}$ m^{-3}, in the limiter configuration. The hard X-ray diagnostics system in HT-7 is the main tool to measure FEB and consists of a vertical X-ray detector array. On HT-7 the CdTe detector was also used in the vertical array since 2001 for its excellent performance and successful application. The CdTe detector here can detect an energy range of X-ray from 20 keV to 200 keV, which is the energy range of non-thermal bremsstrahlung emitted by the fast electrons driven by lower hybrid wave. In the present experiments the feed back controls were applied to keep plasma current, the position and central line averaged density constant.

A typical waveform of the LHCD discharge is shown in the Fig. 1. The plasma current is 150 kA, the line averaged density n_e = 1.6 x10^{19} m^{-3}, 230 kW LHCD was launched from 0.32 s to 1.1 s.

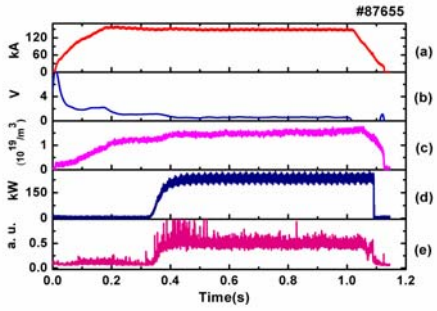

Fig. 1 Waveforms of LHCD discharge no. 87655. (a) is the plasma current, (b) the loop voltage, (c) the center line –average density, (d) the LH power, (e) the center line-integrated FEB emission intensity

For the plasma current scanning experiments it is experimentally and numerically observed that photon temperature increases with the increase in plasma current[5], which is mainly due to the interaction of the residual loop voltage and the fast electrons driven by lower hybrid waves. The population of fast electrons is higher at high plasma currents. Both increment of photon temperature and population of fast electrons at higher plasma currents leads to higher lower hybrid current drive efficiency.

During the plasma density scan experiment, LH power with 500 kW at $n_{//}$ = 2.35 was injected into target plasma having current of 150 kA. The plasma densities scanned shot by shot were (1.2, 1.7, 2.1, 2.5) x10^{19} m^{-3}. The photon temperature of central sight line is derived from FEB spectra, T_{ph} decreases with increasing plasma density [5,6]. At plasma density of 1.2x10^{19} m^{-3} and a fixed plasma current 150 kA, the CD efficiency is lower, that is only 0.33 m^{-2}A/W. The population of fast electron produced by the lower hybrid waves indicated by HX-ray intensity normalized by the line averaged density is low as can be seen in the Fig. 2.

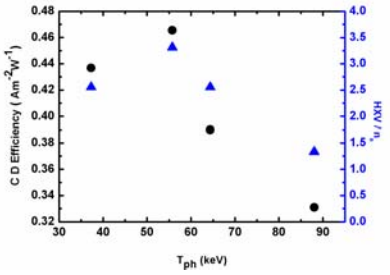

Fig. 2 Lower hybrid current drive efficiency and ratio of intensity of fast electron to density of fast electron versus Photon temperature at I_p= 150kA , P_{LH} = 500kW $n_{//}$ =2.35, (circle and triangle represent CD efficiency and ratio of fast electron population to density respectively).

At the lower line average plasma density of fixed plasma current, the electron temperature of the target plasma is higher, which will generate more resonant electrons with LHW on one hand. On another hand the less frequent collision with bulk electrons at lower plasma density can sustain the fast electron produced by LHW for longer time, which is partially responsible for higher photon temperature, due to lower slowing down time. At higher plasma density of 2.1x10^{19} m^{-3}, the CD efficiency is about 0.44 m^{-2}A/W, while the fast electron population is much higher than the low plasma density case as seen in Fig. 2. For higher density region the target

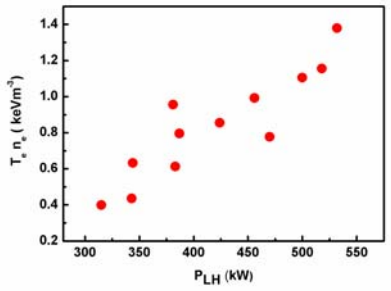

Fig. 3 $\Delta T_e n_e$ versus lower hybrid Power at n_e= 1.5x10^{19}m^{-3}, I_p= 150kA, P_{LH} = (188-532)kW, $n_{//}$ =2.35.

plasma has low temperature at fixed plasma current and faster slowing down will leads a lower photon temperature. The increased population of fast electrons contributes the increased CD efficiency significantly.

Figure 3 shows the increment of $\Delta T_e n_e$ with the LHCD power, which gives a measure of the energy transferring to bulk electrons from LHW. This heating is mainly through the collision of the bulk electrons by the fast electrons generated by LHCD, which slows these fast electrons down. The slowing down time of fast electrons, which is generated primarily at the resonance energy of LHCD [7], is inversely proportional to the bulk electron density. It can be clearly seen from the increment rates of $\Delta T_e n_e$ against LHW power in figures 3 and 4 for the densities of 1.5x10^{19} m^{-3} and 1.0x10^{19} m^{-3}.

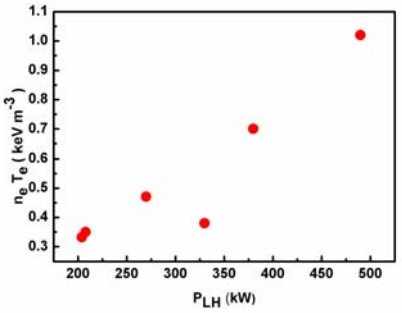

Fig.4 $\Delta T_e n_e$ versus lower hybrid Power at n_e= 1.0x10^{19}m^{-3}, I_p= 150kA, P_{LH} = (204-490)kW.

The slowing down via collisions can be responsible for the energy transferring to the bulk electrons from the fast electrons, which may account for the behavior of the photon temperature versus density. the population of the fast electrons generated by LHCD plays dominated role in generation of the current carried by fast electrons.

References

[1] N. J. Fisch *et al*., Phys. Rev. Lett., **41,** 873 (1978).
[2] Y. Peysson *et al*., Plasma Phys. Control. Fusion, **35**: B253 (1993).
[3] Z. Y. Chen *et al., Chin. Phys. Lett*. **22** 900 (2005).
[4] B. N. Wan, *et al*., J. Nucl. Mater., **313–316**: 127 (2003).
[5] J. Younis *et al*., *Plasma Science & Tech*. **10** 529 (2008).
[6] J. Younis *et al*., submitted to Plasma Phys. Control. Fusion.
[7] J. Wesson *Tokamaks* (Oxford: Oxford University Press) 2003 p 69.

Proceedings of ITC18,2008

ICRF heating in helical reactor

K. Saito, T. Seki, R. Kumazawa, H. Kasahara, T. Mutoh, F. Shimpo, G. Nomura

National Institute for Fusion Science,322-6 Oroshi-cho, Toki 509-5292, Japan

ICRF heating is a favorable high-density plasma heating method since ICRF wave can propagate in high-density plasma. ICRF heating in helical reactor was calculated by using an antenna code and a ray tracing code assuming high-density plasma without resonance layers of α-particles in plasma core. Enough loading resistance and low electric field inside the ICRF antenna was obtained. The strong heating of plasma will be expected in high-density plasma by heating electron and tritium, especially with the configuration of the second harmonic resonance layer of tritium on the magnetic axis shifted onto the saddle point.

Keywords: ICRF heating, helical reactor, LHD, α-particles, ray tracing, ELD/TTMP, second harmonic heating

1. Introduction

Helical fusion reactor [1, 2] has an advantage of steady-state operation since no need for a current drive. Before the ignition in the helical reactor, plasma must be heated by external heating such as ion cyclotron range of frequencies (ICRF) heating, electron cyclotron heating (ECH) and neutral beam injection (NBI). ICRF heating is a favorable high-density plasma heating method since the fast wave launched from ICRF antenna can be transmitted to plasma core even in high-density plasma. In Large Helical Device (LHD) [3], ions were efficiently heated by minority ion heating (hydrogen as minority ions, helium as majority ions) especially by locating ion cyclotron resonance layer on the saddle point of magnetic field strength where the gradient of magnetic field strength is zero, which is characteristic of helical device [4]. Injected energy of 1.6 GJ was achieved mainly using this heating method [5]. Mode conversion heating is also efficient heating method though heating deposition is far off-axis around normalized minor radius of 0.75 [4]. However, there are problems in the ICRF heating in reactor. One is that the loss of fusion-produced α-particles induced by the RF wave [6]. The other is existence of evanescence of the fast wave in vacuum region between plasma and ICRF antennas.

In section 2, resonance configurations to reduce the induced loss of α-particles will be shown. In section 3, calculation of loading resistance and electric field in the ICRF antenna will be shown. Ray tracing analysis will be conducted in section 4. Section 5 is a summary section.

2. Candidate of frequency and magnetic field strength in helical reactor

It was shown by the Monte Carlo simulation that α-particles are well confined without RF field [7]. We propose the configurations where the second harmonic resonance layer of tritium locates at the plasma core and the resonance layers of α-particles locate out of the plasma core to reduce the induced loss of α-particles by RF waves. Figure 1-a shows the ion cyclotron resonance layers at the vertically elongated toroidal section, where $f = n f_{ci}$. Magnetic configuration is the same with that of LHD (R_{ax}=3.75 m, vacuum), except for the scale factor of 3.5. The magnetic field strength on axis B_{ax} is 4.92 T and the RF frequency f is 50 MHz. The second harmonic resonance layers of α-particles do not exist inside of last closed flux surface and only the fundamental resonance layer locates in high-field peripheral region of the plasma. Therefore, loss of high-energy α-particles by RF field is expected to reduce and the energy of α-particles will be sufficiently utilized for plasma heating and the heat load by the α-particles on divertor plates or first wall will be kept low. A second harmonic resonance layer of tritium locates on the magnetic axis, therefore tritium heating is expected as well as electron heating by electron Landau damping (ELD) / transit-time magnetic pumping (TTMP) heating. Figure 1-b shows the resonance layers in the case of B_{ax}=5.10 T and f=50 MHz. A fundamental α-particle

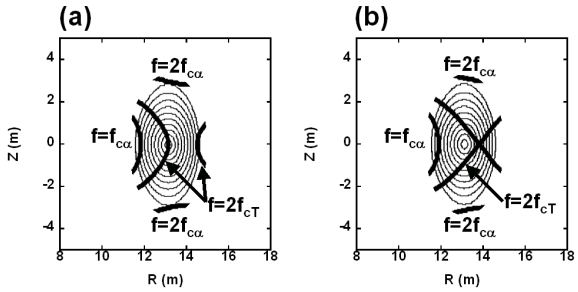

Fig.1 Configurations of ion cyclotron resonance layers. (a) Resonance layer of tritium on magnetic axis (f=50 MHz, B_{ax}=4.92 T). (b) Resonance layer of tritium on saddle point (f=50 MHz, B_{ax}=5.10 T).

author's e-mail: saito@nifs.ac.jp

resonance a little approaches to the plasma core and the resonance layer of tritium does not locate on the magnetic axis, however it locates at the saddle point where the efficient ion heating is expected.

3. Calculation of ICRF antenna performance

The loading resistance and the electro magnetic field around ICRF antenna were calculated by using variational method [8]. In this calculation slab model of plasma was used and infinite area of Faraday shield and back plate was assumed. Wave launched from antenna never returns to antenna. Simplified dielectric tensor of cold plasma was used, where a component of electric field along to magnetic field line is zero. The size of model antenna was 600 mm in strap width, 1000 mm in strap height, 50 mm between Faraday shield and the strap, and 350 mm between the strap and the back-plate. Large distance of 500 mm between plasma and Faraday shield was assumed to avoid the intense heat load on the ICRF antenna. RF frequency was 50 MHz and the magnetic field strength was 4.5 T (constant). Parabolic density profile was assumed with the peak density of 2×10^{20} m^{-3}. Ion species were deuterium and tritium with the same concentration. Power was fed into the two straps of upper and lower antenna by the coaxial lines with the characteristic impedance Z_c of 50 Ω through an outer port at the vertically elongated toroidal section assuming FFHR-2S [2] since it is not necessary to use blanket area for the feed lines. By the calculation, it was found that the loading resistance R was 10 Ω in the case of the opposite current direction on straps. Assuming maximum voltage in the coaxial line V_{max} of 70 kV, which is the twice of the interlock level in LHD, the allowable injection power by two antennas was estimated to be 19.6 MW by using the equation

$$Power = \frac{1}{2} R \left(\frac{V_{\max}}{Z_c} \right)^2 . \qquad (1)$$

Electric field inside the antenna was also calculated. The strength of electric field between Faraday shield and strap was the largest. In the case of 19.6 MW injection, it was 8.1 kV/cm and was smaller than that of breakdown for E⊥B (>30 kV/cm) [9]. Figure 2-a shows the intensity of the component of pointing vector directed to plasma. Peaks locate near the antenna tips. In the case of the same current direction on straps, loading resistance of 9.5 Ω and the power of 18.6 MW is possible. Maximum electric field was 14.2 kV/cm and still allowable level. The peak of intensity of pointing vector located between antennas as shown in Fig. 2-b.

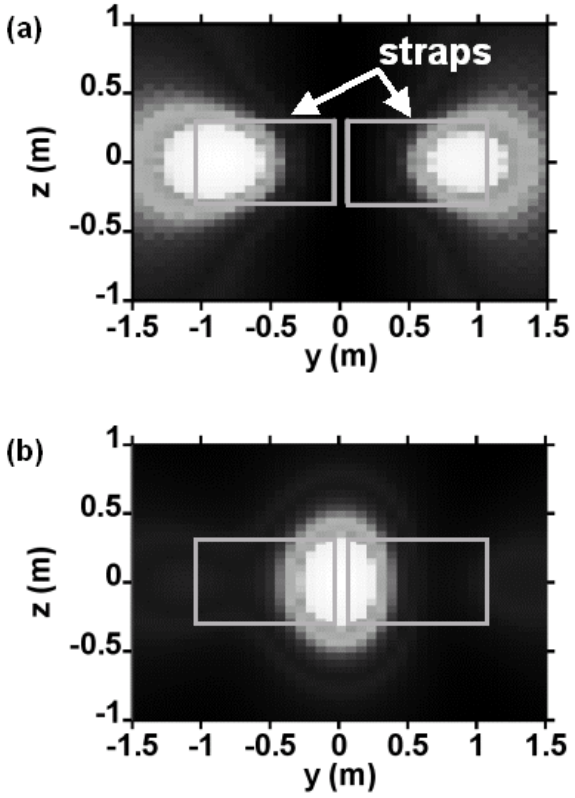

Fig.2 Intensity of the component of pointing vector directed to plasma at the plasma edge. (a) Opposite current direction case. (b) Same current direction case.

4. Ray-tracing calculation of ICRF wave in helical reactor

The ray tracing calculation was conducted using the peaks of pointing vector obtained in section 3 as initial positions. Four combinations of initial wave number parallel to magnetic field line and the wave number perpendicular to the magnetic field line projected on the flux surface of $(k_{//}, k_{\perp})$ =(-0.7 m^{-1}, -0.7 m^{-1}), (-0.7 m^{-1}, 0.7 m^{-1}), (0.7 m^{-1}, -0.7 m^{-1}), (0.7 m^{-1}, 0.7 m^{-1}) were supposed since waves are evanescent for larger wave numbers. In this calculation, magnetic field configuration of LHD was used with the scale factor of 3.5. Dielectric tensor of cold plasma was used for the calculation of ray trajectory and polarization. Absorbed power was calculated by using the absorption ratio Q and the wave energy W,

$$Q = \frac{\varepsilon_0}{2} \omega \vec{E}^* \cdot \vec{K}^a \cdot \vec{E} \qquad (2)$$

$$W = \frac{1}{4\mu_0} \vec{B}^* \cdot \vec{B} + \frac{\varepsilon_0}{4} \vec{E}^* \cdot \frac{\partial \omega \vec{K}^h}{\partial \omega} \cdot \vec{E} \qquad (3)$$

where, $\vec{E}$ is the polarized electric field and $\vec{K}$ is the hot plasma dielectric tensor. The absorbed power was superposed with the same weight ignoring the effect of interference. High density plasma with internal diffusion barrier (IDB) [10] with the following profiles of electron density and temperatures of ions and electrons were supposed,

$$n_e = n_{e0}[0.8\exp\{-(\rho/0.35)^{2.5}\} + 0.1(1-\rho^{6.5}) + 0.1] \quad (4)$$

$$T_{i,e} = T_{i,e0}(1-\rho^4) \quad (5)$$

where, ρ is the normalized minor radius. Deuterium and tritium was the same concentration, and the fusion products and the impurities were ignored. Ion and electron temperatures on magnetic axis $T_{i,e0}$ were 8 keV. The electron density on magnetic axis n_{e0} was scanned from 1×10^{20} m^{-3} to 5×10^{20} m^{-3} supposing high-density ignition.

4-1 Opposite current direction on straps

Ray tracing calculation was conducted from two initial positions where the strength of pointing vector shown in Fig 2-a is the maximum in the case of the opposite current direction on straps. The resonance layer of tritium located on the magnetic axis as shown in Fig 1-a. Figure 3-a shows variation of $k_{//}$. In spite of the small initial $k_{//}$, it was strongly enlarged, especially with the high electron density. The large $k_{//}$ up-shift is the characteristic to helical devices as pointed out in ref. [11]. These large $k_{//}$ is preferable for the direct electron heating by ELD and/or TTMP since the components for electron heating of $\vec{K}^a$ (anti-Hermitian part of $\vec{K}$) are proportional to $\exp\{-(\omega/k_{//}v_{te})^2\}$. In Fig. 3-b, the values of $\exp\{-(\omega/k_{//}v_{te})^2\}$ for different electron densities were shown, and they grew up enough close to one.

Figure 4-1-a shows the integrated absorbed energy by electron and tritium. Absorption increased with the plasma density, and the portion of absorption by electron and tritium was changed. Wave energy was absorbed mainly by tritium at low density, whereas, wave energy was absorbed mainly by electron at high density since before cyclotron resonance of tritium, electrons start to absorb wave energy due to enhanced electron heating at high density. Figure 4-1-b shows power deposition profile. Location of power deposition is near plasma but a little off-axis (ρ≈0.25). Figure 4-2-a shows the absorbed energies in the case of resonance on the saddle point. In this case, the ratio of tritium heating increased since rays experienced the resonance of tritium earlier. Therefore, deposition profile shifted outward as shown in Fig. 4-2-b.

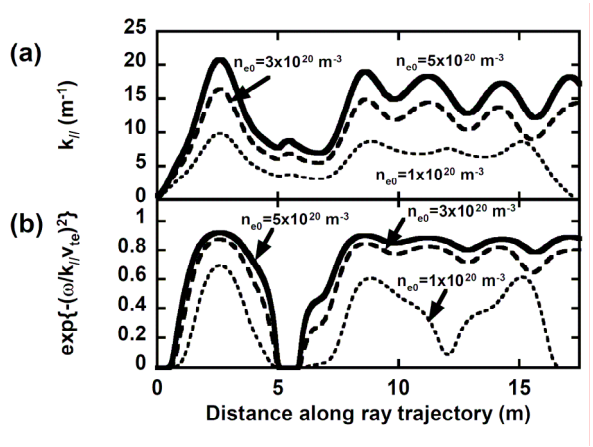

Fig.3 (a) Variation of $k_{//}$ for three electron densities on magnetic axis. (b) Variation of $\exp\{-(\omega/k_{//}v_{te})^2\}$ as an index of ELD/TTMP strength.

4-2 Same current direction on straps

Initial position was set at the outer edge on mid-plane at the perpendicularly elongated plasma section, since the pointing vector was maximum there in the case of the same current direction on straps as shown in Fig 2-b. Ray tracing was conducted for two cases of resonance of tritium on the magnetic axis and the saddle point. As shown in Fig.4-3-a, in the case of resonance on the axis, tritium heating was dominant and power was deposited on the magnetic axis (Fig.4-3-b). One-pass absorption was small when the density was low. However, by the configuration of resonance layer of tritium on saddle point, it increased though the peak of deposition shifted around ρ=0.5 as shown in Figs. 4-4-a and 4-4-b. Therefore the configuration of the magnetic axis on the saddle point may be useful for intense core heating. The magnetic axis was shifted onto the saddle point artificially and resonance layer of tritium was located on the axis. In this case, the intense core heating by tritium was calculated as shown in Figs. 4-5-a and 4-5-b. The second harmonic heating was thought to be enhanced by the effects of large $k_{\perp}$ around the axis and low gradient at the saddle point. Due to the strong absorption by tritium, electrons were not heated. Since the wave energy is dumped at the magnetic axis perfectly before the growing up of $k_{//}$, even if resonance of α-particles exists in plasma by the Doppler effect, the acceleration of α-particles will be avoided.

5. Summary

To reduce the enhanced loss of α-particles by RF waves, the configurations without the cyclotron

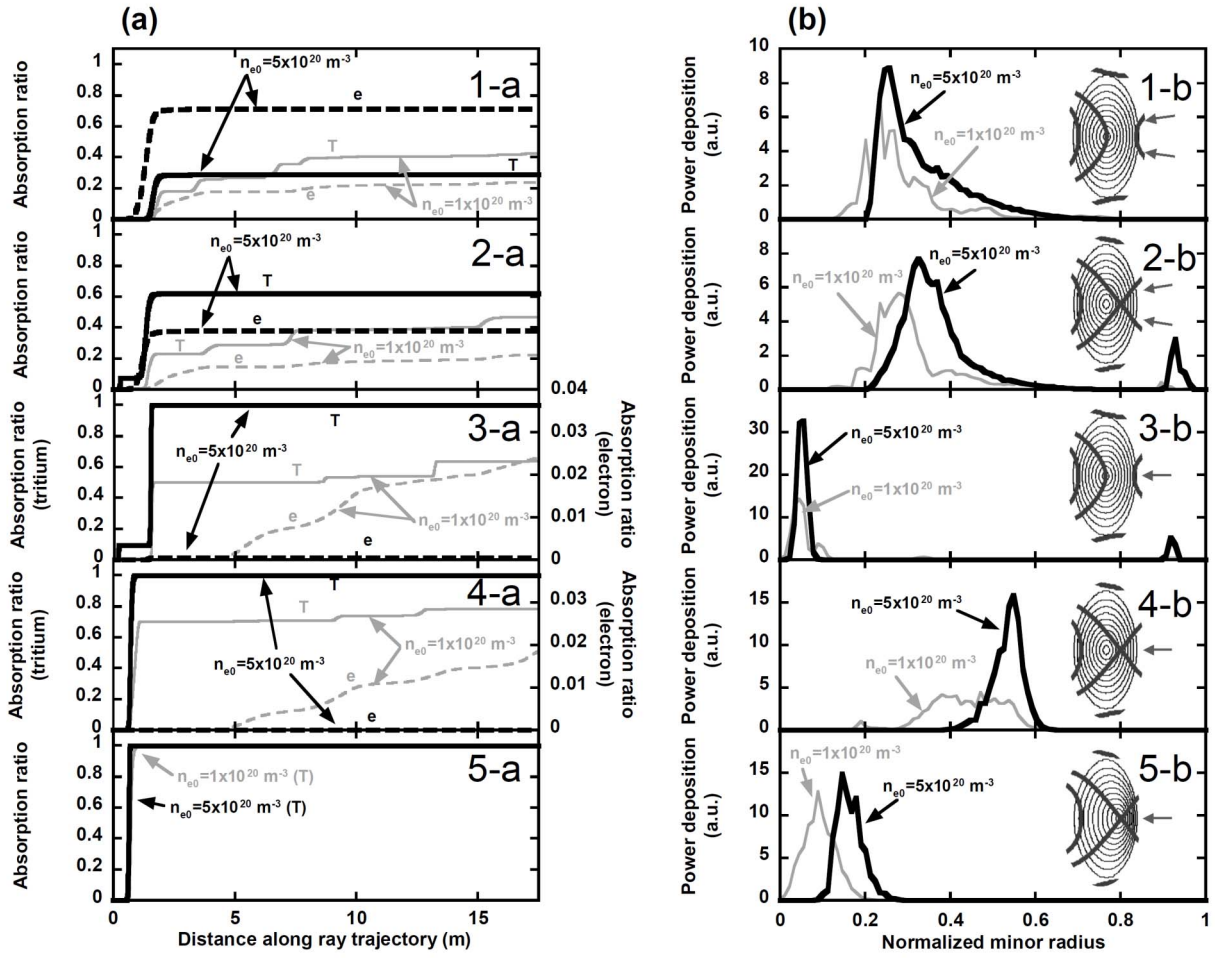

Fig.4 (a) Absorbed wave energy by electron and tritium normalized by initial wave energy for various initial positions and resonance configurations. (b) Deposited power density multiplied by dV/dρ. At the right side, initial positions and resonance configurations are shown.

resonance of α-particles layer in plasma core were selected as candidates for ICRF heating in helical reactor. The second harmonic resonance layer of tritium located at the plasma core. ICRF antenna for the helical reactor was not optimized but the large loading resistance of 10 Ω and the power injection of 20 MW from two antennas were found to be achievable. By the calculation of ray tracing, it was found that the wave number parallel to magnetic field was up-shifted largely especially in high-density IDB plasma even if the initial wave number was small, which enabled ELD/TTMP heating. The configuration of the second harmonic resonance layer on the magnetic axis shifted onto the saddle point makes the intense core heating possible by emitting the RF wave from mid plane.

References

[1] A. Sagara, et al.,Fusion Eng. Des. 83 (2008) 1690-1695.

[2] N. Yanagai, K. Nishimura, A. Sagara, Design of Split-Type Helical Coils for FFHR-2S, NIFS Annual Report, 2006-2007, p.269.

[3] O. Motojima, et al., Nucl. Fusion 47 (2007) S668-S676.

[4] K. Saito, R. Kumazawa, T. Mutoh, T. Seki, T. Watari, Y. Torii, et al., Nucl. Fusion 41 (2001) 1021-1035.

[5] K. Saito, et al., J. Nucl. Mater. 363-365 (2007) 1323-1328.

[6] D. S. Darrow, et al., PPPL Reports, PPPL-3164 (1996).

[7] S. Murakami, H. Yamada, M. Sasao, M. Isobe, T. Ozaki, T. Saida, et al., Fusion Sci. Technol. 46 (2004) 241-247.

[8] K. Theilhaber, J. Jacquinot, Nucl. Fusion 24 (1984) 541-554.

[9] S.J. Wukitch, et al., 2002 proc .19th Int. Conf. on Fusion Energy 2002 (Lyon, France, 2002) (Vienna: IAEA) CD-ROM file FT/P1-14 and http://www.iaea.org/programmes/ripc/physics/fec2002/html/fec2002.htm.

[10] N. Ohyabu, et al., Plasma Phys. Control. Fusion 48 (2006) B383-B390.

[11] N. Takeuchi, et al., J. Plasma Fusion Res. SERIES, Vol.6 (2004) 642-646.

Proceedings of ITC18,2008

Development of 77 GHz-1 MW ECRH system for LHD

Hiromi TAKAHASHI[1)], Takashi SHIMOZUMA[1)], Shin KUBO[1)], Yasuo YOSHIMURA[1)], Hiroe IGAMI[1)], Satoshi ITO[1)], Sakuji KOBAYASHI[1)], Yoshinori MIZUNO[1)], Yasuyuki TAKITA[1)], Takashi MUTOH[1)], Tsuyoshi KARIYA[2)], Ryutaro MINAMI[2)], Tsuyoshi IMAI[2)]

[1)] *National Institute for Fusion Science*

[2)] *Plasma Research Centre, University of Tsukuba, Tsukuba 305-8577, Japan*

In the Large Helical Device (LHD), the development of new 77 GHz gyrotrons of the design value of more than 1 MW for 5 s and 300 kW for CW have started from 2006 as the joint program between NIFS and University of Tsukuba. The replacement of the existing gyrotrons by the 77 GHz-1 MW tubes is in progress. Two 1 MW tubes have been installed in LHD up to now. We have also finished the arrangement of the peripheral components including the transmission line. We have attained the operation of 0.86 MW/ 1.1 s and 0.76 MW/ 5 s for each 77 GHz gyrotron.

Keywords: ECRH, gyrotron, matching optics unit, steady state operation, LHD

1. Inroduction

Electron cyclotron resonance heating (ECRH) is one of the most promising heating methods for fusion plasmas due to its higher power density and lower risk for neutron activation. From the view point of plasma control, ECRH also plays a key role as a control knob for local plasma parameters by local heating or toroidal current drive with a high spatial resolution [1]. Thus, it is substantially important to develop gyrotrons with a capability of high-power generation and long-time oscillation for effective utilization of ECRH as a plasma control knob and extension of parameter regime of long-time sustained plasma.

In the Large Helical Device (LHD) [2], the enhancement of the output power per gyrotron was planed to enlarge the plasma operational regime and the replacement of the existing gyrotrons to high-power ones is progressed. 8 sets of gyrotron are operated and the total injection power of ECRH to plasma is less than 2 MW. We will replace all these gyrotrons to 1 MW-ones and set ultimate goal as the total injection power of 5 MW. The oscillation frequencies of these 1 MW-gyrotrons are selected as 77 or 154 GHz and are different from those of the gyrotrons already installed in LHD. The frequency of 77 GHz is resonant with the fundamental electron cyclotron resonance layer on axis of the standard configuration of LHD, which shows good plasma confinement [3], so a higher electron temperature on the axis and a higher peaking factor of the temperature profile than that obtained previously are expected. Moreover, these gyrotrons have the capability of 300 kW-continuous oscillation, thus the gyrotron will contribute to the expansion of the parameter regime of long-time-sustained plasma. LHD has a capability of long-pulse operation [4] of high temperature/density plasma due to the superconducting coil system and various heating source. Therefore, LHD can be said one of the most appropriate devices for extrapolation to steady-state fusion reactor in terms of the size and the feature.

In this paper, we show the progress of the installation of the 77 GHz 1 MW-gyrotrons for LHD. The paper is organized as follows. In section 2, the ECRH system in LHD is described. Section 3 deals the characteristics of the 1 MW-gyrotrons and the peripheral components. In Section 4, the results of the short/long pulse operation and the achieved operational regime are shown. Final conclusions are presented in section 5.

2. ECRH system in LHD

LHD is the largest heliotron device with R = 3.9 m, a = 0.6 m, which has the pole number of 2 and the toroidal period of 10. The heliotron configurations are produced by a set of helical winding coils and three sets of poloidal field coils, which are all superconducting magnet. Therefore the steady-state formation of magnetic configuration and plasma sustainment has been realized. The magnetic field on axis is ~2.9 T.

In LHD, ECRH system with 8 sets of gyrotron, which frequencies are 77 (Toshiba Electron Tubes & Devices, TETD), 82.7 (Gycom), 84 (Gycom) and 168 GHz (TETD), have been operated for preionization and plasma heating [5]. Among them, the 77-GHz gyrotrons has been newly installed since the experimental campaign of 2007. These are the collector-potential-depression (CPD) type gyrotrons [6] for high efficiency operation

author's e-mail: hiromi.takahashi@LHD.nifs.ac.jp

excluding those of 82.7 GHz. One of the 84 GHz gyrotron has the capability of continuous-wave (CW) oscillation and that is mainly used for steady-state plasma experiments [7]. The type of magnetron injection gun (MIG) is triode for TETD tubes and diode for Gycom tubes, respectively. These gyrotrons are set at the heating equipment room next to the LHD hall. Each ECRH system is composed of gyrotron tube, power supply for gyrotron, matching optics unit (MOU), waveguides, miter bends, arc detectors, dummy load, waveguide switch, antenna and the other components. The millimetre wave power is transmitted to LHD through the corrugated waveguides with the inner diameter of 31.75 mm or 88.9 mm after transformation of the beam to HE_{11} mode at the MOU and injected to the plasma using injection antenas. One of the antennas is mirror type anntena consisted of one focusing mirror and one steering mirror. The other is waveguide anntena used for CW gyrotron. The transmission efficiency of ECW is about 60-95 % depending on the number of the miter bend, the length of the transmission line, and the othe factors.

3. Configuration of 1 MW-Gyrotron

Since July 2007, the installation of the 1 MW-gyrotrons designed by TETD has progressed in LHD and two 1 MW-tubes have been operated in the present circumstance. The design of the gyrotron and the configuration with the MOU are shown in Tab I and Fig. 1. The gyrotron type is CPD and the gun is a triode configuration cathode for controllability. 6 sweep coils are set around the collector and a triangular current of 1.9 Hz is applied to the coils to change the injection point of the spent electron beam temporally in order to avoid the local heat accumulation. $TE_{18,6}$ is selected as the cavity mode taking the cathode configuration, the radio frequency (RF) power loss on the inner wall, matching with the mode converter into consideration. RF beam is projected from output window after the shaping by 4 copper mirrors in the gyrotron. A chemical-vapor-deposition (CVD) diamond disc with high thermal conductivity and low dielectric constant is used for the projection window so a higher output/ longer pulse operation is realized. Moreover, the diamond window allows the projection of RF beam with TEM_{00} mode leading to less power loss in the shaping to HE_{11} mode at the MOU. The diamond disc is also used for injection window to LHD.

A MOU is set as illustrated in Fig. 1. The MOU mirror system consists of 2 copper mirrors with the major axis of 100 mm and the minor axis of 80 mm. A phase distribution of an RF beam is corrected by these mirrors. The mirror surface was designed by the convergence calculation for the height of the bumpy on the mirror

TAB I Design of 77 GHz gyrotrons

Items	Design
Frequency	77 GHz
Power/ Pulse length	1.0 MW/ 5.0s, 0.3 MW/ CW (#1) 1.2 MW/ 5.0s, 0.3 MW/ CW (#2)
Beam Current	≤ 50 A
Cavity mode	$TE_{18,6}$
MIG type	Triode
Collector type	Collector Potential Depression
Output window	CVD Diamond

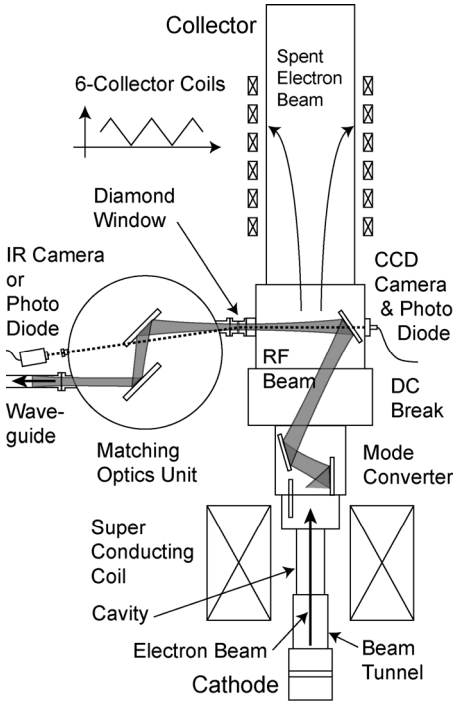

Fig.1 The gyrotron configuration with the MOU.

corresponding to the phase difference between the initial phase distribution and the goal one, which was calculated from the inverse diffraction for HE_{11} mode at MOU projection port. The design value of transmission efficiency of the MOU is 98.8 %. The alignment of the RF beam was done by the adjustment of these two mirrors and the gyrotron final mirror. An arcing in the MOU is monitored through the sapphire window by the arc detector (photo diode) set at the ICF 70 port located on the same surface of the MOU projection port. The temperature profile of the diamond window during an operation is also monitored using an IR camera through the port.

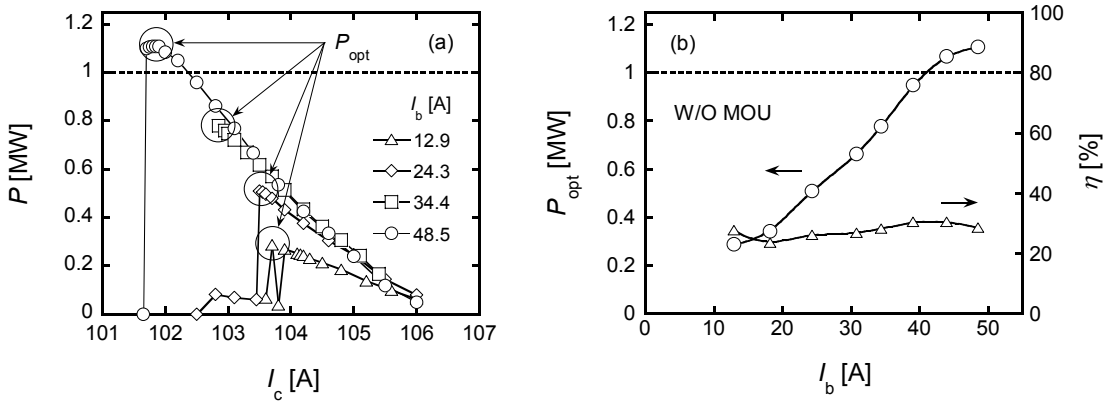

Fig.2 The dependence of (a) the output power on the coil current, (b) the maximum output power and the oscillation efficiency on the electron beam current.

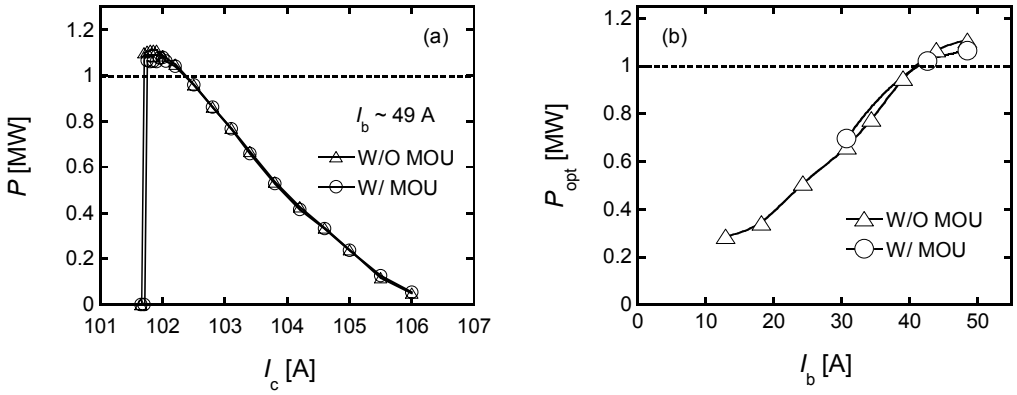

Fig. 3 The dependence of (a) the output power on the coil current and (b) the maximum output power on beam current W/, W/O the MOU. The operation of 1 MW output was attained even with the MOU.

4. Short and long pulse operations

After the arrangement of the cooling system for the gyrotron components, we started the short-pulse test. In this operation, the output power was monitored using short-pulse dummy load connected to the projection port of the gyrotron. Figure 2 shows the dependence of (a) the output power P on the coil current of the superconducting magnet at the cavity I_c, (b) the maximum output power P_{opt} and the oscillation efficiency η on the electron beam current I_b for #1 77 GHz-gyrotron. In this operation, the dummy load was evacuated to ~10^{-4} Torr and the pulse length of the gyrotron oscillation was set for 3 ms. The oscillation region of the operating mode elongated to the lower magnetic field side with I_b increasing and P = 1.1 MW was achieved at I_b = 48.5 A. The maximum oscillation efficiency of 30.5 % was confirmed at I_b = 43.9 A. We also checked the transmission efficiency of the MOU. Figure 3 shows the dependence of (a) P on I_c and (b) P_{opt} on I_b W/, W/O the MOU for #1 77 GHz-gyrotron. It was confirmed that the power loss due to the MOU was small and the 1 MW output was attained even with the MOU. Eventually, we performed the operation of 1.05 MW/ 4 ms.

After 1 MW test for short pulse, we proceeded to a long pulse operation. The conditioning in the long pulse operation was performed using CW-dummy loads. A pre-dummy load is set upon each CW-dummy load in order to absorb reflected waves from the CW-dummy load. The output power from the gyrotron in the long-pulse operation was evaluated as the sum of the absorption power at CW- and pre-dummy load. Figure 4 shows the progress of the extension of the power and the pulse length for #1 ((a), (b)) and #2 gyrotron ((c), (d)), (e) the operational regime and its present boundary in power vs. pulse length until October 16, 2008. In Fig. 4 (e), the open circles and the open squares represent the attained operation regime for #1 and #2 gyrotron, respectively. We operated the gyrotrons for ~200 hours in the cumulative operational time. Up to now, we attained the operation of 860 kW/ 1.1 s, 500 kW/ 5.0s for #1 gyrotron and 760 kW/

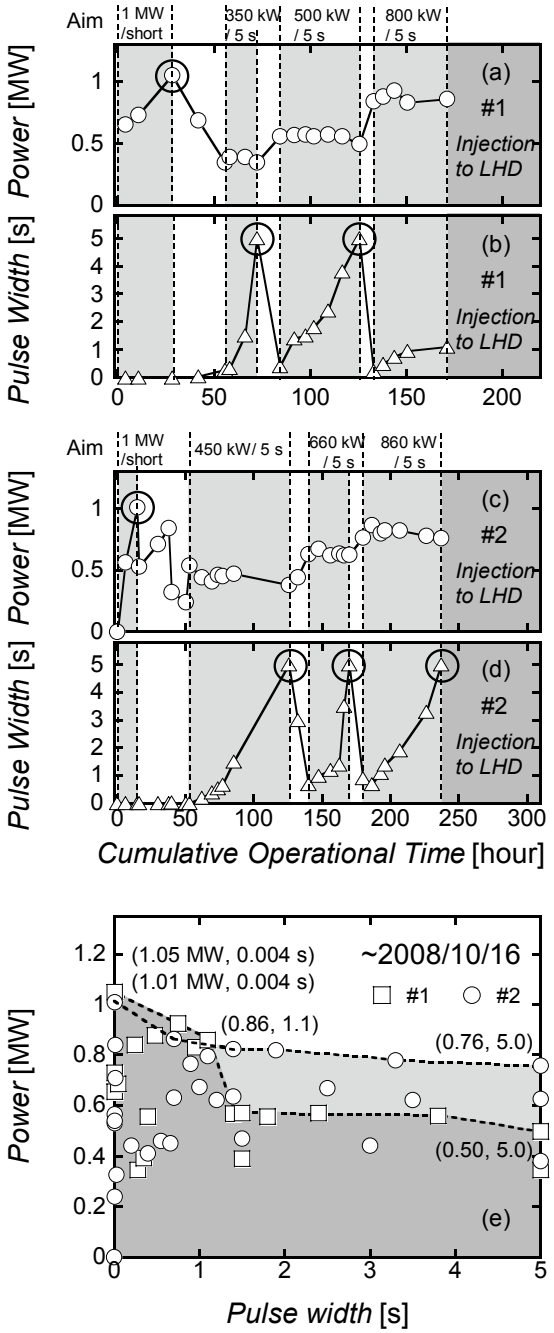

Fig. 4 (a)-(d) the progress of power and the pulse length, (e) the attained operational regime and its present boundary.

5.0 s for #2 one. Finally, we show the typical oscillation of high power output for 5.0 s. Figure 5 shows the time evolution of (a) collector, body and anode voltage V_C, V_B, V_A, (b) beam and anode current I_b, I_A and (c) output power P. Although the output power exceeded 800 kW at the beginning of the oscillation, it decreased gradually with the beam current decrease. We now try to apply a temporal heater boosting with preprogram to compensate the beam current decrease.

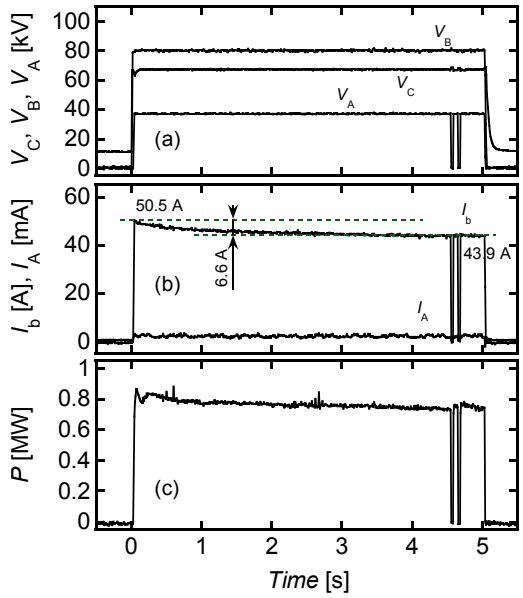

Fig. 5 The time evolution of (a) collector, body and anode voltage, (b) beam and anode current and (c) output power.

5. Summary

77 GHz gyrotron of the design value 1 MW/ 5 s and 300 kW/ CW was newly installed in LHD and the arrangement of the peripheral component has already done. We have attained the operation of 0.86 MW/ 1.1 s and 0.76 MW/ 5 s for each 77 GHz gyrotron. In future work, we will extend the operational regime to 1 MW/ 5 s or 1.2 MW/ 5s and 300 kW/ CW. In parallel to that, we start the installation of second 77 GHz gyrotron (1.5 MW/ several sec., 300 kW/ CW), which has already developed.

Acknowledgment

We wish to acknowledge useful discussions with Professor K. Sakamoto. We are grateful to Dr. Y. Mitsunaka for the development of the gyrotron. This work was supported by NIFS grants, ULRR501, ULRR503, ULRR512, ULRR514 and ULRR518.

References

[1] V. Erckmann and U. Gasparino, Plasma Phys. Control. Fusion **36**, 1869 (1994).
[2] O. Motojima *et al.*, Nucl. Fusion **45**, No 10, S255 (2005).
[3] H. Yamada *et al.*, Nucl. Fusion **41**, No 7, 901 (2001).
[4] T. Mutoh *et al.*, Nucl. Fusion **47**, No 9, 1250 (2007).
[5] S. Kubo *et al.*, Plasma Phys. Control. Fusion **47**, No 5A, A81 (2005).
[6] K. Sakiamoto *et al.*, Phys Rev. Lett. **73**, 3532 (1994).
[7] T. Shimozuma *et al.*, Fusion Eng. Des. **53**, 525 (2001).
[8] T. Notake *et al.*, Plasma Phys. Control. Fusion **47**, 531 (2005).

Proceedings of ITC18,2008

Flux supply of a field-reversed configuration by NBI heating

Fusaki P. Iizima and Toshiki Takahashi

Dept. of Electronic Engineering, Gunma University, 1-5-1 Tenjin-cho, Kiryu 376-8515, Japan

It is shown that the magnetic flux of a field-reversed configuration plasma can be supplied by neutral beam injection heating. Although the beam ion current leads a flux decay due to interaction between fast ions and electrons that carries the current dominantly, the thermal force affects sustainment of the flux. The azimuthal electric field is the only source of flux supply in the newly developed model.

Keywords: neutral beam injection, field-reversed configuration, flux supply, resistive decay, thermal force, Monte-Carlo simulation

1. Inroduction

Neutral beam injection (NBI) is most effective way to maintain a field-reversed configuration (FRC) plasma. Because of its high-beta nature a commonly-used wave heating method is believed unfortunately inapplicable. Therefore, NBI is a key issue of steady state operation of FRC plasmas.

Recent numerical studies are focused on heating of FRCs. Takahashi *et al*. showed an FRC plasma with the trapped flux of 4.7 mWb confines well 15-keV beam ions injected tangentially to the plasma current [1]. A study of the flux supply by NBI, on the other hand, has not been as yet investigated. The theoretical model to discuss the flux supply of an FRC plasma is needed to develop.

It has been thought that the presence of the beam current could augment the confinement field according to the Ampère's law, and then the flux is thought to be supplied. However, the resistive force between beam particles and electrons can cause the flux decay, when one employs the simplified Ohm's law and the Faraday's law. This suggests that the azimuthal component of electric field should be modified. Being examined the azimuthal force on the electron fluid element the thermal force [2]

$$\mathbf{R}_{\mathrm{T}} = -\frac{3}{2}\frac{n_{\mathrm{e}}}{\omega_{\mathrm{e}}\tau_{\mathrm{e}}}\frac{\mathbf{B}}{B}\times\nabla T_{\mathrm{e}} \qquad (1)$$

can contribute to the flux supply of an axisymmetric FRC. Here, $n_{\mathrm{e}}, \omega_{\mathrm{e}}, \tau_{\mathrm{e}}, T_{\mathrm{e}}$ are the electron density, the electron cyclotron frequency, the electron collision time, and the electron temperature in Joule, respectively. When the core plasma is heated by fast ions, the electron pressure gradient enhances; it can lead the flux supply.

In the present paper, we will develop a calculation model to discuss flux supply and show its possibility by NBI heating.

2. Heating by NBI

Neutral beam injection into the FRC plasma is firstly demonstrated at the FIX (FRC Injection Experiment) machine [3]. The FRC lifetime is extended by NBI; it is thought that it results from suppression of a global motion of the FRC by a beam ion ring formed near the X-point [4]. Power deposition by beam ions to the plasma is calculated by tracing orbits of beam ions [5, 6]. Since the beam ions are injected obliquely with respect to the geometric axis, they suffer from the end loss significantly. Therefore, the deposition power is at most 10 % of the injection power. Contrary to the axial injection, tangential NBI (TBNI) can suppress orbit losses of beam ions drastically [1]. We study now heat generation of electrons by Coulomb collisions with beam ions.

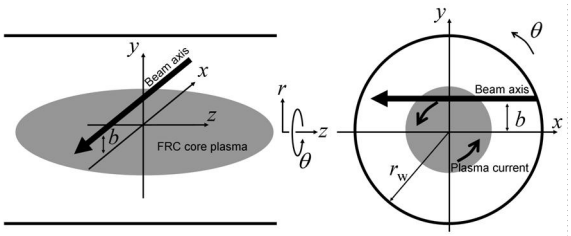

Fig.1 Geometry of tangential neutral beam injection.

An equilibrium state is calculated by the Grad-Shafranov equation. Neutral beam particles are injected tangentially as shown in Fig. 1. We consider the case that the field resistively decays as

$$\frac{\partial \psi}{\partial t} = -r\eta J_{\theta}\,. \qquad (2)$$

Ionization of neutral particles is reproduced by a Monte-Carlo method [5]. Orbits of beam ions are calculated by integrating numerically the equation of motion that includes the slowing-down collision term. Electron heat generation term is written as

$$Q_{\mathrm{eb}} = -\mathbf{R}_{\mathrm{eb}} \bullet \left(\mathbf{u}_{\mathrm{e}} - \mathbf{u}_{\mathrm{b}}\right), \qquad (3)$$

where $\mathbf{R}_{\mathrm{eb}}$ is the friction force by beam ions acting on the electron fluid. Heat generation of beam ions can be

author's e-mail: m07e0607@gs.eng.gunma-u.ac.jp

neglected, because the mass of electron is much smaller than the mass of beam ions. The R. H. S. of Eq. (3) is calculated from the friction force of individual beam ion by using the PIC method [7].

Numerical results are shown in Fig. 2, 3, and 4, where neutral beam particles are injected at $r = 0.24 r_{\mathrm{w}}$ and $z = 0.1 z_{\mathrm{M}}$. Here, r_{w} and z_{M} are the wall radius and the axial length from the midplane to the mirror end. The beam ion density is shown in Fig. 2. In our calculation, injection is done only at $t = 0$ (the top figure). We show also the case $t = 10 t_{\mathrm{A0}}$ (the middle) and $t = 20 t_{\mathrm{A0}}$ (the bottom). It is found that beam ions moves axially toward the midplane; this implies beam ions exhibit the betatron orbit. The azimuthal flow velocity of beam ions is also presented in Fig. 3. The current of beam ions generates the poloidal field, and it contributes to flux supply. On the other hand, interaction between beam ions and electrons cause the azimuthal electric field. This results in the electron current and flux decay. From Fig. 3, the flow of beam ions directs in the ion diamagnetic current initially. A paramagnetic beam flow can be found in $0.1 z_{\mathrm{M}} \le z \le 0.5 z_{\mathrm{M}}$. The orbit of beam ions changes from the betatron to gyrating motion with time. By comparing with Fig. 2, the number of gyrating particle is relatively few, because the beam ion density is low in this region. Electron heat generation occurs dominantly near the midplane and geometric axis. Therefore, it is possible that the electron temperature increases near the field-null. If so, the electron temperature gradient enhances with time. By the thermal force written in (1), the magnetic flux can be augmented.

3. Flux supply by heating

We will demonstrate maintenance of the magnetic flux of an FRC plasma numerically. Suppose that electron heat generation is done as

$$Q_{\mathrm{e}} = Q_{\mathrm{e0}} \left(\frac{r}{r_{\mathrm{w}}} \right)^2 \left[1 - \left(\frac{r}{r_0} \right)^2 \right] \exp(-\beta z^2), \qquad (4)$$

where $Q_{\mathrm{e0}}, r_0, \beta$ are parameters that control amount of heat and a region where electrons can be heated. The electron temperature increases as

$$\frac{3}{2} n_{\mathrm{e}} \frac{\partial T_{\mathrm{e}}}{\partial t} = Q_{\mathrm{e}}. \qquad (5)$$

The initial temperature assumed to be uniform in the present calculation. The time derivative of the flux function is written in

$$\frac{\partial \psi}{\partial t} = -r E_\theta. \qquad (6)$$

The azimuthal electric field is

$$E_\theta = \eta J_\theta + R_{\mathrm{T}\theta}, \qquad (7)$$

where $\eta, R_{\mathrm{T}\theta}$ are the anomalous resistivity and the azimuthal component of the thermal force written in (1). We employ the Runge-Kutta method for time integration of Eqs. (5) and (6).

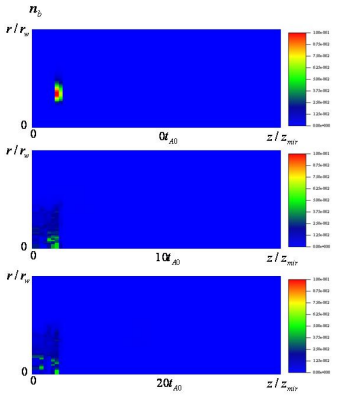

Fig.2 Color contours of the beam ion density. (Top) $t = 0$, (middle) $t = 10 t_{\mathrm{A0}}$, and (bottom) $t = 20 t_{\mathrm{A0}}$.

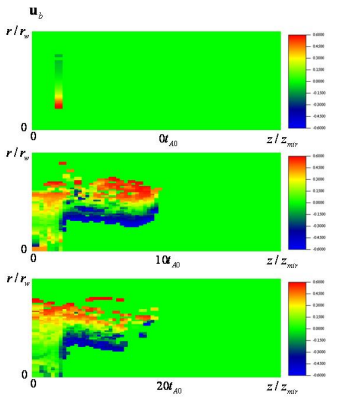

Fig.3 Color contours of azimuthal flow of the beam ions. (Top) $t = 0$, (middle) $t = 10 t_{\mathrm{A0}}$, and (bottom) $t = 20 t_{\mathrm{A0}}$.

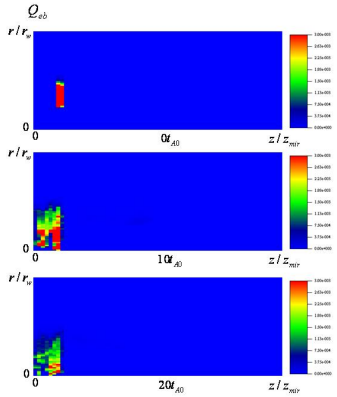

Fig.4 Color contours of electron heat generation by NBI. (Top) $t = 0$, (middle) $t = 10 t_{\mathrm{A0}}$, and (bottom) $t = 20 t_{\mathrm{A0}}$.

The electron temperature profile in *r*-*z* plane is shown in Fig. 5. The peak value becomes 1.6 times higher than the initial temperature T_0 (124 eV). In this calculation, we set

$$Q_{e0} = 5\times10^{-2}\,\frac{n_0 T_0 q_i\,|\psi_w|}{m_i r_w^2},$$

$$r_0 = 0.4 r_w\,,\quad \beta = 15/z_M^2\,.$$

Here, n_0, ψ_w, m_i, q_i are the initial electron density at the field-null, the flux function at the wall and midplane, the ion mass, and the ion charge, respectively. To show the possibility of flux supply by heating, we examine the effect of electron heat generation on time evolution of flux function. The midplane profiles of the flux function and magnetic field are shown in Fig. 6. When we neglect the heat generation term, the flux decays with time as is drawn by the red solid line. On the other hand, if electron heat generation is present, the flux can be sustained. Time evolution of the maximum trapped flux is shown in Fig. 7. When the FRC plasma is heated, no decay of the trapped flux is found. Therefore, we can show successfully the possibility of flux supply by electron heating.

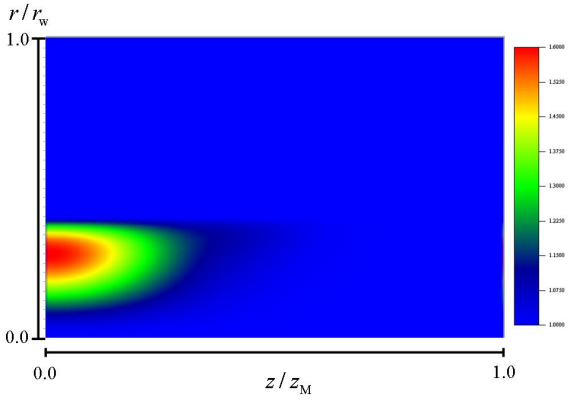

Fig.5 Color contour of the electron temperature at $t = 18.7 t_{A0}$ .The maximum of the temperature reaches 1.6 times higher than the initial value.

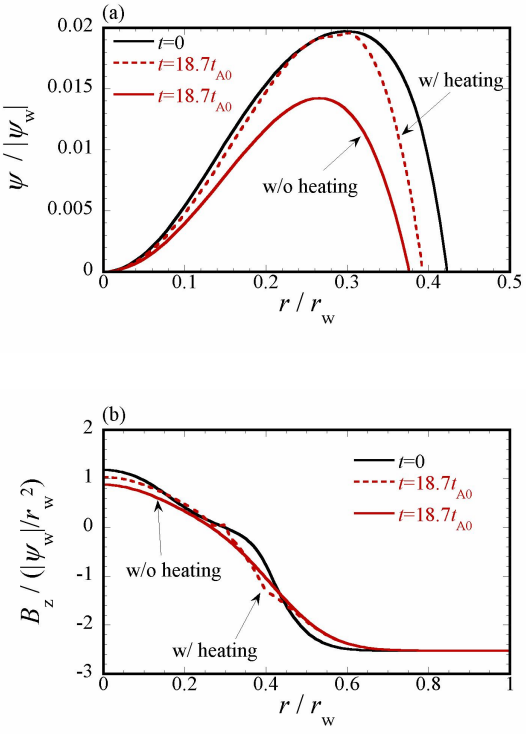

Fig.6 The midplane (z=0) profiles of (a) the magnetic flux function and (b) the magnetic field. The black solid lines indicate the initial profiles.

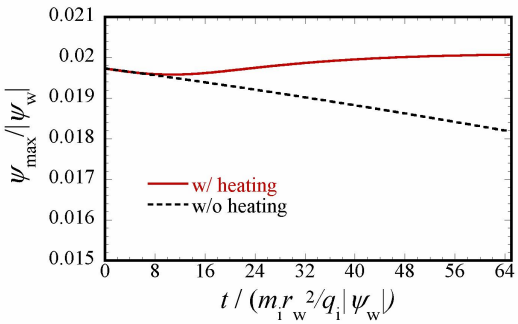

Fig.7 Time evolution of the maximum trapped flux. The red solid line shows flux supply by the electron heat generation. The flux decays resistively for the case of the black solid line.

4. Summary

Electron heat generation by tangential neutral beam injection into a field-reversed configuration has been calculated numerically. The heat generation has been found near the field-null point.

Taking into account the electron thermal force, we have shown the possibility of the FRC flux supply by the electron heating. Numerical results evidently show sustainment of the magnetic flux, when the heat generation is present.

From our result, not only NBI but also such as the electron cyclotron wave heating is also possible method to drive the diamagnetic plasma current.

References

[1] T. Takahashi *et al*., J. Plasma Fusion Res. **81**, 421 (2005).
[2] S. I. Braginskii, *Transport Properties in a Plasma,* in Review of Plasma Physics, M.A. Leontovish (ed.), Consultants Bureau, vol. 1, p. 216 (1965).
[3] T. Asai *et al*., Phys. Plasmas **7**, 2294 (2000).
[4] T. Asai *et al*., Phys. Plasmas **10**, 3608 (2003).
[5] T. Takahashi *et al*. Phys. Plasmas **11**, 3131 (2003).
[6] T. Takahashi *et al*. Phys. Plasmas **11**, 3801 (2003).
[7] C. K. Birdsall and A. B. Langdon, in *Plasma Physics via Computer Simulation* (Institute of Physics Publishing, Bristol and Philadelphia, 1991).

Proceedings of ITC18,2008

2nd Harmonic ECCD experiment using 84 GHz EC-wave in LHD

Yasuo YOSHIMURA, Shin KUBO, Takashi SHIMOZUMA, Hiroe IGAMI, Hiromi TAKAHASHI, Ryosuke IKEDA, Namiko TAMURA[a], Katsumi IDA, Mikirou YOSHINUMA, Yasuhiko TAKEIRI, Katsunori IKEDA, Satoru SAKAKIBARA, Kenji TANAKA, Kazumichi NARIHARA, Kazunobu NAGASAKI[b], Takashi MUTOH and Akio KOMORI

National Institute for Fusion Science, 322-6 Oroshi-cho, Toki 509-5292, Japan
[a] Dept. of Energy Science and Technology, Nagoya Univ., Nagoya 464-8463, Japan
[b] Institute of Advanced Energy, Kyoto University, Uji 611-0011, Japan

Second harmonic electron cyclotron current drive (ECCD) experiments were performed in Large Helical Device (LHD) to investigate the characteristics of the EC-driven current and its profile, and to investigate the possibility of controlling the current and rotational transform profiles by ECCD. By a scanning of EC-wave beam direction, a systematic change of plasma current is observed, and the direction of the plasma current is reversed by a reversal of the beam direction. Motional Stark Effect (MSE) measurement revealed tentative behavior of plasma current profile. At the early phase of ECCD, the EC driven current at the plasma core is mostly cancelled by counter current driven by an inductive electromagnetic force. It takes a few seconds for the inductive electromagnetic force to disappear, and the total plasma current gradually approaches to a constant value.

Keywords: ECCD, current profile, rotational transform, MSE, LHD

1. Introduction

Electron cyclotron current drive (ECCD) is an attractive tool to control plasmas. Using well-focused EC-wave beam, plasma current can be driven locally so that ECCD can control the profiles of plasma current and rotational transform which affect the magnetohydro-dynamics (MHD) activities [1-3]. In tokamak-type plasma confining devices, the effectiveness of ECCD on stabilization of neoclassical tearing mode (NTM) which is one of the harmful MHD activities has been demonstrated by driving current within the magnetic island [4]. Moreover, ECCD can be available for supporting ohmic plasma current startup in tokamaks.

Also for stellarators which do not need plasma current for plasma confinement, the capability of current profile control is effective for fine plasma control. In the Wendelstein 7-AS stellarator, clear ECCD experiments have been carried out and the results were investigated precisely [5]. Also in Heliotron-J [6] and the compact helical system (CHS) [7,8], ECCD was successfully observed.

In this paper, results of ECCD experiment in the large helical device (LHD) are described. LHD and the system for ECCD experiment are briefly explained in Sec. 2. Section 3 describes some results obtained in ECCD experiment such as EC-wave beam direction scan and long pulse ECCD. In Sec. 4, time evolution of plasma current and future plan of ECCD experiment are discussed. Then, the content of this paper is summarized in Sec. 5.

2. LHD and the system for ECCD

The LHD is a helical device with the toroidal period number m = 10 and the polarity l = 2. The magnetic field structure with the rotational transform for plasma confinement is generated totally by the external superconducting coils such as a couple of helical coils and three pairs of poloidal coils [9]. The major radius, or, the position of magnetic axis R_{ax} of LHD plasma can be varied in a range from 3.42 m to 4.1 m. The averaged plasma minor radius is about 0.6 m, and the maximum magnetic field at the magnetic axis is about 3 T. Those values and characteristics of the magnetic field configuration such as rotational transform profile and magnetic field along magnetic axis are dependent on R_{ax}.

The magnetic fields along magnetic axis for 3 cases are plotted in Fig. 1 as functions of toroidal angle. In the case of R_{ax} = 3.75m, the magnetic field on magnetic axis is nearly constant, while with R_{ax} = 3.6 m or 3.9 m magnetic ripples of about 5 % exist. The ECCD experiments described in this paper were performed with the magnetic

author's e-mail: yoshimura.yasuo@lhd.nifs.ac.jp

configuration of R_{ax} = 3.75 m to minimize the effect of magnetic ripple on ECCD. The magnetic field on axis is 1.5 T, that is, the second harmonic resonance field for the frequency of 84 GHz.

The EC-wave beam injection systems of LHD furnish 2-dimensionally steerable mirror which enables the beam direction control. One of the beam injection systems which is used for ECCD experiment is composed of two inner-vessel mirrors. One of them focuses the EC-wave beam radiated from the waveguide inserted to LHD vacuum vessel as a circular Gaussian beam. The other plane mirror is used for changing the beam direction. The focused beam has a beam waist on the equatorial plane with a radius of 30 mm. The injection system is installed at the bottom port of LHD (1.5-L port), and the beam is injected from the low magnetic field side (LFS). The toroidal angle at the 1.5-L port is 0 (or 36) degrees.

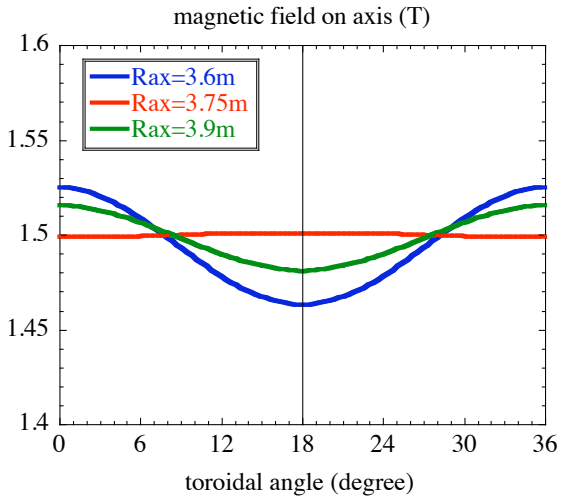

Fig. 1 Distributions of magnetic field along magnetic axis for the magnetic axis positions of 3.6, 3.75 and 3.9 m. With the magnetic axis position of 3.75 m, magnetic ripple is negligible so that trapping effect for electrons near the magnetic axis is minimized.

3. Results of ECCD experiment

The EC-wave beam direction was toroidally scanned keeping the beam aiming position on the magnetic axis. A schematic drawing to clarify the experimental configuration, definitions of EC-wave beam direction ($N_{//}$) and plasma current direction is seen in Fig. 2. $N_{//}$ is defined as a projection of beam unit vector on the toroidal direction.

The plasmas were generated and sustained only by the EC-wave power of 310 kW in the right-hand circular polarization for non-$N_{//}$ case, which is close to X-mode in the case of oblique injection. It has been confirmed that by an obliquely injected EC-wave beam with the left-hand circular polarization, plasmas can not be generated and can not be sustained effectively. The pulse length is limited to 600 ms due to operating duty cycle of used EC-wave power source (gyrotron). For $N_{//}$ = 0, that is, for normal injection case the polarization was set as linear X-mode.

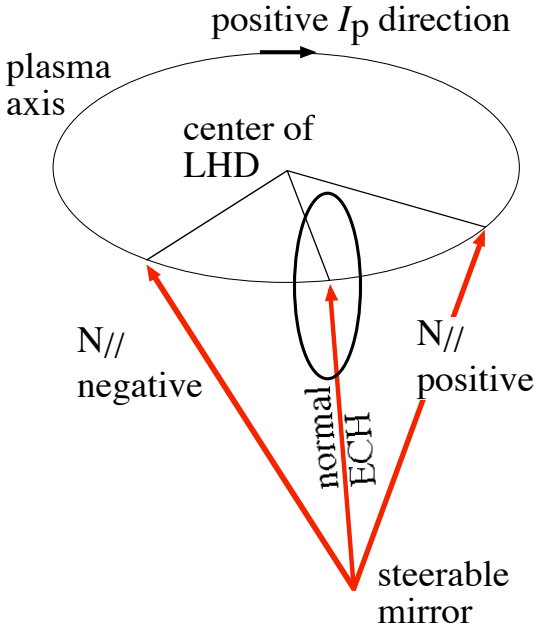

Fig. 2 A schematic drawing showing experimental configuration of EC-wave beam injection and definitions of directions of $N_{//}$ and plasma current.

During the beam direction scanning, electron density was kept at rather low density around 0.08×10^{19} m^{-3}. The plasma current at the end of plasma discharge is plotted against $N_{//}$ in Fig. 3. The total plasma current changes its direction according to the change of the sign of $N_{//}$, and the direction agrees with the theoretical prediction from the Fisch-Boozer theory [10] in the case of the beam injection from LFS. When the toroidal component of EC-wave beam is clockwise with negative $N_{//}$, (counter-clockwise with positive $N_{//}$), the current is driven counter-clockwise (clockwise). Here, the current direction of clockwise (counter-clockwise) is defined as positive (negative) direction.

The total plasma current shows negative and positive peaks against negative and positive variations of $N_{//}$, respectively. The peak values are about +- 1 kA. Though precise dependence of driven current on electron density has not been investigated, higher driven current with higher density can be expected. With the density of 0.5×10^{19} m^{-3} and with $N_{//}$ of 0.2, plasma currents of more than 3 kA by 600 ms pulse width were observed in other discharges. The density region lower than 0.1×10^{19} m^{-3}

might be too low to assure sufficient power absorption.

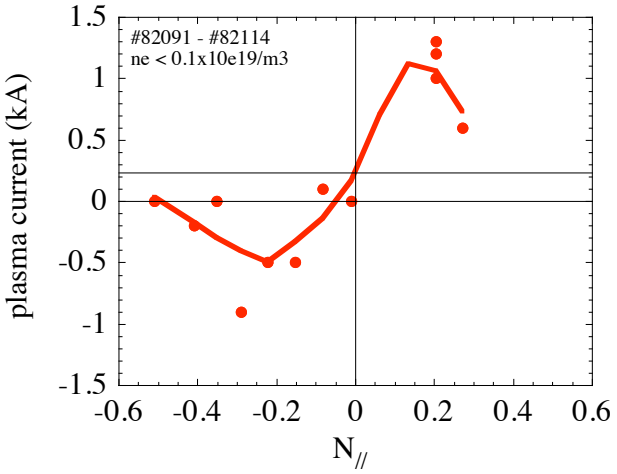

Fig. 3 Dependence of plasma current on EC-wave beam direction. $N_{//}$ is defined as a projection of beam unit vector on the toroidal direction.

Here it should be noted that during the 600 ms pulse width, the plasma current is continuously developing and is not saturated. Figure 4 shows waveforms of plasma current and electron density in a long pulse ECCD experiment done to investigate the long time evolution of plasma current. ECCD was performed with $N_{//}$ of -0.29, rather low EC-wave power of 100 kW and long pulse width of 10 s using a gyrotron which can be operated continuously. Plasma startup was supported by another EC-wave power of 300 ms and the plasma was sustained with the 100 kW EC-wave power for ECCD.

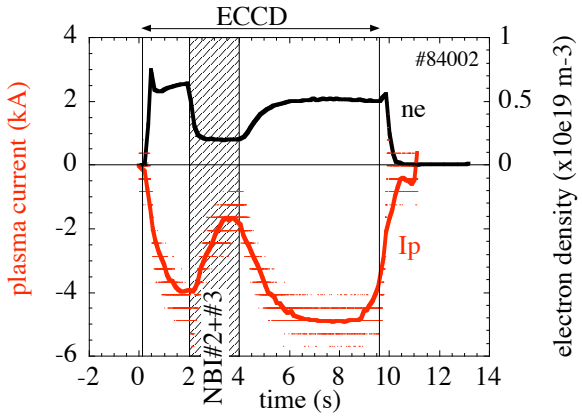

Fig. 4 Time evolution of plasma current and electron density in 100 kW, 10 s ECCD experiment.

Excluding the perturbation by the neutral beam injection (NBI) from 2 to 4 s, it is seen that it takes a few seconds for plasma current to saturate, and the saturated value is about -5 kA. In this case, an ECCD efficiency γ defined using electron density n_e, major radius R, plasma current I_p and absorbed power P_{abs} is evaluated as

$$\gamma = n_e R I_p / P_{abs} = 9\text{x}10^{17}\ \text{A/Wm}^2.$$

This value is comparable to that obtained in Wendelstein 7-AS [5].

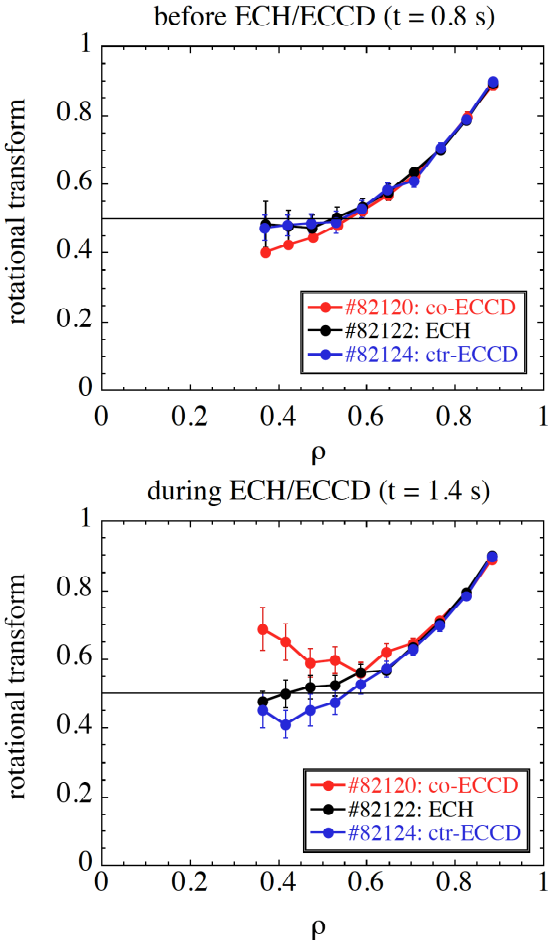

Fig. 5 Distributions of rotational transform measured with MSE measurement for the cases of co-ECCD, counter-ECCD and ECH just before applying ECCD/ECH (0.8 s) and during ECCD/ECH (1.4 s).

Setting the $N_{//}$ values at the optimum ones for ECCD ($N_{//}$ = 0.27 for co-ECCD and $N_{//}$ = -0.29 for counter-ECCD, respectively) and at zero for ECH, distribution of the rotational transform was measured with the motional stark effect (MSE) measurement. The MSE measurement needs NBI. The plasmas were generated and sustained with the NBI power injected from 0.5 s, and the EC-wave power of 370 kW, 600 ms was superposed on the plasma from 1.0 s

to 1.6 s. Just before the EC-wave power injection at 0.8 s, the distributions of the rotational transform in the cases of co-ECCD, counter-ECCD and ECH do not differ so much as seen in Fig. 5. On the other hand, during the superposition of ECCD and ECH at 1.4 s, the distribution of the rotational transform in the case of co- (counter-) ECCD shows significant increase (decrease) from that in the case of ECH at 1.4 s, or those at 0.8 s. The estimated driven currents inside the normalized radius of 0.5 which cause the changes in the rotational transform are more than 10 kA. From this result of MSE measurement, possibility of the control of rotational transform profile by ECCD was proved. Especially, removing of rational surface of 0.5 would be effective for suppression of MHD activities concerning with the existence of the rational surface.

4. Discussion and future plan

In Fig. 5, there is no significant change in rotational transform at the peripheral region, $\rho > 0.7$. It means that though an EC-driven current over 10 kA flows at core region, the EC-driven current is cancelled by a counter-flowing current so that the residual total current is not so much. The counter-current is caused by an inductive electromagnetic force. This is consistent with the fact that in the ECCD experiment with 600 ms pulse width and over 300 kW power, the total plasma current at the end of the discharge measured with a Rogowski coil surrounding the plasma is up to 4 kA. The counter-current should decay with a time constant of L/R (L: plasma inductance, R: plasma resistance here). Simply estimated L/R time for the plasmas in the ECCD experiment exceeds 10 s mainly due to large plasma volume of ~30 m^3 in LHD. So the estimated L/R time qualitatively agrees with the experimental observation of current ramp up time of 3-4 seconds as seen in Fig. 4 but not quantitatively. Precise estimation of L/R time in LHD would be needed.

To clarify the precise evolution of the rotational transform distribution, or, EC-driven current profile, MSE measurement for long pulse ECCD experiment of over 5 s with NBI is necessary. At LHD, construction of ECH system by introducing higher power (up to 0.8 MW for 10 s) gyrotrons with operating frequency of 77 GHz is undergoing [11]. By using new ECH system, higher driven current at higher density can be achievable, and then ECCD would contribute to improvement of plasma performance in LHD.

Also, to investigate characteristics and physics in ECCD for further application of ECCD, basic experiments which reveal the dependences of driven current on plasma density, absorbed EC-wave power, configuration of magnetic field and so on, should be performed.

5. Conclusions

In LHD, 2nd harmonic ECCD experiments were performed using 84 GHz EC-wave. So far, effective ECCD by scanning EC-wave beam direction was successfully observed. A long pulse ECCD experiment of 10 s indicated that the time constant of plasma current saturation is a few seconds. At the early phase of ECCD, counter-current caused by an inductive electromagnetic force exists and cancels the EC-driven current. To evaluate ECCD results and investigate ECCD physics precisely, long pulse ECCD experiment over a few seconds and MSE measurement for it is necessary. New high power, long pulse 77 GHz ECH system would enable the next ECCD experiment.

References

[1] V. Erckmann and U. Gasparino, Plasma Phys. Control. Fusion **36**, 1869 (1994).
[2] B. Lloyd, Plasma Phys. Control. Fusion **40**, A119 (1998).
[3] R. Prater, Phys. Plasmas **11**, 2349 (2004).
[4] H. Zohm *et al*., Nucl. Fusion **39**, 577 (1999).
[5] H. Maassberg *et al*., Plasma Phys. Control. Fusion **47**, 1137 (2005).
[6] K. Nagasaki *et al*., Proc. 22nd IAEA Fusion Energy Conference (2008) EX/P6-15
[7] Y. Yoshimura *et al*., Journal of Korean Physical Society **49**, S197 (2006).
[8] Y. Yoshimura *et al*., Fusion Science and Technology **53**, 54 (2008).
[9] O. Motojima *et al*. Phys. Plasmas **6**, 1843 (1999).
[10] N. J. Fisch and A. H. Boozer, Phys. Rev. Letters **45**, 720 (1980).
[11] H. Takahashi *et al*., to be published in Fusion Science and Technology

Proceedings of ITC18,2008

Optimisation of the magnetic field configuration for the negative ion source of ITER neutral beam injectors

Piero Agostinetti, Vanni Antoni, Marco Cavenago[a], Giuseppe Chitarin, Nicolò Marconato, Mauro Pavei, Nicola Pilan, Gianluigi Serianni, Piergiorgio Sonato

Consorzio RFX, EURATOM-ENEA Association, Corso Stati Uniti 4, I-35127 Padova, Italy

[a]*Laboratori Nazionali di Legnaro-Istituto Nazionale di Fisica Nucleare (LNL-INFN), Viale dell'Università 2, 35020 Legnaro (PD), Italy*

The negative ion source of the neutral beam injectors for ITER requires that the co-extracted electron current is not larger than the negative ion current. To this purpose a suitable magnetic field configuration was adopted, generated by a current flowing in the plasma grid and by two permanent magnets on either side of the source. In the present design of the system however the magnetic field lacks uniformity across the beam.

This paper focuses on strategies aimed at optimising the magnetic field distribution and improving the beam optics, based on two-dimensional magnetic simulations, including permanent magnets, ferromagnetic materials and electrical currents.

A careful distribution of the filter field current can provide a more efficient extraction of negative ions with respect to electrons. The use of ferromagnetic material can reduce the magnetic field downstream from the accelerator, resulting in lower beam deflection. The interference with the permanent magnets of ITER reference design is also discussed.

It is proposed that the path of the plasma grid current is divided between several conductors to minimise the stray field. Moreover, ferromagnetic material should be inserted in the grounded grid. It is shown that the proposed modifications reduce the magnetic field in the region downstream from the grounded grid, with the advantage of a smaller deflection of the beam.

The effect on electrons is discussed. However, a three-dimensional simulation will be necessary to address the issue of electrons as well as the vertical uniformity of the beam, taking into account the effects of finite extension of the permanent magnets, and optimising the return current path.

Keywords: ITER, heating and current drive, negative ion source, beam magnetic deflection, magnetic field computation, numerical computation

1. Introduction

The negative ion source of the neutral beam injectors for ITER requires that the co-extracted electron current is not larger than the negative ion current [1]. To reduce the number of extracted electrons, the reference design [2] is characterised by a magnetic field configuration generated by a current flowing in the plasma grid and by two permanent magnets on either side of the source [3]. In this configuration however the magnetic field is not uniform across the beam.

The present contribution focuses on strategies aimed at optimising the magnetic field distribution and improving the beam optics, based on two-dimensional magnetic field simulations. Specifically the following objectives will be pursued:

- uniformity of magnetic field in the beam source
- reduction of the axial component of the magnetic field in the ion source
- reduction of the horizontal magnetic field inside the accelerator
- reduction of the horizontal magnetic field downstream from the grounded grid.

Several magnetic field configurations have been considered, including the role of ferromagnetic material, suitable current distributions and permanent magnets; the overall aim is to obtain a more efficient and uniform extraction of negative ions with respect to electrons and to reduce the deflection of ions. The path of the filter field current is also carefully analysed to minimise the stray field.

In the following, the sources of the horizontal magnetic field will be introduced along with the numerical model developed in the ANSYS environment; then the results of the best cases will be presented; finally a comparison of the proposed solutions, in terms of $\int B\mathrm{d}l$

author's e-mail: gianluigi.serianni@igi.cnr.it

and particle trajectories, will be given.

2. Magnetic field sources

In the ITER beam source the magnetic configuration results from two different contributions, which can be considered separately in a first analysis. The so-called filter field principally lies on the horizontal plane and should be as parallel as possible to the grids in the region immediately upstream from the plasma grid (PG); it has the aim to reduce the electron current extracted through the plasma grid apertures by forcing the electrons to hit the PG or the source walls, due to their lower Larmour radius than the ions. A vertical magnetic field is generated around the extraction grid (EG) by permanent magnets embedded in the EG, with the purpose of deflecting the co-extracted electrons onto the EG.

The present paper is devoted to a two-dimensional investigation of the horizontal magnetic field; according to the ITER reference design, such field is generated by the current in the PG and by the permanent magnets,.

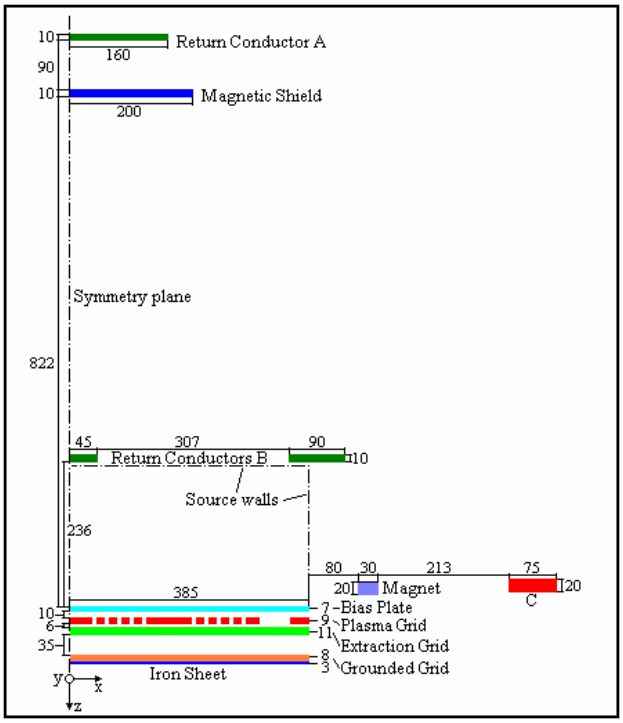

Fig.1 Geometry of the 2D ANSYS model; source walls are also indicated (RF driver not shown). The beam is along *z*; numbers indicate dimensions.

The possibility to improve the magnetic field profiles has been explored. A horizontal section of the ion accelerator was considered; thanks to the intrinsic symmetries, only half of the section has been modelled. The model is shown in Fig. 1: it comprises the area occupied by Bias Plate (BP), PG, EG and Grounded Grid (GG), at the bottom left of the picture; the filter field magnet, and another conductor at the bottom right. Also the conductor for the current return was considered, and different positions and configurations were tested; in the reference design the unique conductor for the return current is located on the back side of the device (Return Conductor A), behind a ferromagnetic shield. Because of the beamlet apertures and the cooling water manifold, the current flowing in the PG is characterised by a non uniform current density; so the PG has been modelled as a plate interrupted as many times as the holes. These "equivalent 2D holes" have a width which is given by the ratio between "vacuum" volume and solid volume, multiplied by grid length and divided by aperture number.

The configurations tested are (see Fig. 1):

a) reference case, comprising magnetic field due to the permanent magnets and to the 4 kA current flowing through the PG and the return conductors A;

b) current return as in a; filter magnets as in a; filter field current divided between the PG, 3 kA, and two guard conductors, labelled C in fig 1 (2x1.5 kA); 3 mm soft iron sheet inside the GG;

c) same as b, but return current divided in the three Return conductors B, located on the back side of the plasma source, between the RF drivers: central conductor carrying a 3 kA current; those in the side 1.5 kA each;

d) same as case c, without permanent magnets.

In cases b,c, and d the PG current is within the limits of the original specifications for ITER.

In Fig. 2 the magnetic flux lines in the ion accelerator for the four different cases are compared; the line density convention is not the same in the panels: it is easy to see from cases a through d that the density of magnetic flux lines outside of the accelerator is lower than in the plasma source and such difference is strongly enhanced by the soft iron in the GG (cases b,c,d). Moreover, in cases a and b, several magnetic flux lines connect the holes of the lateral beamlet group to the plasma located upstream from the central beamlet group, thus facilitating the co-extraction of electrons; in case c only some flux lines which come from the source sides enter some apertures, whereas in case d the flux lines which reach the holes come from the region between BP and PG where the plasma has a lower density. So case d should reduce the number of electrons extracted from PG. Moreover, eliminating the permanent magnets reduces the intensity of the magnetic field at the side of the PG, and so the magnetic-mirror effect for electrons.

3. Particle deflection

The main objectives of the present work are the reduction and the uniformity of the effect of the magnetic field on the trajectories of negative ions. Hence the various magnetic configurations have been compared in terms of the deflection of the particle trajectories.

As the beamlet trajectories are mainly along the z direction, the x component of the magnetic field, which is given by PG current and permanent magnets, generates a vertical deflection (along y).

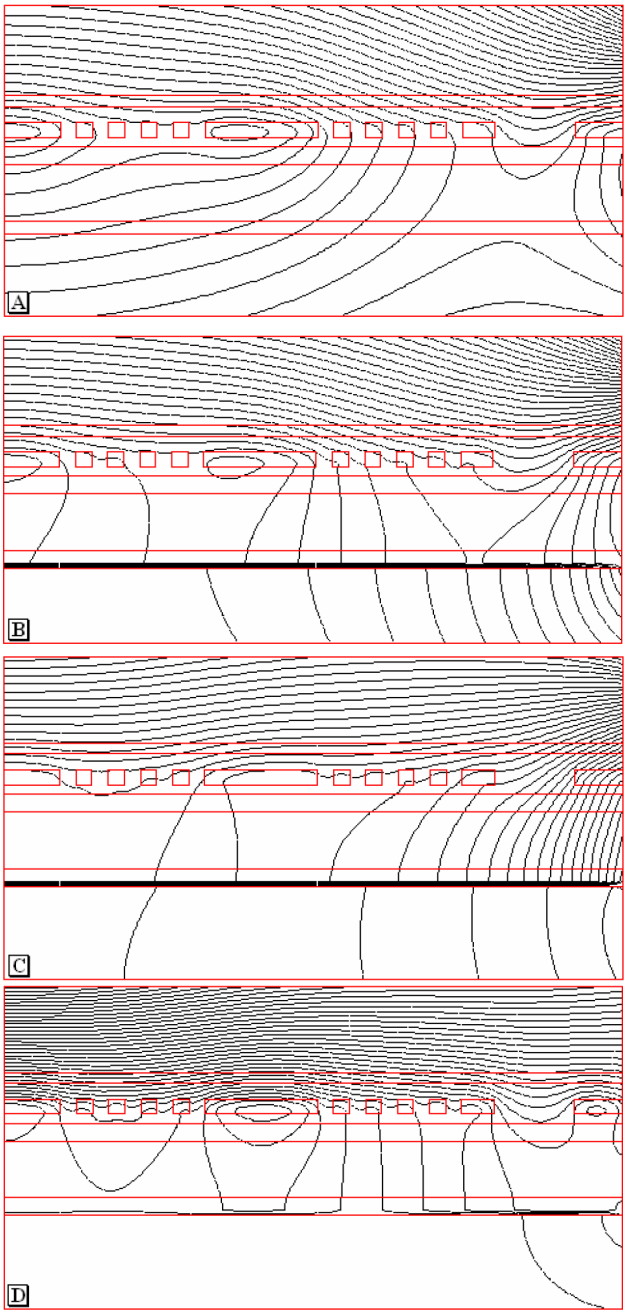

Fig.2: Magnetic flux lines for the four cases investigated. A discontinuity is produced by a 3 mm soft iron plate in the GG (cases b,c,d).

The vertical deflection angle, ϑ, can be defined, in the vertical plane, as the angle between the beamlet direction and the geometrical axis of the apertures. The vertical offset, defined as the vertical distance between beamlet centre and geometrical axis, is approximately proportional to the deflection angle for a given accelerator and position.

The code EAMCC (Version 3.1) [4] was used to calculate the beamlet trajectories inside the accelerator. Table 1 shows that the difference between the deflection angles calculated at the "Central" and "Lateral" positions, 18 mm downstream from the GG, is about 2 mrad with magnetic configuration a, about 1 mrad with configuration b, about 0.5 mrad with configuration c and about 0.2 mrad with configuration d.

	Deflection angle "Central" beamlet [mrad]	**Deflection angle "Lateral" beamlet [mrad]**	**Differential deflection between beamlets [mrad]**
Case a	-3	-1	2
Case b	+0.5	+1.5	1
Case c	+1.5	+2	0.5
Case d	+1	+0.8	0.2

Table 1: Deflection of "Central" and "Lateral" beamlets for the four cases investigated.

Hence, it is confirmed that the magnetic configuration d gives the best results in terms of deflection uniformity.

The evaluation of the vertical deflection of the beamlets by the EAMCC code is a time-consuming task when the computation must be carried out for a long distance downstream from the GG.

In the paraxial approximation, using conservation of energy along the particle path and neglecting the contribution of focusing gaps of the accelerator give the following approximation for the deflection:

$$\vartheta = \frac{q\int B_x(z)\,dz}{\sqrt{m^2 v_0^2 + 2qm(U_0 - U(z))}} \qquad (1)$$

where U is the electric potential on the z axis, U_0 its value at the extraction and v_0 the speed at the extraction. This integration has been numerically carried out along z in the paraxial approximation.

The results of the integrals are shown in Fig. 3 for all cases under investigation and 1 m downstream from the PG. It is clear that the vertical deflection of all beamlets has been greatly reduced with the proposed magnetic configuration, from around 20 mrad to about 0.5 mrad; moreover, the maximum difference among the beamlets

decreased from 5 mrad to 0.4 mrad.

The magnetic configuration of case d has already been implemented in the mechanical design of the beam source for SPIDER, the test facility for ITER ion source (Fig. 4). The two conductors for forward PG current are copper bars having a section of 100×15 mm^2 each and are connected in parallel to the PG at the top and bottom of the ion source.

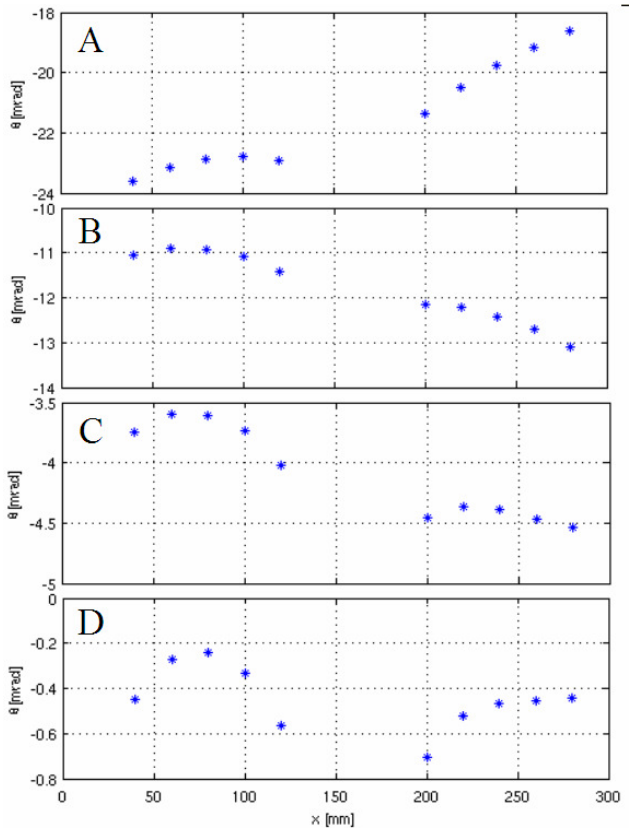

Fig. 3 Calculation of the deflection integral up 1 m downstream from the PG for each beamlet.

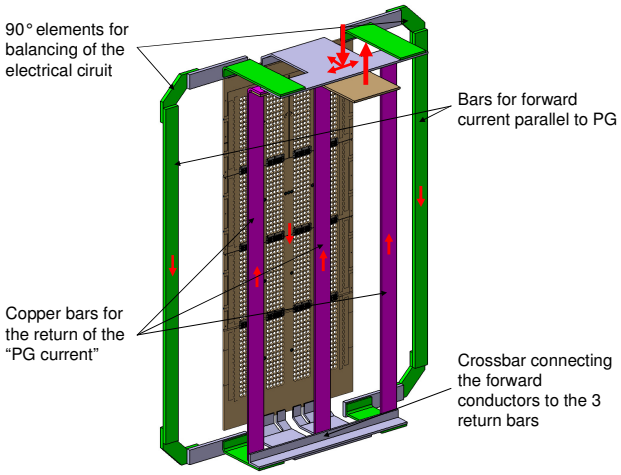

Fig. 4 Implementation of the electrical circuit in the beam source.

The sharing of the current flowing through the PG and the two parallel bars is accomplished by changing the resistance of the 90° elements that connect the two vertical straight bars at the top and bottom. At the bottom of the source the forward currents are connected through a crossbar to the three return bars. The return current is in fact distributed on three parallel copper bars (having a section of 90×10 mm^2 each) that are placed between the copper and the stainless-steel driver plates of the RF source and are insulated from them. At the top of the beam source all conductors are connected to the in-vacuum end of the power supply transmission line.

5 Conclusions

The configuration proposed in the present work represents a major improvement in terms of the reduction of the vertical deflection of beamlets. The final deflection is in the range of 1 mrad for all beamlet groups.

The best solution seems case d, which requires that forward and return currents are split in three conductors, and the return current paths are located within the driver plate; no permanent magnets are required, which makes the magnetic configuration more flexible and fully controlled from the outside.

3D computations are on-going, in order to assess the vertical uniformity of the configuration, including the realistic path of the current at the edges. The proposed configuration heavily affects the behaviour of electrons after the GG: since the magnetic field is greatly reduced, electrons can reach far away downstream. The 3D model will address the effect of the proposed magnetic configuration on electrons; it will also allow the analysis of the horizontal deflection of beamlets.

Acknowledgments

This work was supported by the European Communities under the Contract of Association between EURATOM and ENEA. The views and opinions expressed herein do not necessarily reflect those of the European Commission.

References

[1] R.S. Hemsworth *et al.*, Rev. Sci. Instrum. **79**, 02C109 (2008).
[2] ITER Technical Basis 2002, "Neutral beam heating & current drive (NB H&CD) system", Detailed Design Document (section 5.3 DDD5.3) (Vienna: IAEA)
[3] R.S. Hemsworth, *et al.*, Rev. Sci. Instrum. **67**, 1120 (1996)
[4] G. Fubiani *et al.*, Phys. Rev. STAB **11**, 014202 (2008)

Proceedings of ITC18, 2008

Fast wave electron heating experiments focusing on competition between damping mechanisms on Large Helical Device

Takuya Oosako[1)], Hiroshi Kasahara[2)], Yuichi Takase[1)], Kenji Saito[2)], Tetsuo Seki[2)], Ryuhei Kumazawa[2)] and Takashi Mutoh[2)]

[1)]*Graduate School of Frontier Sciences, The University of Tokyo, Transdisciplinary Science Bldg. 413, Kashiwanoha 5-1-5, Kashiwa 277-8561, Japan*

[2)]*National Institute for Fusion Science,322-6 Oroshi-cho, Toki 509-5292, Japan*

Fast Wave electron heating experiments were performed in Large Helical Device. In this experiment, magnetic fields B = 1.5 T and 1.86 T were used. Electron cyclotron emission using modulation techniques of FW injection indicated central electron heating in the 1.5T case with electron cyclotron (EC) and neutral beam (NB). In the 1.86 T case, there was no evidence of direct electron heating. Energetic ions were observed during FW heating of the NB preheated plasma.

Keywords: helical/stellarator configuration, Fast Wave

1 Introduction

The fast wave (FW) can be used for electron heating and current drive in high density, high beta plasmas. FW experiments have been investigated in tokamaks [1-3], and there are many challenging works in helical devices. For a helical demo reactor with very high plasma density (10^{22} m^{-3}), core plasma heating (e.g., by NBI) is key issue. FW is useful for heating the plasma to ignition, because0 there is no high density accessibility limit. Since ion cyclotron heating often creates high energy ions that can damage the antenna and the vacuum vessel, FW electron heating is desirable. In Large Helical Device [4], initial FW electron heating experiments were performed successfully [5]. At high harmonics of ion cyclotron frequency, electron Landau damping (ELD) and magnetic pumping (MP) can dominate over ion cyclotron harmonic damping [6]. However if harmonic number is relative small, there is competition between damping mechanisms. Researching this competition is same issue in toroidal deveice (tokamak and helical). In this experiment, magnetic fields B = 1.5 T and 1.86 T were used. By using this magnetic field, FW run across 2nd, 3rd, 4th, 5th ion cyclotron resonance layer. In the present paper, details of the magnetic configuration is described in Sec. 2. Section 3 describes experimental results. Section 4 is denoted to discussion, and the results are summarized in Sec 5.

2 Locations of electron/ion cyclotron resonance layer

Since the LHD antenna [7] is not arrayed, the $k_{\parallel}$ (wavenumber parallel to the magnetic field) spectrum is broad and centered around zero.For effective Landau damping, $\omega/(k_{\parallel}v_{\rm the}) \cong O(1)$, high electronn temperature is needed. Here ω is the FW angular frequency and $v_{\rm the}$ is the electron thermal velocity. The experiments were conducted under 2 conditions with different magnetic field strength (B=1.5T and 1.86T). Figure 1 shows the layers of cyclotron resonance. In this calculation, $n_{\rm e0} = 3.0 \times 10^{19}{\rm m}^{-3}$ and the wavenumber parallel to the magnetic field line $k_z = 5{\rm m}^{-1}$ are used.In the 1.5 T case, the elenctron second cyclotron resonance layer crosses the magnetic axis, so pre-electron heating is desirable. FW would be coupled with high energy electrons. And the hydrogen second harmonic cyclotron resonance ($2\Omega_{\rm H}$) layer exists around $\rho = 0.5$. There is competition between CD (cyclotron damping) and ELD/MP. In the 1.86 T case, the $2\Omega_{\rm H}$ layer exists around $\rho = 0.9$. If cyclotron damping is week, FW wold be absorbed by electrons.

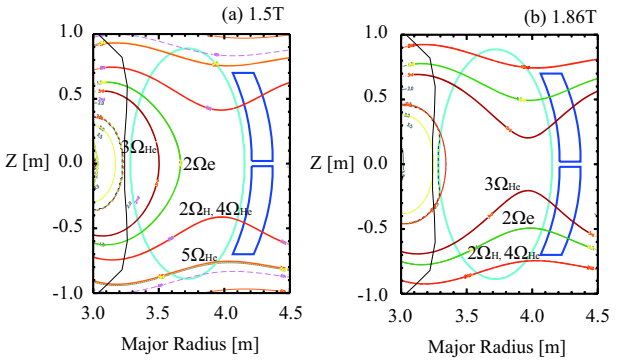

Fig. 1 Cyclotron resonance layers in the case of B = 1.5T (a) and 1.8T (b).

author's e-mail: oosako@fusion.k.u-tokyo.ac.jp

3 Experimental results

3.1 EC electron heating and the high energy ion tail by FW

Figure 2 shows electron temperature profile before and after EC injection in both cases. Horizontal axis indicates Major radius. Electron temperature is measured by Thomson scattering. Bulk electron temperature around plasma center is increased in 1.5T case. In 1.86T case, Electron heating is weak, and there is not clear difference of electron temperature profile between before and after. Figure san shows the time evolution of a FW heating discharge. The electron density was measured with a FIR interferometer, the radiation power was measured with a bolometer, and loading shows coupling between FW and plasma. In this shot, IC power up to 1MW was injected into hydrogen plasma with line integrated densities of $2 \times 10^{19}\mathrm{m}^{-3}$.

The ion energy distribution in the discharge of figure 3 is described in Fig. 4. Plots is the count number of neutral particles for 0.1 s. Label indicates start time of measurements in the discharge of figure san. High energy ion tail were observed in both cases. It might be caused by cyclotron damping (2nd Ω_H). There are high energy ion tail above 120 eV in 1.5T case. On the other hand, no energetic ion was observed in 1.86T case. Ion cyclotron resonant layer in 1.5T case is closer to the plasma center than in 1.86T case, so IC power was absorbed by cyclotron damping in 1.5T case. In both cases, no energetic ions were observed (ne $\sim 3.0 \times 10^{19}\mathrm{m}^{-2}$).

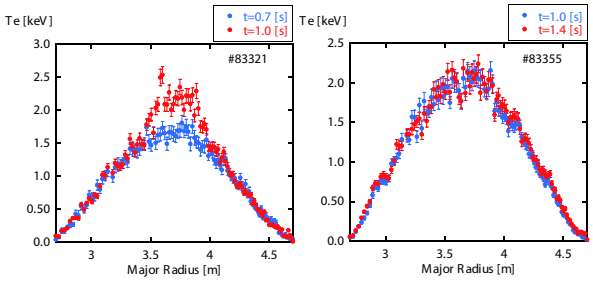

Fig. 2 Te profile measured by Tomson scattering. (a) 1.5T case and (b) 1.86T case.

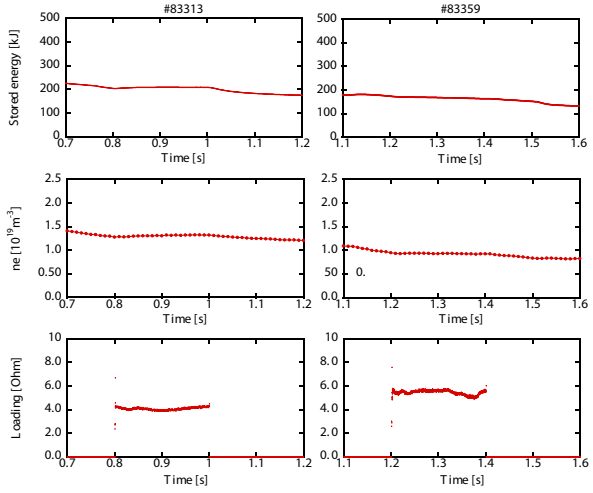

Fig. 3 Time evolution of plasma parameters in hydrogen plasma discharge. (a) -1.5T (b) -1.86T. FW are launched for 0.2 s.

3.2 Power modulation experiments

Power modulation experiments were also performed to calculate FW damping profile. Plasma heating profile using FFT analysis are described in Fig. 5 and Fig. 6. Horizontal axis denotes normalized minor radius. In this calculation, ECE signal component synchronizing RF on/off frequency is derived. In these heating phase, stored energy is $\sim$ 400 kJ and electron density is $3 \times 10^{19}\mathrm{m}^{-3}$, and electron temperature in B = -1.86T is lower than Te in B = -1.5T ($f_{\mathrm{ICH}} \sim$ 10 Hz). Clear central heating is achieved when central electron temperature is high using ECH in -1.5T case.

In -1.86T, phase differences are not changed in each heating phase, and plasma heating position is approximately same, and those are at plasma edge ($\rho \sim 0.8, 0.9$). 2nd ion cyclotron damping is strong candidate in each heating because slowing down time is not much difference and effective heated position is very close to 2nd ion cyclotron resonances.

3.3 Plasma loading

Figure 7 shows that antenna loading comparison between two magnetic field. In this shot, electron density gradually increased by usin gas puffing and electron densities are similar to each discharges. However the characteristics of antenna loading are much different. In spite of increasing electron density, loading decreased. In 1.5T case, antenna loading is gradually decreased and that loading is stable. However, in 1.86T case, antenna loading is drastically changed during FW injection and there are eigen mode and RF injection is unstable.

4 Discussion

As described in Fig. 7, -1.5T case plasma is more suitable for FW injection than -1.86T case. Electron temperature change is conceivable as one the reason of this. Figure 8 shows that time evolution of the electron temperature at the center and edge of the plasma. Electron temperature Te is obviously decreased (from 2 keV to 1.5 keV), and decreasing ratio of the Te is similar at center and edge (-1.5T). There is no difference of Te between t = 0.5s and t = 1.5 s, and Te is kept constant ($\sim$ 2 keV) or very weakly decreased (-1.86T). ELD and TTMP is strongly related to electron beta be, and high Te is required for wave damping through ELD and TTMP when the be has a few %.

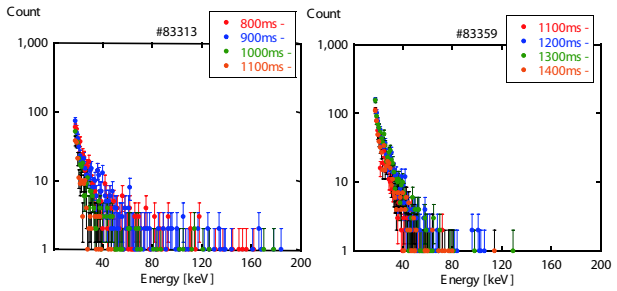

Fig. 4 Temporal change of the ion energy distribution in the discharge of Figure 3.

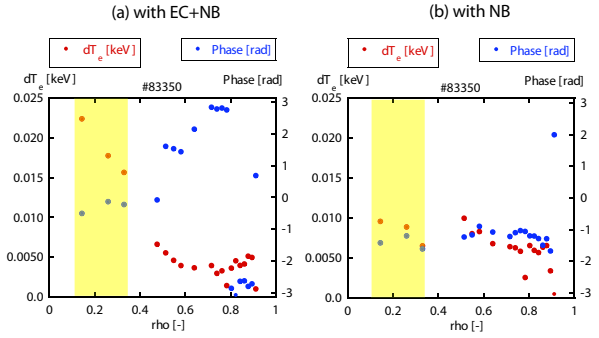

Fig. 5 FW deposition profile in the case of -1.5T. (a)with EC + NB (b)with NB.

5 Conclusions

Comparing cyclotron damping with electron Landau damping (ELD) / transit time magnetic pumping (TTMP), the experiment with different cyclotron resonances (-1.5T, -1.86T) is tried on LHD. Ion acceleration is observed in -1.5T and -1.86T. In -1.5T case, and they are strongly related to electron densities. According to FFT analysis, heating position is much different in -1.5T and -1.86T, and there are no differences of phase delay with -1.86T in each heating phases. The characteristic of antenna loading is different in these ICRF resonances, and the antenna loading is fluctuated in B of -1.86T.

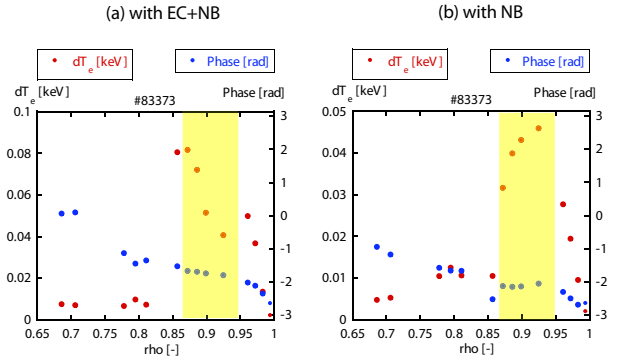

Fig. 6 FW deposition profile in the case of B = -1.86T. (a)with EC + NB (b)with NB

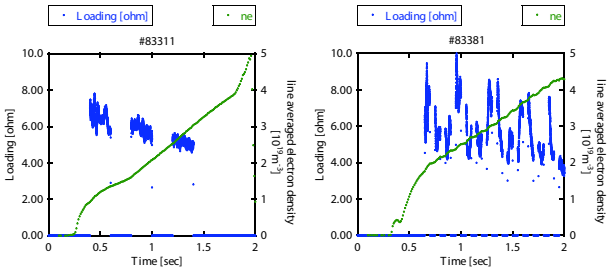

Fig. 7 Dynamic change of the plasma loading and line averaged electron density. Electron density increased by gas puffing.

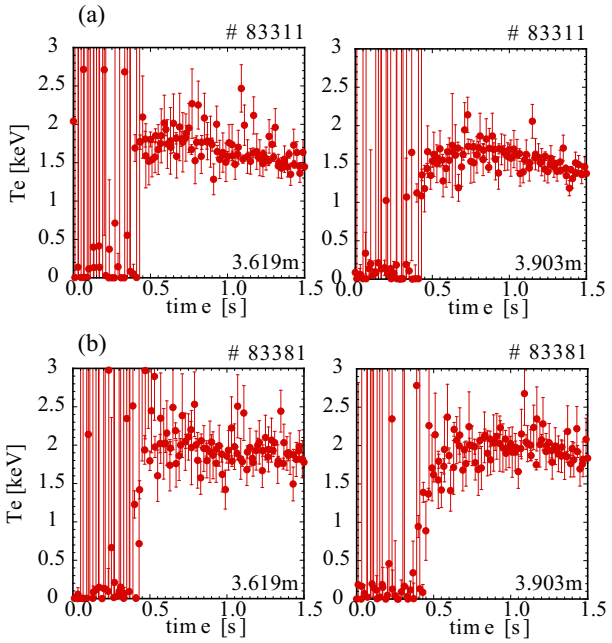

Fig. 8 Time evolution of electron temperature. (a)-1.5T (b)-1.86T.

[1] C. C. Petty, et al., *Proceedings of the 12th Topical Conference in Radio Frequency Power in Plasmas, Savannah, 1997* (American Institute of Physics, Woodbury), p. 225.
[2] L. Colas, et al., Nucl. Fusion **46** (2006) S500-S513.
[3] J. Hosea, et al., Phys. Plasmas **15**, 056104 (2008).
[4] O. Motojima, et al., Phys. Plasmas **6**, 1843 (1999).
[5] H. Kasahara, et al., J. Korean Phys. Soc. **49** (2006) 192-196.
[6] M ono, Phys. Plasmas **2**, 4075 (1995).
[7] H. Kasahara, et al., Fusion Eng. Des. **83** (2008) 253-255.

Proceedings of ITC18,2008

Commissioning the ICRF System and an ICRF Assisted Discharge Cleaning at the KSTAR

Jong-Gu Kwak, Son Jong Wang , Young-Dug Bae, Chul Kyu Hwang, Sung Kyu Kim

Korea Atomic Energy Research Institute, 1045 Daedeok-daero, Yuseong, Daejeon, Korea

KSTAR(Korean Superconducting Tokamak Advanced Research) is a national superconducting tokamak with the aim of high beta operation based on AT(Advanced Tokamak) scenarios, and ICRF(Ion Cyclotron Ranges of Frequency) heating is one of the essential tools to achieve this goal. The ICRF system also contributed to the first plasma experiments of KSTAR through discharge cleaning. The fabrication and HV(high voltage) test of the antenna and matching system were finished in 2006 and the installation of the antenna, matching system and the transmitter at the KSTAR site was completed in 2007. Antenna conditioning was carried out to improve the HV holding condition of the antenna installed on the KSTAR and to check on an EM(Electro-Magnetic) interference with other equipments such as the superconducting magnet monitoring system and other machine and/or plasma diagnostic systems. In this presentation, installation processes of the ICRF system (with an emphasis on the quality assurance procedures of KSTAR), as well as the results from the first RF discharge experiment for a discharge cleaning in and FWEH(Fast Wave Electron Heating) experiment for KSTAR 1st experimental campaign are outlined.

Keywords: KSTAR, ICRF, transmitter, antenna, cleaning

1. Introduction

KSTAR is a Korean national superconducting tokamak aiming at a high beta operation based on AT scenarios, and ICRF is one of the essential tools to achieve this goal.[1] The ICRF system also contributes to the first plasma experiments of KSTAR through discharge cleaning and assisting the discharge startup.

The fabrication and HV test of the antenna and matching system were finished in 2006 and final installation of the antenna, matching system and the transmitter at the KSTAR site was completed in 2007.[2][3] In this presentation, installation processes of the ICRF system including the transmitter (with an emphasis on the quality assurance procedures of KSTAR), as well as the results from the first RF discharge experiment for the discharge cleaning and ICRF experiments in KSTAR, are outlined.

2. Antenna and tuning system

The installed antenna consists of four straps, however, two straps are fed via RDL(Resonant Double Loop) and tuners for the KSTAR 1st experimental campaign. The Faraday shield profile of the installed antenna fits the magnetic surface of the separatrix in the standard diverted plasmas of the KSTAR as shown in Fig.1. The antenna is protected at its sides by two poloidal limiters covered with graphite tiles which intrude into the plasma past the shield by 5 cm. The RF output from the transmitter is fed into two tuners via one coaxial transmission line whose total length is about 80 m. The impedance matching is done by adjusting the two liquid stub-tuners whose matching conditions are checked with a network analyzer. Presently it is tuned at 30 MHz but it could be adjusted to other frequencies by changing the length of the U-link at the resonant loop and the tuning position of the tuners. The tuning position at the ICRF-DC(Discharge Cleaning) is the same as that for a vacuum antenna conditioning. This means that antenna loading resistance is very small at the ICRF-DC.

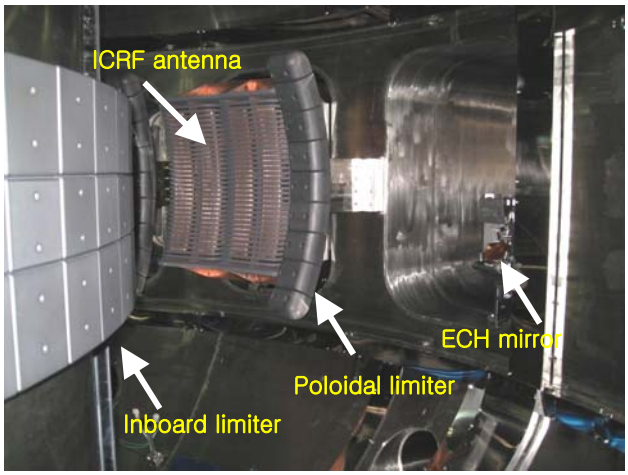

Fig.1. Invessel components and ICRF antenna

author's e-mail: jgkwak@kaeri.re.kr

Unexpected voltage rise is the most harmful or probable event for the ICRF system. The RF voltage exceeding a certain limit (~35 kV for 9-3/16" transmission line) may destroy the RF components. High VSWR, which can be expressed by maximum and minimum RF voltages, also degrades the performance of a transmitter. This event can be caused by a variation of the loading resistance due to the edge plasma fluctuation including an abrupt plasma termination or arcing in the transmission line. To protect the system, three independent methods are provided. The first is a self protection of the transmitter. High VSWR detected at the output of the transmitter cuts the RF input of the transmitter within tens of μs. The input is recovered delayed by several ms automatically. The second is an over voltage protection. If one of the four voltages measured at the resonant loops exceeds a preset value, the input of the transmitter is disconnected within μs. The disconnection will not be automatically recovered and recorded as ICRF fault. The third method is activated by central PCS. When the PCS detects a fault in which the PCS gives up control of the plasma discharge, it activates a no-go signal of the ICRF. The three methods were operated successfully for the first campaign of the KSTAR ICRF.

The functions of the ICRF control and data acquisition system are realized by using six independent digital signal processor (DSP) modules with customized peripheral boards. The number of channels(ADC-18, DAC-4, DIN-16, DOUT-8) for the board is thought to be enough for a specific function. The C codes written in each DSP do not exceed several hundred lines so that their maintenance is relatively simplified. The DSPs are basically connected by local a TCP/IP network which is disconnected to the outer world. Through this network, control and monitor signals which are not sensitive to the sampling time are transferred in a near realtime. At the end of a tokamak shot, the sampled arrays are collected through the same network. The governing controller of this network is made of a single PC with a Linux operating system equipped with a EPICS input/output controller (IOC). Because the most time-demanding functions are reserved to the DSPs, the CPU usage of the PC was less than 10 %.

For a few fast communications, such as an internal interlock or trigger, a optical fiber was connected between the DIN/DOUT of DSPs. The governing PC only knows the post-event for the monitoring purpose.

2. Commissioning the 2 MW transmitter

The ICRF heating and current drive scenario for the KSTAR eventually requires 4 units of 2 MW transmitters with a frequency range from 25 to 60 MHz for achieving final goal. The first KSTAR transmitter is a modified FMIT(Fusion Material Irradiation Test) transmitter consisting of four amplifier stages. Its frequency range is from 30 to 60 MHz and it is planned that a frequency band below 30 MHz is covered by modifying an existing cavity or manufacturing a new cavity. An amplitude-modulated 1mW frequency source drives a 500 watt solid state wideband amplifier, which in turn drives three tuned triode/tetrode amplifier stages. The tube employed in the final power amplifier is a 4CM2500KG tetrode fabricated by CPI(Communications & Power Industries). The anode power supply is a simple rectifier with an ignitron crowbar . After a fabrication of the cavity and power supply was completed in 2004, several failures of the tube during a factory and a site acceptance test occurred before eventually achieving 1.9 MW for 300 s at 33 MHz in 2007. Finally, we also succeeded in achieving 1.9 MW at 45 MHz and 1.8 MW at 60 MHz which is an upper frequency band of the transmitter. The electrical efficiency of the FPA(Final Power Amplifier) is about 70 %. It is well known that the rf power of the tetrode is decreased as the frequency is increased and a stable power generation at high frequency is one of the critical issues for the ITER ICRF system. So this is a very encouraging result for the development of an ICRF transmitter for the ITER. Fig.2 shows the achieved rf power vs. the frequency.

3. ICRF-DC and ICRF experiments

The vessel consists of SUS316 and inboard is partly covered by three rows Graphite tiles. The poloidal limiter is installed at the antenna side to protect the ICRF antenna module and to limit the outer plasma boundary. The material of the poloidal limiter is Graphite. The notable point is that the front surface of the ICRF antenna is coated by B4C. The coating thickness is about 100 um. ECH mirror and some diagnostic windows are located very far from the poloidal limiter and they are also protected by a shutter for a non-used period.

The vacuum vessel mainly comprises of a main vessel, a pumping duct, a long viewport duct, which has 100 m^2 of a total surface area without a port and 100 m^3 of an inner volume including a port. The main pumping unit is composed of eight turbo molecular pumps (TMP) and two cryo-pump systems. Pumping capacities of each TMP and the cryo-pumps are 2,800 liter/s and 10,000 liter/s, respectively. A differential pumped RGA is installed at the end of the pumping duct for measurements of the partial pressures and the RGA partial pressure is calibrated by a comparison with the pressure gauge. The diagnostics for a discharge

cleaning is a differential pumped RGA attached to a pumping duct and a cold cathode and a hot cathode gauge attached to the vessel and the pumping duct respectively. To analyze the discharge characteristics, a microwave interferometer, Bremsstahlung, H-alphas and a TV camera were used.

GDC was performed over-night after a daily tokamak shot and early morning before a tokamak shot. Pure hydrogen discharge was used for the initial 1 hour followed by a He discharge for removing the hydrogen attached to the vessel during the H discharge. The partial pressures of the hydrogen, water, nitrogen and carbon compounds were increased during the He-GDC as shown in Fig.3. ICRF assisted DC was used between the tokamak shots and it lasted for around 10 min. The injected RF power was limited to 30 kW by the high voltage on the transmission line and the antenna from a low antenna loading resistance and the pulse duration was restricted by no water cooling to the antenna straps and the Faraday shield. The operational pressure region was from 10-3 to 10-4 mbar for the He and H discharges. The B_{TF} was varied from 0.5 to 1.4 T. The antenna loading resistance was slightly increased and the plasma density was decreased as the B_{TF} was increased. Depending on the B_{TF} and RF frequency, a selective heating between an ion and an electron could be implemented. Whereas the plasma density was decreased at the flap top region for a successive shot when we applied the ICRF-DC at around shot #900, there is no change in the plasma density regardless of the ICRF-DC. Only the H_2 partial pressure was changed for the ICRF-DC and the calculated H_2 removal rate was about 3.6 Pa-m^3/h. This is less effective than the other machine results. More systematic study on a discharge cleaning with a more refined RGA system is necessary for the next campaign.

The first ICRF experiment was tried using the FWEH heating mode at 1.5 T of B_{TF} . The frequency is 30 MHz and two resonant loops are used. RF power up to 150 kW is delivered to the plasma as shown in Fig 4. The line intensity of C-III and VB is increased during the ICRF pulse, however no changes in Te and Wdia are observed during this pulse. In order to increase the ICRF coupling, we intentionally moved the plasma column closer to the antenna, however, the heating effect is not clear. The front antenna surface is a D-shape however, the first KSTAR plasma is a circular shape and the distance between the antenna and limiter is a little bit longer(5 cm) so that the RF coupling is very low. We expect the heating effect to be clear for the next campaign by upgrade the following things such as using a minority heating mode, shortening the distance between the antenna and the poloidal limiter.

4. Inspection on the antenna after the campaign

After the experimental campaign, the internal structure of the vacuum vessel including the ICRF antenna was inspected for a post-mortem analysis and it was found that some parts of the antenna structure including the poloidal limiter are covered by an unknown material. The non transparent area of the current strap behind the faraday shield is also coated by unknown material as shown in Fig 5(a) and poloidal limiter adjacent to the ICRF antenna is also covered as shown in Fig 5(b). Only the front surface was coated by B_4C and the deposited area is easily removed by sand paper and revealed cooper color. Deposited area of the side surface of the poloidal limiter has a configuration of the antenna shape.

5. Summary

Since 1996, the KSTAR ICRF system has been designed and fabricated and it was finally installed at the KSTAR site in 2007. Finally it contributed to a successful first plasma generation in 2008 via the ICRF-DC. In addition, up to a 150 kW rf power was coupled to the 1st plasma with the FWEH mode. Based on the first experimental campaign, we expect the ion heating to be better for the next campaign by shortening the antenna plasma distance and a using minority heating mode.

References

[1] Lee G.S., et al., Nuclear Fusion 40 (2000) 575.

[2] Bae, Y.D., et al., Nuclear Fusion 43 (2003) 805.

[3] Kwak, J.G., et al., Nuclear Fusion 47 (2007) 463.

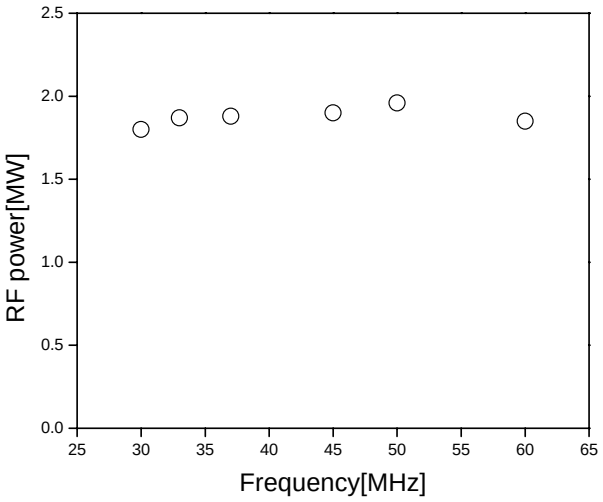

Fig.2. RF power vs. frequency

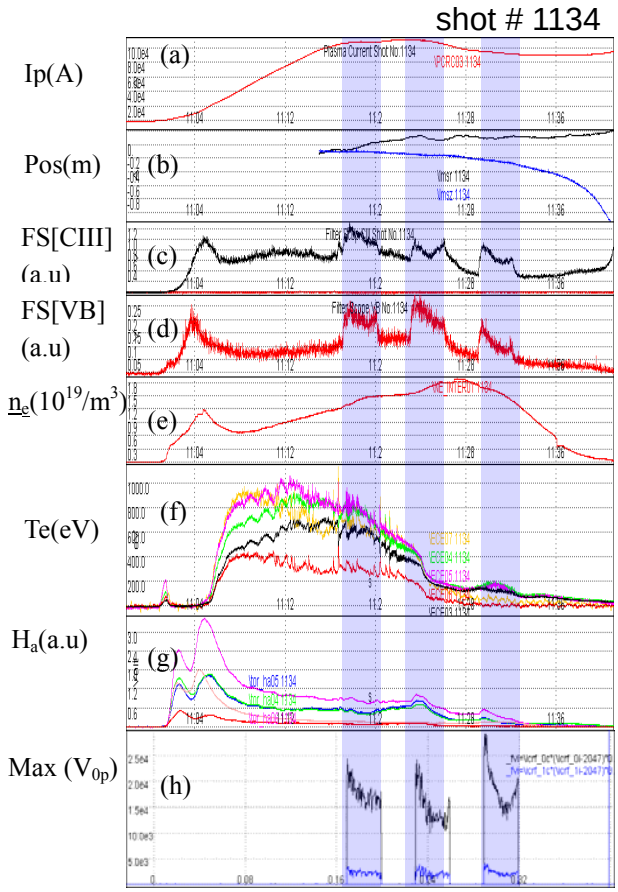

Fig.4. Time evolution of plasma current(a), plasma position(b), impurity(C-III)(c), Bremsstahlung (d), plasma density(e), Te by ECE(f), H-α(g) and Max. voltage on the antenna(h).

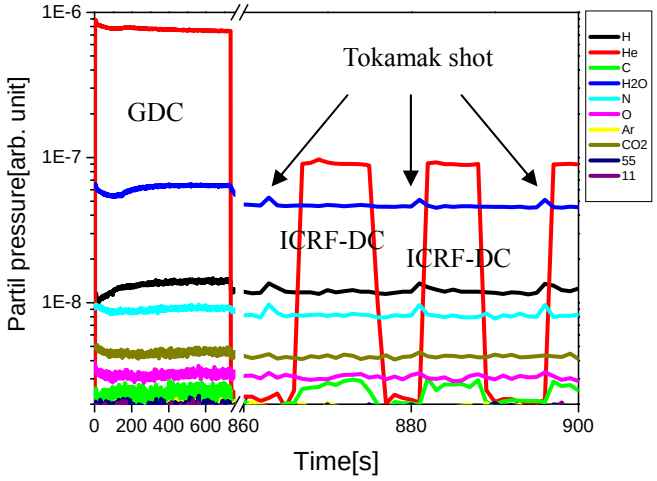

Fig.3. Time evolution of GDC and ICRF-DC

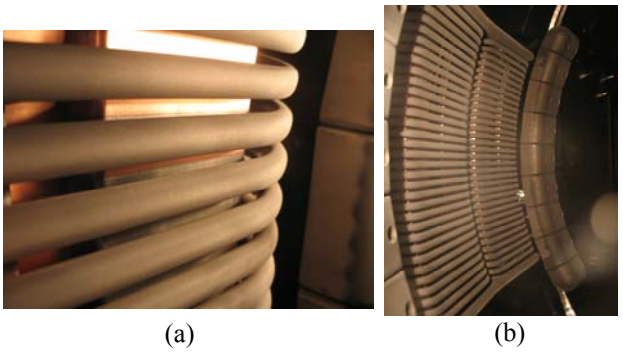

(a) (b)

Fig 5. Deposited area of antenna and poloidal limiter

Proceedings of ITC18, 2008

Behavior of high-pressure gasses injected to vacuum through a fast solenoid valve for supersonic cluster beam injection

Akiyoshi MURAKAMI, Junichi MIYAZAWA,[1)] Takanori MURASE,[1)] Koji YASUI,[1)]
Hayato TSUCHIYA,[1)] Tomohiro MORISAKI[1)], Nari TSUTAGAWA[2)], and Hiroshi YAMADA[1)]

The Graduate University for Advanced Studies, 322-6 Oroshi-cho, Toki 509-5292, Japan

[1)]*National Institute for Fusion Science, 322-6 Oroshi-cho, Toki 509-5292, Japan*

[2)]*Graduate School of Science, Nagoya University, Nagoya 464-8602, Japan*

The supersonic cluster beam (SSCB) injection method is being developed as a new fueling method for the Large Helical Devise (LHD) experiment. As a first step, cluster formation at a room temperature has been investigated for various gasses using a fast solenoid valve for SSCB. Rayleigh scattering of laser light by the cluster is measured by a fast charge coupled device (CCD) camera. In the case of methane, nitrogen, and argon, clear scattering signals are observed at the high backing pressure of more than 3 – 4 MPa. In the case of hydrogen, helium, and neon, on the other hand, no scattering signal is detected at < 8 MPa. The scattering signals from argon and nitrogen clusters show approximately cubic dependence on the backing plenum pressure as expected from a model. Meanwhile, stronger pressure dependence than this has been found in the case of methane, where the scattering signal increases with the fifth power of the backing pressure at 3.2 MPa – 7 MPa, and it is further enhanced at > 7 MPa.

Keywords: fueling method, gas puffing, solenoid valve, cluster, Rayleigh scattering

1. Introduction

A new fueling method of supersonic cluster beam (SSCB) injection, which is expected to be beneficial for deeper penetration of the fuel particles and higher fueling efficiency than that of gas puffing, is being developed for the Large Helical Devise (LHD) experiment. In SSCB, high-pressure hydrogen gas cooled to less than 77 K by a GM refrigerator will be injected to vacuum through a fast solenoid valve with a Laval nozzle. SSCB is an improved version of cluster jet injection (CJI) developed for HL-2M, where liquid nitrogen of 77 K is used for gas cooling [1], or, the supersonic gas injector (SGI) developed for NSTX, where a Laval nozzle is used to generate supersonic gas jet [2].

Although it is expected that SSCB will produce cluster, there is no established theory to predict the cluster size in a free jet expansion. However, it has been shown that the condition to produce cluster can be described by an empirical scaling parameter Γ^* that is proportional to so-called "Hagena parameter", k [3, 4],

$$\Gamma^* = k \frac{(d/\tan\alpha)^{0.85}}{T_0^{2.29}} P_0, \qquad (1)$$

where d is the nozzle diameter in μm, α is the expansion half angle (α = 45° for sonic nozzles, α < 45° for supersonic), P_0 is the backing plenum pressure in 10^{-4} MPa, and T_0 is the pre-expansion temperature in Kelvin.

e-mail murakami.akiyoshi@LHD.nifs.ac.jp

Massive condensation, where the cluster size exceeds 100 atoms/cluster, is generally observed for Γ^* > 1000 [3, 4]. The parameter Γ^* as a function of the gas temperature is shown in Fig. 1, where d = 500 μm, α = 45°, and P_0 = 4 MPa are assumed. The nozzle diameter of d = 500 μm is equal to that of the valve used in this study. In this calculation, species-dependent k of 184, 3.85, 2360, 528, 185, and 1650 are used for H_2, He, CH_4, N_2, Ne, and Ar, respectively [3]. The result implies that the gasses except helium are expected to form clusters at a room

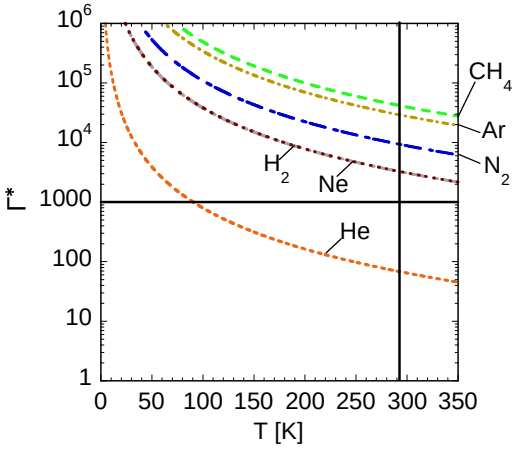

Fig.1 Calculated results of the scaling parameter Γ^*, where d = 500 μm, α = 45° , P_0 = 4 MPa. The gasses except helium satisfy the condition of massive condensation Γ^* > 1000 at room temperature (293 K).

temperature.

Before applying SSCB to LHD, the solenoid valve for SSCB has been tested at a room temperature in a test vacuum chamber. Various gasses shown in Fig.1 are used in the experiment to investigate the clustering condition.

2. Experimental Setup

The experimental setup is shown in Fig. 2. A solenoid valve of Parker-Hannifin Pulse Valve Series 99B07 with a 500 μm diameter orifice is used. This valve is equipped with a tapered nozzle. The available backing pressure is up to 8 MPa. This valve is set inside the vacuum chamber. The pressure in the vacuum chamber is measured by a pressure gauge of MKS Baratron capacitance manometer (MODEL#617A) set at the opposite side of the valve. When the valve is open, the gas flows from left to right in Fig. 2. Various gasses of H_2, He, CH_4, N_2, Ne, and Ar are used in the experiment. A semiconductor laser of NEOARK LDP2-6535A with 650 nm standard wavelength and 35 mW power is set inside the chamber to perpendicularly intersect the gas flow. A beam dump is set at the opposite side of the laser and the valve is rolled by black tape in such a way that the stray light is suppressed. The distance between the valve exit and the laser chord is variable from 3.5 mm to 4.0 mm. The CCD camera of 1280 × 1024 pixels is arranged in the direction perpendicular to both the gas flow and the laser beam. An example CCD image is shown in Fig. 3.

The total Rayleigh scattering signal S_{RS} is proportional to the product of the scattering cross section σ and the number density of clusters n_c. The cross section σ is proportional to the square of the averaged cluster size N_c which is defined by the averaged number of atoms per cluster. n_c is approximately given by the monomer density before becoming cluster, n_0, divided by N_c, i.e., $n_c \approx n_0/N_c$. The scattering signal S_{RS} is proportional to P_0N_c since the monomer density is proportional to the backing plenum pressure P_0. Farges et al. showed that $N_c \propto P_0^{1.8\text{-}2.1}$, assuming a multilayer icosahedral model [5, 6]. This means that the scattered light signal S_{RS} should vary as

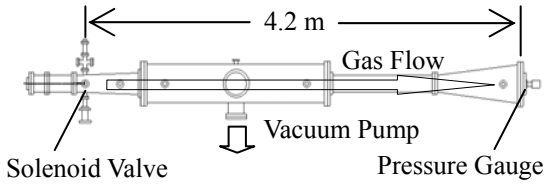

Fig. 2 Schematic of the experimental setup. The distance from the solenoid valve to the baratron pressure gauge is 4.2 m. Inside the chamber is pumped to less than 10^{-4} Pa. The laser is set inside the chamber.

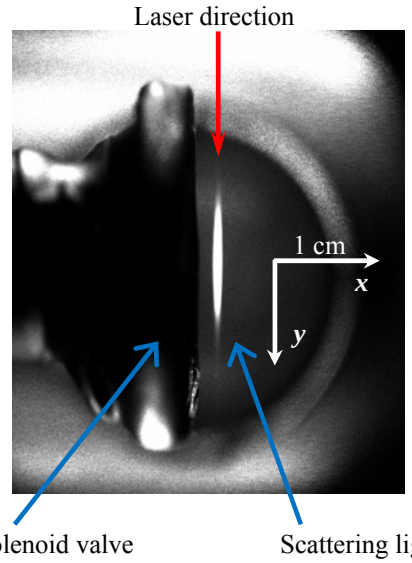

Fig. 3 The scattering light image detected by the CCD camera in the case of CH_4. The backing pressure is 8.0 MPa, and the exposure time is 10 ms. The laser beam direction (y) is perpendicular to the gas flow (x).

below,

$$S_{RS} \propto P_0^{2.8-3.1}. \quad (2)$$

3. Results

Figure 4 shows the temporal behavior of the

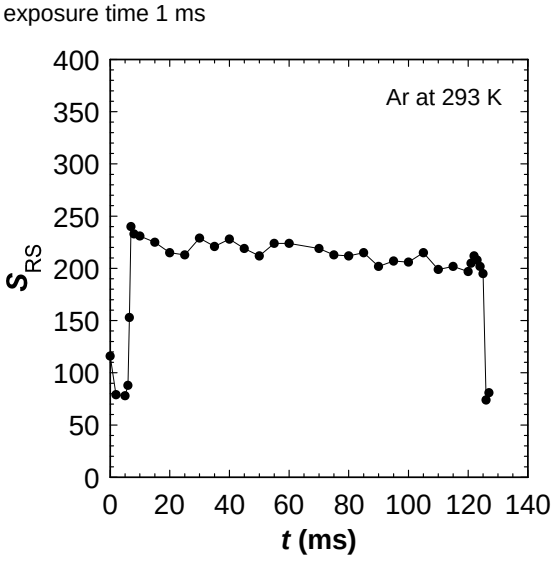

Fig. 4 Typical temporal behavior of the scattering signal intensity. The working gas is Ar and the backing pressure is 7.1 MPa.

scattering signal intensity in the case of Ar. The valve is opened from 0 – 120 ms. The camera exposure time is fixed to 1 ms. As seen in the figure, the scattering light signal intensity is approximately constant during the valve open. Hereinafter, the valve opening time of 40 ms and the CCD camera trigger timing of 35 ms are fixed.

Typical scattering signal profiles in the case of CH_4 are shown in Fig. 5. The direction y in Fig. 5 is parallel to the laser light (see Fig. 3). The backing plenum pressure P_0 is varied from 6.0 MPa to 8.0 MPa. While the exposure time of the CCD camera is fixed to 10 ms. Nearly symmetric profiles are also observed for N_2 and Ar.

Maxima of scattering signals are plotted in Fig. 6. The scattering signal increases with $\sim P_0^{2.8}$ for Ar (Fig. 6(a)) and $\sim P_0^{3.2}$ for N_2 (not shown) at room temperature. These results are similar to the expectation of Eq. (2) and the results of Ref [3]. However, for CH_4 at room temperature (Fig. 6(b)), it is found that the backing pressure dependence is stronger than expected, i.e., $S_{RS} \propto P_0^{4.8}$ at $P_0 < 7$ MPa and $S_{RS} \propto P_0^{8.6}$ at $P_0 > 7$ MPa. This result is different from $S_{RS} \propto P_0^{2.8\text{-}3.1}$ (Eq.(2)).

The scattering signal is detected when the backing plenum pressure is above 3.2 MPa, 3.0 MPa, and 4.0 MPa for CH_4, Ar, and N_2, respectively. In the case of H_2, He, and Ne, no scattering signal is detected up to 8.0 MPa of the backing plenum pressure. Although both hydrogen and neon satisfy the condition of $\Gamma^* > 1000$, no cluster is detected. When the first scattering signal is detected by the CCD camera, Γ^* is 31000, 22000, and 9000 for CH_4, Ar, and N_2, respectively. These are much higher than the condition of massive condensation, $\Gamma^* > 1000$ reported in Refs. [3, 4].

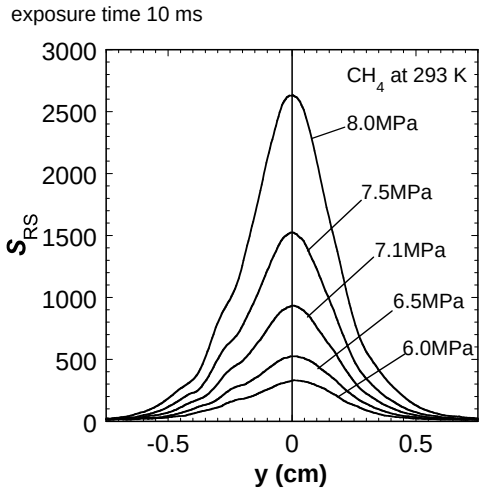

Fig. 5 Typical scatter signal profiles in the case of CH_4. The direction y is parallel to the laser light. The backing pressure P_0 is scanned from 6.0 MPa to 8.0MPa while the gas puff pulse length of 40 ms and the CCD camera trigger timing of 35 ms and the exposure time of 10 ms are fixed.

(a)

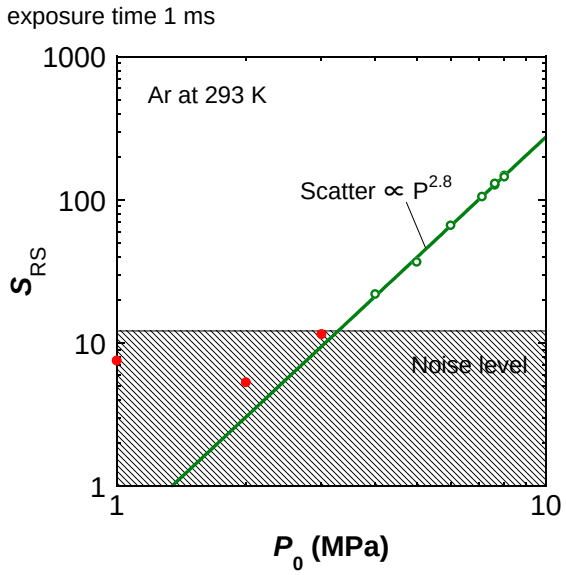

(b)

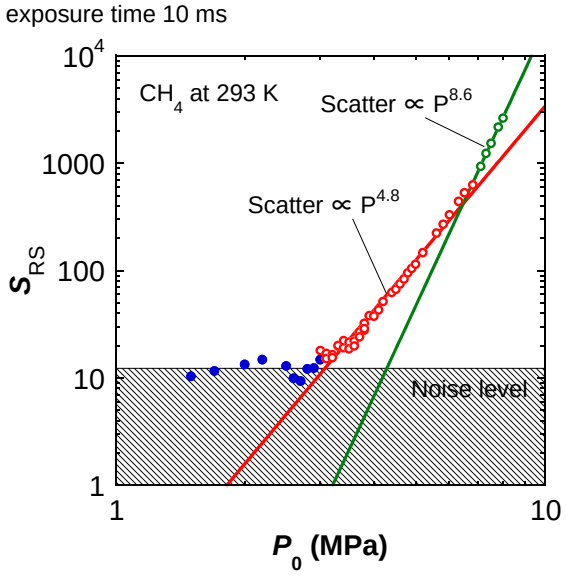

Fig. 6 Peak scattered signal as a function of the backing pressure for (a) argon at 293 K, and for (b) methane at 293 K.

Chem. Phys. **84**, 3491 (1986)

4. Summary

Clustering condition for various gasses at a room temperature has been investigated using the fast solenoid valve for SSCB. The Rayleigh scattering signal is detected by the CCD camera when the backing plenum pressure is above 3.2 MPa, 3.0 MPa, and 4.0 MPa for CH_4, Ar, and N_2, which correspond to 31000, 22000, and 9000 of Γ^*, respectively. In the case of H_2, He, and Ne, no scattering signal is detected. Nearly symmetric shapes of the scattering signal profile in CH_4, Ar, and N_2 are observed by the CCD camera. It has been found that the scattering signal intensity dependence on the backing pressure is similar to the expectation of Eq. (2) and the results of Ref [3] for N_2 and Ar. In the case of CH_4, stronger backing pressure dependence is observed, i.e., $S_{RS} \propto P_0^{4.8}$ below 7 MPa and $S_{RS} \propto P_0^{8.6}$ at $P_0 > 7$ MPa. These are different from $S_{RS} \propto P_0^{2.8\text{-}3.1}$ (Eq.(2)) expected from the result of Farges et al.[5, 6]. Farges et al. estimated this relation assuming a multilayer icosahedral model for Ar cluster. This model seems to be reasonable also for N_2, which shows similar pressure dependence as Ar. However, new structure model is required to determine the cluster size of CH_4, which shows stronger backing pressure dependence than Ar and N_2.

In this work, no signal is detected in the case of H_2 and Ne, although the massive condensation condition is satisfied. Possible causes of this might be ; the noise level was larger than the scattering signal, or the laser power was too low. In order to observe the scattering signals of hydrogen and neon clusters, it is necessary to improve the experimental setup.

In SSCB, high-pressure gas cooled to less than 77 K will be injected to the fusion plasma through a fast solenoid valve with a Laval nozzle. At a low temperature below 77 K, Γ^* for H_2 increases to the similar level as those of Ar and CH_4 at a room temperature (see Fig. 1) where clear Rayleigh scattering signals are observed in this study. Therefore, it is expected that hydrogen cluster beam will be easily formed below 77 K.

Acknowledgments

This work has been financially supported by NIFS08ULPP517.

References

[1] L. Yao *et al*. Nucl. Fusion **47**, 139 (2007).
[2] V.A.Soukhanovskii *et al*. Rev Sci Instrum.**75**, 4320 (2004)
[3] R. A. Smith *et al* Rev Sci Instrum. **69**, 3798 (1988).
[4] O. F. Hagena Z. Phys. D **4**, 291 (1987)
[5] O. F. Hagena and W. Obert, J. Chem. Phys. **56**,1793 (1972)
[6] J. Farges, M. F. de Feraudy, B. Raoult, and G. Torchet, J.

Proceedings of ITC18, 2008

Effects of gas-fueling by Supersonic Molecular Beam Injection on plasma performance in Heliotron J

Tohru Mizuuchi, Shinji Kobayashi, Satoshi Yamamoto, Hiroyuki Okada, Kazunobu Nagasaki, Shinya Watanabe[a], Kiyofumi Mukai[a], Katsuyuki Hosaka[a], Yusuke Kowada[a], Shiori Mihara[a], Hyunyong Lee[a], Yu Takabatake[a], Shintaro Kishi, Yuji Nakamura[a], Kiyoshi Hanatani, Nobuhiro Nishino[b], Shigeru Konoshima, Katsumi Kondo[a] and Fumimichi Sano

Institute of Advanced Energy, Kyoto University, Gokasho, Uji 611-0011, Japan
[a]Graduate School of Energy Science, Kyoto University, Gokasho, Uji, Japan
[b]Graduate School of Engineering, Hiroshima University, Higashi-Hiroshima, Japan

A gas fueling by supersonic molecular beam injection (SMBI) is successfully applied to ECH/NBI plasma in Heliotron J. Although the optimization of this fueling method for the Heliotron J experiment is in progress, increase/decrease of electron temperature and its target density dependence are observed for ECH plasma. In a combination heating condition of ECH (~ 0.35 MW) and NBI (~ 0.6 MW), the stored energy reached ~ 4.5 kJ, which is about 50 % higher than the maximum one achieved so far under the conventional gas-puffing in Heliotron J. Two different types of propagation of perturbations in the radiation profile are also observed after the SMBI for ECH+NBI plasma.

Keywords: fueling control, supersonic molecular-beam injection, gas-puffing, transport, Heliotron J

1. Introduction

The selection of gas fueling method is one of the most important factors to obtain a high density and good performance plasma from two aspects; (1) the profile control of the core plasma density through the controlled penetration depth of neutral particles and (2) the reduction of neutral particles in the peripheral region. Although injection of ice pellets is well known as a technique to realize favorable fueling from these aspects and used in rather large devices, the system is complicated and it is not easy to make a pellet small enough for density control in medium or small sized devices. On the other hand, a supersonic molecular beam injection (SMBI) technique, which has been developed by L. Yao et al. [1, 2, 3], is an alternative method to obtain the deeper penetration of the neutral particles into the core plasma compared to the conventional gas-puffing. This technique is considered to be effective especially for a medium or small sized device.

The SMBI technique has been used also for plasma diagnostics such as a He-beam probe or gas-puff imaging techniques in some fusion devices [4, 5], where the amount of the injected neutrals can be suppressed as low as possible to prevent the target plasma from being perturbed. Recently high-pressure SMBI is examined as a fueling method for ECH/NBI plasmas in Heliotron J.

This paper reports the first SMBI fueling experiment in Heliotron J. Although the optimization of this fueling method for the Heliotron J experiment is in progress, in a combination heating condition of ECH and NBI, the stored energy of ~ 4.5 kJ was recorded, which is about 50 % higher than the maximum one achieved so far under the normal gas-puff fueling condition [6] in Heliotron J.

2. Experimental Set-up

The Heliotron J device is a medium sized helical-axis heliotron device ($\langle R_0 \rangle / \langle a_p \rangle$ = 1.2/0.17 m, $B_0 \leq 1.5$ T) with an L/M = 1/4 helical coil [7, 8]. Figure 1 schematically shows the arrangement of the heating system, major diagnostic equipments and a SMBI system. The initial plasma is produced by using the second harmonic X-mode ECH (70 GHz, < 0.45 MW, non-focusing Gaussian beam) launched from a top port. The hydrogen neutral (H^0) beam (< 30 keV, < 0.7 MW/beam-line) is injected for NBI plasmas using one or two tangential

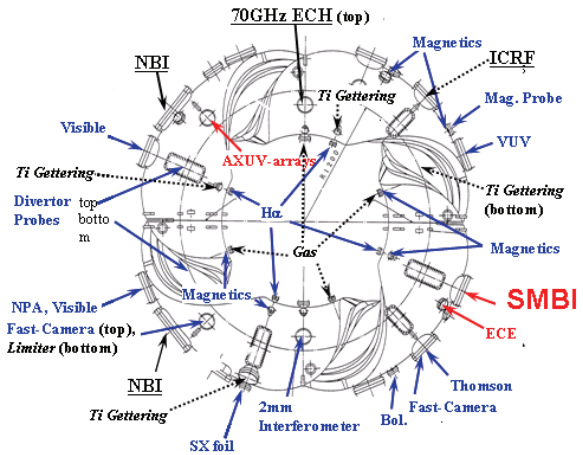

Fig. 1 Experimental set-up

author's e-mail: mizuuchi@iae.kyoto-u.ac.jp

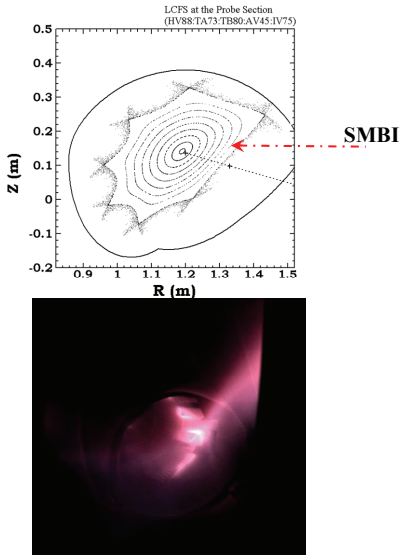

Fig. 2 The poloidal cross-section at the SMBI port (top) and a snapshot of the tangential plasma view (without any optical filter) at the timing of SMBI (bottom).

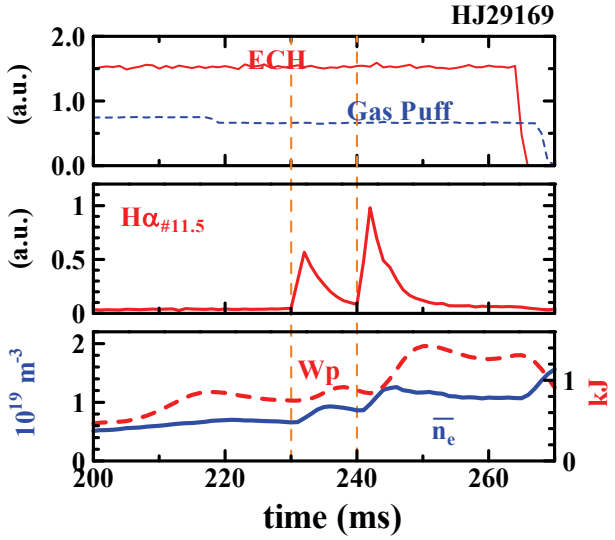

Fig. 3 Example of time traces of the intensity of Hα emission at the SMBI section, the line averaged density, the stored energy with ECH pulse and the gas-puff control voltage. The vertical dashed lines indicate the timing of SMBI.

beam-lines, which are facing each other (BL-1 and BL-2). Selecting one of the two beam-lines or changing the direction of the confinement field, Co- or CTR-injection can be performed.

A conventional gas-puff system with four piezoelectric valves is used to density control in usual experiments, which is installed at the inboard side ports around the torus at ≈90° intervals (see Fig. 1). In addition to this, a SMBI system is equipped on a horizontal port (#11.5 port) in Heliotron J. This system consists of a fast solenoid valve (the diameter of its orifice is 0.1 mm for this experiment.) with a magnetic shield. Although this system is introduced to Heliotron J originally for the diagnostic purpose such as the gas-puff imaging measurement for edge plasma turbulence with a high speed video camera [5], by increasing the plenum gas

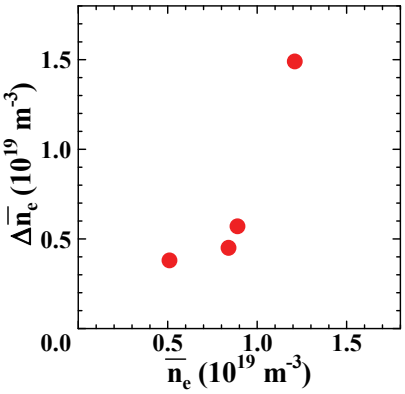

Fig. 4 The increase of $\bar{n}_e$ after a SMBI as a function of the target density (ECH plasma).

pressure (≥ 1 MPa) and the pulse width (0.4-1.0 ms), this system is used for the fueling control. Figure 2 shows a poloidal cross-section at the SMBI port and a snapshot of the tangential plasma view (with no optical filter) at the SMBI timing taken at the Thomson port near the SMBI port (see Fig. 1). By the SMBI fueling, a bright stripe is observed, which seems to be along the field line. Figure 3 shows an example of the time traces of the ECH pulse, the gas-puff control voltage, the intensity of Hα emission at the SMBI section ($H\alpha^{\#11.5}$), the line-averaged density ($\bar{n}_e$) and the stored energy (W_p) for an ECH plasma with SMBI, where the SMBI was fired two times with about 10 ms interval, indicated by the rapid increases of the Hα signal.

3. Experiments and results

3.1. SMBI for ECH plasma

The SMB pulse(s) of hydrogen was injected to ECH (~ 0.35 MW) deuterium plasmas of different line-averaged densities ($\bar{n}_e$) under the standard (STD) configuration [8] with the reversed magnetic field direction. Here, the condition of SMBI was fixed: the pulse width ~ 0.8 ms, the plenum pressure ~ 1.2 MPa. The experiment shows that the increase of $\bar{n}_e$ after a SMBI pulse ($\Delta\bar{n}_e$) seems to depend on the target density as shown in Fig. 4. Since the H-mode transition was observed above a critical density and $\bar{n}_e$ uncontrollably increases after the transition [9], it is difficult in higher $\bar{n}_e$ region to discriminate between the increase by SMBI itself and that due to the improved transport. The target density dependence of $\Delta\bar{n}_e$ observed in the low $\bar{n}_e$ region (< 1×10^{19} m^{-3}), however, suggests the enhanced penetration of neutrals outside the plasma maybe due to the edge cooling by SMBI.

The difference in the $\bar{n}_e$ –W_p relation between the conventional gas-puff and SMBI was not clear for ECH plasma with $\bar{n}_e$ well below the cut-off density. Near the cut-off density, however, the SMBI fueling seems better than the gas-puff from the viewpoint of the accessibility to the higher density and stored energy ECH plasma.

Figure 5 shows the time response of the ECE intensity I_{ECE} from several channels, which corresponding to the different positions. Here the signals of Hα and $\bar{n}_e$ are also plotted. For higher target density plasma (~ 0.8×10^{19}

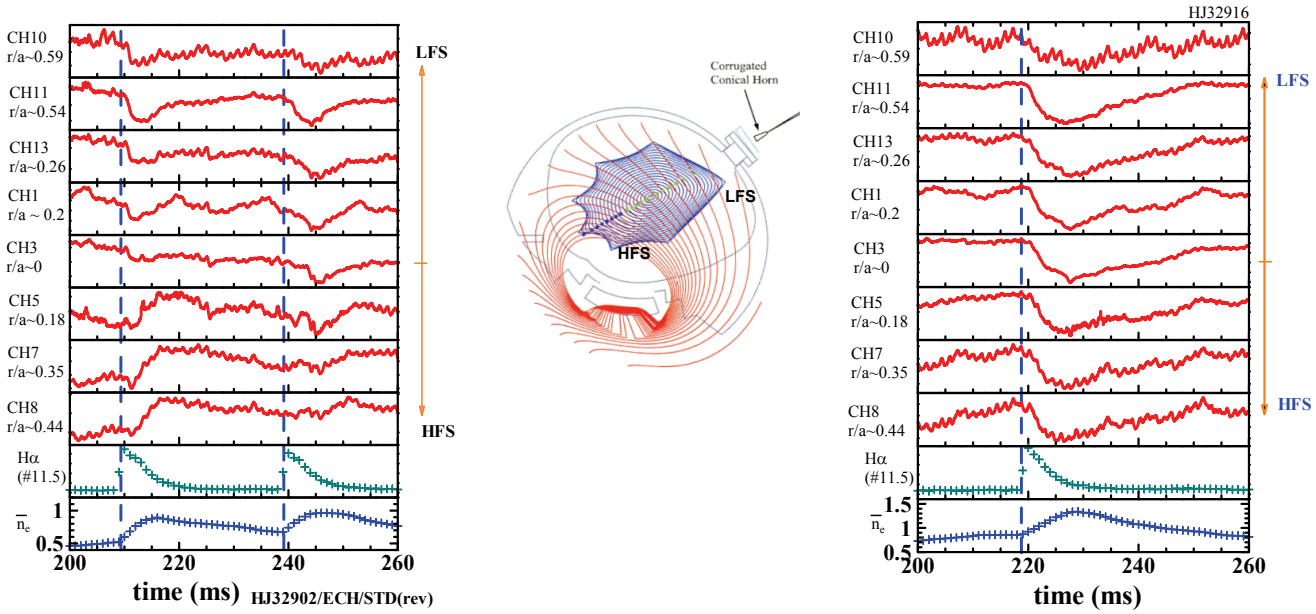

Fig. 5 Time responses of I_{ECE} for a lower (left) and higher (right) target density plasma. (ECH plasma). The intensity of I_{ECE} is adjusted to make clear the response for each channel. The middle figure schematically shows the poloidal section for the ECE measurement.

m^{-3}, Fig. 5 right), I_{ECE} decreases after the SMBI pulse for all positions, indicating the decrease of electron temperature (T_e), and gradually recovers to the level before the SMBI. The start timing of the decrease in I_{ECE} is almost the same for all channels, which might indicate some non-local phenomena. For lower target density plasma ($\sim 0.5\times10^{19}$ m^{-3}, Fig. 5 left), I_{ECE} also decreases after the SMBI for the near side of the SMBI (i.e. the low field side, LFS). However, I_{ECE} increases for the far side (i.e. the high field side, HFS), indicating the increase of T_e. Although we should take care of a local effect on I_{ECE} since the ECE section is very close to the SMBI section, the increase of T_e is interesting. The measurement of T_e is necessary at a position toroidally well apart from the SMBI section. The measurement in more peripheral region is also necessary.

3.2. SMBI for ECH+NBI plasma

For the combination heating of ECH and NBI, the SMBI fueling is also preferable to produce higher $\overline{n_e}$ and higher W_p plasmas. Figure 6 shows the time traces of $\overline{n_e}$, W_p, Hα and the signals from three channels of a SX-array for an ECH+NBI discharge with two pulses of SMBI. Here, the experiment was performed under the STD configuration with the normal field direction. The condition of ECH is almost the same as the experiment described in the previous sub-section and only one beam line (BL-2, ~0.6 MW) is used for NBI, i.e. the Co-injection. The first SMBI successfully increased the $\overline{n_e}$ and W_p, but the effect of the second SMBI was observed only on the slight increase of $\overline{n_e}$. The stored energy started to decrease before the second SMBI and was not increased by the second SMBI. Figure 7 shows the $\overline{n_e}$ dependence of W_p for the similar ECH+NBI plasmas. Under the conventional gas-puff fueling, the stored energy are limited at ~ 3 kJ, By using the SMBI fueling, the stored

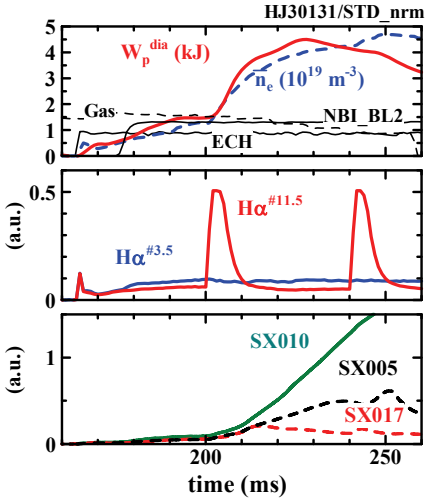

Fig. 6 Time traces of $\overline{n_e}$, W_p, Hα and I_{SX} for an ECH+NBI discharge with SMBI.

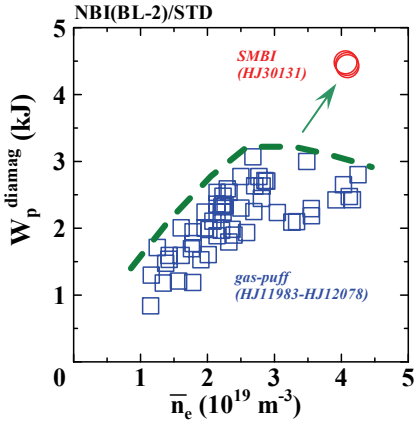

Fig. 7 The density dependence of the stored energy. (ECH+NBI plasma) □ are the data obtained with the gas-puff fueling and ○ are the data with the SMBI fueling.

energy reached ~4.5 kJ, about 50 % higher than the maximum value achieved under the conventional gas-puff fueling condition.

Relating to the SMBI effects on the plasma performance, propagation of perturbations caused by SMBI are observed in a chord-profile of radiation from the plasma measured with an AXUV-array. Here, the AXUV array with 1μm^t-Al filter was used for detection of radiation above ~500eV [10]. The discharge condition is a combination heating of ECH (~0.35 MW) and NBI (BL-1 and BL-2) under the STD configuration with the reversed field direction. Figure 8 shows the time responses of Hα, $\overline{n_e}$, W_p and the normalized chord-profile of the radiation measured with the AXUV-array. As shown in the figure, we can observe two types of propagating perturbations in the radiation profile caused by a SMBI pulse; one is pinch-like perturbation near the center and the other is expansion observed in the peripheral region. Since the radiation is a function of the density and temperature, direct measurements of the temperature and density is necessary to understand this observation.

4. Summary

A gas fueling method with SMBI is successfully applied to ECH/NBI plasma in Heliotron J.

Interesting time responses caused by the SMBI are observed: increase/decrease of T_e and its target density dependence for ECH plasma, two different types of propagation of perturbations in the radiation profile caused by the SMBI for ECH+NBI plasma.

In a combination heating condition of ECH and NBI, the stored energy reached ~4.5 kJ, which is about 50 % higher than the maximum one achieved so far under the conventional gas-puff fueling condition in Heliotron J.

In order to understand these interesting observations and to make use of these findings for improving plasma performance, more detailed studies and the refinement of the SMBI tourniquet are necessary. The optimization of this fueling technique for the Heliotron J experiment is in progress.

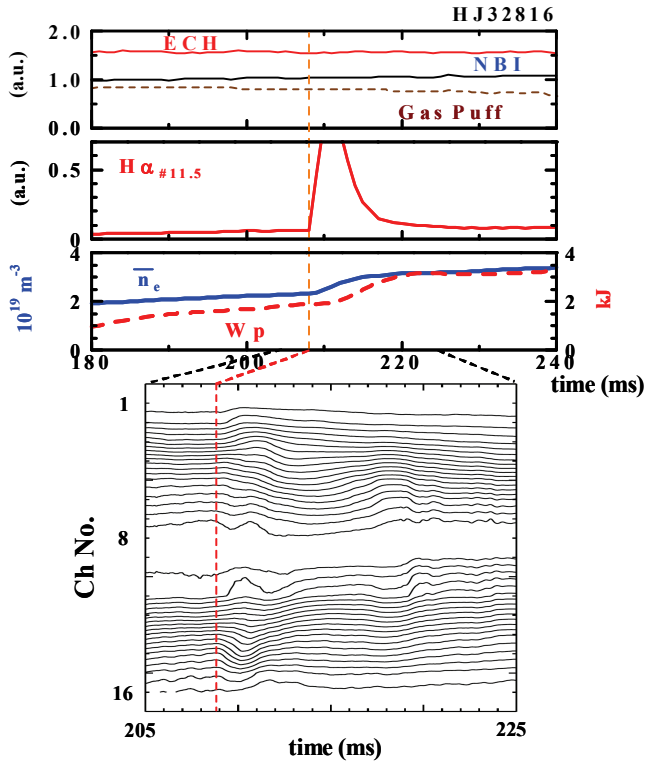

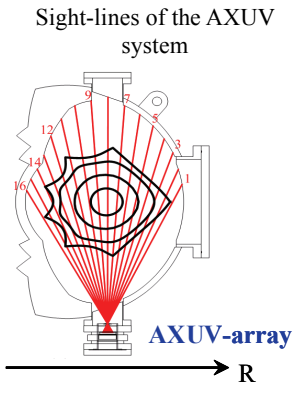

Fig. 8 Time responses of Hα, $\overline{n_e}$, W_p and the normalized chord profile of radiation measured with the AXUV-array.

Acknowledgement

The authors are grateful to the Heliotron J supporting group for their excellent arrangement of the experiments. The authors give special thanks to Profs. L. Yao, Q.W. Yang and their colleagues for the fruitful discussions. This work is performed with the support and under the auspices of the JSPS-CAS Core University Program, the Collaboration Program of the Laboratory for Complex Energy Processes, IAE, Kyoto University, the NIFS Collaborative Research Program (*NIFS04KUHL001, NIFS04KUHL002, NIFS04KUHL003, NIFS04KUHL004, NIFS04KUHL005, NIFS05KUHL007, NIFS06KUHL007, NIFS06KUHL009, NIFS06KUHL010, NIFS06KUHL011, NIFS06KUHL014, NIFS06KUHL015*) and the Formation of International Network for Scientific Collaborations as well as the Grant-in-Aid for Sci. Research.

References

[1] L. Yao, in "New Developments in Nuclear Fusion Research" (Nova Sci. Pub, 2006)) pp. 61-87.
[2] L. Yao et al., Proc. 20th EPS Conf. on Controlled Fusion and Plasma Phys. (Lisbon, 1993) vol. **17C(I)**, p303.
[3] L. Yao et al., Nucl. Fusion **47** (2007) 1399.
[4] B. Branas, et al., Rev. Sci. Instrum., **72** (2001) 602.
[5] N. Nishino, et al., J. Nucl. Mater., **337-339** (2005) 1073.
[6] T. Mizuuchi, et al., J. Plasma Fusion Res., **81** (2005) 949
[7] F. Sano, et al., J. Plasma Fusion Res. SERIES **3**, 26 (2000).
[8] T. Obiki, et al., Nucl. Fusion **41**, 833 (2001).
[9] F. Sano, et al., Nucl. Fusion **45**, 1557 (2005).
[10] S. Watanabe, et al., in this conference.

Proceedings of ITC18, 2008

Spectroscopic diagnostics for spatial density distribution of plasmoid by pellet injection in Large Helical Device

G. Motojima, R. Sakamoto, M. Goto, H. Yamada and LHD experimental group

National Institute for Fusion Science,322-6 Oroshi-cho, Toki 509-5292, Japan

In order to investigate the behavior of the plasmoid which is the pellet ablatant ionized by background plasma, two-dimensional imaging measurements of high-speed spectroscopy using a fast camera has been developed in the Large Helical Device. The diagnostic system provides the density distribution of the plasmoid. The density distribution is determined by the Stark broadening width of Balmer-β line. The Stark broadening profile can be evaluated from the intensity ratio measured with narrow-band optical filters having different full width at half maximum. The two-dimensional images of the plasmoid by the fast camera connected to a bifurcated fiber scope with two objective lenses are obtained. As an initial result from the imaging measurements, it is shown that the plasmoid density is in the order of 10^{23} m^{-3}.

Keywords: pellet injection, plasmoid, helical device, two-dimensional imaging measurements, spectroscopy

1 Introduction

Solid hydrogen pellet injection is a primary technique for efficient core plasma fueling in fusion devices. The pellet injection is sure to play a important role in next-step devices such as ITER and also will be one of promising candidates for particle refueling in a future fusion reactor. In particular, the importance of the pellet injection is increased in the high central density operation required for a helical reactor [1].

When pellets are injected into a hot, magnetically confined plasma, pellet particles are ablated by heat flux from a background plasma. The pellet is immediately surrounded by its neutral cloud which is generated by the ablation of the pellet. The neutral cloud has a effect of shielding from the ambient background plasma. Subsequently the neutral cloud is ionized and expanded in the direction parallel to the magnetic field lines. Here, the ionized pellet material is referred to as a plasmoid.

The pellet ablation and subsequent behavior of the plasmoid are key elements to determine the characteristics of pellet fueling. Extensive experiments have been devoted to the clarification of fueling characteristics of the pellet [2]. In particular, recent studies have been focused on the drift of the plasmoid [3]. The drift of the plasmoid may be attributed to an $\boldsymbol{E} \times \boldsymbol{B}$ drift that arises from a vertical polarization in the ablation cloud due to the magnetic field gradient [4]. The behavior of the plasmoid following ablating process has a primary effect on the pellet mass deposition. Therefore, the understanding of not only the pellet ablation but also subsequent behavior of the plasmoid allows the optimization of the pellet fueling. As for the pellet ablation, the identification of the position in the pellet ablation is of great importance. In LHD, three-dimensional observation system with stereoscopic analysis using a fast camera has been developed [5]. The position of the pellet ablation can be precisely identified by using this method. Concerning the behavior of the plasmoid, the quantitative evaluation of the pellet particles transferred by the plasmoid provides the understanding of the homogenization process of the plasmoid. The process of the homogenization has been demonstrated in numerical calculations. Moreover, the density and temperature of the plasmoid has been measured by spectroscopic diagnostics [6, 7]. However, quantitative two-dimensional evaluation of the plasmoid parameters has not yet been achieved. The objective of this study is to evaluate the two-dimensional density distribution in the plasmoid quantitatively by imaging measurements with high-speed spectroscopic diagnostics.

The rest of the paper is organized as follows. The principle of the high-speed spectroscopic analysis is described in Section 2. In Section 3, the experimental setup is presented. The initial experimental results are shown in Section 4. Summary is given in Section 5.

2 Imaging measurements of High-speed spectroscopy

The spectrum of Balmer-line depends on the density and temperature of the plasmoid. Here, the emission from the background plasma can be ignored, since the density of the plasmoid is about several hundred times larger than that of the background plasma, resulting that the emission from the plasma is much smaller than that from the plasmoid. The electron density can be determined from the Stark broadening profile of the Balmer-α or Balmer-β line. Figure 1 shows examples of spectra in the range of wavelength from 400 to 800 nm for (a) low density (n_e = 1.0×10^{22} m^{-3}) and (b) high density (n_e = 9.0×10^{23} m^{-3}). The same electron temperature is assumed at 1.0 eV for both cases (the value is based on the results from ref. [7]). Here, the spectra are estimated from the fitting with the the-

author's e-mail: gen@lhd.nifs.ac.jp

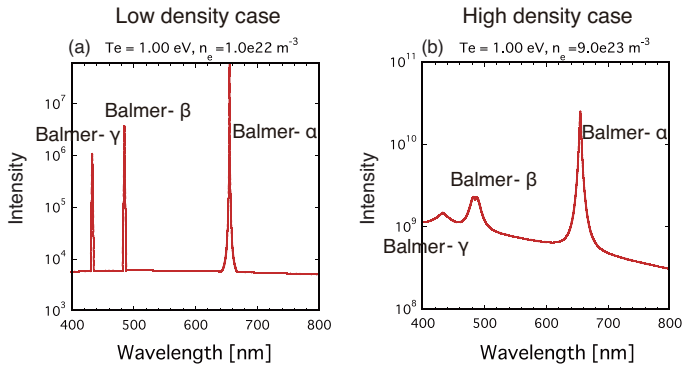

Fig. 1 Spectra in the range of wavelength from 400-800 nm for (a) low density ($n_e = 1.0\times10^{22}$ m^{-3}) and (b) high density ($n_e = 9.0\times10^{23}$ m^{-3}). The same electron temperature is selected. Intensity is expressed in logarithmic scale.

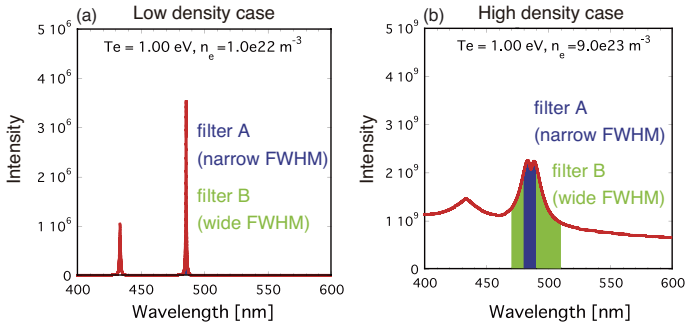

Fig. 2 Spectra of the Balmer-β and Balmer-γ lines with a constant background for (a) low density ($n_e = 1.0\times10^{22}$ m^{-3}) and (b) high density ($n_e = 9.0\times10^{23}$ m^{-3}). Intensity is expressed in linear scale.

oretical data based on the collision-radietive model [8, 9]. Only the Balmer-α, β, and γ lines appear as discrete lines and other series lines appear as a continuum spectrum. In low density case, the line profile is peaked. While, in high density case, the line profile is broader. It is found that the line profile depends on the electron density. The characteristics make possible the evaluation of the electron density.

The Stark broadening width can be estimated from the intensity ratio measured with narrow-band optical filters having different full width at half maximum (FWHM). Figure 2 shows the extended figure of Fig. 1 around Balmer-β line. In low density case, there is almost no difference in the intensity between wide and narrow FWHMs due to the peaked line profile. While, in high density case, the intensity difference becomes large due to the broader line profile, resulting that the ratio of intensity measured with narrow FWHM to that measured with wide FWHM becomes small.

In this study, we concentrate on the Balmer-β line (center wavelength : 486.1 nm) to evaluate the density of plasmoid. The filter parameters suitable for various presumed densities (10^{22} – 10^{24} m^{-3}) and temperatures (0.9-1.2 eV) in a plasmoid were selected using the spectra es-

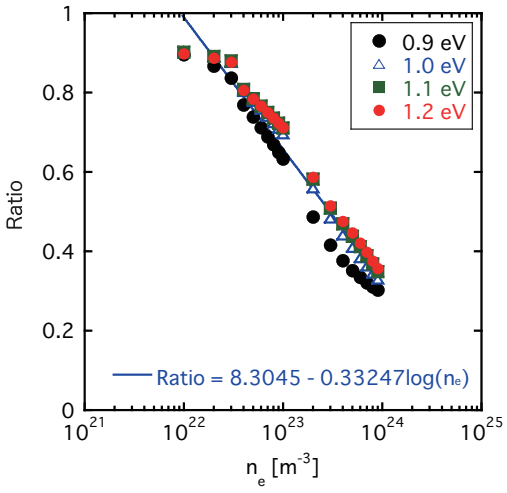

Fig. 3 Dependence of the logarithm of density on the ratio of the intensity measured with FWHM of 5 nm to that measured with wide FWHM of 20 nm. Solid line shows logarithm fitting of the data. The fitting line is used in analysis.

timated from theoretical data. The ranges of density and temperature are assumed by the results from spectrometer measurement of plasmoid in LHD [7]. Figure 3 shows the dependence of the logarithm of electron density on the ratio of the intensity measured with FWHM of 5 nm to that measured with wide FWHM of 20 nm. The ratio is approximately proportional to the logarithm of plasmoid density. The ratio is small with increasing electron density. With this filter combination, dependence of the plasmoid temperature can be ignored, and we are able to measure the plasmoid density in the range from 10^{22} to 10^{24} m^{-3}.

3 Experimental Setup

In this section, the spectroscopic diagnostics system for density distribution of plasmoid is explained. Figure 4(a) shows a horizontally elongated poloidal cross section of the LHD and in-situ pipe gun type 10 barrel pellet injector. The plasmoid can be observed just behind the pipe gun pellet injector and parallel to the injection axis :namely, the line of sight is consistent with the pellet injection axis. The emission from the plasmoid is evenly divided by a half mirror, as shown in Fig. 4(b).

A bifurcated fiber scope with two objective lenses is used in this spectroscopic system [5]. The scope is composed of a pair of 50000 element quarts fiber scopes with a stainless-steel flexible protective tube. The overall length is 15 m and the bifurcated portions are about 5 m in length. Each objective lens, which has a field of view of 15 degree, with different filters selected in Sec. 2 is used. Two images which are viewed from the same line of sight just behind the pellet injector are obtained.

The images are focused onto a single fast camera (Vision Research Inc., Phantom V7) so that the simultaneity

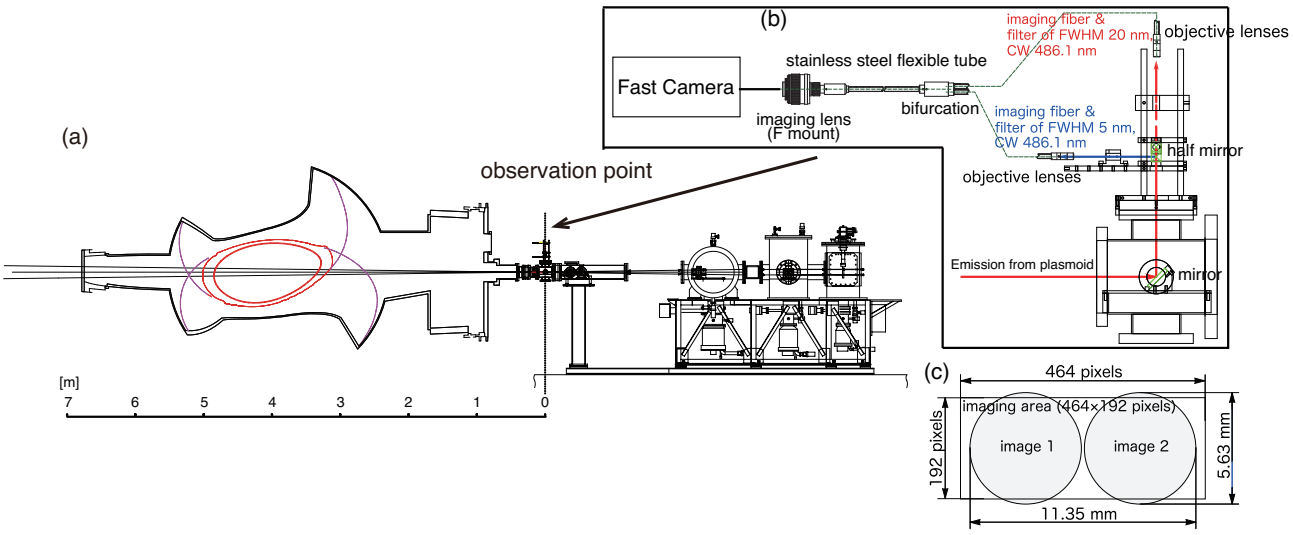

Fig. 4 (a) Cross-sectional drawing of the LHD vacuum vessel and fuelling pellet injector, which is equipped with 10 barrels independent barrels (b) enlarged view of observation point where the imaging measurements are equipped (c) imaging area on the sensor of the fast camera.

is ensured. The fast camera is equipped with a 12 bit self-resetting complementary metal oxide semiconductor sensor (SR-CMOS). The frame rate and the exposure time are selected to be 2000 fps with a resolution of 464 × 192 pixels and 2 μs, respectively. The bundled end is connected to an imaging lens which can project a pair of images onto the imaging sensor, as shown in Fig. 4(c).

4 Results

The initial results of two-dimensional imaging measurements by high-speed spectroscopy were obtained. Figure 5 shows typical images of the plasmoid with the filters having (a) FWHM 5 nm and (b) FWHM 20 nm. The pellet is injected to the NBI plasma with central electron temperature of 1.5 keV. Here, the identity of the two fields of view is confirmed by the strong correlation between two images. The intensity of the image with the filter of FWHM 20 nm is stronger than that of image with the filter of FWHM 5 nm. The plasmoid seems to be expanded to the direction parallel to the magnetic field line. The emission intensity distribution of two images in the direction perpendicular to the magnetic field line passing through the maximum intensity point is shown in Fig. 6(a). The difference of intensity is observed in the pellet ablatant. Since it is difficult to evaluate the ratio of intensity in the outer region of the plasmoid due to small intensity and/or lower density than that of assumption, the analysis is limited to the region around the plasmoid. Figure 6(b) shows the ratio of intensity between two images in the direction perpendicular to the magnetic field line passing through the maximum intensity point. In the center of plasmoid which has strong intensity, the ratio is close to 1 that means the density in the order of 10^{22} m^{-3}. On the other hand, in the region around the center of plasmoid, minimum of the ratio is about 0.6 that means the density in the order of 10^{23} m^{-3}. Figure 7(a)

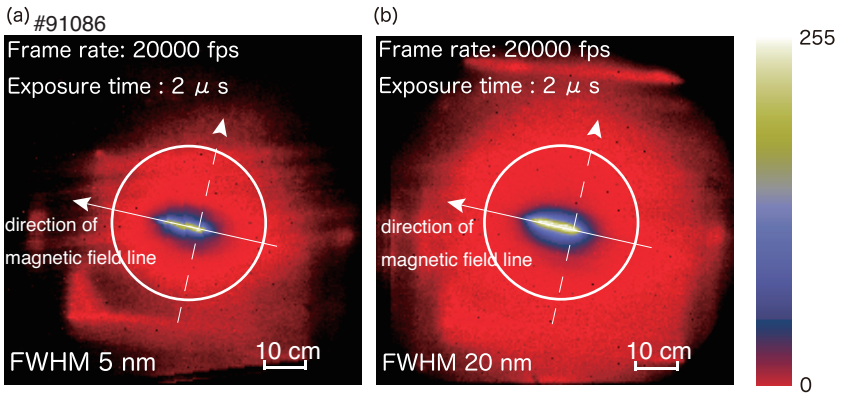

Fig. 5 Typical images of plasmoid with the filters having (a) FWHM of 5 nm and (b) FWHM of 20 nm. Analysis is made within the circular line. Solid line shows the direction of the magnetic field line and dot line shows the direction perpendicular to the magnetic field line.

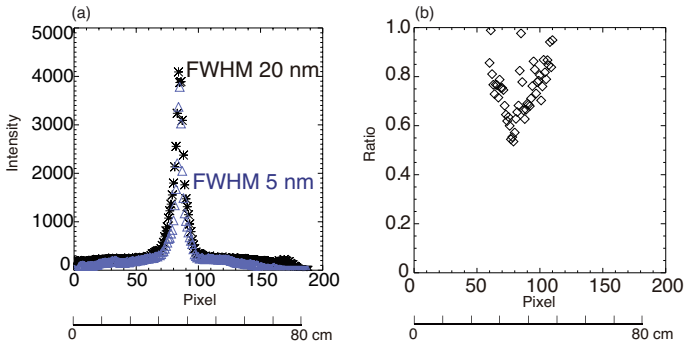

Fig. 6 (a) Emission intensity distribution and (b) ratio of two images in the direction perpendicular to the magnetic field line passing through the maximum intensity point. Asterisk symbol shows the intensity with FWHM of 20 nm and triangle symbol shows the intensity with FWHM of 5 nm.

shows the density distribution in the plasmoid. Here, gray zone shows the region having large error because of small intensity. The density of the plasmoid is over 10^{22} m^{-3} and the plasmoid measures 20 cm wide. The plasmoid density is in the order of 10^{23} m^{-3} except for the center region of the pellet ablatant. In the center region of the plasmoid, the density seems to be lower. The reason may be attributed to the unexpected temperature range. However, further studies are necessary. Figure 7 (b) shows the electron density distribution in the direction perpendicular to the magnetic field line passing through the maximum intensity point. The maximum electron density at 2.3×10^{23} m^{-3} is observed.

5 Summary

In order to obtain the two-dimensional plasmoid density distribution quantitatively, imaging measurements of high-speed spectroscopic system using a fast camera has been developed. The density of the plasmoid is evaluated by the width of the Stark broadening in Balmer-β line. The Stark broadening can be estimated by comparing the difference in emission intensity from the plasmoid between narrow-band optical filters having different FWHM. The most suitable a pair of filters which have the same central wavelength of 486.1 nm and different FWHM of 5 nm and 20 nm was selected by the spectra estimated from the fitting with the theoretical data. As an initial result, the density distribution of the plasmoid by imaging measurements was obtained. Here we show that the plasmoid density is in the order of 10^{23} m^{-3}. In future, the three-Dimensional distribution of the density in the plasmoid will be evaluated by using tomography under the assumption that the structure of the plasmoid is rotational axial-symmetry around the magnetic field line.

Acknowledgements

The authors are grateful to the LHD operation group. This study was supported by NIFS08ULPP521.

[1] O. Mitarai *et al.*, Proc. 22nd IAEA Fusion Energy Conference, Geneva, FT/P3-19 (2008); also available at http://www-pub.iaea.org/MTCD/Meetings/FEC2008/ft_p3-19.pdf
[2] B. Pégourié, Plasma Phys. Control. Fusion **49**, R87 (2007).
[3] P. T. Lang *et al.*, Phys. Rev. Lett. **79**, 1487 (1997).
[4] V. Rozhansky *et al.*, Plasma Phys. Control. Fusion **37**, 399 (1995).
[5] R. Sakamoto *et al.*, Rev. Scient. Inst. **76**, 103502 (2005).
[6] D. H. McNeill *et al.*, Phys. Fluids B **3**, 1994 (1991).
[7] M. Goto *et al.*, Plasma Phys. Control. Fusion **49**, 1163 (2007).
[8] C. Stehle and R. Hutcheon, Astron. Astrophys. Suppl. Ser. **140**, 93 (1999).
[9] T. Fujimoto, Plasma Spectroscopy (Oxford: Oxford University Press) (2004).

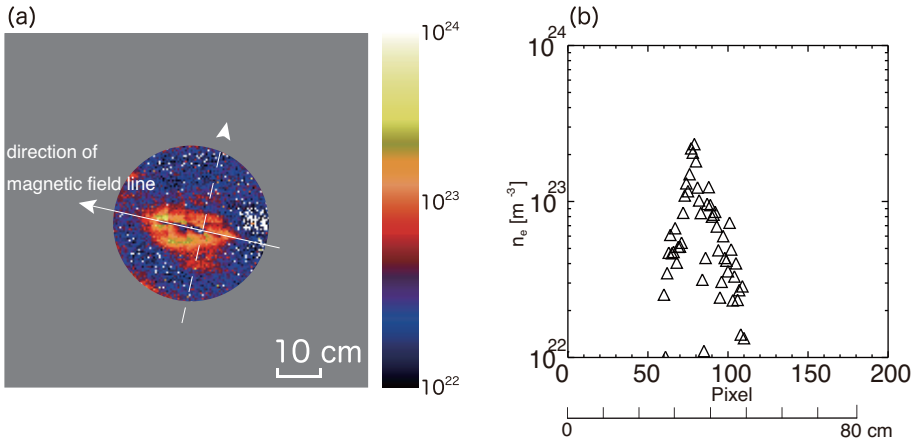

Fig. 7 (a) Density distribution in plasmoid and (b) electron density distribution along the dot line in the direction perpendicular to the magnetic field line passing through the maximum intensity point. Here, dot line shows the direction of the magnetic field line and dot line shows the direction perpendicular to the magnetic field line.

Proceedings of ITC18, 2008

Plasmoid behavior in LHD plasmas

Ryuichi ISHIZAKI and Noriyoshi NAKAJIMA

National Institute for Fusion Science, Toki 509-5292, Japan

In order to clarify the difference on the motion of a plasmoid created by a pellet injection between tokamak and helical plasmas, MHD simulation including ablation processes has been carried out. In LHD plasma, the plasmoid drifts to the lower field side similarly to tokamak. However, it is found that the drift direction is reversed after several Alfvén transit times in the case that the plasmoid is located at the inner side of the torus on the horizontal elongated poloidal cross section.

Keywords: pellet, drift, tire tube force, MHD, CIP

1 Introduction

Injecting small pellets of frozen hydrogen into torus plasmas is a proven method of fueling [1]. The physical processes are divided into the following micro and macro stages. The micro stage is the ablation of mass at the pellet surface due to the high temperature bulk plasma which the pellet encounters. The neutral gas produced by the ablation is rapidly heated by electrons and ionized to form a high density and low temperature plasma, namely a plasmoid. The macro stage is the redistribution of the plasmoid by free streaming along the magnetic field lines and by MHD processes which cause mass flow across flux surfaces. The micro stage is well-understood by an analytic method [2] and numerical simulation [3]. The drift motion of the plasmoid is investigated in the macro stage [4]. Since the plasmoid drifts to the lower field side, the pellet fueling to make the plasmoid approach the core plasma has succeeded by injecting the pellet from the high field side in tokamak. On the other hand, such a good performance has not been obtained yet in the planar axis heliotron; Large Helical Device (LHD) experiments, even if a pellet has been injected from the high field side [5]. The purpose of the study is to clarify the difference on the motion of the plasmoid between tokamak and helical plasmas.

In order to investigate the motion of the plasmoid, the three dimensional MHD code including the ablation processes has been developed by extending the pellet ablation code (CAP) [3]. It was found through the comparison between simulation results and an analytical consideration that the drift motion to the lower field side in tokamak is induced by a tire tube force due to the extremely large pressure of the plasmoid and a $1/R$ force due to the magnetic pressure gradient and curvature in the major radius direction as shown in Ref. [6]. In the study, the motion of the plasmoid is investigated in the LHD plasma in four cases that the plasmoids are initially located at the inner and outer sides of the torus on the vertical and horizontal elongated poloidal cross sections. The plasmoids drift to the lower field sides in all cases. However, in the case that it is located at the inner side of the torus on the horizontal elongated poloidal cross section, it is found that the drift direction is reversed after several Alfvén transit times, namely it drifts to the higher field side.

author's e-mail: ishizaki@nifs.ac.jp

2 Basic Equations

Since the plasmoid is such a large perturbation that the linear theory can not be applied, a nonlinear simulation is required to clarify the behavior of the plasmoid. The drift motion is considered to be a MHD behavior because the drift speed obtained from experimental data [1] is about several % of v_A, where v_A is an Alfvén velocity. Thus, the three dimensional MHD code including the ablation processes has been developed by extending the pellet ablation code (CAP) [3]. The equations used in code are:

$$\frac{d\rho}{dt} = -\rho\nabla\cdot\mathbf{u}, \tag{1a}$$

$$\rho\frac{d\mathbf{u}}{dt} = -\nabla p + \mathbf{J}\times\mathbf{B} + \nu\rho\left[\frac{4}{3}\nabla(\nabla\cdot\mathbf{u}) - \nabla\times\omega\right], \tag{1b}$$

$$\frac{dp}{dt} = -\gamma p\nabla\cdot\mathbf{u} + (\gamma-1)\left[H + \eta J^2 + \nu\rho\left(\frac{4}{3}(\nabla\cdot\mathbf{u})^2 + \omega^2\right)\right], \tag{1c}$$

$$\frac{\partial\mathbf{B}}{\partial t} = \nabla\times(\mathbf{u}\times\mathbf{B} - \eta\mathbf{J}), \tag{1d}$$

$$\mathbf{J} = \nabla\times\mathbf{B}, \tag{1e}$$

$$\omega = \nabla\times\mathbf{u}. \tag{1f}$$

ρ, $\mathbf{B}$, $\mathbf{u}$ and p are normalized by ρ_0, B_0, v_A and B_0^2/μ_0 at the magnetic axis, respectively, where μ_0 is the magnetic permeability. $\gamma = 5/3$, $\nu = 10^{-6}v_A L_0$ and $\eta = 10^{-6}\mu_0 v_A L_0$ are used as the ratio of the specific heats, viscosity and

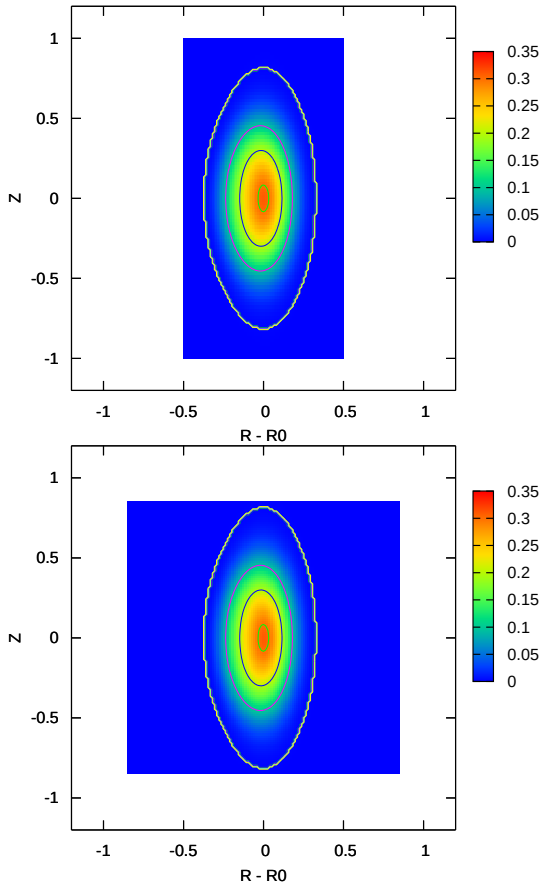

Fig. 1 Pressure contours on the vertical elongated poloidal cross sections at $\phi = 0$ in (a) the HINT and (b) the CAP codes expressing the LHD plasma with $R_0 = 3.82$. The last closed surfaces are defined by the contour lines of 0.5% of the maximum pressure.

electric resistivity, respectively, where L_0 is a characteristic length; 1 m. Heat source H is given by:

$$H = \frac{dq_+}{dl} + \frac{dq_-}{dl}, \quad (2)$$

where $q_\pm$ is the heat flux model dependent on electron density and temperature in the bulk plasma and the plasmoid density. l is the distance along the field line. The subscript + (−) refers to the electrons going to the right (left). Then, the heat source can be calculated on each field line. Assuming Maxwellian electrons incident to the plasmoid, a kinetic treatment using a collisional stopping power formula leads to the heat flux model, $q_\pm$ [3] which is used in construction of the ablation model [2].

In order to investigate the plasmoid motion in LHD plasmas, an equilibrium obtained by the HINT code [7] is used as the bulk plasma. Although the HINT code uses the rotational helical coordinate system, the CAP code uses the cylindrical coordinate system (R, ϕ, Z) because of preventing numerical instability induced by a locally and extremely large perturbation of the plasmoid. The colors in Figs. 1(a) and (b) show the pressure contours in the

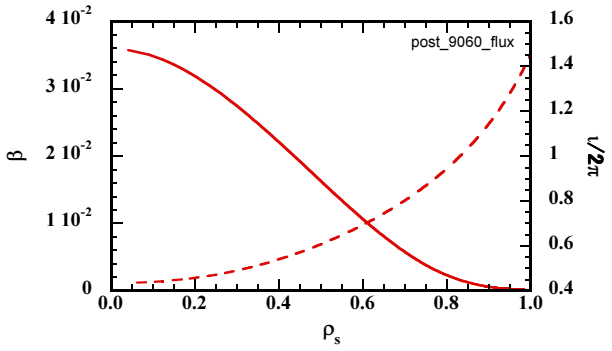

Fig. 2 The plasma beta β (solid line) and rotational transform $\iota/2\pi$ (dashed line) as a function of normalized minor radius ρ_s in the LHD plasma.

poloidal cross sections at $\phi = 0$ in the HINT and CAP codes, respectively. The yellow lines show the last closed surfaces defined by the contour line of 0.5% of the maximum pressure. The domain of the CAP code is larger than one of the HINT code because it is necessary for the last closed surface to be within the simulation box. In other words, the HINT code can not provide all data required by the CAP. Equations (1) are thus solved only in the inside of the last closed surface in the CAP code. Therefore, it is difficult to evaluate accurately the plasmoid motion around the last closed surface, but it is possible to carry out more stable simulation than one in the rotational helical coordinate. The Cubic Interpolated Psudoparticle (CIP) method is used in the code as a numerical scheme [8].

3 Drift motion of plasmoid in LHD plasma

When a plasmoid is heated in tokamak plasmas, it is expanding along the magnetic field and simultaneously drifts to the lower field side due to a tire tube force and a $1/R$ force induced by the magnetic field with curvature [6]. In the study, the motion of the plasmoid is investigated in the LHD plasma. Figure 2 shows the plasma beta β and rotational transform $\iota/2\pi$ in the bulk plasma as a function of normalized minor radius ρ_s used in the code. Figure 3 show four initial locations of the plasmoids. The colors in Figs. 3(a) and (b) show the pressure contours in the poloidal cross sections at $\phi = 0$ (vertical elongated one) and $2\pi/20$ (horizontal elongated one), respectively. The plasmoids denoted by circles A and C are located at the inner side of the torus, and those denoted by circles B and D are located at the outer side of it. Namely, the plasmoid A is at the highest field side and the plasmoid D is at the lowest field side among them. Those plasmoids are located on the same flux surface of $\rho_s = 0.4$, which is corresponding to $\iota/2\pi = 0.54$ as shown in Fig. 2. The peak values of density and temperature of the plasmoid are 1000 times

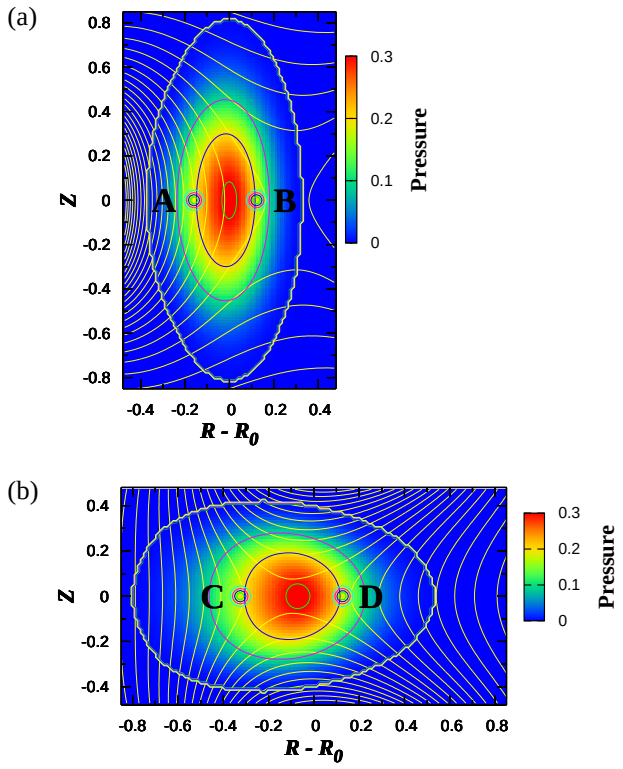

Fig. 3 Four initial locations of the plasmoids in the LHD plasma with $R_0 = 3.82$. The colors show the pressure contours in the poloidal cross sections at (a) $\phi = 0$ (vertical elongated one) and (b) $\phi = 2\pi/20$ (horizontal elongated one). The last closed surfaces are defined by the contour lines of 0.5% of the maximum pressure. The yellow lines show the contour of the magnetic pressure. The plasmoids denoted by circles A, B, C and D are located on the same flux surface of $\rho_s = 0.4$.

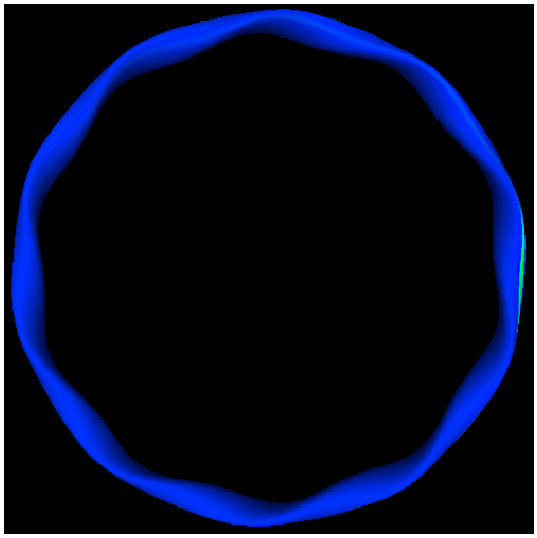

Fig. 4 The contour of the mass flow ρu_r of the plasmoid D across the flux surface $\rho_s = 0.4$ at $t = 5\tau_A$.

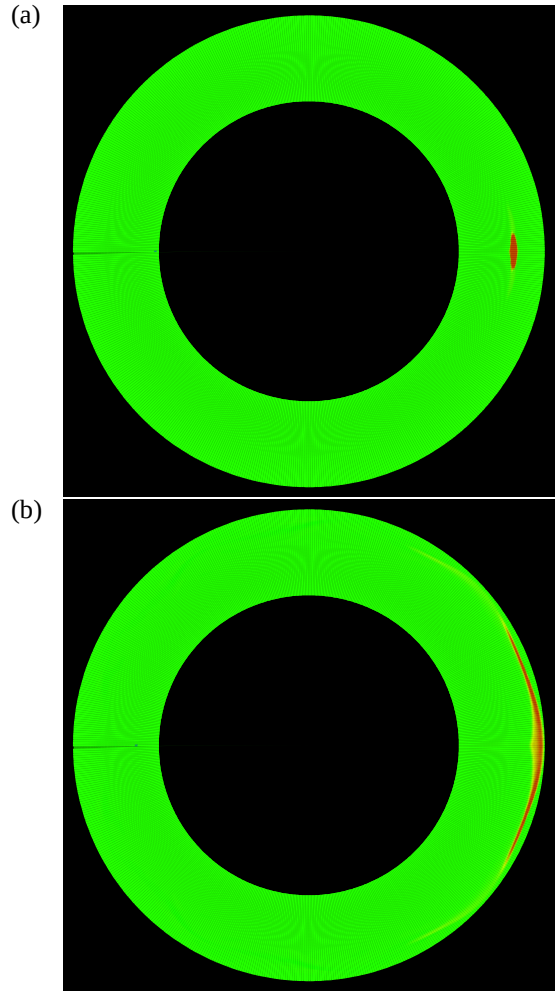

Fig. 5 The projection of the density in the direction of Z of the plasmoid D at (a) $t = 2\tau_A$ and (b) $t = 10\tau_A$.

density and 1/1000 times temperature of the bulk plasma, respectively. The plasmoid, whose half width is 0.03, encounters the electrons with fixed temperature 2 keV and density 10^{20} m^{-3}.

Simulations have been carried out in four cases A, B, C and D. Figure 4 shows the contour of the mass flow ρu_r of the plasmoid D across the flux surface $\rho_s = 0.4$ at $t = 5\tau_A$, where τ_A is the Alfvén transit time. Figures 5(a) and (b) show the projection of the density in the direction of Z at $t = 2\tau_A$ and $10\tau_A$, respectively, of the plasmoid D. It is found from Figs. 4 and 5 that the plasmoid is expanding along the magnetic field line with about 10% of the Alfvén velocity and simultaneously drifts across the flux surface in the direction of the major radius with about 1% of the Alfvén velocity. Figures 6(a) and (b) are the averaged density and averaged mass flow on the flux surfaces, respectively, of the plasmoid A (red line) and B (blue line). Solid and dashed lines show ones at $t = 2\tau_A$ and $10\tau_A$, respectively. The plasmoid A drifts toward the magnetic axis because it drifts to the lower field side due to the tire tube and $1/R$ forces. Thus, the mass flow becomes negative, and

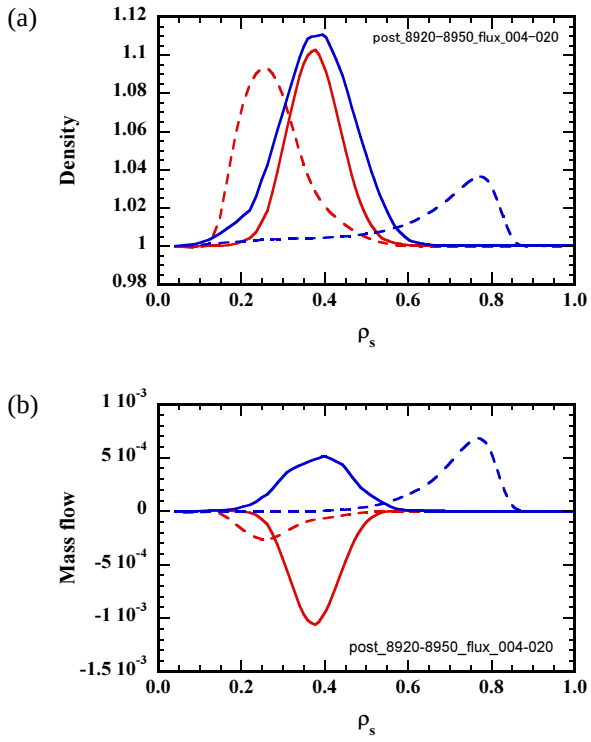

Fig. 6 (a) The averaged density and (b) the averaged mass flow on the flux surfaces as a function of the normalized minor radius, ρ_s. Red and blue lines show ones of the plasmoid A and B, respectively. Solid and dashed lines show ones at $t = 2\tau_A$ and $10\tau_A$, respectively.

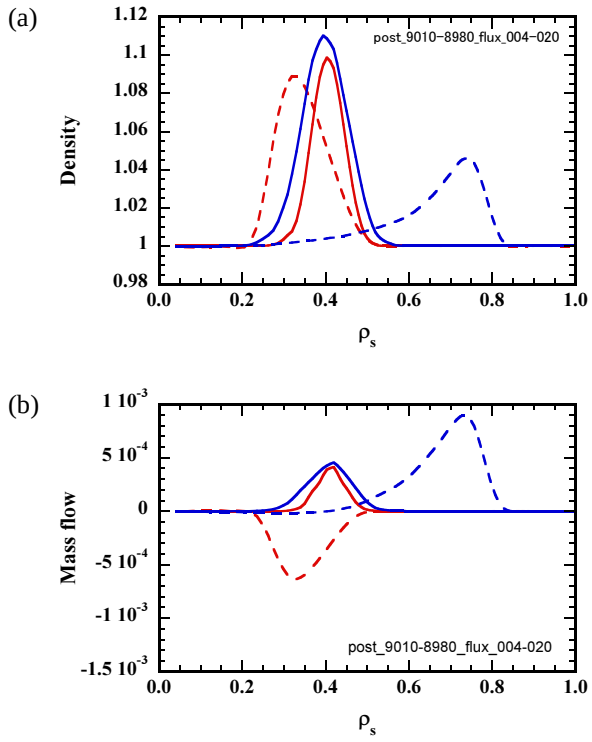

Fig. 7 (a) The averaged density and (b) the averaged mass flow on the flux surfaces as a function of the normalized minor radius, ρ_s. Red and blue lines show ones of the plasmoid C and D, respectively. Solid and dashed lines show ones at $t = 2\tau_A$ and $10\tau_A$, respectively.

the peak density drifts in the negative direction of ρ_s. Since the plasmoid B is initially located in the region where the gradient of the magnetic pressure is negative because a saddle point of one is at $R - R_0 \sim 0.27$ as shown in Fig. 3(a), it drifts in the direction of the major radius. Thus, the mass flow becomes positive, and the peak density drifts in the direction of ρ_s. Figures 7(a) and (b) are the averaged density and averaged mass flow on the flux surfaces, respectively, of the plasmoid C (red line) and D (blue line). Solid and dashed lines show ones at $t = 2\tau_A$ and $10\tau_A$, respectively. The plasmoid C had a positive mass flow at $t = 2\tau_A$, but it has a negative one at $10\tau_A$. Namely, the plasmoid drifts in the negative direction of the major radius, and subsequently drifts in the positive direction of it. Since the plasmoid C is initially located in the region where the gradient of the magnetic pressure is positive, it is reasonable that the plasmoid drifts in the negative direction of the major radius at first. The plasma beta of the plasmoid becomes ~ 1 because the magnetic well is induced by the extremely large pressure. Therefore, the drift direction is considered to be reversed due to the change of the magnetic pressure and curvature induced by such a high beta. The detail will be clarified in the future work. The plasmoid D located in the lowest field side among the four cases drifts in the direction of the major radius. The mass flow thus becomes positive and the peak of the density drifts in the direction of ρ_s.

4 Summary

It is verified by simulations using the CAP code that the plasmoid with a high pressure induced by heat flux drifts to the lower field side for several Alfvén transit times in the LHD plasma. Such a drift is induced by a tire tube force and $1/R$ force caused by an extremely large pressure of the plasmoid similarly to tokamak. However, it is found that the drift direction is reversed in the case that an initial location of the plasmoid is the inner side of the torus on the horizontal elongated poloidal cross section. That fact is considered to be caused by the change of the magnetic pressure and curvature induced by the high beta, but the detail analysis will be required to clarify the physics mechanism.

[1] Y. W. Muller et al. Nucl. Fusion, **42**, 301 (2002).
[2] P. B. Parks and M. N. Rosenbluth. Phys. Plasmas, **5**, 1380 (1998).
[3] R. Ishizaki et al. Phys. Plasmas, **11**, 4064 (2004).
[4] P. B. Parks et al. Phys. Rev. Lett., **94**, 125002 (2005).
[5] R. Sakamoto et al. *in proceedings of 29th EPS conference on Plasma Phys. and Control. Fusion.*
[6] R. Ishizaki et al. IAEA-CN-149/TH/P3-6 (2006).
[7] K. Harafuji et al. J. Comp. Phys., **81**, 169 (1989).
[8] H. Takewaki et al. J. Comput. Phys., **61**, 261 (1985).

Proceedings of ITC18,2008

Plasma Diagnostics in the Formation Stage of "LCDC"

The Local Cold and Dense Compress Formed by Injected Pellets

Masaru. Irie[1], Miyoko.Kubo-Irie[2], FBX Team[1]
[1]*Waseda University, Tokyo, Japan*
[2]*Denji Ohyoh Kenkyuujyo (Research Institute for Applied Electro-Magnetism), Tokyo, Japan*

The most efficient fueling scheme so far is said to be a frozen deuterium pellet injection, even though it is still very difficult to accomplish central fuelling (to inject fuel into the burning plasma core) into nuclear fusion reactors. On the other hand, this scheme forms very cold (~10^1eV)and very dense (~10^{23}) plasma along the magnetic field line on the rational surface in the time scale of about 10^0ms. This is called LCDC (Local Cold Dense Compress). The detailed experimental observation has not been reported so far because of the difficulty stated below. This paper deals with the experimental proposal in this direction. The fundamental diagnostic scheme is 3D image reconstruction technique developed in our laboratory. This is originally developed in nuclear fusion research as a Soft X-ray Tomography. This technique is going to be used in many fields: CXT (Constrained X-ray Tomography)in medical field, CEBT (Constrained Electron Beam Tomography) in biological field and quantum entanglement detection for quantum computer research.

Keywords: LCDC (Local Cold and Dense Compress), Pellet Injection, Bremsstrahlung radiation , ablation, plasmoid

Inroduction

The injected pellet goes under intense heat up and is ablated by bulk plasma and evaporated. The neutral hydrogen vapour-clusters go under free diffusion until they are ionized. These clusters form dense plasmoid, which is partially ionized plasma above the order of $10^{25}/m^3$. Because of the high collisionality, this plasmoid shields the solid pellet core from the main plasma and it travels almost the same speed as the injection speed crossing many rational surfaces. In their simulation, Nakamura and Wakatani estimated the plasmoid parameters as below in 1986 and well within the experimentally obtained parameters.

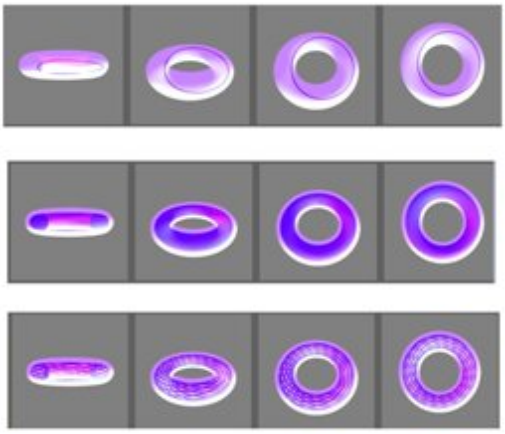

Fig.1. LCDC on the rational surfaces.
The plasma diffusion allows the LCDC density decay about 100 times faster on q=1.01 than on q=1.1 magnetic surface.
1st raw q=1.0, 2nd raw q=1.01 3rd raw q=1.1

Pellet core : ~10^1K , $10^{30}/m^3$
Plasmoid: $10^{24}/m^3$, 10^0 eV
Bulk Plasma: $10^{20}/m^3$, 10^4 eV

This plasmoid in this phase contains neutral hydrogen and radiates strong spectral emission. Because of this nature the plasmoid has been studied both intensively and extensively.
In due course, after about duration of 10^{-4} sec, the plasmoid develops to be nearly fully ionised and the radiation changes into continuum. Because of the fast

author's e-mail: fbx3@waseda.jp

diffusuion in the direction parallel to the magnetic field, the plasma diffuses rapidly into the magnetic surfaces. However on the rational surfaces, because of the short connection length, the low temperature and high density plasma forms a filament type local loop called LCDC (Local Cold and Dense Compress) and show quite different behavior from those on the irrational surface, Irie [1]. Fig.1 shows the basic image of this LCDC near q=1, q=1.01 and q=1.1 surface. The plasma diffusion velocity along the magnetic field line is about a half km/s. So the LCDC volume is minimum at q=1 and the volume is roughly 100 times larger at q=1.01.

The plasma density in the latter decays about two orders of magnitude lower than the former within few ms.

Here we would like to show the diagnostic scheme of thermalization and diffusion process of this LCDC plasma with the fundamental technique used in our laboratory in the field of the quantum computation.

Radiation Intensity estimation

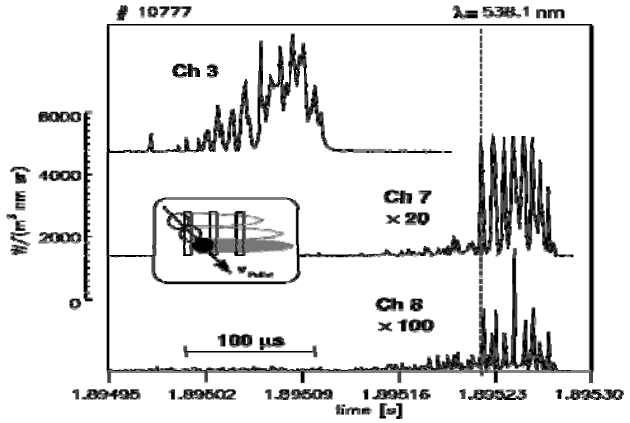

Fig.2. High density plasma drift with Continium radiation measurement in ASDEX-U
W.M.Muller et al. Phys.Rev.Lett, 83,p2199 (1999)

In 1999 W. M. Muller and his co-workers published their experimental result of pellet injection into the ASDEX-U tokamak as shown in Fig.1[2]. The pellet is injected from the high field side and the plasmoid drifts to lower field side. The plasmoid is striated and split into many clouds. The radiation is observed through many slits and each plasmoid blocks shows each plasmoid sequentially as in the figure. a train observed spectral radiation the Balmer line spectra decays in due course. The movement is monitored with an array of slits as shown in the figure. Drifting plasmoids initially radiates clear and strong Balmer line spectra similar to those in Channel.3 and when it reaches to the plasma center, Channel.8, the radiation in 5384.1 even though their intensity becomes weaker by few orders of magnitude but still keeps well distinguishable sequential radiation peak. In their paper they do not mention the detailed radiation process, however here we would like to write down the fundamental Bremsstrahlung formula for reference.

$$\varepsilon = 6.8\times10^{-33} Z^2 n_e n_i T^{-1/2} g_n \exp(-h\nu/kT) \mathrm{Wm^{-3}Hz^{-1}} \qquad (1)$$

This clearly shows the strong density dependence and indicates the possibility to detect these emission from the LCDC plasma along the magnetic field line in the downstream zone of the Balmer radiation points.

Density estimation: Diffusion Equation

In their web page V. M. Timokhin, et al, in the State Polytechnical University of St. Petersburg, Russia shows a

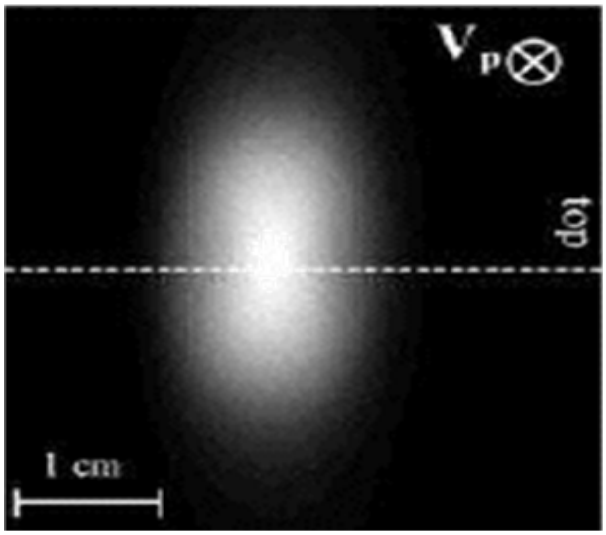

Fig.3. Plasmoid from carbon pellets in the W7-AS Plasma.
V. M. Timokhin, et al. (2005)

nice picture of the plasmoid form the carbon pellet shown in Fig.3.

The three dimensional diffusion equation with non-isotropic diffusion coefficient is

$$\frac{\partial N}{\partial t} = D_x \frac{\partial^2 N}{\partial x^2} + D_y \frac{\partial^2 N}{\partial y^2} + D_z \frac{\partial^2 N}{\partial z^2}$$

$$N(r,z,t) = \frac{1}{8(\pi t)^{3/2} D_r (D_z)^{1/2}} \exp\left[-\frac{(r-r_0)^2}{4D_r t} - \frac{(z-z_0)^2}{4D_z t} \right] \qquad (2)$$

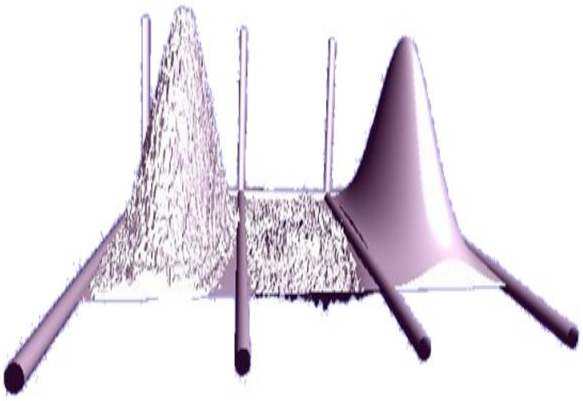

Fig.4. The three dimensional plot of the radiation intensity (left), the best fit surface of this image profile based on the equation (2) (right) and the difference between the two surfaces profiles (middle). The agreement is within 0.5% in this case.

This image and the classical diffusion model agrees very well as shown above. The three dimensional plot of the intensity (left), the best fit surfaces of these image profiles based on the equation (2) (right) and the difference between the two profiles (middle) is shown in Fig.4. This simple model with only two adjustment parameters describes the basic feature of the radiation profiles well within our requirement. The mean discrepancy is less than 0.5% in this case. In this model we can trace around where and around when the LCDC are most probable to exist.

Three dimensional reconstruction detection

The next problem is how to distinguish the LCDC radiation out of the strong background radiation from the edge plasma. Let us see the example. In fug.5 the picture of ELM filament in MAST Spherical Tokamak is presented taken from Dudson et al[3]. The image is in focus a little behind the center colum so the front ELM filament is strongly blurred and the rear ELM filament is less blurred. If the physical If the physical system is optically thin and the Dynamic range of the image sensor is broad enough, we should be able to obtain the three dimensional information by using focusing technique based on the geometrical optics.In other word, we should be able to identify the position of the radiation source as shown in Fig.6. The plane at P1 receives the converging ray from the source. The plane P2 the ray is just in focus and The plane at P3 receives the diverging ray from the source. In P2 plane clear two dimensional image is recorded but on the other plane the image is blurred and the spatial correlation factor is larger than the focusing plane.

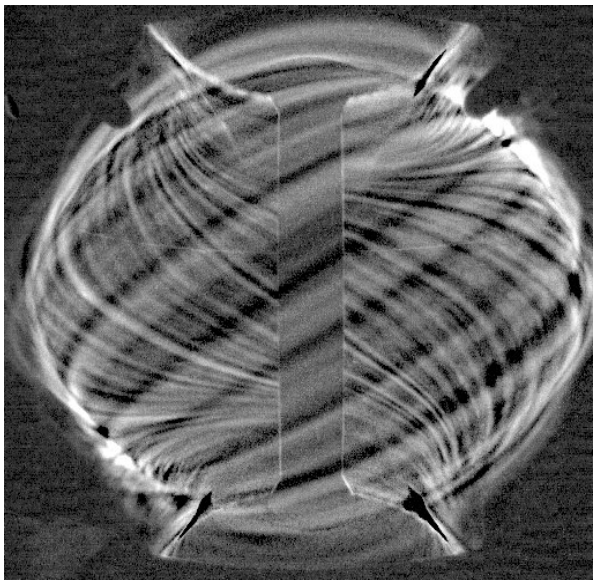

Fig.5. The sample of off-focus image taken from
The ELM filament in MAST L-Mode plasma
B. Dudson et al. p.92, Programme 35th EPS Conf. Plasma Phys. 2008.

The two dimensional image taken on the camera sensor plate is understood as the convolution of all the ray passing through the lens.

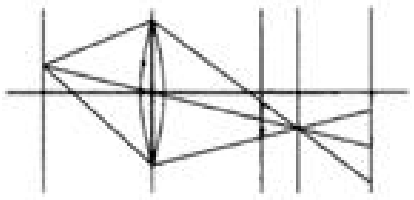

Fig.6. Out of focus blurred image in geometrical optics / ray tracing model. The plane at P1 receives the converging ray from the source. The plane P2 the ray is just in focus and The plane at P3 receives the diverging ray from the source.

The simplest imaging method to meet this requirement is attained by tandem camera system shown in Fig.7 , which is in principle modified version of the conventional 3-CCD camera for RGB separation in instrumental engineering sense. Here spatial resolution is determined by the lens aperture and the camera position. The detailed description shall be published elsewhere.

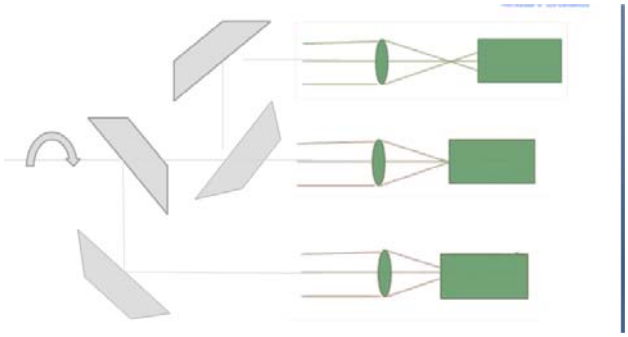

Fig.7. Tandem camera configuration to obtain 3-dimensional spatial resolution.

For LCDC measurement, strong background radiation is originated from the plasma boundary and LCDC is within the main plasma region. The image distance should be clearly distinguished even with conventional camera lens aparture and modidied version of the conventional 3-CCD camera system similar to Fig.7. At the same time on the wave optical assumption, we can expect the image co-relation in the off-focus plane.

Low intensity detection

Even though the emission intensity of LCDC itself is expected to be few orders of magnitude higher than the main plasma, this localized nature means total volume observed by the camera is again few orders of magnitude samaller than the peripheral

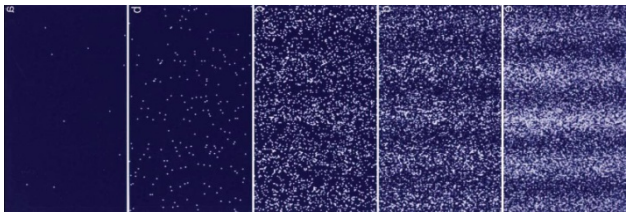

Fig.8 Schematic example of low intensity photon imaging
（Electron Beam version of Young's Double Slit)
Taken from
Build-up of an electron interference pattern.
Numbers of electrons are
10 (a), 200 (b), 6,000 (c), 40,000 (d), and 140,000 (e).
Tonomura A,, Proc. Natl. Acad. Sci. USA 102 No. 42 (2005): 14952.

plasma. In this sense it is difficult to detect unless the initial estimation of the position is vague or the plasma perturbation is not small to shift the rational surface. In these occasion the photon correlation type detection is necessary. This sort of problems is solved in the developing stage of Thomsom Scattering Experiment neary half a century ago.

In Fig.8, we show the similar classical example. This is the Young's double slit experiment by Tonomura.This nature is also seen in the quantum entanglement experiment aiming for the quantum computer.

Conclusion

We have discussed the fundamental diagnostic plans for

LCDC (THE LOCAL COLD AND DENSE COMPRESS)

narrow filamentary plasma channel which is supposed to lie on the rational surface. Even though this zone occupies only local zone but it shows very interesting diagnostic information. The detailed assumptions identifies the rough estimation of their nature.
The starting point should be identified from the time history started from initial plasmoid phase from Balmer Radiation. The radial density profile is well assumed to be in Gaussian Profile and it lies on the Magnetic field line.

References

1. M.Irie & M. Kubo-Irie et al.
   35th EPS Conf. Plasma Phys. 2008.
2. Y.Nakamura, H.Nishighara and M.Wakatani, Nuclear Fusion 26,907(1986)
3. W.M.Muller et al.
   Phys.Rev.Lett, 83,p2199 (1999)
4. V. M. Timokhin, et al.
   32th EPS Conf. Plasma Phys. 2005
5. B. Dudson et al.
   35th EPS Conf. Plasma Phys. 2008.
6. Tonomura A.,
   Proc. Natl. Acad. Sci. USA 102 No. 42 (2005): 14952.

Proceedings of ITC18, 2008

Microscopic deformation of tungsten surfaces by high energy and high flux helium/hydrogen particle bombardment with short pulses

M. Tokitani [a], N. Yoshida [b], K. Tokunaga [b],
H. Sakakita [c], S. Kiyama [c], H. Koguchi [c], Y. Hirano [c], S. Masuzaki [a]

[a] *National Institute for Fusion Science, Toki, Gifu 509-5292, Japan*
[b] *Research Institute for Applied Mechanics, Kyushu University, Kasuga, Fukuoka 816-8580, Japan*
[c] *National Institute of Advanced Industrial Science and Technology, Tsukuba, Ibaraki 305-8568, Japan*

High energy and high flux helium and hydrogen particles were irradiated with polycrystalline tungsten specimen by using neutral beam injection (NBI) facility in National Institute of Advanced Industrial Science and Technology (AIST). Incidence energy and flux of NBI shot are 25 keV and 8.9×10^{22} ions/m^{2}s, respectively. Duration time of each shot was 30 ms with 6 min interval. Surface temperature may be reached over 1800 K. In the cases of helium irradiation, total fluence was selected 2 cases of 1.5×10^{22} ions/m^{2}s and 4.1×10^{22} He/m^{2}s. The former case, large sized blisters with the diameter of 500 nm were densely observed. While, the latter case, blisters was disappeared and fine nano-branch structures appeared instead of blisters. Cross-sectional transmission electron microscope (TEM) observation was performed by using focused ion beam (FIB) technique. Fig. 1 shows that TEM image after irradiated with 4.1×10^{22} He/m^{2}s. It was clear that very dense fine helium bubbles with the size of 1-50 nm were observed, the density of tungsten matrix was drastically decreased by void swelling with growth of helium bubbles. In the hydrogen irradiation case, these damages were not observed.

Keywords: Helium, Hydrogen, High energy and high fluence, Tungsten, Nano-scale structure, Blister, Bubble

1. Introduction

Tungsten is a candidate of divertor armor materials in international thermonuclear experimental reactor (ITER). In ITER conditions, strong erosion and radiation damages on the divertor surface caused by high heat and particle loading due to the disruptions and edge localized modes (ELMs) are critical issues for achievement of its good thermal and mechanical properties. Thus, heat loading tests or particle loading tests have been performed using several electron beam [1,2] or plasma machines [3,4], respectively. However, evaluation of the synergistic loading effects of high heat and particles with short pulses is necessary for confirming the reliability of tungsten armor tiles. Although some proceeded experiment about it has already been performed [5-7], they have mainly focused on the micro scale or macro scale phenomena. For understanding the fundamental mechanism of the damage evolution, we have to focus on nano-scale structures.

Especially, helium irradiation effects with high heat loads should be noted because helium once injected into metals causes serious damaging effects and it does not release until high temperature due to the strong interaction with lattice defects such as vacancies and dislocation loops [8]. Actually, tungsten irradiation tests to divertor plasmas in Large Helical Device (LHD) indicated that synergistic effects due to high heat and helium/hydrogen particle load lead to damage and erosion of tungsten surface [9,10].

Therefore, the helium or hydrogen irradiation experiment with high heat loading is important for not only elucidation of the damage evolution but also safety assessment of tungsten walls for fusion devices. In this study, high energy and high flux helium and hydrogen particles were irradiated with polycrystalline tungsten specimen by using neutral beam injection (NBI) facility in National Institute of Advanced Industrial Science and Technology (AIST). After the exposure, nano-scale deformation and damage evolution were investigated by using focused ion beam (FIB) fabrication technique and transmission electron microscope (TEM) observation. Furthermore, to investigate the effect of bombardment of helium and hydrogen particles, optical reflectivity was measured by means of spectrophotometer for the wavelength between 190 and 2500 nm. It is expected that from the investigation of correlativity of reflectance and damage evolutions, radiation damages caused by heat and particle loads may be able to be predicted from measurement of optical reflectivity.

author's e-mail: tokitani.masayuki@LHD.nifs.ac.jp

This study is fundamental research focused on the nano-scale damage evolution in tungsten due to the energetic particle bombardment under high heat loading.

2. Experimental procedures

2.1. Material irradiation in NBI facility

High current and high current-density NBI beam system with strong focusing characteristics for measure to the behavior of alpha particle characteristics in nuclear fusion device were successfully developed in AIST [11]. Another application of this focused beam is the irradiation test of materials.

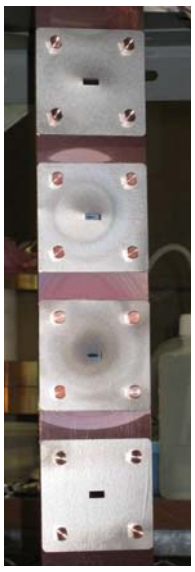

Fig. 1 Specimen stage

High purity (~99.95 %) powder metallurgy (PM) tungsten specimens of 10 × 5 × 1 mm^3 were mounted in the focused point of the NBI beam by using special specimen stage as shown in Fig. 1 and then, irradiated with helium, hydrogen and He+H NBI beam. Incidence energy and beam current were fixed as 25 keV and 40 A, respectively. The diameter of the focused beam was estimated as ~60 mm. Then, the power density and flux were 300 MW/m^2 and 8.8×10^{22} particles/m^2s. Duration time of each shot was 30 ms with 6 min interval. Total irradiation time and fluence of each irradiation pattern were summarized in table. 1. In the case of He+H irradiation, the ratio of hydrogen and helium was estimated at about He : H = 7.9 : 2.1 [12]. Although surface temperature was measured by using an optical pyrometer and thermocouples embedded to just behind the specimen, unfortunately, its exact value was not able to be measured. The expected temperature from optical pyrometer is near 1800 K.

2.2. Material analysis

After the exposure, surface morphology was analyzed by means of scanning electron microscopy (SEM). For clarify the depth distribution of nano-scale damages, cross-sectional microscopic observation was conducted by using focused ion beam (FIB) fabrication technique and transmission electron microscopy (TEM) observation.

Furthermore, to investigate the effect of bombardment of helium and hydrogen particles on optical reflectivity, change of optical reflectivity was measured by means of spectrophotometer.

	Pulse x shot	Total Irr. time	Power density	Fluence
He	~30ms x 7shot	171ms	300MW/m²	1.5x10²²He/m²
	~30ms x 16shot	461ms	300MW/m²	4.0x10²²He/m²
H	~30ms x 5shot	146ms	300MW/m²	1.3x10²²H/m²
He+H	~30ms x 15shot	447ms	300MW/m²	3.9x10²²He+H/m²

Table 1 Total irradiation time, power density and total fluence for each irradiation pattern.

3. Results and discussions

3.1. Surface morphology

Fig. 2 shows surface photo and SEM image of tungsten specimens after irradiated with helium, hydrogen and He+H beams. Irradiated area on specimens was about 8 × 3 mm^2. In the cases of helium irradiation, total fluence was selected 2 patterns of 1.5×10^{22} He/m^2 and 4.1×10^{22} He/m^2. The former pattern, surface color was changed to gray and large blisters with the diameter of 500 nm were densely observed. While, the latter pattern, blisters were disappeared due to the sputtering erosion, and surface become smoother at low magnification SEM image. However, at high magnification image, fine nano-branch structures appeared instead of blisters. This structure must be affected the degradation of optical reflectivity in visible wavelength, actually, the surface color has been turned to dark brown. The detailed discussion of optical reflectivity will be mentioned in section 3.5.

In the case of hydrogen irradiation, although intensive grain growth was observed, remarkable deformation did not show any sign. These discrepancies between hydrogen and helium seem to be the result of the difference of the behavior of them in metals. In the case of helium, surface modifications are considered to be due to the formation, coalescence and migration of helium bubbles near the surface during the pulse high heat loading. While, in the case of hydrogen, these effects does not occur. It is known that retention of hydrogen isotopes in tungsten is low in general, and this is one of

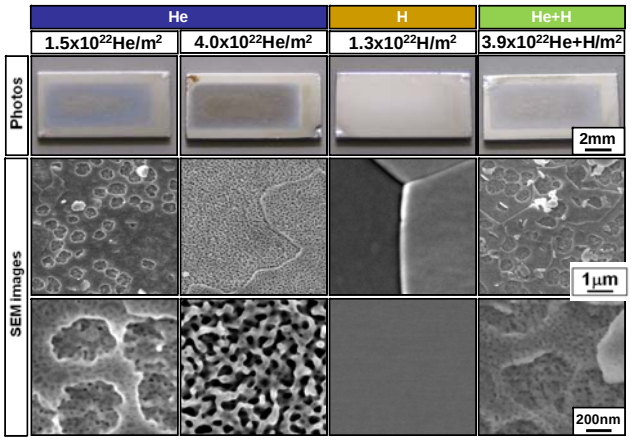

Fig. 2 Surface photo and SEM image of tungsten specimens

the advantages of this material [13].

Furthermore, in the case of simultaneous irradiation of He and H, surface morphology was quite similar to the lower fluence case of helium irradiation (1.5×10^{22} He/m^2). This means that damage evolution of the surface does not depend on the hydrogen irradiation.

3.2. Depth distribution of nano-scale damages

To clarify depth distribution of radiation damages, we need cross-sectional image of the sub-surface region in nanometer level. FIB fabrication technology was used for obtain the cross-sectional TEM samples for nano-observations. Fig. 3-(a~d) shows TEM images of four exposure patterns. In the case of lower helium irradiation (a), helium bubbles with size of about 1~50 nm were densely observed up to the depth of 200 nm. One should note that many of the bubbles are larger than 20 nm and some of them have an oddly shaped image like an ellipse or even a gourd. This indicates that the bubbles have grown by coalescence with the abrupt temperature increase and the non-equilibrium shape is “frozen” by rapid cool-down after the termination of the NBI beams. Although average penetration depth of 25 keV-He in tungsten was estimated to be about 60 nm by TRIM-code, heavy damaged region was much deeper than that of this value. We can consider that this discrepancy is caused by not only diffusion of injected helium atoms but also void swelling of the surface. In the case of (b), highest helium irradiation, helium bubbles with size of about 1~100 nm were densely observed with nano-branch structures, many of the bubbles are larger than 50 nm. It was much larger than that of case (a). Thus, density of tungsten matrix was drastically decreased by void swelling, and its depth distribution was over 300 nm. On the surface of this specimen shown in Fig. 2, blisters lid which can be observed in case (a) was already disappeared due to the sputtering erosion. In this irradiation stage, the accumulation of helium atoms by implantation in the matrix and loss by sputtering erosion and exfoliation of blisters has reached a balance. Therefore, if the helium were continuously irradiated, nano-branch structures will not be disappeared.

In the case of hydrogen irradiation, (c), nano-scale damages scarcely formed, which corresponds to the surface observation result as shown in Fig. 2. It is considered that since hydrogen atoms scarcely interact with lattice defects, radiation damages could not form even at the high energy and high flux condition.

Furthermore, result of a simultaneous irradiation of hydrogen and helium, (d), shows that size and density of helium bubbles and its depth distribution were very similar to the case (a). As mentioned above, damage evolution does not depend on the hydrogen irradiation. In contrast, helium once injected into metals, they cause serious damaging effects due to the strong interaction with lattice defects such as vacancies and dislocation loops. Thus, helium irradiation effects in tungsten indicate that serious consideration should be given to the surface erosion of tungsten walls.

3.5. Optical reflectivity

Fig. 4-(a~d) shows the optical reflectivity of tungsten specimens after exposed to NBI beams. Reflectivity of virgin specimen was also plotted together. It is clear that strong reduction of reflectivity has occurred in all helium irradiation cases (a, b, d). In particular, about 500 nm or less is remarkable. Referring to our previous study [14], it is considered that reduction of optical reflectivity is due

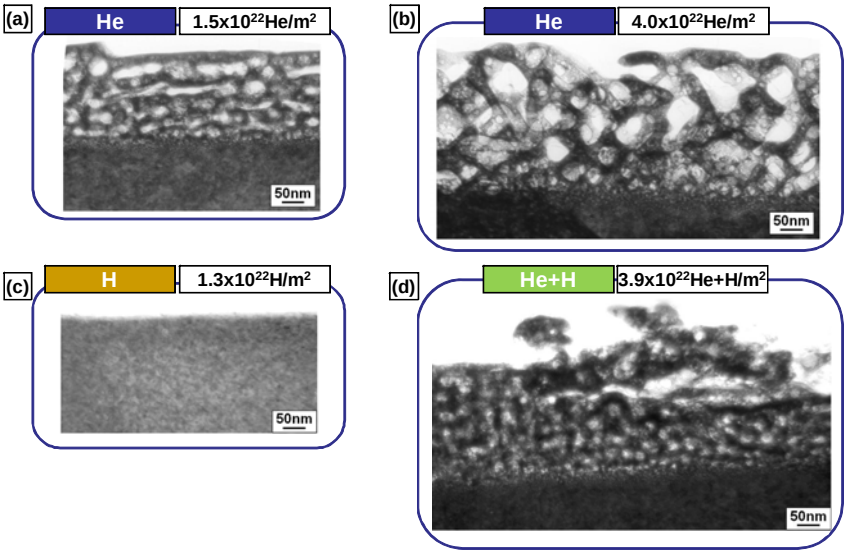

Fig. 3 Cross-sectional TEM images after irradiated with
(a): 1.5×10^{22} He/m^2, (b): 4.0×10^{22} He/m^2, (c): 1.3×10^{22} He/m^2, (d): 3.9×10^{22} He+H/m^2

to the multiple scattering of light by the dense helium bubbles in the sub-surface region. In the case of (a) and (b), the spectrum is very similar in the range of 190 to 2500 nm. We can consider that since surface morphology and depth distribution of nano-scale damage of them were similar in Fig. 2 and Fig. 3, reduction of reflectivity may be dependent on them.

On the other hand, highest helium irradiation, (b), although drastic degradation has occurred in short wave length (190~1000 nm), its recovery has identified in long wave length (2000~2500 nm). We can consider the following mechanisms for this phenomenon. Reduction of reflectivity must be due to the surface roughening and fine bubble formation, drastic degradation in short wave length was caused by formation of nano-branch structures with nano-scale helium bubbles as shown in Fig. 3-(b). While, in the long wave length region, its recovery has been caused by smoothening the surface due to the progress of the sputtering erosion as shown in Fig. 2.

In the case of hydrogen irradiation, (c), although slight degradation was observed in the long wave length (1500-2500 nm), remarkable degradation was not confirmed in whole wave length regions. We should note that effect of helium bombardment for optical reflectivity is also much higher than that of hydrogen bombardment. This result is important for the design and operation of plasma diagnostics using first mirror.

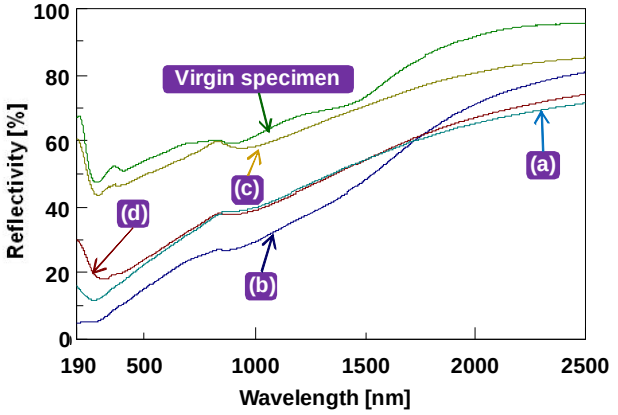

Fig. 4 Optical reflectivity of specimen after exposed to NBI beams. (a): 1.5×10^{22} He/m^2, (b): 4.0×10^{22} He/m^2, (c): 1.3×10^{22} He/m^2, (d): 3.9×10^{22} He+H/m^2

4. Summary

High energy and high flux helium and hydrogen particles were irradiated with tungsten specimen by using NBI facility in AIST, and then, nano-scale deformation and damage evolution in tungsten were investigated.

In the case of helium irradiations, very dense fine helium bubbles with the size of 1~100 nm were observed, the density of tungsten matrix was drastically decreased by void swelling with growth of helium bubbles. In the hydrogen irradiation case, these damages were not observed.

To investigate the effect of bombardment of helium and hydrogen particles, optical reflectivity was measured. The hydrogen irradiation case, it was scarcely changed before and after irradiation. However, reduction of reflectivity has occurred in helium irradiation case, and it near 500 nm or less and also infrared region was remarkable. It is considered that reduction of optical reflectivity is due to the multiple scattering of light by the helium bubbles in the sub-surface region.

High energy and high flux helium irradiation effects in tungsten indicate that serious consideration should be given to the surface erosion of tungsten walls. Furthermore, if we use the tungsten for first mirror, its design and operation will become also serious problems.

Acknowledgement

A part of this study was financially supported by the Budget for Nuclear Research of the Ministry of Education, Culture, Sports, Science and Technology of Japan, based on the screening and counseling of the Atomic Energy Commission.

References

[1] K. Tokunaga et al., Fus. Eng. Des. 81 (2006) 133-138
[2] X. Liu et al., J. Nucl. Mater. 329-333 (2004) 687-691
[3] D. Nishijima et al., Materials Transactions Vol.46 No.3 (2005) 561-564
[4] D. Nishijima et al., J. Nucl. Mater. 313-316 (2003) 97-101
[5] K. Tokunaga et al., J. Nucl. Mater. 307-311 (2002) 130-134
[6] K. Tokunaga et al., J. Nucl. Mater. 329–333 (2004) 757-760
[7] S. Tamura et al., J. Nucl. Mater. 337–339 (2005) 1043–1047
[8] T. Baba et al., Materials Transactions Vol.46 No.3 (2005) 565-567
[9] M. Tokitani et al., J. Nucl. Mater. 337-339 (2005) 937-941
[10] M. Tokitani et al., J. Nucl. Mater. 363-365 (2007) 443-447
[11] H. Sakakita et al., Proc. of IAEA Fusion energy conf. 2006, FT/P5-2
[12] H. Sakakita et al., submitted to J. Plasma Fus. Res. Series
[13] N. Yoshida, Y. Hirooka J. Nucl. Mater. 258-263 (1998) 173-182
[14] A. Ebihara et al., J. Nucl. Mater. 363-365 (2007) 1195-1200

Proceedings of ITC18,2008

Study on electrode of solid electrolyte hydrogen (isotope) sensor for application to liquid blankets

T. Ohshima[a,b], M. Kondo[b,c], M. Tanaka[c], T. Muroga [b,c]

[a]*TYK Co. Ltd., 3-1 Obata-cho, Tajimi 507-8607, Japan*

[b]*Department of Fusion Science, The Graduate University for Advanced Studies, 322-6 Oroshi-cho, Toki 509-5292, Japan*

[c]*National Institute for Fusion Science, 322-6 Oroshi-cho, Toki 509-5292, Japan*

The control of hydrogen isotopes is one of the key issues for liquid blankets. For this purpose, monitoring of hydrogen isotopes using on-line sensors is the essential technology. In the present study, the hydrogen sensor using solid electrolyte ceramics was developed for fusion blanket application. Because of very corrosive environment of liquid breeders, Pd membrane electrodes, which will be more protective of the ceramics relative to the conventional porous Pt electrodes, were fabricated and tested. The Pd membrane electrode was shown to perform well in gaseous environment.

Keywords: Blanket, Hydrogen senor, Solid electrolyte, Electrode, Palladium, Flibe, Flinak, Pb-17Li, Li

1. Introduction

Molten salt LiF-BeF_2 (Flibe), molten lithium (Li), and molten lead-lithium (Pb-17Li) are candidate blanket tritium breeding materials for fusion reactors. For the blankets with those liquid breeders, control of tritium is the key issue. For this purpose, on-line sensing of tritium in the high temperature melts is the essential technology.

The hydrogen partial pressures of the three melts are extremely different, with very high pressure for Flibe, medium for Li-Pb and very low for Li [1].

Proton conductive solid electrolyte is the functional ceramics that can allow hydrogen to permeate selectively. It is used as the hydrogen sensor for molten aluminum, molten copper and so on [2,3]. The hydrogen sensors need electrodes on the ceramic surfaces. Porous platinum (Pt) has been used as the electrode. Though Pt electrodes show good performance, they do not protect well the ceramics from the atmosphere because of their open structure.

Palladium (Pd) has high conductivity and hydrogen permeation function and thus a candidate for the protective electrode if flawless coating on the ceramics is possible. Pd porous electrodes have been examined in the previous studies [4, 5]. However, application of Pd to the membrane electrodes has not been examined yet. In this study, fabrication and characterization of Pd membrane on proton conductive ceramics are carried out and the applicability to liquid blankets is examined.

2. The principle of hydrogen sensor

The principle of the hydrogen sensor for gaseous medium is shown in Fig.1. Proton conductive electrolyte ceramics partitions the sensor into two compartments in which flow of gases with different partial pressure of hydrogen is made. In this case, the electrode with higher hydrogen partial pressure acts as anode. The reactions of the electrodes are given bellow;

Anode: $H_2 \rightarrow 2H^+ + 2e^-$ (1)

Cathode: $2H^+ + 2e^- \rightarrow H_2$ (2)

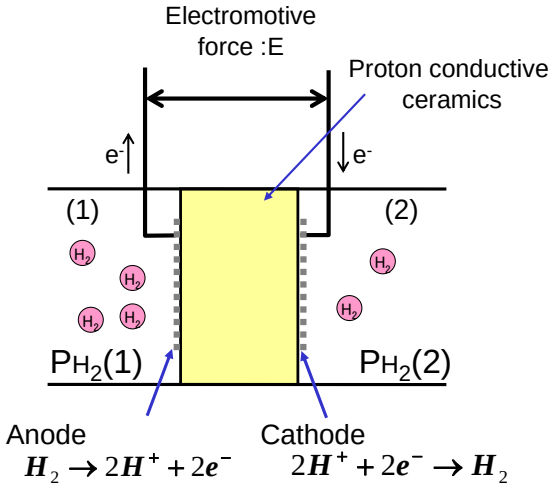

Fig.1 Principle of hydrogen sensor.

These reactions are induced by electromotive force (EMF) between the two electrodes. The EMF is given below according to the Nernst's equation

author's e-mail: t.ohshima@tyk.jp

$$E = \frac{RT}{2F} \ln \frac{PH_2(1)}{PH_2(2)} \quad (3)$$

where F is Faraday constant, R is a gas constant and T is absolute temperature. $PH_2(1)$ and $PH_2(2)$ are partial pressure of hydrogen in compartments (1) and (2), respectively.

3. Fabrication of sensors with Pd electrodes

The hydrogen sensor used cap-shaped $CaZr_{0.9}In_{0.1}O_{3-a}$ as proton conductive ceramics. The sensor's dimension was 3.8mm for the outer diameter, 2.5mm for the inner diameter, and 37mm for the length. The outer surface of the sensor cell was coated with Pd paste and was baked twice at 1673K to make membranous electrode. Inner sensor cell was coated with Pt paste and was baked at 1273K to make a porous electrode. The ceramic sensor was fixed to an Al_2O_3 tube by low melting glass seal.

For measuring EMF of the sensor, Pt wires were fixed to the outer and the inner electrodes, and a stainless tube was inserted to flow the reference gas into the inner electrode. The same structures of the probes having Pt porous electrode or Pd membrane electrode on the both side of the sensor cell were also made. The system of measuring EMF is shown in Fig. 2. Three probes, a thermocouple and tubes for gas inlet to and outlet from the Al_2O_3 protection tube, were inserted and fixed to the silicon stopper. The protection tube was set into the electric furnace and the temperature was kept constant during the flow of H_2-Ar mixed gas.

The EMF was measured at 873K, 773K and 673K with 1%H_2-Ar gas as the reference gas flowing in the inner electrode. At the outer electrode, H_2-Ar mixed gases with several H_2 levels flowed. The 34970A data acquisition switch unit by Agilent was used to measure EMF of the three probes.

4. Characterization of the sensors

4-1 Microstructures

The surface and section of the outer electrode were observed using SEM. The images are shown in Fig. 3. The surface of Pt electrode showed grains of 1 to 5μm and with high density of pores. The diameter of the pores was below 10μm. There were, however, areas where the pore density was locally low. The cross section of Pt electrode showed porous structure with the thickness of 5 to 10μm. There were pores penetrating the electrodes.

The surface of Pd electrode showed grains of 10 to 50μm. The surfaces were smooth and contained very low density of pores. The sections of Pd electrode showed membrane structure with the thickness of 10 to 20μm. The pores observed in the membrane did not penetrate throughout the electrode.

4-2 Performance in gaseous environments

The results of the measurement of EMF are shown in Fig. 4. The dashed lines are the theoretical EMF by Nernst's equation for each H_2-Ar mixed gas with the reference 1%H_2-Ar gas at 873K.

The EMF of all probes changed immediately to the value observing Nernst's equation when the mixture of the flowing H_2-Ar gas was changed in the Al_2O_3 protection tube. The EMF of the three probes agreed with the theoretical values of Nernst's equation. The change of the gases in the Al_2O_3 protection tube was carried out twice and the reproducibility was confirmed.

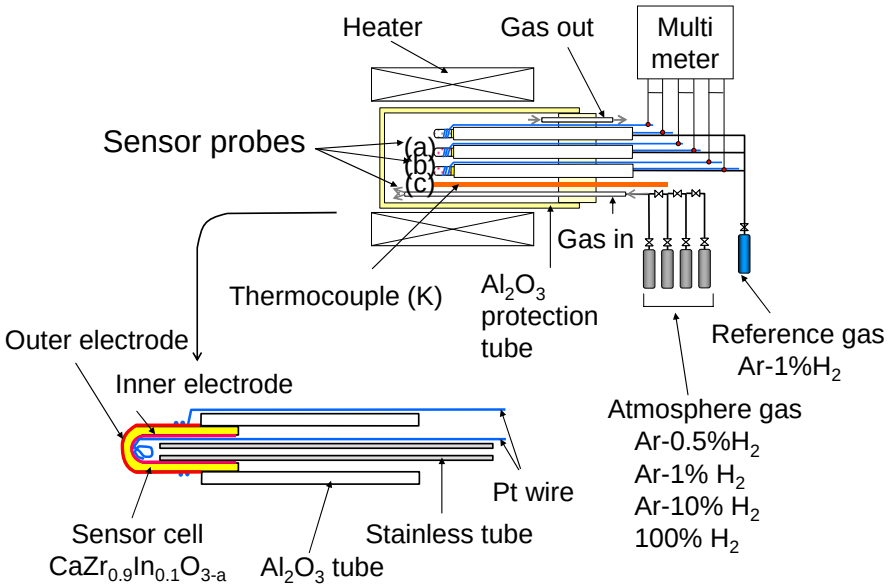

Fig. 2 System for measuring EMF and combination of outer electrode and inner electrode on sensor surface (a) Pt/Pt electrode, (b) Pd/Pt electrode, (c) Pd/Pd electrode

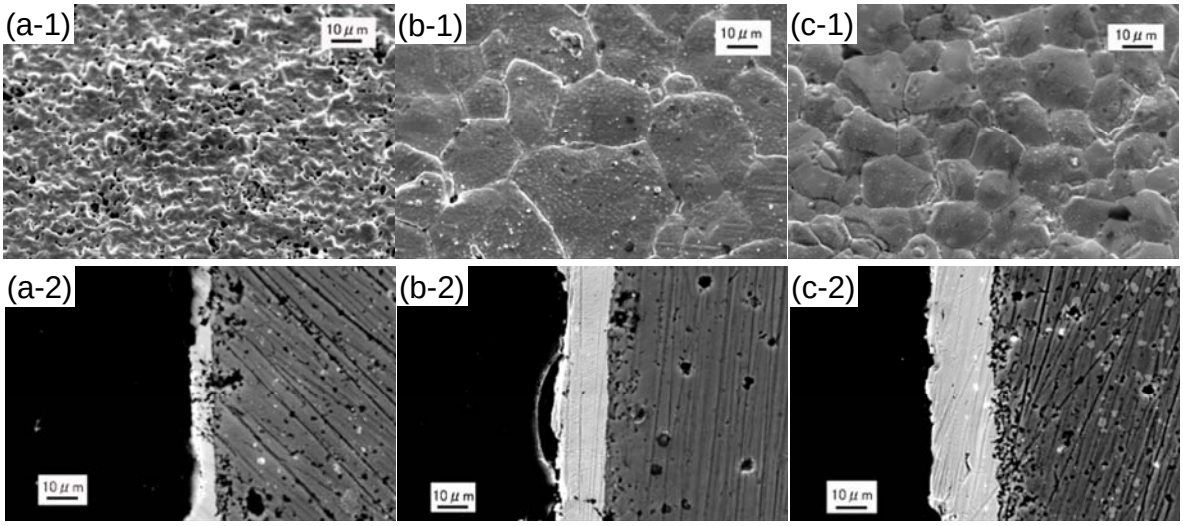

Fig. 3 The SEM images of the surface and the cross section of electrodes.

The measurement of EMF was also carried out at 673K and 773K. Fig. 5 shows the temperature dependence of the measured EMF for various gaseous environments. The probes using Pd electrode obeyed well the theory at all temperatures. The probe with Pt electrode, however, showed lower EMF than that of the theory at 673K.

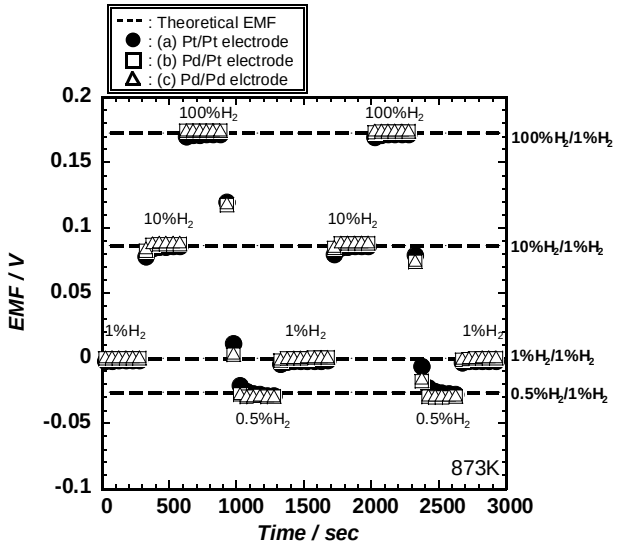

Fig. 4 The measurement of EMF in gaseous environments at 873K.

5. Discussion

In the case of porous Pt electrode, the environmental gas penetrates into the open pores and reaches the ceramics. The position where the surface of the ceramic cell contacts with Pt electrode and the atmospheric gas is called three-phase boundary [6]. The electrode reaction model at the three-phase boundary is schematically shown in Fig. 6(a).

The Pd electrode doesn't have the open pores but has the membrane structure. In this case, the electrode reaction takes place at the interface of the electrode and the ceramic cell, which is called two-phase boundary [7]. The electrode reaction model at the two-phase boundary is schematically shown in Fig. 6(b).

Because no direct contact of the ceramics sensor cell with the environment is expected, the Pd membrane electrodes are thought to be more resistant to corrosion than the porous Pt electrodes.

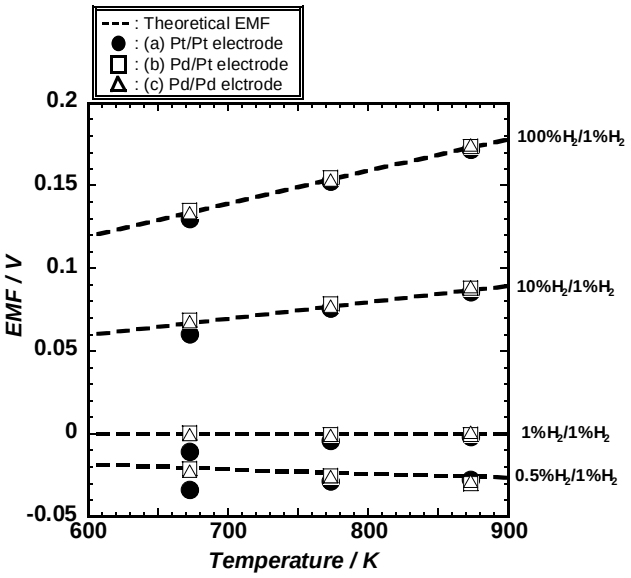

Fig. 5 The temperature dependence of EMF.

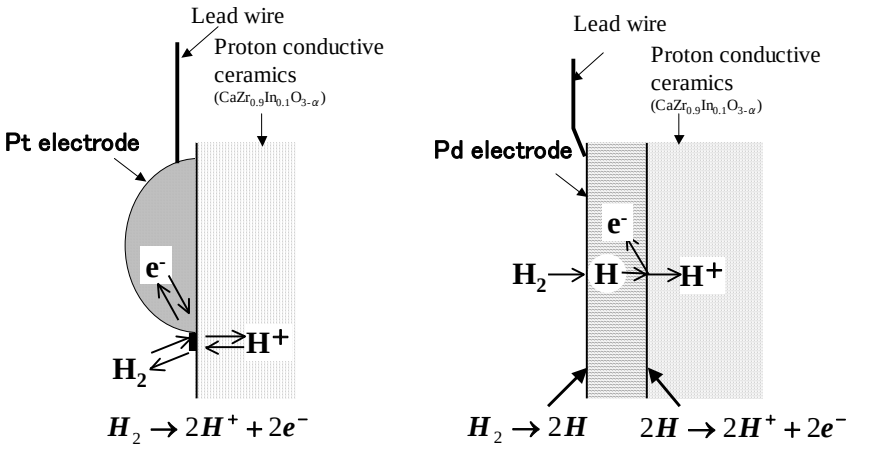

(a) The model of three-phase boundary **(b) The model of two-phase boundary**

Fig.6 Electrode reaction model. (a) Three-phase boundary electrode, (b) Two-phase boundary electrode

6. Conclusion

The fabrication and the performance test of the Pd membrane electrodes for the hydrogen sensor for application to low oxygen or corrosive environments such as liquid breeders were carried out. The conclusions are as follows.

(1) The Pd membranes without open pores were fabricated successfully on the ceramics sensor cell.

(2) The sensor cells with the Pd membrane responded quickly to the change of hydrogen concentration of the flowing gas with high reproducibility.

(3) The EMF with the Pd electrodes was shown to be almost equal to that with the porous Pt electrode in the gaseous environment, indicating that the two-phase boundary of the Pd electrodes works similarly to the three-phase boundary of the Pt electrodes. Furthermore, since the EMF of the Pd electrode obeyed the Nernst's equation better than Pt electrode at lower temperature such as 673K, the sensor using Pd electrode may be used in lower temperature than Pt electrode as well as in the corrosive atmosphere.

References

[1] M. Kondo T. Muroga, K. Katahira, T. Oshima, ICONE**15**, 10588 (2007)
[2] T. Yajima, K. Koide, H. Takai, N. Fukatsu, H. Iwahara, Solid State Ionics **79**, 333 (1995)
[3] N. Fukatsu, N. Kurita, K. Koide, T. Ohashi, Solid State Ionics **113**, 219 (1998)
[4] G. Marnellos, A. Kyriakou, F. Florou, T. Angelidis, M. Stoukides, Solid State Ionics **125**, 279(1999)
[5] S. Zisekas, G. Karagiannakis, M. Stoukides, Solid State Ionics **178**, 2929(2005)
[6] H. Iwahara, J of The Surface Finishing Society of Japan **56**, 486(2005)
[7] H. Matsumoto, Materia Japan **44**, 226(2005)

Proceedings of ITC18, 2008

Voltage Enhancement of the DC Power Supplies for Dynamic Current Control of LHD Superconducting Coils

Hirotaka CHIKARAISHI[1)], Tomoyuki INOUE[1)], Shigeyuki TAKAMI[1)], Koji AOYAMA[2)], Tomoyuki HAGA[3)] and LHD Group[1)]

[1)]*National Institute for Fusion Science,322-6 Oroshi, Toki, Gifu 509-5292, Japan*
[2)]*Aichi Electric Co., Ltd., Aichi 1, Kasugai, Aichi 486-8666, Japan*
[3)]*Asort Co., Ltd., Nishiakashi 5-15-16, Akashi, Hyougo 673-0011, Japan*

The fundamental operation of the helical-type reactor will be performed under the dc magnetic field. But in some situations such as start up of excitation, dynamic control of magnetic field will be required. Also the LHD operation requires dynamic control of magnetic field, and the output voltage of power supplies are enhanced using additional pulse power supplies for this purpose. With the pulse power supplies, the magnetic axis swing operation was realized. This configuration of the power supply is also adaptive to the fusion reactor.

Keywords: helical type reactor, dynamic current control, superconducting coil, pulse power supply

1 Introduction

The fundamental operation of the helical-type reactor will be performed under the dc magnetic field and the power supplies to excite the superconducting magnets will be optimized for the steady state excitation to minimize the loss, but in some situations such as start up of excitation, dynamic control of magnetic field will be required. For this dynamic operation, some additional power supply will be required. The LHD operation has similar situations. Its usual plasma operations are performed under the steady state magnetic field and the power supplies are optimized to the steady state operations. With the progress of the fusion plasma research, more dynamic experiments are planed and they require the dynamic control of magnetic field. For this purpose, the output voltages of power supplies are enhanced using additional pulse power supplies. This paper introduces the outline of the enhanced power supplies for the LHD superconducting coils and the test results using them.

2 Outline of the LHD power supplies

For the LHD, the superconducting coils are excited by six power supplies shown in Figure 1. To design the pulse power supplies for the LHD, the required voltages to dynamic magnetic axis control for the standard confinement are calculated. As the result, it was shown that the output voltage of the power supplies for IS and IV coils are bottle neck and we decided to boost these power supplies with construction of the additional high voltage power supplies.

Figure 2 shows the circuit diagram of the IV power supply. The steady state power supply shows the current power supply shown in Figure 2 and the pulse power supply means the additional one. As shown in figure, these

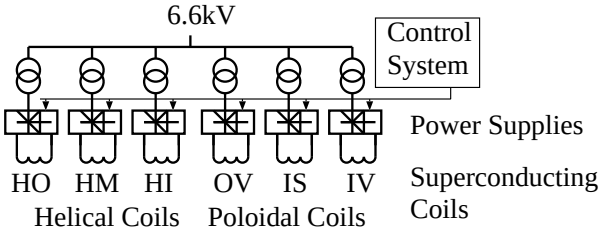

Fig. 1 Block diagram of the power supplies for LHD superconducting coils.

two power supplies are connected in series and the both output voltages are induced to the coil. When some problem for the operation of super conducting coil is occurred, the pulse power supply must not disturb the operation of the protection circuit, so the insertion point is chosen as shown in the figure.

Table 1 shows the specifications of current power supply and additional power supply for IV coil. The output currents of steady-state power supplies are set to realize the 3 T of magnetic field at the plasma center. The output currents of pulse power supplies are decreased to reduce the construction cost.

Table 1 Specifications of the power supplies for IV coil

	current power supply	pulse power supply
Output voltage	33V	180 V
Output current	15.6kA	6.2 kA
Operating time	continuous	120 s
Duty ratio of operation	-	1/15

Because of the limitation of the operating current and

author's e-mail: hchikara@nifs.ac.jp

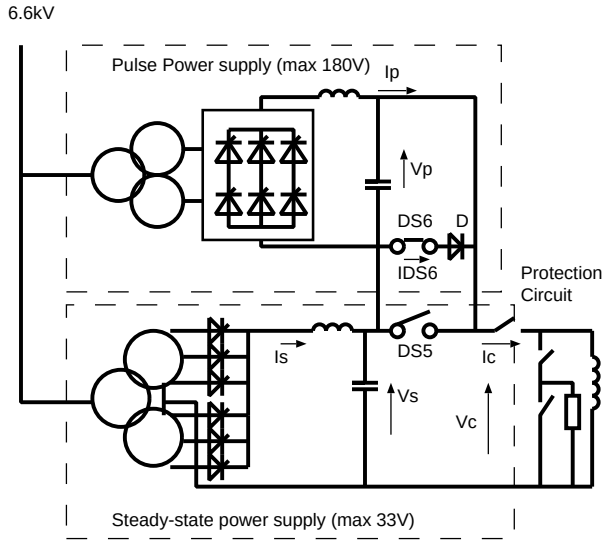

Fig. 2 Circuit diagram of the power supply for IV coil.

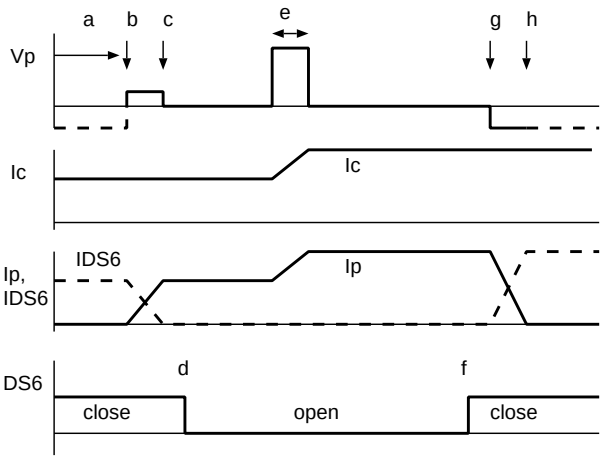

Fig. 3 Sequence of connection and disconnection of the pulse power supply.

time of the pulse power supply, two bypass switches are connected as shown in Figure 2. In the figure DS5 is a large current but slow operation switch and DS6 is medium current but quick operation switch. For the high magnetic field operation, which requires the higher current than 6.2kA, the DS5 is closed and the coil is excited by the steady state power supply only.

For the low magnetic field operation using pulse power supply, the DS5 is opened. In this situation, for the steady state operation, DS6 is turned on; the coil is excited by the DC power supply and the pulse power supply standby for operation. When the high voltage is required, DS 6 is turned off quickly then the pulse power supply is inserted in series and the coil current flows through the pulse power supply.

3 Connection and disconnection sequence of pulse power supply

The connection and disconnection of pulse power supply must be performed under the condition, that the coil current are flowing, without serge voltage occurred by the operation. Also any rush current in the circuit must be avoided in the sequence. Especially DS6 makes parallel circuit to the output of the pulse power supply, so additional diode D is inserted in series with DS 6 to block the shirt circuit current.

The insertion sequence of the pulse power supply is shown in Figure 3. The sequence runs as follows;

a Before the pulse operation, the DS 6 is close and the pulse power supply generate negative voltage. In this situation, the coil current I_c flows through DS6.

b When the signal to start of pulse operation is triggered, the pulse power supply generate the positive voltage, then I_c to pulse power supply from DS 6 and the current flowing DS 6 I_{sw} decrease to zero. [c] At this time, a reverse voltage for the series diode D is induced and D cut off. With this diode, short circuit current flowing DS 6 is blocked.

d When I_{sw} becomes zero, DS 6 turned off and the pulse power supply output voltage is controlled to zero immediate.

After the connection sequence, the output voltage V_c can be swing to control I_c with high ramp rate. The current swing is finished, the pulse power supply returns to zero voltage state. The time delay to connect the pulse power supply is less than 1 s and is enough short for the plasma experiment.

The disconnection sequence is simpler as follows;

f DS 6 is closed and the pulse power supply turns to the regeneration mode. The coil current transfers to DS6 from the pulse power supply.

g When Ip becomes zero, the pulse power supply stop automatically and all coil current flows through DS6 again. [h]

Even though the power supplies are in the sequence of connection and disconnection, the coil current must be regulated with current controller described in the next section. This regulation is performed by the steady state power supplies, which works in this sequence.

4 Current control

The coil current control must be performed with seamless even if the pulse power supply is inserted or not. For this reason the control system is modified. Figure 4 shows the block diagram and inside of the dashed line is additional part. The current regulator receive the current reference I_c* and the actual current I_c, which is measured by the current

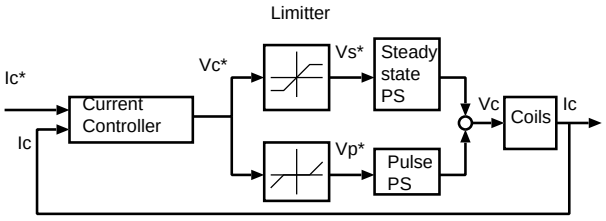

Fig. 4 Block diagram of the current controller.

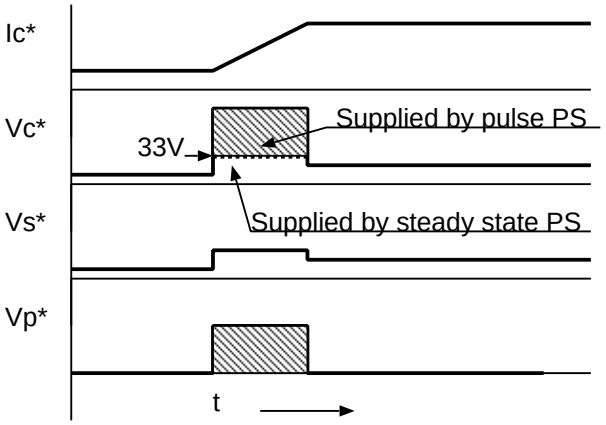

Fig. 5 Simplified drawing of the waveforms of voltage references

sensor set in the steady state power supply, and calculate the necessary voltage V_c*. In the steady state operation, V_c* is fit in 33 V, which is upper limit of the steady state power supply, and it is transferred to the steady state power supply as it reference V_s*. In the pulse operation, V_c* may reach to 218 V, which is sum of the output voltages of the steady state power supply and pulse power supply. When the V_c* over the limit of steady state power supply, the excess part limited by the limiter and generates V_s* At the same time, the excess part is picked up as a voltage reference for pulse power supply V_p*. A simplified drawing of waveforms is shown in Figure 5. With this configuration, two voltage references, which are V_s* and V_p* are generate without any switching of the control system.

5 Excitation test operation result

With the pulse power supply, some test operations were performed. Figure 6, 7 and 8 show some of the operation results.

Figure 6 shows the current and voltage waveforms when DS6 was just turn off and on. With this operation test, it is confirmed that the insertion and disconnection of pulse power supplies are done without large turbulence. When the pulse power supplies are inserted, the output voltage references of then are kept zero, but some voltage

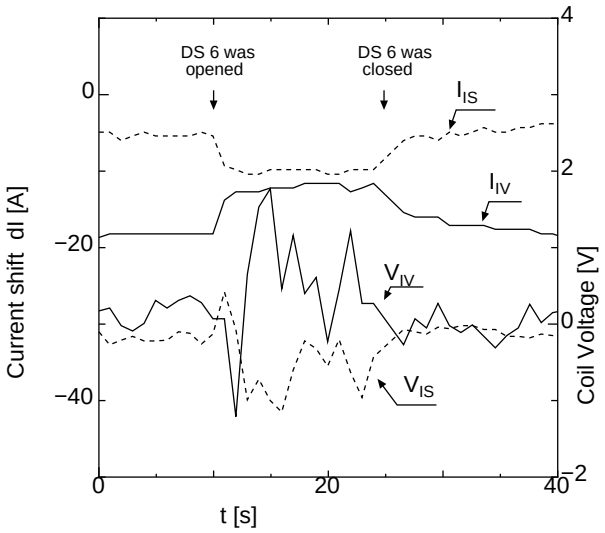

Fig. 6 Voltage and current waveforms when DS6 is turned off and on.

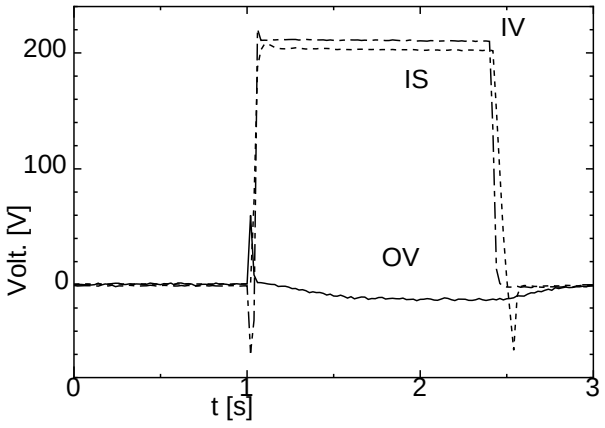

(a) Voltage waveforms.

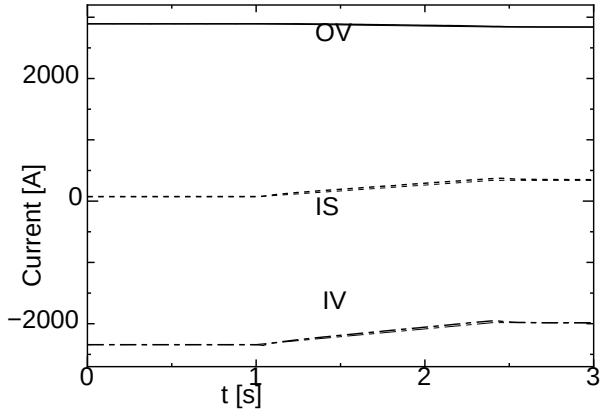

(b) Current waveforms.

Fig. 7 Waveforms when the dynamic current control is performed.

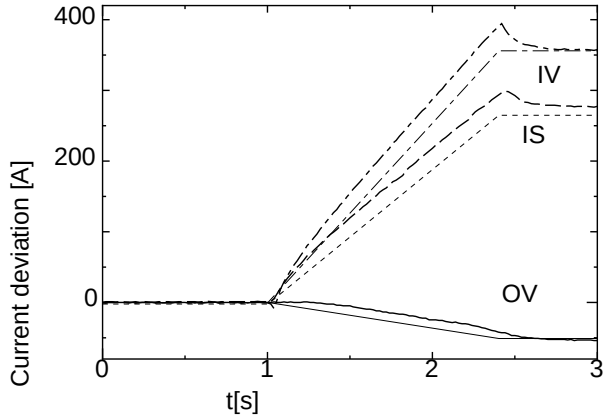

Fig. 8 Current change when the dynamic current control is performed.

turbulences are occurred and coil currents shift about 5A. These current shifts are relatively small for the operation current, but it should be smaller.

Figure 7 show the waveforms when the coil currents are swept using pulse power supplies. At $t = 1$, the current sweep starts and $t = 2.5$ the sweep finished. The coil voltages are ramp up and down quickly, and the voltage waveforms of IS and IV coils became rectangular as shown in Figure 7 (a). At the ramp up and down, the overshoot and the under shoot is observed for IV and IS voltage but it does not affect the current control.

The coil currents are swept smoothly as shown in Figure 7 (b). The detail of current change is shown in Figure 8. In these figures, the thin lines mean the coil current references and the thick lines are actual coil currents. In the figure, there are offset between the reference and actual current for IV and IS coils when currents ramp up. The offset is about 40 A and it causes the overshoot at the end of ramp up. These current offsets are caused by the reaction of the induced current flowing in the plasma or strictures such as coil can or supporting shell of the LHD. The current path in them works as resistive components connected in parallel to the coil equivalently. The effective resistance is about 5 ohms and the time constant is about 0.2 s. The feedback time constant of the controller is about 10 s and is not enough to compensate the reaction. Except this current overshoot, there is not other turbulence such as ringing and it is confirmed that the seamless control for current regulation is confirmed. With this test, it was certificated that the dynamic current control using pulse power supplies are performed without problem.

6 Conclusion

For the LHD plasma experiments, the high voltage power supplies and the control system for them were constructed to make the dynamic coil current control. In the system, it is necessary to connect or disconnect the pulse power supply without stop the system. For this purpose, a new sequence is designed and installed. Also the seamless current control using two power supplies is required and built. The operation tests using LHD coils are performed and it is confirmed that the dynamic connection sequence for the pulse power supply works as designed and the seamless current control has enough performance. The new power system is now works as powerful equipment for the dynamic plasma experiments. The proposed configuration, which uses two power supplies connected in series, is also considered in the design activity of the helical-type reactor.

Acknowledgment

In the constriction and test operation of the power supplies, many staffs of NIFS help us. The authors would like to thank these stuffs.

[1] H. Chikaraishi, S. Takami, T. Inoue, T. Ise, H. Niwa, T. Haga, Fusion Engineering and Design, **83** 260-264 (2008).

Proceedings of ITC18,2008

Framework of Collaboration Investigation on Neutron Effect on Superconducting Magnet Materials

Arata NISHIMURA[a], Takao TAKEUCHI[b], Shigehiro NISHIJIMA[c], Yoshinobu IZUMI[c], Kosuke TAKAKURA[d], Kentaro OCHIAI[d], Tsutomu HENMI[e], Gen NISHIJIMA[f], Kazuo WATANABE[f], Isamu SATO[f], Hiroaki KURISITA[g], Minoru NARUI[g], Tatsuo SHIKAMA[g]

[a] *National Institute for Fusion Science, 322-6 Oroshi, Toki 509-5292, Japan*
[b] *National Institute for Materials Science, 1-2-1 Sengen, Tsukuba 305-0047, Japan*
[c] *Graduate School of Osaka University, 2-1 Yamadaoka, Suita 565-0871, Japan*
[d] *Japan Atomic Energy Agency, 2-4 Shirakata Shirane, Tokai, Naka 319-1195, Japan*
[e] *Japan Atomic Energy Agency, 801-1, Mukoyama, Naka 311-0193, Japan*
[f] *Tohoku University, 2-1-1 Katahira, Aoba, Sendai 980-8577, Japan*
[g] *Tohoku University, 2145-2 Narita, Ooarai 311-1313, Japan*

A fusion reactor will generate D-T neutron and the kinetic energy of the neutron will be converted to the thermal energy and electrical energy. The neutron has huge energy and will be able to penetrate a shielding blanket and stream out of ports for neutral beam injections. The penetrated and streamed out neutrons will reach superconducting magnets and make some damages on the magnet system. To investigate the neutron irradiation effects on the superconducting magnet materials, a collaborative network must be organized and the irradiation researches must be performed. This report will describe the framework of the collaboration investigation which has been established among neutronics, superconducting magnet and fusion system. After showing the collaboration scheme, some new results on 14 MeV neutron irradiation effect are presented. Then, a three years new project which was adopted as one of "Nuclear basic infrastructure strategy study initiatives" by MEXT will be introduced as an example of collaborative program among superconducting materials, fission reactor and high magnetic field technology.

Keywords: collaborative research, neutron irradiation effect, superconducting magnet materials, Nb_3Sn, Nb_3Al, fusion device, pinning, knock-on effect.

1. Introduction

International Thermonuclear Experimental Reactor (ITER) project is in progress, and design activity of DEMO plant will start as part of ITER broader approach (BA) program. ITER will generate D-T neutron (14 MeV) and shielding blankets will be installed in the plasma vacuum vessel [1]. The neutron will be able to penetrate the blanket and stream out of the neutral beam injection ports. So, the neutrons will reach superconducting magnets and cause activation and changes in the superconducting properties [2,3]. In case of JT-60SA which will be constructed under the ITER BA program, the device will not have the shielding blankets and D-D neutron (2.45 MeV) will easily irradiate the superconducting magnets. To reduce the irradiation, some resin with boron will be arranged on the outside surface of the vacuum vessel.

Since the superconducting magnets will be irradiated by fusion neutrons and the properties of the magnet materials will be changed by the irradiation, the database of the neutron irradiation must be constructed and the mechanisms of the property change and the general tendency of the irradiation effects must be discussed and clarified. To study the neutron irradiation effect on the superconducting magnet materials, the neutron irradiation facility must be arranged. Also, the evaluation system of the superconducting properties after irradiation must be installed in the radiation controlled area, because the samples will be activated by the neutron irradiation.

On the design of the fusion reactor system, the collaborative investigations among researchers in system engineering, neutronics, superconducting magnet, power supply and so on have to be performed considering the construction and operation of the superconducting magnet system. The exchange of the knowledge and discussion is very important and fruitful to understand the background of each research field and carry out the reasonable design. In this study, the special collaboration scheme among fission reactor engineering, neutronics, superconducting materials, fusion engineering has been organized and the framework has been constructed little by little under the inter-University scheme.

Author's e-mail: nishi-a@nifs.ac.jp

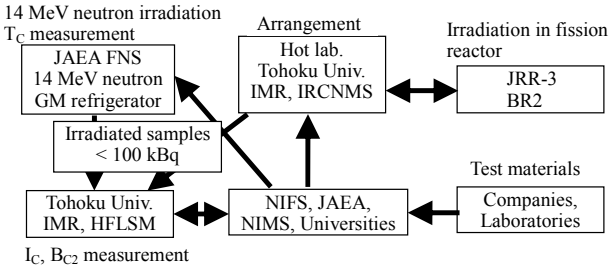

Fig. 1 Collaboration network for neutron irradiation effect on superconducting magnet materials.

In this paper, the collaboration network established will be explained and some test results obtained in the collaborative work will be presented. Also, the outline of the new project to install the superconducting magnet in a radiation controlled area will be introduced.

2. Collaboration Network

The collaboration scheme is shown in Fig. 1. There is a core meeting controlling all activities on the neutron irradiation investigation performed within this framework. Originally, the basic activity of the meeting has been supported by NIFS collaboration research program started in 2004. The samples are provided by NIFS, NIMS, JAEA and some companies and send to Fusion Neutronics Source (FNS) in Japan Atomic Energy Agency (JAEA) or JRR-3 (fission reactor) in JAEA through International Research Center for Nuclear Materials Science (IRCNMS, so-called Ooarai center) of Tohoku University. The irradiated samples are kept at radiation controlled areas in FNS and Hot Lab in Ooarai center and are sent to High Field Laboratory for Superconducting Materials (HFLSM) in Tohoku University after checking the residual radioactivity. Since the maximum Bq per one sample is limited to 100 kBq in HFLSM, some samples must wait for the reduction of residual radioactivity. The superconducting properties of non-irradiated and irradiated samples are evaluated in HFLSM using 28 T hybrid superconducting magnet. After measuring the properties, the samples are transferred back to FNS or Ooarai center and kept in usual way.

The participants in the frame work have meetings to expand the investigation to two directions, the application research and the basic research as described above. To realize the fusion reactor, the systematic study must be performed. However, the present status is on the phase developing the test facilities and test procedures for activated samples. The collaboration network established here is expected to be strengthened and widened more.

3. Change in Superconducting Properties

For the irradiation tests, NbTi, Nb_3Sn and Nb_3Al strands were taken up firstly and 14 MeV neutron irradiation tests started at FNS. After irradiation, the critical current and the critical magnetic field were measured at HFLSM. The irradiated samples were soldered on the sample holder in a radiation controlled area at Laboratory of α-Ray Emitters neighboring to HFLSM in Katahira campus of Tohoku University and then the sample holder was brought into the 28 T hybrid superconducting magnet.

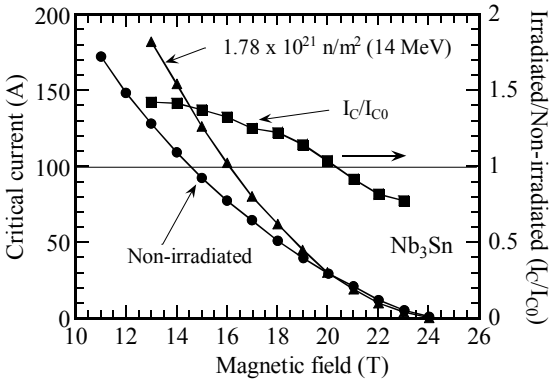

Fig. 2 Change in critical current of Nb_3Sn strand (0.7 mm diameter) against magnetic field. Non-irradiation and after 14 MeV neutron irradiation of 1.78 x 10^{21} n/m^2 at room temperature are compared.

A special cup was attached to the sample holder to reduce the scattering of small particles when the sample should be melt away in liquid helium during the critical current measurement. Also, a filter was inserted in the recovery line of the helium gas to collect the activated particles when melting should occur. After the test, the cryostat and surrounding area was investigated by a survey meter for safety.

The test results are shown in Fig. 2. Since the NbTi and Nb_3Al strands did not show the clear change after the irradiation as far as the data obtained, only the Nb_3Sn strand data was plotted. After the 14 MeV neutron irradiation of 1.78 x 10^{21} n/m^2, the critical current increased remarkably around 13 T. The critical magnetic field (B_{C2}) which was measured by shifting the magnetic field under the constant current of 0.1 A showed no clear change after the irradiation and it was about 25.5 T. It is recognized that the increment of the critical current depends on the magnetic field and it becomes zero at the higher magnetic field because of no change in B_{C2}.

The relation between the ratio of I_C/I_{C0} and neutron fluence is shown in Fig. 3. Where I_C is the critical current of irradiated sample and I_{C0} is the non-irradiated one. The data were referred from [4-6]. Some tendencies are observed in the figure. (1) I_C/I_{C0} increases once and decreases. But there is materials (samples) dependence. (2) Improved samples by the third element addition show lower increment of I_C. (3) The peak position of I_C/I_{C0} is shifting to the smaller fluence direction depending on the higher energy neutron irradiation. (KUR: Fission reactor.

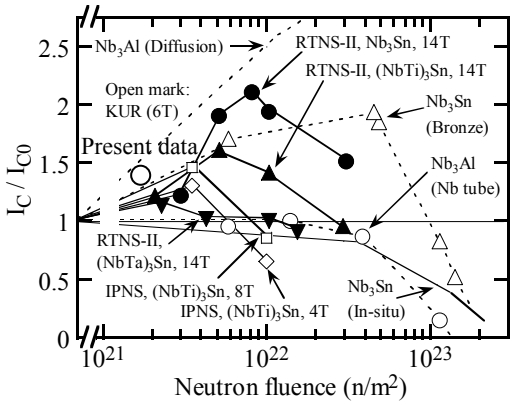

Fig. 3 Summary of neutron irradiation effect on critical current of Nb_3Sn wires. Round and triangle open symbols show the results at Kyoto University Research Reactor. Irradiation was done at around 355 K. Others were irradiated at cryogenic temperature.

RTNS-II: 14 MeV neutron source. IPNS: Spallation neutron source.) (4) Nb_3Sn made by bronze process without the third element showed higher I_C/I_{C0} at peak position, while the sample by in-situ process was not improved. (5) Nb_3Al showed the different results depending on the fabrication process, diffusion process and Nb tube process.

The present results at 13 T and 14 MeV neutron fluence of 1.78 x 10^{21} n/m^2 was plotted with a rather larger round open symbol. The increment of the I_C is very clear and I_C/I_{C0} becomes larger than previous data sets. It is not easy to explain the mechanisms of the I_C increment because the material and fabrication process are different. However, it is considered that the pinning force and/or number of pinning sites will be increased by the knock-on effect of the high energy neutron. The data will be obtained more in near future and the discussion will be performed systematically.

Voltage-current curves of Bi2223 tapes are shown in Fig. 4. The neutron irradiation was carried out in JRR-3 and the V-I curve measurement was performed in the hot lab in Ooarai center. The test conditions were at 77 K and

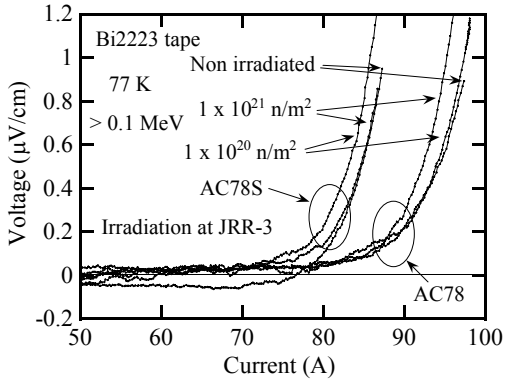

Fig. 4 V-I curves of Bi2223 tapes at 77 K.

under self-magnetic field. Although the data is a little scattered, there is no clear difference on the V-I curve. So, it would be concluded that there is no irradiation effect of neutron up to 1 x 10^{21} n/m^2.

4. New Proposal on Neutron Irradiation Study

A high magnetic field superconducting magnet is needed at the radiation controlled area to perform the tests of superconducting properties after neutron irradiation. To reduce the He gas load to air conditioning in the radiation controlled area, the magnet will have thermal conduction cooling system and not require a lot of liquid helium. Also, 500 A class current lead with thermal conduction system will be useful and the sample temperature will be controlled to be variable constant.

To prepare a superconducting magnet and the current lead, a proposal was composed and sent to MEXT in Japanese Government. The research frame was "Nuclear Basic Infrastructure Strategic Study Initiatives" and the area was the "Promotion of Effective Utilization of Hot Labs." The representative of the proposal is Professor Tatsuo Sikama at Tohoku University and NIFS, NIMS and HFLSM in Tohoku University are the collaborative institutions. The proposal title is "Study on neutron irradiated superconducting magnet materials at cryogenic temperatures and under high magnetic fields" and the investigation duration is three years. The purpose of this study is "Establishment of Center of Excellence for radioactive materials research at cryogenic temperatures and under high magnetic field." Fortunately, the proposal was adopted by the government and the activity started at the autumn in 2008. To realize the above purpose, the following facilities will be installed at the radiation controlled area in Ooarai center.

- Cryogenic system for 15.5 T superconducting magnet.
- Control system for 15.5 T superconducting magnet.
- 15.5 T superconducting magnet.
- Variable temperature insert and current leads.
- Measurement system.
- Magnetic field evaluation including shielding structure.
- 500 A power supply for sample.
- Support facilities.

The engineering design of the conduction cooled 15.5 T superconducting magnet and the cryogenic system already started. The inner bore diameter is 52 mm and it is room temperature space. The conceptual design of the variable temperature insert also started to discuss among the core members of the collaborative investigation network. It is the first trial in the world to cool down the sample by thermal conduction under the condition of 500 A related current. The final performance test of the facility will be carried out in winter of 2011. The project is a good success of the collaborative network.

In addition to the initiative program, the investigation and discussion on a cryogenic neutron irradiation system in a fission reactor began. The Japan Materials Testing Reactor (JMTR) locates at Ooarai in Ibaraki prefecture is now under repair work. It will restart in 2010 and the reopening of the irradiation service to Universities and Institutions is scheduled in 2011. In timing with this repairing, the cryogenic system for keeping the sample temperature less than 10 K during neutron irradiation will be designed and installed. A superconducting sample with lead wires for four probe method will be in the capsule and set in near the core of the fission reactor. On the conceptual design, the gamma-ray heating is assumed to be around 0.1 W/g (Fe) and the maximum neutron fluence will be around 2x 10^{22} n/m^2. To avoid the complicated procedures of High Pressure Gas Safety Law in Japan, the several GM refrigerators for 4 K will be combined and one cryogenic system with about 10 W at 4 K will be formed.

The sample will be irradiated at less than 10 K and the irradiated sample will be inserted into the 15.5 T superconducting magnet to measure the superconducting properties without rising the sample temperature up to 300 K. It will be a good simulation for superconducting magnet for fusion application

5. Summary

On the progress of design and fabrication of the D-D or D-T burning plasma devices and plants, the collaboration among various disciplines becomes more important and essential. To realize the special components for fusion plats, collaborative investigation is absolutely imperative. In this paper, the new trial to establish the collaborative project was introduced and the new results on neutron irradiation effects were presented. In addition, the contents of the new proposal adopted by MEXT, Japanese Government, were described.

The collaborative research network on neutron irradiation effect on superconducting magnet materials has been established. There are mainly two purposes. One is for design and fabrication activity providing the database. The other is academic activity to clarify the mechanism of the change in superconducting properties by neutron irradiation.

Under the collaboration of newly established network on neutron irradiation study, the superconducting property of Nb3Sn, Nb3Al and NbTi wires was investigated. As the results, it was clarified that the critical magnetic field did not change remarkably after 14 MeV neutron irradiation of 1.78 x 10^{21} n/m^2, though the critical current at lower magnetic field increased. Also, it was observed that the critical current of Nb3Al did not increase at the magnetic field range of 20 T to 25 T. As for the Bi2223 tapes, after the irradiation of 14 MeV neutron of 8.69 x 10^{20} n/m^2 and fission neutron of 1 x 10^{21} n/m^2, V-I curves were measured at 77 K under self-magnetic field, and no clear change was observed.

A new proposal entitled “Study on neutron irradiated superconducting magnet materials at cryogenic temperatures and under high magnetic fields” has been adopted by MEXT, Japanese Government, as a “Nuclear Basic Infrastructure Strategic Study Initiatives.” The promotion of integrated researches of various disciplines will be accelerated through the program, and the new facilities such as a 15.5T superconducting magnet will be opened for researchers at Universities and Institutions as special equipment for inter-University research. This new collaborative network will be expected to boost the realization of the component integration and DEMO plant.

Acknowledgments

The authors would like to express their thanks to Y. Hishinuma, T. Tanaka, T. Muroga at National Institute for Fusion Science, M. Sakamoto at The Graduate University for Advanced Studies, M. Yamasaki at Tohoku University, T. Konno, K. Okuno at Japan Atomic Energy Agency for the contribution to perform the study, and also to Furukawa Electric Corporation Ltd., Sumitomo Electric Industries Ltd. and Toshiba Corporation for providing the samples.

Part of this work was supported by a Grant-in-Aid for Scientific Research (#16560725, #17656098, #1936035), NIFS collaboration research programs (NIFS04KOBF008, NIFS07KOBF014), Fusion Engineering Research Center program at NIFS (NIFS06UCFF013, NIFS06UCFF005, NIFS08UCFF005), and Budget for Nuclear Research of the MEXT.

The work at high magnetic field was performed at the High Field Laboratory for Superconducting Materials, Institute for Materials Research, Tohoku University.

References

[1] ITER Design Description Document (DDD), 11, Magnet (N 11 DDD 177 04-05-12 W 0.2) (2004).

[2] A. Nishimura et al., Advances in Cryogenic Engineering **52**, 208 (2006).

[3] A. Nishimura et al., Journal of Plasma Fusion Research **83**, 30 (2007) (in Japanese).

[4] H. Weber, Advances in Cryogenic Engineering **32**, 853 (1986).

[5] M. W. Guainan, P. A. Hahn, and T. Okada, Summary Report on RTNS-II Collaboration Research, UCID 21298 (1988).

[6] T. Kuroda, K. Katagiri, H. Kodaka, M. Yuyama, H. Wada, . Inoue, and T. Okada, J. of Atomic Energy Society Japan **37**, 652 (1995) (in Japanese).

Proceedings of ITC18,2008

Conceptual Design and Development of an Indirect-cooled Superconducting Helical Coil in FFHR

Hitoshi Tamura, Kazuya Takahata, Toshiyuki Mito, Shinsaku Imagawa, Akio Sagara

National Institute for Fusion Science, 322-6 Oroshi-cho, Toki, Gifu 509-5292, Japan

FFHR is the name for a conceptual design of a heliotron fusion reactor being developed at the National Institute for Fusion Science. All the coils in the FFHR are made of superconductors. Several cooling schemes have been proposed for the helical coils and indirect cooling is considered a good candidate. In this study, we investigated the possibility of using an indirect-cooled superconducting magnet for the FFHR. In parallel with this design study, we developed the Nb_3Sn superconductor, jacketed with an aluminum alloy, for use in an indirect-cooled magnet. The results of performance tests for a sub-scale superconductor showed good feasibility for application in the FFHR helical coil. Stress distribution in the helical coil was also analyzed, and the stress and strain were confirmed to be within the permissible range.

Keywords: large helical device, helical reactor, indirect-cooled superconducting magnet, Nb_3Sn superconductor, cable-in-conduit-conductor, stress analysis

1. Introduction

Experimental results of the large helical device (LHD) have revealed that an LHD-type helical reactor is well suited as a demonstration device of a fusion power plant [1]. FFHR is the name for the conceptual design of an LHD-type heliotron fusion reactor. The magnet system of the FFHR includes one pair of superconducting helical coils and two pairs of superconducting poloidal coils. Several cooling schemes have been proposed for these superconducting helical coils—forced-flow and indirect cooling are considered good candidates. The former with a cable-in-conduit conductor (CICC) has been chosen for designs of many large-scale experimental fusion magnets, such as the poloidal coils of the LHD, the main coils of ITER, Wendelstein 7-X, and JT-60SA, because of its mechanical strength and electrical/thermal stability. On the other hand, indirect cooling solves the problem of pressure drops in the CICC. Furthermore, a superconducting magnet with indirect cooling is considered to have better mechanical rigidity, since its structural components, such as the superconducting strands, cabling jacket, insulators, cooling panels, and coil case, are completely in contact with each other.

In this study, we investigated the possibility of using an indirect-cooled superconducting magnet for the FFHR. In parallel with this study, we developed Nb_3Sn superconductors, jacketed with an aluminum alloy, for use in the indirect-cooled magnet. The "react-and-wind" process can be performed on a large superconducting coil using this type of superconductor, since the jacketing can be performed after heat treatment of the superconducting strands by friction stir welding (FSW). The development details of sample conductors and the results of performance tests for the sub-scale superconductor are also shown.

author's e-mail: tamura@nifs.ac.jp

2. Structure of the Coil

Fig. 1 shows a schematic of the cryogenic components in the FFHR. The major and minor radii of the helical coils are approximately 14–16 and 4 m, respectively. The total magnet energy of the coils is 120 GJ. The electromagnetic force generated by these coils is sustained by inner and outer supporting structures. The magnetic field at the plasma center is 6.18 T. The cross sectional dimension of the helical coil was determined by considering the geometry of the plasma facing components. Fig. 2 shows a conceptual design of the cross section of the helical coil. It has a rectangular cross-section, 1.8 m in width and 0.9 m in height. There were 432

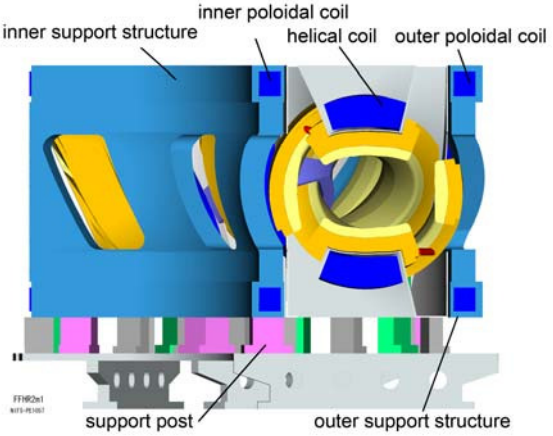

Fig.1 Schematic of the cryogenic components in the FFHR.

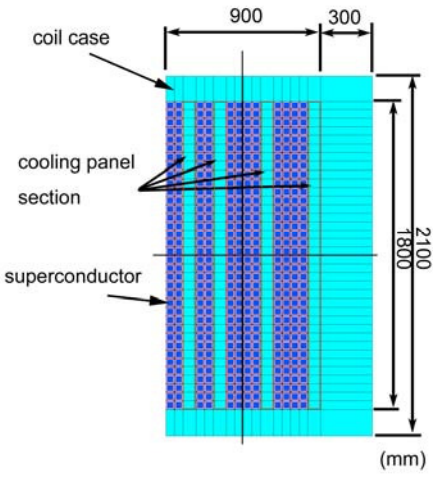

Fig. 2 Cross-sectional view of the conceptual design of the indirect-cooled helical coil.

superconductors (36 turns, 12 layers) made of Nb_3Sn and a jacketing material. An aluminum alloy was chosen as the jacketing material, because it offers high thermal conductivity and mechanical strength. The cooling panels were placed at every two or four turns of the winding. Each cooling panel is 75 mm thick and the superconductor is indirectly cooled by this cooling panel. The coil is wound along the coil case made of stainless steel (SS) and covered with a lid. The LHD-type helical reactor does not require plasma current so there is little AC loss in the magnet. The heat load to the coil during reactor operation comes mainly from nuclear heating. Takahata et al. calculated the elimination of this steady state heat load and showed that an aluminum jacket superconductor with a cooling panel could resolve this issue [4].

3. Development of the Aluminum Alloy Jacketed Superconductor

3.1 Specification and fabrication process

The fundamental geometry of the superconductor is a 50 mm square shape, including insulation. Since the maximum magnetic field at the coil region is around 13 T, Nb_3Sn wires can be used. The operating current is 100 kA and the overall current density is 40 A/mm^2. Since the melting point of aluminum alloy (933 K) is lower than that of the heat treatment temperature of the Nb_3Sn wires (1000 K), the jacketing must be performed after the heat treatment of the wires. We developed a conductor fabrication process, using a FSW technique that uses friction heating, to avoid the temperature rise in the welding region. The superconducting wire is embedded in the aluminum alloy jacket with a solder material and the lid is welded by the FSW. The solder can be automatically melted and it fills the void around the superconducting

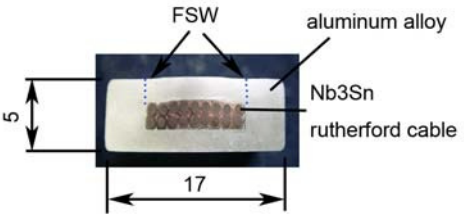

Fig. 3 Photo of the cross-section of reduced size 4.7 kA class sample superconductor.

wire. A prototype 10 kA class superconductor with 17 mm square shape was made to demonstrate the fabrication process and the performance of the conductor. It showed 19 kA transport current at 8 T and confirmed that although there was some degradation in the critical current, it was not due to the fabrication process, but the difference in thermal contraction between Nb_3Sn and aluminum alloy [4].

3.2 Reduced size sample test

To confirm the allowable bending deformation, 4 kA class superconductors, made of Nb_3Sn cable and aluminum alloy jackets using the same production process as the previous 10 kA class sample, were manufactured. The packing factor of the superconductor inside the aluminum jacket was increased from 60% to 80%. Fig. 3 shows the cross-sectional structure of the sample conductor and its dimensions. The following two samples were tested: (1) without bending, and (2) bent once along a rig, with a radius of 150 mm then bent back to the original straight shape (R150S). Fig. 4 shows the experimental results of current-carrying capacity tests. The open plot indicates the critical currents (definition; 1 μV/cm) of the test conductor at 4.4 K and the error bars represent the maximum and

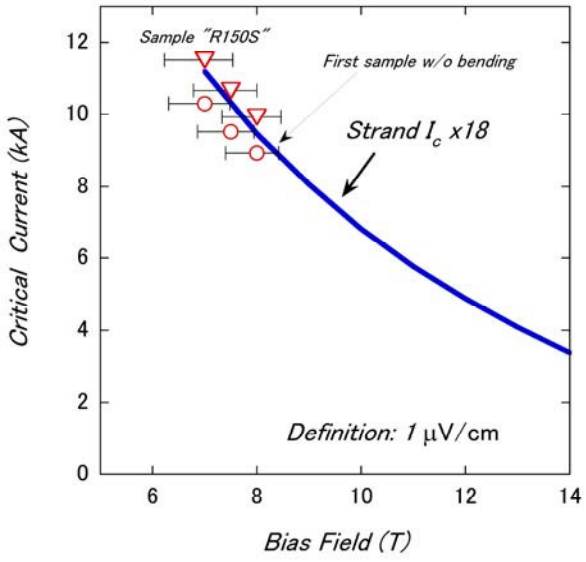

Fig. 4 Critical currents of the reduced size superconductor, with and without bending.

minimum magnetic field inside the conductor. The solid line indicates the critical current of the strand, multiplied by 18 (the number of strands). We succeeded in carrying a current of 11 kA at 8 T with the sample R150S. This confirms that the critical current was not affected by bending. Furthermore, the critical current of sample R150S might be increased by the pre-bending effect [5].

4. Comparison with CICC

Here we simply compared the apparent rigidity between the indirect-cooled and CICC type superconductors. Fig. 5 shows models of the superconductors. The indirect-cooled superconductor has a 50 mm square shape and a 32 mm square Nb_3Sn superconducting region filled with solder. The ratio of the superconductor to the solder is 8:2. The superconductor includes an 18-mm-thick aluminum alloy (6061 T6) and 1-mm-thick insulation. The CICC type has 90 kA of operating current with 480 superconductors made of Nb_3Sn. The conduit is 1.6 mm thick and the conductor is embedded in the internal plate. Both components are made of SS. There is an insulator between the conduit and the internal plate.

The longitudinal rigidity was estimated according to the rule of mixture, using the area fraction of each structural component. The cross-sectional rigidity was calculated by modeling each conductor type with the finite element method (FEM) model. In this case, the plane strain model was adopted, and the rigidity was calculated from the result of reaction force against the force displacement at the top of the conductor. In the indirect-cooled type, the material properties of the superconducting region were selected according to the rule of mixture. On the other hand, in the superconducting region in the CICC type it was assumed that it did not contribute to the mechanical rigidity of the cross-sectional direction. The other components were treated as isotropic materials. The material properties of the components at a cryogenic temperature (4 K) [6-8] were used in the analytical model. The material properties used in the calculation are shown in Table 1.

The longitudinal rigidity of indirect-cooled and CICC superconductors were estimated at 82 and 109 GPa, respectively. The former coil has a cooling panel, which also contributes to coil rigidity. If the cooling panel has a longitudinal rigidity of 163 GPa, the indirect-cooled coil can provide reasonable overall rigidity compared with the CICC coil. Assuming that the cooling panel consists of a SS case and a cooling mechanism, 20% of the cooling panel area can be used for the mechanism. The cross-sectional rigidity of the indirect-cooled and CICC types were 79 and 56 GPa, respectively.

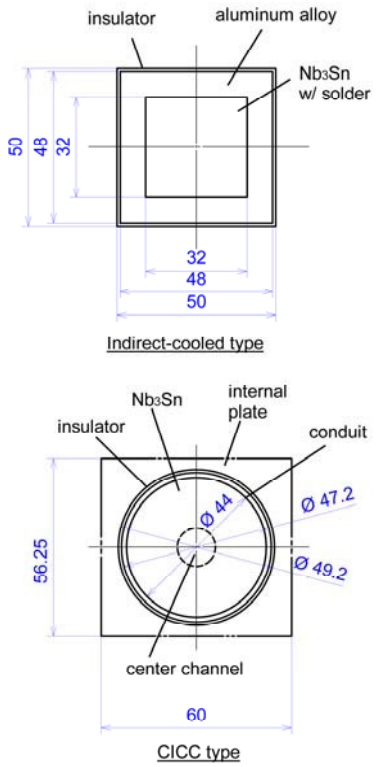

Fig. 5 Rigidity evaluation model for the indirect -cooled (upper) and CICC (lower) superconductors.

Table 1. Material property of components.

	Young's modulus (GPa)	Poisson's ratio	note
Nb_3Sn	100	0.3	
Aluminum	77	0.327	6061-T6
Insulator	80	0.3	Alumina w/ epoxy
Stainless steel	208	0.284	SS316
Solder	40	0.3	Pb free

5. Coil rigidity evaluation

5.1 Analytical model

The helical coil of the FFHR has a three-dimensional structure, with a change in its curvature in the toroidal angle. It is believed that a circular coil with an average curvature similar to that of an actual helical coil can estimate the mechanical behavior of the coil [9]. We calculated the stress and strain distribution inside the coil to confirm the stress and strain levels. The average radius of curvature of the helical coil was 5.5 m at the center of the cross section of the coil. The cross-sectional structure of the helical coil, shown in fig. 2, was used to create the FEM model. The radius from the central axis to the center of the coil cross section was set at the average of the curvature of the helical coil. The insulator used in the superconductors was assumed to be made of alumina

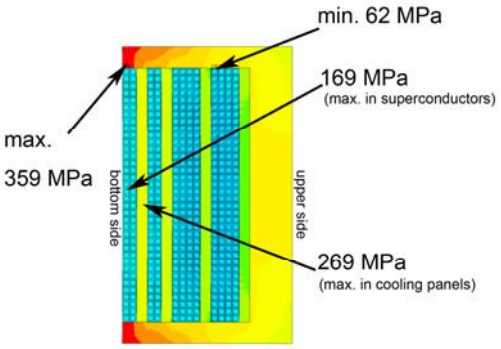

Fig. 6 Hoop stress distribution by the radial electromagnetic force.

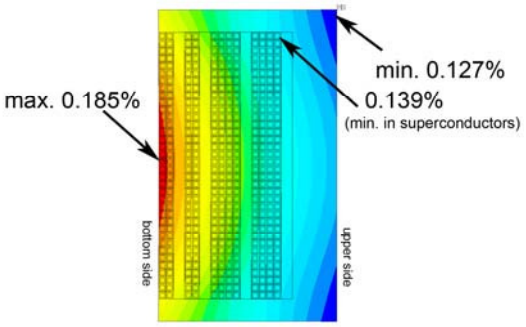

Fig. 7 Circumferential strain distribution by the radial electromagnetic force.

ceramics and resin. The SS coil case, with a thickness of 300 mm at the top and 150 mm on both sides of the coil section, was used.

An electromagnetic force was applied as the body force by multiplying the current density and the magnetic field in every single superconducting region to ensure that the electromagnetic force was precisely applied to the coil. The electromagnetic force considered here was in the radial direction of the circular coil since it generated the hoop force inside the coil. The hoop force is more effective for the superconductor than the overturning force at a point of strength of the coil structure. Although the magnetic field intensity was different at every cross section, an averaged magnetic field was applied at every single superconducting position along the circumference. Furthermore, a constant value was added to the averaged magnetic field so that the total hoop force in the cross section was equal to the maximum overall hoop force. ANSYS version 11.0 was used, and the three-dimensional axisymmetric solid element was adopted.

5.2 Result

The material properties were set using the values described in section 4. It was assumed that the cooling panel had 80% of Young's modulus for SS316. Figs. 6,7 show the results of the hoop force analysis with respect to the hoop stress distribution, the hoop strain distribution, and the radial displacement distribution, respectively. The maximum hoop stress of 359 MPa appeared in the side wall of the coil case. In the coil winding section and the cooling panel section, the maximum stress was 169 and 269 MPa, respectively. The strain from hoop force was 0.185% at the bottom center of the superconductor. The components in the coil were subjected to compressive stress towards the coil center region. All stress and strain levels for each component were within the permissible values.

6. Conclusions

In conceptual design studies of the FFHR, indirect-cooled superconducting helical coils have been proposed. The aluminum-alloy-jacketed Nb_3Sn superconductors with a cooling panel can prove the feasibility of this approach. The following results were obtained in this study: (1) A reduced sample size of the aluminum-alloy-jacketed Nb_3Sn superconductor showed good performance and the critical current did not degrade by bending. (2) The cooling panel requires a longitudinal rigidity of 163 GPa to provide same rigidity as a helical coil using CICC. (3) The indirect-cooled type superconductor has much higher cross-sectional rigidity than the CICC. (4) Stress and strain distributions in the indirect-cooled helical coil, investigated by the FEM model, were confirmed to be within the permissible range.

Acknowledgments

The authors wish to express their thanks to Mr. M. Sugimoto of the Furukawa Electric Co., Ltd. for his efforts in developing a superconductor for the candidate system. This work was supported by the National Institute for Fusion Science (08ULAA107, 08ULAA117).

References

[1] O. Motojima *et al*., Fusion Eng. Des. **81** 2277 (2006).
[2] A. Sagara *et al*., Nucl. Fusion **45** 258 (2005).
[3] A. Sagara *et al*., Fusion Eng. Des. **81** 2703 (2006).
[4] K. Takahata *et al*., Fusion Eng. Des. **82** 1487 (2007).
[5] G. Nishijima *et al*., IEEE. Trans. Appl. Supercond. **16** 1220 (2006).
[6] Cryocomp software (Eckels Engineering and Cryodata Inc., 1997).
[7] D. Mann, *LNG Materials and Fluids* (National Bureau of Standards, 1977).
[8] N. Mitchell, Cryogenics **45** 501 (2005).
[9] H. Tamura *et al*., Journal of Physics: Conference Series **97** 012139 (2008).

Proceedings of ITC18,2008

Long-term thermal stability of reduced activation ferritic/martensitic steels as structure materials of fusion blanket

Yanfen LI[1,2)], Takuya NAGASAKA[3)], Takeo MUROGA[3)]

[1)] *The Graduate University for Advanced Studies, 322-6 Oroshi, Toki, Gifu 509-5292, JAPAN*
[2)] *Institute of Plasma Physics, Chinese Academy Sciences, Hefei, Anhui, China*
[3)] *National Institute for Fusion Science, Oroshi, Toki, Gifu 509-5292, JAPAN*

In this work, the effect of thermal ageing on mechanical properties of JLF-1 (JOYO-II HEAT) and CLAM (HEAT 0603) steels have been studied at temperatures in the range of 823 - 973 K. The results showed that the hardness increased slightly and the creep properties improved after ageing at 823 K for 2000 h for the both steels. On the other hand, the hardness decreased after ageing above 823 K, especially at 973 K for 100 h, and the creep property degraded at 973 K for 100 h. The Larson-Miller parameter was shown to be appropriate for predicting the long-term creep properties from the short-term experiments at higher temperature with higher stress. By extrapolation to the typical design limit for the blanket, 823 K for 100 000h, the rupture stress was estimated to be about 135 MPa for the both steels. The present thermal aging treatments influenced the rupture stress by ~15 MPa.

Keywords: fusion blanket, reduced activation ferritic / martensitic steel, thermal stability, thermal ageing, creep properties, Larson-Millar parameter

1. Introduction

Blanket is one of the important components of fusion reactors, which provides the primary heat transfer and tritium breeding systems. Currently, reduced activation ferritic / martensitic (RAFM) steels are considered as the primary candidates for blanket structural materials because of their most matured industrial infrastructure and relatively good radiation resistance [1].

In fusion applications, they need to withstand high temperature under long-term loading. When the absolute service temperature was higher than about 698 K, the creep deformation of these steels will occur [2]. Since the maximum operating temperature of blanket structural materials will be determined by the thermal creep deformation, evaluation of the thermal creep performance in the blanket condition is the key necessity [3]. In addition, the thermal ageing during the operation may affect the creep properties [4]. However, the research to understanding the thermal ageing effects on the creep deformation is quite limited.

Since testing materials for the actual operating time is extremely costly and time-consuming, prediction of creep rupture performance based on the results of short-term creep experiments at higher temperature with higher stresses has been explored using stress-time parameters. Many efforts to estimate the long-term creep properties have been done for the steels which are being used in fission power plant [5,6], but limited data are available for RAFM steels [7]. No effort has been made to include the thermal aging effect on the prediction of the long-term creep performance of RAFM steels.

In this work, thermal ageing at temperatures in the range of 823 - 973 K on JLF-1 and CLAM steels was carried out and the creep properties were tested. As the aging temperature, 823 K was chosen to test at the upper temperature limit in fusion blanket, and 973 K to accelerate the aging effects. The Larson-Miller parameter and Monkman-Grant equation was proposed to describe the long-term behavior necessary for the blanket design.

2. Experimental Procedure

The materials used are JLF-1 (JOYO-II-HEAT) and CLAM (HEAT 0603) steels. The chemical compositions of these two steels (in weight) are 9.00% Cr, 1.98% W, 0.49% Mn, 0.20% V, 0.083% Ta, 0.09% C, and balance Fe for JLF-1 and 8.94% Cr, 1.45% W, 0.44% Mn, 0.19% V, 0.15% Ta, 0.13% C, and balance Fe for CLAM. The heat treatments included quench and tempering. The quench treatments were carried out by heating at 1323 K for 60 minutes for JLF-1 and 1253 K for 30 minutes for CLAM and then cooled by air. The tempering treatments were carried out by heating at 1053 K for 60 minutes for JLF-1 and 1033 K for 90 minutes for CLAM and then cooled by air.

The SSJ specimens with a gauge size of 5 x 1.2 x 0.25 mm^3 were machined along the roll direction. Then, these specimens underwent ageing experiments in the temperature range of 823 to 973 K under high vacuum in order to avoid high oxidation of the material.

Author's e-mail:li.yanfen@nifs.ac.jp

The Vickers hardness was measured by using a Vickers Hardness Testing Machine under a load of 300 g with loading time of 30 s at room temperature.

The uniaxial creep tests up to rupture were performed at 823 to 923 K with the applied stress between 150 and 300 MPa in a vacuum of < 1 x 10^{-4} Pa. The loading was carried out by a simple suspension, which had a high stability. Creep strain was measured by double linear variable differential transformers (LVDTs) with increased precision.

3. Results

3.1 Hardness Measurement

The hardness results are plotted in Fig. 1. It shows that the hardness values of CLAM steel were higher than those of JLF-1 at all conditions. After ageing at 823 K for 2000 h, the hardness increased slightly for the both steels. On the contrary, softening occurred above 823 K. The softening of JLF-1 steel was smaller than that of CLAM.

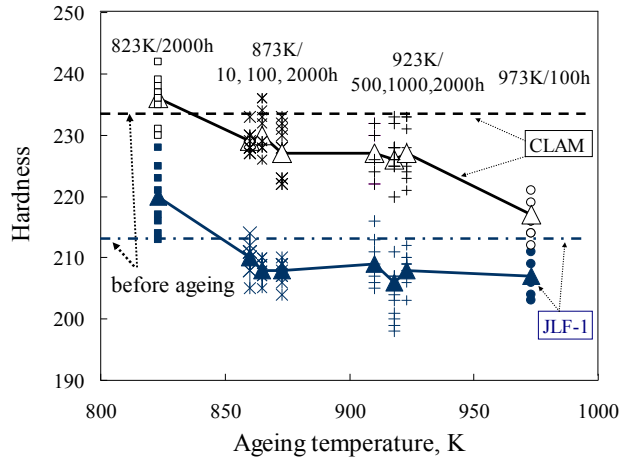

Fig. 1 Hardness change of JLF-1 and CLAM steels by thermal ageing.

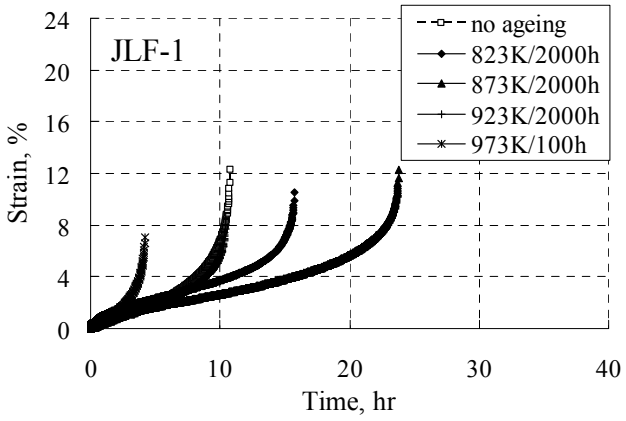

Fig. 2 Creep curves of JLF-1 steel at different ageing conditions (tested at 823 K with 250 MPa).

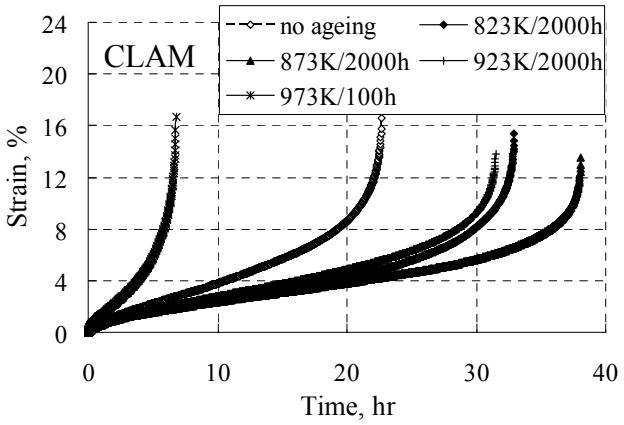

Fig. 3 Creep curves of CLAM steel at different ageing conditions (tested at 823 K with 250 MPa).

3.2 Creep Properties

The uniaxial constant load creep tests were conducted at 823 to 923 K with the applied stress between 150 and 300 MPa. Figs. 2 and 3 show the strain dependence of the creep curve for different ageing conditions. The typical creep curves of the present steels, similar to that observed in other RAFMs, were composed of the primary or transient region, where the creep rate decreases with time, steady state region which is a linear process, and the tertiary or accelerated creep region characterized by an increased creep rate after reaching a minimum creep rate until the material rupture.

For CLAM steel, after ageing at 823 to 873 K up to 2000 h, the minimum creep rate decreased and the rupture time increased. Similar to CLAM, the creep rupture time increased by ageing at 823 and 873 K for 2000 h for JLF-1. But further ageing at 923 K for 2000 h returned the properties to almost the level of no aging. On the other hand, ageing at 973 K for 100 h caused a significant degradation in creep properties, which is consistent with the results of hardness measurements. Although the minimum creep rate is smaller and rupture time is longer for CLAM than those of JLF-1, CLAM is more susceptible to thermal ageing than that of JLF-1.

4. Discussion

4.1 Larson-Miller Parameter

Prediction of long-term creep rupture performance based on the results of short-term creep experiments at higher temperature with higher stresses has been carried out based on stress-time parameters. Larson-Miller parameter is one of the popular methods, which is based on the model of the rate processes [8]:

$$r_c = A \times \exp(-Q/RT) \qquad (1)$$

where

r_c = minimum creep rate

A = constant
exp = natural logarithm base
Q = activation energy for process
R = gas constant
T = absolute temperature

Assuming the times of primary and tertiary creep are much shorter than that of the secondary creep and the tertiary creep begins when total strain reached a critical value (ε_r), the creep curve is simplified as schematically presented in Fig. 4. In this case, Equation (1) can be written as

$$1/t_r = B \times \exp(-Q/RT) \qquad (2)$$

where t_r is the time to rupture and B is the constant.

Taking the logarithm for Equation (2), the Larson-Millar equation (LMP: Larson-Miller Parameter) can be derived:

$$T(C + \log t_r) = Q/2.3R = LMP \times 1000 \qquad (3)$$

where C = log B

The Larson-Miller equation assumes that the activation energy Q, hence LMP, is independent from T and t_r but only the function of the applied stress σ. Assuming $LMP = P_0 - \alpha\sigma$, applied stress σ and $LMP(=T(C+\log t_r)\times 0.001)$ should show linear relation (Larson-Miller diagram).

Larson-Millar parameter assumes that temperature and time can be interchanged, provided no important microstructural changes occurred during the test. When the creep mechanism changes, the use of this parameter for predicting long time performance is not accurate. It was also suggested to use the Monkman-Grant equation [9] together with the Norton law [10] for predicting creep properties of 9%Cr steels:

$$\log r_c = -1/n \times \log t_r + D \qquad (4)$$

where n and D are the constants.

Figs. 5 and 6 present the minimum creep rate (r_c) as a function of rupture time (t_r) for JLF-1 and CLAM steels. From the figures, it can be seen that the constant n in eq. (4) is almost equal to 1. This means that the simplification shown in Fig. 4 and thus the Larson-Miller parameter are appropriate for the present prediction.

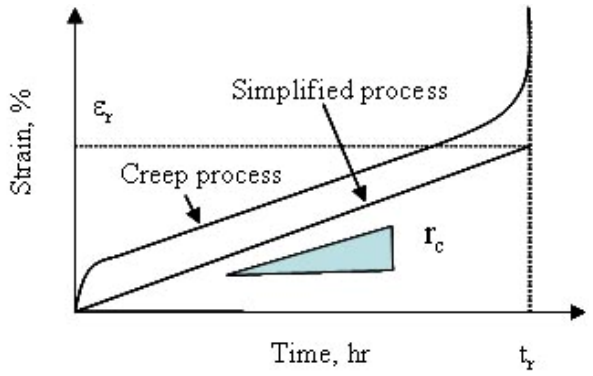

Fig. 4 Schematic illustration the creep curve and simplified process.

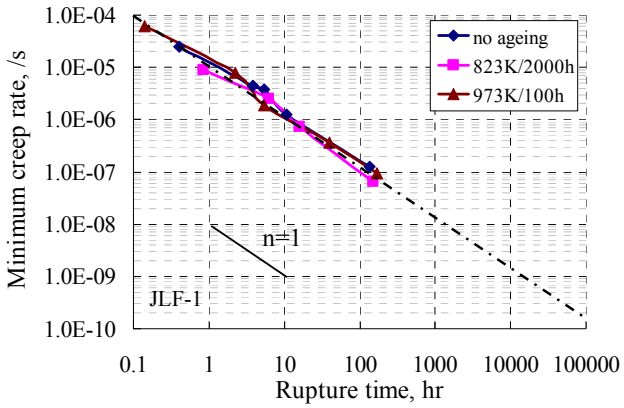

Fig. 5 Minimum creep rate as a function of rupture time (Monkman – Grant equation) for JLF-1 steel.

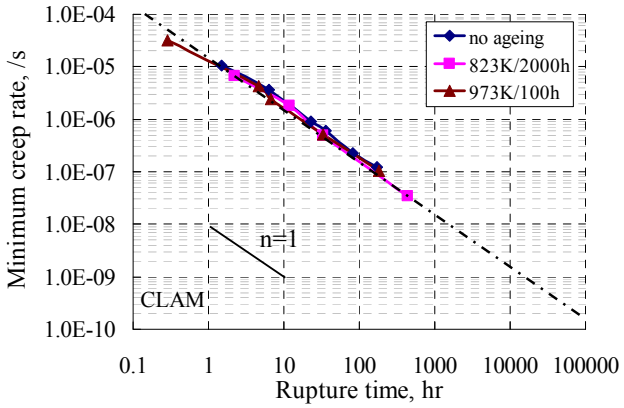

Fig. 6 Minimum creep rate as a function of rupture time (Monkman – Grant equation) for CLAM steel.

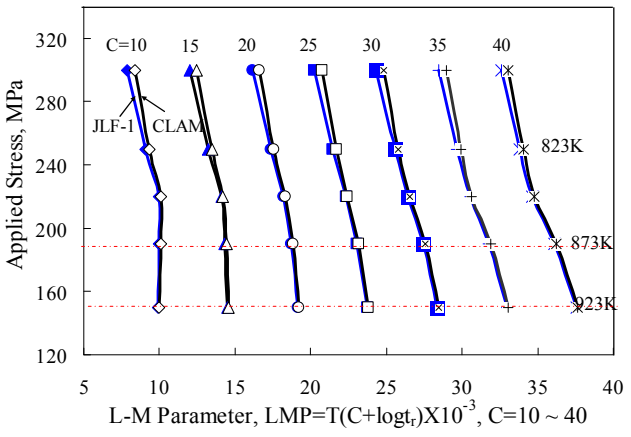

Fig. 7 Fitting of the Larson-Millar parameter with applied stress for various values of C for JLF-1 and CLAM steels before ageing

The C in Larson-Miller equation is a material constant. By the fitting of the present experimental data, the C = 30 is considered to be suitable for JLF-1 and CLAM steels, as shown in Fig. 7.

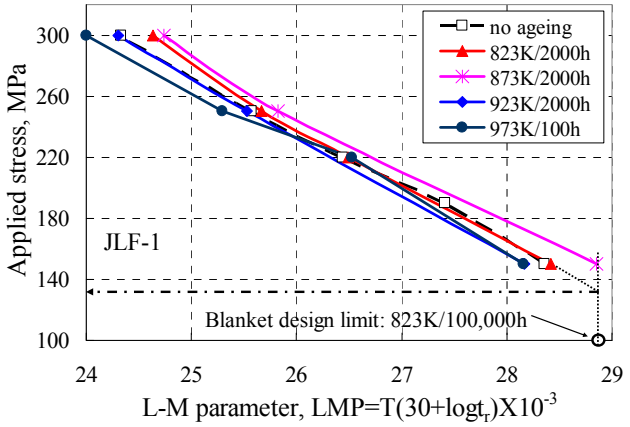

Fig. 8 Applied stress as a function of Larson-Millar Parameter for JLF-1 steel.

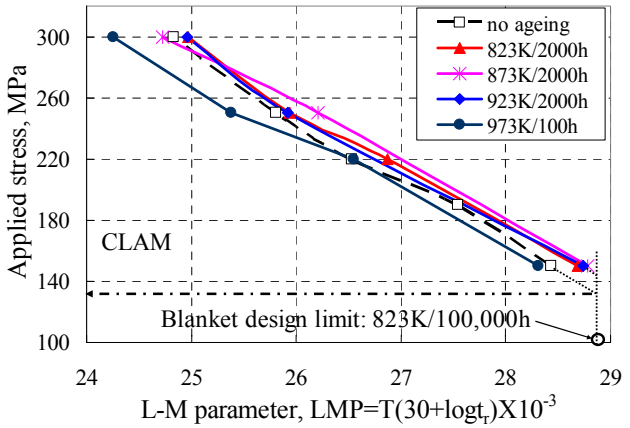

Fig. 9 Applied stress as a function of Larson-Millar Parameter for CLAM steel.

Figs. 8 and 9 present a Larson-Miller diagram with different aging conditions. The diagrams show the increase of LMP by ageing at 823 and 873 K and the decrease by ageing at 973 K. In addition, the rupture stress was estimated to be about 135 MPa by predicting the typical design limit for blanket, 823 K for 100 000h.

Figs. 8 and 9 also show that the estimated rupture stress can be change by about 15 MPa by the prior thermal ageing. These uncertainty need to be considered as the possible thermal ageing effect during the thermal creep processes.

Based on ASTM VIII guideline, acceptable stress limit of $2/3\times135=90MPa$ is derived for the both steels.

4.2 Thermal Activation Analysis

The present experiments and analysis showed that hardening and increase in the creep activation energy took place by aging at 823 K, and softening and the decrease in the creep activation energy occurred by aging at 973 K. In this section correlation of the hardness data is attempted based on the thermal activation process.

In this analysis ageing is assumed to be induced by migration of the constituent species (most probably C) with activation energy of E_m. The total number of jumps of the species during the aging is given by:

$$\upsilon = \upsilon_0 \times \exp(-E_m / kT) \times t_a \qquad (4)$$

where

υ_0 = jump frequency, 10^{13}/s
E_m = migration energy, eV
k = Boltzsman energy, $0.8625*10^{-4}$ ev/K
T = absolute temperature, K
t_a = aging time

Figs. 10 and 11 show the hardness change against the total number of jumps assuming the migration energy of 1.6, 2.0 and 2.4 eV for JLF-1 and CLAM, respectively. As shown in the figures, the total number of jumps is not an appropriate correlation parameter in any case of the activation energy. This means that the hardness change by aging is not thermally activated processes with a particular activation energy.

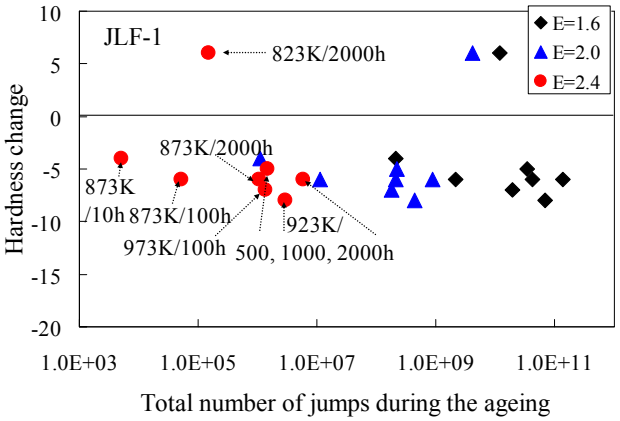

Fig. 10 Hardness change vs total number of jumps in different ageing conditions for JLF-1 steel.

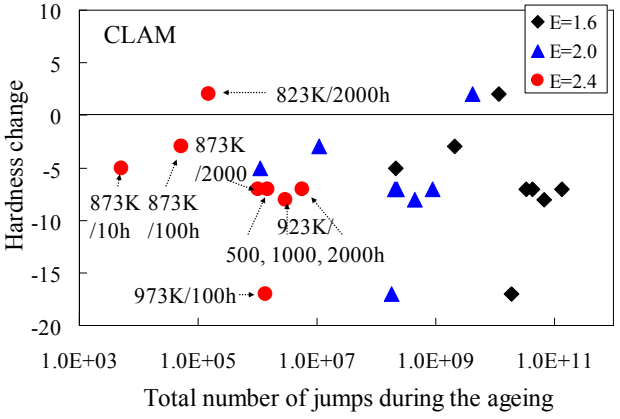

Fig. 11 Hardness change vs total number of jumps in different ageing conditions for CLAM steel.

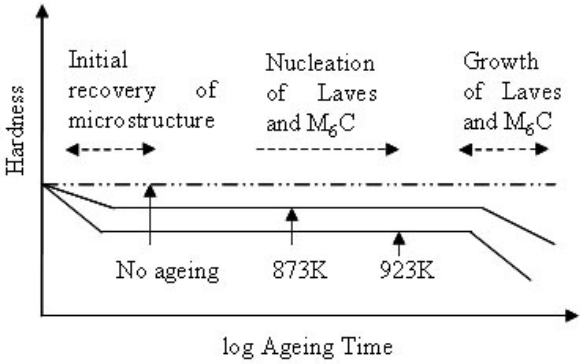

Fig. 12 The proposed dependence of hardness on ageing time at 873 to 923 K for JLF-1 and CLAM steels.

The authors' previous study showed that the hardening by aging at 823 K for 2000 h is due to the formation of fine TaC precipitates [11]. Therefore, the increase in the creep activation energy by ageing at 823 K for 2000 h was also considered to be originated from the precipitation of TaC.

However, by the ageing at 873 to 923 K, the hardness is almost independent from the aging time as shown in Figs. 10 and 11. It seems that the softening took place only in the initial ageing time as schematically shown in Fig. 12. In this case further softening needs formation of new phases such as Laves and M_6C. This is consistent with the observed precipitation in F82H by Tanigawa et al [12], which showed that the present aging conditions are before the formation of those phases.

5. Summary

The ageing experiments were carried out for JLF-1 and CLAM in the temperature range of 823 to 973 K followed by mechanical properties tests. The conclusions of the study are listed below:

(1) The hardness increased slightly after ageing at 823 K for 2000 h for the both steels. However, ageing at > 823 K caused a decrease in hardness.

(2) The minimum creep rate decreased and the rupture time increased after ageing at 823 and 873 K for 2000 h for the both steels, which suggested that the activation energy for the creep process increased. However, the creep property degraded significantly after ageing at 973 K for 100 h, indicating the decrease in the energy.

(3) The Larson-Miller parameter was used to predict long-term creep performance from the short-term experiment at higher temperature. The rupture stress of 135 MPa was predicted for the typical design limit of blanket, 823 K for 100 000h. The present thermal aging treatments influenced the rupture stress by ~15 MPa.

(4) From the activation analysis, it was suggested that the present ageing conditions are located after the initial microstructural recovery and before the softening and by formation of Laves and M_6C phases.

Acknowledgements

This work was carried out based on NIFS Budget Code NIFS07UCFF003 and NIFS07GCFF003. This work was also supported by JSPS-CAS Core University Program.

Reference

[1] T. Muroga, M. Gasparotto and S. J. Zinkle, Fusion Eng. & Des., **61-62**, 13 (2002).
[2] A. -A.F. Tavassoli, J. Nucl. Mater., **302**, 73 (2002).
[3] F. Abe, Mater. Sci. and Eng. A, **319-321**, 770 (2001).
[4] J. Lapeña, M. Garcia-Mazario, P. Fernández, *et al.*, J. Nucl. Mater. **283-287**, 662 (2000).
[5] P.J. Ennis, A. Zielinska-Lipiec, O. Wachter, *et al.*, Acta Mater., **45**, 4901 (1997).
[6] G. Dimmler, P. Weinert, and H. Cerjak, Int. J. Press. Vess. Pip., **85**, 55 (2008).
[7] P. Fernández, A.M. Lancha, J. Lapeña, *et al.*, Fusion. Eng. & Des. **75-79**, 1003 (2005).
[8] F.R. Larson and James Miller, Trans. ASTM, **74**, 765 (1952).
[9] F.C. Monkman, *N.J. Grant, Proc ASTM*, **56**, 593 (1956).
[10] F.H. Norton, McGraw hill publishing Co. Ltd. 1929) p. 67.
[11] Y.F. Li, T. Nagasaka and T. Muroga, presented in 18th-Topical Meeting on the Technology of Fusion Energy, San Francisco, USA, Sep. 28-Oct.2, 2008.
[12] H. Tanigawa, K. Shiba, S. Jitsukawa, *et al.*, 13th-International Conference on Fusion Reactor Materials, Nice, France, Dec. 10-14, 2007.

Proceedings of ITC18,2008

Real-time Video Streaming System for LHD Experiment Using IP Multicast

Masahiko Emoto, Takashi Yamamoto, Makoto Hasegawa[a)], Masanobu Yoshida, and Yoshio Nagayama

National Institute for Fusion Science,322-6 Oroshi-cho, Toki 509-5292, Japan

[a)]Research Institute for Applied Mechanics, Kyushu University, 6-1 Kasuga-kouen, Kasuga, Fukuoka

In order to accomplish smooth cooperation research, remote participation plays an important role. For this purpose, the authors have been developing various applications for remote participation for the LHD (Large Helical Device) experiments [1], such as Web interface for visualization of acquired data [2]. The video streaming system is one of them [3]. It is useful to grasp the status of the ongoing experiment remotely, and we provide the video images displayed in the control room to the remote users. However, usual streaming servers cannot send video images without delay. The delay changes depending on how to send the images, but even a little delay might become critical if the researchers use the images to adjust the diagnostic devices. One of the main causes of delay is the procedure of compressing and decompressing the images. Furthermore, commonly used video compression method is lossy; it removes less important information to reduce the size. However, lossy images cannot be used for physical analysis because the original information is lost. Therefore, video images for remote participation should be sent without compression in order to minimize the delay and to supply high quality images durable for physical analysis. However, sending uncompressed video images requires large network bandwidth. For example, sending 5 frames of 16bit color SXGA images a second requires 100Mbps. Furthermore, the video images must be sent to several remote sites simultaneously. It is hard for a server PC to handle such a large data. To cope with this problem, the authors adopted IP multicast to send video images to several remote sites at once. Because IP multicast packets are sent only to the network on which the clients want the data; the load of the server does not depend on the number of clients and the network load is reduced. In this paper, the authors discuss the feasibility of high bandwidth video streaming system using IP multicast.

Keywords: remote participation, monitoring, streaming, IP multicast, SINET3

1. Introduction

Large scale experiment such as Large Helical Device (LHD) experiment in NIFS has been executed under the corporation of many researchers work at various places. Therefore, for such an experiment, a remote participation facility plays an import role to accomplish smooth cooperation. For example, motional image data is useful in that it can help researchers recognize not only the status of the experiment, but dynamic behaviors of plasma, including plasma-wall interactions and impurity transport at the plasma periphery. Commonly, video streaming over a limited network is sent in lossy compressed formats such as RealVideo, MPEG, QuickTime, and the like. For example, Shoji developed the Video on Demand system for LHD experiments to monitor plasma behavior [4]. That system provides MPEG1 or MPEG2 format images by the network. Using these formats, the video data can be shrunk to a tenth of its original size or smaller, whereas with the lossless compression algorithm, the data shrinks only tens of percents at the most. However, the disadvantage of using lossy compression is that information is lost when it is compressed. This does not matter if the image is used solely for monitoring, but it

Fig.1 Control room in NIFS

author's e-mail: emo@nifs.ac.jp

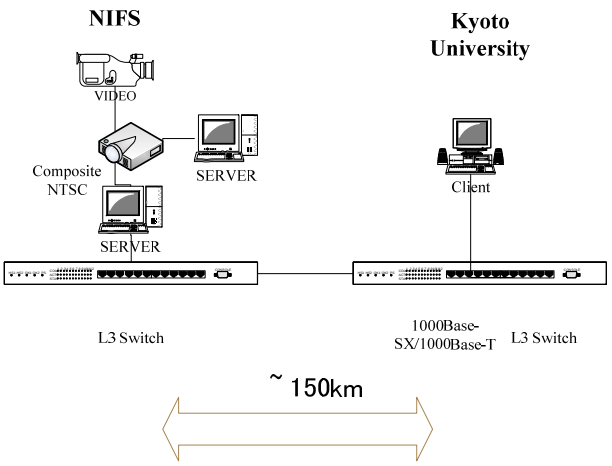

Fig 2. System overview

cannot be used for further scientific analysis. Another disadvantage is delay. Because these lossy compression uses motion compensation to reduce sizes; it detects the difference between consecutive frames and send only differences. However, because of this scheme, it needs to store the previous frames to determine the next images. Therefore, the delay is inevitable.

To solve this problem the authors has been developing the real-time monitoring system that send lossless images.

2. Real-time Monitoring System

In the control room of NIFS, there is a 150-inch projector to display the summary graph of the latest acquired data and the video image of the plasma to monitor the current going experiment (Fig.1). This information is helpful to the researchers in NIFS to monitor the ongoing experiment. Because the authors thought it was also helpful to the researchers at the remote sites, the authors have developed a system to send this image to the other universities. Fig 2 is the overview of this system. The network connecting NIFS and Kyoto University is Super SINET [5], an optical fiber based network. The server in NIFS sends the video images displayed by the projector to the client in Kyoto University. The source of the image is captured from the composite signal out from the video switcher using NTSC format. NTSC is widely used by video recorder and video capture in Japan, and is an easy format to handle. Although the output signal from the PC is RGB signal, it is converted into NTSC signals. The captured data is composed of VGA-size 24bit RGB images. The server and clients use two TCP/IP ports to communicate with each other; one for sending image data, the other for flow control.

While the authors were testing this system, several problems were found. First, the system uses NTCS video signals while the output signal from PC is RGB digital signal. The number of scan lines of NTSC is 525 while

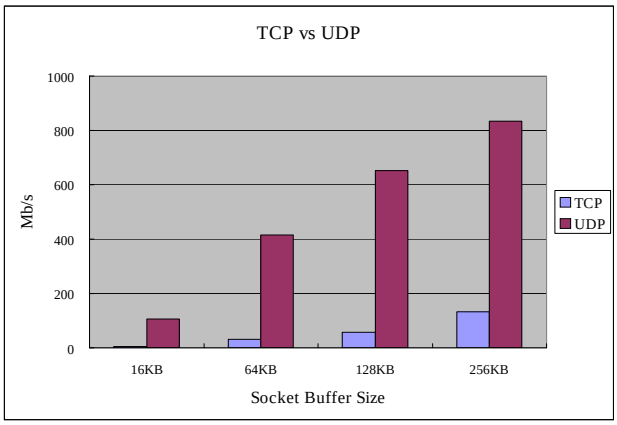

Fig. 3 Network speed between NIFS and Kyoto University using Super SINET

the vertical resolution of the PC signal is 1024. Thefore, the image is deteriorated and it is hard to read the small text in the summary graph.

The second problem is transfer ratio. The system uses TCP connection to send video images. Using TCP, the sender must confirm that the client receives the packet before it will send the next packet. Therefore, if there is a large latency between the sender and receiver, the total transfer ratio decreases. For example, the total TCP transfer ratio between NIFS and Kyoto University becomes 6 ~ 130 M bit/sec depending on socket buffer size while they are connected by 1Gbits/sec capability network (Fig. 3) [6]. On the other hand, the maximum transfer ratio of UDP reaches more than 800 Mb/sec.

The third problem is its scalability. Because the server must send images to each client one by one, the server's CPU and network load increase proportional to the number of clients. Judging from the current network bandwidth (less than 1Gbps), one server can handle only a few clients

3. New System

To solve the problems of the previous system, the author has been developing a new monitoring system. First, the new system uses VGA capture device to capture video signal out from PC directly. Second, in order to solve large latency problem, the new system uses IP multicast that uses UDP instead of TCP. When the sender uses UDP, it doesn't have to wait for the client's reply, and

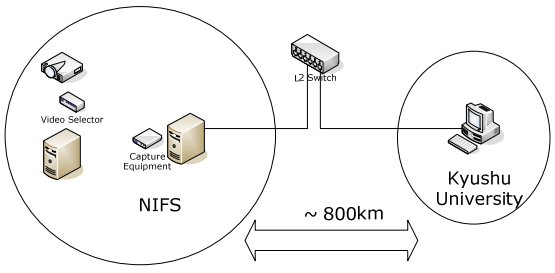

Fig.4 New system

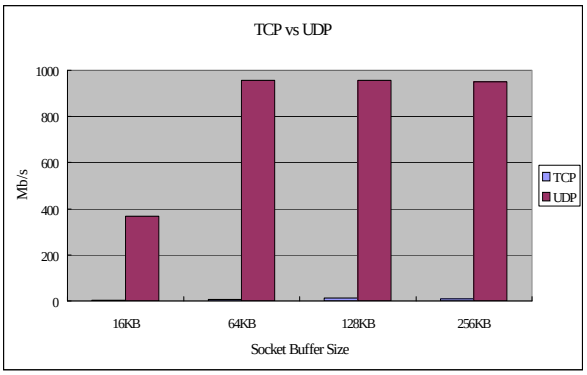

Fig. 5 Network Speed between NIFS and Kyoto University using SINET3

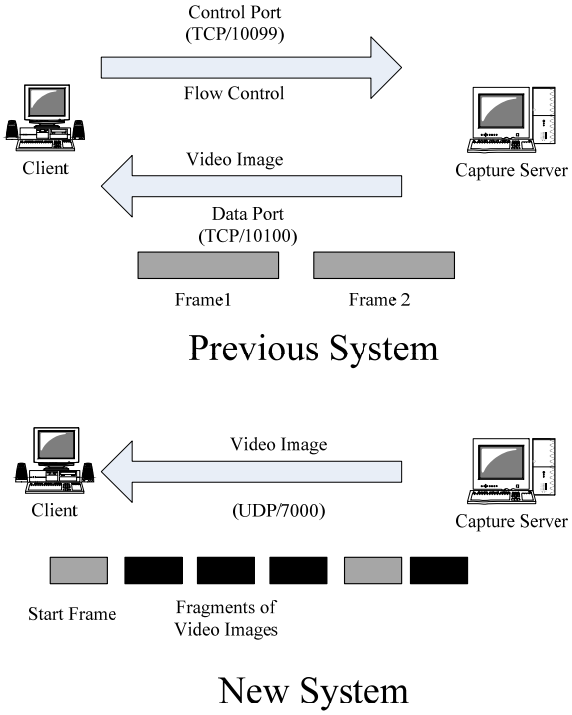

Fig. 6 Protocols of the video streaming system.

the system can take full advantage of the network capability. On the other hand, there is a drawback of UDP; it is not reliable because the sender doesn't confirm whether client receives the packets or not, therefore, packets may be lost. If the system send the experimental data by UDP, this drawback becomes critical even if the number of lost packets is few. However, for sending video images for monitoring, it is not critical because the user can still identify the images if the number of lost packets is few. Using IP multicast also solve the scalability problem because multicast packets are sent only to the sub-nets on which the clients want the data, and the load of the server does not depend on the number of clients.

Fig 4 shows the overview of this system. The newly developed system uses a signal duplicator to duplicate the signal input to the projector. It is RGB signal of 1280 x 1024 pixels and its frame ratio is 60 frames / sec, and the NTSC signals from the VTR is converted to RGB signal. To capture the signal, the system uses a video capture device, Epiphan system's VGA2USB LR [7]. It is a USB device and connected to the server. The operating system of the server is Linux, and the image is captured using Video4Linux API.

The network connecting NIFS and Kyushu University is SINET3 [5], the latest inter-university network integrating the former Super SINET and SINET. The server and the client are connected by L2 switches, and they don't send packets via routers or L3 switches. Fig.5 shows the TCP and UDP transfer ratio. Same as the previous system, TCP transfer ratio is not good considering it is 1Gbp network. However, that of UDP reaches 950 Mb/sec, and it is almost upper limit of the network speed.

While the server of the previous system sent each frame one by one using TCP protocol, the new system sends fragment of a frame using IP Multicast, i.e. UDP protocol. (Fig.6)

4. Results

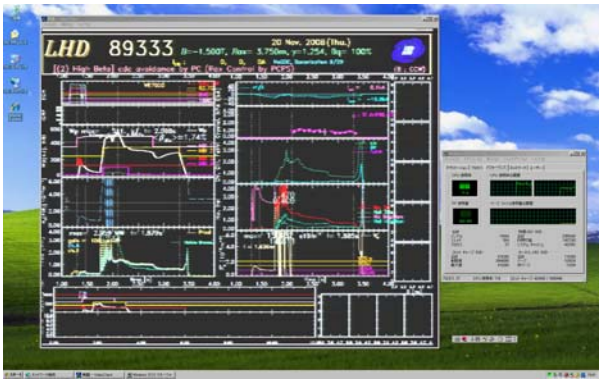

Fig.7. Client Program

Fig.7 shows the display of the client PC. The center window shows the same image displayed in the control room in NIFS. The actual frame ratio sent from the server is 23 frames /sec, and the total transfer ratio becomes 420 Mb/s.

The captured image is divided into pieces, and the server sends each piece as a multicast packet. Therefore, if

	Server	Client
OS	Fedora 9 (i386)	Windows XP
CPU	Intel Core 2 Duo E6550 (2.33GHz)	Intel Core 2 Duo T8100 (2.1GHz)
Memory	2GB	2GB

Table 1. Specification of the server and client PC

the client doesn't catch up with the packet flow, it will drop packets and area of the images corresponding to the dropped packets are missing. Seeing the images of the client PC, no packet loss is observed. However, the CPU load becomes almost 80% during this test. Therefore, computers less powerful than this PC might drop the packets. The specification used for this system is listed in table. 1.

It is difficult to measure the exact delay of the video images between NIFS and Kyushu University, but it is estimated 220 msec. This estimation is the sum of 200 msec, which is the delay of images measured between two PCs located at the local LAN, and 20 msec, which is the time to send IP packets from NIFS to Kyushu University.

5. Discussion & Conclusion

The authors demonstrated the feasibility of real-time monitoring system using IP multicast. Judging from the frame ratio of 23 frames / sec and the delay of 220 msec, the system may not be used for real-time control, but can be used for monitoring. However, the authors experienced the excessive increase of CPU load of the L3 switch while the system was tested using local area network; the CPU load of the network switch increased to 100%, and it became an obstacle to other functions. This is probably because the multicast function of this switch is implemented by software and consumed CPU power. On the other hand, the excessive CPU load increase was not observed for NIFS-Kyushu University network. One of the reason of this is it is L2 connection, and it doesn't relay L3-level transportation. From this fact, the multicasting high quality video images needs enough power, and the multicast function should be implemented as wired logic.

Acknowledgements

This work was partly supported by Cyber Science Infrastructure (CSI) development project of the National Institute of Informatics.

References

.

[1] M. Emoto, T. Yamamoto, S. Komada and Y. Nagayama, Fus. Eng. Des. **81** 2051 (2006)

[2] M. Emoto, S. Murakamib, M. Yoshida, H. Funabaa and Y. Nagayama, Fus. Eng. Des. **83** 453 (2008)

[3] M.Emoto, K.Watanabe, S.Masuzaki, N.Ohno, and H.Okada, Rev. Sci. Inst. **74** 1766 (2003)

[4] M.Shoji, et al., PCaPAC2000, Hamburg, Oct. 2000

[5] http://www.sinet.ad.jp/

[6] M.Emoto, NIFS-MEMO-**51** 42 (2006)

[7] http://www.epiphan.com/

Proceedings of ITC18, 2008

Development of a High Speed VUV Camera System for 2-Dimensional Imaging of Turbulent Structure in LHD

M. Takeuchi, S. Ohdachi and LHD experimental group

National Institute for Fusion Science, 322-6 Oroshi-cho, Toki 509-5292, Japan

In fusion plasmas, a turbulent transport effects greatly on a plasma confinement. In order to clarify the role of the turbulent transport, measurements of fluctuations with high time and spatial resolutions are necessary. In this case, if 2-dimensional structures are observed, the more detailed characteristics of turbulence can be clarified, since a propagation direction of the fluctuations and the mode number are found in visually. Therefore, a high speed vacuum ultraviolet (VUV) camera system for 2-dimensional imaging of turbulent structures was developed and installed in LHD. This optical system is composed of 2 multi-layer mirrors made of Mo / Si and a micro-channel plate (MCP). An emission from plasma reflects at the multi-layer mirrors with high reflectivity and images on the MCP. The VUV emission near 13.5 nm of impurity carbon (n = 4-2 line of C VI) can be observed. In analysis of the camera image, an inverse transformation of the line-integrate data is required for the deviation of the turbulent structure. In this paper, the constitution of this VUV camera system and an analytical method are described in detail, and moreover preliminary results observed in LHD are shown.

Keywords: 2-dimensional imaging, vacuum ultra-violet, impurity carbon, turbulent structure

1. Inroduction

In fusion plasmas, a turbulent transport effects greatly on a plasma confinement. For edge transport barrier plasmas, the turbulence suppressions by sheared E x B flow have been observed [1]. Recently, oscillating E x B flows called zonal flows have emerged as an important part of the overall turbulence physics [2].

The measurement of turbulence needs both high temporal and high spatial resolutions. We want to know a 2-dimensional turbulent structure to clarify a propagation direction of fluctuations, the mode number and so on. In a large helical device (LHD), an edge transport barrier plasma and an internal diffusion barrier plasma are observed and researched in recently. The clarification of the turbulent structure in the plasmas is important to clarify physical mechanisms of these transport barriers.

Therefore, we developed a new 2-dimensional imaging diagnostics for turbulent structures, which called “a high speed vacuum ultraviolet (VUV) camera system”. This VUV emission from impurity carbon reflects an impurity fluctuation, and a fluctuation of an electron density can be estimated as a result. This system has an advantage that a light intensity is larger than that of a pinhole type optical system. This high speed VUV camera system was installed on LHD and preliminary data were obtained.

2. High speed VUV camera system

A high speed VUV camera system is constituted by multi-layer mirrors, an MCP and a high speed camera as shown in Fig.1. VUV light can only travel in a vacuum region, therefore the system is composed in vacuum chamber except the high speed camera.

The multi-layer mirror is made of Mo / Si (typical thickness is 6.66 nm, dMo : dSi = 4 : 6) and the reflectivity is about 50-60 % [3]. This mirror is mainly reflect the VUV light of 13.5 nm (half band width is about 1-2 nm). This wavelength is corresponds to the impurity carbon line (n = 4-2 line of C VI) [4]. There are two multi-layer mirrors in the system. One of these mirrors reflects the VUV light from plasma by the convex mirror (curvature radius is 144.5 mm), the other reflects the light and images on the MCP by the concave mirror (curvature radius is 390 mm).

The MCP (Tokyo instruments, inc.) is an electron-multiplier device which multiply electrons detected 2 dimensionally. Since the MCP has sensitivity for not only electron but also ion, VUV light and X-ray, the MCP is also used for those detected devices. The MCP has the phosphor screen of 48 mm in diameter in order to image the output signal optically. In experiment, the MCP is biased high voltage to observe the VUV light. The MCP has two layers and one layer is the output of rhe assembly (Vo), the other is the input of the assembly (Vi). The phosphor screen is applied upto +3.0 kV, Vo is connected to ground and Vi is applied upto -1.5 kV. The output intensity can be controlled by changing the value of the high voltage.

The 2-dimensional image of the phosphor screen of MCP is recorded by a high speed camera. We used the

author’s e-mail: m-takeuchi@nifs.ac.jp

Phantom v4.2 camera of the Vision Research, Inc. This camera can record up to 15300 pictures per second (pps) in 256 × 128 pixels. The obtained data is transferred to the PC through an optical fiber and stored in there.

The overall view of the high speed VUV camera system together with LHD vacuum vessel and plasma is shown in Fig.2 and the top view of that is shown in Fig.3. The focal length of the multi-layer mirrors is about 7 m, thus the mirror is placed from the plasma center by the length. The plasma image is reduced by 1 / 60 by mirror optic and focused on the MCP screen. Since the diameter of the port, we are using now, is smaller than initial design, only the 1 / 3 of the image (5.5 mm at the entrance of the MCP) can be measured now.

3. Analytical method

The obtained 2-dimensional data do not directly reflect the plasma fluctuations because of the line integrated effect. Particularly, the situation in the helical plasma is more complicated than that in the tokamak plasma. The obtained data need to be reconstructed in order to know the actual 2-dimensional fluctuation data.

In order to analyze the turbulent structure, it is supposed that a radiation along magnetic field lines is constant. We need to know the equivalent field lines of sight in the region of the view line [5]. The Fourier – Bessel expansion method [6, 7] will be used in the reconstruction of the radiation intensity.

Moreover, the simulation of the profiles of the emission of impurity carbons is needed to predict the experimental emission profile. The IONEQ code [8] for LHD developed by Dr. A. Weller will be used to simulate the emission.

4. Experimental results

Preliminary data was obtained by using the high speed VUV camera system in LHD. The following data was measured by camera speed of 2000 pps and 256 × 128 pixels.

Figure 4 shows the time evolutions of neutral beam injection (NBI), plasma stored energy (W_p), line integrated density (nL), power of radiation (P_{rad}), H_α emission, C III emission and measured VUV emission at the position of (x, y) = (119, 65) pixel where is the center of the MCP. This plasma was heated by four NBIs and hydrogen pellets were injected for t = 2.6-2.9 s. A time evolution of the emission at (x, y) = (119, 65) is similar to C III emission, P_{rad} and H_α emission. A rapid small increase at t = 3.465 s in VUV emission is also observed for C III emission, however, not observed for P_{rad} and H_α emission. Therefore, the observed emission may reflect carbon impurity emission of 13.5 nm. Since there is a possibility that the observed emission includes the low-energy light which wave length is not 13.5 nm, we will improve the high speed VUV camera system by using a low-energy-cut filter.

The 2-dimensional image at t = 2.8205 s is also shown in Fig.4. The emission inside of the imaging area (< 5.5 mm in diameter) was observed. The emission outside the imaging area may be a stray light. The analysis of this 2-dimensional VUV emission is now proceeding.

5. Summary

A high speed VUV camera system was developed and preliminary data was obtained. The 2-dimissional VUV emission was successfully observed. It is necessary to improve this system to observe the VUV light of higher strength for measurement of the turbulent structure at a high resolution time. This new diagnostics have a possibility to become a useful and powerful tool for 2-dimensional imaging of turbulent structures in fusion plasma.

Acknowledgments

This study is supported by NIFS budget code NIFS07ULHH509 and is also partially supported by the Ministry of Education, Science, Sports and Culture, Grant-in-Aid for Scientific Research (B), 17360446, 2005-, by the IAEA TEXTOR agreement (NIFS07KETE001) and by the "SPS-CAS Core-University Program" in the field of "Plasma and Nuclear Fusion".

We wish to express our gratitude for Dr. Kuninori Sato's having lent us his MCP.

References

[1] P.W. Terry, Rev. Mod. Phys. **72**, 109 (2000)
[2] P.H. Diamond *et al*., Plasma Phys. Control. Fusion **47**, R35 (2005)
[3] H. Takenaka *et al*., Transactions of MRS-Japan **28**, 95 (2003)
[4] D. Stutman *et al*., Rev. Sci. Instrum. **77**, 10F330 (2006)
[5] S. Ohdachi *et al*., Plasma Sci. & Tech. **8**, 45 (2006)
[6] Y. Nagayama, J. Appl. Phys. **62**, 2702 (1987)
[7] N. Iwama and S. Ohdachi, J. Plasma Fusion Res. **82**, 399 (2006)
[8] A. Weller *et al*., JET-IR(87)10

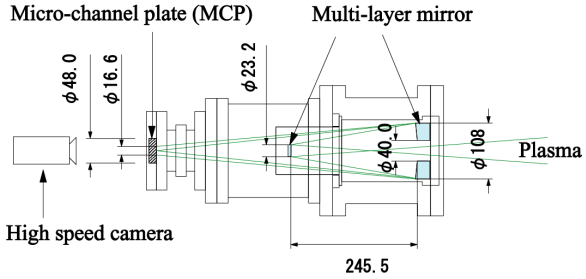

Fig.1 High speed VUV camera system.

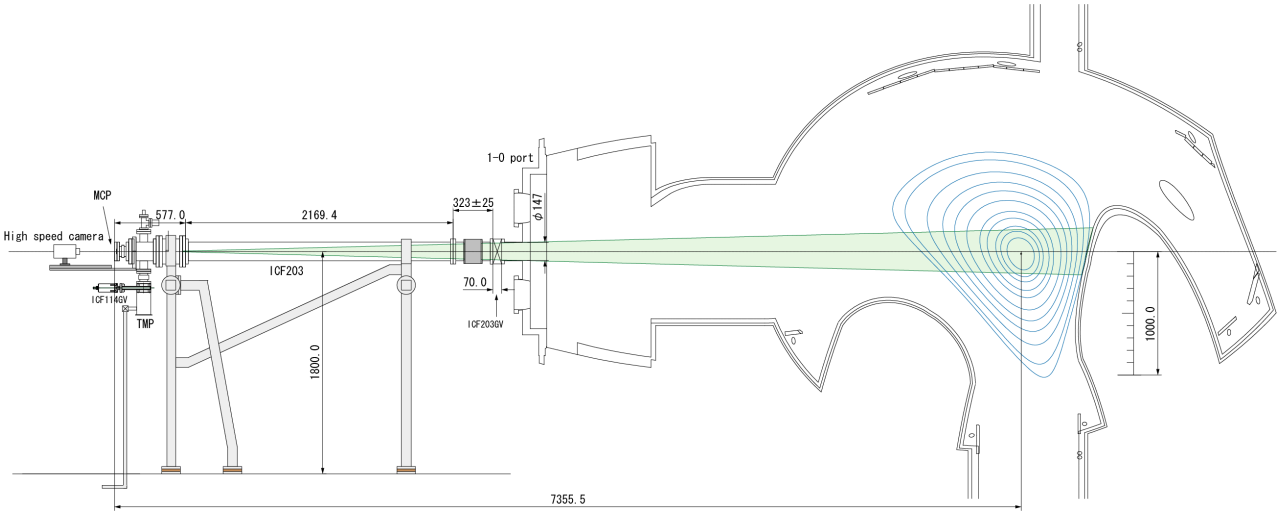

Fig. 2 The overall view of the high speed VUV camera system together with LHD vacuum vessel and plasma.

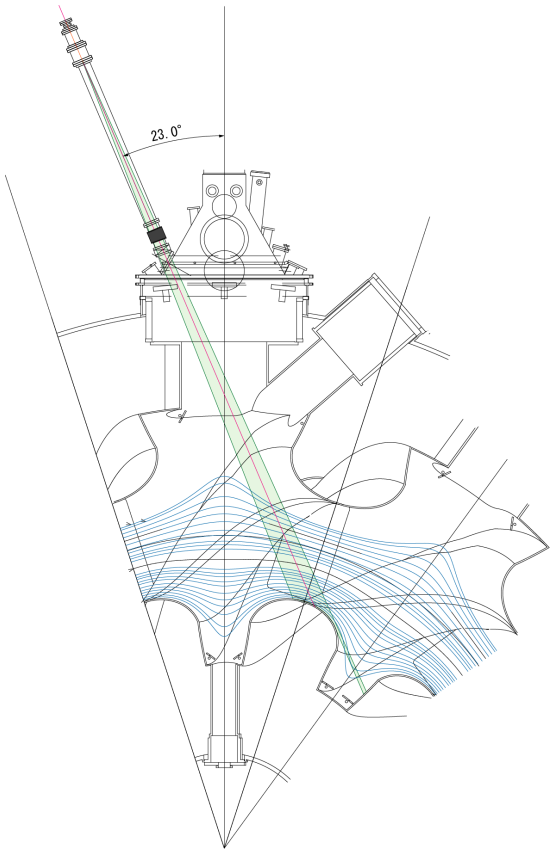

Fig.3 The top view of the high speed VUV camera system together with LHD vacuum vessel and plasma.

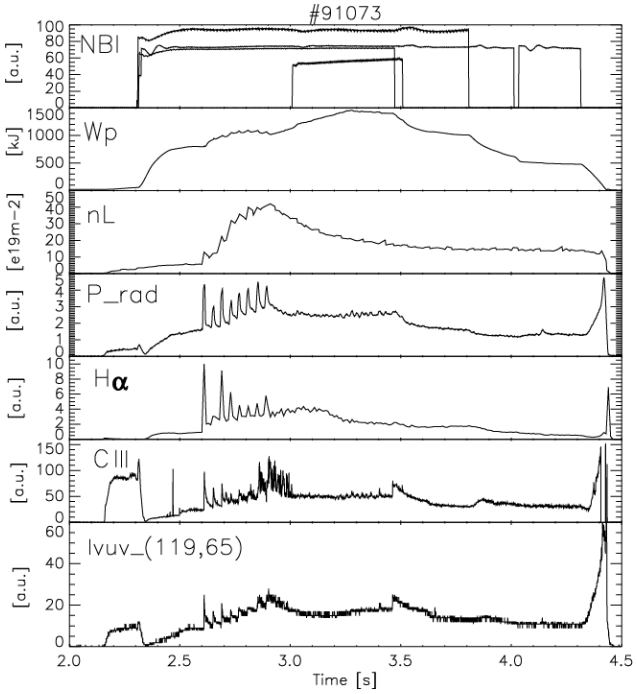

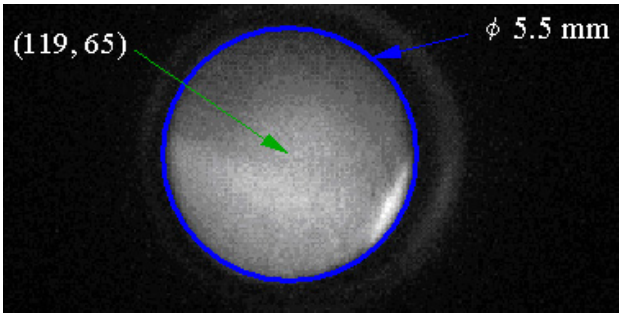

Fig.4 Time evolutions of NBI, Wp, nL, Prad, H_α, C III and VUV emission at (x, y) = (119, 65) pixel where is the center of the MCP and an image of camera at t = 2.8205 s in #91073. The imaging region is inside the circle of 5.5 mm in diameter.

Proceedings of ITC18, 2008

Collective Thomson Scattering Study using Gyrotron in LHD

Shin KUBO[1)], Maski NISHIURA[1)], Kenji TANAKA[1)], Takashi SHIMOZUMA[1)], Yoshinori TATEMATSU[2)], Takashi NOTAKE[2)], Teruo SAITO[2)], Yasuo YOSHIMURA[1)], Hiroe IGAMI[1)], Hiromi TAKAHASHI[1)], Namiko TAMURA[3)]

[1)]*National Institute for Fusion Science,322-6 Oroshi-cho, Toki 509-5292, Japan*
[2)]*Research Center for Development of FIR Region, Univ. of Fukui, Fukui, 910-8507, Japan*
[3)]*Dept. of Energy Science and Technology, Nagoya Univ., Nagoya, 464-8463, Japan*

The collective Thomson scattering (CTS) is one of the most promising methods for evaluating the ion velocity distribution function. The study of CTS diagnostic has been started utilizing the gyrotron and antenna/transmission systems installed in LHD for high power local electron heating. One of the high power gyrotrons at 77 GHz is selected as a probing power source and a set of highly focused antenna system is used for the probing and receiving antenna. The specific feature of the system, receiver design are described and preliminary data obtained in for ECRH plasma in LHD are discussed.

Keywords: Collective Thomson scattering, ECRH, ECE, Gyrotron, Gaussian beam, Ion temperature

1 Introduction

The direct and local measurement of the ion velocity distribution function is important in any fusion relevant plasma to study the behaviors of not only the bulk but also the high energy ions. The collective Thomson scattering (CTS) has long been attracted and intensively studied as one of the most promising diagnostic methods for the ion distribution function[1]. Frequency range required for the CTS in the fusion relevant plasma is determined from the collective scattering condition and scattering angle that gives the spatial resolution. This frequency range lies from infrared to millimeter wave[2, 3, 4]. Mainly due to a small scattering cross section, or scattering efficiency, CTS requires high power probe beam source with sharp single frequency spectrum and highly sensitive receiver near the frequency but avoiding a direct contamination of the probe frequency that requires a sophisticated stray suppression. The other important factor required for the spatially well resolved measurement of CTS is the well defined probe and receiving beams and their controllability. High power, sharp spectrum, and highly focussed well defined Gaussian beam are already realized for the electron cyclotron resonance heating (ECRH) system using gyrotron and high power transmission/antenna in LHD. We have started the trial of CTS study utilizing the existing ECRH system in LHD[5] as well as that utilizing higher frequency (400 GHz) gyrotron that is under development[6]. Expected necessary frequency range to deduce ion velocity distribution is ± 3 GHz at the center frequency. In section 2 are discussed the characteristic feature of the ECRH system in LHD as a CTS probe and receive beam. Electron cyclotron emission (ECE) is expected to be the main source of noise for CTS diagnostic. The ECE spectrum expected at the line of receiving beam is discussed in section 3. Receiver system is described in section 4. Finally the preliminary data obtained with the system described here are shown in section 5.

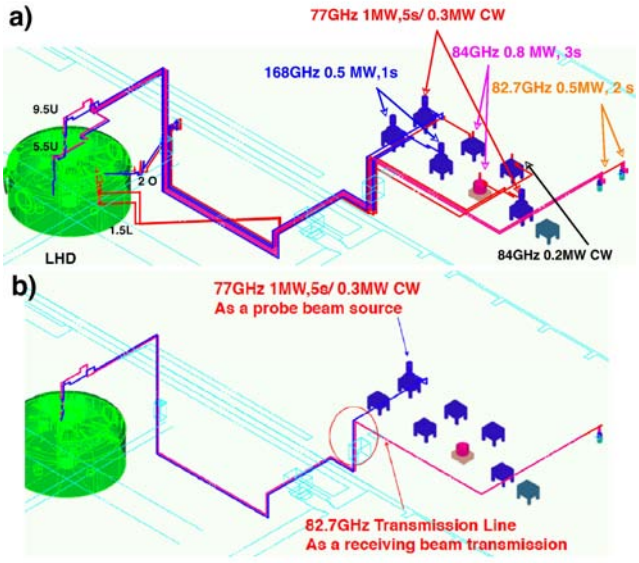

Fig. 1 a) Two sets of injection antenna system are installed on 4-ports of LHD, (5.5U, 9.5 U, 1.5L and 2O). b) A set of transmission line/ antenna on the 9.5U port is selected for CTS. The set that 77GHz 1MW power is available is used for probe beam.

2 ECRH system as a probe beam and receiver antenna for CTS

One of the newly installed 77 GHz gyrotrons in LHD have achieved more than 1MW over 3 s[7]. The present ECRH system is illustrated in Fig. 1 a). Nine gyrotrons are in operational and eight corrugated transmission lines (6- 88.9

author's e-mail: kubo@LHD.nifs.ac.jp

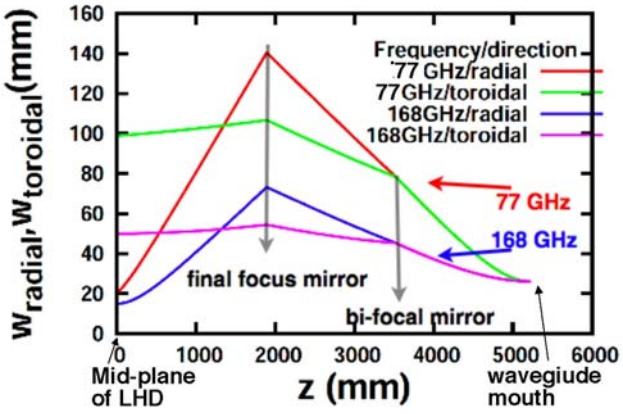

Fig. 2 Beam evolution at 9.5 U port antenna. Originally the focusing mirrors are originally optimized for 168 GHz to focus the symmetric Gaussian beam radiated from 88.9 mm corrugated waveguide to an elliptical Gaussian beam on the mid-plane of LHD to have *1/e* waist size of 15 mm and 50 mm in radial and toroidal direction, respectively. Re-calculated beam evolutions for 77 GHz are plotted. The waist size for 77 GHz are also elliptical Gaussian with the waist size on the LHD-midplane 20 and 100 mm.

id and 2-31.75 mm id) are connected to LHD. Two sets of injection antenna are installed on each 4-LHD ports (5.5U, 9.5U, 2-O and 1.5L). The 9.5 U port antenna set is selected as a CTS probe and receiving antenna, since 77 GHz high power is available for the probing beam and the beam controllability is well established and confirmed [8]. This gyrotron has a triode gun that allows high frequency power modulation without degrading oscillating mode which is one of the important feature for the CTS. This gyrotron is connected to one of the Gaussian mirror antenna set. This antenna set includes one another Gaussian beam mirror suitable for receiving the scattered power from definite scattering volume. The injection antenna used was originally designed for 168 GHz. The beam evolutions for 77 GHz is re-calculated using the same mirror sets and configurations as 168 GHz, using the mirror curvature and phase plane transformation relation:

$$\frac{\cos\phi}{\rho_\sigma} = \frac{1}{2R_{\sigma,\mathrm{in}}} + \frac{1}{2R_{\sigma,\mathrm{out}}} \tag{1}$$

here, ϕ is the injection/reflection angle, $R_{\sigma,\mathrm{in}}$, $R_{\sigma,\mathrm{out}}$ and ρ_σ are the phase radius of input and output beams and mirror curvature radius in σ =toroidal or poloidal directions. Actual beam configuration is shown in Fig. 3 for the case where the center of the scattering volume lies near $\rho \approx 0.7$. The upper half of the flux surfaces of $\rho = 0.1$ and 1.0 are also shown for reference. The effective scattering volume can be calculated by integrating over the space using the

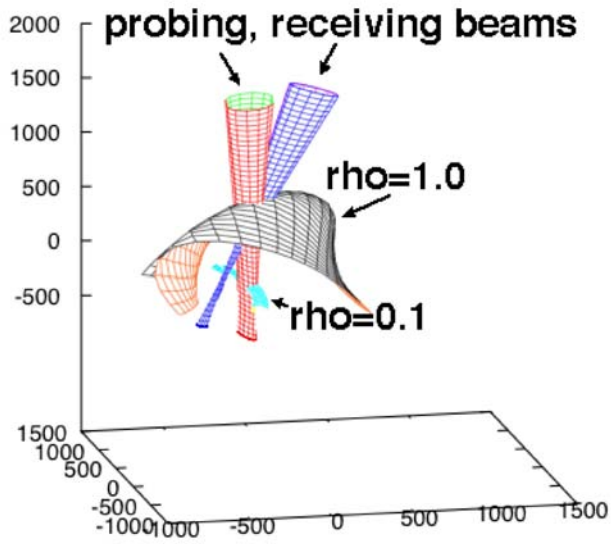

Fig. 3 3-D image of the probe and receiving beams.

following formula

$$\iint \exp\left(-\frac{x^2}{w_{0,\mathrm{x}}^2+\frac{\lambda^2(z-z_{0,\mathrm{x}})^2}{\pi^2 w_{0,\mathrm{x}}^2}} - \frac{y^2}{w_{0,\mathrm{y}}^2+\frac{\lambda^2(z-z_{0,\mathrm{y}})^2}{\pi^2 w_{0,\mathrm{y}}^2}}\right) \exp\left(-\frac{x'^2}{w_{0,\mathrm{x}'}^2+\frac{\lambda^2(z'-z_{0,\mathrm{x}'})^2}{\pi^2 w_{0,\mathrm{x}'}^2}} - \frac{y'^2}{w_{0,\mathrm{y}'}^2+\frac{\lambda^2(z'-z_{0,\mathrm{y}'})^2}{\pi^2 w_{0,\mathrm{y}'}^2}}\right) \delta(\boldsymbol{r}' - \overleftrightarrow{\boldsymbol{T}} \cdot \boldsymbol{r})\mathrm{d}\boldsymbol{r}\mathrm{d}\boldsymbol{r}'. \tag{2}$$

Here, λ is the wavelength, $w_{0,\sigma}$, $z_{0,\sigma}$ are the waist size and waist position in $\sigma = x, y, x', y'$. (x, y, z) is the local coordinate of injection beam and (x', y', z') is that of receiving beam and $\overleftrightarrow{\boldsymbol{T}}$ is the conversion tensor of both local coordinates. The scattering volume for the case shown in Fig. 3 is about 700 cm^3. This volume is distributed over the minor radius 0.78 ± 0.2 as shown in Fig. 4. This figure defines the spatial resolution of the CTS measurement using this antenna set.

3 Background ECE as a main noise source

Main competing background noise source for CTS is the electron cyclotron emission (ECE). The background ECE level on the line of sight toward the receiver antenna should be estimated taking account of the actual antenna configuration. The calculation of the background ECE spectrum is performed by solving the radiation transfer equation back along the line of sight. The method is described in ref[9]. For use of this 77 GHz gyrotron as a probing beam, operational magnetic field should be selected so as to exclude the fundamental and second harmonic resonances of 77 GHz on the line of sight inside the plasma confinement region, in order to reduce the ECE background that is considered to be the largest noise source. The relations be-

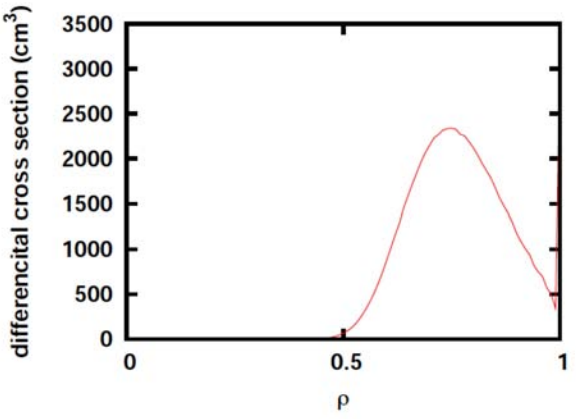

Fig. 4 Differential cross section of the scattering volume as a function of effective minor radius ρ. The scattering volume center is placed at z=0.5 m, R=3.6 m on the vertically elongated poloidal cross section in LHD. Total effective scattering volume is about 700 cm^3 in this case.

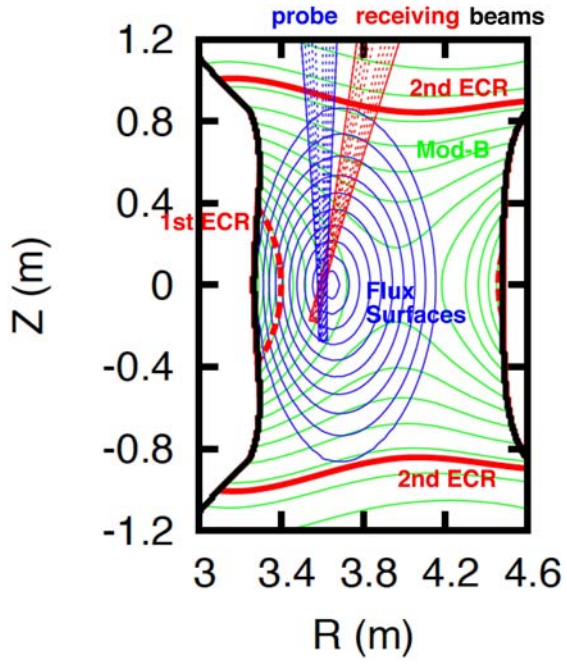

Fig. 5 Relation between probing, receiving beams, flux surfaces and EC resonances for the case of magnetic field setting B_0=2.2 Tesla on the vertically elongated cross section in LHD.

tween resonances and probing, receiving beam on the vertically elongated cross section in LHD are shown in Fig. 5. Setting higher magnetic field would place the fundamental resonance layer inner to the higher electron temperature region, causing higher background ECE level taking into account of the multi-reflection. On the other hand, setting lower magnetic field would place the second harmonic resonance layer on the receiving line of sight. In Figure 6 are shown the calculated O and X mode ECE spectrum for the cases of central electron temperature $T_{e,0}$= 5 keV and 1 keV. By setting the magnetic field near 2.2 Tesla, one can expect the background ECE level minimum, although the multi-reflection effect can increase the contribution from fundamental resonance. Due to its complexity of magnetic field structure in LHD, there exists fundamental and second harmonic resonance simultaneously in any settings of magnetic field strength. In such configurations, some adjustment of setting magnetic field would necessary to minimize the ECE background and at the same time to avoid the absorption of scattered power.

4 Receiver system for CTS

A receiver system is installed on the upstream of the transmission line, which is normally used for high power transmission line for ECRH. A waveguide switch is attached on the 88.9 mm id corrugated waveguide transmission system at the marked position in Fig. 1 b). A heterodyne receiver is placed at the output of the waveguide switch. The receiver consists of a high sensitive heterodyne radiometer. The circuit diagram is shown in Fig. 7 a).

At the front end, two multi-stage notch filters with the 3 dB band width of 300 MHz and attenuation -120 dB at the center frequency, 76.95 GHz, are placed to avoid the high level stray radiation that can damage the mixer or make ghost signal at the mixer and make saturation of the intermediate frequency (IF) amplifier. A pin-switch is also inserted to block the spurious mode which might be excited at the turn on or off of the gyrotron out of the notched but sensitive frequency. Band pass filter from 72 to 82 GHz to filter out the lower side band of the mixer of the local frequency at 74 GHz is also placed in front of the mixer. Intermediate frequency from 300 MHz to 10 GHz at the upper side band of the mixer is amplified by low noise amplifier and splitted to filter bank. Since the gyrotron oscillating frequency can subject to the shift of the order of 100 MHz during the oscillation or at the ramping up phase

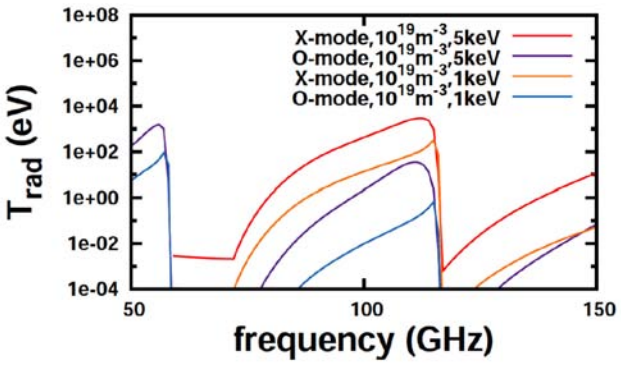

Fig. 6 Calculated ECE spectrum for the line of sight of CTS receiving antenna. Electron temperature is assumed to have $T_{e,0}(1-\rho^2)^2$. Here the magnetic field is set B=2.2 Tesla.

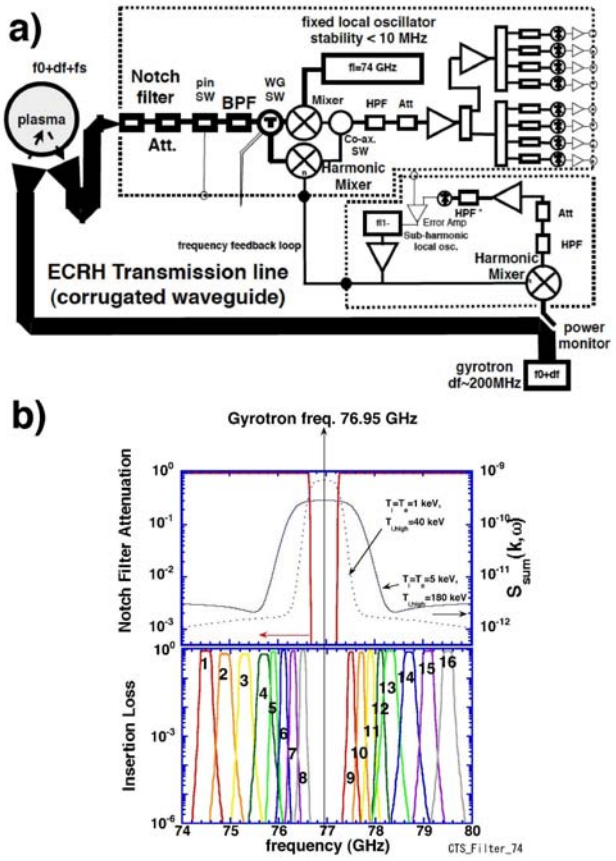

Fig. 7 a) Block diagram of the heterodyne receiver for CTS in LHD. The notch filter, band pass filter and pin-switch are placed in front of the mixer. Fixed local frequency at 74 GHz is normally used. b)Characteristics of the filter prepared for the local frequency at 74 GHz expected from the characteristic curve at the IF. Expected notch filter response with calculated CTS spectrum are shown in the upper column.

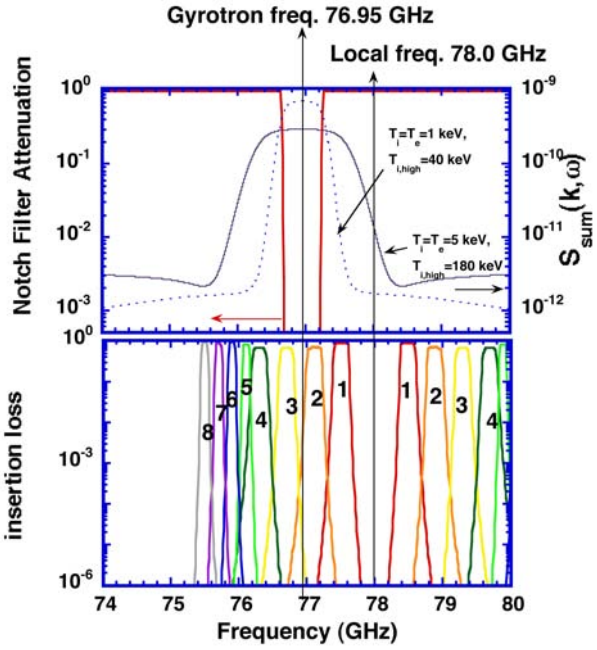

Fig. 8 Characteristics of the filter prepared for the local frequency at 78 GHz expected from the characteristic curve at the IF. Expected notch filter response is shown above.

of the anode voltage, IF center frequency tracking system using harmonic mixer will be also attached for the precise estimation of the bulk component. Filter bank consists of 8 to 16 filters at the first trial. Fig. 7 b) are shown the expected response of the notch and bank filters in the upper and lower column, respectively. Here, calculated CTS spectrum for the cases where the bulk ion and electron temperatures are 1 keV with high enegy ions of 40 keV and 5 keV with 180 keV high energy ions are over plotted in the upper column.

5 Preliminary Results

At the adjustment phase of the CTS receiver system, the local oscillator was damaged and the Gunn oscillator at 78 GHz is used in stead of 74 GHz. With this local frequency, expected frequency response of the receiver is shifted as shown in Fig. 8. In this case, channel 1 to 4 becomes sensitive at both upper and lower side bands of the local frequency. As is expected from the calculated CTS spectrum, channel 1 to 4 are sensitive to the bulk ion temperature and channel 5 to 8 are more sensitive to high energy ion components. Preliminary signals were obtained from the ECRH plasma without NBI at the magnetic field of 2.75 Tesla. Electron density levels was 1×10^{19} m^{-3}. Plasma parameters are kept only by the 77 GHz ECRH which is also used as a probing beam. Nominal electron temperature was 3 keV at the center. The injected power is 100% modulated at the frequency of 50 Hz from 0.25 to 1.15 s, 1.25 to 1.75 s and 1.85 s to 2.25 s. In Fig. 9 are shown detected signals at each filer channel from 1 to 8 indicated in Fig. 8. Raw signals contain sharp spikes at each modulation that may be attributed to the spurious mode oscillation from the gyrotron. These spikes are almost subtracted but failed from 1.3 to 1.6 s in this figure. The signals during on and off phases are separated and displayed by red and green lines. It seems that the background ECE level and scattered signal level are well separated at channels 1 to 4 and barely at channel 5 and 6. Shown in Fig. 10 are the expanded signals in time from 1.0 to 1.1 s. These signals show clear characteristics of the scattering signals in contrast to the change of the ECE background which is small and should be continuous. Although several checks are to be done, these signals show expected feature of the scattering signals. The sensitivity calibration of each channels are underway. The deduction of the CTS spectrum from these data would be possible after this calibration.

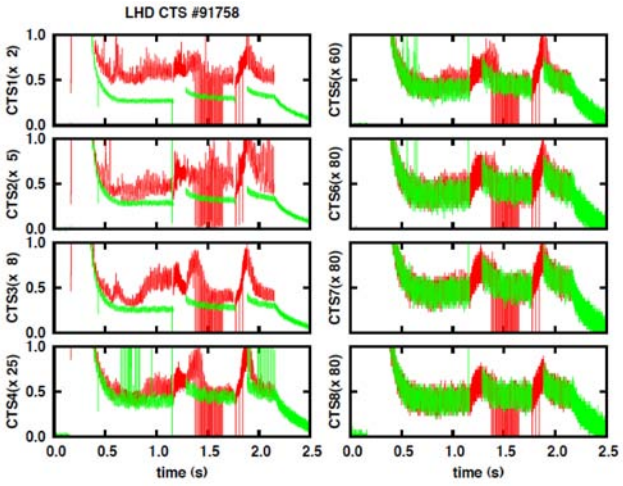

Fig. 9 Preliminary data from each filter bank channel as indicated in Fig. 8. Detected signals are separated by on and off phase of the probing beam and indicated by red and green lines.

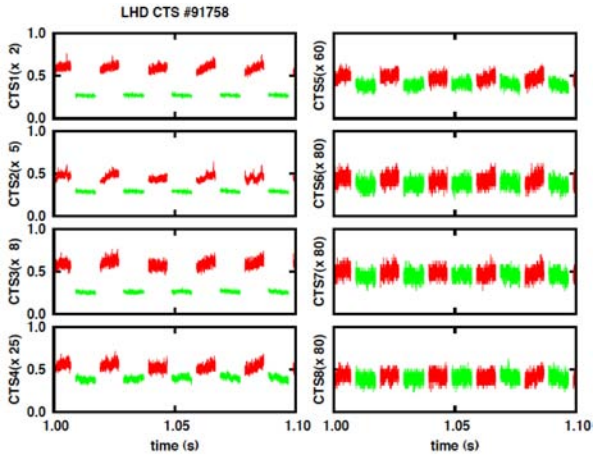

Fig. 10 Expanded figure in time from 1.0 to 1.1 s of Fig. 9. The increase of the ECE background can well be separated from the step-wise increase/ decrease at turn-on and -off time especially in channels 1 to 6.

Summary

The CTS system is conformed utilizing the characteristic features of the LHD ECRH system. These features includes well controlled and strongly focused Gaussian beam antenna, high power low loss transmission lines. From the expected Gaussian beam, the method of estimating the beam cross section is established and shown the spatial resolution of CTS measurement. CTS receiver is designed and constructed to detect the scattering signals in the range of ± 3 GHz at 77 GHz. Preliminary signals are obtained for ECRH plasma at the density of 1×10^{19} m^{-3}. Furthermore check and calibration is necessary to confirm and deduce ion velocity distribution function from these data.

[1] H. Bindslev, S. K. Nielsen, L. Porte, J. A. Hoekzema, S. B. Korsholm, F. Meo, P. K. Michelsen, S. Michelsen, J. W. Oosterbeek, E. L. Tsakadze, E. Westerhof, and P. Woskov, Phys. Rev. Lett. **97**, 205005 (2006).

[2] T. Kondoh, S. Lee, D. P. Huchinson and R. K. Richards, Review of Scientific Instruments **72**, 1143 (2001).

[3] S. Michelsen, S. B. Korsholm, H. Bindslev, F. Meo, P. K. Michelsen, E. L. Tsakadze, J. Egedal, P. Woskov, J. A. Hoekzema, F. Leuterer and E. Westerhof, Review of Scientific Instruments **75**, 3634 (2004).

[4] F. Meo, H. Bindslev, S. B. Kolsholm, E. L. Tsakadze, C. I. Walker, P. Woskov G. Vayakis, Review of Scientific Instruments **75**, 3585 (2004).

[5] M. Nishiura, K. Tanaka, S. Kubo, T. Saito, Y. Tatematsu, T. Notake, K. Kawahata, T. Shimozuma, T. Mutoh, Review of Scientific Instruments **79**, 10E731 (2008).

[6] T. Notake, T. Saito, Y. Tatematsu, S. Kubo, T. Shimozuma, K. Tanaka, M. Nishiura, A. Fujii, La Agusu, I. Ogawa, T. Idehara, Rev. Sci. Instrum. **79**, 10E732 (2008).

[7] H. Takahashi, T. Shimozuma, S. Kubo, S. Ito, S. Kobayashi, Y. Yoshimura, H. Igami, Y. Mizuno, Y. Takita, T. Mutoh, T. Kariya, R. Minami, T. Imai, Submitted to Fusion Science and Technology.

[8] S. Kubo, T. Shimozuma, Y. Yoshimura, H. Igami, H. Takahashi, *et al.*, Proc. 22nd IAEA Fusion Energy Conference, 13-18 October 2008 Geneva, Switzerland. EX/P6-14.

[9] S. Kubo, H. Igami, Y. Nagayama, S. Muto, T. Shimozuma, Y. Yoshimura, H. Takahashi and T. Notake, Proc. of International Congress on Plasma Physics 2008, 8-12 September 2008, Fukuoka Japan; Submitted to Plasma and Fusion Research.

Proceedings of ITC18, 2008

Simultaneous measurement of electron and ion temperatures with helium-like argon spectrum

Motoshi GOTO and Shigeru MORITA

National Institute for Fusion Science, Toki 509-5292, Japan

The helium-like argon spectrum is measured for the plasma in the Large Helical Device (LHD). The electron temperature T_e derived from the intensity ratio of the resonance line ($1s^2\,{}^1S_0 - 1s2p\,{}^1P_1$) to a dielectronic satellite line ($1s^22p\,{}^2P_{1/2} - 1s2p^2\,{}^2D_{3/2}$) is consistent with the central T_e measured with the Thomson scattering method when the electron density n_e has a peaked profile. The ion temperature T_i is simultaneously determined from the Doppler broadening width of the resonance line and the establishment of thermal equipartition between electrons and ions, i.e., $T_i = T_e$, due to the increase of n_e is experimentally confirmed.

Keywords: X-ray spectroscopy, helium-like argon, dielectronic satellite line, electron temperature measurement, ion temperature measurement

DOI:

1 Introduction

The x-ray spectroscopy has played an important role to measure the central ion temperature T_i in the fusion experiments. In LHD (the Large Helical Device), the temporal development of T_i is measured for every discharge from the Doppler broadening of the helium-like resonance line of argon, i.e., Ar XVII $1s^2\,{}^1S_0 - 1s2p\,{}^1P_1$ [1].

Besides the ion temperature measurement, the helium-like spectrum has found various uses for the plasma diagnostics in the core region. The helium-like spectrum here means a group of several emission lines corresponding to the transitions from $n = 2$ levels, where n is the principal quantum number, to the ground state of helium-like ion and numerous satellite lines of lithium-like ion which appear in the same wavelength range as the former.

The measurement of the electron temperature T_e with the intensity ratio of the dielectronic satellite line to the resonance line is an example of the applications of the helium-like spectrum [2, 3]. This method utilizes the different T_e-dependence of the rate coefficients for the electron impact excitation and dielectronic capture processes. The reliability of the derived parameter naturally depends on the accuracy of the atomic data.

Many efforts have been made to improve the theoretical calculation method for the required atomic data. In TEXTOR the measured spectra were compared with synthetic ones based on the newly calculated data and a comprehensive consistency between them was obtained [5]. Similar comparison was also made in NSTX [3], where it was demonstrated that the temporal behaviour of the derived electron temperature was consistent with the result of the Thomson scattering measurement.

In this paper, the temporal behaviors of T_i and T_e are simultaneously derived from the helium-like argon spectra taken for LHD and their consistency with the change of the background plasma condition is examined.

author's e-mail: goto@nifs.ac.jp

2 Experimental setup

The measurement is made for a discharge with the magnetic configuration of $R_{ax} = 3.8$ m and $B_{ax} = 2.539$ T, where R_{ax} and B_{ax} are the major radius of the magnetic axis and the magnetic field strength on the magnetic axis, respectively. The temporal development of the discharge is shown in Fig. 1. The plasma is started up with the electron cyclotron heating (ECH), and is sustained with three neutral beams (NBI). The argon gas-puff is provided at $t = 0.3$ s with the 10 ms pulse width. Eight hydrogen pellets are sequentially injected with a 40 ms interval from $t = 0.7$ s.

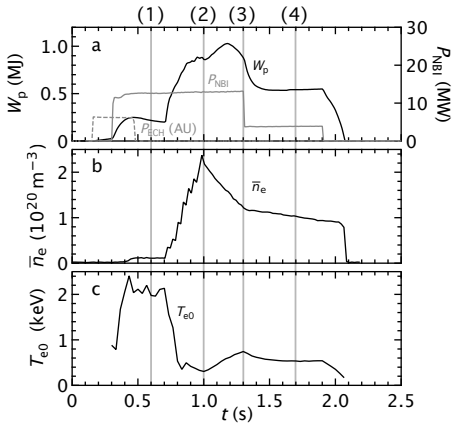

Fig. 1 Several parameters for the discharge analyzed here (#69260): (a) the ECH and NBI powers, P_{ECH} and P_{NBI}, respectively, and the stored energy W_p, (b) the line-averaged electron density $\bar{n}_e$, and (c) the central T_e by Thomson scattering method. T_e and n_e profiles at the timings (1)–(4) are shown in Fig. 6.

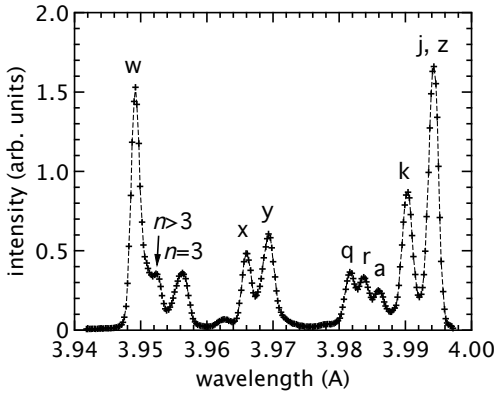

Fig. 2 Example of the measured spectrum made up of the data from two identical LHD discharges #69258 and #69260. The data are summed over from $t = 1.5$ s to $t = 1.7$ s. The line notation follows Ref. [4].

The line-averaged electron density $\overline{n}_e$ is derived from the radial profile data measured with the Thomson scattering method but the interferometer data in the initial low density phase are used to calibrate the absolute value. It is clearly seen that $\overline{n}_e$ stepwise increases synchronizing with each pellet injection. The central electron temperature T_e is immediately lowered after the pellet injection is started.

The helium-like argon spectrum is measured with a Johann-type crystal spectrometer which is basically the same as that described in detail in Ref. [1] but the radius of curvature of the quartz crystal (2020) has been changed from 3000 mm to 1500 mm. This modification aims at observing a wider wavelength range in a single measurement. The lattice spacing of the crystal is 4.2554 Å. The Bragg angle and the wavelength dispersion at $\lambda = 3.9492$ Å, which is the wavelength of the helium-like argon resonance line ($1s^2\,{}^1S_0 - 1s2p\,{}^1P_1$), are 68.1320 degree and 874.049 mm/Å, respectively.

A charge coupled device (CCD) is used as the detector. The detection area consists of 1024 pixels (in the direction of wavelength dispersion) times 256 pixels and the pixel size is $26 \times 26\,\mu m^2$. The spectra is obtained every 4 ms.

Figure 2 shows an example of the measured spectra for the discharge in Fig. 1. Here, the data are summed over the time period from $t = 1.5$ s and $t = 1.7$ s. The notation of lines follows Gabriel's definition [4]. The w, x, y, and z lines correspond to the transitions $1s^2 - 1s2l$ of helium-like ion and other lines indicated in Fig. 2 to the representative transitions of doubly excited lithium-like ion, i.e., $1s^2 2l' - 1s2l2l'$. The two groups of lines designated as $n = 3$ and $n > 3$ correspond to the transitions $1s^2 nl' - 1s2lnl'$ with $n \geq 3$.

It should be noted here that the detector size is insufficient to get the entire spectrum in Fig. 2 with a single discharge. The spectrum in Fig. 2 is made up of the data from successive two discharges which are almost identical. In the first measurement the wavelength range involving the w to y lines is observed and for the subsequent discharge the detector position is shifted so that the wavelength range involving the y to z lines is covered. The amplitude of the data taken in the second measurement is normalized to that of the first measurement at the y line which is involved in the both measurements. Here, the signal count is summed every eight channels and is represented by a single point in Fig. 2.

3 Model calculation

Here, we focus on the line intensity ratio of the k and w lines which is known to have a strong T_e-dependence [3]. Figure 3 shows a part of the energy level diagram of argon ion relevant to those lines. The upper level of the w

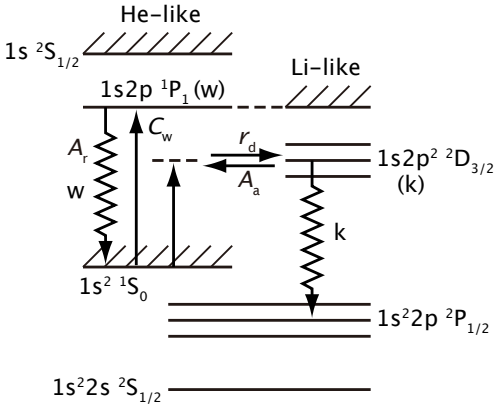

Fig. 3 Schematic energy level diagram relevant to the w and k lines of helium-like and lithium-like ions.

line $1s2p^1P_1$, which is also denoted by w here, is considered to be in corona equilibrium, namely, its population is determined so that the excitation from the ground state $1s^2{}^1S_0$ and the radiative deexcitation to the ground state are balanced. Under corona equilibrium the populations of the ground state and the w level, n_g and n_w, respectively, should satisfy the equation

$$C_w n_g n_e = A_w n_w, \tag{1}$$

where C_w is the excitation rate coefficient due to electron impact from the ground state to the w level, A_w is the spontaneous radiative transition probability from the w level to the ground state, and n_e is the electron density. The right-hand-side of Eq. (1) is nothing but the intensity or the photon emission rate of the w line.

The upper level of the k line, which is also denoted by k here, is the doubly excited state of lithium-like ion $1s2p^2{}^2D_{3/2}$. The k level is mainly populated through the dielectronic capture by the ground state helium-like ion which is indicated with an arrow labeled as r_d in Fig. 3. The dominant population outflow processes are the autoionization and radiative decay to the singly excited level

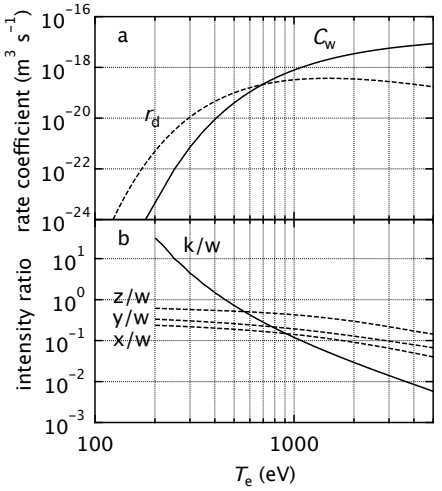

Fig. 4 T_e-dependence of the rate coefficients C_w and r_d (a) and intensity ratios between helium-like lines k/w, x/w, y/w, and z/w (b).

$1s^2 2p^2 P_{1/2}$. The latter process is called the stabilizing transition. The k level population, n_k, is determined so that these processes are balanced as

$$n_g n_e r_d = n_k (A_r + A_a), \tag{2}$$

where r_d is the rate coefficient of the dielectronic capture, and A_r and A_a are the probability for the stabilizing transition and the autoionization, respectively.

Since the dielectronic capture is the reverse process of the autoionization, r_d and A_a should satisfy the detailed balance equation under thermodynamic equilibrium as

$$\left[n_g n_e r_d = n_k A_a \right]_E , \tag{3}$$

where $[\cdots]_E$ indicates the condition of thermodynamic equilibrium. The rate coefficient r_d is expressed as

$$r_d = \left[\frac{n_k}{n_g n_e} \right]_E A_a = Z_k A_a, \tag{4}$$

where

$$Z_k = \frac{g_k}{2 g_g} \left(\frac{h^2}{2\pi m k T_e} \right)^{3/2} \exp\left(-\frac{\chi_{gk}}{k T_e} \right) \tag{5}$$

is the Saha-Boltzmann coefficient. Here, g_g and g_k are the statistical weights of the helium-like ground state and the level k, respectively, χ_{gk} is the energy level difference between these levels, and h, m, and k are the Planck constant, electron mass, and Boltzmann constant, respectively. Substituting Eq. (4) into Eq. (2) one obtains

$$n_k = \frac{A_a}{A_r + A_a} Z_k n_e n_g. \tag{6}$$

The intensity of the k line is obtained as $n_k A_r$.

The intensity ratio of the k to w lines I_k/I_w is now expressed as

$$\frac{I_k}{I_w} = \frac{A_r A_a Z_k}{C_w (A_r + A_a)}. \tag{7}$$

The T_e-dependence of C_w and r_d are shown in Fig. 4 (a) and I_k/I_w is shown in Fig. 4 (b). The values C_w, A_r, and A_a are taken from Ref. [5]. The strong T_e-dependence of I_k/I_w stems from the different T_e-dependence of C_w and r_d. Intensities of other helium-like ion lines, x, y, and z, can be obtained from a relation similar to Eq. (1). Figure 4 also shows the intensity ratios of x, y, and z lines to the w line. The advantage of use of the k/w ratio in comparison with other line ratios for the T_e measurement is clearly observed.

4 Results and discussion

The intensities of the w and k lines are derived from the measured spectra: each line profile is fitted with a Gaussian function and its intensity is obtained as the integral of the function.

The temporal development of the k to w line ratio is shown in Fig. 5. The electron temperature is readily determined from the calculation result in Fig. 4. The result is shown in Fig. 5. In Fig. 5 the central electron temperature measured with the Thomson scattering method is also shown. Before pellet injection ($t < 0.7$ s) the discrepancy between two results is large. After starting the pellet injection the both values immediately coincide with each other.

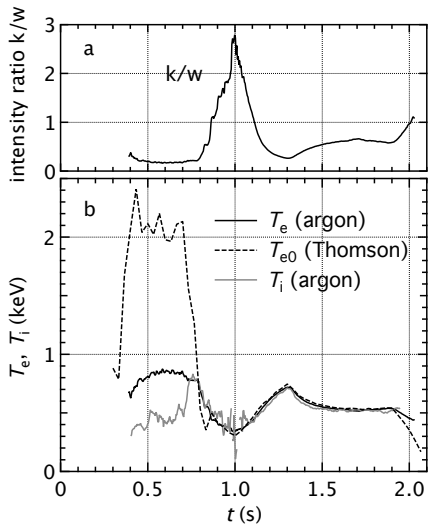

Fig. 5 Measured intensity ratio of the k and w lines for the discharge in Fig. 1 (a) and T_e derived from the k/w ratio, central T_e by Thomson scattering, and T_i from Doppler broadening of the w line (b).

The disagreement between the two measurements in the early time period can be understood from the fact that the present result is based on a line-integral measurement. Figure 6 shows the radial profiles of T_e and n_e measured at the timings indicated in Figs. 1. In the initial low density phase the T_e has a peaked profile while n_e profile is hollow. Roughly speaking, the line intensity is proportional to the product of n_i and n_e, here n_i stands for the helium-like ion

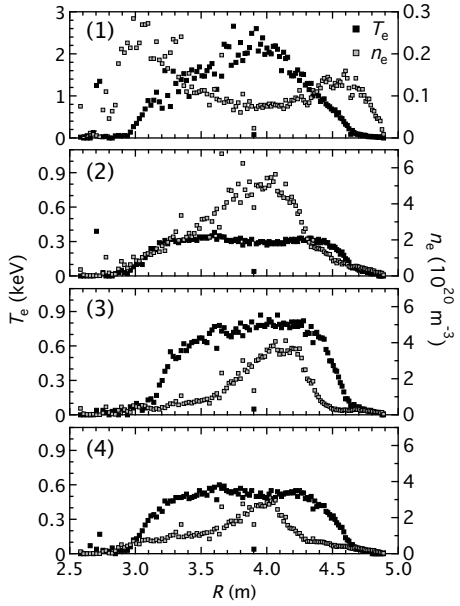

Fig. 6 Radial profiles of T_e and n_e measured with the Thomson scattering method at different four stages ((1)–(4)) of the discharge in Fig. 1.

density. Although the density profile of helium-like ion is probably peaked at the center, the line intensities could have a broad profile due to the relatively high n_e in the edge region. Therefore, the contribution of the edge emission in the observed line intensity might be so large that the apparent T_e is lowered.

After starting the pellet injection the T_e profile becomes rather flat and n_e is peaked at the center. Such characteristics, i.e., peaked n_e and flat T_e profiles, are sustained until the end of discharge although the highest values are dynamically changed. Since T_e profile is flat in this time period, the value derived with the present method can be regarded as that at the plasma center. As seen in Figure 5, the present result shows a good consistency with the Thomson's data, and the reliability of the present method is demonstrated.

We next consider the line profile for the T_i measurement. The ion temperature can be, in principle, derived from the Doppler broadening profile of an appropriate emission line. However, since the measured line profile is generally a convolution of the instrumental profile and the Doppler profile, deconvolution of the measured line profile into two profile components is necessary to determine T_i.

The instrumental profile, which is here approximated with a Gaussian function and represented by its width w_{inst}, is evaluated as follows. When the density is so high that equilibrium between the electron and ion temperatures, namely, $T_i = T_e$, can be assumed, the Doppler (Gaussian) width w_D is estimated from the measured T_e. Since the measured line width w_{obs} has a relationship with w_{inst} and w_D as

$$w_{obs}^2 = w_D^2 + w_{inst}^2, \tag{8}$$

w_{inst} is derived. Here, w_{inst} for the w line at $t = 1.7$ s is determined and thereby T_i in the entire discharge time is derived. The relation among w_{obs}, w_{inst}, and w_D at $t = 1.7$ s is shown in Fig. 7 and the eventually derived T_i is shown in Fig. 5.

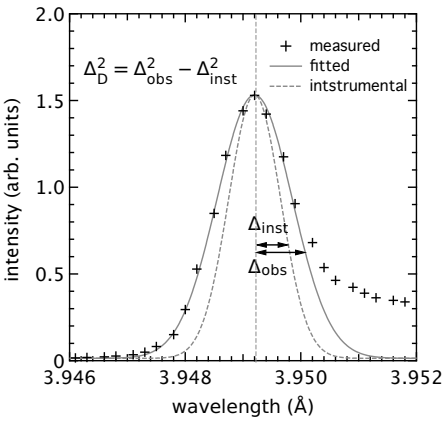

Fig. 7 Measured profile of the w line and instrumental width evaluated at $t = 1.7$ s.

Here, we focus our interest on T_e and T_i derived with argon spectra. Since they are derived from emission lines of the same ion, they should reflect the plasma condition at the same location though the detailed location is unclear. It is observed in Fig. 5 that electrons and ions have yet to reach thermal equipartition before pellet injection. Once n_e is increased, T_i shows the same temporal development with T_e until the end of discharge.

From all these results shown here, one may say that the T_e measurement technique with helium-like ion spectrum has arrived at the level for a practical use as well as the T_i measurement although an attention should be paid to the location where the dominant radiation takes place. This problem can be solved if a higher Z ion is adopted so that the emission is certainly localized at the plasma center.

Acknowledgements

The authors are grateful for the support of LHD experimental group to conduct the experiment in LHD. This study has been made in part under the financial support by the LHD project (NIFS08ULPP527).

[1] S. Morita et al., Rev. Sci. Instrum. **74**, 2375 (2003).
[2] M. Bitter, Phys. Rev. Lett. **43**, 129 (1979).
[3] M. Bitter, Phys. Rev. Lett. **91**, 265001 (2003).
[4] A. H. Gabriel, Mon. Not. R. astr. Soc. **160**, 99 (1972).
[5] O. Marchuk, *PhD thesis* (2004).

Proceedings of ITC18,2008

Conceptual Design of dispersion interferometer using ratio of modulation amplitudes

T. Akiyama, K. Kawahata, S. Okajima[a] and K. Nakayama[a]

National Institute for Fusion Science, 322-6 Oroshi-cho, Toki 509-5292, Japan

[a)] *Chubu University, 1200, Matsumoto-cho,Kasugai 487-8501, Japan*

Since a dispersion interferometer is free from mechanical vibrations, it does not need a vibration compensation system even if a wavelength of a probe beam is short (e.x. infrared and near infrared region). This paper describes a new signal processing of the dispersion interferometer using a ratio of modulation amplitudes with a photoelastic modulator. The proposed method is immune to changes in detected signal intensities and the signal processing system becomes simple. Designs of the optical system of the dispersion interferometer for proof of principle, especially specification of a nonlinear optical crystal, are also shown.

Keywords: interferometer, dispersion interferometer, non-linear crystal, photoelastic modulator, CO_2 laser

1. Introduction

High reliability and resolutions are required for electron density measurements in fusion devices in order to control plasmas and to understand the plasma physics.

A conventional heterodyne interferometer is widely used for the electron density measurement and has a high density resolution. It, however, suffers from fringe jump errors, which degrade reliability of the interferometer, in a high density range. These days the Large Helical Device (LHD) developed a high density operation regime whose central electron density is up to several times 10^{20} m^{-3} [1], and the expected density range in ITER is about 1 $\times 10^{20}$ m^{-3} [2]. Hence the problem of the fringe jump is becoming more significant. While a short-wavelength laser can reduce probabilities of the fringe jumps, phase errors caused by mechanical vibrations become significant. They should be suppressed with a vibration isolator or be compensated by adopting the two-color interferometry, which consists of two probe beams with different wavelengths (light sources). Even so, it is difficult to eliminate the vibration components completely because of slight differences in the optical path and wavefronts of probe beams and an optical system becomes complex and expensive.

One candidate of the solutions is a density measurement with a polarimeter based on the Faraday effect [3-5] or the Cotton-Mouton effect [6-8]. Although density resolutions of polarimeters are less than these of the interferometers, it does not suffer from fringe jump errors and immune to mechanical vibrations principally. The other candidate is a dispersion interferometer [9]. It is also insensitive to mechanical vibrations and hence does not need the vibration isolator and the two-color interferometry system even if the short-wavelength laser, for example a CO_2 laser and a YAG laser, is used.

This paper describes a new signal processing of the dispersion interferometer using a ratio of modulation amplitudes. The proposed method makes the signal processing simple and can remove measurement errors due to changes in the detected signal intensity. Section 2 briefly explains the principle of the dispersion interferometer and the new proposed signal processing. Section 3 shows a design of the proposed dispersion interferometer for the proof of the principle. Summaries are given in Sec. 4.

2. Principle of dispersion interferometer

2.1. Basic dispersion interferometer

Figure 1 shows the principle of the basic dispersion interferometer [9]. A probe beam whose angular frequency is ω passes through a type-I nonlinear crystal to generate the second harmonic whose polarization angle is perpendicular to that of the fundamental. And then, the fundamental and the second harmonic components propagate along almost the same optical path. Phase shifts due to changes in the optical path length Δd by

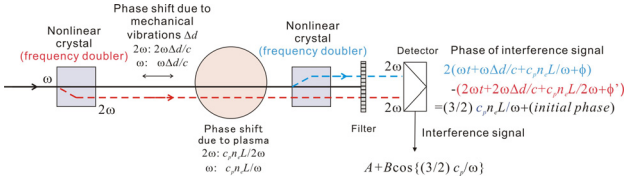

Fig.1 Basic dispersion interferometer

author's e-mail: takiyama@lhd.nifs.ac.jp

mechanical vibrations are $\omega\Delta d/c$ and $2\omega\Delta d/c$, respectively. The phase shifts due to a plasma are $c_p\bar{n}_eL/\omega$ and $c_p\bar{n}_eL/(2\omega)$, where $c_p = e^2/(2\varepsilon_0 m_e c)$, $\bar{n}_e$ is the line averaged electron density and L is the optical path length in the plasma. After passing through the plasma the frequency of the fundamental wave is doubled again with the other nonlinear crystal. The remaining fundamental, which is not converted into the second harmonic, is cut by a following filter and the second harmonic components only go into a detector. Phases of these second harmonic components φ_1 and φ_2 (second harmonics which are generated by the first and the second nonlinear crystals are noted as 1 and 2, respectively) are given as follows:

$$\begin{aligned}\varphi_1 &= 2(\omega t + \omega\Delta d/c + c_p\bar{n}_eL/\omega + \phi_1)\\ \varphi_2 &= 2\omega t + 2\omega\Delta d/c + c_p\bar{n}_eL/(2\omega) + \phi_2\end{aligned} \quad (1)$$

where ϕ_1 and ϕ_2 are initial phases of second harmonics. The detected interference signal I between these second harmonic components becomes

$$\begin{aligned}I &= A + B\cos(\varphi_1 - \varphi_2)\\ &= A + B\cos\left(\frac{3}{2}\frac{c_p\bar{n}_eL}{\omega} + \phi\right).\\ A &= I_1 + I_2,\ B = 2\sqrt{I_1I_2}\\ I_1, I_2 &: \text{intensities of second components}\\ \phi &= \phi_1 - \phi_2 : \text{initial phase}\end{aligned} \quad (2)$$

As shown in Eq. (2), the phase shift due to mechanical vibrations is canceled out automatically. Hence, the phase of the interference signal is determined by only the dispersion of the plasma and is free from mechanical vibrations even with a short wavelength laser.

2.2. Dispersion interferometer with a phase modulation

Since Eq. (2) is the almost the same as the interference signal of a homodyne interferometer, the basic dispersion interferometer has the same disadvantage as the homodyne one: (i) restriction of the phase where Eq. (2) is a monotonic function (ii) necessity of calibration experiments of the detected intensity A and B and their variations during discharges lead to phase errors. The phase modulation method [10] with an electro-optical modulator (EOM) can reduce the influence of the intensity variations. The EOM, which is operated with a drive signal of $\pi\sin\Omega t$, is inserted between the first nonlinear crystal and the plasma. It gives a phase modulation of $\pi\sin\Omega t$ only for the second harmonic components. As a result, the following modulated interference signal I_{pm} is detected.

$$I_{pm} = A + B\cos\left(\pi\sin\Omega t + \frac{3}{2}\frac{c_p\bar{n}_eL}{\omega} + \phi\right) \quad (3)$$

I_{pm} is directly digitized with a higher sampling frequency than Ω. Due to the phase modulation the amplitude of I_{pm} changes between maximum (A+B) and the minimum (A-B). A and B are assumed constants during one modulation period and the DC component A and the amplitude B are evaluated from the digitized signal. And then, A is subtracted from the digitized signal and the amplitude of I_{pm} is normalized by B. The drive signal of the EOC is also digitized coincidently and the times t_0 when $\sin\Omega t_0 = 0$ are determined. At the t_0, normalized signal I_{pm}^{norm} becomes

$$I_{pm}^{norm} = \cos\left(0 + \frac{3}{2}\frac{c_p\bar{n}_eL}{\omega} + \phi\right). \quad (4)$$

The line averaged electron density can be calculated from the arcosine of Eq. (4).

2.3. Dispersion interferometer using a ratio of modulation amplitudes

Now we are designing a dispersion interferometer with a use of a photoelastic modulator (PEM) instead of

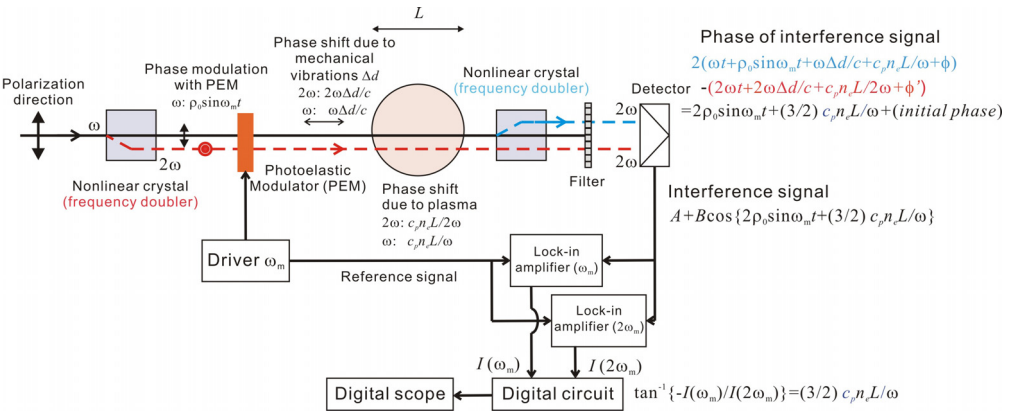

Fig.2 Dispersion interferometer with a photoelastic modulator (PEM) and a signal processing using ration of modulation amplitudes

the EOM, whose modulation frequency is stable. Figure 2 shows the schematic view. The modulator axis of the PEM is arranged parallel to the polarization direction of the fundamental in order to give phase modulations only to the fundamental. In this configuration, the following interference signal $I(t)$ is obtained.

$$\begin{aligned} I(t) &= A + B\cos\left(2\rho_0 \sin\omega_m t + \frac{3}{2}\frac{c_p \bar{n}_e L}{\omega} + \phi\right) \\ &= A + B\left\{\cos(2\rho_0 \sin\omega_m t)\cos\left(\frac{3}{2}\frac{c_p \bar{n}_e L}{\omega} + \phi\right)\right\} \\ &\quad - B\left\{\sin(2\rho_0 \sin\omega_m t)\sin\left(\frac{3}{2}\frac{c_p \bar{n}_e L}{\omega} + \phi\right)\right\} \end{aligned} \quad (5)$$

where ρ_0 is the maximum retardation of the PEM, which is determined by the applied voltage to the PEM, ω_m is the modulation frequency of the PEM. Here, $\cos(2\rho_0 \sin\omega_m t)$ and $\sin(2\rho_0 \sin\omega_m t)$ can be expanded with the Bessel function of order of n J_n.

$$\begin{aligned} \cos(2\rho_0 \sin\omega_m t) &= J_0(2\rho_0) + 2\sum_{n=1}^{\infty} J_{2n}(2\rho_0)\cos(2n\omega_m t) \\ \sin(2\rho_0 \sin\omega_m t) &= 2\sum_{n=1}^{\infty} J_{2n-1}(2\rho_0)\sin\{(2n-1)\omega_m t\} \end{aligned} \quad (6)$$

In this way, the detected interference signal $I(t)$ can be expanded with harmonic components of ω_m. The following amplitudes of fundamental and the second harmonic components I_{ω_m} and $I_{2\omega_m}$ of the modulation frequency ω_m can be measured with lock-in amplifiers.

$$\begin{aligned} I_{\omega_m} &= -2BJ_1(2\rho_0)\sin\left(\frac{3}{2}\frac{c_p \bar{n}_e L}{\omega}\right) \\ I_{2\omega_m} &= 2BJ_2(2\rho_0)\cos\left(\frac{3}{2}\frac{c_p \bar{n}_e L}{\omega}\right) \end{aligned} \quad (7)$$

From the ratio of these amplitudes, the line averaged electron density $\bar{n}_e$ is obtained.

$$\begin{aligned} \frac{I_{\omega_m}}{I_{2\omega_m}} &= \tan\left(\frac{3}{2}\frac{c_p \bar{n}_e L}{\omega}\right) \\ \therefore \bar{n}_e &= \frac{2}{3}\frac{\omega}{c_p L}\tan^{-1}\left\{\frac{I_{\omega_m}}{I_{2\omega_m}}\right\} \end{aligned} \quad (8)$$

Here, ρ_0 is set at 1.3 radian by applying the adequate voltage to the photoelastic material for $J_1(2\rho_0) = J_2(2\rho_0)$. This new method of the phase extraction is completely free from variations of detected intensities A and B. In addition, it is simpler than that in Ref [10] and suits to real time measurements.

Table 1 Optical parameters of $AgGaSe_2$ for 10.6 μm

Transparency (μm)	0.8-18
Refractive index n_o (10.6 μm)	2.5912
Refractive index n_e (10.6 μm)	2.5579
Refractive index n_o (5.3 μm)	2.1634
Refractive index n_e (5.3 μm)	2.5808
Phase-matching angle (deg.)	55.4
d_{eff} (definition: $P=dE^2$)	2.47×10^{-22}
Surface damage threshold P_{sd} (kW/cm^2, CW)	33-45
Thermal-lensing threshold P_l (kW/cm^2)	2
Thermal conductivity (W/cm/K)	0.011
Absorption coefficient (cm^{-1})	0.09

3. Conceptual design of dispersion interferometer using a ratio of modulation amplitude

For the proof of the principle, we are designing a dispersion interferometer with a CO_2 laser whose wavelength is 10.6 μm. The CO_2 laser to be used is GN-802-GES with an output power (MPB Technology Inc.) of 7.5W or LC-25 (DEOS) with 25 W. Either one of them will be selected according to a signal-to-noise ratio (SNR). One of important components for good SNR is the nonlinear crystal for second-harmonic generation (SHG) because the power of the second harmonics strongly depends on the specifications of the nonlinear crystal.

3.1. Design of a nonlinear crystal for SHG

Silver gallium selenide ($AgGaSe_2$) is commonly used for SHG of 10.6 μm laser light. Table 1[11, 12] summarizes properties of $AgGaSe_2$. The conversion efficiency $\eta = P_{2\omega}/P_{\omega}$, where $P_{2\omega}$ and P_{ω} are the powers of the second harmonic and the fandamental, is given by [13]

$$\eta = 2\left(\frac{\mu}{\varepsilon_0}\right)^{3/2}\frac{\omega^2 {d_{\text{eff}}}^2 l^2}{n^3}\left(\frac{P_\omega}{\pi\omega_0^2}\right)\left\{\frac{\sin(\Delta k l/2)}{\Delta k l/2}\right\}^2 \quad (9)$$
$$\Delta k \equiv k_{2\omega} - 2k_{\omega}$$

where ω is the laser frequency, d_{eff} is the effective nonlinearity, l is the length of the crystal, n is the refractive index of the fundamental, ω_0 is the beam waist, $k_{2\omega}$ and k_{ω} are wavenumbers of the second harmonics and the fundamental, respectively. The last term, which includes Δk, stands for the phase matching condition. As is mentioned in Sec. 3.2, that is determined by the angle between the beam path and the optic axis of the crystal. Here, the phase matching condition is assumed to be satisfied and the term is given to be unity. It is noted that Eq. (9) presumes a plane wave for an incident light. This is approximately valid when the length of the crystal is less than the confocal focusing length $z_0 = \pi\omega_0^2 n/\lambda$ of the Gaussian beam.

Generally, η of the second harmonic of a continuous-wave laser light is small, an order of 0.1%. Hence, it is favorable for good SNR to increase the power of the second harmonic as much as possible. Eq. (9)

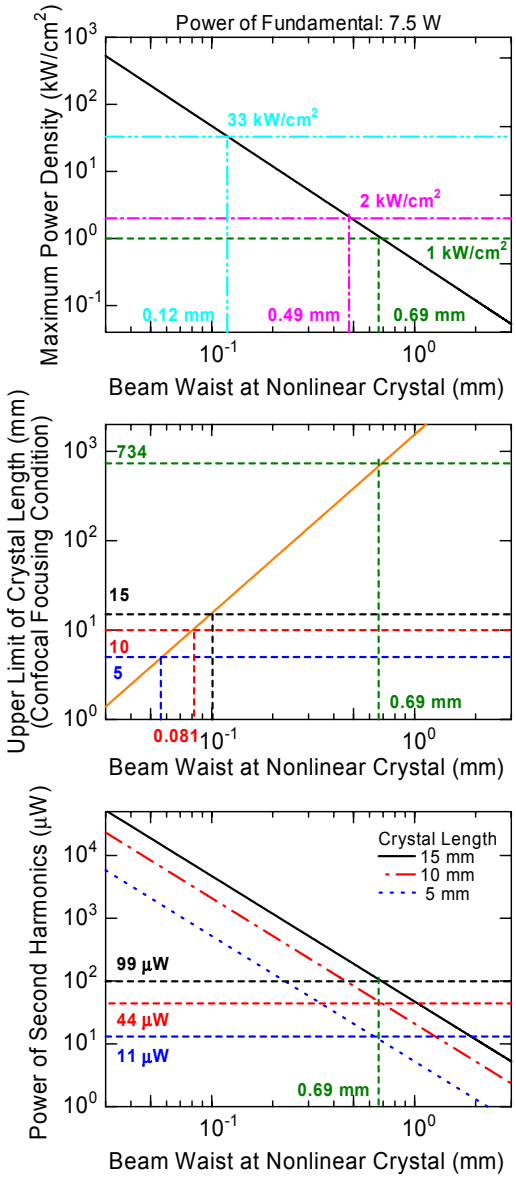

Fig.3 Dependence of (a) maximum power density, (b) upper limit of crystal length and (c) power of second harmonic component on a beam waist at a nonlinear crystal in the case of an incident beam with a power of 7.5 W. The nonlinear crystal is $AgGaSe_2$.

indicates that η increases with the power density of the incident beam. However, there are some following limitations in the power density and the crystal length.

The maximum power density $P_0 = 2P_{total} / (\pi\omega_0^2)$ of the focused Gaussian beam into the nonlinear crystal should be smaller than a surface damage threshold P_{sd} of 33 kW/cm^2 for a cw laser. Here, P_{total} is the total incident power and ω_0 is the beam waist (1/e^2 power radius). In the case of $AgGaSe_2$, the thermal-lensing effect, which decreases the SHG efficiency, should be considered. This is due to the small thermal conductivity, which is comparable to glass, for example. A threshold P_l for the thermal-lensing effect of 2 kW/cm^2 reported in Ref. 11 and is smaller than P_{sd}, allowable beam waist is determined by P_l. In this design, the maximum power density is set at the half of P_l, 1 kW/cm^2, for safety. The resultant beam waist focused in the center of the crystal is 0.69 mm as shown in Fig. 1(a) for a total incident power of 7.5 W.

The commercially available length of the $AgGaSe_2$ crystal is up to 20 mm at present. The upper limit of the crystal length which is determined by the confocal focusing length is much larger than available length for a beam waist of 0.69 mm as shown in Fig.1(b).

Figure 1(c) shows the power of the generated second harmonic calculated with Eq. (9). In the case of 15 mm-long crystal, 99 μW is generated from an incident beam with a power of 7.5 W and with a beam waist of 0.69 mm. The transmissivity at the second harmonic of zinc sellenide ZnSe with anti-reflection coating at the fundamental, which is used for the PEM and two vacuum windows (not shown in Fig.2), is about 0.65. That of IR filter made of sapphire which eliminates the fundamental (see Fig.2) is about 0.7. Hence the total transmissivity of the second harmonics which is generated in the first nonlinear crystal is $0.65^3*0.7=0.19$. When the thermoelectrical cooled IR photovoltaic detector PVI-3TE-5 (Vigo system, Responsivity: 2 (A/W)) with the preamplifier STCC-04 (Vigo system, Transimpedance: 10^5 (V/A)) are used, the output voltages I_1 and I_2 becomes as follows.

$I_1 = (99*10^{-6})*0.19*2*10^5 = 3.8$ V

$I_2 = (99*10^{-6})*0.7*2*10^5 = 14$ V

Considering the efficiency of interference and reflectivity of mirrors and so on, the detected power will be slightly smaller. Nevertheless, these generated powers of the second harmonics are enough to be detected.

3.2. Phase matching condition

The second harmonic is continuously generated along the optical path in the nonlinear crystal. If phases of the second harmonic which is generated at the entrance region and the central region in the crystal, they interfere each other and the total power of the second harmonic decreases. In order to suppress that, the phase of the second harmonic should be matched (phase matching condition). For that purpose, the fundamental is injected into the crystal in the certain angle θ_m against the optic axis of the crystal to satisfy $n_e^{(2\omega)} = n_o^{(\omega)}$ based on the birefringence. In the case of the type-I nonlinear crystal, which is used in this dispersion interferometer, the fundamental and the second harmonic are ordinary and extraordinary wave, respectively. θ_m is given by following expression [13].

$$\sin^2\theta_m = \frac{\left\{n_o^{(\omega)}\right\}^{-2} - \left\{n_o^{(2\omega)}\right\}^{-2}}{\left\{n_e^{(2\omega)}\right\}^{-2} - \left\{n_o^{(2\omega)}\right\}^{-2}} \quad (10)$$

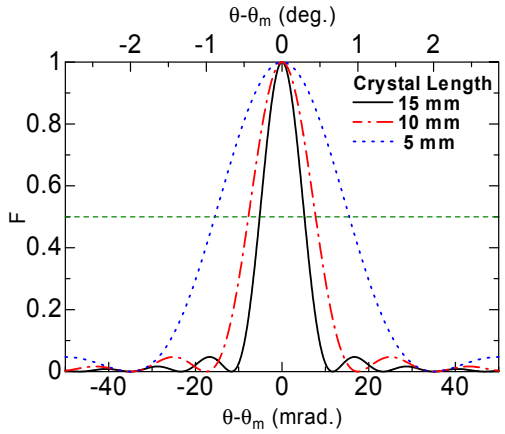

Fig.4 Phase matching condition for $AgGaSe_2$

Assigning refractive indexes, θ_m of $AgGaSe_2$ becomes 55.4 deg. Δk is also given by

$$\Delta kl/2 = \frac{\omega l}{c}\left\{n_e^{(2\omega)}(\theta_m) - n_o^{(\omega)}\right\} \approx -\frac{\omega l}{c}\sin(2\theta_m)\frac{\left\{n_e^{(2\omega)}\right\}^{-2} - \left\{n_o^{(2\omega)}\right\}^{-2}}{2\left\{n_o^{(\omega)}\right\}^{-3}}(\theta - \theta_m) \quad (11)$$

and $F = \left\{\sin(\Delta kl/2)/(\Delta kl/2)\right\}^2$ is plotted in Fig. 4. The half width of F for the 15-mm long crystal is only 0.3 deg. Since a beam deviation angle of the CO_2 laser beam caused by a density gradient is an order of 0.01 deg. in the case of a LHD plasma with a density profile of 1×10^{20} $(1-\rho^8)$ m^{-3}, for example. However, it should be pay attention to the reduction of the power of the second harmonic in the high density range where the beam deviation angle becomes large.

3.3. Temperature raise of the nonlinear crystal

The temperature of the nonlinear crystal raises due to absorption of the laser power. The absorbed power P_{abs} is given by

$$P_{abs} = P_{total}\left[1-\exp(-\alpha l)\right] \quad (12)$$

where α is an absorption coefficient. 0.09 cm^{-1} is reported for $AgGaSe_2$, then P_{abs} becomes 0.95 W. The heat balance between the crystal and surrounding air is written by

$$T = T_0 + P_{abs}/(hS) \quad (13)$$

where h is the heat transfer coefficient, S is the surface area of the crystal, T is the crystal temperature, T_0 is the air temperature (here, 27°C). Assuming the heat transfer coefficient is 10 $Wm^{-2}K^{-1}$ pessimistically, the crystal temperature raises up to 371°C for the 5×5×15 mm-size crystal (S=2.25 cm^2 excluding the bottom plane 5×15 mm^2). In case that the surface area is increased up to 50 cm^2 by attaching a heat sink, the crystal temperature is only 47°C. Although the temperature is uniform inside the crystal in this rough estimation, the small thermal conductivity of $AgGaSe_2$ makes heat gradient between the central region and the surface. Hence it is necessary to have enough temperature margins for designing of the heat sink and cooling.

4. Summary

A dispersion interferometer is one of candidates of reliable electron density measurement. We propose the dispersion interferometer using a ratio of modulation amplitudes with a PEM. This method removes measurement errors from changes in the detected signal intensity and makes the signal processing simple and easy to use for real time feedback control. $AgGaSe_2$ is selected for SHG of a CO_2 laser dispersion interferometer for proof of the principle and the power of the generated second harmonics is estimated.

Acknowledgements

This work was supported by Grant-in-Aid for Young Scientists (B) (20760584).

References

[1] N. Ohyabu, T. Morisaki, S. Masuzaki, R. Sakamoto, M. Kobayashi, J. Miyazawa, M. Shoji, A. Komori, O. Motojimi, and LHD Experimental Group, Phys. Rev. Lett. **97**, 055002 (2006).

[2] Y. Shimomura, R. Aymar, V.A. Chuyanov, M. Huguet, H. Matsumoto, T. Mizoguchi, Y. Murakami, A.R. Polevoi, M. Shimada, Nucl. Fusion **41**, 309 (2001).

[3] Y. Kawano, S. Chiba and A. Inoue, Rev. Sci. Instrum. **72**, 1068 (2001).

[4] T. Akiyama, K. Kawahata, Y. Ito, S. Okajima, K. Nakayama, S. Okamura, K. Matsuoka, M. Isobe, S. Nishimura, C. Suzuki et al., Rev. Sci. Instrum. **77**, 10F118 (2006).

[5] M. A. Van Zeeland, R. L. Boivin, T. N. Carlstrom, and T. M. Deterly, Rev. Sci. Instrum. **79** 10E719 (2008).

[6] Ch. Fuchs and H. J. Hartfuss, Phys. Rev. Lett. **81**, 1626 (1998).

[7] T. Akiyama, K. Kawahata, Y. Ito, S. Okajima, K. Nakayama, S. Okamura, K. Matsuoka, M. Isobe, S. Nishimura, C. Suzuki et al., Rev. Sci. Instrum. **77,** 10F118 (2006).

[8] A. Boboc, L. Zabeo, and A. Murari, Rev. Sci. Instrum. **77**, 10F324 (2006).

[9] V. P. Drachev, Yu. I. Krasnikov and P. A. Bagryansky, Rev. Sci. Instrum. **64** 1010 (1993).

[10] P. A. Bagryansky, A. D. Khilchenko, A. N. Kvashnin *et. al.*, Rev. Sci. Instrum. **77** 053501 (2006).

[11] S. Ya Tochitsky, V. O. Petukhov, V. A. Gorobets, V. V. Chuakov and V. N. Jakimovich, Appl. Optics **36**, 1882 (1997).

[12] Cleverland Crystals Inc.

[13] A. Yariv, "Optical Electronics in Modern Communications fifth edition", Oxford University Press.

Proceedings of ITC18,2008

Development of a microwave AM reflectometer for electron density profile measurement in Heliotron J

K. Mukai[a,b], K. Nagasaki[c], V. Zhuravlev[d], T. Fukuda[e], T. Mizuuchi[c], H. Okada[c], S. Kobayashi[c], S. Yamamoto[c], S. Konoshima[c], S. Watanabe[a], K. Hosaka[a], Y. Kowada[a], S. Mihara[a], H. Y. Lee[a], Y. Takabatake[a], S. Kishi[a], K. Minami[a], K. Kondo[a], F. Sano[c]

[a]*Graduate School of Energy Science, Kyoto University, Gokasho, Uji, 611-0011, Japan*

[b]*Japan Society for the Promotion of Science Research Fellow*

[c]*Institute of Advanced Energy, Kyoto University, Gokasho, Uji, 611-0011, Japan*

[d]*RRC "Kurchatov Institute", Institute of Nuclear Fusion, Moscow,123182, Russia*

[e]*Osaka University, 2-1 ,Yamadaoka, Suita, 565-0871, Japan*

A microwave reflectometer is developed for electron density profile measurement in Heliotron J. An amplitude modulation (AM) type system is adopted to reduce density fluctuation effects. The carrier frequency ranges from 33 to 56 GHz, and the modulation frequency is 100 MHz. The X-mode is selected as the propagation mode in order to measure a hollow density profile typically which is observed in ECH plasmas. A test-bench examination using an aluminum reflection plate shows that the measured phase shift agrees well with that expected from the change in the plate position if the dependence on the RF signal power is taken into account. A numerical program to reconstruct density profile from the measured phase shift data has been also developed. The result confirms that the program works well for modeled flat or hollow density profiles.

Keywords: reflectometer, amplitude modulation, electron density profile, Heliotron J

1. Introduction

Measurement of electron density is one of the important issues to understand the plasma confinement and transport. Microwave reflectometer is widely used for density profile and density fluctuation measurements [1, 2]. The advantage of electron density profile measurement by reflectometer is that the time evolution of local electron density profile is possible to measure during a plasma discharge with good time and spatial resolutions. It has few limitation of installation port and does not need any assumption of the shape of magnetic surfaces.

Several types of reflectometer have been developed such as a frequency modulation (FM) reflectometer, an amplitude modulation (AM) and a pulse radar reflectometer. The electron density profile measurement by AM reflectometer has been carried out in T-10 tokamak [3], W7-AS [4], TJ-II [5] and HL-2A [6]. The advantages of the AM method are that it can suppress the effect of density fluctuations in profile measurement and that it can avoid the fringe jump by setting the whole of phase shift less than 2π.

In Heliotron J, it is an urgent task to obtain the electron density profile. The goal of this study is to develop a microwave reflectometer for Heliotron J and to investigate the particle transport from the density profile measurement.

In this paper, we describe current status of a microwave AM reflectometer system for electron density profile measurement in Heliotron J. We show results of characteristics test in a test stand and the program to reconstruct the density profile from the measured phase shift data.

2. Design of the reflectometer system

2.1 Basic design

Heliotron J is a medium-sized helical-axis heliotron device ($\langle R_0 \rangle$ = 1.2 m, $\langle a \rangle$ = 0.17 m, $B_0 \leq 1.5$ T) with an L/M = 1/4 helical coil [7]. The main purpose is to explore the optimization of the field configuration in helical-axis heliotron. The plasma heating systems are a second-harmonic X-mode ECH (70GHz, 500 kW), a two-loop-antennae ICH system (19-23.2MHz, 600 kW) and two tangential beam NBI systems (30kV, 700 kW). The electron density ever attained is $\bar{n}_e \leq 4.0\times10^{19}$ m^{-3}.

The main goal of this reflectometer is to measure the electron density profile in the wide confinement region. As a first step, however, the low density plasma ($\bar{n}_e \leq 1.0\times10^{19}$ m^{-3}) is targeted. The sweeping time of the carrier frequency is set as less than 1 ms, which is shorter than the typical energy confinement time of Heliotron J plasma.

author's e-mail: mukai@center.iae.kyoto-u.ac.jp

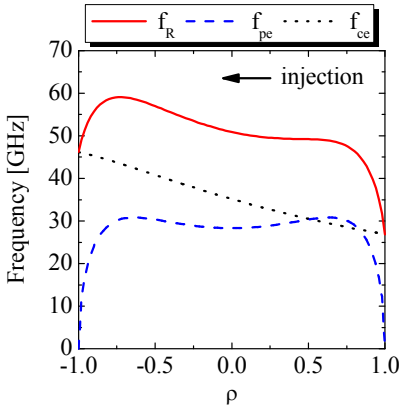

Fig.1 Characteristic frequencies along the line-of-sight of reflectometer for a hollow electron density profile

Figure 1 shows the radial profiles of the right-hand cut-off frequency, f_R, the plasma frequency, f_{pe}, and the electron cyclotron frequency, f_{ce}, along the line-of-sight. The electron density profile is assumed to be hollow, given by

$$n_e(r) = n_e(0)\{1-(r/a)^6\}[1-0.4\times\{1-(r/a)^2\}] \qquad (1)$$

Here $n_e(0)$ is determined to satisfy the condition, $\bar{n}_e=1.0\times10^{19}$ m^{-3}.

In helical systems, a hollow density profile is typically observed in ECH plasma. In such a profile, the central density cannot be measured by using the O-mode. Since there is an appropriate gradient of magnetic field in Heliotron J, the X-mode is selected as the propagation mode. By using the carrier frequency of 33-56 GHz (nearly Q-band), it is possible to obtain density profile over the full range of plasma radius for low-density plasmas.

2.2 Schematic of the AM reflectometer

Figure 2 shows the schematic of the designed AM reflectometer. A pulse generator supplies a triangular-wave of 1 kHz to a voltage controlled oscillator (VCO) of 8.25-14 GHz. The frequency band of 33-56 GHz is generated by the VCO and a ×4 frequency multiplier. A Q-band waveguide transmission of 8 m long is used for transmission in order to suppress the resonant attenuation which is observed when using oversized waveguides. After transmission, the microwaves are modulated in amplitude with the frequency of 100 MHz by using a PIN modulator. Low-pass filters are assembled to remove the effect of 70 GHz ECH. Horn antennae are used for launching and receiving microwaves. A heterodyne detection system is applied to detect the reflected signal. A phase meter consists of a frequency down-converter (from 100 MHz to 5 MHz) and a phase detector. The phasemeter also measures the RF signal

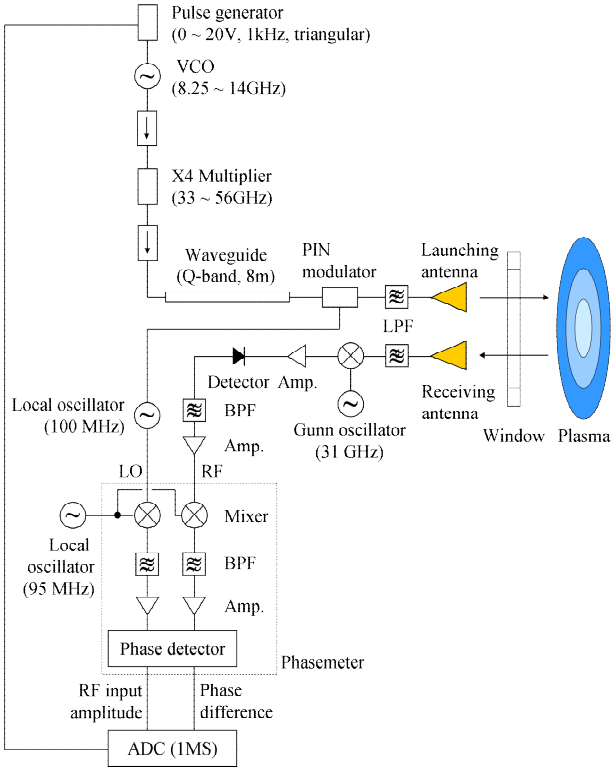

Fig.2 Schematic of the AM reflectometer.

power to correct the power dependence of the phase comparator. The outputs of the pulse generator, the RF input amplitude and the phase difference are stored by a data acquisition system with the sampling time of 1 μsec.

3. Measurement results in test stand

The performance of each microwave component has been measured in a test stand before installing the system in Heliotron J. Figure 3 shows the dependences of the frequencies and intensities of the VCO and the multiplier on the VCO input voltage. The output frequencies are controlled stably by the VCO input voltage, and the output intensities are almost constant for the operation range of the VCO input voltage. Figure 4 shows the phase outputs and signal intensities of the modulated signal at the front and end of the 8 m Q-band waveguide transmission. In the whole range of carrier frequencies, the phase output is

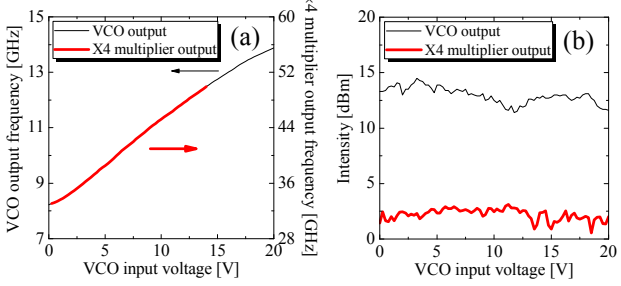

Fig.3 Dependence of VCO and ×4 multiplier output (a)frequencies and (b)intensities on VCO input voltage.

almost flat. However, since the intensity is weak, it needs to amplify the signal for reliable measurement.

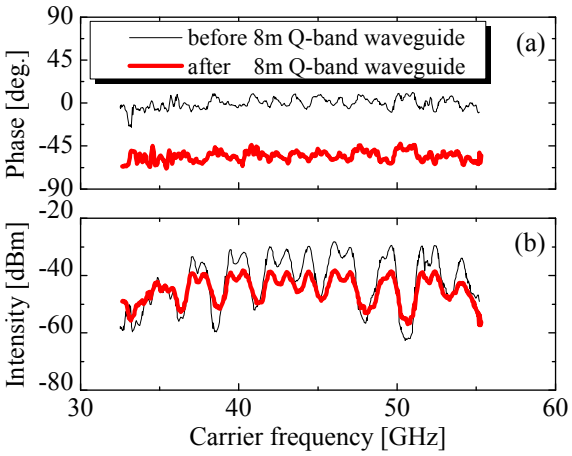

Fig.4 Dependence of (a) the phase output and (b) the modulated signal intensities on the carrier frequency before and after the 8 m Q-band waveguide transmission.

The phase measurement has been conducted by using an aluminum reflection plate instead of plasma. The length of the transmission line is changed by moving the plate in the range of 30 cm at an 1 cm interval. Figure 5 (a) shows the dependence of the phase shift on the plate displacement. It can be seen that the phase output of the phasemeter depends on the RF input amplitude. This dependence is caused by the characteristic of the limiting amplifier in the phasemeter. Figure 5 (b) shows the corrected phase shift data by using the calibration data of the phase output. The calibration reduces the root-mean-square error from 2.4 degree to 1.4 degree. The phase shift agrees well with that expected from the change of the plate position when the amplitude dependence is taken into account.

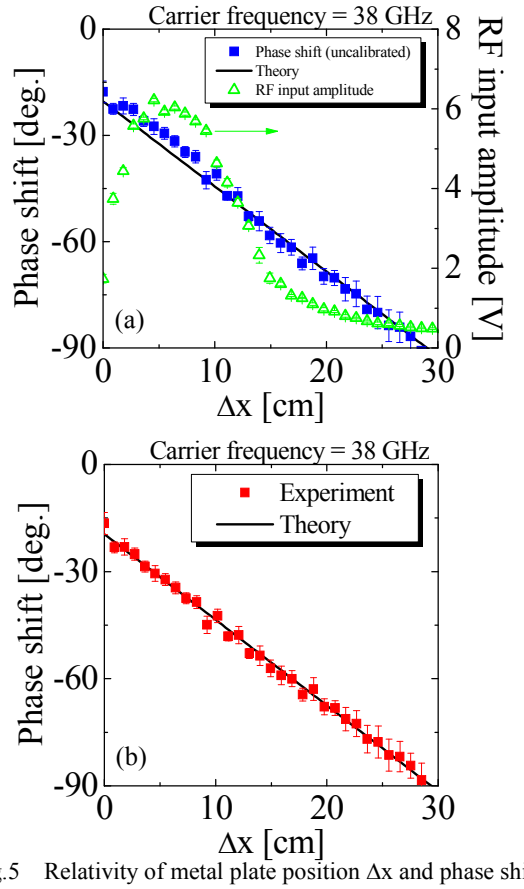

Fig.5 Relativity of metal plate position Δx and phase shift (a)uncalibrated and (b)calibrated.

4. Density profile reconstruction method

4.1 Algorithm of profile reconstruction

The phase shift of the probe signal from the reference signal is written as

$$\phi(f_n) = \frac{4\pi f_n}{c}\int_a^{r_n} N_X(r, f_n)\mathrm{d}r \qquad (2)$$

where f_n is the carrier frequency, r_n is the position of cutoff layer corresponding to f_n and N_X is the refractive index of X-mode. By using Eq. (2), the position of the cutoff layer is determined, and the density profile can be reconstructed.

The algorithm to reconstruct the density profile is as follows. By considering the difference between two phase shift data, the phase shift caused by the difference of the transmission length outside LCFS between the probe and the reference signals can be removed.

$$\begin{aligned}&\frac{4\pi f_{n+1}}{c}\int_{r_n}^{r_{n+1}} N_X(r, f_{n+1})\mathrm{d}r \\ &= \phi(f_{n+1}) - \phi(f_n) \\ &\quad - \left[\frac{4\pi f_{n+1}}{c}\int_a^{r_n} N_X(r, f_{n+1})\mathrm{d}r - \frac{4\pi f_n}{c}\int_a^{r_n} N_X(r, f_n)\mathrm{d}r\right] \end{aligned} \qquad (3)$$

At the cutoff layer, the left-hand side of Eq. (3) can be approximated as $\Delta r_n\ N_X(r_n, f_{n+1})/2$ since $N_X(r, f_{n+1})=0$. Here $\Delta r_n = r_{n+1} - r_n$ is given by

$$\begin{aligned}\Delta r_n = \frac{2}{N_X(r_n, f_{n+1})}\Bigg[&\phi(f_{n+1}) - \phi(f_n) - \frac{4\pi f_{n+1}}{c}\int_a^{r_n} N_X(r, f_{n+1})\mathrm{d}r \\ &+ \frac{4\pi f_n}{c}\int_a^{r_n} N_X(r, f_n)\mathrm{d}r\Bigg]\end{aligned} \qquad (4)$$

The integral term of Eq. (4) can be calculated by using a trapezoid formula. Consequently, the density profile can be reconstructed if the initial density value is determined by other diagnostics, for example, Langmuir probe.

4.2 Results of reconstruction using model profiles

In order to validate the reconstruction algorithm, model electron density profiles are reconstructed by the program calculating Eq. (4). The profile is chosen as a flat or hollow density one. The electron density is assumed as the line-averaged density, $\bar{n}_e = 1.0\times10^{19}$ m^{-3}, and the edge density, $n_e(\rho=1) = 0.2\times10^{19}$ m^{-3}. Here ρ denotes the normalized minor radius.

The reconstruction results are shown in Fig. 6. Here,

the cutoff layer position of 33 GHz is assumed to be located at ρ=1. At the both profiles, the density profiles are reconstructed with the error less than 5 % in the center region. This indicates that the program can reconstruct density profile in the whole plasma region with the sufficient accuracy for density profile measurement. For a high-density model (2.0×10^{19} $m^{-3}\leq \bar{n}_e \leq 3.0\times10^{19}$ m^{-3}), the density gradient at the edge region can be evaluated within 10 % accuracy.

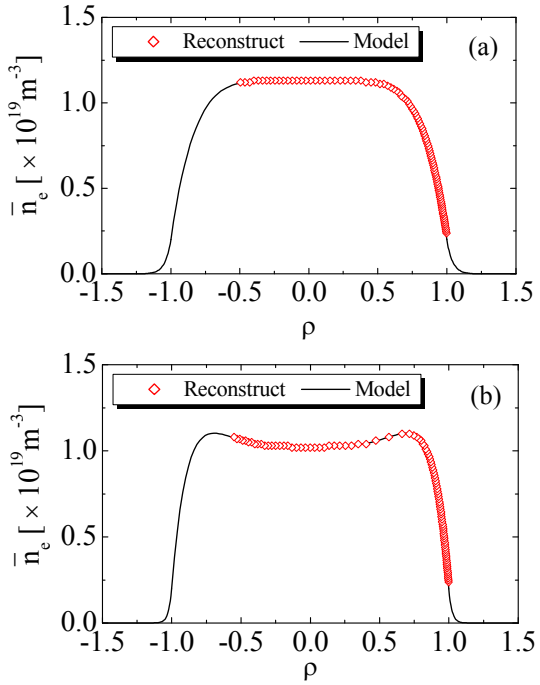

Fig.6 Reconstructed profiles, (a) flat density profile and (b) hollow density profile at $\bar{n}_e=1.0\times10^{19}$ m^{-3}.

5. Summary

The AM reflectometer is developed for the electron density profile measurement in Heliotron J. The measurement results in a test stand show that each microwave component works well and the phase shift is measured as designed.

A program to reconstruct density profile from the relative phase shift data has been developed. The program has been examined by using modeled density profiles such as flat and hollow ones. The result confirms that the program works well for the modeled shapes of the density profile model with accuracy of fewer than 5 % for low density at the plasma central region.

The reflectometer system is under installation in Heliotron J. In order to measure the profile with satisfactory accuracy, it is necessary to improve detection system sensitivity and S/N ratio. Therefore, we plan to install more sensitive detector and Q-band microwave amplifier. The electron density profile will be measured in ECH, NBI and ICRF plasmas in the near future.

Acknowledgements

The authors are grateful to the Heliotron J team for their excellent arrangement of the experiments. This work was partly supported by NIFS/NINS under the NIFS Collaborative Research Program (NIFS04KUHL005) and the project of Formation of International Network for Scientific Collaborations.

References

[1] C. Laviron, *et al*., Plasma Phys. Control. Fusion **38** 905 (1996)
[2] E. Mazzucato, Rev. Sci. Instrum. **69** 2201 (1996)
[3] V. Zhuravlev, Proc. 26th EPS Conf. on Controlled Fusion and Plasma Phys. (Maastricht, 1999) Vol. **23J**, p857.
[4] M. Hirsh, *et al*., Rev. Sci. Instrum., **67** 1807 (1996).
[5] T. Estrada, *et al*., Plasma Phys. Control. Fusion **43** 1535 (2001)
[6] W. Xiao, *et al*., Plasma Science & Technology, Vol. **8**, No. 2 (2006)
[7] T. Obiki, *et al*., Nucl. Fusion **41**, 833 (2001)

Proceedings of ITC18, 2008

Clustered Data Storage for Multi-site Fusion Experiments

NAKANISHI Hideya, KOJIMA Mamoru, OHSUNA Masaki, IMAZU Setsuo, NONOMURA Miki, YAMAMOTO Takashi, EMOTO Masahiko, NAGAYAMA Yoshio, KAWAHATA Kazuo, LHD exp. group, HASEGAWA Makoto[1)], HIGASHIJIMA Aki[1)], NAKAMURA Kazuo[1)], and YOSHIKAWA Masayuki[2)]

National Institute for Fusion Science, 322-6 Oroshi-cho, Toki 509-5292, Japan
[1)]RIAM, Kyushu Univ., 6-1 Kasuga-kouen, Kasuga 816-8580, Japan
[1)]PRC, Univ. of Tsukuba, Tsukuba 305-8577, Japan

LABCOM data acquisition and management system has already provided full functions in both the local and remote participations for the LHD experiments. This study newly added the function to deal with experimental raw data not only in one experimental device but also from multiple distant sites. Its original distributed structure has enabled the multi-site modification with a minimum change mainly within the data location indexing database for clustered storage. However, the access permission and restriction for each site's data and users should be strictly implemented. The system has started its operation since 2008 under bilateral collaboration between LHD, QUEST, and GAMMA10 experiments, aiming to organize "Fusion Virtual Laboratory" in Japan.

Keywords: LABCOM, clustered storage, SINET3, LHD, QUEST, GAMMA10, Fusion Virtual Laboratory

1 Introduction

Remote participation technology is one of the most important fundamentals for modern fusion experiments [1, 2]. It is recently based on over 10 Gbps information highways, in which many Giga-bytes or sometimes Tera-bytes experimental data are shared by distributed collaborators.

On the other hand, the amount of experimental data which continuously keep growing (Fig. 1) often causes the operational staffs too heavy management burden. Such the increasing costs of data management will possibly be optimized by an intensive administration of the data storage system through the ultra-wideband networks. The Internet Data Center (IDC), which provides centralized monitoring and control for data resources, is a typical example to streamline the data management in commercial fields. This solution would be also required in physics research experiments.

SINET3 is Japanese academic information highway operated by National Institute of Informatics (NII) having 10 or 40 Gbps backbone [3]. It also serves Layer-2 or Layer-3 IP virtual private network (VPN) exclusively for fusion research community whose name is "SNET" [4]. It is intrinsically equipped with both the wide bandwidth and high security.

SNET has been hosted by NIFS since 2001 fiscal year, at first for the LHD remote participation activities [5, 6]. From 2005 FY, the bilateral collaboration programs between NIFS and research centers of other universities has additionally come into operation. The most typical example of it is the All-Japan spherical tokamak (ST) research program [7] where remote data acquisition can be realized between its new experimental device "QUEST" and LHD's data repository.

In this study, we have modified the LHD data acquisition and management system to be able to deal with multiple experiments and their data simultaneously. In the following sections, required specifications and applied implements are described with their effectiveness.

2 Objective: Access controls for multiple sites

As mentioned in the previous section, one of the most important objective of this study is to build easily extendable data storage with the centralized management. LHD data repository has already possessed multiple disk volumes and the FibreChannel based storage area network (FC-SAN) by way of yearly increase of their capacity. FC-SAN is *de facto* standard of massive-size storage shared for various uses.

LABCOM data system can already provide full functions in both the local and remote participations for the LHD fusion experiments [8, 9]. In this study, however, we have to add a new function to deal with acquired raw data not only in one experimental device but also from multiple distant sites.

When sharing the clustered storage volumes among different experimental sites, a clear distinction should be given to the access permission and restriction for data and users of each site. These access controls shall be implemented on the indexing database by adding a new "site" key to prior "diagnostic (data) name" and "shot number"

author's e-mail: nakanishi.hideya@lhd.nifs.ac.jp

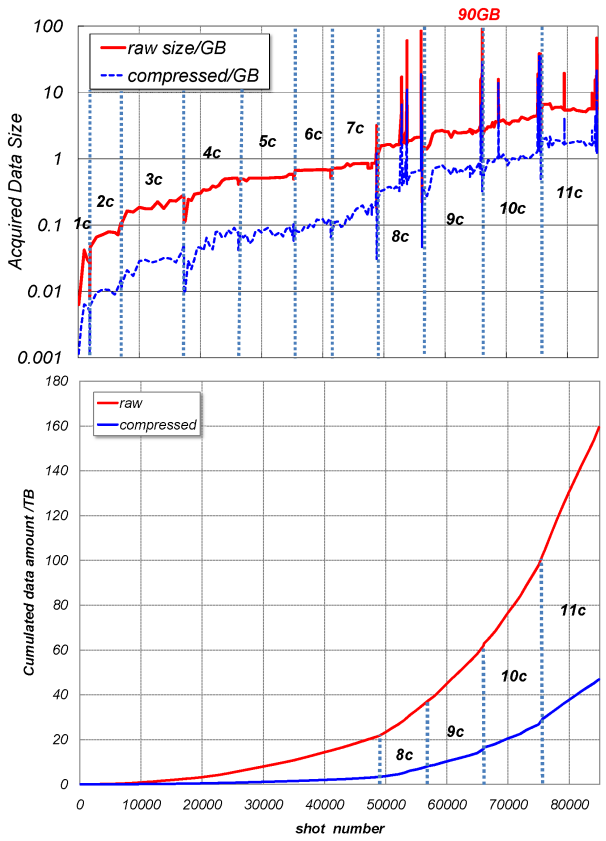

Fig. 1 Data growth in LHD, per-shot size (top) and cumulative amount (bottom): 1c~11c mean annual experimental campaigns of LHD. 90 GB/shot is the world record of acquired raw data in one plasma experimental discharge. All the acquired data are kept online to be accessible for every collaborators.

keys. The "site" should control both the diagnostic data and the user groups. Table 1 shows the essential part of this upgrade.

3 New LABCOM/X data acquisition and management system

R&D for LABCOM data acquisition and management system has been started since 1995, aiming for constructing a new plasma diagnostic data system for Large Helical Device (LHD) experiment in NIFS. As the first plasma was established in March 1998 [10], it has experienced ten years' annual campaigns until now.

One of the most remarkable achievements was to establish a new world record of diagnostic data amount acquired in one fusion plasma discharge. It has been achieved by means of a brand-new technology of ultra-wideband real-time data acquisition whose maximum performance is up to 160 MB/s for each digitizer front-end [11].

The LABCOM system has originally a distributed structure in which data acquisition and storage elements are completely separated on fast network [12]. When wide-area networks (WAN) could be equivalent to local

Table 1 Related tables in "facilitator" database; components of main "shot" table (left) and contents of new "site" table (right): Bold-typed **shot#, diag#,** and **site#** are the primary keys.

Column	Modifiers
shot	not null
subshot	not null
diag_id	not null
host_id	not null
media_id	not null
regist_no	not null
note_id	not null
site_id	not 0 default 1

site_id	site_name
1	lhd
2	quest
3	gamma10

one (LAN) on its throughput, there is no logical difference between them. The multi-site modification was, therefore, realized with a minimum change mainly on the facilitator database which informs the data locations shown in Fig. 2.

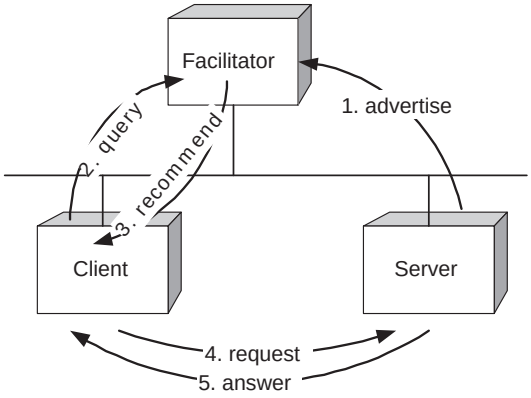

Fig. 2 Recommend-type facilitator model: The facilitator never mediate the requests but only recommend the appropriate server to send them [13]. It is suitable for the distributed data store and retrieval system which must transfer many binary large objects (BLOBs) without any bottlenecks.

The access restriction between multi-sites' data and user groups has been implemented by a combination of database's user account corresponding to site's user group and its access permission to registered IP addresses. It means that every stored data belong to their own site, and also the data retrieval computers are independently registered for each site.

The main "shot" table shown in Table 1 contains more than 14 million entries of the experimental data. By means of database's embedded acceleration of key indexing, however, a query search be answered in about 0.14 second.

The multiple sites' data handling system has started the operation since September 2008, under bilateral collaborations between LHD in NIFS, QUEST in RIAM, Kyushu Univ., and GAMMA10 in PRC, Univ. of Tsukuba. Due to such the topological evolution, we newly name the data system as "LABCOM/X". Fig. 3 show the schematic

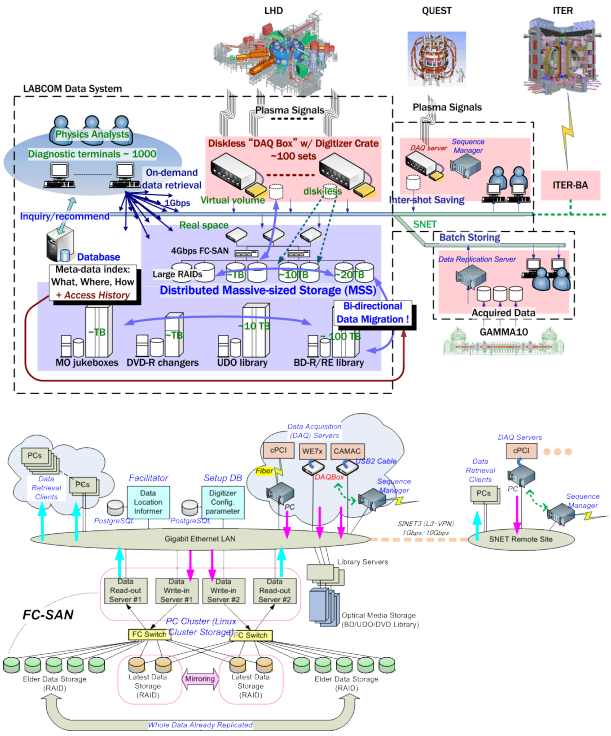

Fig. 3 Multi-site data acquisition and management system based on SNET; physical view (top) and logical scheme (bottom).

views.

4 GFS2 storage cluster and data replication

For a multi-sites' data repository, it will be quite essential that plural I/O servers should work redundantly and even in load-balancing. The cluster filesystem provides the synchronization mechanism of the content data among them. We use Red Hat Global File System (GFS) [14] and its version 2 (GFS2) afterward, whose I/O performance is almost the same as ordinary local ones like xfs or ext3 (Table 2).

Generally, cluster filesystems such as Sun's Lustre File System or IBM's General Parallel Filesystem (GPFS) provides better performance in writing huge data volumes by means of split I/O into many storage nodes. To keep the consistency among their distributed chunks, it usually needs at least one metadata server or service process. On the other hand, GFS never split a file into many or distributed chunks. It only provides a distributed file locking mechanism to synchronize the file appearance among the cluster node computers. So, it is also possible for us to use GFS volume as a local filesystem without any metadata server. This feature is quite advantageous when some GFS volumes are filled and changed to be read-only ones, as shown in Fig. 3.

Another possibility to make data replication was hardware or software mirroring. When using a number of huge

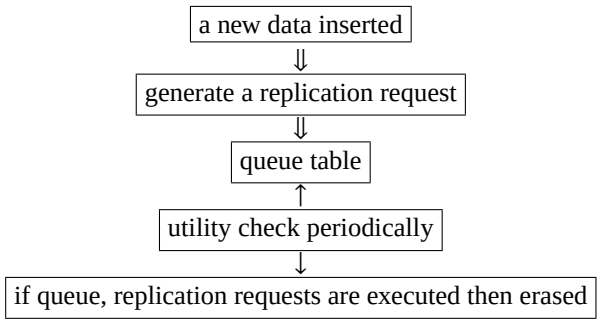

Fig. 4 Replication queuing algorithm between database table and the utility.

disk arrays, however, it would be more disadvantageous due to the extremely long rebuilding time in recovery when inconsistency disorders happened.

After above mentioned discussions, we have made a specific utility to replicate newly appeared data files which runs in cooperation with the facilitator database. Applied replication scheme is a simple combination of request queuing and their cyclic batch execution, as shown in Fig.4. It never check the equality between the source and destination volumes, only making the incremental copies of newly appeared files. Such the loosely tied data mirroring mechanism is rather preferable for flexible storage operations.

We have also changed the data migration scheme. Between the distant data acquisition (DAQ) servers and storage ones, we previously adopted the network filesystem (NFS) to share the cluster volume on local-area network, in other words, within a single LHD site. However, it could be less reliable for the distant data sharing because NFS was designed basically to be used on LAN. Moreover, over seventy NFS clients were constantly connected to the NFS server during the experimental sequences and occasionally caused overloads on server.

For the above reasons, we have abandoned NFS and applied the ftp-based method for it. As its client only establishes a network session during the file transfer and will be disconnected when completed, the server-side load efficiency has been much improved. It also has an advantage to be easily replaced by some higher-throughput parallel-session ftp, such as GridFTP [15], both for the future extension and far distant migration.

Table 2 Throughput difference between local (ext3, xfs) and cluster (gfs2) filesystems: These are the results from 100 MB write tests of "`dd if=/dev/zero of=outfile bs=1024 count=102400`" and "`count=1048576`".

filesystem	I/O rate (100 MB)	I/O rate (1 GB)
ext3	0.635 s 165 MB/s	8.63 s 124 MB/s
xfs	0.811 s 129 MB/s	8.53 s 126 MB/s
gfs2	0.869 s 121 MB/s	6.68 s 161 MB/s

5 Conclusion and remarks for future

The LABCOM storage cluster has proved the effectiveness for the use of multiple fusion experiments. It is on-demand extendable with FibreChannel storage area network (FC-SAN) and multiple disk volumes.

Considering about the preprogrammed sequential operation and the data granularity of fusion experiments, the simple network locking algorithm provided by GFS2 seems more preferable for us to fast split I/O cluster filesystems having a metadata server. Newly developed replication utility also provides a good flexibility for sustaining the data protection on it. The ftp-based new migration scheme has proved its reliability having no trouble during one year experiment on LHD.

We will further advance the "Fusion Virtual Laboratory" in Japan to demonstrate the next-generation and coming ITER and ITER-BA multi-site experiments.

Acknowledgments

This work is performed with the support and under the auspices of the NIFS Collaborative Research Program; NIFS08ULHH503, KUTR031, KUTR035 and NIFS07-KUGM021. It is also supported by Cyber Science Infrastructure (CSI) development project of the National Institute of Informatics (NII).

References

[1] J. How and V. Schmidt, Fusion Eng. Design **60**, pp. 449–457 (2002).
[2] J. Vega *et al.*, Rev. Sci. Instrum. **74**, pp. 1773–1777 (2003).
[3] NII, *SINET3* http://www.sinet.ad.jp/ (2007).
[4] *SNET* http://snet.nifs.ac.jp/ (2006) [in Japanese].
[5] M. Emoto, T. Yamamoto, S. Komada and Y. Nagayama, Fusion Eng. Design **81**, pp. 2051–2055 (2006).
[6] K. Tsuda, Y. Nagayama, T. Yamamoto, R. Horiuchi, S. Ishiguro and S. Takami, Fusion Eng. Design **83**, pp. 471–475 (2008).
[7] *All-Japan ST Research Program* http://www.nifs.ac.jp/kenkyo/icr/st.html (2008) [in Japanese].
[8] H. Nakanishi, M. Ohsuna, M. Kojima, S. Imazu, M. Nonomura, Y. Nagayama and K. Kawahata, Fusion Eng. Design **82**, pp. 1203–1209 (2007).
[9] M. Ohsuna, H. Nakanishi, S. Imazu, M. Kojima, M. Nonomura, M. Emoto, Y. Nagayama and H. Okumura, Fusion Eng. Design **81**, pp. 1753–1757 (2006).
[10] O. Motojima *et al.*, Phys. Plasmas **6**, pp. 1843–1850 (1999).
[11] H. Nakanishi, M. Ohsuna, M. Kojima, S. Imazu, M. Nonomura, M. Emoto, H. Okumura, Y. Nagayama, K. Kawahata and LHD exp. group, J. Plasma Fusion Res. **82**, pp. 171–177 (2006) [in Japanese].
[12] H. Nakanishi, M. Kojima and S. Hidekuma, Fusion Eng. Design **43**, pp. 293–300 (1999).
[13] K. Kawagome *et al.*, *Distributed Objects Computing* (Kyoritsu Publishing, Tokyo, Japan, 1999) [in Japanese].
[14] Red Hat, Inc., *Global File System* http://www.redhat.com/docs/manuals/enterprise/RHEL-5-manual/Global_File_System/ (2007).
[15] *GridFTP* http://www.globus.org/toolkit/data/gridftp/ (2008).

Proceedings of ITC18,2008

Multi-channel neutron emission and triton burn-up measurement on JT-60U using Digital-Signal-Processors

K. Ishii, K.Shinohara [a], M. Ishikawa [a], T. Okuji [b], M. Baba [b], M. Isobe [c], S. Kitajima, M. Sasao

Department of Quantum Science and Energy Engineering, Tohoku Univ., Sendai 980-8579, Japan

[a]Japan Atomic Energy Agency, 801-1, Mukoyama, Naka 311-0193, Japan

[b]Cyclotron and Radioisotope Center, Tohoku Univ., Sendai 980-8578, Japan

[c]National Institute for Fusion Science, 322-6 Oroshi-cho, Toki 509-5292, Japan

In JT-60U, the multi channel neutron profile monitor measured the line-integrated neutron emission. A digital-signal processing (DSP) system was applied to every neutron detector of the neutron profile monitor. A new 2D mapping method of DSP data analysis was developed to discriminate neutrons from γ-rays. The combination of DSP and the 2D map enabled the simultaneous measurement of DD and DT neutrons with one detector. The time evolution of DD and that of DT neutrons showed different response to the ITB formation, depending on the viewing chord.

Keywords: JT-60U, neutron diagnostics, Digital-signal-Procssors, triton burn-up

1. Introduction

The information on the energetic ion behavior in deuteron heated deuterium plasma can be obtained by measuring the line-integrated neutron emission rate with neutron detectors viewing the plasma along a number of chords (a neutron profile monitor) [1]. To avoid contamination of γ-rays and the scattering component in a neutron profile measurement, it is important to use a detector that discriminates neutrons from γ-rays and is insensitive to low-energy neutron. To discriminate neutrons from γ-rays, several kinds of scintillators, such as NE213, Stilben crystals, NE451 have been used [1], combined with sophisticated discrimination electronics, which require a finite process time and hence prevent the high counting rate measurement.

In JT-60U, a digital-signal processing (DSP) system was developed and applied to all neutron detectors of the multi channel neutron profile monitor of seven viewing chords [2-6], to overcome this problem in the count rate. Then, it is important to develop a fast and reliable n-γ discrimination logics and the software for the digital data analysis.

In the present study, a new 2D n-γ discrimination mapping method was introduced and applied to the DSP data from the neutron profile monitor of JT-60U. The neutron profile measurement was successfully carried out during the 2008 campaign of JT-60U, using this new system.

In JT-60U, DD neutrons were produced in a deuterium plasma heated by D^0-beams. The DT neutrons were produced as well by triton burn-up, and their time evolution can be used to predict 3.5MeV α-particle behavior in a fusion reactor. The separation of DT neutrons form that of DD was clearly performed, and the time evolutions of both DD and DT neutrons were obtained. They showed different behaviors depending on the viewing chord.

keiichi.ishii@ppl2.qse.tohoku.ac.jp

2. Neutron Profile Monitor of JT-60U

In JT-60U, the multi channel neutron profile monitor had seven viewing chords; six chords view the plasma poloidaly and one chord views vertically. Details of the viewing and collimation systems were described in Ref. 2.

2. 1 Hardwares

Each viewing chord equipped a neutron detector of stilben crystal. A stilben crystal is sensitive not only to neutrons but also to γ-rays. It is necessary to discriminate neutrons from γ-rays. An analog neutron-γ pulse shape discrimination circuit had been used in order to measure collimated neutron flux [2]. However, the maximum count rate of the analog n-γ discrimination circuit was limited below ~$1x10^5$ cps. To overcome this problem in the count rate, a digital-signal processing (DSP) system was developed for neutron detectors [3, 5]. In this DSP system, output pulses from an anode of a photo multiplier tube (PMT) of a detector are recorded as continuous waveform using a fast flash analog-to-digital converter (flash ADC) [6]. One pulse decayed typically within ~100ns. Therefore, the flash ADC was required

with a nano-sec range sampling rate of digitizing outputs.

This DSP system had been extended to seven chords of the neutron collimator system [6]. The recorded data size was 7GB per discharge. A sampling rate was usually 200 M-samples/s, which was chosen from the optimization between the pulse shape discrimination quality and the time period covered by the system, though the maximum sampling rate was 5 G-samples/s [5,6]. With the ADC sampling rate of 200 M-samples/s, the time duration covered by the data acquisition scheme was about 2.68 s. A recorded data was stored once in the flash ADC, and it was transferred to a HDD of a PC after the measurement.

A recorded data was analyzed with an off line software, (1) to discriminate neutrons from γ-rays, (2) to obtain a pulse height spectrum to separate DD and DT neutrons in every time bin, typically 10 ms, and (3) to obtain the time evolution for both DD and DT neutrons.

2.2 Pulse shape analysis

To discriminate neutrons from γ-rays, a charge integration method was used in the software, using the difference in the decay time of an output pulse. This system successfully achieved the counting rate capability higher than ~1x10^5 counts/s [5]. The software for the pulse shape analysis had following function: (1) catches the maximum of the digitized pulse height for each pulse, and saves it as "height", (2) produces 3 integrals "fast", "slow", and "total", (3) rejects pile up events. The neutron-γrays (n-γ) discrimination was done using the charge integration method in which each pulse is was integrated for two time intervals as shown in functions of software. The integral for the time interval near the pulse peak was defined as "fast", and the other was called "slow". A value of "total" was integrated from the time when pulse rises up to the end of the interval for the slow.

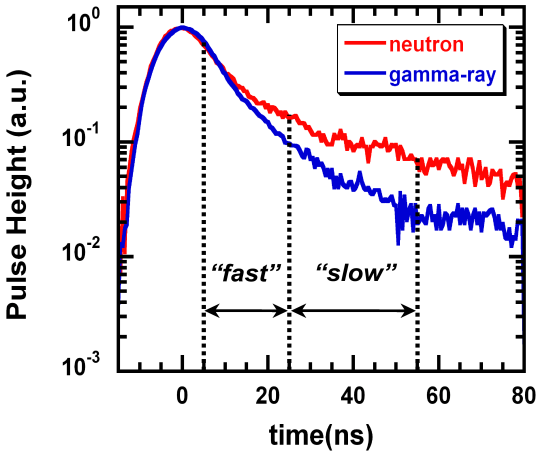

Fig.1 An example of a pulse shape digitized with 2 G-samples/s. Time intervals of fast and slow are indicated by dotted lines. The decay time of neutron is longer than that of γ-ray.

Fig.1 shows pulse shape digitized in 2 G-samples/s, and time intervals of fast and slow. As shown in Fig.1, a decay time of neutron is longer than that of γ-ray. In the other word, charges of neutron are lager than that of γ-rays which has the same pulse height as that of neutron. Using three values, "fast", "slow", and "height" for one pulse, a two dimensional (2D) map in height–slow normalized with (fast+slow) space can be plotted to discriminate neutrons as shown in Fig.2. One dot is plotted against one pulse. Neutrons are discriminated graphically using this 2D map.

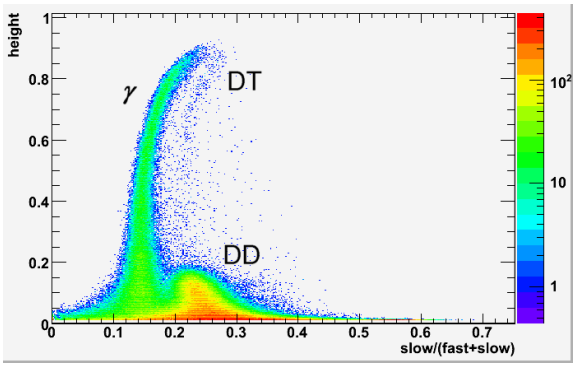

Fig.2 A 2D map in height – slow space for n-γ discrimination.

In Fig.2, there are two peaks at ~0.15 and ~0.25 of the normalized slow. The peak that has small charge is γ-ray. Most of pulses due to neutrons are distributed in low height region below the height of 0.2. Pulses distributes in this region is considered as DD neutrons. A few neutrons distributed above the height of 0.2 can be DT neutrons, which are produced in the DT fusion reaction emitting 14 MeV. In figure 2, neutron events are not separated from that of γ–rays in the low energy of the height below 0.05, and in the high energy region above 0.7. To solve the problem in the low energy region, a value of "total", which was the integration over the whole pulse, was used. fast/total and slow/total were used as the parameters of a 2D map shown in Fig.3.

There are two groups in Fig.3, and neutrons are discriminated clearly from γ–rays comparing with Fig.2. To investigate feature of a new n-γdiscrimination, we selected neutron region in Fig.3 and plotted these pulses again in the conventional 2D map whose parameter was height and slow/(fast+slow). As a result, the separation was successful for low energy. However, it was found that some high-energy γ–rays were counted as neutron. Therefore, a conventional height–slow space discrimination was further done for the neutron events selected by the new 2D map of the normalized fast-slow space (double 2D discrimination).

To obtain the profile of DT neutron emission rate, it is important to discriminate DT neutrons for all detectors. The time interval of the charge integration method was the same value for all detectors on supposition that all detectors had the same pulse shape. However, some detectors did not discriminate DT neutrons from energetic γ-rays. To solve this problem, the pulse shape analysis was done using pulses recoded in high sampling rate (2 G-samples/s). As a result, it was found that pulse shape was different for each detector. The time intervals were changed for each detector in the software, and then all detectors achieved success in discriminating DT neutrons from energetic γ-rays.

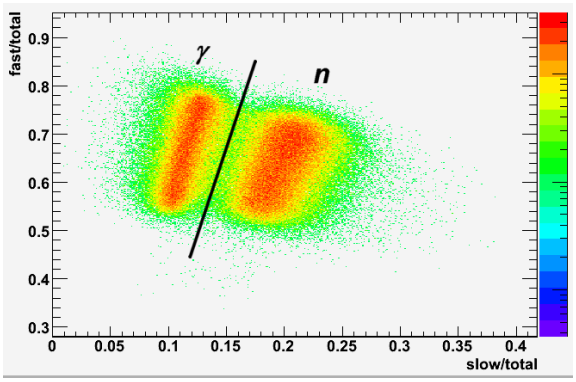

Fig.3 A new 2D map in fast-slow space normalized with total. Neutrons are discriminated from γ-rays clearly.

3. Triton burn-up

In JT-60U, DD neutron was measured mainly because energetic deuterium was injected as neutral beam (NB) into the deuterium plasma. Not only 2.5 MeV neutrons but also 1MeV tritons are produced through the DD fusion reaction. When tritons are confined in the bulk plasma and slow down to the energy region suitable for DT reaction by collision with mainly electrons, they may react with deuteron and then produces 14.1MeV neutron. In the DSP system, DT neutron was measured as well as DD neutron simultaneously using the same detector. Fig.4 shows a pulse height distribution of neutrons that is discriminated from γ-rays using the double 2D discrimination. In Fig.4, the edge near 0.15 of height is considered as the DD neutron edge. The counts distributing above 0.15 are DT neutrons, showing that the DSP system successfully achieves DT neutron detection. High neutron counts in the low energy region is considered to be scattered neutron component.

To obtain the time evolution of DD neutrons and DT neutrons respectively, two regions were defined in the height distribution. As shown in Fig.4, one region defined for DD neutrons is from 0.05 to 0.15, the region for DT neutrons is above 0.4. A histogram of neutron in the each region is produced against time, and then the time distribution of neutrons is obtain as shown in Fig.5 (e) - (h). The DT neutron emission rate is less than that of the DD neutron by the order of 2-3 in Fig.4, similar to the ratio reported from other large tokamaks [1]. Therefore, it is necessary that a counting time interval of DT neutron is longer than that of DD neutron to raise statistical precision. In Fig.5, the time interval for DT neutron is ten times longer than that for the DD neutron. Therefore, the time evolution of DT neutron is shown with dots due to low time resolution. If the DT neutron emission rate is higher, the time resolution can be higher.

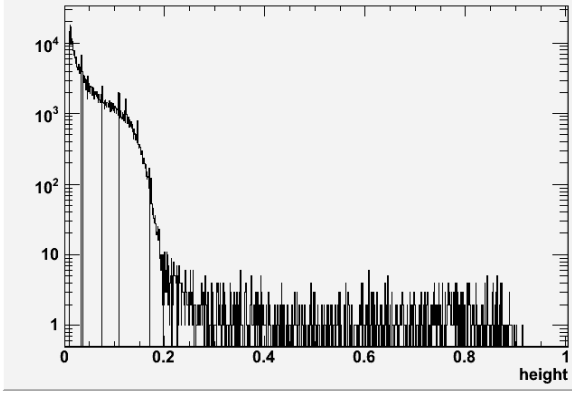

Fig.4 A height distribution of neutrons discriminated from γ-rays. In the DSP system, DT neutron is measured as well as DD neutron simultaneously using the same detector.

Fig.5 shows the time evolution of neutron emission rate measured by the DSP system and plasma parameters. In this discharge, the plasma was heated by the 13 MW positive ion based neutral beams (PNBI) and ~2.9 MW electron cyclotron heating (ECH). The plasma current was 1.2MA and the toroidal magnetic field was 3.7T. The plasma was disrupted at 7.4s.

The DSP system measured the line-integrated neutron emissivity, not local neutron emissivity. An absolute value of the line-integrated neutron emission rate in a chord cannot be compared with that in others because the geometrical efficiency and the detection efficiency have not yet considered. During the measurement of the DSP system, power of PNB was almost constant and ECH was injected from 6.0 s. Electron temperature and density increased remarkably from 6.3 s in the core region. Namely an internal transport barrier (ITB) was formed. Total neutron emission rate measured by the fission chamber increased gradually from 6.5s until the disruption. The time evolution of DD neutron measured by DSP system is similar to that of fission chamber. However, the DD neutron emission rate in the central chord (chord 7) increased more than that in the peripheral chord (chord 6) after the ITB formation. It is

considered that the DD neutron emission reflected the density almost linearity because the dominant DD fusion component was not the thermal but that of the beam-plasma interaction and the input power of PNB was almost constant.

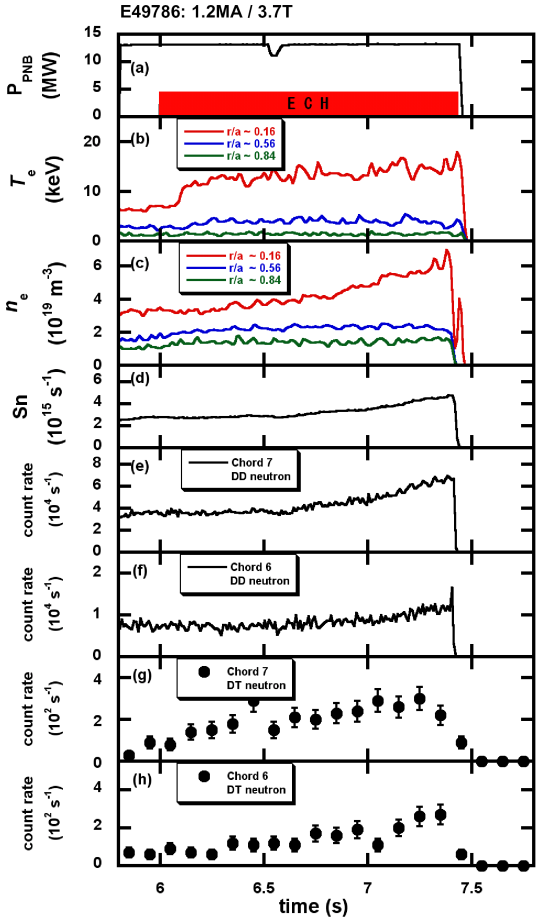

Fig.5 The time evolution of: (a) input power of PNB and ECH, (b) electron temperature, (c) electron density, (d) total neutron emission rate measured by a fission chamber, (e) count rate of DD neutron in chord 7 which views the core region of plasma, (f) count rate of DD neutron in chord 6 viewing the edge region, (g) count rate of DT neutron in chord 7 and (h) count rate of DT neutron in chord 6.

The DT neutron emission showed the different time evolution in each chord. In chord 7, the count rate of DT increased more than a factor 3 after ITB formation. The DT emission rate in every chord changed time to time more the statictics, and it was less steady than the DD emission. In general the time response of DT neutrons is delayed by the slowing down time, typically over 1 second in the present case, and therefore it is affected by the change of diffusion, MHD instability, stochasity and so on [7]. In the present case, the change of classical diffusion can be excluded because the typical deflection time is longer than 1second. Further analysis of discharges and the study of relation with various parameters are needed.

4. Summary

A digital-signal processing (DSP) system was applied to every neutron detector of the neutron profile monitor of JT-60U. A double n-γ discrimination mapping method of DSP data analysis was developed, where a new 2D map in a fast-slow space normalized with total was introduced. By using this system, DT neutrons were measured as well as DD neutrons in the DD plasma simultaneously with a same detector. The time evolution of DT neutron was obtained for all chords.

DD neutron emission rate in central chord increased more than that in the chord viewing the edge region after appearance of the ITB. The time evolution of DT neutron showed the difference for each chord, which can nor be explained by the classical energetic ion diffusion.

Acknowledgments

The authors would like to express their appreciation to the JT-60U team for their contribution to operate and the experiments of JT-60U. This work was performed partially under support of a Grant-in-Aid from the Ministry of Education, Culture, Sports, Science, and Technology of Japan, “Priority area of Advanced Burning Plasma Diagnostics”

References

[1] M. Sasao, et al., Fusion Sci.& Tech. **53**, 604-639 (2008).

[2] M. Ishikawa, T. Nishitani, A. Morioka, M. Takechi, K. Shinohara, M. Shimada, Y. Miura, M. Nagami, Rev. Sci, Instrum. **73**, 4237 (2002).

[3] M. Ishikawa, T. Itoga, T. Okuji, M. Nakhostin, K. Shinohara, T. Hayashi, A. Sukegawa, M. Baba, T. Nishitani, Rev. Sci. Instrum.**77**, 10E706 (2006).

[4] M. Ishikawa, M. Takechi, K. Shinohara, C.Z. Cheng, G. Matsunaga, Y. Kusama, A. Fukuyama, T. Nishitani, A. Morioka, M. Sasao, M. Baba and JT-60 team, Nucl. Fusion, **47**(8), 849-855 (2007).

[5] T. Itoga, M. Ishikawa, M. Baba, T. Okuji, T. Onishi, M. Nakhostin and T. Nishitani, Radiat. Prot. Dosimetry, **126**, 380 (2007).

[6] K. Shinohara, T. Okuji, M. Ishikawa, M. Baba and T. Itoga, Rev. Sci. Instrum., **79**, 10E509 (2008).

[7] W. W. Heidbrink, G. J. Sadler, Nucl. Fusion, **34**(4), 535-615 (1994).

Proceedings of ITC18, 2008

Radiation measurement in Heliotron J by using an AXUV photodiode array with multiple optical filters

S. Watanabe, K. Nagasaki [a], Y. Kowada, T. Mizuuchi [a], H. Nishio [b], H. Okada [a], S. Kobayashi [a], S. Yamamoto [a], N. Tamura [c], C. Suzuki [c], K. Mukai, K. Hosaka, S. Mihara, H. Y. Lee, Y. Takabatake, S. Kishi, S. Konoshima [a], K. Kondo, F. Sano [a]

Graduate School of Energy Science, Kyoto University, Gokasho, Uji, Kyoto 611-0011, Japan

[a] Institute of Advanced Energy, Kyoto University, Gokasho, Uji, Kyoto 611-0011, Japan

[b] Department of Electronic Science and Engineering, Kyoto University, Kyoto, 606-8501, Japan

[c] National Institute for Fusion Science,322-6 Oroshi-cho, Toki 509-5292, Japan

The characteristics of spectrally-resolved plasma radiation with several heating methods have been investigated in Heliotron J by using an absolute extreme ultraviolet photodiode (AXUVD) array with multi-optical filters. Utilization of the multi-optical filters makes it possible to study the radiation characteristics separately in different photon energy ranges. For ECH and ECH+ICH plasmas at the density of 0.3-0.4×$10^{19}$$m^{-3}$, the radiation in the energy range of 20~70eV is dominant near the edge (ρ~0.6-0.8) region. The radiation increase in this energy range cased by the superposition of ICH to ECH qualitatively agrees with the increase of line emission from impurities such as C, O, Fe and Ti. For NBI plasma, the chord-integrated radiation for the photon energy ranges of ≥200eV is more concentrated in the core region compared to that in ECH plasma. Comparison of different filtered data suggests that the radiation in the photon energy range of ~500eV is important for NBI plasmas.

Keywords: Heliotron J, AXUVD, radiation measurement, radiation profile, spectrally-resolved measurement

1. Introduction

Radiation from magnetically confined toroidal plasmas plays an important role in a power balance of the plasma and affects the accessible density limit. In order to investigate the radiation loss from the plasma, metal-foil bolometers and/or silicon photodiodes have been used in various fusion plasma experiments. Recently a wide-band silicon p-n junction photodiode has been developed by IRD, Inc., which is referred to as the absolute extreme ultraviolet photodiodes (AXUVD) [1]. AXUVD can measure the photon from visible to x-ray region (1.127eV to 100keV) due to the absence of a doped surface dead-region and zero surface recombination [1]. Other advantages of AXUVD are (1) fast time response and (2) insensitivity to long wavelength radiation like microwaves from the electron cyclotron heating system and (3) insensitivity to low-energy (< 500 eV) neutral particles. Since the intensity of radiation from plasma depends on the photon energy (or wave-length) range, the energy spectrum must be studied for detailed investigation of the radiation characteristics. In order to measure the radiation in the vacuum ultraviolet (VUV) and soft X-ray region, a filtered AXUVD has been utilized [2, 3] .

Recently an AXUD array system with multiple foil filters has been installed on Heliotron J. By using the filters the characteristics of radiation can be studied separately in the photon energy ranges. In this paper, we describe the characteristics of spectrally-resolved radiation from plasmas heated by different heating methods in Heliotron J.

author's e-mail: w.shinya@center.iae.kyoto-u.ac.jp

2. AXUVD array system for Heliotron J

Heliotron J is a medium-sized helical-axis heliotron device (<R_0> = 1.2 m, a = 0.1-0.2 m, B_0 < 1.5 T) with a low magnetic shear [4]. For plasma production and heating, second-harmonic X-mode ECH (70 GHz, 0.4 MW) [5], ICH (19-23.2 MHz, 0.6 MW) [6] and two tangential NBI (0.7 MW/beam-line, 30 kV H^0-beam) [7] are applied.

Figure 1 shows the design of the AXUVD-array system. An aluminum plate of thickness 50 μm^t with a slit of 0.4mm × 5mm is set in front of an AXUVD-array (AXUV16ELO/G, IRD, Inc.). The distance from the diode to the slit is 30 mm. The AXUVD array is set at a bottom port of Heliotron J and views the whole poloidal cross section as shown in Fig. 2. The viewing area of the center chord (ch-8) of the array, which views the plasma center, is 32mm × 146mm on the equatorial plane. The solid angle for this case is ~1×10^{-5} sr. The diode current I is described by Eq. (1),

$$\frac{I}{S_{res}T_{trans}} = \int\int_{S_{obs}} \varepsilon \cdot \frac{\Omega}{4\pi} dSdl \qquad (1).$$

Here S_{res} is the spectral responsivity in the diode, T_{trans} is

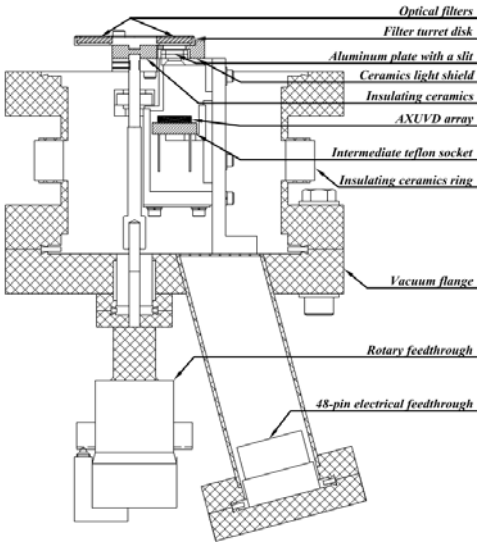

FIG. 1 The design of the AXUVD system.

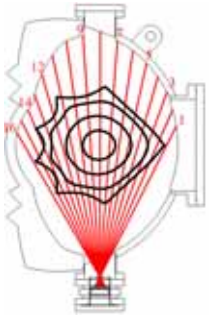

FIG. 2 The lines of sight of the AXUVD system (red) and magnetic flux surfaces (black).

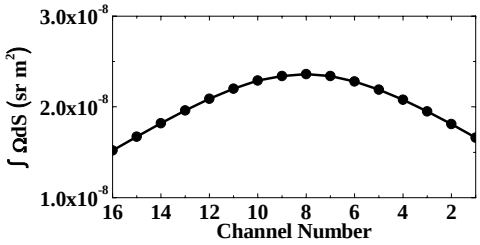

FIG. 3 Surface integral solid angle at each channel.

the transmittance of the optical filter, ε is the emissivity, S_{obs} is the observation area and Ω is the solid angle for a small area of S_{obs}, dS. Assuming that ε is constant on S_{obs}, the right part of Eq. (1) can be described by $\int \varepsilon \int \Omega dS dl$. When the distance from plasma to the diode is sufficiently longer than that from the slit to the diode, $\int \Omega dS$ can be assumed to be constant along a line of sight. The value of $\int \Omega dS$ at each channel is estimated as shown in Fig. 3. Then the $\int \varepsilon dl$ can be obtained from the observed diode current by using Eq. (1).

As a filter system, two aluminum foils with thickness of 1.0μm^t and 0.2μm^t (tolerance ±10%), an interference filter (Al/LiF/Parylene) are mounted on a turret disk, located in front of the slit plane. The Al foils and the interference filter are supported by copper mesh

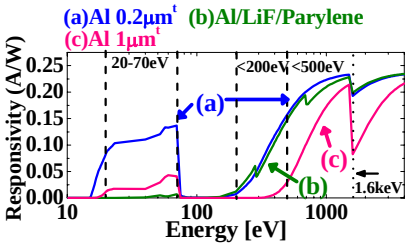

FIG. 4 Spectral responsivity of AXUVD with optical filters.

(a pitch of 360μm, a mesh bar size of 19μm). The transmittance of the mesh can be estimated to be about 86% in the interesting energy range.

Figure 4 shows the spectral responsivities of the AXUVD with each filter, which are estimated by using the catalog data [8]. The application of the multi-optical filters makes it possible to estimate the radiated power in several separate photon energy ranges. The applications of the Al/LiF/Parylene and Al 1μm^t filters can limit the effective sensitive photon energy range to ≥200eV and ≥500eV, respectively. Here, we set the lowest limit of the sensitive photon energy range as 10% of the maximum responsivity (~0.24A/W). On the other hand, the radiation in the photon energy band of 20~70eV can be estimated by subtracting the data measured with the Al 0.2μm^t filter from those measured with Al/LiF/Parylene filter for identical discharges.

3. Radiation characteristics under different heating scenarios

3.1 ECH+ICH plasma

Measurement of radiation for photon energy ranges of ≥500eV and 20~70eV has been carried out for ECH plasma with the line-averaged density of 0.3-0.4×10^{19}m^{-3} for the standard (STD) Heliotron J configuration. In this experiment, a pulse of ICH (~0.3MW) is superposed on the ECH (~0.35MW) plasma.

Figure 5 shows an example of the time evolution of the line averaged density, $\bar{n}_e$, and the intensity of the AXUVD signals at center chord (ch-8), I_{AXUV}(ch-8), for

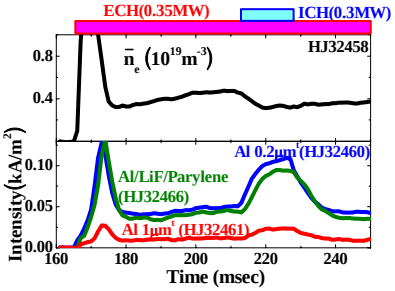

FIG. 5 Time evolution of the density and AXUV signals with different optical filters. An ICH pulse is superposed on ECH plasma during 213- 228ms.

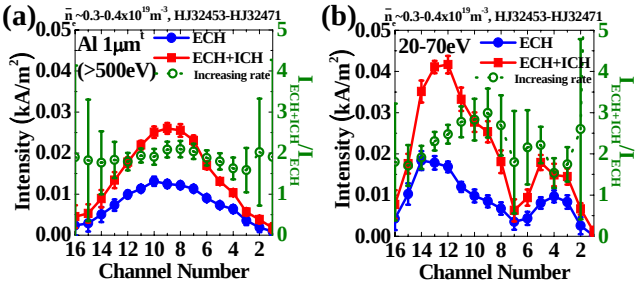

FIG. 6 The chord integral profiles of radiation in AXUVD with (a) 1μm^t -Al filter and (b) estimated energy of 20~70eV on ECH and ECH+ICH plasmas.

three filters cases. The signal intensity is increased for all the cases by the superposition of ICH, while $\bar{n}_e$ is decreased slightly.

Figure 6 shows the chord-integrated profiles of the radiation for the photon energy range of (a) ≥500eV and (b) 20~70eV. In the ECH plasma, the observed profile suggests that the radiation for the photon energy range of ≥500eV is dominant near the plasma core, and that the radiation in the energy range of 20~70eV is dominant at the edge chords which are tangent to the surface near ρ~0.6-0.8 (chs-4, 13).

In the ECH+ICH phase, the signal intensity in each photon energy range is increased compared to those at the ECH-only phase. The ratio of I_{AXUV} at ECH+ICH phase to I_{AXUV} at ECH-only phase is also plotted in Figs. 6 (a) and (b). The increase ratios of the total intensities for the energy range of ≥500eV and 20~70eV are about factors of 1.9 and 2.2, respectively. During the ICH superposition phase, it is observed that the line emission from impurities such as O, C, Ti and Fe are increased. Figure 7 shows the VUV spectra measured with a VUV polychoromator for the ECH-only and ECH+ICH phases. Here, the observed wave-length range corresponds to the photon energy range of 32-73eV. This suggests that the increase of the line emission from the impurities might contribute to the increase of the radiation in the photon energy range of 20~70eV.

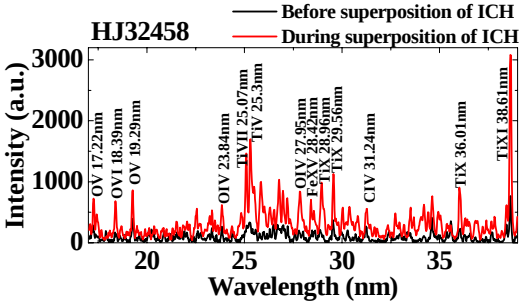

FIG. 7 VUV spectra in the range of 17-39nm (32-73eV) before and during the superposition of ICH to ECH plasma.

3.2 NBI plasma

The difference of radiation characteristics between ECH (~0.35MW) and NBI (~0.35MW) plasmas has been investigated at the density of 0.9×10^{19}m^{-3} under the STD configuration.

Figure 8 shows the time evolution of $\bar{n}_e$, the stored energy (W_p), I_{AXUV}(ch-8) with the 1μm^t-Al foil. The density and the stored energy increase after NBI and reach their maxima around t=200-210ms and then are kept almost constant. On the other hand, I_{AXUV}(8ch) increases until t~220ms and then it keeps a slightly lower level.

Figure 9 shows the difference in the I_{AXUV} profiles between ECH and NBI plasmas for the photon energy range of ≥200eV and ≥500eV. Here the time-averaged data at t=230-250ms (the hatched phase in Fig. 8) are plotted. The I_{AXUV} profile in NBI plasma is centrally peaked compared to that in ECH plasma for both the energy ranges. The value of I_{AXUV} (ch-8) is about five times higher than that for ECH plasma, while I_{AXUV} at ch-(1-5) and ch-(11-16) which correspond to ρ>0.5 is almost the same for both the ECH and NBI plasmas. The peaking factor of I_{AXUV} profiles, which is defined as the ratio of I_{AXUV}(ch-8) to the total intensity for all channels, is also plotted in Fig. 8. It is shown that the peaking factor also continue to increase until t~220ms and then is kept almost constant.

The total intensity in the photon energy range of

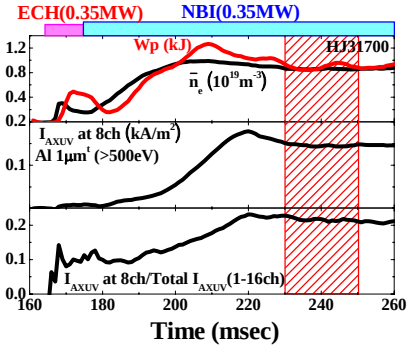

FIG. 8 Time evolution of $\bar{n}_e$, Wp, I_{AXUV} (ch-8) with 1μm^t-Al filter and the peaking factor of the chord-integral radiation profile for NBI plasma.

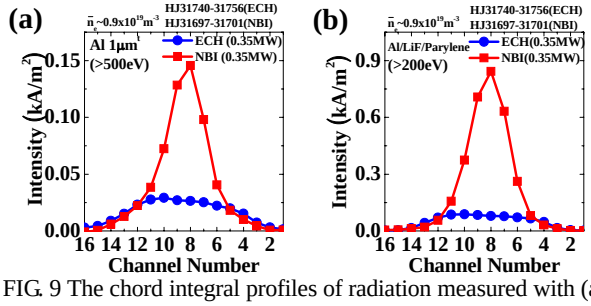

FIG. 9 The chord integral profiles of radiation measured with (a) 1μm^t-Al and (b) Al/LiF/Parylene filters on ECH and NBI plasmas.

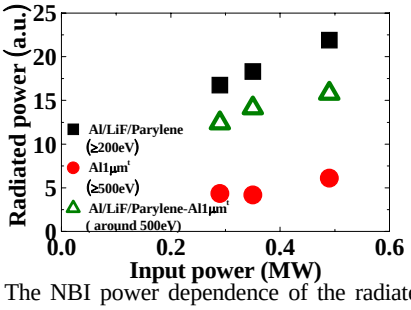

FIG. 10 The NBI power dependence of the radiated power measured with 1μm^t-Al and with Al/LiF/Parylene filters by using averaged sensitivity.

≥500eV is about 2 twice higher for NBI plasmas compared to that for ECH plasma, while that in the energy range of ≥200eV is about 4 times higher than that for ECH plasmas. On the other hand, the total intensity for all channels with Al/LiF/Parylene filter in NBI plasmas is about 5 times higher than that with the 1μm^t-Al foil.

A difference of spectral responsivity between with Al 1μm^t and with Al/LiF/Parylene filters arises in the photon energy ranges of ~500eV and ~1.6keV as shown in Fig.3. It is considered, however, that the difference of spectral responsivity in the energy range of ~1.6keV is not be important for this NBI data set since the pulse height analysis of the soft X-ray data for these plasmas indicate that the number of photons in the energy of ≥1.6keV is a few orders smaller than that in the energy of ≤1keV. In order to discuss the relative radiated power between different photon energy ranges, we estimate the "averaged sensitivity" for each sensitive energy range by averaging the spectral responsivity over the sensitive photon energy range; the averaged responsivity with Al/LiF/Parylene and Al-1μm^t filters are 0.18A/W (200eV~1.5keV) and 0.15A/W (500eV~1.5keV), respectively.

Figure 10 shows the NBI power dependences of the total intensity for the data observed with 1μm^t-Al and with Al/LiF/Parylene filters. The intensity is corrected by using the averaged sensitivity. The intensity increases with the NBI power. The intensity observed with the Al/LiF/Parylene filter (square symbol) is about 3-5 times higher than that observed with 1μm^t-Al filter (circle symbol) for this NBI power range. Since the difference of the intensity come from the difference in the spectral responsivity shown in Fig. 3, the observation mentioned above suggests that the radiation from NBI plasmas might be dominated by that around 500eV.

4. Summary

The characteristics of spectrally-resolved radiation have been investigated for ECH, ECH+ICH and NBI plasmas in Heliotron J by using AXUVD array with multi-optical filters. Utilization of the multi-optical filters makes it possible to study the radiation characteristics separately in different photon energy ranges.

For ECH and ECH+ICH plasmas at the density of $0.3\text{-}0.4\times10^{19}$m^{-3}, the radiation in the photon energy range of 20~70eV is dominant near the edge (ρ~0.6-0.8) region. It is somewhat consistent with a general picture of the high temperature plasma radiation that the hollow profile with a large peak near the boundary consists of the low energy photons. The superposition of ICH to ECH plasma increases the radiation in the two photon energy ranges (20~70eV and >500eV). The increase in the 20-70eV range qualitatively agrees with the increase of line emission observed with the VUV policrometer from impurities such as C, O, Fe and Ti.

For NBI plasma, the I_{AXUV} profile is highly peaked compared to that in ECH plasma for the photon energy ranges of >200eV. The comparison of the data measured with 1μm^t-Al to those with Al/LiF/Parylene filters suggests that the radiation from NBI plasmas might be dominated by the photons with the energy range around 500eV. Although the source of the radiation increase has not been identified yet, the results indicate the importance of the radiated power in this energy range for the power balance analysis in the NBI plasmas.

The energy-resolved radiation monitor described in this paper would provide important information in plasma operation. An optical filter for the radiation of lower energy (<20eV) will be set up in the next experimental campaign in order to extend the photon energy region.

Acknowledgements

The authors are grateful to the Heliotron J team for their excellent arrangement of the experiments. This work was partly supported by NIFS/NINS under the NIFS Collaborative Research Program (NIFS04KUHL005, NIFS07KUHL014).

References

[1] Korde R et al., Metrologia **40** S145-S149 (2003)

[2] Gray DS et al., Rev. Sci. Insutrum. **75** 376 (2004)

[3] Suzuki C et al., Rev. Sci. Insutrum. **75** 4142 (2004)

[4] Obiki T et al., Nucl. Fusion. **41** 833 (1999)

[5] H. Shidara et al., Fusion Sci. Technol. **45**, 41 (2004)

[6] H. Okada et al., Nucl. Fusion **47** 1346 (2007)

[7] S. Kobayashi et al., 34th European Physical Society Conference on Plasma Physics, **P4-162** (2007)

[8] http://www.ird-inc.com/

Proceedings of ITC18, 2008

Extension of the energy-resolved soft X-ray imaging system using two CCD cameras in LHD

Chihiro SUZUKI, Katsumi IDA, Mikirou YOSHINUMA and LHD Experimental Group

National Institute for Fusion Science, 322-6 Oroshi-cho, Toki 509-5292, Japan

An existing imaging system using a soft X-ray CCD (Charge Coupled Device) camera and beryllium (Be) filters installed to a tangential viewport of the Large Helical Device (LHD) has been utilized not only for the measurement of the flux surface shape, but also for the energy resolved imaging in long pulse discharges. In order to obtain simultaneously soft X-ray energy spectra necessary for the analyses of the imaging results, we have extended the present diagnostic system by adding another soft X-ray CCD camera mainly used for the photon counting mode. This new camera has been installed in a vertical viewport and equipped with two mounting disks rotating independently. This setup enables us to choose any combination of Be filter thickness and slit width according to the amount of photon flux, and it can be combined with the kinetic mode operation if temporal resolution is the first priority. The details and capability of the simultaneous measurements of the soft X-ray images and energy spectra are described.

Keywords: soft X-ray, CCD camera, imaging, photon counting, energy spectrum, LHD

1. Introduction

Soft X-ray imaging technique using a CCD (Charge Coupled Device) camera sensitive directly to soft X-ray photons has ever been applied to the diagnostics of magnetically confined high temperature plasmas [1, 2, 3, 4]. In the Large Helical Device (LHD) experiment, an imaging system using the soft X-ray CCD camera and beryllium (Be) filters has already been installed to a tangential viewport. This existing system is mainly utilized for the measurement of flux surface shape, especially the derivation of the magnetic axis shift (Shafranov shift) from the fitting of the pre-calculated equilibria to the measured soft X-ray profile assuming that the emissivity profile could be expressed by Fourier-Bessel expansion [3].

On the other hand, information on a soft X-ray energy spectrum is often necessary for further analyses of recent experimental results of the soft X-ray imaging. In the analysis of the energy resolved soft X-ray imaging demonstrated recently [5], for example, the evaluation of the contribution of K_α spectral lines from impurity ions to the measured signal intensity is important especially in higher energy range. Another example is hollow soft X-ray emissivity profiles often observed in high ion temperature discharges together with the formation of carbon impurity hole. Since this phenomenon is considered to be closely related to impurity transport, it is important to determine which impurity line or continuum radiation dominantly contributes to the observed hollow soft X-ray profile. Therefore it would be helpful for further discussions on the results of the imaging if soft X-ray energy spectra are measured simultaneously.

CCD cameras can also be utilized for the measurements of soft X-ray energy spectra by operating them in photon counting mode [1, 2]. Furthermore, spatial and energy resolutions of this method are expected to be better than those of conventional X-ray pulse height analyzer (PHA). Therefore we are planning to extend the existing system by adding another soft X-ray CCD camera mainly used for the photon counting mode. The arrangements of the sights of the two cameras are illustrated in Fig. 1, where a top view of horizontal cross section at the equatorial plane and a vertical cross section are drawn. The existing and new cameras have been installed in tangential and vertical viewports, respectively. The details and capability of the measurements of the soft X-ray images and energy spectra by the two cameras are described in this article.

author's e-mail: csuzuki@lhd.nifs.ac.jp

2. Recent imaging results

As mentioned in the previous section, two examples which indicate the importance of soft X-ray energy spectra are found in the recent imaging results obtained by the existing camera. These results are reviewed in this section. Since the details of the existing system have already been published elsewhere [5], only a brief explanation is given here. The system consists of a soft X-ray CCD camera (Andor Technology, DO435-BV) together with a pinhole, a pneumatic mechanical shutter, and a remotely rotatable filter disk which mounts eight Be filters. The quantum efficiency curve of the CCD chip ranges roughly from 1 to 10 keV. In order to adjust cutoff energy of photons, filter thickness is selectable from 50–1650 μm. The camera is equipped with a back illuminated CCD chip of frame transfer type of which image area is 13.3×13.3 mm^2 composed of 1024×1024 pixels. The output of the CCD camera is

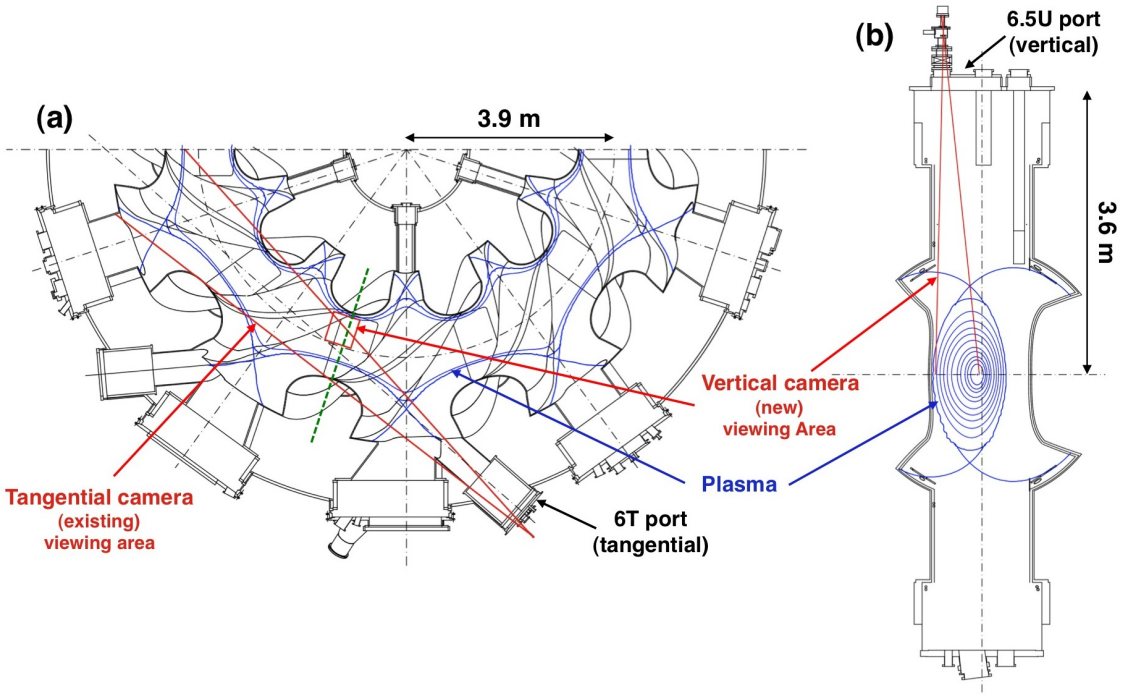

Fig. 1 Arrangement of the viewing areas of the existing and new soft X-ray CCD cameras. (a) Top view of horizontal cross section at the equatorial plane and (b) vertical cross section at the green broken line in (a) are drawn. The existing and new cameras have been installed in the tangential (6T) and the vertical (6.5L) viewports, respectively.

read out by a 1 MHz analog-to-digital (A/D) converter with a resolution of 16 bit. The total readout time is about 0.6 s for 2×2 pixel binning. The diameter of the pinhole can also be chosen out of 0.05, 0.1, 0.2 and 0.4 mm.

The differential images of specific photon energy range obtained in the energy resolved soft X-ray imaging have also been reported in ref. [5]. The measurement has been carried out by changing the Be filter thickness during a long pulse discharge sustained for several minutes [6] whose electron density and temperature are of the order of 10^{19} m^{-3} and 1 keV, respectively. Eight two-dimensional images with different cutoff energies are measured by rotating a filter disk. Assuming continuum radiation and spatially uniform effective charge, it can possibly be applied to the measurements of line-averaged effective electron temperature and change in soft X-ray profile due to locally distorted electron energy distribution. However, if the measured soft X-ray emissivity contains not only the continuum but also K_α spectral lines from impurity ions, they would affect the signal intensity especially in higher energy range. Therefore the simultaneous measurement of the soft X-ray energy spectra would be helpful for further discussions.

Another example of the recent results is given in Fig. 2 which shows tangential soft X-ray images in a high ion temperature discharge accompanied by the formation of carbon impurity hole. The soft X-ray emissivity profile suddenly changes from peaked one to hollow one when the formation of carbon impurity hole (around 2.25 s) is observed in charge exchange spectroscopy [7]. Since the filter thickness is 450 μm corresponding to a cutoff energy of about 4 keV, K_α lines from titanium (4.8 keV), chromium (5.7 keV) and iron (6.6 keV) would possibly contribute to the measured intensity together with the continuum radiation due to bremsstrahlung. Since this phenomenon is considered to be closely related to impurity transport, it is important to determine which impurity line or continuum radiation dominantly contributes to the observed hollow soft X-ray profile.

3. Energy calibration

As described previously, CCD cameras can also be utilized for the measurements of soft X-ray energy spectra by counting pulse heights in the photon counting mode. We have prepared another soft X-ray CCD camera (Andor Technology, DO432-FI) for this purpose. The camera is equipped with a front illuminated CCD chip of which image area is 28.1×25.9 mm^2 composed of 1250×1152 pixels. Before the installation of this camera, energy sensitivity and resolution were evaluated by the calibration using standard X-ray sources. Radiations from the X-ray sources of Fe^{55}, Am^{241}, and Cd^{109} were measured repeatedly by this camera in the photon counting mode with an appropriate integration time. The results of this procedure are summarized in Fig. 3.

Figure 3 (a) shows the histogram of the CCD signal counts generated by individual incoming photons, which

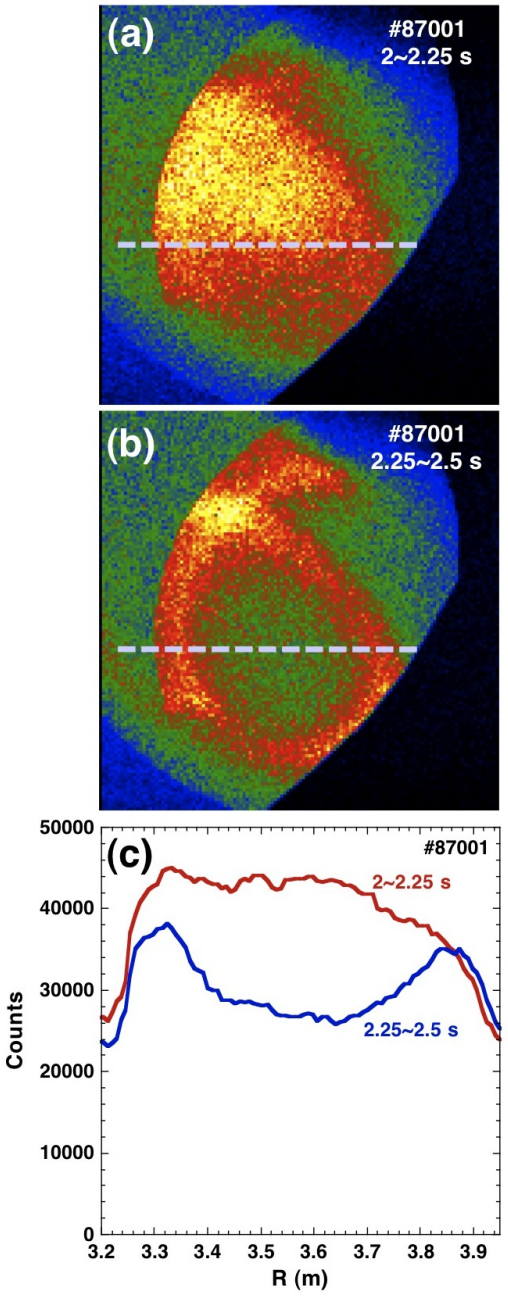

Fig. 2 An example of soft X-ray emissivity profile in a high ion temperature discharge with the formation of carbon impurity hole. The profile suddenly changes from (a) peaked one to (b) hollow one around 2.25 s when the formation of carbon impurity hole is observed in the charge exchange spectroscopy measurement. The change in the horizontal profile along the broken lines indicated in (a) and (b) is drawn in (c). The thickness of the Be filter is 450 μm.

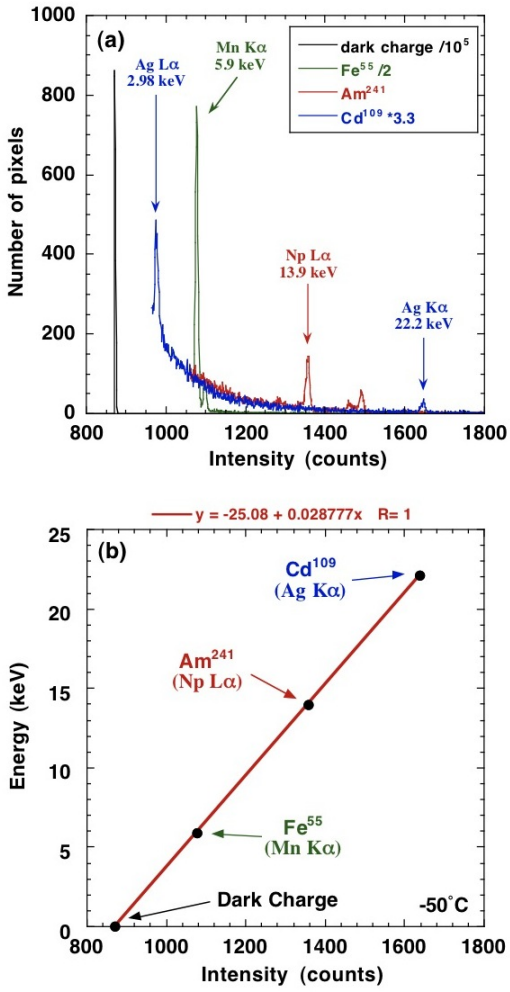

Fig. 3 Calibration of energy sensitivity and resolution of the new soft X-ray CCD camera. (a) Energy spectra obtained by several standard X-ray sources. (b) Plot of photon energy versus CCD count to obtain energy sensitivity from the slope.

corresponds to the energy spectra since the generated charges are proportional to the incoming X-ray photon energy in the photon counting mode. Several sharp peaks of K_α and L_α lines corresponding to the characteristic X-rays of known energies are clearly observed. The highest peak around 870 counts (indicated by a black line) is not from the X-ray, but is due to the dark charge of the CCD chip. As a result, a relation between the X-ray energy and the signal intensity (in counts) is derived as shown in Fig. 3 (b).

The energy resolution is evaluated to be 230 eV at the photon energy of 5.9 keV from the width of the spectral line. This value is better than that of conventional X-ray PHA. The sensitivity evaluated from the linear slope of Fig. 3 (b) is 29 eV/count. These results indicate that the energy resolution and sensitivity of this camera is good enough as an alternative way to measure the soft X-ray energy spectra.

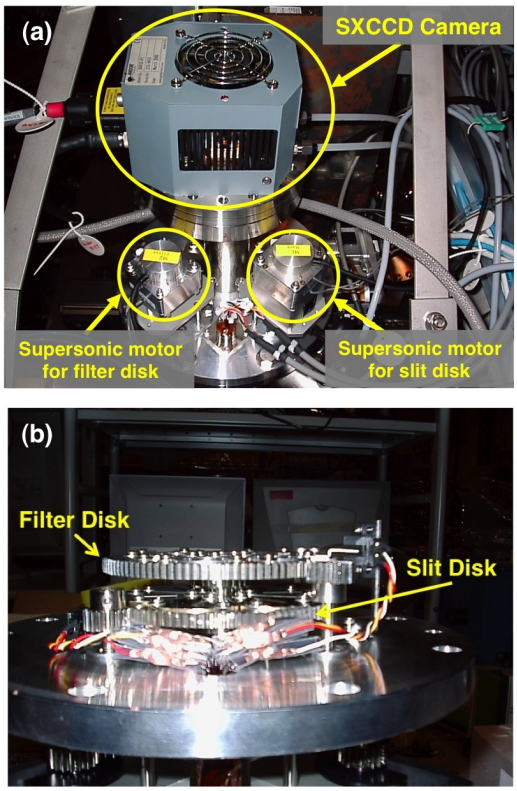

Fig. 4 Photographs of the installation of the new soft X-ray CCD camera system. (a) Installed CCD camera and two supersonic motors. (b) Filter and slit disks installed in front of the camera.

4. Installation of new CCD camera

Though the setup of the newly added system is basically similar to the existing one, it has been installed in the upper viewport as shown in Fig. 1. A photograph of the installed CCD camera and supersonic motors for the mounting disks are shown in Fig. 4 (a). The specification of the A/D converter and pinhole are the same as those of the existing CCD camera. A unique feature of this system is that two mounting disks which rotate independently are equipped in front of the camera as shown in Fig. 4 (b). Be filters are mounted on the first disk to control the cutoff energy, while several slits with various widths are attached to the second disk so as to limit the photon illumination to the top rows of the CCD chip. The slits are used in the kinetic mode operation of the CCD if temporal resolution is the first priority. Namely, images are exposed only on a part of rows at the top of the CCD array and other rows are masked for temporary storage by using a slit. Time resolution (minimum frame rate) in this mode is determined by the vertical shift speed of charges, which is much faster than that in the normal acquisition mode. The fast kinetics mode combined with the photon counting mode can be applied to the one-dimensional electron temperature measurement.

5. Summary and prospects

The importance of information on soft X-ray energy spectra has been revealed in the analyses of the recent imaging results of the diagnostic system using a soft X-ray CCD camera and Be filters in LHD. In order to obtain soft X-ray energy spectra, we have extended the existing diagnostic system by adding another soft X-ray CCD camera mainly used for the photon counting mode, and installed it in a vertical port of LHD. The high sensitivity and energy resolution of the new camera is expected according to the calibration using X-ray sources. Two independently rotating disks for Be filters and slits allow us flexible control of photon flux on the CCD chip. They can be combined with the kinetic mode operation if temporal resolution is the first priority.

In the near future, algorithms for the photon counting mode from the CCD readout will be prepared. After the complete installation of the new camera, the effect of line emissions from impurities will be studied during the next experiment. Finally, this extended diagnostic system will be applied in the future to the trial of the detection of difference in two-dimensional soft X-ray image by energy range caused by local generation of non-Maxwellian electrons in a stable long pulse discharge by electron cyclotron resonance heating (ECRH).

Acknowledgments

This work has been partly supported by a grant-in-aid for scientific research from MEXT. This work was carried out under budget code NIFS08ULPP544.

[1] Y. Liang, K. Ida, S. Kado, I. Nomura and T. Minami, Rev. Sci. Instrum. **71**, 3711 (2000).
[2] Y. Liang, K. Ida, S. Kado, T. Minami, S. Okamura, I. Nomura, K. Y. Watanabe, H. Yamada, CHS Group and LHD Group, Rev. Sci. Instrum. **72**, 717 (2001).
[3] Y. Liang *et al.*, Plasma Phys. Control. Fusion **44**, 1383 (2002).
[4] T. Kobuchi, K. Ida, H. Yamada, M. Yokoyama, K. Y. Watanabe, S. Sakakibara, M. Yoshinuma, and the LHD Experimental Group, Plasma Phys. Control. Fusion **48**, 789 (2006).
[5] C. Suzuki, K. Ida, T. Kobuchi, M. Yoshinuma, Rev. Sci. Instrum. **79**, 10E929 (2008).
[6] R. Kumazawa *et al.*, Nucl. Fusion, **46**, S13 (2006).
[7] M. Yoshinuma *et al.*, this conference.

Proceedings of ITC18,2008

Toroidal flow velocity profile of an impurity ion in a Field-Reversed Configuration plasma

Tatsuya Ikeda, Toshiki Takahashi, Tomohiko Asai[a], Tsutomu Takahashi[a]

Department of Electronic Engineering, Gunma University, kiryu 376-8515, Japan

[a]College of Science and Technology, Nihon University, Tokyo 101-8308, Japan

Particle orbits of impurity ions are calculated to estimate their toroidal flow velocity. If the impurity ion flow differs from the ion flow, the Doppler shift measurement of impurity spectra requires a suitable modification of experimental results. At the field-null, the carbon ion flow coincides with the deuterium ion flow due to the friction force between them. At the separatrix, however, impurity and plasma ions have their own flow velocities. It is found that the diamagnetic drift that is dependent on the charge and mass of each fluid species dominates the toroidal flow velocity.

Keywords: field-reversed configuration, toroidal flow velocity, Doppler shift measurement, orbit calculation, resistive flux decay

1. Introduction

The rotational instability with the toroidal mode number n=2 limits the lifetime of field-reversed configuration (FRC) plasmas [1, 2]. Several works showed application of external multipole fields suppresses time variation of the line-integrated electron density [3, 4]. These experiments reveal elliptical deformation of FRC plasmas is inhibited by multipole fields. Internal structure, on the other hand, can be deformed to a complex dumbbell-like shape [5], even when no deformation of the separatrix shape can be found. Therefore, we need to clarify the origin of rotation to prolong the FRC lifetime.

Particle loss [6] and end-shorting [7] are now considered as two most promising mechanisms. Recently, Belova *et al*. claimed that particle loss associated with resistive flux decay may contribute to the rotation [8]. We have shown that the flux decay can contribute directly to the toroidal spin-up [9]. Suppose the FRC plasma is axisymmetric. This assumption is valid until the rotational instability is triggered. In this case, the canonical angular momentum

$$P_\theta = mv_\theta r + q\psi(r,z) \qquad (1)$$

of every particle is conserved, where m, q are the mass and charge, v_θ is the toroidal velocity component, and $\psi(r,z)$ is the poloidal flux function. If the poloidal flux decays due to a resistivity and toroidal axisymmetry is still valid, then

$$m\Delta(v_\theta r) = -q\Delta\psi \ . \qquad (2)$$

Equation (2) shows every ion gains the angular momentum in the ion diamagnetic direction, when the trapped poloidal flux decays. Generally, the separatrix radius decreases during the decay phase. If the guiding center r is also decreased, the toroidal velocity v_θ is further increased. The toroidal velocity for ions is calculated by averaging v_θ .

The toroidal velocity measurement is important to find its time evolution and spatial profile. Conventional method to find flow velocities is the Doppler shift measurement of impurity ion spectra such as C III and C V. If impurity ions rotate with the same velocity as plasma ions, then the Doppler shift measurement offers accurate information of plasma flow. Otherwise we need modification of the experimental result to obtain the rotation velocity.

In the present paper, we study numerically the impurity ion (carbon ion) velocity in an FRC plasma that decays resistively and therefore rotates according to Ref. 9.

2. Numerical Model

Since the discussion above is based on a single-particle picture, we need to confirm a collective effect due to the flux decay. A number of super-particles are traced numerically in the decaying FRC plasma. The poloidal flux decay is reproduced by

$$\frac{\partial\psi}{\partial t} = -r\eta J_\theta \ . \qquad (3)$$

Here, the electric resistivity η equals $A\eta_{\mathrm{cl}}$, where A is the anomaly factor and η_{cl} is the classical resistivity. Note that $\psi > 0$ inside the separatrix region in our paper. The flux lifetime is controlled by the parameter A . By integrating Eq. (3) with use of the Runge-Kutta method, a flux function at a calculation point is found. The

author's e-mail: m08e602@gs.eng.gunma-u.ac.jp

electromagnetic fields are then written by the obtained ψ as

$$\mathbf{B} = \nabla \times \mathbf{A} = \nabla \times \left(\frac{\psi}{r} \mathbf{e}_\theta \right), \quad \mathbf{J} = \frac{1}{\mu_0} \nabla \times \mathbf{B}, \quad \mathbf{E} = \eta \mathbf{J} \,. (4)$$

The plasma and impurity ions (C^{4+}) are traced as super-particles in the field given by Eq. (4). The weight of a super-particle is estimated initially from the Maxwell distribution. The friction term due to collisions is included in the equation of motion. The Pitch angle scattering is simulated with use of a Monte-Carlo method [10]. The density and particle flux of both plasma and impurity ions are calculated by the PIC method [11].

3. Results and Discussion

The orbit of an impurity ion is calculated in a prescribed field given in Eqs. (3) and (4). To compare our results with an FRC experiment, the flux decay time obtained by our calculation is set to be equal to the flux lifetime of the NUCTE (Nihon University Compact Torus Experiment)-III device. As noted before, the flux decay time is controlled by the anomaly factor A.

The time evolution of the trapped flux in the NUCTE-Ⅲ experiment is shown in Fig. 1. The FRC plasma is formed in 0-10 μs. The rotational instability with the toroidal mode number n=2 is caused at 35 μs, and the magnetic configuration collapses. From the end of the formation phase (t=10μs in Fig. 1), therefore the FRC plasma keeps axisymmetry for 25μs; it corresponds to $23 t_{A0}$, where t_{A0} is the Alfvén time $t_{A0} \equiv r_w / v_{A0}$, and $v_{A0} \equiv B_{ex} / \sqrt{\mu_0 m_i n_0}$ (B_{ex} : the initial external magnetic field, m_i : the plasma ion mass, n_0 : the initial density at the field-null). The decrement of the trapped flux for $23 t_{A0}$ is about 0.26 mWb. By controlling the anomaly factor, we obtain the time evolution of the flux shown in Fig. 2, where the decrement of the flux for $23 t_{A0}$ is almost the same as the experimental result.

According to Ref. [9], presence of the resistive flux decay cause rotation of the FRC plasma. The calculated plasma ion density and toroidal velocity profile are shown by the color contour in Figs. 3 and 4. We can see that the plasma ions diffuse out from the separatrix by collisions. As the magnetic flux decays, ions can gain the toroidal momentum near the separatrix. This rotation velocity results from particle loss and the direct effect of flux decay.

The profiles of impurity ion density and flow velocity obtained by our calculation are presented in Figs. 5 and 6. The initial impurity density is set as $10^{-5} n_i$, where n_i is the ion density. We assume the impurity ion temperature is same as the plasma ion temperature, since collisions for thermal equilibrium are frequent in the formation phase.

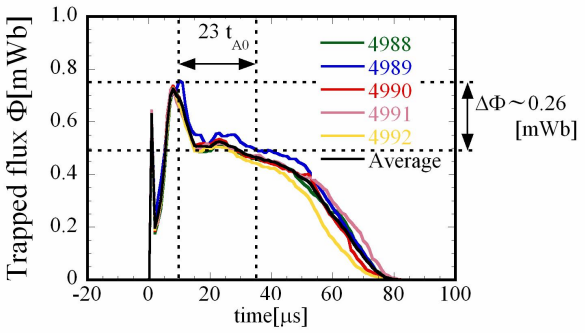

Fig.1 The time evolution of the trapped flux in the experiment that is used NUCTE-Ⅲ.

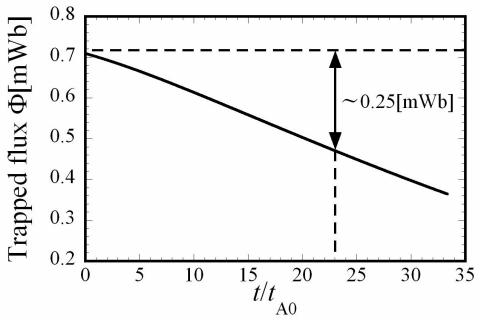

Fig.2 The time evolution of the maximum trapped flux obtained by the numerical calculation.

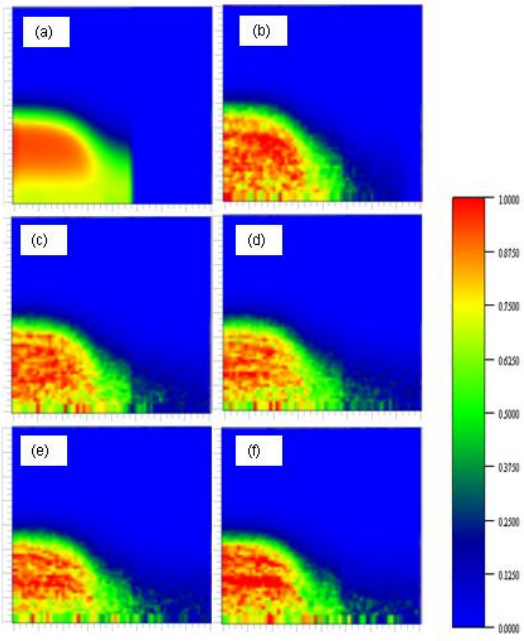

Fig.3 Color contours of the plasma ion density whose values are normalized by the initial density at the field-null. The figures are shown at (a) $t = 0$, (b) $t = 2t_{A0}$, (c) $t = 4t_{A0}$, (d) $t = 6t_{A0}$, (e) $t = 8t_{A0}$, and (f) $t = 10t_{A0}$.

The temperatures of both ions and impurity ions are 124 eV here. It is found that the impurity ions concentrate gradually at the field-null due to the $\mathbf{E}\times\mathbf{B}$ drift. The difference seen in the density profile between plasma and impurity ions results from their collision frequency. We also found the impurity ion density at the separatrix reduced significantly; it cause reduction in the diamagnetic drift velocity of impurity ions. From Fig. 6, we find the toroidal velocity peaks at the field-null point. At the separatrix, on the other hand, the rotation velocity vanishes after $t = 6t_{A0}$. The time evolution of toroidal velocity at the field-null is presented in Fig. 7. Significant time variation of ion velocity is caused by shortage of the number of super-particles. Also, averaged Larmor radius of deuterium ions is larger than the radial mesh interval. To reduce the amplitude of the oscillation, we need more super-particles as deuterium ions. It appears from Fig. 7 that the toroidal velocity of impurity ions follows the time averaged (coarse-grained in time) ion velocity. We can say that the Doppler shift measurement of impurity ion spectra is valid at the field-null point. Contrary to Fig. 7, the separatrix velocity of impurity ions deviates considerably as shown in Fig. 8. Although the ion density gradient is sustained, the impurity ions near the separatrix distributes uniformly. Therefore, the diamagnetic drift velocity reduces for the impurity ions. At the field-null point, the friction force acting on the impurity ion dominates the toroidal velocity, and then the velocity

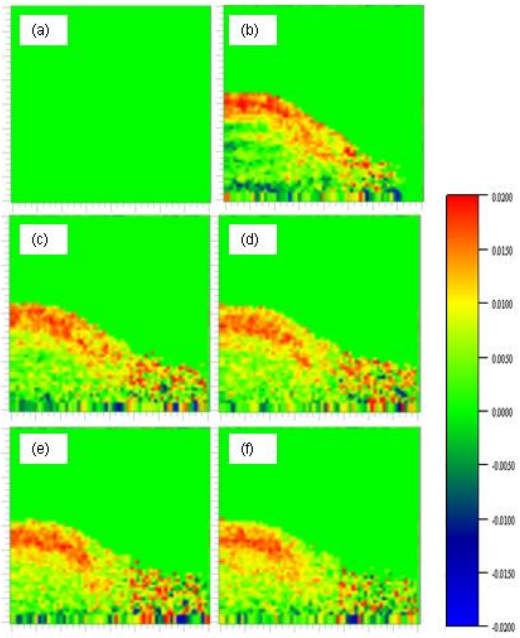

Fig.4 Color contours of the toroidal flow velocity for plasma ions. The velocity is normalized by r_w/τ, where $\tau \equiv m_i r_w^2/(q_i|\psi_w|)$. The output time is the same as Fig. 3.

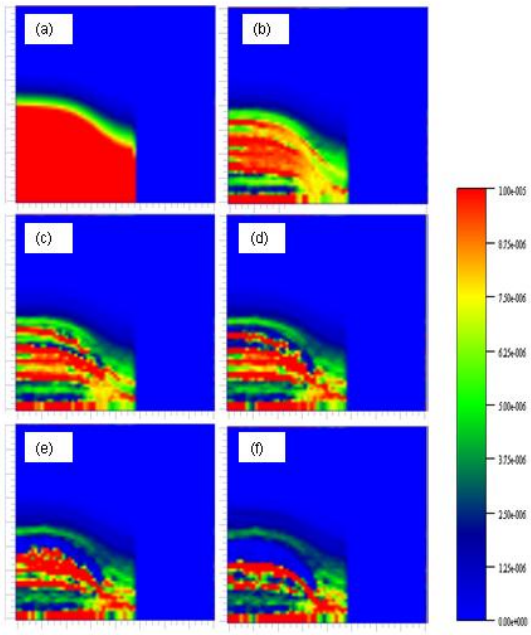

Fig.5 Color contours of the impurity ion density. Figures are shown in the same manner as Fig.

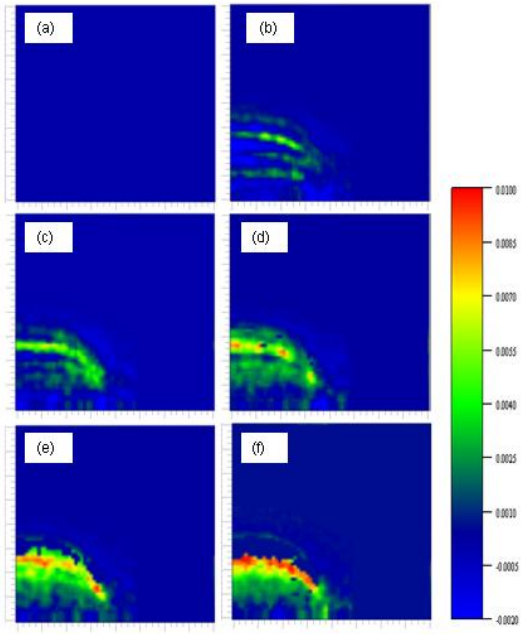

Fig.6 Color contours of the toroidal flow velocity for impurity ions. Figures are shown in the same manner as Fig. 3.

tends to coincide with the plasma velocity. At the separatrix, however, it is not necessary the case that the toroidal friction force results in the toroidal flow because of relatively strong fields.

The toroidal velocity of impurity ions measured by the Doppler shift of the spectral line is shown in Fig. 9.

The line of sight is shifted away from the geometric axis by 4.5 cm; it locates between the field-null and the separatrix. We find the toroidal velocity of the impurity ions is about $0.065 v_{A0}$ after $t = 9 t_{A0}$ from the formation of the FRC plasma. This velocity measured by the experiment sits between the field-null and separatrix flow velocity obtained by our calculation. However, a detailed comparison of the flow profile should be done in a near future. Also, we need to add the electron pressure gradient term in the electric field for a more valid estimation of the impurity flow velocity.

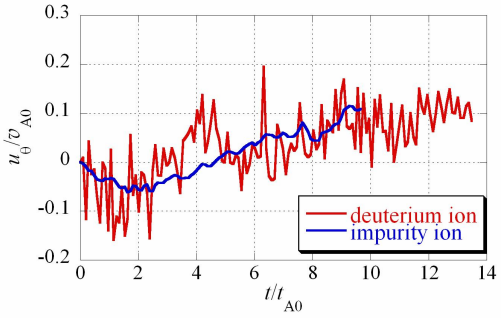

Fig.7 The time evolution of the toroidal velocity at the field-null point for the deuterium ions (the red line) and the impurity ions (the blue line).

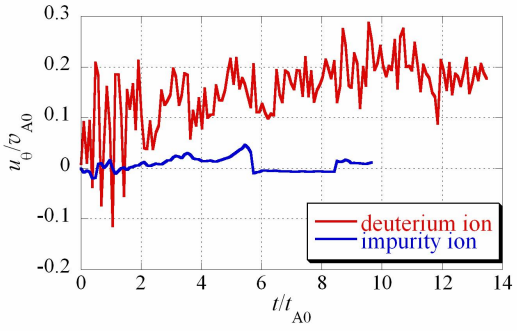

Fig.8 The time evolution of the toroidal velocity at the separatrix and midplane for the deuterium ions (the red line) and the impurity ions (the blue line).

4. Summary

We have calculated numerically orbits of the impurity ions (C^{4+}) to study the difference of the toroidal rotation velocity between impurity and plasma ions in a field-reversed configuration (FRC) plasma. The flux of the FRC plasma decays resistively, and plasma ions gradually gain the toroidal momentum. The impurity ions also spin-up at the field-null point due to the friction force from the plasma ions, and their rotation velocity gives close agreement with the flow velocity of the plasma. The separatrix flow velocity for impurity ions, however, tends to deviate from the plasma ion velocity. Because of a relatively strong field at the separatrix, the friction force between plasma and impurity ions is found to affect little their rotation velocity. Therefore, we consider modification of the Doppler shift measurement is necessary for the toroidal velocity near the separatrix.

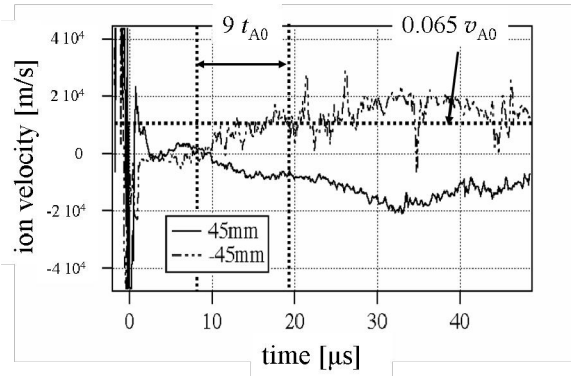

Fig.9 The time evolution of the toroidal velocity of impurity ions that is measured by the Doppler shift measurement.

References

[1] M. Tuszewski, Nucl. Fusion **28**, 2033 (1988).
[2] D. J. Rej et al., Phys. Fluids B **4**, 1909 (1992).
[3] S. Ohi *et al*. Phys. Rev. Lett. **51**, 1042 (1983).
[4] S. Shimamura and Y. Nogi, Fusion Technol. **9**, 69 (1986).
[5] T. Asai *et al*, Phys. Plasmas **13**, 072508 (2006).
[6] D. S. Harned and D. W. Hewett, Nucl. Fusion **24**, 201 (1984).
[7] L. C. Steinhauer, Phys. Plasmas **9**, 3851 (2002).
[8] E. V. Belova *et al*., Nucl. Fusion **46**, 162 (2006).
[9] T. Takahashi *et al*., Plasma Fusion Res. **2**, 002 (2007).
[10] A. H. Boozer and G. K.-Petravic, Phys. Fluids **24**, 851 (1981).
[11] C. K. Birdsall and A. B. Langdon, in *Plasma Physics via Computer Simulation* (Institute of Physics Publishing, Bristol and Philadelphia, 1991).

Proceedings of ITC18, 2008

Development of microwave imaging reflectometry at NIFS

Y. Nagayama[1)], D. Kuwahara[2)], Z. B. Shi[3)], S. Yamaguchi[4)], T. Yoshinaga[1)], S. Iio[2)], S. Sugito[1)], Y. Kogi[5)], and A. Mase[5)]

[1)]*National Institute for Fusion Science, 322-6 Oroshi-cho, Toki 509-5292, Japan*
[2)]*Tokyo Institute of Technology, 2-12-1 Ohokayama, Meguro-ku 152-8550, Japan*
[3)]*The Graduate University for Advanced Studies, 322-6 Oroshi-cho, Toki 509-5292, Japan*
[4)]*Kansai University, 3-3-35 Yamate-cho, Suita 564-8680, Japan*
[5)]*KASTEC, Kyushu University, 6-1 Kasuga Koen, Kasuga 816-8580, Japan*

February 2, 2009

The Microwave Imaging Reflectometry (MIR) is under development at National Institute for Fusion Science (NIFS) in order to observe density fluctuations. The MIR makes a image of cutoff surface on the imaging detector array. The first MIR system, which is installed in the TPE-RX RFP device, uses the 20 GHz wave and the 4×4 plenary Yagi-Uda antenna array. The second MIR system, which is installed in the large helical device (LHD), uses the 60 GHz wave and the 8×5 horn antenna array. Those imaging detectors are newly invented in this research.

1 Introduction

The research object of the National Institute of Natural Sciences (NINS), to which the National Institute for Fusion Science (NIFS) belongs, is science of complex systems. Imaging, such as microscope and telescope, is a strong tool to investigate complex systems, and the NINS has started Imaging Science Project.

In terms of the illumination, imaging is divided by two: one is the ”passive” imaging and another is the ”active” imaging. In the case of the passive imaging, the observer uses only a imaging detector to take a picture with natural illuminations or self radiation from the object. In the case of the active imaging, the observer uses both a imaging detector and a illumination.

One of the most attractive imaging for the magnetically confined fusion plasma is the microwave with the following reasons: (1) The plasma radiates microwave as the electron cyclotron emission (ECE), of which intensity is proportional to the electron temperature; (2) The plasma reflects the microwave at the cutoff electron density. Since different frequencies of ECE or the reflection correspond to different locations, the cross-sectional image can be also observed [1]. As ECE is very sensitive to the variation of the electron temperature, the ECE imaging is very powerful tool to investigate MHD instabilities [2, 3]. As the microwave reflection at the cutoff surface is very sensitive to the variation of the electron density, the reflectometry is very powerful tool to investigate both MHD instabilities and electro-static instabilities [4]. Electro-static instabilities causes the variation of electron density.

The ECE imaging is a passive microwave imaging and the microwave imaging reflectometry (MIR) is an active microwave imaging, as shown in Fig. 1. The microwave imaging system consists of a imaging optics, a microwave illumination system, a imaging detector array, a multi-channel frequency separator, DC circuits, and digitizers, as shown in Fig. 1. The frequency separator consists of bandpass filters and RF amplifiers. The frequency width of a bandpass filter for ECEI is wide. Since the ECE is a blackbody radiation, the signal intensity of ECE is higher as the bandwidth is wider. The frequency width of a bandpass filter for MIR is narrow. Since the MIR signal is the reflection of the illuminated wave, the noise intensity of MIR is lower as the bandwidth is narrower. In order to reduce the bandwidth for MIR, the frequency difference between the illumination wave and the local wave should be well stabilized.

Despite of the usefulness of the microwave imaging, only one group has been successful to observe the plasma with microwave imaging in the world [6]. They obtain a 2-D cross-sectional image of the electron temperature with a 1-D imaging detector array and a frequency separator array [5, 6]. Their imaging detector uses dual-dipole antenna with a substrate lens. This antenna is attached with a long balun to transform the circuit from the antenna balanced circuit to the unbalanced antenna circuit. Since balun and antenna is on the same substrate, their detector array should be one dimensional.

One of key technologies of the microwave imaging is a imaging detector array. No 2-D imaging detector array has been used in the microwave imaging for plasma diagnostics yet. A muli-channel frequency separator is another issue. A microwave imaging system uses many imaging detector channels and tremendous number of frequency separator channels. For example, a 8×5 2-D imaging detector array has 40 channels. If each detector channel is connected to a frequency separator dividing 8 frequency channels, the total channel number is 480. Both the cost

author's e-mail: nagayama.yoshio@nifs.ac.jp

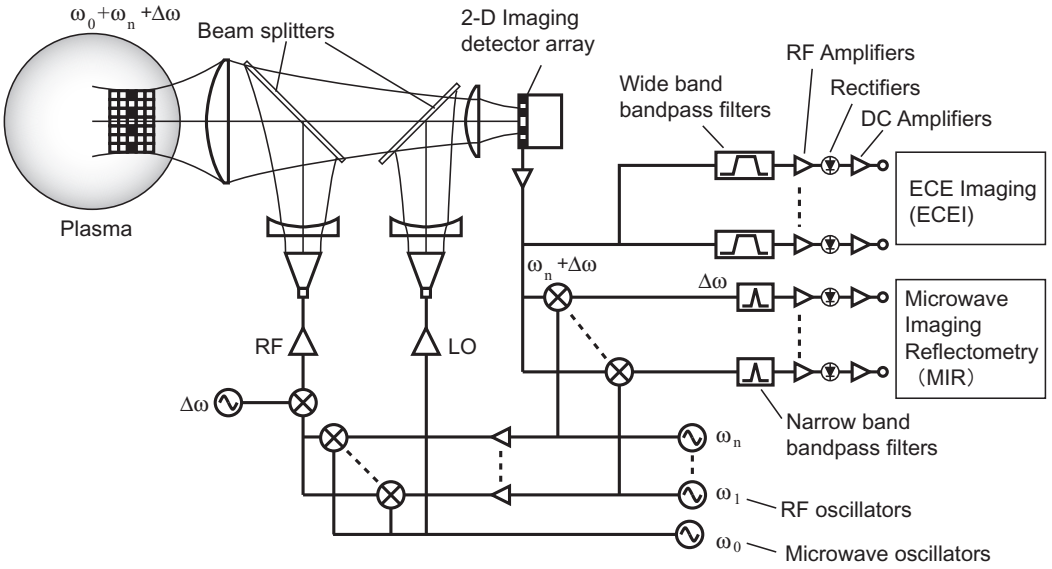

Fig. 1 Schematic view of microwave imaging system.

and the size should be very small to be installed. In the imaging science project, a 8×5 60 GHz 2-D imaging detector arrays [8] and a 8 channel frequency separator [9] have been developed.

The microwave imaging is under development as a NINS imaging science project at NIFS. The prototype of the MIR was installed in 2006 [**?**, **?**]. The prototype MIR has 3 frequencies (53, 66, 69 GHz) for illuminating wave and 3 horn antennas to receive reflection wave. A 4×4 20 GHz 2-D imaging detector array using planer Yagi-Uda antenna has been developed. The first MIR system was developed and installed in the TPE-RX reversed field pinch device at the National Institute of Advanced Industrial Science and Technology (AIST) in 2007 [12, 13]. This system uses the 20 GHz 2-D imaging detector array. The second MIR system has been developed to be installed in the LHD at NIFS. This system uses the 60 GHz 2-D imaging detector array. This paper presents those MIR systems developed at NIFS.

2 Proto type MIR System in LHD

Figure 2 shows a schematic diagram of the prototype MIR system in LHD. The illumination wave (RF) is generated by 3 high power (0.5 W) IMPATT oscillators, whose frequencies are 53, 66 and 69 GHz, respectively. These oscillators used to be installed 5 m far from LHD. However, the operation of the IMPATT oscillators was interfered by the leakage of the magnetic field. Actually, the output power of the IMPATT oscillators reduces as the magnetic field increases, and finally no output power are observed. After enclosing in 5 mm thick soft-iron shield case, the power was dropped by 30 %. Therefore the microwave sources are installed 15 m far from LHD and the microwave is transferred using oversized rectangular waveguides (X-band, WR-90) and 90 degree H bends. By using optical system, the illumination wave radiated from a horn antenna (WR-15) is formed to a parallel beam with a diameter of 20 cm at the reflection layer in the plasma. The illumination wave is reflected by the three cutoff layers, which are determined by the local density and the magnetic field in the case of X-mode reflection.

The primary imaging mirror (M1) is installed in the LHD vacuum vessel. This is an elliptic concave mirror with the size of 43×50 cm and the focal length of 106.5 cm. The distance between the mirror M1 and plasma is 210 cm. The mirror M1 is remotely manipulated by the use of ultrasonic motors (USMs). Since the LHD plasma is twisted, toroidal and poloidal angles of the main mirror should be controlled within 1 degree in order to obtain reflection from plasma.

The reflected wave is accumulated by the primary imaging mirror. ECE and the reflected wave are separated by a dichroic plate (DP), which is a high pass filter with a sharp cut-off frequency of 70 GHz. This dichroic plate is an 8 mm thick aluminum alloy plate with many circular holes. The diameter of each hole is 2.5 mm and they are separated by 2.8 mm. The hole has the angle of 45 degree to the plate so that ECE wave more than 70 GHz efficiently passes through the dichroic plate.

The reflected beam and the illumination beam are separated by the beam splitter (BS), which is a 3 mm thick Plexiglas plate. The reflected illumination beam by BS and the transmitting illumination beam through DP are absorbed by microwave absorbing forms (ECCOSORB CV-3) in order to reduce background noise. Because of microwave absorbers and beam separation, the leakage of the illumination wave to the receiver is significantly reduced, so that the background level in the signal is drastically reduced.

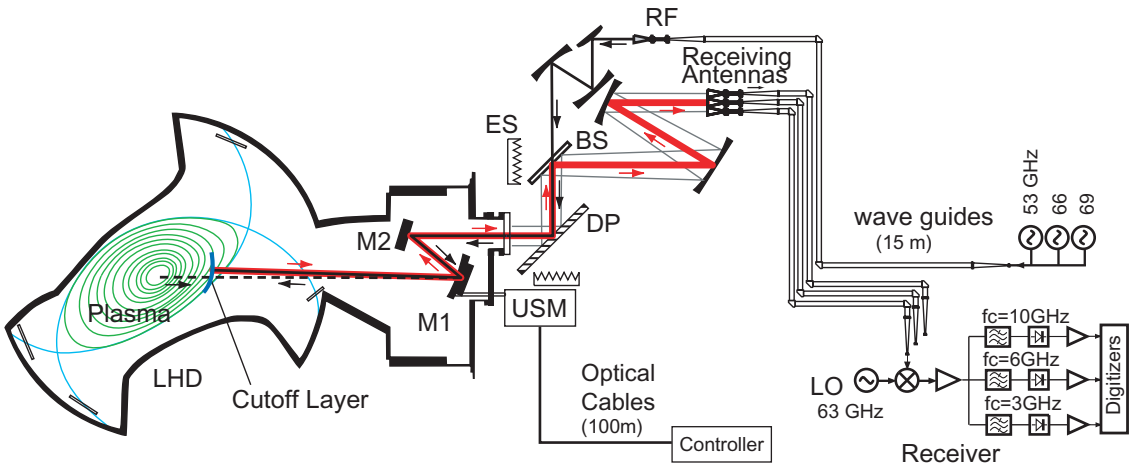

Fig. 2 Schematic view of the prototype of MIR system in LHD. M1: Adjustable concave mirror, M2: Plane mirror, DP: Dichroic plate (70GHz), BS: Beam splitter, US: Ultrasonic motor, ES: ECCOSORB CV3.

The plasma image is formed on the front end of receiving horn antenna (WR-15) array by the mirror optics. The pair of antennas is separated by 8.4 cm in the poloidal direction, and another pair by 10.7 cm in the toroidal direction on the cutoff layer. Received reflection wave is transmitted to the heterodyne receiver with oversized waveguides (X-band). In the heterodyne receiver, reflected wave is mixed with the wave from local oscillator (LO) with the frequency of 63 GHz to make intermediate frequency (IF) signals. IF signals selected by band-pass-filters with the bandwidth of 10 % of the central frequency are amplified by modular RF amplifiers. Finally they are rectified by Schottky barrier diodes, amplified by DC amplifiers and digitized by PXI digitizer modules.

By using this system, the edge harmonic oscillations are observed [14].

3 MIR System in TPE-RX

TPE-RX is a large reversed field pinch (RFP) in the world. The major radius is 172 cm and the minor radius is 45 cm. With 20 GHz reflectometry, of which cutoff density is $0.5\times 10^{19}\mathrm{m}^{-3}$, the density fluctuation can be observed when $n_{av} > 0.4\times 10^{19}\mathrm{m}^{-3}$. In the typical TPE-RX plasma, the cutoff frequency near the field reversal surface, where the toroidal field changes the direction, is about 20 GHz. Therefore, we use 20 GHz for MIR in TPE-RX.

Figure 3 shows a schematic diagram of the MIR system in TPE-RX. The quartz window of the TPE-RX viewing port is located at $r = 67$ cm, the illumination wave (RF) can pass through the window. The primary mirror (M_1), which is an elliptic concave mirror with the size of 40×43 cm, makes a parallel illumination beam in the plasma. The reflected wave is collected by M_1 and is separated from the illumination beam by the first beam splitter (BS_1). The local oscillation (LO) wave and the reflected wave is mixed with the second beam splitter (BS_2). These beam splitters are 3 mm thick Plexiglas plates. The RF wave reflected by BS_1 and the LO wave passing through BS_2 are absorbed by a microwave absorber in order to reduce background noise. An image of the reflection layer is made on the 2-D mixer array by the Teflon lens (L_1).

In this experiment, two types of 2-D mixer array are used. One is a 2-D array of coax to waveguide adapters with diodes. The waveguide is for the frequency bandwidth of 18 – 26.5 GHz and has the inner size of 1.07×0.43 cm. These adapters are separated by 2.24 cm. Another is a 2-D planar Yagi-Uda antenna array on a Teflon printed circuit board (PCB) with the thickness of 0.254 mm. In the 2-D Yagi-Uda antenna array, four elements are set on a PCB with a distance of 12 mm, and 4 PCBs are stacked with a distance of 15 mm. Each element consists of a planar Yagi-Uda antenna, a balun, a beam lead type Schottky barrier diode (SBD) and an IF amplifier. In this system, a tapered balun is used, and this is different from the original planer Yagi-Uda antenna system. On the design of antenna system, a computer code for electro-magnetic field is employed. This Yagi-Uda antenna has 3 guiding elements, a pair of dipole and a reflector element. The IF amplifier consists of surface acoustic wave (SAW) bandpass filters and RF amplifiers. Also the mixer element has two voltage regulators for the power supply of amplifier and the DC bias of SBD. The signal output is a MMCX straight PCB jack connector. The 2-D mixer array is contained in a shield box that has 16 SMA connectors for the signal output. The MMCX and SMA are connected with a coaxial cable inside the shield box.

The LO wave ($\omega + \omega_1$) is made by mixing the RF wave (ω: 20 GHz) and the lower frequency wave generated by a crystal oscillator (ω_1: 110 MHz) at an up-converter. Lenses L_1 and L_2 make a spot of LO wave with the diameter of 10 cm on the 2-D mixer array. By mixing the reflected wave with the frequency of ω and the LO wave,

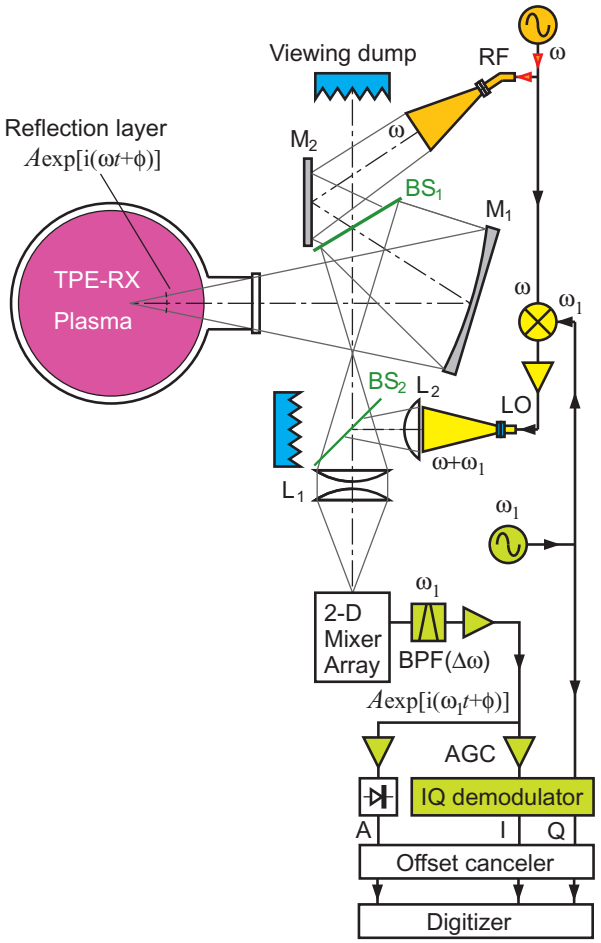

Fig. 3 Schematic view of MIR system in TPE-RX.

the 2-D mixer array makes IF signal with the frequency of ω_1. Since the IF frequency ω_1 is well stabilized, the noise can be significantly reduced because the bandwidth of the IF amplifier is narrow (4 MHz).

The reflective wave contains the amplitude A and the phase ϕ, as, $A\exp[i(\omega t+\phi)]$, where the amplitude A and the phase ϕ is generated by a density fluctuation in the plasma. The phase ϕ indicates the vibration motion of the reflection layer. The IF signal also contains the amplitude and the phase, as $A\exp[i(\omega_1 t+\phi)]$. The amplitude is obtained by rectifying the IF signal with microwave monolithic integrated circuit (MMIC). The phase is obtained by comparing the IF frequency and the signal by the IQ demodulator. I and Q signals correspond to $\cos\phi$ and $\sin\phi$, respectively.

Due to RF noise, the rectified RF signal contains large offset. This offset is removed by an offset canceler, which consists of a differential amplifier and a sample-hold circuit. The sample-hold circuit works as follows: a digitizer samples the MIR data at $t = 0$ and hold it in a digital memory, then an digital to analog converter makes analog output. By using the differential amplifier the offset that is the analog output of the sample-hold circuit is removed from the MIR signal.

By using this system, MHD turbulences in RFP plasmas are observed [13].

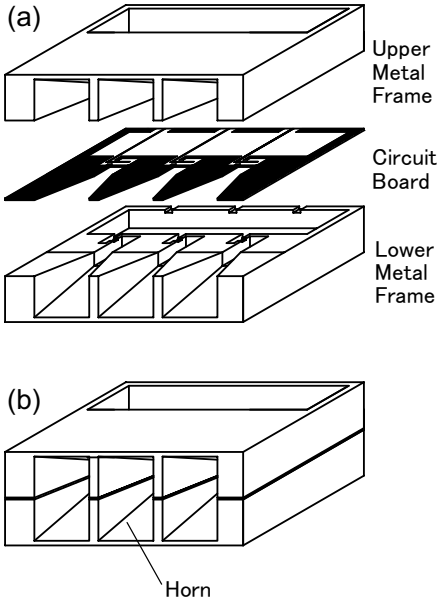

Fig. 5 Schematic view of an assembly of horn antenna array. (a) Parts; (b) Completed form.

4 2-D MIR System in LHD

Figure 4 shows a schematic diagram of the 2-D MIR system in LHD. he optical system is almost the same as the prototype MIR system. The difference is optics for the LO wave and thickness of the beam splitters. Since the 2-D detector contains mixers, the LO wave illuminate the 2-D detector by using a beam splitter.

The illumination wave (RF) is the mixture of the LO wave (frequency: ω_0) and the IF frequency (frequency: ω_L) with an up-converter. Due to small leak of original frequency, the RF wave includes a small amount of ω_0 and a major part of $\omega_0 + \omega_L$. If this wave is used as LO wave, the detector generates an IF signal of ω_L without reflection. Since the reflection is much weaker than the illumination, a strong LO wave is required to make an IF signal. In this case, the IF frequency is 110 MHz, which is generated by a crystal oscillator.

The local oscillation (LO) for the heterodyne detection is made by up-converting the VCO signal and a crystal oscillator's signal, to generate an intermediate frequency (IF) of 110 MHz. We are also developing band-pass filter-banks, IF amplifiers and I-Q demodulators. The band-pass filter-bank uses the microwave strip line technology. The I-Q demodulator is a phase detector of reflected signals.

A schematic view of an assembly of the imaging detector array is shown in Fig. 5. This detector array is made of 3 major parts, such as the upper metal frame, a circuit board and a lower metal frame, as shown in Fig. 5(a). The upper and lower metal frame are made of aluminum alloy,

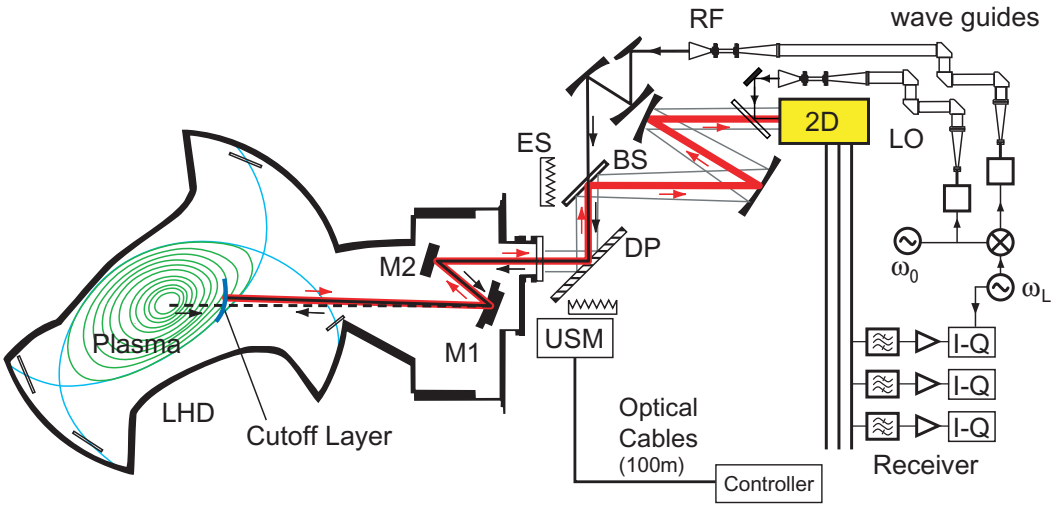

Fig. 4 Schematic view of the 2-D MIR system in LHD.

and horn shape and waveguide slots are made by electrical discharge machining. By attaching these slots, a horn antenna is formed, as shown in Fig. 5(b). In the upper structure, another slot is formed for passing the micro-strip-line. On the circuit board the mixer diode, filters and RF amplifiers are mounted. The circuit is produced by the micro-strip-line technology. The horn antenna receives both RF and LO waves and the mixer generates a intermediate frequency (IF) signal. The mixer bias is supplied from a DC power supply through an inductor, and the bias current is optimized. The IF amplifiers is low-cost GaAs microwave monolithic ICs with the frequency range of DC to 10 GHz and the 13 dB. Its power is supplied from RF output through the choke inductor and the current limit resistor. The DC-blocking capacitors are needed after the output of the amplifier. By stacking this 1-D array, a 2-D array (5 in toroidal and 8 in toroidal directions) is formed.

The frequency response the reflectivity of different 90 degree beam splitters is shown in Fig. 6. Here, a mylar sheet (thickness: 0.2 mm), plane acrylic glasses (thickness: 1 mm and 2 mm) and a high refractive index board (thickness: 2.54 mm) are tested. The amount of reflection differs as the polarization differs. Despite of the polarization, a transparent frequency window is observed in thick beam splitters. In the case of 90 degree beam splitter with the thickness of 2 mm, the transparent frequency is 47.2 GHz, of which wavelength is 6.35 mm in vacuum. In the case of 180 degree beam splitter with the thickness of 2 mm, the transparent frequency is 42.2 GHz, of which wavelength is 7.1 mm in vacuum. An acrylic glass with the thickness of 1 mm is used as a beam splitter.

The I/Q demodulator is under development to measure the phase difference between the probe wave and the reflected wave. It outputs the three components of $\cos\phi$, $\sin\phi$ and the reflected power of the 110 MHz intermediate frequency (ϕ is the phase difference between the probe wave and reflected wave). The I/Q demodulator consists of a low-price quadrature demodulator IC-chip (the unit price is about 15 dollars) with the auto-gain control function. The output frequency range is DC - 1 MHz, which is higher than the typical frequency range of 1 - 500 kHz of the density fluctuation in LHD. The input power is automatically adjustable between -80 and -30 dBm. The low-cost version of the I/Q demodulator with the unit price of less than 100 dollars is now under development in NIFS.

5 Conclusion

Microwave Imaging Reflectometry is under development in order to obtain the 2-D/3-D image of the electron density fluctuation in the TPE-RX RFP device and in the Large Helical Device. The MIR becomes a powerful tool to investigate the micro-turbulence and the magneto-hydrodynamic instability in the magnetically confined plasma. By using the microstrip line technology three key devices are under development for the LHD plasma experiment and the industrial applications. The 2-D detector array is developed by stacking of 1-D detector arrays of the planar Yagi-Uda antenna for 20 GHz and the horn antenna for 60 GHz. The intermediate frequency receiver with the bandpass filter and the RF amplifiers is installed on the same board of the antenna array. The I/Q demodulator is under development for the multi-channel phase measurement of the phase difference between the probe wave and the reflected wave. These devices enable the multi-channel microwave imaging system for 2-D/3-D observation in the plasma diagnostics.

Acknowledgement This works is supported by National Institute for Fusion Science (Grant No. NIFS08ULPP525) and by National Institute of Natural Sciences (Grant No. NIFS08KEIN0021).

[1] Y. Nagayama, Rev. Sci. Instrum. **65**, 3417 (1994).
[2] Y. Nagayama, et al., Phys. Plasmas **3**, 2631 (1996).

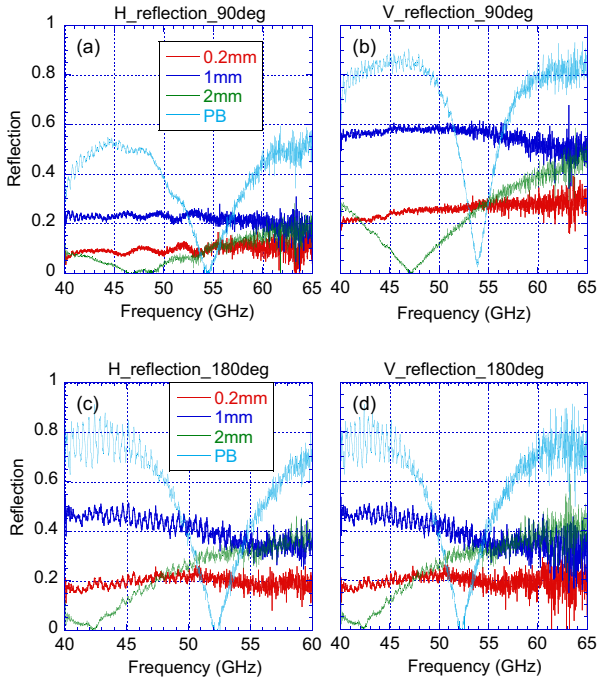

Fig. 6 The refectivity of 90 degree beam splitters. (a) The polarization is perpendicular to the beam splitter. (b) The polarization is parallel to the beam splitter. Numbers indicates thickness of acrylic glass of beam splitter. PB is a high reflactive index board with the thickness of 2.54 mm.

[3] Y. Nagayama, et al., Phys. Plasmas **3**, 1647 (1996).
[4] E. Mazzucato, Rev. Sci. Instrum. **69**, 2201(1998).
[5] C.W. Domier, et al., Rev. Sci. Instrum. **77**, 10E924 (2006).
[6] H. Park, et al., Phys. Rev. Letters, **96**, 195003 (2006).
[7] Z. Shen, et al. Plasma Fus. Res, , **2**, S1019 (2007).
[8] D. Kuwahara, et al., ”Development of 2-D Antenna Array for Microwave Imaging Reflectometry in LHD”, Plasma Fusion Res. JPFR Series (to be published in 2009).
[9] Y. Kogi, et al., Rev. Sci. Instrum. **79**, 10F115 (2008).
[10] S. Yamaguchi, et al., Rev. Sci. Instrum. **77**, 10E930 (2006).
[11] S. Yamaguchi, et al., Plasma Fusion Res. **2**, S1038 (2007).
[12] Y. Nagayama, et al., Plasma Fusion Res. **3**, 053 (2008).
[13] Z.B. Shi, et al., Plasma Fusion Res. **3**, S1045 (2008).
[14] S. Yamaguchi, et al., ”Observation of MHD mode with higher harmonics in the edge plasma region in the Large Helical Device”, (submitted to Phys. Plasmas).

Proceedings of ITC18,2008

Development of Reconfigurable Analog and Digital Circuits for Plasma Diagnostics Measurement Systems

Amit Kumar Srivastava, Atish Sharma, Tushar Raval

Institute for Plasma Research, Gandhinagar - 382 428, Gujarat, India

In long pulse discharge tokamak, a large number of diagnostic channels are being used to understand the complex behavior of plasma. Different diagnostics demand different types of analog and digital processing for plasma parameters measurement. This leads to variable requirements of signal processing for diagnostic measurement. For such types of requirements, we have developed hardware with reconfigurable electronic devices, which provide flexible solution for rapid development of measurement system. Here the analog processing is achieved by Field Programmable Analog Array (FPAA) integrated circuit while reconfigurable digital devices (CPLD/FPGA) achieve digital processing. FPAA's provide an ideal integrated platform for implementing low to medium complexity analog signal processing. With dynamic reconfigurability, the functionality of the FPAA can be reconfigured in-system by the designer or on the fly by a microprocessor. This feature is quite useful to manipulate the tuning or the construction of any part of the analog circuit without interrupting operation of the FPAA, thus maintaining system integrity. The hardware operation control logic circuits are configured in the reconfigurable digital devices (CPLD/FPGA) to control proper hardware functioning. These reconfigurable devices provide the design flexibility and save the component space on the board. It also provides the flexibility for various setting through software. The circuit controlling commands are either issued by computer/processor or generated by circuit itself.

Keywords: reconfigurable analog circuit, reconfigurable digital circuit, field programmable analog arrays, plasma diagnostics measurement, field programmable gate arrays, fpaa, fpga

1. Introduction

The time duration of tokamak discharge has been prolonged in accordance with the development of fusion research. In the next generation tokamak like SST-1 and ITER [1] the discharge time of the order of 1000 sec. is planned. At the same time demand for more no. of acquisition channels from different diagnostics is increasing. Various diagnostics demand different types of analog and digital processing for plasma parameters measurement. This leads to variable requirements of signal processing for diagnostic measurement. For such types of requirements, we have developed hardware with reconfigurable electronic devices, which provide flexible solution for rapid development of measurement system. Here the analog processing is achieved by Field Programmable Analog Array (FPAA) integrated circuit while reconfigurable digital devices (CPLD/FPGA) achieve digital processing. FPAA's provide an ideal integrated platform for implementing low to medium complexity analog signal processing. Recent trends in hardware design have seen a marked increase in the use of programmable devices such as CPLDs (Complex Programmable Logic Device) and FPGAs (Field Programmable Gate Arrays), and more recently field-programmable analog arrays (FPAA). Programmable devices reduce the time and cost of hardware prototyping. Design using field-programmable devices is automated through the use of sophisticated computer-aided design (CAD) tools, which synthesize circuits from schematic, high-level, or behavioral descriptions into usable hardware. This automated CAD flow reduces the need for detailed design expertise in developing working hardware and thus makes hardware design open to a greater number of users. These reconfigurable devices provide the design flexibility and save the component space on the board.

2. Reconfigurable Measurement system

The hardware design of reconfigurable measurement system is presented as block diagram in figure 1. The block diagram shows how various elements

author's e-mail: amit@ipr.res.in

are connected with each other for achieving the following described functions:

- Signal conditioning of the sensor/transducer signal
- Configuring analog circuits in FPAA integrated circuit to achieve analog processing as per diagnostics requirements
- Analog to digital conversion
- Configuring digital circuits in FPGA integrated circuit to process on-board digital data for acquisition and control

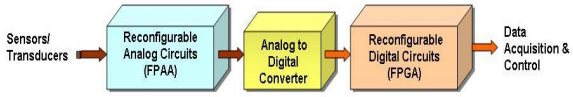

Fig. 1 Block Diagram of Measurement system using Reconfigurable devices

We have developed the reconfigurable measurement system for plasma diagnostics for variable requirements. Implementation and testing of our analog designs has been done through FPAA development board while digital processing has been achieved with in-house developed FPGA based CAMAC digitizer.

3. Reconfigurable Analog Circuits

Reconfigurable analog circuits have been implemented using FPAA device for variable analog signal processing requirements. A field programmable analog array is a powerful and flexible integrated circuit for quickly, efficiently, and accurately designing a wide variety of circuits, including multiple-pole filters and other related circuits. FPAAs may soon prove themselves in applications requiring fast and complex analog circuit prototyping and flexibility in the final analog circuit design. Design using field-programmable devices is automated through the use of sophisticated computer-aided design (CAD) tools, which synthesize circuits from schematic, high-level, or behavioral descriptions into usable hardware. Figure 2 shows schematic and simulation in the FPAA development software for our analog circuit configuration. We have configured the FPAA for various signals conditioning task like amplification, offset removal, filtering etc. For analog processing, we have tested various circuits like variable gain circuit, comparator, filter, wave rectifier etc. The advantage we get with these devices is that we can configure the circuits as per our diagnostics requirements. We can also simulate the circuit through software before placing actual circuit in FPAA device. With dynamic reconfigurability, the functionality of the FPAA can be reconfigured in-system by the designer or on the fly by a microprocessor. This feature is quite useful to manipulate the tuning or the construction of any part of the analog circuit without interrupting operation of the FPAA, thus maintaining system integrity.

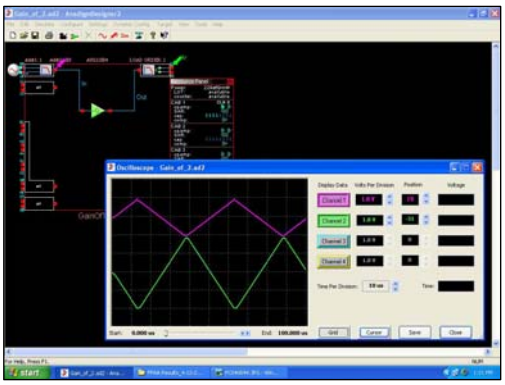

Fig. 2 Schematic and simulation in FPAA development software to configure analog circuit.

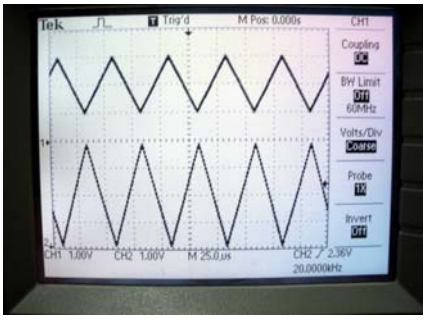

Fig. 3 Measured signal on oscilloscope of input and output of FPAA based amplification circuit

4. Reconfigurable Digital Circuits

Reconfigurable digital circuits have been implemented using FPGA device and analog to digital converter circuitry for on-board data processing requirements of data acquisition and control [2]. The designed module is a FPGA based CAMAC digitizer. The FPGA is used for all system module logic function and on-board data processing. The main aim to design this CAMAC module is to process the data, acquired from various channels, in real time and to output it for further action. The module can be used for monitoring, control and acquisition [3]. The real time processing has been implemented with VHDL hardware description language. The module can be configured to acquire data from up to eight channels with real time processing capability using VHDL code with FPGA as target device. The processed data can also be output through Digital to Analog Converter. VHDL code is a hardware description language for reconfigurable digital devices

(CPLD/FPGA). We can easily configure the digital logic and can verify the design though simulation before actual implementation in device. We have tested the circuit for various data processing algorithm like addition, multiplication etc.

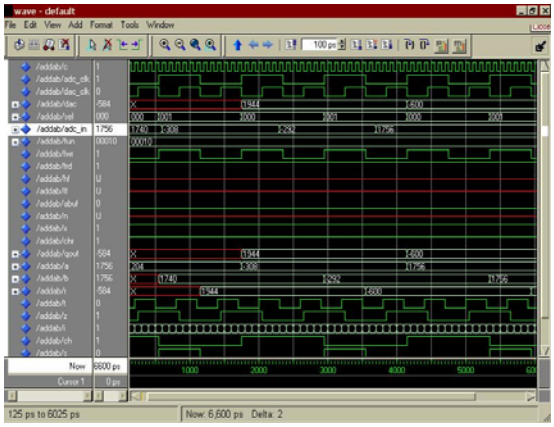

Fig. 4 Digital Design verification: VHDL code simulation.

5. Graphical User Interface

A user-friendly Graphical User Interface (GUI) has been developed with LabVIEW application software for acquisition through developed hardware. This provides a convenient display and analysis platform for acquired data. The main feature that distinguishes LabVIEW from other data acquisition application software is its highly modular graphical programming language and large library of mathematical and statistical functions.

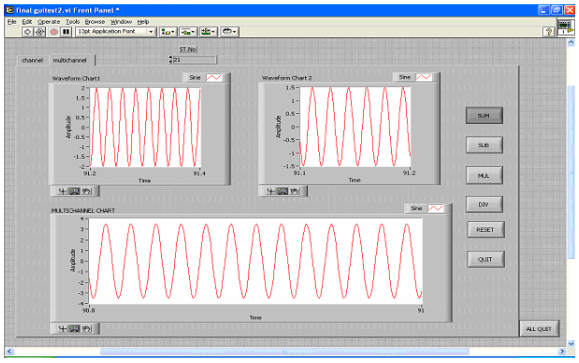

Fig. 5 GUI developed in LabVIEW for acquisition and to configure FPGA for various processing algorithms

The advantage of graphical programming is that the code is flexible, reusable, and self-documenting. Subroutines can be saved in a library and reused without modification in other programs. This dramatically reduces development time and enables researchers to develop or modify their own programs.

6. Results & Discussion

We have tested the developed reconfigurable analog and digital hardware for different analog signal conditioning circuits and digital signal processing algorithms. The developed CAMAC module has been tested in CAMAC data acquisition system with precise test and measurement equipments. The testing has been performed with GUI developed in LabVIEW application software. We have tested the DC performance as well as AC performance of hardware with utility developed in LabVIEW software. We have found the results quite satisfactory. These reconfigurable technologies may be quite useful, in future, for development of variable requirement plasma diagnostics measurement systems for different interfaces.

7. Acknowledgement

The authors express their sincere thanks to all the members of SST-1 Data Acquisition Division for their kind co-operation.

References

[1] P.H.Rebut, ITER the first experimental fusion reactor, *Fusion Engineering and Design*, Vol. **30,** pp. 85, (1995).

[2] P.C. Van Haren and N.A. Oomens, Data acquisition systems for fusion devices, *Fusion Technology*, Vol. **24,** pp. 391–402, (1993).

[3] Eriko Jotaki and Satoshi Itoh, Continuous Monitoring and Data Acquisition System for Steady-State Tokamak Operation, *Fusion Technology*, Vol.**27,** pp.171-175, (1995).

Proceedings of ITC18, 2008

Measurement of divertor heat flux in helical-axis Heliotron-J device using a thermal probe

Hiroto MATSUURA[1)], Ken NAKANO[1)], Katsuyuki HOSAKA[2)], Kenichi NAGAOKA[3)], Takashi MUTOH[3)], Hiroyuki OKADA[4)], Shinji Kobayashi[4)], Tohru MIZUUCHI[4)], Katsumi KONDO[3)], and Fumimichi SANO[4)]

[1)]*Graduate School of Engineering, Osaka Prefecture University, Osaka 599-8531, Japan*
[2)]*Graduate School of Energy Science, Kyoto University, Uji 611-0011, Japan*
[3)]*National Institute for Fusion Science, Gifu 509-5292, Japan*
[4)]*Institute of Advanced Energy, Kyoto University, Uji 611-0011, Japan*

Direct measurement of divertor heat flux is an important task. But heat flux calibration is often difficult since heat diffusion in sensors is slower process than discharge duration time of present experiments. In this paper, using unsteady heat conduction model, heat flux in Heliotron J edge plasma is firstly measured. Obtained heat flux value, although it is time averaged, does not contradict edge plasma parameters.

Keywords: Thermal probe, divertor, Heliotron-J, Heat flux, Heat conduction

1 Introduction

It is well known that there exist the sheath regions between plasmas and solid components which face to plasmas and that current through these sheath is determined by the sheath potential drop. According to sheath theory, momentum and heat flux through the sheath is also the function of the sheath potential drop. Recently Combined force-Mach- Langmuir probe[1] and thermal probe[2, 3] were proposed to measure these flux and to obtain not only electron parameters but also ion information such as its temperature. Recently, the first result on ion temperature measurement with thermal probe is reported in [4], but importance of energy reflection coefficient on thermal probe measurement is pointed [5].

It is also very important to measure the heat flux itself in divertor plasma. In the design of fusion reactors like International Tokamak Experimental Reactor(ITER), vast heat flux($> 10[\mathrm{MW/m^2}]$) is expected to flow onto divertor target plate through this sheath boundary. In order to check proposed methods to reduce this heat load such as "detached plasma formation", direct measurement of heat flux is indispensable, since relation between heat flux and plasma parameter is very complicated. Moreover ion temperature contribution could not be ignored as usual text books, since ion temperature is larger than electron temperature in divertor plasma [6] . So development of direct measurement tools for divertor heat flux would be an important task.

In this paper, first results of heat flux measurement for Heliotron J edge plasma are given. In section 2, an experimental setup is described. In section 3, unsteady heat conduction model is applied for thermal probe data in Heliotron J. Some results are shown in Sec.4.

author's e-mail: matsu@me.osakafu-u.ac.jp

2 Experimental Setup

Heliotron J is a medium sized helical axis Heliotron device with a helical winding coil of $L = 1/M = 4$. The details of Heliotron J are described in Refs. [8] and [9]. Last year the Hybrid Directional Probe (HDP) used in Compact Helical System [7] were moved to Heliotron-J device under Collaboration with NIFS. HDP is composed of 1 magnetic probe sensor(Pin 6) and 7 Langmuir probe tips(Pin 1-5, 7-8), 5 tips of which are equipped with type-K thermocouples(TC) and available also as thermal probes. In this paper, data of Pin 3 and 4 are mostly used. These pins are made of oxygen-free-cupper and the diameter and length are 4.5 and 11[mm] respectively.

HDP has a driving system of three parameters $(R_p, \theta_p, \alpha_p)$ and positions of its pins and can be changed shot by shot. R_p is the HDP probe head shift along the major radius direction in mm unit. θ_p is the swing angle in degree unit along the poloidal direction, although in this paper data only for $\theta_p = 0$ are used. α_p is the rotation angle in degree unit around the axis of cylindrical HDP head. Due to the mechanical limitation, only half rotation data are available. α_p can be scan $-110 \sim 10$ and difference of initial position of Pin3 and Pin4 is 60.

HDP is installed to port 7.5 cross section of Heliotron J and so called X-point can be studied. Figure 1 shows outer part of port 7.5 section (Toroidal angle is 163[deg.]) and magnetic surface in standard configuration. Horizontal solid line at $Z = 0.271$[m] is the trajectory of HDP head axis for $\theta_p = 0$. When $R_p \sim 135$, the top of HDP head reaches the Last Closed Flux Surface(LCFS). Two symbols (cross and dagger) in this figure are the position of Pin3

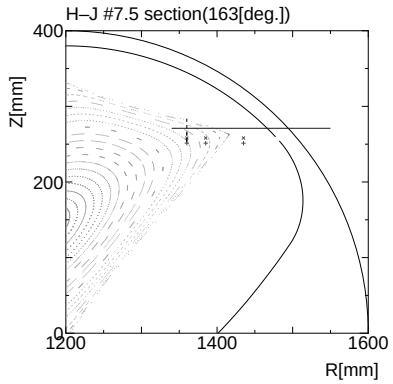

Fig. 1 Probe pins position of the Hybrid Directional Probe (HDP) on port 7.5 cross section. HDP head moves along horizontal solid line at $Z = 0.271$[m] with setting parameter R_p. Probe pins move along vertical dashed line at $R = 1.36$[m] with α_p.

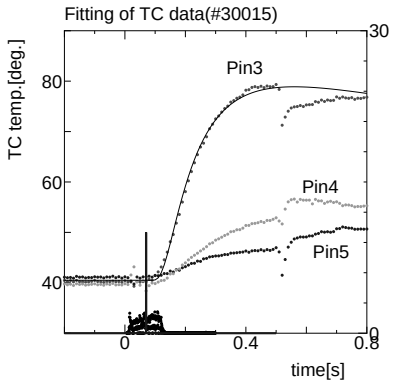

Fig. 2 Example of TC data and fitting result for the HDP. The position of Pins are $R = 1.36$[m](Pin3 and 4), 1.38[m](Pin5), and $Z = 0.25$[m](Pin3 and 5), 0.26[m](Pin4). Solid line fitting Pin3 data is obtained by eq.(1) with $x_{tc} \sim 1.07 \times 10^{-2}$[m] and $q\Delta t \sim 2.9$[J/mm^2].

and Pin4 for $R_p = 210, 185$, and 135. Small vertical dashed line at $R = 1.36$[m] shows the movement of Pin3 and Pin4 with α_p scanning at $R_p = 210$.

3 Heat conduction model

Basic concept of thermal probe is very simple. From the probe tip temperature (T_p) data, heat flux to probe surface Q can be deduced by solving heat conduction problem. For DC discharge plasma, we can use the simple steady relation such that $Q \sim \Delta T_p$. However, heat flux calibration of thermal probes of HDP has not yet completed, mainly since discharge pulse length ($\Delta t \sim 0.1$[s]) is shorter than thermal diffusion time in a probe tip (about 1[s]) and steady state heat conduction model is not available. Figure 2 shows the example of thermocouple data measured at $(R_p, \theta_p, \alpha_p) = (210, 0, 0)$ for NBI plasma. Temperature increases almost after main discharge terminates and reaches maximum value about at $t = 0.5$[s]. After that TC signal show the abnormal jump, which is thought to be due to helical coil current noise.

As the first step, we used a very simple model to analysis heat conduction in probe pins. A probe pin is treated as semi-infinite plane and plasma heat flux is treated as Delta-function type short pulse. Then temperature in a probe pin is the function of time t and distance from the pin surface x and given as

$$\begin{aligned} \Delta T &= T(x,t) - T_\infty \\ &= \frac{q\Delta t}{k}\sqrt{\frac{a}{\pi(t-t_0)}}\exp(-\frac{x^2}{4a(t-t_0)}) \end{aligned} \qquad (1)$$

where k is heat conductivity, a is thermal diffusivity, q is the averaged heat flux density, T_∞ is initial temperature, and t_0 is the time when heat pulse reaches the pin surface, which is indicated as a vertical line at $t = 0.07$[s] in Fig. 2.

For fixed x, temperature response to the heat pulse shows a peak at $t = \frac{x^2}{2a}$. If temperature increment becomes maximum ($\Delta T = \Delta T_{max}$) at $t = t_{max}$, TC sensor is expected to locate at $x_{tc} = \sqrt{2a(t_{max} - t_0)}$. From the Pin3 data in Fig. 2, $x_{tc} \sim 1.07 \times 10^{-2}$[m]. And total heat that the probe pin receives ($q\Delta t$) can be estimated by

$$k\Delta T_{max} = q\Delta t\sqrt{\frac{a}{\pi(t_{max}-t_0)}}\exp(-\frac{1}{2}) \qquad (2)$$

If $q\Delta t \sim 2.9$[J/mm^2] is assumed, eq.(1) well reproduces time evolution of Pin3 data in Fig. 2.

It must be noted that x_{tc} is not exactly corresponding to real position of TC connection point. Type-K TC used in HDP has the sheath material around connection point and it works as heat resistance and $t_{max} - t_0$ may become longer than that expected from real TC position.

By using $\Delta t = 0.1$[s], Pin3 is estimated to receive heat flux of about 400[W] in main discharge. On the other hand, ion saturation current measured with the same pin was ~ 100[mA] near LCFS. Although no electron temperature data is obtained by this probe pin, estimated heat flux is the same order as $\gamma T_e I_{is}$, if $T_e = 100$[eV] and heat transmission factor γ of order of 10 are assumed.

According to eq.(1), if TC position can be moved toward probe surface or TC sheath is removed, then x_{tc} would become smaller, TC signal response would be improved, and real time monitoring of heat flux might be possible. To study this improvement more precisely, the second improved model for probe pin heat conduction is now developing.

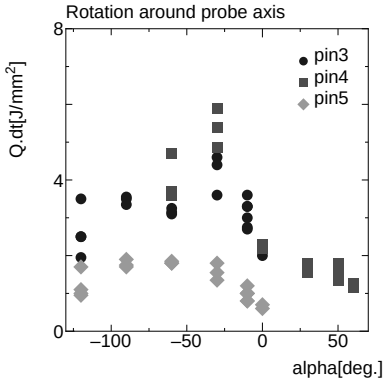

Fig. 3 Heat flux profile around HDP head. Holizontal axis is angle around HDP(α) and vertical axis is the heat received during whole discharge ($q\Delta t$). For rotation angle $\alpha_p = 0$, Pin3 (and Pin5) is at $\alpha = -10$[deg.] and Pin 4 is at $\alpha = 50$[deg.].

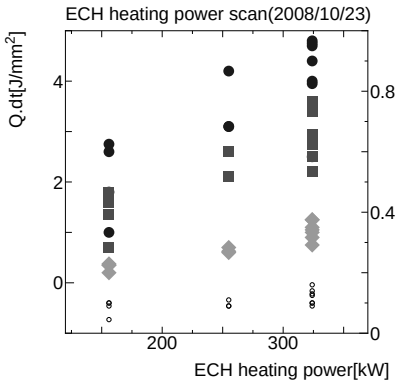

Fig. 4 ECH power scan effect on heat flux. Data symbols is the same as Fig. 3. Small open circles are also plotted for diamag monitor value(right axis with arbitrary unit).

4 Heat flux just inside LCFS

Figure 3 shows heat flux profile around the HDP head. Holizontal axis is angle around HDP(α) and vertical axis is the heat received during whole discharge ($q\Delta t$). R_p(= 210) and θ_p(= 0) are fixed and α_p is scanned. Pin3 (and Pin5) covers $\alpha = -120 \sim 0$[deg.] and Pin4 covers $\alpha = -60 \sim 60$[deg.]. As shown in Fig. 1, probe pins reach LCFS at $\alpha = -120$[deg.](mechanical limit) and they go most deeply into main plasma at $\alpha = 0$[deg.]. So if the gradient of plasma parameter(density, temperature, potential etc.) is significant, heat flux would show the maximum at $\alpha = 0$[deg.] and the minimum at $\alpha = -120$[deg.]. But although data is limited and shows scattering, the maximum heat flux is found around $\alpha = -50$[deg.]. Similar profiles have been obtained for ion saturation current. So most probable explanation for these profiles is the existence of plasma flow, which directs toward $\alpha = -50$[deg.] or $\alpha = 130$[deg.]. If this hypothesis is true, angular profile must has periodicity of 180[deg.]. Unfortunately, present heat flux data does not confirm the clear minimum value around $\alpha = 40$[deg.]. Farther measurement will be necessary.

Figure 4 shows the change of heat flux with plasma heating power.(In this case, only ECH was used as the plasma heating device.) Data symbols is the same as Fig. 3 (Pin3: circles, Pin4: squares, Pin5: diamonds). R_p and θ_p are also same as Fig. 3 and α_p is kept to be 0, which means that rotation angle of Pin3 (and Pin5) is $\alpha = -10$[deg.] and that Pin 4 is $\alpha = 50$[deg.]. As increasing plasma heating power, estimated heat flux for each pins also increases. But data scattering is rather large, since keeping line-averaged density nearly constant for different ECH heating power is difficult. For high power ECH, strong gas puffing is necessary to overcome the so-called density clamping. When ECH power is reduced, extra gas puffing sometimes terminates main discharge. One example is given in Fig. 5. ECH power of shot number 32435 and 32436 is the same (about 156[kW]). But discharge of #32435 terminates during ECH heating pulse and discharge time is only 40% of #32436, while stored energy is almost the same around $t = 200$[ms].

The $q\Delta t$ data for #32435 in Fig. 4 is also much smaller than #32436. For Pin3, $q\Delta t$ is about 1.0[J/mm^2](#32435) and 2.6[J/mm^2](#32435). If real discharge time, not ECH heating pulse length, is used as Δt, averaged heat flux is nearly equal for these two shots. So, in order to study the relation of heating power and heat flux measured with thermal probe method and present heat conduction model, knowledge on real discharge time would be necessary. On the other hand, although preset method of measuring heat flux can not obtain time variation of it, it could be used as monitoring tool to watch shot reproductivity as likely as ion saturation current. If probe position or bias voltage is kept the same and TC signal (or estimated heat flux) after a shot changes, we can see something wrong has happened in the shot.

5 Summary

Obtained results in this paper are summarized like the following.

- Heat conduction models to calibrate heat flux detected with HDP are constructed.
- Using TC evolution data, averaged heat flux in Heliotron J edge plasma is firstly estimated, which does not contradict with the value calculated from probe current data with most simple sheath theory.
- By rotating HDP around its axis, heat flux angular profile is measured. Obtained profile indicates the existence of some kind of plasma flow.

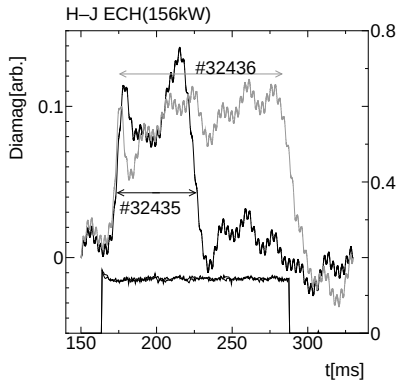

Fig. 5 Diamag monitor signal for two successive shot with the same ECH power and slightly different gas puffing control.

- As increasing plasma heating power, estimated heat flux also seems to increase. But knowledge on real discharge time is necessary to estimate heat flux exactly.

In order to monitor heat flux during main plasma discharge, improvement of TC response is necessary. One method is to reduce heat resistance between TC and probe pins by removing TC sheath material. Another is to move connecting points of TC toward pin surface where plasma irradiation occurs. Design and construction of new thermal probe with considering these improvements are left for the future work.

Acknowledgements

The authors are grateful to the Heliotron J supporting group for their excellent arrangement of experiments. One of Authors (H.M.) acknowledges Prof. Y.Nakamura and Dr. S.Yamamoto of Kyoto University for their advice on Heliotron J magnetic configuration and data acquisition system. This work is partially performed with the support and under the auspices of the NIFS Collaborative Research Program(NIFS08KUHL021).

[1] T.Lunt et al., Proc. 32nd EPS Conf. on Plasma Phys.,P1-005, Tarragona, Spain(2005).
[2] E.Stamate et al., Appl. Phys. Lett. **80** (2002) 3066.
[3] H.Matsuura et al.,Contrib. Plasma Phys. **46** (2006) 406.
[4] K.Kurihara et al., Plasma Fusion Res., **2** (2007) S1082.
[5] H.Matsuura et al., Proc. 2nd IFHT., Tokyo, Japan(2004)93.
[6] M.Kočan et al.,Plasma Phys. Control. Fusion. **50** (2008)125009.
[7] K.Nagaoka et al., Plasma Fusion Res. **2** (2007) S1092.
[8] T.Obiki et al., Nucl. Fusion **41** (2001) 833.
[9] F.Sano et al., Nucl. Fusion **45** (2005) 1557.

Proceedings of ITC18, 2008

Movable Thomson Scattering System Based on Optical Fiber (TS-probe)

K. Narihara, H. Hayashi

National Institute for Fusion Science, 322-6 Oroshi-cho, Toki 509-5292, Japan

This paper proposes a movable compact Thomson scattering (TS) system based on optical fibers (TS-probe). A TS-probe consists of a probe head, optical fiber, a laser-diode, polychromators and lock-in amplifiers. A laser beam optics and light collection optics are mounted rigidly on a probe head with a fixed scattering position. Laser light and scattered light are transmitted by flexible optical fibers, enabling us to move the TS-prove head freely during plasma discharge. The light signal scattered from an amplitude-modulated laser is detected against the plasma light based on the principle of the lock-in amplifier. With a modulated laser power of 300W, the scattered signal from a sheet plasma of 15 mm depth and n_e~10^{19} m^{-3} will be measured with 10% accuracy by setting the integrating time to 0.1 s. The TS-probe head is like a 1/20 model of the currently operating LHD-TS.

Keywords: Thomson scattering system, fiber laser, divertor plasma, TS-probe, LHD

1. Introduction

In fusion-oriented plasma experiments, Thomson scattering (TS) is a standard method to obtain electron temperature (T_e) and density (n_e) profile data. Its advantage lies in that it gives local values of T_e and n_e with a high confidence and accuracy. There are, however, disadvantages: the small probability of TS ($n_e \sigma L<10^{-11}$) necessitates bright optics and high efficient detectors even with the currently available high-energy pulse lasers; and precise laser beam alignment is often required. As a result of these, a TS usually requires a high cost and tedious labor in construction and maintenance, which preventing an easy use of TS at various locations in a plasma confinement device. As an example of a way out of this disadvantageous situation, this paper proposes an idea of a "TS-probe" which is compact and movable, like a Lagmuire probe, to a desired position around a plasma without necessity of laser beam alignment. We have already proposed a similar idea 13 years ago [1], but it have not yet realized because of absence of the suitable optical components. With recent substantial progresses in the necessary optical components, we reexamine the idea in this paper.

author's e-mail: narihara@nifs.ac.jp

2. Description of a TS-probe

A schematic view of a TS-probe designed for measuring a divertor-leg plasma of 15 mm depth is given in Fig. 1.

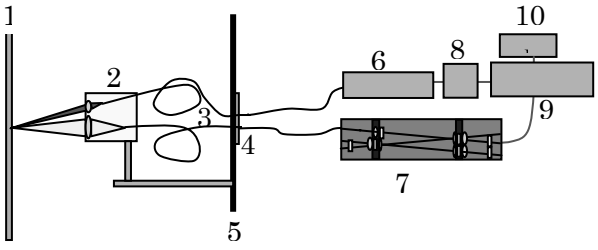

Fig.1. Schematic view of a TS-probe: 1. divertor-leg plasma; 2. TS-probe head; 3. optical fibers; 4. fiber feed-through; 5. vacuum chamber wall; 6. laser diode; 7. polychromator; 8. pulse generator; 9. lock-in amplifier; 10. data acquisition and computer.

It consists of: a probe head; optical fibers; optical fiber feed-through; laser diode; polychromator; lock-in amplifiers. These are described in details in what follows.

(1) A probe head delivers laser energy and collects a backwardly scattered light from a fixed scattering position. A key point is to collect as many TS-photons as possible while keeping background plasma light at the smallest level. For this, it is important to form the image of the laser beam just onto the surface of the light collection fiber with a well-adjusted size slit. Figure 2 shows the scattering configuration. From a simple geometry, the image of the oblique line (laser beam), which intersects the L2's optical axis at the angle α, intersects the optical axis at β, which are related by $\tan\alpha/\tan\beta=m$. Here $m=75/175=1/2$ is the magnification.

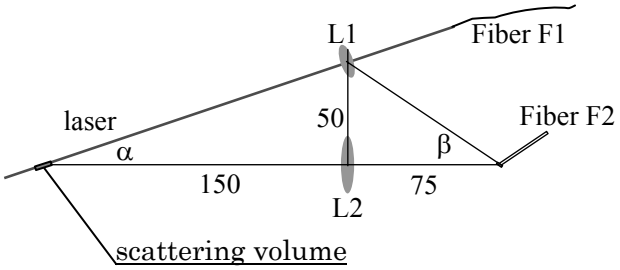

Fig. 2. Thomson scattering optics configuration.

An expanded view of the end of the optical fiber is shown in Fig. 3. The incident angle $\theta1=90°-\beta$ is chosen so that the light incident to the fiber is reflected as little as possible. If the laser beam and hence the scattered light is properly polarized (p-wave), the reflectance at the fiber surface is less than 1 % for $45°<\theta1<63°$ as shown in Fig. 4. Unfortunately the fiber supposed to be used depolarizes the propagating laser light even if initially polarized. The unpolarized light reflects on the surface of the fiber by 5% on average for $45°<\theta1<63°$ as shown in Fig. 4. We choose the central incident angle to be $\theta1=56°$ and hence $\beta=34°$ and $\alpha=17°$ for m=0.5. The end of the fiber is cut at 56° so that the central incident light propagates along the axis of the fiber after the refraction. A slit of 1mm in length and 0.5 mm in width set at the obliquely cut surface of the fiber defines the scattering cylindrical volume of L=3 mm in length and D=1mm in diameter located at the waist point of the laser beam shaped by L1 lens. The L1 lens has focal length f=34 mm and diameter ϕ30, which matches the NA=0.22 of the fiber F1 with the core diameter of 0.5 mm.

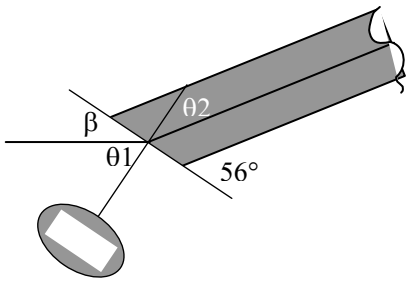

Fig. 3. Magnified view of the optical fiber for collecting TS-light.

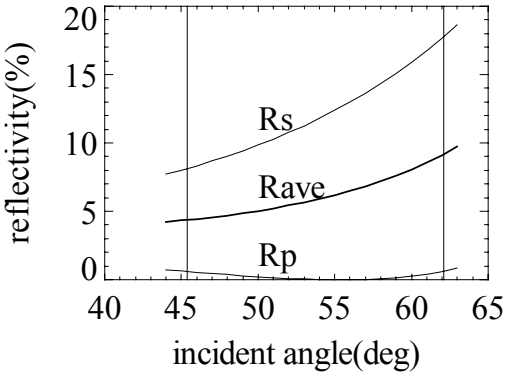

Fig. 4. Reflectivity at the end surface of the fiber as a function of incident angle.

The L2 lens has the focal length f=52 mm and 40 mm diameter with a 34mm×40 mm square aperture which match the acceptance angle of the fiber F2. The aperture gives the solid angle of $\Delta\Omega=25$ msr. All optical components consisting the TS-probe is housed in a box of 100×100×50 mm^3 size. The scattering configuration is similar to a 1/20 model of the LHD-TS.

(2) **Optical fiber**: Two optical fibers are used: F1 is for delivering high power laser energy; and F2 is for transporting the scattered light to a polychromator.

Contrary to our intuition, it is reported that a step index type optical fiber made of pure silica can transmit a high power density [2]: A 400μm core diameter fiber can transmit 2000 W CW light and a 1MW/mm^2 light pulse width <1ms. Considering available laser diode of 300W CW output, core diameter of 400 μm is large enough for F1 fiber. The f=52 mm lens (L1) with 20×30mm^2 aperture focuses the scattered light onto the end surface of F2 fiber of 1mm in diameter cut at the Brewster angle. Both fibers set insides vacuum chamber is flexible enough enabling us to move the TS-prove head freely to a large extent. A simple metallic screen will shield the fiber against plasma radiation that would otherwise heats up the fibers. Unavoidable exposure to hard x-rays and neutrons, if present, will result in a gradual drop in the transmission of the fibers and fluorescent emission from the body of the fibers. The latter problem will not be serious for the present case in which a modulated laser beam is used. The former problem will be alleviated greatly by suitably selecting the fiber material and the wavelength of laser light (900-1100 nm) transmitted in the fiber. Raising the temperature of fibers, which may occur naturally or intentionally, will cure the defects introduced inside the fibers.

(3) **A Fiber feed-through** interfaces the fibers set in the inside and outside of a vacuum chamber. There is commercially available fiber feed-through that can be used for an ultra-high vacuum (UHV) environment of 10^{-10} mbar [3]. The durability against high power transmission is an issue not yet checked.

(4) **Laser diode:** A light source for a TS is required to be intense enough to yield sufficient signal and to have a wavelength width narrow enough to discern the Doppler broadening of the scattered spectrum due to thermal motion of plasma electrons. The allowable width ($\Delta\lambda$) depends on the minimum-measurable electron temperature T_{e_min}(eV) as follows: $\Delta\lambda/\lambda << T_{e\_min}^{0.5}/500$. Examples: for T_{e_min}=10eV, $\Delta\lambda/\lambda << 6/1000$; for T_{e_min}=1eV, $\Delta\lambda/\lambda << 2/1000$. These imply that it is not absolutely necessary to use lasers operating in a cavity, e.g., an Nd:YAG laser with $\Delta\lambda/\lambda << 10^{-6}$, as a TS-light source. Laser diodes, which are widely used for pumping the laser rod and for industrial application such as welding and cutting, seem to be suitable for the present purpose. For example, LIMO GmbH produces a fiber coupled laser diode module that delivers 980 nm 350 W light from a 400μm core fiber with NA=0.22 [4]. The specified line width (FWHM) $\Delta\lambda$<8 nm will allow the Te measurement down to T_{e_min}~30eV, which is rather high for edge plasma measurement. Recently it was reported [5] that a Bragg grating stabilizes a diode laser to yield power of 330 W from a fiber in $\Delta\lambda$=0.5 nm line width at λ=967 nm, which allowing a TS measurement down to a few eV. These above data are for a CW operation. As described later, the laser diode should be modulated at a high frequency. Whether there is degradation in high power delivering capability when used in modulation mode is an open question.

(5) **A polychromator** spectrum-analyze the scattered light transported by fibers. We will use a conventional three-filter polychromator. The principle of operation is based on the transmission and reflection characteristics of a combination of filters arranged to form a zigzag optical path. A key issue in the polychromator is to prevent the stray light with the wavelength at the laser from entering the light detector such as avalanche photo diode (APD). In the case of LHD-TS, each filter in the polychromator blocks the light at 1064 nm (Nd:YAG laser wavelength) with the blocking factor of 10^5 (OD5). Even with this high blocking factor, some polychromators suffer from the stray light problem. Considering the absence of the beam dump in the present case, the filters with a much higher OD blocking will be necessary. A setting a notch filter with OD~4 at the laser wavelength at the exit of the fiber-lens may be a solution to this. In addition to the high blocking, the steepness of the edge of the filters is of importance related with the lowest detectable Te (T_{e_min}).

(6) **Lock-in amplifiers** are used to pickup weak scattered signals modulated at frequency f_m in the presence of an overwhelming background noise mainly arising from plasma light. In considering that the spectrum of plasma density fluctuation and the resultant plasma light fluctuation monotonically

decreases down to a sub-MHz region, the reference frequency f_m higher than 1MHz is favorable for reducing the noise contribution. There is a commercially available lock-in amplifier operating at frequency as high as 200 MHz: SR844 (Standard Research System) [6].

3. Signal to Noise Ratio

We suppose to measure a sheet like divertor leg plasma of 15 mm in depth that has *Te* less than 100 eV and *ne* ranging from 10^{18} m^{-3} to 10^{19} m^{-3} with a modulated laser diode of P_{LASER} =300W and λ_{LASER} = 980 nm.

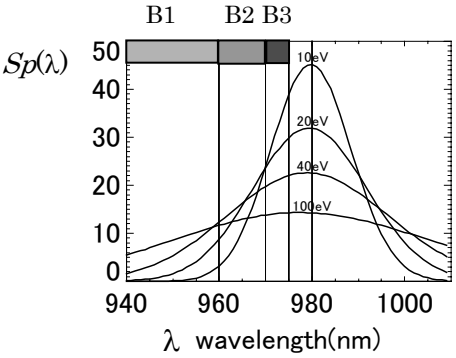

Fig. 5. TS spectra for various Te. Three color bands are indicated.

The backward TS spectrum is shown in Fig. 5 for various *Te*, which are discriminated by three color channels with pass bands B1=[940, 960], B2=[960, 970] and B3=[970, 975] in nm unit. The light power fed to a polychromator is the sum of the scattered light P_{sct} plus the plasma radiation P_{rad}, which are given respectively as

$$P_{sct} = P_{LASER}\, ne\, L(\, d^2\sigma/d\Omega d\lambda)\Delta\Omega\Delta\lambda$$

$$\approx 1.2\,(\,P_{LASER}/300W)(\,ne/10^{-19}m^{-3})(L/3mm)$$

$$*(\Delta\Omega/25msr)Sp(\lambda)d\lambda/\lambda_{\,LASER}\quad pW \qquad (1)$$

and

$$P_{rad} = j_v \Delta\nu\Delta V\Delta\Omega$$

$$\approx 110\,(Z_{eff}/3)(ne/10^{-19}m^{-3})^2(Te/100eV)^{-1/2}*(G/10)$$

$$(\Delta\Omega/25msr)(V_{obs}/10mm^3)*(\Delta\lambda/nm)(1\mu m/\lambda)^2 \qquad (2)$$

Here $Sp(\lambda)$ is the TS spectrum shown in Fig. 5, λ_{LASER}=980 nm is the laser wavelength, j_v is the Bremsstrahlung emissivity, Z_{eff} is the effective ion charge, G is the Gaunt factor enhanced ~5 times to take account of enhanced radiation due to recombination and line radiation, $V_{obs}\sim\pi D^2/4*15\sim10mm^3$ is the effective plasma volume that the collection optics see. The light power that falls in i-th filter's pass band is incident to the i-th APD, inducing a current

$$j_i = \int d\lambda\,(P_{sct}+P_{rad})F_i(\lambda)/h\nu$$

$$= \int d\lambda\,(P_{sct}+P_{rad})\,F_i\,(\lambda)/\lambda/hc \qquad (3)$$

$$\equiv j_{si.} + j_{bi}$$

Here $F_i(\lambda)$ is the filter transmittance η_{FIL} times quantum efficiency η_Q of the the i-th channel: $F_i(\lambda)=\eta_{FIL}.(\lambda)\,\eta_Q(\lambda)$. We assume an idealized filter with η_{FIL} =0.9 in the i-th pass band and η_{FIL}=0 otherwise. The responsivity (A/W) and its associated quantum efficiency η_Q (%) of an APD are shown in Fig. 7 as function of wavelength, from which we reasonably set η_Q=0.75 for the three pass bands (940 nm <λ<975 nm).

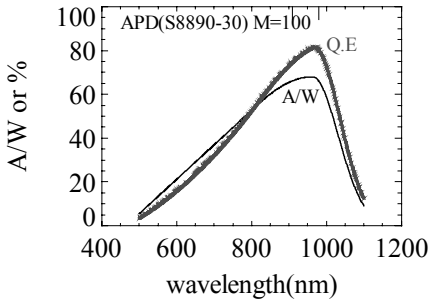

Fig. 6. Responsivity and quantum efficiency of an APD (Hamamatsu S8890).

For later use, we define x_i by

$$x_i \equiv j_{si}/ne \qquad (4)$$

Figure 7 (a) and (b) show j_{bi} and $j_{si.}$ for plasma with ne=$10^{-19}m^{-3}$ as a function of *Te*. We note that the scattering signals $\{j_{si};\ i=1,2,3\}$ are deeply buried in the plasma Bremsstralung signals $\{j_{bi};\ i=1,2,3\}$. The outputs of the APDs, which is proportional to $j_i=j_{si}+j_{bi}$ are fed to three lock-in amplifiers. A lock-in

amplifier is a kind of a Fourier analyzer if the reference input is fed by a precise sinusoidal signal, which is also used to modulate the laser diode. The frequency spectrum of the output of an APD is composed of two terms: one is a very narrow TS-signal centered at the modulation frequency f_m; other is broad band noise mainly generated by shot noise. The current in the APD $j_i=j_{si}+j_{bi}+j_d$ generates the shot noise whose power spectrum is given by

$$<i_n^2> =2e(j_{si}+j_{bi}+j_d)M^2Fn(M)\Delta f. \quad (5)$$

where M~100 is the multiplication factor of the APDs and j_d~1 nA is the dark current in the APD, Fn(M) is an excess noise factor and Δf is the bandwidth.

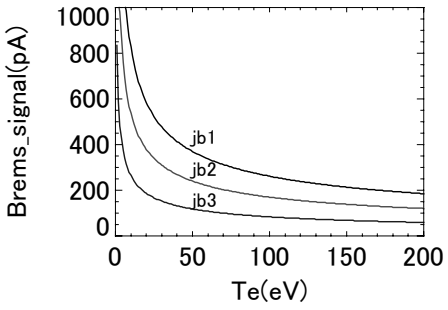

Fig.7 (a) APD currents induced by Bremsstrahlung. *ne*=10^{-19}m^{-3}.

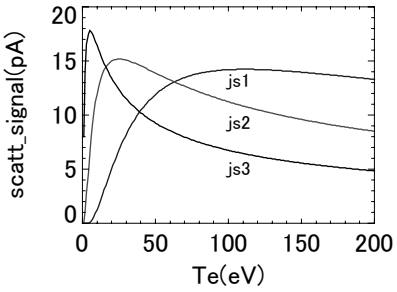

Fig.7 (b) APD currents induced by Thomson scatted light. *ne*=10^{-19}m^{-3}.

The appearance of Fn(M) implies an enhanced noise in the avalanche process in APD [7,8,9]. Fn(M) is dependent on the ratio of hole ionization to electron ionization. By suitable design and selection of processing material, Fn(M) can be less than 4 for M=100 [9]. In this paper we assume Fn(M)=10. The RC-type integration time τ of a lock-in amplifier gives the spectrum width Δf given by the relation $\Delta f=1/4\tau$. Then, the output of the lock-in amplifier is expressed as

$$y_i= j_{si} \pm [e(j_{si}+j_{bi}+j_d)/2\tau]^{1/2} \equiv j_{si}\pm\delta_i. \quad (5)$$

Hence, however deeply the TS-light is buried in the plasma radiation, it is possible to pickup the TS-signal by taking a long enough integration time. With these data $\{y_i;\ i=1,2,3\}$ we can estimate the errors on the deduced *Te* and *ne* by following the standard method. The two ratios $j_{s1}/j_{s3} \equiv g1(Te)$ and $j_{s2}/j_{s3} \equiv g2(Te)$ are functions of *Te* alone as shown in Fig. 8. Conversely, the observed ratios y1/y3 and y2/y3 give two *Te*: $Te1=g^{-1}(y1/y3)$ and $Te2=g^{-1}(y2/y3)$. Here g^{-1} is the inverse function of g.

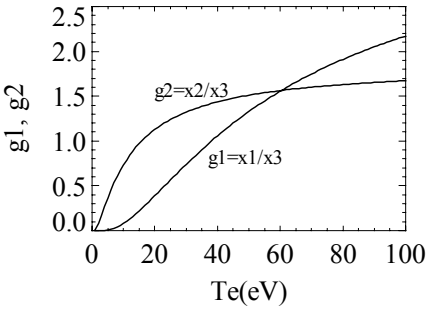

Fig. 8. Two ratios among the TS-signals from three-color channels.

The errors on *Te1* and *Te2* are calculated as

$$(\delta Te1)^2=(\partial g1^{-1}(x)/\partial x)^2(\delta y1^2/y3^2+y1^2\delta y3^2/y3^4) \quad (6)$$

$$(\delta Te2)^2=(\partial g2^{-1}(x)/\partial x)^2(\delta y2^2/y3^2+y2^2\delta y3^2/y3^4) \quad (7)$$

$$(\delta yi)^2=e(j_{si}+j_{bi}+j_d)/2\tau \quad (6)$$

With the variance $(\delta Te)^2$ defined by

$$1/(\delta Te)^2 =1/(\delta Te1)^2 +1/(\delta Te2)^2 \quad (8)$$

the most probable *Te* is given by

$$Te=(Te1/(\delta Te1)^2+Te2/(\delta Te2)^2)(\delta Te)^2 \quad (9)$$

The errors on *ne* is obtained, for example, from

$$ne = j_{s3}/ x_3 \quad (10)$$

$$(\delta ne/ne)^2=(\delta j_{s3}/j_{s3})^2+(\partial x_3(Te)/\partial Te)^2 (\delta Te)^2 \quad (11)$$

In what follows, we shows relative errors in *Te* and *ne*, $\sqrt{(\delta Te)^2}/Te$ and $\sqrt{(\delta ne)^2}/ne$, as a function *Te* for several combinations of parameters that gives the relative errors less than 20%. First we show the relative errors for P_{LASER}=300W, $ne=10^{19}m^{-3}$ and τ=0.1s in Fig. 9. Errors in both *Te* and *ne* are less than 10% for 6eV<*Te*<90eV. This implies that a plasma with $ne\geq10^{-19}m^{-3}$can be measured with time resolution around 0.1s.

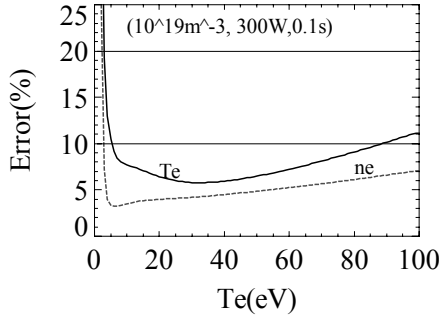

Fig. 9. $\sqrt{(\delta Te)^2}/Te$ and $\sqrt{(\delta ne)^2}/ne$ for P_{LASER}=300W, $ne=10^{19}m^{-3}$ and τ=0.1s.

For a ten times more dense plasma, $ne=10^{20}m^{-3}$, an integration time of 0.05 s is necessary for the same P_{LASER} =300W as shown in Fig. 10.

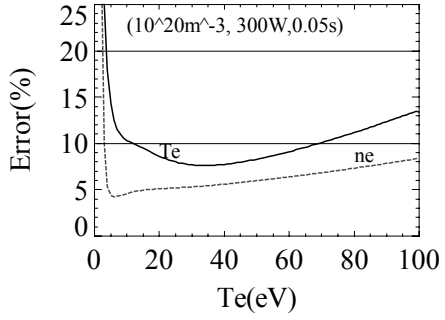

Fig.10. $\sqrt{(\delta Te)^2}/Te$ and $\sqrt{(\delta ne)^2}/ne$ for P_{LASER} =300W, $ne=10^{20}m^{-3}$ and τ=0. 05s.

Even a smaller laser power of P_{LASER} =100W yields a reasonable data quality with a longer integration time of 0.5 s as shown in Fig. 11.

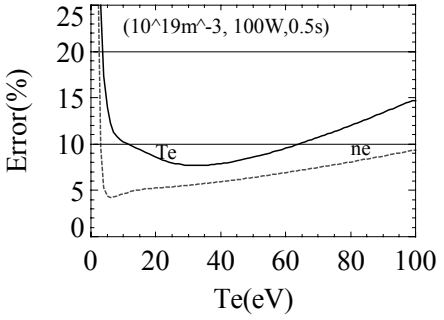

Fig.11. $\sqrt{(\delta Te)^2}/Te$ and $\sqrt{(\delta ne)^2}/ne$ for P_{LASER} =100W, $ne=10^{19}m^{-3}$ and τ=0.5s.

Even lower density plasma of $ne=10^{18}m^{-3}$ can be measured with P_{LASER} =300W by integrating much longer time of 1 s as shown in Fig.12.

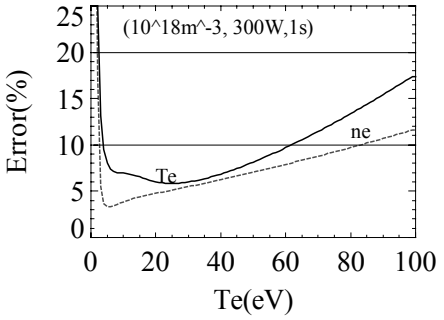

Fig.12. $\sqrt{(\delta Te)^2}/Te$ and $\sqrt{(\delta ne)^2}/ne$ for $ne=10^{18}m^{-3}$, P_{LASER} =300W and τ=1s.

4. Discussions

We showed the feasibility of a TS-probe based on optical fibers and the recently developed high power laser-diode with narrow line width. It was shown that the currently available laser diode of 300W can yield accurate *Te* and *ne* data for plasma of $ne\sim10^{-19}m^{-3}$ with integration time of 0.1s. If there were no enhancement in APD noise, the noise power spectrum in Eq. (5) is proportional to M^2 . In this case, the errors in *Te* and *ne* are much reduced and

an integration time of 0.01 s is long enough to yield accurate data as shown in Fig.13.

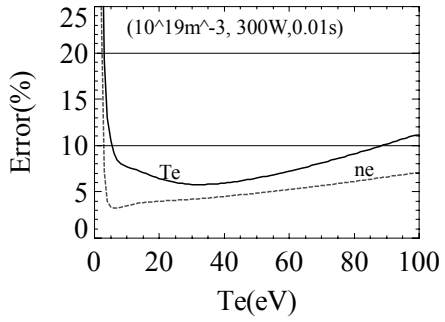

Fig.13. $\sqrt{(\delta Te)^2}/Te$ and $\sqrt{(\delta ne)^2}/ne$ for P_{LASER} =300W, ne=10^{19}m^{-3} and τ=0.01s when no enhanced noise is added to APDs.

In this view, developing photo detectors with smaller noise are worthwhile [9]. With the presently available APDs, time integration longer than 0.1 s is necessary for measuring plasma with 10^{19}m^{-3} ≥ne. Hence, the proposed TS-probe is suitable only for long pulse discharge experiments. For measuring a fast phenomenon a shorter integration time less than 0.1s is desirable. A way to improve this is to raise the TS-light power. The key element of the TS-probe is intense light transmission in a fiber. A ϕ1.2 fiber, which is still flexible, can transmit light of 2kW CW and 1MW pulse with duration less than 1ms. If 1MW laser of 0.1 ms pulse width is available, it will give enough accuracy with τ=0.01 ms as shown in Fig.14.

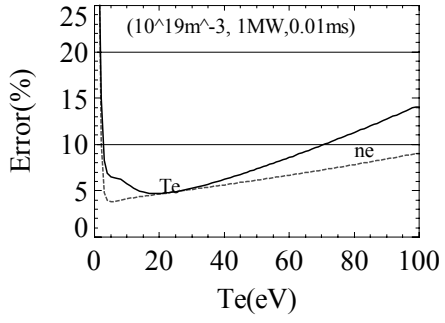

Fig.14. $\sqrt{(\delta Te)^2}/Te$ and $\sqrt{(\delta ne)^2}/ne$ for P_{LASER} =1MW, ne=10^{19}m^{-3} and τ=0.01ms.

Up to this point, we have assumed that there is no plasma light fluctuation around the frequency of the laser diode modulation f_{m}~ 1MHz. This assumption may be supported by the fact that there is no success report on detecting turbulent density fluctuation by Bremsstlahlung measurement. A key point in the present TS-probe is the smallness of V_{obs}~ 10mm^3, which helps to reduce the plasma radiation power entering to the light collection optics. This is accomplished by matching the slit size on the light collecting fiber to the size of the image of the laser beam whose size is reduced down to ϕ1mm. The beam size largely depends on the fiber diameter and the N.A. The smaller diameter and smaller NA are favorable for reducing the beam size. If it is possible to mount a laser diode on the TS-probe head, the beam size at the focal point can be reduced much less than ϕ0.1, thus lowering V_{obs} and P_{rad} several orders of magnitude. This approach of design will be given elsewhere.

REFERENCES

[1] K. Narihara, et al., Fusion Engineering and Design **34-35,** 67 (1997).
[2]Diaguide, Mitsubishi-cable Catalog 2000.07 (in Japanese).
[3] www.lewvac.co.uk
[4] www. LIMO.de
[5] Laser Focus World Japan 2008-8, p52.
[6] www. Thinkers.com/products/SR844.htm
[7] A. van der Ziel, *Noise*, Prentice-Hall, Inc, 1954.
[8] R.J. McIntyre, IEEE Trans. on Electron Devices, **ED-13**, 164 (1966).
[9] 'The Avalanche Photodiode Catalog', Advanced Photonix, Inc.

Proceedings of ITC18,2008

Development of the UV and Visible Impurity Influx Monitor (Divertor) for ITER

Atsushi Iwamae, Hiroaki Ogawa, Tatsuo Sugie, Satoshi Kasai, Yoshinori Kusama

Japan Atomic Energy Agency, Mukoyama 801-1, Naka, Ibaraki,311-0193, Japan

Nippon Advanced Technology, Tokai, Ibaraki, 311-1112, Japan

We have developed a spectroscopic diagnostics system in the wavelength region of 200 - 1000 nm for monitoring ITER divertor plasmas, such as the influx of impurity elements, position of the ionization front, electron temperature and density. An equivalent size prototype of the optical components for the upper port spectroscopic diagnostics system has been fabricated and assembled as part of the system to estimate quantitative light throughput. Collisional-radiative models estimate the line intensities of helium ash and carbon ions. The reflection of tungsten and carbon fiber composite, which comprise the plasma facing materials of the divertor, is measured. The reflection of the surface of the tungsten divertor material is 23% at λ656nm. There is an anisotropic aspect to the surfaces of W and CFC.

Keywords: iter divertor plasma, spectroscopic diagnostics, impurity influx, in-site calibration method, reflection of divertor component materials

1. Introduction

Generating electric power by means of nuclear fusion, DEMOs, and the next generation of tokamak- and heliotron-type reactors of ITER, has been proposed, including the SlimCS [1]. In order to realize the potential of a DEMO reactor, the plasma diagnostics in the harsh environment of D-T fusion plasmas, i.e., high levels of neutrons, gamma-rays and plasma particle bombardment as well as nuclear heating, should be strictly tested during the ITER phase. The impurity influx monitor (divertor) through ultra-violet (UV) and visible spectroscopic measurements [2-4] is responsible primarily for monitoring influx from the plasma-facing components of beryllium, carbon, and tungsten, for sensing the position of the ionization front, and for determining the ion temperature in divertor plasmas [5]. The impurity influx monitor also has the secondary functions of monitoring electron temperature and density (T_e and n_e), as well as the fuel ratios (n_H/n_D or n_T/n_D) of divertor plasmas. The impurity influx monitor also supplements information about the radiation power and profiles in the divertor and the X-point/MARFE regions, and gives information about the densities of neutral atoms and molecules.

The neutron flux and energy deposition in mirror materials and the vacuum window are estimated in Ref. [6]. Estimates of the neutron flux and nuclear heating at the first mirror located ~1m behind the first wall are 1.2×10^8 m^{-2} s^{-1} and 20 kW/m^3, respectively. It is known that neutron irradiation of 1.4×10^8 n m^{-2} on the molybdenum mirror has no effect on the mirror surface [7]. Divertor systems are planned for the upper #01, equatorial #01 and divertor #02 ports. The fist mirrors of these systems are made of molybdenum. From each of the upper and equatorial ports, we may observe the divertor plasma with lines of sight in a 71 chord fan array. From the divertor port we observe the plasma with viewing chords in a fan array placed in a gap between the divertor cassettes. The optical design of the viewing chords for observing strike divertor plate is undergoing to fit inside the new divertor dome box. Here we report on the present status of development of the divertor for ITER on the upper port.

2. Prototype optical properties

We have assembled the optical components into a scale size model viewing system. Figure 1 shows the arrangement of the upper port optical system. The prototype of the upper port fan array viewing chords is manufactured with fifty lines of sight, though seventy-one lines are planned for the production model. The front-end optics placed close to the main plasma consists of three metallic mirrors. The material of the first and second mirrors is molybdenum. The second is an off-axis paraboloid mirror. The third is a plane aluminum. The distance from the first mirror to the divertor dome is about eight meters. The fifty lines of sight cover 1.4 m in the poloidal direction. Emissions from the divertor plasma collected with the front-end optical optics are transferred via a dog-leg, using two aluminum-coated glass mirrors with a 190 mm effective diameter to a Cassegrain telescope.

author's e-mail: iwamae.atsushi@jaea.go..jp

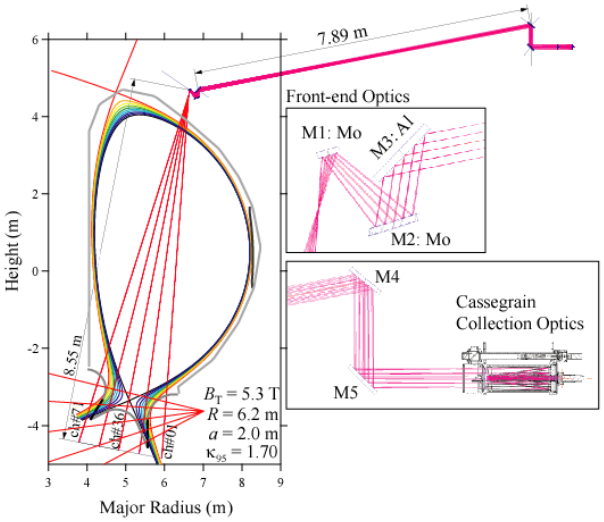

Fig.1 The upper port optical system of the impurity influx monitor (divertor). Front-end optics consists of three metallic mirrors: a plane M1(Mo), an off-axis paraboloid M2(Mo), and a plane M3(Al). Fan array lines of observation are planned to total seventy-one chords from the upper port.

At the focus plane of the Cassegrain collection optics, a micro-lens array is coupled with fifty optical fibers whose 200-micrometer core diameter is contained within a 220-micrometer clad. The micro lens array (MLA) is made of synthetic silica and contains in one unit, ten biconvex lens with a radius, length, and height of 3.3 mm, 6.7 mm, and 2mm, respectively. These five units are bonded with a binding material. Fifty optical fibers of two meters each transfer the light to a spectrometer, each of which has an FC coupler.

We measured the light throughput coefficient of the prototype. A calibrated standard xenon light source irradiated a Spectralon reflectance target at a distance of 50 cm. The target was placed 30 cm in front of the first mirror. A compact optical fiber-coupled spectrometer was used to record the spectral properties. Light to the spectrometer was relayed via a 20-meter length of the 200-220 FC-SMA optical fiber which prevents an anisotropic mode inside the core of the optical fiber.

Figure 2 shows the spectral throughput coefficients of three chords of #01, #26 and #50. In the visible wavelength region, the coefficient is almost flat at 4×10^{-11} m^2sr, and gradually decreases in the red wavelength region. Below a wavelength of 300 nm, the signal to noise ratio is rather low because of the spectrometer grating and detector efficiency. Above 800 nm no calibration data are available for the light source. Future experiments in the longer wavelength region will employ a calibrated integral sphere.

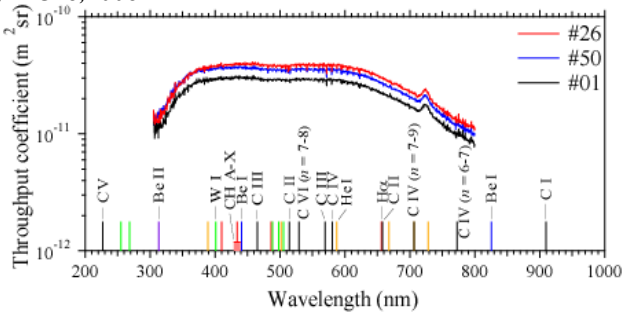

Fig.2 Measured light throughput coefficients for the upper port prototype. The peaks at the 730 nm are the pseudo-peak of the xenon line from the light source.

The observable region of the MLA was assessed by means of inserting light from a halogen lamp into each of the optical fibers. The MLA image when focused at the target plate at a distance of 8.55 m from the first mirror and gathered through the collection and front-end optical components, is shown as an example in Fig.3. The widths of the examined lens image at 90% intensity range from 27 to 34 mm. This satisfies the ITER requirement of a 50 mm resolution. The surface of lens #01 is rather rough, such that the light throughput of this chord is relatively low. Where a micro lens array with a biconvex radius of r = 2.45 mm and length of 7.45 mm is feasible, light collection efficiency increases at least three times.

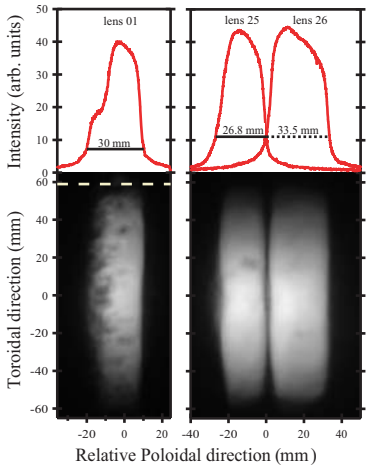

Fig.3 MLA image in the divertor region. The size of the image in the poloidal direction satisfies the ITER requirement of 50 mm.

3. Emission intensity estimation

Emission intensity of the ITER divertor plasma using the B2-EIRENE code package [8] has been calculated with the following conditions: I_p = 15 MA, B_T = 5.3 T, P_{fusion} = 600 MW, (Q = 20, P_{NBI} = 30 MW), a deuterium flux from the core of 9×10^{21} s^{-1}, and a gas-puff

rate of 1.4×10^{23} s^{-1}[9]. A two-dimensional plasma parameter distribution (T_e and n_e) and helium atom and ion density distributions are obtained from the code. Near the strike points in front of the inner and outer divertor targets, the plasma temperature is $T_e < 1$ eV and the density is $n_e > 1\times10^{21}$ m^{-3} I, leading to the conclusion that a detached plasma is formed. The line integrated emission intensity of He I lines is estimated with a collisional-radiative (CR) model [10,11]. Figure 3 shows one example (He I $2^3P - 3^3D$, λ587.6 nm emission line radiance) of six emission lines of He I (n = 3 – 2), for both (a) ionizing and (b) recombining components. The chord-integrated intensity along the line-of-sight portrayed in Fig. 1 from the upper port is shown in Fig. 5. The peak intensity is 7×10^{17} ph $s^{-1}m^{-2}sr^{-1}$. The ionizing component is dominant for all of the observation chords since both strike points at the divertor plates are not observable from the upper port. The intensity ratios of the $I_{667.8\ nm}/I_{728.1\ nm}$ and $I_{728.1\ nm}$ / $I_{706.5nm}$ emission lines are often used to estimate n_e and T_e. The singlet and triplet emission line-integrated intensities are plotted on a logarithmic scale as shown in Fig. 6. In order to obtain the n_e and T_e distributions, it is required to measure the radiance on the order of 10^{15} ph $s^{-1}m^{-2}sr^{-1}$.

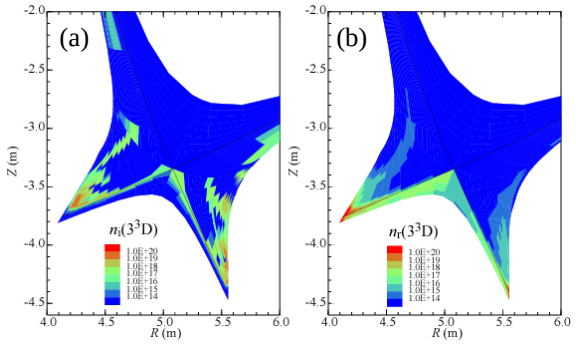

Fig.4 The population distribution of the n(3^3D) state, with (a) the ionizing component from helium atoms and (b) the recombining component from helium ion shown separately.

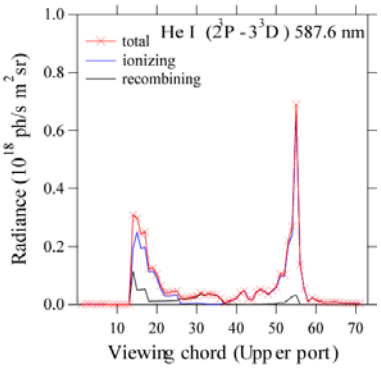

Fig.5 Chord-integrated emission intensity of the He I 587.6 nm (2^3P – 3^3D) transition. The ionizing component is dominant for all viewing chords.

The optical throughput coefficient is around 4×10^{-11} m^2sr, and peak photon intensity is 7×10^{17} ph $s^{-1}m^{-2}sr^{-1}$. If we divide the signal among three spectrometers, (UV, filter and High resolution), the efficiency of the split optical fibers is 12%. The light is transferred from the ITER port to the diagnostic room via one hundred meters of optical fiber with a transmission rate of 70%. If we use a spectrometer with a diffraction efficiency of ~50% and a back-illuminated CCD whose quantum efficiency is 60%, then 7.1×10^5 photoelectrons s^{-1} are detectable, i.e. 710 photoelectrons/ms. Helium ash that has a higher signal is observable with a 1 ms time resolution. However, to obtain special information on n_e and T_e, a certain amount of time is required. B2-EIRENE code also provides a C^{3+} and C^{4+} ion density map. We have estimated the C IV emission intensity using the CR model [12]. Results are shown in Fig. 7. The C IV (n= 6–7) 772.6 nm line is used to estimate ion temperature [13]. The upper port observes the divertor plasma through the high-temperature core plasma. Figure 8 shows the estimated bremsstrahlung continuum emission intensity along the central chord of the fan array view. The continuum emission is the same order for helium and the C IV emission intensity evaluated here.

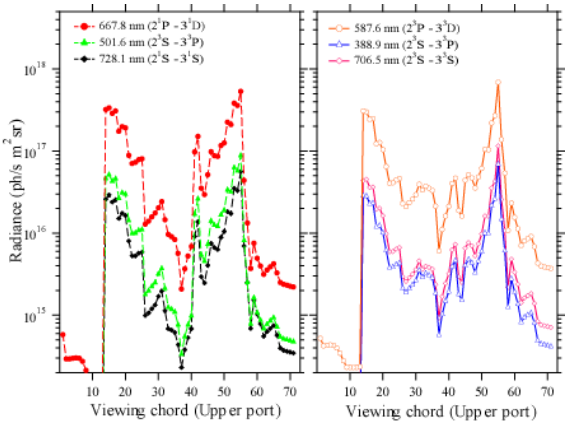

Fig.6 Chord-integrated emission intensity of the He I n = 3 to n = 2 levels.

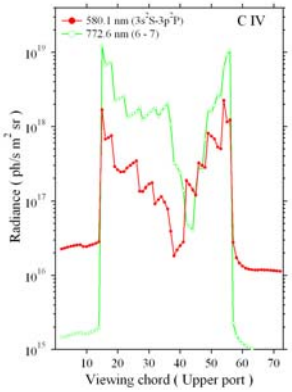

Fig.7 Chord-integrated emission intensity of C IV.

Signal level shifts in the continuum radiation also are taken into account in evaluating the impurity emission intensities.

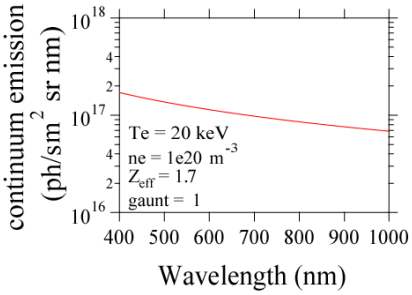

Fig.8 Bremsstrahlung intensity is the same order across impurity emission lines.

4. Spatial resolution with computer tomography

The position of the ionization front can be measured through a multi-chord observation. Spatial distribution with a full width of 10-cm at a half-maximum (FWHM) Gaussian distribution is examined as a model case. In the #01 section we have an upper and equatorial fan array view, though the angle between the two views is rather narrow. Neither strike points are covered by both upper and equatorial views. We have employed the maximum entropy method [12,13] of the computerized tomopgraphy in order to reconstruct the two-dimensional special distribution. The distribution of the reconstructed model is elongated along the vertical direction by a factor of four, compared to the original distribution. In order to improve this situation we have proposed a gap-viewing fan array of 72 chords at divertor port #02 in the left gap of the central cassettes, looking radially inward. We have to assume that the following reconstruction is based on toroidal symmetry at ports #02 and #01 of about 20 degrees in the toroidal direction. Figure 9 shows the suggested gap-viewing chords and the reconstructed image. The reconstructed image with the upper port view and the gap fan array view provides a good estimate of the original distributions.

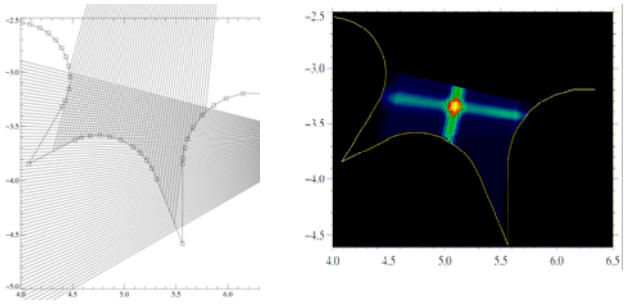

Fig.9 The gap-viewing chords and the CT image.

5. Reflection of the plasma-facing components.

The upper baffles of the inner and outer divertor and the dome are made of pure tungsten. The strike points are carbon fiber composite (CFC). We have examined the direct reflections of both divertor materials with injection light beams up to five degrees away from normal. Spectral reflection measurements have been carried out with a spectrophotometer (JASCO V570 with a SLM468 unit). Figure 10 shows the results for the CFC and tungsten divertor components. CFC reflection is negligible, with a reflection peak of 0.5% at λ250 nm. However, the reflection of tungsten is as high as 23% at λ656 nm (Dα line). There is an anisotropic aspect to the reflection because of the curved cutting by the milling machine. We will investigate the bidirectional reflection distribution functions of the divertor material for lines at various wavelengths.

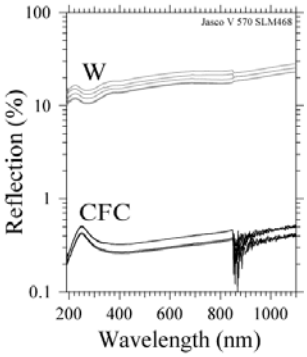

Fig.10 The five degree nominal reflections for W and CFC. At a wavelength of 850 nm, the grating of the monochromator is changed, and the detectors are switched from a photomultiplier to a PbS sensor.

References

[1] K. Tobita *et al.*, Nucl. Fusion **47**, 892 (2007).
[2] T. Sugie *et al. Burning Plasma Diagnostics* (AIP, New York 2008) p. 218.
[3] T. Sugie, J. Plasma Fusion Res **79**, 10 (2003).
[4] H. Ogawa *et al.* Plasma and Fusion Res. **2**, S1054 (2007).
[5] A. Costley, *System Require Document (SRD) Diagnostics* PBS 55 (2008).
[6] H. Iida *et al. Nuclear Analysis Report* G 73 DDD 2 W 0.2 (2004).
[7] T. Nishitani *et al*. Fusion Eng. Des. **42**, 443 (1998).
[8] R. Schneider *et al*. J. Nucl. Mater. **266-269** 175 (1999).
[9] A.S. Kukushkin *private communication*.
[10] M. Goto, J. Quant. Spectro. Radiat. Trans. **76** 331 (2003).
[11] M. Goto and T. Fujimoto, NIFS-DATA-043 (1997).
[12] T. Nakano *et al*. Nucl. Fusion **47** 1458 (2007)..
[13] T. Nakano *et al.* J. Plasma Fusion Res. **80**, 500 (2004).
[14] N. Iwama and S. Ohdachi, J. Plasma Fusion Res. **82**, 399 (2006).
[15] K. Fujimoto *et al*. Plasma Fusion Res. **2** S1121 (2007).

Proceedings of ITC18,2008

Recent progress in development of Nd:YAG laser for ITER edge Thomson scattering diagnostics

T. Hatae, T. Hayashi, S. Kajita[1)], H. Yoshida[2)], H. Fujita[2)], M. Nakatsuka[2)], J.-H. Lee[3)], K. Yahagi[4)], K. Shinobu[4)], T. Ono, Y. Kusama

Fusion Research and Development Directorate, Japan Atomic Energy Agency, 801-1 Mukoyama, Naka, Ibaraki 311-0193, Japan, [1)] Nagoya university, [2] Osaka university, [3)]National Fusion Research Institute, [4)]NEC Engineering, Ltd.

We are developing a high-energy (5J) and high repetition-rate (100Hz) laser system for ITER. Optical design of the laser system has been conducted. The design is based on the design of Nd:YAG laser for Thomson scattering system for JT-60U. A prototype laser amplifier has been designed, and developed experimentally. Two laser rods and four flash lamps are installed in the prototype laser amplifier. From initial tests of the prototype laser amplifier, it has been confirm that the net laser energy of ~1.3J is extracted from one laser rod.

Keywords: ITER, Thomson scattering, YAG laser, stimulated Brillouin scattering, phase conjugate mirror, laser oscillator, laser amplifier

1. Inroduction

An edge Thomson scattering system for ITER is a diagnostic system which measures electron temperature (T_e) and density (n_e) at a peripheral region of the plasma [1]. The edge Thomson scattering system is required to measure T_e and n_e over a relatively narrow spatial area (r/a>0.9) but with a high spatial resolution (5 mm at the midplane). The requirements are summarized in Table 1. A high-energy (5J) and high-repetition-rate (100Hz) Q-switched Nd:YAG laser system is necessary for this system. We are developing a high-energy and high repetition-rate laser system for ITER based on the laser design in JT-60U[2-5]. In this article we report recent progress in development of Nd:YAG laser for the edge Thomson scattering system in ITER.

Table 1. Requirement for ITER edge Thomson scattering system

Parameter	Area*	Range	Resolution		Accuracy
			temporal	spatial	
T_e	$r/a > 0.9$	0.05 – 10 keV	10 ms (100Hz)	5 mm	10%
n_e		5×10^{18} – 3×10^{20} m^{-3}			5%

*Measurement area of 0.85<r/a<1.07 has been considered recently.

2. Target performance of the Nd:YAG laser and technical issues

A laser system having energy of 5J, repetition rate of 100Hz, and pulse width of 10 ns is necessary in order to realize the ITER measurement requirement. Nd:YAG laser is possible to realize the performance. The Q-switched laser which simultaneously has energy of 5J and the repetition rate of 100Hz is categorized as a high average power laser. It generally requires advanced technology in order to make the high-average-power laser. The 5-J, 100-Hz Q-switched laser has not been made until now. The technical issues of development the high-average-power laser are as follows.

(1) Limitation of the output energy by thermal lensing effect which are caused by the temperature gradients across the active area of the laser rod.

(2) Decreasing of the beam quality by deplolarization which are caused by thermally induced birefringence.

(3) Decreasing of the output energy by parasitic oscillation which originates from multistage and high gain amplifiers.

The stimulated-Brillouin-scattering phase conjugate mirror (SBS-PCM) is an important tool for improving the performance of high-average-power laser systems [6]. It is possible that the SBS-PCM compensates the thermally induced wavefront distortion such as the thermal lensing effect, and improves the depolarization caused by thermally induced birefringence. Furthermore, the parasitic oscillation due to the amplitude spontaneous emission (ASE) is suppressed by threshold of the stimulated Brillouin scattering. In the Nd:YAG laser system for Thomson scattering in JT-60U, SBS-PCMs has been utilized, and successfully achieved energy of 7.46J and repetition rate of 50Hz[2-5]. The ITER laser system is designed based on design of the JT-60U laser system.

author's e-mail: hatae.takaki@jaea.go.jp

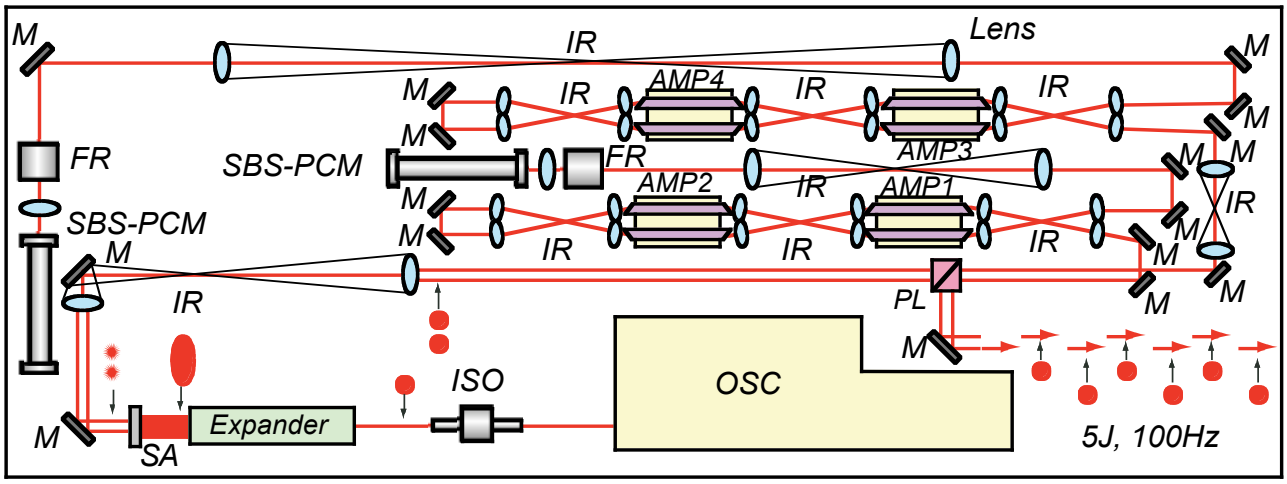

Fig.1 Optical layout of Nd:YAG laser for edge Thomson scattering system in ITER

3. Design of Nd:YAG laser for edge Thomson scattering system in ITER

In the optical configuration of the laser system, MOPA configuration is adopted. The oscillator produces single-longitudinal-mode (SLM) laser pulse (Energy =20mJ, repetition rate=100Hz, pulse width=30ns) [1,7]. The laser beam from the oscillator is shaped from a circular pattern to elliptic pattern using a beam expander composed of cylindrical lenses. The elliptic pattern is divided into two beams, and converted to top-hat profiles employing a dual serrated aperture (SA) and a successive spatial filter. Relay imaging optics (IR) are installed to maintain the top-hat profile. Each beam is amplified by an amplifier stage utilizing an SBS-PCM. There are two high-power amplifiers in the amplifier stage, and four laser rods are used in the laser system. Double-pass amplified beams by the SBS-PCM are extracted by a polarizer (PL). To reduce the thermal effect, each amplifier stage is fired at 50Hz, and dual beams are amplified alternately by dual amplifier stages. Finally, 100-Hz, 5-J beam is obtained. The optical layout is shown in Fig.1. Note that the dual beams are automatically aligned by the phase conjugate effect, and shapes and positional relation of dual input beam before dual amplifier stages and final output beams are always identical at the polarizer.

Output energy is roughly estimated from the performance of JT-60 amplifier. Net extract energy which is defined difference between the output energy and the input energy of a rod was measured using JT-60 amplifier (14mm of Nd:YAG rod diameter, 90 mm in length). Since the maximum extract energy is 1.86 J, total extract energy using four rods is expected 7.44J. If effective amplification is carried out, the output energy over 5J is expected in the case of ITER laser system.

4. Design of prototype laser amplifier

For the compact optical layout, two Nd:YAG laser rods (14mm in diameter, 100mm in length, 5.35° of wedge angle, concentration of Nd is 1.1 atomic%) and four xenon flash lamps are installed in a prototype amplifier. Each laser rod is pumped by two flash lamps, the electric energy of ~100J is supplied to two flash lamps at 50Hz of repetition rate. The average electric power of 10kW is supplied per one amplifier. The efficiency of Nd:YAG laser is ~2%, generally. Most of the electric power is changed to the heat in the amplifier. Therefore, ~10kW of heat removal is required for the amplifier, effective cooling techniques are necessary. Fig.2 shows a schematic of the prototype amplifier. Bolosilicate-glass flow tubes are installed to effectively cool for laser rods and flash lamps. Gap between the laser rod (flash lamp) and the flow tube is 1mm. The reflector is gold-plated mirror, and is cooled by cooling water.

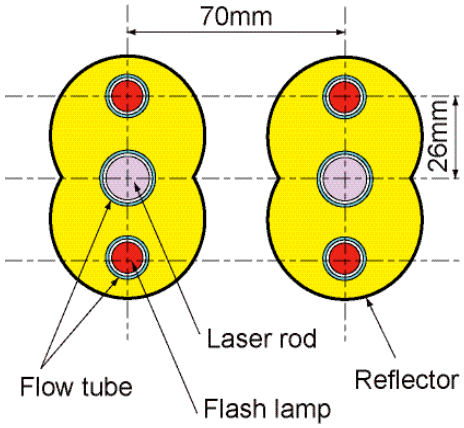

Fig.2 Schematic of prototype amplifier (cross section)

5. Initial tests for prototype amplifier

The small signal gain (SSG) of new amplifier has been measured using the ITER SLM oscillator. The SSG and the extracted energy measurement are shown in Fig.3. Though the SSG monotonously increases in the low charged energy region, the SSG is saturated around 65J as shown in Fig.3(a). The SSG of ITER amplifier is lower than that of JT-60 at the full pump (100J of charge energy). The maximum extracted energy is ~1.3J at the full pump as shown in Fig.3(b). JT-60 laser system is used to measure the extract energy of ITER amplifier.

Since intensity of the flash lamp emission increases with increasing of the charged energy, it seems that the laser rod is pumped normally. Further more, significant ASE is not observed. Influence of repetition rate and flow rate of cooling water upon SSG is examined. The SSG decreases with increasing of the repetition rate. This means the SSG decreases when the heat load increases. Even if the flow rate of cooling water for one laser rod is changed from 2.6 to 4.1L/min at 20°C, the SSG is not drastically improved. We think that the rod center is not cooled sufficiently.

As for the laser crystal, the gain profile shifts to the long wavelength side when the temperature of the crystal

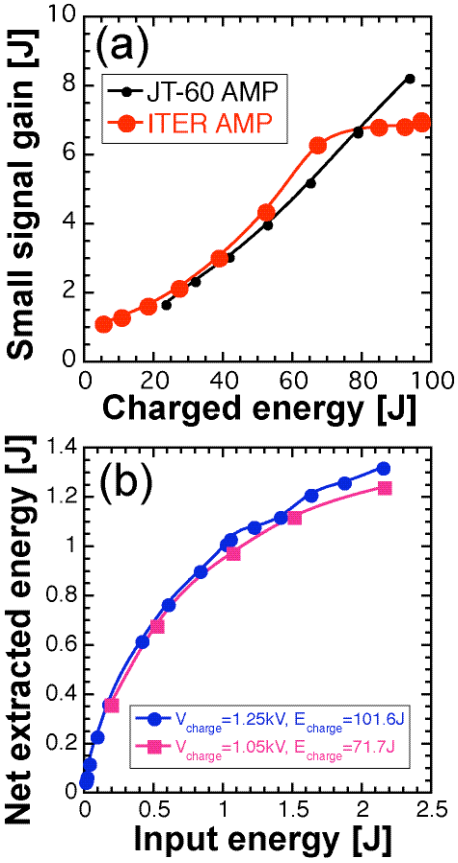

Fig.3 (a) Small signal gain versus charged energy for flash lamps (repetition rate 50Hz). (b) Net extracted energy versus input energy to ITER amplifier.

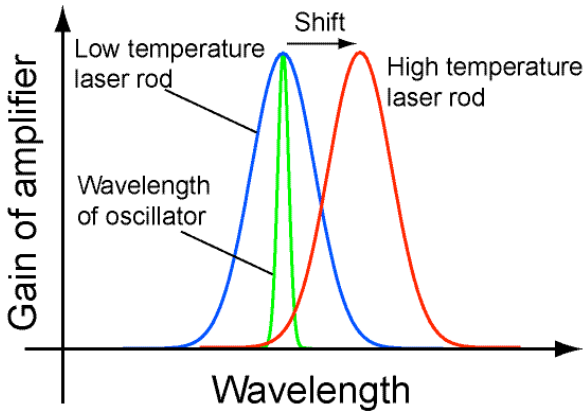

Fig.4 Gain profile shift of laser amplifier with changing the rod temperature

rises as shown in Fig.4 [8]. From the characteristics, we think that the laser beam of the oscillator can not be sufficiently amplified due to the mismatch of gain profile and wavelength of oscillator. Since it is difficult to lower the temperature of the rod center, the gain profile control is also difficult. To amplify in the best gain, we consider that matching the wavelength of oscillator with gain profile of the amplifier is effective. We will measure their spectra to verify this hypothesis.

6. Conclusion

A Nd:YAG laser for ITER edge Thomson scattering system is developing. The target performance is 5J, 100Hz. Design of the laser is based on that of laser system for Thomson scattering in JT-60U. New laser system will utilize stimulated-Brillouin-scattering phase conjugate mirrors to solve issues for high average power lasers. To get high reflectivity of the phase conjugate mirror, a laser oscillator with the single longitudinal mode has been developed. A prototype laser amplifier has been produced experimentally. From the initial tests, it found that the small signal gain was saturated around the maximum pumping. We are investigating the causes. As one possibility, we consider the mismatch of amplifier's gain profile and wavelength of oscillator causes saturation of small signal gain. We will measure their spectra to verify this hypothesis. Producing improved four amplifiers, and the assembling of the new laser system will be started in 2009.

Acknowledgment

This work is performed under the auspices of JAEA collaboration research program and Institute of Laser Engineering (Osaka university) collaboration program. This work is supported in part by Grant-in-Aid for Scientific Researches on Priority Area "Advanced diagnostics for burning plasma" from Ministry of

Education, Culture, Sports, Science and Technology (No. 17044009, 20026011).

References

[1] T. Hatae *et al*., Trans. Fusion Sci. Tech. **51**, 58 (2007).
[2] H. Yoshida *et al.*, Jpn. J. Appl. Phys. **42**, 439 (2003).
[3] H. Yoshida *et al.*, Jpn. J. Appl. Phys. **43**, L1038 (2004).
[4] T. Hatae *et al*., J. Plasma Fusion Res. **80**, 870 (2004).
[5] T. Hatae *et al*., Rev. Sci. Instrum. **77**, 10E508 (2006).
[6] D. A. Rockwell, IEEE J. Quanum Electron. **24**, 1124 (1988).
[7] T. Hatae *et al*., "Design of single-longitudinal-mode laser oscillator for edge thomson scattering system in ITER", JAEA-Technology 2006-021.
[8] A. Kaminskii, Laser crystals, Their Physics & Properties (Springer-Verlag, Berlin, 1990) p335.

Proceedings of ITC18,2008

Comparison of Au and Pt foils for an imaging bolometer

B. J. Peterson, E. A. Drapiko, D. C. Seo[a], J. Kodaira, N. Ashikawa
National Institute for Fusion Science,322-6 Oroshi-cho, Toki 509-5292, Japan
[a] National Fusion Research Institute, Daejeon 305-806, Rep. of Korea

The imaging bolometer is a fusion reactor relevant diagnostic for the measurement of radiated power. Essential to its ability to make accurate temporally and spatially resolved measurements of radiated power is the detailed calibration of the thin metal foil that converts the radiated power to infrared radiation measured by an infrared camera. The choice of the foil material is critical to optimizing the sensitivity of the imaging bolometer. Calibration of the foil provides information on the actual sensitivity of the foil which can help in selecting the best foil material. In this work thermal properties of the 0.63 micron thick Au and 0.87 micron thick Pt foils are investigated by heating the foils with a chopped 25 mW HeNe laser and observing the temperature change, ΔT, of the foil and the rise/decay times, $\tau_{rise/decay}$, of the foil temperature. For a foil in which the cooling is dominated by diffusion, since the sensitivity of the foils is proportional to the ratio of the thermal diffusivity to the thermal conductivity of the foil, κ/k, which is proportional $\Delta T/\tau$, where τ is the average of the decay and rise times, we can compare the relative sensitivities of the foils by comparing these ratios for Pt and Au foils. The results surprisingly indicate that Pt is more than 9 times more sensitive than Au even though standard thermal properties indicate that Au should be 14% more sensitive than Pt. This inconsistency is largely due to a slightly smaller decay time, τ, which is inconsistent with a 5 times smaller κ, in the case of the Pt compared to Au. While the 5 -6 times larger temperature rise, ΔT, is somewhat consistent with 3.2 times smaller kt for the Pt foil compared to Au foil. This inconsistency in the thermal times, along with observed differences between the rise and decay times, indicate that the IR radiation is dominant over diffusion in the cooling of the foil. In that case the sensitivity should be evaluated by $1/k \sim \Delta T$ which indicates that Pt is 8 times more sensitive than Au, while the ratio of thermal conductivities indicates that it should be only 4 times more sensitive.

Keywords: bolometer, diagnostics, infrared, imaging, calibration,

1. Introduction

Bolometer diagnostics are essential for the measurement of radiated power loss from fusion devices [1]. The InfraRed imaging Video Bolometer (IRVB) has been under development for application to a fusion reactor due to its durability vis-à-vis neutrons and gammas and its lack of in-vessel wires and the numerous vacuum feedthroughs which plague conventional resistive bolometers [2,3,4]. Also it provides an image of the radiation from the plasma which can be useful for steady-state reactor operation [5].

An IRVB consists of a thin metal foil mounted in a copper frame which absorbs the radiation from the plasma through an aperture. Viewing the foil from the opposite side is an IR camera which is used to measure the change in the foil temperature due to the absorbed radiation. The radiation profile on the foil is obtained by solving the two-dimensional heat diffusion equation for the foil. In order to do so the thermal characteristics of the foil including the product of the thermal conductivity , k, and the foil thickness, t_f, the thermal diffusivity, κ, and the blackbody emissivity, ε, must be determined. Since the foil is blackened with a graphite coating for good IR emissivity, and due to non-uniformity in the manufacturing of the foils, these properties can vary considerably across the foil and from the standard values found in reference handbooks [6]. Therefore it is important to measure these properties carefully to insure the calibration of the diagnostic and to evaluate which foil material is the most sensitive.

The noise equivalent power density, S_{IRVB}, of the IRVB is given by the following equation [7]

$$S_{IRVB} = \frac{\sqrt{2}kt_f\sigma_{IR}}{\sqrt{f_{IR}N_{IR}}}\sqrt{\frac{5N_{bol}^3 f_{bol}}{A_f^2} + \frac{N_{bol} f_{bol}^3}{\kappa^2}} \quad (1)$$

in terms of the IR camera parameters: sensitivity, σ_{IR}, frame rate, f_{IR}, and number of pixels, N_{IR}, the foil properties: area, A_f, thickness, t_f, thermal conductivity, k, and thermal diffusivity, κ, and the IRVB parameters: frame rate, f_{bol} and number of channels, N_{bol}. The blackbody

author's e-mail:peterson@LHD.nifs.ac.jp

radiation term is not included since it is negligible for background temperatures below 1000 K. In normal applications the term on the right side under the radical dominates, therefore we can write $S_{IRVB} \propto kt_f / \kappa$. This should be as small as possible for high sensitivity, therefore we can write the sensitivity of the IRVB in terms of the foil parameters as κ/kt_f.

Recently several candidate foils materials have been suggested for an IRVB. These include Au, Pt and Ta. Au is not a good choice for a reactor since it has a high neutron cross-section which has been observed to lead to transmutation to Hg [8]. Calibration work with Ta showed that its value of kt_f was two times larger than the standard values indicating a halving of its sensitivity [6]. In this paper we consider Pt for the first time and compare it to Au with which we have much experience. The objective of this study is to determine which foil material would be most sensitive for future use on LHD and KSTAR, two large experiments without sizable amounts of neutrons.

2. Experimental technique

In order to evaluate the relative merits of gold and platinum foils we use a laser calibration technique to evaluate the sensitivity of the two foils. Foils with a nominal thickness of 2.5 microns are selected since the target is applications to LHD or KSTAR for which that thickness is sufficient to stop energetic photons. However when samples of the foil material were measured with a microbalance the average thicknesses were calculated to be 0.87 microns for the Pt foil and 0.63 microns for the Au foil. The foils are mounted in copper frames to expose an area of 7 cm x 9 cm then sprayed on both sides with graphite as shown in Figure 1and then mounted in a vacuum flange with a ZnSe IR window. Then the flange is mounted on a vacuum chamber as shown in Figure 2. A chopped HeNe laser (~20 mW) is used to heat the foil at each of twenty positions on the foil starting in the center of the foil and moving step by step in 1 cm increments in both dimensions to cover one quadrant of the foil. A FLIR SC500 IR camera (microbolometer, 8 – 12 microns, 60 fps, 256 x 320 pixels with a close up lens) is used to measure the foil temperature. At each laser position the IR camera data is taken as a series of four 200 frame captures. The first is without the laser to provide a background image, the second is during the temperature rise after the laser shutter is opened, the third records the steady-state temperature profile due to the laser heating of the foil and the fourth records the decay of the foil temperature after the shutter is closed. The background temperature measurement is averaged over the 200 frames and subtracted from the remaining 600 frames. The steady state series is then averaged over the 200 frames and the

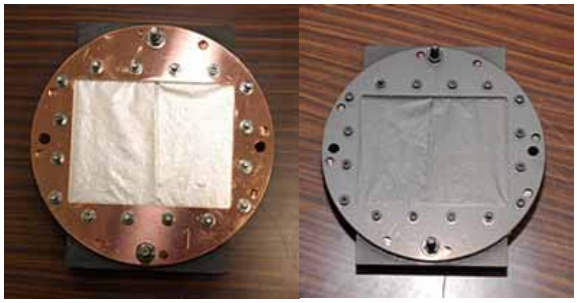

Fig.1 Platinum foil mounted in copper frame before (left) and after (right) blackening with graphite.

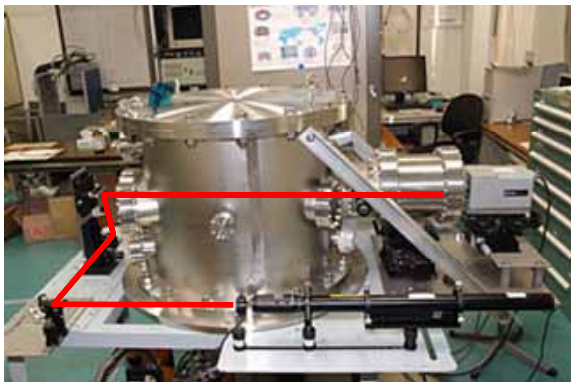

Fig.2 Test stand showing laser path (red).

peak of the temperature profile, ΔT, is found and measured. The temperature rise and decay are fit to a modified Gaussian [4] to find the rise and decay times, respectively, which are averaged to give an effective thermal time, τ, in order to partially remove the effect of the IR radiation. If we neglect the blackbody radiation from the foil then $\tau \propto 1/\kappa$ and $\Delta T \propto 1/kt_f$ and therefore the sensitivity can be written as

$$\kappa / k_f \propto \Delta T\, t / \tau S \quad (2)$$

where S is the laser power density. By comparing these parameters we can evaluate the relative sensitivity of the Au and Pt foils.

3. Results

The vertical and horizontal ΔT profiles when the laser is located at the center of the foil are shown in Figure 3 for the Au and Pt foils. One notes that the temperature rise on the Pt foil is 38.5C while that of the Au foil is 7.65C or 5 times lower. When averaged over 20 points on the foil the average is 44.2C for Pt and 7.15C for Au giving a difference of a factor of 6. In Figure 4 the foil temperature decays are shown for the peak ΔT position with the central laser position for the Pt

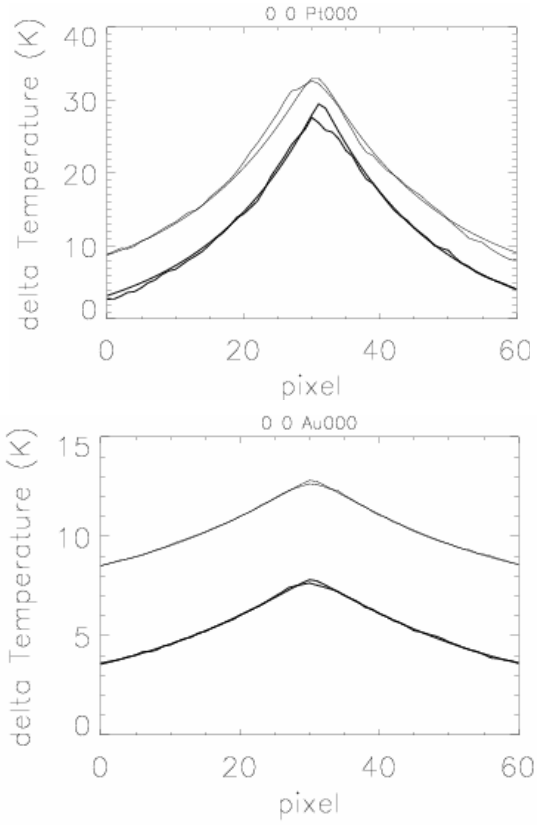

Fig.3 Temperature profiles for Pt (upper) and Au (lower) foils. In each plot upper profile is vertical profile and is offset by 5 C and lower profile is horizontal profile. Fits to a modified two-dimensional Gaussian are also shown.

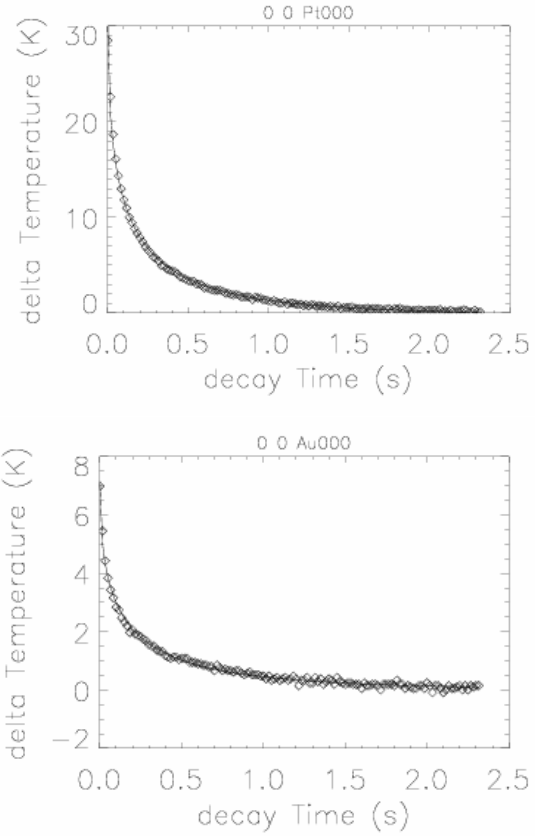

Fig.4 Temperature decays (symbols) for Pt (upper) and Au (lower) foils and modified exponential fits (lines).

and Au foils. The decays are fit to a modified Gaussian as shown in the figure giving decay times of 0.341 s (Pt) and 0.368 s (Au). Not shown are the temperature rise data when the shutter is opened which when fit to the modified Gaussian give rise times of 0.367 s (Pt) and 0.459 s (Au). Taking the average of the rise and decay times for each point and averaging over the 20 points on the foil gives effective thermal times of 0.321 s (Pt) and 0.360 s (Au). If we combine τ, ΔT and slight variations in the laser power according to Equation 2 then we get relative sensitivities of 5.4 Cμm/smW (Pt) and 0.59 Cμm/smW (Au). Therefore Pt is considered to be 9.2 times more sensitive than Au.

4. Discussion

Several observations deserve comment and discussion. First of all, regarding the steady state temperature rise, ΔT, we observed that this is 5 to 6 times higher for Pt than for Au. Since $\Delta T \propto 1/kt_f$, this may be partially explained by the difference in kt, which for the Au foil is 3.2 times greater than that of the Pt foil since Pt has a thermal conductivity which is 4.4 times smaller than that of Au.

Secondly, regarding the rise and decay times, we observe that the rise time is longer than the decay time. This is presumably due to the radiative cooling of the foil by infrared radiation. We attempt to mitigate the effect of this on our comparison of the two foil sensitivities by averaging the decay and rise times. Although this is not the correct way to compensate for this effect, it should remove it partially. In the same sense the temperature rise, ΔT, should also be affected by the infrared cooling. The higher the temperature rise the greater the cooling, therefore we estimate that the Pt data should be more strongly affected by the IR cooling, hence we expect that the actual difference between the two sensitivities should be even larger. Also regarding the thermal times, τ, we note that Pt has a slightly shorter thermal time than that of Au. However, for cooling of the foil dominated by diffusion $\tau \propto 1/\kappa$, we expect that the thermal time for Pt should be 5 times greater than that for Au due to a five times smaller thermal diffusivity. This discrepancy, in addition to the previously described difference in the rise and decay times, indicates that blackbody (IR) radiation is more dominant than diffusion in the cooling of the foil.

This would explain also why the Pt foil cools faster than the Au foil since its temperature is higher due to smaller *k* and therefore the IR cooling effect is greater. This would also explain why Pt is more than 9 times more sensitive than Au even though a comparison of the ratio of their thermal diffusivity to thermal conductivities would suggest that Au should be slightly more sensitive than Pt.

This indicates that our criteria for evaluating the sensitivity given by Eq. 2 may not be correct since this is based on the assumption that diffusion is dominating the cooling of the foil and the experimental evidence that we have is to the contrary (especially the difference between the rise and decay times). Therefore we should consider another criteria for the sensitivity, namely

$$1/k_f \propto \Delta T\, t / P \quad (3)$$

where P is the laser power. When this is considered the experimental values show that Pt is 8.1 times more sensitive that Au while the ratio of the thermal conductivities is 4.4. Therefore based on this criteria the Pt is still 8 times more sensitive than Au while the standard thermal parameters indicate that it should be only 4 times more sensitive.

.

We can conclude that Pt would be 8 or more times more sensitive than Au as long as the radiation dominates over the diffusion in the cooling of the foil. We should confirm at which power levels the IR radiation dominates over the diffusion in the foil and make sure that the balance of these two cooling channels is properly handled in the solution of the heat diffusion equation for the incident radiated power. Also this effect should be checked in a thicker foil such as the 2.5 microns we plan to use eventually in KSTAR and LHD and the 10 microns that would be necessary for ITER.

This result indicates that we can raise the sensitivity of the IRVB by a factor of 8 or more by using Pt instead of Au. This should be an advantage for the IRVB compared to resistive bolometers since the resistive bolometer thermal time is determined by the diffusion through the insulating layer to the metal grid and not by blackbody radiation.

By raising the temperature of the foil and frame above that of the surrounding background we should be able to insure that the IR radiation term dominates over the diffusion and thereby remove diffusion from the foil power balance. This will enable an instantaneous measurement of the radiated power that will no longer require solution of the heat diffusion equation. We plan to test this in the near future.

Acknowledgement

This work was supported in part by a Grant-in-Aid for Science Research from the Japanese Ministry of Education, Culture,Sports, Science and Technology, 'Priority Area of Advanced Burning Plasma Diagnostics' (16082207) by NIFS Grant # ULPP-528 and by the Japan Korea Fusion Collaboration Program.

References

[1] A. W. Leonard *et al.*, Rev. Sci. Instrum. **66** 1201 (1995).
[2] B. J. Peterson, Rev. Sci. Instrum. **71** 3696 (2000).
[3] B. J. Peterson *et al.*, Rev. Sci. Instrum. **74** 2040 (2003).
[4] H. Parchamy *et al.*, Rev. Sci. Instrum. **77** 10E515 (2006).
[5] B. J. Peterson *et al.*, J. Nucl. Mater. **363-365** 412 (2007).
[6] B. J. Peterson *et al.*, Rev. Sci. Instrum. **79** 10E301 (2008).
[7] B. J. Peterson *et al.*, Plasma Fusion Res. **2** S1018 (2007).
[8] T. Nishitani et al., Fusion Eng. Des. **63-64**, 437 (2002).

Proceedings of ITC18, 2008

Numerical study on formation process of helical nonneutral plasmas using electron injection from outside magnetic surfaces

Kazutaka NAKAMURA[1)], Haruhiko HIMURA[1)], Mitsutaka ISOBE[2)], Sadao MASAMUNE[1)] and Akio SANPEI[1)]

[1)]*Department of Electronics, Kyoto Institute of Technology, Matsugasaki, Sakyo Ward, Kyoto 606-8585, Japan*
[2)]*National Institute of Fusion Science, Toki 509-5292, Japan*

In order to investigate the formation process of helical nonneutral plasmas, we calculate the orbits of electron injected in the stochastic magnetic field when the closed helical magnetic surfaces is correspond with the equipotential surfaces. Contrary to the experimental observation, there are no electrons inward penetrating.

Keywords: Orbit calculation, Nonneutral plasmas, Helical, Electron injection, Stochastic magnetic region

1 Introduction

Research on nonneutral plasmas confined on toroidal magnetic surfaces has been intensively conducted in recent years [1, 2]. Despite the closed magnetic surfaces, no break-up of those is required when the plasmas are produced. In experiments on devices of the Compact Helical System (CHS) [3] and the Heliotron J [4], an electron-gun (hereafter, e-gun) has been installed in the stochastic (or ergodic) magnetic region (SMR) [5] surrounding the last closed flux surface (LCFS) and just ejected thermal electrons in the SMR. Then, within the order of 10 μs after the injection, those have penetrated deeply in the helical magnetic surfaces (HMS), spread rapidly in the whole of the closed surfaces, and finally formed a helical nonneutral plasma there [6].

Regarding the mechanism of the inward penetration of electrons, recent three dimensional orbit calculations including two experimental findings which are that (1) there is a electrostatic potential and (2) the center of equipotential surfaces (EPS) is shifted from that of HMS have finally outputted some outward orbits that extend to inward part of closed helical vacuum magnetic region [7]. Data have clearly shown that the pitch angle of electron injected into the stochastic magnetic region is scattered considerably due to the presence of self space potential ϕ_s. Eventually, the injected electron turns to be a helically trapped particle [9, 10], and start an inward movement along one of the $|B_{min}|$ contours [3, 7, 10]. Once penetrating deeply, the electron can never escape from the LCFS because the negative ϕ_s acts as a potential barrier.

In this paper, we report the result of orbit calculation and the velocity map in the case that the center of EPS is corresponded with that of HMS. Then no electrons penetrate across the HMS. In Sec. 2, the model employed in this computation is briefly explained. Data obtained from the calculation and the velocity map are given in Sec. 3. Finally, a summary is given in Sec. 4.

author's e-mail: nakamu6t@nuclear.es.kit.ac.jp

2 Calculation Model

As mentioned, when the center of the EPS is shifted from that of HMS, it has known that some electrons injected in the SMR can penetrate the HMS and are trapped [7]. So we ensure the orbits when the center of the EPS is correspond with that of HMS. We mention the calculation model as follows.

Firstly, in experiments, substantial ϕ_s (down to ~ -400V) has been clearly measured [6] in the SMR just after thermal electrons are injected from the e-gun with the acceleration voltage V_{acc} is -1.2kV. This is because the lines of force in the SMR are chaotic, the connection lengths of those to the grounded chamber wall are very long. Therefore, there are no doubt that the thermal electrons injected from the e-gun are confined there. So we assume the presence of the EPS which extend to the SMR and model a radial profile of ϕ_s from the experimental data, as seen from the solid curve in Fig. 1. Figure. 2 shows the ϕ_s distribution at the $\phi = 0^o$ plane. On the SMR and its

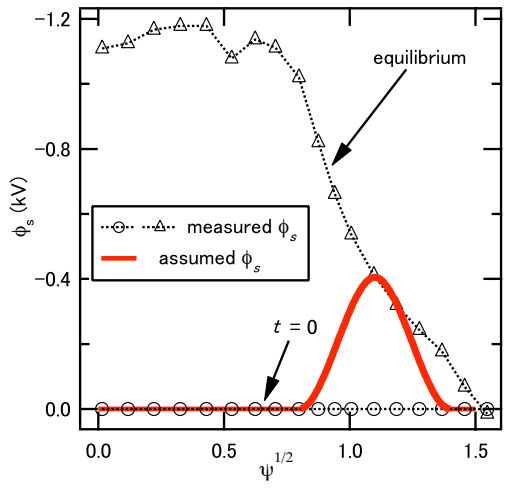

Fig. 1 The modeled self electrostatic potential ϕ_s in the stochastic magnetic region (SMR) and its vicinity. The profile is determined from the measured data.

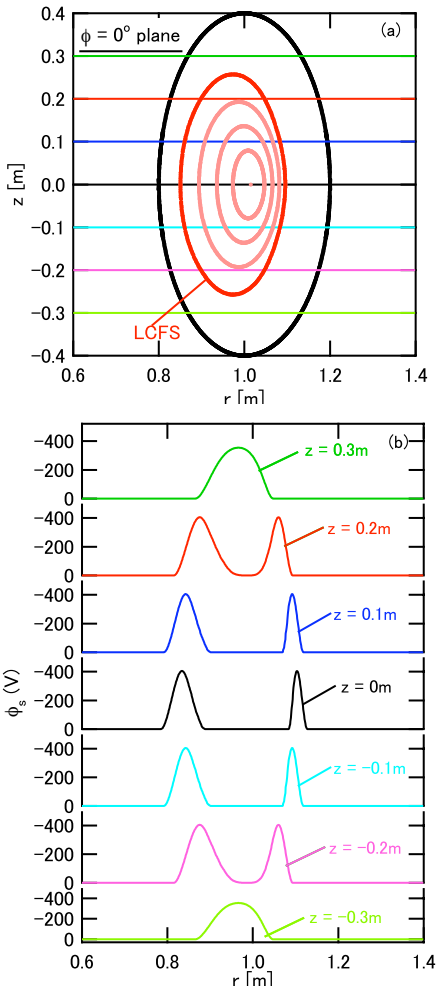

Fig. 2 The example of ϕ_s distribution (a) at the $\phi = 0^o$ poloidal plane and (b) on horizontal line. At this calculation, the value of ϕ_s is calculated as the function of normalized minor radius.

vicinity, there is electrostatic potential, as experimentally.

Secondly, to calculate full gyro-orbits of the electron ijected in the SMR, we solve the equation of motion $\dot{\mathbf{v}} = -e(\mathbf{v} \times \mathbf{B} + \mathbf{E})/m_e$, we employ the 6^{th} order Runge-Kutta-Verner method in cylindrical coordinates. Here, q and m_e are the charge and mass of an electron, respectively. In calculation, we have varied the injection angle a of the e-gun. Other parameters listed below are fixed as follows; the strength of $\mathbf{B}$ at manetic axis $R_{ax} = 101.6$ cm is 0.9 kG and the value of V_{acc} is -1.2kV. The injection position of a single electron is at $\Psi^{1/2} = 1.1$ on the equatorial plane at the $\phi = 29.5^o$ cross-section, where $\Psi^{1/2}$ is the normalized minor radius and ϕ is the toroidal angle, respectively. These are exactly the same condition as the experimental setting.

3 Calculation Results

In calculation, we have varied the initial absolute value of velocity and pitch angle of the e-gun. We show the calculation results as follows.

3.1 Passing Orbit

In this subsection, we show the orbit whose initial pitch angle is 16^o. Figure 3 shows the time evolutions of all parameters of injected electron. The injected electron sticks around the LCFS, as shown in Fig.3 (a). For this case, as recognized from Fig. 3 (b), the electron rotates the torus at all times from $t = 0\,\mu$s to the calculation end. No transition electron or helically trapped one can be found for this case at all. The injected electron has been in the state of passing particle, all the time.

Precisely, the penetration across the HMS is happened when the pitch angle of injected electron is scattered by the electrostatic field and the electron turns to

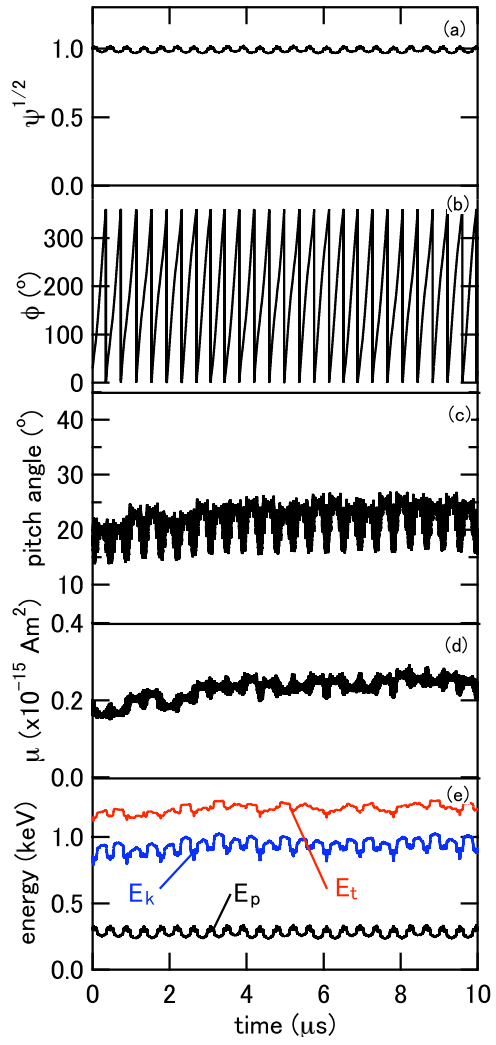

Fig. 3 Time evolutions of (a) normalized position, (b) toroidal angle, (c) pitch angle, (d) magnetic moment and (e) total energy E_t, kinetic energy E_k and potential energy E_p of the injected electron, for the case of $v_\perp/v_\parallel \sim 16^o$. In this case, the electron has been always in the state of passing particle in the SMR.

become a helically trapped particle[7]. Then, the helically trapped electron travels inwardly along $|B_{min}|$ contours where the strength of **B** is weaker compared to the neighborhood region on each magnetic surface, which is just same as the motion of helically trapped electron of neutral plasmas[5, 10]. But in this case, the variation of the pitch angle of injected electron is very small, as seen from Fig. 3 (c). Consequently, no penetration of theinjected electron occurs, because the transition to a helically trapped particle is never happened.

As long as ϕ_s is independent of time and depends only on coordinates, it follows from the equations of motion that total energy E_t is conserved;

$$\begin{aligned} 0 &= \mathbf{v}\cdot\dot{\mathbf{v}} - \frac{q}{m_e}\mathbf{v}\cdot(\mathbf{v}\times\mathbf{B}+\mathbf{E}) \\ &= \mathbf{v}\cdot\dot{\mathbf{v}} + \frac{q}{m_e}\dot{\mathbf{r}}\cdot\nabla\phi_s \\ &= \frac{d}{dt}\left(\frac{v^2}{2}+\frac{q}{m_e}\phi_s\right), \end{aligned} \tag{1}$$

so eqn.(1) can be written as

$$\text{const} = \frac{m_e v^2}{2} + q\phi_s. \tag{2}$$

As seen from Fig. 3 (d, e), magnetic moment μ and E_t of the injected electron are conserved.

3.2 Helically Trapped Orbit

In the case of initial pitch angle $\sim 126^o$, but the penetration across the HMS is not observed, either. Figure 4 shows the time evolutions of all parameters of injected electron. As seen from Fig. 4 (b, c), the injected electron doesn't move to toroidal direction and becomes helically trapped particle. But in this case, the injected electron hits the grounded chamber wall, doesn't penetrate across the HMS. This is because the injected electron must become a helically trapped particle on the inboard $|B_{min}|$ contours[7]. So in this case, the penetration of injected electron is not observed.

3.3 Velocity Mapping

As explained above, the inward penetration across the HMS has depend on whether the transition to a helically trapped particle occurs or not, and moreover, the transition is affected much by the initial pitch angle of the injected electron. Thus, we have performed a mapping of the initial pitch angle of the pitch angle with changing its kinetic energy V_{acc} (equivalently, beam energy in experiments): V_{acc} = −0.8 and −0.4 kV.

Figure 5 shows the velocity map for electrons injected in the SMR. Orbit calculations are conducted up to 20 μs. The symbol of × on the map represents in-successful penetration. As recognized from Fig. 5, the inward penetration across the HMS is independent of initial V_{acc} and pitch angle. This is because that when the center of EPS is correspond with that of HMS, the electrostatic field is always perpendicular to magnetic force line. As mentioned, the pitch angle of the injected electrons must be scattered on the inboard $|B_{min}|$ contours. Then, the electrostatic field which is parallel to magnetic force line operates powerfully to this scattering, because the scattering results from the change of the value of $v_{\|}$. Figure 6 shows the contours of strength of $E_{\|}$ when the center of EPS is shifted from that of HMS. As seen higher right from Fig. 6, there are regions that have large $E_{\|}$. So when the center of the EPS is shifted from that of HMS, we enter into that the electrons decelerated the motion of direction of the magnetic

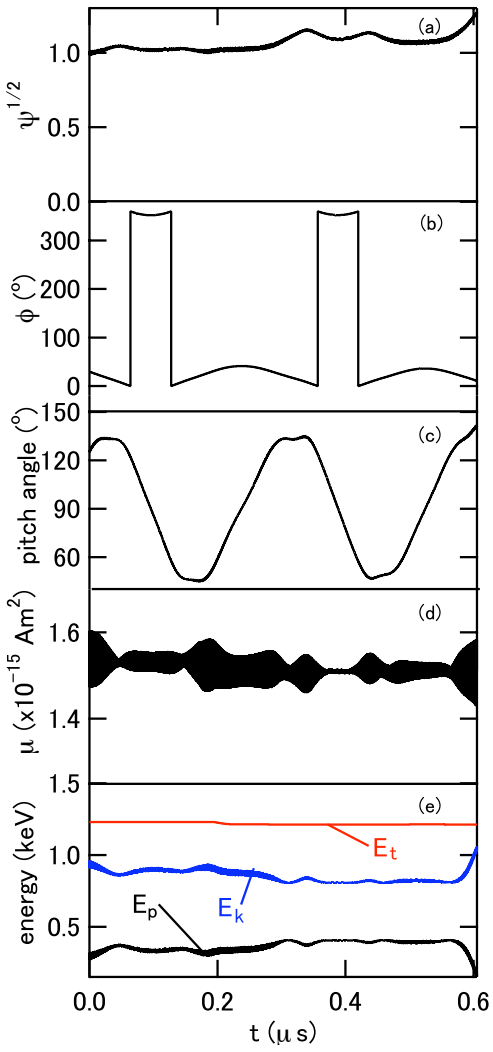

Fig. 4 Time evolutions of all parameters for the case of $v_{\perp}/v_{\|} \sim 126^o$. Parameters here are the same as those in Fig. 3, for reader's convenience. As recognized, no penetration of the injected electron occurs for this case, too. In this case, the electron is reflected from magnetic mirror and finally hits to the grounded chamber wall at $t \sim 0.6\mu$s.

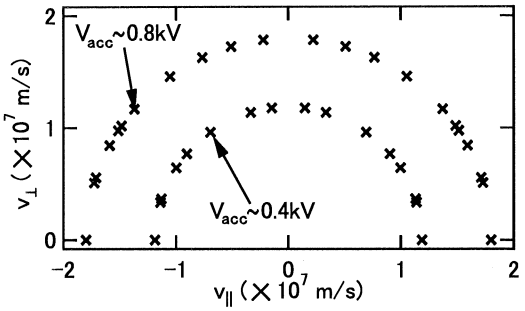

Fig. 5 The velocity map for the electron launched from the e-gun placed at the point (r, θ, z) =(1.183, 29.5, 0). As recognized, there are no electrons which happen the inward penetration across the HMS.

force line in this region become helically trapped particle, and some electrons injected in the SMR penetrate across the HMS [11].

4 Summary

In order to investigate the formation process of helical non-neutral plasmas, we have numerically performed a mapping of velocity space of outward electrons whose orbits extend to inward part of closed helical vacuum magnetic region of the Compact Helical System machine, especially in the case the center of EPS is correspond with that of HMS. In calculations presented here, the magnetic axis R_{ax} is fixed to be R_{ax} = 101.6 cm and the magnetic field strength is B = 0.9 kG. Those are exactly the same as those in the settings of actual experiments. And, in this computation, electron full orbits are solved using the 6^{th} Runge-Kutta method to include the effect of Larmor motion.

In experiments on CHS, it is observed that electron penetrating across the closed HMS any ejecting angle. However data show that in the case the center of EPS is correspond with that of HMS, no penetration is observed in computation with any value s of $v_\perp/v_\parallel$. This is because no electrostatic field which is parallel to magnetic field line, so pitch angle of the injected electron is not scattered effectively.

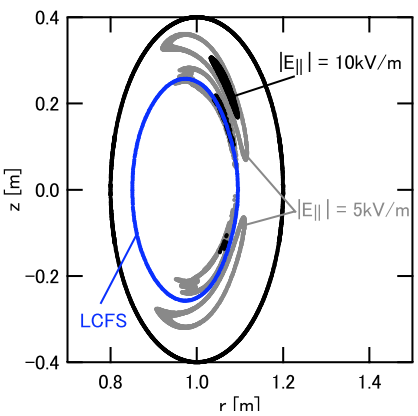

Fig. 6 The contours of strength of $E_\parallel$ when the center of EPS is shifted from that of HMS at $\phi = 0^o$ poloidal plane. This shift cause large $E_\parallel$ in the SMR.

Acknowledgment

The authors are grateful to Drs. A. Shimizu, K. Matsuoka, and S. Okamura of NIFS for their continuous encouragements. This work is performed under the aupices of the NIFS CHS Research Collaboration, No. NIFS07KZPH002.

[1] H. Himura *et al.*, Phys. Plasmas **14**, 022507 (2007).
[2] M. Hahm *et al.*, Phys. Plasmas **15**, 020701 (2008).
[3] S. Okamura *et al.*, Nucl. Fusion **39**, 1337 (1999).
[4] T. Obiki *et al.*, Plasma Phys. Control. Fusion **42** 1151 (2000).
[5] M. Isobe *et al.* Nucl. Fusion **41**, 1273 (2001).
[6] H. Himura *et al.*, Phys. Plasmas **11**, 492 (2004).
[7] K. Nakamura *et al.*, submitted to Phys. Plasmas (2008).
[8] M. H. Redi *et al.* Phys. Plasmas **6**, 3509 (1999).
[9] A. Shishkin *et al.* Nucl. Fusion **47**, 800 (2007).
[10] T. Watanabe *et al.* Nucl. Fusion **46**, 291 (2006).
[11] K. Nakamura *et al.*, submitted to J. Plasma Fusion Res. SERIES (2008).

Proceedings of ITC18, 2008

Studies of Nonneutral Plasmas Confined on Helical Magnetic Surfaces of Heliotron J

Daichi SUGIMOTO[1)], Haruhiko HIMURA[1)], Kazutaka NAKAMURA[1)], Sadao MASAMUNE[1)], Akio SANPEI[1)], Hiroyuki OKADA[2)], Satoshi YAMAMOTO[2)], Shinji KOBAYASHI[2)], Tohru MIZUUCHI[2)], and Fumimichi SANO[2)]

[1)]*Department of Electronics, Kyoto Institute of Technology, Matsugasaki, Kyoto 606-0855, Japan*
[2)]*Institute of Advanced Energy, Kyoto University, Gokasho, Uji, Kyoto 611-0011, Japan*

Nonneutral plasmas confined on helical magnetic surfaces becomes have different characteristics from those of neutral plasmas. The most significant one observed in experiments is that both space potential ϕ_s and plasma density n_e are not constant on closed magnetic surfaces. This strongly implies that such plasma parameters vary also along each magnetic field line (B-field line) with which closed magnetic surfaces are formed. In this paper, we have numerically estimated the variations of ϕ_s and n_e along helical B-field lines of the Heliotron J machine. Data show that on the magnetic axis, variatios of ϕ_s and n_e are about 7 V and 2×10^7 m^{-3} for the case of $B \sim 0.3$ kG. Other accessible B-field lines and the estimated variations of ϕ_s and n_e on them are also presented.

Keywords: toroidal nonneutral plasmas, pure electron plasmas, magnetic surface confinement, equilibrium of helical nonneutral plasmas, variation of plasma parameters on magnetic surface

1. Introduction

Experiments on nonneutral plasmas have been conducted on various machines such as the Penning trap [1], Paul trap [2], and toroidal devices.[3] Recently, experimental studies on toroidal nonneutral plasmas confined on helical magnetic surfaces (HMS) have been initiated. Contrary to toroidal neutral plasmas, both space potential ϕ_s and electron density n_e of toroidal nonneutral one are nonconstant on HMS[4]-[6]. This phenomenon can be approximately explained by the theory [7] which shows that in nonneutral plasmas, parallel electrostatic force balances with the parallel pressure gradient force. This actually calls for variations of ϕ_s and n_e along magnetic field lines (B-field lines) on closed magnetic surfaces.

However, variations of ϕ_s and n_e are so far observed on the HMS, not along B-field lines. Obviously, in order to compare the observed variations with the theory, studies on those plasma parameters must be conducted along B-field lines.

In this paper, we have numerically estimated the variations of ϕ_s and n_e along helical B-field lines of the Heliotron J machine. Data show that on the magnetic axis, variatios of ϕ_s and n_e are about 7 V and 2×10^7 m^{-3} for the case of $B \sim 0.3$ kG. Other accessible B-field lines and the estimated variations of ϕ_s and n_e on them are also presented.

2. Apparatus

Experiments of nonneutral plasmas confined on the HMS are performed in a middle size machine of quasi-advanced stellarator, Heliotron J. The averaged major and minor radii of the machine are 1.2 and 0.38 m, respectively. Figure 1 shows a poloidal cross-section of Heliotron J on which an electrostatic probe is installed in the vacuum chamber.

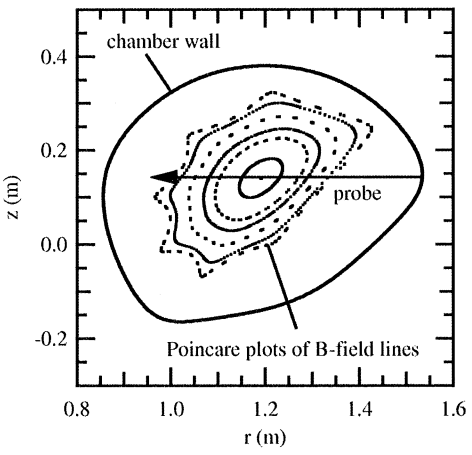

Fig. 1 A view of the 11.5 cross-section of Heliotron J. The chamber wall is drawn by the black solid curve. Poincare plots of B-field lines are shown. The solid arrow shows the location of the probe. The shaft length of the probe is about 60 cm so that values of plasma parameters can be mesured at two different points on each magnetic surface.

Electrons are injected by an electron gun (e-gun), which has a LaB_6 emitter as the cathode. [8] The e-gun is inserted horizontally along the r axis and set on 1 cm outside from the last closed flux surface (LCFS). The acceler-

author's e-mail: sugimo07@nuclear.es.kit.ac.jp

ation voltage V_{acc} of the electrons are variable. But, typically, it is fixed to $V_{acc} = -600$ (V). The pulth width of V_{acc} is also variable in the range between $\sim$ 10 (μs) and $\sim$ 100 (ms). Plasma parameters of ϕ_s, n_e and electron temperature T_e are measured by an emissive and Langmuir probe. The e-gun and the probe are located on poloidal cross-sections at $\varphi = 71.05°$ and $\varphi = 251.05°$ (henceforth, called the 3.5 and 11.5 cross-sections, respectively). Here, φ is the toroidal angle. The shaft of the employed probe is long enough, which can reach the edge of LCFS at the inboard side. The magnetic field (B-field) is operated as static for this experimental study, and the maximum strength of B-field on the magnetic axis at the 11.5 cross-section is about 3×10^{-2} T.

3. Brief review of observed variation

Figure 2 shows a set of preliminary results of measured radial profiles of ϕ_s, n_e, T_e of helical nonneutral plasmas produced on Heliotron J, and calculated B strength. The radial position is described by $\Psi^{1/2}$, where $\Psi^{1/2} = 0$ and 1 correspond to the the magnetic axis and the LCFS, respectively. As mentioned, all values of ϕ_s, n_e, T_e and $|B|$ are measured at two different measurement points on each HMS. The dark and black colors indicate the data on the inboard - and the outboard side, respectively. Clearly, considerable variation of ϕ_s is recognized in the HMS. The observed variation becomes larger near the LCFS. On the other hand, the variation of n_e is seen even in the plasma core. Contrary to those, little variation of T_e is so far measured. Anyhow, data strongly suggest that those plasma parameters are varied along B-field lines.

4. Magnetic field line tracing

To precisely measure both ϕ_s and n_e along helical B-field lines, we must exactly know where each B-field line circulates in the vacuum vessel. For the purpose, we have numerically traced the helical B-field lines in Heliotron J. Figure 3 explains two examples of B-field lines for which the B-field line tracing is conducted. The black circle shows the B-field line which passes through the magnetic axis at $\Psi^{1/2} = 0$, while the black triangle is one of B-field lines that is off the magnetic axis where $\Psi^{1/2} \sim 0.25$. For both cases, the B-field line tracing is started from the 11.5 cross-section.

Figure 4 shows the strength of $|B|$ along the B-field line on the magnetic axis. It is seen from the data that the value of $|B|$ changes slightly for the case. On the other hand, for the B-field line at $\Psi^{1/2} \sim 0.25$, the change in $|B|$ is larger, as shown in Fig. 5. It should be noted here that the value of $|B|$ on the cross-section at $\varphi = 251.05°$ is different when the B-field returns there after a single toroidal circulation. This is due to the rotational transform that causes the B-field get back to a different position on the cross-section.

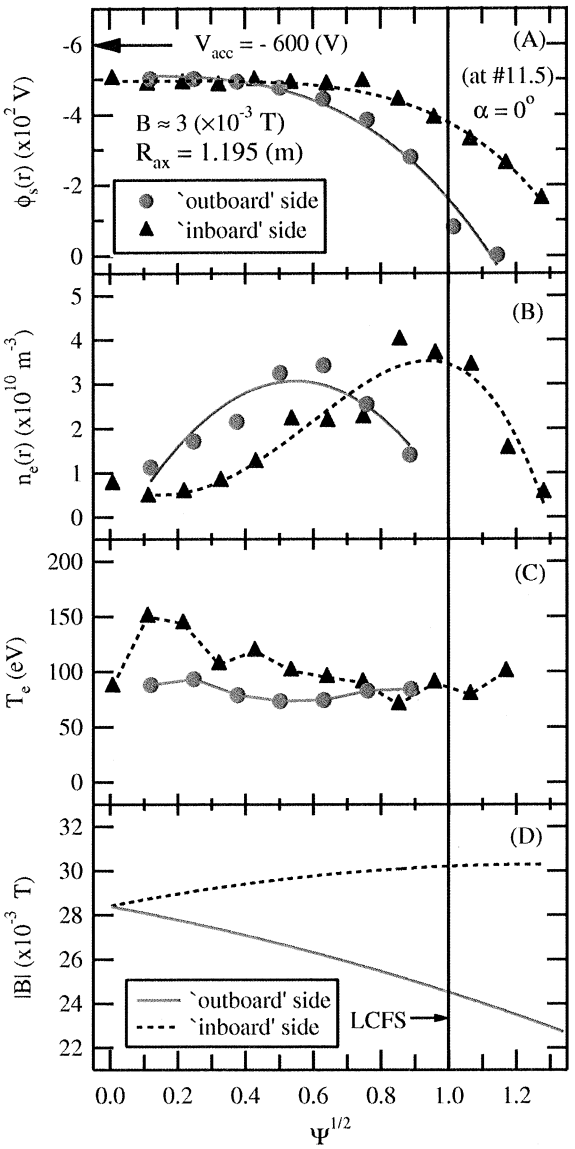

Fig. 2 First resalt of nonneutral plasmas confined on Heliotron J. (A) ~ (D) show measured radial profiles of space ptential $\phi_s(r)$, electron density $n_e(r)$, electron temperature $T_e(r)$ and B-field strength $|B|(r)$ at the 11.5 cross section. The horizontal axis is the normalized minor radius.The light marks and solid lines are outboard side profiles and darks and broken lines are inboard side profiles.

5. Estimated variations of ϕ_s and n_e

In this section, we estimate values of expected variations along B-field lines. As presented in Sec. 3, apparent differences in ϕ_s have been observed on each magnetic surface. On the other hand, the B-field strength is also varied on them. Using these results, we can thus relate the difference in ϕ_s with the B-field strength. Figure 6 shows the relationship between the potential variation $d\phi_s$ and the B-field strength. From this result, we assume

$$d\phi_s \propto (\Psi^{1/2})^2, \tag{1}$$

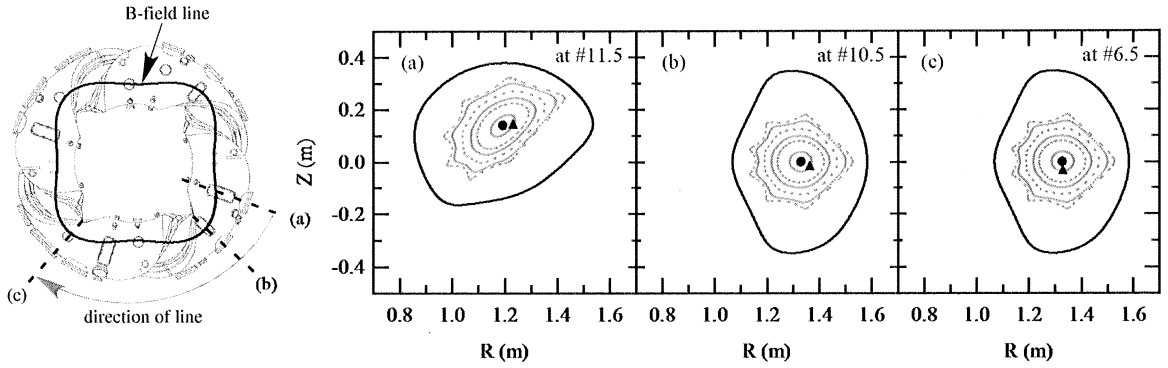

Fig. 3 Top view of Heliotron J and poloidal cross-sections at different toroidal angles. The cutting planes labeled as (a), (b) and (c) in the left figure correspond to the cross sections in the right one. The dotted points show Poincare plots of B-field lines. The circle and the triangle show B-field lines at $\Psi^{1/2} = 0$ (on the magnetic axis) and ~ 0.25 (off the magnetic axis).

$$dB \propto \Psi^{1/2}. \tag{2}$$

Thus, the value of $d\phi_s$ can be written as

$$d\phi_s \propto (dB)^2. \tag{3}$$

From the experimental data, we can obtain

$$d\phi_s \approx -242(\Psi^{1/2})^2 + 28.5, \tag{4}$$

and

$$dB \approx 5.7 \times 10^{-3}\Psi^{1/2}. \tag{5}$$

Therefore, the relationship between $d\phi_s$ and dB is represented as

$$d\phi_s \approx -75.8 \times 10^5 (dB)^2 + 28.5. \tag{6}$$

Assuming that the Eq. (6) holds also along B-field lines, we calculate variations of both ϕ_s and n_e. For the case of B-field line at $\Psi^{1/2} = 0$ (on the magnetic axis), the difference in $|B|$ between the 11.5 and 6.5 cross-sections is about $dB \sim -1.67 \times 10^{-3}$ (T). The obtained negative value of dB means that the value of $|B|$ at the 11.5 cross-section is larger than that at the 6.5 cross-section. Thus, the value of $d\phi_s$ can be calculated to be ~ 7.4 (V). On the other hand, for the case of B-field line at $\Psi^{1/2} \sim 0.25$, two values of dB are existed, as mentioned in Sec. 4. When $dB \approx -2.19 \times 10^{-3}$ (T) is applied, $d\phi_s$ is about -7.80 (V). If $dB \approx -5.63 \times 10^{-4}$ (T) is used, $d\phi_s \sim 26.1$ (V) is obtained.

Secondly, regarding the n_e variation, we consider the fluid force balance equation for a low density pure electron plasmas. The variation of n_e along a B-field line is expressed as

$$\frac{dn_e}{n_e} \approx \left(\frac{a}{\lambda_D}\right)^2 \frac{d\phi_s}{\phi_s}. \tag{7}$$

Here, a is the typical scale length so that we regard it as the averaged minor radius of Heliotron J. Also, $\lambda_D = \sqrt{\epsilon_0 \kappa T_e / n_e e^2}$ shows the Debye length[7]. Substituting the value of $d\phi_s$ for Eq. (7), the value of dn_e is estimated to be $\sim -2.22 \times 10^7$ (m^{-3}) for the B-field line at $\Psi^{1/2} = 0$ (on the magnetic axis). For the case of B-field line at $\Psi^{1/2} \sim 0.25$ (off the magnetic axis), dn_e is about $1.61. \times 10^8$ (m^{-3}) at the 6.5 cross section, while -5.38×10^8 (m^{-3}) at the 10.5 cross section.

As understood from above results, the estimated dn_e is much smaller than n_e, which calls for better resolution for measurements in the next series of Heliotron J experiments. Another important thing to perform next experiments would be to either increase n_e or decrease T_e. This is because λ_D is the key parameter to decide the variation of n_e along B-field lines. In fact, smaller λ_D gives rise to larger dn_e. Since T_e is probably affected by V_{acc} strongly, experiments using smaller V_{acc} should be required. In fact, if T_e becomes $1/10$ times smaller, dn_e would then become 10 times larger. Experiments will be performed soon.

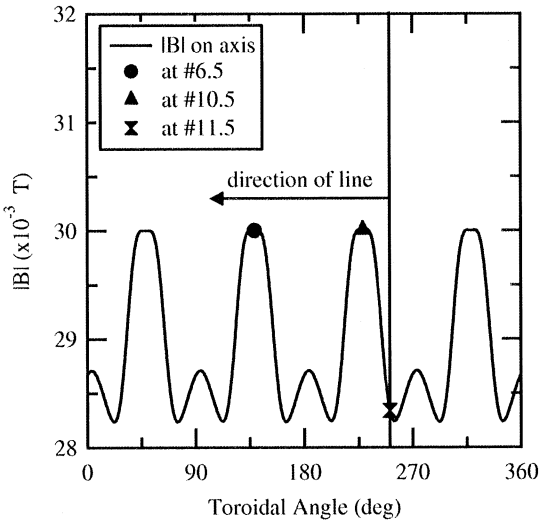

Fig. 4 The variation of B-field strengh $|B|$ along the B-field line at $\Psi^{1/2} = 0$ (on the helical magnetic axis).

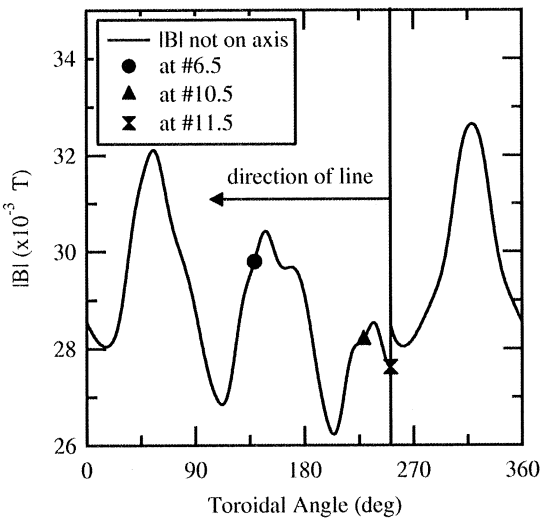

Fig. 5 The variation of B-field strengh $|B|$ along the B-field line at $\Psi^{1/2} \sim 0.25$ (off the helical magnetic axis).

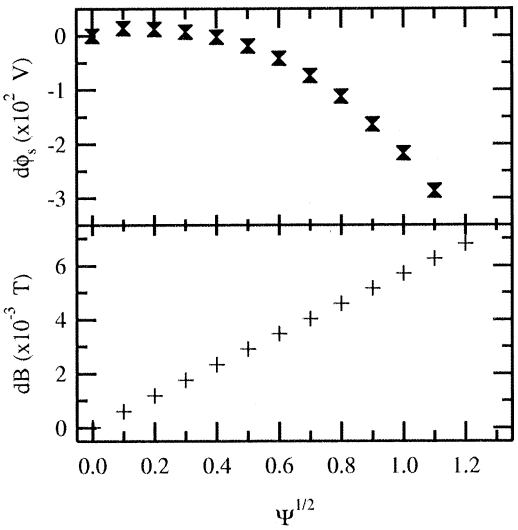

Fig. 6 Dependences of both $d\phi_s$ and dB on $\Psi^{1/2}$. Here, $d\phi_s$ and dB present differences in ϕ_s and B on each magnetic surface, respectively.

Acknowledgment

The authors are greatful to the Heliotron J group at Kyoto University, especially Mr. T. Senju for his technical support.

[1] F. M. Penning, Phisca **3**, 873 (1936).
[2] H. Friedburg, W. Paul, Naturwissenschaft **38**, 159 (1951).
[3] J. D. Daugherty, J. E. Eninger, and G. S. Janes, Phys. Fluids **12**, 2677 (1969).
[4] H. Himura, H. Wakabayashi, M. Fukao *et al.*, Phys. Plasmas **11**, 492 (2004)
[5] H. Himura, H. Wakabayashi, Y. Yamamoto, M. Isobe, S. Okamura, K. Matuoka, A. Sanpei and S. Masamune, Phys. Plasmas **14**, 022507 (2007)
[6] Michael Hahn, Thomas Sunn Pedersen, Quinn Marksteiner, and John W. Berkery, Phys. Plasmas **15**, 020701 (2008)
[7] Remi G, Lefrancois and Thomas Sunn Pedersen, Phys. Plasmas **13**, 120702 (2006)
[8] H. Himura, H. Wakabayashi, Y. Yamamoto, A. Sanpei, S. Masamune, M. Isobe, S. Okamura and K. Matsuoka, Hyperfine Interactions **174** pp.83-88, 2007.

Proceedings of ITC18,2008

Charging of Positively Charged Dust Particle in Weak Magnetic field

Yukihiro TOMITA[1)], Gakushi KAWAMURA[1)] and Osamu ISHIHARA[2)]

[1] *National Institute for Fusion Science, 322-6 Oroshi-cho, Toki 509-529,2 Japan*

[2] *Faculty of Engineering, Yokohama National University, Yokohama 240-8501, Japan*

The absorption cross-section of the charge particle to the spherical dust particle with positive charge in a weak magnetic field is investigated analytically and numerically. The closest radius of electrons becomes larger than that in the absence of magnetic field due to the Lorentz force, indicating the absorption cross-section smaller. In order to investigate the parameter dependence of the electrostatic force and the magnetic field on the electron orbits, the closest radius of an electron is approximated by the linear dependence of the strength of magnetic field. From this expression of the closest radius one can obtain the absorption cross-section and can calculate the charge state of the dust particle.

Keywords: dust, charging, magnetic field, absorption cross-section

1. Introduction

The generation, growth and transport of dust particles in fusion plasmas are one of the interesting topics. One of the remarkable points is related with absorption of radioactive tritium, which is one of the fusion fuels of the D-T fueled fusion [1, 2]. After operation of plasma discharges, the treatment, collection and disposal of the radioactive dust particles are one of key issues from the viewpoint of the safety.

In order to study behavior of the dust particle in fusion plasmas the charge state of the dust particle in magnetic field is one of the essential issues. In this study absorption cross-section of a spherical dust particle with positive charge by an electron/ion is studied in weak uniform magnetic field. The absorption cross-section in the absence of magnetic field was expressed by the OML (Orbit Motion Limited) theory [3, 4]. The OML theory, where energy and angular momentum of a charged particle are conserved in an infinite Debye length limit, has been widely used to charging of a dust particle in space plasmas as well as laboratory plasmas. An orbit of a charged particle (an ion or an electron) heading to a charged dust particle at rest along the magnetic field is analyzed analytically and numerically. Because of the Lorentz force in the presence of magnetic force, the charged particle with the same sign as the dust charge approaches closer to the dust than the orbit without magnetic field, indicating larger absorption cross section. On the other hand the charged particle with the opposite sign of dust charge leaves further the dust, indicating the absorption cross section smaller than that in the absence of magnetic field. The dust particle immersed in relatively low temperature plasma is charged negatively because of large mobility of electrons. On the other hand, in the case of the hotter plasma than few hundreds eV, the dust particle is charged positively due to the strong thermionic emission [5]. In the previous research the charging of the negatively charged dust particle in the weak magnetic field was analyzed [6], where we clarified 1) the magnetic field effectively affects the orbit of an electron compared to an ion, 2) the charge state of the floating dust particle with a radius of 1 mm increases from 6.63×10^5 to 6.86×10^5 for the 1 eV ions and electrons in the magnetic field of 10 G and for the higher energy of plasmas with 10 eV, dust charge is found to increase from 6.63×10^6 to 6.70×10^6 due to the effects of magnetic field.

2. Dynamics of Dust in Weak Magnetic Field

The charged particle orbits of j-th species ($j = e, i$) in the magnetic field are analyzed in the cylindrical coordinates (ρ, θ, z), where the uniform magnetic field B_0 is applied to the axial z- direction. The unmovable point dust particle is located at the origin (O) with the charge q_d. The charged particle with the charge q_j starts to move from the initial position ($\rho = b_{in}$, $\theta = 0$, $z = z_{in}$) with the velocity ($v_\rho = v_\theta = 0, v_z = v_{j,in}$) . The equations of motion of the j-th charged particle in this axisymmetric system are,

radial direction:

$$m_j[\frac{d^2\rho}{dt^2} - \rho(\frac{d\theta}{dt})^2] = q_j E_r \frac{\rho}{r} + q_j B_0 \rho \frac{d\theta}{dt} \qquad (1)$$

and axial direction:

$$m_j \frac{d^2 z}{dt^2} = q_j E_r \frac{z}{r} \qquad (2)$$

Here m_j is the mass of the charged particle, r is the radial

author's e-mail: tomita@nifs.ac.jp

particle position from the origin (O) ($r^2 = \rho^2 + z^2$) and E_r is the radial electrostatic field due to the charged dust particle. The azimuthal motion is determined from the conservation of canonical angular momentum P_θ:

$$\frac{d\theta}{dt} = \frac{1}{m_j \rho^2}\left(P_\theta - \frac{q_j B_0}{2}\rho^2\right). \tag{3}$$

The initial conditions ($\rho = b_{in}$, $\mathrm{d}\theta / \mathrm{d}t = 0$) give the constant value of P_θ:

$$P_\theta = \frac{q_j B_0}{2} b_{in}^2 . \tag{4}$$

The normalized equations of motion become

$$\frac{d^2\bar{\rho}}{d\bar{t}^2} = \frac{\alpha_j}{2}\frac{\bar{\rho}}{\bar{r}^3} + \frac{\mu_j^2}{4}\frac{1-\bar{\rho}^4}{\bar{\rho}^3}, \tag{5}$$

$$\frac{d^2\bar{z}}{d\bar{t}^2} = \frac{\alpha_j}{2}\frac{\bar{z}}{\bar{r}^3}, \tag{6}$$

where the distances, velocity and time are normalized by the impact parameter b_{in}, the initial speed $v_{j,in}$ and $b_{in}/v_{j,in}$, respectively. The system in the absence of magnetic field is determined by the parameter α_j,

$$\alpha_j \equiv \frac{q_j q_d}{4\pi\varepsilon_0 b_{in}} \Big/ \frac{m_j v_{j,in}^2}{2}, \tag{7}$$

which is the ratio of the electrostatic potential energy at the distance of the impact parameter to the initial kinetic energy and the parameter μ_j indicates the effect of the static magnetic field,

$$\mu_j \equiv b_{in} \Big/ \frac{m_j v_{j,in}}{|q_j B_0|}, \tag{8}$$

which is the ratio of the impact parameter b_{in} to the Larmor radius with respect to the initial speed $v_{j,in}$. The parameter μ_e of the electron is much larger than that of the ion for the case of ions with the sound speed c_s and the thermal speed of the electron v_{the}:

$$\frac{\mu_e}{\mu_i} = \frac{m_i v_{i,in}}{Z_i m_e v_{e,in}} \simeq \frac{m_i c_s}{Z_i m_e v_{the}} \simeq \sqrt{\frac{m_i}{m_e}}, \tag{9}$$

where Z_i is the charge state of the ion. This relation indicates the effect of the magnetic field on the ion is much smaller than that of the electron (see Eq. 5).

In high plasma temperature there is a possibility to charge positively due to the thermionic emission from the dust particle. In this study we investigate the electron absorption cross-section of positively charged dust particle. In order to investigate the electron orbit numerically, the start position ($z = z_{in}$) should be determined. In Fig.1 the dependence of the closest radius ($r = r_{min}$) to the dust, where the radial velocity of the charges particle is vanishing ($dr/dt = 0$), on the initial axial position (z_{in}) is

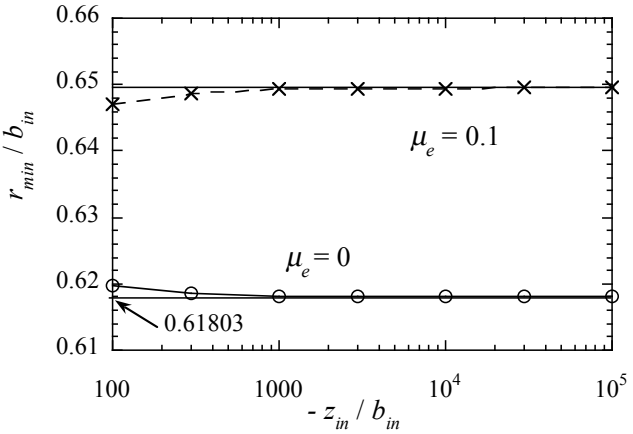

Fig.1 The closest positions as a function of initial axial position (z_{in}), where α_e = - 1.0 and μ_e = 0 and 0.1.

shown with the parameters α_e = - 1.0 and μ_e = 0 and 0.1. In the case without magnetic field (μ_e = 0) the closest radius is obtained from the OML theory as r_{min} / b_{in} = 0.61803. The orbit of the closer start to the dust deviates due to the strong Coulomb force of the dust. This figure shows that the initial position should be far from - 1000 b_{in} with the 10^{-3} accuracy. The Coulomb force is proportional to the parameter α_e, so the start point is determined as z_{in} = - 10^3 b_{in} α_e.

The typical orbit of an electron near the negatively charged dust, which is located at the origin ($\rho = z = 0$), is shown in Fig.2, where α_e = 1.0 and μ_e = 0.01. The closest radius in the presence of in the axial magnetic field (solid line in Fig.2) becomes smaller than that in the absence of magnetic field. The orbit of a charged particle in magnetic field is characterized by three-dimensional nature rather than the two dimensional orbit. The particle

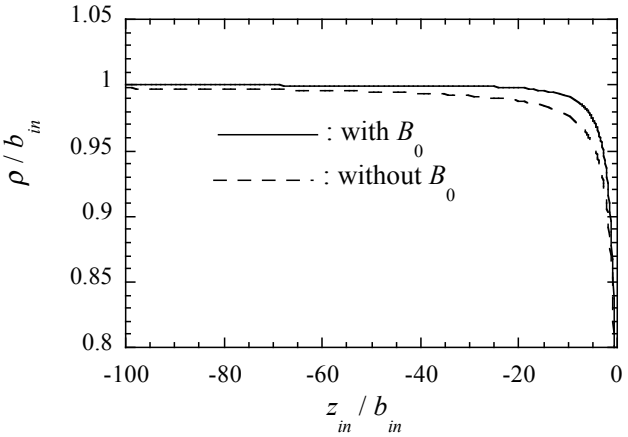

Fig.2 Typical orbit of an electron near the positively charged dust for the case α_e = - 1.0 and μ_e = 0.01. The solid and dashed lines are the orbits with and without magnetic field, respectively.

has a radial velocity due to the radial electric field. This radial velocity pushes an electron in the azimuthal direction by the Lorentz force. This azimuthal velocity makes the radial force by the axial magnetic field. Thus the magnetic field has the second order effect on the orbit without magnetic field, see Eq. 5. As a result the radial force balance of the particle between the Lorentz force and the centrifugal force determines the radial motion of a charged particle. The radial equation of motion is expressed from Eq. 1,

$$m_j \frac{d^2\rho}{dt^2} = q_j E_r \frac{\rho}{r} + m_j \rho (\frac{d\theta}{dt})^2 + q_j B_0 \rho \frac{d\theta}{dt} . \quad (10)$$

where the first term of the RHS is the electrostatic force by the dust particle, the second one is the centrifugal force and the third one indicates the Lorentz force. From the relation of the conservation of the canonical angular momentum (Eqs. 3 and 4), the summation of the centrifugal force and the Lorentz force is expressed as:

$$m_j \rho (\frac{d\theta}{dt})^2 + q_j B_0 \rho \frac{d\theta}{dt} = \frac{1}{m_j \rho^3} (P_\theta^2 - \frac{q_j^2 B_0^2}{4} \rho^4)$$

$$= \frac{q_j^2 B_0^2}{4 m_j \rho^3} (b_{in}^4 - \rho^4) . \quad (11)$$

For the case of the orbit of the charged particle with the opp0site sign as the dust charge, its radius ρ is smaller than the initial one (b_{in}) due to the radial electrostatic force, which means the centrifugal force is stronger than the Lorentz force all the time. This deference makes the closest radius larger than that without magnetic field, Fig. 2. On the other hand the charged particle with the same sign of the dust charge approaches to the dust.

For the weak magnetic field, i.e. small μ_e, the closest radius r_{min} is linearly proportional to the strength of magnetic field or μ_e,

$$\bar{r}_{\min}(\alpha_e, \mu_e) = \bar{r}_{\min 0}(\alpha_e) + \gamma_e(\alpha_e)\mu_e . \quad (12)$$

Here γ_e is the constant of proportion, which depends on α_e and $\bar{r}_{\min 0}$ is the closest radius in the absence of magnetic field, which is obtained from the OML theory:

$$\bar{r}_{\min 0}(\alpha_e) = \frac{1}{2}(\alpha_e + \sqrt{\alpha_e^2 + 4}) . \quad (13)$$

In Fig.3 the closest radius is shown by the dashed line for the small μ_e, where the parameter α_e = - 1.0, where the linearly approximated line is shown by the solid line. The linear approximation is valid in the range $\mu_e < 0.3$ for α_e = - 1.0. The dependence of the coefficient γ_e on the parameter α_e is investigated numerically, Fig.4. The least square curve (solid line in Fig.4) indicates

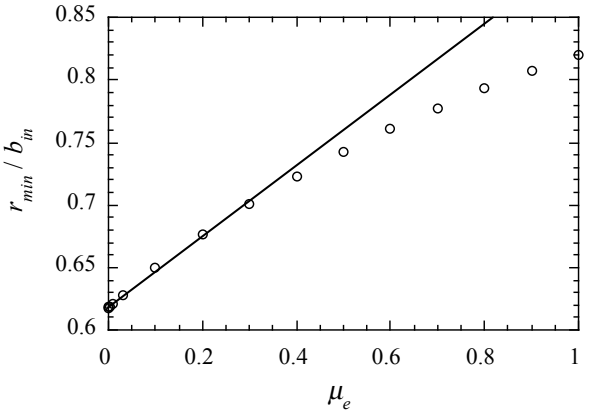

Fig.3 The closest radius as a function of parameter of magnetic field μ_e, where α_e = - 1.0.

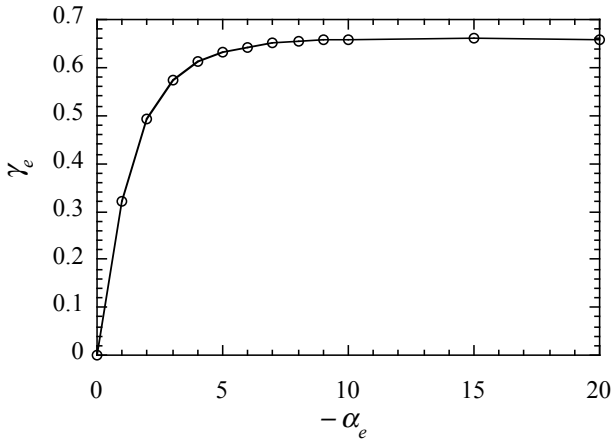

Fig.4 The dependence of the coefficient γ_e on the parameter α_e. The least square and the approximated curves are shown by the solid and the dashed lines, respectively.

$$\gamma_e = 0.658\,[1 - \exp(0.679\,\alpha_e)] . \quad (14)$$

By using Eq. (14), the absorption cross-section is obtained. The un-normalized closest radius is expressed from Eq. 12:

$$r_{\min}(\alpha_e^*, \mu_e^*) = r_{\min 0}(\alpha_e^*)$$

$$+0.658\,[\,1 - \exp(0.679\,\alpha_e^* / b_{in})]\,\mu_e^*\, b_{in}^2 , \quad (15)$$

where

$$r_{\min 0}(\alpha_e^*) = \frac{1}{2}(\alpha_e^* + \sqrt{\alpha_e^{*2} + 4 b_{in}^2}) , \quad (16)$$

$$\alpha_e^* \equiv b_{in}\alpha_e = \frac{-e q_d}{4\pi\varepsilon_0} / \frac{m_e v_{e,in}^2}{2} , \quad (17)$$

$$\mu_e^* \equiv \mu_e / b_{in} = \left| eB_0 \right| / m_e v_{e,in} . \quad (18)$$

This closest radius corresponds to the effective finite dust

radius R_d to the absorption. From this result, Eq. (15), the absorption cross-section of an electron to the dust is obtained easily.

6. Conclusion

The absorption cross-section of the positively charge particle to the spherical dust particle in a weak magnetic field was investigated analytically and numerically. The closest radius of electrons becomes larger than that in the absence of magnetic field due to the Lorentz force, indicating the absorption cross-section smaller. In order to investigate the parameter dependence of the electrostatic force and the magnetic field on the electron orbits, the closest radius of an electron is approximated by the linear dependence of the strength of magnetic field. From this expression of the closest radius one can obtained the absorption cross-section and can calculate the charge state of the dust particle. These results can be important to analyze the dynamics of the dust particle in plasmas immersed in the magnetic field. The higher order approximation of the effects of magnetic field, the absorption cross-section of electrons to the positively charged dust particle and the velocity distribution of the charged particles are left as future issues. The effects of stronger magnetic field, where the strong Larmor motions are dominant, can be studied by the statistical approach of the particle orbits.

Acknowledgments

This work was supported in part by a Grant-in-Aid for scientific research from Ministry of Education, Science and Culture of Japan (No. 19055005).

References

[1] G. Federici *et al.*, Nucl. Fusion **41**, 1967 (2001).

[2] J. Winter, Plasma Phys. Control. Fusion **46**, B583 (2004).

[3] H. Mott-Smith and I. Langmuir, Phys. Rev. **28**, 727 (1926).

[4] J. E. Allen, Phisica Scripta **45**, 497 (1992).

[5] R. D. Smirnov, A. Yu. Pigarov, M. Rosenberg, S. I. Krasheninnikov and D. A. Mendis, Plasma Phys. Control. Fusion **49**, 347 (2007).

[6] Y. Tomita, G. Kawamura, T. Yamada and O. Ishihara, to be appeared in J. Plasma Fusion Res.

Proceedings of ITC18,2008

Numerical Analysis of Slow-Wave Instabilities in Oversized Sinusoidaly Corrugated Waveguide Driven by Finitely Thick Annular Electron Beam

K. Otubo, K. Ogura, M. Yamakawa and Y. Takashima

Graduate School of Science and Technology, Niigata University, 950-2181, Japan

There are three kinds of model for beam instability analyses, which are based on solid beam, infinitesimally thin annular beam, and finitely thick annular beam. In high power experiments, the shape of electron beam is annulus having finite thickness. We present slow-wave instability driven by finitely thick annular beam in oversized sinusoidaly corrugated waveguide for K-band operation. Our analysis is based on a new version of self-consistent liner theory considering three dimensional beam perturbations. The dependence of Cherenkov and slow cyclotron instabilities on the annular thickness and guiding magnetic field are examined.

Keywords: thin-walled annular beam, oversized sinusoidaly corrugated waveguide, Cherenkov instability, slow cyclotron instability

1. Introduction

The backward wave oscillator (BWO) can be driven by an axially injected electron beam and is one of high-power microwave sources. In BWOs, a periodically corrugated slow-wave structure (SWS) is used to reduce the phase velocity of the electromagnetic mode close to the beam velocity. In order to increase the operation frequency and/or the power handling capability, oversized SWSs are used. The diameter of oversized SWS is larger than free-space wavelength of output electromagnetic wave by several times or more. In many high power experiments, cold cathodes are used and the shape of electron beam is a thin-walled annulus. In order to confine the electron beam, a guiding magnetic field is applied. In the interactions between the beam and the electromagnetic wave, the cyclotron instability as well as the Cherenkov instability plays an important role [1-2]. Near the cyclotron resonance or with relatively low magnetic field, the beam motion perpendicular to the magnetic field cannot be ignored and more definite study of BWO is required by taking into account vertical perturbation of the beam. A pioneering work can be seen in Ref. [3], considering a coupling between a sheet beam and a microwave circuit. A new version of self-consistent field theory considering three-dimensional beam perturbations are developed based on a solid beam [4-5] and an infinitesimally thin annular beam [6]. For infinitesimally thin annular beam, the sheet boundary is modulated due to the transverse modulation of annular surface. Analyses of infinitesimally thin annular beam need to be based on a different theory from thin-walled annular and solid beam. For a finitely thick annular beam, a numerical code has been developed and eigen modes and slow-wave instabilities are analyses in Ref. [7], in which a dielectric-loaded SWS is used for simplicity. The boundary condition at the beam surface is different from the infinitesimally thin annular beam. Solid beam and thin-walled annular beam are based on the same beam boundary condition, but the number of the boundary is different. Thin-walled annular beam has outside and inside surface, and solid beam has only outside surface.

In this work, we develop a numerical code for a sinusoidaly corrugated waveguide with a finitely thick annular beam and analyze slow-wave instabilities in oversized sinusoidaly corrugated waveguide designed K-band operations in a weakly relativistic region less than 100 kV. The organization of this proceeding is as follows. In Sec. 2, we describe numerical method of thin-walled annular beam. In Sec. 3, dispersion relation of oversized sinusoidaly corrugated waveguide driven by thin-walled annular beam is presented. The dependence of growth rate on the annular thickness and guiding magnetic field are examined. In Sec. 4, conclusion of this paper is given.

2. Numerical method

We consider a periodically corrugated cylindrical waveguide in Fig. 1. The wall radius $R_w(z)$ varies along the axial direction z as $R_0+h\cos(k_0z)$, where average radius R_0=1.57 cm, corrugation amplitude h=0.17 cm, pitch length z_0=0.34 cm and corrugation wave number $k_0=2\pi/z_0$. A guiding magnetic field B_0 is applied

author's e-mail: fo8e056f@mail.cc.niigata-u.ac.jp

uniformly in the axial direction. An electron beam is propagating along the guiding magnetic field and the shape of electron beam is finitely thick annulus. The beam is uniformly distributed from inside radius R_{ba} to outside radius R_{bb} with beam thickness $\Delta_p(=R_{bb}-R_{ba})$. The outside and inside regions of the beam are a vacuum. The temporal and spatial phase factor of all perturbed quantities is assumed to be $\exp[i(k_z z+m\theta-\omega t)]$. Here, m is the azimuthal mode number and k_z is the axial wave number. Based on this model, the dispersion relation can be derived self-consistently considering the three-dimensional beam perturbations and boundary condition. For the beam, the relativistic effects are considered.

In the system with magnetized beam such as Fig.2, electromagnetic modes are the hybrid mode of transverse magnetic (TM) and transverse electric (TE) mode due to the perturbed perpendicular motion to the magnetic field. Two letters of EH and HE is used, to designate the hybrid mode. In this paper, TM is dominant in EH mode and TE is dominant in HE mode.

An electron beam surface is modulated as beam is propagating. For finitely thick annular beam, the transverse moderation appears as the surface electric charge at the fixed boundary as shown in Figs.2. Thin-walled annular beam has two surfaces because there is a vacuum region inside the beam.

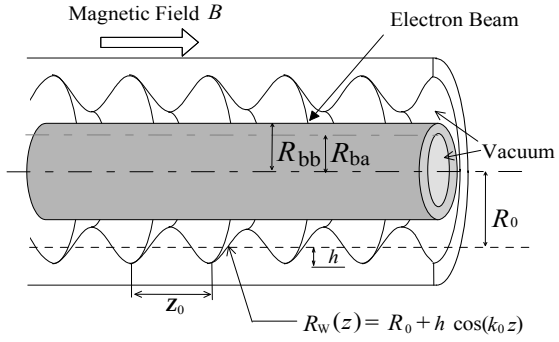

Fig. 1 Model of analysis. The wall of cylindrical waveguide is corrugated sinusoidally.

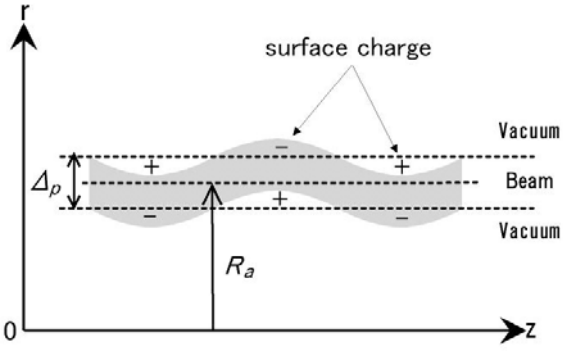

Fig. 2 Beam surface of finitely thick annular beam.

Since the SWS is spatially periodic with z_0, the fields in SWS are expressed by a sum of spatial harmonic series, so-called Floquet's series. The eigen functions for the cylindrical system are the Bessel functions, i.e., J_m and N_m, which have been used in the Floquet's series for non-oversized BWO cases. The electromagnetic modes are volumetric waves having the strong field near the axis. For the oversized BWO, the electromagnetic field is localized near the SWS wall as shown in Fig. 3. All spatial harmonics are evanescent wave in the radial direction. If the spatial harmonics are expressed by J_m and N_m, they have extremely large imaginary number. This causes serious problems in numerical calculations. To avoid this difficulty, the expressions of spatial harmonics should be the modified Bessel functions, i.e., I_m and K_m. We improve the new self-consistent analysis by replacing the Bessel functions to the modified Bessel functions.

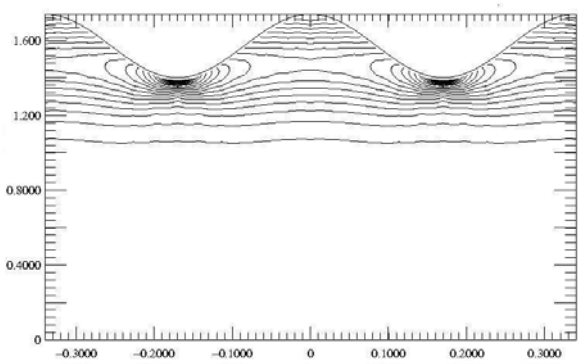

Fig. 3 The electric field distribution of TM_{01} mode in the K-band SWS at the π point.

3. Numerical result

We analyzed the dispersion relation of oversized sinusoidaly corrugated waveguide driven by a finitely thick annular beam. Figure 4 shows the dispersion curves of EH_{01} mode with the beam energy 80 keV, current 200 A, beam thickness Δ_p=0.1 cm and B_0=0.4 T. Four beam modes exist on the axially streaming beam. They are fast and slow space charge modes, fast and slow cyclotron modes. The slow space charge and slow cyclotron modes couple to EH_{01} mode, resulting in the Cherenkov and slow cyclotron instabilities. The growth rate of slow cyclotron instability is shown Fig. 5 for m=-1, 0 and 1. The nonaxisymmetric instabilities are almost the same as the axisymmetric instability. Since the perturbation is assumed to be $\exp[i(k_z z+m\theta-\omega t)]$, the electromagnetic wave propagate helically. The rotating direction is rightward (leftward) in the laboratory frame of reference with positive (negative) m. For oversized BWO, the growth rates are not affected by the rotational direction.

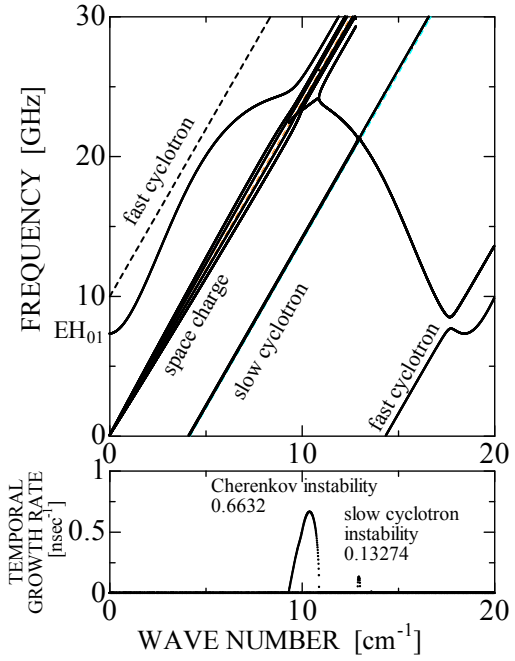

Fig.4 The dispersion curves of axisymmetric mode (m=0) with beam energy 80 keV, current 200 A, outside radius R_{bb} =1.35 cm, inside radius R_{ba}=1.25cm and external magnetic field B_0=0.4 T.

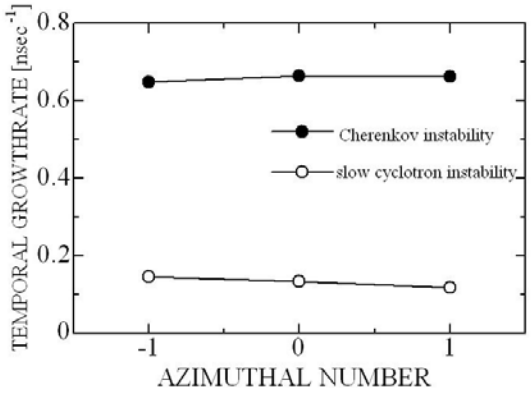

Fig. 5 The temporal growth rate of Cherenkov and slow cyclotron instability versus rotational direction of the electromagnetic field.

Figure 6 shows the dependence of the temporal growth rate on beam thickness Δ_p, for EH_{01} mode. The beam outer radius is fixed to 1.35 cm, and beam inner radius has been changed with a fixed line charge density. The growth rate of Cherenkov instability increases by decreasing Δ_p. The growth rate of slow cyclotron instability also increases by decreasing the beam thickness. But, in the region of Δ_p < 0.022 cm, the growth rate decreases.

In the limit that the beam inner radius is zero, the growth rate of Cherenkov and slow cyclotron instabilities of thin-walled annular beam approaches the growth rate of solid beam, ▲ in Fig.6. In the other limit that $\Delta_p \rightarrow 0$, the corresponding growth rates are those of an infinitesimally thin annular beam model with Δ_p=0 and are depicted by ● in Fig. 6. Two models based on finite and zero Δ_p give almost the same results for the Cherenkov instability. For the slow cyclotron instability, the growth rates are different between two models. This might be caused by the difference of annulus: one has an internal structure between the inner and outer surface and the other is just a sheet without any internal structure.

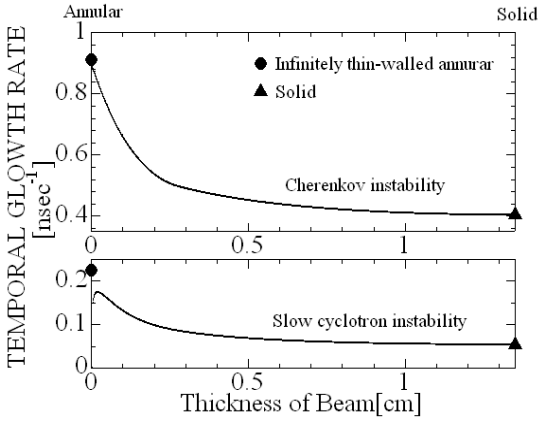

Fig. 6 The dependence of the temporal growth rate on beam thickness.

For EH_{01} mode, the dependence of the temporal growth rate of Cherenkov instability on the guiding magnetic field is shown in Fig.7, and that of slow cyclotron instability in Fig.8. The growth rate of Cherenkov instability hardly changes by the variation of magnetic field. But, in the region of B_0 < 0.18T, the growth rate increases. In this region, the slow cyclotron instability merges into the Cherenkov instability. The dip of growth rate in the vicinity of 1.8T is attributed to the resonant interaction of space charge mode and fast cyclotron mode. Electromagnetic energy excited by the space charge mode is absorbed by the beam due to the fast cyclotron interaction.

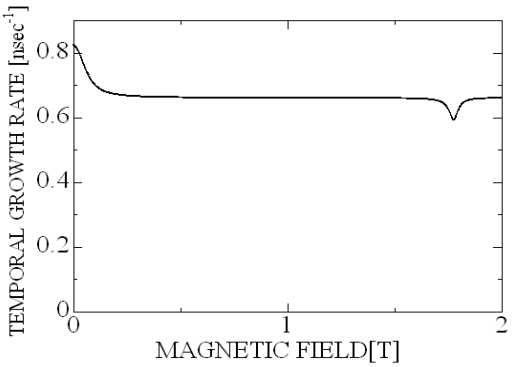

Fig.7 Dependence of Cherenkov instability on the guiding magnetic field. The beam parameter is the same as Fig. 4.

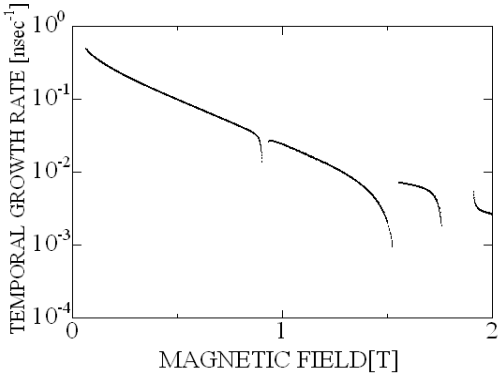

Fig. 8 Dependence of slow cyclotron instability on the guiding magnetic field. The beam parameter is the same as Fig. 4.

The growth rate of slow cyclotron instability decreases by increasing magnetic field. Slow cyclotron mode shifts to the right and fast one to the left in Fig. 4. In the vicinity of 0.9T and 1.8T, the slow and fast cyclotron modes are interacting and the growth rate becomes discontinuous. In the vicinity of 1.5T, the slow cyclotron mode begins to cross EH_{01} mode at the 2π point with a very small growth rate, at point 1 in Fig. 9. Other interaction points 2 and 3 in the forward region appear as Fig. 9. After passing this point, interacting point 1 and 2 merge and disappear as the magnetic field rises. The slow cyclotron mode couples to EH_{01} mode at point 3 only, leading to the discontinuity of growth rate near 1.5 T. In summary, the slow cyclotron mode couples to EH_{01} mode in the backward region of 0-1.5 T and 1.8-2.0 T. From 1.5-1.8 T, the slow instability occurs in the forward region.

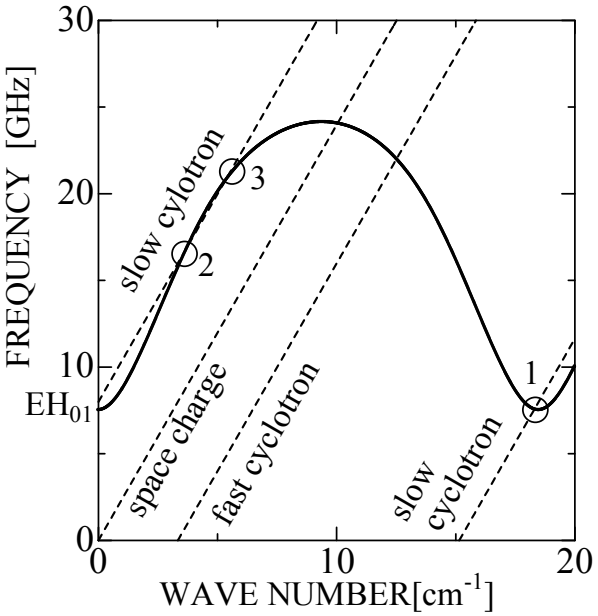

Fig. 9 Dispersion curve of EH_{01} mode. Three beam lines of space charge, fast cyclotron and slow cyclotron modes are plotted for B_0=1.5T.

4. Conclusion

We develop a numerical code for a sinusoidaly corrugated waveguide with a finitely thick annular beam considering three-dimensional beam perturbations. The self-consistent field analysis is improved and the slow cyclotron and Cherenkov instabilities of oversized BWO are numerically examined. Nonaxisymmetric instabilities are excited even in the completely axisymmetric system. The growth rates are almost the same among nonaxisymmetric and axisymmetric instabilities. The slow cyclotron and Cherenkov instabilities depend on the annular thickness. The Cherenkov instability has a week dependence on the guiding magnetic field, while the slow cyclotron instability strongly depends on the magnetic field.

Acknowledgments

This work was partially supported by Grant-in-Aid for Scientific Research from the Ministry of Education, Science, Sports and Culture of Japan, and by NIFS Collaboration Research Program.

References

[1] K. Ogura *et al*., IEEJ Trans. FM. **125**, 733 (2005).
[2] Y. Takamura *et al*., Plasma Fusion Res. **3**, S1078 (2008).
[3] J. R. Pierce, *Traveling-Wave Tube* (Van Nostrand, Toronto, 1950).
[4] O. Watanabe, *et al*., Phys. Rev. E. **63**, 056503 (2001).
[5] K. Ogura *et al*., Jpn. J. Appl. Phys. **42**, 7095 (2003).
[6] K. Ogura *et al*., J. Plasma Phys. **72**, 905 (2006).
[7] S. Tamura *et al*., Plasma Fusion Res. **3**, S1020 (2008)

Proceedings of ITC18, 2008

Algebraic analysis approach for multibody problems II: Variance of velocity changes

Shun-ichi OIKAWA, Koichiro HIGASHI, Hideo FUNASAKA, and Yu KITAGAWA

Graduate School of Engineering, Hokkaido University, Sapporo 060-8628, Japan

The algebraic model (ALG) proposed by the authors has sufficiently high accuracy in calculating the motion of a test particle with all the field particles at rest. When all the field particles are moving, hoewver, the ALG has poor prediction ability on the motion of the test particle initially at rest. None the less, the ALG approximation gives a good results for the statistical quantities, such as variance of velocity changes or the scattering cross section, for a sufficiently large number of Monte Carlo trials.

Keywords: multibody problems, algebraic model

1 Introduction

Since it is difficult to rigorously deal with multibody Coulomb and gravitational collisions, the current classical theory considers them as a series of temporally-isolated binary Coulomb collisions within the Debye sphere. The efficient and fast algorithms to calculate inter-particle forces include the tree method [2, 3], the fast multipole expansion method (FMM) and the particle-mesh Ewalt (PPPM) method [4]. Efforts have been made to use parallel computers, and/or to develop special purpose hardware to calculate interparticle forces, e.g. the GRAPE (GRAvity PipE) project [1].

Some of the authors have developed an algebraic model for multibody problems, and have shown that the momentum transfer cross-section with our model is in good agreement with the exact one [1]. As shown in Fig. 1

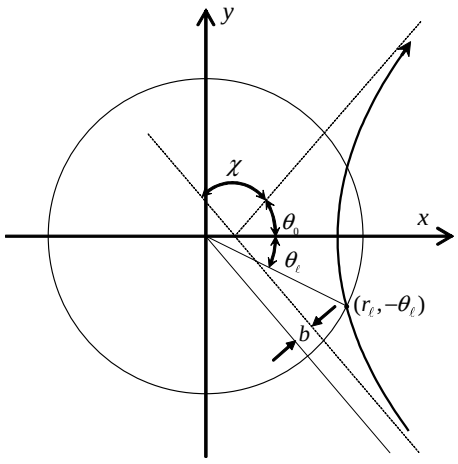

Fig. 1 Unperturbed relative trajectory $r = r(\theta)$ in an orbital plane. The scattering center is at the origin. An impact parameter is $b = b_0 \tan\theta_0$. Interaction region is inside the circle with a radius $r_\ell = \Delta\ell/2$.

author's e-mail: oikawa@fusion.eng.qe.hokudai.ac.jp

its scattering angle, $\chi \equiv \pi - 2\theta_0$, is given by $b = b_0 \tan\theta_0$, where b is the impact parameter, $b_0 \equiv e^2/4\pi\varepsilon_0\mu g_0^2$ corresponds to $\chi = \pi/2$ scattering, and g_0 the initial relative speed at $r = \infty$ and $\theta = -\theta_0$.

The angular component of the equation motion gives the well-known invariant of

$$r^2 \frac{\mathrm{d}\theta}{\mathrm{d}t} = \text{const} = b g_0, \tag{1}$$

and the radial component is given by

$$\frac{\mathrm{d}g_r}{\mathrm{d}t} = \frac{g_0^2 b_0}{r^2}\left(1 + \frac{b_0}{r}\tan^2\theta_0\right), \tag{2}$$

where $g_r \equiv \dot{r}$ denotes the radial velocity. The first term in the parentheses on the right hand side of Eq. (2) stands for the Coulomb force $F_\mathrm{c} \propto r^{-2}$. This force is much smaller for small angle scatterings, i.e. $\chi \ll 1$, than the second term F_a which scales as $\propto r^{-3}$ and results from the conservation of angular momentum Eq.(1), since, at the closest point $r_\mathrm{min} = r(\theta = 0)$ shown in Fig. 1, we have

$$\frac{b_0 \tan^2\theta_0}{r_\mathrm{min}} \simeq \frac{2}{\chi} \gg 1. \tag{3}$$

Thus the main force on the particle is not the Coulomb force F_c, but F_a due to the conservation of angular momentum.

2 Algebraic Approximation for Multibody Interaction

Since the r-dependence on $F_\mathrm{a} \propto r^{-3}$ is steeper than that on $F_\mathrm{c} \propto r^{-2}$, the momentum change in $\mu\boldsymbol{g}$ is almost due solely to F_a near $r = r_\mathrm{min}$. As a consequence, the exact hyperbolic trajectory for the particle can be approximated as a broken line with an impulse force of

$$\mu\Delta\boldsymbol{g} = 2\mu g_0 \cos\theta_0 \boldsymbol{e}_x \tag{4}$$

near the closest point as shown in Fig. 2.

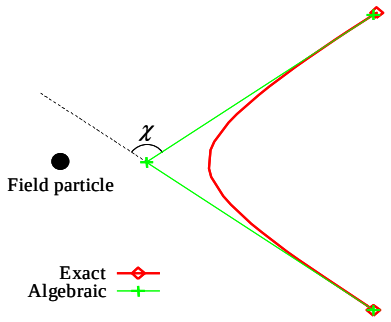

Fig. 2 Algebraic trajectory (broken line) and exact trajectory (curved line) which is a part of a hyperbola. A field particle (black circle) is on the left.

With this in mind, we have approximated a multibody problem to a series of binary deflections near their closest point as shown in Fig. 2, in which a test particle starts at the lower-right point, and its final point is at the upper-right point due to the interaction with a field particle at rest.

2.1 Coordinate transformation

In order to apply the above binary interaction approximation (ALG) shown in Fig. 2 to multibody cases, first we seek for a field particle that gives the test particle an impulse force *at the earliest time*. For this purpose, it is convenient to transform the coordinate system from $(x,\ y)$ to (ξ,η), in such a way that the initial position of the test particle is at the origin $(\xi,\eta)=(0,0)$ and the relative velocity $\boldsymbol{g}\equiv\boldsymbol{v}_i-\boldsymbol{v}_j$ is $(g_\xi,g_\eta)=(0,g)$. Then the relative position $\boldsymbol{r}_{ij}$ has an η-coordinate of

$$\eta_{ij}=\left(\boldsymbol{r}_i-\boldsymbol{r}_j\right)\cdot\boldsymbol{g}/g. \tag{5}$$

The particle moves along the η-axis with a constant velocity of g, and is to interact at $\left(0,\eta_{ij}\right)$ with this field particle in a time interval of $\Delta t_{ij}\equiv\eta_{ij}/g$ sec. Accordingly, the field particle that the test particle is given an impulse force at the earliest time has the smallest positive η_{ij}, i.e.

$$\eta_{\min}\equiv\min(\max(0,\eta_{ij})),\ \text{for } 1\le i,j\le N, \tag{6}$$

We have ignored the effect of field particles with $\eta_{ij}<0$, since the interaction is completed at $\eta=0$ in our approximation. In other words, such field particles have already interacted with the test particle in the past.

When the test particle moves to the position of $(0,\eta_{\min})$, it changes the relative velocity by $\Delta\boldsymbol{g}_{ij}$ as

$$\Delta\boldsymbol{g}_{ij} = -2g\sin\frac{\chi_{ij}}{2}\,\boldsymbol{e}_\xi, \tag{7}$$

$$\chi_{ij} \simeq 2\arctan\frac{b_0}{\xi_{ij}}, \tag{8}$$

where the pair i and j satisfies Eq. (6), and we have approximated that the impact parameter is given by $b=\xi_{ij}$ in Eq. (4) as shown in Fig. 3. Thus, in the (ξ,η) coordinate

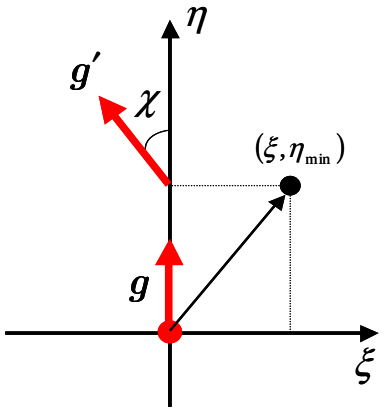

Fig. 3 Coordinate transform from the (x,y) to (ξ,η). In this coordinate system, the scattering angle χ, i.e. the impact parameter b and the time of the interaction Δt are approximately given by ξ and η, respectively.

system, the field particle position ξ_{ij} and η_{ij} correspond to the velocity change $\Delta\boldsymbol{g}_{ij}$ and the time of the interaction Δt_{ij}, respectively. This procedure will be repeated until the test particle leaves the prescribed interaction region, i.e. $r<\Delta\ell/2$ as depicted in Fig. 1.

3 Calculation

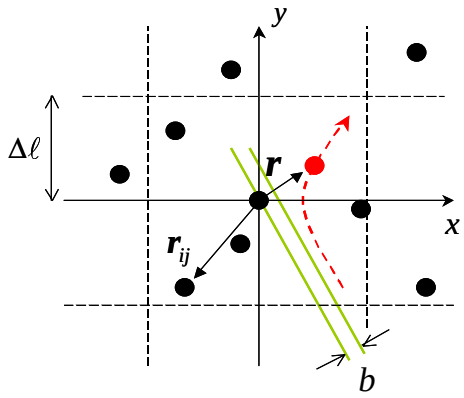

Fig. 4 Typical initial particle positions. The almost-uniformly-distributed black circles are field particles. For Case 1, a gray circle (or red in color) is the test particle at $\boldsymbol{r}$ with an impact parameter b. Initial conditions for Case 2 is that all the field particles are moving, and the test particle locates at the orign at rest.

The numerical results with using the *direct integration method*, DIM, hereafter refers to that obtained by solving the following equation of motion a particle-i with a charge q_i, a mass m_i, and velocity $\boldsymbol{v}_i$ at a position $\boldsymbol{r}_i$

$$m_i\frac{\mathrm{d}\boldsymbol{v}_i}{\mathrm{d}t} = q_i\sum_{j\neq i}^{N}\frac{q_j}{4\pi\varepsilon_0}\frac{\boldsymbol{r}_i-\boldsymbol{r}_j}{\left|\boldsymbol{r}_i-\boldsymbol{r}_j\right|^3}, \tag{9}$$

where $\boldsymbol{r}_j$ are the field particles' positions. As the DIM in this study, we will use the 6-stage 5-th order Runge-Kutta-Fehlberg method known as the RKF65 [7, 8] with the absolute numerical error tolerance of 10^{-16}.

In the following, we will assume that, except a test particle, the field particles on the average are randomly distributed in the phase space $(\boldsymbol{r}, \boldsymbol{v})$. In configuration space, field particles are distributed with the average interparticle separation, $\Delta\ell$. We will consider two cases: all the field particles are fixed at their initial positions, the Case 1, and moving field particles, Case-2. The typical initial condition for Case 1 are depicted in Fig. (4)

3.1 Case 1: All the field particles at rest [5]

In Case 1, all the field particles are at rest, and one of them locates at the origin. The test particle starts from the position of $(b, -\Delta\ell/2)$ with a velocity of $(0, v_0)$. Thus b is the impact parameter against the field particle initially at the origin.

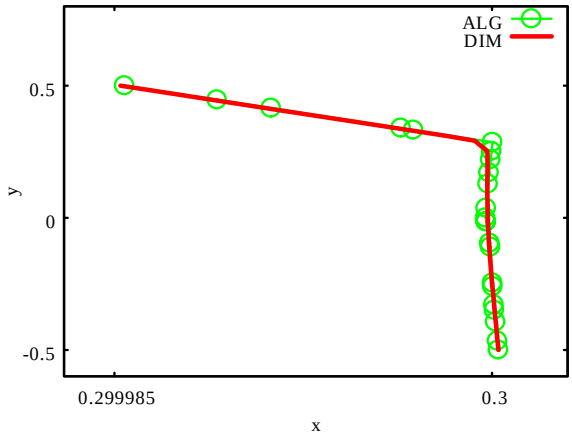

Fig. 5 Comparison of algebraic trajectory (denoted by ALG) and the exact trajectory (denoted by DIM, direc inegration method) in the case of 442-body Coulomb collisions with an impact parameter $b = 0.3\Delta\ell$. Coordinates (x, y) are normalized by $\Delta\ell$. The circles in the figures for the algebraic trajectories stand for the positions at which the test partcile is given the impulse force by one of 441 field particles. See Ref. [5] for more detail.

Figure 5 is an example out of 10^5 Monte Carlo calculations for an impact parameter $b = 0.3\Delta\ell$, and compares the algebraic (ALG) trajectory and the exact (DIM) trajectory normalized by the interparticle separation $\Delta\ell$. Note that the DIM results are accurate up to of the order of 10^{-16} which is the absolute error tolerance adopted. The circles in the figure indicate the positions at which the test partcile is given the impulse force by one of 441 field particles. The algebraic (ALG) approximation agrees well with the direct integration method, DIM, in most cases as shown in Fig. 5.

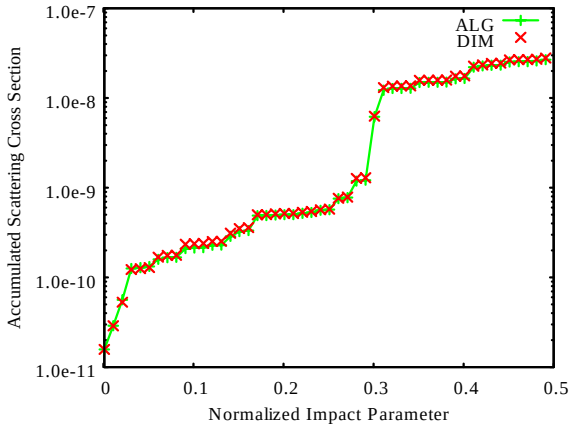

Fig. 6 Accumulated Coulomb scattering cross section $\sigma_{\rm acc}(b)/\Delta\ell^2$ vs normalized impact parameter $\bar{b} = b/\Delta\ell$ in the case of $N = 442$-boby.

Depicted in Fig. 6 is the *accumulated* scattering cross section $\sigma_{\rm acc}(b)$ as a function of the impact parameter b defined by

$$\sigma_{\rm acc}(b) = \int_0^b \left(\frac{\Delta g}{g}\right)^2 \pi b db. \tag{10}$$

The agreement with the exact one is also excellent. It should, however, be noted that all the field particles are at rest throughout the calculation in this case [5]. The CPU time required for the algebraic approximation is only about 20 min using a personal computer, whereas the exact analysis requires 15 hours to integrate the entire set of multibody equations of motion.

3.2 Case 2: Moving field particles.

In Case 2, we will loosen the above restriction on the field particle motion, and have applied the algebraic model to the 10-body problem, in which there are 9 moving field particles and a test particle initially at rest. The change in position $\Delta\boldsymbol{r}$ (results not shown) of the field particles are in good agreement with the exact one, since they are moving so that $\Delta\boldsymbol{r}_i \sim \boldsymbol{v}_i(0)\,\Delta t$ to a good approximation. Although, the absolute value of the change in velocity $|\Delta\boldsymbol{v}|$ of each particle by the ALG are of the same order as the exact one, the orientation of $\Delta\boldsymbol{v}$ are not correct as shown in Fig. 7, in which The test particle is given impluse forces as marked with circles. Also depicted in Fig. 7 is the final point at $t = \Delta t$ by using the BIA, the binary ineraction approximation, proposed by some of the authors [6]. Note that the BIA accurately predicts the final point of the DIM with the absolute error tolerance of 10^{-16}.

In spite of poor accuracy in the individual particle motion, the ALG approximation gives a good results for the statistical quantities, such as variance of velocity changes for a sufficiently large number of Monte Carlo trials. Figure 8 shows the variance of changes in velocity, $\left\langle(\Delta\boldsymbol{g})^2\right\rangle$, of

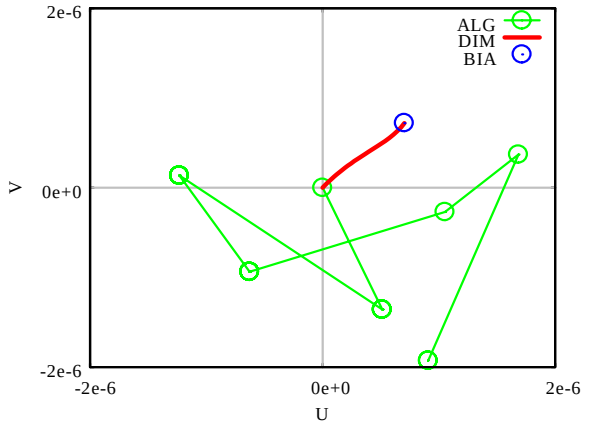

Fig. 7 Case 2: Trajectory of the test particle initially at rest, in the velocity space (U, V) normalized by a thermal speed. There are 9 moving field particles.

the test particle initially at rest, in the case of $N = 10$-boby. For small numbers of trials $N_{\rm MC}$, such as $N_{\rm MC} \sim 2 \times 10^4$ in Fig. 8, the ALG differes significantly from the DIM. Several jumps seen in the figure are due to the close encounters, i.e. the large angle scatterings. The ALG sometimes results in the false close encounters, especially at $N_{\rm MC} \sim 2 \times 10^4$, which have led to numerical errors. Such errors in variance by the ALG becomes smaller for larger $N_{\rm MC} \sim 10^6$, since the large angle scattering seldom occurs in plasmas. The variance calculated by using the BIA, perfectly agrees with the DIM as was shown in Fig. 8.

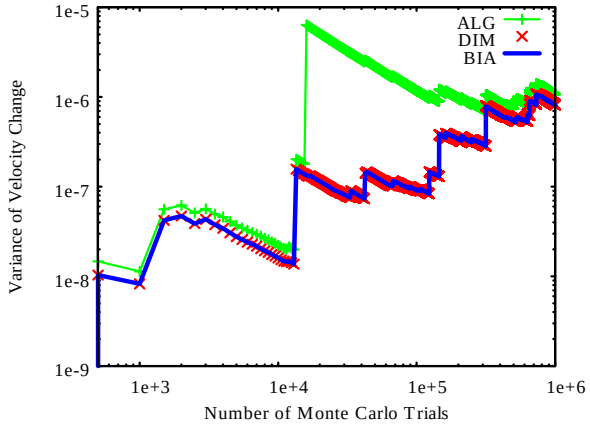

Fig. 8 Variance of the change in velocity of the test particle initially at rest, $\left\langle (\Delta \boldsymbol{g})^2 \right\rangle$, in the case of $N = 10$-boby. The DIA stands for the direct integration method, ALG the algebraic approximation, and BIA the binary ineraction approximation [6].

4 Conclusion

The algebraic model (ALG) proposed by the authors has sufficiently high accuracy in calculating the motion of a test particle with all the field particles at rest. When all the field particles are moving, hoewver, the ALG has poor prediction ability on the motion of the test particle initially at rest. None the less, the ALG approximation gives a good results for the statistical quantities, such as variance of velocity changes or the scattering cross section, for a sufficiently large number of Monte Carlo trials.

Acknowledgement

The author would like to thank Dr. A. Wakasa, Prof. Y. Matsumoto and Prof. M. Itagaki for their fruitful discussions on the subject. The author would also acknowledge the continuous encouragement of the late Prof. T. Yamashina.

[1] J. Makino and M. Taiji, GRAPE-4: A MASSIVELY PARALLEL SPECIAL-PURPOSE COMPUTER FOR COLLISIONAL *N*-BODY SIMULATIONS. APJ **480**, 432–446(1997).

[2] A. W. Appel, An Efficient Program for Many-Body Simulation, *SIAM J. Sci. Stat. Comput.* **6** 85–103 (1985)

[3] J. E. Barnes and P. Hutt, A hierarchical $O(N\log N)$ force-calculation algorithm, *Nature* **324** 446–449 (1986)

[4] P. P. Brieu, F. J. Summers and J. P. Ostriker, Cosmological Simulations Using Special Purpose Computers: Implementing P^3M on GRAPE *ApJ* **453** 566 (1995)

[5] S. Oikawa, H. Funasaka, Algebraic analysis approach for multibody problems. J. Plasma Fusion Res. **36** (2008) S1073.

[6] H. Funasaka, S. Oikawa, K. Higashi, and Y. Kitagawa, Binary Interaction Approximation to *N*-Body Problems, *this conference*, P2-61.

[7] E. Fehlberg. Low-order classical Runge-Kutta formulas with step size control and their application to some heat transfer problems. NASA Technical Report 315 (1969).

[8] E. Fehlberg. Klassische Runge-Kutta-Formeln vierter und niedrigerer Ordnung mit Schrittweiten-Kontrolle und ihre Anwendung auf Warmeleitungsprobleme, *Computing* (Arch. Elektron. Rechnen), vol. 6, (1970) pp. 61–71.

Proceedings of ITC18, (2008)

Experimental Study on Performance of Slow Cyclotron Maser in Weakly Relativistic Region

K. Bansho, K. Ogura, H. Oe, Y. Kazahari, H. Iizuka, A. Sugawara

Graduate School of Science and Technology, Niigata University, Niigata 950-2181, Japan

[a] Plasma Research Center, University of Tsukuba, Tsukuba 305-8577, Japan

(Received day month year / Accepted day month year should be centered 10-point type)

Studies of slow cyclotron maser operation of slow–wave device are reported. The beam voltage is weakly relativistic, less than 100 kV. The slow-wave structure is periodically corrugated oversized waveguide, whose target operation frequency due to the Cherenkov interaction is in K-band. By using rectangular corrugation having the relatively small ratio of corrugation width to periodic length of about 20%, the dispersion curve around the upper cut-off becomes flat and the effect of second harmonic slow cyclotron resonance is observed in the low energy region near 30kV. By using the sinusoidal corrugation and the rectangular corrugation having the ratio of corrugation width to periodic length of 50%, the effect of the fundamental and the second harmonic slow cyclotron maser is observed in the low energy region.

Keywords: slow-wave device, weakly relativistic region, rectangular corrugation, slow cyclotron maser

1. Introduction

Backward wave oscillators (BWOs) are one of high-power microwave sources. In BWO, a slow wave structure (SWS) is used to reduce the phase velocity of electromagnetic wave to beam velocity. Axially streaming electron beam interacts with the electromagnetic field to generate high-power microwaves. In order to increase the power handling capability and/or the operating frequency, oversized SWS have been used successfully. The term "oversized" means that the diameter D of SWS is larger than free-space wavelength λ of output electromagnetic wave by several times or more.

In Ref. [1], the combined resonance operation of the Cherenkov interaction and the second harmonic slow cyclotron interaction is reported by using rectangularly corrugated SWS. Although the radiations based on the conventional Cherenkov interaction are predicted to be independent of the magnetic field strength, some strong magnetic field dependence of output power can be seen. The electromagnetic field properties of beam in a finite strength magnetic field are still far from being fully elaborated. And the magnetic field dependence of slow-wave device is a still unsettled issue. In this study, we investigate how operating characteristics of slow-wave devices are depend on the magnetic field from a viewpoint of slow cyclotron interaction.

2. Slow Wave Structure (SWS)

The cylindrical SWS is periodically corrugated. The corrugation is rectangular or sinusoidal. In Fig.1, the rectangular SWS is shown. Dispersion characteristics of SWS are determined by the average radius R_0, corrugation amplitude h and periodic length z_0. The corrugation wave number is given by $k_0=2\pi/z_0$. For the rectangular SWS, one more parameter is added, that is, the corrugation width d. The dispersion characteristics of structure are controlled by changing R_0, h, d and z_0.

Dispersion curves of rectangular SWS are obtained by a numerical method based on the mathematical formula in Ref. [2]. Figure 2 shows the dispersion relation of fundamental axisymmetric transverse magnetic (TM_{01}) mode for two types, whose parameters are listed in table 1. In Fig.2, beam lines of space charge mode $\omega= k_z v$ and slow cyclotron mode $\omega= k_z v-\Omega$ are also plotted. Here, ω, k_z, v and Ω are angular frequency, axial wave number, beam velocity and relativistic cyclotron frequency, respectively. The slow space charge and the slow cyclotron modes couple to fundamental TM_{01} mode, leading to the Cherenkov and slow cyclotron instabilities. For A parameter, the slow-wave device operates as BWO based on the Cherenkov instability by 80 keV beam. The beam interaction point with TM_{01} is close to the upper cut-off at π -point. For B parameter, the dispersion curve around the upper cut-off becomes flat. And the interaction point

author's e-mail: f08e078g@mail.cc.niigata-u.ac.jp

between the 80 keV slow space charge mode and TM_{01} mode shifts toward a traveling wave region. Decreasing beam energy to 30 keV, the interaction point moves to a backward wave region as shown in Fig.2.

Table 1 Parameters of rectangular SWS

	R_0 [mm]	h [mm]	z_0 [mm]	d/z_0 [%]
A	15.1	1.1	3	50
B	15.38	1.38	2.2	22.7

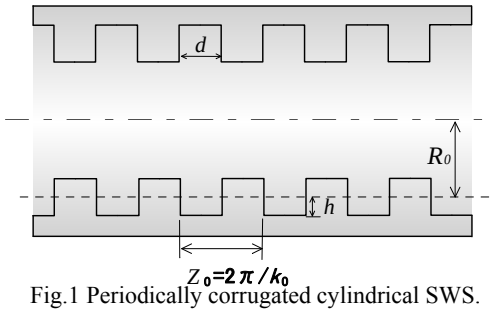

Fig.1 Periodically corrugated cylindrical SWS.

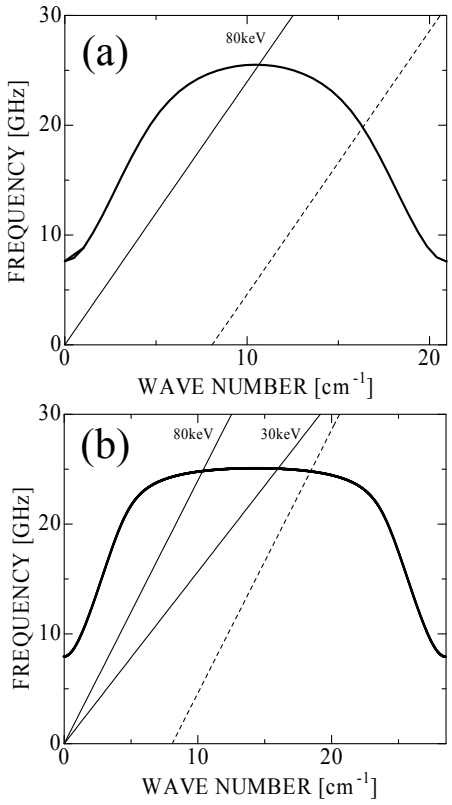

Fig.2 Dispersion characteristics of TM_{01} for rectangular SWS, (a) for A type SWS and (b) B type SWS. Solid lines and dashed lines are slow space charge mode and slow cyclotron mode, respectively.

Dispersion curves like Fig. 2(a) are obtained by sinusoidal corrugations. However, the flat pattern like Fig. 2(b) requires relatively small value of d/z_0 and cannot be realized by sinusoidal corrugations. In this paper, the dispersions like Fig. 2(a) and 2(b) are called A type and B type, respectively. In Fig.3, a photograph of B corrugation is shown. We examine the performance of slow cyclotron maser in the weakly relativistic region using rectangular corrugated SWS and sinusoidal corrugated SWS.

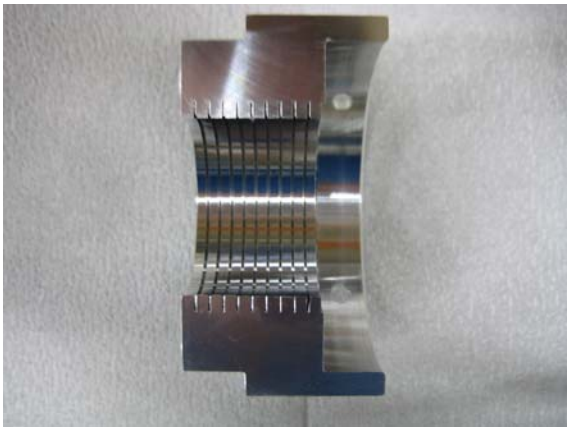

Fig.3 Rectangular corrugation of type B.

3. Experimental results

The experimental setup is schematically shown in Fig.4. Output voltage up to 100 kV from the pulse forming line is applied to the cold cathode. A disk cathode proposed in Ref. [3] is used as a cold cathode. A uniform axial magnetic field B_0 for the beam propagation is provided by ten solenoid coils. The value of B_0 can be changed from zero to about 1T. The microwave outputs are picked up by a rectangular horn antenna typically located 600 mm away from the output window.

Figure 5 shows an example of detected signals. The beam voltage and current are about 100kV and 300A, at the microwave peak time. The microwave signal is split into two branches. One consists of a short waveguide and forms a prompt signal. The other branch is a delay line and forms a delayed signal. The operation frequency estimated from delay time is about 26GHz.

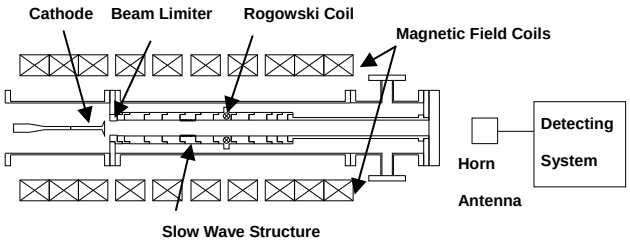

Fig.4 Schematic diagram of the experimental setup.

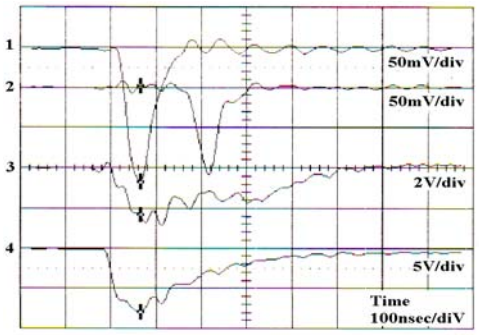

Fig.5 Waveform of measured signals: 1 prompt signal, 2 delayed signal, 3 beam current and 4 beam voltage.

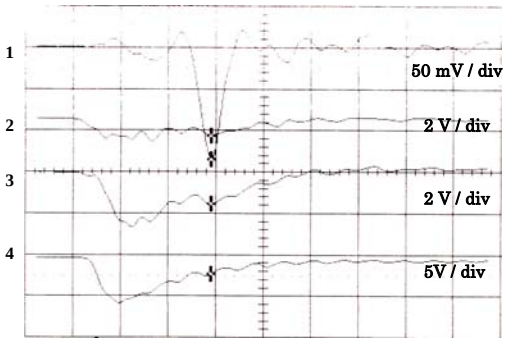

Fig.6 Waveform of measured signals: 1 microwave output, 2 cathode current, 3 beam current and 4 beam voltage.

There exists a critical beam voltage for the meaningful radiations based on the Cherenkov interaction [4]. The starting voltage is more critical than the starting current for the oversized BWOs. Figure 5 corresponds to the radiation above the starting voltage for A type.

Figure 6 is an example of the waveform of measured signals for B type. Microwave radiations like A type are not observed. In Fig.6, the applied beam voltage is about 75kV. However, no radiation starts until the voltage decreases to 30kV. As explained in the previous section (Fig.2), the space charge mode intersects in the travelling wave region with the beam voltage above about 60 keV. And hence, BWO operation based the Cherenkov interaction will not start. The oscillation mechanism rather than the Cherenkov works. Figure 7(a) is a power dependence on B_0 for B type SWS. The radiation resonantly increases at about 0.65 T. This may be the effect of slow cyclotron interaction, as discussed later.

For Fig. 7(a), disks corresponding to rectangular corrugation are fabricated and are integrated into one piece. The manufacturing accuracy may be inferior. The accuracy may be improved by fabricating the corrugation as one piece. Figure 3 is the improved corrugation with a manufacturing accuracy of the order of 0.01mm. Figure 7(b) is power dependence on B_0 by using the improved SWS. Compared with Fig.7(a), the microwave output increases about three times.

By changing the condition at SWS end, the radiation mode can be controlled as reported in Refs. [1,3]. For Figs.7(a) and (b), a straight cylinder with 68 mm is placed at the beam entrance of SWS. The radiation patterns are measured and show the radiation mode is nonaxisymmetric hybrid HE_{11} mode for Fig.7. By changing the cylinder length before SWS to 34mm, the radiation mode changes to axisymmetric TM_{01} mode. The power dependence on B_0 becomes like Fig.8. The effect of slow cyclotron interaction is observed above 0.6 T. However, the outputs decrease around 0.7 T. This might be caused by the effect of the absorption due to the fast cyclotron interaction in the straight cylinder before and after SWS as discussed latter.

In Fig.9, the power dependence on B_0 for sinusoidal corrugation is shown. The microwave outputs become a peak at about 0.9 T and 0.45T. This might be caused by a resonance between slow cyclotron and Cherenkov interactions. For rectangular corrugated SWS with the ratio of corrugation width to periodic length of 50%, similar power dependence on B_0 is observed. However, the fundamental operation is not clear compared with the sinusoidal corrugation.

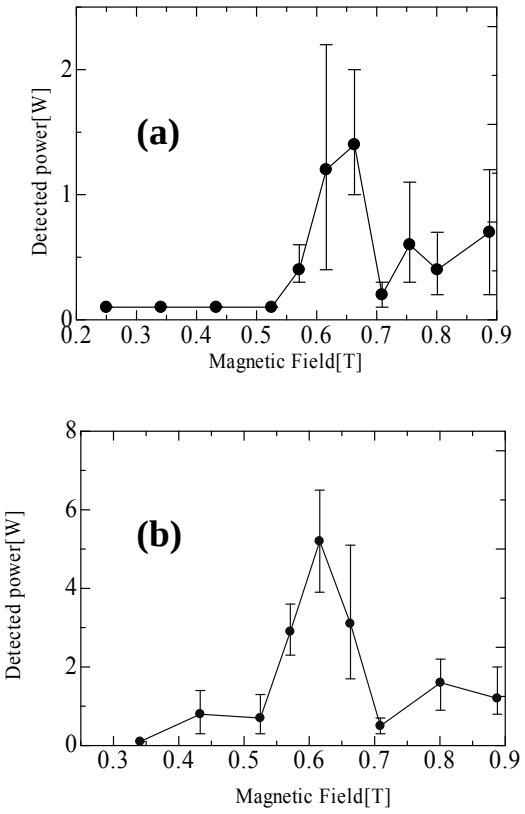

Fig.7 Output powers versus the magnetic field for a 10-period B SWS. The upper is the disk-integrated SWS and the lower is the improved SWS. The beam voltage is about 30kV.

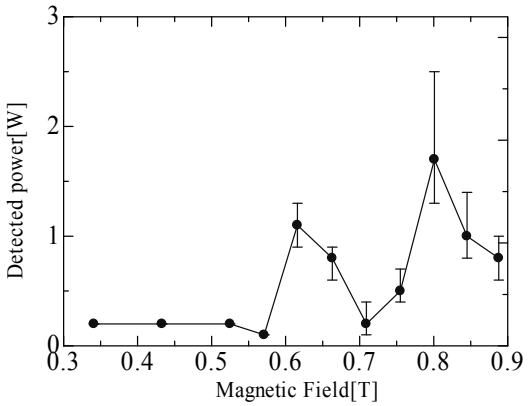

Fig.8 Output powers versus the magnetic field for a 10-period SWS of B type. The beam voltage is about 30kV.

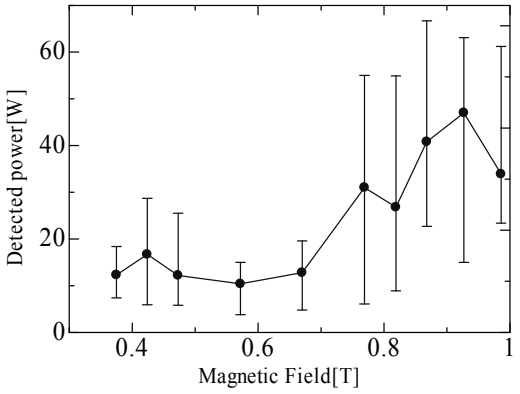

Fig.9 Output powers versus the magnetic field for a 50-period sinusoidal corrugated SWS. The beam voltage is about 40kV

4. Discussion and Conclusion

The dispersion curve of axisymmetric TM_{01} mode for sinusoidal corrugated SWS is shown in Fig.10. Beam space charge effects are included in the Cherenkov interaction, using a field theory based on an infinitesimally thin annular beam in Ref. [5]. The slow cyclotron mode depends on the axial magnetic field B_0. By increasing B_0, the beam line of slow cyclotron mode $\omega = k_z v - \Omega$ shifts to the right in Fig.10. The Cherenkov interaction synchronizes resonantly with the slow cyclotron interaction at the fundamental frequency around 0.84T. This is a slow cyclotron maser operation reported in Refs. [6, 7]. The output peaks in the region of 0.9 T and 0.45 T in Fig.9 respectively correspond to the combined resonance operation at the fundamental and the second harmonic frequencies of slow cyclotron interaction.

For B type, the combined resonance occurs at 1.25 T. In Fig.7, the outputs increase around 0.6 T can be explained by the combined resonance of the Cherenkov interaction and the second harmonic slow cyclotron interaction.

In Fig.8, the microwave power is once increased around 0.6 T. In this case, the absorption by the straight cylinder before and after SWS is occurred around 0.7 T in addition to the amplification due to the combined resonance. In Fig.8, the absorption is stronger than the amplification and the microwave power is decreased. It is necessary to control the absorption effect as well as amplification effect. More definite study of the synergistic interaction should be required.

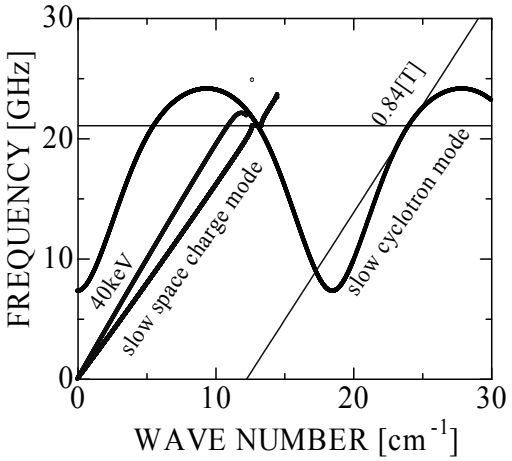

Fig.10 Dispersion curves of fundamental TM_{01} for type B SWS. The beam energy is 40 keV.

Acknowledgments

This work was partially supported by Grant-in-Aid for Scientific Research from the Ministry of Education, Science, Sports and Culture of Japan, and by NIFS Collaboration Research Program.

References

[1] Y. Takamura et al., Plasma Fusion Res. 3 (2008) S1078.

[2] P. J. Clarricoats and A. D Olver, *Corrugated Horns for Microwave Antenna* (Peter Peregrinus, London, 1984).

[3] K. Ogura,et at., IEEJ Trans. FM, **127**, 681 (2007).

[4] K. Ogura,et at., J. Plasma Fusion Res. SERIES, **6**, 703 (2004).

[5] K. Ogura,et at., J. Plasma Phys., **72**, 905 (2006).

[6] K. Ogura,et at., Phys. Rev. E, **53**, 2726 (1996).

[7] K. Ogura,et at., J. Phys. Soc. Jpn., **67**, 3462 (1998).

Proceedings of ITC18, 2008

Preliminary Study on Uncertainty-Driven Plasma Diffusion

Tsuyoshi OIWA, Shun-ichi OIKAWA, and Takahiro SHIMAZAKI

Graduate School of Engineering, Hokkaido University, Sapporo 060-8628, Japan

Quantum mechanical plasma diffusion is studied using a semi-classical model with two different characteristic lengths; one is the average interparticle separation, and the other is the magnetic length. The diffusion coefficients D by the model give similar dependence to experiments on many parameters, such as the temperature T, the mass m, the density n, and the magnetic field B. The numerical values of D is larger than that of the neo-classical diffusion.

Keywords: neo-classical theory, anomalous diffusion, quantum mechanical diffusion, uncertainty.

1 Introduction

A classical particle obeys the deterministic equation of motion which gives the particle trajectory in the phase space $(\boldsymbol{r}, \boldsymbol{v})$ at a time t. The actual *trajectory* of a particle with a mass m, however, is stochastic in the phase space with uncertainties in position $\Delta\boldsymbol{r}$, in velocity $\Delta\boldsymbol{v}$, and in energy ΔE in a time interval Δt because of the uncertainty relation:

$$\Delta r \Delta v > \frac{\hbar}{m}, \ \Delta E > \frac{\hbar}{\Delta t}, \tag{1}$$

where $\hbar = 1.05457 \times 10^{-34}$ Joule·sec stands for Planck constant. Equation (1) tells us that (i) lighter particle has larger uncertainty in phase space, and (ii) the uncertainty in energy ΔE is larger for shorter time intervals.

Since, for a given time interval Δt, there are three unknowns Δr, Δv, and ΔE in Eq. (1), we need to find/impose another relation among these uncertainties. For this purpose, let L be a length that the particle travels during some characteristic time interval, i.e. $L \equiv v_0 \Delta t$, where v_0 is the initial particle speed.

In the presence of a uniform magnetic field $\boldsymbol{B}$, the classical particle's energy $E = m\boldsymbol{v}^2/2$ is a constant of the motion:

$$\Delta E = m\Delta\boldsymbol{v} \cdot \left(\boldsymbol{v}_0 + \frac{\Delta\boldsymbol{v}}{2}\right) = 0. \tag{2}$$

In the case of a quantum mechanical particle, ΔE is not necessarily zero, as

$$\Delta E \sim m\boldsymbol{v}_0 \cdot \Delta\boldsymbol{v} > \frac{\hbar}{\Delta t}. \tag{3}$$

Comparing the above with the uncertainty relation in Eq. (1), we have

$$\Delta r < L, \quad \Delta v > \frac{\hbar}{mL}. \tag{4}$$

Thus, the square of the uncertainty in the cyclotron center $\boldsymbol{r}_G = \boldsymbol{r} + \boldsymbol{v} \times \boldsymbol{\omega}/\omega^2$ is given by

$$(\Delta\boldsymbol{r}_G)^2 = (\Delta\boldsymbol{r})^2 + \left(\frac{m\Delta\boldsymbol{v}}{qB}\right)^2 \sim L^2 + \left(\frac{\hbar}{qBL}\right)^2. \tag{5}$$

author's e-mail: aiueoiwa@fusion.eng.qe.hokudai.ac.jp

2 Semi-Classical Model for Motion

Let us assume that a charged particle with a positive charge $q > 0$ is moving in the presence of a uniform magnetic field $\boldsymbol{B} = (0, 0, B)$ in the z-direction. First, we integrate the equation of motion for the classical particle for the time interval of Δt to get the classical position in the phase space $(\boldsymbol{r}(\Delta t), \boldsymbol{v}(\Delta t))$.

$$\boldsymbol{r}(\Delta t) = \boldsymbol{r}(0) + \int_0^{\Delta t} \boldsymbol{v}(t)\ \mathrm{d}t, \tag{6}$$

$$\boldsymbol{v}(\Delta t) = \boldsymbol{v}(0) + \int_0^{\Delta t} \boldsymbol{v}(t) \times \boldsymbol{\omega}\ \mathrm{d}t, \tag{7}$$

where $\boldsymbol{\omega} = q\boldsymbol{B}/m$ is the cyclotron frequency vector.

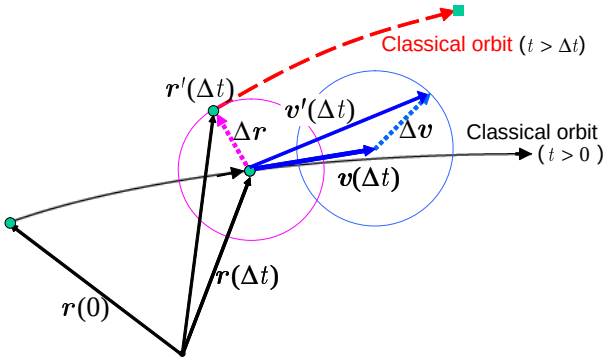

Fig. 1 Semi classical model for quantum motion. The particle initially at $r(0)$ *classically* moves to $\boldsymbol{r}(\Delta t)$ with a velocity $\boldsymbol{v}(\Delta t)$ at $t = \Delta t - 0$. At this time, it suffers the quantum mechanical deviations in position, $\Delta\boldsymbol{r}$, and in velocity $\Delta\boldsymbol{v}$. The particle is at $\boldsymbol{r}'(\Delta t)$ with a velocity $\boldsymbol{v}'(\Delta t)$ at the time $t = \Delta t + 0$.

As shown in Fig. 1, next we add the randomly-oriented uncertainties $\Delta\boldsymbol{r}$, and $\Delta\boldsymbol{v}$ to $\boldsymbol{r}(\Delta t)$, and $\boldsymbol{v}(\Delta t)$, the

magnitude of which is given by Eq. (4), as

$$\boldsymbol{r}'(\Delta t) = \boldsymbol{r}(\Delta t) + \Delta \boldsymbol{r}, \quad (8)$$

$$\boldsymbol{r}'(\Delta t) = \boldsymbol{v}(\Delta t) + \Delta \boldsymbol{v} \quad (9)$$

This procedure is repeated until the time t reaches $\tau_c \equiv 2\pi/\omega$, i.e. the cyclotron period.

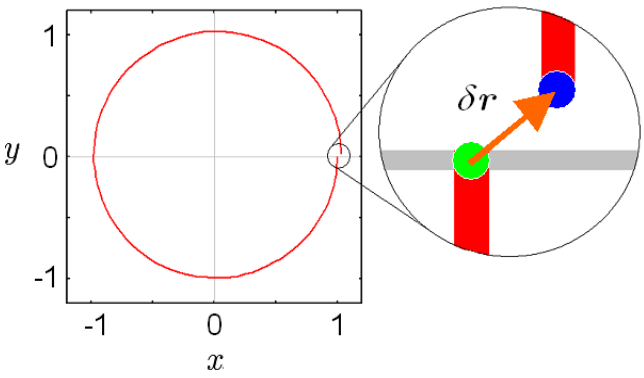

Fig. 2 Deviation of cyclotron motion, $\delta \boldsymbol{r} \equiv \boldsymbol{r}(\tau_c) - r(0)$, due to uncertainty in one gyration for a given characteristic length $L = v_0 \Delta t$. Lengths are normalized by the cyclotron radius $\rho = mv_0/qB$.

Figure 2 shows the particle trajectory during one cyclotron period, in which a deviation $\delta \boldsymbol{r} \equiv \boldsymbol{r}(\tau_c) - r(0)$ from the classical motion is seen.

In the following subsections we will choose the average interparticle separation, $\Delta \ell \equiv n^{-1/3}$, and the magnetic length [1], $\ell_B \equiv \sqrt{\hbar/qB}$, as the characteristic length L.

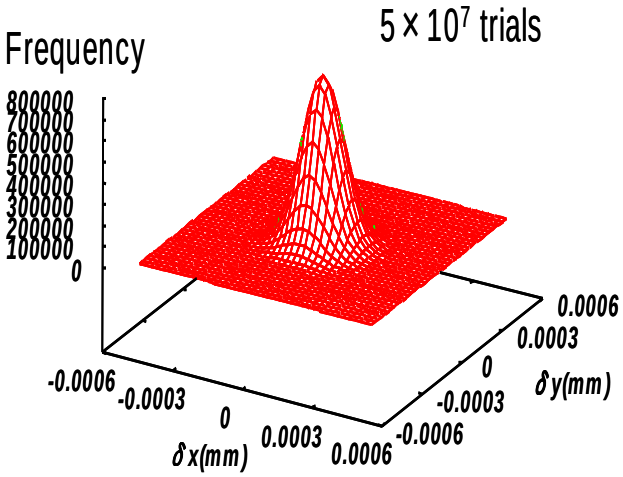

Fig. 3 Histgram for $\delta \boldsymbol{r} = (\delta x, \delta y)$ for $N_{MC} = 5 \times 10^7$ Monte Carlo trials.

It should be noted that the magnetic length $\ell_B = \sqrt{\hbar/qB}$ is the spatial size of wave packet in the plane perpendicular to the magnetic field [1], i.e.

$$|\psi(\boldsymbol{r}_\perp, t)|^2 = \frac{1}{\pi \ell_B^2} \exp\left[-\frac{(\boldsymbol{r}_\perp - \langle \boldsymbol{r}_\perp(t) \rangle)^2}{\ell_B^2} \right], \quad (10)$$

where $\psi(\boldsymbol{r}_\perp, t)$ stands for the wavefunction, $\langle \boldsymbol{r}_\perp(t) \rangle$ the classical position of the particle in the plane perpendicular to $\boldsymbol{B}$.

From many Monte Carlo calculations (tyipically $N_{MC} \sim 10^4$ turns out to be enough in this study for convergence) of such the diffusion coefficient

$$D \sim \frac{\left\langle (\delta r)^2 \right\rangle}{\tau_c} \quad (11)$$

will be obtained for a particular choice of the characteristic length L, where $\langle \cdot \rangle$ stands for the ensemble average. Figure 3 shows the histgram of $\delta \boldsymbol{r}$ for $N_{MC} = 5 \times 10^7$ Monte Carlo trials, which resembles the probability density function of a wavefunction in quantum mechanics.

2.1 CASE-A: L = interparticle separation, $\Delta \ell$

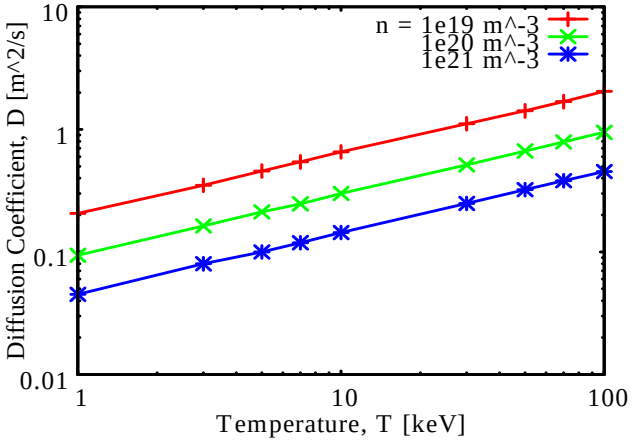

Fig. 4 CASE-A: Temperature T and density n dependence of diffusion coefficient D [m^2/s] in the case of $L = \Delta \ell$, the interparticle separation.

If we choose the characteristic length $L \equiv \Delta \ell$, where $\Delta \ell \equiv n^{-1/3}$ stands for the average interparticle separation, then the uncertainty in energy is given as $\Delta E \sim mv_0 \Delta v$. Thus, from Eq. (4), we have

$$\Delta r \sim \Delta \ell, \text{ and } \Delta v \sim \frac{\hbar}{m \Delta \ell}. \quad (12)$$

The particle is assumed to be in typical fusion plasmas of $T = 1-100$ keV, and $n = 10^{19}-10^{21}$ m^{-3}, and $B = 1-10$ Tesla. The initial particle speed v_0 is selected as the thermal speed $v_{th} = \sqrt{2T/m}$. The above calculation for a fixed T, n, and B is repeated $N_{MC} = 10^4$ times.

Figure 4 shows the temperature and density dependence of the diffusion coefficient $D = D(T, n)$, which leads to the scaling of

$$D_{\text{CASE-A}} \sim 0.094 \sqrt{\frac{T_{\text{keV}}}{A}} \left(\frac{10^{20}}{n} \right)^{\frac{1}{3}} \propto \sqrt{\frac{T}{m}} n^{-1/3}, \quad (13)$$

where $A = m/m_p$ is the mass number with m_p being proton mass. It is interesting to note that the diffusion coefficient D does not depend on the magnetic field B, but on the particle mass $m^{-1/2}$. The latter is known as the isotope effect [3, 4] .

2.2 CASE-B: L = magnetic length, ℓ_B.

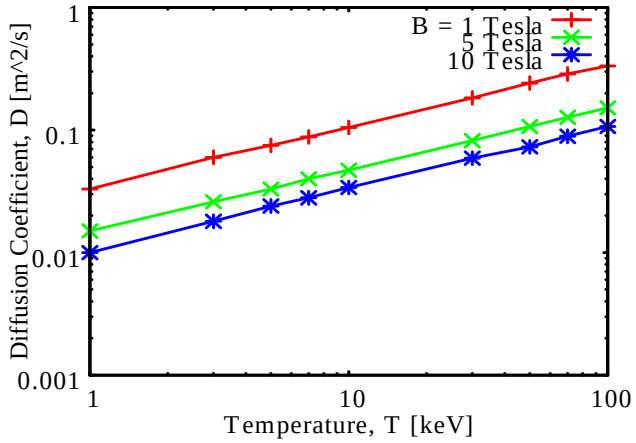

Fig. 5 CASE-B: Temperature T and the magnetic field B dependence of diffusion coefficient D [m^2/s]in the case of $L = \ell_B$, the magnetic length.

The uncertainties for $L = \ell_B$, say the CASE-B, are

$$\Delta r \sim \ell_B, \text{ and } \Delta v \sim \frac{\hbar}{m\ell_B}. \tag{14}$$

The particle is assumed to be in typical fusion plasmas of $T = 1 - 100$ keV, and $B = 1 - 10$ Tesla. Note that the density n does not enter into this case. Monte Carlo calculations similar to the CASE-A are made. Figure 5 shows the temperature T and the magnetic field B dependencies of the diffusion coefficient D, which leads to the scaling of

$$D_{\text{CASE-B}} \sim 0.033\sqrt{\frac{T_{\text{keV}}}{AB}} \propto \sqrt{\frac{T}{mB}}, \tag{15}$$

in which $\sqrt{T/m}$ scaling is the same as Eq. (13) for the CASE-A.

3 Discussion

Table 1 summarizes the dependence of D on plasma parameters, such as T, n and B. The parameters' ranges are $1 \le T \le 100$ keV, $1 \le B \le 10$ Tesla, and if applicable $10^{19} \le n \le 10^{21}$ m^{-3}. The ITER-89 dependence of D in the table assumes $D \propto \rho^2/\tau_E$, where τ_E is the energy confinement time in the ITER-89 scaling law. The diffusion coefficients D by these models give similar dependence to experiments on many parameters, such as the temperature T, the mass m, the density n, and the magnetic field B, as well as its values of the order of the anomalous diffusion.

Table 1 Parameter dependence of D, The parameters' ranges are $1 \le T \le 100$ keV, $10^{19} \le n \le 10^{21}$ m^{-3}, $1 \le B \le 10$ Tesla. The ITER-89 dependence of D in the table assumes $D \sim \rho^2/\tau_E$.

Model	$D \propto T^\alpha m^\beta n^\gamma B^\delta \cdots$	Values
ITER-89	$\sqrt{\frac{P}{m}}\, n^{-0.1} B^{-0.2}$	~ 1 m^2/s
CASE-A: $\Delta\ell = n^{-1/3}$	$\sqrt{\frac{T}{m}}\, n^{-1/3} B^0$	0.1-2
CASE-B: $\ell_B = \sqrt{\frac{\hbar}{qB}}$	$\sqrt{\frac{T}{m}}\, n^0\, B^{-0.5}$	0.01-0.3
Neo-classical	$\sqrt{\frac{m}{T}}\, n\, B^{-2}$	~ 0.01

In the case of the most common fusion plasma (e.g. $T = 10$ keV, $n = 10^{20}$ m^{-3} and $B = 3$ T), however, the value of the diffusion coefficients by our model are $D_{\text{CASE-A}} \sim 0.30$ m^2/s and $D_{\text{CASE-B}} \sim 0.08$ m^2/s, both of which are one order smaller than the anomalous diffusion. Moreover, which characteristic length L is right one is an open question.

From Eq. (5), the diffusion coefficient D_G of the gyration center is

$$D_G \sim \frac{\left\langle (\Delta r_G)^2 \right\rangle}{\tau_c} = v_0 L \left\{ 1 + \left(\frac{\hbar}{qBL^2} \right)^2 \right\}. \tag{16}$$

For $L \gg \ell_B = \sqrt{\hbar/qB}$, the diffusion of the gyration center is determined by L, i.e. $D_G \sim v_0 L$, otherwise $D_G \sim v_0 \ell_B^4/L^3$. In most fusion plasmas, the interparticle separation is much shorter than the magnetic length, i.e. $\Delta\ell \gg \ell_B$, so that $D_G \sim v_0 \ell_B$. This leads to $\sqrt{T/m}$ scaling of the diffusion coefficient D, irrespective of the selection of the length scale L.

4 Conclusion

The diffusion coefficients D by our model give similar dependence to experiments on many parameters, such as the temperature T, the mass m, the density n, and the magnetic field B, as well as its values larger than the neo-classical diffusion.

Acknowledgement

The author would like to thank Dr. A. Wakasa, Prof. Y. Matsumoto and Prof. M. Itagaki for their fruitful discussions on the subject. The author would also acknowledge the continuous encouragement of the late Prof. T. Yamashina.

[1] L. D. Landau and E. M. Lifshitz, *Quantum mechanics: non-relativistic theory*, 3rd ed., translated from the Russian by J. B. Sykes and J. S. Bell (Pergamon Press, Oxford, 1977)
[2] P. Yushmanov et al., *Nucl. Fusion* **30** 1999(1990).
[3] R. J. Hawryluk, Rev. Mod. Phys. **70**, 537(1998).
[4] V. Sokolov and A. K. Sen, Phys. Rev. Lett. **92**, 165002 (2004)

Proceedings of ITC18, 2008

Binary Interaction Approximation to *N*-Body Problems

Hideo FUNASAKA, Shun-ichi OIKAWA, Koichiro HIGASHI and Yu KITAGAWA

Graduate School of Engineering, Hokkaido University, Sapporo 060-8628, Japan

The binary interaction approximation (BIA) to the N-body problems is proposed. The BIA conserves total linear momenta in principle. Other invariants, such as the total angular momentum and total energy, are conserved as much effective digits as at least 12 for a two dimensional hydrogen plasma of $T = 10$ keV and $n = 10^{20}$ m^{-3}. It is found for such a plasma that the total CPU time of the BIA approximately scales as $N^{1.9}$.

Keywords: N-body problem, algebraic approximation, binary interaction approximation, variable step size.

1 Introduction

In an isolated N-body charged particle system as shown in Fig. 1, the non-relativistic equation of motion for the i-th particle with an electric charge q_i and a mass m_i is as follows:

$$m_i \frac{\mathrm{d}\boldsymbol{v}_i}{\mathrm{d}t} = q_i \sum_{j\neq i}^{N} \frac{q_j}{4\pi\epsilon_0} \frac{\boldsymbol{r}_i - \boldsymbol{r}_j}{|\boldsymbol{r}_i - \boldsymbol{r}_j|^3}, \tag{1}$$

where $\boldsymbol{r}_i$ and $\boldsymbol{v}_i$ stand for the position and the velocity of the i-th particle. Hereafter, the calculation using the above equation of motion Eq. (1) will be referred to as the DIM, direct integration method.

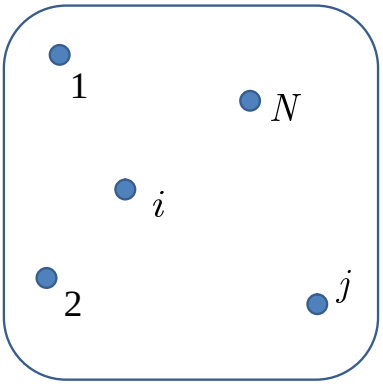

Fig. 1 An N-body system.

When $N \geq 3$, it is well known that no exact/analytical solution can be obtained, and one should be content with approximated solutions using one of numerical integration methods. In principle, to arbitrary error levels the numerical solution can be found. However, it is practically impossible for the large number of particles, i.e. $N \ggg 1$, since the number of force calculations on the right hand side of Eq. (1) is in proportion to N^2. Moreover, the time step tends to decrease with increasing N, thus the total CPU time should scale as N^3.

author's e-mail: plasaka@fusion.qe.eng.hokudai.ac.jp

The efficient and fast algorithms to calculate interparticle forces include the tree method [1, 2], the fast multipole expansion method (FMM) and the particle-mesh Ewalt (PPPM) method [3]. Efforts have been made to use parallel computers, and/or to develop special purpose hardware to calculate interparticle forces, e.g. the GRAPE (GRAvity PipE) project [4]. The authors have recently developed an algebraic model for multibody problems [5], and have shown that the momentum transfer cross-section with our model is in good agreement with the exact one [5,6]. Unfortunately, this model turns out to lack in enough accuracy in predicting individual particle motion [6].

As shown in Fig. 2 the scattering angle, $\chi \equiv \pi - 2\theta_0$, is given by $b = b_0 \tan\theta_0$, where b is the impact parameter, $b_0 \equiv e^2/4\pi\varepsilon_0\mu g_0^2$ corresponds to $\chi = \pi/2$ scattering, and g_0 the initial relative speed at $r = \infty$ and $\theta = -\theta_0$. In

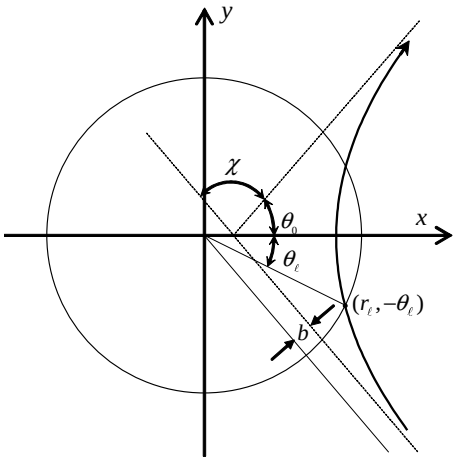

Fig. 2 Unperturbed relative trajectory $r = r(\theta)$ in an orbital plane. The scattering center is at the origin. An impact parameter is $b = b_0 \tan\theta_0$.

the binary system with an impact parameter b, a typical velocity change Δg in the relative velocity is given by

$$\Delta g = 2g_0 \sin\frac{\chi}{2} \sim \epsilon g_0, \ \epsilon \equiv \frac{b_0}{\Delta\ell}, \tag{2}$$

where $\Delta\ell$ is the average interparticle separation.

In N-body systems with $\epsilon \ll 1$, such as the fusion plasmas, Eq. (2) suggests that three-or-more body interaction is of order of ϵ^2 and can be ignored. It should be noted that the Debye lengths λ_D in fusion plasmas generally satisfy $\lambda_D \gg \Delta\ell$, thus typical binary interaction is characterized by the nondimensional parameter ϵ. This parameter is of order of U/K, where U and K stand for the potential and kinetic energies.

In this study, we will propose the binary interaction approximation (BIA) to the N-body systems with $\epsilon \ll 1$, and compare it with the direct integration method (DIM), both using the 6-stage 5-th order Runge-Kutta-Fehlberg (RKF65) integrator [7, 8] with an absolute numerical error tolerance of 10^{-16}.

2 BIA: Binary Interaction Approximation to N–body problems.

The equation of relative motion for the particle pair (i, j) in an N–body system used by the binary interaction approximation, the BIA, is

$$\mu_{ij}\frac{\mathrm{d}\boldsymbol{g}_{ij}}{\mathrm{d}t} = \frac{q_i q_j}{4\pi\epsilon_0}\frac{\boldsymbol{r}_{ij}}{r_{ij}^3} \tag{3}$$

where $\boldsymbol{r}_{ij} = \boldsymbol{r}_i - \boldsymbol{r}_j$ stands for the relative position, $\boldsymbol{g}_{ij} = \boldsymbol{v}_i - \boldsymbol{v}_j$ the relative velocity, and $\mu_{ij} = m_i m_j/\left(m_i + m_j\right)$ the reduced mass. In the BIA, the above equation is integrated, completely ignoring the other particles, from $t = 0$ to $t = \Delta t$ to give $\Delta\boldsymbol{r}_{ij}$ and $\Delta\boldsymbol{g}_{ij}$. The total number of integration is ${}_N\mathrm{C}_2 = N\left(N-1\right)/2$ for an N–body problem. The individual changes in position $\Delta\boldsymbol{r}_i$ and velocity $\Delta\boldsymbol{v}_i$ of the i–th particle are as follows

$$m_i\Delta\boldsymbol{r}_i = m_i\boldsymbol{v}_i\Delta t + \sum_{j\neq i}^{N}\mu_{ij}\left(\Delta\boldsymbol{r}_{ij} - \boldsymbol{g}_{ij}\Delta t\right) \tag{4}$$

$$m_i\Delta\boldsymbol{v}_i = \sum_{j\neq i}^{N}\mu_{ij}\Delta\boldsymbol{g}_{ij} \tag{5}$$

for $i = 1, 2, \cdots, N$. Note that the term within the parentheses, i.e. $\delta\boldsymbol{r}_{ij} \equiv \Delta\boldsymbol{r}_{ij} - \boldsymbol{g}_{ij}\Delta t$, on the right hand side of Eq. (4) vanishes when the interaction between the pair (i, j) vanishes. In other words, the BIA scheme is exact for free particles. It should also be noted that the total momenta $\boldsymbol{P} \equiv \sum_{i=1}^{N} m_i\boldsymbol{v}_i$ is kept constant with this approximation, since, from Eq. (5) and $\mu_{ij} = \mu_{ji}$,

$$\sum_{i=1}^{N} m_i\Delta\boldsymbol{v}_i = \sum_{i=1}^{N-1}\sum_{j=i+1}^{N}\mu_{ij}\left(\Delta\boldsymbol{g}_{ij} + \Delta\boldsymbol{g}_{ji}\right) = 0, \tag{6}$$

which also ensures the center of mass position $\boldsymbol{R}_{\mathrm{CM}}$ to be exact:

$$\boldsymbol{R}_{\mathrm{CM}}\left(\Delta t\right) = \boldsymbol{R}_{\mathrm{CM}}\left(0\right) + \boldsymbol{G}_{\mathrm{CM}}\left(0\right)\Delta t, \tag{7}$$

where $\boldsymbol{G}_{\mathrm{CM}}$ is the center of mass velocity.

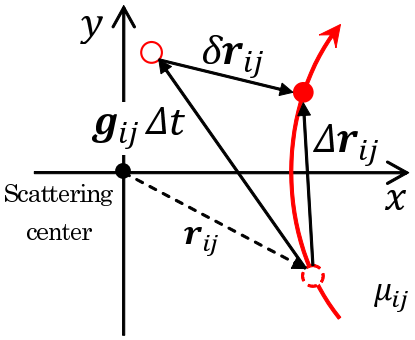

Fig. 3 Relative motion for the particle pair of (i, j). A scattering center is at the origin. The change in position of the particle with a mass μ is $\Delta\boldsymbol{r}_{ij}$. If there is no interaction, the change in position is $\boldsymbol{g}_{ij}\Delta t$ during a time interval of Δt.

3 Calculation

3.1 Initial condition for an $N = 122$–body problem.

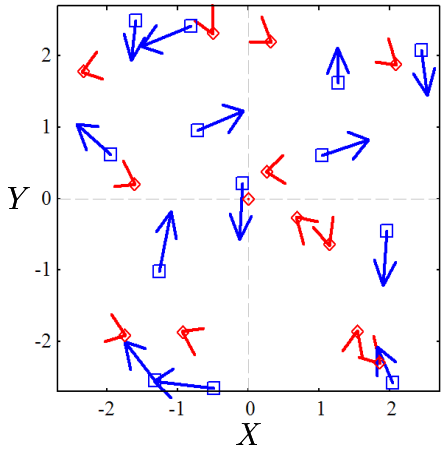

Fig. 4 Initial positions normalized by the interparticle separation $\Delta\ell \equiv n^{-1/3}$ of an $N = 122$–body problem. Only 26 particles near the origin are depicted. Squares with arrows in blue stand for the electron positions and velocities, and diamonds with arrows in red for the protons. Spatial distribution is uniform both for protons and electrons. The Maxwellian velocity distribution is adopted for a given temperature $T = T_{\mathrm{electron}} = T_{\mathrm{proton}}$.

Figure 4 depicts the initial condition for a two-dimensional $N = 122$–problem, in which there are 61 protons and 61 electrons. Note that only 26 particles near the

origin are depicted in the figure. In this and the following figures, positions are normalized by the interparticle separation $\Delta\ell \equiv n^{-1/3}$, and velocities by the relative thermal speed among electrons, $g^{ee}_{\rm th} = \sqrt{2}v^{e}_{\rm th}$. Squares with arrows in blue in Fig. 4 stand for the electron positions and velocities, and diamonds with arrows in red for the protons. Spatial distribution is uniform and the velocity distribution is maxwellian for both species with temperatures of $T = T_{\rm electron} = T_{\rm proton} = 10$ keV. The number density $n = 10^{20}$ m^{-3} is assumed, which leads to the parameter $\epsilon = 1.67 \times 10^{-7} \ll 1$.

3.2 Trajectories of a proton and an electron.

The 122-body system is integrated for $\Delta t \equiv \Delta\ell/g^{ee}_{\rm th}$, i.e. the time for the electron with its thermal speed to travel the average interparticle separation $\Delta\ell \equiv n^{-1/3}$. Figures 5 and 6 show the trajectories in the configuration space (X, Y) on the left and velocity space (U, V) on the right for a proton initially at rest, and a moving electron, respectively. In both figures, the diamonds labeled 'initial' are initial points at $t = 0$. The lines are trajectories solved by using the DIM. Triangles indicate the final points at $t = \Delta t$ by the BIA. The agreement between the BIA and the DIM is excellent.

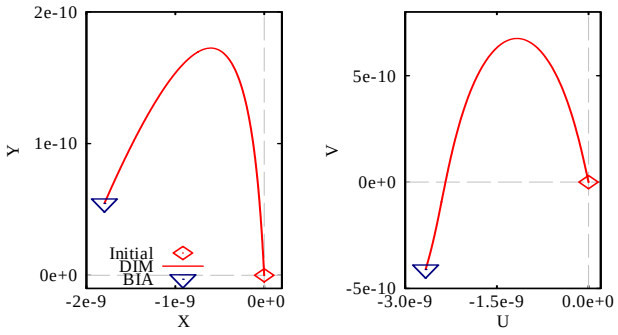

Fig. 5 A proton motion initially at rest in the configuration space on the left, and in the velocity space on the right, for the N =122-body system. Symbols represent the initial and final position calculated by the BIA. The particle starting at the diamonds goes along lines which are calculated by the full N-body integration, i.e. the DIM.

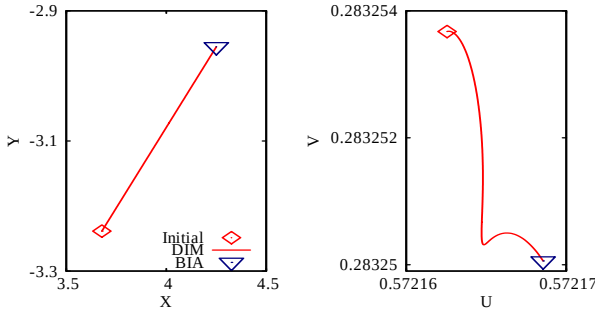

Fig. 6 An electron motion for the N =122-body system. Legends are the same as Fig. 5.

As is typically seen on the right in Fig. (6), the complicated velocity change in time, or the accelleration, is reproduced well by the BIA, in which three-or-more body intractions are ignored.

3.3 Errors and effective digits of invariants.

There are four invariants of motion in an isolated two dimensional system; the total linear momenta $\boldsymbol{P}$, the total angular momentum L_Z, and the total energy E. Effective digits for calculated invariants of motion and CPU time for $N = 122$ are listed in Table 1, in which, with $\boldsymbol{r}_i = (X_i, Y_i)$ and $\boldsymbol{v}_i = (U_i, V_i)$,

$$P_X = \sum_{i=1}^{N} m_i U_i, \tag{8}$$

$$P_Y = \sum_{i=1}^{N} m_i V_i, \tag{9}$$

are the total linear momenta,

$$L_Z = \sum_{i=1}^{N} m_i \left(X_i V_i - Y_i U_i\right), \tag{10}$$

the total angular momentum, and

$$E = \frac{1}{2}\sum_{i=1}^{N} m_i \boldsymbol{v}_i^2 + \frac{1}{4\pi\epsilon_0}\sum_{i=1}^{N-1} q_i \sum_{j=i+1}^{N} \frac{q_j}{|\boldsymbol{r}_i - \boldsymbol{r}_j|}, \tag{11}$$

the total energy of the system.

Table 1 Effective digits for calculated invariants of motion and CPU time for $N = 122$. P_X and P_Y are the total linear momenta, L_Z the total angular momentum, E the total energy of the system.

method	$P_{\rm X}$	$P_{\rm Y}$	$L_{\rm Z}$	E	CPU time
DIM	16	15	16	16	3.4
BIA	16	15	15	12	0.2
unit	digit				sec

Note that the effective digits of 15-16 is the maximum for 64-bit calculation on the computer used in this study. In the case of the DIM, all the effective digits for invariants reach this maximum, while the total energy conservation for the BIA is 12 digits, worse than the DIM which is generally the case. The angular momentum conservation for the BIA happens to be 15 digits for this particular initial conditions for $N = 122$–body problem. The conservation in L_Z, however, is generally close to that in E for different initial conditions and the number of particles N.

As for the CPU time, the BIA is 17 times faster than the conventional DIM for $N = 122$. Since the speed up ratio depends essentially on the number of particles N, calculations for different N will be examined in the following subsection.

3.4 CPU time dependence on N

We made similar calculation to the foregoing section varying the number of particles, N. The CPU time dependence on N with fitting lines are depicted in Fig. 7, in which CPU time inversions are found for the DIM, i.e. longer CPU time $\tau^{\rm CPU}_{\rm DIM}(N) > \tau^{\rm CPU}_{\rm DIM}(N')$ for less number of particles $N < N'$ at around $N \sim 700$ and 1600. Such inversions can occur because the integrator RKF65 used here controls the time step size during the calculation according to the given error tolerance. The CPU time for the direct integration method scales as $\tau^{\rm CPU}_{\rm DIM} \propto N^{2.7}$, and the binary interaction approximation $\tau^{\rm CPU}_{\rm BIA} \propto N^{1.9}$ both using the RKF65 with the same absolute error tolerance of 10^{-16}. Also BIA 1 is the CPU time to calculate only one particle, which scale as $\tau^{\rm CPU}_{\rm BIA1} \propto N^{1.0}$. If we are interested in motion of only one test particle-i at a time $t = \Delta t$ from initial conditions at $t = 0$, it is possible with the BIA to calculate $\boldsymbol{r}(\Delta t)$ and $\boldsymbol{v}(\Delta t)$, since it is based on the principle of superposition of $\Delta \boldsymbol{r}_{ij}$ and $\Delta \boldsymbol{v}_{ij}$ using Eqs. (5) and (4).

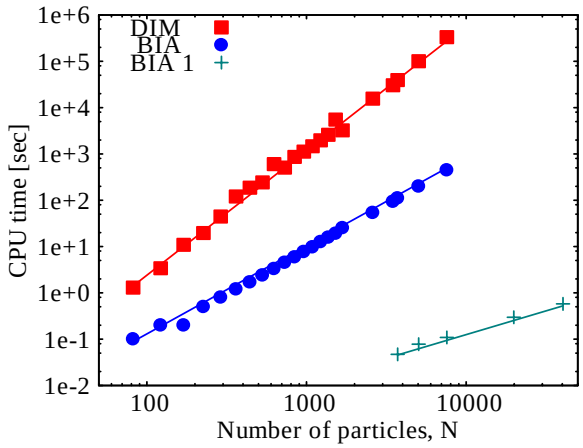

Fig. 7 CPU time $\tau^{\rm CPU}$ dependence on the number of particles N on a typical PC. Red squares stand for the CPU time for the DIM with a fitting line in red, $\tau^{\rm CPU}_{\rm DIM} \propto N^{2.7}$. Blue circles stand for the CPU time for the BIA with a fitting line in blue, $\tau^{\rm CPU}_{\rm BIA} \propto N^{1.9}$. Also BIA 1 is the CPU time to calculate only one particle, which scale as $\tau^{\rm CPU}_{\rm BIA1} \propto N^{1.0}$

As was shown on the right in Fig. 6, the temporal electron acceleration is complicated due to its small mass. For a given numerical error tolerance, this tends to make the common time step smaller, and consequently make the total CPU time $\tau^{\rm CPU}$ longer especially in the DIM. On the other hand, the BIA with the same error tolerance as the DIM is a *pair wise* variable time step scheme, since the time step for the pair (i, j) is independent from that for any other pairs (i, j').

4 Summary and Discussion

The binary interaction approximation, the BIA, to the N-body problems is proposed. The BIA conserves total linear momenta in principle, and is a *pair wise* variable time step scheme when used with the integrator using the embedded formula such as the Runge-Kutta-Fehlberg scheme [7, 8]. Other invariants, such as the total angular momentum and total energy, are conserved as much effective digits as at least 12 for a two dimensional hydrogen plasma of $T = 10$ keV and $n = 10^{20}$ m^{-3}, in which $\epsilon \sim 1.67 \times 10^{-7}$. The CPU time of the BIA scales as $\tau^{\rm CPU}_{\rm BIA} \propto N^{1.9}$ for such a plasma. It should also be noted that with the BIA it is possible to calculate only one particle's motion [6] with the CPU time in proportion to N.

The numerical results presented here is for two dimensional systems with low density and high temperature, i.e. $\epsilon \ll 1$, which is the most appropriate for the BIA. We will soon apply the BIA to three dimensional cases, and/or to systems with $\epsilon \sim 1$, such as the gravitational N-body systems, in the near future.

Acknowledgement

The author would like to thank Dr. A. Wakasa, Prof. Y. Matsumoto and Prof. M. Itagaki for their fruitful discussions on the subject. The author would also acknowledge the continuous encouragement of the late Prof. T. Yamashina.

[1] A. W. Appel, An Efficient Program for Many-Body Simulation, *SIAM J. Sci. Stat. Comput.* **6** 85–103 (1985)

[2] J. E. Barnes and P. Hutt, A hierarchical $O(N\log N)$ force-calculation algorithm, *Nature* **324** 446–449 (1986)

[3] P. P. Brieu, F. J. Summers and J. P. Ostriker, Cosmological Simulations Using Special Purpose Computers: Implementing P^{3}M on GRAPE *ApJ* **453** 566 (1995)

[4] J. Makino, M. Taiji, T. Ebisuzaki, and D. Sugimoto, GRAPE-4: A Massively Parallel Special-Purpose Computer for Collisional N-Body Simulations, *APJ* **480**, 432–446(1997).

[5] S. Oikawa and H. Funasaka, Algebraic analysis approach for multibody problems. J. Plasma Fusion Res. **36** (2008) S1073.

[6] K. Higashi, S. Oikawa, H. Funasaka, and Y. Kitagawa, Algebraic analysis approach for multibody problems II: Variance of velocity changes. *this conference*, P2-58.

[7] E. Fehlberg. Low-order classical Runge-Kutta formulas with step size control and their application to some heat transfer problems. NASA Technical Report 315 (1969).

[8] E. Fehlberg. Klassische Runge-Kutta-Formeln vierter und niedrigerer Ordnung mit Schrittweiten-Kontrolle und ihre Anwendung auf Warmeleitungsprobleme, *Computing* (Arch. Elektron. Rechnen), vol. 6, (1970) pp. 61–71.

Proceedings of ITC18,2008

Micro-spectroscopic Investigation of the Plasma-surface Interaction in the Microwave Carbothermic Reduction of the Powdered Magnetite

Akihiro Matsubara[1], Kazuya Nakayama[1], Shigeki Okajima[1], Sadatsugu Takayama[2], and Motoyasu Sato[2]

[1]*Chubu University, 1200, Matsumoto, Kasugai, Aichi, 487-8501, Japan*

[2]*National Institute for Fusion Science, 322-6 Oroshi, Toki, Gifu, 509-5292, Japan*

The plasma-surface interaction in microwave carbothermic reduction of magnetite was experimentally investigated with the Integrated Microscopic Imaging System. It was found that luminous body with burst/jet structure is formed on the specimen during reduction period. Its emission spectrum has a continuous spectrum of thermal radiation, and laser beams are scattered significantly by the luminous body. These facts suggest presence of plasma-powder mixture. The formation of the mixture, position in dust plasma, and the relation to the PSI in fusion science are described.

Keywords: plasma-surface interaction, plasma-powder particle mixture, microwave carbothermic reduction, spectroscopic measurement, luminous body, dust plasma, self-organization.

1. Introduction

Plasma-surface interaction is one of crucial issues in fusion research as well as plasma processing, but in some cases it has been also studied in the field of the material processing associated with thermally activated processes based on microwave heating. A typical example is microwave iron production presented here. High-purity pig irons have been produced successfully in a multimode microwave test reactor from powdered iron ores (magnetite) with carbon as a reducing agent in a nitrogen atmospheric pressure [1]. The microwave iron making has the advantage that the CO_2 emissions can be reduced by tens of percent compared with that in conventional blast furnaces, if the electric power for the microwave is generated by renewable energy, such as solar, hydro and nuclear power. A feature of the microwave method is the sudden rise in temperature of the material surface from ~700 °C to ~1000 °C accompanied by light emission of atmospheric plasma [2]. The nature of the temperature jump has been seen simply an emergence of an additional energy flow to the material through the plasma. Such plasma has been observed in almost all similar experiments.

In order to investigate the plasma-surface interaction in the microwave iron making, visible emission spectroscopy has been introduced. The light emission after the temperature jump consists of strong atomic/molecular lines. These lines have been well assigned as spectra listed in the spectrum database based on the spark and arc discharge [2], indicating the presence of plasma electrons with several electron volts in the electron temperature. The multipoint pyrometric and spectroscopic measurements demonstrated that the microwave heating mode changes from direct volumetric heating by microwave into surface heating by plasma, when the atmospheric plasma is generated [2]. It was found that the structure of emission spectrum near-UV range (240 nm - 310 nm) changes drastically from the continuous spectrum to line spectra of iron, with progressing reduction process [2].

The present paper provides micro-spectroscopic observation indicating that the plasma formed on the material takes on an aspect of plasma-powder mixture. It will be shown that burst/jet structure with continuous emission spectrum appears just above the specimen during reduction dominated period. The aspect of plasma-powder mixture dismisses the simple view that the plasma is just an independent medium as a microwave absorber for heating the material; rather, that aspect requires consideration of modification of microwave propagation and absorption in the plasma-powder mixture. Such feedback leads to the self-organization of the three-body mixture consisting of the microwave field, plasma-powder mixture, and powdered-material (specimen). It will also described about the position in the category so called *dust plasma*. The relation to the plasma-surface interaction in fusion devices also briefly mentioned.

2. Experimental setup

Figure 1 shows the microwave single mode cavity (TE_{103} at cw 2.45 GHz) and its diagnostics system located at the National Institute for Fusion Science. In this experiment the specimen was set at the anti-node of the electric-field standing wave, i.e., the electric field heating.

author's e-mail: MATSUBARA.Akihiro@sti.chubu.ac.jp

The specimen was made of magnetite (Fe_3O_4) and graphite powders of which grain sizes were <1 μm and *ca.* 5 μm, respectively. The mixing ratio was M_{Fe3O4} : M_C = 90 : 10 by mass. Corresponding mol ratio was n_{Fe3O4} : n_C = 1.0 : 2.0 that is equivalent mole portions for the carbothermic reduction of magnetite, $Fe_3O_4 + 2C \rightarrow 3Fe + 2CO_2$ − 317 kJ/mol. The composite powder (total mass: 0.619 g) was shaped into a cylindrical rod of 8-mm in diameter and 10-mm in length. The specimen was set inside the quartz cell (12.5 mm in inner diameter and 200 mm in length). Before starting the microwave irradiation, the quartz cell was evacuated by the rotary pump and refilled with helium gas. During the irradiation, a continuous helium gas flow of 20 ml/min was used with a pressure a little higher than ambient pressure.

The microscopic spectroscopy was performed with the Integrated Microscopic Imaging System as shown in Fig. 2. A feature of it is integration of a microscope and a 2D-imaging spectrometer. This allows us to observe emission spectrum in parallel with watching the appearance of the specimen through the microscope image. The emission light from the specimen is condensed by the objective lens; then, it is split in two by half mirror. The transmitted light is detected by the microscope, and the reflected light is introduced into the magnification lens, scanning mirror, and finally the imaging spectrometer that is a lens-slit Czerny-Turner configuration. The camera lens as the collimator in the spectrometer minimizes aberration of astigmatism due to the collimator mirror in a common spectrometer. In present experiment no mirror scanning mode is taken for enhancing dynamic range. The slit-shaped observation region on the specimen is fixed at a center of the observation region of the microscope [see Fig. 4]. The exposure time was 20 ms for the microscope, and 580 ms for the spectrometer.

Two InGaAs pyrometers [labeled as IR1 and IR2 shown in Fig. 1] were taken for measurement of the specimen temperature. IR1 and IR2 were directed to the specimen top surface and side surface, respectively. The neutral gas pressure in the cell was monitored with the electrical-resistance strain-gage type transducer. Flow rate of exhaust gas was measured by the mass flow meter, and exhaust gas analysis was performed with the quadrupole mass analyzer.

3. Experimental results

Figure 3 shows time evolutions of various parameters measured during the heating. There are three stages associated with the change of phenomena as I - III depicted schematically above the upper axis of Fig. 3(a):

I. Pre-reduction stage (t < 200 s) characterized by microwave direct volumetric heating.

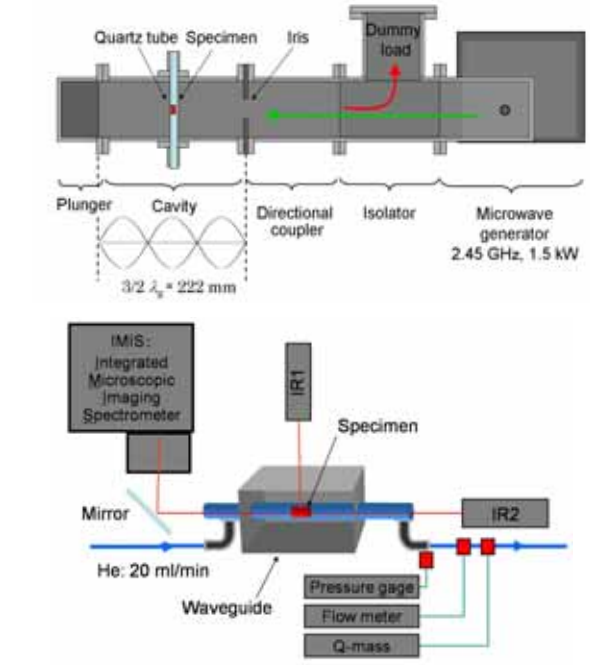

Fig. 1. Experimental setup of the microwave heating in the single mode cavity in the upper frame and diagnostics system in the lower frame.

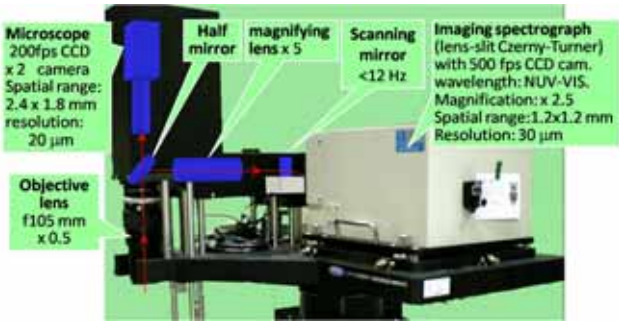

Fig. 2. Integrated Microscopic Imaging Spectrometer and its structure and specification.

II. Reduction-dominated stage (t = 200 ~ 320 s) with the significant plasma surface interaction and exhaust gas generation.

III. Post-reduction dominated stage (t > 320 s).

These stages are equivalent fundamentally to that found in previous experiments for microwave iron making [2].

In the first stage, the temperature of the top and side surfaces increases in the same way as shown in Fig. 3(a), indicating homogeneous direct microwave heating. There are almost no exhausted gases detected.

The beginning of the stage II is triggered by the plasma ignition. As shown in Fig. 3(a) the temperature of the top surface inherently jumps up from 512 °C at t = 200 s, and it reaches 1160 °C within 4 s. The side-surface temperature rises gradually and reaches 1160 °C taking for ~100 s. The exhaust gas flow rate keeps higher level

in this stage as shown Fig. 3(b). In addition constituent of the exhaust gas is mainly CO_2 and CO [see Figs. 3(c)-3(f)]. It should be noted that the exhaust flow rate is several times overestimated because of the mass flow meter is for helium gas. The time when CO_2- and CO- gas arrives at the flow meter is supposed at ~222 s, corresponding to the sudden rise of the flow rate. By using the flow rate of ~50 ml/min before the sudden rise, the total amount of gas generated in this period (~2 min) can be comparable within the order of magnitude to the amount of mass loss of the specimen (0.16 g); thus it is appropriate interpretation that the reduction process is dominated in this period.

Figure 4(a) shows the typical microscope image captured by IMIS during the stage II. The field of view was placed to include the top surface of the cylindrical specimen. It is found that the burst occurs frequently with jet structure. The duration of the burst is less than 50 ms in this case, but in some cases it reaches 100 ms. It is also found that the space just above the specimen is filled by luminous body. The spectral image displayed in Fig. 4(c) for which the field of view is depicted as the vertical line in Fig. 4(a) indicates that there is strong continuous spectrum corresponding to that luminous body. In addition a few line emission spectra are superimposed on the continuous spectrum. Figure 4(b) shows the spectrum above the specimen [y = 1.33 mm; indicated by the marker in Fig. 4(c)]. Peaks with arrow can be assigned as iron atomic spectrum. The strong peaks at 569 nm and 590 nm are Na I. Although the constituent concentration of sodium is under 0.01% in the raw material, transition probability for Na I (3s-3p) is quite large; it makes the intensity of the spectrum stronger.

As the stage changes into III (post reduction period), the exhaust gas flow rate decreases, and finally almost no exhaust gas is generated [see Fig. 3(b)]. It should be noted that the bright plasma emission around the specimen was still visible with the naked eye; however as shown in Fig. 5(a) in microscopic observation it is found that there is no luminous body as found in the reduction period of stage II. In fact the spectral image has no strong continuous spectrum as seen in stage II, rather molecular band spectra of both C_2 ($A^3\Pi_g$ - $X\,^3\Pi_u$) and CO ($B^1\Sigma$-$A^1\Pi$) appear clearly at the edge of the material.

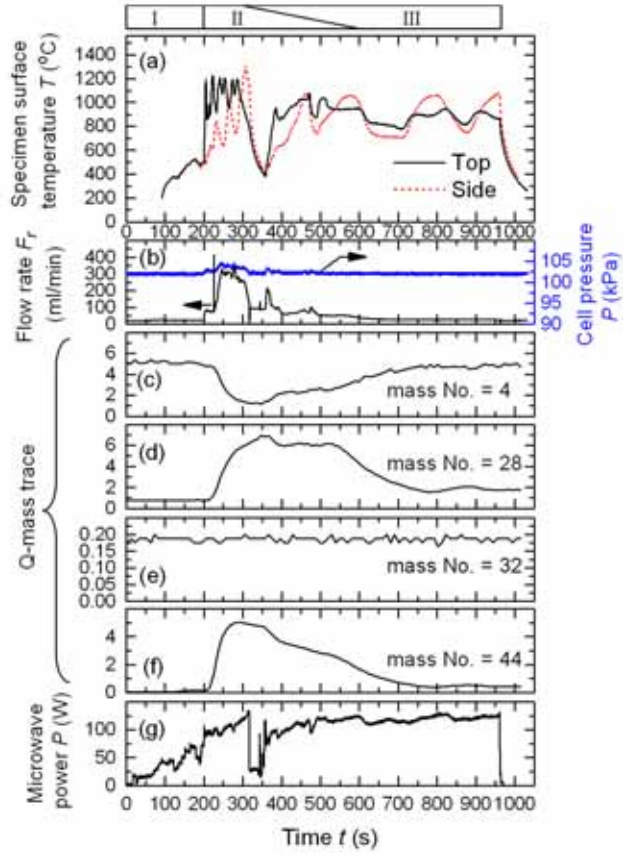

Fig. 3. Evolution of specimen temperatures in (a), the exhaust flow rate and cell pressure in (b), relative intensities of the signal in the quadrupole mass-analyzer in (c) – (f), and the net microwave power absorbed in the single mode cavity in (g).

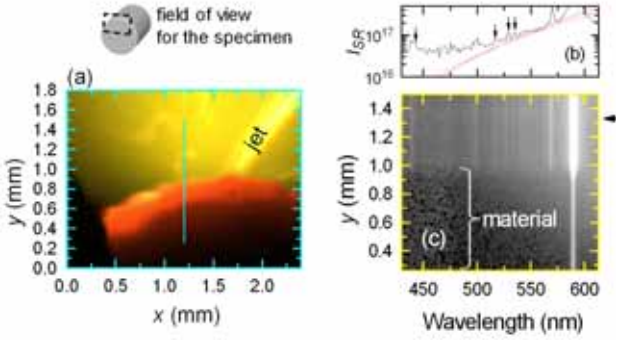

Fig. 4. Typical visible (a) and spectral (c) images of the upper part of specimen for the reduction dominated period (the stage II; t = 234 s). The vertical line in (a) depicts the field of view for the spectral image of (c). Arrows in (b) shows spectra assigned as Fe I. The unit of I_{SR} is photons m^{-2} s^{-1} nm^{-1} sr^{-1}.

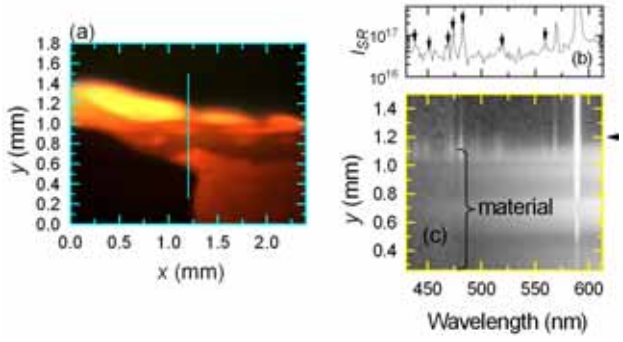

Fig. 5. Typical visible (a) and spectral (c) images captured in the post reduction period (the stage III; t = 505 s). Arrows in (b) shows spectra assigned as CO ($B^1\Sigma$-$A^1\Pi$) and C_2 ($A^3\Pi_g$ - $X\,^3\Pi_u$).

4. Discussion

The luminous body (with burst and jet) and continuous spectrum just above the specimen during reduction period (the stage II) imply presence of plasma-powder mixture generated by strong plasma-surface interaction. A part of the continuous spectrum can be due to the thermal radiation of the powder in the plasma. Three thermal radiation spectrums for temperature range of 1200 - 1400 °C and emissivity range of 0.1 - 1.0 are drawn as red dotted lines in Fig. 4(b). That temperature range is comparable to or somewhat higher than that of specimen temperature measured by pyrometers. This situation inspires us to consider inclusion of powder particles from the specimen into the plasma.

The intensity of the observed spectrum is higher than that of the thermal spectrum for shorter wavelength. This can be connected with the results reported in the previous paper [2]. It was found that the intensity of continuous emission spectrum near-UV range (240 nm - 310 nm) is more three order magnitude larger than that of black body spectrum. A candidate of the continuous spectrum was considered as a cathodoluminescence of magnetite (reported wavelength range: 310-620 nm with twin peaks at 390 nm and 480 nm) due to the impingement of a plasma electron onto the specimen surface of magnetite.

The view of the plasma-powder mixture has been supported by the similar experiment for the measurement of CO_2 concentration with CO_2-laser absorption. An He-Ne laser beam (633 nm) was aligned along the CO_2 laser beam, in order to monitor influence of laser-light scattering due to the powder particles inside the plasma. It was found that the transmissivities for both CO_2- and He-Ne lasers drop to 0.1 during reduction dominated period. This value is much less than that based on gas absorption, indicating almost scattering (~ 90 %) by powder particle.

The plasma-powder mixture can be formed in such a way that the powder is blown into the space by the burst and jet as mentioned above. The burst and jet can result from reduction reaction and/or an adiabatic expansion by localized heating (likely due to a micro scale arc discharge), and those consist of CO/CO_2 gas and powder particles. On the other hand disappearance luminous body in the post reduction period (stage III) will be explained as depletion of the raw powder (i.e., as progress of reduction). Emergence of molecular spectrum of CO ($B^1\Sigma$-$A^1\Pi$) indicates that electron plasma temperature is higher for post reduction period than that for the reduction period. The waning of the plasma-powder interaction suppresses the power loss through thermal radiation and reduction reaction of the powder particle in the plasma.

It would be mentioned about the possibility that the plasma-powder mixture plays not merely a part of microwave absorber/heater; rather, it behaves as a component in self-organization of the system consisting of microwave field, plasma-powder mixture, and powder material (specimen). The hot spots on the surface causing the burst/jet can be attributed to microwave focusing due to a kind of edge effects; however the propagation and absorption of microwave itself will be modified by the plasma-powder mixture.

The plasma-powder mixture presented here would be categorized into *hot dust plasma*, since thermal- and secondary-electron emissions should not be neglected [3]. There are some similarities with a hot-dust plasma so called *ball lightning* generated in the concentrated microwave field [4, 5]. The luminescence of the ball lightning has been explained as chemical emission due to re-oxidation of nano-particles generated by reduction reaction through the localized arcing in the surface layer of material. The micro-scale structure observed in present experiment supports qualitatively above explanation.

Finally, relationship to the plasma-surface interaction in fusion science would be mentioned briefly. The condition that plasma faces to the metal oxide-graphite mixture can be materialized in fusion device, if graphite particles are re-deposited on or implanted into metal oxide layer on the first wall. Formation of such metal-oxide layer is supposed to be rare case depending on leak of air or H_2O. When the significant heat flux from the plasma typically induced by an edge localized mode (ELM) strikes the deposition area, the metal oxide is reduced by graphite and resultant CO/CO_2 gas takes the deposited particles toward the plasma. The contamination of the dust particles can change the propagation and absorption of high frequency electromagnetic wave [6].

Acknowledgement

This research is supported in part by a Grant-in-Aid for Scientific Research on Priority Areas (465) of the Ministry of Education, Culture, Sports, Science and Technology in Japan.

References

[1] K. Nagata, *et al*., *Proc. of 4th Int. Cong. on Sci.&Tech. of Steel Making*, Gifu, 632 (2008).
[2] A. Matsubara1, *et al*., Plasma Fusion Res. **3**, S1085 (2008).
[3] P. K. Shukla, Phys Plasma **8**, 1791 (2001).
[4] J. Abrahamson and J. Dinniss, Nature **403** 519 (2000).
[5] V. Dikhtyar and E. Jerby, PRL **96** 045002 (2006).
[6] S. Takamura, J. Plasma Fusion Res. **78** 295 (2002).

Proceedings of ITC18,2008

Investigation of Laser Pulse Propagation in Plasma using the PIC Simulation Method

Hassan Hoseinkhani, Amir Hossein Esmailian, Ardavan Kouhi
Department of Inertial Confinement, Plasma Physics & nuclear Fusion Research School, Nuclear Science & Technology, Research Institute, AEOI.
P.O. 14395-836, Tehran, Iran

In this paper, the propagation of high power and short laser pulse in plasma medium is investigated. To do this aim, the particle model of plasma and particle-in-cell (PIC) computational method is used. The Maxwell equations are solved on a lattice and the relativistic Lorentz equation, by interpolation of the electromagnetic fields on the particles, leads to the temporal evolution of the phase space of the particles. The sources (ρ and J) are interpolated self-consistently. The equations are discretized with finite difference method and the Leapfrog differencing method is used to perform the computations for fields. The results are in a very good consistency with the current theories of the wave propagation in plasmas. The energy loss, dispersion and the change in the shape of the pulse due to the interaction with the electrons are shown and discussed. The obtained results can be used in the study of laser-plasma interactions especially in fast ignition approach to laser fusion process.

Keywords: Particle-in-cell (PIC), Laser-Plasma Interaction, Particle Simulation, Fast Ignition, Pulse Propagation in Plasma.

1. Introduction

A plasma medium can be considered as a large number of charged particles moving in their self-consistent electric and magnetic fields. The physics of such system can be studied by computer modeling simulation. Among the most successful models for computer simulation of plasma are particle models. This model becomes more practical in near-critical plasma. In this region the equations of state are not accessible and therefore the fluid description of the system can be no longer valid.

The particle behavior of the plasma also becomes dominant during the interaction of high power short pulse laser $(10^{-5}s)$ with the charge particle. For this interaction regime, the electron motion in the presence of intense light wave is highly relativistic. As we wish to model our system in high-temperature, the effects are very weak, so the plasma can be considered as a large number of collisionless particles. Therefore the propagation of the laser pulse in the plasma medium can be investigated by using particle-in-cell (PIC) computer simulation method.

On physical grounds the particle simulation of plasma in the region mentioned above is in focus of interest for study the relativistic laser-plasma interaction in laser fusion experiments especially in fast ignition approach. Many researchers have also studied the phenomena which accrue in laser plasma accelerators and X-ray lasers by PIC method. Since we are interest in systems containing more than $N \simeq 3\times10^4$ particles, the total number of arithmetic operations required to evaluate directly the force on each particle due to all other particles of the system will be of the order of $\eta = 10N^2$. Calculation of this magnitude is totally impractical for exploring the physics of plasma. For this reason one may view each particle in a simulation as representing many particles of a real plasma namely superparticle. In addition, instead of computing direct interactions between particles we use particle-mesh model in our calculations.

author's e-mail: hhosseinkhani@aeoi.org.ir

2. Particle in cell (PIC) method

In this scheme, particles are defined in continuum space in both position and velocity whereas fields are defined at discrete locations in space. The values of particle and field are advanced sequentially in time. The equations of motion of particle evolve in each time step $\Delta t / 2$, using electromagnetic fields interpolated from the discrete grid to the continuous particle locations. The term for charge and current sources, ρ and J, are interpolated self consistently on the discrete mesh points and the Maxwell equations are then advanced on time step. This procedure will be repeated in the next time step. The electromagnetic fields evolve according to the Maxwell equations:

$$\frac{\partial \mathbf{B}}{\partial t} = -\nabla \times \mathbf{E}\,, \tag{1}$$

$$\frac{\partial \mathbf{D}}{\partial t} = -\nabla \times \mathbf{H} - \mathbf{J}\,, \tag{2}$$

subject to initial conditions:

$$\nabla . \mathbf{D} = \rho\,, \tag{3}$$

$$\nabla . \mathbf{B} = 0\,. \tag{4}$$

The particle positions and velocities obey the Newton-Lorentz equations of motion:

$$\frac{d}{dt}\gamma m\mathbf{v} = \mathbf{F} = q\left(\mathbf{E} + \mathbf{v} \times \mathbf{B}\right), \tag{5}$$

$$\frac{d\mathbf{x}}{dt} = \mathbf{v}\,, \tag{6}$$

where the relativistic factory γ is given by

$$\gamma = \sqrt{\frac{1}{1-\left(v/c\right)^2}} = \sqrt{1+\left(\frac{u}{c}\right)^2}\quad,\ u = \gamma v\ . \tag{7}$$

Eqs. (5) and (6) are discretized using the second-order leapfrog scheme. The leapfrog finite-difference approximations to Eqs. (5) and (6) are

$$\frac{u^{t+\Delta t/2} - u^{t-\Delta t/2}}{\Delta t} = \frac{q}{m}\left(\mathbf{E}^t + \frac{u^{t+\Delta t/2} - u^{t-\Delta t/2}}{2\gamma^t} \times \mathbf{B}^t\right), \tag{8}$$

$$\frac{x^{t+\Delta t} - x^t}{\Delta t} = \frac{u^{t+\Delta t/2}}{\gamma^{t+\Delta t/2}}\,, \tag{9}$$

With $\gamma^t = \left(\gamma^{t-\Delta t/2} + \gamma^{t+\Delta t/2}\right)/2$.

The instability of above equations can be verified through the Boris's algorithm. Based on this algorithm the term, $u^{t+\Delta t/2}$ can only appear in one side of Eq. (7). The general finite-difference forms of Eqs. (1) and (2) can be written as :

$$\delta_t D_i = \delta_j H_k - \delta_k H_j\,, \tag{10}$$

$$\delta_t B_i = -\delta_j E_k + \delta_k E_j\,, \tag{11}$$

Where i, j and k denote the indices of an orthogonal right-handed set of coordinates. δ_q denotes some finite-difference operator with respect to the variable q. In order to perform the numerical implementation of Eqs. (9) and (10) in PIC codes we use a centre difference for the differentials δ, and place the fields on the mesh. In this manner D, E and J are defined at the midpoints of the segments connecting mesh nodes. The centre difference forms of Eqs. (9) and (10) on a uniform mesh become:

$$\frac{D_i^t - D_i^{t-\Delta t}}{\Delta t} = \frac{H_{k,x_j+\Delta x_j/2}^{t-\Delta t/2} - H_{k,x_j-\Delta x_j/2}^{t-\Delta t/2}}{\Delta x_j} - \frac{H_{j,x_k+\Delta x_k/2}^{t-\Delta t/2} - H_{j,x_k-\Delta x_k/2}^{t-\Delta t/2}}{\Delta x_k} - J_i^{t-\Delta t/2}\,, \tag{12}$$

$$\frac{B_i^{t+\Delta t/2} - B_i^{t-\Delta t/2}}{\Delta t} = \frac{E_{k,x_j+\Delta x_j/2}^{t} - E_{k,x_j-\Delta x_j/2}^{t}}{\Delta x_j} + \frac{E_{j,x_k+\Delta x_k/2}^{t} - E_{j,x_k-\Delta x_k/2}^{t}}{\Delta x_k}\,. \tag{13}$$

To complete the discrete model we require prescriptions for obtaining the charge density at mesh points from the distribution of superparticles and for obtaining the forces at superlattice positions from the mesh-defined electric fields. The charge density at mesh point p is given by the total charge in the cell surrounding mesh point p divided by the cell volume:

$$\rho_p^n = \frac{qN_s}{4}\sum_{i=1}^{N_p} W\left(x_i^n - x_p\right) + \rho_0\quad, \tag{14}$$

Where N_s, H, ρ_0, x_j and $x_p = pH$ are the number of electrons per unit length, the cell width, background density charge, the position of the superparticle i in the cell and coordinate of particle p, respectively. The charge assignment function W used in Eq.(14) is :

$$W(x) = \begin{cases} 1 & |x| < \dfrac{H}{2}\quad,\quad x = \dfrac{H}{2} \\ 0 & \text{elsewhere} \end{cases} \tag{15}$$

3. Results and Conclusions

In the present work, we have performed the numerical code based on PIC method to investigate the propagation of laser pulse in a plasma medium. To do so, the envelope spatial shape of the laser pulse has been considered as a Gaussian-shaped profile. We also assumed that the pulse propagates in the z direction.

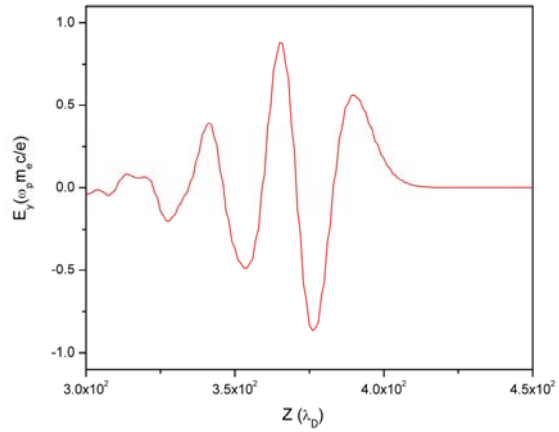

Fig.1. The spatial shape of the pulse in the plasma medium.

The time width of the pulse is $0.3\,\omega_p^{-1}$ which for electron density $n = 10^{17}/\mathrm{cm}^3$ will be of the order of 10 fs and the power of the pulse is ~ TW. Evolution of the pulse in the medium is evaluated by solving the equations of motion and Maxwell equations consistently using initial boundary conditions.

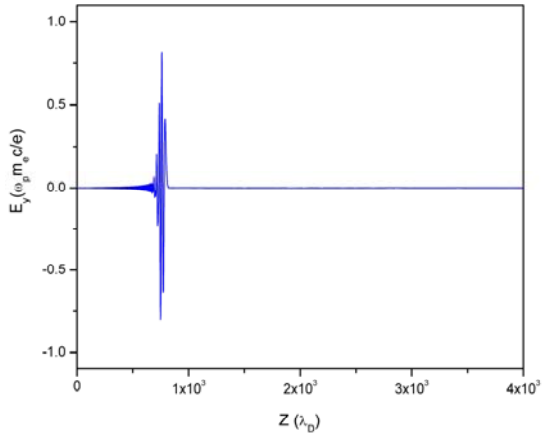

Fig.2. Propagation of laser pulse in plasma for scaled time $10\,\omega_p^{-1}$.

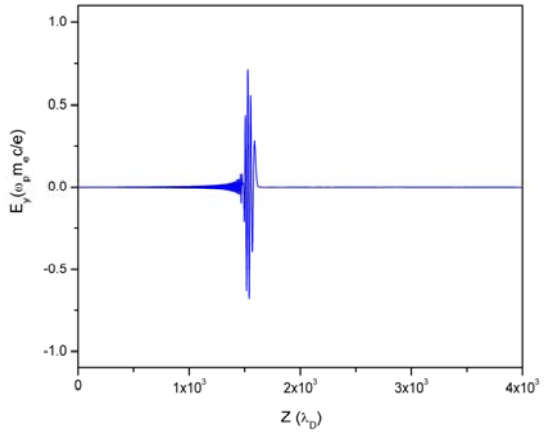

Fig.3. Same as Fig.1 for $20\,\omega_p^{-1}$.

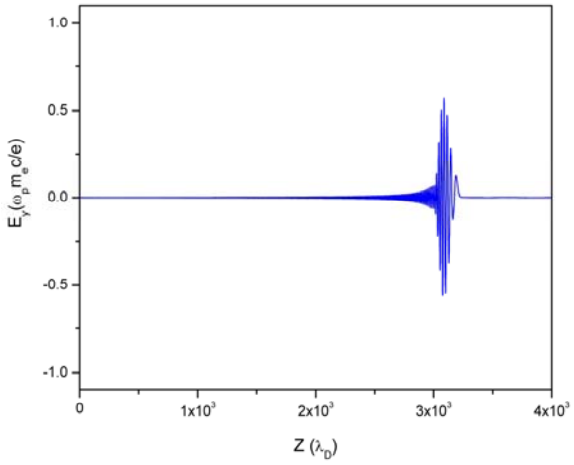

Fig.4. Same as Fig.1 for $40\,\omega_p^{-1}$.

The spatial shape of the pulse in the plasma medium is illustrated in figure (1). In figures (2)-(4) the results obtained for scaled times, $10\,\omega_p^{-1}$, $20\,\omega_p^{-1}$, and $40\,\omega_p^{-1}$ have been shown. Here $\omega_p = \sqrt{ne^2/\varepsilon_0 m_e}$ is plasma frequency and $\lambda_D = \sqrt{\varepsilon_0 kT/ne^2}$ is the Debye wave length.

References

[1] J. M. Dawson, Rev. Mod. Phys. **55**, 403 (1983).

[2] C. K. Birdsall and A. B. Langdon, Plasma Physics via Computer Simulation, (The Adam Hilger Series on Plasma Physics, 1991).

[3] R. W. Hockney and J. W. Eastwood, Computer Simulation Using Particles, (New York: McGraw-Hill, 1981).

[4] M. Tabak. et al, Phys. Plasmas. **1**, 1626 (1994).

[5] J. Meyer-ter-vehn, Plasma. Phys. Control. Fusion. **47**, A231 (2001).

[6] R. Bingham, J.T. Mendoca and P.Shukla, Plasma Phys. Control. Fusion, **46**, R1 (2004).

[7] D. C. Eder. et al, Phys. Plasma **1**, 1744 (1994).

[8] J. P. Verboncoeur, Plasma Phys. Control. Fusion **47**, A231 (2005).

Proceedings of ITC18, 2008

Kinetic Simulation of Heating and Collisional Transport in a 3D Tokamak

Andres BUSTOS[1,4)], Francisco CASTEJON[1,4)], Luis A. FERNÁNDEZ[2,4)], Victor MARTIN-MAYOR[2,4)], Alfonso TARANCÓN[3,4)] and José L. VELASCO[3,4)]

[1)]*Lab. Nac. de Fusión – Asociación Euratom/Ciemat, 28040-Madrid, Spain.*
[2)]*Dep. de Física Teórica I. Universidad Complutense, 28040-Madrid, Spain.*
[3)]*Dep. de Física Teórica. Universidad de Zaragoza, 50009-Zaragoza, Spain.*
[4)]*BIFI: Instituto de Biocomputación y Física de Sistemas Complejos, 50009-Zaragoza, Spain*

The microwave plasma heating has a strong influence on collisional transport, experimentally observed both in stellarators and tokamaks. The estimate of the interplay between heating and collisional transport implies solving a 5D kinetic equation. We deal with this problem using a recently developed code (ISDEP: Integrator of Stochastic Differential Equations for Plasmas) in a tokamak with ripple as a test device, introducing the heating effects. In this work we develop a method for a non-linear computation of the time-dependent plasma temperature profile, based on several linear calculations. The influence of heating on the relevant transport parameters, on plasma rotation and on the velocity distribution function is studied.

Keywords: Ion cyclotron resonance heating, ion transport, non-linear simulation.

1 Introduction

Transport and heating are usually described as separated processes. The former is customarily solved by fluid equations and the latter, which is considered as a source term of the transport set of equations, is calculated in the framework of kinetic theory. However, there exist several phenomena that show that transport is modified by the heating effects (see e.g. [1, 2]), due to the interplay between microwave plasma heating and transport, and must be estimated solving the 5D kinetic equation (3D in space and 2D in momentum space).

In this work we solve simultaneously the ion transport and heating in the non-linear regime, taking advantage of the equivalence between the linear Fokker Planck (FP) and Langevin equations [4]. As it is well-known, the FP equation is a collective description of the system, i.e. an equation for the distribution function in phase space $f(t, x)$. An equivalent form is describing the system with a Langevin equation, which is a Stochastic Differential Equation (SDE) for a single particle, where the variation of x_i, the phase space coordinate, depends on a deterministic term, proportional to dt, and on a random term dW^i that describes a Wiener process [4].

We use ISDEP, a Monte Carlo code that calculates the ion kinetic transport by following the guiding centre orbits in the presence of electric field, including ion-ion [3] and ion-electron collisions [5]. We introduce in the equations a new term that estimates the microscopic quasi-linear wave-particle interaction and was firstly written in Langevin form in [6]. As we deal with ion transport, the heating method that we will consider is direct Ion Cyclotron Resonance Heating (ICRH), in the range of second harmonic of ion cyclotron resonance frequency, which is based on launching resonant electromagnetic waves from the edge of the confined plasma. In our case, the randomness represented by the Wiener processes of the interaction is related to the collisions with the background plasma and with the random relative phase between particles gyromotion and waves. In this work, we do not introduce any kind of turbulent transport yet. The wave-particle interaction is formally the same as in the ECRH case, i.e., it can be considered as a resonant diffusion in momentum space. We will include the nonlinear evolution of the background temperature using a self consistent method, updating the temperature at each step.

We choose a tokamak device with ripple instead of a complex device, since we are interested in studying the influence of the heating on transport rather than on the confinement properties of a given magnetic configuration. This application shows the the usability of stellarator tools in 3D problems that appear in tokamaks.

author's e-mail: andres.debustos@ciemat.es

2 Modeling of collisional transport and heating.

2.1 The Langevin Equations for the system

The dynamics of the test particles is given by a set of Langevin equations. This includes several physical features and approximations. We study the evolution of the guiding center position, the velocity square and the pitch: $x^i = (\vec{r}_{gc}, v^2, \lambda)$, $\lambda = v_{\|}/v$. We also consider Coulombian collisions with the background using the Boozer-Kuo Pe-

travic collision operator.

The quasilinear wave-particle interaction used in this work is a resonant process in phase space. The resonant condition is satisfied with very small probability, but the influence on (v^2, λ) is very strong. We take a Gaussian deposition profile centered at the magnetic axis. As we will see, the final result is a global increase of the energy.

Schematically, the equations we are solving are:

$$\begin{aligned} \mathrm{d}\vec{r}_{\mathrm{gc}} &= \vec{v}^{\,\mathrm{gc}}(x)\,\mathrm{d}t, && (1)\\ \mathrm{d}v^2 &= \left(F^{\mathrm{gc}}_{v^2}(x) + F^{\mathrm{coll}}_{v^2}(x) + F^{\mathrm{ICH}}_{v^2}(x)\right)\mathrm{d}t \\ &\quad + G_{v^2}(x)\circ \mathrm{d}W^{v^2} + G_{vA}(x)\circ \mathrm{d}W^{A} && (2)\\ &\quad + G_{vB}(x)\circ \mathrm{d}W^{B}, && (3)\\ \mathrm{d}\lambda &= \left(F^{\mathrm{gc}}_{\lambda}(x) + F^{\mathrm{coll}}_{\lambda}(x) + F^{\mathrm{ICH}}_{\lambda}(x)\right)\mathrm{d}t \\ &\quad + G_{\lambda}(x)\circ \mathrm{d}W^{\lambda} + G_{\lambda A}(x)\circ \mathrm{d}W^{A} && (4)\\ &\quad + G_{\lambda B}(x)\circ \mathrm{d}W^{B}. && (5) \end{aligned}$$

The Wiener process is an independent increment stochastic process (Gaussian distributed) such that:

$$\mathrm{d}W^j(0) = 0, \qquad \langle \mathrm{d}W^j(t)\rangle = 0, \tag{6}$$

$$\langle \mathrm{d}W^j(t)\mathrm{d}W^k(t)\rangle = \delta^{jk}dt. \tag{7}$$

This process introduces diffusion phenomena in the system evolution. Using Eqs. (1), (3) and (5) we can follow particle trajectories in the confined plasma, affected by electromagnetic fields using the guiding centre approximation: $\vec{v}^{\,\mathrm{gc}}$, $F^{\mathrm{gc}}_{v^2}$ and $F^{\mathrm{gc}}_{\lambda}$ [7] and collisions with other particles via the Boozer operator: F^{coll}_{v}, $F^{\mathrm{coll}}_{\lambda}$ G_{v^2} and G_{λ} [8]. The functions $F^{\mathrm{ICH}}_{v^2}$, $F^{\mathrm{ICH}}_{\lambda}$, G_{vA}, G_{vB}, $G_{\lambda A}$ and $G_{\lambda B}$ can be found in [6], although some misprints have been corrected. Even though the work in [6] was developped for ECRH, we take this model for 2^{nd} harmonic of ICRH. The symbol "$\circ$" indicates that we are using Stratonovich algebra for the SDE system [4].

The Monte Carlo method is used to integrate a large number of independent trajectories and calculate the main confinement properties as the average energy, particle and heat fluxes, confinement time, etc. One of the main advantages of following independent trajectories is that the simulations scale perfectly in massive parallel clusters. In fact, all the calculations presented in this work have been done using grid computing techniques, see e.g. [9].

2.2 Introduction of non linear effects

Linearizing the Boltzmann equation is equivalent to study the test particles keeping fixed the background plasma. This makes impossible the study of heating effects during plasma evolution because no temperature rising will be observed despite the fast ions will transfer their energy to the background. To overcome this limitation while keeping the benefits of the equivalence between the FP and the Langevin approach, we allow time dependent temperature profiles: $T(\rho, t)$, which we shall fix self-consistently by identifying the time evolution of the temperature of the test particles with that of the field particles [5]. Note that time dependent profiles are allowed in a linear FP equation, the iterative method is the key point to introduce non linearities, as will be explained below. In this work we keep constant the background density, assuming that the sources are able to supplement the particle losses.

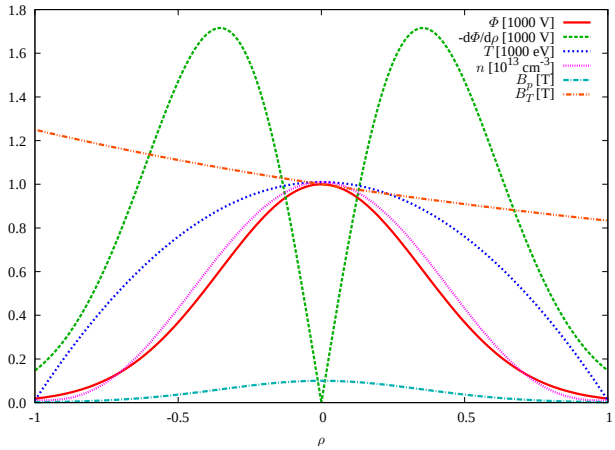

Fig. 1 1D profiles: electrostatic potential (Φ) and its derivative, proportional to the electric field ($\mathrm{d}\Phi/\mathrm{d}\rho$), temperature ($T$), density ($n$) and poloidal ($B_p$) and toroidal ($B_T$) magnetic fields. In this picture, the values with $\rho < 0$ correspond the high magnetic field side of the device while $\rho > 0$ refers to the low field side. All the profiles except B_T are symmetric in the poloidal angle.

We use as temperature profile the average kinetic energy in an interval of $\Delta\rho = 0.1$ centered in ρ at a time t: $v^2(\rho, t)$. Let q_i be the quotient of the average kinetic energy in the i-th iteration with ICH and the energy without ICH. Then, in the iteration $i+1$ we take as temperature the initial profile multiplied by q_i:

$$q_i(\rho, t) = \frac{v_i^2(\rho, t)}{v^2(\rho, t)}, \qquad T_{i+1}(\rho, t) = T_0(\rho)\, q_i(\rho, t)\,. \tag{8}$$

We stop iterating when $T_{i+1}(\rho, t) = T_i(\rho, t)$ within errors, which is our self-consistent profile.

2.3 The tokamak model

In our test device, the plasma is a circular torus with major radius $R_0 = 1$ m and minor radius $a = 0.2$ m. The main magnetic field ($B_0 = 1$ T) as well as a small ripple, ($\sim 0.01\, B_0$) is created by 32 toroidal coils. The expression for the rippled magnetic field is obtained from [10]. The ripple does not modify the toroidal magnetic flux in an appreciable way ($\sim 0.01\%$, estimated by numerical integration), so we can take the usual expression $\rho = r/a$. ICH microwaves are launched by two antennae located in opposite angles of the torus. We plot the shape of the main profiles in Fig. 1.

3 Numerical results

We use a *Kloeden-Piersen* algorithm [4] for solving our SDE system. It is similar to a second order Runge Kutta method for a given SDE for $X(t)$:

$$\mathrm{d}X^i = F^i(X,t)\,\mathrm{d}t + G^i_j(X,t)\circ \mathrm{d}W^j, \tag{9}$$

$$\begin{aligned} X^i_{n+1} &= X^i_n + \frac{\delta}{2}\left(F^i(X_n) + F^i(X_p)\right) + \\ &\quad \frac{1}{2}\left(G^i_j(X_n) + G^i_j(X_p)\right)\Delta W^j, \end{aligned} \tag{10}$$

$$X^i_p = X^i_n + F^i(X_n)\delta + G^i_k(X_n)\,\Delta W^k. \tag{11}$$

This method converges weakly (for the averages, see [4]) with order δ^2 ($\delta = t_{n+1} - t_n$.) for a 1D multiplicative noise. Unfortunately, we are dealing with 4D multiplicative noises and we find convergence up to order δ (specially in the ICH case).

We perform several linear simulations updating the temperature according to (8) and we stop iterating when we reach the self-consistent profile in v^2 (Fig. 3). The main results of this work are the comparison of fluxes, velocities, distribution functions and other relevant quantities between simulations with and without heating. In Fig. 2 we show the time evolution of several plasma features in both cases: persistence $\mathcal{P}$ (defined as the fraction of surviving particles), effective radius and kinetic and total energy. It can be seen that the persistence of particles falls faster in the case of ICH. This is not surprising since the average energy is increased and so does the outward flux. We calculate the confinement times fitting $\mathcal{P}(t)$ to $e^{-t/\tau}$. The average radius also increases in the case of ICH for times larger than the typical collision one, showing again the increase of the outward particle flux. The average energy rises for times larger than 10^{-3} s, showing the obvious effect of plasma heating and the typical time scale in which the power absorption is relevant. The change of the average squared velocity is, not surprisingly, very similar to the energy one.

Also we calculate the toroidal and poloidal velocity profiles (Fig. 3). We see that the poloidal velocity does not change because it depends mostly on the $\vec{E}\times\vec{B}$ drift, and it is not modified in the system. On the other hand, v_ϕ is strongly influenced by ICH, because if v^2 grows while v_θ is constant, then v_ϕ increases. This increment, focused on $\rho \simeq 0$, is propagated radially via transport processes.The evolution of the particle flux profile is plotted in Fig. 4, which shows that this is always larger in the presence of heating, especially for $t > 10^{-3}$ s, which is the typical time scale for plasma heating to be relevant. The steady state flux is monotonic, as corresponds to the absence of sources or sinks. The heat flux profile evolution (Fig. 5) is again monotonic in steady state ($t = 5\cdot 10^{-2}$ s), but the gradient in the centre of the device is much larger in the case of ICH than in the one without heating, since the heat source is located close to $\rho = 0$.

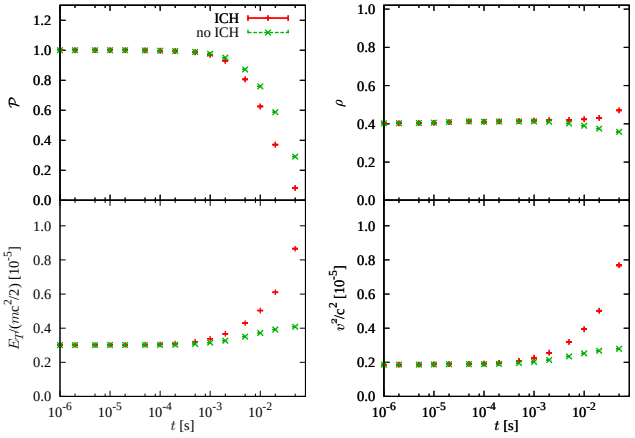

Fig. 2 Evolution (with and without ICH) of the persistence $\mathcal{P}$ (upper left), average effective radius, ρ (upper right), total energy E_T (lower left) and kinetic energy (lower right) in units of $mc^2/2$. Confinement times are $\tau = 0.0387(8)$ s and $\tau_{\mathrm{ICH}} = 0.0212(9)$ s. We can observe the heating effect for $t > 10^{-3}$ s.

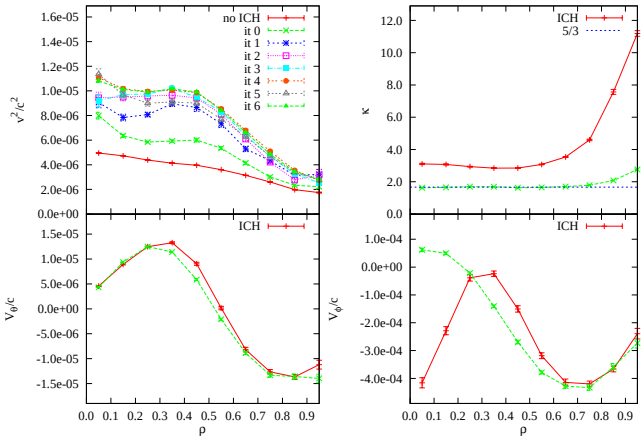

Fig. 3 Iterations of the v^2 profile (upper, left), Binder cumulan (upper, right), poloidal velocity (lower, left) and toroidal velocity (lower, right), measured in $t = 5\cdot 10^{-2}$ s.

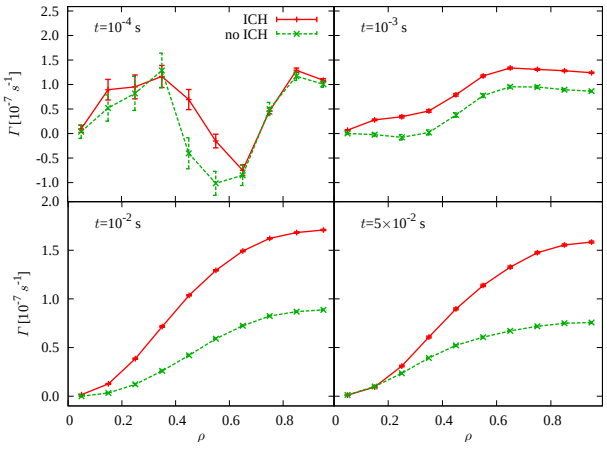

Fig. 4 Particle fluxes.

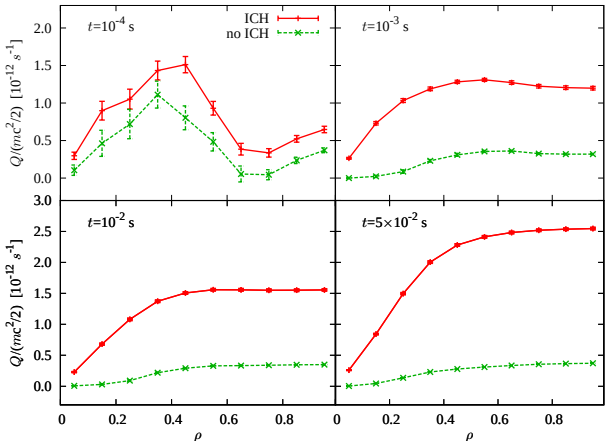

Fig. 5 Heat fluxes.

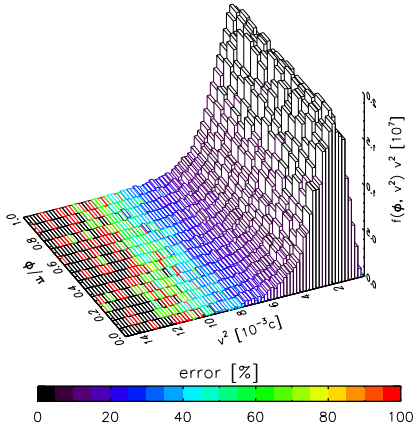

Fig. 7 Velocity probability distribution functions with ICH.

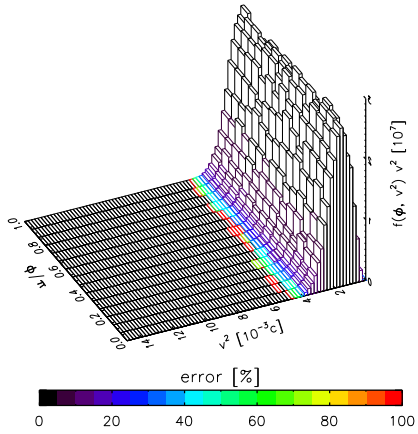

Fig. 6 Velocity probability distribution functions, as a function of the velocity and the toroidal angle without ICH.

We compute and compare the probability distribution function ($v^2 \cdot f(v,\phi)$), in terms of v and ϕ (Fig. 6). We find that with a small ripple (1%) $f(v,\phi)$ does not depend on ϕ in any case, which implies that the parallel transport is able to overcome the local heating produced by the antennae as well as the ripple effects. It is clear that the effect of heating tends to make the distribution function wider , rising its tail and creating an important number of suprathermal ions. The Binder cumulant, defined as $\kappa := \langle v^4\rangle/\langle v^2\rangle^2$, measures deviations from the Maxwellian distribution (Fig 3). In the plasma without ICH, the cumulant is equal to 5/3 at every time, except in the outer plasma radius where an increase of fast particles due to the transport is observed. The ICH plasmas show clear effects of heating with a cumulant larger than the Maxwellian value.

4 Conclusions

We have estimated for the first time the combined effects of ion collisional transport and heating outside the frame of the linear approximation. To do that, we have developed a nonlinear kinetic method based on Langevin equations for transport and quasi linear heating. For the moment, we have considered a non-realistic model for the electric field created by ICRH waves. We modify the background temperature with an iterative method, allowing a real increment of the particle energy. This method makes possible the numerical solution, for any geometry and wave, of the collisional transport in phase space. The only approximations are considering collisional transport in a frozen electrostatic potential and assuming that wave-particle interaction is well described by quasi-linear theory. We have particularized our model to the geometry of a tokamak with ripple, avoiding for the moment the effects of more complex geometries to concentrate ourselves in the heat and transport interplay. This computer code can be easily adapted to another geometries and plasma profiles, like stellarator or ITER geometries.

The authors would like to thank the EGEE Project (EGEE-II INFSO-RI-031688) for enabling grid computing capacity for the calculations performed in this work and T. Happel for his help with some figures.

[1] F. Castejón *et al.*, Nucl. Fusion **42**,271,(2002).
[2] M. A. Ochando, F. Medina and the TJ-II Team, Plasma Phys. Control. Fusion **45**, 221 (2003).
[3] F. Castejón *et al.*, Plasma Phys. Control. Fusion **49** 753, (2007).
[4] P. E. Kloeden and E. Platen, *Numerical Solutions for Stochastic Differential Equations*, Springer-Verlag, (1992).
[5] J. L. Velasco *et al.*, Nucl. Fusion **48**, (2008).
[6] F. Castejón and S. Eguilior, Plasma Phys. Control. Fusion **45**, 159 (2003).
[7] J. P. Chistiansen and J. W. Connor, Plasma Phys. Control. Fusion **46**, 1537(2004).
[8] A. H. Boozer and G. Kuo-Petravic, Phys. Fluids **24**(5), 851 (1981).
[9] F. Castejón *et al.*, Computing and Informatics **27**, 261 (2008).
[10] A. H. Boozer, Review of Modern Physics **76**, 1071 (2005).

AUTHOR INDEX